

Randall Allemang · James De Clerck · Christopher Niezrecki  
Alfred Wicks *Editors*

# Special Topics in Structural Dynamics, Volume 6

Proceedings of the 31<sup>st</sup> IMAC, A Conference on Structural  
Dynamics, 2013



# Conference Proceedings of the Society for Experimental Mechanics Series

*Series Editor*

Tom Proulx

Society for Experimental Mechanics, Inc.,

Bethel, CT, USA

For further volumes:

<http://www.springer.com/series/8922>





Randall Allemang • James De Clerck • Christopher Niezrecki • Alfred Wicks  
Editors

# Special Topics in Structural Dynamics, Volume 6

Proceedings of the 31st IMAC, A Conference on Structural  
Dynamics, 2013

*Editors*

Randall Allemang  
University of Cincinnati  
Cincinnati, OH, USA

Christopher Niezrecki  
Department of Mechanical Engineering  
University of Massachusetts Lowell  
Lowell, MA, USA

James De Clerck  
The Enterprise Program  
Michigan Technological University  
Houghton, MI, USA

Alfred Wicks  
Department of Mechanical Engineering  
Virginia Polytechnic Institute and State University  
Blacksburg, VA, USA

ISSN 2191-5644                      ISSN 2191-5652 (electronic)  
ISBN 978-1-4614-6545-4            ISBN 978-1-4614-6546-1 (eBook)  
DOI 10.1007/978-1-4614-6546-1  
Springer New York Heidelberg Dordrecht London

Library of Congress Control Number: 2013940179

© The Society for Experimental Mechanics, Inc. 2013

This work is subject to copyright. All rights are reserved by the Publisher, whether the whole or part of the material is concerned, specifically the rights of translation, reprinting, reuse of illustrations, recitation, broadcasting, reproduction on microfilms or in any other physical way, and transmission or information storage and retrieval, electronic adaptation, computer software, or by similar or dissimilar methodology now known or hereafter developed. Exempted from this legal reservation are brief excerpts in connection with reviews or scholarly analysis or material supplied specifically for the purpose of being entered and executed on a computer system, for exclusive use by the purchaser of the work. Duplication of this publication or parts thereof is permitted only under the provisions of the Copyright Law of the Publisher's location, in its current version, and permission for use must always be obtained from Springer. Permissions for use may be obtained through RightsLink at the Copyright Clearance Center. Violations are liable to prosecution under the respective Copyright Law.

The use of general descriptive names, registered names, trademarks, service marks, etc. in this publication does not imply, even in the absence of a specific statement, that such names are exempt from the relevant protective laws and regulations and therefore free for general use.

While the advice and information in this book are believed to be true and accurate at the date of publication, neither the authors nor the editors nor the publisher can accept any legal responsibility for any errors or omissions that may be made. The publisher makes no warranty, express or implied, with respect to the material contained herein.

Printed on acid-free paper

Springer is part of Springer Science+Business Media ([www.springer.com](http://www.springer.com))

# Preface

*Special Topics in Structural Dynamics Volume 6: Proceedings of the 31st IMAC, A Conference on Structural Dynamics, 2013* represents one of seven volumes of technical papers presented at the 31st IMAC, A Conference and Exposition on Structural Dynamics, 2013 organized by the Society for Experimental Mechanics, and held in Garden Grove, California February 11–14, 2013. The full proceedings also include volumes on Nonlinear Dynamics; Experimental Dynamics Substructuring; Dynamics of Bridges; Dynamics of Civil Structures; Model Validation and Uncertainty Quantification; and, Modal Analysis.

Each collection presents early findings from experimental and computational investigations on an important area within Structural Dynamics. *Special Topics in Structural Dynamics* represents papers on enabling technologies for Modal Analysis measurements such as Sensors & Instrumentation, as well as applications of Modal Analysis in specific application areas. Topics in this volume include:

- Teaching Experimental & Analytical Structural Dynamics
- Sensors & Instrumentation
- Aircraft/Aerospace
- Bio-Dynamics
- Sports Equipment Dynamics
- Advanced ODS & Stress Estimation
- Shock & Vibration
- Full-Field Optical Measurements & Image Analysis
- Structural Health Monitoring
- Operational Modal Analysis
- Wind Turbine Dynamics
- Rotating Machinery
- Finite Element Methods

The organizers would like to thank the authors, presenters, session organizers, and session chairs for their participation in this track.

Cincinnati, OH, USA  
Lowell, MA, USA  
Houghton, MI, USA  
Blacksburg, VA, USA

Randall Allemang  
Christopher Niezrecki  
James De Clerck  
Alfred Wicks



# Contents

<b>1</b>	<b>Safety Improvement of Child Restraint System by Using Adoptive Control</b> .....	<b>1</b>
	Takayuki Koizumi, Nobutaka Tsujiuchi, and Shin Ito	
<b>2</b>	<b>Dynamic Response and Damage Estimation of Infant Brain for Vibration</b> .....	<b>11</b>
	Takayuki Koizumi, Nobutaka Tsujiuchi, Keisuke Hara, and Yusuke Miyazaki	
<b>3</b>	<b>Mechanical Strength of Bone Cement with and Without Adjuvant Screw Fixation</b> .....	<b>19</b>
	Ryan Keyser, Robert Migliori, Tessa Morgan, Steven R. Anton, Kevin M. Fariholt, and R. Michael Meneghini	
<b>4</b>	<b>Development of a Bench for Testing Leg Prosthetics</b> .....	<b>35</b>
	H. Giberti, F. Resta, E. Sabbioni, L. Vergani, C. Colombo, G. Verni, and E. Boccafogli	
<b>5</b>	<b>Application of Modal Testing and Analysis Techniques on a sUAV</b> .....	<b>47</b>
	Kaci J. Lemler and William H. Semke	
<b>6</b>	<b>Progress in Operational Analysis of Launch Vehicles in Nonstationary Flight</b> .....	<b>59</b>
	George James, Mo Kaouk, and Tim Cao	
<b>7</b>	<b>Influence of Test Conditions on Comfort Ranking of Road Bicycle Wheels</b> .....	<b>77</b>
	Julien Lépine, Yvan Champoux, and Jean-Marc Drouet	
<b>8</b>	<b>Direct Measurement of Power on a Gravity Independent Flywheel-based Ergometer</b> .....	<b>83</b>
	F. Braghin, M. Bassetti, P. Crosio, and D. Locati	
<b>9</b>	<b>Instrumented Treadmill for Cross-Country Skiing Enhanced Training</b> .....	<b>87</b>
	M. Bassetti, F. Braghin, and S. Maldifassi	
<b>10</b>	<b>Instrumenting a Rowing Ergometer for Improved Training</b> .....	<b>93</b>
	G. Cazzulani, M. Bassetti, G. Picardi, L. Mariella, J. Verdonkschot, A. Benecchi, and Dario Dalla Vedova	
<b>11</b>	<b>A Laboratory Technique to Compare Road Bike Dynamic Comfort</b> .....	<b>99</b>
	Yvan Champoux, Julien Lépine, Philippe-Aubert Gauthier, and Jean-Marc Drouet	
<b>12</b>	<b>Exploring Experimental Structural Dynamics in EMA/ME 540 at UW-Madison</b> .....	<b>107</b>
	Matthew S. Allen	
<b>13</b>	<b>The ABRAVIBE Toolbox for Teaching Vibration Analysis and Structural Dynamics</b> .....	<b>131</b>
	Anders Brandt	
<b>14</b>	<b>Structural Dynamics Teaching Example: A Linear Test Analysis Case Using Open Software</b> .....	<b>143</b>
	Per-Olof Stuesson, Anders Brandt, and Matti Ristinmaa	
<b>15</b>	<b>Testing Anti-Ram Barrier Protection Systems</b> .....	<b>155</b>
	Kurt Veggeberg	

<b>16</b>	<b>Fiber Optic Accelerometers and Sensors for Dynamic Measurements</b> .....	161
	Kurt Veggeberg	
<b>17</b>	<b>Nonlinear Model Tracking for Varying System Geometries</b> .....	167
	Timothy A. Doughty, Matthew R. Dally, Mikah R. Bacon, and Nick G. Etzel	
<b>18</b>	<b>Fuzzy Arithmetical Assessment of Wave Propagation Models for Multi-Wire Cables</b> .....	177
	Christoph Schaal and Michael Hanss	
<b>19</b>	<b>A Vibro-Haptic Human-Machine Interface for Structural Health Monitoring Applications</b> .....	187
	Christina Brown, Martin Cowell, C. Ariana Plont, Heidi Hahn, and David Mascareñas	
<b>20</b>	<b>Technologies for Seismic Safety Management of Existing Health Facilities</b> .....	199
	C. Rainieri and G. Fabbrocino	
<b>21</b>	<b>Wave-Induced Vibration Monitoring for Stability Assessment of Harbor Caisson</b> .....	207
	So-Young Lee, Thanh Canh Huynh, Han-Sam Yoon, Jeong-Tae Kim, and Sang-Hun Han	
<b>22</b>	<b>Damage Assessment of a Beam Using Artificial Neural Networks and Antiresonant Frequencies</b> .....	217
	V. Meruane and J. Mahu	
<b>23</b>	<b>Case Studies of Tools Used in Teaching Structural Dynamics</b> .....	225
	Kurt Veggeberg	
<b>24</b>	<b>“Structural System Testing and Model Correlation”: An Industry-University Collaborative Course in Structural Dynamics</b> .....	233
	Michael Todd, Dustin Harvey, David Gregg, Bill Fladung, Paul Blelloch, and Kevin Napolitano	
<b>25</b>	<b>Visualizing Structural Vibrations Using Stroboscopic Light in a Novel Setup</b> .....	241
	Markus J. Hochrainer	
<b>26</b>	<b>Analytical and Experimental Learning in a Vibrations Course at the University of Massachusetts Lowell</b> ..	249
	Pawan Pingle and Peter Avitabile	
<b>27</b>	<b>Around the World in 80 Courses</b> .....	265
	David Ewins	
<b>28</b>	<b>Review of a Pilot Internet System Dynamics Course</b> .....	271
	C.C. Claeys, S. Leuridan, D. Brown, and J. Connor	
<b>29</b>	<b>Using Random Response Input in Ibrahim Time Domain</b> .....	281
	Peter Olsen and Rune Brincker	
<b>30</b>	<b>Modal Parameter Identification of New Design of Vertical Axis Wind Turbine</b> .....	289
	Prasad D. Chougule and Søren R.K. Nielsen	
<b>31</b>	<b>Predicting Dynamic Strain on Wind Turbine Blade Using Digital Image Correlation Techniques in Conjunction with Analytical Expansion Methodologies</b> .....	295
	Jennifer Carr, Javad Baqersad, Christopher Niezrecki, Peter Avitabile, and Micheal Slattery	
<b>32</b>	<b>Dynamic Characterization of a Free-Free Wind Turbine Blade Assembly</b> .....	303
	Javad Baqersad, Christopher Niezrecki, Peter Avitabile, and Micheal Slattery	
<b>33</b>	<b>Harmonic Analysis on a Lévy Plate and Its Application to Fatigue Analysis</b> .....	313
	Nam-Gyu Park, Jung-Min Suh, and Kyeong-Lak Jeon	
<b>34</b>	<b>Vibration Level Assessment of Nuclear Power Plant Powerhouse Hall</b> .....	321
	G.G. Boldyrev and A.A. Zhivaev	
<b>35</b>	<b>Study on the Band Structure of Trigonal Chiral Structures</b> .....	329
	Shiyin Xu, Xiuchang Huang, and Hongxing Hua	
<b>36</b>	<b>FEM Sensitivity Vector Basis for Measured Mode Expansion</b> .....	339
	Robert N. Coppelino	

<b>37 Estimation of Unmeasured DOF's on a Scaled Model of a 4-Storey Building</b> .....	347
Anders Skaftø and Rune Brincker	
<b>38 Estimation of Rotational Degrees of Freedom by EMA and FEM Mode Shapes</b> .....	355
A. Sestieri, W. D'Ambrogio, R. Brincker, A. Skaftø, and A. Culla	
<b>39 Real-Time Dynamic Stress Response Estimation at Critical Locations of Instrumented Structures Embedded in Random Fields</b> .....	367
Eric M. Hernandez and Kalil Erazo	
<b>40 Strain Estimation in a Glass Beam Using Operational Modal Analysis</b> .....	375
Manuel L. Aenlle, Anders Skaftø, Pelayo Fernández, and Rune Brincker	
<b>41 Pressure Measurement Sensor for Jointed Structures</b> .....	383
G. Chevallier, H. Festjens, F. Renaud, and J.-L. Dion	
<b>42 Modal Analysis of Machine Tools Using a Single Laser Beam Device</b> .....	389
Christian Brecher, Stephan Bäumlner, and Alexander Guralnik	
<b>43 Valvetrain Motion Measurements in Firing Conditions by Laser Doppler Vibrometer</b> .....	395
P. Castellini, P. Chiariotti, M. Martarelli, and E.P. Tomasini	
<b>44 Using High-Speed Stereophotogrammetry to Collect Operating Data on a Robinson R44 Helicopter</b> .....	401
Troy Lundstrom, Javad Baqersad, and Christopher Niezrecki	
<b>45 Principles of Image Processing and Feature Recognition Applied to Full-Field Measurements</b> .....	411
John E. Mottershead and Weizhuo Wang	
<b>46 Model Updating Using Shape Descriptors from Full-Field Images</b> .....	425
Weizhuo Wang, John E. Mottershead, Eann Patterson, Thorsten Siebert, and Alexander Ihle	
<b>47 Shape-Descriptor Frequency Response Functions and Modal Analysis</b> .....	437
John E. Mottershead, Weizhuo Wang, Thorsten Siebert, and Andrea Pipino	
<b>48 Dynamic Simulation of the Lunar Landing Using Flexible Multibody Dynamics Model</b> .....	447
Huinam Rhee, Sang Jin Park, Tae Sung Kim, Yong Ha Kim, Chang Ho Kim, Jae Hyuk Im, and Do-Soon Hwang	
<b>49 A New Approach for a Train Axle Telemetry System</b> .....	453
M. Bassetti, F. Braghin, F. Castelli-Dezza, and M.M. Maglio	
<b>50 Triaxial Multi-range MEMS Accelerometer Nodes for Railways Applications</b> .....	463
M. Bassetti, F. Braghin, G. Cazzulani, and F. Castelli-Dezza	
<b>51 Acoustical Excitation for Damping Estimation in Rotating Machinery</b> .....	473
Bram Vervisch, Michael Monte, Kurt Stockman, and Mia Loccupier	
<b>52 Numerical Simulations on the Performance of Passive Mitigation Under Blast Wave Loading</b> .....	481
Oruba Rabie, Yahia M. Al-Smadi, and Eric Wolff	
<b>53 Finite Element Model Updating Using the Shadow Hybrid Monte Carlo Technique</b> .....	489
I. Boulkaibet, L. Mthembu, T. Marwala, M.I. Friswell, and S. Adhikari	
<b>54 Pseudo Velocity Shock Data Analysis Calculations Using Octave</b> .....	499
Howard A. Gaberson	
<b>55 Analysis and Dynamic Characterization of a Resonant Plate for Shock Testing</b> .....	515
Richard Hsieh, R. Max Moore, Sydney Sroka, James Lake, Christopher Stull, and Peter Avitabile	
<b>56 Resonances of Compact Tapered Inhomogeneous Axially Loaded Shafts</b> .....	535
Arnaldo J. Mazzei and Richard A. Scott	
<b>57 Modelling Friction in a Nonlinear Dynamic System via Bayesian Inference</b> .....	543
P.L. Green and K. Worden	



<b>58</b>	<b>Optimum Load for Energy Harvesting with Non-linear Oscillators</b> .....	555
	A. Cammarano, A. Gonzalez-Buelga, S.A. Neild, D.J. Wagg, S.G. Burrow, and D.J. Inman	
<b>59</b>	<b>Harvesting of Ambient Floor Vibration Energy Utilizing Micro-Electrical Mechanical Devices</b> .....	561
	Joshua A. Schultz and Christopher H. Raebel	
<b>60</b>	<b>Robust Optimization of Magneto-Mechanical Energy Harvesters for Shoes</b> .....	571
	Stefano Tornincasa, Maurizio Repetto, Elvio Bonisoli, and Francesco Di Monaco	
<b>61</b>	<b>Optimization of an Energy Harvester Coupled to a Vibrating Membrane</b> .....	577
	Levent Beker, H. Nevzat Özgüven, and Haluk KÜlah	
<b>62</b>	<b>Experimental Localization of Small Damages Using Modal Filters</b> .....	585
	G. Tondreau and A. Deraemaeker	
<b>63</b>	<b>Output Only Structural Identification with Minimal Instrumentation</b> .....	593
	Suparno Mukhopadhyay, Raimondo Betti, and Hilmi Lus	
<b>64</b>	<b>Simulation of Guided Wave Interaction with Defects in Rope Structures</b> .....	603
	Stefan Bischoff and Lothar Gaul	
<b>65</b>	<b>Estimation of Modal Parameters Confidence Intervals: A Simple Numerical Example</b> .....	611
	Elisa Bosco, Ankit Chiplunkar, and Joseph Morlier	
<b>66</b>	<b>A Bayesian Framework of Transmissibility Model Selection and Updating</b> .....	621
	Zhu Mao and Michael Todd	
<b>67</b>	<b>Monitoring of Torsion of Guyed Mast Shafts</b> .....	627
	Shota Urushadze and Miroš Pirner	

# Chapter 1

## Safety Improvement of Child Restraint System by Using Adoptive Control

Takayuki Koizumi, Nobutaka Tsujiuchi, and Shin Ito

**Abstract** Wearing a child restraint system (CRS) greatly improves the crash-safety of children. However, the number of children's injuries in traffic accidents hasn't decreased. Therefore much further improvement of CRS is requested. Recently, active control of restraint systems for occupants has been studied to improve crash-safety and their effectiveness has been shown. We proposed active harness control for CRS and showed its effectiveness. We constructed a simulation model without harness control. It consists of a child dummy model and a CRS model. We attached a mechanism that changed the harness length in the CRS model. Additionally, we constructed a control system. In this system, head acceleration is fed back as a state quantity and the controller changes the belt length. However, measuring head acceleration in actual car crashes is unrealistic. Therefore we constructed a child linear model and estimate child's head acceleration in crashes. Also, we designed a controller that determines the harness length from estimated head acceleration. Simulations were executed and the injury risks were decreased compared to the model without control of the harness. Thus we clarified the effectiveness of active control of CRS in numerical simulations.

**Keywords** Child restraint system • Adoptive control • Crash-safety • Property estimation • Optimization

### 1.1 Introduction

According to a National Police Agency survey in 2011, the quotient of death or severe injury in car crashes for child restraint system (CRS) users is 0.72%, while that for occupants not using a CRS is 2.71 [1]. With these statistics, the utility of the CRS is confirmed. However, since children continue to be injured even though they are wearing CRSs, further crash-safety improvement is required [2] and the research had been done to improve CRSs by attaching safety devices [3].

To improve crash-safety, continuous restraint systems have been researched for occupants, and their effectiveness has been shown [4, 5]. Therefore, we proposed a controlling harness that continuously restrains a child to a CRS and showed its effectiveness.

Currently, many crash experiments and numerical simulations have investigated child crash-safety and designed safety devices. Numerical simulations are more effective than experiments, especially for repeated trials.

In this study, we created a retractor model in a CRS model and attached the harness to the retractor model to create a CRS model control harness to show the effectiveness of controlling harnesses. Numerical simulation employed the CRS and dummy models using the acceleration pulses acquired from sled tests that simulated frontal crashes. The supplied acceleration is compliant with ECE R44. The control harness, we attached a mechanism that changed the harness length in the CRS model. Additionally, we constructed a control system. In this system, head acceleration is fed back as a state quantity and the controller changes the belt length. However, measuring head acceleration in actual car crashes is unrealistic. Therefore we constructed a child linear model and estimated a child's head acceleration in crashes.

Next, injury criteria were set to the objective functions, and the controller gains were set to the optimizing parameters to minimize the objective function. Using an optimized controller, we simulated the effectiveness of the controlling harness and clarified our improved CRS for greater crash-safety.

---

T. Koizumi • N. Tsujiuchi • S. Ito (✉)

Department of Mechanical Engineering, Doshisha University, 1-3, Tataramiyakodani, Kyotanabe-city, Kyoto 610-0321, Japan  
e-mail: [tkoizumi@mail.doshisha.ac.jp](mailto:tkoizumi@mail.doshisha.ac.jp); [ntsujiuc@mail.doshisha.ac.jp](mailto:ntsujiuc@mail.doshisha.ac.jp); [dtl0325@mail4.doshisha.ac.jp](mailto:dtl0325@mail4.doshisha.ac.jp)

## 1.2 Accident Data

In this section, we analyze the accident data to identify the current CRS problems and clarify what should be improved.

Table 1.1 shows the accident data by crash type of children injured while wearing CRSs [2]. Frontal crashes comprise the largest number of fatalities and severe injuries. Figure 1.1 shows the accident data of children less than 6-year-olds who were injured while wearing CRSs [6]. The bulk of the data consists of head, neck, and thorax injuries. Therefore, in this study, we assessed the crash-safety of children by head, neck, and thorax injury criteria in frontal crashes.

## 1.3 Simulation Model

In this section, we constructed a non-control model without a harness control. It consists of a child dummy model and a current CRS model. The details of each are described below. Next, we attached a mechanism that changed the harness length in the current CRS model. Additionally, we constructed a control system for the harness and a simulation model that can control the harness in collisions.

### 1.3.1 Dummy Model

In this study, we adopted the Hybrid III 3-year-olds dummy model, whose overview is shown in Fig. 1.2. We modeled the Hybrid III 3-year-olds dummy model, which is generally used for the CRS assessment of front collisions [7]. Since the model exists in the MADYMO database, it has enough validity as a Hybrid III 3-year-olds dummy [8]. This model consists of 28 rigid bodies and 18 joints, and its calculation time is far shorter than finite element models.

### 1.3.2 CRS Model

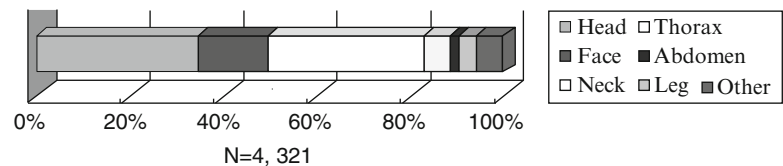
The CRS model consists of a main part, a 3-point harness, and an ECE test seat (Fig. 1.3). The main part of the CRS model consists of ten rigid bodies interconnected by joints. The 3-point harness was modeled by the finite element and represents the physical harness. The ECE test seat was modeled by two rigid planes, and the CRS model was connected to the reference place by belt elements. To evaluate this model's validity, we conducted a sled test using the Hybrid III 3-year-olds dummy based on ECE R44 [9]. Displacement of the dummy head, the CRS, and the resultant acceleration of the head were compared in experiments and simulations. Figure 1.3 shows the results of frontal crashes and the CRS model's validity.

Next, we modeled the retractor in the cushion of the CRS model constructed above and attached it to the harness. Therefore, the CRS model has a mechanism that changed the harness length (Fig 1.4).

**Table 1.1** Accident data of crash type of injured children wearing CRSs

	Number of cases	Number of fatality and severe injured	Fatality and severe injured rate [%]
Frontal crash	3,005	50	1.66
Side crash	1,438	22	1.53
Rear-end crash	3,245	9	0.28

**Fig. 1.1** Accident data of injured areas of children under 6-year-olds wearing CRSs



**Fig. 1.2** Hybrid III 3-year-olds dummy model



**Fig. 1.3** CRS model

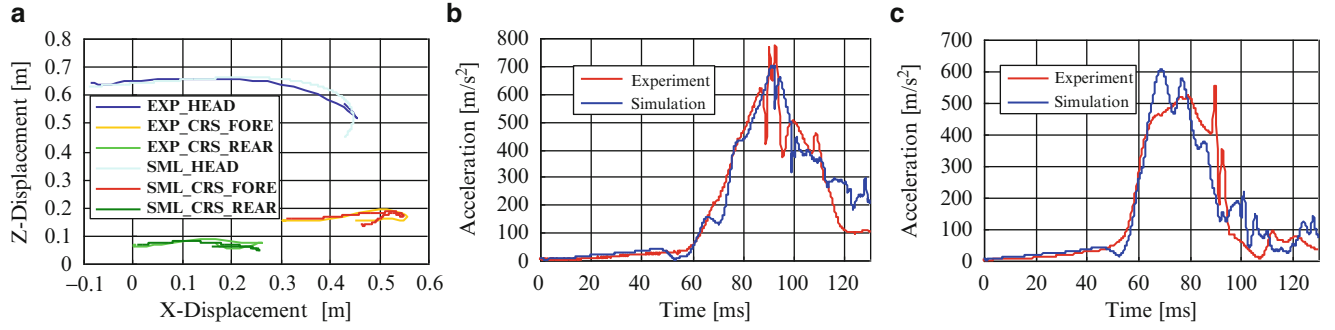


## 1.4 Linear Model

In a paper related to the study of active control, the occupant's head acceleration is chosen as the property to control. However it is difficult to measure head acceleration in a crash. Therefore we construct a linear model to estimate the infant's head acceleration.

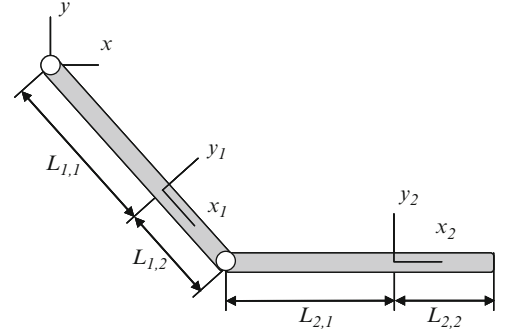
### 1.4.1 Infant Model

About the linear model in Fig. 1.5, the restraint equation of motion below holds.



**Fig. 1.4** Results of CRS calibration tests in frontal crashes calibration tests in frontal crash (a) Trajectories of head and CRS, (b) Head resultant acceleration, (c) Thorax resultant acceleration

**Fig. 1.5** Example of link model



$$\Phi(\mathbf{q}, t) = \begin{bmatrix} x_1 - L_{1,1} \cos \phi_1 \\ y_1 - L_{1,1} \sin \phi_1 \\ x_2 - L_{2,1} \cos \phi_2 - x_1 - L_{1,2} \cos \phi_2 \\ y_2 - L_{2,1} \sin \phi_2 - y_1 - L_{1,2} \sin \phi_2 \end{bmatrix} \quad (1.1)$$

The generalized coordinate is  $\mathbf{q} = [x_1, y_1, \phi_1, x_2, y_2, \phi_2]^T$ . When external force applied to each link is  $F_{x_i}, F_{y_i}$  and torque applied to the linear model is  $T$ , the generalized force is  $\mathbf{Q} = [F_{x_1}, F_{y_1}, T, F_{x_2}, F_{y_2}, -T]^T$ . A differential algebraic equation is represented below.

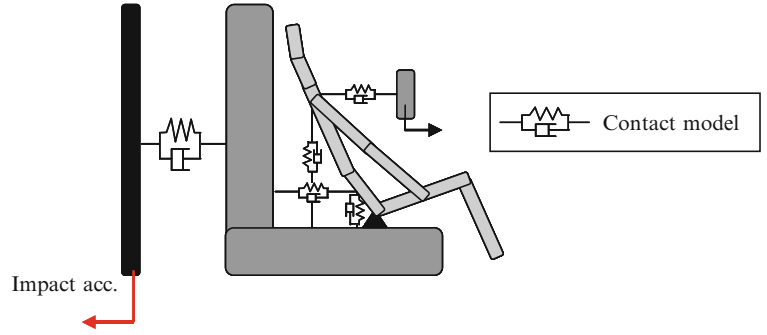
$$\begin{bmatrix} \mathbf{M} & \Phi_{\mathbf{q}}^T \\ \Phi_{\mathbf{q}} & \mathbf{0} \end{bmatrix} \begin{bmatrix} \ddot{\mathbf{q}} \\ \lambda \end{bmatrix} = \begin{bmatrix} \mathbf{Q}^A \\ \Gamma \end{bmatrix} \quad (1.2)$$

$$\Phi_{\mathbf{q}} = \left[ \frac{\partial \Phi_i}{\partial q_i} \right]$$

$$\Gamma = \Phi_{\mathbf{q}} \ddot{\mathbf{q}}$$

$M$  is mass matrix.  $\lambda$  is Lagrange constant number. Using the above method, we solved the differential algebraic equation of the linear model with eight rigid bodies and seven joints in Fig. 1.6. Each rigid link represents head, neck, thoracic cavity, abdomen, crural area, leg area, brachial region and antebrachial region. As its length, mass, and inertial moment, the values of the HybridIII 3-year-olds dummy model were adopted. Its joints represent an infant's arthrogonous characteristics. We illustrate the joint characteristics in the next section. We made the initial position and, initial angle of each link correspond to the dummy model's initial posture. The CRS was modeled as an object having only mass.

We defined the five-contact model, which represents the restraint between the car body and the CRS, and the CRS and the infant. We adopted the Voight model as the contact model. Moreover, we enabled the contact model to move between the thoracic cavity and the CRS to represent the variance of harness length by changing the contact point. We define inter-joint

**Fig. 1.6** Link model

force and the restraint force calculated by the contact model as the generalized acting force. The generalized acting force was calculated by inter joint force and the contact model, and the differential algebraic equation of the infant linear model was analyzed by the four-dimensional Runge–Kutta method.

### 1.4.2 Joint Characteristic

The infant model's joints are modeled by rigid links and enabled to rotate. These joints' characteristics should be those of the HybridIII 3-year-olds dummy model, but data related to the dummy model does not exist. Therefore, we calculate the 3-year-olds infant's joint characteristics by scaling of the adult characteristics that was proposed by Y.K. Yang and Robert and substitute the calculated data. We used the geometric scaling method to calculate the joint characteristics. This method is the way to calculate various physical quantities by consulting human body measurement. Regarding the representative length of each item, we defined the adult's data as  $X$ ,  $Y$  and  $Z$ , and the infant's data as  $x$ ,  $y$  and  $z$ . Then, the scaling coefficient of the lengths  $\lambda_x$ ,  $\lambda_y$  and  $\lambda_z$  is represented as below.

$$\begin{aligned}\lambda_x &= x/X \\ \lambda_y &= y/Y \\ \lambda_z &= z/Z\end{aligned}\quad (1.3)$$

When using the scaling coefficient of the Young's modulus  $\lambda_E$ , the scaling coefficient of the load is represented as below.

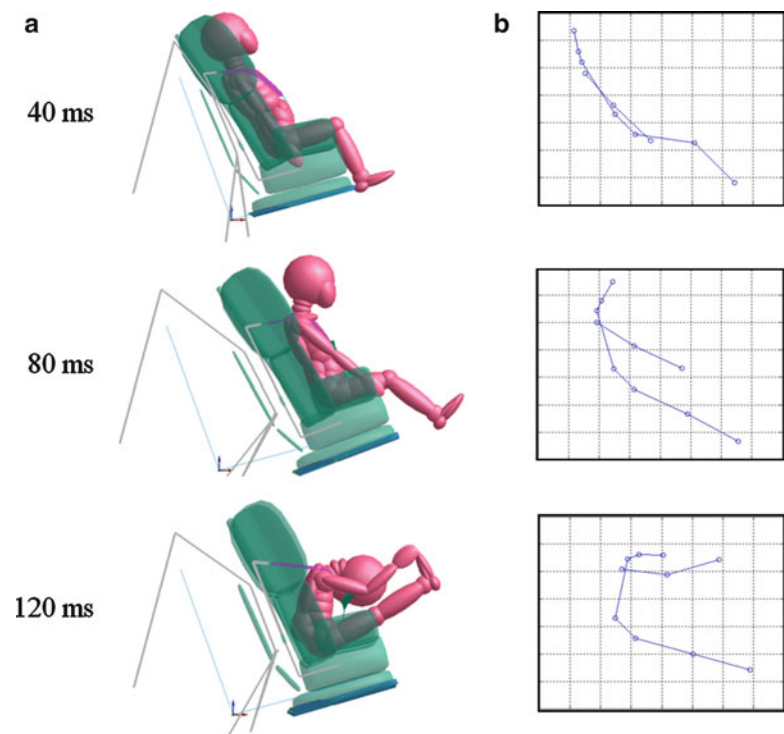
$$\begin{aligned}f_X/F_X &= \lambda_E \lambda_Y \lambda_Z \\ f_Y/F_Y &= \lambda_E \lambda_Z \lambda_X \\ f_Z/F_Z &= \lambda_E \lambda_X \lambda_Y\end{aligned}\quad (1.4)$$

The scaling coefficient of the load multiplied by the scaling coefficient of the moment arm equals the scaling coefficient of the torque. The torque is as below.

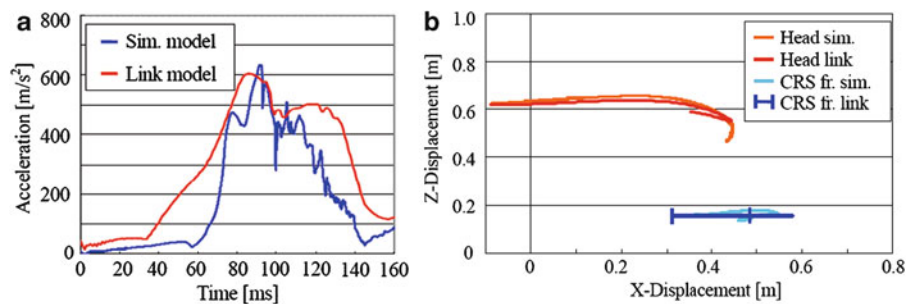
$$\begin{aligned}t_X/T_X &= \lambda_E \lambda_X \lambda_Y^2 \\ t_Y/T_Y &= \lambda_E \lambda_Y \lambda_X^2 \\ t_Z/T_Z &= \lambda_E \lambda_Z \lambda_Y^2\end{aligned}\quad (1.5)$$

As the scaling coefficient of the Young's modulus, we used scaling of the Young's modulus of the ligament. We assumed the infant's range of movement equals the adult's. As the viscosity characteristic related to each joint's rotation, we used that of the adult's estimated by Aoki.

**Fig. 1.7** Comparison of behavior between the simulation and link models (a) Simulation model, (b) Link model



**Fig. 1.8** Comparison of simulation and link model (a) Head resultant acceleration, (b) Trajectories of head and CRS



### 1.4.3 Validity Verification

To verify the validity of the constructed linear model, we compared it to the simulation model constructed in the previous chapter. In a way similar to the previous chapter, simulations were executed without the control of the harness using the acceleration gained by the sled test. Figure 1.7 shows the comparison of the behavior between the linear model and the simulation model in car crashes. From this figure, there is a little difference of the behaviors of the leg between using the linear model and not using. The cause may be that the contact model is not defined between the leg and the CRS. However Fig. 1.8 shows that the head acceleration, head displacement and CRS displacement of the linear model correspond to those of the simulation model. Thus, the validity of the linear model constructed in this paper is confirmed.

## 1.5 Control System

### 1.5.1 Block Diagram

We designed a PI controller to control the harness length of the CRS model in collisions using MATLAB/Simulink software. Next we constructed a control system to decrease the risk of injuries to the head, neck, and thorax.

**Fig. 1.9** Block diagram of experimental control system

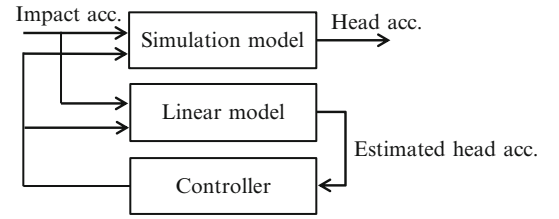


Figure 1.5 shows our constructed block diagram. The dummy model sits on the CRS model, and the collision acceleration is input. The PI controller controls the harness length by feeding back the output head accelerations estimated by the constructed linear model to the controller (Fig 1.9).

### 1.5.2 Optimization

In this section, head and thorax injury criteria were set to the objective functions, and the controller gains were set to the optimizing parameters to minimize the objective function. The optimization of the controller gains was performed with optimization software called modeFRONTIER. Numerical simulations were executed repeatedly and parameters were optimized. These parameters were applied to the controller and reconstructed a controller system. A simulation model with this optimized control system is called a control model.

### 1.5.3 Objective Functions

In this study, the crash-safety of children was assessed by head, neck, and thorax injury criteria in frontal crashes. *HIC36*, *Nij*, and *Thorax Acceleration Tolerance* were chosen as the injury criteria and set to the objective functions that should be decreased.

The head injury criterion (*HIC*) is formulated below.

$$HIC = \max \left\{ (t_2 - t_1) \left[ \frac{1}{t_2 - t_1} \int_{t_1}^{t_2} a dt \right]^{2.5} \right\} \quad (1.6)$$

$a$ : Head resultant acceleration

*HIC36* is set as  $t_2 - t_1 = 36$  [ms] and is widely used in the collision safety field [10]. A threshold value of 1,000 was applied to the Hybrid III 3-year-olds dummy, and we assumed a risk of injury if the criterion exceeded 1,000.

The neck injury criterion (*Nij*), which is formulated below, had four kinds of values determined by the combination of axial force and bending moment. The combination of tension and extension is NTE, the combination of tension and flexion is NTF, the combination of compression and extension is NCE, and the combination of compression and flexion is NCF. *Nij*, which is their maximum value, is set to an objective function.

$$Nij = \frac{F_x}{F_{xc}} + \frac{M_{oc_y}}{M_{yc}} \quad (1.7)$$

$F_x$ : Neck axial force [N]

$F_{xc}$ : Critical value of axial force [N]

$M_y$ : Neck bending moment[Nm]

$M_{yc}$ : Critical value of bending moment[Nm]

A threshold value is 1.0 because *Nij* is regularized by critical values and might cause injury if the criterion exceeds this value.



As a thorax injury criterion, we chose thorax acceleration tolerance, because it is directly calculated from spinal acceleration. This criterion is peak spinal acceleration sustained for 3 [ms]. The threshold value of thorax acceleration tolerance is 60 G and might cause injury if the criterion exceeds this value.

### 1.5.4 Optimizing Algorithm

We adopted the genetic algorithm as an optimizing algorithm in this study.

The genetic algorithm imitates the inheritance and the evolution of life, based on the idea of evolution to a better design by assuming that one design is one gene and repeating such operations as the crossover of two genes, mutation, and natural selection.

Sixteen designs were generated as the first generation by semi-random sampling and evolved until the 40th generation. The mutation rate was assumed to be 5%.

### 1.5.5 Control Model

Optimization that minimizes the objective functions was done using the algorithm, and many Pareto optimum solutions were obtained. A Pareto optimum solution means that a better solution doesn't exist among the solutions, although it is not necessarily more dominant than all other solutions. Therefore, evaluation function  $J$  was formulated in this study, and the Pareto optimum solutions were judged by the evaluation function, which regularizes by dividing the injury values of the head, the neck, and the thorax by each threshold value, as described below.

$$J = \left(\frac{HIC}{1000}\right)^2 + \left(\frac{Nij}{1.0}\right)^2 + \left(\frac{Thorax\ tolerance}{60\ G}\right)^2 \quad (1.8)$$

The evaluation function  $J$  selected a Pareto optimum solution as a preferred solution. This preferred solution was applied to the controller gains to reconstruct a controller system. In this study, a simulation model with this optimized control system is called a control model.

## 1.6 Simulation Results

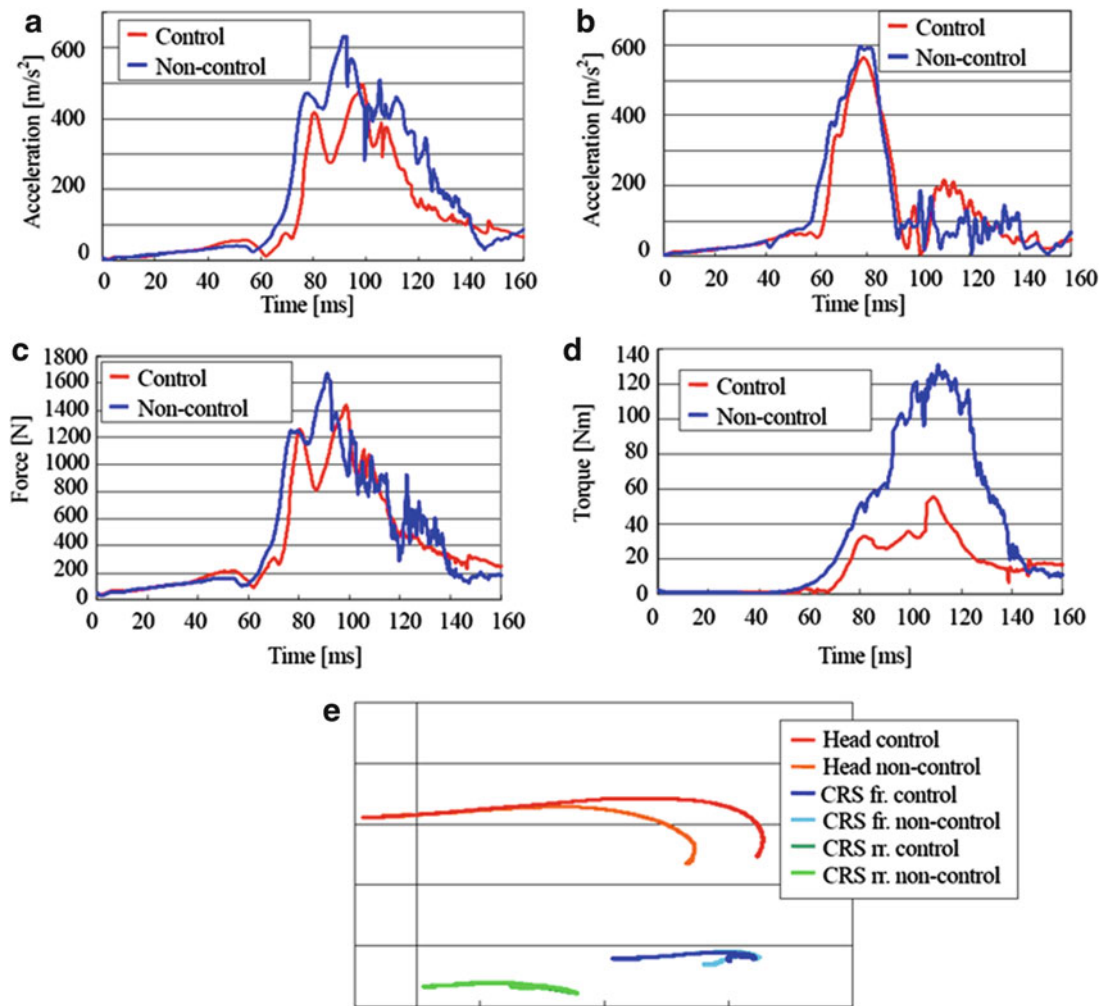
To clarify the optimization effect of the harness controller, simulations were executed using the non-control and control models and we compared these models. The control model is the simulation model that consists of the dummy model and the current CRS model without a harness control system. Table 1.2 compares the injury values of the non-control and control models. Additionally, Figs. 1.10 and 1.11 compare responses and behaviors.

First, we compared and discussed the responses of both models. Table 1.2 shows that all injury risks of a control model were substantially decreased compared to a non-control model. This results shows that CRS improved crash-safety.

Additionally, in Fig. 1.10d, each value temporarily decreased at about 90 [ms], perhaps because the controller changed the length of harness rapidly and harness was loosened temporarily. Figure 1.10a shows the head resultant accelerations. The peak value in the control model is smaller than in the non-control model. Therefore, the head injury value decreased from 596 to 305, and head injury risks decreased. Figure 1.10b shows the thorax resultant accelerations. The peak value in the control model is smaller than in the non-control model and the acceleration increased earlier. Perhaps because the belt was immediately fastened after the impact and the peak value decreased. Therefore, the thorax injury value decreased from

**Table 1.2** Comparison of the injury values between the non-control and the control models

Injury value (Threshold value)	<i>HIC</i> (1,000)	<i>Nij</i> (1.0)	<i>Thorax acceleration tolerance</i> (60 G)
Non-control	593.9 (59[%])	2.29 (229[%])	60.0 G (100[%])
Control	304.8 (30[%])	1.25 (125[%])	56.3 G (94[%])
Ratio of decrease to threshold value	29[%]	104[%]	6[%]



**Fig. 1.10** Response comparison between non-control and control models (a) Head resultant acceleration, (b) Thorax resultant acceleration, (c) Neck axial force, (d) Neck bending moment, (e) Trajectories of head and CRS

60 G to 56 G, and the thorax injury risk decreased as a result. Figure 1.10d show the neck axial force and the neck bending moment. Even though major differences of the peak values in the control and non-control models are not seen in the neck axial force, the peak value decreased in the neck bending moment. As a result, the neck injury value decreased from 2.91 to 1.25, and neck injury risks decreased. From Fig. 1.10e, the maximum head displacement became 0.65 [m] in the non-control model and 0.80 [m] in the control model, and the displacement difference was 0.15 [m]. In the control model, the head displacement increased because the controller lengthened the harness to prevent head, neck, and thorax injuries.

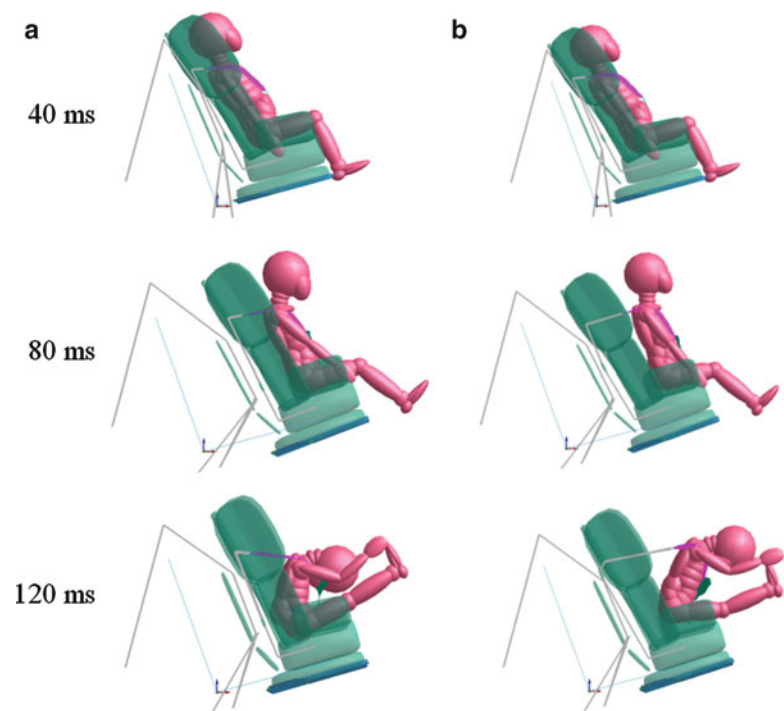
The crash-safety of CRS was improved by optimized harness controller.

## 1.7 Conclusion

The following conclusions were drawn from this study.

1. Attaching the concept of the adoptive control for the CRSs, the possibility of improving the crash safety was clarified.
2. We constructed a child linear model and estimated a child's head acceleration to control the harness length.
3. The numerical simulations showed that the head, the neck, and the thorax injury risk decreased with PI controller designed for controlling of the harness.

**Fig. 1.11** Comparison of behavior in non-control and control (a) Non control model, (b) Control model



**Acknowledgements** This work was partially supported by Grant-in-Aid for Scientific Research (C) (23560272), Japan Society for the Promotion of Science.

## References

1. Transportation Authority of National Police Agency (2011) Incidents of transportation accident in 2011 (in Japan)
2. Yoshida R, Goto S, Mori K (2002) The study of child restraint system safety based on ITARDA field survey. In: Proceedings of the 2002 JSAE congress, Kyoto, Japan
3. Koizumi T, Tsujiuchi N, Kurumisawa J (2008) Optimization of child restraint system with load limiter and airbag using child FE human model in frontal crash. In: International conference on noise and vibration engineering, Leuven, Belgium
4. Gabriella G, Paul L, Edwin van den E, Arjan van L, Cees van S, John C (2007) Real time control of restraint systems in frontal crashes. In: SAE World Congress and Exhibition, Detroit, MI USA
5. Ewout van den L, Bram de J, Frans V, Maarten S, Ellen van N, Dehlia W (2004) Continuous restraint control systems: safety improvement for various occupants tiofidelity rating of MADYMO three-year-olds child FE human model. In: The 18th international technical conference on the enhanced safety of vehicles, Nagoya, Japan
6. Institute for Traffic Accident Research and Data Analysis (1999) Investigative research report on effect of wearing CRS, ITARDA pp 13–29
7. Kathleen DeSantis K, Roger AS, Gaston A, Stanley B, Michael K (1996) Techniques for developing child dummy protection reference values. NHTSA biomechanics reports
8. TNO Automotive (2004) MADYMO theory manual version 6.2
9. ECE Regulation No. 44. Uniform provision concerning the approval of restraining devices for child occupant of power-driven vehicles
10. Workgroup Data Processing Vehicle Safety (2004) Crash analysis criteria description version 1.6.1

## Chapter 2

# Dynamic Response and Damage Estimation of Infant Brain for Vibration

Takayuki Koizumi, Nobutaka Tsujiuchi, Keisuke Hara, and Yusuke Miyazaki

**Abstract** The purpose of this paper is to clarify the mechanical generation mechanism of acute subdural hematoma, which is a severe injury in infants, by performing experiments and finite element analysis. The acute subdural hematoma in infants is caused by accidents such as falling or abuse such as shaking. This paper describes the shaking events.

In the experiments, we used a 6-month-old anthropometric dummy and a vibration exciter, which can set the parameters. The dummy was fixed to the exciter at the chest, which it was given the vibration. The head model of the dummy is transparent, and the brain behavior can be visualized. In finite element analysis, we used a model that has been converted to the 6-month-old head through the adult head by the method of free-form deformation (FFD) and scaling. Also, we performed the simulation of shaking events as input acceleration and angular velocity of the head obtained in the experiments.

We measured the stretch ratio of the bridging veins, which connect the skull and the brain, then compared this with the ratio to the threshold (1.5). In this study, we examined the effect on the infant head of shaking action, along with the risk.

**Keywords** Infant • Acute subdural hematoma (ASDH) • Shaken baby syndrome • Finite element analysis • Material properties • Frequency

## 2.1 Introduction

Currently in Japan, the leading cause of death in children under a year old is accident, and this has not changed since 1960 [1]. Intentional injury such as abuse experienced by children has also become a problem, and physical abuse involving infant head trauma is considered the highest risk to life.

Among severe cases of infant head trauma, acute subdural hematoma (ASDH) is prominent. The mortality rate due to this is high, and the survivors suffer from heavy permanent damage. When assessing ASDH, it is not easy to ascertain whether its cause is abuse by shaking or an accident such as a fall. Judgment of abuse or accident in medical institutions that relies on experience and intuition lacks a scientific basis. Shaken baby syndrome is well known as a form of head injury caused by abuse. However, it is not clear whether the shaking action itself is fatal from previous study. Therefore, it is necessary to clarify the generating mechanism of ASDH in infants and to provide a scientific basis to make the judgment.

ASDH occurs by the relative rotational motion between the skull and the brain with a rupture of bridging veins. However, with the traditional dummy that has a rigid head, it is not possible to visualize the relative rotational motion between the skull and brain during shaking.

Therefore, in this study, we use an infant anthropometric dummy that has a realistically shaped physical model of an infant head to visualize the relative motion between the skull and the brain. Also, we perform experiments to evaluate the

---

T. Koizumi • N. Tsujiuchi • K. Hara (✉)

Department of Mechanical Engineering, Doshisha University, 1-3, Tataramiyakodani, Kyotanabe-city, Kyoto 610-0321, Japan  
e-mail: [tkoizumi@mail.doshisha.ac.jp](mailto:tkoizumi@mail.doshisha.ac.jp); [ntsujiuc@mail.doshisha.ac.jp](mailto:ntsujiuc@mail.doshisha.ac.jp); [dum0517@mail4.doshisha.ac.jp](mailto:dum0517@mail4.doshisha.ac.jp)

Y. Miyazaki

Department of Information Environment, Graduate School of Information Science and Technology, Tokyo Institute of Technology, 2-12-1, Ookayama, Meguro-ku, Tokyo 152-8552, Japan  
e-mail: [y-miyazaki@mei.titech.ac.jp](mailto:y-miyazaki@mei.titech.ac.jp)

behavior of the dummy head for vibration input that assumes a shaking act with a vibration exciter. The vibration exciter can set the parameters such as frequency and amplitude.

In addition, we constructed a finite element model of the infant head and simulated the shaking. The model faithfully reproduced the shape. By performing the simulation, we examined the stretch ratio of the bridging veins and relative motion between the brain and skull when shaking.

## 2.2 Anthropometric Dummy

### 2.2.1 Six-Month-Old Anthropometric Test Dummy

In this experiment, we used a CRABI 6-month-old (CRABI 6-Mo) [2], whose height is 67 cm and weight is 7.8 kg. The neck is shaped in soft rubber, and attributes such as bending and stretching are close to the actual biology. The dummy reproduced the highest biological characteristics of the infant in current commercial dummies. The x axis is aligned in the anterior posterior direction, with positive x indicating the anterior direction. The y axis is aligned in the lateral directions, with the positive y indicating the dummy's left side. The z axis is aligned in the superior-inferior direction, with positive z indicating the superior direction.

### 2.2.2 Transparent Skull Model

In this study, we used the transparent skull model to visualize the behavior of the brain [3]. Figure 2.1 shows the model. This model reproduces the shape of the head of an infant. The skull is composed of polycarbonate with high transmittance. The brain model is composed of left and right cerebrum, cerebellum and brain stem, and manufactured with silicon gel, the dynamic viscoelastic properties of which are equivalent to the real brain. This brain model was inserted into the skull model and then the gap between brain and skull was filled with water as cerebrospinal fluid (CSF). Flax and tentorium were modeled with a polyurethane sheet, the Young's modulus of which was equivalent to the real one; then it was affixed to the inner surface of the skull. Thus, the brain movement was confined.

We constructed the infant dummy, which can visualize brain behavior, by attaching the transparent skull model to CRABI 6-Mo. Figure 2.2 shows the dummy.

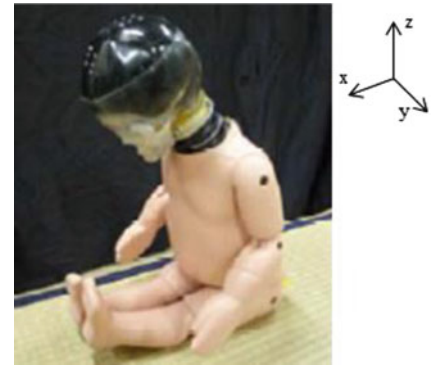
## 2.3 Experiments

The shaking vibration by humans is not constant. Therefore, in this study, we performed the experiments using a vibration exciter to set the input parameters such as frequency and amplitude.

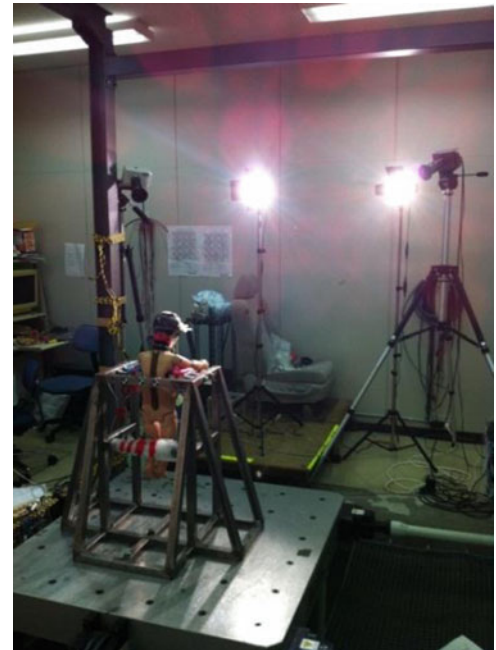


Fig. 2.1 Head physical model

**Fig. 2.2** Infant dummy (CRABI 6-Mo)



**Fig. 2.3** Appearance of shaking experiment by vibration exciter

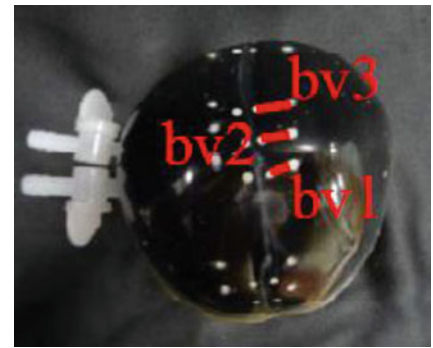


### 2.3.1 Methods

Figure 2.3 shows the experiment aspect. The dummy was fixed on a board it was to transmit vibration of the vibration exciter to the chest. We set up an angular velocity sensor and acceleration sensors on the head of the dummy and attached an acceleration sensor on the chest; then, we measured the acceleration and angular velocity. We applied white markers to the inner surface of the skull and the brain surface to measure the relative movement between the skull and brain. We set to bv1-bv3 each combination of markers of brain and skull. Figure 2.4 shows the combination of markers. Head behavior was taken at a sampling rate of 500 fps or 200 fps with two high-speed cameras (D-III: Detect). The displacement time history of markers was measured by the digital image correlation method. Then, we measured the relative displacement of the markers of bv1-bv3 by converting the three-dimensional displacement method using the Direct Linear Transformation (DLT) method. In addition, we smoothed each three-dimensional displacement by the three-point moving average method. We calculated the stretch ratio ( $\lambda$ ) between two points as the evaluation strain parameters of bridging veins of the attached positions by the three-dimensional displacement. The stretch ratio ( $\lambda$ ) is defined by the following equation using the distance ( $l_0$ ) of the bv1-bv3 in the video frame and the distance ( $l$ ) of the bv1-bv3 in the initial position. We defined the value obtained by the following equation as the bridging vein stretch ratio.

$$\lambda = \frac{l}{l_0}$$



**Fig. 2.4** Makers positions

### 2.3.2 Input Vibration

In previous studies, we concluded that the vibration in the vertical direction has less impact on the infant head. Therefore, we have performed experiments for only the X axial, which is the main component of the shaking vibration. Input vibrations were a total of 12 patterns, combining 3 amplitude patterns [30.0 mm, 40.0 mm, 50.0 mm] in the X axial with 4 frequency patterns [1.5 Hz, 2.0 Hz, 2.5 Hz, 3.0 Hz].

To reproduce the human act of shaking infants, input amplitudes are set to the value around the one with which people shake the infant dummy. In addition, input frequencies were set at a lower value than the maximum high-risk frequency (around 3.0 Hz) obtained by previous studies. In the previous study, the dummy's head, which was a rigid model, was swung the most on the 3.0-Hz frequency.

## 2.4 Results and Discussion

Results are reported in Fig. 2.5 in terms of the bridging vein stretch ratio of bv1-bv3 obtained by the experiments and time history and in Fig. 2.6 in terms of the maximum ratio of results and amplitudes.

The maximum of the bridging vein stretch ratio tends to increase with the increasing amplitude at any frequency in Fig. 2.6. Therefore, the breaking risk of bridging veins is high as amplitude increases.

For 40 mm or more amplitude on 3.0-Hz frequency, the stretch ratio exceeds the 1.5 threshold, which is the breaking value of bridging veins reported by Lee and others [4]. Particularly, for 50.0-mm amplitude, the stretch ratio is significantly higher than the threshold. For 30.0-mm amplitude, the stretch ratio is significantly below the threshold even though the frequency is 3.0 Hz, which is high-risk. Therefore, bridging veins are likely to break above 40.0-mm amplitude on 3.0-Hz frequency, and the risk is especially high in 50.0-mm amplitude, while there is no risk in 30.0 mm amplitude. In other words, we can prove mechanically that ASDH is likely to occur for severe vibration.

In Fig. 2.6, the stretch ratio is significantly below the threshold in any amplitude of 2.5 Hz and under. In other words, bridging veins don't break for 2.5 Hz and under. Therefore, we can conclude that ASDH due to breaking bridging veins does not occur with the vibrations resulting from cradling.

## 2.5 Simulation

### 2.5.1 Construction of Model and Material Properties

The finite element model of an infant head has been developed very little, even though the head model of adults has been developed in many studies. For constructing a finite element model of the infant head, it is not appropriate to obtain it from scaling the adult head model. A highly accurate infant head model cannot be constructed because the characteristics of skull shape are different for infants and adults.

In this study, we used the finite element model of a 6-month-old head, which is newly constructed. Figure 2.7 shows the new model and Table 2.1 shows the dimensions. We retrieved the three-dimensional shape data of the head by CT images of a

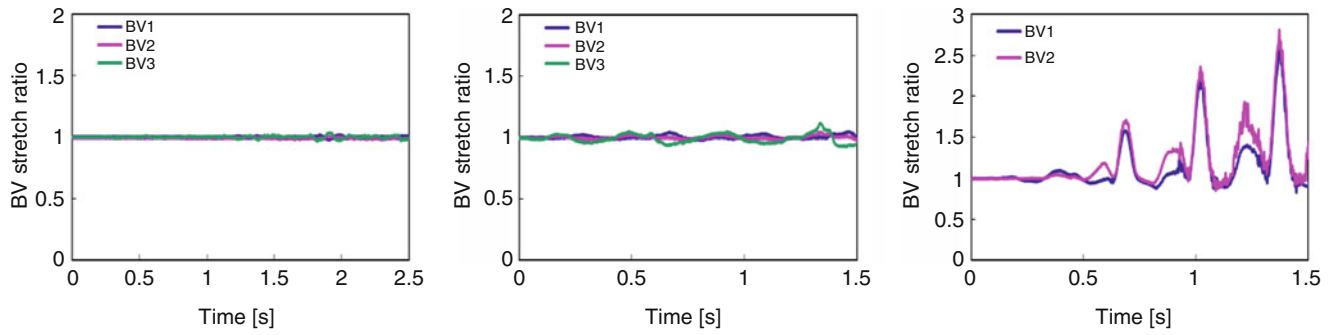


Fig. 2.5 Bridging vein stretch ratio responses with high speed camera images

Fig. 2.6 Max bridging vein stretch ratio responses with high speed camera images

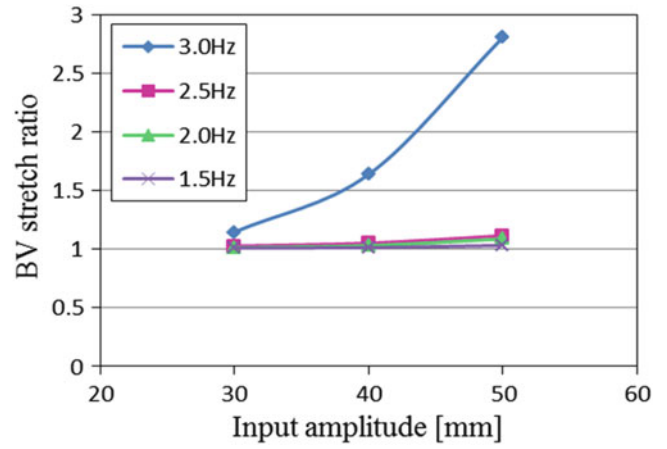


Fig. 2.7 Finite element model

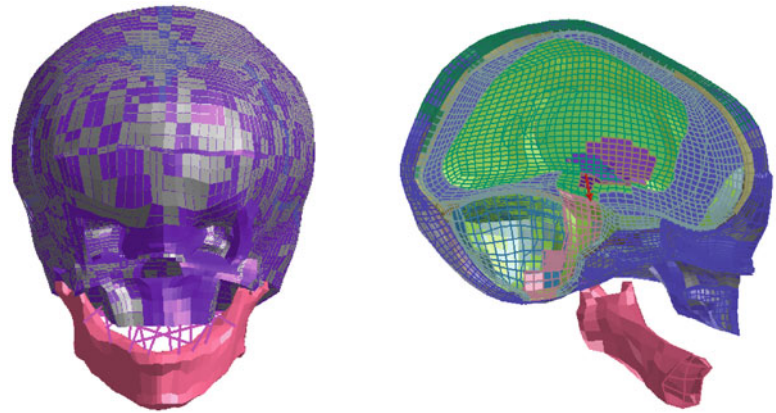


Table 2.1 Dimension of 6-Mo head [mm]

Length	Breath	Height
154.9	119.4	147.3

particular 4-month-old head. Then, we converted the shape of the finite element model of an adult head into the 4-month-old head model based on the shape data with the free-form deformation transformation (FFD) method. The 6-month-old infant head finite element model that is used in this study is constructed by scaling the dimensions of a 4-month-old head which have been converted to the shape of the CRABI 6-Mo head.

The head finite element model is composed of a skull including structure and anterior fontanel, cerebrospinal fluid (CSF), brain (left and right cerebrum, cerebellum and brainstem), and membrane (dura mater, pia mater, flax and tentorium).



**Table 2.2** Material properties (1)

Part	Material property	Density $\rho$ [kg/m <sup>3</sup> ]	Young's modulus E [GPa]	Poisson's ratio $\nu$
Right cerebrum	Linear_Visco_Elastic	1,040	K = 2.19	
Left cerebrum				
Cerebellum				
Brain stem				
Pia mater				Elastic
Dura mater		1,133	$3.15 \times 10^{-2}$	0.45
Falx		1,133	$3.15 \times 10^{-2}$	0.45
Tentorium		1,133	$3.15 \times 10^{-2}$	0.45
Sagittal sinus		1,133	$3.15 \times 10^{-2}$	0.45
CSF	Linear_Visco_Elastic	1,060	K = 2.19	
Ventricle				
Skull diploe	Elastic	2,150	$421 \times 10^{-3}$	0.22
Structure			$4.2 \times 10^{-3}$	
Mandible	Elastic	2,150	4.6	0.05
Inner table	Elastic	2,723	15	0.21
Outer table				
Bridging vein	Elastic	1,133	$9.62 \times 10^{-3}$	0.45

**Table 2.3** Material properties (2)

Part	Density [kg/m <sup>3</sup> ]	Bulk modulus [Gpa]	Short time shear modulus [GPa]	Long time shear modulus [GPa]	Decay constant [s <sup>-1</sup> ]
Brain	1,040	2.19	$2,710 \times 10^{-9}$	$891 \times 10^{-9}$	166
CSF	1,060	2.19	500	$5.0 \times 10^{-7}$	500,000
Ventricle					

**Table 2.4** Properties of the modified material (1)

Part	Material property	Density $\rho$ [kg/m <sup>3</sup> ]	Young's modulus E [GPa]	Poisson's ratio $\nu$
Brain	Linear_Visco_Elastic	1,040	K = 2.19	
Falx	Elastic	1,133	$3.15 \times 10^{-2}$	0.45
Tentorium		1,133	$3.15 \times 10^{-2}$	0.45
Skull	Elastic	1,200	2.45	0.33

**Table 2.5** Properties of the modified material (2)

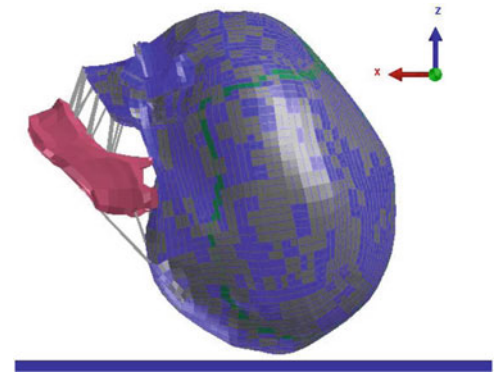
Part	Density [kg/m <sup>3</sup> ]	Bulk modulus [Gpa]	Short time shear modulus [GPa]	Long time shear modulus [GPa]	Decay constant [s <sup>-1</sup> ]
Brain	1,040	2.19	$2,704 \times 10^{-9}$	$886 \times 10^{-9}$	166
CSF	1,060	2.19	500	$5.0 \times 10^{-7}$	500,000

Tables 2.2 and 2.3 shows the material properties of each tissue. Suture and skulls of infants are soft as ossification is not complete compared with adults. Thus, the material properties used the average value of the measurement results of 1–12 months, which are obtained in the three-point bending test of Margulies et al. [5]. Material testing at 6 months has not been carried out. Therefore, the suture material property used is for 11 months. The CSF property used is a viscosity elastic property, almost like water. In addition, other properties given are the adult properties.

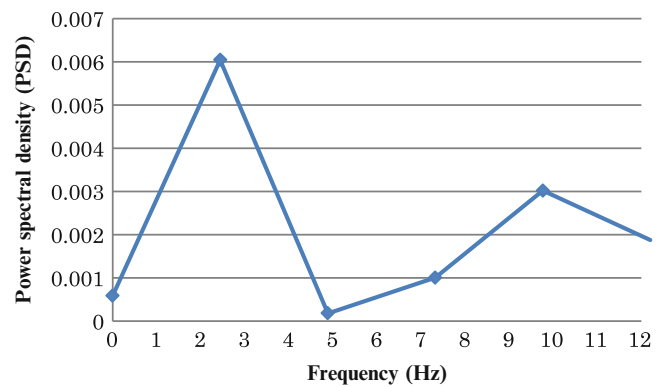
We can verify the operational state of the load and the deformation of the intimal structure such as skull and brain by using a finite element modal.

### 2.5.2 Simulation and Result

In this study, we have carried out a simulation to verify the frequency response of the brain. In the simulation, we constructed the finite element model of the dummy's head. We developed the model by modifying the material properties because the dummy's head and the finite element model are equal for shape and structure. The dummy's head is composed skull, brain, flax, tentorium and CSF. Therefore, the simulation model is standardized of dummy's configuration. Tables 2.4 and 2.5 shows the properties of the modified material.

**Fig. 2.8** Simulation condition**Table 2.6** Input values

Initial velocity (x) [m/s]	Initial velocity (z) [m/s]	Initial angular velocity (y) [rad/s]
2.86	-4.43	-27

**Fig. 2.9** Power spectral density obtained by FFT

We simulated the event of falling impact from the back head to ground with the simplified model of the above using the PAM\_CRASH solver. The skull model was defined as rigid body and given a translational velocity and angular velocity when upset from 1 m high to the center of gravity position. And then, we examined the response of the elements of the brain surface. Figure 2.8 and Table 2.6 show the conditions of simulation.

As a result of the simulation, the resonant frequency is detected at around 2.5 Hz. Figure 2.9 shows the power spectral density, which is obtained by fast Fourier transform (FFT) of the acceleration obtained by simulation. In the experiment, it is found the 3.0 Hz vibration is the high risk to break the bridging veins for the infant head. Therefore, the brain of the infant will resonate between 2.5 and 3.0 Hz, and the vibration in this frequency band is dangerous to influence significantly the brain.

## 2.6 Conclusion

1. In the experiment, ASDH is likely to occur for severe vibration such as the frequency is 3.0 Hz and the amplitude is 50.0 mm. And also, ASDH due to breaking bridging veins does not occur with the vibrations resulting from cradling since bridging veins don't break for 2.5 Hz and under.
2. In the simulation, the resonant frequency is detected at around 2.5 Hz. Therefore, the resonant frequency of an 6-month-old brain is between 2.5 and 3.0 Hz, and it is dangerous to vibrate the infant in this frequency band.

**Acknowledgements** This work was partially supported by Grant-in-Aid for Scientific Research (C) (23560272), Japan Society for the Promotion of Science.

## References

1. Science Council of Japan, Committee of clinical medicine birth and development subcommittee (2008) I in order to establish a preventing system child injury by accident. Recommendations Science Council of Japan (in Japanese)
2. Kazuko A et al. (2003) Calibration method and structure of Q3 and CRABI 6-month-old dummy. *Automot Res* 25(7): 293–298 (in Japanese)
3. Tuyoshi N, Yusuke M, Asami Y, Yoshihumi N, Tatsuhiro Y (2011) Measuring the relative motion between the brain and skull during shaking using a physical model of the infant head. In: Proceedings of the 23th conference on bioengineering, Kumamoto University in Japan, pp 127–129 (in Japanese)
4. Lee M-C, Haut RC (1989) Insensitivity of tensile failure properties of human bridging veins to strain rate: implications in biomechanics of subdural hematoma. *J Biomech* 22(6–7):537–542
5. Coats B, Margulies SS (2006) Material properties of human infant skull and suture at high rates. *J Neurotrauma* 23(8):1222–1232

# Chapter 3

## Mechanical Strength of Bone Cement with and Without Adjuvant Screw Fixation

Ryan Keyser, Robert Migliori, Tessa Morgan, Steven R. Anton, Kevin M. Fariholt, and R. Michael Meneghini

**Abstract** Knee replacement surgery is a challenging, invasive procedure, so it is prudent that reliable components are used to minimize the likelihood of implant failure and subsequent risky, post-operation corrections. Each artificial component is adhered to a bone interface by composite acrylic-based cement. It is theorized that the structural integrity and, by extension, longevity of bone cement used to fill voids in knee replacement surgery is augmented by adjuvant screws embedded in the cement and anchored in bone, analogous to rebar-reinforced concrete. While the screw fixation method has exhibited positive results in arthroplasty patients, no conclusive evidence has been produced demonstrating its value over cement without screw fixation. It was the purpose of this research to examine which, if either, method is more effective. Porous polyurethane blocks were used to emulate human bones, in which uniform defects were generated and filled with bone cement in two cases, with and without the addition of screws. To test their mechanical properties, the specimens were loaded in compression by a material testing machine to mimic the forces created by the body, with focus on micro-motion of the cement. Additionally, nondestructive damage detection techniques were performed during fatigue testing by high frequency interrogation using piezoceramic actuators and sensors. Damage detection and classification algorithms were explored from attained data.

**Keywords** Total knee replacement • TKR • Adjuvant screw fixation • Mechanical testing • Structural health monitoring • Bone cement

---

R. Keyser  
Los Alamos National Laboratory, W-13, 87544 Los Alamos, NM, USA  
e-mail: [rrkeyser@msn.com](mailto:rrkeyser@msn.com)

R. Migliori  
New Mexico Institute of Mining and Technology, 87801 Socorro, NM, USA  
e-mail: [migliori@nmt.edu](mailto:migliori@nmt.edu)

T. Morgan  
Oklahoma State University, 74074 Stillwater, OK, USA  
e-mail: [tessajme@okstate.edu](mailto:tessajme@okstate.edu)

S.R. Anton (✉)  
Los Alamos National Laboratory, INST-OFF, 87544 Los Alamos, NM, USA  
e-mail: [sranton@lanl.gov](mailto:sranton@lanl.gov)

K.M. Fariholt  
Commonwealth Center for Advanced Manufacturing, 23842 Disputanta, VA, USA  
e-mail: [kevin.farinholt@ccam-va.com](mailto:kevin.farinholt@ccam-va.com)

R.M. Meneghini  
Indiana University School of Medicine, 46202 Indianapolis, IN, USA  
e-mail: [rmeneghi@iuhealth.org](mailto:rmeneghi@iuhealth.org)

## 3.1 Introduction

### 3.1.1 Background

Total knee replacement (TKR) is one of the most common medical procedures performed today (along with total hip replacement). It is usually performed in response to various forms of arthritis, most prominently osteoarthritis, but also rheumatoid and psoriatic, and other miscellaneous factors. Hundreds of thousands of knee replacement surgeries are performed every year in the U.S. alone.

Early knee implants were crude devices, typically constraining joint rotation to a single axis, incongruous with actual knees that can rotate slightly about the long axis of the leg. Today, a typical TKR implant is comprised of titanium or cobalt-chrome femoral and tibial components that accurately imitate the motion of the knee. The tibial component has a polyurethane surface and represents the load-bearing meniscus; the femoral component replaces the kneecap cartilage. An adhesive intermediary, typically polymethylmethacrylate (PMMA) or “bone cement”, is used to bind artificial components to organic interfaces (bone). Together, these components assume the role of the knee joint in both form and function.

Much of the early research for artificial knee implants was directed towards making the implants perfectly mimic the human knee, functionally and structurally. Fortunately, this goal has garnered enough attention that focus may be shifted towards some of the other difficulties associated with TKR. One important focus area has been the relationship between body and implant, a significant factor in increasing longevity.

In general, critical failure in an implant occurs when it becomes dissociated from organic material enough to engage in relatively large motion, a few millimeters, perhaps, within the body. Such dissociation is a consequence of a variety of factors, including poor placement during surgery, infection, autoimmune responses, which may attack bone material surrounding an implant, and a host of other complications. The result is typically the same: surgery.

### 3.1.2 Motivation

A significant hurdle surgeons must overcome when repairing a knee implant are *bone defects*, harmful voids in the tibia or femur that develop within cancellous tissue as a result of removing or repositioning the implant during surgery or in parallel with the failure mechanisms listed above. It is imperative that defects be repaired, for they induce structural instability, not only in the bone itself, but also in the security of the implant connection to bone by decreasing available surface area.

The standard procedure for repairing defects is by *block augmentation*. In this operation, an inert implant, usually a titanium block, is seated in a defect area that has been excavated and anchored in bone by a long metal rod. Alternatively, some physicians choose to fill a defect with the same bone cement used elsewhere in the TKR procedure. Others, still, supplement this filling with screws, drilled into bone and immersed in the cement, based on the theory that they reinforce the structure.

Several factors make the cement methods preferential to block augmentation. Most prominently, the cement methods are *cheap* and *easy*. Additionally, little to no bone matter must be removed, allografts are not a requirement, and the cement is pliable and may be molded to fit the defect. Although block augments are durable and effective, some difficulties are associated with the technique. Foremost is that block augments are not generally customized, but made in a few specific shapes and sizes, so that the defect area itself must be shaped for the implant. This translates to the removal of significant bone matter, a legitimate concern.

Furthermore, the bone cement technique requires less than \$100 worth of materials, contrary to block augmentation, which is relatively difficult, complicated, and more expensive. Although the cement techniques have exhibited success in practice [1], little quantitative data illustrating their *functional* effectiveness over any other method, or in particular over each other, has been produced. However, one study of particular interest focuses on the mechanical strength of cement-less tibial components [2], and is referred to for a baseline in testing methodology for this experiment.

### 3.1.3 Objectives

Accordingly, the primary aim of this study is to scientifically examine the two cement methods – with and without screws – and evaluate their performance with respect to each other as a technique for filling bone defects affiliated with TKR. Results are based on the micro-motion (the recoverable, essentially elastic motion that does not entail damage) of the cement relative

to the bone during testing, measured by a Linear Variable Differential Transformer (LVDT). The health and recovery time of the implant and, heretofore, the patient, is dependent on the micro-motion of the bone/cement interface, especially during the first few weeks of recovery. Less motion is better because it protects the interface and allows proper meshing with the body.

The secondary directive of this study is to apply damage detection techniques to forge damage metrics for data collected by piezoceramic sensors/actuators (PZTs or lead zirconate titanate) [3] from the bone/cement constructs, with particular focus on the integrity of the bone/cement interface. Algorithms adapted from structural health monitoring (SHM) techniques [4–6] are investigated to determine ways to predict damage before the construct failure. The outcome of this study may provide operating physicians, and the medical community as a whole, with reliable information on identifying early failure of knee replacements.

## 3.2 Experimental Procedures

### 3.2.1 Test Samples

In this study, bone is emulated by specialized blocks of cellular rigid polyurethane foam (Sawbones) designed specifically for orthopedic research. The original blocks were  $13 \times 18 \times 4$  cm with a density of 0.32 g/cc. Defects are represented by approximately quarter-sphere pits of various depths (summarized in Table 3.1) reamed into the edges of the foam blocks by an orthopedic surgeon according to surgical requirements, as shown in Fig. 3.1a.

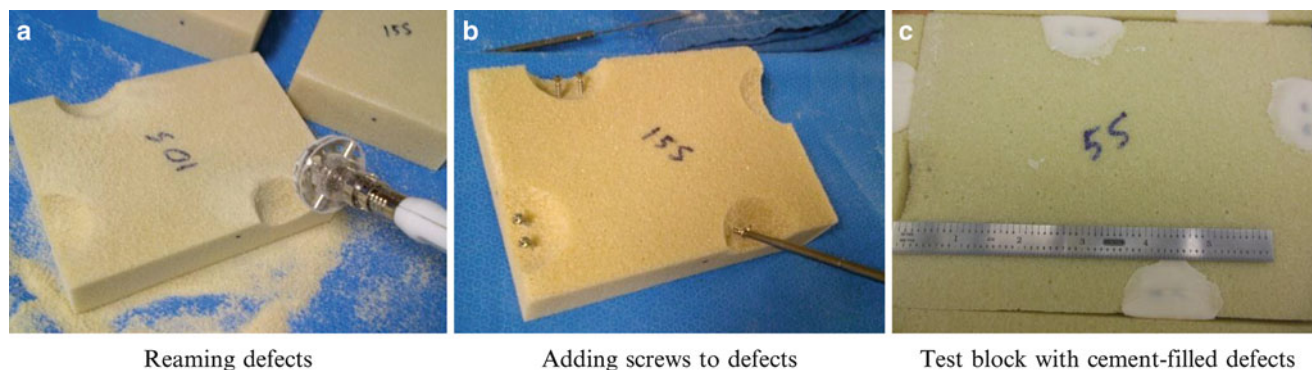
The defects were filled with PMMA bone (Stryker) cement, either with or without a pair of embedded screws (4 mm Stryker stainless steel screws, 40 mm in length, “fully threaded cancellous”). Figure 3.1 depicts these test specimens, prepared by an orthopedic surgeon.

Once received, the blocks were cut to approximately  $5.4 \times 5.4 \times 4$  cm (see Fig. 3.2a), so that the smaller blocks contained only one cement-filled defect each, which was centered on one edge. The cement surfaces were sanded to be level with the rest of the foam for a more even and consistent surface. The blocks were labeled by the defect depth (5, 10, or 15 mm) and presence of screws with a letter to distinguish between the duplicates. For example, block 5SB has a 5 mm defect with screws and is the “B block” or second block of that type. Block 5B has the same description, but without screws.

Next, the blocks were outfitted with PZTs (APC International). Quarter-inch diameter PZTs (actuators) were bonded to the front faces of the cement and half-inch diameter PZTs (sensors) were bonded to either to the top or back faces of the blocks (see Fig. 3.2b). Various PZT configurations were investigated; the final locations were based on the arrangement that gave the strongest, most clear signals. For the 5 mm defect samples, this was the top of the block; for the 10 and 15 mm

**Table 3.1** Number of test specimens

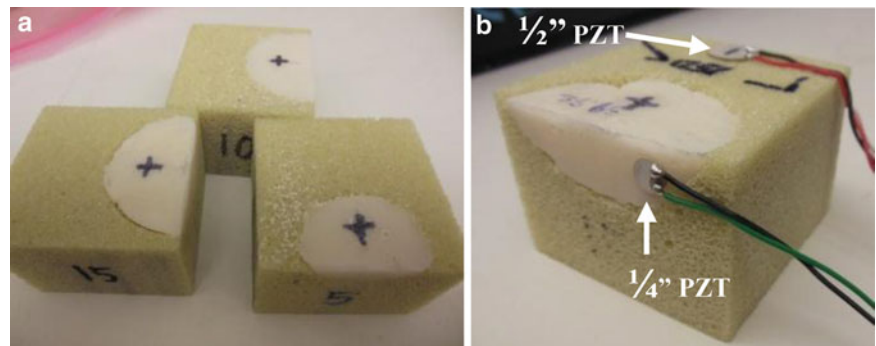
Defect depth (mm)	Defects with cement only	Defects with cement and screws
5	4	3
10	4	3
15	4	3



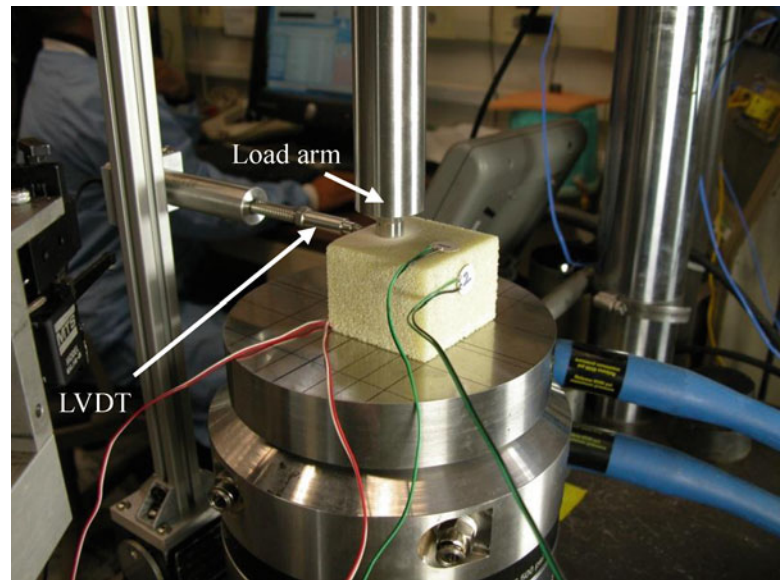
**Fig. 3.1** (a), (b) and (c): Preparation of test specimens. (a) Reaming defects, (b) Adding screws to defects, (c) Test block with cement-filled defects



**Fig. 3.2** (a) Cut test blocks and (b) Test specimen outfitted with PZTs



**Fig. 3.3** Experimental setup for mechanical testing of samples



samples, the sensors were attached to the back of the block. The actuator was offset from the center of the defect to make room for the LVDT, which contacted the block in the center of the cement on the front face of the block.

### 3.2.2 Test Methodology

#### 3.2.2.1 Loading Conditions

Two types of loading conditions were applied to the test specimens by a materials testing machine (MTS 880): (1) Force-controlled cyclic compression and (2) Compression-to-failure at a constant strain rate. The contact surface of the stainless steel load applicator was 12 mm in diameter and was applied to the approximate geometric center (marked by a plus sign on each block, as shown in Fig. 3.2 of the semicircle of the cemented defects. The application of the load arm can be seen in Fig. 3.3.

First, the specimens were subjected to the cyclic mechanical loading to emulate the forces due to walking seen by the bone/cement assembly after TKR, with focus on the micro-motion of the cement relative to its host. Originally, the cyclic load ranged from 50 to 700 N. However, due to a lack of detectable micro-motion, the cyclic ceiling was incrementally increased to 1,700 N. Following cyclic testing, the specimens were compressed by the MTS to critical failure at a constant strain rate of 0.2 mm/s until 6% strain was reached. The purpose of the second compression test was to observe the failure mechanisms experienced by the specimens, particularly at the bone/cement interface. For both tests, the MTS machine catalogued time, vertical displacement, and force. The primary quantity of interest, horizontal displacement of the cement face, was also measured by the MTS but via an external LVDT.

### 3.2.2.2 LVDT

An LVDT (Omega LD621-10 LVDT and BK Precision 9123A Single Output Programmable DC Power Supply) was used to measure the micro-motion of the cement relative to the bone as it was being subjected to compressive forces. A mount was developed to ensure repeatability in the placement of the LVDT between test specimens. The LVDT was mounted to a rigid part of the MTS so that the direction of motion of the LVDT was normal to and centered on the top of the cement face of the test specimen (Fig. 3.3). The measurements were sampled at a rate of 60 Hz throughout both the cyclic and compression tests.

### 3.2.2.3 PZT Measurements

Passive and active measurements achieved with acoustic waves, generated at the cement faces by PZT actuators, were taken throughout the procedure. Actuators were driven by a high-speed Morlet waveform generator (National Instruments PXI 8186 Embedded Controller, PXI 4461 card, and LabVIEW version 8.6) for wave propagation. An amplifier (Krohn-Hite Corporation Wideband Amplifier) and oscilloscope (Tektronix TDS Four Channel Color Digital Phosphor Oscilloscope) were used. For the high-speed Morlet waveform generator, the most sensitive frequencies at which the waves propagated proved to be 90 kHz for the 5 mm samples, 130 kHz for the 10 mm samples and 110 kHz for the 15 mm samples. During the cyclic testing, all of the specimens were only passively monitored.

Prior to each cyclic test, a specimen was loaded in the MTS with a pre-load of about 10 N, and a baseline measurement was taken by interrogating using the block's designated active sensing method. During the cyclic test, only passive monitoring was done so as not to disturb the test specimen and contaminate the passive sensing data. At the completion of the cyclic tests, the sample was unloaded to about 10 N and, again, interrogated with the PZTs. Throughout the compression-to-failure testing, the active sensing measurements were taken repeatedly.

## 3.3 Results and Discussion

### 3.3.1 LVDT Measurements

Figure 3.4 illustrates two examples of horizontal displacement measurements (blue) recorded by the LVDT during cyclic testing. The data contours allude to approximately sinusoidal motion at the cement face, with the same period and ostensibly in response to the oscillatory encumbrance. This feature is clearly visible in the left panel of Fig. 3.4, and, although occluded by noise, in the right panel too. Aggregate horizontal motion of the samples was taken as the amplitude of a sine function computationally fit to the LVDT data. This operation provides a displacement representative of each measurement en masse, eliminating the need for tedious analytical techniques. Examples of such fits are plotted red and overlaid on blue LVDT data in Fig. 3.4.

Error in horizontal displacement was taken as a "by inspection" vertical range of noise about a peak. While such bounds are illustrated in both panels of Fig. 3.4, they are exemplified in the right-side graph. Multiple term sine fits were also investigated, but deemed unnecessary as the difference in amplitudes between them were negligible compared to the error bounds depicted in Fig. 3.4.

#### 3.3.1.1 Motion During Cyclic Testing

The procedure outlined above was performed for all 21 measurements. The results are depicted in Fig. 3.5. Data from a 5 mm sample, 5SB, was deliberately excluded because it was determined to be an outlier.

Due to the magnitude of the uncertainty in the measurements, only enough information to ascribe a general trend to the results of cyclic testing exists, leading to two general conclusions. The first being, with one prominent exception (15SA), samples with screws tended to displace more than those without. The second is that larger defects tended to displace less than smaller ones (where displacement is always horizontal and at the cement face).



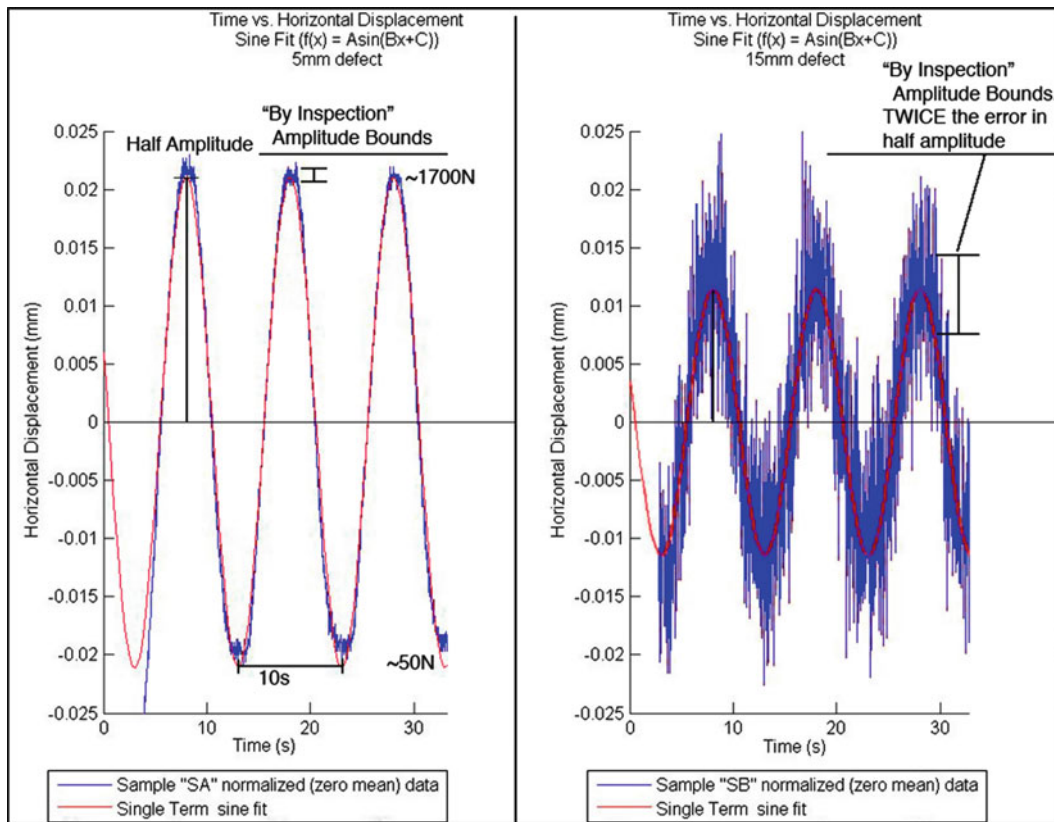


Fig. 3.4 Two examples of sine fit overlaid on raw LVDT displacement data (horizontal)

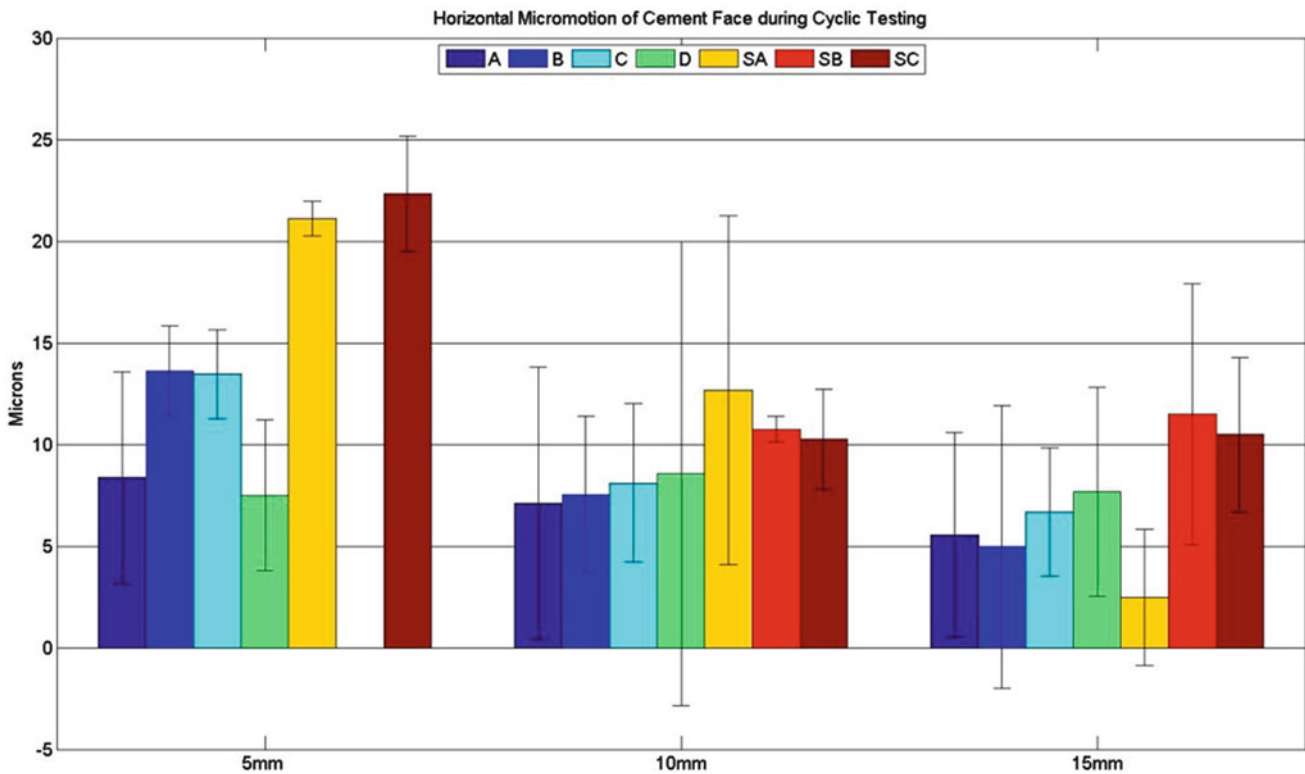
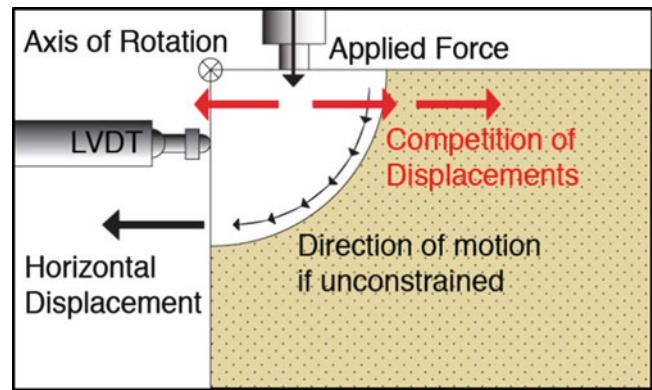
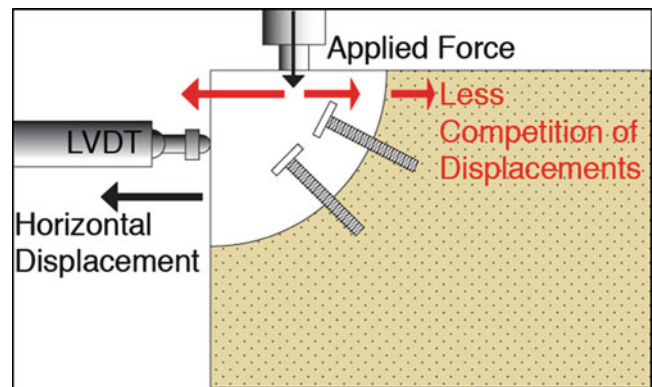


Fig. 3.5 Cyclic results-half amplitude from sine fit with error bar

**Fig. 3.6** Caricature of screw-less test sample cutaway to median



**Fig. 3.7** Caricature of test sample with screws cutaway to median



### 3.3.1.2 Discussion

The foremost conclusion drawn from analysis of measurements taken from the cyclic testing with the LVDT is contradictory to the initial hypothesis. That is, it was expected that samples with screws would displace less than those without, the opposite of what was determined by the measurements. In response, an investigation was launched that aimed to understand these results and potentially to improve the experiment for future work. The preliminary results of this examination are as follows.

Figure 3.6 is a caricature of a screw-less test sample shown, with a few important features illustrated, as it would be during cyclic or compressive testing.

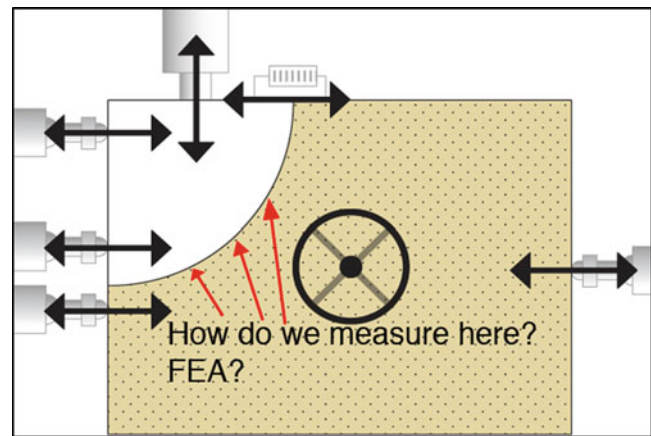
Figure 3.6 is meant to expose two important oversights in the techniques used to measure micro-motion in test samples. The first, and perhaps most apparent, is that the cement filling has a propensity to rotate about a fixed point when loaded at either face (in this case, at the surface), simply due to its curved geometry. Assuming the cement does indeed rotate, it is likely that motion at the cement face falls increasingly outside the measurable range of the LVDT as the rotational axis is approached. That is, motion close to the axis is so minimal as to be absorbed by noise. The LVDT used to measure horizontal displacement was placed lamentably, although often necessarily, near this location.

Second, most materials tend to expand in directions contrary to the applied load when compressed. It is possible that, as the steel actuator compressed the cement, a competition of displacements between the cement and bone occurred (as the bone yielded to the cement's expansion), where each worked effectively to cancel the other's movement. Such an event may have led to diminished displacement at the cement face, even though various movements would have occurred elsewhere within the sample. Although total cancellation almost certainly did not occur (as it does in Fig. 3.6, displacement competition depicted in red), motion at the face may have diminished enough to, again, be immeasurable to the LVDT or otherwise corrupted by this effect.

Conversely, the qualities that may diminish horizontal motion at the cement face or misrepresent aggregate horizontal displacement in screw-less samples are exactly those countered by the presence of screws (Fig. 3.7). That is, the screws help the cement resist rotation, and may reduce the proclivity of the bone to yield to the cement (i.e. strengthening it), forcing the cement to expand outward and into the LVDT as it is compressed, thus eliminating both factors that contribute to diminished motion at the front face.

Thus, it is by nature that the two samples produce results contrary to what was expected. However, it is unknown if in either case motion at the bone/cement interface was transmitted proportionally to the LVDT during experimentation. In other

**Fig. 3.8** Caricature of screw-less sample cutaway to median. Possible test setup shown sine-transparent



words, it is not clear that horizontal displacement at the cement face is representative of interfacial motion (at least in the way assumed by this research).

Accordingly, if this research is pursued, it is highly recommended that motion of the test construct be thoroughly, even redundantly, recorded. It is also imperative that motion across the interface be recorded directly, and it is recommended that this motion be compared to that at faces (if applicable).

A variety of options could be explored to accomplish the measurements necessary to properly characterize a bone/cement construct, particularly with concern to interfacial micro-motion. Preeminently, alternative geometries could be explored, specifically those conducive to inspection of the interface. For, the geometry used in this research makes the regions indicated (by red arrows) in Fig. 3.8 especially difficult to measure.

However, if alternative geometries are not a preferable option, the experiment can still be otherwise performed satisfactorily. For example, by a stereoscopic DIC (digital image correlation) derivative, where cameras are used to record movement in three dimensions. This choice, although likely expensive and extremely data intensive, would mitigate the factors described previously. Furthermore, a DIC technique could be particularly useful in correlating to or validation of a finite element model that is compiled primarily to render the interface. It is highly recommended that, if geometry that obstructs most or all of the interface is adopted in future research, either DIC be performed on the sample or the interface be modeled by FEA (finite element analysis). Ideally, both DIC and a FEA would be performed and correlated.

If neither different geometries nor DIC/FEA are viable options, a setup such as that illustrated in Fig. 3.8 is the final recommendation of the authors. It is most important that that motion across the regions indicated be measured; the particulars of the setup are up to future investigators. However, if “displacement gauges” and LVDT’s are employed, as in Fig. 3.8, it is recommended that they are high resolution, specifically of order one or two microns.

### 3.3.1.3 Motion During Compression Testing

It was previously stated that the presence of screws strengthens the bone, even while leading (indeed, as a result of) to greater motion at the cement face. While this statement cannot be directly proven by data attained during this project, it is clear from data taken during compression testing that the screws perform a strengthening role, but in the *vertical* direction. Compare Figs. 3.9 and 3.10.

Both Figs. 3.9 and 3.10 show data received (from 5 mm samples) during compression testing of the samples (with illustrative markings). Referring to Fig. 3.9, it is clear (indicated in two cases) that, at a given force, samples with screws tend to displace less than those without in the vertical direction. Precisely the opposite is the case in the horizontal direction (Fig. 3.10), indicating that screws add strength in the vertical direction at, apparently, the cost of motion at the lower face. Further, it appears that samples with screws also fail at much higher forces (Fig. 3.9) than those without. Again, indicating that screws augment the integrity of the construct.

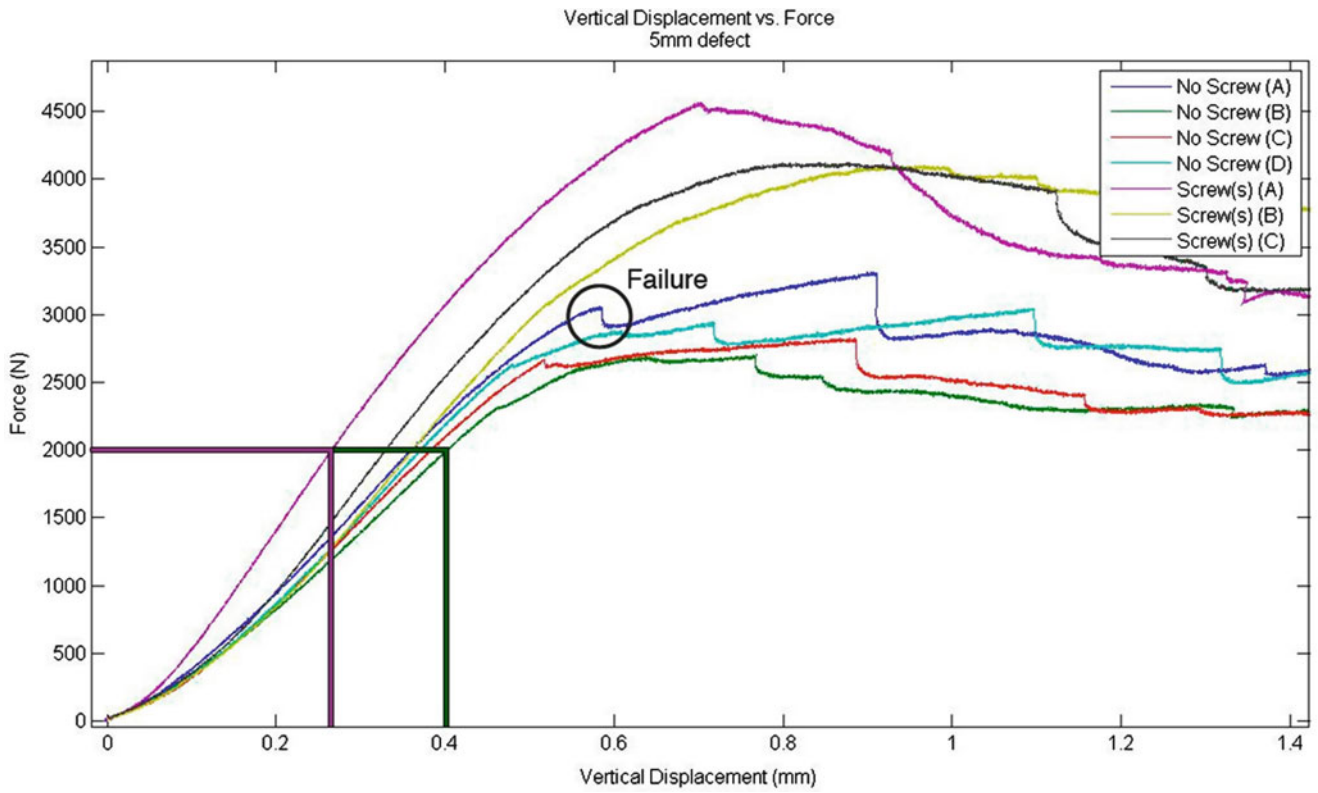


Fig. 3.9 Compression test data: vertical displacement versus force

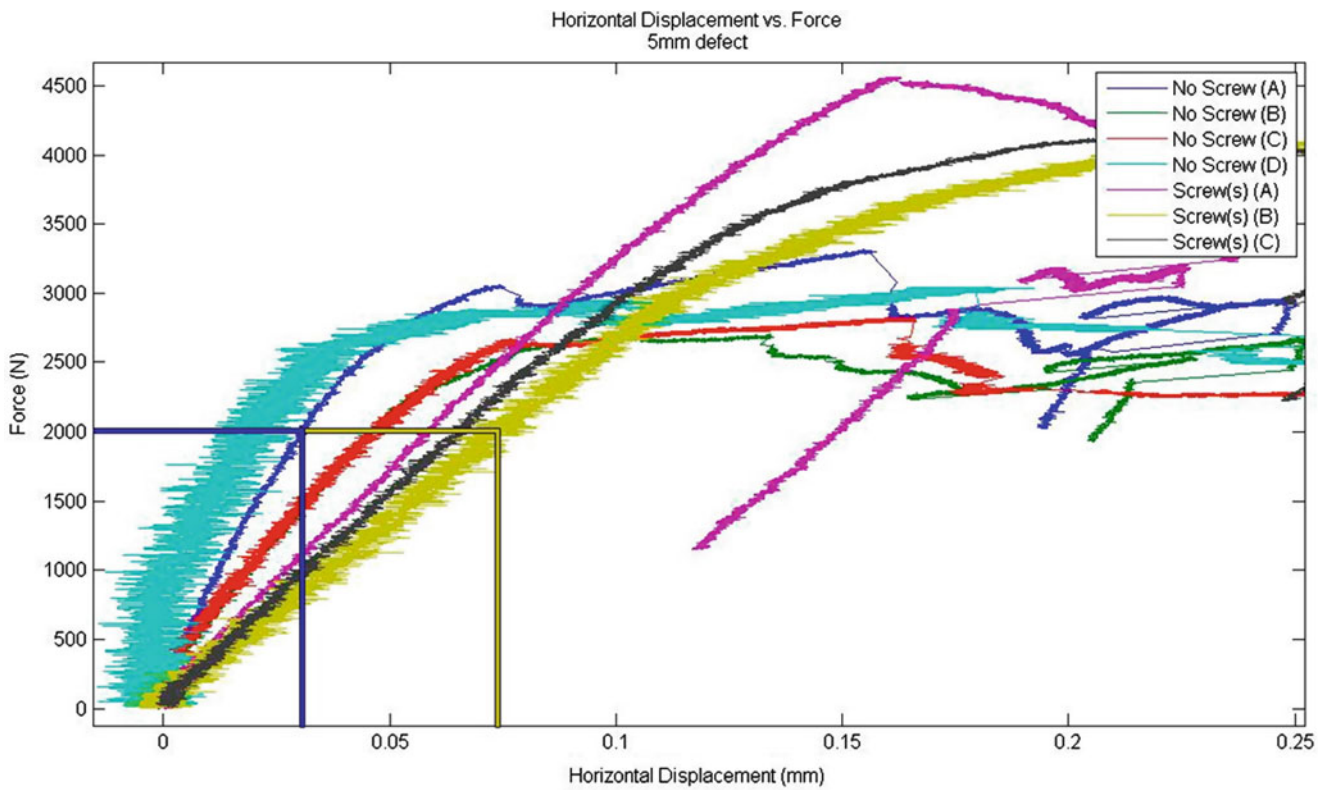
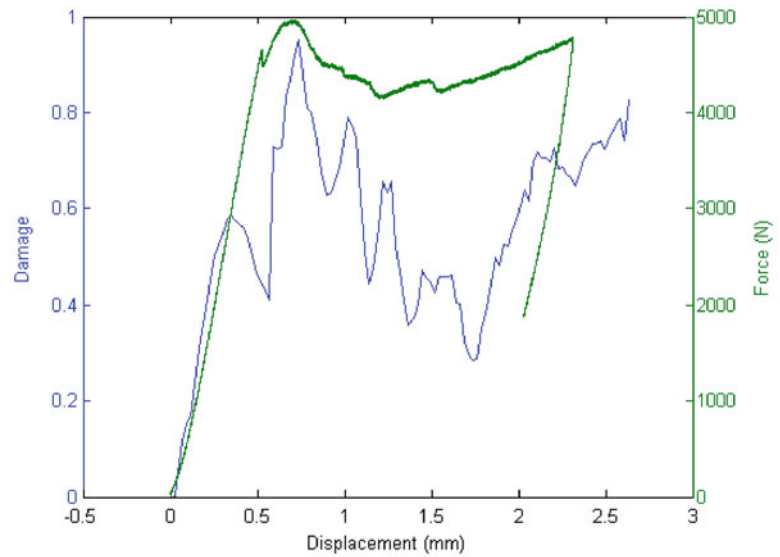


Fig. 3.10 Compression test data: horizontal displacement versus force

**Fig. 3.11** ICMBF method for sample 10A



### 3.3.2 PZT Measurements

The sensor data from the wave propagation during the compression-to-failure tests underwent interrogation in effort to determine how to establish reliable damage metrics. Variations that were produced as loading, and sequentially damage, was incurred includes frequency intensity changes, frequency shifts, and power changes. Thus, various damage metrics were established to analyze these changes. The damage metrics created fall into the following four categories: (1) frequency intensity changes, (2) frequency shifts, (3) power changes, and (4) exponential regression of the Fast Fourier Transform (FFT) data time constant tracking. The objective in creating these damage metrics was to see whether damage could be detected with them, and not necessarily to analyze the quality of each metric. No metric shows maturity adequate to be used in an implant thus far, but most show potential for use in the future.

#### 3.3.2.1 Frequency Intensity Changes

Of the damage metrics developed, two utilized tracking change in the intensity of a given frequency as the compression test proceeded. The first was the Intensity Changes of the Maximum Baseline Frequency (ICMBF) method. This method checks the baseline measurement for the frequency with the greatest intensity. The damage detection metric for the ICMBF method follows (3.1):

$$D_{\text{ICMBF}} = \frac{|A_f - A_{f,\text{baseline}}|}{A_{f,\text{baseline}}} \quad (3.1)$$

In the above equation,  $A_f$  is the intensity at each measurement point of the frequency that had the greatest intensity in the baseline measurement. This metric was computed for each of the samples with wave propagation data and overlaid on the force-displacement graph created by the mechanical test data. Figure 3.11 shows the damage metric and force-displacement curve of Sample 10A.

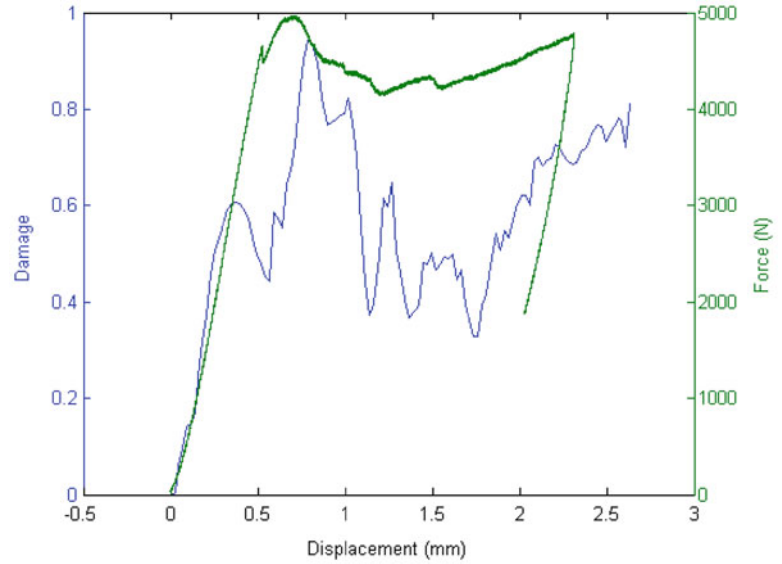
As seen in Fig. 3.11, there is a generally increasing trend in this damage metric for this sample. This was not the case in all samples, but it shows that this metric can sometimes detect damage.

Another damage metric of this type is the Intensity Changes of Drive Frequency (ICDF) method. This method tracks the intensity of the drive frequency, the frequency that the actuator is excited. The formula (3.2) for this damage metric follows:

$$D_{\text{ICDF}} = \frac{|A_{df} - A_{df,\text{baseline}}|}{A_{df,\text{baseline}}} \quad (3.2)$$



**Fig. 3.12** ICDF method for sample 10A



In (3.2),  $A_{df}$  is the amplitude of the drive frequency at each measurement point. This metric was computed for each of the samples with wave propagation data and overlaid on the force-displacement graph created by the mechanical test data. Figure 3.12 shows the damage metric and force-displacement curve of Sample 10A.

Like Figs. 3.11 and 3.12 shows a generally increasing trend in the damage metric for this sample. Again, this was not the case for all samples, but this shows that this metric, too has potential as a damage metric.

Both the ICMBF and ICDF methods show some potential for being able to detect damage, but they are far from robust enough to be used in a medical application.

### 3.3.2.2 Frequency Shifts

Another of the damage metrics explored was that of determining how frequencies shift as the sample is compressed. The Bounded Drive Frequency Shift (BDFS) method was used to analyze the data recorded from each sample. This method finds the highest intensity frequency in the range bounded by the drive frequency plus or minus a deviation value. The deviation value used in this metric for the sawbones data was 10 kHz. The equation for this metric is:

$$D_{BDFS} = \frac{|F_m - F_{m, \text{baseline}}|}{F_{m, \text{baseline}}} \quad (3.3)$$

In (3.3),  $F_m$  is the highest intensity frequency in the range bounded by the drive frequency plus or minus a deviation value of 10 kHz. The BDFS method was computed for each sample and its force-displacement curve was overlaid. Shown below is the BDFS for Sample 5A in Fig. 3.13.

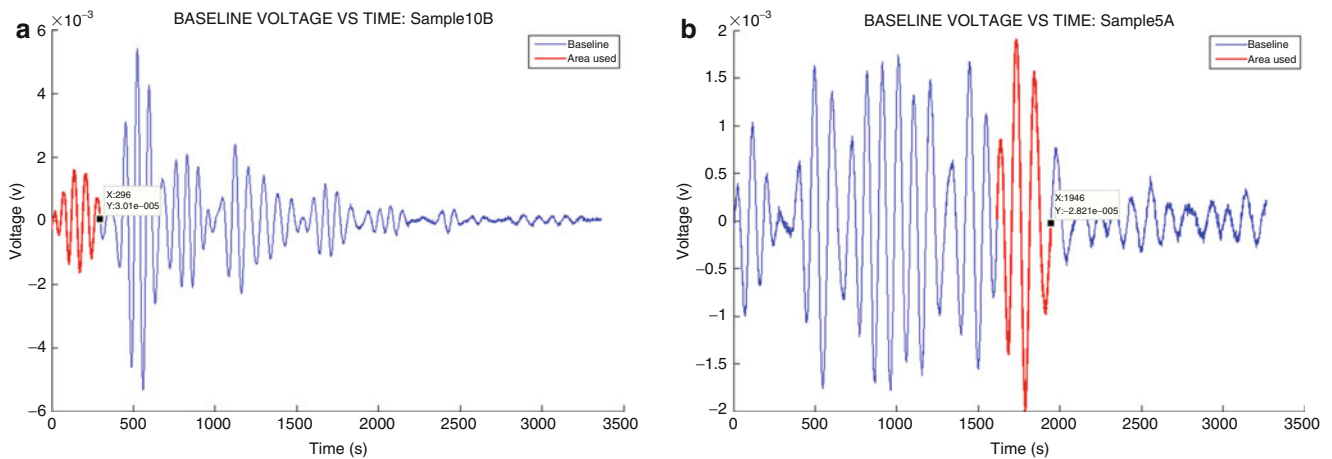
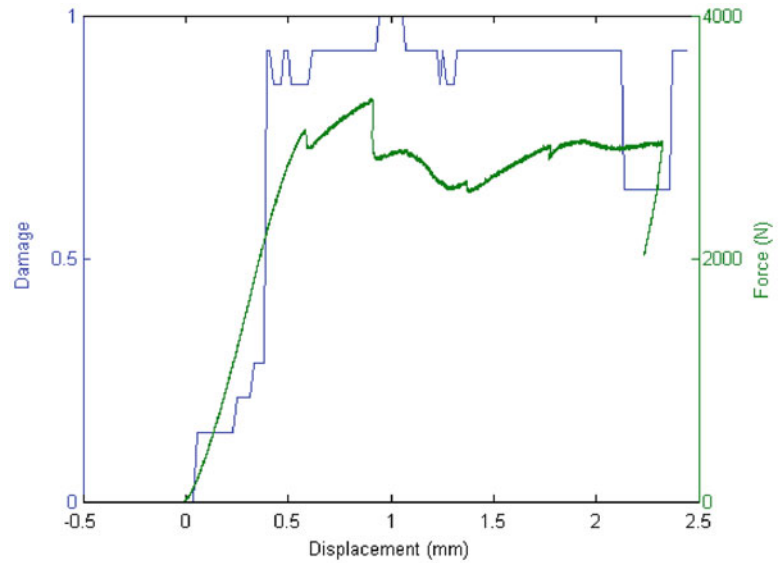
As shown in Fig. 3.13, as damage is about to incur, there is a sudden increase in the BDFS metric. This is useful because it shows damage slightly before failure occurs. Unfortunately, due to the amount of data per run, computation of the FFT produced frequency results of poor resolution, and, thus, caused the shape of the function of Fig. 3.13. Overall, this metric provides some useful information about damage, but the implementation may not be ideal for the medical community.

### 3.3.2.3 Power Changes

The third metric explored was that of looking how power changes in the signal as damage incurred. For this type, a Power Spectral Density (PSD) is computed over a region of the time domain data for each measurement as the sample is being loaded. The area is computed under the PSD curve. The general equation for the PSD metric can be seen below:

$$D_{PSD} = \frac{(|A_{PSD} - A_{PSD, \text{baseline}}|)}{A_{PSD, \text{baseline}}} \quad (3.4)$$

**Fig. 3.13** BDFS method for sample 5A

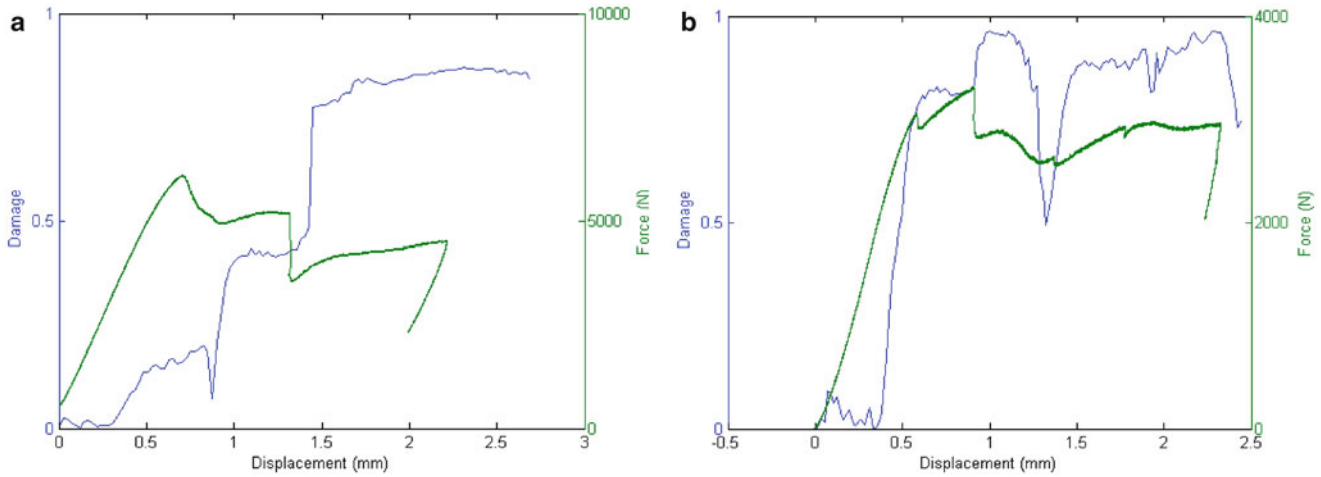


**Fig. 3.14** (a) First packet and (b) Greatest amplitude packet

In (3.4),  $A_{\text{PSD}}$  is the area under the PSD curve for each measurement. The PSD method was computed in two fashions, the first of which is done on the first “packet” of data. This is the most pure signal with the least constructive and destructive interference from reflections. For the sake of consistency, the first four wavelengths are analyzed with this method. How the data was selected can be seen shown in red in Fig. 3.14a. The second PSD method was implemented on the three peaks surrounding the wave in the time domain with the greatest amplitude. Typically, the greatest amplitude in the measurements is due to constructive interference. In theory, this makes our metric more susceptible to detecting small changes. How the data was selected for this method can be seen shown in red in Fig. 3.14b.

The two variations of the PSD metric were computed for each sample and the sample’s force-displacement curve was overlaid, results shown in Fig. 3.15.

Shown in Fig. 3.15a is the PSD metric on the first packet of data. Noticeably, the metric increase as damage occurs. Particularly interestingly, in Sample 5A, each damage site in the force-displacement curve is followed by a steep increase in the damage metric value. This shows that this metric can detect damage. It may not do a good job at detecting the early signs of damage however. Figure 3.15b depicts the PSD metric on the three peaks surrounding the wave of highest amplitude in the time response. Notably the damage metric increases dramatically right before the first sign of damage in the force-displacement curve. Of the techniques explored thus far, the PSD on the three wavelengths about the maximum amplitude wave shows the most potential.



**Fig. 3.15** (a) PSD metric for first packet data of sample 10B and (b) PSD metric for greatest amplitude packet of sample 5A

Overall, the PSD metrics both convey that damage can be detected with the explored methods. Conversely, though damage can be seen, no quantitative evidence has been produced thus far to show the reliability of this method. More analysis is recommended before being used in the medical community.

### 3.3.2.4 Exponential Regression of the Fast Fourier Transform (FFT) Data Time Constant Tracking

An exponential decay was fit through the frequency data from 0 to 5 MHz using a linear least squares (LLS) method. The exponential regression was of the form:

$$Y = A * e^{t/\tau} \quad (3.5)$$

In (3.5),  $\tau$  is the time constant. The time constant when this regression is applied to frequency data is subject to how frequencies are distributed in the frequency domain, the relative amplitude differences amongst those frequencies, and where the dominant frequencies lie in the frequency domain. Notably, all of these factors are worth considering when looking for damage (as seen in methods A, B, and C). Figure 3.16 shows an example of how the exponential regression was fit through the FFT of Sample 10A.

Using (3.6), the damage metric for the Exponential Time Constant (ETC) method is shown:

$$D_{ETC} = \frac{|\tau - \tau_{baseline}|}{\tau_{baseline}} \quad (3.6)$$

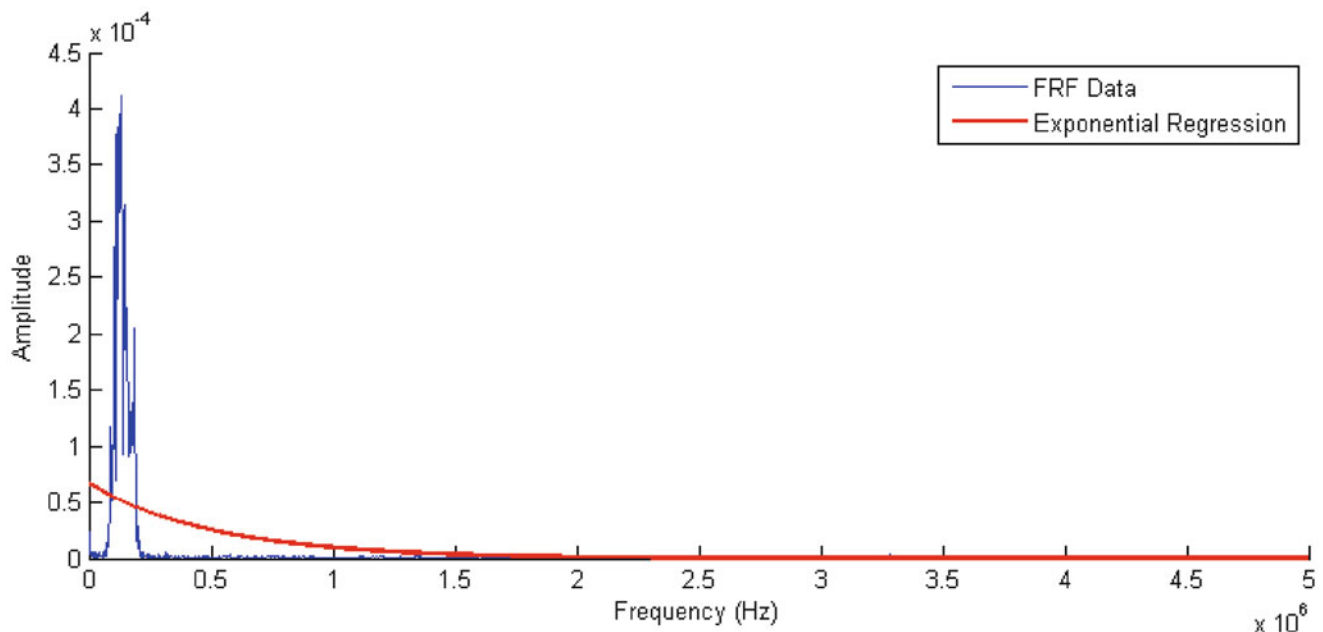
Where  $\tau$ , the exponential time constant, is calculated at each point as the sample is loaded. Shown in Fig. 3.17 is the ETC metric for Sample 10A.

As shown in Fig. 3.17, the ETC metric does show a generally increasing trend as desired in a metric, however, the trend may not serve as the best indicator for the onset of damage. The ETC method is the least understood of the damage detection methods highlighted in this paper, and thus, it is certainly not robust enough for the medical community. With further work, this method may offer some potential.

## 3.4 Conclusions and Recommendations

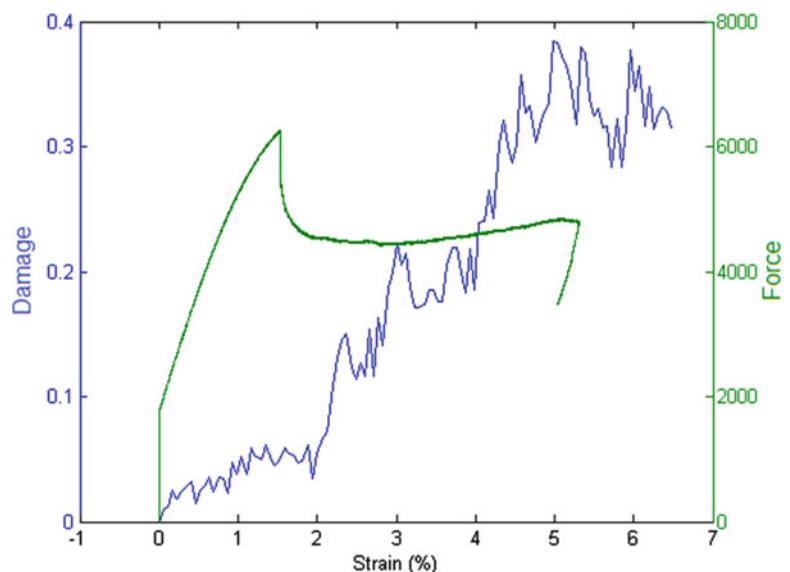
The hypothetical outcome of this research was that bone defects repaired with adjuvant screws would minimize interfacial micro-motion, compared to those without, when loaded in a manner analogous to conditions produced at the surface of the tibia by ambulatory motion, expediting patient recovery. A cyclic test, designed to mimic these conditions, was developed and





**Fig. 3.16** Exponential fit of FFT for sample 10A

**Fig. 3.17** ETC method for sample 10A



executed on the available samples. Contrary to preliminary predictions, the results of this test showed that samples without screws displaced less horizontally than those with. In response, an investigation to determine the origin of these defiant results was performed, from which it was found that the test methodology, along with other possible contributing factors, insufficiently represented motion at the interface. A set of recommendations was compiled to assist in future investigation of this research, the most desirable of which were different sample geometries or a finite element analysis, possibly with experimental validation. Nevertheless, it is believed that adjuvant screws perform a structurally favorable role in bone defects repaired by PMMA cement, particularly at the interface. Although this conclusion is supported by results drawn from cyclic and compression testing, it is not sufficiently to deem further research unnecessary.

As for the damage detection algorithms, no metric shows maturity adequate to be used in an implant thus far, but most show potential for use in the future. Hopefully, this research will stimulate further research towards monitoring the health of knee implants. Like an early warning system, this is in the interest of preventing critical failure of an implant and subsequent emergency surgery. It is the hope that damage detection metrics and classification schemes might one day be adapted for

use with an *in situ* that would reside within a knee implant and broadcast structural health data wirelessly. Such sensors would be non-invasive and alert physicians (and patients) of imminent failure, allowing repair or replacement to occur prior to catastrophic failure.

**Acknowledgements** The authors would like to acknowledge support for this work provided by Los Alamos National Laboratory as part of the Los Alamos Dynamic Summer School. Additionally, the authors extend thanks to Manny Lovato of Materials Science and Technology at Los Alamos National Laboratory for his help and guidance performing the mechanical testing.

## References

1. Ritter M, Harty L (2004) Medial screws and cement: a possible mechanical augmentation in total knee arthroplasty. *J Arthroplast* 19(5):587–589
2. Amer L, Stone B, Warren C, Cornwell P, Meneghini RM (2009) Initial mechanical stability of cementless highly-porous titanium tibial components. In: *Proceedings of the IMAC-XXVII*
3. Inman D, Cudney H (2000) Structural and machine design using piezoceramic materials, a guide for structural design engineers. NASA report, grant no. NAG-1-1998, April 2000
4. Doebling S, Farrar C (1998) A summary review of vibration-based damage identification methods. *Shock Vib Dig* 30(2):91–105
5. Farrar C, Worden K (2007) An introduction to structural health monitoring. *Philos Trans R Soc A* 365(1851):303–315
6. Sohn H, Farrar C, Hemez F, Shunk D, Stinemas D, Nadler B, Czamecki J (2004) A review of structural health monitoring literature: 1996–2001. Los Alamos National Laboratory report, LA-13976-MS

# Chapter 4

## Development of a Bench for Testing Leg Prosthetics

H. Giberti, F. Resta, E. Sabbioni, L. Vergani, C. Colombo, G. Verni, and E. Boccafogli

**Abstract** The present paper deals with the development of a bench for testing prostheses for legs. The bench includes a fake leg (from femur to foot) and it allows rotations of femur (up to  $40^\circ$ ) and of tibia with respect to femur (up to  $40^\circ$ ). Lockable gas springs allow stopping tibia and femur rotations. An hydraulic actuator applies a load to the hip, while a sled driven by an electric motor moves the foot simulating walking. Attachment between foot and sled has been designed to allow load transfer from heel to forefoot. Once maximum rotations for tibia and femur are reached, the leg is lifted and swings. As a first application, the test bench will be used to test transtibial prosthetics, including the knee socket, but it has been designed so that it could allow testing, with a limited number of adjustments, also transfemoral, foot and ankle prosthetics.

Design of test bench components and definition of control strategy for moving and synchronizing actuators, has been achieved through co-simulation of a Multi-Body model of the bench developed using ADAMS/View and a model of the control system and actuation devices developed using MatLab/Simulink.

Results of preliminary experimental tests on a transtibial prosthesis are shown.

**Keywords** Transtibial prosthetics • Lower-limb amputee • Test bench design • Multi-body model • Co-simulation

### 4.1 Introduction

The present paper deals with the development of a bench for testing prostheses for, which is carried out within a research project supported by the centre for testing and application of prosthetics and orthopaedics of INAIL (Istituto Nazionale per l'Assicurazione contro gli Infortuni sul Lavoro-Italian National institute for industrial insurance). The test bench includes a fake leg constituted by elements reproducing femur, tibia, ankle, foot, knee and knee socket (Fig. 4.1). Aim of the bench is to test prostheses considering working conditions more similar to real ones with respect to methodologies provided by standards [1, 2], although, as it will be explained later on, it doesn't completely reproduce walking. Moreover, while standards provide methodologies for testing a single prosthesis type (foot, ankle, etc.), the proposed bench would allow to contemporarily test prostheses for different parts of the leg with a few adjustments.

In this paper the design of the test bench is discussed, considering its application to transtibial prostheses used by lower-limb amputees (Fig. 4.2). The bench has therefore to guarantee the sequential replication of loads on the prosthesis and it has to reproduce relative rotations between femur and tibia during walking, also allowing the adaptability to different patients.

A series of assumptions have been made in the test bench design:

- Although the movement of the leg is a 3D motion, only the plane of walking is taken into account (sagittal plane). Loads and stresses in the other two planes (frontal and transversal) are indeed neglected, since reasonably lower. Under this assumption, the structure undergoes a bi-dimensional loading system;

---

H. Giberti • F. Resta • E. Sabbioni (✉) • L. Vergani • C. Colombo

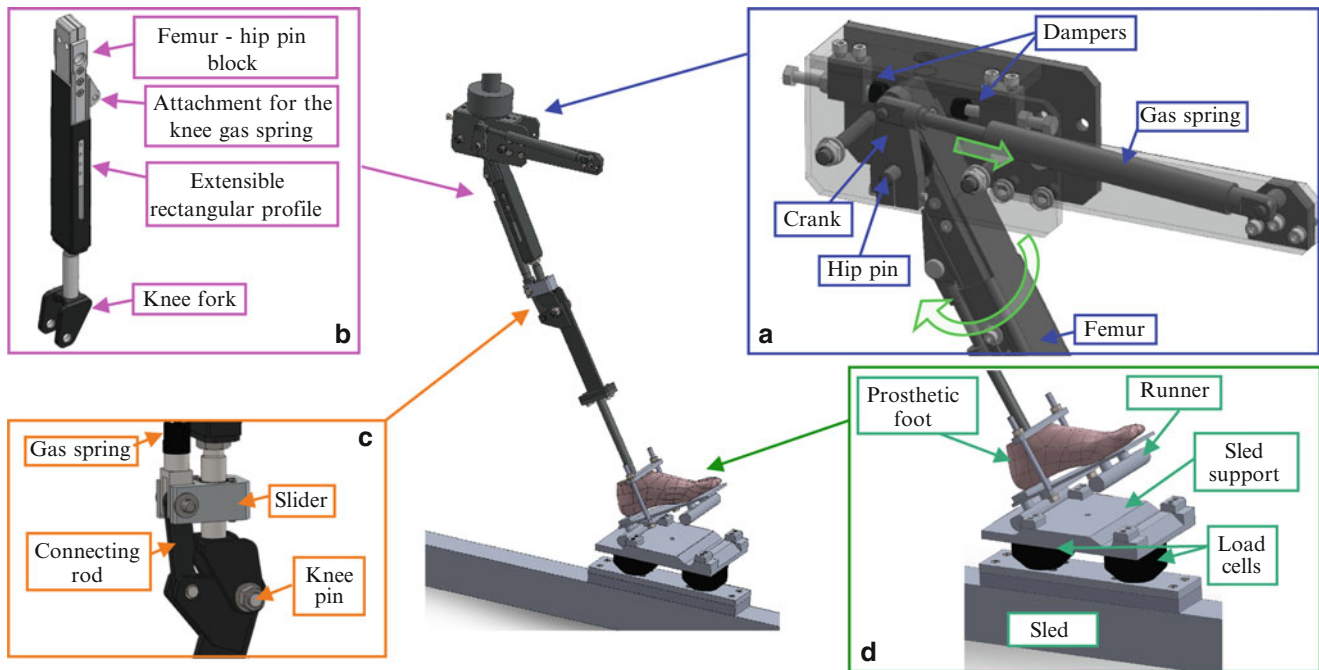
Department of Mechanical Engineering, Politecnico di Milano, Via La Masa 1, Milan, MI 20156, Italy

e-mail: [hermes.giberti@polimi.it](mailto:hermes.giberti@polimi.it); [ferruccio.resta@polimi.it](mailto:ferruccio.resta@polimi.it); [edoardo.sabbioni@polimi.it](mailto:edoardo.sabbioni@polimi.it); [laura.vergani@polimi.it](mailto:laura.vergani@polimi.it); [chiara.colombo@polimi.it](mailto:chiara.colombo@polimi.it)

G. Verni • E. Boccafogli

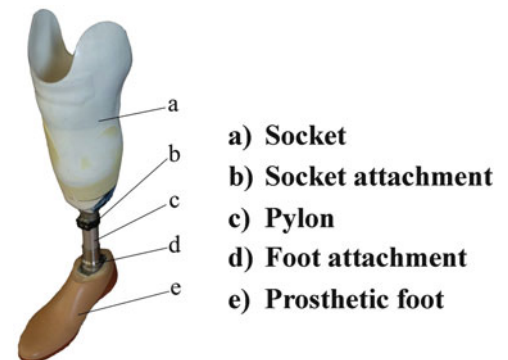
INAIL, Centro per la sperimentazione ed applicazione di protesi e presidi ortopedici, Via Rubina 14, Vigorso di Budrio, BO 40054, Italy

e-mail: [g.verni@inail.it](mailto:g.verni@inail.it); [e.boccafogli@inail.it](mailto:e.boccafogli@inail.it)

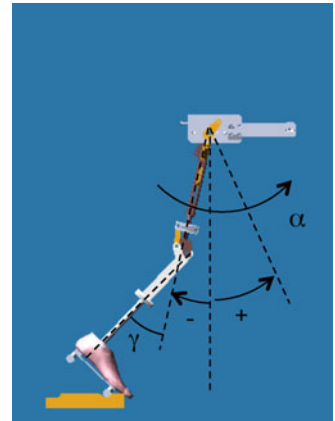


**Fig. 4.1** Assembly of the test bench and some of its details: (a) hip assembly; (b) femur; (c) knee system; (d) foot and sledge joint

**Fig. 4.2** Components of a transtibial prosthesis



- Despite hip and knee can be regarded as roto-translational joints, they are introduced in the test bench as revolute joints (i.e. hinges);
- No relative rotations between tibia and foot are allowed since, generally speaking, in transtibial prostheses used by lower limb amputees, the prosthetic foot is clamped to the pylon reproducing tibia and fibula bones;
- Hip can only move along vertical direction. This assumption implies that motion of leg parts can only be achieved by imposing a motion to the foot. As it will be explained later on, motion of the hip and the load acting on it (reproducing the patient weight) are applied by an hydraulic actuator, while the foot is moved by a sled driven by an electric motor. This assumption represents a significant difference with respect real walking, even if reproduction of relative rotations between leg components is allowed;
- Rotations of femur (angle  $\alpha$ ) and of tibia respect to femur (angle  $\gamma$ , see Fig. 4.3) are applied one after the other, while during real walking, they take place simultaneously;
- Femur rotations (angle  $\alpha$ , see Fig. 4.3) in the range  $[-10^\circ; 30^\circ]$  and rotations of tibia respect to femur (angle  $\gamma$ , see Fig. 4.3) in the range  $[0^\circ; 30^\circ]$  are considered (in amplitude). Although literature gait analysis [3] and experimental tests performed at INAIL labs have shown that femur rotation varies from  $30^\circ$  at the beginning of the stance phase to  $-10^\circ$  before the beginning of the swing phase, and that tibia-femur relative rotation (angle  $\gamma$ , see Fig. 4.3) is almost zero during the stance phase, but reaches values of approximately  $60^\circ$  in amplitude before the swing phase, largest stresses in the prosthetic components are reached during the stance phase, this justifying the selected range for angles  $\alpha$  and  $\gamma$ .

**Fig. 4.3** Angles and conventions

## 4.2 Design of the Test Bench

Figure 4.1 shows the test bench designed under the assumptions reported in the previous section. Motion and load conditions to the fake leg are provided by a hydraulic actuator and a sled driven by an electric motor. The hydraulic actuator drives the vertical motion and the vertical load applied to the hip. The sled instead provides the foot motion.

Components of the test bench can be divided between passive and active.

Passive components are:

- A rectangular profile reproducing the femur (Fig. 4.1b). It has a variable length between 350 and 450 mm, corresponding to lengths ranging between the 50% percentile of women and 95% percentile of men;
- The knee articulation mechanism connecting femur and tibia. This mechanism must be included inside the reproduction of an amputee stump fitting the knee socket, to allow its testing. Dimensions of the mechanism must thus be limited since, in the knee region the geometry of the amputee stump decreases and the maximum allowed section is  $80 \times 80 \text{ mm}^2$ ;
- A continuous pylon representing the tibia, bolted at the desired length;
- The prosthetic foot, bolted to the tibia;
- The attachment of the prosthetic foot to the linear sled (runner, Fig. 4.1d). The foot is clamped in a structure including a platform connected with two semi-cylinders. Contact occurs between the semi-cylinders and the sled support. This attachment is needed to allow the sled to hook and drag the foot. Geometry of attachment has partially been inspired by ISO-10328 [1]. At the beginning of gait, contact occurs only on the rear cylinder (i.e. the heel), then it moves to the front one (i.e. the forefoot). Distance between the two regions has been defined according to ISO-10328.

All the above components can be replaced with the prostheses to be tested. In particular, in the application considered in this paper, tibia is replaced by a transtibial prosthesis, including the knee socket.

Active elements of the bench needed to provide the desired motion and load conditions to the prostheses to be tested are:

- An hydraulic actuator is attached one side to the hip and the other to a fixed frame. As already mentioned, it drives the vertical motion of the hip and the load applied on it. Load is provided in agreement with ISO-22675 [2] and it depends on the leg positions during walking. A load cell measures the force provided by the hydraulic actuator, while a LVDT measures its displacement;
- A lockable gas spring between hip and femur. The air spring can be locked pressing an on-off button. An automatic system constituted by a small hydraulic piston has been designed and interfaced with the control logic to commute the air spring condition from locked to unlocked and viceversa during the work cycle. When the air spring is locked, femur rotations are prevented, while when it is unlocked femur rotations are allowed (Fig. 4.1a);
- A lockable gas spring between femur and tibia. The air spring acts on a kinematic mechanism consisting of a slider, with an axial bearing, and a connecting rod, which allows relative rotations between tibia and femur (Fig. 4.1c). This mechanism has been design to fit the morphology of the socket. In the knee region, in fact, the geometry of the amputee stump decreases and it allows only limited dimensions for the components to be used (maximum section  $80 \times 80 \text{ mm}^2$ ). When the air spring is locked, relative rotations between knee and femur are blocked.
- A sled moving on a linear guide driven by an electric motor. Length of the linear guide is 1.5 m to reach the desired rotations of the leg parts. The linear guide has been selected on the basis of the maximum vertical load that must be applied to the leg (2,600 N during static tests). On the sled are placed two load cells placed in correspondence of the semi-cylinders of the foot platform.

All rotating elements, such as hip and knee pins, are provided with bushings.

Dimensions of mechanical components are obtained considering structural integrity both for static loads and infinite fatigue life.

To select the electric motor driving the sled, the hydraulic actuator and the gas springs and to evaluate the loads of the elements constituting the test bench for their dimensioning, a Multi-Body model of the test bench has been developed.

### 4.3 Model of the Tests Bench

Selection of the actuators and assessment of the capability of the designed test rig of simulating the work cycle for fatigue tests (i.e. a step) has been achieved through co-simulation of a Multi-Body (MB) model of the test bench, implemented in ADAMS/View environment, and a model of the control strategy including actuating devices (hydraulic actuator, electric motor and gas springs), implemented in MatLab/Simulink environment. The control strategy has been developed in MatLab/Simulink environment to be directly transferred on the Real-Time (RT) board driving the actuators of the test bench.

Figure 4.4 shows the mechatronic MatLab/Simulink model; the ADAMS\_sys block represents the MB model of the test bench developed using ADAMS/View: inputs of the MB model are the torque provided by the electric motor driving the sled, the force provided by the hydraulic actuator moving the hip and the forces provided by the gas springs. Outputs of the MB model are the electric motor angular speed (from which the position of the sled is derived) and force and displacement of the hydraulic actuator, i.e. the measurements carried out on the test bench. During co-simulation, the MB model of the test bench and the model of the control logic and of the actuating devices run at the same time exchanging inputs and outputs values at predefined time steps.

In the following, the two co-simulating models are described.

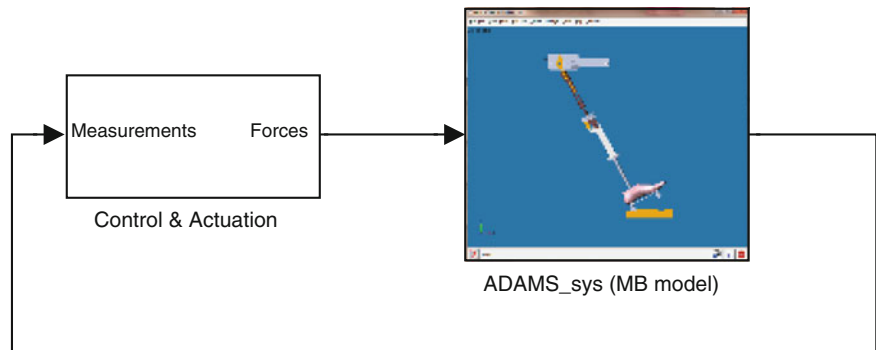
#### 4.3.1 MB Model of the Test Bench

The MB model of the test bench is shown Fig. 4.5. A 3D model has been considered, to account for actual contact geometry between foot and runner. Further developments in fact include the study of different solutions for the foot runner to improve reproduction of foot-ground contact.

Contact forces between foot and runner and between runner and sled have been modeled using the function CONTACT [4, 5]. Making reference to Fig. 4.6, normal contact force is calculated according to:

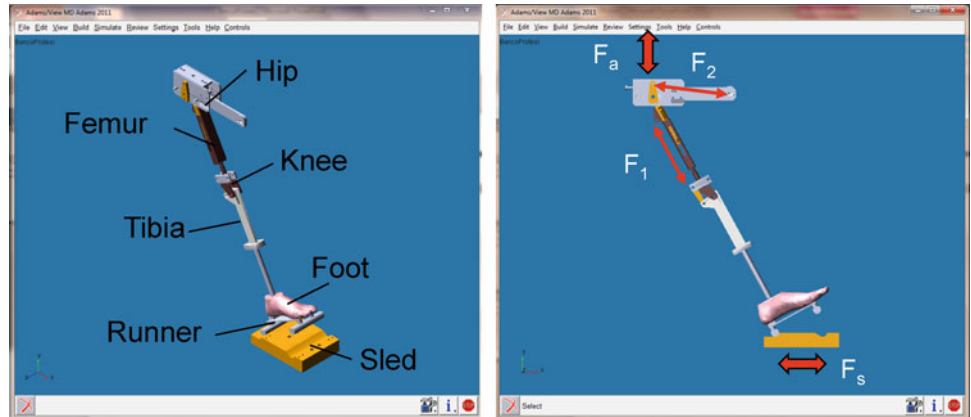
$$F_n = \begin{cases} k \Delta x^n + c (\Delta x) \Delta \dot{x} & x < a \\ 0 & x \geq a \end{cases} \quad (4.1)$$

Normal component of contact force is equal to zero when there isn't penetration between the bodies (i.e. there is no contact between the bodies). When bodies get in contact, force is given by an elastic and a damping contribution. The elastic component is proportional to the penetration  $\Delta x$ . Exponent  $n$  is called penalty factor. To avoid discontinuities, the damping coefficient  $c$  is increased from zero to its maximum value through a cubic law (Fig. 4.7a).

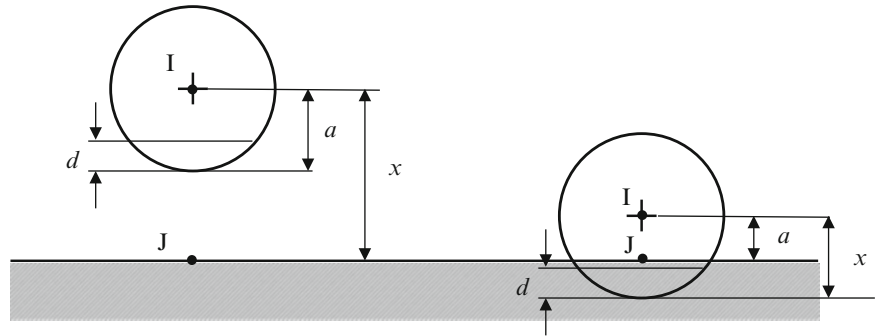


**Fig. 4.4** Mechatronic model for co-simulation

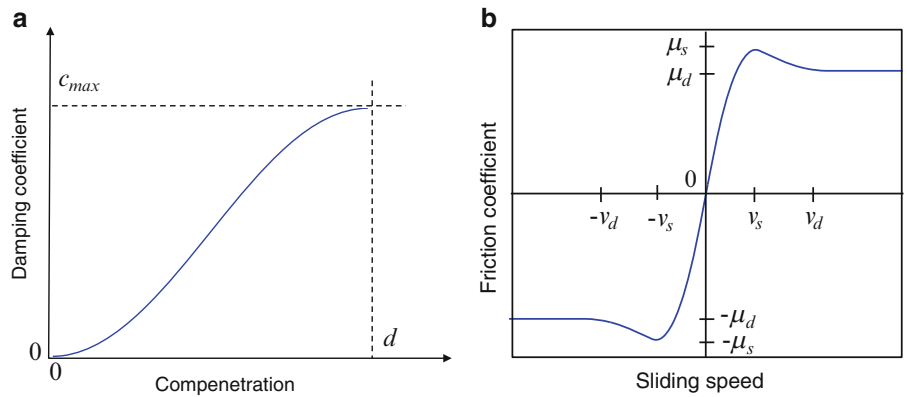
**Fig. 4.5** MB model of the test bench



**Fig. 4.6** Scheme for normal contact force calculation



**Fig. 4.7** (a) Damping coefficient vs. penetration; (b) Friction coefficient vs. sliding speed



The tangential contact force is defined according to Coulomb law:

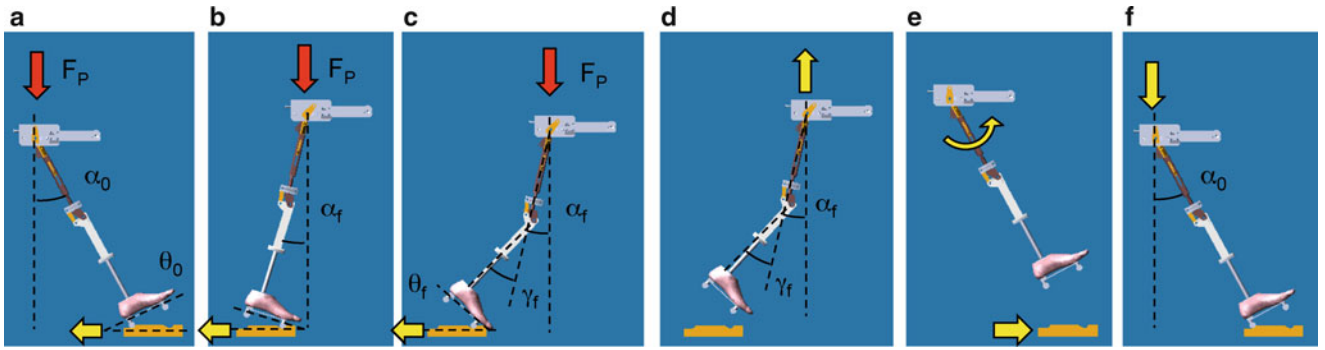
$$F_t = \mu (v_{slip}) F_n \tag{4.2}$$

The friction coefficient is a function of the sliding speed as shown in Fig. 4.7b. Joints compliance is included into the model.

### 4.3.2 Control Strategy and Model of the Actuating Devices

#### 4.3.2.1 Model of Actuating Devices

The hydraulic actuator (force  $F_a$ , see Fig. 4.5) driving the motion of the hip is modeled through the following equations ([6]):



**Fig. 4.8** Phases of the work cycle

$$\begin{cases} F_a = p_L A \\ \frac{V_0}{2\beta} \dot{p}_L + C^* p_L = K_q x_v - A \dot{y}_a \end{cases} \quad (4.3)$$

where  $p_L$  is the pressure drop across the piston rod,  $F_a$  is the force provided by the actuator,  $\beta$  is the bulk modulus of the oil,  $K_q$  is the servo-valve flow gain coefficient,  $C^*$  is the servo-valve total flow pressure coefficient,  $A$  is the piston area,  $V_0$  is the volume of the hydraulic actuator chamber,  $x_v$  is the displacement of the spool valve and  $y_a$  is the displacement of the piston rod.

Dynamics of the electric motor driving the motion of the sled has instead been introduced by means of a first order time lag.

Finally, gas springs between hip and femur and between femur and tibia (forces  $F_1$  and  $F_2$ , see Fig. 4.5) are modeled as follows:

$$F_i = \begin{cases} F_{Preload} & \text{locked} \\ k_i \Delta l_i & \text{unlocked} \end{cases} \quad (i = 1, 2) \quad (4.4)$$

When the gas spring is locked, it provides a constant force  $F_{Preload}$ . On the contrary, when the gas spring is unlocked, it provides an elastic restoring force ( $k_i$  is the spring stiffness, while  $\Delta l_i$  is the spring deflection).

### 4.3.2.2 Control Logic

The control strategy has been developed assuming the following measurements:

- Force and displacement of the hydraulic actuator driving the hip motion;
- Angular speed of the electric motor driving the sled.

From this latter measurement, position of the sled is derived.

In this preliminary stage of the research, these measurements are the only available on the test bench. As a further development, sensors able to measure actual femur and tibia rotations will be added.

In the following, the phases of the developed control strategy are schematically described making reference to Fig. 4.8. As it will be explained later on, phases are triggered based on the position of the sled. Preliminary simulations have been carried out to identify the sled positions correspondent to the desired rotations of femur and tibia. At the purpose, it is worth remembering that aim of the test bench is not the complete reproduction of walking and rotations of femur and tibia are not simultaneous, but they are applied one after the other.

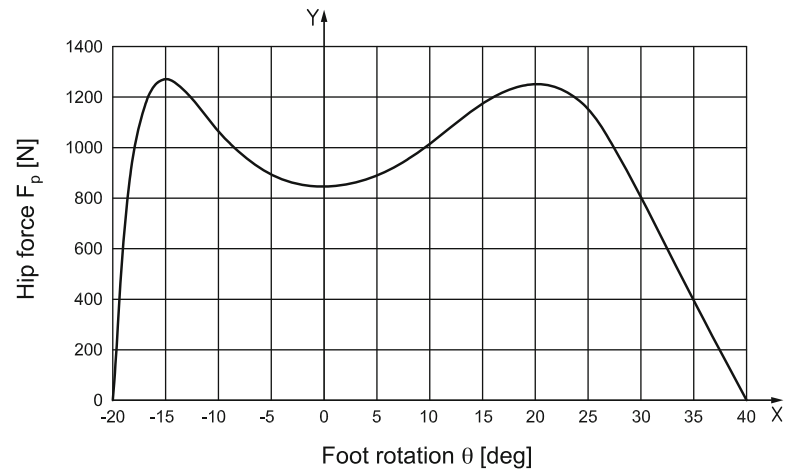


---

Phase 1 (Fig. 4.8a, b)	<p>In the initial condition, no load is applied from the hydraulic actuator, femur is rotated of an angle <math>\alpha_0 = 30^\circ</math>, there is no relative rotation between femur and tibia (Fig. 4.8a), sled and foot runner are in contact and the sled stands still. Then the sled is accelerated dragging the foot runner and rotating the femur clockwise. To allow femur rotation the spring between hip and femur is unlocked (force <math>F_2</math>, see Fig. 4.5). The phase ends when the sled reaches the position correspondent to the final rotation of femur <math>\alpha_f = -10^\circ</math>.</p> <p>During this phase and the following, the hydraulic actuator provides a force according to ISO 22675 (see Fig. 4.9, [2]). At the purpose, the force provided by the hydraulic is controlled in feedback by means of a PID regulator acting on the servo valve position <math>x_v</math>. The scheme of the force feedback control is shown in Fig. 4.10.</p> <p>During this phase, there is no relative rotation of tibia with respect of femur. This is achieved by locking the gas spring placed between femur and tibia (force <math>F_1</math>, see Fig. 4.5).</p>
Phase 2 (Fig. 4.8c)	<p>Once the sled has reached the position correspondent to the femur rotation <math>\alpha_f</math>, the gas spring placed between femur and tibia is unlocked to allow knee rotations. Any further rotation of femur is instead prevented by a bumpstop. As already mentioned, even during this phase, the hydraulic actuator provides a force according to ISO 22675. Phase 2 ends when the sled reaches a position correspondent to a relative rotation between tibia and femur equal to <math>\gamma_f = 30^\circ</math>.</p>
Phase 3 (Fig. 4.8d)	<p>The leg is lifted and the sled is stopped. To prevent rotations of femur and tibia, both the gas springs are locked. During this phase, hydraulic actuator control is switched from force to displacement feedback. The scheme of displacement feedback control is shown in Fig. 4.11.</p> <p>Displacement feedback control is applied also in the next 3 phases.</p>
Phase 4 (Fig. 4.8e)	<p>Once the leg is completely lifted, both the gas springs are unlocked. Thus the leg swings and, after oscillations have extinguished, it gets back to the initial condition, i.e. rotation of femur equal to <math>\alpha_0 = 30^\circ</math> and no relative rotation between femur and tibia.</p> <p>Meanwhile the sled is accelerated to return to the initial position. Once the sled has reached its initial position, it is stopped.</p>
Phase 5 (Fig. 4.8d)	<p>The leg is brought down till the foot runner returns in contact with the sled.</p> <p>The gas spring placed between femur and tibia is locked.</p> <p>Then hydraulic actuator control is switched from displacement to force feedback and the work cycle re-starts from phase 1.</p>

---

**Fig. 4.9** Reference hip force vs. foot runner rotation



## 4.4 Simulation Results

Figure 4.12 shows the results of the implemented model during one working cycle, i.e. one step.

The hydraulic actuator force and displacement, the contact force at the foot runner-sled interface, rotations of femur and foot runner and relative rotation between femur and tibia are depicted versus the work cycle percentage. Number of phases is also reported.

Transition from force to displacement feedback control of the hydraulic actuator is clearly visible after the end of phase 2.

As it can be seen, almost half of the cycle (contrarily to real gaits) is used to lift the leg, let it swing and get it back to the initial position.

Relative rotation between femur and tibia reaches a maximum value of  $30^\circ$ , while the foot rotates of  $75^\circ$  (from  $-30^\circ$  to  $45^\circ$ ). These values are coherent the ones prescribed for prosthetics tests [2] and the ones collected during amputees gait analysis [3].

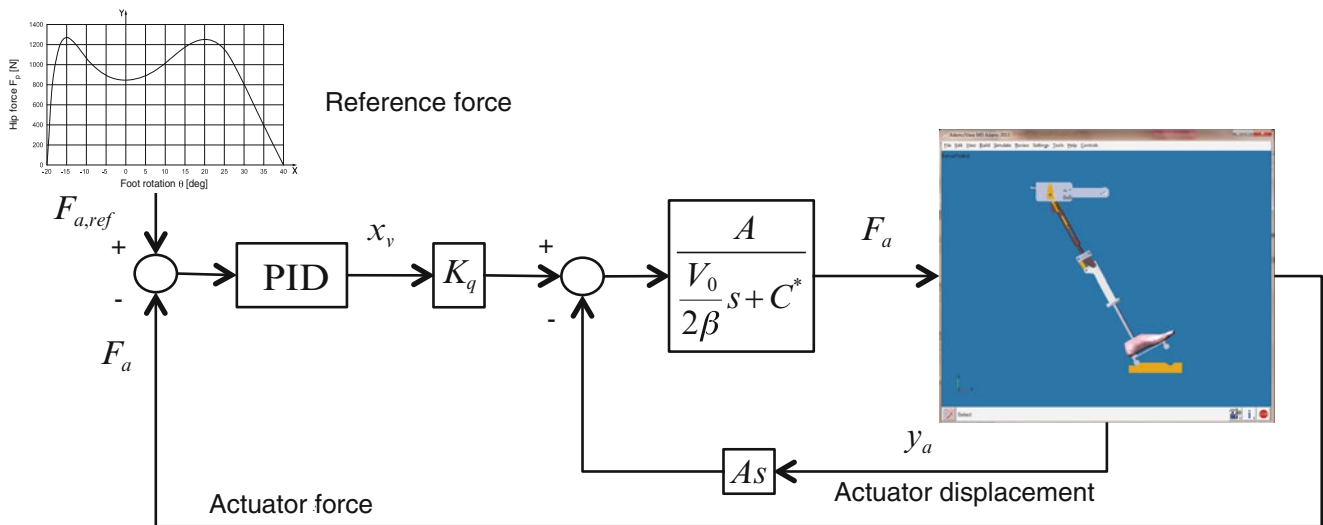


Fig. 4.10 Feedback control of hydraulic actuator force

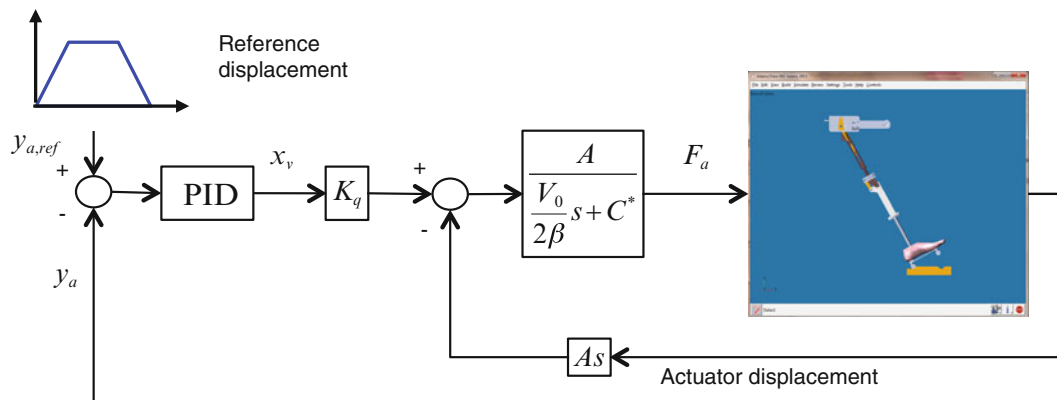


Fig. 4.11 Feedback control of hydraulic actuator displacement

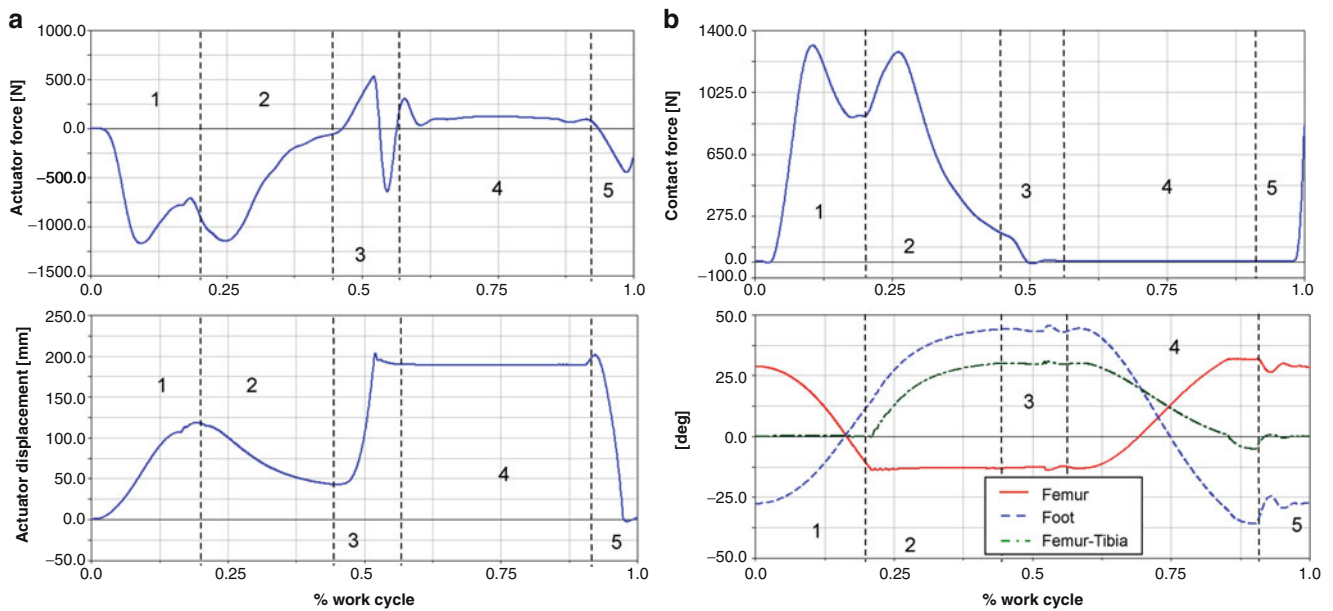
Even foot-sled contact force is coherent with the one indicated in ISO 22675 [2]. Transition from heel to forefoot contact can be clearly seen in the last part of phase 1.

Actuators have been selected to allow the execution of the complete work cycle in 1 s, almost the duration of one step.

## 4.5 Preliminary Experimental Results

The developed model allowed to select the actuators for the test bench (electric motor, hydraulic actuator and gas springs) and to implement the control logic to driving the motion of the test bench elements. Then a prototype of the test bench has been built (Fig. 4.13).

Preliminary experimental tests have been carried out on a transtibial prosthesis. Thus, the element representing the tibia has been modified to fit the knee socket (Fig. 4.2). At the purpose, based on a 3D scan of the amputee stump, coverage for the tibia (cut in correspondence of the amputation level) has been built. The gap between coverage and the stump has been filled with polyurethane foam, to simulate the muscular tissues. For this reason, a mould for the stump was developed, as well as a system to hang the tibial structure. It must be stressed that the knee mechanism, as already mentioned, is included inside the foam coverage, which fits the knee socket. Thus when rotations between femur and tibia occur, both the foam coverage and the knee socket are bended, similarly to real walking conditions. This is of course essential for properly testing the knee socket.



**Fig. 4.12** (a) Hydraulic actuator motion and displacement vs. work cycle percentage; (b) Contact force and femur, foot and femur-tibia relative rotations vs. work cycle percentage

**Fig. 4.13** Test bench



Figure 4.14 shows the different steps of design and production stages of the component. In Fig. 4.14a a 3D image of the complete structure is shown: foam has to fit the stump shape and to allow movements of the structure. Foam thickness has been chosen in order to have a higher stiffness in correspondence of the most stressed contact points: during stance phase the stump is pressed against the socket in correspondence of the knee stressing in particular the lower patellar region and the popliteal fossa, while during the swing phase, the socket is hanged to the condyle regions. In Fig. 4.14b the mould and the positioning of the structure is shown, before foam casting. Figure 4.14c shows the obtained stump, which is joined to the rest of the designed structure of the test bench (Fig. 4.14d).

**Fig. 4.14** (a) Design of the tibial coverage to fit the stump shape; (b) Placement of the tibial structure in the mould; (c) Obtained artificial stump; (d) Test bench in the final configuration

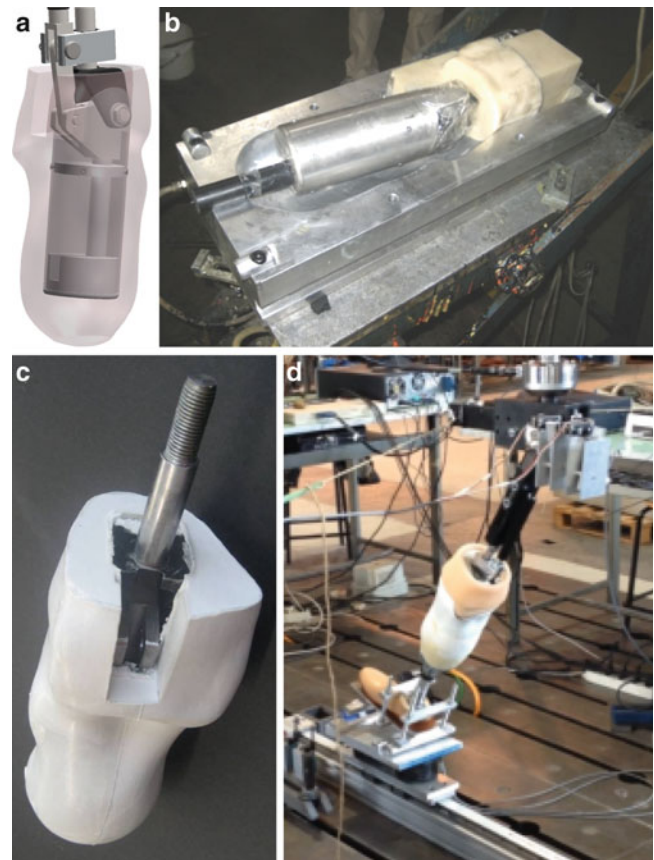


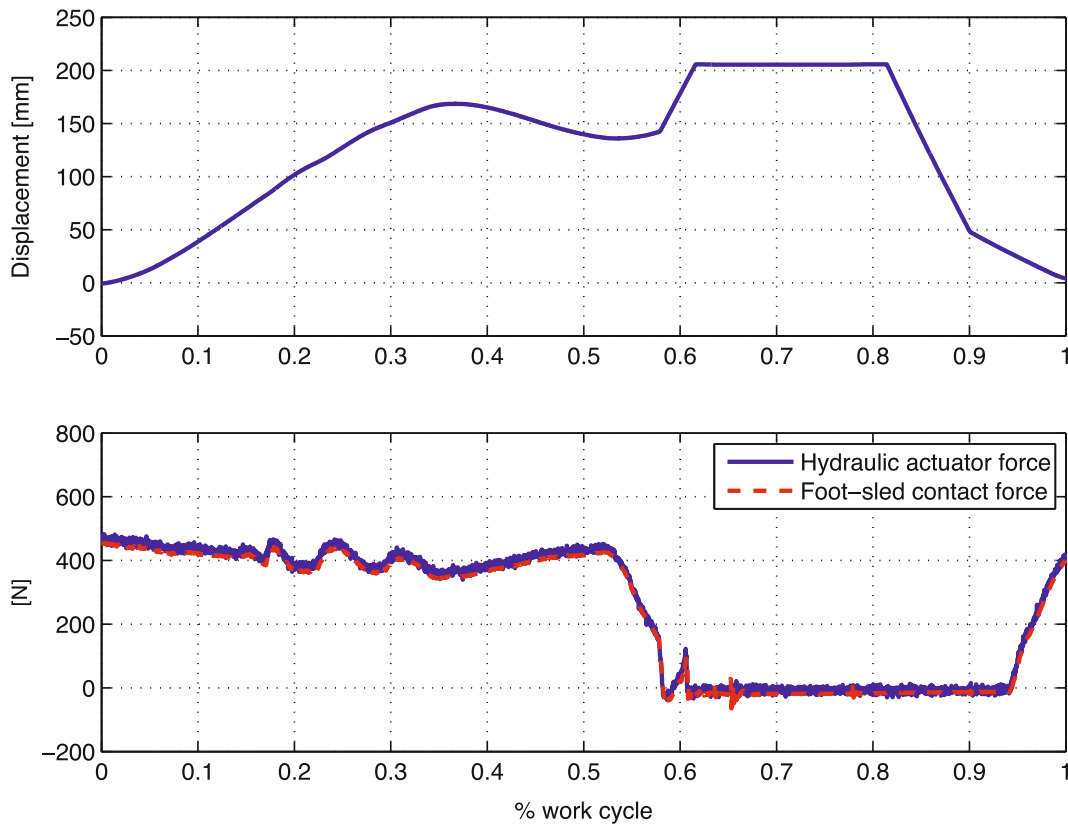
Figure 4.15 shows the results of preliminary experimental tests. A work cycle (i.e. one step) is performed, according to the control logic previously described. It is to point out that, during the experimental test, load on the hip is maintained constant, while in the previously described work cycle it was varied according to ISO 22675. Hydraulic actuator displacement and force are reported as a function work cycle percentage. The hydraulic actuator force is compared, in the lower part of the figure, with the foot-sled contact force (dashed line), obtained by summing up the measurement provided by the two load cells placed in the sled support.

As it can be seen, contact force and hydraulic actuator force are in good agreement and force feedback control is able to maintain a constant load on the hip while the sled is moved. About the 40% of the cycle is used for lifting and lowering the leg and for the swing phase. With respect of the simulated cycle the stance phase is thus longer.

## 4.6 Concluding Remarks

The design of a test bench for testing prostheses for legs has been presented in this paper. The test bench is constituted of a fake leg (from femur to foot). Hip motion and load are provided by a hydraulic actuator, while the foot is moved by a sled driven by an electric motor. Lockable gas springs block/allow femur rotations and femur-tibia relative rotations. In order to properly select actuators and to dimension test bench components, a model of the bench as been implemented. It is constituted of a MB model of the fake leg, a model of the actuating devices and the control logic regulating the leg motion.

After assessed the test bench performance through simulations, a prototype has been built. Some preliminary tests have been performed on a transtibial prosthesis.



**Fig. 4.15** Hydraulic actuator displacement and force and foot-sled contact force vs. work cycle percentage

## References

1. ISO 10328: 2006 Prosthetics – structural testing of lower-limb prostheses – requirements and test methods
2. ISO 22675: 2006 Prosthetics – testing of ankle-foot devices and foot units – requirements and test methods
3. Perry J (1992) Gait analysis, normal and pathological function. SLACK Inc, Thorofare
4. MD Adams (2010) Online help
5. Faik S, Witteman H (2000) Modeling of impact dynamics: a literature survey. In: International ADAMS user conference, Orlando, pp 3–10
6. Merritt HE (1967) Hydraulic control system. Wiley, New York

# Chapter 5

## Application of Modal Testing and Analysis Techniques on a sUAV

Kaci J. Lemler and William H. Semke

**Abstract** This paper's focus is on experimental structural analysis using contemporary testing techniques for a small unmanned aerial vehicle (sUAV). Testing was performed to find the bending and torsional modes of the wings and tail utilizing multiple methods. Data acquisition and analysis were performed using ModalVIEW, a structural analysis program supported by LabVIEW. The aircraft was excited with random excitation using a single mechanical shaker. These techniques were applied in a case study on the BTE Super Hauler airframe, a small UAS operated by the Unmanned Aircraft Systems Engineering (UASE) Laboratory at the University of North Dakota. The aircraft is primarily used for flight testing of multiple payloads, including an antenna system designed for use in sense and avoid applications. This application requires the addition of wing pods to the current airframe to avoid electro-magnetic interference from the engine of the UAS. Therefore, the effects of the two wing pods on the structural dynamic behavior of the UAS, as well as flutter analysis, were performed on the aircraft and the results are presented and compared. In addition, a statistical method of critical sensor placement for accurate modal information with limited accelerometers is discussed.

**Keywords** Modal analysis • Unmanned aerial vehicle • Sensor placement • Flutter analysis • ModalVIEW

### 5.1 Introduction

Modal analyses were performed on a small Unmanned Aircraft Systems (UAS) both with and without wing pods and the results were compared to find the effect the wing pods have on the structural characteristics of the aircraft. A study on channel reduction was also performed and a novel sensor location identification method using a laser vibrometer was developed. Finally, the results were examined to determine the airworthiness of the aircraft with the wing pods installed.

As UAS are being integrated into the National Air Space (NAS) it is important that steps be taken to develop and implement sense and avoid systems into said UAS [1]. These systems are necessary to enable UAS to sense and avoid obstacles such as uncooperative aircraft, birds, power lines, buildings, and other obstacles [2]. The Unmanned Systems Aircraft Engineering (UASE) team at the University of North Dakota has done work in the field of sense and avoid systems for small UAS. One system that was developed uses an Automatic Dependent Surveillance-Broadcast (ADS-B) transponder to track cooperative aircraft that also have ADS-B transponders. This system works well to predict and avoid collision scenarios with cooperative aircraft but doesn't assist in sense and avoid applications for uncooperative obstacles. Therefore, work is also being done on a small phased array radar system that can be installed into the small UAS along with the ADS-B to provide the ability to track cooperative and uncooperative obstacles. This phased array radar system includes an antenna that locates objects by radiating a narrow beam of electromagnetic energy in the direction of interest. This beam is also steerable so that it can locate objects at all locations around the UAS [2]. Because this antenna radiates electromagnetic energy, it needs to have a clear field of view, containing no metal components, between it and its target [3]. This introduces a need to mount the antennas on the wings to eliminate the engine, landing gear, and assorted fuselage components that could block the view of the antennas if they were mounted in the fuselage. The use of wing pods eliminates any unwanted

---

K.J. Lemler • W.H. Semke (✉)

Unmanned Aircraft Systems Engineering Laboratory, School of Engineering and Mines, University of North Dakota,

Grand Forks, ND 58202, USA

e-mail: [kaci.lemler@gmail.com](mailto:kaci.lemler@gmail.com); [william.semke@engr.und.edu](mailto:william.semke@engr.und.edu)





**Fig. 5.1** Unmanned aircraft system engineering team with the UAS they operate

view interference and provides a payload bay on the wings in which to mount the antennas. The wing pods can dramatically change the structural and flight characteristics of the aircraft, making an experimental structural analysis study necessary to prove airworthiness of the modified aircraft.

The UASE team consists of a mix of undergraduate and graduate students in Mechanical Engineering and Electrical Engineering. The purpose of the lab is to design, build, and flight test payloads for UAS. UASE has performed over 80 missions and has developed payloads relating to phased array radar, search and rescue, precision agriculture, sense and avoid, laser communications, and more. Flight testing is performed at Camp Grafton South, a military training facility in central North Dakota. This facility has restricted airspace, allowing UASE to safely and legally operate its UAS fleet. UASE owns and operates multiple UAS, one of which is the Bruce Tharpe Engineering Super Hauler, (henceforth referred to as the Super Hauler). The Super Hauler the red and white aircraft on the right in Fig. 5.1 and is a gas powered UAS constructed of plywood, balsa wood, and Monokote. It has a 12 foot wingspan and a dry weight of 48 lb. The engine is a 2-cylinder, 9.8 hp engine. The Super Hauler is capable of carrying payloads that weigh up to 30 lb and has an electromagnetic shielded payload bay measuring 21 in. by 11 in. by 12 in..

## 5.2 Test Overview

The structural modes and natural frequencies of a structure can be obtained through ground vibration tests (GVTs). Ground vibration tests are important tests to perform on an aircraft as they are used to predict flutter and assess the significance of modifications made to the structure [4]. The main tool used in a GVT is the frequency response function (FRF). This function can be based on the displacement, velocity, or acceleration response of a system [5]. The expression for any FRF can be written as

$$H_{jk}(\omega) = \frac{X_j}{F_k} \quad (5.1)$$

where  $X_j$  is the harmonic response in one of the degrees of freedom,  $j$ , caused by  $F_k$  which is a harmonic force at a different degree of freedom,  $k$  [6]. Modal analysis is performed by curve-fitting the FRF obtained from the testing to obtain modes then applying that data to a model of the structure to find the associated mode shapes.

As stated previously, modal analyses on the Super Hauler were made necessary by the addition of wing pods. The wing pods used to hold the antennas were designed and built by members of UASE. The pods are made entirely of polycarbonate to eliminate any electromagnetic interference [3]. The aerodynamic shape of the pods results in less drag thus decreasing the effect of the pods on flight performance. The payload pods mount at the intersections of the wing segments using an aluminum mounting rib that follows the contour of the wing at this location. The overall dimensions of the pods are 7.75 in.

**Fig. 5.2** Wing payload pod on the Super Hauler



**Fig. 5.3** The Super Hauler in the test rig while instrumented with accelerometers

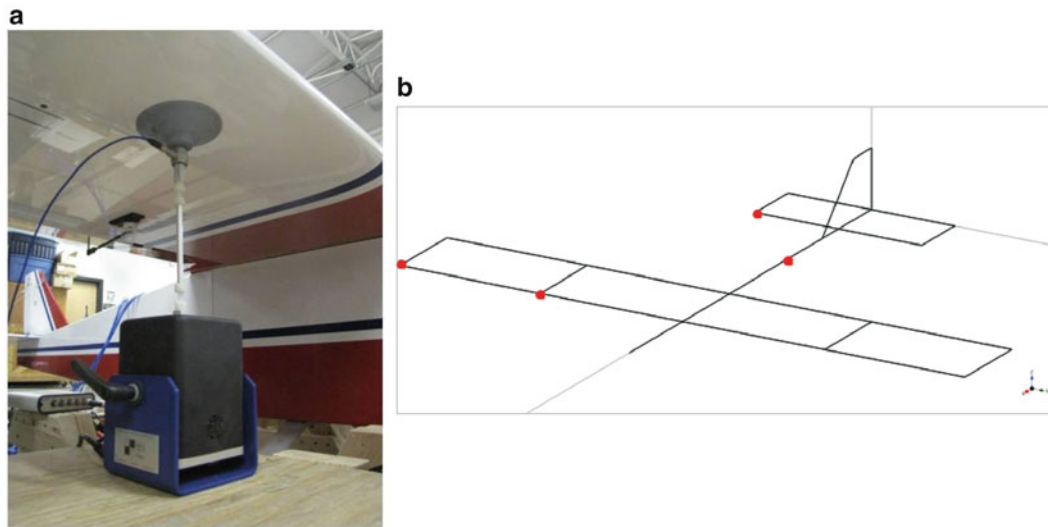


long by 11 in. wide by 2.5 in. deep and each pod can carry up to 5 lb. The pods will most often be used in pairs to equalize the wing loading and provide a symmetric load on the airframe. The electrical and power connectors and wiring are run inside of the wing to keep them out of the airflow over the wing. Figure 5.2 shows the wing pods mounted on the Super Hauler.

For the modal testing, the Super Hauler was isolated by suspending it on bungee cords in a test rig so that all the wheels were 1.25 in. off of the ground. This setup simulates a free-free boundary condition. The Super Hauler was then instrumented with uni-axial and tri-axial accelerometers in key locations. The instrumented Super Hauler in the test rig can be seen in Fig. 5.3. Tests were performed with and without the wing pods installed. For all of the tests with the pods, weight was added to the pods so that a total weight of 5 lb was attached to each wing. There was no payload in the payload bay during the testing.

Excitation of the Super Hauler was achieved by a small shaker. The shaker that was used was the Mini SmartShaker™ with an integrated power amplifier from The Modal Shop Inc. The setup of the shaker can be seen in Fig. 5.4a where it was attached to the aircraft through the use of a suction cup. A load cell was attached in line with the shaker's stinger to measure input force. The aircraft was excited at several different locations, all in the Z direction, that are identified by the red dots in Fig. 5.4b.





**Fig. 5.4** (a) The shaker setup with stinger, load cell, and suction cup (b) Excitation locations

**Fig. 5.5** National Instruments cDAQ-9178 data acquisition board used for the testing

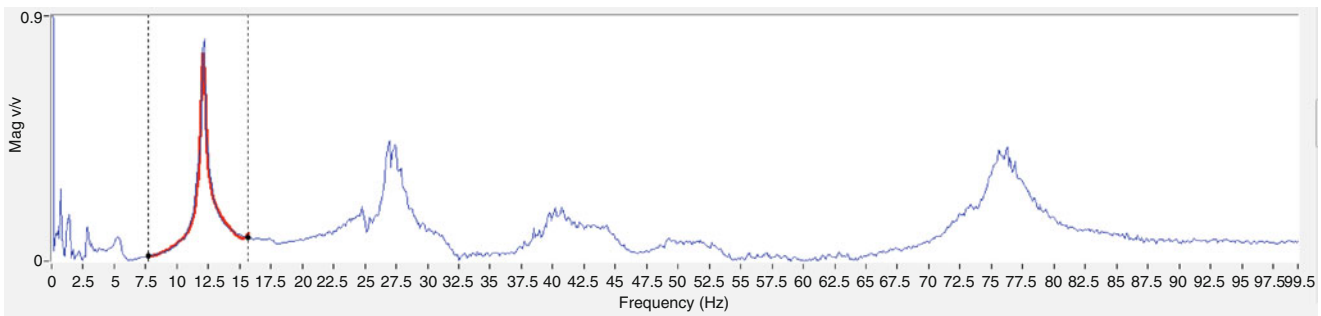


**Table 5.1** Test equipment information

Description	Model	Sensitivity
Uni-axial accelerometer	PCB Piezotronics 352C18	10 mV/g
Uni-axial accelerometer	PCB Piezotronics 352C33	100 mV/g
Tri-axial accelerometer	PCB Piezotronics 356A32	100 mV/g
Load cell	PCB Piezotronics 208C02	50 mV/g
Shaker	The Modal Shop Inc. K2007E01	
Data acquisition board	National Instruments cDAQ-9178	
Data acquisition modules	National Instruments 9234	

The accelerometers and excitation devices were routed to a National Instruments data acquisition board that was connected directly to a computer. The DAQ that was used was a National Instruments cDAQ-9178 with eight National Instruments 9234 DAQ modules installed. This setup can be seen in Fig. 5.5 (Table 5.1).

Data capture and analysis was performed using ModalVIEW, a software designed specifically for modal testing and analysis. The settings in ModalVIEW were as follows. The shaker was set to random excitation with a Hanning window applied. The measurement type was set to FRF-EMA for an experimental modal analysis. The sampling rate was left at the default of 1651.61 Hz and the resolution was set to 0.1 Hz. The shaker was activated so that the Super Hauler was excited with random excitation, then ModalVIEW was told to record data from the accelerometers. ModalVIEW would then gather data for a period of time and when it was done the shaker was turned off. This was repeated so that two data sets were gathered at each loading and excitation configuration then the shaker was moved to the next excitation location and the process was rerun.



**Fig. 5.6** Sample frequency response function with curve fit on the targeted mode

Once all of the vibration data was gathered, analysis was performed using ModalVIEW and followed the steps outlined below. First, ModalVIEW automatically generated a frequency response function (FRF) for each channel from the response that was measured. A curve could then be fit to the FRF to find the modes by selecting a frequency range for ModalVIEW to analyze and the number of modes within that range. The fit of the curve could be checked and, if the fit looked good, the mode(s) would then be added to the mode list for that test. This can be seen in Fig. 5.6. This was repeated through the FRF until a list of modes and natural frequencies was created for each test. ModalVIEW was then used to build a model of the Super Hauler. The accelerometers were assigned to their respective nodes and degrees of freedom. The structure could then be animated with the motion and mode shape associated with each natural frequency that was found.

### 5.3 Base Model

The base model consisted of a planar model of the aircraft with 12 uni-axial accelerometers and 4 tri-axial accelerometers in the locations shown in Fig. 5.7a. All of the uni-axial accelerometers were mounted to measure acceleration in the Z direction except for the one on the vertical stabilizer, which was mounted to measure in the Y direction. The test was performed both with and without pods. When the pods were installed, four more uni-axial accelerometers were added to measure the motion of the pods. The pod accelerometer locations are shown in Fig. 5.7b where the two on the side of the pod were mounted in the Y direction and the two on the bottom of the pod were mounted in the Z direction.

Figure 5.8 shows the mode shapes that were found and lists the corresponding natural frequencies without the pods and with the pods. The first mode shape that was observed was mode 1 type bending in the wings. The second mode shape consisted of tail torsion while the wingtips bent in opposite directions of each other. The third mode shape showed wingtip, wing, tail, horizontal stabilizer, and vertical stabilizer torsion while the wingtips also bent. The fourth mode shape only appeared in the no pods configuration and consisted of wing torsion while the horizontal stabilizer bent slightly. The fifth mode shape showed wing torsion in the same direction. The sixth mode shape showed the wingtips bending in opposite directions of each other while the tail moved side to side and the horizontal stabilizer underwent torsion and bending. The seventh mode shape showed the wingtips bending in opposite directions of each other while the tail moved side to side. The eighth mode shape only appeared in the no pods configuration and showed horizontal and vertical stabilizer torsion. The ninth mode shape only appeared in the no pods configuration and showed the horizontal stabilizer under bending and torsion with mode 2 bending in the wings and vertical stabilizer torsion. The tenth mode shape showed the wings experiencing mode 2 type bending with horizontal stabilizer bending and torsion. The eleventh mode shape showed wing and horizontal stabilizer torsion in the same direction. The twelfth mode shape only appeared with the pods and showed the wings in torsion and the horizontal stabilizer in bending and torsion. The thirteenth mode shape showed wing torsion in opposite directions from each other while the horizontal stabilizer and the body both bent. The fourteenth mode shape showed wing mode 2 bending and torsion with horizontal stabilizer torsion. The fifteenth mode shape showed horizontal stabilizer torsion while the wings underwent mode 2 wing torsion.

The results are summarized in Table 5.2. It can be seen that the natural frequencies with the pods are 8–30% smaller than the corresponding natural frequencies without pods. This was expected since, when installed, the wing pods account for 20% of the total weight of the aircraft.

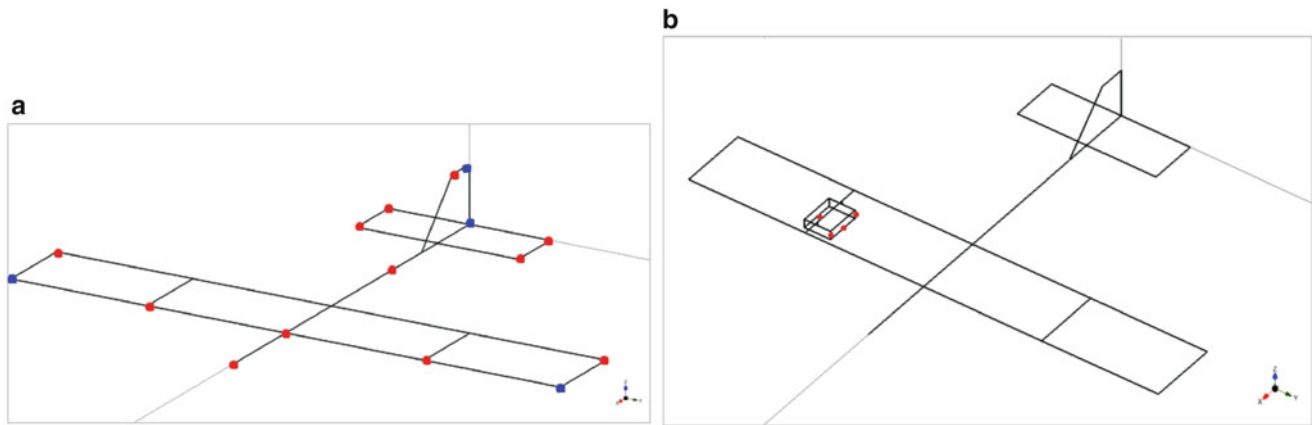


Fig. 5.7 Base model accelerometer locations (*red* = uni-axial, *blue* = tri-axial)

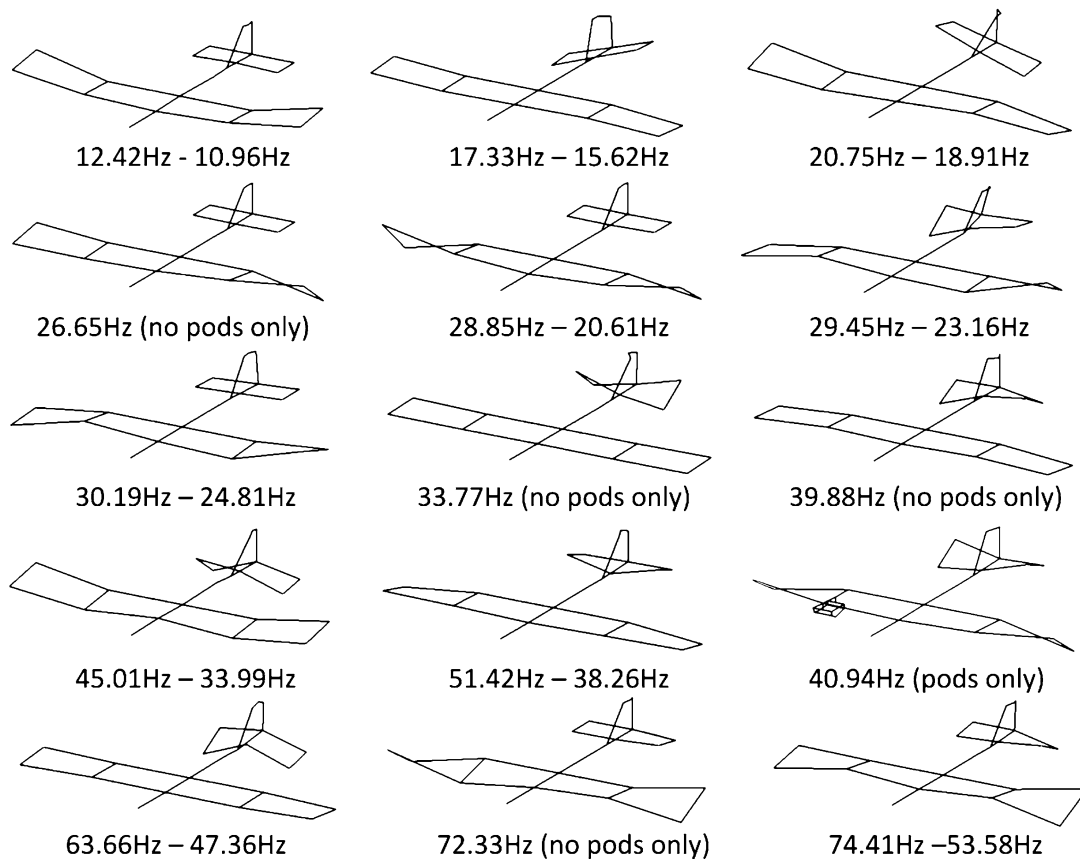


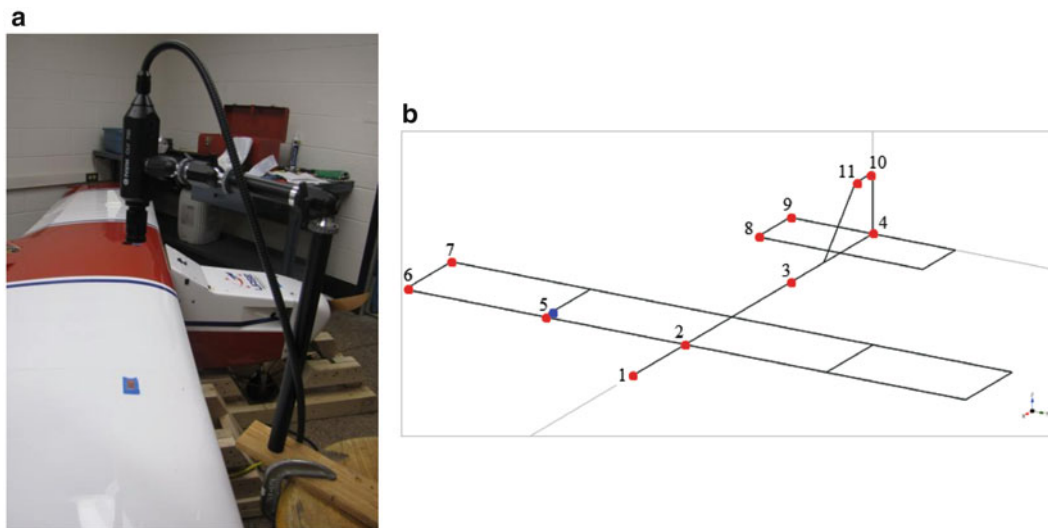
Fig. 5.8 Base model mode shapes and natural frequencies

#### 5.4 Sensor Location Identification Method and Channel Reduction

Channel reduction is an important topic in modal analysis. With every extraneous channel there are associated costs. These costs include an extra sensor and the time spent installing, indexing, and logging the sensor as well as processing and analyzing the data obtained from said accelerometer. Because of this, it is important to use as few channels as possible while still keeping enough to identify the modes of the structure [7]. A key point in channel reduction is sensor location selection. Several methods for identifying important locations for sensors have been developed.

**Table 5.2** Summarized natural frequencies for the base model with and without pods

No Pods	Pods	%Diff	Description
12.42	10.96	11.69	Mode 1 wing bending
17.33	15.62	9.89	Tail torsion, wingtip bend opposite
20.75	18.91	8.88	Wingtip, wing, tail, HS, VS torsion, wingtip bend
26.65			Wing torsion, slight HS bend
28.85	20.61	28.58	Wing torsion in same direction
29.45	23.16	21.37	Wingtips bend opposite, HS bend/torsion, tail wag
30.19	24.81	17.81	Wingtips bend opposite, tail wag
33.77			HS, VS torsion
39.88			HS bend/torsion, mode 2 wing bend, VS torsion
45.01	33.99	24.48	Mode 2 wing bend, HS bend/torsion, VS torsion
51.42	38.26	25.58	Wing torsion, HS bend/torsion
	40.94		Mode 2 wing torsion, HS bend/torsion
63.66	47.36	25.61	Wing torsion opposite, HS bend, body bend
72.33			Mode 2 wing bend, torsion opposite, HS torsion
74.41	53.58	27.99	HS torsion, mode 2 wing torsion



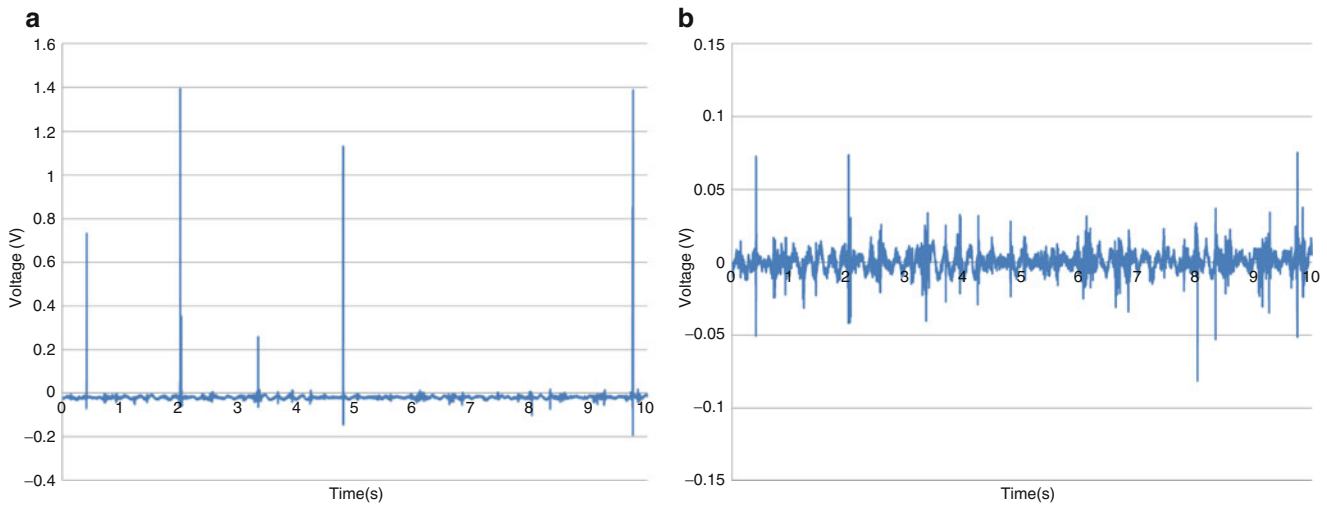
**Fig. 5.9** (a) Laser vibrometer testing setup (b) Excitation (blue) and measurement (red) locations for laser vibrometer tests

One methodology uses a finite element model in which sensor sets are found which maximize the ability to observe modes while constraining each sensor to contribute unique information [8]. Another method selects sensor locations that make the corresponding target mode shape partitions as linearly independent as possible while maximizing the signal strength of the target modal responses within the sensor data [9]. Yet another method uses a genetic algorithm to identify sensor locations by starting with a relatively small number of possible final locations and evolving these locations to the best set [10].

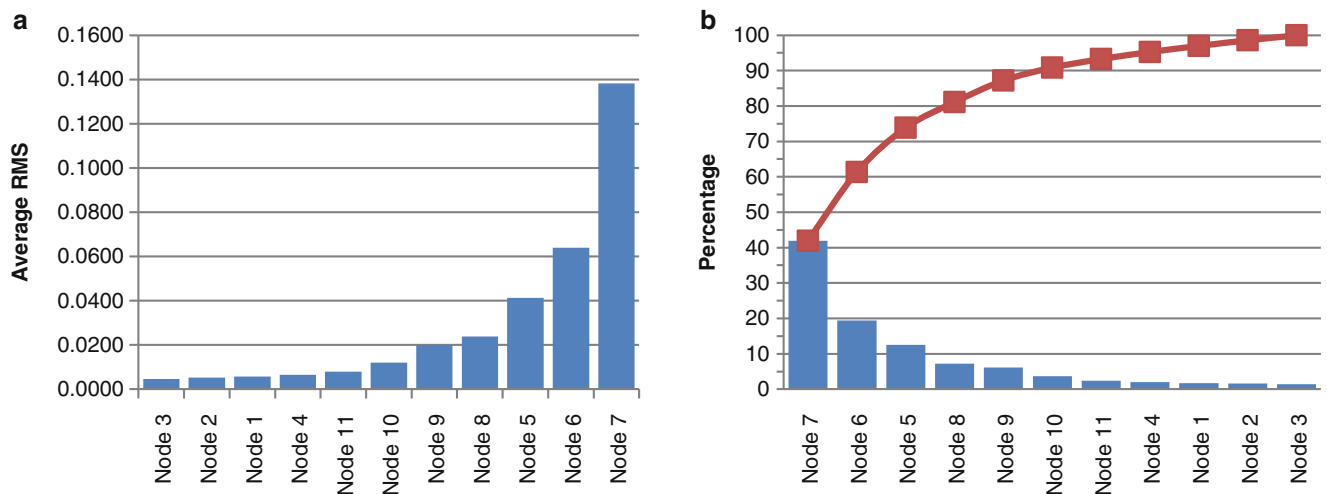
There are several more methods for sensor location identification but the majority of them require extensive finite element modeling, algorithm development, mathematical modeling, or a combination thereof [11]. It was desired to develop a relatively quick and easy, non-contact, experimental method with which to identify important sensor locations for complex systems that are difficult and time consuming to model. This was achieved through the use of a laser vibrometer. A laser vibrometer is a good tool to use for this purpose because of its mobility and its capability to gather vibration data in a non-contact manner. The laser vibrometer was used to measure the velocity of the surface of the aircraft at several locations. These values were then used to identify locations of high interaction.

The laser vibrometer that was used for the tests was a Polytech OFV 2601 Laser Vibrometer Controller with a Polytech CLV Laser Unit and a Polytech CLV 700 Laser Head. To perform the laser vibrometer testing, the Super Hauler was placed in the test rig and the shaker was attached in the location marked by the blue dot in Fig. 5.9b. The Super Hauler was in the no pods and unloaded condition.

The laser vibrometer was mounted on a stand and directed to measure the vibration of the aircraft at the locations shown in Fig. 5.9b. All measurements were in the Z direction except for the two on the vertical stabilizer which were in the Y direction. The first step in the test procedure was to move the laser vibrometer to a measurement location and focus the



**Fig. 5.10** (a) Raw laser vibrometer data. (b) Data with outliers removed and adjusted for an average of zero



**Fig. 5.11** (a) Average RMS values for laser vibrometer measurement locations and (b) Pareto diagram

laser to get a strong, clear signal. Next, the shaker was activated to vibrate the aircraft with random excitation. A LabVIEW program was then run that recorded and logged the data from the vibrometer over a 10 second period. These steps were repeated until three sets of data were gathered from each measurement location.

A sample of the data gathered is shown in Fig. 5.10a. The graph shows the voltage measurements taken by the laser vibrometer of a test location versus time with the voltage corresponding to amplitude. As can be seen, the data wasn't centered around zero and there were some outliers due to noise in the laser vibrometer. Post processing was performed in Excel to remove the outliers and then shift the data sets so that they had an average of zero. The sample data set after post processing can be seen in Fig. 5.10b.

To find an effective measure of the magnitude of vibration at each location, (5.2) was used to calculate the Root Mean Square (RMS) value for each data set.

$$x_{rms} = \sqrt{\frac{1}{n} (x_1^2 + x_2^2 + \dots + x_n^2)} \quad (5.2)$$

A representative RMS value for each measurement location was then found by calculating the average of the three RMS values from the three data sets at each location. The average RMS values at each node can be seen in Fig. 5.11a.

Once the average RMS values were calculated, it was desirable to establish a statistical method to select the important modes at which accelerometers need to be placed. The method that was selected was a Pareto diagram. Pareto diagrams were



**Table 5.3** Summary of natural frequencies for channel reduction tests

Base	95%	90%	75%	Description
12.42	12.40	12.40	12.40	Mode 1 wing bending
17.33	17.47	17.48	17.52	Tail torsion, wingtip bend opposite
20.75	20.80	20.79	20.96	Wingtip, wing, tail, HS, VS torsion, wingtip bend
26.65	25.99	26.01	25.87	Wing torsion, slight HS bend
28.85	28.17	28.14	28.10	Wing torsion in same direction
30.19	30.82	30.82	30.71	Wingtips bend opposite, tail wag
33.77	36.49	36.11		HS, VS torsion
39.88	39.70	39.83	39.80	HS bend/torsion, mode 2 wing bend, VS torsion
45.01	44.93	44.93	44.67	Mode 2 wing bend, HS bend/torsion, VS torsion
51.42	51.00	51.73	50.58	Wing torsion, HS bend/torsion
63.66	61.06	62.86	64.08	Wing torsion opposite, HS bend, body bend
72.33	73.27	71.97	71.87	Mode 2 wing bend, torsion opposite, HS torsion
74.41	75.92	75.88	75.76	HS torsion, mode 2 wing bend and torsion

introduced in the field of quality control and are used to determine the most significant aspects of a body of information [12]. Resources can then be used on the important aspects and not wasted on trivial aspects. The Pareto diagram method was applied to this test by first assuming the important motion of the aircraft was captured by the measured locations. Selecting the measurement locations is an important step in this process since a location has to be measured to be included in the analysis of important sensor placement locations. The average RMS values were then ordered from largest to smallest and the individual percentages of the total were calculated. These percentages were then summed to find a running cumulative percentage of total aircraft motion captured. These results were then graphed and are shown in Fig. 5.11b where the blue bars are individual percentages of the total, and the red line is the cumulative percentage. A thorough screening of potential sensor locations must be conducted to help ensure that all the motion of interest is captured. The use of a laser vibrometer makes this process effective due to the efficiency of data collection.

This Pareto diagram can be used to determine which locations should be measured. To capture 75% of the motion, nodes 5, 6, and 7, which are the nodes on the wings, should be instrumented. Alternatively, to capture 90% of the motion, nodes 8 and 9, on the horizontal stabilizer, would have to be instrumented as well. To capture even more motion, nodes 10 and 11 on the vertical stabilizer could be instrumented as well to bring the measured motion up to 95%. The values chosen in this case were chosen because they coincide with the various surfaces of the aircraft. Since the correct level is case dependent, this value should be left to user discretion. To examine the effects of channel reduction, tests were performed with these levels. A summary of the natural frequencies and mode shapes found in the channel reduction tests compared to the natural frequencies for the base model with no pods can be seen in Table 5.3.

It can be seen that the 95% test captured all of the natural frequencies that were seen in the base model. However, as would make sense from the data that was removed, any motion in the fuselage was undetectable using the 95% data. There was relatively little activity in the fuselage when compared to the rest of the structure, though, so the inability to observe that motion is fairly insignificant. The 90% test also captured all of the natural frequencies that were seen in the base model. However, any motion in the fuselage or vertical stabilizer was undetectable using the 90% data. Depending on the application, the inability to observe this motion could be acceptable since the fuselage and vertical stabilizer don't experience much motion and all of the modes were detected. The 75% test captured almost all of the natural frequencies that were seen in the base model, missing one mode at 33.77 Hz. However, any motion in the body or tail was undetectable using the 75% data. The inability to detect a mode at 33.77 Hz can be traced to this fact since that mode consists solely of horizontal and vertical stabilizer motion. This is a significant lack of data because of the inability to detect a mode. It also factors into airworthiness determinations because of the inability to see motion in the horizontal stabilizer. One important note in the data analysis is as sensors are removed, the relative magnitudes in the FRFs can change, introducing a potential for identifying modes that hadn't been recognized before or missing modes that had been previously identified.

## 5.5 Determination of Airworthiness

One of the main reasons that a ground vibration test on the Super Hauler was conducted was to determine if the aircraft was still airworthy after the addition of wing pods. A major concern in aircraft is aeroelastic flutter. Aeroelastic flutter is defined as involving the interaction of aerodynamic, elastic, and inertia forces on structures that produces an unstable oscillation that often results in structural failure [13]. Flutter is typically observed on surfaces, such as wings and tails, that encounter

**Table 5.4** Summary of wing modes

No Pods	Pods	Description
12.42	10.96	Mode 1 wing bending
28.85	20.61	Wing torsion in same direction
29.45	23.16	Wingtips bend opposite, HS bend/torsion, tail wag
30.19	24.81	Wingtips bend opposite, tail wag
45.01	33.99	Mode 2 wing bend, HS bend/torsion, VS torsion
51.42	38.26	Wing torsion, HS bend/torsion
63.66	47.36	Wing torsion opposite, HS bend, body bend

**Table 5.5** Summary of potential horizontal stabilizer flutter modes

No Pods	Pods	Description
29.45	23.16	Wingtips bend opposite, HS bend/torsion, tail wag
39.88		HS bend/torsion, mode 2 wing bend, VS torsion
45.01	33.99	Mode 2 wing bend, HS bend/torsion, VS torsion
	40.94	Mode 2 wing torsion, HS bend/torsion

**Fig. 5.12** The Super Hauler in flight with the wing pods installed

large aerodynamic loads [14]. Flutter occurs when the aerodynamic forces associated with motion in two modes of vibration (i.e. wing bending/torsion) cause the modes to couple adversely [15]. An uncontrolled increase in vibration amplitude is observed when the aircraft is moving fast enough that the structural damping is insufficient to quell the motion coming from aerodynamic energy being added to the surface [16].

New aircraft are put through rigorous testing to identify flutter. These tests include both ground vibration tests and flight tests that include structural excitation, response measurement, and data analysis for stability [13]. The Super Hauler had been flown for several missions prior to the development of the wing pods so the stability of the aircraft had been established. The tests were performed to see if the addition of the wing pods changed the modes of the aircraft to the extent that flutter would be introduced in normal flight operations.

The primary location on an aircraft where flutter is a concern is the wings. The natural frequencies were examined to see if the addition of the pods changed the frequencies so that a wing bending mode would coincide with a wing torsional mode. Table 5.4 summarizes the modes that were dominated by wing motion and it can be seen that none of the frequencies aligned so that flutter conditions were created.

The modes that were observed to contain potential for flutter with a combination of bending and torsional modes were noticed in the horizontal stabilizer and are summarized in Table 5.5. As flight loadings are smaller on the horizontal stabilizer, flutter is not as significant of a problem on this surface. However, this discovery will lead to the UASE lab increasing the tension in the stabilizer wires to combat the flutter tendencies shown in the horizontal stabilizer.

The Super Hauler was flown in July 2012 with the wing pods attached. Dummy weights were placed in the pods to simulate a payload. The weights added brought the total weight of the pods to 5 lbs each. An image that was taken during the flight in which the pods are visible is shown in Fig. 5.12. The flight was successful with no problems during flight and there was no noticeable change in the flight characteristics or the handling of the aircraft.

## 5.6 Conclusion

A full modal analysis investigating the effect of wing pods on a small UAS was presented. The pods were shown to lower the natural frequencies for corresponding mode shapes but no wing flutter was introduced into the system. This led to the conclusion that the wing pods were a safe addition to the aircraft, which was demonstrated by a successful flight with the wing pods installed. A novel channel reduction method, using a laser vibrometer, was presented. This method was shown to provide a quick, non-contact, and experimental way to determine important sensor locations through the use of a Pareto diagram. This method provides the user with the flexibility to determine the level of information they desire to capture. A study was done on channel reduction and three different tests were performed and analyzed. The sensors along the body of the aircraft, as well as on the vertical stabilizer, were found to be unnecessary for this testing while the sensors on the wings were imperative.

**Acknowledgements** This research was supported in part by Department of Defense contract number FA4861-06-C-C006 “Unmanned Aerial System Remote Sense and Avoid System and Advanced Payload Analysis and Investigation,” the Air Force Research Laboratory, “MEMS Antenna for Wireless Communications Supporting Unmanned Aerial Vehicles in the Battlefield,” and the North Dakota Department of Commerce, “UND Center of Excellence for UAV and Simulation Applications.” The authors would like to also acknowledge the contributions of the Unmanned Aircraft Systems Laboratory team at UND.

## References

1. Alme J (2009) Vivaldi antenna design for X Band electronically-steered antenna arrays and phased array radars. Department of Electrical Engineering, University of North Dakota
2. Hajicek D (2009) Electronically-steered phased array antenna design for integration into small unmanned aircraft systems. Department of Electrical Engineering, University of North Dakota
3. Lemler KJ, Semke WH (2012) Structural analysis of the effects of wing payload pods on small UAS. In: Proceedings of the 30th international modal analysis conference (IMAC), Jacksonville, Feb 2012
4. Kehoe MW (1987) Aircraft ground vibration testing at NASA Ames-Dryden Flight Research Facility. National Aeronautics and Space Administration
5. Simisiriwong J (2009) Structural testing of an ultralight UAV composite wing and fuselage. Department of Aerospace Engineering, Mississippi State University
6. Ewins DJ (2000) Modal testing: theory, practice, and application, vol 2. Research Studies Press, Baldock
7. Carne TG, Dohrmann CR (1995) A modal test design strategy for model correlation. In: Proceedings of the 13th international modal analysis conference, Nashville
8. Stephan C (2011) Sensor placement for modal identification. *Mech Syst Signal Process* 27:461–470
9. Kammer DC, Tinker ML (2004) Optimal placement of Triaxial accelerometers for modal vibration tests. *Mech Syst Signal Process* 18:29–41
10. Stabb M, Belloch P (1995) A genetic algorithm for optimally selecting accelerometer locations. In: Proceedings of the 13th international modal analysis conference. Nashville, Tennessee, pp 13–16
11. Papadimitriou C (2005) Pareto optimal sensor locations for structural identification. *Comput Methods Appl Mech Eng* 194(12–16):1655–1673
12. Lawson J, Erjavec J (2001) Modern statistics for engineering and quality improvement. Duxbury, Pacific Grove
13. Kehoe MW (1995) A historical overview of flight flutter testing. National Aeronautics and Space Administration
14. De Marqui C, Jr Rebolho DC, Belo EM, Marques FD (2006) Identification of flutter parameters for a wing model. *J Braz Soc Mech Sci Eng* 28(3):339–346
15. Wright JR, Cooper JE (2007) Introduction to aircraft aeroelasticity and loads. Wiley, Chichester
16. Hebert C, Cowan D, Attar PJ, Weisman CD Exploring structural dynamics. AIAA



# Chapter 6

## Progress in Operational Analysis of Launch Vehicles in Nonstationary Flight

George James, Mo Kaouk, and Tim Cao

**Abstract** This paper presents recent results in an ongoing effort to understand and develop techniques to process launch vehicle data, which is extremely challenging for modal parameter identification. The primary source of difficulty is due to the non-stationary nature of the situation. The system is changing, the environment is not steady, and there is an active control system operating. Hence, the primary tool for producing clean operational results (significant data lengths and data averaging) is not available to the user. This work reported herein uses a correlation-based two step operational modal analysis approach to process the relevant data sets for understanding and development of processes. A significant drawback for such processing of short time histories is a series of beating phenomena due to the inability to average out random modal excitations. A recursive correlation process coupled to a new convergence metric (designed to mitigate the beating phenomena) is the object of this study. It has been found in limited studies that this process creates clean modal frequency estimates but numerically alters the damping.

**Keywords** Operational modal analysis • Signal processing • Hilbert transform • Correlation function • Damping estimation

### 6.1 Introduction

The spacecraft launch environment is a highly complex and non-stationary event that is characterized by high amplitude input forces, highly variable loads, a wide spectrum of responses, constantly changing vehicle mass, active control interactions, staging, and limited instrumentation. At the same time, structural response analyses and loads estimations must be performed with models that are only partially validated using ground test data due to the fact that access to diagnostic and environmental ground tests are limited. To compound matters, project managers tend to reduce uncertainty factors designed to protect for loads increases and model unknowns. As a result, the designs progress rapidly before loads and structural problems are uncovered. This means that there are very few tools available to recover from structural dynamics issues in such a highly dynamic environment without costly redesigns late in the design cycle or in early operations.

Traditional modal testing applies a known input to the structure (or components/test articles) and structural dynamic parameters are then extracted. In spite of the relatively pristine data, these dedicated tests are often difficult to schedule or afford (and rarely achieve flight-like loading conditions). The inclusion of operational modal testing and analysis tools can be used to offset these limitations by providing additional cost and schedule effective opportunities for diagnostic information extraction. These opportunities are available on the ground and during flight as well as on full-up systems, subsystems, components, and test articles.

---

G. James (✉) • M. Kaouk • T. Cao

Loads and Structural Dynamics Branch, NASA Johnson Space Center, Houston, TX 77058, USA  
e-mail: [george.h.james@nasa.gov](mailto:george.h.james@nasa.gov); [timothy.t.cao@nasa.gov](mailto:timothy.t.cao@nasa.gov)

## 6.2 Technical Background

The technology for extracting structural dynamic properties from structures (i.e. modal testing) has rapidly improved over the last several decades. Operational modal analysis (OMA) is one of the specialized spin-offs that have grown in importance over the last 20 years. In OMA, a known and measured input is not artificially imparted to the structure to drive the known responses but measurements are made in-situ and processed to obtain a subset of the desired modal data. This approach is very useful for large in-service structures that cannot be removed from service effectively (e.g. bridges, buildings, wind turbines, off-shore structures, etc.). One of the earliest OMA techniques was the Natural Excitation Technique (NExT) [1]. This development showed that for a class of inputs, the auto and cross-correlation functions could be processed as time decay functions to estimate the modal frequencies and modal damping properties. Time domain estimators, such as Polyreference [2] or the Eigensystem Realization Algorithm (ERA) [3] have been used to process such data. [Appendix 1A](#) contains the theoretical background for this technique. Recent years have seen the OMA field become rich with other advanced techniques having broad applicability [4]. However, NExT has continued to spawn on-going efforts to improve, expand, and further understand the approach [5–10].

### 6.2.1 *Alternative Approaches for Traditional OMA*

There are two general classes of algorithms for performing stationary linear OMA: (1) time history-based techniques that are generally related to Stochastic Subspace Identification (SSI) and frequency domain-based techniques that are related to Frequency Domain Decomposition (FDD) [1, 4, 11–14]. Early time domain approaches included tools like the Random Decrement and Maximum Entropy Methods [15–18]. The technical basis for the NExT approach mentioned previously involved converting measured responses into auto and cross-correlation functions and processing with standard time domain modal analysis routines [1]. However, the more general SSI techniques directly integrate the correlation calculations and modal processing algorithms into a single step rooted in discrete time system identification theory [12, 14]. The earliest manifestations of FDD were peak picking and half-power bandwidth estimation schemes operating on the Power Spectral Density (PSD) functions [13]. However the advanced FDD algorithms refine the modal parameter estimates using powerful tools like the Singular Value Decomposition (SVD) [4, 13]. An interesting direction for frequency domain approaches involves the use of Hilbert transforms applied to PSD's to obtain biased Frequency Response Function (FRF) estimates [4, 19].

There is another direction in operational testing that involves estimating the forces acting on the system. This would allow more traditional FRF-based approaches to be used for system identification. These forces can be estimated via known mass changes to the system or via hybrid analytical/experimental data [20, 21]. For non-stationary systems, Wavelet Analyses represents one possible approach [22, 23]. Another possible approach is via the Wagner-ville developments [24]. For non-linear and non-stationary systems, the empirical Hilbert-Huang method is a possibility [25–27].

### 6.2.2 *Launch Environment Analyses*

There have been a limited number of reported attempts to analyze flight data to extract modal parameter information, although there are certainly many other unreported attempts. The time domain approaches based on correlation and SSI are generally used for flight data analyses as the rapidly changing vehicle properties do not allow the full advantages of the frequency-domain approaches to be realized. The responses are generally broken into a series of time windows, each of short duration (and quite often significant overlap), that are processed individually. If the loading and system characteristics are fairly constant over each window, then estimates of the changing parameters can be obtained as a function of flight time [28–35].

Three of the references listed above show that one trajectory for NExT has been to act as a pathfinder for the development of operational analysis techniques to process launch data [28–30]. This effort is doubly challenging as modal damping is one of the most sought after parameters from the launch environment, which is difficult to extract even in well controlled stationary environments. However, flight damping during launch becomes a critical part of the discussions during the design and operations of space vehicles due to the control over the response of structures and components. Hence, modal damping has become an important metric for the utility flight data and flight data analyses.

Reference [28] discusses the earliest work in the application of the NExT/OMA approach to launch data from a missile-based system. The work used tight narrow-band filters to limit the data under processing to one or two modes at time. Also,

the time windows generally covered 2–4 cycles of the modes and had significant overlap. In order to make this analysis tenable, the modal engine (ERA [3]) had to be called automatically. Even with tight filtering and the processing software able to call ERA when needed, this analysis was a very labor intensive process. The manual effort involved assessing the results of the processing for each window, making decisions on the selected roots, resetting parameters if required, and restarting the processing when needed. However, the traces for modal frequency and damping look fairly reasonable and smooth (except for the first mode damping in first stage flight).

Reference [29] discusses a later launch analysis from the Space Shuttle. For this analysis and automation process called AUTO-ID was added to the tool [36, 37]. The addition of this technique eased the computational burden of extracting parameters in a consistent manner from the multitude of correlation functions calculated from the sliding time window segments of the random time histories to allow a rapid assessment of the data. This was a much less labor-intensive process than the original processing effort as discussed in Ref. [28]. As a result many more modes were assessed in much less time than seen in the previous case study. However, the results were not a pristine and more excursions in the frequency and damping were allowed as a result. The reported data for modal damping still shows trends and excursions during flight.

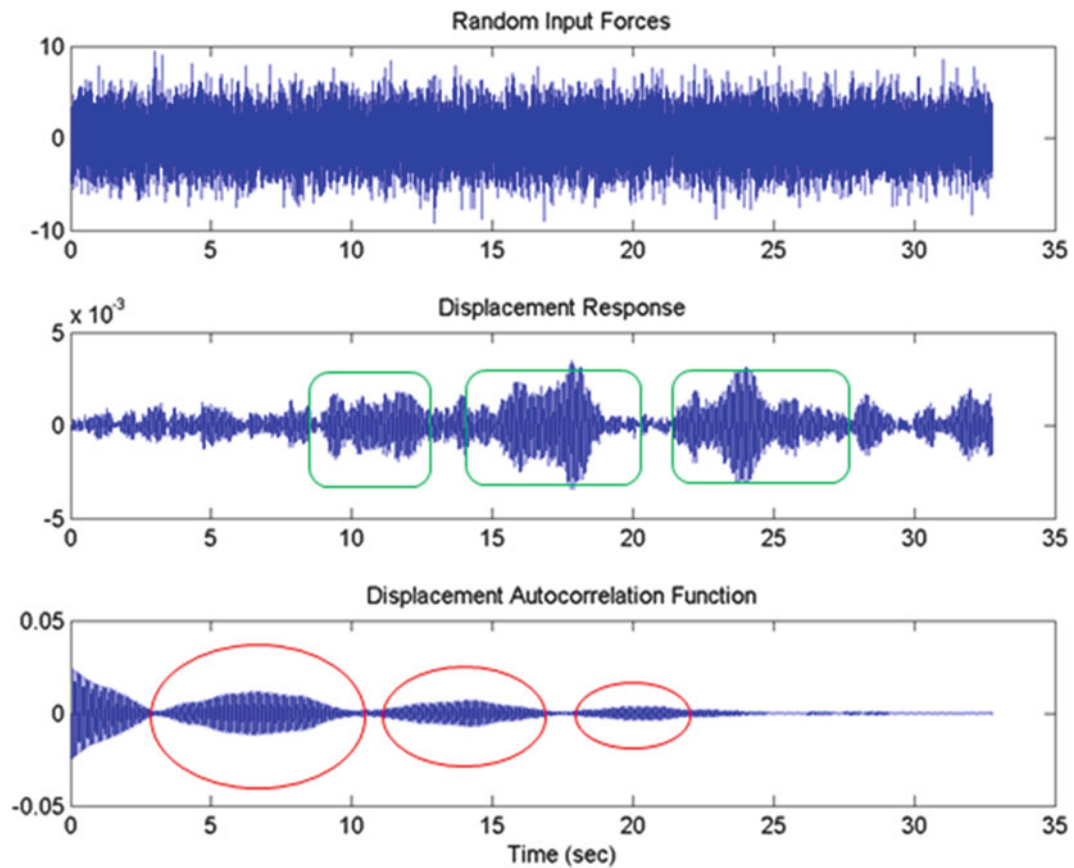
Reference [30] is a recent study performed on the PA-1 test flight. This test flight provided a very challenging data set with a very short flight time and extremely rapidly changing modal frequencies. Autonomous identification was not used and the amount of frequencies studied was less than the study discussed in Ref. [29]. The user effort required was intermediate between the two previous studies discussed. Since the user interacted with data to a greater extent than previously and the experience of the previous exercises was available, two problems were for immediate attention: beat-like phenomena in the correlation functions of short time records and potential interactions between the vehicle control systems and extracted damping in the lowest bending modes of the vehicles. A working hypothesis for the first problem (beat-like phenomena) has been developed in which the phenomena are apparent increases in correlation due to the lack of ability to temporally average out the random characteristics of the responses. A limited number of potential mitigations for this effect are in-hand as well plans to assess other non-correlation based approaches. This work continues an effort to study a mitigation which uses multiple correlation processes as applied to short time histories [38]. The second problem of potential control system interactions is still being scoped.

### 6.3 Study of Recursive Correlation and an Associated Convergence Metric

A most significant complexity associated with operational analysis of launch systems is the unsteadiness due to rapidly changing mass properties. This usually drives the available time records to be very short due to the need to utilize some type of sliding window analysis (at least for a process that assumes stationarity). The analysis of several recent data sets has shown that one effect (at least on the correlation-based processing approaches) is a “beating” or “blooming” phenomena which limits the amount of the correlation functions that can be used for processing [30, 35, 39]. Although the first low-lag points in the correlation functions are relatively unaffected, the higher-lag time data points are relatively useless for analysis.

#### 6.3.1 Previous Findings

Figure 6.1 illustrates the beating phenomena as illustrated by a simple one DOF analytical model of a 10 Hz mode with 1% damping excited by random white noise using Newmark-Beta integration. The 32,768 length time history has a time step of .001 s. The random input is shown in the top plot of Fig. 6.1. The displacement response of the 10 Hz system is shown in the middle plot. Displacement is used as opposed to the more easily measured acceleration as it illustrated the issue with more clarity. Notice that the response shows random excitations of the 10 Hz system mode, which eventually damps out. The lower plot provides the autocorrelation function of the displacement shown in the middle plot. The beating phenomena are clearly seen as the correlation increases at longer lags. Note that the “beating” terminology is adopted as the correlation function looks like a time history of closely spaced modes interacting or “beating”. The periodic increases in correlation deviates from the theoretical damped sinusoids that are expected from OMA/NEX correlation functions and limit the utility to separate closely space modes as only early lags can be used for analysis [1]. The working hypothesis for this phenomena is that the random “blooms” in the response data (middle plot of Fig. 6.1) result as the internal modes are randomly excited by the input. During the correlation process these “blooms” in the response data become the beating phenomena in the correlation functions (see bottom plot of Fig. 6.1).



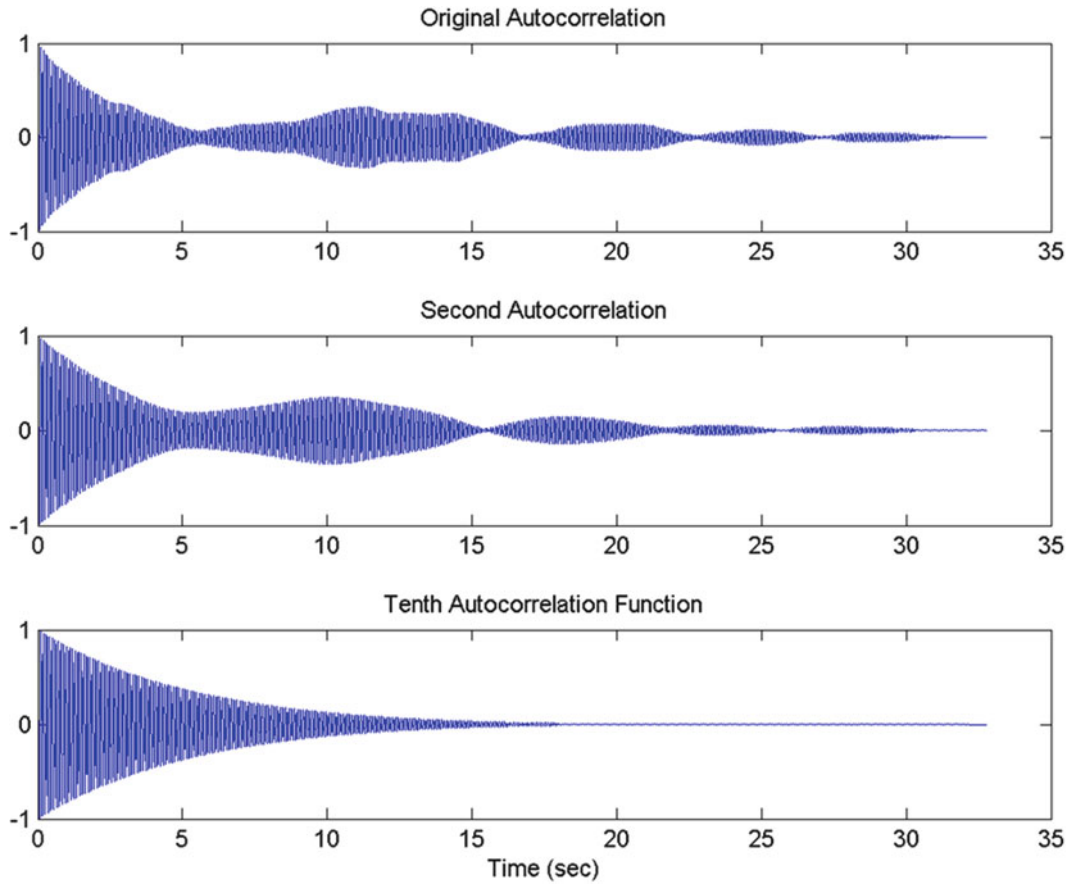
**Fig. 6.1** Beating phenomena in correlation functions in single DOF analytical data

Previous work to address this issue suggested that the beating effects can be reduced via repeated correlation calculations using the same parent time data. Figure 6.2 shows the effectiveness of this approach. The top plot shows an autocorrelation function of a 10 Hz single DOF system excited randomly. If a another correlation calculation is performed using the first autocorrelation function as the parent data then the correlation function shown in the middle plot results. The bottom plot results after performing an additional eight correlation calculations using the function shown in the middle plot as the parent data (10 correlation calculations total). This obviously produces a damped sinusoidal function as expected. It can be seen that the proper damping seemed to result after a number of these correlations are performed. However, the application of additional correlations does numerically alter the extracted damping. Hence, this approach needs a convergence metric to allow the analyst to know when to stop performing additional correlations [30]. A metric was presented in Ref. [38] and will be repeated here. However the ongoing effort has discovered that there are numerical issues with the recursive correlation approach that need to be understood as validation of the technique is proving elusive.

### 6.3.2 Development of a Convergence Metric

The problem at hand involves performing additional specialized averaging (in the form of autocorrelation functions) on the randomly excited data. The desired result is a mathematical function that more closely matches the theoretical expectation of damped sinusoids. The primary issue in the current single pass correlation functions is not the sinusoidal content but the incomplete capture of the decaying exponential envelope. Hence, the first step will be to extract the envelope. To do this we start by generating an analytic function using the Hilbert transform of the first pass correlation functions:

$$C_{ij}(t) = R_{ij}(t) + \sqrt{-1} * H_{ij}(t); \text{ where} \quad (6.1)$$



**Fig. 6.2** Use of repeated correlation calculations to reduce beating phenomena

$R_{ij}$  is correlation function between outputs  $i$  and  $j$ ;  
 $H_{ij}$  is the Hilbert transform of  $R_{ij}$ ; and  
 $C_{ij}$  is the analytic function associated with  $R_{ij}$  and  $H_{ij}$ .

The Hilbert transform is defined as follows:

$$H_{ij}(t) = \frac{1}{\pi} \int_{-\infty}^{\infty} \frac{R_{ij}(\tau)}{(t - \tau)} d\tau. \quad (6.2)$$

The envelope is then the amplitude of the complex analytic function:

$$A_{ij}(t) = \sqrt{R_{ij}^2(t) + H_{ij}^2(t)}. \quad (6.3)$$

Figure 6.3 contains an example of the previous functions. The top plot is the numerical displacement response of a single-mode 10 Hz system with 1% damping as excited with random inputs. The middle plot shows the autocorrelation function from the data in the top plot. The bottom plot shows the associated envelope as described by (6.3) above. Now the theoretical result suggests that the correlation function looks a decaying sinusoid, hence for this single-mode system, the envelope should look like an exponential decay:

$$A_{ij}(t) \approx A_0 e^{-at} \quad (6.4)$$

Therefore for this simplified system, we can take the natural log to simplify:

$$\ln(A_{ij}(t)) \approx \ln(A_0) + \ln(e^{-at}) = a_0 - at. \quad (6.5)$$

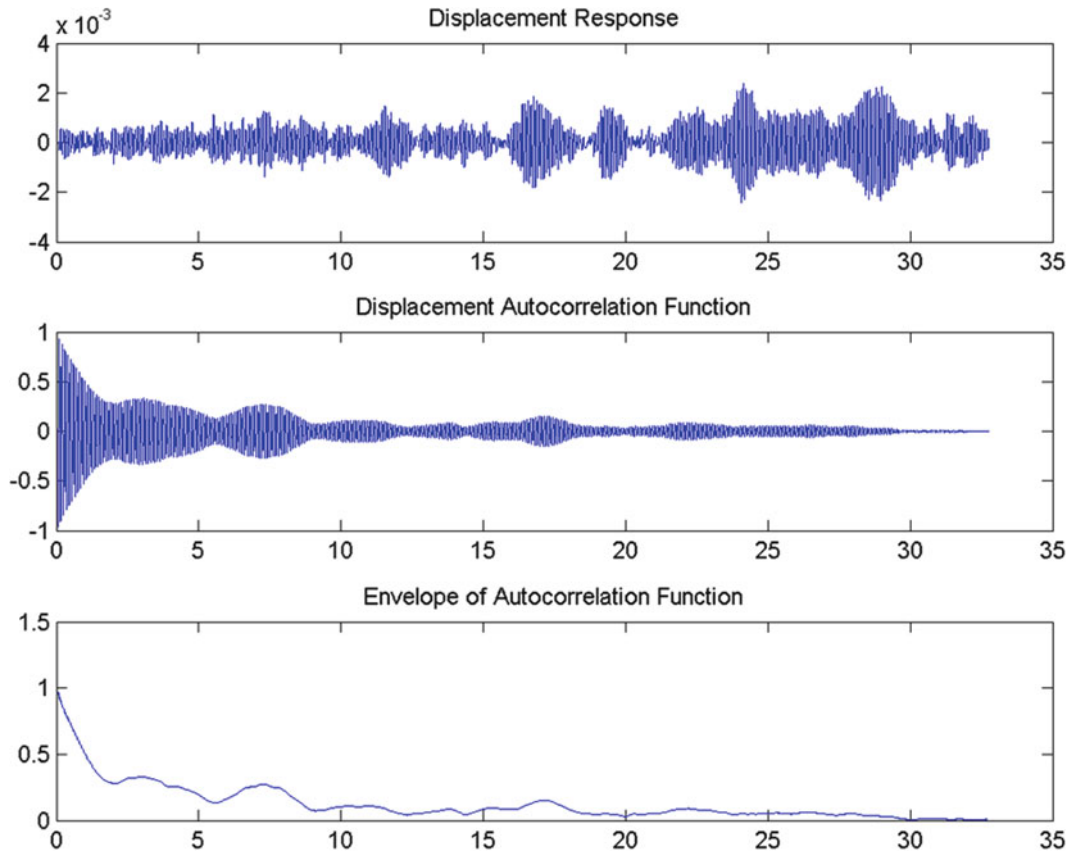


Fig. 6.3 Envelope of correlation function of a single DOF analytical data

There are two possible approaches to determine estimates of the exponential parameter from the log envelope. The first approach is to fit a line to the natural log of the envelope with the offset providing  $a_0$  and the slope ( $a$ ) parameter. For subsequent discussions, this approach shall be referred to as the “linear slope” approach and the slope parameter designated as “ $a_1$ ”. The alternative approach is to take a mean value of the differences between any two values of the log envelope and divide by the time step. This approach will be referred to as the “mean difference” and the slope parameter designated as “ $a_2$ ”. Figure 6.4 shows those two approaches and the best fit estimates for the first half of the records of the log envelope given in Fig. 6.3.

In order to further increase the content of the modal response and reduce the effects of the random forcing function, the current correlation function is subjected to another pass through the correlation processing step. Correlation processing (in a time domain sense) involves a summation process of all data separated by the same number of time steps (or correlation lags in this case):

$$R_{ij}(\tau) = \sum_{t=0}^{t_{\max}-\tau-1} x(t+\tau)y(t) \quad \tau \geq 0$$

$$R_{ij}(\tau) = R_{ij}(-\tau) \quad \tau < 0 \quad (6.6)$$

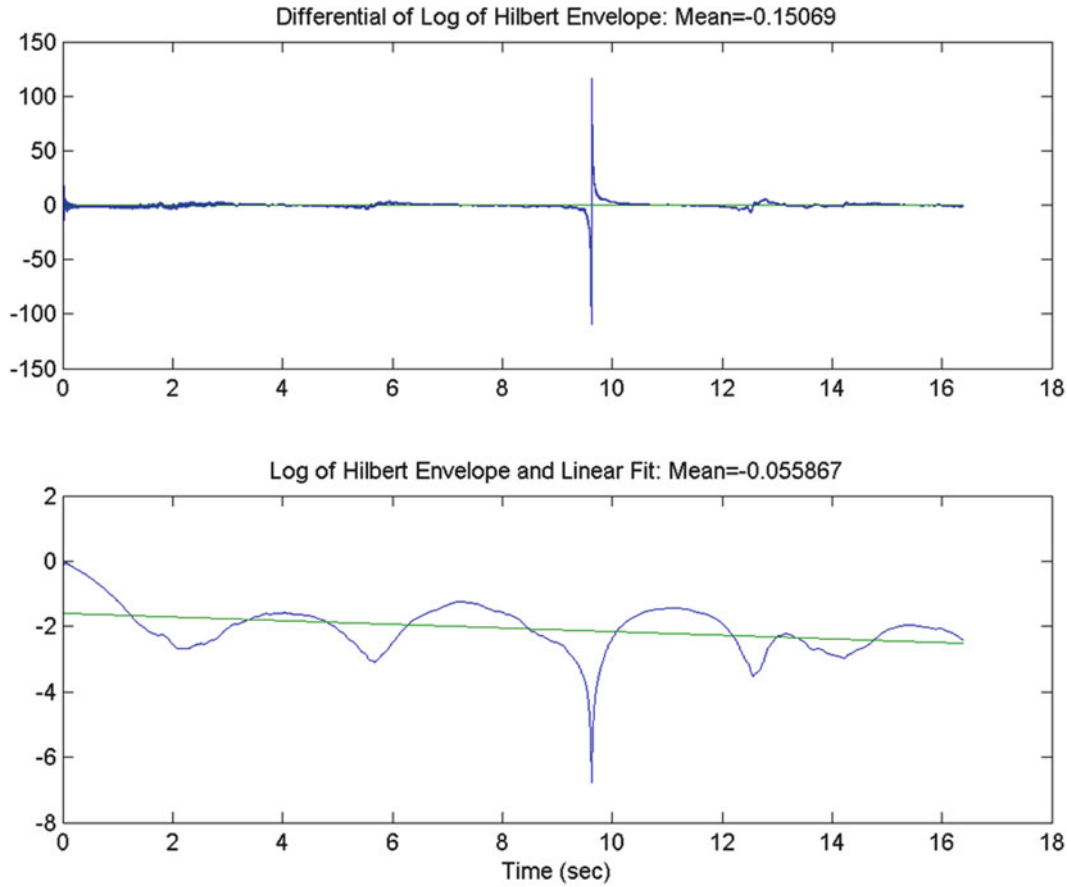
Now if we substitute the original time history products for the current correlation function and add a subscript to denote the iteration or number of the successive correlation steps ( $k$ ):

$$R_{ijk}(\tau) = \sum_{t=0}^{t_{\max}-\tau-1} R_{ijl}(t+\tau)R_{ijl}(t) \quad \tau \geq 0$$

$$R_{ijk}(\tau) = R_{ijk}(-\tau) \quad \tau < 0 \quad (6.7)$$

Where  $l = k-1$ .





**Fig. 6.4** Fits to log envelope of a single DOF analytical correlation function

Hence, the variables of interest will be estimated at each iteration and will receive a “ $k$ ” subscript:  $H_{ijk}(t)$ ,  $C_{ijk}(t)$ ,  $A_{ijk}(t)$ ,  $a_{0k}$ ,  $a_{1k}$ , and  $a_{2k}$ . The slope parameters are updated each iteration and compared to the previous value and scaled with respect to the first slope value to produce a convergence metric (labeled as  $b_{0k}$  and  $b_{1k}$ ). Hence for the linear slope metric:

$$b_{1k} = 100 * \left( \frac{a_{1k} - a_{1l}}{a_{1l}} \right). \quad (6.8)$$

And for the mean difference metric:

$$b_{2k} = 100 * \left( \frac{a_{2k} - a_{2l}}{a_{2l}} \right). \quad (6.9)$$

Figure 6.5 shows typical convergence histories for these two metrics. The top plot provides the actual values of the slope parameters (as illustrated in Fig. 6.4) for multiple subsequent correlation iterations. The lower plot shows the traces of the related convergence metrics. For this example the process was ended when the convergence metric was lower than 1% in either parameter. Typically the mean difference converges first. Figure 6.6 shows the fits to the converged log envelopes. Although there are some obvious numerical issues for longer lag times, the overall trends are much closer to the expected exponential decay model. Figure 6.7 shows the final correlation trace after convergence in the top plot. The middle plot contains the final envelope of the correlation trace. These plots show the expected decaying exponential shape. After performing a modal identification on the data shown in Fig. 6.7, the resulting modal frequency is found to be 10.1 Hz with .99% damping. The resulting synthesis to the converged data is provided in Fig. 6.8. The final extracted frequency and damping is used to generate damped sine and cosine functions which are least-squares fit to the correlation data to generate the synthesis.

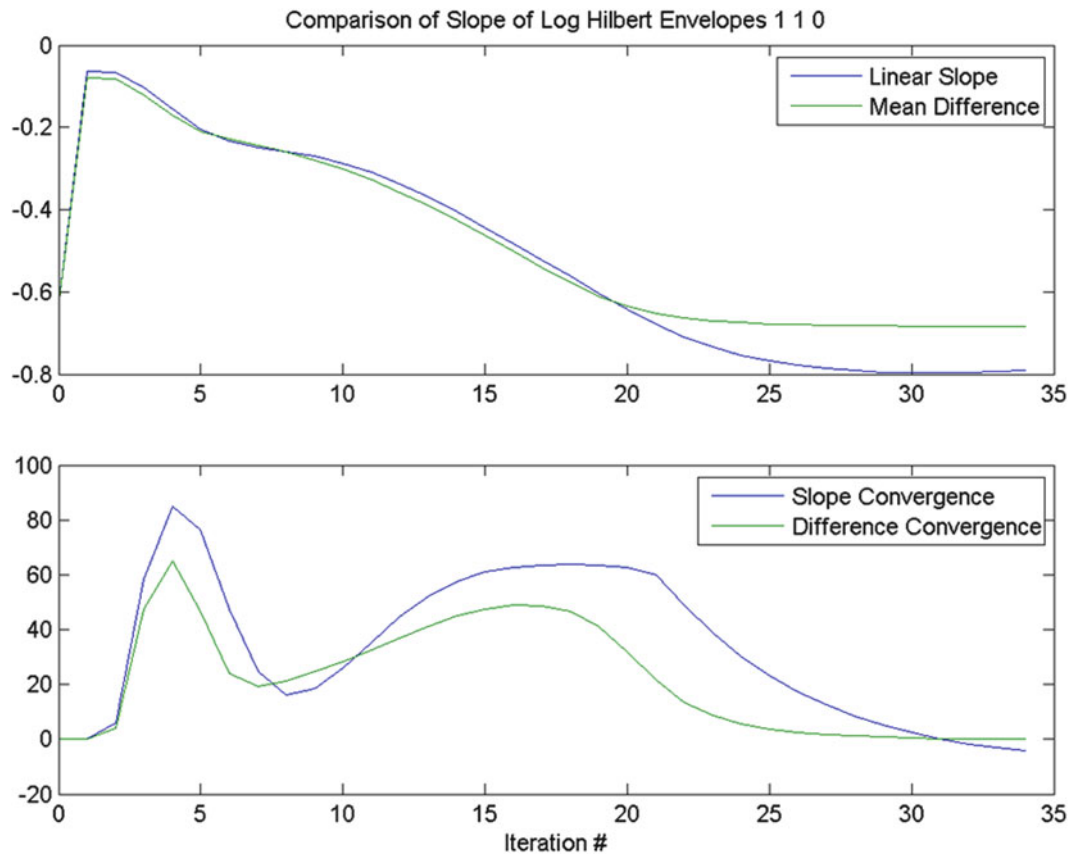


Fig. 6.5 Convergence of multiple correlations of single DOF analytical data

### 6.3.3 Numerical Assessment of Recursive Correlation/Convergence Metric Approach

The data provided above to study and develop a mitigation strategy for correlation beating on short time records is subject to several simplifying factors that will have to be assessed before the process becomes truly useful. These include multiple modes, data stationarity, multiple sensors, numerical round-off error, system noise, the role that the phase of the analytic function may play, digital parameter shifting (as seen in numerical integration algorithms), and the order to apply the cross-correlation and iterative autocorrelations when using data from different sensors. However, the most critical unknown to be removed before this mitigation process is useful for short time record launch data analysis are the actual effects of data record length. Hence, a scoping study of the effects was performed some critical features of the overall technique were uncovered.

This scoping study involved utilizing several different data record lengths of data to develop estimates of the modal frequency and modal damping to assess the trends in the parameters. For the 10 Hz analytical data with 1% damping, data lengths from 1,024 samples to 32,768 length data record were assessed in increasing data record length increments of 1,024 samples for 32 different analyses. Figure 6.9 provides the results of this study. The top plot shows the variation of the extracted frequency as the data record length processed in increased. The frequency variations are exaggerated due to the scale and are not significantly problematic. However, the lower damping plot shows a clear trend of increasing damping estimates away from the 1% expected value as the record length is increased. This is an issue that must be dealt with as damping is a critical parameter in these studies and the shorter time records are the region that launch data processing will be utilizing. The good news from the initial study was that the process break-down appeared to be stochastic with a clear monotonic trend. This was the state of the work as reported in Ref. [38].

Further work to understand short time history effects lead to an unfortunate finding. Figure 6.10 shows the same scoping study if the damping is increased from 1% to 10%. In this study, the damping was seen to continue to converge to 1%. Several other input values of damping were exercised with very similar results. Hence the extracted damping values of the recursive correlation technique were completely numerical in origin.



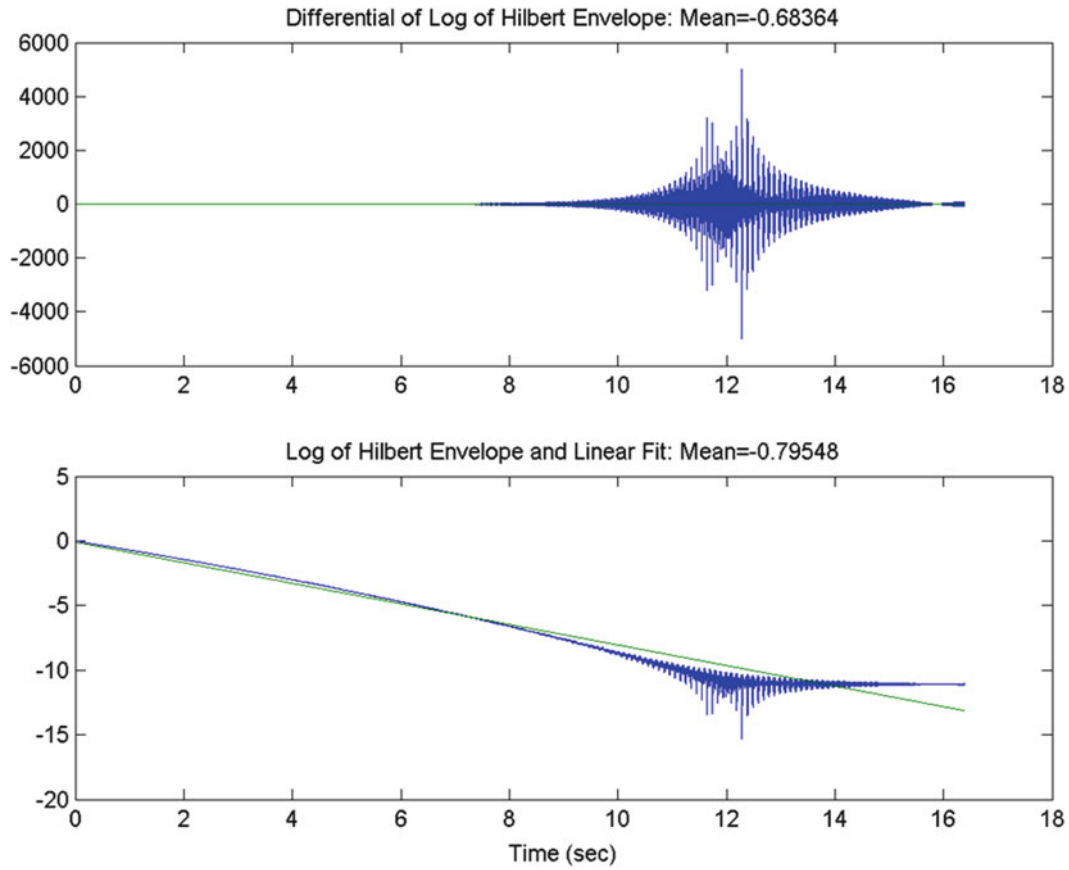


Fig. 6.6 Converged fits to log envelope of single DOF analytical data

### 6.3.4 Analytical Study of Recursive Correlation Damping

In order to study the short time history and recursive correlation effects, assume a damped cosine function (see [Appendix 1](#) for the theoretical basis of this assumption):

$$x(t) = e^{-\delta\omega t} \cos(\omega t). \quad (6.10)$$

The autocorrelation function could then be defined as:

$$R_{xx}(\beta) = \int_{\alpha_1}^{\alpha_2} x(\alpha + \beta)x(\alpha)d\alpha. \quad (6.11)$$

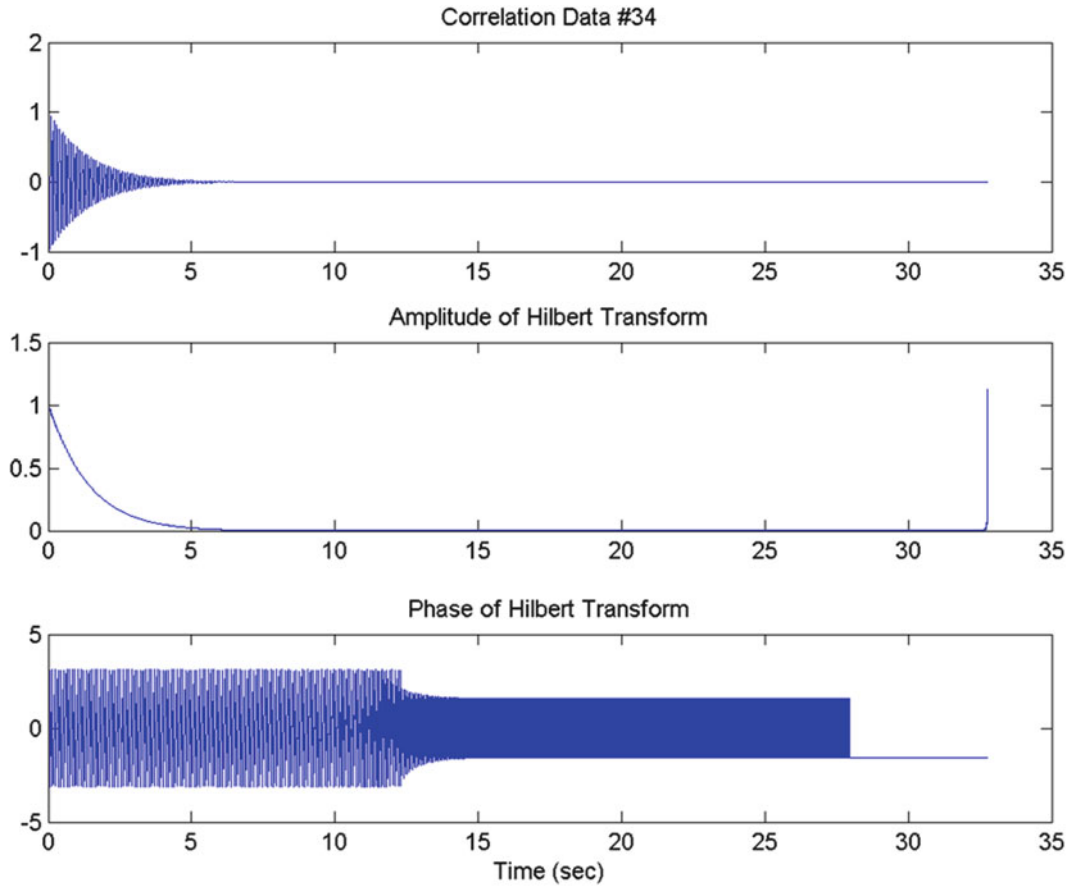
With the following definitions feeding (6.11):

$$\alpha = \delta\omega t. \quad (6.12)$$

$$\beta = \delta\omega\tau. \quad (6.13)$$

$$\alpha_1 = 0; \quad (6.14)$$

$$\alpha_2 = \delta\omega(t_f - \tau) = \alpha_f - \beta; \quad (6.15)$$



**Fig. 6.7** Envelope of converged correlation function of single DOF analytical data

$$x(\alpha) = e^{-\alpha} \cos\left(\frac{\alpha}{\delta}\right); \text{ and} \quad (6.16)$$

$$x(\alpha + \beta) = e^{-\alpha} \cos\left(\frac{\alpha}{\delta}\right) e^{-\beta} \cos\left(\frac{\beta}{\delta}\right) e^{-\alpha} \sin\left(\frac{\alpha}{\delta}\right) e^{-\beta} \sin\left(\frac{\beta}{\delta}\right). \quad (6.17)$$

After rearranging the following equation results:

$$R_{xx}(\beta) = \int_{\alpha_1}^{\alpha_2} \left\{ A(\alpha) e^{-\beta} \cos\left(\frac{\beta}{\delta}\right) - B(\alpha) e^{-\beta} \sin\left(\frac{\beta}{\delta}\right) \right\} d\alpha. \quad (6.18)$$

With the following definitions used to generate (6.18):

$$A(\alpha) = \frac{1}{2} e^{-2\alpha} \left[ 1 + \cos\left(\frac{2\alpha}{\delta}\right) \right]; \text{ and} \quad (6.19)$$

$$B(\alpha) = \frac{1}{2} e^{-2\alpha} \sin\left(\frac{2\alpha}{\delta}\right). \quad (6.20)$$

Now when the following assumption is used:

$$\delta^2 \approx 0. \quad (6.21)$$

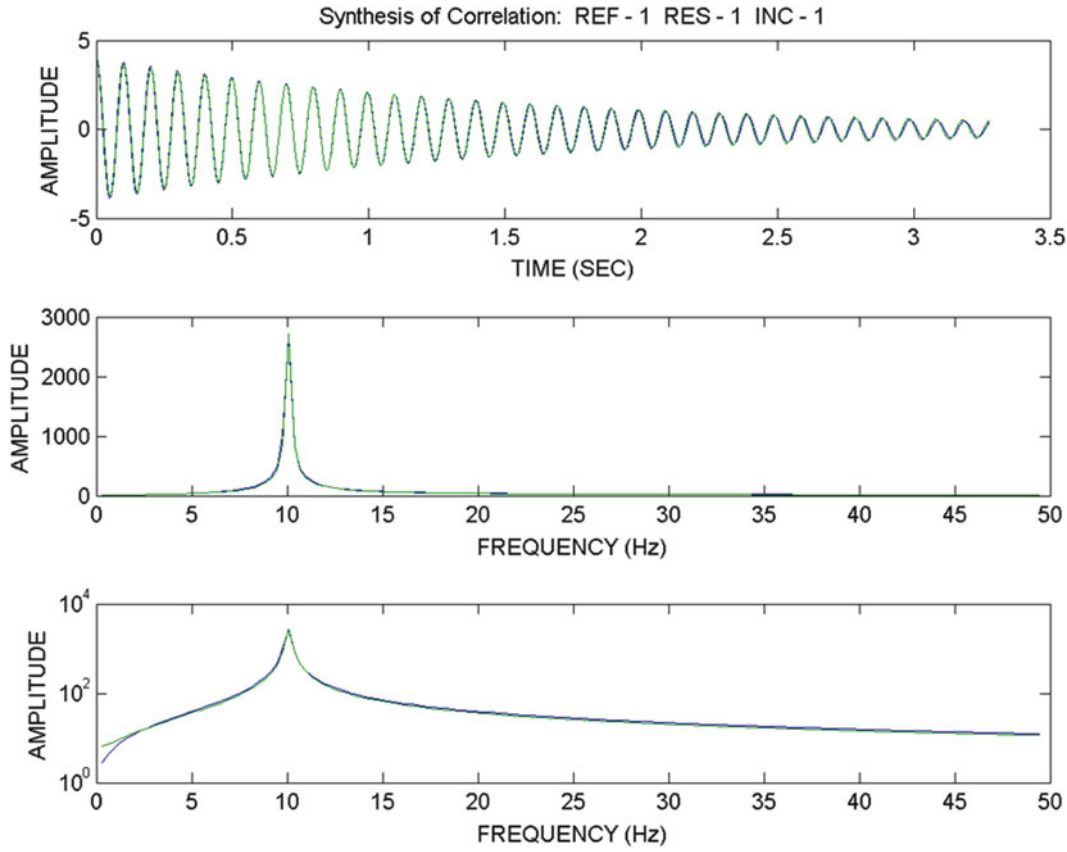


Fig. 6.8 Data and synthesis of modal fit to converged correlation of analytical data

These simplifications result:

$$\int_{\alpha_1}^{\alpha_2} A(\alpha) d\alpha \approx \frac{1}{4}(1 - e^{-2\alpha_2}) + 0; \text{ and} \quad (6.22)$$

$$\int_{\alpha_1}^{\alpha_2} B(\alpha) d\alpha \approx 0. \quad (6.23)$$

With these simplifications, the autocorrelation reduces to the following:

$$R_{xx}(\beta) \approx \frac{1}{4} [1 - e^{-2(\alpha_f - \beta)}] e^{-\beta} \cos\left(\frac{\beta}{\delta}\right). \quad (6.24)$$

Equation 6.24 can also be written as the following:

$$R_{xx}(\tau) \approx \frac{1}{4} [1 - e^{-2\delta\omega(t_f - \tau)}] e^{-\delta\omega\tau} \cos(\omega\tau). \quad (6.25)$$

Now for the case of  $\omega = 10$  Hz,  $\delta = 1\%$ ,  $t_f = 1$  s, the function  $1 - e^{-2\delta\omega(t_f - \tau)}$  is shown in Fig. 6.11.

As the final time gets larger, the resulting function shown in Fig. 6.11 rapidly approaches 1.0 for most lags in the correlation function. Figure 6.12 shows the function for a 10 s time history and Fig. 6.13 for a 100 s data record. Hence for short time records the damping will be significantly affected by each correlation processing step that is used. For longer time histories, the numerical damping effects are limited to the last few lags of the resulting correlation function. However, these limited longer time history effects apparently build up over time to reach some steady-state value of numerical damping. It is very interesting that the modal frequency is largely unaffected by this numerical error.

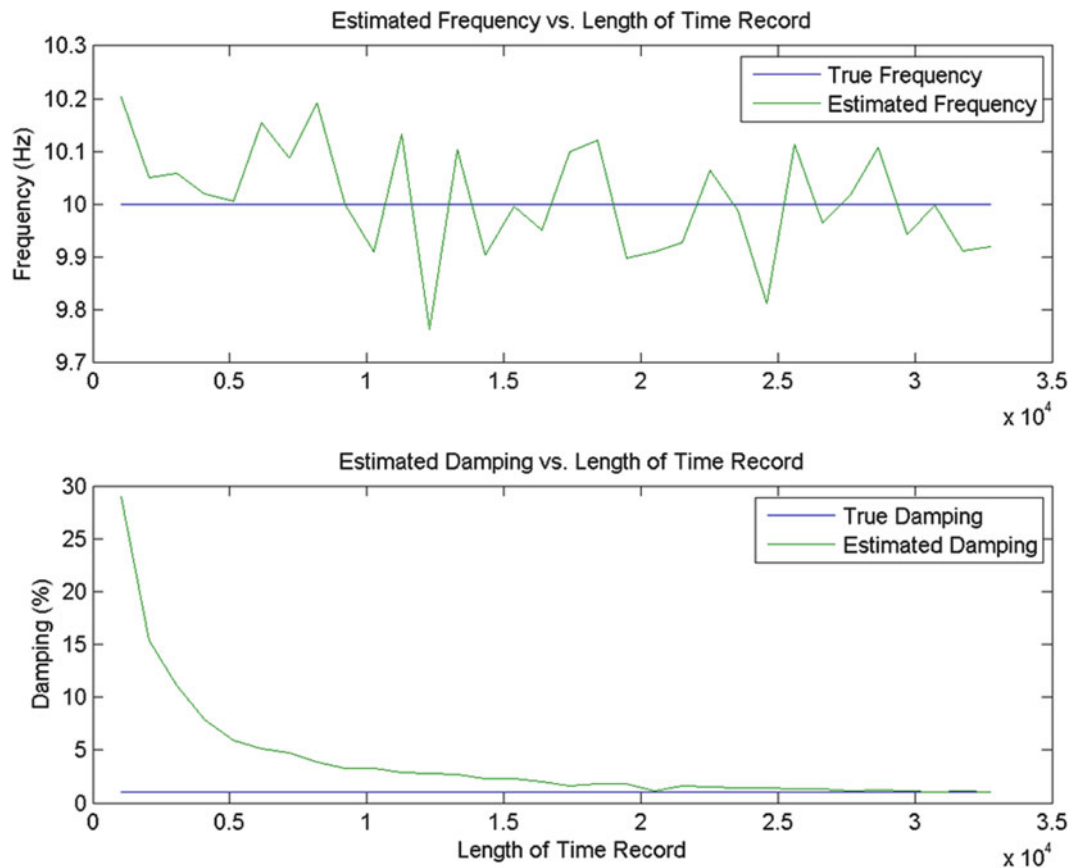


Fig. 6.9 Effect of data record length using single DOF analytical data – 1% damping

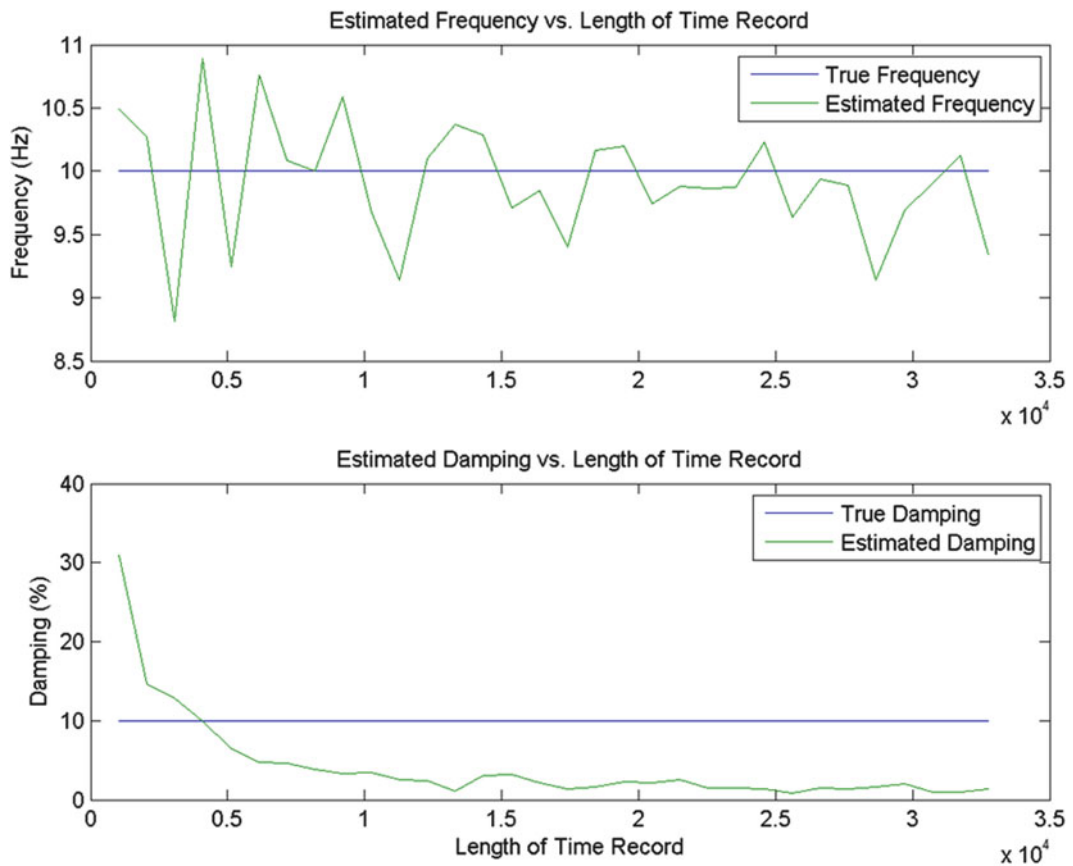
### 6.3.5 Recommended Follow-on Work

The direct use of the suggested convergence metric for recursive correlation functions to extract modal damping is not a promising activity based on this work. Although, a more in-depth study of the damping modification build-up as a function of recursion step and the subsequent information contained in the phase of the analytic function are promising avenues to increase understanding. However, the ability clean up randomly excited data and extract well-behaved frequency estimates is an advantage to be pursued. A suggested next step would be to verify the frequency stability based on a larger set of increasingly realistic data characteristics as was mentioned above. If successful modal frequency extraction is seen, then these estimates could be used to drive a supplemental extraction process for damping. Such supplemental processes might be based on wavelet functions (see Refs. [22] and [23]) as a first recommended trial study.

## 6.4 Conclusion

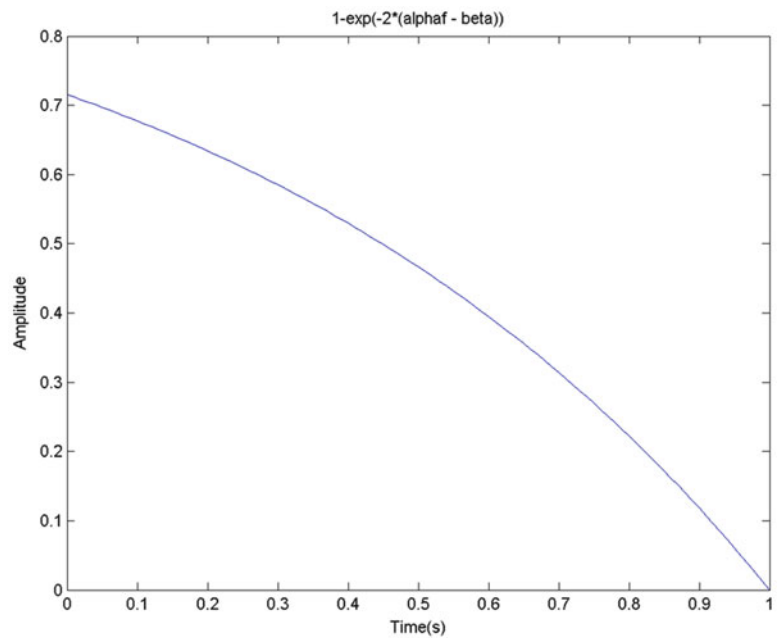
The process of identifying modal parameters during launch is a difficult and challenging process. In this work, the launch phase of flight is assumed to be processed with small moving windows that are intended to keep the variations in modal parameters to a minimum such that stationary assumptions can hold. A more specific assumption of this work is that acceleration data in each window are processed into cross- and autocorrelation functions. It has been found that this process is hampered by “beating” or “blooms” in the correlation functions. These unwanted features limit the amount of data that can be used in the subsequent time domain algorithm processing. In typical ground based applications, these effects are rarely seen as frequency-domain averaging using long stationary time histories is highly effective at eliminating the issue.

An alternative approach has been reported that may be applicable in launch processing is the use of multiple iterations of correlation processing using the same base data. This mitigation had been hampered until recently by the lack of a



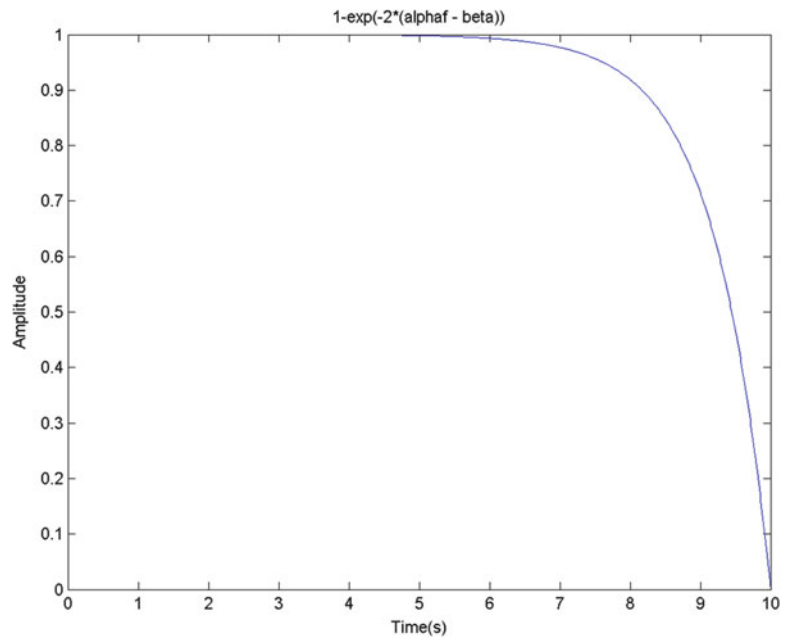
**Fig. 6.10** Effect of data record length using single DOF analytical data – 10% damping

**Fig. 6.11** Numerical scaling factor for autocorrelation function based on a 1 s time history

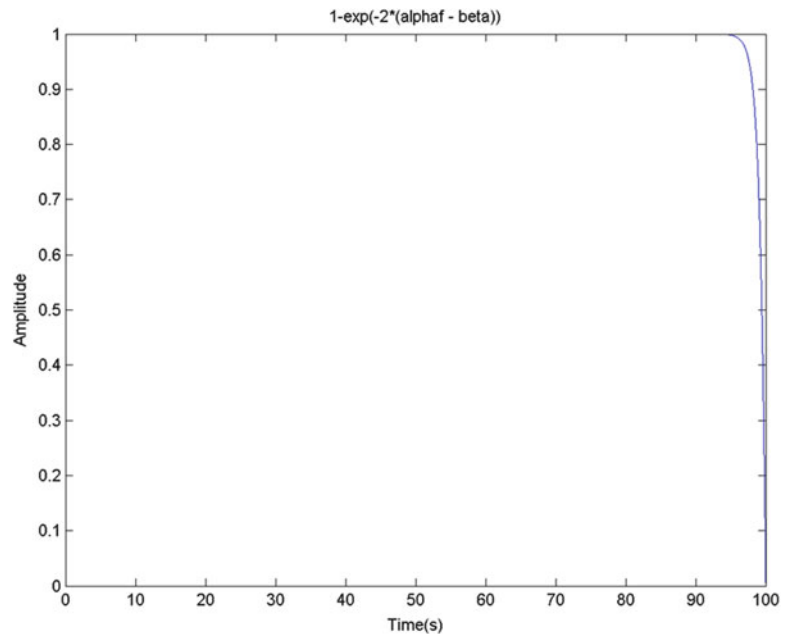


convergence metric to allow the process to terminate. The recent development of a convergence metric has allowed this recursive correlation process to be subjected to further scrutiny. The convergence metric utilized a Hilbert transform of the resulting correlation function from each recursive step to generate an analytic representation of the data. The envelope of each correlation function can thus be extracted from the analytic function. The natural log of this envelope is then used to set

**Fig. 6.12** Numerical scaling factor for autocorrelation function based on a 10 s time history



**Fig. 6.13** Numerical scaling factor for autocorrelation function based on a 100 s time history



the data into a format where a linear slope can be estimated. A significant finding is that for a limited class of data studied to-date (single dominant mode) is that these slope parameter estimates converge. Previously, this convergence seemed to produce an estimate of the proper damping for long enough time histories with a deterministic bias affecting shorter time histories.

Work reported herein has shown that the proper modal damping is replaced with a fairly consistent value of numerical damping by repeated correlations. However, the modal frequency is left intact in this process. Subsequent mathematical studies have suggested that there is an expected numerical modification of the modal damping when short time history correlation processing is used. Furthermore this study has suggested that longer time histories will also be subjected to numerical damping modification via repeated correlation processing based on the same limitations of the correlation functions. There are some fruitful follow-on studies that can be envisioned to further understand the numerical effects on damping such as a mathematical assessment of multiple correlations and the information available in the phase of the analytical function.

The modal frequency estimation process becomes a much more refined activity and this advantage needs to be studied and pursued. If this holds after subsequent studies with more realistic data sets, then a supplemental process to extract damping can be pursued with refined estimates of frequency available. Wavelet technology has been suggested as one potential basis for such a supplemental process.

## A.1 Appendix 1A: Theoretical Basis for an OMA Process, NExT

A critical step in the development of NExT was to find a function that could be measured from operational data, but possessed a clear relationship with and a dependence on the modal parameters of the structure. For NExT, the function selected was cross-correlation functions between responses without a measurement of the input force. This section outlines the development of the relationship between the cross-correlation function and modal parameters. The full details of this development can be found in multiple Refs. [1, 40, 41].

The derivation begins by assuming the standard matrix equations of motion:

$$[M] \{\ddot{x}(t)\} + [C] \{\dot{x}(t)\} + [K] \{x(t)\} = \{f(t)\} \quad (6.26)$$

where

[M] is the mass matrix;

[C] is the damping matrix;

[K] is the stiffness matrix;

{f} is a vector of random forcing functions;

{x} is the vector of random displacements; and t is time.

Equation 6.26 can be expressed in modal coordinates using the standard modal transformation and diagonalized matrices (assuming proportional damping). A solution to the resulting scalar modal equations can be performed via the convolution or a Duhamel integral and assuming a general forcing function {f} with zero initial conditions [42]. The solution can be converted back into physical coordinates and specialized for a single input force and a single output using appropriate mode shape matrix entries. The following equation results:

$$x_{ik}(t) = \sum_{r=1}^n \psi_{ir} \psi_{kr} \cdot \int_{-\infty}^t f_k(\tau) g^r(t-\tau) d\tau \quad (6.27)$$

where  $g^r(t) = 0$ , for  $t < 0$ ;  $g^r(t) = \frac{1}{m^r \omega_d^r} \exp\left(-\zeta^r \omega_n^r t\right) \sin\left(\omega_d^r t\right)$ , for  $t \geq 0$ ;  $\omega_d^r = \omega_n^r \left(1 - \zeta^{r2}\right)^{1/2}$  is

the damped modal frequency;

$\omega_n^r$  is the  $r^{th}$  modal frequency;

$\zeta^r$  is the  $r^{th}$  modal damping ratio;

$m^r$  is the  $r^{th}$  modal mass;

n is the number of modes;

$\psi_{ir}$  is the  $i^{th}$  component of mode shape r; and

t is the time.

The next step of the theoretical development is to form the cross-correlation function of two responses ( $x_{ik}$  and  $x_{jk}$ ) due to a white-noise input at a particular input point k. The cross-correlation function  $\mathfrak{R}$  as the expected value of the product of two responses evaluated at a time separation of T,

$$\mathfrak{R}_{ijk}(T) = E[x_{ik}(t+T) x_{jk}(t)] \quad (6.28)$$

where E is the expectation operator [13, 43].

Substituting (6.27) into (6.28) and recognizing that the force  $f$  is the only random variable, then the expectation operator functions only on the forcing function. Using the definition of the autocorrelation function [17], and assuming for simplicity that the forcing function is white noise (this is only approximately true), then the expectation operation collapses to a scalar times a Dirac delta function. The Dirac delta function collapses one of the Duhamel integrations embedded in the cross-correlation function. The resulting equation can be simplified via a change of variable of integration ( $\lambda = t - \tau$ ). Using the definition of  $g$  from (6.27) and the trigonometric identity for the sine of a sum results in all the terms involving  $T$  being separated from those involving  $\lambda$ . This separation allows terms that depend on  $T$  to be factored out of the remaining integral and out of one of the modal summations. This results in:

$$\Re_{ijk}(T) = \sum_{r=1}^n \left[ A_{ijk}^r \exp\left(-\zeta^r \omega_n^r T\right) \cos\left(\omega_d^r T\right) + B_{ijk}^r \exp\left(-\zeta^r \omega_n^r T\right) \sin\left(\omega_d^r T\right) \right] \quad (6.29)$$

where  $A_{ijk}^r$  and  $B_{ijk}^r$  are independent of  $T$ , are functions of only the modal parameters, contain completely the remaining modal summation, and are shown below.

$$\left\{ \begin{array}{c} A_{ijk}^r \\ B_{ijk}^r \end{array} \right\} = \sum_{s=1}^n \frac{\alpha_k \psi_{ir} \psi_{kr} \psi_{js} \psi_{ks}}{m^r \omega_d^r m^s \omega_d^s} \cdot \int_0^\infty \exp\left(-\zeta^r \omega_n^r - \zeta^s \omega_n^s\right) \lambda \cdot \sin\left(\omega_d^s \lambda\right) \left\{ \begin{array}{c} \sin\left(\omega_d^r \lambda\right) \\ \cos\left(\omega_d^r \lambda\right) \end{array} \right\} d\lambda. \quad (6.30)$$

Equation (6.29) is now the key result of this derivation because many time-domain modal analysis algorithms utilized impulse response functions as the input data for estimating the modal parameters. We see that (6.29) shows that the cross-correlation function has the same characteristics as the impulse response function, a sum of decaying sinusoids with the same damping and frequency as the impulse response function. Thus, cross-correlation functions can be used in place of impulse response functions in these time-domain modal parameter estimation algorithms. Consequently, (6.29) provides us with the desired function that can be measured from operational data and used to extract the modal parameters. The reader can refer to the provided references for more details of the intermediate steps in this derivation [1, 14, 15]. These references also provide verification of this derivation, using the maximum of an autocorrelation function and a cross-correlation identity.

## References

1. James G, Carne T, Lauffer J (1995) The Natural Excitation Technique (NExT) for modal parameter extraction from operating structures. *SEM Int J Anal Exp Modal Anal* 10(4):260–276
2. Vold H, Rocklin T (1982) The numerical implementation of a multi input modal estimation algorithm for mini-computers. In: *Proceedings of IMAC I*, Orlando
3. Juang J-N, Pappa R (1985) An eigensystem realization algorithm for modal parameter identification and model reduction. *AIAA J Guidance Control Dyn* 8(4):620–627
4. Brinker R, Kirkegaard P (2010) Editorial in the special issue on operational modal analysis. *Mech Syst Signal Process* 24(5):1209–1212
5. Hermans L, Van der Auweraer H (1997) On the use of auto and cross-correlation functions to extract modal parameters from output-only data. In: *Proceedings of structural dynamics: recent advances*, Southampton, 14–17 July 1997
6. Cao T, Zimmerman D, James G (1998) Identification of Ritz vectors from ambient test data. In: *Proceedings of IMAC XVI*, Santa Barbara, 2–5 Feb 1998
7. Zhang L, Brinker R, Andersen P (2001) Modal indicators for operational modal identification. In: *Proceedings of IMAC XIX*, Kissimmee
8. Mohanty P, Rixen D (2003) Modifying the ERA identification for operational modal analysis in the presence of harmonic perturbations. In: *Proceedings of the 16th ASCE engineering mechanics conference*, Seattle, 16–18 July 2003
9. Calcedo J, Dyke S, Johnson E (2004) Natural excitation technique and Eigensystem realization algorithm for phase I of the IASC-ASCE Benchmark problem: simulated data. *J Eng Mech* 130(1):49–60
10. Chiang D-Y, Lin C-S (2012) Identification of modal parameters from nonstationary ambient vibration data using correlation technique. In: *Proceedings of IMAC XXX*, Jacksonville, Jan 30–Feb 2, 2012
11. Carne T, James G (2010) The inception of OMA in the development of modal testing technology for wind turbines. *Mech Syst Signal Process* 24(5):1213–1226
12. Brownjohn J, Carden P (2007) Reliability of frequency and damping estimates from free vibration response. In: *Proceedings of the 2nd international operational modal analysis conference*, Copenhagen, pp 23–30
13. Zhang L, Wang T, Tamura Y (2010) A frequency-spatial domain decomposition (FSDD) method for operational modal analysis. *Mech Syst Signal Process* 24(5):1227–1239



14. Magalhães F, Cunha A, Caetano E, Brinker R (2010) Damping estimation using free decays and ambient vibration tests. *Mech Syst Signal Process* 24(5):1274–1290
15. Campbell R, Vandiver J (1980) The estimation of natural frequencies and damping ratios of offshore structures. In: *Proceedings of the 12th annual offshore technology conference*, Houston
16. Briggs M (1981) Multichannel maximum entropy method of spectral analysis applied to offshore structures. WHOI-81-69, Woods Hole Oceanographic Institute
17. Ibrahim S (1977) Random decrement technique for modal identification of structures. *J Spacecraft Rockets* 14(4):183–198
18. Asmussen J, Ibrahim S, Brinker R (1998) Random decrement: identification of structures subjected to ambient excitation. In: *Proceedings of IMAC XVI, Santa Barbara*, 2–5 Feb 1998
19. Agneni A, Crema LB, Coppotelli G (2010) Output-only analysis of structures with closely spaced poles. *Mech Syst Signal Process* 24(5): 1241–1249
20. Bjerg I, Hansen S, Brinker R, Aenlle ML (2007) Load estimation by frequency domain decomposition. In: *Proceedings of the 2nd international operational modal analysis conference*, Copenhagen, pp 669–676
21. James G, Carne T, Wilson B (2007) Reconstruction of the space shuttle roll-out forcing function. In: *Proceedings of the IMAC XXV, Orlando*, 19–23 Feb 2007
22. Freudinger L, Lind R, Brenner M (1997) Correlation filtering of modal dynamics using the Laplace Wavelet, NASA CR-97-207066
23. Lind R, Brenner M, Haley S (1997) Estimation of modal parameters using a Wavelet approach, NASA TM-97-206300
24. Gröchenig K (2001) *Foundations of time-frequency analysis*, Birkhäuser, Basel, Switzerland, p 386
25. Huang NE et al (1998) The empirical mode decomposition and the Hilbert spectrum for non-linear and non-stationary time series analysis. *Proc R Soc Lond* 454:903–993
26. Chen J, Xu YL (2002) Identification of modal damping ratios of structures with closely spaced modal frequencies. *Struct Eng Mech* 14(4): 417–434
27. Xu YL, Chen SW, Zhang RC (2003) Modal identification of Di Wang Building under Typhoon York using the Hilbert-Huang transform method. *Struct Des Tall Special Buil* 12(1):21–47
28. James G, Carne T, Marek E (1994) In-situ modal analysis of STARS missile flight data and comparison to pre-flight predictions from test-reconciled models. In: *Proceedings of the 15th IES aerospace testing seminar*, Manhattan Beach, 11–13 Oct 1994
29. James G (2003) Modal parameter estimation from space shuttle flight data. In: *Proceedings of IMAC XXI, Kissimmee*, 3–6 Feb 2003
30. James G et al (2012) Operational analysis in the launch environment. In: *Proceedings of IMAC XXX, Jacksonville*, Jan 30–Feb 2, 2012
31. Kim H, Van Horn D, Doiron H (1994) Free-decay time-domain modal identification for large space structures. *J Guid Contr Dyn* 17(3):513–519
32. Le Gallo V, Goursat M, Gonidou L (2007) Damping characterization and flight identification. In: *Proceedings of IMAC XXV, Orlando*
33. Goursat M, Döhler M, Mevel L, Andersen P (2010) Crystal clear SSI for operational modal analysis of aerospace vehicles. In: *Proceedings of IMAC XXVIII, Jacksonville*
34. Franssen S, Rixen D, Henriksen T, Bonnet M (2010) On the operational modal analysis of solid rocket motors. In: *Proceedings of IMAC XXVIII, Jacksonville*
35. Bartkowicz T, James G (2011) Ares 1-X in-flight modal identification. In: *Proceedings of 52nd AIAA/ASME/AHS/ASC SDM conference*, Boulder, 4–8 Apr 2011
36. James G, Chhipwadia K, Zimmerman D (1999) Application of autonomous modal identification to traditional and ambient data sets. In: *Proceedings of IMAC XVII, Kissimmee, FL USA*
37. Pappa R, James G, Zimmerman D (1999) Application of autonomous modal identification of the Space Shuttle tail rudder. *AIAA J Spacecraft Rockets* 35(2):163–169
38. James G (2012) Development of operational modal analysis techniques for launch data, AAS-12-627, American Astronautical Society
39. James G, Cao T, Fogt V, Wilson RL, Bartkowitz T (2011) Extraction of modal parameters from spacecraft flight data. In: *Proceedings of IMAC XXIX, Jacksonville*
40. James GH, Carne TG, Lauffer JP (1993) The Natural Excitation Technique (NExT) for modal parameter extraction from operating wind turbines, SAND92-1666, Sandia National Laboratories, Albuquerque
41. James GH, Carne TG, Lauffer JP, Nord AR (1992) Modal testing using natural excitation. In: *Proceedings of IMAC X, San Diego*, 3–7 Feb 1992
42. Crandall SH (1958) *Random vibration*. Wiley, New York
43. Papoulis A (1965) *Probability, random variables, and stochastic processes*. McGraw-Hill, New York

# Chapter 7

## Influence of Test Conditions on Comfort Ranking of Road Bicycle Wheels

Julien Lépine, Yvan Champoux, and Jean-Marc Drouet

**Abstract** In the past few years, the dynamic comfort of bicycles has become a hot topic in the cycling industry. To improve comfort, a wide variety of dynamic tests is used to characterize and compare bikes. Because these tests usually involve a cyclist, and since the tires have a non-linear effect on the system, test protocols are expected to have an impact on the dynamic characteristics and bicycle ranking. With the objective of establishing good practices when comparing wheel comfort, this paper presents the influence of several test parameters on the vibrations induced to the cyclist at the hands and buttocks. The influence of two excitation surfaces on bicycle dynamics is studied: a flat excitation surface and an irregular surface that locally deforms the tire. The type of excitation, such as white noise, impacts and typical road excitation, are also investigated. Results with regard to the effect of the cyclist's mass are also presented. The conclusion of this study shows that even if those parameters have a significant influence on the vibration levels transmitted to the cyclist, they do not affect the transmissibility ranking of two wheelsets. It should be noted however that the changes observed in the cyclist's posture and position on the bicycle can affect wheelset ranking. Great care is therefore advised in controlling the cyclist's posture and attitude on the bicycle during the tests.

**Keywords** Bicycle dynamic comfort • Bicycle wheel • Vibrations transmission • Vibration measurement • Excitation techniques

### 7.1 Introduction

Vibrational comfort is a somewhat vague term used in several fields and is related to the level of vibration transmitted from vibrating objects to humans. Several studies have focused on vibrational comfort, especially in the field of health and safety at work and in the field of passenger transport. Two ISO standards have been developed to establish protocols to measure accelerations transmitted to humans [1, 2]. These standards serve as guidelines for measurement and analysis of the vibration level transmitted to humans taking into account human sensitivity to vibrations, which varies with frequency. The vibration transmitted to humans is also the subject of several studies in sports such as ice hockey [3], baseball [4] and golf [5]. The vibrational comfort of road bicycles is also an important issue for bicycle manufacturers and, in the past decade, has become an important design criterion for their products. In this regard, it is essential to have an in-depth understanding of the vibrational behaviour of the bicycle-cyclist system as well as an adequate assessment of the vibration induced to the cyclist/biker (VIB), [6, 7].

Of the main bicycle components, the vibrational behaviour of the wheels has received a lot of attention. Lépine et al. [8] and Petrone and Giubilato [9] have assessed differences in transmissibility of force and acceleration between wheels using test rigs that simulate the cyclist's weight. Olieman et al. [10] have compared wheel comfort with a cyclist riding on different roads. The acceleration at the saddle and handlebars was measured using the same bike for different sets of wheels. For the tested wheelsets, the results of this study did not show any significant difference in the VIB. Using in situ collected data, Giubilato and Petrone [11] have also compared the VIB in acceleration level using different sets of wheels. They observed

---

J. Lépine (✉) • Y. Champoux • J.-M. Drouet  
VélUS Research Group, Department of Mechanical Engineering, Université de Sherbrooke, 2500 boul. de l'Université,  
Sherbrooke, QC J1K 2R1, Canada  
e-mail: [julien.lepine@usherbrooke.ca](mailto:julien.lepine@usherbrooke.ca); [yvan.champoux@usherbrooke.ca](mailto:yvan.champoux@usherbrooke.ca); [Jean-Marc.Drouet@USherbrooke.ca](mailto:Jean-Marc.Drouet@USherbrooke.ca)

significant differences in the VIB for different wheelsets. According to these results, the comfort ranking of wheels is related to the road surface condition. This same conclusion is also shared by Velo News magazine [12, 13].

With regard to the aforementioned studies, there is no unanimous conclusion regarding the influence of the wheels on the VIB and ultimately, on the comfort ranking of wheels. Because test conditions such as the excitation level or the excitation surface seem to be related to the VIB, the aim of this study was to further investigate their influence on the VIB and on the comfort ranking of road bicycle wheels. Using the same bike, the VIB measured using two wheelsets are compared using two cyclists, four excitation types (white noise, road replication, shaker impact, treadmill impact) and two shaker contact surfaces (flat and dowel). This paper presents the results of this investigation.

## 7.2 Methods

Two different wheelsets are used in this paper and identified as wheelset A and wheelset B. Their selection was based on a vibration transmissibility ranking carried out in a previous study [8]. According to the results of this previous study in which six wheels were tested, wheelset A is the one which transmitted most and wheelset B is the one which transmitted least.

All the tests are carried out using the same bicycle. Wheel tires are inflated at eight bar. Two laboratory apparatuses are used: (1) a road simulator equipped with two hydraulic shakers enables us to control the vertical displacement under both wheels (Fig. 7.1a); (2) a homemade bicycle treadmill with a wooden dowel attached to the belt to generate an impact on the wheels (Fig. 7.1b).

During each test, the cyclist's posture is controlled as follows:

- The cyclist assumes as natural a position on the bike as possible, with the hands resting on (but not grasping) the brake levers.
- The cyclist applies and maintains a constant static vertical force at the hands. This force is measured using an instrumented stem.
- The bike cranks are fixed in a horizontal position with the left crank at the front.
- The cyclist does not pedal.

To assess the VIB, the vertical acceleration ( $a_{VIB}$ ) and the transmitted vertical force at the stem and at the saddle ( $F_{VIB}$ ) are measured. At the saddle, the acceleration is measured using a PCB 352C68 accelerometer fixed on the upper part of the seat post and the force is measured using strain gauges located on the seat post (Fig. 7.2). At the stem, the force is measured with an instrumented stem [14] and the acceleration is measured with a PCB 352C65 accelerometer attached near the handlebar clamp (Fig. 7.3).

The signals from the accelerometers and the force transducers at the stem and at the saddle are filtered according to standards ISO 2631 [2] (sensitivity of the hand in all directions) and ISO 5349 [1] (whole body sensitivity to vertical vibration) respectively. The RMS value of filtered signals is a measure to assess the VIB. This method allows us to compare

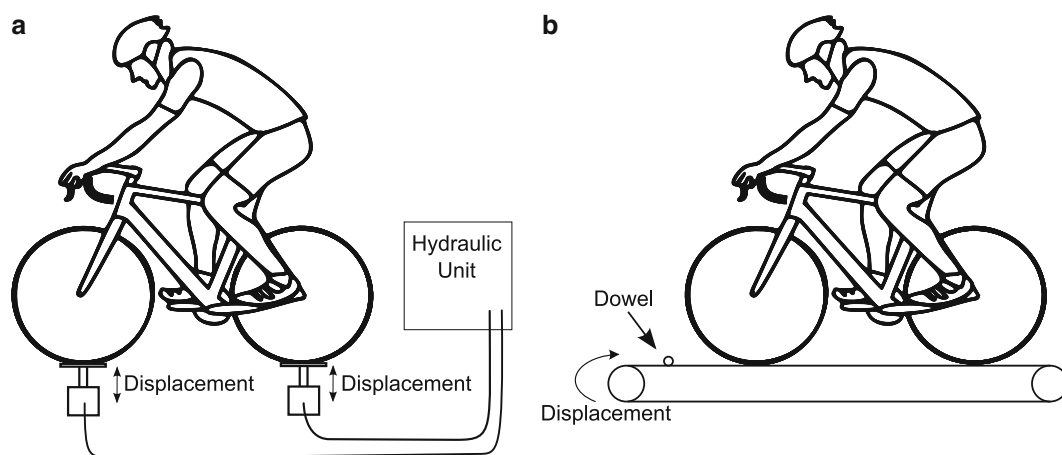
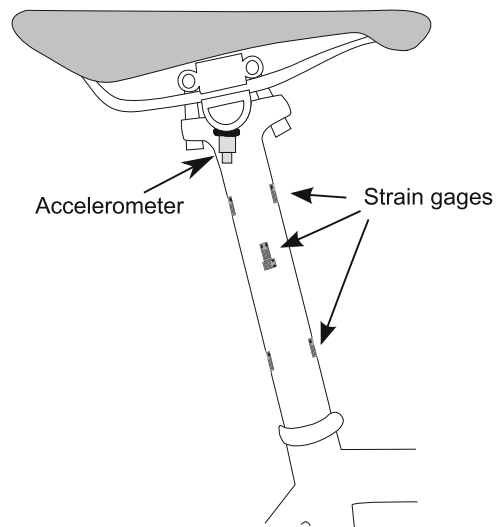
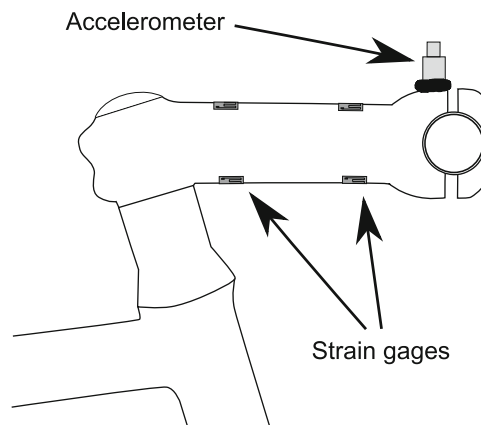


Fig. 7.1 (a) hydraulic actuator excitation; (b) treadmill excitation



**Fig. 7.2** Instrumented seat post



**Fig. 7.3** Instrumented stem

the tests with a single RMS value, thus facilitating the analyses. In this study, the bicycle-cyclist system was considered as a stochastic system. Measurements were repeated in a random order to increase the power of the statistic test used to compare the wheelsets.

The three test condition categories considered are as follows:

- *Type of excitation*

*White noise*: Random white noise excitation up to 100 Hz with 0.3 mm of RMS amplitude generated by the hydraulic shakers (Fig. 7.1a). This amplitude corresponds to the shakers' upper limit.

*Road*: Road excitation replication generated by the hydraulic actuators (Fig. 7.1a) [15].

*Shaker impact*: Vertical impacts of 25 ms duration and 45 mm amplitude created by the hydraulic actuators (Fig. 7.1a).

*Treadmill impact*: Vertical and horizontal impacts created by a 16 mm diameter wooden dowel attached to the treadmill belt rolling at 26 km/h (Fig. 7.1b).

- *Shaker contact surface*

*Flat*: a flat surface in contact with the tires (Fig. 7.4a).

*Dowel*: a penetrative surface in contact with the tires (Fig. 7.4b).

- *Cyclist*

To evaluate the effect of the cyclist's mass, two cyclists are used as testers: cyclist #1–1.82 m, 70 kg; cyclist #2–1.80 m, 92 kg.

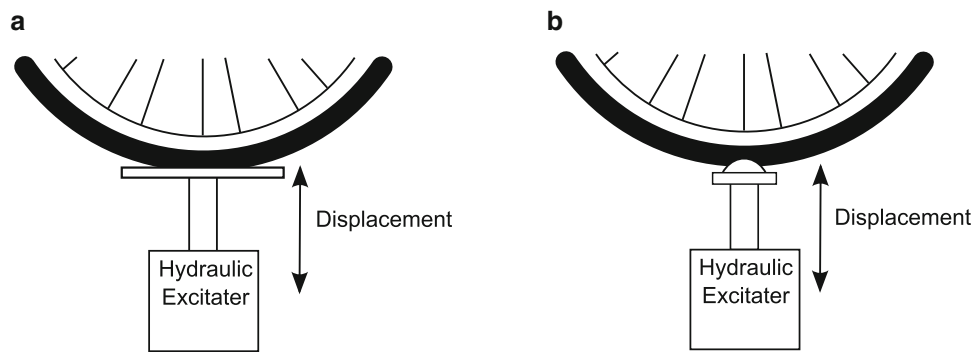


Fig. 7.4 Shaker contact surfaces: (a) Flat; (b) Dowel

### 7.3 Results

The mean values of  $a_{VIB}$  and  $F_{VIB}$  of the test replications are presented for wheelsets A and B. For each of the three test condition categories, the results are displayed using four graphs in a  $2 \times 2$  configuration representing (1) the mean values of  $a_{VIB}$  at the saddle (upper left graph); (2) the mean values of  $a_{VIB}$  at the stem (upper right graph); (3) the mean values of  $F_{VIB}$  at the saddle (lower left graph); (4) the mean values of  $F_{VIB}$  at the stem (lower right graph). Test results are also presented with a confidence interval at 95% estimated with Fisher's LSD (least significant difference) method [16]. To ensure the validity of this method, the normality of the RMS value residues distribution has been checked.

### 7.4 Discussion

As shown by the results presented in this paper, it is possible to establish a transmissibility ranking of wheels based on the VIB in terms of acceleration and transmitted force. The VIB due to wheelset A is on the whole higher than to the one with wheelset B. White noise and treadmill impacts excitations only allow us to significantly distinguish between wheelset A and wheelset B based on  $a_{VIB}$  at the saddle (Fig. 7.5a). Road excitation allows us to significantly distinguish between wheelset A and wheelset B based on  $a_{VIB}$  at the saddle and stem and based on  $F_{VIB}$  at the stem (Fig. 7.5a, b, d). Shaker impact excitation only allows us to significantly distinguish between wheelset A and wheelset B based on  $a_{VIB}$  at the stem (Fig. 7.5b). No significant difference between wheelset A and wheelset B can be established using  $F_{VIB}$  at the saddle. Treadmill impact excitation allows us to significantly distinguish between wheelset A and wheelset B based on  $a_{VIB}$  at the saddle and the stem (Fig. 7.5a, b).

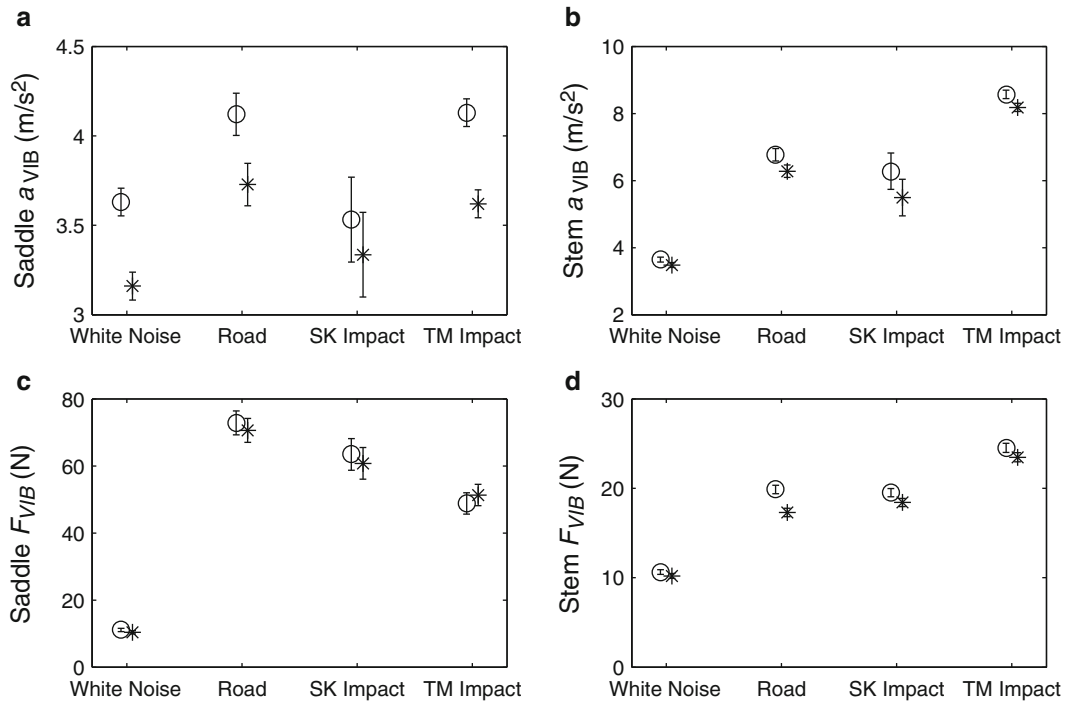
Both shaker contact surfaces yield similar results when it comes to distinguishing between wheelset A and wheelset B (Fig. 7.6). However, lower values of  $a_{VIB}$  and  $F_{VIB}$  at both the saddle and the stem are observed when the excitation surface is penetrating into the tires (dowel).

Even though results presented in Figs. 7.5 and 7.6 were obtained with cyclist #1, measurements for cyclist #2 were also carried out. Results for cyclist #2 exhibit the same trend as those presented for cyclist #1. Nonetheless, and as shown on Fig. 7.7, results for both cyclists differ in level. Higher acceleration levels are transmitted to cyclist #2 but higher force levels are transmitted to cyclist #1.

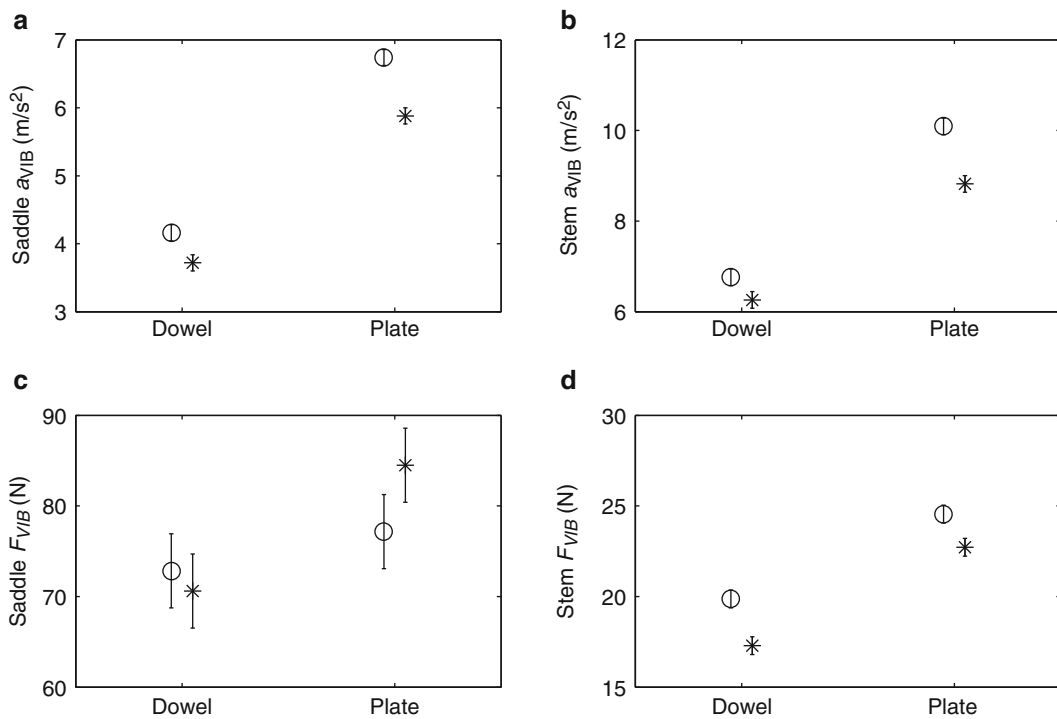
Some precautions were taken during acceleration and force measurements to reduce the effect of cyclist inter-variability. It was observed that the cyclist's influence on the vibrational behaviour of the bicycle is not constant. The cyclist always moves slightly on the bicycle even if he tries to maintain the same posture and attitude. These small postural displacements are detrimental to the repeatability of the tests. Proper statistical analysis must be performed for these tests to be compared.

### 7.5 Conclusion

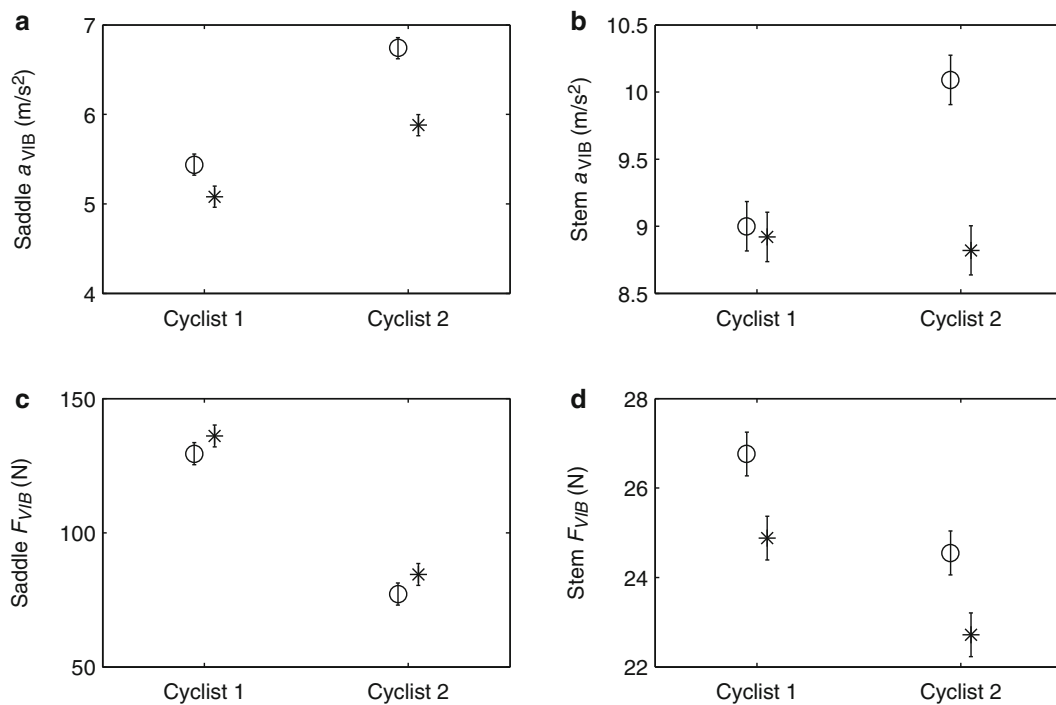
With the objective of establishing good practices when comparing wheel comfort, this paper presented the influence of several test parameters on the vibrations induced to the cyclist at the hands and buttocks. The influence on the bicycle dynamics of two excitation surface was studied: a flat excitation surface and an irregular surface that locally deforms the tire. The type of excitation, such as white noise, impacts and typical road excitation, were also investigated. Results with regard to the effect



**Fig. 7.5** Effect of the excitation type in discriminating between wheelset A (○) and wheelset B (\*) with cyclist #1. SK impact means shake impact. Treadmill impacts (TM impact) were applied to the rear wheel only for graph a and c and to the front wheel only for graph b and d. Uncertainty bars correspond to high and low end values of 95% confidence interval



**Fig. 7.6** Effect of the excitation type in discriminating between wheelset A (○) and wheelset B (\*) with cyclist #1. Uncertainty bars correspond to high and low end values of the 95% confidence interval



**Fig. 7.7** Effect of the cyclist's mass in discriminating between wheelset A (○) and wheelset B (\*) with cyclist #1. Uncertainty bars correspond to high and low end values of the 95% confidence interval

of the cyclist's mass are presented. Even if these parameters have a significant influence on the vibration levels transmitted to the cyclist, they did not affect the transmissibility ranking of the two wheelsets used in this study. It should be noted however that observed changes in the cyclist's posture and attitude on the bicycle can impair measurement of  $a_{VIB}$  and  $F_{VIB}$  and hence affect the wheelset ranking. Great care should therefore be taken to control the cyclist's posture and attitude on the bicycle during the tests. Even with a proper posture and attitude control, measurements must be considered as a result of a stochastic process. No conclusion can be drawn on the basis of a single measurement. Tests must be replicated and statistically analysed.

## References

- ISO 5349-1 (2001) Mechanical vibration – measurement and evaluation of human exposure to hand-transmitted vibration – Part 1: general requirements
- ISO 2631-1 (1997) Mechanical vibration and shock – evaluation of human exposure to whole-body vibration – Part 1: general requirements
- Hunt L, Garcia I (2012) Implementation of a vibration absorber for composite hockey goalie sticks. *Procedia Eng* 34(0):349–354
- Russell DA (2006) Bending modes, damping, and the sensation of sting in baseball bats. *The Eng. Sport* 6:11–16
- Roberts JR, Jones R, Mansfield NJ (2005) Evaluation of vibrotactile sensations in the 'feel' of a golf shot. *J Sound Vib* 285(1–2):303–319
- Champoux Y, Richard S, Drouet J (2007) Bicycle structural dynamics. *Sound Vibr* 41(7):16–24
- Wojtowicki J, Champoux Y, Thibault J (2001) Modal properties of road bikes Vs. ride comfort. *Proceedings of IMAC-XIX*, 1:648–652
- Lépine J, Champoux Y, Drouet JM (2012) Technique to measure the dynamic behavior of road bike wheels. *Topics Modal Anal II* 6:465–470
- Petrone N, Giubilato F (2011) Comparative analysis of wheels vibration transmissibility after full bicycle laboratory tests. *Proceedings of AIAS 40°*
- Olieman M, Marin-Perianu R, Marin-Perianu M (2012) Measurement of dynamic comfort in cycling using wireless acceleration sensors. *Procedia Eng* 34(0):568–573
- Giubilato F, Petrone N (2012) A method for evaluating the vibrational response of racing bicycles wheels under road roughness excitation. *Procedia Eng* 34(0):409–414
- Zinn L (2012) Getting the most from your post. *Velo News* 41:88–94
- Fretz C, Nick L, Zinn L (2011) Tech and training: endurance bike test. *Velo News* 40:84
- Drouet J, Champoux Y (2012) Development of a three-load component instrumented stem for road cycling. *Procedia Eng* 34(0):502–507
- Lépine J, Champoux Y, Drouet J (2011) Excitation techniques for testing bike vibration transmission in the laboratory. *Proceedings of IMAC-XXIX*, 6:35
- Montgomery DC (2009) *Design and analysis of experiments*. Wiley, Hoboken



# Chapter 8

## Direct Measurement of Power on a Gravity Independent Flywheel-based Ergometer

F. Braghin, M. Bassetti, P. Crosio, and D. Locati

**Abstract** YoYo Technology™ commercializes a training instrument called YoYo Squat™, a gravity independent flywheel-based ergometer, that allows to train quadriceps and adductors as well as supporting trunk and core muscle groups unloading the shoulder and spine. This ergometer, however, is equipped only with an optical sensor (encoder) to measure the rotation of the flywheel thus making it almost impossible to determine the instantaneous power generated by the athlete as well as the force as a function of the number of repetitions. It was therefore decided to equip the YoYo Squat™ with miniaturized single axis load cells, a linear position transducer parallel to the strap and strain gauge force plates for both feet. This has allowed to assess not only the above mentioned quantities but also the point of application of the normal load on the two feet thus further improving the training output and the feedback to both the athlete and the trainee for improved performance and/or more focused training.

**Keywords** Flywheel ergometer • Training • Power measurement • Yo-Yo • Dynamometric plates

### 8.1 Introduction

Gravity flywheel based ergometers are widely used for sport training since they activate the extensor muscles of the knee and ankle joints while performing the leg press exercise. Resistance is provided independent of gravity by using the inertial focus of a flywheel. The commercial available systems are lacking in force measurement. The system described in this paper introduces an innovative way to measure the real athletes' performance and measure only the inertial flywheel angular speed.

### 8.2 Description of the System

The flywheel-based ergometer described in this paper, has been designed and developed at the Department of Mechanical Engineering Politecnico di Milano. As shown in Fig. 8.1, it is composed of a gravity independent flywheel and two independent dynamometric plates.

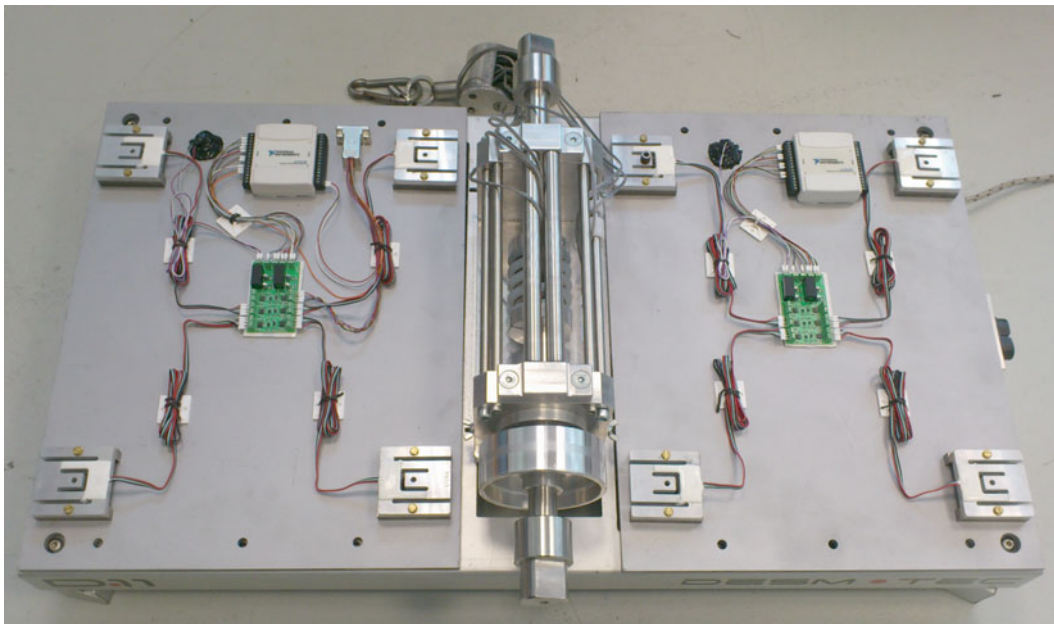
The gravity flywheel assembly, the part collocated in the middle, is composed of twelve elements: the shaft, two pillars, a plate, four load cells, two bearings, a rope and an inertial flywheel. Figure 8.2 shows all these components.

This independent flywheel assembly has been designed in order to allow different installations, such as on the floor or on the wall. The device can be used to train different muscles by means of the linear displacement in the vertical direction under a given load. The shaft is free to rotate along its axis and it is supported by bearings fixed into the pillars. A rope has been fixed around the shaft in order to transform the force applied at its extremity in a torque applied to the shaft that moves

---

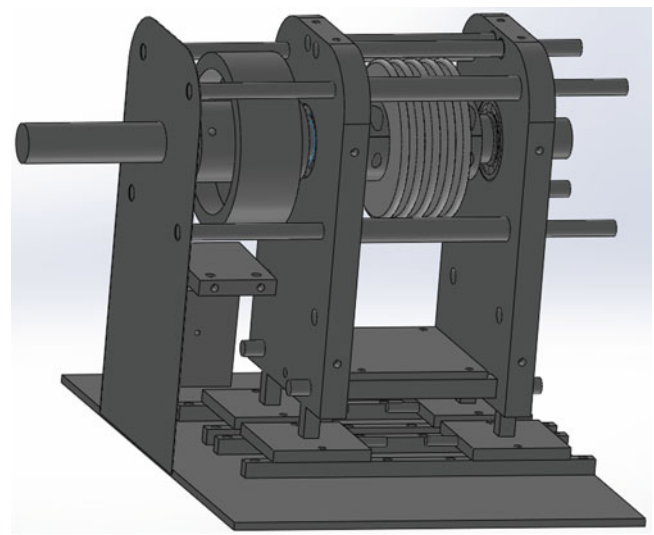
F. Braghin (✉) • M. Bassetti • P. Crosio  
Department of Mechanic, Politecnico di Milano, Via La Masa 1, 20156 Milan, Italy  
e-mail: [francesco.braghin@polimi.it](mailto:francesco.braghin@polimi.it); [marco.bassetti@polimi.it](mailto:marco.bassetti@polimi.it); [pietro.crosio@polimi.it](mailto:pietro.crosio@polimi.it)

D. Locati  
Federazione Italiana Sport Invernali, Via Piranesi 46, 20137 Milan, Italy  
e-mail: [dany.locati@yahoo.it](mailto:dany.locati@yahoo.it)



**Fig. 8.1** Flywheel ergometer designed by the Department of Mechanic

**Fig. 8.2** Gravity flywheel assembly

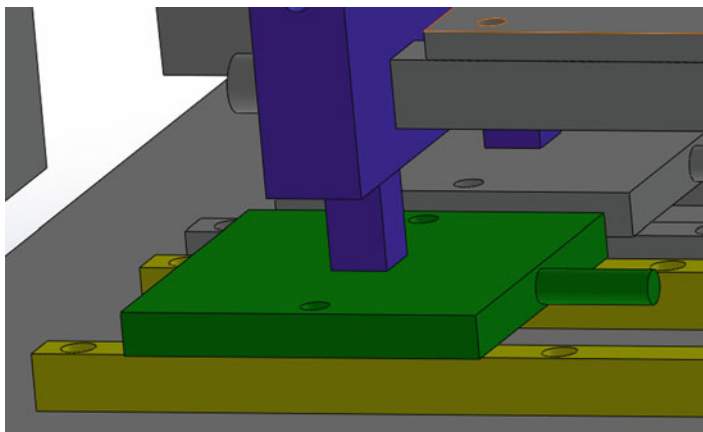


the inertial flywheel installed at the end. The inertial flywheel can be changed in order to vary the load applied. The force is transmitted to the ground through the two pillars linked to the bearings of the shaft. Figure 8.3 shows the position of the load cell (in green) as opposed to the pillar (in blue).

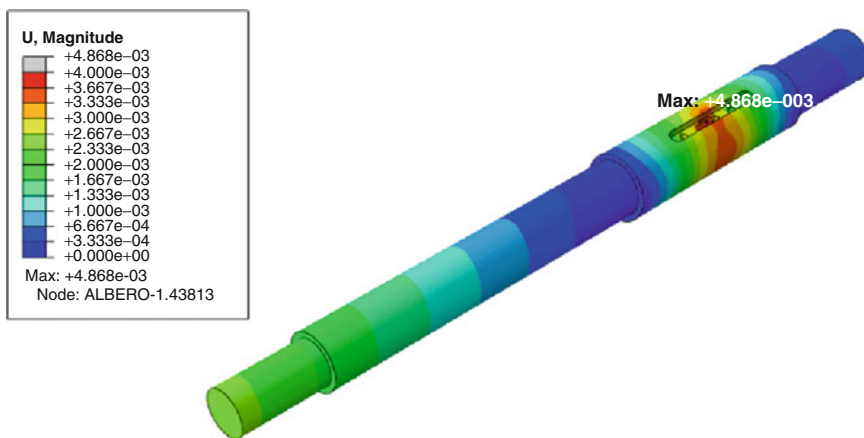
Four load cells have been installed under the pillars in order to measure the forces applied. Thanks to them, it is possible to identify the vertical load applied by the athlete and the moment along the lateral axis. The longitudinal moment is transmitted to the pillars through the bearings and because of that it is negligible. The rotation of the shaft is measured using an optical encoder which gives the speed of revolution of the shaft. Thanks to this measure, it is possible to recognize the value of instantaneous power generated by the athlete and the total energy of the work done by him/her. In order to guarantee a training instrument suitable for professional skiers, the value of the full scale load has been set from the experience. From the preliminary test performed with a YoYo Squat™, it resulted that skiers are able of 3000 N. The load cells used are selected in order to allow a total overload of about 150% of the full scale. The shaft, and the position of the bearings supporting it, are designed by means of FE analysis in order to have a maximum vertical displacement -under the full scale load- less than 0.01 mm, as shown in Fig. 8.4.

In order to provide a security device, an emergency brake has been applied to the shaft. Due to the design of the whole system, the time of braking depends on the inertia installed on the shaft. The emergency brake is visible in Fig. 8.5.

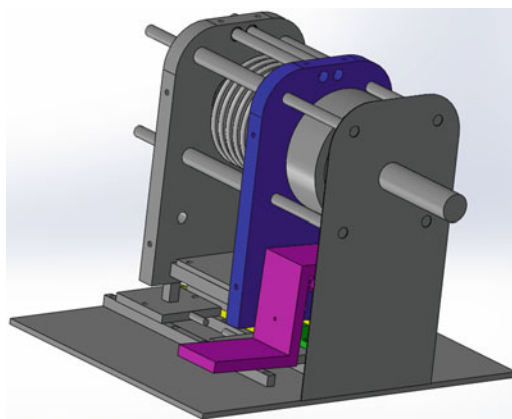
**Fig. 8.3** Load cell and pillars disposition



**Fig. 8.4** FEA design for optimize displacement



**Fig. 8.5** Emergency brake shown in purple



Aluminium and stainless steel have been chosen during the design of the whole system in order to obtain a light weight, low cost, and long lasting device.

### 8.3 Conclusions

In sport, training is very important. However it is very difficult to judge athletes' performance objectively. This paper presents a new way to reach such objectivity.

# Chapter 9

## Instrumented Treadmill for Cross-Country Skiing Enhanced Training

M. Bassetti, F. Braghin, and S. Maldifassi

**Abstract** In order to meet the need for indoor training, Rodby has developed a special ski-skating treadmill that allows cross-country skiers to test their physical performance under laboratory conditions, using classical and freestyle techniques on roller skis by adjusting both the inclination of the slope as well as its speed. However, both inclination and speed are adjusted manually by an operator or set at the beginning of the test thus making it very difficult to recreate real skiing conditions. Thanks to the cooperation with the Italian national ski team, the treadmill was equipped with some additional sensors that allowed to continuously adjust the slope to simulate a real track of cross-country skiing as well as the speed to account for the different skiing performances of the athletes under test. Both the design of the additional measurement system as well as of the control algorithm is presented.

**Keywords** Nordic ski • Treadmill • Simulator • Ultrasound sensor • Real-time

### 9.1 Introduction

In modern sprint cross-country skiing, strength and maximal speed are major determinants of performance. While strength can be improved using traditional training systems, increasing the maximal speed requires outdoor training or the training using machines that allow to correctly reproduce the skiing movement. For this purpose, treadmills have been adopted [1–3]. Modern treadmills, besides allowing a regulation of the speed, also allow to control the inclination of the track. However, the typical tests performed on such treadmills are, using a control term, feed-forward tests since speed and inclination are pre-imposed and the skier has to adjust kinematics not to fall off the treadmill. Moreover, most tests are done not to improve performances but to assess actual performances both in terms of maximal speed, peak oxygen uptake ( $\dot{V}O_{2peak}$ ), oxygen uptake at anaerobic threshold ( $\dot{V}O_{2Th}$ ), produced lactate and peak heart rate [4–6].

The aims of this study is to develop a treadmill based cross-country ski simulator that is able to reproduce the slopes of a real track and regulates the speed of the treadmill as a function of the athlete's speed thus allowing to closely reproduce a real outdoor test. Thus, real training sessions can be performed. Moreover, to allow athletes to “feel” the track, also a video reproduction of the track is implemented (at present, only a 2D video is used but in the next future also 3D video or even virtual reality could easily be implemented). This allows athletes to optimize race strategies, i.e. decide how to distribute the effort along the track.

---

M. Bassetti (✉) • F. Braghin  
Department of Mechanics, Politecnico di Milano, Via La Masa 1, 20156 Milan, Italy  
e-mail: [marco.bassetti@polimi.it](mailto:marco.bassetti@polimi.it); [francesco.braghin@polimi.it](mailto:francesco.braghin@polimi.it)

S. Maldifassi  
Comitato Olimpico Nazionale Italiano, Largo Lauro De Bosis 15, 00135 Rome, Italy  
e-mail: [stefanomaldifassi@fisi.org](mailto:stefanomaldifassi@fisi.org)

## 9.2 Simulator Components

The treadmill based cross-country ski simulator is mainly made up of a treadmill (Fig. 9.1) that allows to set both the speed and the inclination. For safety reasons, only positive slopes can be set. Thus, as will be explained later on, special features have been implemented to reproduce downhill slopes.

Usually, speed and inclination values are set by trainers. For being able to closely reproduce outdoor tests, speed has to be set by the athlete's skiing speed while inclination has to be set according to the reached position along the track. Thus, the athlete's skiing speed has to be measured to define the treadmill's speed and integrated in order to set the treadmill's inclination. This is done by using relative displacement sensors: if the athlete moves forward along the treadmill with respect to its reference position, the treadmill's speed is increased; if the athlete moves back, the treadmill's speed is decreased. Knowing the treadmill's speed at any time instant, it is possible to evaluate the athlete's travelled distance and thus the position of the athlete along the track. Since, during cross-country skiing, arm motion could "blind" one sensor, three relative motion sensors are used in parallel pointing at three different points on the chest of the athlete.

Sensor signals are acquired using a low-cost National Instruments USB acquisition board (NI USB-6009 board) at a sampling rate of 100Hz and are elaborated in real-time using a laptop on which the control logic, implemented in LabView Real-Time, is running. The treadmill's speed and inclination are adjusted every 0.05 s through the RS232 port on Rodby's treadmill.

As said in the introduction, in order to allow the athlete to "feel" the track and optimize strategies, it is necessary to show to the athlete her/his position along the track. To do this, the track to be reproduced on the simulator has to be shot using an HD video high speed camera with integrated GPS (in our case, a Contour GPS video camera with full HD 50fps has been used). Thus, given the distance travelled from the start, by interpolating GPS data it is possible to determine the corresponding video frame that has to be projected (using a traditional video). This task is also carried out by the laptop on which LabView Real-Time is running every 0.05 s.

Finally, in order to acquire the forces exerted by the athlete during the tests, both skirolls and ski poles have been instrumented with strain gauges. The rugged data logger ( $100 \times 20 \times 10$  mm in order to fit into a grip or elsewhere on the athlete), with 12 integrated strain gauge bridge amplifiers and 16bit ADC, acquires data independently from the treadmill. Thus, this "wearable" cross-country ski acquisition system will not be described in the present paper.

## 9.3 Sensors

As said in the previous paragraph, there are only three relative displacement sensors on the cross-country ski simulator. The first decision is whether to use contact or contactless sensors. To provide the athlete with the most natural feeling, contactless sensors were chosen. Among the various types of contactless sensors, ruggedness and insensitivity to surface conditions



**Fig. 9.1** Rodby's ski-skating treadmill used for the simulator

**Fig. 9.2** Adopted narrow beam sonar sensor



and color were main requirements for the considered application. Thus, sonar sensors were considered the best possible choice. To detect people high sensitivity, yet minimal side-lobes are required. Moreover, very short to long-range detection is required.

The chosen sensor (Fig. 9.2) has the following characteristics:

- Designed for outdoor or indoor environments
- Precise narrow beam
- High sensitivity
- Sensor operates at 42 kHz
- Continuously variable gain
- Object detection includes zero range objects
- Low power 3.0–5.5 V operation
- Detects objects from 0 to 6.5 m with 25 mm resolution
- Compact, robust PVC housing, designed to meet IP67

In order to account for the blinding of sensors due to arm motion if one sensor experiences an output variation greater than 1 V/s is rejected by the control logic and only the signal of the other sensors are considered. As an example, Fig. 9.3 shows a typical output of the adopted sensors.

## 9.4 Real-Time Control

The real time control, implemented in LabView Real-Time running on a laptop, carries out the following tasks:

- Check that the gradient of the outputs of the three signals is below a given threshold; if not, the corresponding sensor output is neglected in the further calculations
- Comparison of the mean sensor outputs  $S$  with the reference output  $S_{ref}$  (reference position of the athlete on the treadmill); if the difference  $\varepsilon = S_{ref} - S$  is different from zero, increase or decrease the speed  $\Delta v$  of the treadmill through a predefined (by Rodby) command on the RS232 port according to a classical PID controller:

$$\Delta v = k_p \varepsilon + k_d \dot{\varepsilon} + k_i \int_0^t \varepsilon dt \quad (9.1)$$

$k_p$  being the proportional gain,  $k_d$  being the derivative gain and  $k_i$  being the integrative gain

- Integration of the speed in order to determine the travelled distance and set of the inclination of the treadmill through a predefined (by Rodby) command on the RS232 port that corresponds to that travelled distance; it should be noted that, due to the fact that no speed nor rotation feedback is available on Rodby's treadmill, nominal speed is considered for determining the travelled distance; however, thanks to dedicated tests with additional sensors on the treadmill, it was seen that the speed variations delay are proportional to  $\Delta v$ ; thus, a corrective contribution was added
- Interpolation of the travelled distance on the GPS data acquired along the track with Contour GPS camera and identification of the corresponding frame that is outputted to the video projector port

Figure 9.4 shows a screenshot of the developed program.



## Analog Voltage Response for Near and Distant Objects

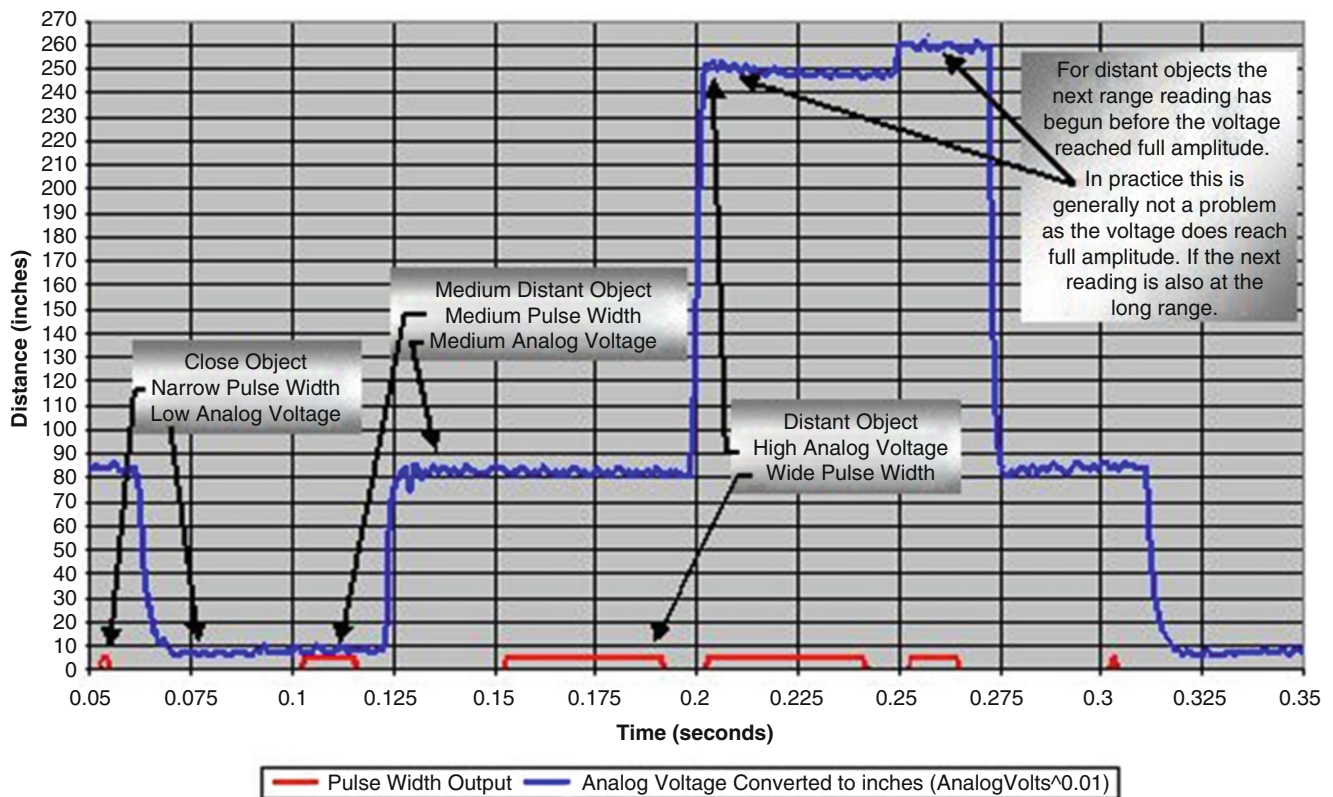


Fig. 9.3 Typical sonar sensor output

One comment is required for the simulation of downhill slopes: due to the fact that, for safety reasons, only uphill inclinations can be produced by the treadmill, no “natural” downhill slopes can be reproduced by the simulator. Thus, two possibilities are available, either modify the track by removing all downhill slopes or try to simulate the slopes by blocking the athlete relative position on the treadmill and by increasing the speed of the treadmill according to the athlete’s acceleration along the slope. The first solution is easier to implement but leads to nonrealistic and much more tiring tracks. The second solution require the introduction of a blocking system (an elastic band) and a numerical model that modifies the treadmill’s speed according to the athlete’s acceleration. Obviously, the second solution was chosen.

To simplify the modeling, the athlete’s was assumed to be a point mass acceleration along a downhill slope according to the gradient of the slope, the friction coefficient between snow and skies and the aerodynamic drag of the skier. Thus, athlete’s mass, friction and drag coefficients are required by the real-time code for being able to reproduce downhill slopes. One final comment: the elastic band is positioned 1,000 mm behind the athlete’s reference position (in order to avoid that a deceleration of the athlete is stopped by the elastic band) and a smooth transition algorithm is implemented to pass from uphill to downhill solpes and viceversa.

Results from preliminary tests carried out on the virtual track shown in Fig. 9.5 will be shown at the conference. Special algorithms were implemented to account for safety procedures (abrupt stopping of the athlete, falling of the athlete, ...).

## 9.5 Conclusions

The present paper describes how a traditional Rodby treadmill has been turned into a realistic cross-country ski simulator for enhanced training. To achieve this result, three sonar sensors and a PC based real-time controller were used. To achieve a more realistic effect of the simulator, also visual feedback was provided to the athletes.



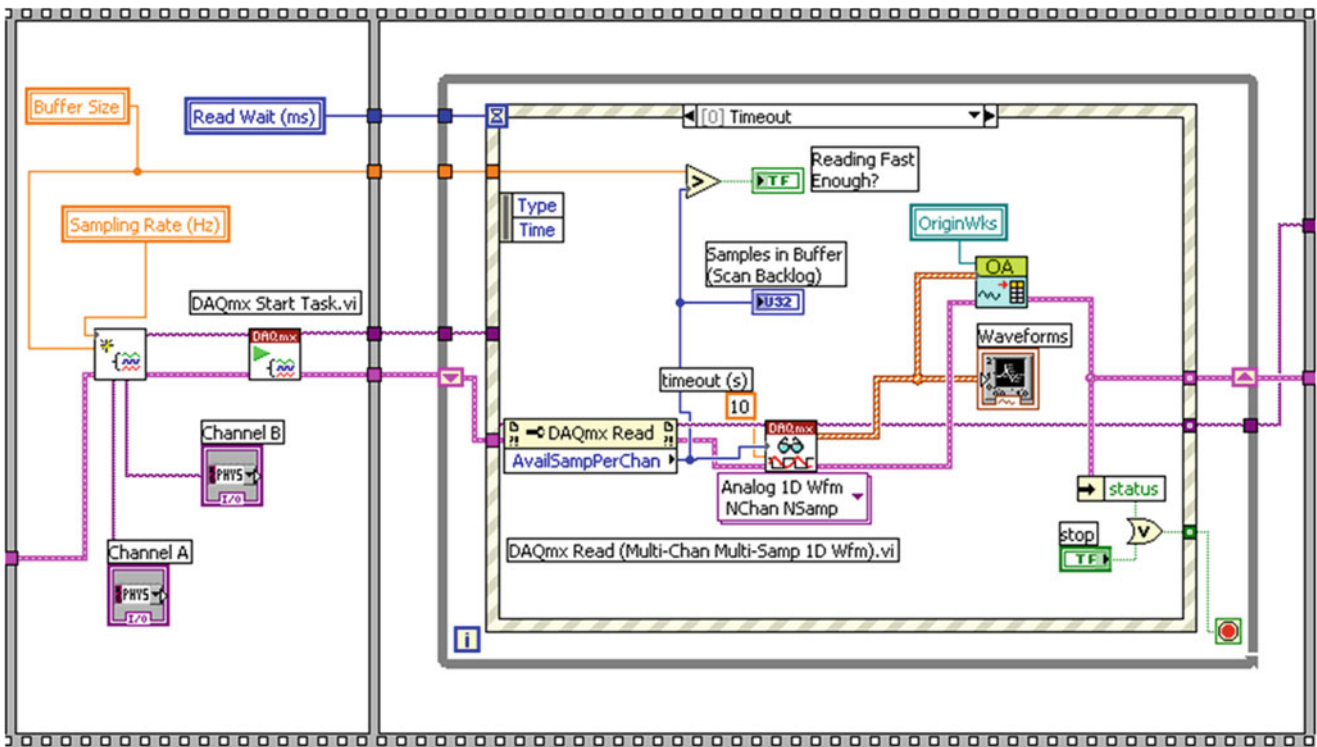


Fig. 9.4 Screenshot of the real-time controller implemented



Fig. 9.5 Virtual track used for the preliminary tests

## References

1. Heitkamp H-C, Moll D, Nieß A, Horstmann T, Mayer F, Dickhuth H-H (1998) Performance diagnostic tests and competition performance in Nordic skiing. *Deutsche Zeitschrift für Sportmedizin* 49(11–12):347–350
2. Stöggl T, Lindinger S, Müller E (2007) Analysis of a simulated sprint competition in classical cross country skiing. *Scand J Med Sci Sports* 17(4):362–372
3. Stöggl T, Enqvist J, Erich M, Holmberg H-C (2010) Relationships between body composition, body dimensions, and peak speed in cross-country sprint skiing. *J Sports Sci* 28(2):161–169
4. Fabre N, Balestreri F, Leonardi A, Schena F (2010) Racing performance and incremental double poling test on treadmill in elite female cross-country skiers. *J Strength Cond Res* 24(2):401–407
5. Popov DV, Vinogradova OL (2012) Comparison of the aerobic performance of leg and arm muscles in cross-country skiers. *Hum Physiol* 38(5):508–513
6. Haug RC, Porcari JP, Brice G, Terry L (1999) Development of a maximal testing protocol for the NordicTrack cross-country ski simulator. *Med Sci Sports Exerc* 31(4):619–623

# Chapter 10

## Instrumenting a Rowing Ergometer for Improved Training

G. Cazzulani, M. Bassetti, G. Picardi, L. Mariella, J. Verdonkschot, A. Benecchi, and Dario Dalla Vedova

**Abstract** Rowing ergometers are used by athletes for indoor training and performance improvement. Typical commercial ergometers provide some information (for example power output and covered distance), but these indications are typically estimated starting from the fan speed and thus are not very reliable as already pointed out in the literature. The present paper presents the work done to fully instrument a commercial rowing ergometer in order to directly measure all relevant quantities for improved training: the seat, the handlebar and the stretchers have been redesigned and equipped with force and displacement sensors able to measure both the dynamic and kinematic behavior of the athlete. In this way the interaction of the athlete with the rowing machine is fully known, together with the direct measurement of the instantaneous rowing power output. Some results are also presented and discussed.

**Keywords** Rowing ergometer • Performance optimization • Training • Wireless acquisition system • Load transducers

### 10.1 Introduction

Rowing ergometers are training machines aimed at reproducing the rowing dynamics [1]. In typical ergometers a handlebar replaces the oars while the energy dissipation due to the boat motion in water is reproduced by an air fan.

Athletes use rowing ergometers for indoor training and to improve their position and efficiency [2–5]. For this purpose, typical commercial rowing ergometers provide some information to the athlete (e.g. power output, covered distance, speed). Anyway, all these indications are typically estimated from the fan speed, since no direct measurements are available. As a consequence, due to the nonlinearities associated to air dissipation, indications are not very reliable as already pointed out in the literature [6]. Moreover, no information is provided about the interaction between the athlete and the machine (athlete position, forces, . . .).

This layout can be effective for training, but it does not provide significant information for posture and performance optimization. For this reason, in the last years, some researches have been carried out to study the aspects of the rowing mechanics and to find the best rowing layout in terms of power output and boat speed. In detail, [7] and [8] focused on the stretcher, studying the effect stretcher height and comparing fixed and floating stretchers; [9] described a system for the measurement of the forces on the seat; [10] proposed an instrumented rowing machine that measures the forces on the handlebar and on the stretcher.

---

G. Cazzulani (✉) • M. Bassetti • G. Picardi  
Department of Mechanical Engineering, Politecnico di Milano, Via La Masa 1, Milan, 20156 Italy  
e-mail: [gabriele.cazzulani@mail.polimi.it](mailto:gabriele.cazzulani@mail.polimi.it); [marco.bassetti@polimi.it](mailto:marco.bassetti@polimi.it); [gianmarco.picardi@gmail.com](mailto:gianmarco.picardi@gmail.com)

L. Mariella  
Ferrari S.P.A., Via Emilia Est 1163, Modena, Italy  
e-mail: [Luciano.Mariella@ferrari.com](mailto:Luciano.Mariella@ferrari.com)

J. Verdonkschot • A. Benecchi  
Federazione Italiana Canottaggio, Viale Tiziano 74, Rome, 00196 Italy  
e-mail: [josi@verdonkschot.nl](mailto:josi@verdonkschot.nl); [a.benecchi@me.com](mailto:a.benecchi@me.com)

D.D. Vedova  
Comitato Olimpico Nazionale Italiano, Largo Lauro De Bosis 15, Rome, 00135 Italy  
e-mail: [dario.dallavedova@coni.it](mailto:dario.dallavedova@coni.it)

Anyway, as previously pointed out, all these studies focus only on some aspects of the rowing mechanics, without providing a full information about the rowing kinematics and dynamics and about the athlete-machine interaction.

This paper presents the work done to fully instrument a commercial rowing ergometer called “Concept 2” in order to directly measure all relevant quantities for improved training and rowing optimization: the seat, the handlebar and the stretcher have been re-designed and equipped with force and displacement sensors able to measure both the dynamic and kinematic behaviour of the athlete. In detail:

- Two displacement sensors mounted on the seat and on the handlebar, together with a 3D camera system allow measuring the motion of both the athlete and the moving parts of the rowing ergometer (the seat and the handlebar);
- Four single axis load cells under the seat allow measuring the normal load on the seat as well as the longitudinal and lateral position of the application point of this normal load;
- Five single axis load cells between the stretchers and the structure of the rowing ergometer allow measuring the normal and longitudinal load applied by the athlete on the stretcher as well as the longitudinal and lateral position of the application point of this normal load;
- One single axis load cell at the handlebar allows measuring the applied force.

In this way the interaction of the athlete with the rowing machine is fully known, together with the direct measurement of the instantaneous rowing power output.

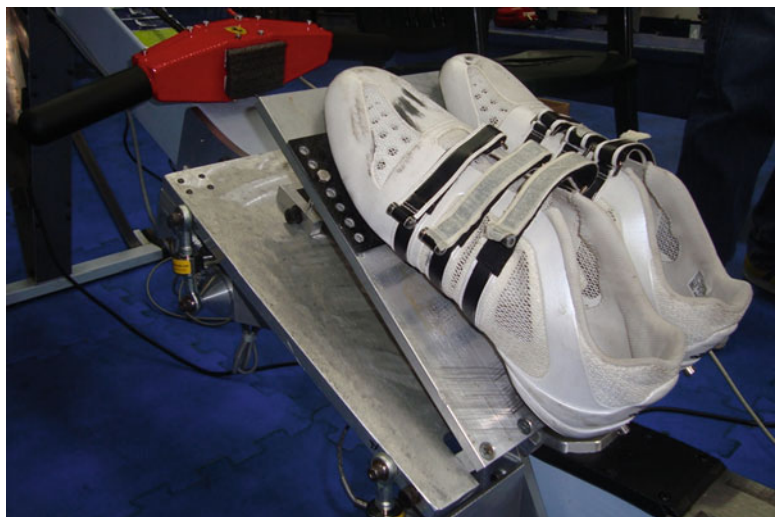
In the following, the first three sections describes the project of the re-designed stretcher, seat and handlebar respectively and the corresponding measurement layout. Section 10.5 describes the 3D camera system that measures the athlete’s motion. Finally, in Sect. 10.6 some results are presented and discussed.

## 10.2 The Stretcher

Boat stretchers (or footrests) are typically designed in order to optimize the rowing performance: the stretcher inclination can be adjusted in order to adapt it to the athlete’s ergonomic characteristics and the feet are kept as close as possible one to the other in order to reduce the boat width and, as a consequence, the drag force on it. On the contrary, the stretcher inclination of Concept 2 ergometer is fixed. Moreover, the distance between the feet is greater than that on the boat due to the presence of the supporting structure between them.

For this reason, the ergometer stretcher has been completely re-designed, in order to make it as similar as possible to the one mounted on boats. The footrest inclination can now be adjusted from a 38° angle to a 52° angle with respect to the ground. Figure 10.1 shows the design of the new proposed stretcher.

The stretcher is equipped with five single-axis force sensors in order to measure the longitudinal and vertical force applied by the athlete. The load cells are inserted into the rods connecting the footrest and the chassis. In this way, they sense only an axial force and the measurement is not affected by moments or shear forces. In detail, one load cell measures the longitudinal force, while the remaining 4 ones measure the vertical forces. Due to the symmetry of the ergometer rowing, the lateral force is assumed negligible and not measured.



**Fig. 10.1** The re-designed stretcher for concept 2 ergometer



The coordinates of the point of application of the normal force on the stretcher can be calculated knowing the total vertical force  $F_{tot}$  (the sum of the four vertical load cells) and the moment of the vertical forces with respect to the transversal and longitudinal axes of the ergometer ( $x$  and  $y$ ) as

$$\begin{cases} P_x = \frac{M_y}{F_{tot}} \\ P_y = \frac{M_x}{F_{tot}} \end{cases} \quad (10.1)$$

where

$$\begin{cases} M_x = (F_1 - F_2 - F_3 + F_4) b \\ M_y = (F_1 + F_2 - F_3 - F_4) a \end{cases} \quad (10.2)$$

while  $a$  and  $b$  represent the distance between the vertical load cells along the  $x$  and  $y$  directions;  $F_1$ ,  $F_2$ ,  $F_3$  and  $F_4$  represent the measurements of the front-left, rear-left, rear-right and front-right load cells respectively. The knowledge of the centre of forces allows the trainer to correct the athlete posture, in order to avoid unwanted asymmetries in his rowing dynamics.

### 10.3 The Seat

Due to the changes on the stretcher, also the seat has been modified. In particular, since the stretcher height increased, the vertical position of the seat has been increased of the same quantity, in order to keep the athlete position unchanged. Figure 10.2 show the design of the new seat. Four vertical single-axis load cells have been mounted under the seat to measure the vertical forces applied by the athlete. In this case, both the lateral and longitudinal forces are negligible, due to the rowing symmetry and to the longitudinal sliding of the seat respectively. For this reason no longitudinal nor lateral load cells have been mounted on the seat. Anyway, an horizontal rod has been placed between the seat and its chassis. As explained in Sect. 10.2 for the stretcher (equations 10.1 and 10.2), the centre of forces has been calculated also for the seat.

The seat position with respect to the rowing ergometer chassis is measured by means of a linear encoder. Since the seat slides with respect to the ground, in order to simplify the wiring all its sensors are measured using a new National Instruments wireless acquisition board (NI 9191).

### 10.4 The Handlebar

The handlebar of the rowing ergometer has been completely re-designed in order to insert a force and displacement measurement. The force is measured through a single-axis load cell, while the displacement is measured through a linear



Fig. 10.2 The re-designed seat

**Fig. 10.3** Top view of the new handlebar of the rowing ergometer



encoder equal to the one used for the seat. Moreover, the speed of the fan is acquired. These sensors allow collecting different useful indicators for the athlete training, summarising as:

- The exact athlete power output, calculated multiplying the force on the handlebar and the first time derivative of the displacement; in this way, starting from this calculation, some other indicators can be obtained, such as the mean power of a rowing cycle, the global mean power and the maximum power;
- The rowing frequency;
- An estimation of the boat speed and covered distance, calculated starting from the fan speed.

Figure 10.3 shows a picture of the modified handlebar.

## 10.5 The 3D Camera System

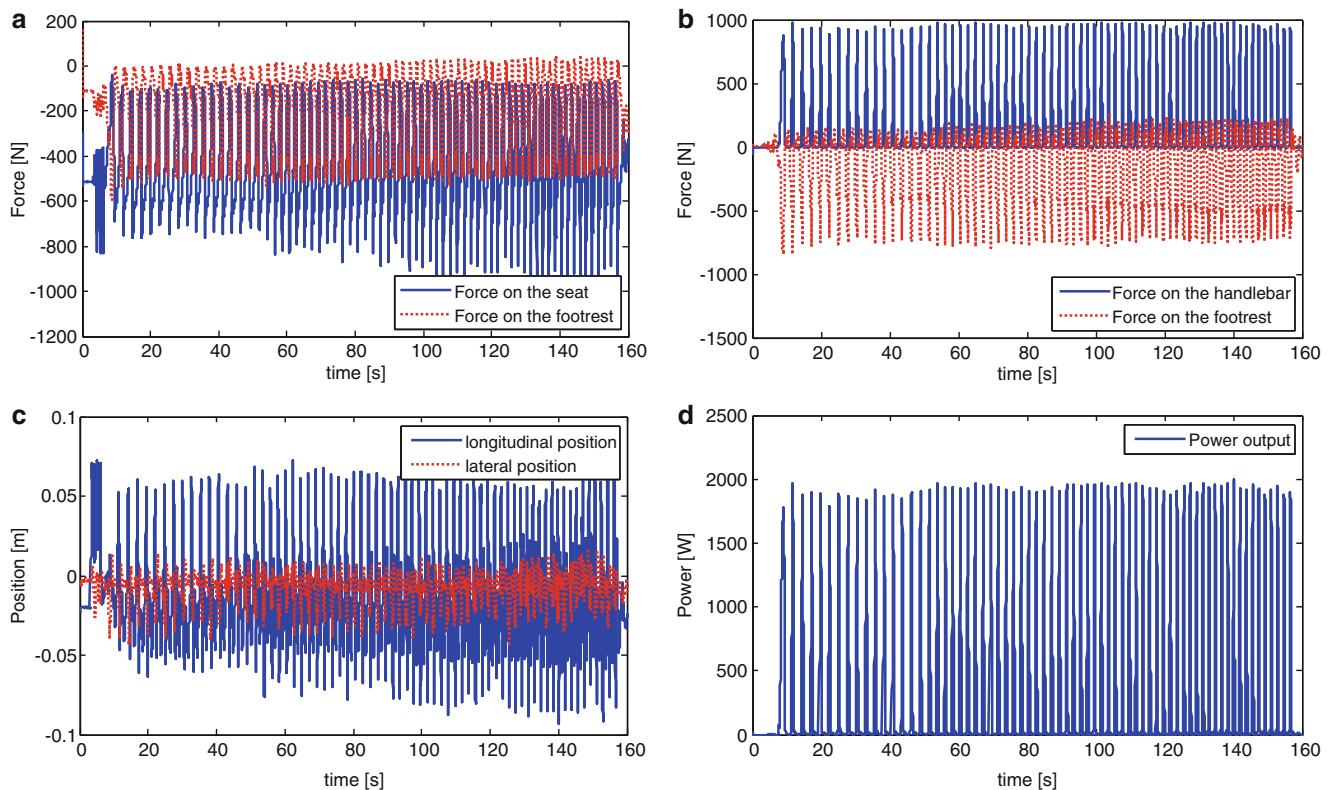
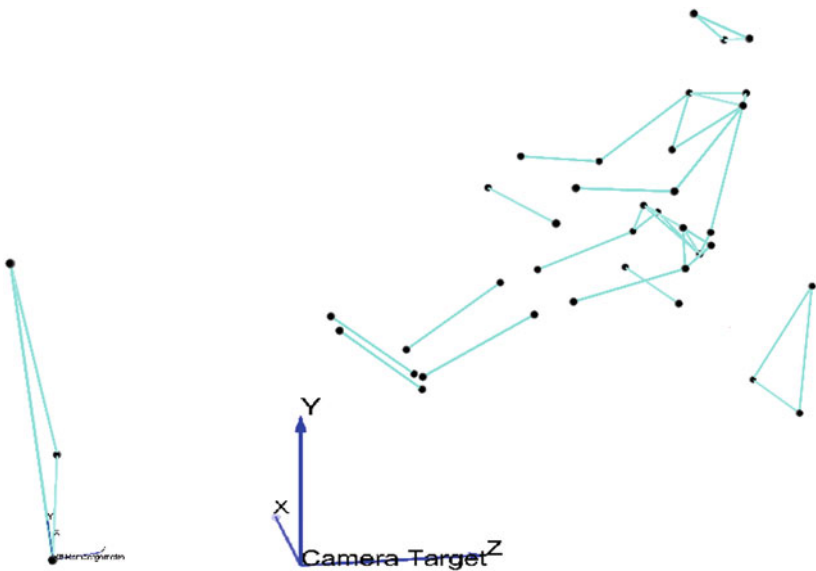
The previous sections explain the work done to measure all the relevant quantities describing the dynamic interaction between the athlete and the rowing machine. However, in order to provide a complete training tool, those dynamic quantities may not be sufficient to fully describe the athlete behaviour during rowing. For this reason, the previously described measurement setup has been integrated with a 3D kinematic measurement of the athlete motion.

All the kinematic joints of the athlete (ankles, knees, hip and so on) together with the moving parts of the rowing ergometer (the seat and the handlebar) are mapped with markers. Then, a set of six cameras is considered to measure the position of all the markers and to reconstruct the athlete motion during the rowing training. Figure 10.4 shows an example of the output of the 3D camera system. The black circles represent the position of the markers with respect to the global reference system.

## 10.6 Results and Discussion

In this section, some experimental results obtained with the proposed instrumented rowing ergometer are shown. The results shown in Figs. 10.5 and 10.6 refer to a test of the female Italian rowing team member. In the test the athlete increases the rowing frequency from a minimum value of 22 strokes/min to a maximum value of 35 strokes/min. The test is performed with a footrest inclination equal to 45° and without sliders between the rowing ergometer and the ground. Figure 10.5 shows the time histories of the complete test, while Fig. 10.6 shows the time history of a single rowing cycle.

**Fig. 10.4** Identification of the athlete's body motion through the 3D kinematic measurement system



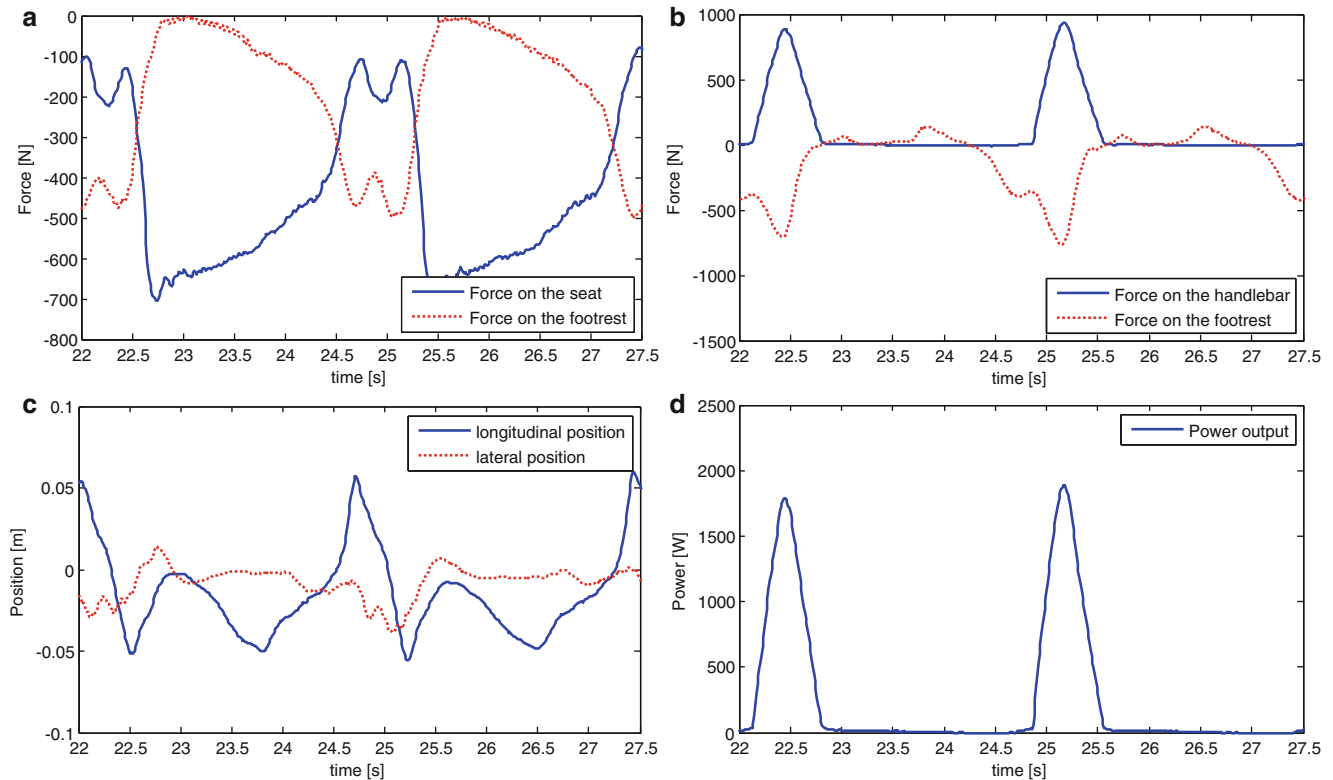
**Fig. 10.5** Results of a rowing test: vertical forces on the seat and on the footrest (a), horizontal forces on the footrest and on the handlebar (b), point of application of the normal force on the seat (c) and instantaneous athlete power output (d)

## 10.7 Conclusion

The present work described the project of an instrumented rowing ergometer for athlete training and performance improvement.

A commercial ergometer has been instrumented with force and displacement sensors in order to provide a complete information about the athlete motion and its dynamic interaction with the ergometer. This sensor layout is integrated with a 3D camera that measures the motion of the athlete during rowing.





**Fig. 10.6** Zoom on a single rowing cycle: vertical forces on the seat and on the footrest (a), horizontal forces on the footrest and on the handlebar (b), point of application of the normal force on the seat (c) and instantaneous athlete power output (d)

The tests performed with the female Italian rowing team show the effectiveness of the proposed training tool. The collected information can be used to optimize the athlete's posture and to correct possible defects, thus improving the athlete's performance.

## References

- Schabert EJ, Hawley JA, Hopkins WG, Blum H (1999) High reliability of performance of well-trained rowers on a rowing ergometer. *J Sports Sci* 17(8):627–632
- Hawkins D (2000) A new instrumentation system for training rowers. *J Biomech* 33(2):241–245
- Macfarlane DJ, Edmond IM, Walmsley A (1997) Instrumentation of an ergometer to monitor the reliability of rowing performance. *J Sports Sci* 15(2):167–173
- Henry JC, Clark RR, McCabe RP, Vanderby R Jr (1995) An evaluation of instrumented tank rowing for objective assessment of rowing performance. *J Sports Sci* 13(3):199–206
- Bassetti M, Braghin F, Cheli F, Maldifassi S (2012) Instrumented rowing machine for optimized training. *Conf Proc Soc Exp Mech* 6:499–506
- Soper C, Hume PA (2004) Reliability of power output during rowing changes with ergometer type and race distance. *Sports BiomechInt Soc Biomech Sports* 3(2):237–248
- Caplan N, Gardner TN (2005) The influence of stretcher height on the mechanical effectiveness of rowing. *J Appl Biomech* 21(3):286–296
- Colloud F, Bahaud P, Doriot N, Champely S, Chèze L (2006) Fixed versus free-floating stretcher mechanism in rowing ergometers: mechanical aspects. *J Sports Sci* 24(5):479–493
- Murphy AJ, Chee STH, Bull AMJ, McGregor AH (2010) The calibration and application of a force-measuring apparatus on the seat of a rowing ergometer. In: *Proceedings of the institution of mechanical engineers, Part P: J Sports Eng Technol* 224(1):109–116
- Torres-Moreno R, Tanaka C, Penney KL (2000) Joint excursion, handle velocity, and applied force: a biomechanical analysis of ergometric rowing. *Int J Sports Med* 21(1):41–44

# Chapter 11

## A Laboratory Technique to Compare Road Bike Dynamic Comfort

Yvan Champoux, Julien Lépine, Philippe-Aubert Gauthier, and Jean-Marc Drouet

**Abstract** Comfort is an important characteristic in road bikes, and a major source of discomfort is the vibration transmitted to the cyclist. Since human memory tends to forget the perceived vibration stimulus strength soon after the perception is no longer present, a comparison between two situations must be done rapidly. Laboratory testing is therefore frequently used to investigate and document perception. This paper presents a laboratory technique enabling us to subject the cyclist to various types of bike vibration stimuli. The technique is based on the use of a bicycle simulator that generates vertical displacement under both wheels of a bike. A commercial bicycle is used to replicate vibration outputs at the saddle and the stem of different bikes. The strategy to determine the appropriate driving signals of each simulator actuator is presented in this paper. This requires solving an inverse problem. The results indicate that the measured and the reproduced PSD spectrum shapes are very similar. The main factor influencing the quality of reproduction is cyclist intervariability.

**Keywords** Vibration • Bicycle • Perception • Reproduction • Comfort • Excitation techniques

### 11.1 Introduction

One of the primary desirable characteristics of a road bike is its capacity to filter road excitation in order to reduce the vibration transmitted to the cyclist. Vibrations generated by road surface defects are a significant source of discomfort and fatigue and are a disincentive to ride. Comfort is fundamentally related to the cyclist's perceptions. The cognitive dimensions of the rider's own assessments of "dynamic comfort" therefore need to be examined, and this involves a quantification of thresholds and parameters that can influence the cyclist's ability to perceive and differentiate variations in vibration levels. A road bicycle is a very compliant and lightweight structure. Because of its weight and added damping, the cyclist has the greatest influence on the bike's response [1, 2]. Moreover, while riding, the posture and position of the cyclist also influence the contact point vibration response [3]. Split testing, which compares A versus B in different situations, is an efficient technique that can be used to assess human perception.

To study the cognitive parameters related to cyclist perception, laboratory testing must be used, but the test environment should be as realistic as possible. The notion of ecological validity, first introduced by Gibson [4] in the visual and later extended to the auditory modality [5, 6], expresses the need to study human perception and performance under ecological conditions by preserving or recreating the contextual and environmental cues that are meaningful for the task at hand. An experimental protocol is ecologically valid only if the participants react to some extent as if they were in a natural situation. On methodological grounds, it is critical to re-create an experimental protocol that resembles a naturalistic situation so that participants recognize and treat the stimuli as natural or potentially familiar experiences [7]. To facilitate the reactivation of cognitive processes elaborated in a previous cycling experience, we decided to design an experimental protocol enabling participants to use a real bicycle instead of an artificial structure such as a saddle and a handlebar driven by shakers.

---

Y. Champoux (✉) • J. Lépine • P.-A. Gauthier • J.-M. Drouet  
VélUS Research Group, Department of Mechanical Engineering, Université de Sherbrooke, 2500 boul. de l'Université,  
Sherbrooke, QC, J1K 2R1 Canada  
e-mail: [Yvan.Champoux@USherbrooke.ca](mailto:Yvan.Champoux@USherbrooke.ca); [julien.lepine@usherbrooke.ca](mailto:julien.lepine@usherbrooke.ca); [Philippe-Aubert.Gauthier@USherbrooke.ca](mailto:Philippe-Aubert.Gauthier@USherbrooke.ca);  
[Jean-Marc.Drouet@USherbrooke.ca](mailto:Jean-Marc.Drouet@USherbrooke.ca)

For the proposed technique, the laboratory reproduction system requires a commercially available bike as well as a cyclist to ride it. This so-called “reproduction bike” has its own dynamic behavior. A valid question must then be asked: Is it possible, by providing adequate excitation inputs only, to accurately reproduce vibrational outputs of a different brand of bicycle? Providing the answers to this question was the motivation behind the work presented in this paper. The test environment is described in the first part of the paper. First of all, using input and output measurements on the reproduction bike only, the accuracy of reproduction was investigated. In a final step, the target output signals measured on a different commercial bike were compared to the reproduced signals in order to evaluate the quality of the reproduction.

### 11.2 Methods

A road bike simulator that was developed for testing road bike dynamic behavior in previous studies was used in this study. Two Xcite model 1100–7 hydraulic shakers were used to impose a vertical displacement under each wheel as shown in Fig. 11.1.

The bike is held vertically by using horizontal bungees attached near the seatpost clamp and to a lab fixture. The cyclist is not required to pedal. The shakers’ amplifier electric signal inputs  $s_1(t)$  and  $s_2(t)$  generate a vertical displacement under the wheels that corresponds to an existing road profile [8].

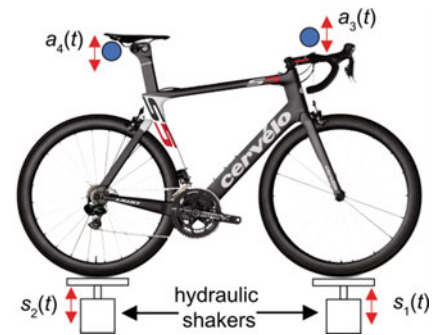
Output acceleration signals  $a_3(t)$  and  $a_4(t)$  were measured using PCB accelerometers model PCB 352C65 at the stem–handlebar connection and model PCB 352C68 under the saddle at the saddle–seatpost connection. An LMS SCADA Recorder and LMS Testlab software were used to acquire and analyze data. The TestLab MIMO FRF software package was used to playback pre-recorded waveform signals.

The reproduction system can be represented by a MIMO two inputs–two outputs system (Fig. 11.2). The inputs  $S_1(\omega)$  and  $S_2(\omega)$  are the frequency spectrum respectively of  $s_1(t)$  and  $s_2(t)$  while  $A_3(\omega)$  and  $A_4(\omega)$  are the output Frequency spectrum for  $a_3(t)$  and  $a_4(t)$ . Front wheel excitation with the stem acceleration is considered to be a direct path. Similarly, the rear wheel excitation is the direct path to the saddle acceleration response. When both excitations are provided, part of the front wheel excitation is responsible for the saddle output and part of the rear wheel excitation is responsible for the stem output. These are the coupling terms responsible for the crosstalk.

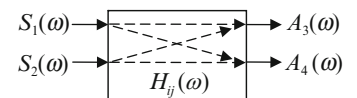
Equation 11.1 represents in the frequency domain the input–output relationship. The FRF system matrix  $[H]$  contains four terms.

$$\begin{Bmatrix} A_3 \\ A_4 \end{Bmatrix} = \begin{bmatrix} H_{31} & H_{32} \\ H_{41} & H_{42} \end{bmatrix} \begin{Bmatrix} S_1 \\ S_2 \end{Bmatrix} \tag{11.1}$$

The off diagonal terms  $H_{32}$  and  $H_{41}$  are the coupling terms. It is important to underline that the system matrix  $[H]$  is always measured with a cyclist riding on the bike. It should also be noted that a typical road excitation input is used to measure  $[H]$ .



**Fig. 11.1** Road bike simulator and the measurement points



**Fig. 11.2** MIMO representation of the system showing the direct path and the coupled transfer path

The inverse matrix  $[Y] = [H]^{-1}$  can be calculated frequency by frequency. All the calculation are done with MATLAB. The inverse problem allows calculating in the frequency domain the system inputs using the outputs as indicated in (11.2)

$$\begin{Bmatrix} S_1 \\ S_2 \end{Bmatrix} = \begin{bmatrix} Y_{13} & Y_{14} \\ Y_{23} & Y_{24} \end{bmatrix} \begin{Bmatrix} A_3 \\ A_4 \end{Bmatrix} \quad (11.2)$$

The reproduction system (bicycle and cyclist) impulse responses  $y_{ij}(t)$  can be obtained by calculating the inverse Fourier transform of the corresponding term  $Y_{ij}$ . One can then calculate the time signal  $s_1(t)$  and  $s_2(t)$  by summing the contribution of the time signal output  $a_3(t)$  and  $a_4(t)$  convoluted (\*) by the respective impulse responses as shown in (11.3) and (11.4).

$$s_1(t) = y_{13}(t) * a_3(t) + y_{14}(t) * a_4(t) \quad (11.3)$$

$$s_2(t) = y_{23}(t) * a_3(t) + y_{24}(t) * a_4(t) \quad (11.4)$$

The time functions  $y_{ij}(t)$  being the impulse responses, each term of (11.3) and (11.4) corresponds to a filtering process of acceleration signals using a Finite Impulse Response (FIR) filter with coefficients provided by the time functions  $y_{ij}(t)$ .

### 11.3 Experimental Validation

The reproduction procedure developed in this work is implemented as follows:

- (i) Acceleration signals  $a_3(t)$  and  $a_4(t)$  measured simultaneously on several different bikes being tested. These signals can be obtained on the road or in laboratory conditions with a cyclist riding the bike. The phase relationship between these two signals must be maintained.
- (ii) The selected reproduction bike is installed on the simulator. With a cyclist sitting on the bike, the system is characterized by measuring its system matrix  $[H]$ .
- (iii) Using the previously measured quantity in step (i), the shakers' excitation signals  $s_1(t)$  and  $s_2(t)$  are calculated using (11.3) and (11.4).

Having a set of  $s_1(t)$  and  $s_2(t)$  for several bikes, it becomes possible to implement comparison perception tests such as split testing.

#### 11.3.1 Validation Using the Reproduction Bike Only

The quality of the reproduction was first investigated using data measured with the reproduction bike only. Three different tests were done to obtain this data:

Test (a)  $H_{31}$  and  $H_{41}$  measured simultaneously when the front shaker only is activated.

Test (b)  $H_{32}$  and  $H_{42}$  measured simultaneously when the front shaker only is activated.

Test (c)  $s_1(t)$ ,  $s_2(t)$ ,  $a_1(t)$  and  $a_2(t)$  measured simultaneously when both shakers are activated.

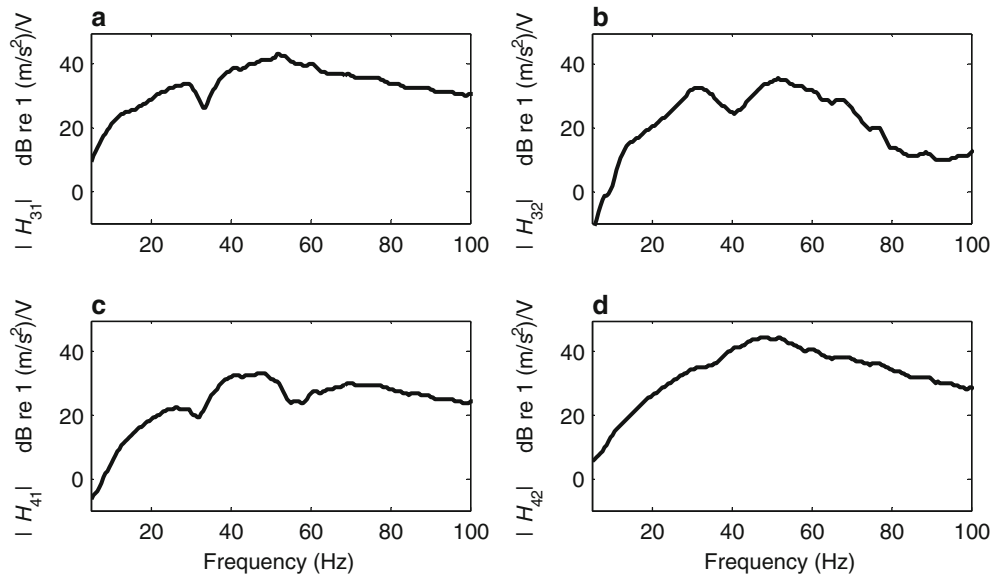
The same road signal was used for both shakers and with the same cyclist on the bike.

Figure 11.3 shows the measured system matrix amplitude  $[H]$  of the reproduction bike with a cyclist on the bike.

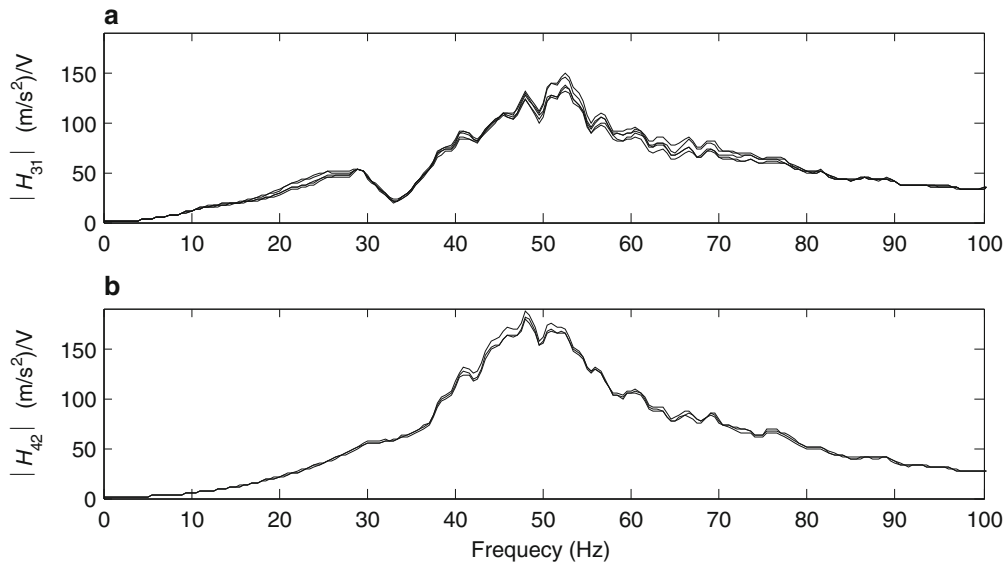
The system matrix measurement was repeated several times in a row to evaluate measurement variability. Between two consecutive tests, the cyclist was asked to dismount. Figure 11.4 shows the FRFs  $H_{31}$  and  $H_{42}$ . The vertical axis is not expressed in dB for this figure. At each frequency, the ratio between the minimum and maximum amplitude of all the curves was calculated. The maximum ratio for all the frequency range 0–100 Hz is 1.25 (1.9 dB) for  $H_{31}$  and 1.06 (0.5 dB) for  $H_{42}$ .

Figure 11.5 shows the matrix  $[Y]$  which is simply the inverse of  $[H]$  calculated frequency by frequency. All calculations were done in MATLAB with no filtering or matrix regulation.

To calculate the FIR filter coefficients  $y_{ij}(t)$ , the inverse Fourier transform of each term  $Y_{ij}$  was calculated. Prior to this calculation, the DC value and the first frequency components were zeroed using a simple cosine taper high pass filter with a cutoff frequency set at 3 Hz. The frequency band of interest is 3–100 Hz. A low pass filter with a cutoff frequency set to 150 Hz was also used to remove the high frequency content. The sampling frequency was set at 8,192 Hz and the FFT record length was 2 s. The numerical impulse response duration was 2 s yielding to a 16,384 coefficients FIR filter.



**Fig. 11.3** System matrix amplitude  $[H]$  of the reproduction bike. (a)  $H_{31}$ , (b)  $H_{32}$ , (c)  $H_{41}$ , (d)  $H_{42}$ . A cyclist is riding the bike



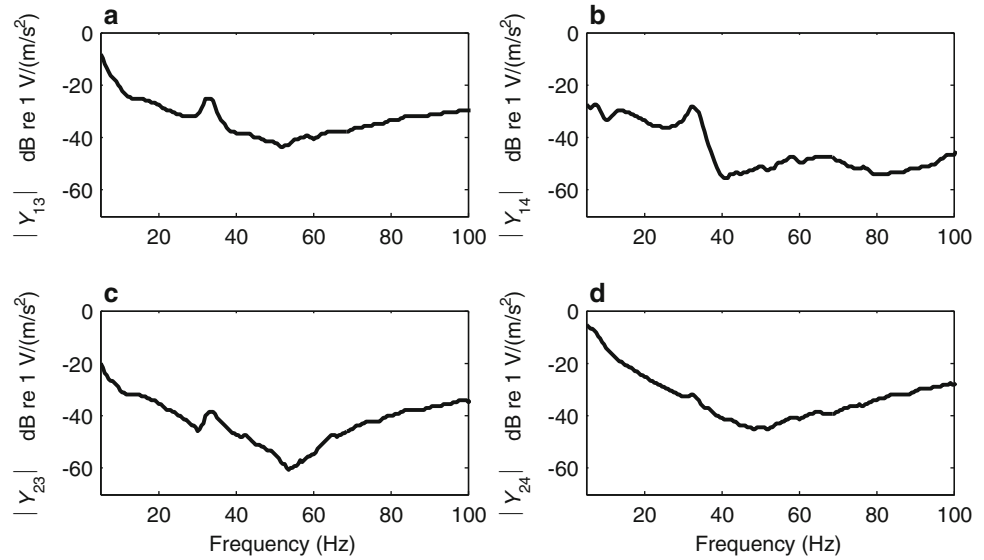
**Fig. 11.4** Measurement variability for  $H_{31}$  and  $H_{42}$  (a)  $H_{31}$  five tests; (b)  $H_{42}$  three tests

The filter coefficients were rearranged to obtain an impulse response with evanescent ends to minimize the truncation errors. Figure 11.6 shows the calculated four impulse response functions.

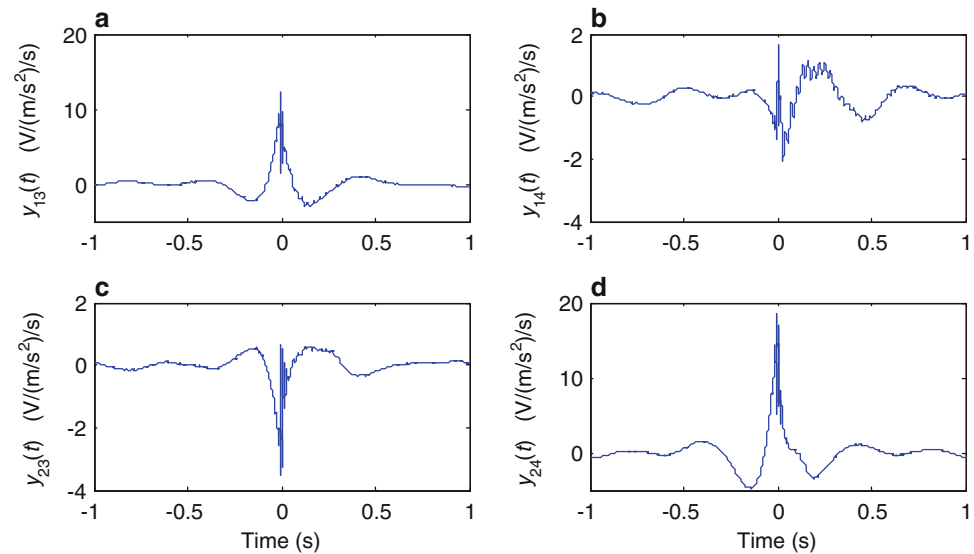
This first validation test used measurements obtained only from the reproduction bike. The input and output signals were measured simultaneously as indicated previously in the description of Test (c). Using the output signals  $a_3(t)$  and  $a_4(t)$  in (11.3) and (11.4), it was possible to solve the inverse problem and calculate the inputs  $s_1(t)$  and  $s_2(t)$ .

The first validation test consists of comparing the calculated and the measured inputs. Figure 11.7 allows us to compare the measured and the calculated inputs signal  $s_1(t)$  for a typical short time segment. The PSD of the measured and reproduced shaker input signals  $G_{s_1s_1}$  and  $G_{s_2s_2}$  are compared in Fig. 11.8. The mean discrepancy between the calculated and the measured PSD is 0.2 dB and the maximum discrepancy is 2.3 dB. The ratio between the measured and the calculated total power for  $s_1(t)$  is 0.98 and 0.94 for  $s_2(t)$ .

**Fig. 11.5** Inverse cyclist-bike system matrix  $[Y]$  of the reproduction bike. (a)  $Y_{13}$ , (b)  $Y_{14}$ , (c)  $Y_{23}$ , (d)  $Y_{24}$



**Fig. 11.6** Impulse response (filter coefficients) for the four terms of  $[Y]$ . (a)  $y_{13}$ , (b)  $y_{14}$ , (c)  $y_{23}$ , (d)  $y_{24}$

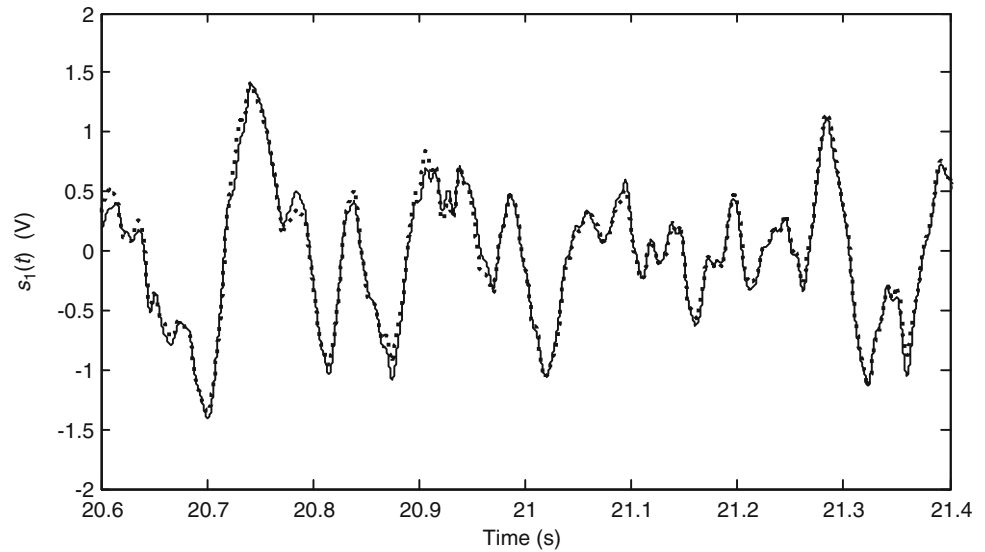


### 11.3.2 Reproduction Quality Assessment

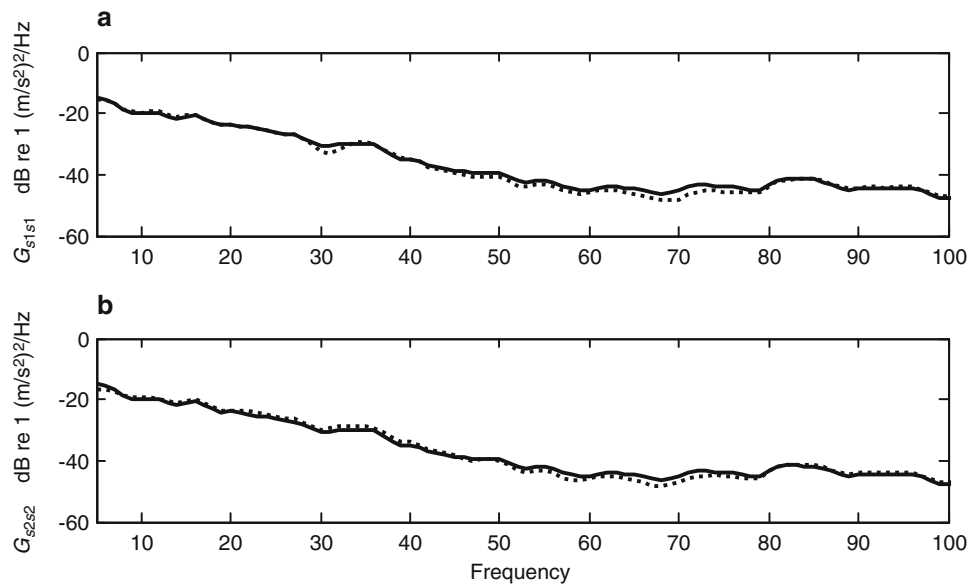
To explore how the proposed approach of using a reproduction bike succeed to reproduce the vibrational behavior of different bikes, a road bike named the “target bike” of a different model and brand than the reproduction bike was selected and tested. The target bike was installed on the simulator and the same shaker road input signals were used. The seatpost and saddle acceleration levels  $a_{3t}(t)$  and  $a_{4t}(t)$  were measured. These signals and their respective frequency spectrum  $A_{3t}$  and  $A_{4t}$  are the target signals. Using the procedure presented previously, the signals  $s_{1t}(t)$  and  $s_{2t}(t)$  were calculated. These signals were then used to drive the shakers, and then the reproduced output acceleration signals  $a_{3r}(t)$  and  $a_{4r}(t)$  were measured. Comparing the target and the reproduced signals is the ultimate way to check the validity of the approach. An accurate reproduction would show a perfect match between reproduced and target signals.

Figure 11.9 shows the comparison of the reproduced and the target acceleration PSD at the stem and at the saddle. A third curve (thick line) shows the measured PSD when the original road signals were used. The shape change of the curves from the thick line to the solid line demonstrates how the reproduction bike outputs are modified by changing the input signals.

**Fig. 11.7** Comparison of the measured shaker input signal  $s_1(t)$  with the calculated signal. *Solid line*: measured signal; *dotted line*: calculated signal exciter



**Fig. 11.8** Comparison of the measured and calculated PSD for the shaker input signals (a) Front exciter  $G_{s1s1}$  (b) rear shaker  $G_{s2s2}$



## 11.4 Discussion

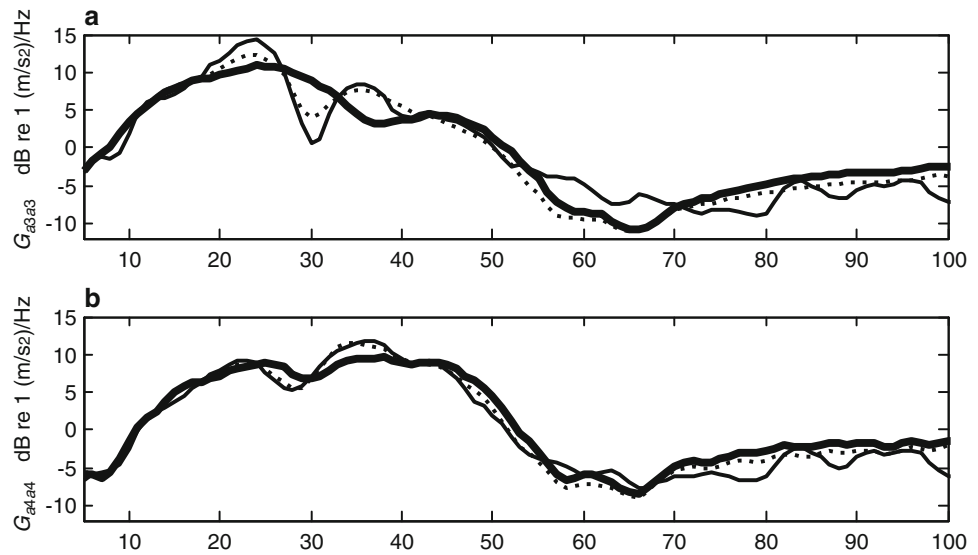
The problem investigated in this study is somewhat similar to what is known as crosstalk cancellation in the audio research community. Crosstalk cancellation is often applied to binaural sound reproduction at a single listener's ears using two or more loudspeakers [9–12]. For audio applications, crosstalk cancellation is somewhat complicated by: (i) the propagation time between sources and receivers and (ii) the full audio bandwidth. In the case studied in this paper, the mostly non-resonant and highly damped behavior of the reproduction bike is sufficient to simplify the derivation of the inverse, crosstalk cancellation, filter and simple inverse processing.

The identification of natural frequency using Fig. 11.3 is difficult because there is no well-defined peak in the FRFs. Modal analysis showed that the peak and valley in  $H_{31}$  around 30 Hz is associated with the front and back cantilever beam mode of the bicycle fork and front wheel.

Several parameters can influence cyclist-bike system behavior [3]. In this paper, a cyclist sits on the bike during all tests for the following reasons: (i) the human body part vibrational behavior in contact with a vibrating structure is recognized to have some non-linearity; (ii) the normal stiffness of road bike tire changes drastically with preload. Testing at running



**Fig. 11.9** Comparison of the target and measured acceleration PSD at the stem and the saddle. (a) Saddle acceleration PSD  $G_{a3a3}$ . (b) Seatpost acceleration PSD  $G_{a4a4}$ . Solid line: replicated PSD, dotted line: target PSD, Thick line: reproduction bike PSD output when shakers are driven by the original road signal



preload levels imposed by the cyclist allows a reduction of the nonlinear effect. One of the main elements that must be taken into account when testing bicycle vibration is the cyclist's "posture" [3] which is related to the way the cyclist leans on the bike, leans onto the handlebar, sits on the saddle and contracts his muscles. These elements have an important effect on the vibrational behavior of the cyclist–bicycle system. For studying bike design modifications in relation to its dynamic behavior and comfort, the inherent variability of the cyclist must be taken into account, and testing techniques must be developed to minimize its impact on test variability. Figure 11.4 shows measurement variability of the matrix  $[H]$ .

The inverse matrix system  $[Y]$  is directly calculated in MATLAB from  $[H]$ . No regulation of the matrix is required. To obtain the impulse response, it is necessary to get rid of the DC component and the few first frequency lines for all  $Y_{ij}$ . Because a piezoelectric accelerometer is used, the first few lines of the FRFs for  $[H]$  are not measured correctly and the amplitude is close to zero. Consequently, the corresponding lines of  $Y_{ij}$  have very high amplitude and must be removed. Figure 11.6 shows the impulse responses. No time windowing was necessary and the use of 16,384 coefficients seems to be adequate so that both ends of each impulse response asymptotically converge toward zero amplitude.

Figures 11.7 and 11.8 provide a first indication of the quality of the reproduction. Because in this case the measurements were done on the same bike, one would expect that the measured and the calculated shaker excitation signals would be identical. Indeed, Figs. 11.7 and 11.8 show that the discrepancies between the target and the measured values are relatively small. The system matrix and the reproduction measurement require three different tests. The intervariability of the cyclist's position and posture could explain most of the discrepancies.

The last validation test results are shown in Fig. 11.9. The target signals (stem and saddle PSDs) are compared with the reproduced PSDs. The response of the reproduction bike (thick line) was definitively reshaped by the use of a different shaker input signals for reproducing the target bike outputs. A frequency span of 5–100 Hz is used to plot the graphs. The capacity of hand and buttock to perceive vibration varies with frequency as described in the ISO standards [13, 14]. Taking the hand and buttock sensitivity into account and the fact that most of the vibrational power shown in  $G_{a3a3}$  and  $G_{a4a4}$  is below 55 Hz, it would be justified to judge the reproduction quality between 5 and 50 Hz. The reproduction quality at the saddle is better than the one at the stem. This is expected because typically two-third of the cyclist's mass is on the saddle and the intervariability of a subject is lower at the saddle. In Fig. 11.9a the replicated amplitude is overestimated around 23 Hz when compared to the target signal. The results are taken from a single measurement and in a certain way this could be considered as a worst case scenario. In any case, the frequency spectrum shapes of both the target and the reproduced signals are very similar.

## 11.5 Conclusion

For perception studies of comfort in a laboratory, a commercial bike was used to develop a reproduction system. The use of vibrational output signals to calculate the required inputs for driving the shakers is essentially an inverse problem. It was shown in this paper that inverting the system is quite straightforward and no specific matrix or system regulation is required. The capacity of the reproduction system to reproduce vibration accelerations at the stem and saddle was examined

and it was shown that the frequency spectrum shapes are well reproduced. Nonetheless, some amplitude discrepancies were observed, mainly at the stem. This approach requires that a cyclist sit on the bike during all tests as well as when characterizing the system. The reproduction system includes both the cyclist and the bike. Practical testing considerations related to nonlinearities were raised to justify including a cyclist. The current challenge to studying comfort is related to the fact that the cyclist has a strong influence on the vibrational response of the bike – cyclist system and a change in position or posture can introduce important variability. The results presented in this paper are based on a single measurement. Repeating all measurements over several days will prove to be worthwhile. It will also be interesting to consider the effect of different cyclists. Finally, we also need to ask if, in order to maximize the quality of the reproduction, it would be necessary to repeat all measurements, including the system matrix characterization, for each cyclist.

**Acknowledgements** The authors gratefully acknowledge financial support from the National Science and Engineering Council of Canada (NSERC) and the participation of Cervélo and Vroomen-White Design.

## References

1. Richard S, Champoux Y (2004) Modal analysis of a road bike's front components. In: Proceedings of IMAC XXII, Dearborn, Feb 2004
2. Champoux Y, Richard SE, Drouet J (2007) Bicycle structural dynamics. *Sound Vib* 41(7):16–24
3. Lépine J, Champoux Y, Drouet JM (2013) Influence of test conditions in comfort ranking of road bicycle wheels. Paper accepted for the IMAC XXXI, Garden Grove, Feb 2013
4. Gibson J (1979) *The ecological approach to visual perception*, 1986 ed. Houghton Mifflin, Boston
5. Gaver W (1993) What in the world do we hear? An ecological approach to auditory event perception. *Ecol Psychol* 5(1):1–29
6. Guastavino C, Katz B, Polack JD, Levitin D, Dubois D (2005) Ecological validity of soundscape reproduction. *Acust United Acta Acust* 91(2):333–341
7. Guastavino C (2009) Validité écologique des dispositifs expérimentaux. In: Dubois D (ed) *Le Sentir et le Dire. Concepts et méthodes en psychologie et linguistique cognitives*. L'Harmattan (Coll. Sciences Cognitives), Paris, pp 229–248
8. Brassard F (2010) Développement d'un simulateur de vibration pour vélo de route. Master degree thesis, Université de Sherbrooke, Sherbrooke
9. Nelson PA, Rose JFW (2005) Errors in two-point sound reproduction. *J Acoust Soc Am* 118:193–204
10. Kirkeby O, Nelson PA (1999) Digital filter design for inversion problems in sound reproduction. *J Audio Eng Soc* 47(7/8):583–595
11. Norcross SG, Soulodre GA, Lavoie MC (2004) Subjective investigations of inverse filtering. *J Audio Eng Soc* 52(10):1003–1028
12. Lentz T (2006) Dynamic crosstalk cancellation for binaural synthesis in virtual reality environments. *J Audio Eng Soc* 54(4):283–294
13. ISO 2631–1 (1997) Mechanical vibration and shock – evaluation of human exposure to whole-body vibration–Part 1: general requirements
14. ISO 5349–1 (2001) Mechanical vibration – measurement and evaluation of human exposure to hand-transmitted vibration–Part 1: general requirements

# Chapter 12

## Exploring Experimental Structural Dynamics in EMA/ME 540 at UW-Madison

Matthew S. Allen

**Abstract** One of the highlights of the experimental structural dynamics course at the University of Wisconsin-Madison is a final project in which the students perform a modal test of a structure and explain how the identified modal parameters affect the performance of the structure. This is a 500 level course, typically taken by a half-and half mix of senior undergraduate students and graduate students. This paper discusses the topics that were covered in the course in the Fall of 2011 and shows highlights from the students' final projects. The different software packages that are used, both commercial and those created in Matlab for the course, are also discussed. The projects have included: a modal test on a wing in a wind tunnel to diagnose a vibration problem, a modal test of a wine glass to relate the modes of the glass to the sound that is heard when it is excited by friction between the rim of the glass and a finger rubbed around the circumference of the rim, and many others.

**Keywords** Laboratory • Experimental • Structural dynamics • Experimental modal analysis • Structural modification

### 12.1 Introduction

The goal of EMA/ME 540: Experimental Vibration and Dynamic System Analysis is to reinforce the students understanding of vibrations theory through hands on experiments while exposing them to state of the art structural dynamic testing methodologies and improving their laboratory skills. The course is intended for both undergraduates and graduate students, so it necessarily includes a review of undergraduate vibrations theory that takes the first 4 or 5 weeks of the course. Those concepts are then built upon over the next several weeks as the students are exposed to the discrete Fourier transform, experimental modal parameter identification, Ritz theory for continuous systems and structural modification theory. The students spend the last several weeks of the course working on a project of their choice the includes both testing *and some analysis* to show how the test results would be useful in the application of interest.

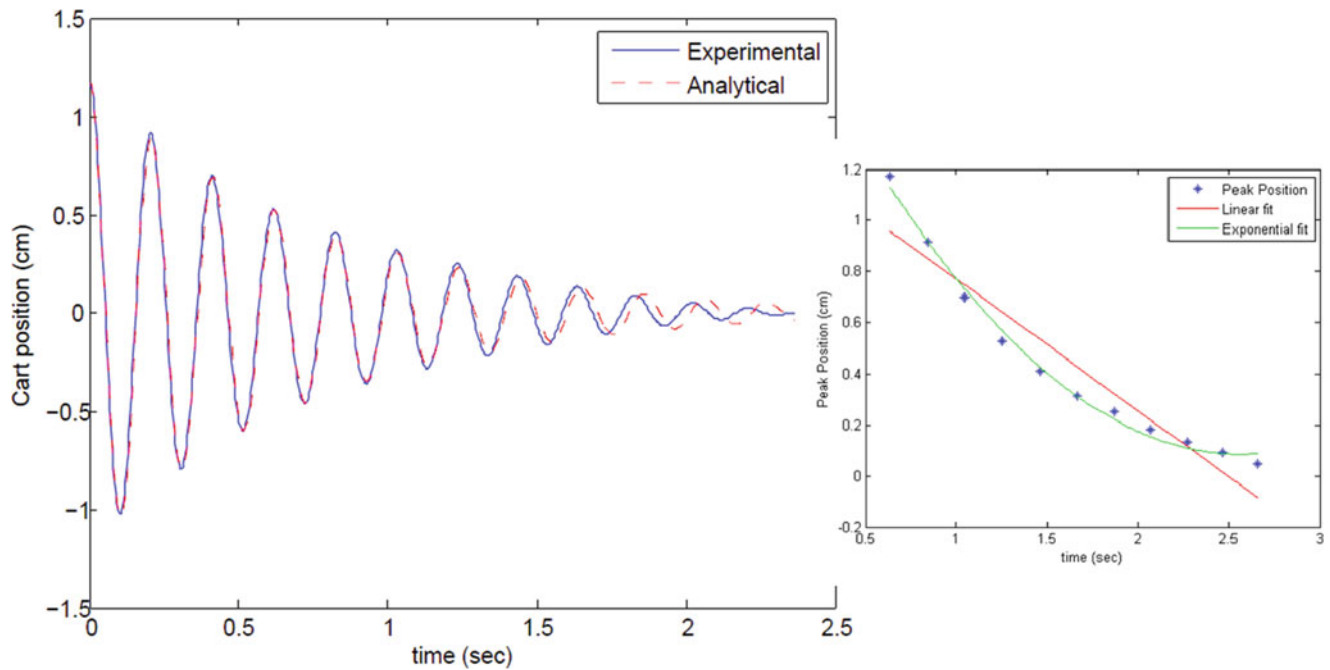
The instructor has found that it is critical to demand that the students think carefully about the meaning of the measurements that they are acquiring and strives to set this expectation with the very first lab report. This lab covers free vibration of mass-spring systems (carts with helical springs) that are conceptually extremely simple yet in fact can exhibit some interesting dynamics. The students receive a low grade on this report if they fail to thoroughly explore the meaning of their measurements. For example, Fig. 12.1 shows a comparison between the measured and predicted time response for the SDOF system from a team who scored quite high. They took great care to carefully calibrate their analytical model, and hence they were able to observe how Coulomb damping begins to affect the response towards the end of the time record.

Further information regarding this course is presented in the syllabus and lab handouts which are provided in the Appendices of this document.

---

M.S. Allen (✉)

Department of Engineering Physics, University of Wisconsin-Madison, 1500 Engineering Drive, 535 ERB, Madison, WI 53706-1609, USA  
e-mail: [msallen@engr.wisc.edu](mailto:msallen@engr.wisc.edu)



**Fig. 12.1** Time history from one team's report for Lab 1 that shows a thorough comparison between analysis and experiment. The period and effective damping in the system change at small amplitudes due to Coulomb friction in the system

## 12.2 Course Outcomes: Final Projects

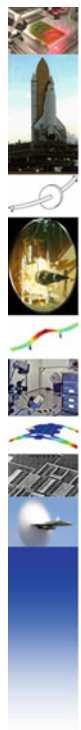
This section presents a sampling of slides from final project presentations that the students have presented over the past few years. Figures 12.2–12.5 describe a project in which a team sought to diagnose a vibration problem in the University's wind tunnel that had been observed when aluminum plates were added to the ends of a wing to force the flow to become more two-dimensional. In this configuration the wing exhibited excessive vibration making tests unsafe at high flow velocities. The team found that the lowest modes of the wing were most strongly excited (suggesting that this was not a flutter problem); apparently the addition of the end plates reduced these frequencies enough to significantly increase their response.

Another team studied the vibration and noise emitted by a crystal glass when a finger is rubbed along the rim of the glass. They performed a modal survey of the glass, taking care to mass load the glass as little as possible, and then acquired measurements of the sound emitted as the glass was excited by friction between a finger and the rim of the glass. They found that the frequency that dominated the audible spectrum corresponded to a pair of four-lobe ovaling modes of the glass (Figs. 12.6 and 12.7).

## 12.3 Conclusions

The goal of this course is to develop the students' understanding of vibration theory and their experimental abilities. Their performance on the final project is usually a good indicator of their understanding of structural dynamics and how it impacts the performance of their chosen system of interest, as well as their persistence and work ethic. Results to date have been good suggesting that many of the students obtain a good level of proficiency as a result of the class. The instructor also has several graduate research assistants who were former students in this class and has found that they tend to be quite capable with measurement and analysis of measurements following the class. Of course there is certainly room for improvement. The primary challenge at the moment is how to construct a review of vibrations theory that allows the class to draw from a large pool of students (with varied pre-requisites) while encouraging a solid mastery of the important material. The instructor is also constantly seeking new ways to encourage the students to think more deeply and seek further insights into the issues that they confront in their projects. On the other hand, the instructor himself has learned a tremendous amount over the past few years teaching this course and so he suspects that this is a never-ending quest.

**Fig. 12.2** Slide 1 from wind tunnel vibration project presentation outlining the problem



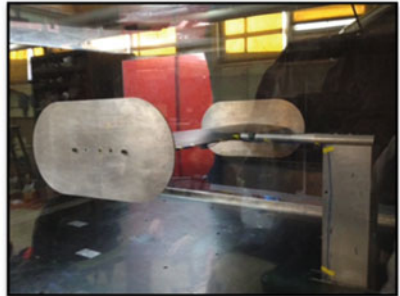
## PROBLEM

Large displacements when plates are added!!!

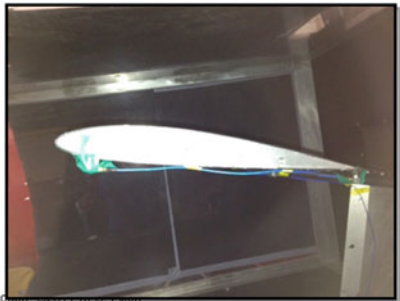
## OBJECTIVES

- Find shifts in natural frequencies between wing with and without plates (EMA)
- Find which modes are causing the largest displacements (OMA)

### 2-D flow

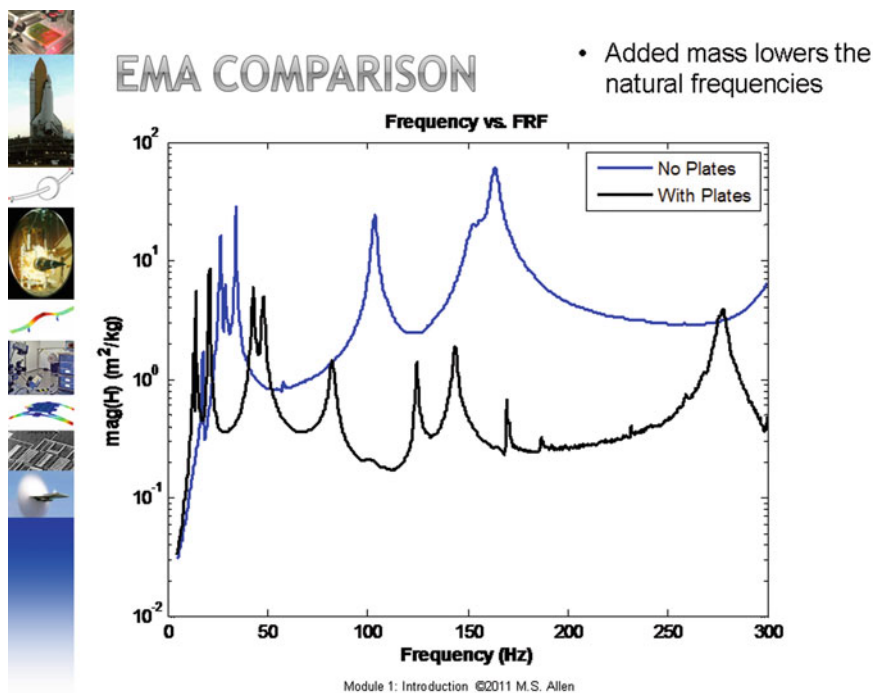


### 3-D flow

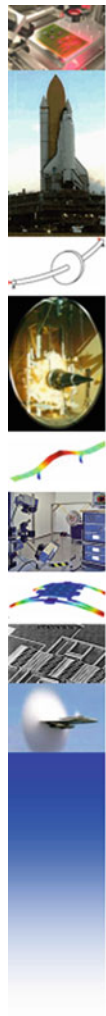


Module 1: Introduction

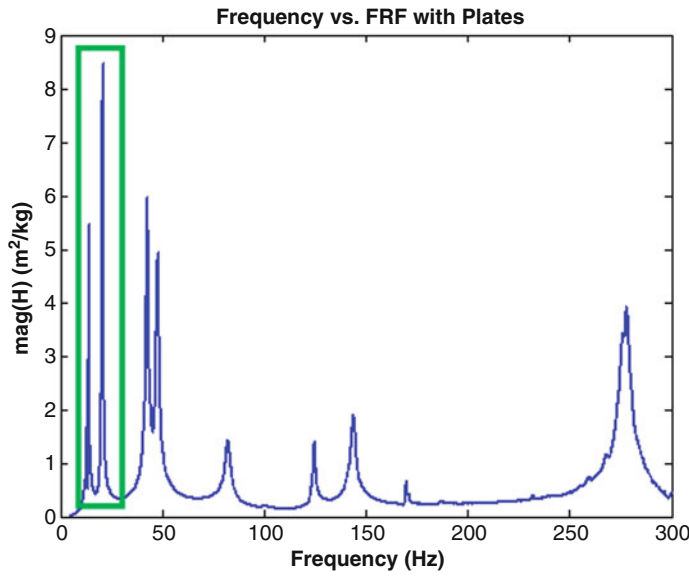
**Fig. 12.3** Slide 2 from wind tunnel vibration project presentation summarizing the differences between the frequency responses of the system with and without the end plates



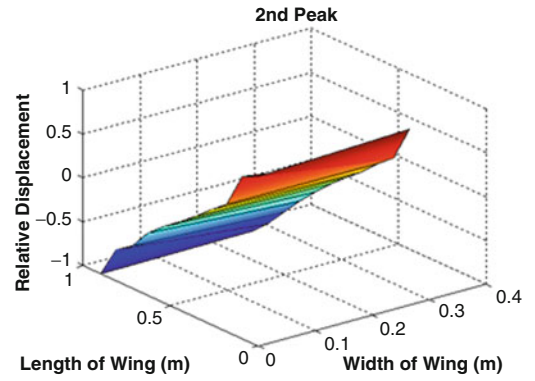
**Acknowledgements** The author would like to thank Dr. Peter Avitabile for the many helpful comments and materials that he supplied when Dr. Allen first created this course in 2009. His comments and ideas were extremely influential in shaping this course. The author would also like to thank Tom Carne for the many questions he answered and the insights and advice that he offered regarding this course.



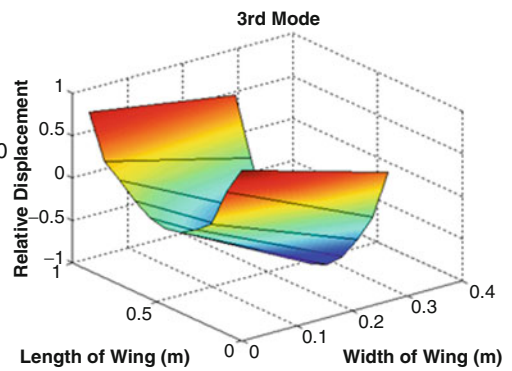
# EMA WITH PLATES



## 1<sup>st</sup> Mode: Stinger Torsion



## 2nd Mode: Stinger Bending

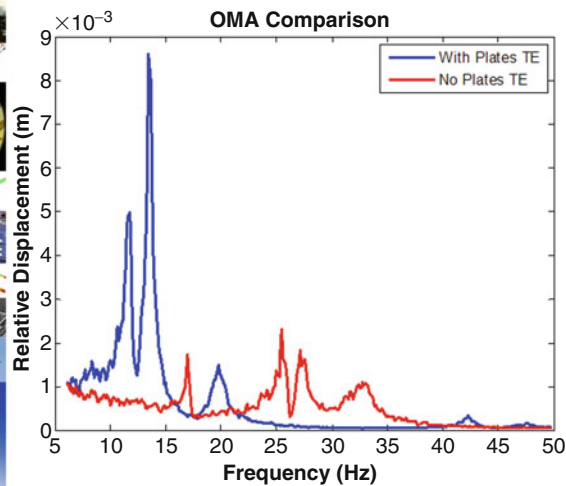


Module 1: Introduction ©2011 M.S.Allen

Fig. 12.4 Slide 3 from wind tunnel vibration project presentation showing the shapes of the modes that are thought to be dominant

Fig. 12.5 Slide 4 from wind tunnel vibration project presentation showing the difference in behavior of the system in operation with and without the end plates

# OMA COMPARISON



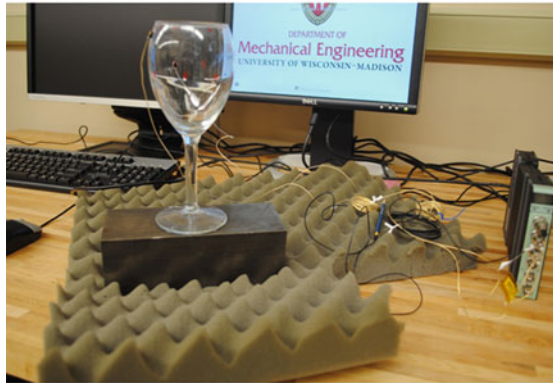
- The displacements of the wing with the plates are much larger than the displacements with out plates
- The lower natural frequencies seem to be in a regime of stronger excitation!

Module 1: Introduction ©2011 M.S.Allen



**Fig. 12.6** Slide 1 from crystal glass project presentation showing experimental setup

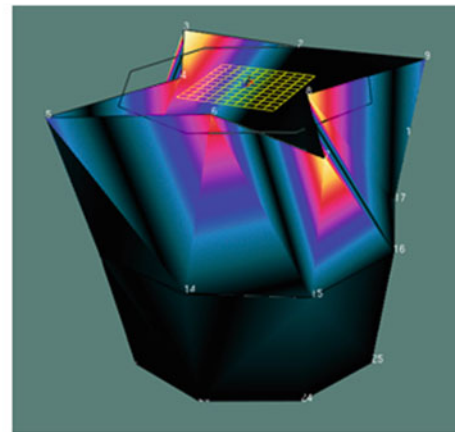
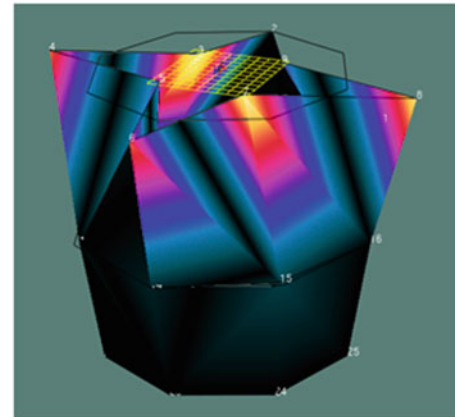
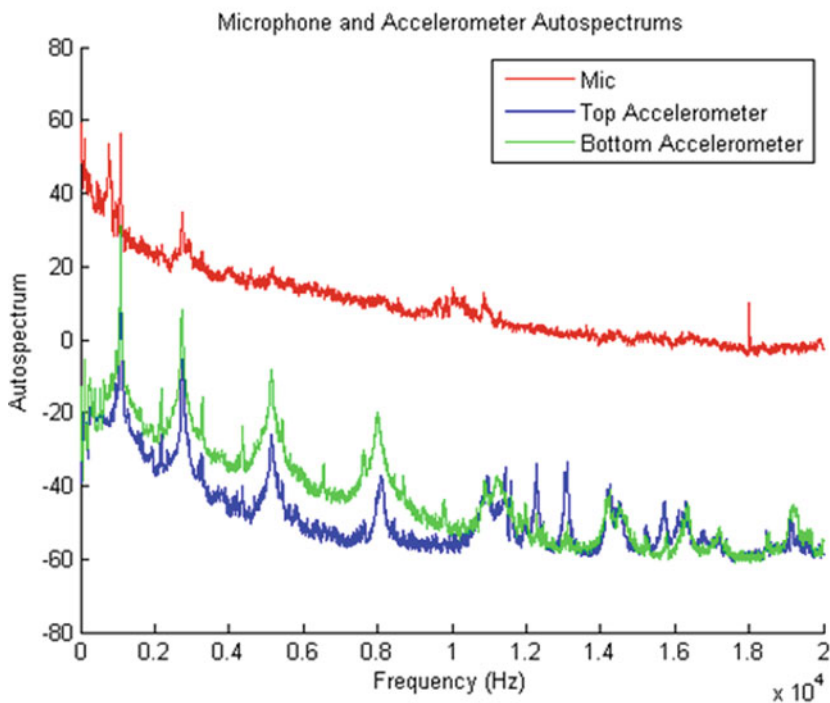
## Modal Analysis of a Crystal Glass



Module 1: Introduction ©2011 M.S. Allen

[1]  
4

## Correlating Noise and Modes of Vibration



**Sound apparently generated by pair of third ovaling modes**

Module 1: Introduction ©2011 M.S. Allen

5

**Fig. 12.7** Slide 2 from crystal glass presentation highlighting experimental results. The modes that contribute most to the audible sound were found to be a pair of four-lobe ovaling modes



## A.1 Appendix 1: ME/EMA 540 Course Syllabus, Fall 2011

### A.1.1 Experimental Vibration and Dynamic System Analysis

**Instructor:** Prof. Matt Allen

Department of Engineering Physics

**Office Hours:** M/Tues 2-3PM, Th 12:30–1:30 PM, or by appointment

**Prerequisites:** ME 340, ME 440, EMA/ME 545 or Instructor Consent

**Course Home Page:** <https://ecow2.engr.wisc.edu/courses/course/view.php?id=1531#section-2> Lecture notes, homework, lab handouts and solutions will be posted on course web site.

**Textbook:** Mechanical and Structural Vibrations: Theory and Applications, Jerry H. Ginsberg [1]. An excellent reference and used for homework assignments.

**Online course description:**

Application of digital data acquisition to the investigation of mechanical components, structures and systems using time histories, transforms and response functions to characterize free, forced and transient inputs. Introduction to sensors, instrumentation and methods appropriate for dynamic system response.

**Evaluation:**

- **Homework sets** – A few homework sets will be assigned throughout the semester to help you review some important concepts from vibrations. Homework sets are due as noted on the course website when they are assigned (syllabus lists expected due dates, which are subject to change). Late homework will not be accepted unless prior arrangements have been made with the instructor. Consulting with your peers is allowed so long as it is done responsibly.
  - If you are ill or otherwise unable to turn in an assignment, contact Prof. Allen immediately by phone or email to make arrangements to turn the assignment. Late homework will not be accepted unless prior arrangements have been made.
- **Exams**
  - None planned, although the instructor reserves the right to give a few quizzes for homework credit if he deems that it would be beneficial.
- **Lab Reports**
  - Most labs will be completed within the scheduled class time, although they require analysis that will be performed outside of class. Lab reports are required for most of the labs and these will be done in teams.
  - Lab reports will be evaluated based on their professionalism, clarity and the insight that they demonstrate into the subject matter. A professional report will contain a short introduction, results, and conclusions, will be neat and will contain enough explanation to guide the reader through your results. *To receive an “A” you must show that you have thought deeply about the results and what they mean; a cursory coverage of the required tasks will earn only a passing grade.*

Brevity and efficiency in the text of your report will be rewarded, although you are encouraged to include as many figures/discussion as needed to present your results. Avoid providing a “data dump;” present your results so that the conclusions and key findings clearly stand out. You do not need to include a detailed description of the procedure that you used unless your procedure deviated from that given to you in the lab assignment (as it may in the later labs).
- **Final Exam Period: 12/17/2011, Saturday, 2:45–4:45 PM**
  - In lieu of a final exam, each lab team will give a presentation to the class on their final project.
- Grades in the course will be decided with the following weighting:
  - Homework Sets 20%
  - Lab Reports 60%
  - Final Project 20%

**General Topic Areas Covered:**

- Review of Free and Forced Harmonic vibration of SDOF and MDOF systems.
- Discrete Fourier Transform, Nyquist sampling theorem and analog to digital conversion.
- Transient modal testing for continuous systems (including impact, step relaxation, etc. . . .).

Date <sup>1</sup>	Week	Topic	Due dates <sup>1</sup>
9/6	1	Introduction, start SDOF free (1.1-1.4)	HW#1 assigned
9/8		Finish SDOF free, MATLAB example (2.1-2.2)	
9/13	2	MDOF systems: free response/generalized eigenvalue problem (4.1, 4.2.1-3)	<b>HW#1 due</b> HW #2 assigned
9/15		MDOF systems: orthogonality (4.3.1,2,4,6)	HW #3 assigned
9/20	3	Lab 1: SDOF/MDOF transient response (2145ME)	<b>HW#2 due</b>
9/22		SDOF forced response (2.3.1,3.1-2)	
9/27	4	MDOF systems: frequency domain TF, intro. to experimental modal analysis (5.1-2, notes)	<b>HW#3 due</b> HW #4 assigned
9/29		MDOF systems: vibration absorber, sensors: accelerometer, strain gauge and LDV (5.3, notes)	<b>L1 report due</b>
10/4	5	Fourier series, DFT, sampling, FRF estimation (3.7 all)	<b>HW #4 due</b> HW# 5 assigned
10/6		Lab 2: frequency response of SDOF/MDOF sys	
10/11	6	Lab 2: continued (2163 ME)	
10/13		Intro to continuous systems/Ritz (6.1.1)	
10/18	7	Ritz method for beams (6.1.3-4, 6.2)	HW #6 assigned <b>L2 report</b> <b>HW #5 due</b>
10/20		Lab 3: sensor comparison (B331 EH)	
10/25	8	Ritz method continued (6.3)	
10/27		MAC, MSF and support conditions (notes)	
11/1	9	Modal parameter estimation (1/2 lecture) (notes)	<b>HW #6 due</b>
11/3		Lab 4a: impact modal test of F-F beam (2163 ME)	
11/3		Lab 4a: continued	<b>L3 report due</b> HW #7 assigned
11/8	10	Lab 4a: continued	
11/10		Structural modification/substructuring (~9.1~)	Assign/discuss projects
11/15	11	Lab 4b: structural modification	<b>L4a report due</b>
11/17		Operational modal analysis (notes)	
11/22	12	Lab 5: output-only modal test of downhill skis	<b>L4b report due</b> Choose projects/teams
11/24-		<b>Thanksgiving recess 11/24-11/27</b>	
11/29	13	Intro to nonlinear vibrations (notes)	
12/1		Testing/analysis for final projects	<b>HW #7 due</b>
12/6	14	Testing/analysis for final projects	<b>L5 report due</b>
12/8		Testing/analysis for final projects	
12/13	15	Testing/analysis for final projects	
12/15		Testing/analysis for final projects	
12/17		<b>Project presentations during</b>	<b>Each group present a summary of their final projects</b>
<b>Final exam period, 12/17/2011, Saturday, 2:45–4:45 PM</b>			

<sup>1</sup>Note: All of the dates below are approximate. The instructor will adjust the schedule as necessary

- Ritz Series models for continua and relationship to experimentally derived models and structural modification.
- Common vibration sensors including: piezoelectric accelerometers and load cells, Laser Doppler Vibrometers (LDV)/ Interferometers, strain gauges, etc. . . .
- Identification of modes with close natural frequencies using Mode Indicator Functions (MIFs) and MIMO identification.
- Introduction to vibration of nonlinear systems.

**Final Project:** Each team will chose a system to study for their final project. The final project focuses on performing an accurate dynamic test and explaining how the modal parameters that you identify affect the performance of the system. The list below gives a sampling of ideas for a final project.

- Test a crystal glass to identify the shape of the mode(s) that contribute to sound generation when a finger is rubbed along the top of the glass. What other modes are present in the frequency range that do not generate sound? Why?
- Hard Drive: Perform modal survey of the case. How do modes compare with the nominal drive frequency and its harmonics? At what spindle speed would you expect to encounter vibration problems with the hard drive?

- Sporting equipment such as a tennis racquet (or similarly for baseball, hockey, etc. . . .): Compare the dynamic properties of two racquets (or one racquet in multiple configurations, e.g. with a vibration absorber.) How would the modes that you observed affect the way a ball is hit or the way it feels to the user? (e.g. simulate the impact of a ball with the racquet using the modal model that you've developed.)
- Perform a modal test on a guitar and use the result to explain the amplification of certain notes in the sound produced.
- Use operational modal analysis to find the modes of the ERB or the second floor of ME.
- For RC enthusiasts: Perform a Modal test of an RC plane to identify the first few bending and torsional modes. Compare the natural frequencies and predict which bending-torsion mode combination is most likely to lead to flutter at high airspeeds.

#### Links:

- Articles giving easy to understand explanations of various concepts from vibrations and experimental modal analysis:
  - <http://macl.caeds.eng.uml.edu/umlspace/mspace.html>
- U Michigan Matlab tutorial:
  - <http://www.engin.umich.edu/group/ctm/basic/basic.html>
- Some very basic Matlab tutorials:
  - <http://www.cyclismo.org/tutorial/matlab/>
- If you need additional help, Matlab tutors are generally available in Wendt library during the walk-in tutoring on Sunday, Monday, Tuesday, and Wednesday nights. See <http://studentservices.engr.wisc.edu/classes/tutoring/> for more details.

## B.1 Appendix 2: Sample Laboratory Assignments

### B.1.1 Lab 1: Free Vibration of SDOF/MDOF Systems

#### B.1.1.1 Lab Report

You will be required to turn in a lab report summarizing your findings. Pay special attention to the questions in bold-italics throughout the lab handout. You do not need to discuss the hardware setup in detail or other items that were given in this handout.

#### B.1.1.2 Objective

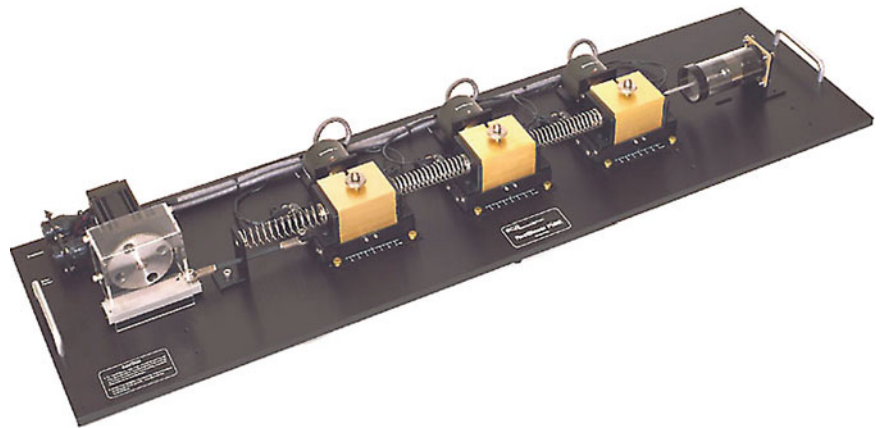
The purpose of this lab is to understand the basic features of the free response of underdamped single-degree-of-freedom (SDOF) and multi-degree-of-freedom (MDOF) systems. You will acquire measurements from a real system and estimate the system's parameters (e.g.  $\omega_n$ ,  $\zeta$ , etc. . . .) for both SDOF and MDOF systems. For the SDOF case, you will carefully compare the measured response to the analytical response that is expected. Your key focus with that comparison is to seek to ascertain to what degree the analytical model is capable of describing the motion of the real system.

In this lab, translational single DOF mass-spring systems will be examined. It is important to note that all physical systems contain some damping, even if no external damper is attached (you will not use the external damper in this lab).

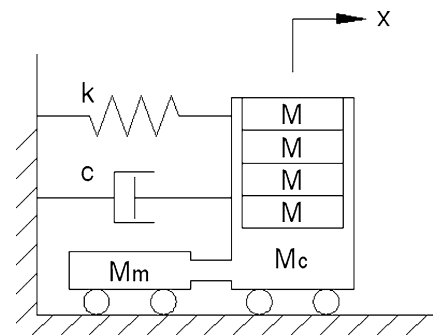
Figure B.1 shows the rectilinear system that will be used for this experiment. Figure B.2 shows a schematic version of the actual systems used in this experiment.

None of these parameters will be given to you except for the mass of the brass blocks ( $M = 0.59$  kg, even if we gave you the others they wouldn't be accurate). All of the other parameters must be determined from experimental data. Of course, one could determine the stiffness of the springs using statics and weigh the parts to estimate  $M_m$  and  $M_c$  the system, but there are some potential disadvantages to that approach. Instead, we shall use dynamic measurements to determine the unknown stiffness  $k$  and the mass of the entire cart  $M_m + M_c = m_1$ . Note that you will not connect the external dashpot, but the system still has some damping. You will also investigate a two-DOF system whose schematic is shown below. Note that you should use identical springs so  $k_1 = k_2$  and you should not connect the dashpot (Fig. B.3).

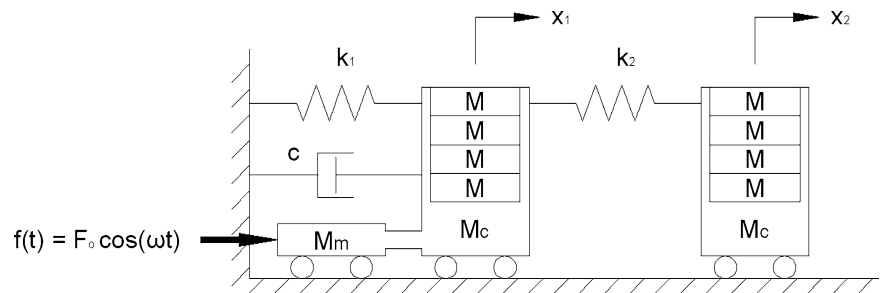
**Fig. B.1** Rectilinear lumped-element dynamic system



**Fig. B.2** Translational system schematic



**Fig. B.3** Two-DOF translational system schematic



### B.1.1.3 Instructions

1. **SDOF SYSTEM:** Use the data acquisition system to capture and save the response of the system to various initial displacements from equilibrium. See the appendix for detailed instructions regarding how to setup the data acquisition system.

- Record the response of the system to initial displacements of about 1–3 cm.
- Add a known mass to the system ( $m_2$ , so the total mass of the system is now  $m_1 + m_2$ ) and repeat the experiment once again for initial displacements of about 1–3 cm.

(i) **ANALYSIS:** Find the natural frequency and damping ratio for the system with and without mass and use them to compute the mass, stiffness and damping ( $m$ ,  $c$  and  $k$ ) constants of the system. **How uncertain are the natural frequency and damping ratio? What about ( $m$ ,  $c$  and  $k$ )?** Make sure your units are correct. **Are your answers reasonable?**

(ii) **ANALYSIS:** Create a plot of the measured response for at least one of the cases in (a) (no mass added) and compare it with the analytically reconstructed response (see detailed instructions in the Appendix for hints).

- It is likely that, even after very carefully tuning your model, you may still not have perfect agreement between the test and model. Think carefully about the following questions to explore this.

2. *How does the measured response compare with theory? Pay special attention to the damping envelope of the response and the frequency of the oscillations.*
  3. *If there are discrepancies, are these due to errors in your estimates for  $\zeta$  and  $\omega_n$ , or are you observing physics (e.g. Coulomb damping) that cannot be described by a linear, viscous model? If we assume viscous damping, how uncertain is the damping ratio?*
2. **MDOF SYSTEM:** Remove any masses from the carts and connect a second spring between the first and second carts. Make a note of what type of spring you used (thick or thin).
- (a) Displace one of the carts about 2 cm and record the response. You should now see a multi-harmonic response since the system is now a two-DOF system. Include a plot in your report.
  - (b) Displace both carts to the right by about the same amount and observe the response. If you displace them exactly in the pattern of the first mode of vibration, then they should oscillate in unison at the same frequency. Can you realize this experimentally? Record the best (closest to harmonic) response that you can obtain on the computer and save it so you can plot it for your lab report. *Use your plot to estimate the mode shape and natural frequency of the first mode.*
  - (c) Displace the carts in opposite directions by about the same amount and record the response. *Can you displace them such that they oscillate in a pure second mode? Record the best response that you can obtain. Is this more or less difficult than the previous case? Why or Why not? Use your plot to estimate the mode shape and natural frequency of the second mode.*

#### B.1.1.4 Summary of What to Include in Your Lab Report

##### 1. Plots

- (a) Comparing the response of the SDOF system with  $m = m_1$  and  $m = m_1 + m_2$ .
- (b) Comparing analytical response of SDOF (tuned to agree as closely as possible) to measured response with  $m = m_1$ .
- (c) Of MDOF system response to ICs  $x_1 \approx 2, x_2 \approx 0$ .
- (d) Of MDOF system response with ICs that you determined to isolate each of the two modes.

##### 2. Results:

- (a) Identified natural frequencies and damping ratios for SDOF system with  $m = m_1$  and  $m = m_1 + m_2$ . Also discuss the uncertainty and how you estimated it.
- (b)  $m_1, k_1, c_1$  and  $c_2$  computed from the modal parameters above
- (c) Identified natural frequencies and mode shapes of the MDOF system, found from the plots in (1d).

##### 3. Answers to the questions found in bold-italics throughout this lab report.

4. You will also include any other plots, tables and analysis that is important to understanding the uncertainty in your results, why your results deviate / or do not deviate from the analytical model, etc. . . .

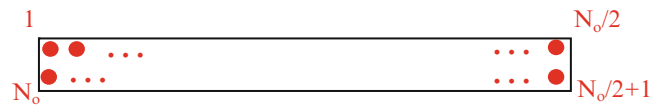
### B.1.2 Lab 4a: Impact Modal Test of Free-Free Beam

In this lab you will perform a modal test to determine the first six modes of a beam in free-free conditions. The beam is made of aluminum and is two inches wide and between 3/16 and 1/4 inches thick. Each team will have a beam of a slightly different length.

#### B.1.2.1 Before Class

Please review the video posted on the course website that describes how to perform a hammer modal test using the B&K software. Download a copy of the **ModalHammer\_ME540.plt** template to use for this lab.

**Fig. B.4** Measurement grid for modal test of free-free beam



### B.1.2.2 In the Lab

Perform a roving input modal test to find the FRFs of the beam. Create a measurement grid on your beam consisting of  $N_o$  points, where  $N_o$  is at least 20, as shown in Fig. B.4. Fix a low sensitivity (5 mV/g) accelerometer to the back side of the beam **behind measurement point 1**. This will be your reference node.

Choose a sample rate and number of samples to avoid leakage (the anti-aliasing filters on the data acquisition hardware should take care of aliasing, although it is still wise to avoid exciting modes that are outside of the measureable bandwidth.). Before you begin saving a complete set of measurements, estimate the natural frequencies of the first six modes and the damping ratio of the first two modes of the beam and determine how long you will need to sample to obtain adequate frequency resolution in the FRF for those modes. Also view the autospectrum of the input force from the hammer, to be sure that it adequately excites the frequency band of interest. Set up an exponential window and record the parameters of the exponential window that you have used. Once you are comfortable that you know how to acquire good FRFs, save anything that you need to answer the questions below and then you may begin acquiring your  $N_o$  point measurement set.

**Initially, do not use a response or hammer window.** Focus on getting a good set of measurements to make sure you know the measurement process. Later there will be time to improve the measurements using a window if that is necessary.

### B.1.2.3 Questions

1. *How did you assure that your sample rate and number of samples were adequate to avoid leakage? Make a note of the settings that you used and list them in your lab report.*
2. *What was the bandwidth of the input force supplied by the hammer? Save a plot of the autospectrum of the input from one of your measurements and include it in your lab report.*

Use the B&K software to acquire and save a complete set of  $N_o$  FRFs of the beam. Use **three averages per point**. Make sure that each of the three measurements that you are averaging is reasonably clean. Severe double hits will visibly contaminate your measurements. Use the “Undo Hit” feature when needed and go back and re-test any points where the measurement is noisy.

Save your project file (\*.pls) file so you can go back and view/export your measurements as needed. Then export a set of FRFs to a \*.uff file that you can load into Matlab (see the instructions at the end of this handout).

### B.1.2.4 Analysis

#### 1. Peak Picking for first few modes:

- (a) Load your FRFs into Matlab using the “loaduff” function on the course website. If you have correctly numbered your input and response points, this should create an  $N_f \times N_o$  FRF matrix from your measurements, where  $N_f$  denotes the number of frequency lines in each measurement. If you run into difficulty, you may need to assemble your FRF matrix manually (see instructions at the end of this handout).
- (b) Create and plot a composite or average of your FRFs using the “comp\_FRF” function, or by simply computing the average of the magnitude of your  $N_o$  FRFs.
- (c) Use peak picking and the half-power bandwidth method to estimate the natural frequency and damping ratio of the first **two** modes of the beam. Estimate each mode shape by assuming that it is proportional to the FRF at the peak. (Note that this is essentially the same procedure that the B&K software uses to produce the mode shape animations that you saw in the lab.)

#### 2. AMI Identification:

- (a) Use the AMI modal parameter identification algorithm to extract the natural frequencies, damping ratios and mode shapes of the first six modes from the measurements. *Include a plot of AMI’s GUI (figure 1000) in your lab report.*

- (b) *How well does AMI's modal model reconstruct your measurements? If there are discrepancies, what might they be attributed to?*

### 3. Compare Experimental Results with Analytical Model:

- (a) Estimate the analytical bending natural frequencies of your beam using the measured dimensions and nominal material properties for aluminum. Compare the analytical bending natural frequencies with those that you measured. There is some uncertainty regarding  $E$  and  $\rho$ , so you can adjust those to bring the results into as good of agreement as possible. *After adjusting those parameters, how do the natural frequencies compare? What do you attribute the differences to?*
- (b) **Bending Modes:** Generate the analytical mode shapes of the beam using the equations in the textbook for bending, and plot them with your experimentally obtained mode shapes overlaid. *Include a plot of your mode shapes in your lab report. How do they compare? What do you attribute the differences to?*

Note that the comparison will be easier if you create two sets of the analytical mode shapes as follows

$\{\phi_{\text{exper}}\}_r$ : ( $N_o \times 1$ ), experimentally measured mode shape vector for  $r$ th mode

$\{\phi_{\text{an}}\}_r$ : ( $N_o \times 1$ ), analytically derived mode shape vector for  $r$ th mode, mass normalized

$\{\phi_{\text{an.fine}}\}_r$ : ( $N_{\text{plot}} \times 1$ ), analytically derived mass-normalized mode shape vector for  $r$ th mode at 100 points evenly distributed between 0 and  $L$ .

To scale these modes for plotting, define the following:

$$(S_{\text{exper}})_r = \|\{\phi_{\text{exper}}\}_r\|$$

$$(S_{\text{an}})_r = \|\{\phi_{\text{an}}\}_r\|$$

Where  $\|x\|$  is the norm of  $x$  (use Matlab's "norm" function). Then you can plot the following to obtain a comparison of the mode shapes that is not affected by the scale of the vectors.

$$\frac{\{\phi_{\text{exper}}\}_r}{(S_{\text{exper}})_r} \quad \frac{\{\phi_{\text{an.fine}}\}_r}{(S_{\text{an}})_r}$$

For modes 1 and 2 your plots should show the shape you got using peak picking, AMI's shape, and the analytical shape. For modes 3–6 compare only the AMI shapes and the analytical shapes.

- (c) **Torsion Modes:** You should identify at least one torsion mode of the beam. Plot it(them) as well but you do not need to compare it(them) with an analytical shape.
- (d) Compute the Modal Assurance Criterion (MAC) matrix between your experimental mode shapes and your analytically predicted bending mode shapes (see MAC\_plot.m). *Are all of your mode shapes distinguishable on the measurement set that you used?*
- (e) Compute the Modal Scale Factors (MSFs) between your experimental and analytical bending mode shapes (you don't need to do this for the torsion modes). *How well do the scales of the shapes compare?* To mass-normalize the analytical shapes from Appendix C in Ginsberg, divide them by  $(\rho AL * \mu_{nd,k})^{1/2}$ , where

$$\mu_{nd,k} = \int_0^1 \psi_k(x')^2 dx'$$

The values of  $\mu_{nd,k}$  are 1.0359, 0.99845 and 1.0001 for  $k = 1, 2$  and  $3$  respectively, and  $\mu_{nd,k} = 1$  for  $k > 3$ .

### B.1.3 Appendix

Definition of MAC and MSF between mode vectors  $cr$  and  $dr$ , where  $()^H$  is the transpose for real vectors (or the Hermetian or complex conjugate transpose for complex vectors).



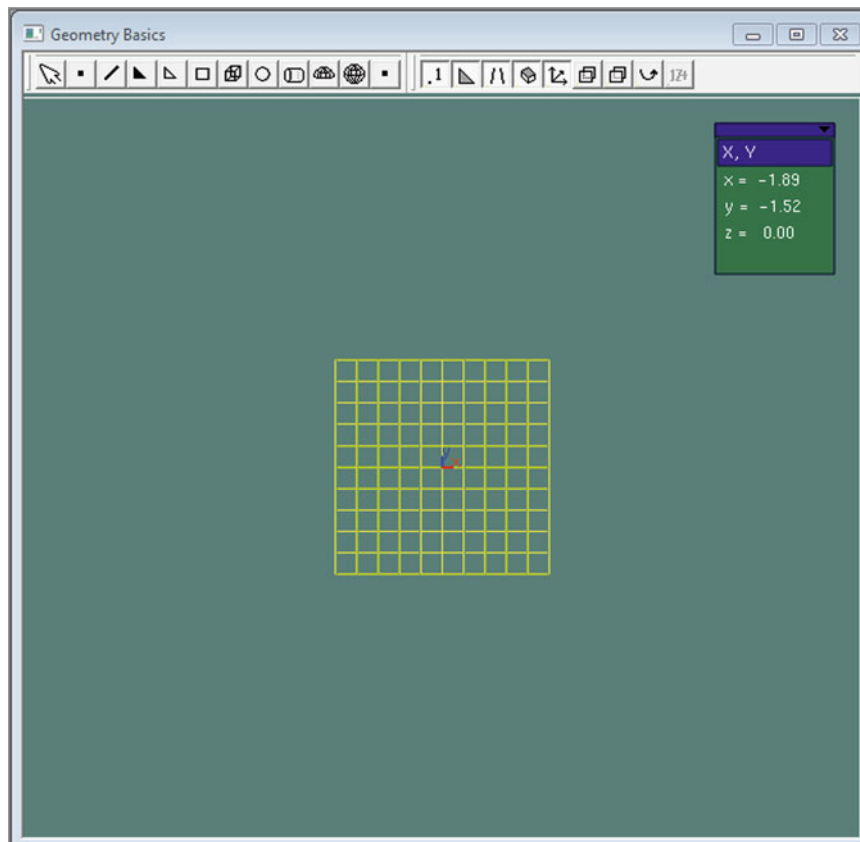
$$MAC_{cdr} = \frac{|\{\psi_{cr}\}^H \{\psi_{dr}\}|^2}{\{\psi_{cr}\}^H \{\psi_{cr}\} \{\psi_{dr}\}^H \{\psi_{dr}\}} = \frac{\left(\{\psi_{cr}\}^H \{\psi_{dr}\}\right) \left(\{\psi_{dr}\}^H \{\psi_{cr}\}\right)}{\{\psi_{cr}\}^H \{\psi_{cr}\} \{\psi_{dr}\}^H \{\psi_{dr}\}}$$

$$MSF_{cdr} = \frac{\{\psi_{cr}\}^H \{\psi_{dr}\}}{\{\psi_{dr}\}^H \{\psi_{dr}\}}$$

## B.1.4 B&K Labshop Instructions

### B.1.4.1 How to Create Geometry in PULSE Labshop

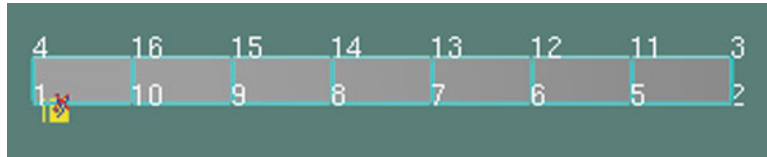
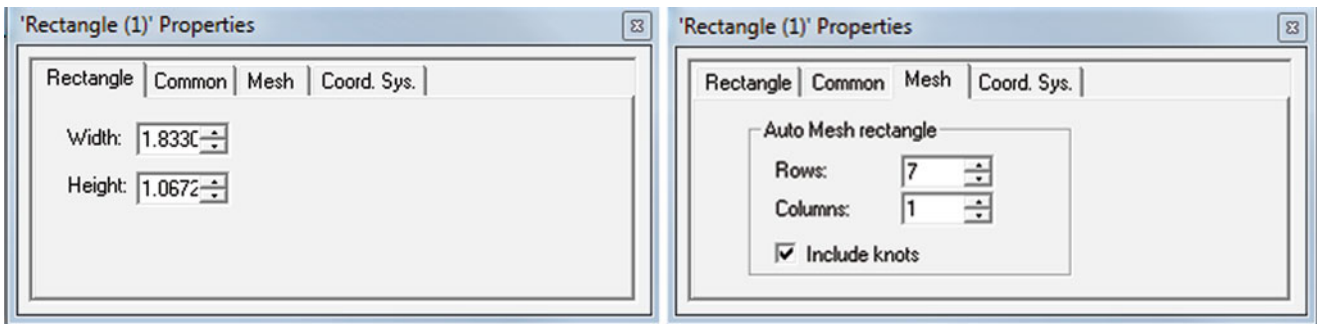
Navigate to Setup>Geometry in the task bar on the left side of the screen. The following screen should appear. Since the test specimen is a beam, a simple rectangle will represent this geometry well enough.



In the geometry window above, click on the rectangle button above (red circle), then drag and click to create the arbitrary rectangle. Note that you should first view the XY plane before creating the geometry. To do this, right click in the window and select view>x,y.

The window (bottom left) with the rectangle properties will allow you to change the dimensions of the beam (adjust accordingly).

Now, select the Mesh tab (top right). Selecting the number of rows will create various points on the beam. These points will represent the inputs for the experiment. Note that the relative distance between the points is irrelevant for this lab. Keep track of the point number and its location on the beam. The measurements will be saved referencing these nodes. After collecting measurements at each grid point, you can export all the results to a .uff file. Export the measurements by navigating to **Measurements>Export** in the side task bar. The following screen should appear.



Be sure to select all measurements to export, and that you are exporting only the Frequency Response Functions H1. Next, click on the **Settings** button, which brings up a window shown below.

Export in ASCII Universal File format, type ASCII, and PC platform. Select which folder you'd like to export to. Once this is done, return to the prior screen and select **Export**.

Load the UFF file into MATLAB using 'loaduff.m' (call in Matlab is `>>data = loaduff`). Note that the data will be structured in cells, and each measurement is located in a cell. For example:

`Data{n}` displays all of the fields in the  $n$ th measurement

`Data{n}.measData` is the complex amplitude of the FRF ( $H_{np}$ ) where  $p$  is the drive point and  $n$  is the response point.

`Data{n}.x` is the frequency vector.

The measurement number, units and other information regarding the measurement is stored in the cell structure. Use the variable editor in Matlab to look at these.

Note that if you have done everything correctly you can use the shortcut:

```
[data,dinfo,H,ws,rsp,refs] = loaduff;
```

Then, `H` will be the FRF matrix with your measurement points listed in ascending order in the columns and `ws` will be the corresponding frequency vector in radians per second. The names of your reference and response measurement points will be in `rsp` and `refs`. For example, if `rsp.name{5}='+3x'` then `H(:,5)` corresponds to the FRF at measurement point 3 in the  $+x$  direction.

Pay close attention to the order of your measurement points when plotting. You may need to re-order the columns of `H` (or from the mode shapes that you get from `H`) in order to plot the mode shapes correctly.

#### B.1.4.2 Additional Help

To use 'pickpeaks.m' you first need to plot the magnitude of the average of all your FRFs. For example:

```
Haverage = sum(H,2)/size(H,2);
```

or use

```
Haverage = comp_FRF(H);
```

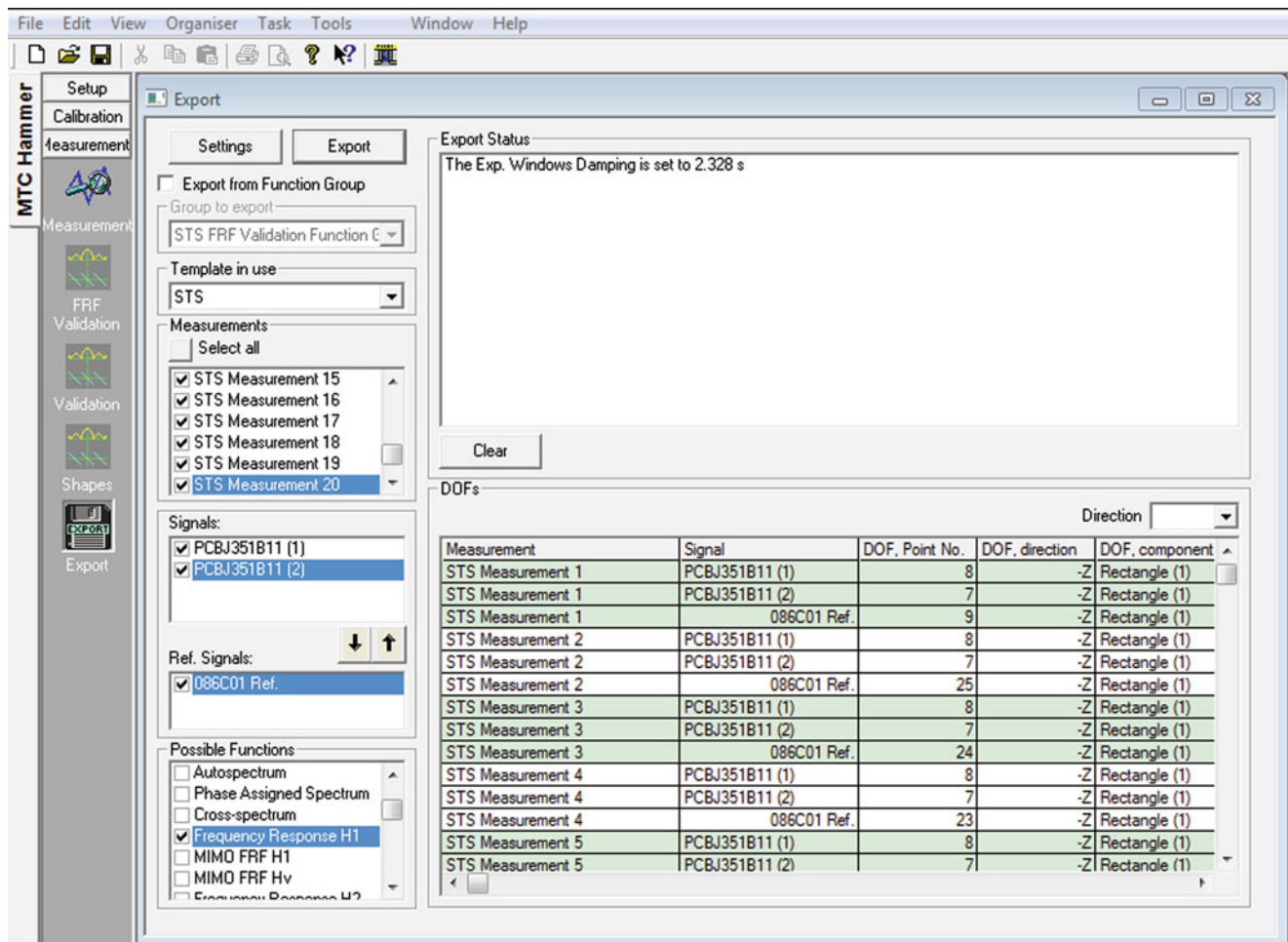
then

```
plot(ws,abs(Haverage));
```

or all in one line

```
plot(ws, comp_FRF(H));
```

The 'pickpeaks.m' function allows you pick points on the active Matlab plot window and extracts the 'x' and 'y' value of the point that you pick. The function returns the index locations of the x-value of the point you picked. So, suppose my `ws` vector is [3 5 8 9 10]. If I picked a point on the plot near `ws = 8`. Then, 'inds' would return 3, the value of the index in `ws` that corresponds to `ws(inds)=8`; Then, you can go back into you full `H(ω)` matrix and extract the rows corresponding to



'inds'. What does one of these rows mean? Well, remember that near a natural frequency (which is a peak in the FRF) the formula

$$\{H(\omega)\} = \sum \frac{\{\phi_r\} \phi_{pr}}{\omega_r^2 - \omega^2 + i\omega 2\zeta_r \omega_r} \quad (12.1)$$

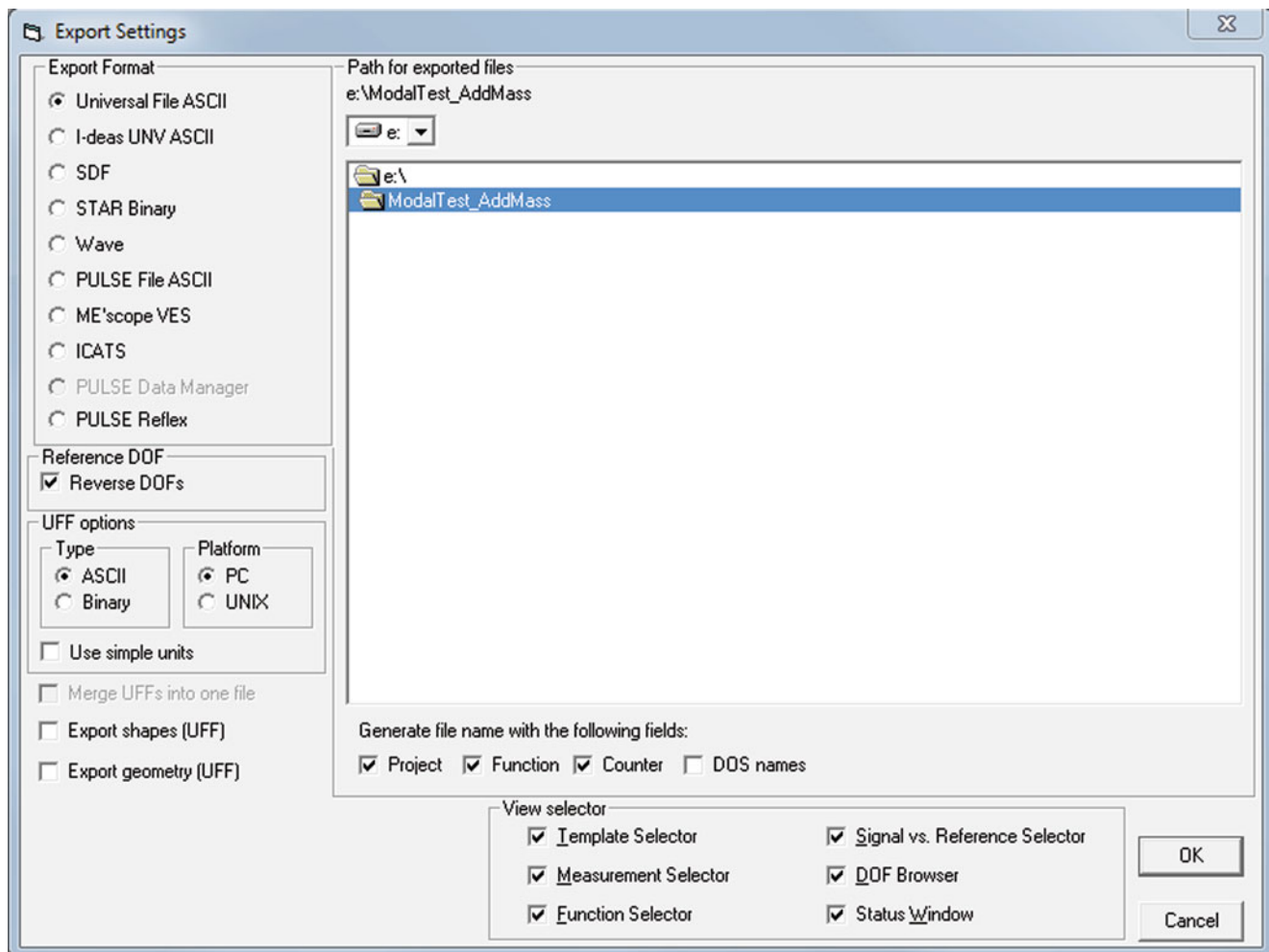
goes to

$$\{H(\omega)\} = \frac{\{\phi_r\} \phi_{pr}}{i\omega 2\zeta_r \omega_r}, \quad (12.2)$$

However, we have accelerometer measurements, so our measurements are related to the mode shapes by:

$$\{H(\omega)\}_{accel} = \frac{-\omega^2 \{\phi_r\} \phi_{pr}}{i\omega 2\zeta_r \omega_r}, \quad (12.3)$$

$\{\phi_r\}$  in (12.3) is the experimental mode shape that we are after, so **the imaginary part** of the vector of FRF measurements is proportional the true mode vector.



### B.1.4.3 To Run AMI and Extract Modes

Type the following commands to set up AMI:

```
global AMISET
AMISET = AMIG_def_opts;
AMISET.DVA = 'A'; % this tells AMI that the data is acceleration/force FRFs
AMISET.LM = 'on'; % this makes the file smaller if you save the AMI fit.
ami(H,ws,AMISET) % where H is the Nf by No FRF matrix and ws is the frequency
vector in radians per second.
```

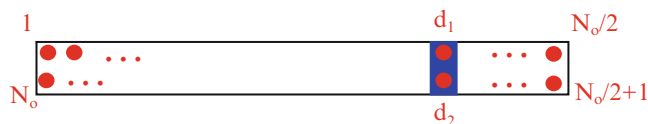
At this point you run through the AMI fitting process. If you are having trouble with this or do not understand it, come in to talk to the instructor or the TA.

After completing the fitting process, run these lines of codes to get to the natural frequencies, damping ratios, and residue vectors.

```
global AMIMODES % brings AMI's variables into the workspace
fn = AMIMODES.mode_store(:,1)/2/pi; % These are the natural frequencies in Hz
zt = AMIMODES.mode_store(:,2); % These are the damping ratios, zeta
% The following gives the residue vectors
res = (-2*real(diag(conj(AMIMODES.mode_store(:,3)))*AMIMODES.A_store)).';
'res' is a matrix containing "residue" vectors in the columns, each of which is related to a mode shape by,
```

$$res(:,r) = \{\phi_r\} \phi_{rp}$$

which is the numerator of (12.1).

**Fig. B.5** Beam with mass modification

So if your drive point was the first measurement point ( $p = 1$ ), then

$$res(1, r) = \phi_{r1}\phi_{r1} = \phi_{r1}^2, \quad \text{then,} \quad \phi_{r1} = \sqrt{res(1, r)}$$

and

$$res(2, r) = \phi_{r2}\phi_{r1}$$

$$\phi_{r2} = \frac{res(2, r)}{\phi_{r1}}$$

so you can continue the process over the rest of that column to estimate that mode shape and then repeat the process for each of the columns of ‘res’ to obtain all of the mass-normalized mode vectors  $\phi_r$ . Note that the drive point residues will sometimes come out negative leading to non-sense results (imaginary mode shapes). If several drive point residues are negative there is likely a problem with your measurements or you may be using some point other than the true drive point in the equations above. On the other hand, the drive point residue for a mode or two may come out negative even in relatively good measurements, so you may be able to take the absolute value and obtain reasonable results.

It is important to consider the units here. We want our mass normalized modes to have units of  $1/\sqrt{\text{mass}}$ . So, the residue vector components should have units of  $1/\text{mass}$ . However, if your FRF was measured with different units then this might not be correct. So before mass normalizing, convert your units to metric. The units of ‘res’ will be the same as those of your FRF, but converted to displacement. So, if you measured the FRFs in units of  $[\text{g}'\text{s}/\text{lbf}]$ , then the units of res will be  $[\text{g}'\text{s}/\text{lbf}] * (\text{sec}^2)$ . Make the appropriate conversion to change this to units of  $(\text{m}/\text{sec}^2)/\text{N} = 1/\text{kg}$ .

### B.1.5 Lab 4b: Impact Modal Test of Free-Free Beam: Structural Modification

In this part of the lab you will predict the effect of a simple structural modification on the mode shapes and natural frequencies of a beam. Your modification consists of the addition of a mass to the beam. You will use the Ritz method together with your experimentally measured mode shapes and natural frequencies to predict the new natural frequencies and mode shapes of your beam after adding the mass, and compare your predictions with experimental measurements on the beam+mass system.

#### B.1.5.1 Measurements

1. Attach a steel block to your beam as shown below so that it covers two measurement points, which are at the same position along the axis of the beam. We will denote these points  $d_1$  and  $d_2$ . Place the block at the measurement points that are nearest to  $(1/6)L$  from the end of the beam (For example, with  $N_o = 20$  points, 2 in. between points and one inch between the 10th point and the end of the beam, the block should be at points 8 and 13, which are across from each other, and so  $d_1 = 8$  and  $d_2 = 13$ ). The steel blocks measure 0.5 by 1.0 by 2.0 in., so they should cover the entire width of the beam (Fig. B.5).
2. Measure the frequency response functions of the beam along at least one row of points (e.g. 1, 2 . . .  $N_o/2$ ) and use those to extract the true natural frequencies and mode shapes of the beam with the mass added.

#### B.1.5.2 Analysis

1. Use your experimentally measured, mass normalized mode vectors and natural frequencies with a one-term Ritz model to compute the natural frequencies of the beam after adding a 144-g block of steel to your beam. Add half of the beam

mass, or 72-g to each point in your analysis. **How much has each natural frequency shifted? Can you explain why some modes have shifted more than others?**

- Use the mode shapes that you generated analytically (as described in the (4a) handout for this lab) to predict the natural frequencies of the beam with the mass added. This analysis gives the Ritz predictions that you would have obtained from this analysis if your measurements were perfect. **Based on the comparison of all of these results, what is the likely cause of any discrepancies?** Think about both measurement errors and the assumptions inherent in the one-term Ritz model.

### B.1.5.3 Analysis with One-Term Ritz Model

To perform your analysis for parts (1) and (2) you will need to determine an expression for the natural frequency of a mode based on the mass added and the mode shape and natural frequency of the mode. For example, in class we used a one-term Ritz model to derive the following expression for the shift in a natural frequency as a function of an additional stiffness  $\Delta k_i$  added to the  $i$ th measurement point.

$$\Delta\omega_r = \frac{1}{2\omega_r}(\phi_{ir})^2\Delta k_i$$

### B.1.5.4 Optional Analysis with Full Ritz Model

The one-term Ritz model assumes that the mode shapes of the structure do not change with the addition of the mass. This assumption can be relaxed somewhat using an N-term Ritz model (where N is the number of modes identified). This can be created from the modes of the beam without the mass. This model has diagonal mass and stiffness matrices and uses the measured mode shapes as basis vectors. Then one can determine the new mass matrix after adding the block, and use that to compute the new natural frequencies and mode shapes.

This approach is implemented in the `ritzsmod.m` file in the `EMAFun` folder of the course Matlab tools. You may use this function for the N-term analysis, or to debug your one-term model, but it cannot be used exclusively. **Each team must turn in a handwritten derivation and the computer code that they have developed to perform the analysis in parts (1) and (2).** In case you want to also use the `ritzsmod.m` function, it is described below.

First you will need to generate the two following two rigid body modes of the beam (these could be measured experimentally, but that would require some additional work). You will need to include these in your Ritz model for the beam in order to obtain accurate results:

$$\phi_{\text{rigid},1}(x) = 1/(\rho AL)^{(1/2)}$$

$$\phi_{\text{rigid},2}(x) = (x - 0.5)/(\rho AL/12)^{(1/2)}$$

where  $x$  ranges from 0 to 1 (nondimensional) in those equations.

```
% Structural modification using experimentally determined mode vectors as
% a Ritz vector basis set.
%
% Computes the modal parameters of the system modified by adding the masses
% and stiffnesses in the vectors dm and km to nodes ns_m and ns_k;
%
% [wn_mod,zt_mod,phi_mod,M_mod,C_mod,K_mod] =
%ritzsmod(wn,zt,phi,dm,ns_m,dk,ns_k);
%
% ``ritzmod`` requires the following necessary inputs:
% wn - vector of natural frequencies for the un-modified structure.
% zt - (optional) vector of modal damping ratios.
% phi - matrix of mass normalized mode vectors where each column
% corresponds to a natural frequency in wn.
% dm - vector of masses to be added to node numbers listed in ns_m.
```

```
% dk - vector of stiffnesses to be added to node numbers listed in ns_k.
% Each spring is between the node listed and ground.
```

For example, suppose that you measured the beam's mode shapes at 20 points and that your mass attaches to the beam at nodes 8 and 13. Then you would use the following to call ritzmod:

```
[wn_mod,zt_mod,phi_mod] = ritzmod(wn, zt, phi, dm, ns_m, [], []);
```

where  $wn$  and  $zt$  are  $N$  by one vectors of the natural frequencies and damping ratios,  $phi$  is a 20 by  $N$  vector of mass normalized mode vectors (each vector is known at all 20 measurement points).

```
dm = [0.072, 0.072]
```

```
ns_m = [8,13]
```

Notice that we're passing in empty vectors for  $dk$  and  $ns_k$  since we haven't attached any springs to the system.

### B.1.6 Lab 5: Output Only (Natural Excitation) Identification of a Downhill Ski

The performance of downhill skis has been shown to depend on the relationship between the natural frequencies of bending and torsion modes [2]. However, in its natural environment a ski's boundary condition is very difficult to model (e.g. the interaction between the ski and the snow), so tests are needed to determine the in-operation dynamics. Since the forces that the snow applies to a ski cannot be easily measured, one must rely on output only modal analysis techniques. In this lab your task is to identify the natural frequencies of the first seven modes of a downhill ski and the corresponding mode shapes in order to determine whether each is a torsion or bending mode. An unknown excitation is simulated in the lab by tapping the ski at random with a hammer. You will use the spectra of the response alone to identify the modes of the ski. (I know, it would have been more fun to do this on the mountain, but what can we do?)

#### B.1.6.1 Derivation (Before Class)

Suppose a system is excited by forces  $f_1$  and  $f_2$  at two different points  $p_1$  and  $p_2$ . The cross spectrum between each of the forces (and each force and itself) is constant with frequency and denoted  $S_{f_1 f_1} = \text{const}$ ,  $S_{f_1 f_2} = \text{const}$ , etc. . . . Based on what we have covered in class, the frequency response at the  $j$ th location (this is the FFT of  $x_j(t)$ ) is,

$$X_j(\omega) = H_{j,p_1}(\omega)F_1(\omega) + H_{j,p_2}(\omega)F_2(\omega)$$

where the accelerance FRF is defined as follows in terms of the modal parameters.

$$H_{j,p_1}(\omega) = \sum_{r=1}^N \frac{-\omega^2 \phi_{j,r} \phi_{p_1,r}}{\omega_r^2 - \omega^2 + i\omega 2\zeta_r \omega_r}$$

One definition of the cross spectrum between measurements  $x_j$  and  $x_n$  is,

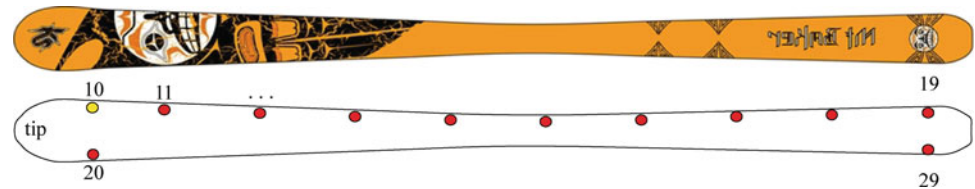
$$S_{x_j x_n}(\omega) = \frac{1}{N_{\text{avg}}} \sum_{m=1}^{N_{\text{avg}}} X_j(\omega)_m X_n(\omega)_m^*$$

This equation also gives  $S_{f_1 f_1}(\omega)$ ,  $S_{f_1 f_2}(\omega)$ , etc. . . . with the appropriate substitutions. The index  $m$  denotes the  $m$ th estimate of the spectra, obtained by taking the FFT of the  $m$ th time series. There are assumed to be a total of  $N_{\text{avg}}$  different measurements that are averaged to estimate the spectra.

Use this expression to show how the mode shape of the  $r$ th mode of vibration is manifest in the cross spectra  $S_{x_j x_n}$  for  $j = 1 \dots N_o$  and  $n$  being a fixed reference point. You will find that you must assume that the output measurements are all acquired simultaneously so that the input spectrum is the same for each. **Turn your handwritten derivation in with your lab report.**



**Fig. B.6** Schematic of measurement grid used when testing the downhill ski



### B.1.6.2 In the Lab

#### Part 1

For this experiment, you will have four (identical) accelerometers mounted along half of the length of the ski. The accelerometer closest to the tip will be set as the reference (since none of the mode shapes has a node at the tip) and called  $x_1$ . The software will be set to compute the autospectrum of the tip response and the cross spectrum between the tip and all other points. (This lab was set up using B&K's OMA template: "Operational Modal Analysis.plt".)

Your task is to determine the following parameters and to acquire an OMA measurement that captures the first seven modes of the ski:

- Number of Averages
- Frequency Bandwidth
- Frequency Resolution (governed by the length of the time window that is processed by the FFT,  $T$ , or the FFT blocksize)

The data acquisition system will already be set to run in free-run mode (no trigger) with a Hanning window.

Choose a sample rate that allows you to capture at least the first 7 bending modes and choose an FFT blocksize that gives reasonable frequency resolution near each peak. You may find that the optimal blocksize is greatly different for the first mode than for the seventh, so feel free to record a few different data sets if time permits to experiment with the settings. **How does the blocksize and number of averages affect the quality of your measurements for a fixed total measurement time?** Tap the ski with the hammer at random times and at random places simulating a random input until the number of averages is reached. You should see the spectra converge as the number of averages increases.

**Hints:** Recall that the frequency spacing in the FFT is  $\omega_1 = 2\pi/T$ , or inversely proportional to the sample length,  $T$ . The frequency spacing must be smaller than the half power bandwidth  $2\zeta_r\omega_r$ , or the peaks will be under-resolved and the damping cannot be accurately estimated. You do not know the damping initially, but when setting up your measurements you can assume that the ski's damping ratios will be at least 0.5% for the skis without bindings and at least 1% for the skis with bindings.

See the Appendix for notes regarding how to save your measurements.

**These steps can be competed in Matlab:** Once you obtain your measurements, use peak picking to determine the natural frequencies of the first 7 modes and plot the corresponding mode shapes using the fact that your derivation has shown that the cross spectrum near each natural frequency,  $S_{x_j x_1}(\omega)$ , is proportional to the mode shape at the  $j$ th measurement point.

#### Part 2

This second part of the lab simulates a more realistic operational modal test where the response sensors must be roved to capture the mode shape at a large enough number of points. In the interest of time the TA has acquired measurements and will provide them to you. The measurements were acquired in seven setups using the measurement grid shown below. (For those who are interested, the ski that was tested is a K2 Mt. Baker Superlight ski, size 174 (yellow), donated in 2007 by K2.) (Fig. B.6).

In all of the measurements, **point 10 near the tip of the ski** was used as a reference, so the cross spectra of all of the other points were computed relative to this point. Since the number of data acquisition channels was limited, the measurements were acquired in seven setups, which are described below. This type of approach is often used when testing large structures to limit the length of the cables that must be used, or when many sensors are desired.

Setup	Sensor 2	Sensor 3	Sensor 4
A	20	21	11
B	12	22	13
C	14	24	23
D	25	26	15
E	27	17	16
F	29	28	18
G	29	20	19

This information is also included in the \*.mat file of the data that you will receive.

In each setup, the accelerometers are located between  $\frac{1}{4}$ " and  $\frac{3}{8}$ " from the edge of the ski. The positions of each measurement point are given below. (For your information, the width of the ski at certain positions is also given, and the taper is approximately linear between those.)

Grid point #	10, 20	11, 21	12, 22	13, 23	14, 24	15, 25	16, 26	17, 27	18, 28	19, 29
Axial pos (in)	2.0	8.75	15.5	22.0	28.75	35.25	42.0	48.5	55.25	62.0
Ski width (in)	4.25	–	–	–	3.5	3.5	–	–	–	4.75

Use the auto and cross spectra provided to estimate the first 10 modes of the ski with the peak picking method. Then use the methods described in class to estimate the mode shapes of the system over the four sensors for each measurement setup. Then, normalize the mode shapes such that the mode shape at the reference sensor is 1.0, in order to stitch the measurements together, and plot the modes. Create a table showing the natural frequencies of each mode and whether it is primarily bending or torsion.

### B.1.6.3 Lab Report

Include the following items in your lab report:

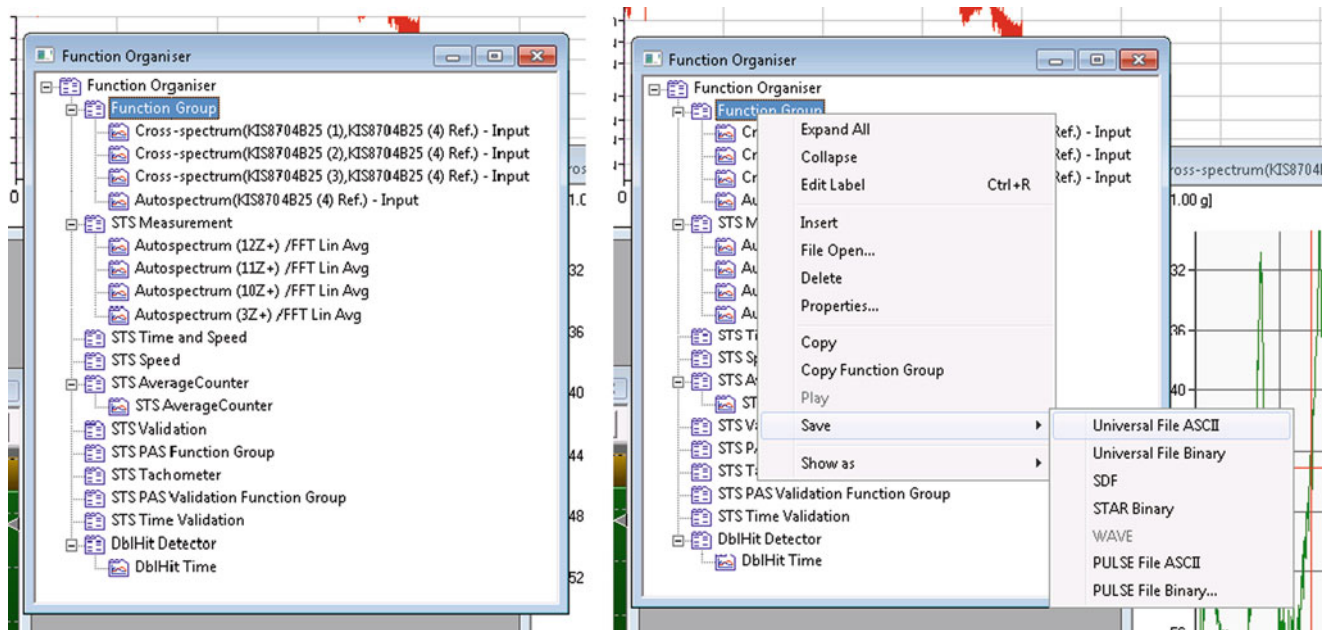
- Plot of the spectra that you measured for part 1, a list of natural frequencies that you identified and a plot of the corresponding mode shapes.
- Plot each of the mode shapes that you identified from the data provided for part 2 and a table showing the natural frequencies and whether each mode is primarily bending or torsion
- Attach your derivations (one per team member) from the “Before Class” section above as an appendix.
- Briefly discuss your results pointing out any interesting features. ***How did this procedure compare with the hammer modal analysis that you performed in Lab 4? Which was easier to perform? Was there any degradation in the quality of the measurements when the OMA technique was used instead of the conventional EMA approach in Lab 4?***

### B.1.6.4 Notes Regarding Data

The data for this lab is contained in the \*.mat file “Lab5\_ref10\_Spectra\_ABCDEFG.mat” on the course website. An  $N_f \times 4$  matrix of auto- and cross-spectral data is supplied for each setup, denoted SA, SB, etc. . . . , where  $N_f$  is the number of frequencies and the four columns each correspond to a sensor. The sensor locations for each setup are given in “>>rspsA.name”; these should agree with the information in the table above. (Specifically, SA (:, 1) contains the autospectra for point 10 in setup A, SA (:, 2) contains the cross spectrum between points 10 and 20, SA (:, 3) the cross spectrum between points 10 and 21, SB (:, 2) the cross spectrum between 10 and 12 for the B setup, etc. . . . )

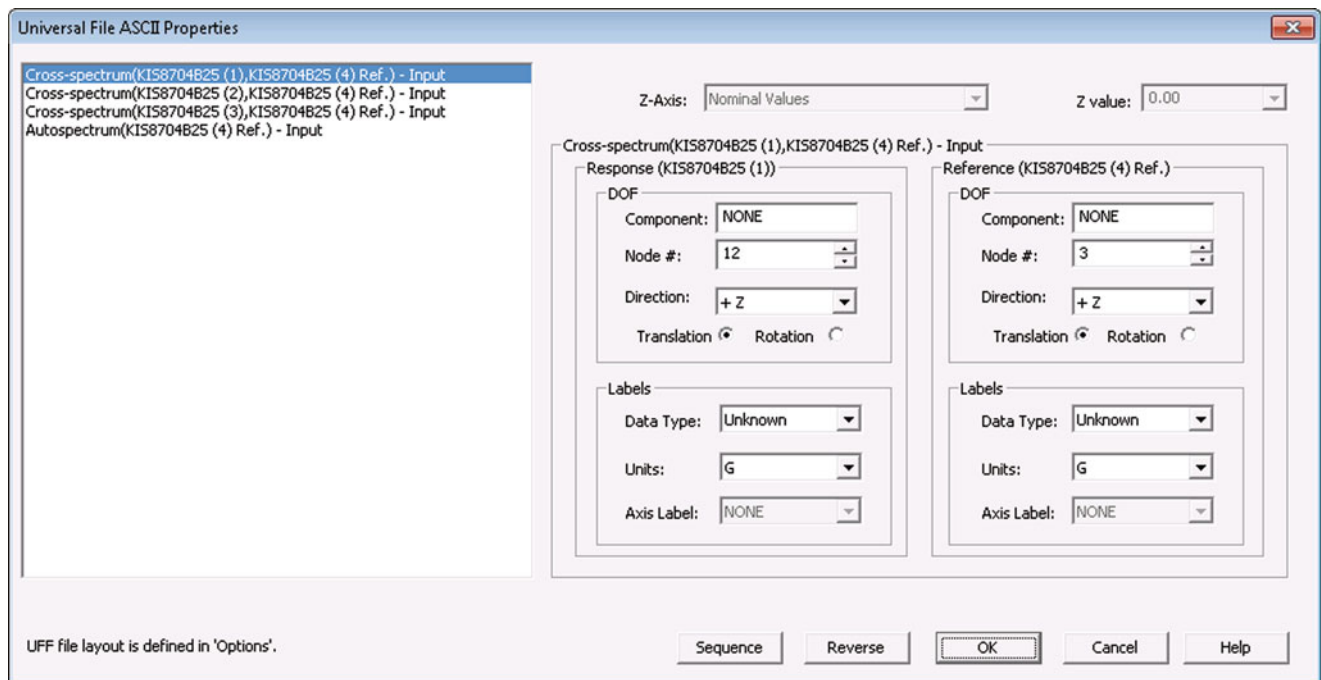
## B.1.7 Appendix

Use the following procedure to export your measurements to a UFF file. You should already have the autospectrum of your reference accelerometer and the cross spectra of the other accelerometers in your function group as shown below.



Right click on the function group (not the individual measurements) and select “Save >> Universal File ASCII”

The following dialog box comes up with options for the UFF file, such as the units or the ability to edit the point numbers. You should be able to simply select “OK” and the UFF file will be written to the current directory.



## B.1.8 Final Project Assignment

### B.1.8.1 Deadlines

- **Nov. 22th** – Select final project group (three students per group) and turn in one-page summary of project plan. (There can be two groups of 2, email me immediately if you want to be in a group of 2.)
- **Dec. 1st** – Must have all hardware ready (and in 2163 if it is portable) to begin testing.
- **Thursday Dec.15th** – presentation due and must be uploaded to course website in a \*.zip file along with all of your measurements and your post-processing scripts, Matlab files, etc. . . . Scan any hand calculations and any other supporting materials and include them in the \*.zip file.
- **Saturday Dec. 17th** – Each group gives a 12–15 min presentation summarizing their results during the final exam period, 2:45–4:45PM on Saturday Dec. 17.

### B.1.8.2 Description

*Your objective is to perform an accurate dynamic test in order to understand some aspect of the dynamic response of your system. You must not only perform the test but also do calculations to explain how the modal parameters that you identify affect the performance of the system.* The list below gives a sampling of ideas for your final project with the associated analysis underlined. You are certainly welcome to propose other ideas as well. Discuss your ideas with the instructor prior to the Nov. 22nd deadline if you are unsure whether they would be feasible.

- Modal test of mass spectrometer hardware (available in lab). Objective is to control the position of the sensor to within one micron ( $10^{-6}$  m). What forcing frequencies should be avoided to accomplish this? What if the system is inadvertently forced at resonance? How large can the forcing be in that case?
- Sporting equipment such as a tennis racquet (or similarly for baseball, hockey, etc. . . .): Compare the dynamic properties of two racquets (or one racquet in multiple configurations, e.g. with a vibration absorber.) Simulate the impact of a ball with the racquet using the modal model that you've developed and use that result to compare how the two will feel to the user, or which will hit the ball farthest?
- Test a crystal glass to identify the shape of the mode(s) that contribute to sound generation when a finger is rubbed along the top of the glass. What other modes are present in the frequency range that do not generate sound? Why might that be?
- Hard Drive: Perform modal survey of the case. How do modes compare with the drive frequency and its harmonics? At what spindle speed would you expect to encounter vibration problems with the hard drive? Remove damping treatments and compare.
- For RC enthusiasts: Perform a Modal test of an RC plane to identify the first few bending and torsional modes. Compare the natural frequencies and predict which bending-torsion mode combination is most likely to lead to flutter at high airspeeds.
- Operational Modal Analysis of Mech. Eng. Building (or ERB): Use OMA techniques to perform a roving sensor modal test of the ME building. Estimate the first few modes of vibration of the 2nd floor walkway surrounding the atrium. Estimate how many people would have to jump in unison on the walkway to obtain three inches of peak displacement.
- Cross Axis Sensitivity: All accelerometers are designed to sense acceleration in one direction, but they are inevitably sensitive to acceleration in other directions as well. Design an experiment on a simple structure, such as a thick beam, to evaluate this. Place several accelerometers perpendicularly on the structure and see to what degree the bending motion is detected by an axially oriented sensor, etc. . . . Look for other anomalies that might help one to detect cross-axis sensitivity (e.g. strange phasing, etc. . . .).

## References

1. Ginsberg JH (2001) Mechanical and Structural Vibrations, 1st edn. Wiley, New York
2. Foss GC, Glenne B (2007) Reducing on-snow vibrations of skis and snowboards. Sound Vib 41:22–27

# Chapter 13

## The ABRVIBE Toolbox for Teaching Vibration Analysis and Structural Dynamics

Anders Brandt

**Abstract** Vibration analysis is a subject where students often find it hard to comprehend the fundamental theory. The fact that we have, in general, almost no intuition for dynamic phenomena, means that students need to explore various dynamic phenomena in order to grasp the subject. For this reason, a MATLAB toolbox (the ABRVIBE toolbox) has been developed as an accompanying toolbox for the recent book “Noise and Vibration Analysis” by the author. This free, open software, published under GNU Public License, can be used with GNU Octave, if an entirely free software platform is wanted, with a few functional limitations. The toolbox includes functionality for simulation of mechanical models as well as advanced analysis such as time series analysis, spectral analysis, frequency response and correlation function estimation, modal parameter extraction, and rotating machinery analysis (order tracking). In this paper, an overview of the functionality is given and recommended use in teaching is discussed. It is also shown how the toolbox can be used for general vibration analysis using data from multichannel measurements. Finally, some laboratory exercises for structural dynamics teaching are discussed.

**Keywords** Vibration analysis • Experimental modal analysis • Order tracking • Spectral analysis • ABRVIBE toolbox

### 13.1 Introduction

This paper describes a toolbox for MATLAB and GNU Octave which was developed as an accompanying toolbox for the book “Noise and Vibration Analysis – Signal Analysis and Experimental Procedures”, [1]. The purposes of the toolbox are at least threefold:

1. To aid teachers in setting up realistic and illustrative examples of the many intriguing things in mechanical vibrations in general, and experimental vibration analysis, in particular,
2. To aid the student’s understanding of mechanical vibrations and analysis of it, by being able to go through each step in calculations etc., in an open fashion, and finally
3. To be a tool for students, researchers, and engineers in industry, to use for analysis of vibrations in an open software environment. For this purpose, the toolbox includes the same functionality as a typical high-end commercial software system (except the data acquisition part), and many extra functions not usually available in commercial systems.

All these purposes are supported by many examples supplied with the toolbox, ordered into separate folders for each chapter of the book. The principle of the toolbox is to allow transparency for the student/user into all the steps in the analysis, so that every single step can be investigated to ensure understanding. The toolbox thus contains high-level commands for standard tasks needed in this field. And each and every function is open, so that the student can open it and investigate it.

All functionality can start with recorded or simulated time data, the latter being found by the author to often being easier to comprehend by students, if they themselves can go through all the typical steps of analysis such as converting data to spectra, then perhaps to frequency response functions, and thereafter for example extracting operating deflections shapes for animation. A teacher using the ABRVIBE [2] toolbox can very easily set up examples to illustrate various aspects of

---

A. Brandt (✉)

Institute of Technology and Innovation, University of Southern Denmark, Campusvej 55, Odense M, DK-5230 Denmark  
e-mail: [abra@iti.sdu.dk](mailto:abra@iti.sdu.dk)

vibration. In assignments, the teacher can also set up example scripts at a level so that the students can accomplish requested results in a reasonable time, for example in time limited lab assignments. Undergraduate students can thus get more “canned” demonstrations, whereas graduate students can be asked to develop more of the tasks themselves.

As an overview, the ABRAVIBE includes, among other things, functionality to

- Store data with header information in a standardized format, which allows for easy implementation of, for example, operating deflection shape analysis and experimental modal analysis,
- Import and export data in universal file format, to allow import from and export to most commercial measurement systems in this field,
- Generate data in the form of frequency response functions (FRFs), or modal parameters, from known mechanical systems described by mass and stiffness matrices and either damping matrices, or modal damping,
- Generate simulated time data for the forced response of mechanical systems, which can be used for understanding mechanical vibrations, as well as for investigating signal analysis techniques on data with known parameters,
- Define signal analysis operations such as filtering, acoustic analysis (1/n octaves, sound level meter integration), etc.,
- Compute statistical functions such as probability density functions, skewness and kurtosis, frame statistics and hypothesis tests for stationarity tests, and data quality assessment,
- Estimate spectra of time signals by linear (rms) spectra, spectral densities, or transient spectra (energy spectral density), with time windowing, averaging etc. by the same algorithms implemented in commercial software, and some more sophisticated methods not yet available commercially,
- Estimate frequency response functions and coherence functions, either from impact testing (using the enhanced method described in [1, 3]), or from shaker testing, with single-input as well as multiple-inputs,
- Perform order tracking functions such as rpm maps, synchronous resampling, order maps etc.
- Extract modal parameters using well-known modal analysis methods, simple SDOF as well as the time domain polyreference MDOF method, and
- Animation of operating deflection shapes and modal analysis results.

All theory that follows is, of course, described in [1]. This will not be referenced but implicitly assumed. In some cases we will, however, give references to background literature.

## 13.2 ABRAVIBE Toolbox Functionality

To simplify the notation below, all toolbox command variables will be written in **bold** letters in the general text, whereas MATLAB code examples will be in `Courier` font.

### 13.2.1 Data Storage Format

The basis for much of the functionality of the toolbox is the way data is stored. First, data from measurements can be stored in a standardized data format which contains information about measurement DOFs etc., to facilitate easy implementation of, for example, experimental modal analysis. Data can be imported from measurement systems in the universal file format, or by writing a function that stores the data in the ABRAVIBE file format. The principles of this data storage format are that

- Each function is stored in a separate file, to allow processing of as much data as possible without memory limitations. A function can for example be a time history, a spectrum, or a frequency response function (FRF).
- Each file consists of two variables: **Data**, containing the function data in a column, and **Header**, which is a structure containing flexible header information, which means that only as much information as needed must be included. New header fields can be added when needed.
- There are high-level commands for reading data into the toolbox for analysis. An example of such a command, is the **data2hmtrx**, which converts single files of FRF data into one FRF matrix and a number of variables with information about the DOFs measured. An example of this function is shown in Sect. 13.2.8.

Another important functionality is to be able to store data into matrices containing multiple-input/multiple-output (MIMO) data. For this purpose, 3-dimensional matrices are used in a standardized fashion,  $\mathbf{H}(\mathbf{f}, \mathbf{d}, \mathbf{r})$ , where

- The first index, **f**, is frequency
- The second index, **d**, is a response location
- The third index, **r**, is a reference location

This means, that if, for example a structure is measured in 35 response points, using two shaker positions, the resulting FRF matrix, **H**, if analyzed with 1,025 frequencies, would be a 1,025-by-35-by-2 matrix. Information about which DOF is located at which address in this matrix can be stored in separate variables.

### 13.2.2 Mechanical System Simulation

Teaching vibrations and structural dynamics often starts with the single-degree-of-freedom (SDOF) system. This system is analyzed for steady-state harmonic response, transient response, etc. It is then shown that multiple-degree-of-freedom (MDOF) systems behave as can be referred to as an extended case of the SDOF system. In the ABRAVIBE toolbox, to aid the understanding of this, the frequency response (FRF) or impulse response (IRF) of a mechanical system with any number of DOFs (within reasonable limits) can be computed with high-level commands. Thus, if the system matrices  $[M]$ ,  $[C]$ , and  $[K]$  are all known, the FRF between a number of input (force) positions, and a number of response locations, can be computed by the command **H = mck2frf(f,M,C,K,indof,outdof,type)**, where **indof** is a vector with each input DOF, and **outdof** is a vector of the output DOFs, and **type** is a variable to produce the FRFs in the form of receptance, mobility, or accelerance. With this single command, an entire FRF matrix, or a subset of it, can thus be computed in one call. Similarly, if only the mass and stiffness matrices are known, modal (viscous) damping can instead be added, and the command **H = mkz2frf(f,M,K,z,indof,outdof,type)**, where **z** now is a vector with the modal damping of each mode.

Next in teaching mechanical vibrations, is often a description of (analytical) modal analysis, where modal parameters (natural frequencies, damping ratios, and mode shapes) are computed from the system matrices. Furthermore, the analysis of the modal solutions are often divided into undamped, proportionally damped, and generally damped systems. In the toolbox, this is supported by the command **mck2modal**. This is a complex command, which can be used in various ways, reflecting the form of damping. Thus, called with only mass and stiffness matrices, it computes the eigenfrequencies and normal modes by the syntax **[fr,V] = mck2modal(M,K)**. If the damping matrix is known, the command instead uses the syntax **[p,V] = mck2modal(M,C,K)** giving the complex poles, **p**, and either the real-valued normal modes if the damping is proportional, or the complex-valued mode shapes using the state-space system formulation, if the damping is non-proportional. This is done for pedagogical reasons, of course, since the state-space formulation could indeed be used in both the latter cases. Finally, for completion, of course the toolbox also contains commands to convert from modal parameters to FRFs. Also, there is, of course, commands to convert from different modal scaling principles, particularly unity modal mass, and unity modal A [1].

### 13.2.3 Time Domain Forced Response

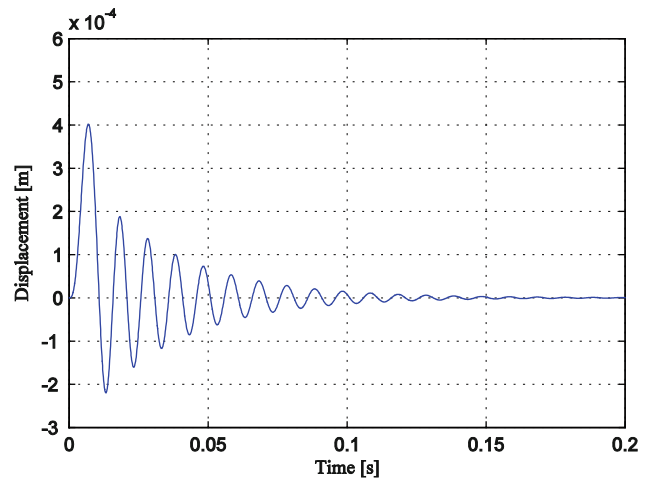
A crucial part of teaching vibrations, is to illustrate the transient versus harmonic forced response, as well as the response to random loads. For vibration analysis, it is many times very important to be able to check an algorithm or method on data with known parameters. For both these purposes, the time domain forced response algorithm implemented in the toolbox is very important. The algorithm is based on a ramp-invariant method of designing digital filters described in [4, 5] which has some very important advantages

1. It is (immensely) faster and much more accurate than standard methods such as Runge–Kutta variants [4],
2. It uses a modal superposition formulation, which means it can use either mass, damping, and stiffness matrices, or mass and stiffness matrices and modal damping, or modal parameters, as input, which makes it very flexible.

The syntax of the command, which is called **timefresp**, is dependent on which of the input parameters are known, but an example is **y = timefresp(x,fs,M,C,K,indof,outdof,OutType)**, where **x** is the force time history or time histories if more than one force, and **indof** and **outdof** are vectors, allowing all requested information to be computed in one call to the command. To illustrate the use, let us define a mechanical SDOF system with natural frequency  $f_r = 100$  Hz, damping  $\zeta_r = 0.05$ , excited by a half sine force, in [N],



**Fig. 13.1** Plot for Example 13.1.  
SDOF response to a half-sine  
input force



$$F(t) = \begin{cases} 100 \sin\left(\frac{\pi t}{T}\right), & 0 \leq t \leq T \\ 0, & t > T \end{cases} \quad (13.1)$$

where the pulse time  $T = 11$  ms. The code to generate the output is found in Example 13.1 and the result plotted in Fig 13.1. A more advanced illustration of the use is found in Sect. 13.2.7.

```

wn=2*pi*100; z=0.05; % Natural frequency in [rad/s] and damping ratio
m=1; k=m*wn^2; c=2*z*sqrt(m*k); % mass, stiffness, and (viscous) damping
T=11e-3; % Pulse time
fs=1e4; % Sampling frequency in Hz
t=(0:1/fs:.2)'; % Time axis in column
F=makepulse(length(t), fs, T, 'halfsine');
F=100*F/max(F); % Scaled force
u=timefresp(F, fs, m, c, k, 1, 1, 'd'); % Transient response in displacement [m]

```

**Example 13.1** Code to generate time forced response of a SDOF system to a transient (half sine) force signal. The result is plotted in Fig. 1.

### 13.2.4 Time Series Analysis

An important part of vibration analysis is signal analysis, so much more because most students taking a class in vibration analysis are mechanical or civil engineers, with lack of background in signal analysis. The ABRVIBE toolbox thus contains commands for in-depth illustration of time series analysis. There are illustrations of convolution, as well as the sampling theorem, which we will not cover here for lack of space. Among more advanced functionality, are digital filter examples for acoustic 1/n octave filtering and A- and C-weighting. In addition, the toolbox includes an RMS (root mean square) integration algorithm which can be used to simulate a sound level meter (SLM), or for vibration comfort analysis, with the command **arms**.

Another important functionality is implemented for integration and differentiation of signals in the time domain. Unlike what is commonly thought, these two fundamental applications are not so readily implemented, and common well-known algorithms such as the trapezoidal rule taught in numerical analysis classes are not suitable for vibration analysis with high dynamic range. Instead, the ABRVIBE toolbox contains state-of-the art digital filter methods for both integration and differentiation with very high accuracy. Finally we should mention the function **psd2time** which can be used to produce Gaussian noise with a specified spectral density.

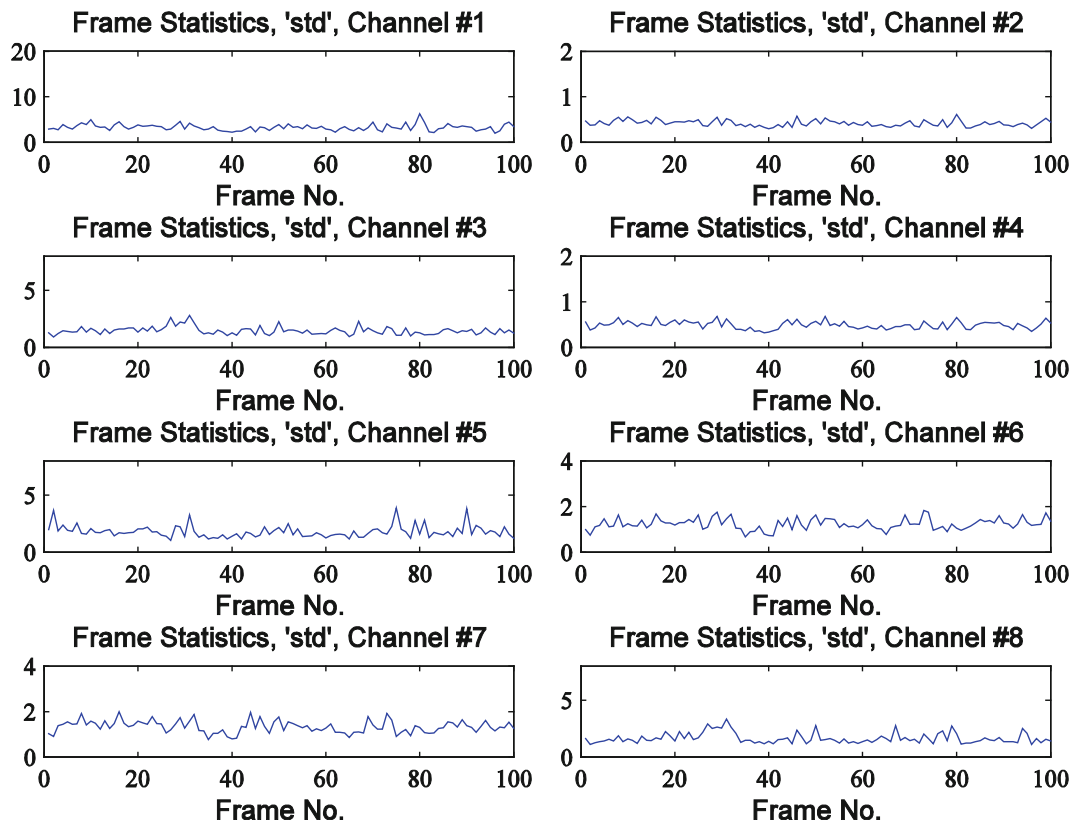


Fig. 13.2 Results of frame statistics in Example 13.2. The standard deviation of each channel is plotted versus frame number

### 13.2.5 Statistics and Data Quality Assessment

Statistical functions are used frequently in vibration analysis, particularly when dealing with field measurement data. There is thus functionality for assessing the statistical properties of signals, testing for stationarity, and for quality assessment of measured signals. The latter will be taken as an example here, as it includes most of the other functionality.

Data quality analysis is essentially based on using a set of statistical measures such as RMS value, min- and max values, skewness, and kurtosis, and to compare these values with known values for signals of good quality, what we can call “normal” values. The analysis is typically done using two time scales; the entire time signal, and a shorter time interval. The entire time signal gives overall statistical values, which may indicate important errors. Shorter intervals, for example 1 s intervals, may instead reveal time restricted errors due to intermittent errors resulting from, for example, cable issues, electrical spikes, etc.

To illustrate an example of a data quality assessment analysis, there are data from eight channels from a measurement on a truck supplied with the toolbox. In Example 13.2 the main code for data quality analysis of these data are shown. The first few lines show a structured way of assessing all files in the data directory, and then looping through all files, which is facilitated by the naming convention of the file names, where the data are stored in files with file names “Truck1.mat”, “Truck2.mat”, . . . “Truck8.mat” in this example. For each channel, the standard deviation is computed as a function of time, for 100 frames, and plotted and the reverse arrangements test is run for each channel. The results of the frame statistics plot are shown in Fig. 13.2. Next the high-level command `statchkf` is used to produce a list of most common statistical variables, and also to log data to two files; a text file called “TruckStats.log”, and a MATLAB file “Truckstats.mat”. The former is typed into MATLAB to produce the results in Table 13.1. The latter is again opened and used to produce a plot of the kurtosis of all channels normalized to the kurtosis of channel 3, which is plotted in Fig. 13.3. The normalization to one of the channels is a good “trick”, to more easily see if there is a discrepancy from what is “normal”.

```

D='..\Data\TruckData\';
DirStruct=dir(strcat(D,'Truck*'));
NoChannels=length(DirStruct);           % Define number of channels
% First, run a frame statistics analysis of all channels, based on standard deviation
for n = 1:NoChannels
    FileName=strcat(D,DirStruct(n).name) % Create file name 'Truck1.mat' etc.
    load(FileName)
    N=floor(length(Data)/100);           % Use 100 frames in total
    subplot(NoChannels/2,2,n)
    F(:,n)=framestat(Data,N,'std',1);    % This command produces the plot, see Fig. 2
    s(n)=teststat(F(:,n),0.02,'reverse'); % s contains Boolean variables true/false
end
% We then compute a reverse arrangements test on channel 3 only (for space reasons)
% Next, we run some standard statistics and log to a file
statchkf(Prefix,1,8,'TruckStats');      % Prefix is entire directory structure...
type TruckStats.log                     % This lists the results in MATLAB
% Next, we plot the overall kurtosis of all channels, from the analysis just made
load TruckStats                          % This file contains the variables used
Kurtosis=Kurtosis/Kurtosis(3)            % Normalize kurtosis to channel 3
bar(Kurtosis)                             % Results of this is shown in Fig. 3

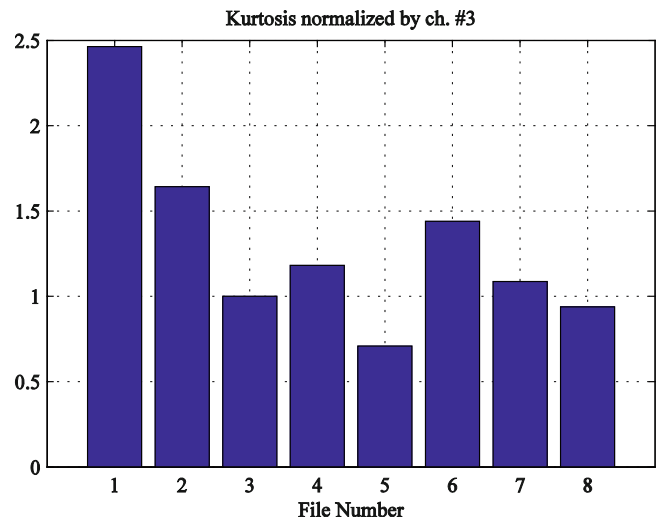
```

**Example 13.2** Data quality assessment of truck data. Some plot commands are omitted here for the sake of brevity

**Table 13.1** Statistical parameters from output of the data quality test in Example 13.2

File #	Max	Min	Mean	Crest	Std dev	Variance	Skewness	Kurtosis
1	51	-69	1.2	18	3.7	13	0.15	11
2	6.4	-7.2	-0.0035	17	0.42	0.18	0.05	7
3	17	-14	0.2	9.5	1.8	3.3	0.042	4.3
4	4.3	-4.8	-0.014	9.8	0.49	0.24	-0.021	5
5	25	-19	0.047	7.5	3.3	11	0.18	3
6	11	-7.2	0.027	8.4	1.3	1.6	0.7	6.1
7	9.9	-8.1	-0.51	6.8	1.4	1.8	0.25	4.6
8	18	-14	0.28	8	2.2	4.8	0.0062	4

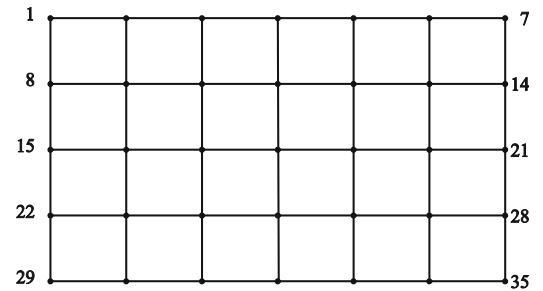
**Fig. 13.3** Kurtosis of the each channels in Example 13.2, normalized to the kurtosis of channel 3. Assuming the kurtosis of channel 3 is good, the plot reveals suspicious kurtosis in at least channels 1, 2, 5, and 6



### 13.2.6 Spectral Analysis

Spectra are perhaps the most commonly used functions for vibration analysis. The ABRAVIBE toolbox therefore include a number of high-level commands to produce spectra of multi-channel recorded or synthesized data. Spectrum types include linear spectrum (also called RMS spectrum), and phase-spectrum, for periodic signals. For random signals, spectral densities can be computed using the very common Welch's method, but also using the smoothed periodogram method. For transients, the transient spectrum and the energy spectral density functions are available. All functions for random signals can also be computed for cross-spectral densities.

**Fig. 13.4** Grid used for reduced mode shapes as well as for EMA of Plexiglas plate



Welch's method for computing spectral densities is well-known and is the method implemented so far, in virtually all commercial software. It will be used in Example 13.3a below. Before introducing this example, however, a few words about the alternative to Welch, the *smoothed periodogram method*, should be mentioned. As described in [1, 6] this method has some advantages over Welch's method that can make it interesting:

1. It can be used with a logarithmic frequency axis, which gives lower random error at higher frequencies, where, usually, a lower frequency resolution is acceptable,
2. It is very practical in cases where unwanted, periodic components present in the noise are to be removed [6].

In any of these cases, the commands **apsdsp**, and **acsdsp** from the ABRVIBE toolbox can be used. Both commands operate similarly to the Welch commands **apsdw**, and **acsdw**, which are going to be used in Example 13.3a.

To illustrate the power of the ABRVIBE toolbox for generating synthetic data, and then performing spectral analysis, we will generate data from a model of a Plexiglas plate [6]. This also illustrates the advanced synthesis models available in the toolbox, and the code for this pedagogic example, developed in the ABRVIBE toolbox and also using the free open CALFEM [7] toolbox, is available in the ABRVIBE toolbox. The example is used thoroughly throughout the ABRVIBE toolbox, and is very similar to the IES plate described in [8]. It is a small, rectangular plate made of Plexiglas (PMMA), and with, essentially, two first modes at very close natural frequencies. The advantages of using such a simple structure are many, for example

- The structure geometry is trivial, so the student can focus on the topic,
- The structure is easily measured with high quality either by impact testing or shaker testing, in relatively short time, which allows for high-quality experimental modal analysis to be incorporated,
- The plate can be modeled relatively simply using inexpensive shell elements [6],
- More than the first ten modes of the plate can be readily described with a mere 5-by-7 grid, either for EMA or for reduced mode shapes for synthesis.

In Example 13.3a we assume that we have access to the eigenfrequencies and the analytical (normal) mode shapes reduced to the experimental grid size of 5-by-7 DOFs as shown in Fig. 13.4. How to obtain such modes are described in [6] (and is, as mentioned, available in the toolbox). We will now show how to use this modal model, by adding some modal damping of 2% to each mode, and then compute time data corresponding to a two-input shaker test using pure random excitation. For this purpose we call the command **timefresp** with the syntax using poles and mode shapes as input. We divide the example into two parts, Example 13.3a to create data, and Example 13.3b to produce the entire cross-spectral matrix.

In Example 13.3b we will now first read the reference data (the force time signals) in, and compute the input autospectral matrix  $G_{xx}$ . Then we will loop through all response channels and compute cross-spectral densities between the two references and the response channel the 3D-matrix  $G_{yx}$ , and store the output autospectral densities in 2D-matrix  $G_{yy}$ . If we have  $R(=2)$  responses, and  $D(=35)$  responses, this analysis thus produces the matrices

- $G_{xx}$   $N/2 + 1$ -by- $R$ -by- $R$ , input autospectral matrix
- $G_{yx}$   $N/2 + 1$ -by- $D$ -by- $R$ , input-output cross-spectral matrix
- $G_{yy}$   $N/2 + 1$ -by- $D$ , output autospectral matrix (no need for cross-spectral densities between outputs)

It should also be mentioned that there are a lot of details in the chapter examples about how to optimize the spectral analysis FFT settings, such as the blocksize, for minimizing bias error etc. It should also be mentioned that there is functionality for many more types of excitation signals, including impact testing, pseudo random noise and burst random. Example 13.3b is just that – an example. It should also be pointed out that the method described in Example 13.3a, could also incorporate known error signals (extraneous noise) either on the input, or output signals, to analyze bias effects when

```

% Part 1 - create data and store in files
indofs=[1 9];           % Force DOFs
outdofs=[1:35];        % Response DOFs
poles=fz2poles(fr,0.02); % Add 2% damping to all eigenfrequencies, to produce complex poles
fs=round(3*max(fr));   % Set a suitable integer sampling frequency
N=100*1024;           % Use 100K samples
Forces=randn(N,length(indofs)); % Create 2 independent Gaussian forces
Header=makehead(1,Forces(:,1),1/fs); % Create Nominal Header
Prefix='PlexiTimeData';
Data=Forces(:,1);      % Next few lines saves the first force
Header.Dof=indofs(1);
Header.Dir='Z+';
Header.Unit='N';
Header.Title='Simulation using Plexi FE model results, and 2 inputs in dofs 1,and 9';
FileName=strcat(Prefix,int2str(1));
save(FileName,'Data','Header'); % Save the first force in file PlexiTimeData1
Data=Forces(:,2);      % Next few lines saves the second force
Header.Dof=indofs(2);
Header.Dir='Z+';
Header.Unit='N';
Header.Title='Simulation using Plexi FE model results, and 2 inputs in dofs 1,and 9';
FileName=strcat(Prefix,int2str(2));
save(FileName,'Data','Header'); % Save the second force in file PlexiTimeData2
% Next, save all responses in following files
for n=1:length(GEOMETRY.node)
    Data=timefresp(Forces,fs,poles,V,indofs,n,'a');
    Header.Dof=outdofs(n);
    Header.Dir='Z+';
    Header.Unit='m/s^2';
    Header.Title='Simulation using Plexi FE model results, and 2 inputs in dofs 1,and 9';
    FileName=strcat(Prefix,int2str(n+2));
    save(FileName,'Data','Header');
end

```

**Example 13.3a** Create synthesized time data from Plexiglas plate using a 5-by-7 grid. The example assumes that eigenfrequencies are in the vector  $\mathbf{fr}$  and normal modes in variable  $\mathbf{V}$ . At the time of writing, this takes approx. 14 seconds on the authors laptop. This includes doubledifferentiating all signals to acceleration

estimating FRFs, for example. Numerous such examples are available among the chapter examples for Chaps. 13 and 14 in [1] which deal with FRF estimation.

### 13.2.7 Frequency Response Estimation

The next natural step after producing auto and cross-spectral density matrices described in the previous section, is to compute the MIMO frequency responses and multiple coherence functions. This can be done immediately after the steps in Example 13.3b, by using the command  $[\mathbf{H},\mathbf{Cm},\mathbf{Cin}] = \mathbf{xmtrx2frf}(\mathbf{Gxx},\mathbf{Gyx},\mathbf{Gyy})$  which computes all FRFs in the matrix  $\mathbf{H}$ , size  $N/2 + 1$ -by- $D$ -by- $R$ , the multiple coherence matrix  $\mathbf{Cm}$ , size  $N/2 + 1$ -by- $D$ , and the input coherence matrix with ordinary coherence between all inputs, in  $\mathbf{Cin}$ , size  $N/2 + 1$ -by- $R$ -by- $R$ .

There is also functionality in the toolbox for estimating FRFs from impact test data. This is done using an enhanced method based on recorded time signals including all impacts. The method is described in [3].

### 13.2.8 Experimental Modal Analysis (EMA)

There is functionality for a variety of EMA operations in the ABRVIBE toolbox. The command **frf2msdof** includes several algorithms for obtaining modal parameters using SDOF approximations. The command **frf2ptime** uses MDOF estimation methods to estimates poles and sometimes modal participation factors (MPFs), using either Prony's method (for one FRF at

```

NoRefs=2;           % Number of references (in first files)
NoResps=35;        % Number of responses (in consec. files)
Prefix='PlexiSynt2Forces';
% Put forces into columns in RefSignal
for n=1:NoRefs
    FileName=strcat(Prefix,int2str(n));
    load(FileName);
    RefSignal(:,n)=Data;
end
fs=1/Header.xIncrement;
% Loop through response channels
for n=1:NoResps
    FileName=strcat(Prefix,int2str(FileNo(n+2)));
    load(FileName);
    RespSignal(:,n)=Data;
end
% Compute all 2-in/35-out auto and cross-spectral densities
[Gxx,Gyx,Gyy,f]=time2xmtx(RefSignal,RespSignal,fs,N); % 50% overlap, Hanning window

```

Example 3b. Processing all time data from the 2-in/35-output synthesized “measurement” into auto and cross-spectral density matrices for MIMO spectrum analysis. On the author’s computer, at the time of writing, this takes approx. 1 sec.

**Example 13.3b** Processing all time data from the 2-in/35-output synthesized measurement into auto and cross-spectral density matrices for MIMO spectrum analysis. On the authors computer, at the time of writing, this takes approx. 1 sec

the time, see [9]), the least squares time domain method (LSCE, see [10]), or by the polyreference time domain method [11]. Mode shapes can then be computed using the command **frfp2modes** which includes a multi-reference least squares frequency domain estimation of residues (mode shapes). Finally animation of the estimated mode shapes can be accomplished by using a GUI-based tool called **animate**. This functionality was supplied externally, see Acknowledgements.

To aid the analysis there is a high-level command that reads in all data and sorts it into variables, the command **data2hmtrx**. This command also rearranges data if coming from an impact test with roving impacts, so that it looks as if it comes from a shaker test to avoid having to deal with both matrix dimensions. There is also a command for mode indication functions, **amif**, which can produce various MIFs, eg. the normal MIF, and the multivariate MIF. There are also two commands to deal with modal assurance criterion (MAC) matrices, **amac** to compute MAC matrices (either auto or cross), and **plotmac** to plot the matrix in Manhattan style display (see Fig. 13.7).

```

Prefix='PlateH';
[H,f,Rdof,Rdir,Fdof,Fdir,FillMtrx]=data2hmtrx(Prefix,1,105);
[p,L,fLimits] = frf2ptime(H,f,400,20,'mvmf','ptd'); % Estimate poles and MPFs
idx=find(f>=fLimits(1) & f<=fLimits(2));
V=frfp2modes(H(idx,:),f(idx),p,L,0.5,Fdof); % Estimate mode shapes
MAC=amac(V); % Compute MAC matrix
plotmac(MAC);

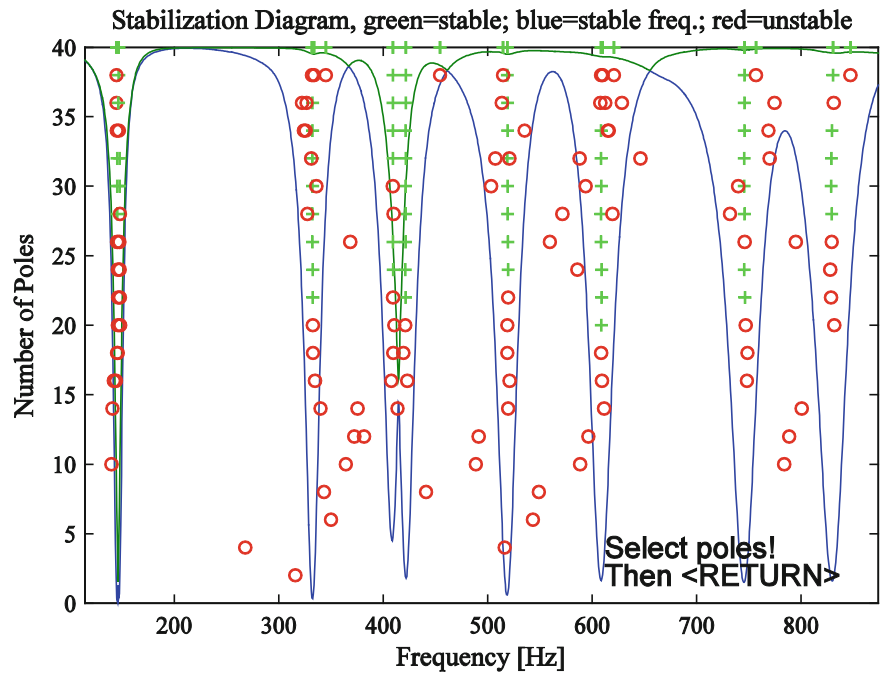
```

Example 4. Experimental modal analysis (EMA) example using data from a 2-reference impact test on a Plexiglas plate.

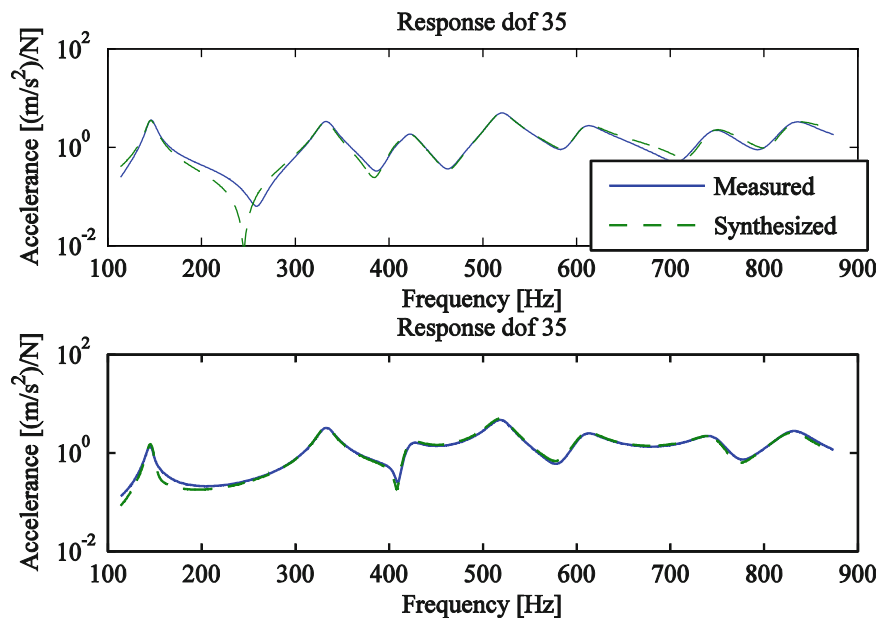
**Example 13.4** Experimental modal analysis (EMA) example using data from a 2-reference impact test on a Plexiglas plate.

To illustrate an EMA example, we will use data from an impact test on the Plexiglas plate mentioned in previous sections. Of course, we could use the FRF matrix computed in Sect. 13.2.7, however, that would not allow us to see how actual measurement data are used for EMA. In Example 13.4 there is thus some code illustrating a multiple-reference analysis using the polyreference time domain method. First the data are read in and sorted using the **data2hmtrx** command. Thereafter the poles and modal participation factors are computed and selected in a stabilization diagram shown in Fig. 13.5. After selecting the poles in this diagram, the residues are estimated using the least squares frequency domain method, using the poles and MPFs from the polyreference method. The command **frfp2modes** also plots each synthesized result as in Fig. 13.6, together with the corresponding measured function, if so is requested. After the mode shapes are thus computed, a MAC matrix

**Fig. 13.5** Stabilization diagram of polyreference time domain estimation for Example 13.4



**Fig. 13.6** Measured and synthesized FRFs from estimation of residues (mode shapes) for dof 35



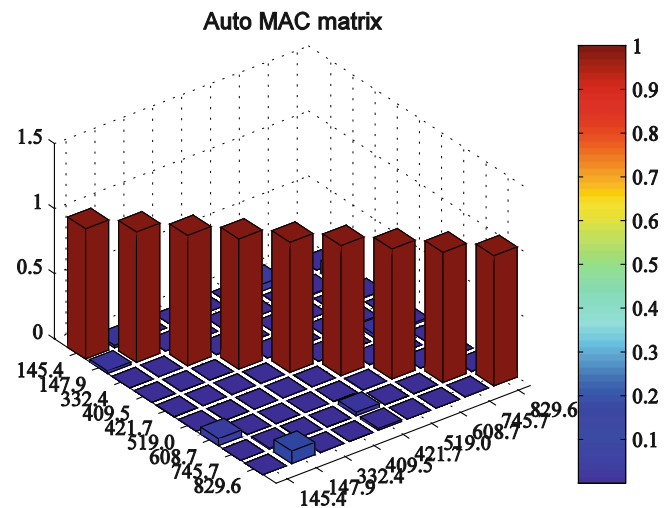
is computed and plotted, as shown in Fig. 13.7. All that remains is to save the modal parameters to a file for subsequent animation, which will not be shown here.

### 13.2.9 Order Tracking

The final topic we shall discuss is analysis of rotating machinery using so-called order tracking. The ABRAVIBE toolbox includes some fundamental functionality for producing RPM-time profiles from a tacho signal. Using the RPM-time profile, RPM maps can then be computed and from those, order tracks can be extracted. There is also functionality for resampling the time signals and from the resampled signals extracting order maps and order tracks.



**Fig. 13.7** MAC matrix of mode shapes from least squares frequency domain estimation using poles and modal participation factors from the polyreference time domain estimation for Example 13.4



### 13.3 Summary

In this paper we have presented a free toolbox for MATLAB or GNU Octave, the ABRAVIBE toolbox, and discussed the toolbox functionality for noise and vibration analysis, with emphasis on teaching vibration analysis and structural dynamics. It was pointed out how the transparency of the open software makes it possible for the student to study the steps involved in the analysis in detail by opening and inspecting the program routines. The flexible nature of the toolbox also enables teachers to customize examples based on the level of the students and the time at hand.

**Acknowledgements** The author would like to express his gratitude to the original author, Dan Lazor, and Dave Brown, University of Cincinnati, for allowing incorporating and distributing the **animate** GUI-based animation software with the ABRAVIBE toolbox.

### References

1. Brandt A (2011) Noise and vibration analysis – signal analysis and experimental procedures. Wiley, Chichester
2. Brandt A (2011) ABRAVIBE, A MATLAB/Octave toolbox for noise and vibration analysis and teaching, revision 1.1. <http://www.mathworks.com/matlabcentral/linkexchange/>
3. Brandt A, Brincker R (2010) Impact excitation processing for improved frequency response quality. In: Proceedings of 28th international modal analysis conference, Jacksonville, Mar 2013 <http://www.abravibe.com/toolbox.html>
4. Brandt A, Ahlin K (2003) A digital filter method for forced response computation. In: Proceedings of 21st international modal analysis conference, Kissimmee
5. Ahlin K, Magnevall M, Josefsson A (2006) Simulation of forced response in linear and nonlinear mechanical systems using digital filters. In: Proceedings of international conference on noise and vibration engineering (ISMA), Catholic University, Leuven
6. Brandt A, Linderholt A (2012) A periodogram-based method for removing harmonics in operational modal analysis. In: Proceedings of the international conference on noise and vibration engineering (ISMA), Leuven
7. Sturesson P-O, Brandt A, Ristinmaa M (2013) Structural dynamics teaching example – a linear test analysis case using open software. In: Proceedings of 31st international modal analysis conference (IMAC), Garden Grove
8. Austrell P-E, Dahlblom O, Lindemann J, Olsson A, Olsson K-G, Persson K, Petersson H, Ristinmaa M, Sandberg G, Wernberg P-A (2004) Calfem – a finite element toolbox, version 3.4. Studentlitteratur AB
9. Proakis JG, Manolakis DG (2006) Digital signal processing: principles, algorithms, and applications. Prentice Hall, Upper Saddle River
10. Brown D, Allemang R, Zimmerman R, Mergey M (1979) Parameter estimation techniques for modal analysis. SAE technical papers 790221
11. Vold H, Kundrat J, Rocklin TG, Russell R (1982) A multiple-input modal estimation algorithm for mini-computers. SAE technical papers 820194

# Chapter 14

## Structural Dynamics Teaching Example: A Linear Test Analysis Case Using Open Software

Per-Olof Sturesson, Anders Brandt, and Matti Ristinmaa

**Abstract** Teaching the topic of structural dynamics in any engineering field is a true challenge due to the wide span of the underlying subjects like mathematics, mechanics (both rigid body and continuum mechanics), numerical analysis, random data analysis and physical understanding. With the increased availability of computers many engineering problems in practice are evaluated by means of numerical methods. The teaching task within the field of structural dynamics thus has to include analytical models in order to create a theoretical basis but also has to include computational techniques with its approximations, and knowledge about their limitations. Equally important is for students to have knowledge of the experimental verification of the obtained models. This paper describes a teaching example where a simple plate structure is modeled by shell elements, followed by a model calibration using experimental modal analysis data. By using open software, based on MATLAB<sup>®1</sup> as a basis for the example, the applied numerical methods are made transparent to the student. The example is built on a combination of the free CALFEM<sup>®2</sup> and ABRVIBE toolboxes, and thus all code used in this paper is publically available as open source code.

**Keywords** Experimental modal analysis • Finite element model • Model calibration • ABRVIBE • CALFEM

### Nomenclature

$h(t)$	Impulse response function
$H(f)$	Frequency response function
$[L]$	Modal participation matrix
$N$	Number of degrees-of-freedom
$\{\psi\}_r$	Mode shape of mode number $r$
$s_r$	Pole of mode number $r$
$u, v, w$	Displacement
$[a]$	Nodal displacement
$[K]$	Global stiffness matrix

---

<sup>1</sup>MATLAB<sup>®</sup> is a trademark of The MathWorks, Inc.

<sup>2</sup>CALFEM<sup>®</sup> is a trademark of the Division of Structural Mechanics, Lund University.

P.-O. Sturesson

Noise & Vibration Center, Volvo Car Corporation, Dept. 91600/PV2C, Gothenburg, SE-405 31 Sweden

e-mail: [per-olof.sturesson@volvocars.com](mailto:per-olof.sturesson@volvocars.com)

A. Brandt (✉)

Institute of Technology and Innovation, University of Southern Denmark, Campusvej 55, Odense M, DK-5230 Denmark

e-mail: [abra@iti.sdu.dk](mailto:abra@iti.sdu.dk)

M. Ristinmaa

Division of Solid Mechanics, Lund University, P.O. Box 124, Lund, SE-221 00 Sweden

e-mail: [matti.ristinmaa@solid.lth.se](mailto:matti.ristinmaa@solid.lth.se)

[M]	Global mass matrix
$[k]_e$	Element stiffness matrix
$[m]_e$	Element mass matrix
[F]	Body force matrix
$\varepsilon, \gamma$	Strain
$\sigma, \tau$	Stress
$E$	Young's modulus
$\nu$	Poisson's ratio
$[N]$	Shape function matrix
$\rho$	Mass density
$t$	Material thickness

## 14.1 Introduction

For transparency in teaching it is advantageous to provide students with a simple case, so that focus can be put on the theory and techniques taught, rather than object related problems. In addition, open source software based on MATLAB<sup>®</sup> or GNU Octave, provides the advantage that the students can follow each step in the process, with direct access to governing equations and variables involved. This transparency is not usually possible with commercial finite element programs. In commercial codes some of these teaching concepts are lost since many of the problems can, in fact, be solved without understanding the underlying physics and numerical methods and their limitations.

The aim of CALFEM<sup>®</sup> [1] was to highlight the link between the mathematical theory and models of a phenomena and its numerical implementation using the finite element method. In such an approach the students are motivated to fully appreciate the intimate relationship between these topics. Also within such an approach it becomes evident for the students that many different physical problems are in fact modeled by the same set of equations, i.e. analogies exist. An additional advantage of open-source code is that the student can also copy a routine and modify it for a specific purpose such as modeling of some special damping.

Model calibration, or correlation theory and methods, are important subjects to teach engineering students. The theory is becoming more and more important for many OEMs who require an efficient and streamlined product development process that enables getting products faster to the market. This is especially important in highly competitive sectors like the automotive industry. Additional efficiency, i.e. cost reduction in product development, may be achieved by means of reducing both the number of prototype build stages and the number of prototypes within a given build stage. Without taking correct countermeasures it is evident that this increases the risk of product quality issues in the field due to errors in the early decision making process.

In order to minimize the risks different actions need to be applied long before hardware builds take place, i.e. before and during the early phase of the product development. These “front loading” actions usually include extensive use of computer aided technologies like CAE in order to enable improved project decision making based on objective data as well as engineering insight but also, which is as important, a more robust process for target setting including subsystem target roll down. A successful outcome of these actions depends heavily on the capability of the applied math methods. The development of new or improving existing math methods is then an important and strategic task that needs to be done outside and upfront to the regular product development work. This task also requires test and CAE communities to thoroughly cooperate in order to be successful. Often organisation and conflicting priorities may be difficult barriers to overcome. Also important in math method development is to address the issue of access to hardware that matches the design. Variability due to manufacturing processes affects the hardware testing and needs also to be considered.

For transparency in teaching it can be an advantage to provide students with a simple case, so that focus can be put on the theory and techniques taught, rather than object related problems. In addition, open source software based on MATLAB<sup>®</sup>, provides the advantage that the students can follow each step in the process, with direct access to governing equations and variables involved. Therefore, in this paper we describe an example of a FE model of a simple PMMA plate, similar to the so-called IES plate [2], made in the popular CALFEM<sup>®</sup> open-source MATLAB<sup>®</sup> toolbox. Experimental modal analysis is then performed and correlation analysis and simple model calibration is performed. For the experimental modal analysis we use the open source ABRAVIBE toolbox, also for MATLAB<sup>®</sup>. If fully free, open source software is wanted, all examples can also be run in GNU Octave, using the same toolboxes.

## 14.2 Theory

### 14.2.1 Experimental Modal Analysis (EMA)

Experimental modal analysis is based on measurements of frequency response functions from which the modal parameters (natural frequencies, relative damping ratios, and mode shapes) are extracted using the relation

$$[H(f)] = \sum_{r=1}^N \frac{Q_r \{\psi\}_r \{\psi\}_r^T}{j\omega - s_r} + \frac{Q_r^* \{\psi^*\}_r \{\psi^*\}_r^T}{j\omega - s_r^*} \quad (14.1)$$

where  $[H(f)]$  is the matrix of frequency responses in receptance form (displacement/force),  $Q_r$  is the modal scaling constant,  $s_r$  the pole of mode number  $r$ ,  $\{\psi\}_r$  the mode shape for mode number  $r$ , and  $N$  is the number of modes (number of degrees-of-freedom). In the typical case, a few, say  $R$ , references are used, either using fixed shakers and roving response sensors (usually accelerometers) which leads to estimates of  $R$  columns from the matrix in (14.1), or by letting  $R$  reference accelerometers be fixed and roving the force around, usually with an impact hammer, which leads to estimates of  $R$  rows of (14.1). In any case, since the frequency response matrix is symmetric, it can easily be transposed if the latter strategy was chosen, so that the formulation may be implemented only for the case of fixed force references.

Instead of the frequency domain relation in (14.1), time domain methods extract the modal parameters by using the relation of the impulse responses in a matrix  $[h(t)]$ , which can be expressed

$$[h(t)] = \sum_{r=1}^N Q_r \{\psi\}_r \{\psi\}_r^T e^{s_r t} + Q_r^* \{\psi^*\}_r \{\psi^*\}_r^T e^{s_r^* t}. \quad (14.2)$$

If two or more poles are very close, several references usually have to be used to correctly extract the corresponding mode shapes. Also, many times the complex conjugate poles and mode shapes are, for simplicity, included in the numbering, so that the sums go from 1 to  $2N$  and only include one term. Equation (14.2) can then be rewritten as

$$[h(t)] = [\Psi] [e^{s_r t}] [L] \quad (14.3)$$

where  $[\Psi]$  is the mode shape matrix with mode shapes in its columns,  $[e^{s_r t}]$  is a diagonal matrix with the complex exponential terms, and  $[L]$  is a matrix with modal participation factors.

A common family of parameter extraction methods for extracting poles are the complex exponential methods; the prony method [3], the least squares complex exponential method [4], and the polyreference time domain method [5]. The latter method can handle closely coupled poles. In all cases, the mode shapes are usually computed in a second step, e.g. by the least squares frequency domain method [6]. These methods are all implemented in the ABRVIBE toolbox [7].

### 14.2.2 Finite Element Method

The finite element method for solving structural dynamic problems is today well established in the industry. More comprehensive reading concerning formulation and basic theory of finite element method can be found in [8–10] while structural dynamic theory can be found in [11].

If an arbitrary linear elastic structure or medium is considered, the equations that describe the dynamic response may be derived by the equilibrium of the work carried out by the external forces acting on structure and the work of the internal, inertial and viscous forces. For a single finite element the work balance yields [8–10]

$$\begin{aligned} & \int_{V_e} \{\delta u\}^T \{F\} dV + \oint_{S_e} \{\delta u\}^T \{\Phi\} dS + \sum_{i=1}^N \{\delta u\}_i^T \{p\}_i \\ & = \int_{V_e} \{\delta \varepsilon\}^T \{\sigma\} dV + \int_{V_e} \{\delta u\}^T \rho \{\ddot{u}\} dV + \int_{V_e} \{\delta u\}^T c \{\dot{u}\} dV \end{aligned} \quad (14.4)$$

where  $\{\delta u\}$  and  $\{\delta \varepsilon\}$  are virtual displacements and corresponding strains,  $\{F\}$  the body forces,  $\{\Phi\}$  the prescribed surface tractions,  $\{p\}_i$  the concentrated point loads with dimension  $n$ ,  $\rho$  the mass density of the material and  $c$  is the viscous material damping parameter.

The variables to be solved in structural mechanics using the finite element approach are usually the displacement field  $\{u\}$

$$\{u\} = \begin{Bmatrix} u \\ v \\ w \end{Bmatrix} \quad (14.5)$$

where  $u$ ,  $v$  and  $w$  are the displacements in  $x$ ,  $y$  and  $z$ -direction using a Cartesian coordinate system. The kinematic relationship between strains and displacement is defined as

$$\{\varepsilon\} = \tilde{\nabla} \{u\} \quad (14.6)$$

where

$$\{\varepsilon\} = \begin{Bmatrix} \varepsilon_x \\ \varepsilon_y \\ \varepsilon_z \\ \gamma_{xy} \\ \gamma_{xz} \\ \gamma_{yz} \end{Bmatrix}, \quad \tilde{\nabla} = \begin{bmatrix} \frac{\partial}{\partial x} & 0 & 0 \\ 0 & \frac{\partial}{\partial y} & 0 \\ 0 & 0 & \frac{\partial}{\partial z} \\ \frac{\partial}{\partial y} & \frac{\partial}{\partial x} & 0 \\ \frac{\partial}{\partial z} & 0 & \frac{\partial}{\partial x} \\ 0 & \frac{\partial}{\partial z} & \frac{\partial}{\partial y} \end{bmatrix} \quad (14.7)$$

By introducing shape functions  $[N]$  the displacement field  $\{u\}$  and its two time derivatives yields

$$\begin{aligned} \{u\} &= [N] \{a\} \\ \{\dot{u}\} &= [N] \{\dot{a}\} \\ \{\ddot{u}\} &= [N] \{\ddot{a}\} \end{aligned} \quad (14.8)$$

where the shape functions are space dependent only and the nodal deformations  $\{a\}$  are dependent of time (or frequency) only. The strains at the nodal degrees of freedom may be derived as

$$\{\varepsilon\} = \tilde{\nabla} \{u\} = \tilde{\nabla} [N] \{a\} = [B] \{a\}. \quad (14.9)$$

By combining (14.4) and (14.8) we get

$$\begin{aligned} \{\delta a\}^T & \left[ \int_{V_e} [N]^T \{F\} dV + \oint_{S_e} [N]^T \{\Phi\} dS + \sum_{i=1}^N [p]_i \right] \\ &= \{\delta a\}^T \left[ \int_{V_e} [B]^T \{\sigma\} dV + \int_{V_e} \rho [N]^T [N] dV \{\ddot{a}\} + \int_{V_e} c [N]^T [N] dV \{\dot{a}\} \right]. \end{aligned} \quad (14.10)$$

Since  $\delta a$  is arbitrary (14.10) can be written as

$$[m]_e \{\ddot{a}\} + [c]_e \{\dot{a}\} + \{f\}_{\text{int}} = \{f\}_{\text{ext}} \quad (14.11)$$

where the element mass and viscous damping matrices are

$$[m]_e = \int_{V_e} \rho [N]^T [N] dV \quad (14.12)$$

$$[c]_e = \int_{V_e} c [N]^T [N] dV \quad (14.13)$$

and the element internal and external force vectors are defined as

$$\{f\}_{\text{int}} = \int_{V_e} [B]^T \{\sigma\} dV \quad (14.14)$$

$$\{f\}_{\text{ext}} = \int_{V_e} [N]^T \{F\} dV + \oint_{S_e} [N]^T \{\Phi\} dS + \sum_{i=1}^N [p]_i. \quad (14.15)$$

In the demonstration example first order shell elements will be used. The shell element consists of combination of a continuous plane stress (2D) element, which describe the membrane behaviour, and a structural plate element, which describe the bending behaviour. Plate theory implies several simplifications and also violations of the fulfilment of solid mechanic field equations. Nevertheless, shell elements are widely used in industry due to less effort in modelling and computational efficiency.

For the membrane behaviour of the shell element, i.e. described by a plane stress element, the following constitutive relation between stress and strain exists [8–10]

$$\{\sigma\} = \begin{bmatrix} \sigma_x \\ \sigma_y \\ \tau_{xy} \end{bmatrix} = \frac{E}{1-\nu^2} \begin{bmatrix} 1 & \nu & 0 \\ \nu & 1 & 0 \\ 0 & 0 & \frac{1-\nu}{2} \end{bmatrix} \begin{bmatrix} \varepsilon_x \\ \varepsilon_y \\ \gamma_{xy} \end{bmatrix} = [D] \{\varepsilon\} \quad (14.16)$$

where  $E$  is the Young's modulus and  $\nu$  Poisson's ratio, respectively. The shape functions for a rectangular four node plane stress element, which has eight degrees of freedom, is

$$[N] = \begin{bmatrix} N_1 & 0 & N_2 & 0 & N_3 & 0 & N_4 & 0 \\ 0 & N_1 & 0 & N_2 & 0 & N_3 & 0 & N_4 \end{bmatrix} \quad (14.17)$$

where

$$N_i = b_i(x - c_i)(y - d_i) \quad (14.18)$$

where  $b$ ,  $c$  and  $d$  are constants. By using (14.9), (14.14) and (14.16) the element stiffness matrix can be derived as

$$[K]_e = \int_{V_e} [B]^T [D] [B] dV \quad (14.19)$$

which is a 8-by-8 matrix in case of a four node plane stress element. For consistency it should be mentioned that in the two-dimensional formulations all rows and columns in (14.7) referring to variables in  $z$ -direction are condensated.

The bending behaviour of the shell element is as mentioned before described by plate theory. More background reading can be found in [12]. In general, a plate is defined as a structure with a thickness  $t$  that is small compared with all other dimensions of the plate. Also, loading occurs only in the direction normal to the plate. In this article Kirchhoff (thin) plate theory is used for finite element implementation. The element stiffness matrix for a plate finite element yields a different formulation compared to a plane stress element. In order to derive the plate element stiffness formulation statics is used for simplicity. The deflection  $w$  in the normal direction of the plate is given by the biharmonic equation

$$\frac{\partial^4 w}{\partial x^4} + 2 \frac{\partial^4 w}{\partial^2 x \partial^2 y} + \frac{\partial^4 w}{\partial y^4} = \frac{12(1-\nu^2)}{Et^3} q \quad (14.20)$$

where  $w$  is the displacement in the normal direction of the plate ( $z$ -direction) and  $q$  the unit load per surface area or using the bending moment as variable

$$\frac{\partial^2 M_{xx}}{\partial x^2} + 2 \frac{\partial^2 M_{xy}}{\partial x \partial y} + \frac{\partial^2 M_{yy}}{\partial y^2} + q = 0 \quad (14.21)$$

using

$$\{M\} = -\frac{t^3}{12} [D] \hat{\nabla} w \quad (14.22)$$

and

$$\{M\} = \begin{Bmatrix} M_{xx} \\ M_{yy} \\ M_{xy} \end{Bmatrix}, \quad \hat{\nabla} = \begin{Bmatrix} \frac{\partial^2}{\partial x^2} \\ \frac{\partial^2}{\partial y^2} \\ 2 \frac{\partial^2}{\partial x \partial y} \end{Bmatrix}. \quad (14.23)$$

The displacement field  $\{u\}$  for a plate finite element consists of, in addition to  $w$ , two rotational degrees of freedom

$$\{u\} = \begin{bmatrix} w \\ \partial w / \partial x \\ \partial w / \partial y \end{bmatrix} \quad (14.24)$$

The deformation or rotation at any arbitrary point in the element is given by

$$\{u\} = [N] \{a\} \quad (14.25)$$

where  $\{a\}$  contains the nodal displacement or rotations. Each node has three deformation degrees of freedom, one displacement and two rotations.

The shape function matrix for all degrees of freedom in a rectangular plate element is given by

$$[N] = \begin{bmatrix} N_1 & 0 & 0 & N_4 & 0 & 0 & N_7 & 0 & 0 & N_{10} & 0 & 0 \\ 0 & N_2 & 0 & 0 & N_5 & 0 & 0 & N_8 & 0 & 0 & N_{11} & 0 \\ 0 & 0 & N_3 & 0 & 0 & N_6 & 0 & 0 & N_9 & 0 & 0 & N_{12} \end{bmatrix} \quad (14.26)$$

The shape function  $N_i$  is given by the field function;

$$\begin{aligned} \phi(x, y) = & c_0 + c_1 x + c_2 y + c_3 x^2 + c_4 y^2 + c_5 x y + c_6 x^2 y + c_7 x y^2 \\ & + c_8 x^3 + c_9 y^3 + c_{10} x^3 y + c_{11} x y^3 \end{aligned} \quad (14.27)$$

or

$$\phi(x, y) = \{x\} \{c\} \quad (14.28)$$

where

$$[x] = [1 \ x \ y \ x^2 \ y^2 \ xy \ x^2 y \ xy^2 \ x^3 \ y^3 \ x^3 y \ xy^3] \quad (14.29)$$

and

$$[c]^T = [c_0 \ c_1 \ c_2 \ c_3 \ c_4 \ c_5 \ c_6 \ c_7 \ c_8 \ c_9 \ c_{10} \ c_{11}]. \quad (14.30)$$

By means of Hermitian interpolation of each shape function  $N_i$  the coefficients  $c_i$  are given by the boundary conditions in terms of ordinates and slopes at each element nodal point.

The derivation of the finite element formulation for the plate element stiffness matrix is more complex than for the plain stress element. For a more comprehensive derivation the reader can read [8–10]. Using (14.21) and deriving its weak form it yields



$$\int_{A_e} [\tilde{B}]^T \{M\} dA = \oint_{S_e} [\nabla N]^T \{n\} M_{nn} dS - \oint_{S_e} [N]^T (V_{nz} + \frac{dM_{nm}}{dm}) dS - \int_{A_e} [N]^T q dA \quad (14.31)$$

where

$$[\tilde{B}] = \hat{\nabla} [N] \quad (14.32)$$

and  $V_{nz}$  and  $M_{nm}$  are the applied forces and moments at the plate element boundary.

The right hand side terms contain the kinematic and static boundary conditions as well as the loads due to body forces. By using (14.22) and the left hand side term of (14.31) the  $12 \times 12$  plate element stiffness matrix yields

$$[K]_e = \int_{A_e} [\hat{B}]^T [\tilde{D}] [\hat{B}] dA \quad (14.33)$$

where

$$[\tilde{D}] = \frac{t^3}{12} [D] \quad (14.34)$$

In this example the shell element formulation has five nodal degrees of freedom. It should be mentioned that in many commercial finite element packages the shell element formulations use six nodal degrees of freedom. The sixth degree of freedom, often referred as “the drilling DOF”, is needed when curved shapes are analyzed.

By means of assembling the element mass and stiffness matrices for each finite element using the model topology the system equations may be derived. Assuming no loads the free vibration equation of motion yields [11]

$$[M] \{\ddot{a}\} + [K] \{a\} = 0 \quad (14.35)$$

and by assuming harmonic motion for each degree of freedom  $u_i$

$$u_i = \bar{u}_i \sin \omega t \quad (14.36)$$

where  $\bar{u}_i$  is the amplitude, then (14.35) yields the eigenvalue problem

$$[-[M] \omega^2 + [K]] \{a\} = 0. \quad (14.37)$$

In the current release of the CALFEM<sup>®</sup> toolbox [13] no finite element formulation for shell element is directly implemented. However, as mentioned earlier the finite element formulation for shell elements is a combination of membrane and plate elements. Both these two finite element formulations are implemented for static analysis. Functions for element mass matrix formulation for shell element has therefore been developed for this demonstration example together with dynamic model check function like mass calculation by means of evaluation of the global mass matrix.

### 14.2.3 Model Verification

There are two common methods to verify an FE model, either using natural frequencies and mode shapes, or using frequency responses [14]. In this paper we will use the latter method. The first comparison is usually to match frequencies of each mode in the FE model with the corresponding mode in the experimental results. For this comparison, the MAC (modal assurance criterion) matrix [15] is used to determine which of the mode in one set should be paired with which mode in the other set. The MAC value between two modes  $r$  and  $s$ , is defined by

$$\text{MAC}(r, s) = \frac{|\{\psi\}_r^T \{\psi\}_s|^2}{\{\psi\}_r^T \{\psi\}_r \{\psi\}_s^T \{\psi\}_s} \quad (14.38)$$

and is similar to the correlation coefficient of the two vectors. For best comparison between test and analytical model, a good EMA test for verification purposes should use sensor positions that minimize the off-diagonal components in the MAC matrix.

After pairing the mode shapes, and comparing the natural frequencies of the EMA results with the eigenfrequencies of the FE model, the FE model should be modified so that eigenfrequencies match the experimental model, within some accuracy limits or if test errors are evident the test sequence should be reworked. Recommended criteria for a verified FE model is that the eigenfrequencies for most important modes lies within 2–10% and the diagonal elements of the MAC matrix are greater than 0.9 and off-diagonal elements are less than 0.1 [14]. For simple structures, like the example used in this article the upper limit of frequency criteria should be less than 5% and the diagonal elements of the MAC matrix should be greater than 0.95. In practice for complex engineering FE models using too stringent correlation criteria provides limited additional benefits but adds time and cost.

Before adjusting any model parameter it is essential to perform an uncertainty assessment of critical parameters. For sheet metal designed structures, especially stamped, the sheet thickness is non-uniform due to the manufacturing process. Properties of joints, e.g. spot welds or glue, are also candidate parameters to be adjusted. Material properties like Young's modulus and Poisson's ratio are well-known for most metallic materials while for complex structures of polymers, where manufacturing process parameters are strongly influencing the material properties, a greater uncertainty exists [16, 17]. In this simple example, parameters to be adjusted are the material properties like the Young's modulus used in the FE model.

More advanced verification could then be done. To find local errors in the FE model, the cross-orthogonality matrix (see [14]) can be used. This requires computing a reduced mass matrix, and will not be done in the current example. The CoMAC (coordinate MAC) [18] can also be used for this purpose. This measure is defined for each DOF  $q$ , by

$$C_q = \frac{\left( \sum_{r=1}^N (\exp \psi_{qr})(f_e \psi_{f_e,qr}) \right)^2}{\sum_{r=1}^N (\exp \psi_{qr})^2 \sum_{r=1}^N (f_e \psi_{f_e,qr})^2} \quad (14.39)$$

i.e. a summation of the correlation coefficients of each DOF over all modes. A CoMAC value different from unity reveals a DOF where there is discrepancy between the FE model mode shapes and the experimental mode shapes. This could, of course, be due to problems in the FE model in which, sometimes, local stiffness of the structure can be hard to model correctly. A low CoMAC value can, however, also be due to a local error in the EMA result, so great care need to be taken when interpreting local discrepancies.

## 14.3 Application

### 14.3.1 Finite Element Model

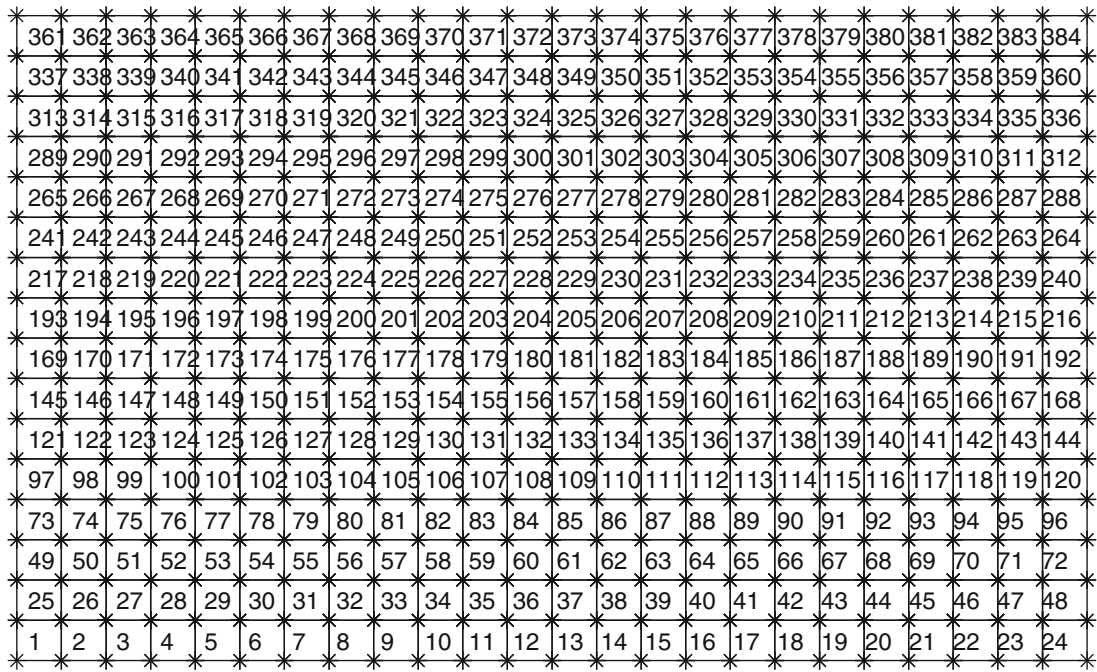
In this demonstration example a simple PMMA plate with dimensions  $533 \times 321$  mm and thickness 20 mm is analyzed. The plate is similar to the so-called IES-Plate proposed in [2], however, for practical reasons, the plate thickness was chosen slightly different from the IES-Plate, by choosing 20 mm thickness, which is a standard thickness in Europe. The Young's modulus for PMMA is reported in [2] to be 4.96 GPa, which is used as a first assumption. For the model in the present case, we use the measured mass density for the actual plate, of  $1.19810^3$  kg/m<sup>3</sup>.

The baseline finite element model, consisting of 16-by-24 elements with a total of 425 DOFs, is shown in Fig. 14.1. This mesh was chosen because it can easily be reduced to the 5-by-7 mesh used for the experiment. To assess the accuracy of the chosen mesh, two alternative meshes, one coarser and one more detailed were also tried, and for each of the three meshes, the ten lowest normal modes were computed. The results of these runs are tabulated in Table 14.1.

The results in Table 14.1 show that there is some increased stiffness for the coarser models, resulting in slightly higher eigenfrequencies. The middle grid density seems reasonable, however, so we decided to use this model.

In CALFEM the following steps were implemented in this demonstration example

1. Generate geometrical topology (nodes).
2. Generate element to nodal degree of freedom topology.
3. For each element calculate mass and stiffness matrices and assemble the data into global matrices.



**Fig. 14.1** FE model with 384 elements, 425 nodes

**Table 14.1** List of eigenfrequencies from normal mode solution of FE models with three different meshes; 7-by-11, 16-by-24, and 34-by-49 elements, respectively

Mode #	Eigenfrequencies, [Hz]		
	Mesh 1	Mesh 2	Mesh 3
1	145.2	145.2	145.5
2	150.0	150.3	150.4
3	340.7	340.5	340.4
4	403.8	401.5	401.0
5	412.8	413.4	413.5
6	522.3	522.0	521.8
7	620.0	616.4	615.3
8	752.5	751.7	750.9
9	846.6	827.5	823.1
10	1002.5	1005.7	1001.4

4. Solve the set of equations (eigenvalue extraction).
5. Post process the results.

## 14.4 Results: Simple Plate

### 14.4.1 FE Results

The first ten eigenfrequencies from a normal mode solution of the FE model with the mid grid density in Table 14.1 are shown in Table 14.2, together with the corresponding values from the EMA test. For the sake of simplicity, the modes are arranged in the order of the experimental modal analysis. Thus the first two FE modes have been swapped, as they appeared in the opposite order. This may be due to the fact that the shell element formulation yields too high bending stiffness. Application of more advanced plate theory could address this.

**Table 14.2** Finite element eigenfrequencies, experimentally obtained undamped natural frequencies and relative damping coefficients from experimental modal analysis of PMMA plate, and relative difference between frequencies

Mode #	FE eigenfreq.	Exp. natural freq. [Hz]	Diff. [%]	Damping [%]	Mode description
1	150.3	145.2	3.4	3.21	First torsion
2	145.3	147.0	-1.1	3.02	First bending, x
3	340.5	332.4	2.4	2.75	Second torsion
4	401.5	409.4	-2.0	2.50	Second bending, x
5	413.4	421.4	-1.9	2.42	First bending, y
6	522.0	518.8	0.6	2.34	Higher-order
7	616.4	608.3	1.3	2.33	Higher-order
8	751.7	745.4	0.8	2.27	Higher-order
9	827.5	830.9	-0.4	2.13	Third bending, x
10	1005.7	992.9	1.3	2.11	Higher-order

#### 14.4.2 EMA Results

Experimental modal analysis was conducted by impact excitation, using two reference accelerometers in two corners along one of the long axes of the plate. A 7-by-5 grid was used for the measurements. The structure was suspended using soft rubber cords which yielded rigid body modes below 5 Hz. Time domain signals were recorded and processed as described in [15, 19]. Shaker excitation is an alternative that could be used with similar results. An advantage with the PMMA plate for teaching purposes is that it is relatively easy to measure with good accuracy.

The polyreference time domain method [5] was used for estimating the poles, followed by a computation of the mode shapes using the frequency domain least squares method, in both cases using available functions in the ABRVIBE toolbox. The results of the experimental modal analysis are shown in Table 14.2, where the first ten modes are tabulated in the third column. It is relatively easy to successfully obtain at least 20 experimental modes, but for correlation with the FE model it is more realistic to select the ten lowest modes. As follows from Table 14.2, the ten lowest undamped natural frequencies ranges from approximately 145 to 993 Hz. Relative damping ratios ranges from 2.1% to 3.2%, and are tabulated in column five of Table 14.2.

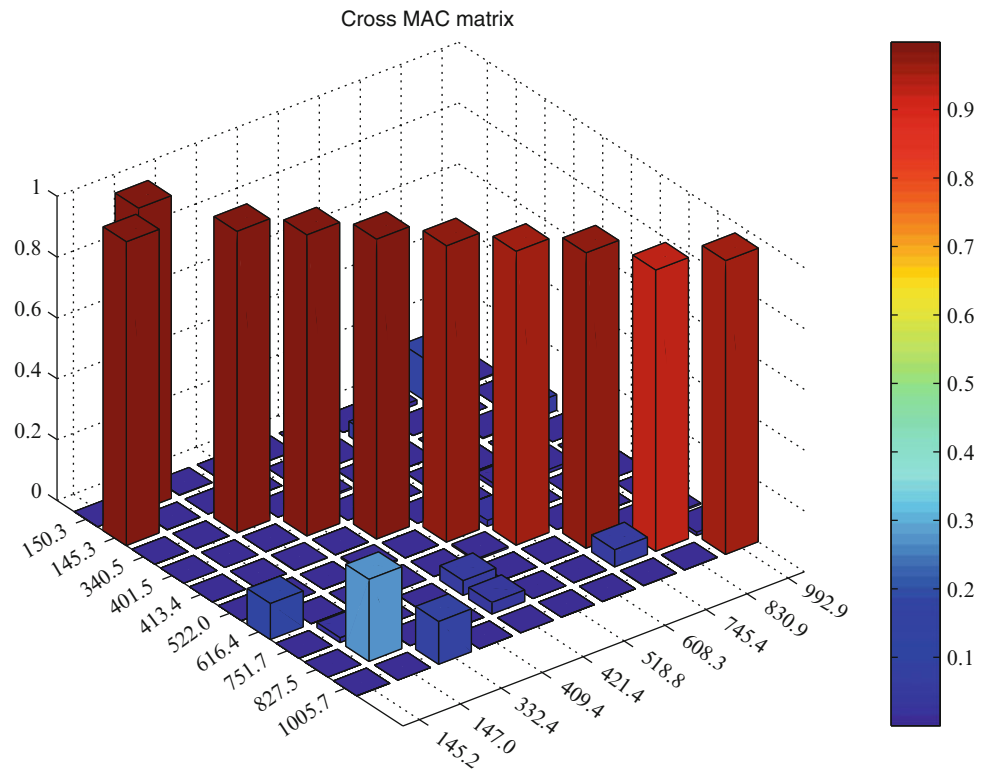
#### 14.4.3 FE Model Calibration

A comparison of the analytical and experimental results in Table 14.2 shows that the frequencies are relatively close, and that the two first modes appear in opposite order in the FE model solution compared to the experiment. For comparison with the experimental mode shapes, the mode shapes from the normal mode solution were reduced to every fourth DOF, corresponding to the 5-by-7 grid used for the experiment. A computation of the cross-MAC matrix showed that the mode shapes were very similar, with MAC values in excess of 0.97 except for mode 9 where the MAC matrix was 0.92. A plot of the cross-MAC is shown in Fig. 14.2.

A simple modification of the FE model is to match the frequency of the first bending mode of the FE model to the corresponding frequency from the experimental results. Since the first bending mode frequency can be assumed to be related to the square root of Young's modulus, this can be obtained by adjusting the Young's modulus by the square of the frequency ratio of the two frequencies. From Table 14.1 we thus get that the new Young's modulus should be approx.  $4.96 \cdot (147.0/145.3)^2 = 5.08$  GPa. The FE model was updated with this new Young's modulus in a second step, and the FE model was again solved for the first ten eigenfrequencies. The results are shown in Table 14.3, where it can be seen that the first bending mode (mode 2) is within 0.04% of the experimental frequency. The difference for the higher order bending modes, marked by asterisks (\*) in the table, are within approx. 1%. The torsion modes, however, are generally slightly overestimated. This is likely a result of the approximations used in the definition of the shell elements used. In our opinion this is good point of the present, simplified exercise, as it gives a reason to discuss the approximations and limitations of various element types.

With the model calibration thus successfully done, the CoMAC values were calculated for all points. The CoMAC values were thus found to be within 0.9–1.0 for all modes. There was therefore not found to be any reason to investigate any local discrepancies between the experimental and analytical mode shapes in this case, which is rather natural considering the simple structure.

**Fig. 14.2** Cross-MAC matrix between experimental modal analysis mode shapes and normal modes of first FE run



**Table 14.3** List of eigenfrequencies of FE model after modifying Young's modulus, and undamped natural frequencies from experimental modal analysis. The bending modes are marked with asterisks (\*) for reference. It is seen that the bending modes are relatively well modelled whereas the frequencies of the torsion modes are typically overestimated by the shell elements

Mode #	Natural frequency [Hz]		Difference [%]
	FE Model	EMA	
1	151.8	145.2	4.37
2	147.0	147.0	0.04*
3	344.0	332.4	3.40
4	406.2	409.4	-0.80*
5	417.0	421.4	-1.06*
6	526.9	518.8	1.52
7	623.0	608.3	2.37
8	759.3	745.4	1.82
9	836.9	830.9	0.71*
10	1016.7	992.9	2.34

## 14.5 Conclusions

The simple test case demonstrates the possibility to teach advanced structural dynamics topics like test-analysis verification using open software. Using open software it is possible to investigate influence of other finite element formulations than in this case a simple shell element with respect to eigenfrequencies and mode shapes. Introduction of pre-test methods using a model reduction scheme like Guyan could also easily be made. Furthermore, the paper discusses some advantages of using a simple structure like the IES plate. The main advantages can be summarized thus:

- Using MATLAB (or GNU Octave) makes it possible for the student to look at variables included such as mass and stiffness matrices, mode shapes etc. for deeper insights into the mathematics involved.
- The structure is easily modeled to a sufficient accuracy using shell elements, which are computationally inexpensive.
- The experimental modal analysis of the plate can be done in a few hours lab time, using either impact testing or shaker testing.
- The correlation and updating of the FE model is done very easily and transparently.
- If more advanced options such as model reduction etc. is wanted, the immediate access to the mass and stiffness matrices in MATLAB is making the process very easy.

## References

1. Ristinmaa M, Sandberg G, Olsson K-G (2000) CALFEM as a tool for teaching university mechanics. *International journal of innovation in science and mathematics education*, 5
2. Gregory D, Smallwood D (1989) Experimental results of the IES Modal Plate. *J Environ Sci*, Nov/Dec: 15–21
3. Proakis JG, Manolakis DG (2006) *Digital signal processing: principles, algorithms, and applications*. Prentice Hall, Upper Saddle River, New Jersey
4. Brown D, Allemang R, Zimmerman R, Mergeay M (1979) Parameter estimation techniques for modal analysis. SAE Technical Paper 790221
5. Vold H, Kundrat J, Rocklin TG, Russell R (1982) A multiple-input modal estimation algorithm for mini-computers. SAE Technical Paper 820194
6. Maia N, Silva J (eds) (2003) *Theoretical and experimental modal analysis*. Research Studies Press, Baldock
7. Brandt A (2012) ABRVIB, A MATLAB/Octave toolbox for noise and vibration analysis and teaching. Revision 1.2. Feb 2013, <http://www.abravibecom>
8. Ottosen N, Petersson H (1992) *Introduction to the finite element method*. Prentice Hall, New York
9. Zienkiewicz OC, Taylor RL (1991) *The finite element method – vol 2. Solid and fluid mechanics, dynamics and non-linearity*, 4th edn. McGraw Hill, London
10. Cook RD, Malkus DS, Plesha ME (1989) *Concepts and applications of finite element analysis*, 3rd edn. Wiley, New York
11. Craig RR Jr, Kurdila AJ (2006) *Fundamentals of structural dynamics*, 2nd edn. Wiley, Hoboken
12. Timoshenko SP, Woinowsky-Krieger S (1959) *Theory of plates and shells*, 2nd edn. McGraw-Hill, New York
13. Austrell P-E, Dahlblom O, Lindemann J, Olsson A, Olsson K-G, Persson K, Petersson H, Ristinmaa M, Sandberg G, Wernberg P-A (2004) CALFEM – a finite element toolbox, version 3.4, KFS i Lund AB, Lund
14. Baker M (1992) Review of test/Analysis correlation methods and criteria for validation of finite element models For dynamic analysis. In: *Proceedings of 10th international modal analysis conference (IMAC)*, San Diego
15. Brandt A (2011) *Noise and vibration analysis – signal analysis and experimental procedures*. Wiley, Chichester
16. Chu J, Saloniemi E-L (2002) Consideration to FEM-formulation in partial damping layers for complex structures such as vehicle floor. Master's Thesis Report, ISSN 0238-8338, Department of Technical Acoustics, Chalmers University of Technology
17. Weber J, Benhayoun I (2010) Squeak, rattle simulation – a success enabler in the development of the new saab 9-5 cockpit without prototype hardware. *SAE Int J Passeng Cars Mech Syst* 3(1):936–947
18. Lieven NAJ, Ewins DJ (1988) Spatial correlation of mode shapes, the coordinate modal assurance criterion (CoMAC). In: *Proceedings of 6th international modal analysis conference (IMAC)*, Kissimmee
19. Brandt A, Brincker R (2010) Impact excitation processing for improved frequency response quality. In: *Proceedings of 28th international modal analysis conference*, Jacksonville

# Chapter 15

## Testing Anti-Ram Barrier Protection Systems

Kurt Veggeberg

**Abstract** This is an overview of the instrumentation system used for full-scale testing of anti-ram barrier protection systems for the U.S. Department of State (DOS) to enhance the security of their facilities while maintaining esthetics by Penn State University's Larson Transportation Institute. The Larson Institute's Crash Safety Research Team has already successfully run crash tests to stop large vehicles traveling at high speeds using this instrumentation system. In these tests, more than 50 channels of dynamic strain, acceleration and temperature were monitored. The tests outlined here focus on innovative and optimized anti-ram barrier designs. It is anticipated that knowledge gained will enhance the nation's infrastructures and capabilities to protect people and facilities against acts of violence and terrorism. An objective is to balance the level of protection and the esthetics necessary to promote a welcoming atmosphere consistent with the U.S. diplomatic mission.

**Keywords** Crash test • Strain gages • Accelerometers • LabVIEW • National instruments

### 15.1 Introduction

Penn State's Thomas D. Larson Pennsylvania Transportation Institute (LTI) established a 5 year cooperative agreement with the U.S. Department of State (DoS) in 2010 to help enhance the security of DoS interests worldwide through research and development related to anti-ram barrier protection systems. The project utilizes the University's full-scale Test Track Facility. Administered by the Larson Institute, the agreement engages faculty, graduate students and researchers from the institute and several academic areas, including affiliates of the Protective Technology Center (PTC) in the Department of Civil and Environmental Engineering, the Department of Mechanical and Nuclear Engineering and the Colleges of Information Sciences and Technology and Arts and Architecture.

LTI's full-scale Transportation Research Facilities include a test track facility designed to accommodate a broad range of research activities. The facility features a 1-mile oval, a large vehicle handling area, and a vehicle durability-testing course that allow additional pavement, vehicle, and appurtenance testing. The facility includes a special test section where test surfaces can be installed on a temporary basis for testing. Current activities include crash testing of anti-terrorist barriers and comprehensive testing of new bus models. A2LA (American Association for Laboratory Accreditation) accredited the Vehicle Systems and Safety program for technical competence in the field of mechanical testing according to ISO/IEC 17025:2005 General Requirements for the Competence of Testing and Calibration Laboratories (Fig. 15.1).

### 15.2 Testing Anti-Ram Barriers

The Protective Technology Center studies effects of blast and high strain rate impact on structures. The Larson Institute's Crash Safety Research Team has already conducted multiple successful crash tests for the DoS using the Chameleon data acquisition system developed by PVI Systems such as lamp and bus stops featured here.

---

K. Veggeberg (✉)  
National Instruments, 11500 N. Mopac, Austin, TX 78759, USA  
e-mail: [kurt.veggeberg@ni.com](mailto:kurt.veggeberg@ni.com)





**Fig. 15.1** Full-scale research facilities at Pennsylvania Transportation Institute

The PTC has a long-standing history related to studying the effects of blast and high strain rate impact on structural systems and components experimentally and computationally. This work has been completed for both government agencies and private sponsors and includes examining protective barrier and sign systems subjected to air-blasts and vehicular collisions.

The Department of State's (DoS) physical security concept is to create a layered or "tiered" defensive system which consists of both active and passive perimeter barriers to delay intruders. The Department had a performance standard and testing procedure for both active entrance barriers and passive perimeter barriers designated as "vehicle-impact rated barriers," or "anti-ram barriers." The previous standard Department of State (DoS) SD-STD-02.01, Vehicle Crash Testing of Perimeter Barriers and Gates, Revision A, dated March 2003 was retired in 2009 in favor of testing under ASTM F2656 – 07 Standard Test Method for Vehicle Crash Testing of Perimeter Barrier [1]. This test method provides a structured procedure to establish a penetration rating for perimeter barriers subjected to a vehicle impact. Knowing the penetration rating provides the ability to select an appropriate barrier for site-specific conditions around a facility.

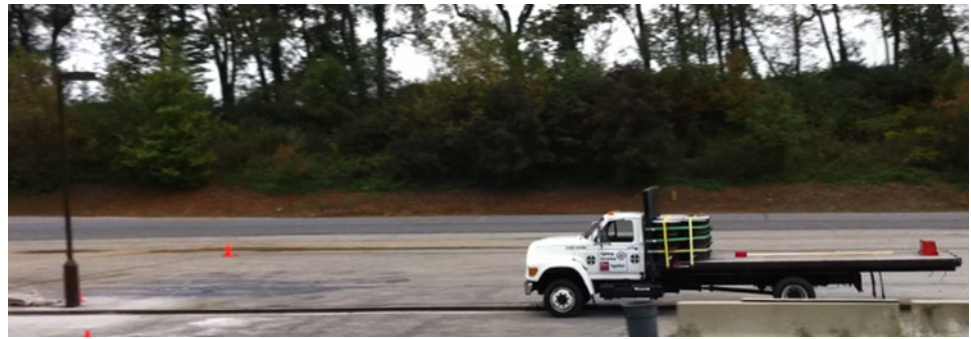
Barrier crash testing is expensive. It must be done at a State Department-authorized facility like the Larson Institute, which instruments the barrier and vehicle, conducts the test, analyzes the instruments and crash films, and issues a test report. A barrier supplier may spend \$100,000 or more to build the prototype, transport it, install it, test it, clean up the debris, and restore the test track.

Research facilities include a rail guidance system for full-scale crash testing at speeds required for specific ratings. High speed cameras are mounted at various locations to provide additional crash test information (Fig. 15.2).

### 15.3 Data Acquisition System

Penn State's Larson Institute needed a turnkey data acquisition system within a short time frame for full-scale tests of anti-ram barrier protection systems for the U.S. Department of State to enhance the security of embassies and other facilities overseas.

**Fig. 15.2** Lamp post barrier testing using truck being towed along rail guidance system



**Fig. 15.3** Data acquisition system and lamp post ready for crash testing



The Chameleon system by PVI Systems was selected. It provides built-in functionality for diverse data acquisition applications for I/O channel synchronization, time and frequency acquisition, live monitoring of all channels, and post-acquisition data display and processing. It supports reconfigurable hardware for multiple test programs, which is important for the variety of tests that will be needed to run. The Chameleon turnkey data acquisition system integrated the National Instruments PXI hardware platform with source control based on NI LabVIEW and data acquisition software capable of measuring over 50 channels of dynamic strain, acceleration and temperature needed for these tests.

The system includes an embedded controller with an 18-slot PXI chassis with space for expansion. The ability of the NI PXIe-4331 high speed bridge input modules to provide the signal conditioning needed for the strain gages and the NI PXIe-4499 dynamic signal acquisition module for accelerometers along with their high speed was a major consideration in the selection. PVI Systems was quickly able to add support for an NI PXIe-4353 32 channel thermocouple module to the data acquisition since it was an NI LabVIEW based application. Additionally, the NI PXI-6682 timing and synchronization module allows precision time-stamping of data (Fig. 15.3).

The Chameleon data acquisition system provides built-in functionality for diverse data acquisition applications for I/O channel synchronization, time and frequency acquisition, live monitoring of all channels, and post-acquisition data display and processing. It supports reconfigurable hardware for multiple test programs, which is important for the variety of tests that will be needed to run in the future.



## 15.4 Conclusion

The Larson Institute's Crash Safety Research Team conducted several successful crash tests for the U.S. Department of State involving various structures designed by the Larson Institute to stop a heavy truck traveling at high speed using this data acquisition system (Figs. 15.4 and 15.5). It is anticipated that knowledge gained from the 5-year cooperative agreement will enhance the nation's capabilities to protect people and facilities against acts of violence and terrorism domestically and abroad. An objective is to balance the level of protection and the aesthetics necessary to promote a welcoming atmosphere consistent with the U.S. diplomatic mission.



**Fig. 15.4** Lamp post crash test aftermath



**Fig. 15.5** Bus stop crash test aftermath

**Acknowledgements** Thanks to Professor Daniel G. Linzell of Penn State University, Associate Professor, Director Protective Technology Center and J.R. Uzzolino of PVI Systems for sharing details from these tests.

## Reference

1. ASTM Standard F2656 – 07 (2009) Standard test method for vehicle crash testing of perimeter barriers. ASTM International, West Conshohocken. doi: [10.1520/F2656-07](https://doi.org/10.1520/F2656-07), [www.astm.org](http://www.astm.org)

# Chapter 16

## Fiber Optic Accelerometers and Sensors for Dynamic Measurements

Kurt Veggeberg

**Abstract** The purpose of this presentation is to provide an understanding of the current state-of-the-art in fiber Bragg grating (FBG) sensors and instrumentation for dynamic and vibration testing. Innovation in the optoelectronics and fiber-optic communication industries has significantly reduced optical component prices and improved quality. By leveraging these economies of scale, fiber-optic sensors and instruments have moved from experimental research applications in the lab to broad usage and applicability in field applications such as structural health monitoring. The main sensing parameters for these tests have been strain and/or temperature and now accelerometers with FBG sensors as the measurement medium. The discussion includes a brief overview of FBG sensors, the functionality of FBG sensors as accelerometers, aspects of commercially available instrumentation for monitoring the accelerometers, and applications where they are being used. Specific applications include the use of optical fiber based sensors in the S Blade wind turbine structural health monitoring project where FBG sensor arrays, along with several other sensing technologies for direct comparison, were surface-mounted and embedded in the composite structure of a wind turbine blade and a structural health monitoring system for restoration work on the historic Duomo di Milano.

**Keywords** Fiber Bragg grating • Accelerometers • Fiber optic sensors • Structural health monitoring • National instruments

### 16.1 Introduction

Optical sensing is ideal for applications where conventional electrical sensors such as foil strain gages, thermocouples, and vibrating wires have proven ineffective or difficult to use due to challenging environmental conditions or measurements taken over long distances. The features and benefits of fiber Bragg grating (FBG) optical sensing include the following:

- Nonconductive
- Electrically passive
- Immune to electromagnetic interference (EMI)-induced noise
- Sensor measurements over very long distances (10+ km)
- Daisy chain multiple sensors on a single fiber

Large and lightweight structures can benefit from the distributed single fiber architecture to simplify installation and reduce weight. The nonconductive and noncorrosive nature of the fiber benefits outdoor and industrial applications where hazardous gases and voltages might be present. Also, the immunity to EMI removes the need for expensive and often difficult signal conditioning required for measurements near noisy sources such as power transformers. FBG optical sensing can benefit many applications in areas such as energy, civil infrastructure, and transportation monitoring. Fiber optic sensors for the measurement of strain, temperature, and pressure are available with performance comparable to traditional sensors.

---

K. Veggeberg (✉)  
National Instruments, 11500 N. Mopac, Austin, TX, 78759 USA  
e-mail: [kurt.veggeberg@ni.com](mailto:kurt.veggeberg@ni.com)

**Fig. 16.1** Micron Optics FBG accelerometer measures acceleration from DC to a few hundred hertz



Applications with severe operating environments are promoting the development of accelerometers based on FBG optical sensing offering the benefits of EMI immunity and lightning and corrosion resistance needed for outdoor installations (Fig. 16.1).

## 16.2 Energy

Monitoring structures that generate, produce, distribute, and convert electrical power introduces many challenges that can be addressed with FBG optical sensing. Whether it is a windmill requiring a lightweight solution or a hydroelectric turbine needing an EMI-resistant system, optical sensing has unique attributes that make it suitable for these traditionally difficult applications.

For example, monitoring the structural integrity of a wind turbine blade with electrical sensors would often result in noisy measurements because of long copper lead wires. With optical sensing, accurate and noise-free strain measurements on wind turbine blades are possible with little added weight to the structure. Furthermore, the nonconductive and distributed nature of optical fibers lends itself well to many uses in oil and gas applications, including pipeline monitoring and downhole monitoring.

Sandia National Labs deployed an FBG optical sensing system based on NI LabVIEW software to monitor wind turbine blades. This resulted in a 94% reduction in cable weight, 90% reduction in installation time, increased measurement capabilities, and removed the need for external calibration. The scan frequency of the Optical Interrogator from Micron Optics allowed a scan rate of 1 kHz, making it possible to measure dynamic strain. New models are being introduced in a PXI format capable of scanning up to 2 Mhz (Figs. 16.2 and 16.3).

## 16.3 Civil

Structural health monitoring (SHM) systems based on electrical sensors often face significant environmental challenges. Consider a suspension bridge across a bay, such as the Donghai Bridge in China. This type of bridge may span a mile and a half or more. It can be exposed to harsh saline environments and could even occasionally be struck by lightning. An electrical monitoring system would require the installation of countless wires, a lightning grounding system, periodic external calibration, and the potential maintenance of corroded and/or degrading sensors.

Deployment of a system based on LabVIEW and PXI hardware that uses both electrical and optical sensors to characterize the structural behavior of the bridge. The system also uses GPS to synchronize the various systems along the bridge (Fig. 16.4).

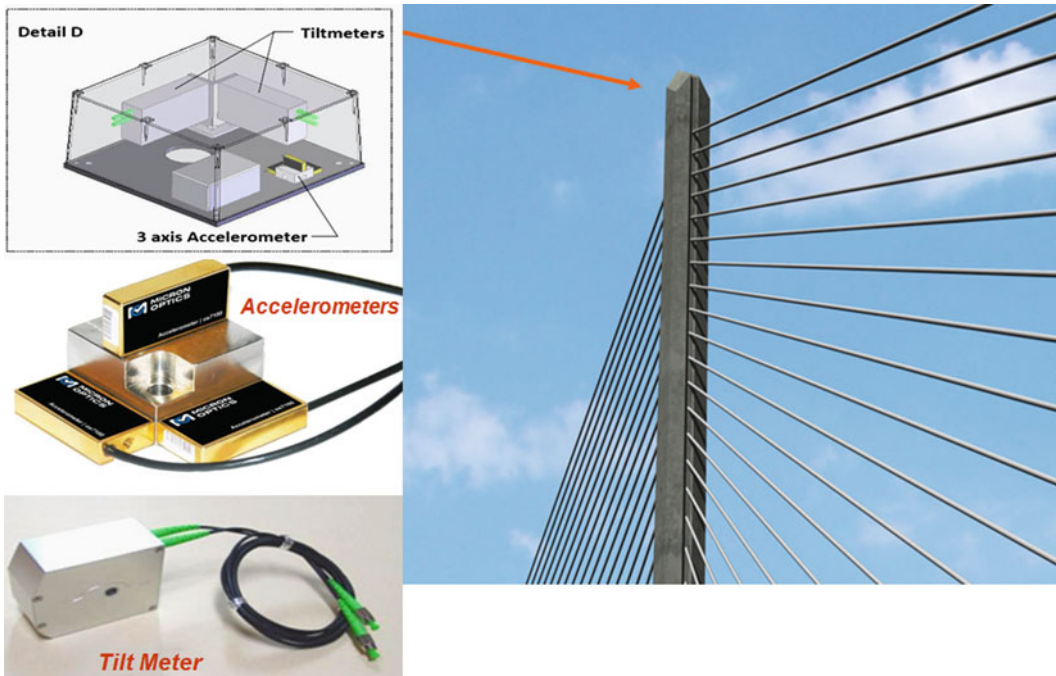
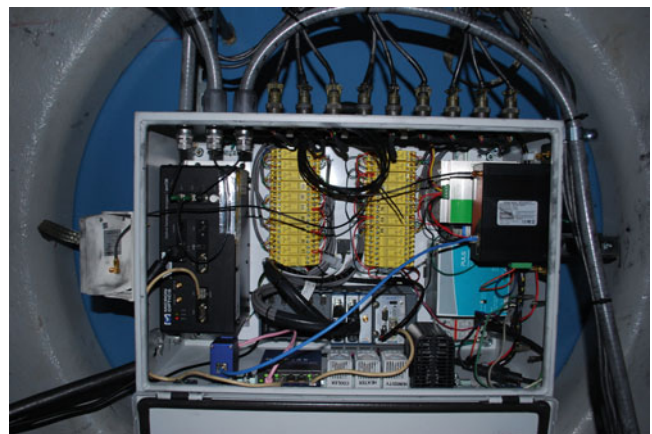
Weight, size, and harsh environmental requirements can pose significant challenges to implementing an electrical monitoring system. FBG optical sensors alleviate these challenges by providing lightweight distributed sensor measurements that are immune to corrosion, high voltage, and EMI-induced noise. Also, because of the longevity and ease of installation of FBG optical sensors and lack of need for external calibration, these sensing systems can be deployed reliably for decades without needing any maintenance – this is especially beneficial for long-term railway and ship hull monitoring. The ability to have multiple sensors on a single, very thin fiber dramatically reduces the weight of the monitoring system, which is especially important in aerospace applications.



**Fig. 16.2** Instrumentation for fiber optic sensors mounted in a “wedding cake” configuration on a wind turbine rotor



**Fig. 16.3** Fiber optic interrogator and data acquisition system mounted on rotor



**Fig. 16.4** Fiber optic accelerometers mounted on bridge tower





**Fig. 16.5** Fiber optic sensors mounted on cupola of the Duomo di Milano

Researchers at the Politecnico di Milano deployed a structural health monitoring system for restoration work on the historic Duomo di Milano [1]. After using NI CompactRIO hardware for the initial phase of monitoring, the researchers transitioned the system to PXI Express hardware to incorporate fiber Bragg grating (FBG) optical sensors for ensuring stable measurements in a challenging environment.

Located in Milan, Italy, the Duomo di Milano is one of the largest and most impressive Gothic structures in the world. Construction of the elaborate Duomo started in 1386 and continued for more than five centuries. In 1762, one of the main features of the Duomo, the main spire, or *Guglia Maggiore*, was erected at a height of 108.5 m and topped with the gold Madonnina statue of the Virgin Mary. In 2010, the Veneranda Fabbrica del Duomo, the organization in charge of the cathedral's preservation and maintenance, undertook the task of restoring the marble of the main spire, which was degraded by weather and pollution.

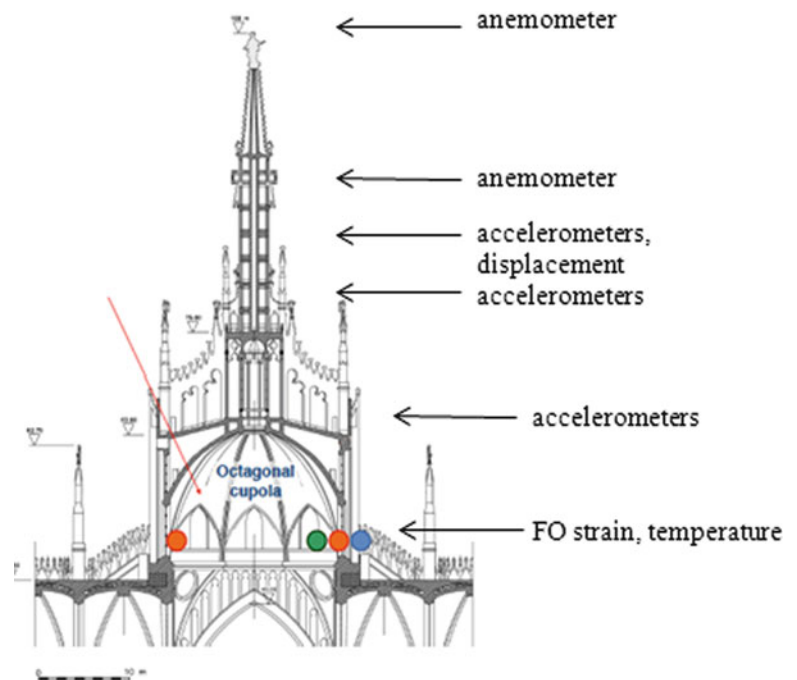
The structure was instrumented with a variety of sensors to monitor wind conditions, the position and movement of the scaffolding and spire, and the load on the cupola. Because of the need for long-term reliable monitoring, and past experiences with lightning destroying previous instrumentation systems, the development team decided to use FBG optical strain gages to monitor the load of the scaffolding on the cupola. Optical strain gages mounted on each of the eight ribs of the octagonal cupola, which supports the main spire, continuously monitor longitudinal deformation of the ribs. Each strain gage is accompanied by an FBG sensor for temperature compensation, and all sensors are multiplexed onto two optical fibers that are routed to the PXI Express system (Fig. 16.5).

The scaffolding and spire are also instrumented with several displacement sensors to measure scaffolding movement relative to the spire, accelerometers to monitor the global dynamic behavior of the spire and scaffolding, linear variable differential transformers (LVDTs) to monitor crack openings, and anemometers to capture wind speed and direction (Fig. 16.6).

The PXI system, located in the bell room near the base of the cupola, includes the NI PXIe-4844 optical sensor interrogator, which acquires data from fiber-optic strain gages and temperature sensors and provides accurate, sensitive, and stable measurements. Currently, the system includes an NI CompactRIO chassis with NI 9,234 dynamic signal acquisition (DSA) modules to acquire data from the electrical accelerometers and LVDTs.

The need to detect very small changes in mechanical strain on the cupola meant that any thermal effects caused by daily temperature cycles on the sensors and on the marble must be accurately compensated for. Therefore, the team set up a

**Fig. 16.6** Sensor locations the Duomo di Milano



system in the Politecnico di Milano laboratory to fully characterize the thermal effects on the measurements. A sample block of marble and a mounted FBG strain sensor were put into an environmental test chamber. An NI PXIe-4844 collected data while the sample and sensor cycled repeatedly from  $-5^{\circ}\text{C}$  to  $40^{\circ}\text{C}$ . The results were used to accurately remove all thermal effects on both the FBG and the marble material.

The need for very stable measurements over long time periods as well as immunity to lightning were two key reasons for using the NI PXIe-4844 optical sensor interrogator and FBG sensors. The PXI system is now continuously monitoring the spire, cupola, and scaffolding through the integrated real-time measurement of both optical and traditional electrical sensors. In fact, the system is now considered a security system by the personnel working on the scaffolding, who have been trained to work with the software and interpret the output. This has proven to be very valuable, as demonstrated after the 2012 earthquakes in Northern Italy. Data collected by the monitoring system was a major help in assessing the integrity of the structures and validating that it was safe to resume restoration work on the spire.

In conclusion, electrical sensing technologies have been successfully deployed in countless applications. However, with the introduction of optical sensing, engineers and scientists can now perform measurements that were previously impractical or, in some cases, impossible with conventional electrical sensors. At present, many real-world applications already use both approaches to harness the combined benefits of electrical and optical sensing. Optical sensing provides reliable and robust solution for very common sensing challenges. It avoids signal corruption or damage from electrical and electromagnetic fields and interference. They can survive in explosive and chemically aggressive environments. They reduce cable costs for large installations. It is possible to instrument DUT with high density of small, lightweight sensors

**Acknowledgements** Thanks to Dr. Alfredo Cigado, Professor of Mechanical Measurements, at the Politecnico di Milano and Tom Graver of Micron Optics for sharing information about applications that they have been involved in.

## Reference

1. National Instruments Fiber-optic strain gages protect restoration of milan cathedral (2011). <http://sine.ni.com/cs/app/doc/pid/cs-14937>

# Chapter 17

## Nonlinear Model Tracking for Varying System Geometries

Timothy A. Doughty, Matthew R. Dally, Mikah R. Bacon, and Nick G. Etzel

**Abstract** Although linear models can successfully explain many behaviors for physical systems, they are unable to describe the complexities of nonlinear systems. Therefore, health monitoring methods based on linear models run the risk of misidentifying nonlinear behavior as failing. Nonlinear Model Tracking (NMT), a health monitoring technique, is used here on a slender cantilevered beam subject to harmonic excitation near the beams second natural frequency, and the fatigue due to excitation. A second order nonlinear differential equation model has been assumed with cubic stiffness. This method uses the Continuous Time based nonlinear system identification technique allowing for model parameter estimation based on stimulus and response. The robustness of this method is demonstrated in its implementation and application to differing system geometries. These geometries studied here illustrate the reliability of this methodology indifferent to the system under observation. This method has shown, with repeatability, the onset of crack initiation and growth, well in advance of catastrophic failure, and has also been shown to work when the healthy system behaves with distinct nonlinearities, where linear techniques fail. The results indicate that NMT can be used for many different systems.

**Keywords** Nonlinear • Vibrations • Nondestructive health monitoring • Modal • Failure

### 17.1 Introduction

In an oscillating system, damage is commonly the result of system fatigue. Plasticity, crack initiation, and crack growth ultimately lead to failure. It is of great interest to develop a method to determine and track damage and its evolution, as failure that is detected early can be avoided. In recent decades the area of Nondestructive Evaluation (NDE) has greatly advanced; see Doebbling et al. [1] for a comprehensive view. Most NDE procedures use linear approximations despite the widespread recognition of nonlinear behavior in all physical systems [2–6] despite the well-established and long-studied nonlinear nature of crack dynamics in vibrating structures [7]. New methods are still emerging for crack detection in vibrating systems as the field of NDE advances [8–11].

Here, The Nonlinear Model Tracking (NMT) is used on a variety of system geometries. System Identification is performed on a slender cantilever beams excited near their second natural frequency. Cantilever beams are understood to be the building block for more complicated structures, and the slenderness allows for more pronounced nonlinear behavior. The second natural frequency is chosen due to dynamic range of the shaker used in the study. Stimulus and response data are fed into the Continuous Time System Identification and the resulting parameter estimates allow for the mapping of the nonlinear parameter over time [12]. This method has been shown to effectively predict catastrophic failure through changes in the nonlinear behavior of the system well in advance of the failure of the beam.

---

T.A. Doughty (✉) • M.R. Dally • M.R. Bacon • N.G. Etzel  
University of Portland, 5000 N Willamette Blvd, Portland, OR 97203, USA  
e-mail: [doughty@up.edu](mailto:doughty@up.edu); [dally14@up.edu](mailto:dally14@up.edu); [bacon14@up.edu](mailto:bacon14@up.edu); [etzell1@up.edu](mailto:etzell1@up.edu)

## 17.2 Background

Previous applications of NMT have shown that, while linear models are easy to work with, they fail to properly track the health of a system behaving nonlinearly accurately. If a linear model is assumed, a healthy system could be misidentified as failing due to a change in behavior that is actually attributed to the system's nonlinearity. For example, some popular linear NDE methods that monitor the natural frequency of a system over time will treat a change in natural frequency as an indication of plastic deformation or crack initiation. Nonlinear models can describe the healthy, complex behavior of systems, as well as the healthy linear behavior. When the nature of the nonlinearity changes, so must the parameters in the model or the model itself. This change in the nonlinearity serves as the early indicator of the onset of failure.

Through ongoing study, it has been shown to successfully detect damage significantly prior to catastrophic failure without exhaustive efforts to identify an accurate nonlinear model. Previous studies have also shown the amount of data required to identify the system parameters is minimal, and that a generic set of data could be used for beams of similar types. This allows the user to identify the healthy system a priori, so the health monitoring can be performed insitu with no pre-operational testing. These findings speak to the method's robustness and relative ease in application.

In short, the method requires establishing a simple nonlinear model to be used for the system studied. It has been determined that the best model for the NMT method was the simplest nonlinear model considered, which included a simple cubic stiffness term [13].

With the best model chosen, Continuous Time System Identification is performed with simultaneously with a range of steady state records of healthy system stimulus and response near resonance, and an updated record of real-time data for the aging beam. Any variation in the system behavior resulted in large changes in the nonlinear parameter estimate. Mapping this nonlinear parameter serves as an indicator of the beam's health.

To collect data for populating the identification algorithm, a typical beam is given an impulse and sweep stimulus to determine estimates of resonance and potential for multimodal response. Then the healthy data is taken as a series of steady state excitation and response records near resonance. Then the beam is excited near-resonant frequency at high excitation levels and allowed to oscillate until failure.

## 17.3 Theoretical Model Development

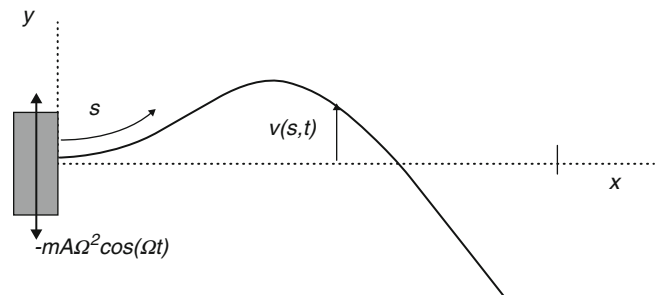
In this study, a horizontally mounted cantilever beam is vertically excited. The excitation frequency is near the beam's second natural frequency, allowing the spatial dependence of the model to be assumed. The theoretical configuration is shown in Fig. 17.1.

In this configuration,  $v$  is the beam's vertical displacement,  $m$  is mass per unit length,  $c$  is damping per unit length,  $D_\xi$  is the bending stiffness,  $A$  is the amplitude of base displacement,  $\Omega$  is the frequency of excitation,  $t$  is time,  $s$  is a reference variable, and  $L$  is the beam length.

The partial differential equation model for the transverse displacement of a cantilevered beam with nonlinear bending stiffness developed in [14] is given with the following partial differential equation and associated boundary conditions:

$$m\ddot{v} + c\dot{v} + D_\xi \left\{ v^{iv} + \left[ v' (v' v'') \right]' \right\} = -mA\Omega^2 \cos(\Omega t), \quad (17.1)$$

$$v(0, t) = v'(0, t) = v''(L, t) = v'''(L, t) = 0. \quad (17.2)$$



**Fig. 17.1** Theoretical configuration for base-excited cantilever beam demonstrating the second mode shape

In the case of the modal excitation, the spatial dependence is assumed to be known. Setting  $\phi(s)$  to be the orthonormalized mode shape which satisfies the stated boundary conditions, we obtain:

$$\Phi(s) = C [\sin(\beta s) - \sinh(\beta s) - \Psi (\cos(\beta s) - \cosh(\beta s))] \quad (17.3)$$

Where:

$$\Psi = \frac{\sin(L\beta) + \sinh(L\beta)}{\cos(L\beta) + \cosh(L\beta)} \quad (17.4)$$

and:

$$\beta L = 4.694. \quad (17.5)$$

Letting  $v(s, t) = a(t) \cdot \phi(s)$ , the nonlinear partial differential equation can be reduced to the form:

$$m\ddot{a} + c\dot{a} + ka + \alpha a^3 = F(t), \quad (17.6)$$

where:

$$k = \left\{ D_{\xi} \int_0^L \phi \phi^{iv} ds \right\}, \quad (17.7)$$

$$\alpha = \left\{ D_{\xi} \int_0^L \phi \phi'^3 + 4\phi \phi' \phi'' \phi''' + \phi \phi'^2 \phi^{iv} ds \right\}, \quad (17.8)$$

and:

$$F(t) = \int_0^L \phi ds (-mA\Omega^2) \cos(\Omega t). \quad (17.9)$$

With this nonlinear model, a collection of forcing,  $F(t)$ , and response,  $a(t)$ , can be used to estimate the system parameters. Note that if  $\alpha$ , the parameter accounting for nonlinearity, is zero then the result is the standard model for a forced mass-spring-damper system. A previous study showed the cubic nonlinearity term outperformed quadratic and combination nonlinearities. The cubic nonlinearity term is understood to be the most significant nonlinearity in base excited cantilever beam systems.

## 17.4 System Identification

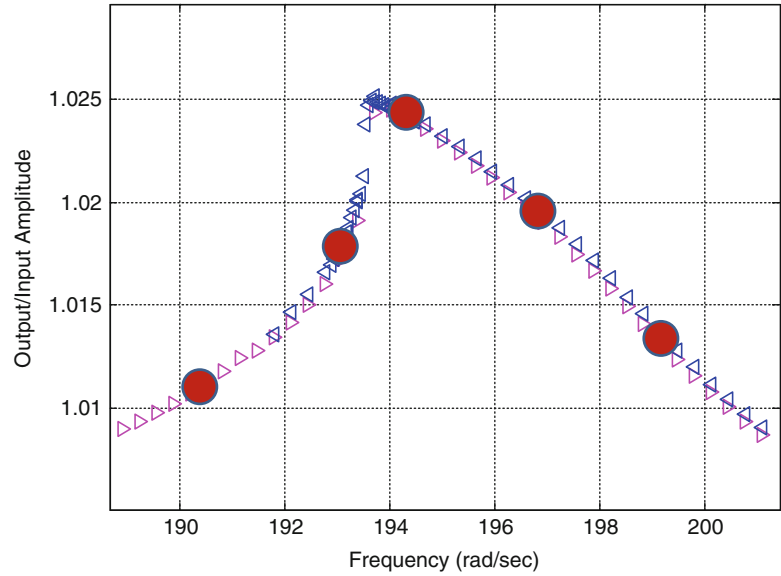
With this nonlinear system model, all system parameters can be estimated based on input and output data ( $F(t)$  and  $a(t)$  respectively). Normally, linear parameters can be estimated through theoretical relationships or experimental validation, but these traditional methods were not used in this study. Disregard for traditional methods was motivated by previous studies which indicated that physically accurate linear parameters was detrimental to the success of the NMT Method. Linear parameters were instead back-solved for in a least squares sense using preliminary time data. (Note: the resulting values may have no physical meaning, but are useful and appropriate for this method.) It is believed that these values differ from expected values because they absorb some of the inaccuracies in the described system model.

Identifying parameters in nonlinear systems is inherently more complex than for linear systems. The system must be excited so that the nonlinear behavior is more pronounced. This nonlinear behavior is then manifested in the data, allowing for the system to be properly identified. Even with suitable data, the method of identification is not obvious. Nonlinear differential equations typically have no analytical solution, so the formulation of the algorithms is dependent on the method of approximating the solution to the governing model. While the methods of Multiple Time Scales and Harmonic Balance have both proven to be effective in identifying nonlinear model parameters [15], the Continuous Time Method was chosen here because of its ease of application and acceptance of transient data.

When applying the Continuous Time Method, input and output accelerations are collected, scaled with respect to node and sensor placement, and integrated to give velocity and position. The position vector is then cubed and the linear vectors



**Fig. 17.2** Example of nonlinear frequency response curve showing steady state record locations (in red)



are collected in a matrix relation. The resulting matrix can then be solved in a least squares sense for parameter estimates. Arranging (17.3) into matrix form gives:

$$[\ddot{a}(t) \quad \dot{a}(t) \quad a(t) \quad a(t)^3] [m \quad c \quad k \quad \alpha]^T = F(t), \quad (17.10)$$

and:

$$\{a(t)^3\} [\alpha] = \{F(t) - \ddot{m}a(t) - c\dot{a}(t) - ka(t)\}. \quad (17.11)$$

Equation 17.10 allows for the direct estimation of the parameter vector. Because of this, (17.10) can be rearranged to (17.11) so that  $\alpha$  is the only unknown in the matrix relation. The nonlinear parameter can then be approximated by solving (17.8) in a least squares sense, where the state vectors are concatenated steady state time responses from select excitation frequencies.

Although, it is not the case, the method can be appreciated if one considers the estimation to be a parametric curve fit to the nonlinear frequency response function for the system. Figure 17.2 is a theoretical representation of this, where the red dots indicate the frequencies selected for the steady state data. The analytic form of the model is not known, so experimental data must be compiled to find the best fit for the curve. With this method it is very important to recognize the importance of collecting steady state data for more than one sinusoidal forcing frequency, as only one steady state frequency would result in poor parameter estimates. For this reason steady state data is collected over a range of frequencies around the system's second natural frequency. Steady state data points were chosen at frequencies near resonance because it has been experimentally shown to accurately identify similar nonlinear models [11, 16].

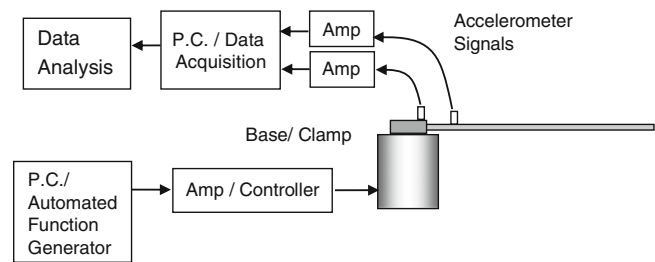
Also, previous investigations have proven that this reuse of preliminary data is effective [13]. Beams of the same type behave the same way. The nonlinear model, parameter estimates, and the healthy steady state data can be used for similar beams, identified by geometry, material, boundary conditions, and mode of response.

Streaming data is used to update the state entries in the system identification code using MATLAB. When the updated data shows a fundamental change in the system, the result is a large change in the estimation of the nonlinear term,  $\alpha$ . In general, changes in the systems response due to changes in the input will not significantly change the estimation of the nonlinear term.

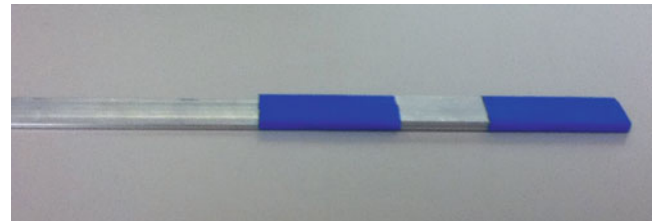
## 17.5 Experiment and Analysis

The testing schematic is shown in Fig. 17.3. The beams that were tested varied in geometry. Geometries tested include (each beam is 6,061 aluminum): (1) a beam with dimensions  $12.7 \times 1.59 \times 500$  mm, (2) a beam with an additional piece of 6,061 of dimensions  $12.7 \times 1.59 \times 120$  mm attached to end of the base beam, as seen in Fig. 17.4 (3) a beam with

**Fig. 17.3** Experimental configuration for fatigue testing



**Fig. 17.4** Close up of attached small (120 mm long) additional section



dimensions of  $12.7 \times 1.59 \times 425$  mm, (4) a beam with control dimensions with an additional piece of 6,061 of dimensions  $12.7 \times 1.59 \times 253$  mm attached to end of the base beam (5) and a beam with control dimensions and an additional piece of 6,061 of dimensions  $12.7 \times 1.59 \times 167$  mm attached to end of the base beam.

Each geometry was excited using a 45 N shaker over a range of frequencies near the second natural frequency for each beam. In conjunction with National Instruments, LabVIEW was used to record accelerations at the beam's base and at 45 mm down the beam. The beam's acceleration was differenced from the base acceleration and then scaled according to the accelerometer's calibration and its location on the beam. The base acceleration was multiplied by mass to give the forcing and then scaled with the mode shape in accordance to (17.9). These new manipulated data sets were then treated as the system's output and input.

Signals from the accelerometers were filtered and amplified to remove any high frequency noise. The filtering was done by fitting the amplified signals with the Fourier Series approximation based on the forcing frequency and its harmonics. The fit functions were then integrated to determine states used in the identification matrices.

In order to determine the resonant frequency of the beams, two sweep tests were performed, one of increasing frequency and the other of decreasing frequency; the resonant frequency was selected as the frequency that displayed the highest ratio of output to input. Once the resonant frequency was determined, steady state data was collected at frequencies near resonance then the linear parameters,  $m$ ,  $c$ , and  $k$  were back solved for using (17.10) and were fixed. These values need not match up with values found from traditional linear estimates, and they do help absorb inaccuracies in the model [12]. This leaves the cubic stiffness value as the only parameter to be estimated.

The initial sweep tests also serve a function in describing the nonlinearity of the systems by showing the two-solution region of the beam's response. The sweeps indicated the expected Hardening Spring Effect, where the maximum response amplitude tends to the lower frequency as the excitation amplitude is increased.

In the fatigue test steady state data collection, a sine wave excitation was used to generate the non-stationary forcing. The sample rate was selected to be 1 kHz. The resonance frequency varied for the different geometries, steady state excitation frequencies were selected near the resonance. At each frequency near resonance, 2 s of data was recorded. This corresponds to approximately 60 cycles of steady state response. The acceleration data was scaled in relation to accelerometer and mode-shape dependence, and then integrated to enter into the system identification matrix.

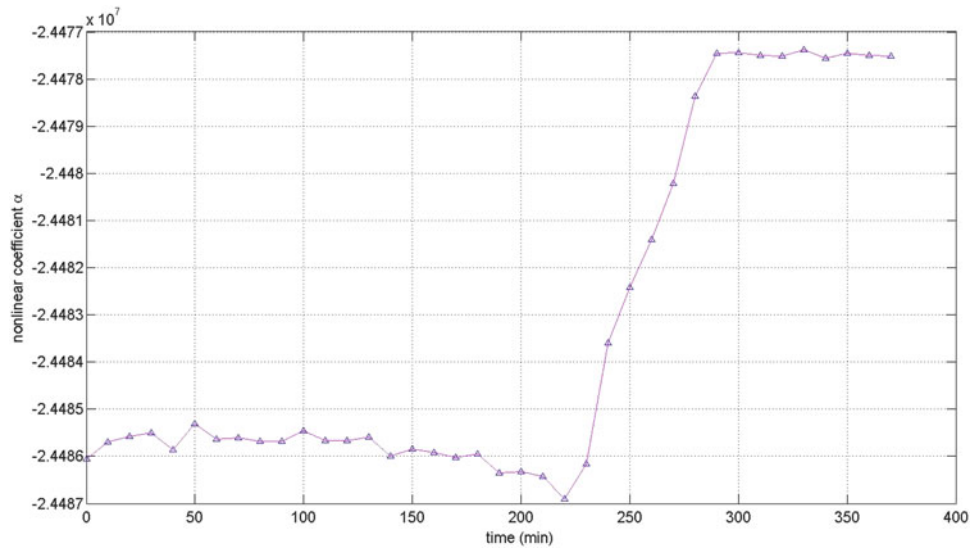
In the final fatigue test, the beams were excited at their respective resonant frequencies and left to shake until failure. The test frequency was held near resonant frequency through the entirety of the test.

## 17.6 Results

During the experiments, repeatable evidence of the success of the NMT was found. The health of the differing geometries, while having differing behaviors, were still accurately tracked by holding the linear parameters constant and allowing the nonlinear parameter to vary. Large changes in the nonlinear term,  $\alpha$ , were evident and corresponded with visual changes in the beam's response to the non-stationary excitation.



**Fig. 17.5** Estimation of  $\alpha$  versus time of a control beam



**Fig. 17.6** Estimation of  $\alpha$  versus time of a beam with a small additional section

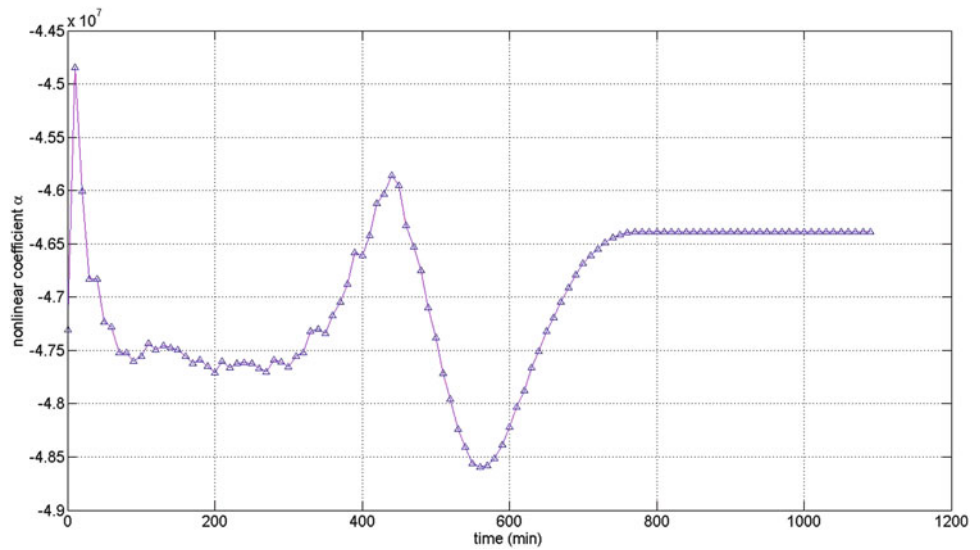


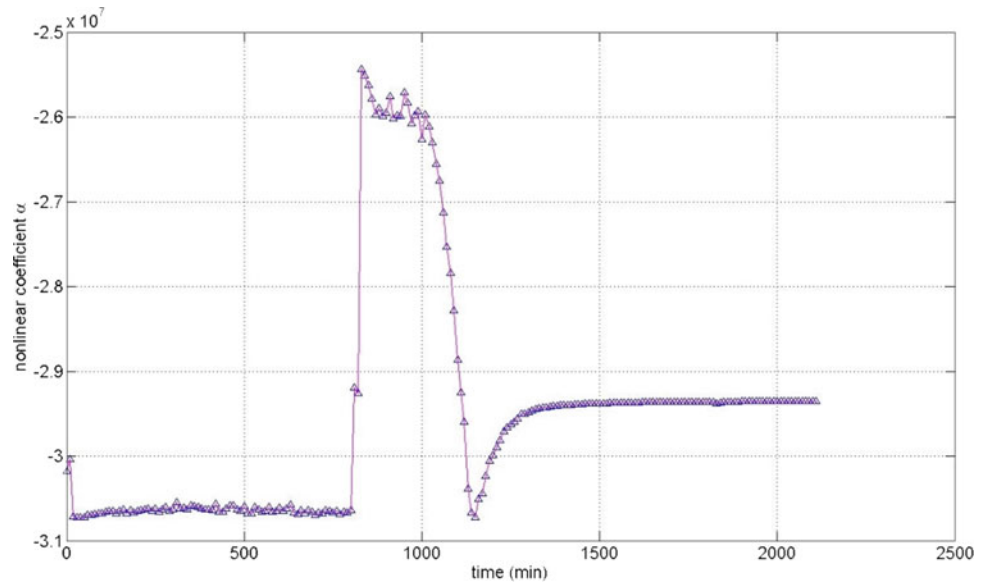
Figure 17.5 shows the health tracking of a control beam of dimensions  $12.7 \times 1.59 \times 500$  mm. In previous experiments, beams of this geometry have been accurately tracked by The NMT [13]. The figure shows that in this particular example, the estimation for the nonlinear parameter is constant up to minute 230, at this point the estimation for  $\alpha$  drastically changes. The beam then fails at minute 370.

The next beam tested was comprised of a control beam with an additional section of 6,061 aluminum attached to the end. An image of one of the modified geometries can be seen in Fig. 17.4. The dimensions of the additional piece are  $12.7 \times 1.59 \times 120$  mm. Figure 17.6 shows the tracking of the nonlinear term  $\alpha$  during the life of the beam. There is some initial settling of the beam, which results in a short variation in alpha. The estimation for the nonlinear term remains relatively constant up until the onset of a crack around minute 350. The estimation for alpha then changes significantly, and levels off until it fails at minute 800.

Figure 17.7 shows the tracking of the nonlinear parameter estimation versus time for the final beam tested. This beam has the dimensions of  $12.7 \times 1.59 \times 425$  mm with no additional piece added to the end. The estimation for  $\alpha$  remains relatively constant until minute 800 where a sharp spike in the nonlinear term’s estimation indicates a crack in the beam has formed. The estimation for the nonlinear term then varies for a couple minutes and then levels out until failure at minute 1,750.

Table 17.1 shows the results of the beams of differing geometries in terms of time to failure and time to drastic change in  $\alpha$ . It is shown that the warning time for the differing geometries ranges from 38% to 56% of the beam’s total life.

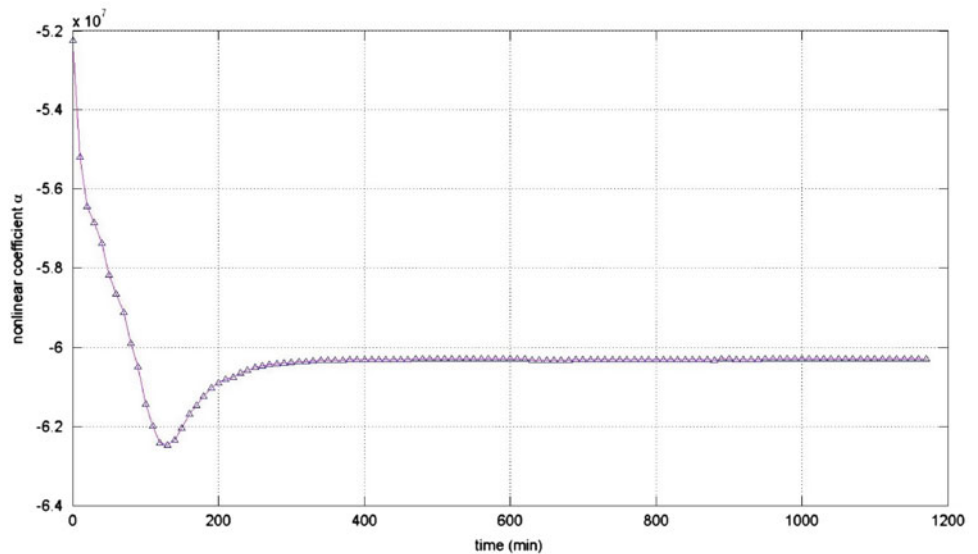
**Fig. 17.7** Estimation of  $\alpha$  versus time of a short beam



**Table 17.1** Failure Results for Different Beam Geometries

Beam figure association	Time to failure	Time at $\alpha$ change	Warning time, % of life time
Control	370 min	230 min	38%
Additional small piece added	800 min	350 min	56%
Shorter beam	1,750 min	800 min	54%

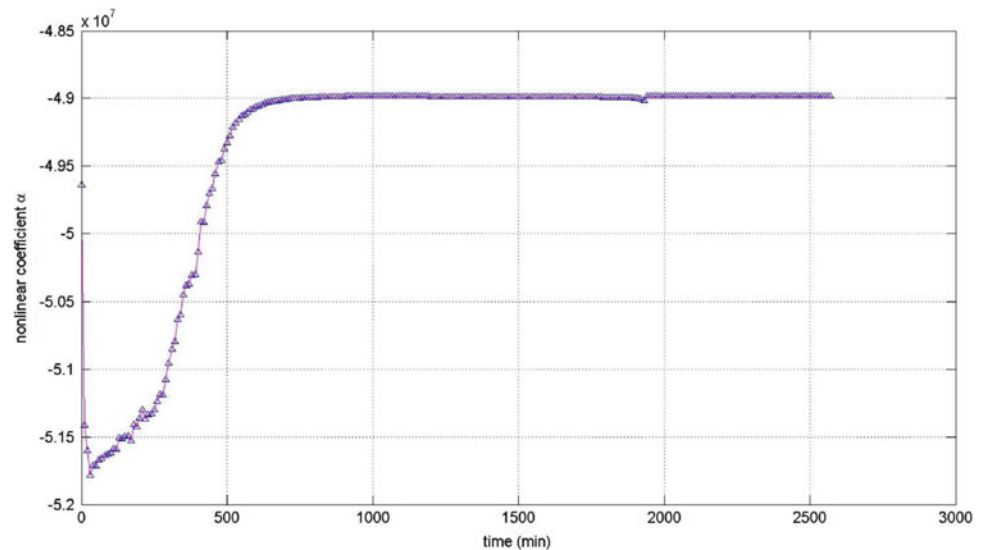
**Fig. 17.8** Estimation of  $\alpha$  versus time of a beam with a large additional section



The results of the other beams tested are displayed in Figs. 17.8 and 17.9. Figure 17.8 is the alpha plot for the beam with the same dimensions as the control beam with an additional piece of 6,061 aluminum of dimensions  $12.7 \times 1.59 \times 253$  mm attached to the end. Figure 17.9 is the alpha plot for the beam tested with the same dimensions as the control beam with an additional section of  $12.7 \times 1.59 \times 167$  mm 6,061 aluminum attached to the end.

Neither of these beams behaved as expected. Speculation as to why is explored in the Discussion section. Another aspect of the alpha plots that could cause false alarm is the early on-set drift phenomena, reasons for which are also explored in the discussion section.

**Fig. 17.9** Estimation of  $\alpha$  versus time of a beam with a medium additional section



## 17.7 Discussion

In each of the experiments done for beams of different geometries, the NMT method used successfully tracked the nonlinear parameter of interest as it changed throughout the experiments. Additionally, the resulting data from each of the different beams tested tracked a change in the nonlinear parameter of the beams for a period of time immediately as data collection began. This phenomenon has been termed early onset drift, and has not been observed in previous experiments. Early onset drift is currently being studied, though this doesn't invalidate the NMT method used in these experiments. As seen in the plot generated from the shorter beam with a length of 425 mm and no additional top section in Fig. 17.7, following the period of early onset drift, the system's nonlinear parameter is observed to be constant for a significant portion of time. Following the portion of time where the nonlinear parameter remained constant, a significant change in the nonlinear parameter is observed which is consistent with observed crack initiation observed in previous experiments of slender cantilevered beams.

A similar trend is apparent for the beam with a small additional top section as seen in Fig. 17.8. Following a period of early onset drift, the nonlinear parameter of the beam with a small additional top section is observed to be constant for a significant amount of time, then the nonlinear parameter changes drastically, signifying plastic deformation and crack initiation in the beam.

Figures 17.10 and 17.11 show cases where the early onset drift may actually be the initial stages of failure. This emphasizes the need to better understand the phenomena. One possibility for the drift may be due to the spacing of the steady state healthy records used in the NMT method. For these figures, the steady state data used in processing for the beams was collected at frequencies very close to resonance. This consequently could have caused the NMT method to be too sensitive to changes in the natural frequency of the beams. Further studies will focus on testing this hypothesis by comparing data processed using multiple steady state data sets collected for different ranges of frequencies near the resonant frequency.

As the phenomenon is new it may be directly associated with the varying geometry study. One hypothesis is that with additional mass, the beams immediately experienced plastic deformation at the clamped end of the beam due to the additional stress. This observation is consistent with previous health monitoring studies, as crack initiation and plastic deformation coincide with a large change in the nonlinear parameter, as is seen in each of the different geometry experiments in which an additional top section was secured to the beam as soon as data collection began. The immediate plastic deformation for these beams could also have occurred because the beams were shaking at a frequency too close to resonance, causing the beams to be shaking at too high of an amplitude, resulting in immediate plastic deformation.

Another possible explanation for the changes observed in the nonlinear parameter in the beginning of the experiments, is a lack of consideration of additional nonlinearities in the model being used for analysis. Both the geometric nonlinearities and the limitations of the physical shaker can contribute to a failed model of the dynamic system. Under heavy loading the shaker may require a warm-up period, or additional vibrations being measured by the accelerometers from the interaction of the observed system with its surroundings.

## 17.8 Conclusion

The NMT method developed in previous studies was shown to be successful in health monitoring experiments for beams of different geometries. Early onset drift in the estimates of the nonlinear parameter is a new phenomenon that occurs in these tests and, while it does not prevent the NMT method's success, it does raise some questions. Further study is underway regarding the observed drift and what it can tell us about the beam failure and about the NMT methodology.

Speculative reasons for explaining the unexpected results seen and early onset drift are, use of steady state data collected too close to the resonance frequency, immediate plastic deformation experienced by the beams with additional top sections mounted to them, or shortcomings in the nonlinear model being used in the NMT. Further studies will work on understanding and explaining the early onset drift phenomenon observed in these experiments, and to optimize and apply the NMT method used to a greater variety of geometries and materials. Once further understood and refined, this model will be applied to more complex models resembling real life systems such as airplane wings, or turbine blade.

## References

1. Doebling SW, Farrar CR, Prime MB (1998) A summary of vibration-based damage identification methods. *Shock Vib Dig* 30:91–105
2. Khiem NT, Lien TV (2004) Multi-crack detection for beam by the natural frequencies. *J Sound Vib* 273:175–185
3. Loutridis S, Douka E, Hadjileontiadis LJ (2005) Forced vibration behavior and crack detection of cracked beams using instantaneous frequency. *NDT E Int* 38:411–419
4. Lee YY, Liew KM (2001) Detection of damage locations in a beam using the wavelet analysis. *Int J Struct Stab Dyn* 1:455–465
5. Gudmundson P (1984) Changes in modal parameters resulting from small cracks. *Proc Int Modal Anal Conf Exhib* 2:690–697
6. Kim J-T, Ryu Y-S, Hyun-Man C, Stubbs N (2003) Damage identification in beam-type structures: frequency-based method vs. mode-shape based method. *Eng Struct* 25:57–67
7. Ding JL, Pazhouh J, Lin SB, Burton TD (1994) Damage characterization by vibration test. *Scripta Metallurgica et Mater* 30:839–834
8. Sih GC, Tzou DY (1984) *Mechanics of Nonlinear Crack Growth: effects of specimen size and loading*. Step. Martinus Nijhoff Publications, Boston, MA, pp 155–169
9. Bovsunovsky A, Bovsunovsky O (2007) Crack detection in beams by means of the driving force parameters variation at non-linear resonance vibrations. *Key Eng Mater* 347:413–420, *Damage Assessment of Structures VII*
10. Andraeus U, Casini P, Vestroni F (2005) Nonlinear features in the dynamic response of a cracked beam under harmonic forcing. In: *Proceedings of the ASME international design engineering technical conferences and computers and information in engineering conference – DETC2005*, v 6 C, 5th international conference on multibody systems, nonlinear dynamics, and control, Long Beach, CA, pp 2083–2089
11. Doughty TA, Leineweber MJ (2009) Investigating nonlinear models for health monitoring in vibrating structures. In: *ASME international mechanical engineering congress and exposition*, Lake Buena Vista, FL
12. Wovk V (1991) *Machinery vibration measurement and analysis*. McGraw Hill, New York
13. Doughty TA, Higgins NS (2010) Effect of nonlinear parametric model accuracy in crack prediction and detection. In: *SEM annual conference & exposition on experimental and applied mechanics*, Indianapolis
14. Crespo da Silva MRM, Glynn CC (1978) Nonlinear flexural-flexural-torsional dynamics of inextensional beams, II. Forced motions. *Int J Solids Struct* 6:449–461
15. Doughty TA, Davies P, Bajaj AK (2002) A comparison of three techniques using steady-state data to identify nonlinear modal behavior of an externally excited cantilever beam. *J Sound Vib* 249(4):785–813
16. Doughty, TA (2002) *System identification of modes in nonlinear structures*. Ph.D. thesis, Ray W. Herrick Laboratories, School of Mechanical Engineering, Purdue University

# Chapter 18

## Fuzzy Arithmetical Assessment of Wave Propagation Models for Multi-Wire Cables

Christoph Schaal and Michael Hanss

**Abstract** To localize damages in engineering structures, such as power lines, ultrasonic wave-based techniques are widely used for Structural Health Monitoring applications. In a cylindrical waveguide, longitudinal, flexural and torsional modes may propagate. Additionally, the wave propagation is generally of dispersive nature. Since cable structures usually consist of several smaller wires, coupling in between individual wires must also be considered. Friction contact causes energy transfer and dissipation as well as mode conversion of propagating waves. Precise transient simulation of wave propagation in multi-wire cables with common FE software results in tremendous computational costs. Therefore, recent research follows a different strategy: only power flows due to propagating waves are considered. Since these models incorporate significant simplifications, a model assessment strategy through advanced fuzzy arithmetic is applied. Uncertainty in model parameters, especially due to simplification and idealization during the modeling process, is considered as epistemic uncertainty. Therefore, the effects of uncertain model parameters represented as fuzzy numbers are investigated by simulations with the use of the Transformation Method. Different models are simulated and an inverse fuzzy arithmetical technique is used to identify parameter uncertainty based on experimentally derived data. Finally, the models' validity is verified.

**Keywords** Structural health monitoring • Guided wave propagation • Epistemic uncertainty • Fuzzy arithmetic • Model assessment

### 18.1 Introduction

Structural Health Monitoring (SHM) methods target multi-wire cable structures, such as overhead power lines or stay cables of suspension bridges. Both types of cables are subject to wind-induced vibrations, temperature changes, corrosion and other static and dynamic loads. Failure of multi-wire cables begins with cracks in individual wires [10] and can eventually lead to a fracture of the entire multi-wire cable. For power lines, this can lead to power outages for millions of households.

In this work, an active ultrasonic wave-based approach for damage localization and characterization in cable structures, as depicted in Fig. 18.1a, is implemented. Ultrasonic waves are excited in the multi-wire cables and are partially reflected and transmitted at discontinuities. Reflections are measured by a sensor, and damage detection algorithms evaluate the structural state. The individual wires of the cable can be considered as waveguides, structures which confine the propagation of waves in one direction. In particular, guided ultrasonic waves qualify for material evaluation, since these waves travel long distances with little decay. However, the multimodal nature of guided wave propagation in cylinders has to be accounted for: in general, several types of waves, referred to as modes, may propagate simultaneously [2]. Also, mode conversion occurs when waves encounter discontinuities [1]. Subsequently, waves often consist of the superposition of several modes with different velocities, requiring sophisticated signal processing. Real cable structures do not consist of a single cylindrical wire but instead are composed of several twisted wires, as shown in Fig. 18.1b. The friction contact between wires further complicates modeling of the multi-wire cables. To avoid high computational costs, recent research on the analysis of wave propagation

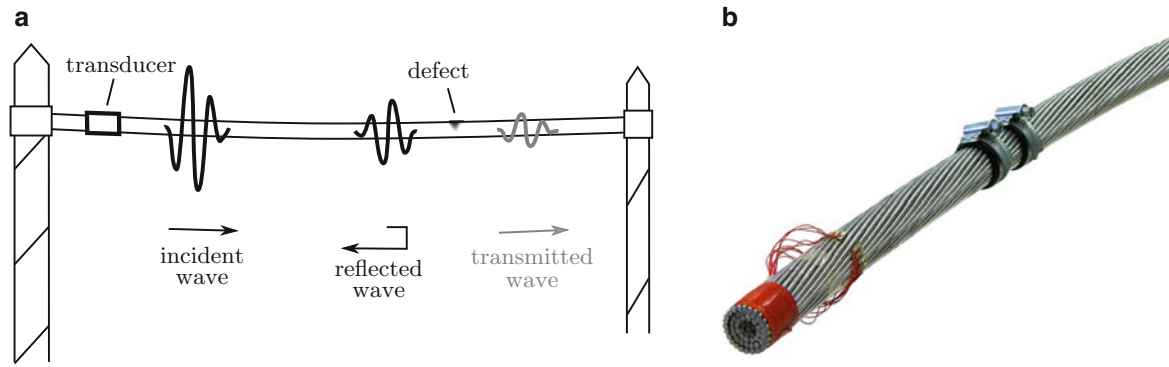
---

C. Schaal (✉)

Institute of Applied and Experimental Mechanics, University of Stuttgart, Pfaffenwaldring 9, D-70550, Stuttgart, Germany  
e-mail: [schaal@iam.uni-stuttgart.de](mailto:schaal@iam.uni-stuttgart.de)

M. Hanss

Institute of Engineering and Computational Mechanics, University of Stuttgart, Pfaffenwaldring 9, D-70550, Stuttgart, Germany



**Fig. 18.1** Structural Health Monitoring concept for overhead power lines using guided ultrasonic waves. (a) Transducer induces guided ultrasonic waves which are partially reflected at defects and detected at the transducer. (b) Power cable, composed of several layers of individual wires (mainly steel and aluminum wires)

in multi-wire cable structures focuses on an energy-based description. Simple models have been derived, describing the dry friction contact between adjacent wires, and have been applied to two-wire systems [11].

Most of today's methods and SHM concepts ignore uncertainty in models and material parameters as well as uncertainty due to simplifications and idealizations during the modeling process. Recently, fuzzy arithmetical approaches dealing with uncertainty in model parameters have emerged rapidly [7]. Pre- and post-processing tools have been developed to provide an efficient implementation in combination with other commercial software packages. Also, an inverse fuzzy arithmetical approach has been developed to identify uncertainty in model parameters [3]. In addition to nominal values, derived from a least-squares identification, measurement values are used to identify uncertainty in model parameters. Furthermore, model validation applications have been investigated to allow for a comparison between different models for a specific physical system.

In this article, the fields of wave propagation for SHM applications and fuzzy arithmetical model assessment are combined and extended. After a brief introduction to applied fuzzy arithmetic, a theoretical background on wave propagation in cylindrical waveguides is given. In the next part, the model development for energy transfers in multi-wire cables is presented. The fourth section introduces the experimental setups and configurations used in this work. Afterwards, various results of the model identification are presented, including numerous experimental and numerical plots. Also, a generalized model validity criterion is defined and evaluated for the energy-based coupling models. In the last section, the results are discussed and an outlook is given.

## 18.2 Theoretical Background

### 18.2.1 Fuzzy Arithmetical Approach

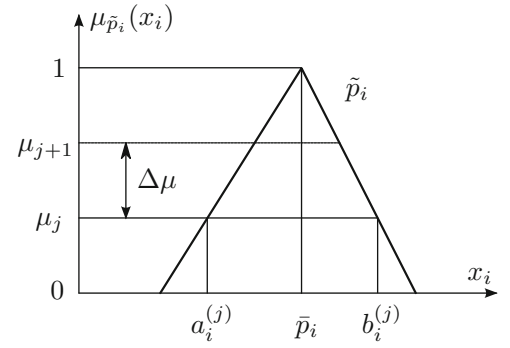
Uncertainty can be classified using various schemes. In this work, the classification into aleatory and epistemic uncertainty is used which was introduced by Hoffman and Hammonds [5]. Causes of aleatory uncertainty are randomness and variability. Epistemic uncertainty is, on the other hand, uncertainty caused by either a lack of knowledge or idealizations and simplifications from the modeling procedure. Aleatory uncertainty is mainly dealt with by probabilistic methods (e.g. [9]), while epistemic uncertainty is mostly handled by possibilistic methods. This work focuses on epistemic uncertainty and fuzzy arithmetical methods.

Fuzzy numbers are a special kind of fuzzy sets featuring exactly one nominal value  $\bar{p}_i$  which is usually the value used for crisp-valued simulations [4]. In order to realize a smooth transition from the nominal value  $\bar{p}_i$  to the worst-case interval  $[a_i^{(0)}, b_i^{(0)}]$ , a membership function  $\mu_{\tilde{p}_i} \in [0, 1]$  is introduced which quantifies the possibility for the occurrence of a specific value. The most commonly used fuzzy number has a triangularly shaped membership function and is therefore also called a linear fuzzy number. An example for the membership function of a triangular fuzzy parameter  $\tilde{p}_i$  is shown in Fig. 18.2.

Models based on uncertain parameters also lead to uncertain outputs. To compute fuzzy-valued outputs  $\tilde{q}_k$ , with

$$\tilde{q}_k = f_k(\tilde{p}_1, \tilde{p}_2, \dots, \tilde{p}_n, s), \quad k = 1, \dots, K, \quad (18.1)$$

**Fig. 18.2** Membership function  $\mu_{\tilde{p}_i}(x_i)$  of a triangular fuzzy number  $\tilde{p}_i$  with  $\alpha$ -cut  $[a_i^{(j)}, b_i^{(j)}]$  at level  $\mu_j$



the Transformation Method is applied [4]. Unmentioned thus far is the independent discrete variable  $s = 1, \dots, S$ , which can be, for example, time  $t$  or frequency  $f$  in common engineering problems. By using the Transformation Method, the propagation of uncertainty in parameters towards the system's outputs can be analyzed. Also, a sensitivity analysis can be used to identify shortcomings in the models and the importance of certain parameters. The worst-case intervals for the fuzzy-valued model parameters, however, mostly rely on expert knowledge. To overcome this deficiency, an inverse fuzzy arithmetical method is used to identify parameter uncertainty on the basis of experimental data.

Before applying inverse algorithms, fuzzy-valued outputs on the basis of measured values are defined. The nominal values are usually model outputs fitted to measured data in a least-squares sense. The worst-case deviation is defined such that all measured values are included within the least conservative bounds. Hence, the membership levels of outputs for each step  $s$  are also of triangular shape (see Fig. 18.2). The idea of the applied inverse fuzzy arithmetical approach, proposed by [4], is to derive a system representation, which is a linear mapping between uncertainty in inputs and uncertainty in outputs for each membership level. This mapping is based on single-sided gain factors which can be determined from initial simulations with the Transformation Method. Even though the inversion of bijective mappings is possible, in general this procedure is not applicable and would lead to an overestimation of the uncertainty [4]. Hence, a quadratic optimization problem is defined such that the resulting uncertainty in the outputs from re-simulations with identified fuzzy-valued parameters is greater than or equal to the uncertainty accrued from measurements [3]. In the presence of an independent variable  $s$ , identified fuzzy-valued parameters and their membership levels also depend on  $s$ , which is undesired for static models. Thus, a method for reducing the obtained  $s$ -dependent sets of fuzzy-valued model parameters to a constant set is applied.

Finally, models can be validated through the results from the inverse fuzzy arithmetical approach. According to [4], the relative imprecision of a general fuzzy number  $\tilde{p}_i$  is given by

$$\text{imp}_{\tilde{p}_i}(\tilde{p}_i) = \frac{1}{2m\bar{p}_i} \sum_{j=0}^{m-1} [(b_i^{(j)} - a_i^{(j)}) + (b_i^{(j+1)} - a_i^{(j+1)})], \quad \text{for } \bar{p}_i \neq 0, \quad (18.2)$$

where  $m$  is the number of  $\alpha$ -cuts and  $a_i^{(j)}$  and  $b_i^{(j)}$  are the lower and upper bounds of the  $j$ th  $\alpha$ -cut, respectively.

By using Eq. (18.2), the model validity criterion  $\Lambda$ , introduced by [3], is generalized to

$$\Lambda = \sum_{i=1}^n |\text{imp}_{\tilde{p}_i}(\tilde{p}_i)| \cdot w(\tilde{q}_k(s), s). \quad (18.3)$$

with the general weighting function  $w(\tilde{q}_k(s), s)$ . If  $w = 1$  is chosen, only the overall uncertainty in model parameters is evaluated.

By choosing  $w = w_1$ , the originally defined criterion appears. In the authors' opinion, however, this criterion may be unfairly dominated by the system's input-output behavior. Therefore,  $w = w_2$  can be used, which reflects the average output uncertainty instead of the accumulated uncertainty:

$$w_1 = \sum_{k=1}^K \left[ \frac{1}{S} \sum_{s=1}^S |\text{imp}_{\tilde{q}_k}(\tilde{q}_k(s))| \right] \quad \text{and} \quad w_2 = \frac{1}{K} \sum_{k=1}^K \left[ \frac{1}{S} \sum_{s=1}^S |\text{imp}_{\tilde{q}_k}(\tilde{q}_k(s))| \right]. \quad (18.4)$$



Alternatively, more conservative weights are defined by

$$w_3 = \max_{k,s} (|\text{imp}_{\tilde{q}_k}(\tilde{q}_k(s))|) \quad \text{and} \quad w_4 = \max_k \left( \left[ \frac{1}{S} \sum_{s=1}^S |\text{imp}_{\tilde{q}_k}(\tilde{q}_k(s))| \right] \right). \quad (18.5)$$

In this paper, the weighting function  $w = w_4$  is used to assess different models, allowing for a comparison of their quality and validity in a worst-case sense without significantly including measurement scatter.

## 18.2.2 Wave Propagation in Cylindrical Waveguides

Guided waves propagate in one direction while having characteristic displacement fields (mode shapes) in all three axes. Bodies which allow for propagation of guided waves are called waveguides. The displacement fields  $\mathbf{u}$  of guided waves can be written in the form

$$\mathbf{u}(\mathbf{x}, t) = \hat{\mathbf{u}}(x, y) e^{j(kz - \omega t)} \quad (18.6)$$

with the angular frequency  $\omega$  and wavenumber  $k$ . The modes are characterized by their respective displacement fields  $\hat{\mathbf{u}}(x, y)$ . For cylindrical waveguides, three types of waves may propagate: longitudinal, flexural and torsional waves [2]. Using common nomenclature, these waves are abbreviated as L(0, $m$ ), F( $n$ , $m$ ) and T(0, $m$ ) with order  $n$  and sequential numbering  $m$ .

In order to develop simplified models for waves propagating in multi-wire cables, an approach solely based on energy flows is used. The kinetic energy  $K$  of a mechanical continuum with volume  $V$  is given by

$$K = \frac{1}{2} \int_V \rho \dot{\mathbf{u}} \cdot \dot{\mathbf{u}} dV \quad (18.7)$$

with the density  $\rho$  and the velocity  $\dot{\mathbf{u}}$ . It can be shown for a longitudinal wave, without loss of generality, that the energy  $E$  of a wave packet in the spatial interval  $[z_0, z_1]$  is

$$E(z) = \text{const} \cdot \int_{z_0}^{z_1} \dot{u}_R^2(z) dz \approx \text{const} \cdot \int_{t_S}^{t_F} \dot{u}_R^2(t) c_g dt = \text{const} \cdot \int_{t_S}^{t_F} \dot{u}_R^2(t) dt \quad (18.8)$$

with the radial velocity  $\dot{u}_R(t)$  at the surface of the waveguide, the group velocity  $c_g$  and the assumption  $dz \approx c_g \cdot dt$ . Note, since propagating waves in cylindrical waveguides are generally dispersive, i.e. group velocity is a function of frequency, a minor error is made by assuming a constant group velocity for all frequencies within the wave packet.

Since measurements are taken at discrete timesteps, the integral transforms into the summation

$$E(z) = \text{const} \cdot \sum_{i=S}^F \dot{u}_R^2(z, t_i(z)) \quad \text{with} \quad t_S(z) \leq t_i(z) \leq t_F(z). \quad (18.9)$$

The times  $t_S$  and  $t_F$  correspond to the start and finish times of the wave packet in the measurement signal, respectively. They can be derived from the position of the measurement  $z$  and the group velocity  $c_g$  of the dominant frequency of the wave packet.

Wavenumbers and group velocities as well as displacement fields  $\mathbf{u}$  and forces  $\mathbf{f}$  of propagating waves in waveguides are efficiently determined by using the Waveguide Finite Element Method (WFEM), introduced by [6]. Only one section  $s$  of the cylindrical waveguide with a thickness  $h$  is considered in the FE modeling process. Assuming periodicity for this section, phase shifts  $\mathbf{u}_L^{s+1} = \lambda \mathbf{u}_L^s$  and  $\mathbf{f}_L^{s+1} = \lambda \mathbf{f}_L^s$  are applied with  $\lambda = e^{jk h}$  and the angular wavenumber  $k$ . By solving the corresponding linear eigenvalue problem, wavenumbers  $k$  and mode shapes for the displacement and traction fields are determined for propagating and non-propagating modes [8]. To determine start and stop times for the analysis of the wave packets in order to calculate their energy, the corresponding group velocities can be calculated with the relation  $c_g = \frac{d\omega}{dk}$ .

### 18.3 Model Development

In order to simplify models describing wave propagation in multi-wire cables, an energy flow based approach is considered. The individual wires are coupled via dry friction. This contact allows for energy transfer from one wire to another. Moreover, energy is not only dissipated due to friction but also due to material damping. For all models, a differential section of a coupled two-rod system is considered, as shown in Fig. 18.3a. Later, the results are generalized for  $n$ -rod systems.

Balancing energy for an individual section (length  $dz$ ) of rod  $i$ , as shown in Fig. 18.3a, yields

$$E_i(z) = E_i(z + dz) + E_{m,i}(z) + E_{ij}(z), \quad (18.10)$$

where  $E_{m,i}$  is dissipated energy due to material damping, and  $E_{ij}$  is the energy transferred from rod  $i$  to  $j$ . The dissipated energy is modeled by

$$E_{m,i}(z) = c_m E_i(z) dz \quad \text{for } i = 1 \dots n, \quad (18.11)$$

with the damping coefficient  $c_m$ , which is identical for all rods of the same material. Equation (18.11) describes the exponential decay of waves propagating in lossy material.

The friction contact facilitating the energy transfer  $E_{ij}$  can be described using different models which are presented in the following.

#### 18.3.1 Distributed Viscous Damper Model

The energy coupling mechanism between the two rods is modeled, in the simplest case, by a distributed viscous damper which connects the differential elements in radial direction, as shown in Fig. 18.3b. This model is already capable of describing energy dissipation and transfer.

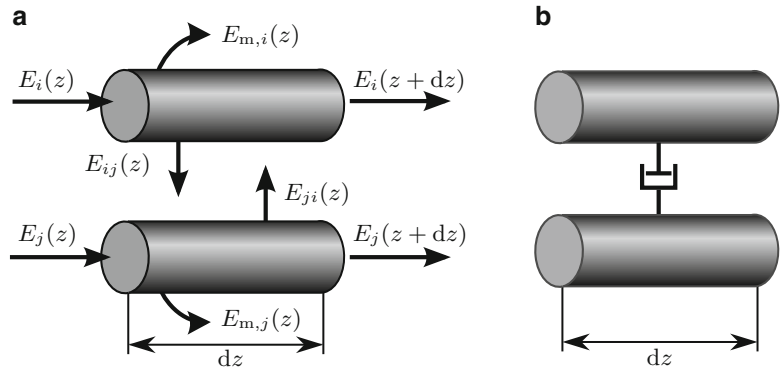
With the force  $F_{ij}$  of the dashpot, the energy transfer  $E_{ij}$  is

$$E_{ij}(z) = F_{ij} \dot{u}_{R,i} dt = c(\dot{u}_{R,i} - \dot{u}_{R,j}) \dot{u}_{R,i} dt, \quad (18.12)$$

where the dashpot coefficient  $c$  is assumed to be equal for the same material combination. Since  $E_i = \text{const} \cdot \dot{u}_{R,i}^2$  and  $c_g = \frac{dz}{dt}$  hold, Eq. (18.12) can be rewritten as

$$E_{ij}(z) = c_c \sqrt{E_i} (\sqrt{E_i} - \sqrt{E_j}) dz \quad (18.13)$$

with the coupling coefficient  $c_c$ . Note,  $E_{ij} = -E_{ji}$  does not hold in general, resulting in energy dissipation in the damper element. Using Eqs. (18.10), (18.11), (18.13), and by taking the limit as  $dz \rightarrow 0$ , one can derive the coupled set of first order nonlinear ordinary differential equations



**Fig. 18.3** Modeling the friction contact between adjacent rods. (a) Energy balance for a differential section of coupled rods. (b) Viscous damper model

$$\begin{aligned}\frac{dE_i(z)}{dz} &= -c_m E_i(z) - c_c \sqrt{E_i(z)} \left( \sqrt{E_i(z)} - \sqrt{E_j(z)} \right), \\ \frac{dE_j(z)}{dz} &= -c_m E_j(z) - c_c \sqrt{E_j(z)} \left( \sqrt{E_j(z)} - \sqrt{E_i(z)} \right).\end{aligned}\quad (18.14)$$

This result can be generalized for  $n$ -rod systems by expressing the state of contact between two rods  $i$  and  $j$  through a binary constant

$$b_{ij} = \begin{cases} 1 & \text{rod } i \text{ and } j \text{ are adjacent} \\ 0 & \text{otherwise} \end{cases}.\quad (18.15)$$

The nonlinear differential equation for the  $i$ th rod can then be written as

$$\frac{dE_i(z)}{dz} = -c_m E_i(z) - c_c \sqrt{E_i(z)} \sum_{j=1}^n b_{ij} \left( \sqrt{E_i(z)} - \sqrt{E_j(z)} \right).\quad (18.16)$$

Initial conditions are chosen as  $E_i(0) = E_{i,0}$ .

### 18.3.2 Extended Damper Model

The model presented in Sect. 18.3.1 has several limitations. In order to handle oscillations of the energy levels, the model is extended with a second-order term with the parameter  $m_E$ . The previously derived Eq. (18.16) is thereby extended to

$$m_E \frac{d^2 E_i(z)}{dz^2} + \frac{dE_i(z)}{dz} = -c_m E_i(z) - c_c \sqrt{E_i(z)} \sum_{j=1}^n b_{ij} \left( \sqrt{E_i(z)} - \sqrt{E_j(z)} \right).\quad (18.17)$$

Additional initial conditions are chosen as  $\frac{dE_i(0)}{dz} = E'_{i,0}$ . Note, the additional second-order term has no direct physical meaning and is added only because of mathematical considerations of the problem to be able to deal with oscillations in the rods' energy levels.

## 18.4 Experimental Investigation

The experimental setup allows for measuring different kinds of multi-rod systems with varying number of rods and twisting angles. Figure 18.4b shows a section of twisted seven-rod system, that is comparable to the core of an overhead power line. The twisting results in a slight helical deformation of the rods. However, considering that the lay angle is small, geometrical alterations can be neglected [12]. For the analysis of the coupling phenomena, a two-rod system is considered in order to



**Fig. 18.4** Experimental setup for the investigation of wave propagation in coupled cylindrical waveguides using a Laser Doppler Vibrometer. Mirrors are used to measure radial velocities from the top and both sides. (a) Vibrometer and mirror setup. (b) Seven-rod structure. (c) Wave excitation with piezo

compare the results with previous work [11]. The two rods (each aluminum [EN AW-6082 T6], 4 mm in diameter, 3 m in length) are twisted to ensure a constant normal force between the rods.

For all setups, the twisted multi-rod system rests on an insulated solid profile. The rods are fixed using rubber clamping near both ends. One rod has a piezoelectric transducer attached to an end, as shown in Fig. 18.4c. This rod is named the active rod, and the other rods are named passive. In the passive rods, waves are only excited via friction contact with the active rod. To induce wave packets in the active rod, an optimized pulse-signal is actuated by the piezoelectric transducer. Measurements are taken with a Laser Doppler Vibrometer (LDV) on both rods at various positions along the cable. Three mirrors, as shown in Fig. 18.4a, are used to orient the laser beam perpendicular to the surface of the measured rod. The mirrors and the LDV are automatically positioned via a two-axis positioning system. Data analysis is conducted using MATLAB.

Using the LDV, radial velocities for both rods are measured and converted to energy levels using Eq. (18.9) for different positions  $z$  along the rods. Data sets of multiple repeated measurements are used for the fuzzy arithmetical analysis of the previously described energy models.

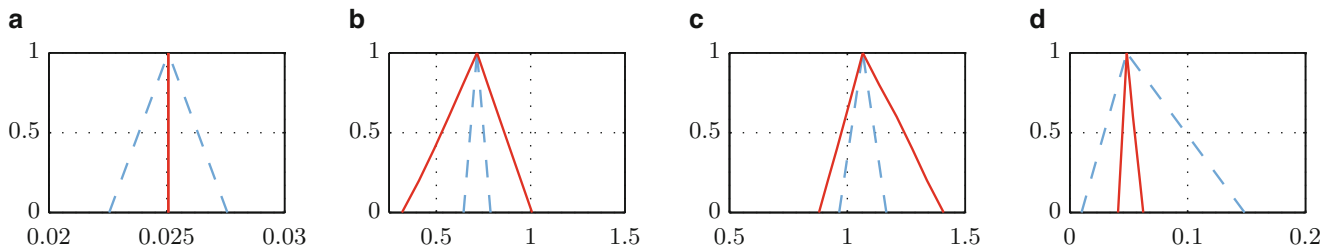
## 18.5 Results

In order to apply the inverse fuzzy arithmetical approach to identify uncertainty in model parameters, as described in Sect. 18.2.1, several measurements are taken. To determine nominal values for the parameters, a crisp-valued identification procedure is applied in a least-squares sense for both the simple distributed viscous damper and the extended damper model.

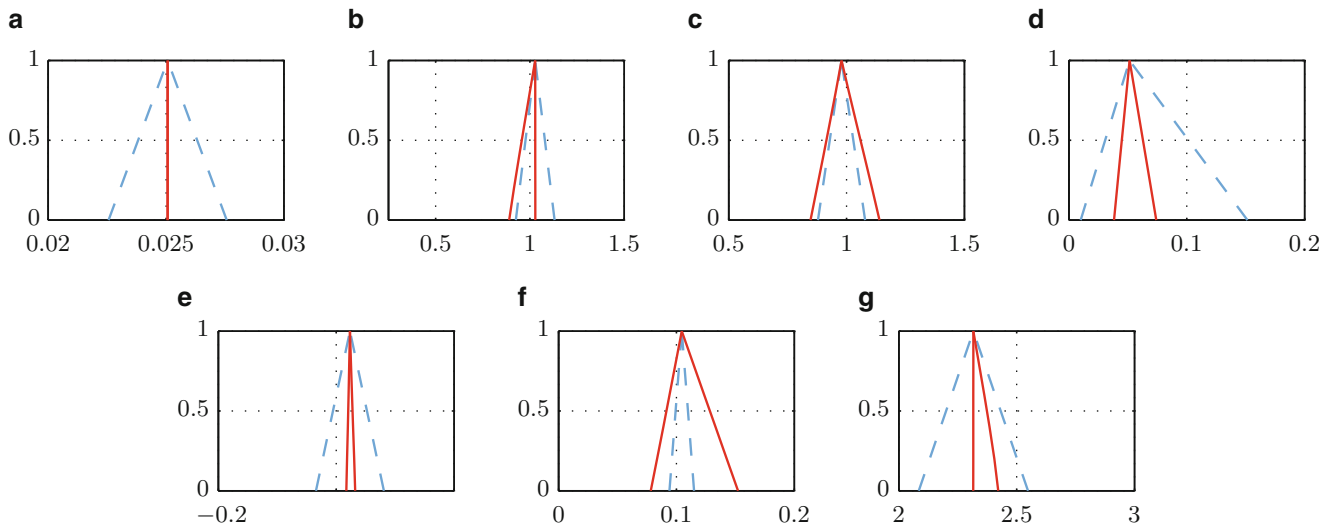
After initial fuzzy-valued simulations of the models are completed to identify the linear system mappings, uncertainty in the model parameters is identified via the inverse algorithm. The fuzzy-valued parameters are shown in Fig. 18.5 for the simple and in Fig. 18.6 for the extended model. Since the models are individually fitted to the measured data in a least-squares sense, the resulting nominal values may differ. The nominal value of the material damping parameter, however, is chosen equally for both systems because its influence on the energy is negligible and the parameter has also been excluded from the crisp-valued fitting.

The identified fuzzy-valued parameters are then used in a re-simulation step and the results are shown in Fig. 18.7a for the simple and in Fig. 18.7b for the extended model. In these figures, the color gradient indicates the corresponding membership level, where a darker color corresponds to a higher membership level.

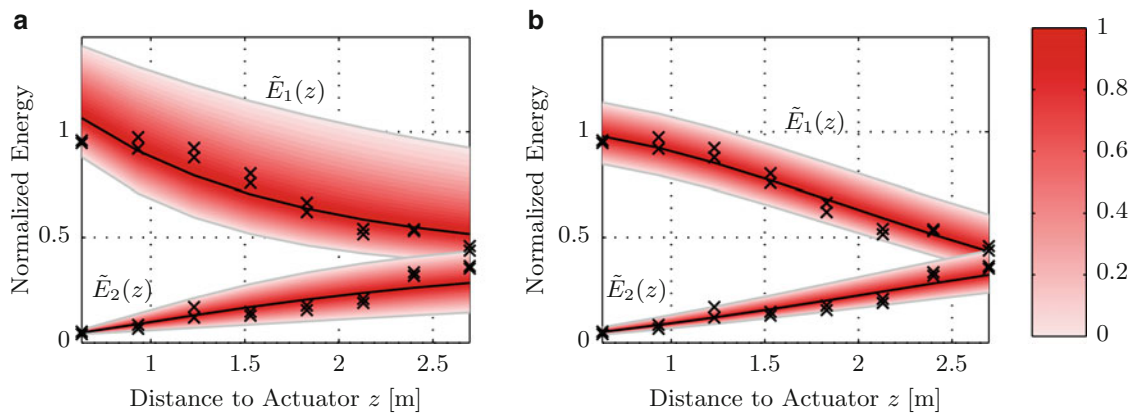
The two models are compared by evaluating the model validity criterion  $\Lambda$  for  $w = w_4$ , as defined in Eqs. (18.3) and (18.5). To evaluate this criterion, the relative imprecisions are calculated for each parameter of the simple and extended model as well as for their energy levels. The results are visualized in Fig. 18.8. Note, the model validity criterion is smaller for the extended model ( $\Lambda = 0.318$ ) than for the simple one ( $\Lambda = 0.4557$ ), i.e. the extended model incorporates less uncertainty. The main reason for this is that the relative imprecisions of the energies  $\tilde{E}_1(z)$  and  $\tilde{E}_2(z)$  in the active and passive rod, respectively, are clearly lower for the extended model. However, the additional model parameters  $\tilde{E}'_{1,0}$  and  $\tilde{E}'_{2,0}$  incorporate comparably large additional uncertainty such that the overall parameter uncertainty of the extended model is similar to the parameter uncertainty of the simple model. These results confirm previous analyses [8].



**Fig. 18.5** Membership levels  $\mu$  of the initially guessed (*dashed, light blue*) and identified (*solid, red*) fuzzy-valued parameters of the simple model. (a)  $\tilde{c}_m \cdot 10^6$ . (b)  $\tilde{c}_c$ . (c)  $\tilde{E}'_{1,0}$ . (d)  $\tilde{E}'_{2,0}$

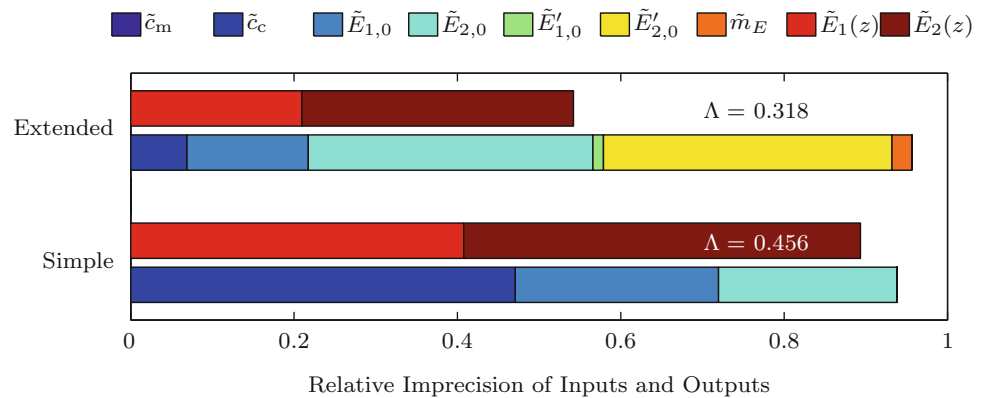


**Fig. 18.6** Membership levels  $\mu$  of the initially guessed (*dashed, light blue*) and identified (*solid, red*) fuzzy-valued parameters of the extended model. (a)  $\tilde{c}_m \cdot 10^6$ . (b)  $\tilde{c}_c$ . (c)  $\tilde{E}_{1,0}$ . (d)  $\tilde{E}_{2,0}$ . (e)  $\tilde{E}'_{1,0}$ . (f)  $\tilde{E}'_{2,0}$ . (g)  $m_E$



**Fig. 18.7** Fuzzy-valued energy plots for the active and passive rod of a twisted two-rod system (simple model and extended model). Worst-case results from experiments are marked by  $\times$ . (a) Fuzzy-valued normalized energies for the simple model. (b) Fuzzy-valued normalized energies for the extended model

**Fig. 18.8** Relative imprecisions of the model parameters and of the energy levels accumulated for each position



## 18.6 Conclusions and Outlook

It has been shown that assessing wave propagation models for coupled waveguides with uncertain parameters is possible through a fuzzy arithmetical approach. Experimental data was used to derive nominal values for the parameters of two energy flow models for multi-wire cables. By implementing an inverse fuzzy arithmetical approach, uncertainty in the systems' parameters has been identified. A re-simulation of the models with the newly identified fuzzy-valued parameters formed the basis for the model assessment. The newly generalized model validity criterion allows for a more adequate analysis. By introducing a more conservative weighting function, the criterion is also no longer dominated by the system's input-output behavior but reflects the system's internal dynamics more appropriately.

With the model validity criterion, it could be shown that the extended damper model is more appropriate for modeling wave propagation and the corresponding energy flows in multi-wire cable structures for Structural Health Monitoring applications. For the extended model, not only are the nominal values of the energy levels closer to measured values, but the overall uncertainty is also lower. Moreover, for different setups, e.g. different twisting and varying surface conditions of the wires, energy transfers can occur such that the passive wire has more energy than the active wire at specific locations, i.e. the energy oscillates between the rods. This behavior cannot be handled by the simple distributed damper model, therefore making the extended model even more appealing. The presented inverse fuzzy arithmetical approach also confirmed that the influence of material damping on guided wave propagation is very small, which confirms the applicability of long range monitoring schemes for multi-wire cable structures.

In the future, the authors plan to develop models with better physical comprehension and to extend the analysis for a seven-wire system. In this seven-wire setup, the inner wire is hidden from measurement and therefore the wave propagation within this wire can only be estimated through simulation. Also, recent improvements to FE models qualify them to be compared with the presented energy models in an effort to prove their validity. Results of fuzzy arithmetical analyses will support the ongoing model development process.

## References

1. Gaul L, Sprenger H, Schaal C, Bischoff S (2012) Structural health monitoring of cylindrical structures using guided ultrasonic waves. *Acta Mech* 223:1669–1680. doi:10.1007/s00707-012-0634-z
2. Graff KF (1991) *Wave motion in elastic solids*. Dover, New York. ISBN:0486667456
3. Haag T, Carvajal González S, Hanss M (2011) Model validation and selection based on inverse fuzzy arithmetic. *Mech Syst Signal Process*. doi:10.1016/j.ymsp.2011.09.028
4. Hanss M (2005) *Applied fuzzy arithmetic – an introduction with engineering applications*. Springer, Berlin. ISBN 3-540-24201-5
5. Hoffman FO, Hammonds JS (1994) Propagation of uncertainty in risk assessments: the need to distinguish between uncertainty due to lack of knowledge and uncertainty due to variability. *Risk Anal* 14:707–712. doi:10.1111/j.1539-6924.1994.tb00281.x
6. Mace BR, Duhamel D, Brennan MJ, Hinke L (2005) Finite element prediction of wave motion in structural waveguides. *J Acoust Soc Am* 117(5):2835–2843
7. Moens D, Hanss M (2011) Non-probabilistic finite element analysis for parametric uncertainty treatment in applied mechanics: recent advances. *Finite Elem Anal Des* 47(1):4–16. doi:10.1016/j.finel.2010.07.010
8. Schaal C, Hanss M (2012) Modeling wave propagation in coupled waveguides with uncertain parameters. In: *Proceedings of ISMA2012–USD2012*. Leuven, Belgium, pp 4945–4958
9. Schuëller GI (2007) On the treatment of uncertainties in structural mechanics and analysis. *Comput Struct* 85(5):235–243. doi:10.1016/j.compstruc.2006.10.009
10. Siegert D, Brevet P (2005) Fatigue of stay cables inside end fittings: high frequencies of wind induced vibrations. *Bull Int Organ Study Endur Ropes* 89:43–51
11. Sprenger H (2011) *Modeling, simulation and experimental analysis of ultrasonic wave propagation in cables with cracked wires*. Der Andere Verlag, Tönning, Germany
12. Treysède F (2007) Numerical investigation of elastic modes of propagation in helical waveguides. *J Acoust Soc Am* 121(6):3398–3408

# Chapter 19

## A Vibro-Haptic Human-Machine Interface for Structural Health Monitoring Applications

Christina Brown, Martin Cowell, C. Ariana Plont, Heidi Hahn, and David Mascareñas

**Abstract** Over the last 10 years, the Structural Health Monitoring (SHM) field has struggled to replace human-based inspections of structures with autonomous sensor networks and classification algorithms. The goal of the SHM community has been to endow structures with an artificial nervous system similar to that of living organisms. This paper proposes a new paradigm which leverages the human nervous system in concert with distributed sensor networks and computational resources. We propose using emerging haptic technology to create a harmonious collaboration between humans, SHM sensor networks, and statistical classification. The neuroscience community has demonstrated haptic-based methods for replacing lost sensations. However, this project explores the possibility of giving humans a new sense – one which reflects the health of a structure. The generation of this sense is achieved through a vibro-haptic human-machine interface. The testbed is composed of a surrogate three-story structure which can be modified to exhibit non-linear dynamic responses on any combination of its three floors. With the use of a vibro-haptic interface, we will study the ability of human users to determine the characteristics of non-linear response. Establishing this intimate connection between humans and structures is the first step in creating a new SHM paradigm that combines human intelligence with distributed measurement capabilities.

**Keywords** Haptics • Sensory substitution • Human-machine interface • Cooperative SHM • Vibro-tactile

### 19.1 Introduction

#### 19.1.1 Background

For years, the Structural Health Monitoring (SHM) community has worked toward building structures that effectively have an integrated nervous system similar to that of a living organism. Much of these research efforts have focused on developing techniques that eliminate the judgment of human structural inspectors by making use of statistical pattern recognition. The statistical pattern recognition SHM paradigm is a multi-step approach consisting of the sequence of operational evaluation, data acquisition & cleansing, feature extraction, and statistical model development [1]. While this methodology has resulted in great improvements in SHM capabilities, the current state-of-the-art techniques still lack the ability to adequately detect, localize, quantify and predict the degree of deterioration seen in a structure for many applications. A major goal of the SHM community has been to remove the human from the SHM loop and build SHM systems that are completely autonomous. Experience shows that the autonomous-SHM paradigm may have severe limitations. Human classification capabilities often exceed those of contemporary classification algorithms [2], and are capable of better adapting to new situations and

---

C. Brown (✉) • C.A. Plont  
Department of Mechanical Engineering, University of New Mexico, Albuquerque, NM 87106, USA  
e-mail: [cbrown92@unm.edu](mailto:cbrown92@unm.edu)

M. Cowell  
Department of Mechanical Engineering, Colorado School of Mines, Golden, CO 80401, USA  
e-mail: [mcowell@mymail.mines.edu](mailto:mcowell@mymail.mines.edu)

H. Hahn • D. Mascareñas  
Los Alamos National Laboratory, Los Alamos, NM 87545, USA  
e-mail: [dmascare@ucsd.edu](mailto:dmascare@ucsd.edu)



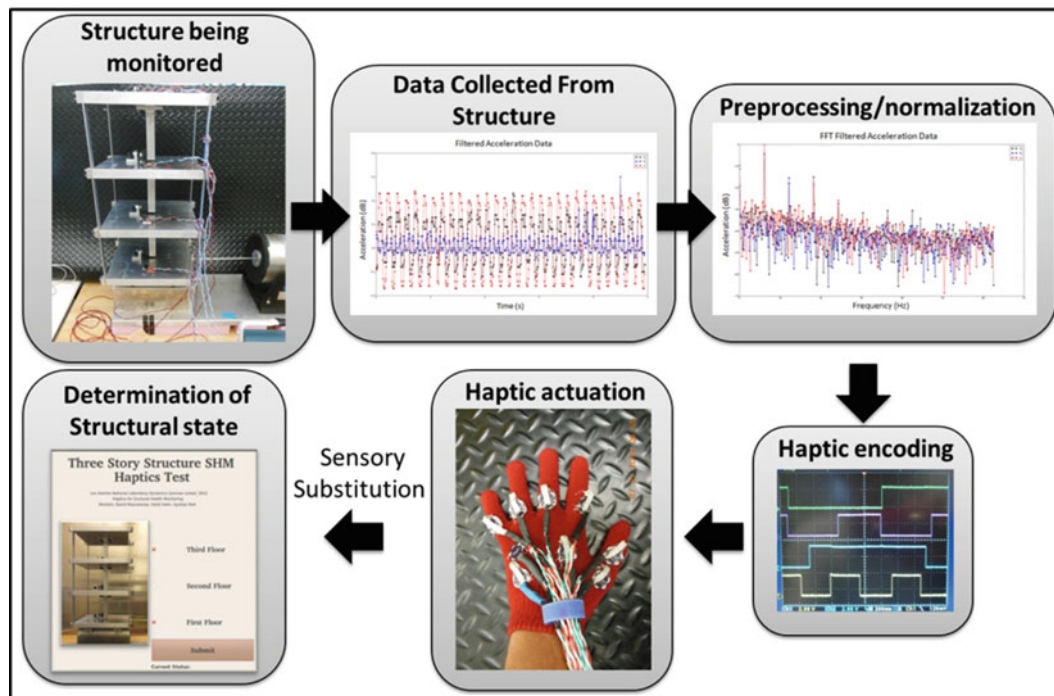
contexts. Furthermore, for life-safety applications there are significant regulatory and liability hurdles that must be overcome before fully autonomous SHM systems will be widely accepted. There are a number of problems with the concept of a fully-autonomous SHM system. In this work we would like to propose the development of a new semi-autonomous SHM paradigm in which novel human-machine interfaces are used to leverage the computational power, precision, and endurance of machines with human adaptivity and judgment. This new paradigm will be referred to as “cooperative SHM.”

The inspiration for this new paradigm comes from a number of sources. In 2005 an online chess playing website hosted a chess tournament in which mixed teams of humans and computers could compete. Teams included chess grandmasters working with several computers as well as the chess-specific supercomputer Hydra [3]. Perhaps unsurprisingly the supercomputers were dominated by strong human players teamed with weak laptops. The surprising result was the winning team consisted of a pair of amateur chess players using three computers at the same time. Chess grandmaster G. Kasparov made the following observation, “Their skill at manipulating and ‘coaching’ their computers to look very deeply into positions effectively counteracted the superior chess understanding of their grandmaster opponents and the greater computational power of other participants. Weak human + machine + better process was superior to a strong computer alone and, more remarkably, superior to a strong human + machine + inferior process. [3]” The formula of “human + machine + better process” for enhanced performance is one of the main ideas behind the concept of cooperative SHM. It may be time to consider merging human intelligence with computational resources. This work aims to explore novel human-machine interfaces that allow humans to naturally leverage computational resources so humans can provide guidance during the inspection process while at the same time increasing the efficiency of inspections. By combining human capabilities with machine capabilities using the proper process and system engineering tools, we hope to build a resulting SHM system that has the judgment and adaptability of a human combined with the scalability of distributed measurement systems and computers.

Inspiration for this concept also came from the neuroscience community. The idea of cerebral sensor plasticity has been explored for a number of years. A prime instance is a study in where the brains of ferrets had been successfully “rewired” to connect optical sensors to the animal’s auditory cortex [4, 5]. The study began with the undeveloped visual and auditory cortices of young ferrets. By stopping the auditory nerve from entering the thalamus, the optic nerve would change paths and grow through the thalamus before arriving to the visual cortex. In this study, half of the ferret’s brain was left unaltered while the other half was “rewired” with the optic nerve double connection. After maturation, it was found that the ferrets’ auditory cortex exhibited the pinwheel design found in the visual cortex instead of the regular linear alignment of auditory cells. Sure enough, when the connection to the visual cortex was severed, the ferrets still reacted to visual cues. This shows that the formation of the cells in the brain is a function of the input as opposed to being a predetermined standard configuration. The principle of “sensory substitution,” [6] based on neural plasticity, has already been leveraged to build new medical devices. An electro-stimulus array was placed on the human tongue in order to help blind people detect spatial forms [7]. This is preliminary work toward a prosthetic device that may 1 day allow blind persons to in some sense “see” using the sensors on their tongue. Another interesting case of human brain plasticity is human echolocation [8]. Some blind people have learned to sense the physical objects in their local surroundings by emitting a series of clicks with their tongue and listening for the resulting echoes. This is the same mechanism used by dolphins and bats to navigate their surroundings as well as look for food. These blind persons have essentially developed a sonar sensing capability to compensate for their lack of sight.

Not only do humans’ and animals’ brains show an ability to adapt to and incorporate unfamiliar methods of sensing, but there are arguments that some humans exhibit a natural instinct that might roughly be described as a “sixth sense.” Two examples of a “sixth sense,” could be the scientist’s “physical intuition” [9] or alternatively the machinist’s “sense of touch” [10]. To elaborate on the sense of touch, machinists often report that they set the speeds and feed rates of their cutting process according to a “sense of touch.” They essentially feel the vibrations being generated by the cutting process and adjust the machine setup accordingly in order to produce the appropriate results. Various devices have been designed to interface with the sense of touch. For example, vibro-haptic devices have been developed that can assist a human with waypoint navigation tasks [11, 12]. Effectively a compass or GPS is replaced with a belt featuring vibrators along its circumference. The vibrators are actuated in a manner that that encodes both distance and bearing. Some users of these devices report an enhanced sense of spatial orientation. Research has also been completed in studying the limits of human perception when multiple tactile inputs are presented to a human simultaneously [13].

The cooperative SHM paradigm arises from the combination of the idea of high-performance humans-machine teaming with the idea of sensory substitution. The goal of the SHM community is essentially to build a “nervous system,” into structures that detects, localizes, and characterizes damage as it appears in a structure. To date we have primarily investigated purely autonomous SHM systems. Perhaps we should consider a new paradigm that interfaces the highly developed human nervous system with a SHM distributed measurement system. We refer to this new paradigm as “cooperative SHM.” In cooperative SHM data collected by a distributed SHM measurement system is interfaced with a human nervous system using the principle of sensory substitution. The hypothesis is that a human interfaced to a structure’s distributed SHM measurement



**Fig. 19.1** Cooperative SHM paradigm

network will develop a sense of the structure’s “pain” as it incurs damage. Furthermore, we are interested in discovering if complex pattern recognition and processing can be performed using haptically-interfaced SHM data, in a manner analogous to human echolocation. This process will be illustrated with an example. In human echolocation the human is essentially generating pulses and, receiving/processing the resulting echoes to develop a spatial map of the human’s surroundings. This set of steps is very similar to the steps that go into performing active, ultrasonic, guided-wave structural health monitoring. We believe that it may be possible to incorporate human intelligence into this SHM process. An ultrasonic signal from a plate structure could be mixed down to the audible frequency range. A human could then listen to the resulting echoes through headphones. The human would then try to pick out patterns in the data corresponding to structural damage. This process is similar to the manner a submarine sonar operator would listen for signals in the sea and pick out ships. To close the loop, damage identified by a human operator could be fed into the training set of a supervised learning-based classifier. The classifier could then work with the human to reduce human workload and improve the overall performance of the system. This would be an example of cooperative SHM that incorporates the principles of sensory substitution as well as human-machine teaming.

### 19.1.2 Cooperative SHM Paradigm

We suspect that the proposed cooperative SHM paradigm can be applied to a wide variety of problems in SHM and potentially problems in other fields as well. In general the cooperative SHM paradigm consists of the steps outlined in Fig. 19.1. First, a structure of interest is instrumented with a distributed measurement system. Next data is collected from the distributed measurement system. The data is then sent to a preprocessing and normalization step. This preprocessing could involve a combination of a wide variety of techniques (e.g. filtering, classification, trend removal, data reduction). Once the data has been preprocessed the next step is to encode the data in a form that can be sent to a haptic device. The nature of this encoding will depend on many factors including the type of haptic actuation been used, the dynamic characteristics of the haptic actuators, the location on the body where the haptic actuation will be applied, the dynamic characteristics of the portion of the body the actuators are applied to, the number of available haptic actuators, the characteristics of the basis that can represent the pre-processed data in the most sparse fashion, and the representative spatial/temporal timescales of the data. The resulting “haptic code,” is then used to modulate the actuation of a set of haptic actuators that are interfaced to a human. The hypothesis at this point is that over time the human will develop a sense of the state-of-health of the structure in

a manner similar to the phenomenon of “sensor substitution”. The idea is that as the human becomes aware of changes in the structure as a result of communication from the haptic interface, the human would make decisions and classifications that indicate the structural state, and what if any remedies should be applied.

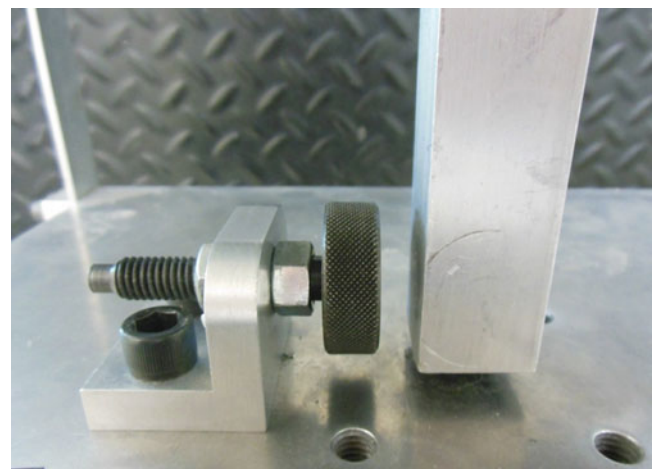
## 19.2 Proposed Proof of Concept Experiment

### 19.2.1 Proposed Proof-of-Concept Experimental Structure

For the proposed proof-of-concept research, a simple three-story structure is chosen as a test platform (Fig. 19.2). This structure is mounted on horizontal rails and is excited with an electromagnetic shaker vibrating at a single frequency. Mounted on the ceiling of each story are vertical columns that descend toward the floor below. Mounted on the floors below are adjustable bumpers that can be engaged or disengaged to interact with the descending columns during shaking (Fig. 19.3). The interaction between bumper and column during excitation produces a nonlinear rattling that simulates damage in the structure. Exciting the structure while no bumpers are engaged produces a linear dynamic response of the structure, while engaging any bumper combination results in a non-linear dynamic response. By varying the number and location of engaged

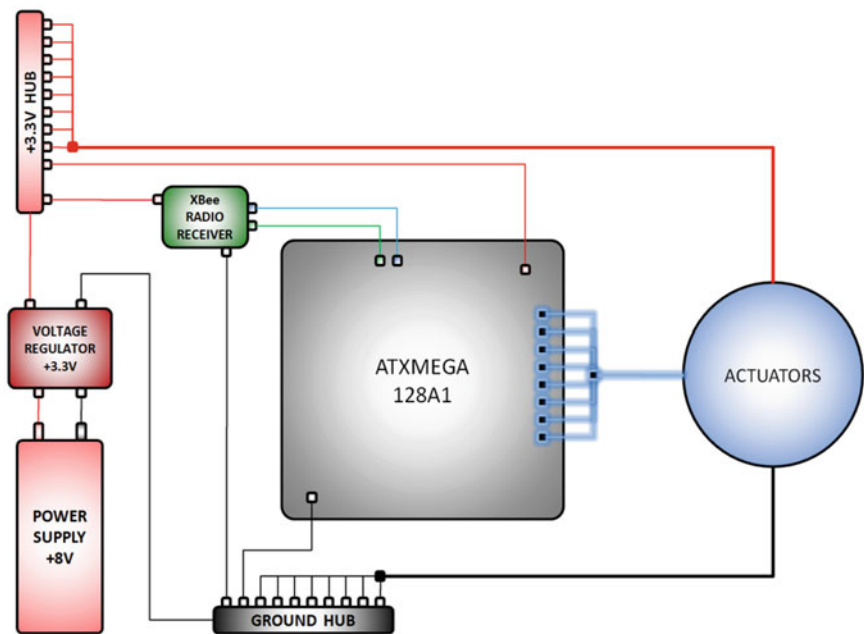


**Fig. 19.2** Surrogate three-story structure & shaker



**Fig. 19.3** Disengaged bumper

**Fig. 19.4** Control system wiring diagram



bumpers the structure can be imbued with a variety of damage scenarios. The dynamic characteristics of this structure have been studied in depth, and can be found in [14]. In the undamaged scenario (no bumpers engaged) the structure displays three dominant modes, plus a rigid body mode. The natural frequencies of the modes are 30.7, 54.2, and 70.7 Hz. As bumpers are engaged the response becomes nonlinear, and additional frequency components arise in the measurements that correspond to multiples of the excitation frequency.

To simulate damage, an electromagnetic shaker was utilized to excite the structure. Accelerometers stationed on each level of the structure transmitted data to a base station computer. The base station computer is used to aggregate the data, perform the data pre-processing and normalization step, as well as generate an appropriate haptic code to modulate the actuators. The generated haptic codes are transmitted to the microcontroller that modulates the haptic actuators. A microcontroller system transmits the haptic code to the corresponding vibrational actuator. The actuators attach to the human-machine interface. In this instance the interface is in the form of a vibrohaptic glove. Once the human subject experiences the haptic code through the actuator array, they will respond by entering into a graphical user interface (GUI) which of the structure's floors they believe the damage is being inflicted upon.

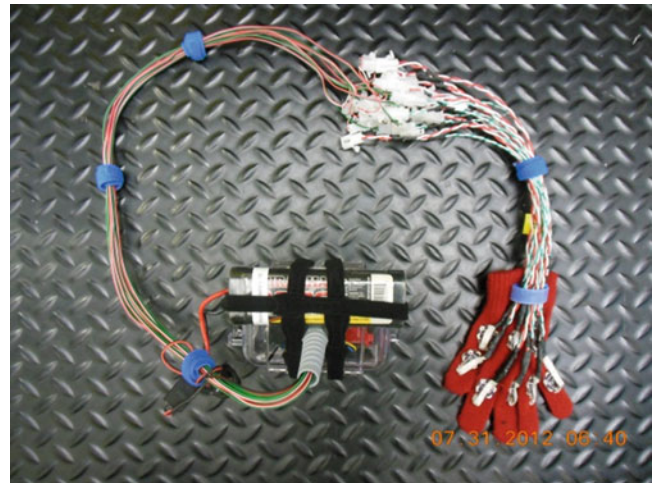
### 19.2.2 Hardware Design

The architecture of the actuator control system relies on embedded code within an ATXMEGA 128A1 microcontroller (MC) to deliver signals to the actuators (Fig. 19.4). Figure 19.5 shows the prototype cooperative SHM human-machine interface. It features 8 vibro-haptic actuators build into a glove. Eight haptic code bytes are received by the XBee radio receiver and transmitted over the USART to the microcontroller. Each byte passed to the microcontroller encodes the response of one of the eight actuators present in the haptic interface. By mapping the location of each actuator on the interface, signals can be tailored to align groups of actuators in tandem – creating sweeping, alternating, circling, or more complex patterns. The goal is to generate patterns that correspond to patterns present in the structure.

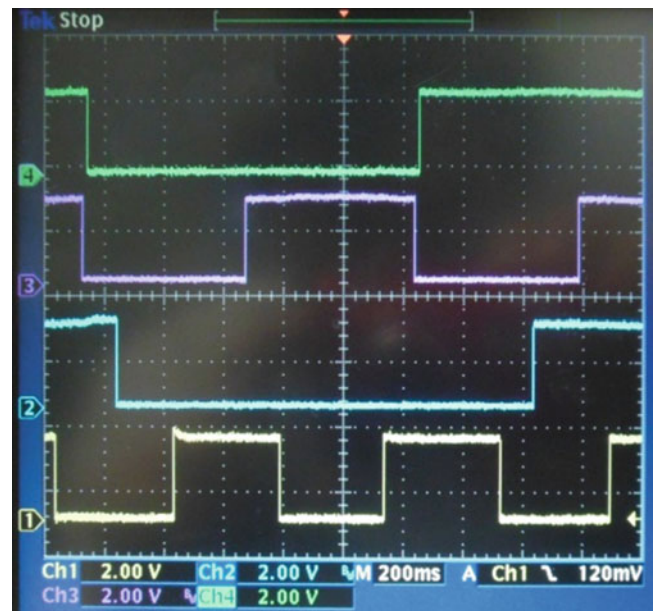
Patterns present in the structural data are encoded as eight-bit information and sent wirelessly to a microcontroller that is worn by the user. Once the signals are received by the microcontroller an embedded program distributes square wave signals to the actuators to initiate vibration. The frequency, phase, duty cycle and duration of these waves comprise the haptic input that is received by the user (Fig. 19.6). The goal of this process is to have the user determine which bumpers are engaged or disengaged in the structure through haptic input alone. This proposed experiment acts as a proof of concept that haptic data interrogation techniques can combine the computational power of a computer with the data classification capabilities of the human brain. The MC, radio receiver, and actuators are packaged with a power supply to be a completely mobile unit. In the design's final invocation this mobility allows the user to roam around a structure to interrogate specific areas in question.



**Fig. 19.5** Experimental haptic device for the proposed cooperative SHM experiments



**Fig. 19.6** Representative square-wave signals generated by the microcontroller from a haptic code



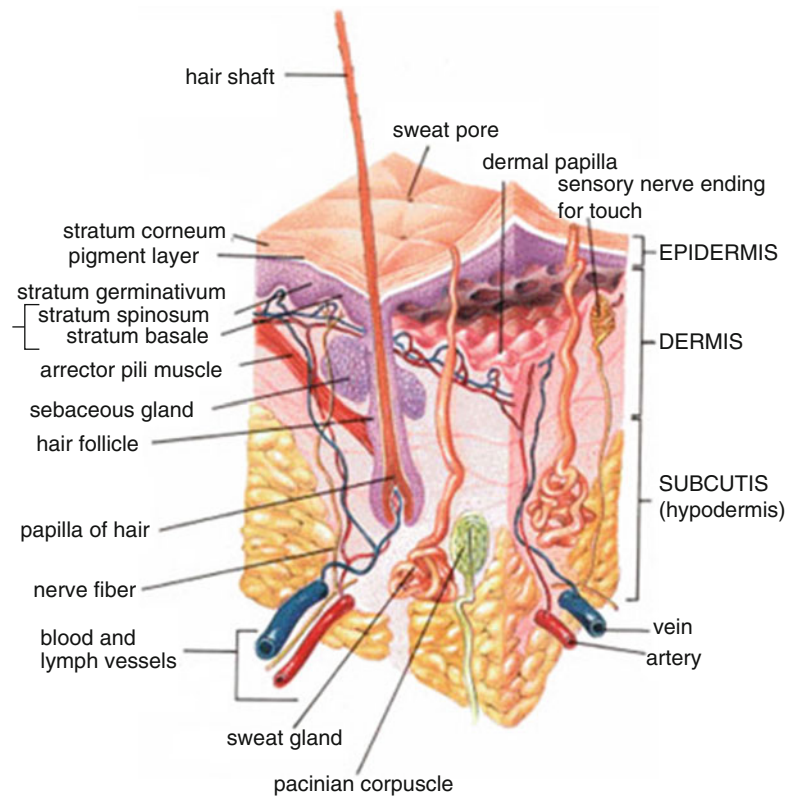
The vibrating actuators selected to be used in this initial research exhibit a characteristic vibrational frequency when supplied with power. The pulses sent by the microcontroller to the actuators act to turn the vibrators on and off.

### ***19.2.3 Considerations for Design of Haptic Cooperative SHM Human-Machine Interface***

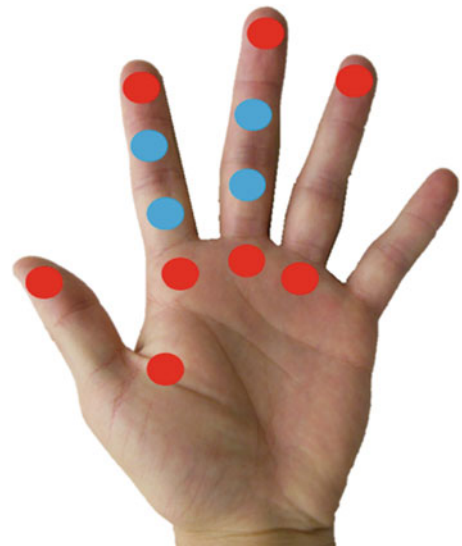
For our interface we aim to capitalize on the sense of touch by targeting Pacinian corpuscles in the hand (Fig. 19.7). Pacinian corpuscles are a type of mechano-receptor that are highly receptive to vibrations. These corpuscles dominate the response for vibrations higher than 80 Hz [16]. Though the range of human sensation extends up to 1,000 Hz, studies have shown that peak reactivity lies between 200 and 300 Hz [17], which is the range that is important to consider when we focus on human subjects testing.

The glove for the interface is a common winter glove, composed of a mesh that expands to the user's hand in a fit that is comfortable yet tight enough to remain next to the skin. The vibrational actuators are attached to the outside of the glove with the actuator facing down, allocated to the Pacinian corpuscles distribution of the hand [18–22]. Two designs were created based on the distribution of sensitivity of the hand to vibration. In the first design the accelerometers are placed on the palm of the hand. This design roughly maps to the Pacinian corpuscles in the human palm (Fig. 19.8). The second model situates

**Fig. 19.7** PC location in a skin sample [15]



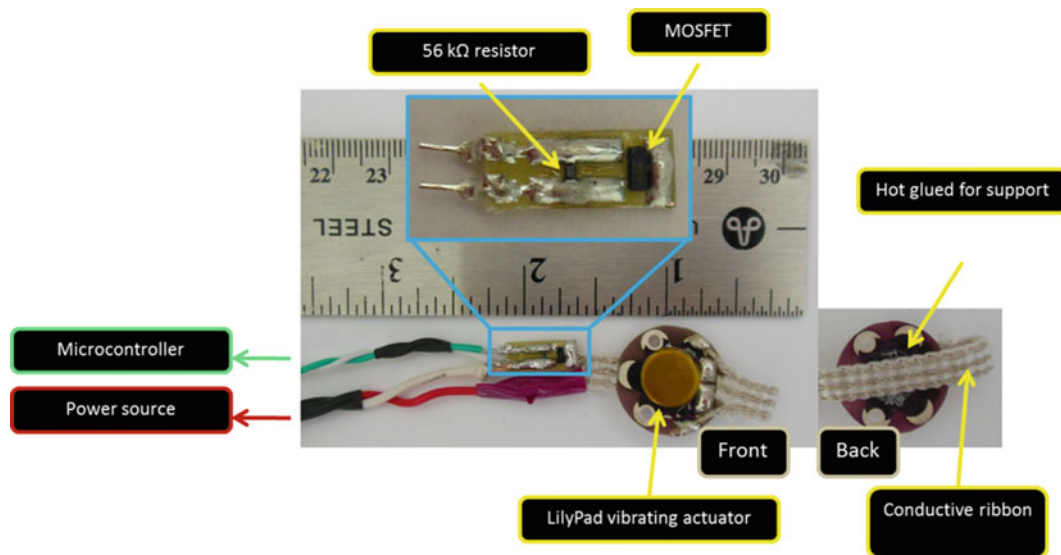
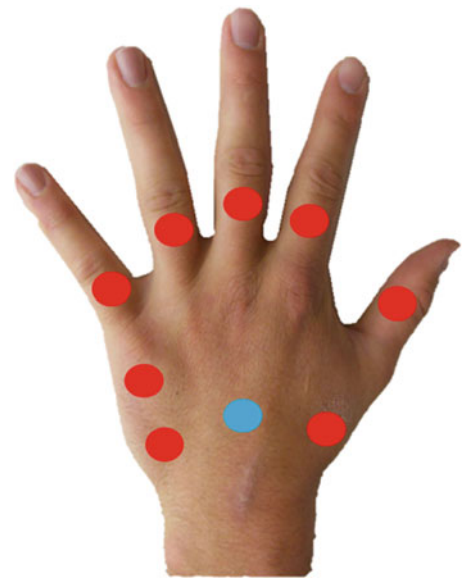
**Fig. 19.8** First design, based on the research done by Johansson [20]. *Red dots* signify definite actuator placements. *Blue dots* stand for locations which are variable



the actuators on the back of the hand and combines several blueprints of Pacinian corpuscles and mechanoreceptor locations (Fig. 19.9). The back of the hand may be advantageous since it has been found that vibrations are best sensed on bony, hairy skin [19, 22]. While there are few PCs in the back of the hand, PCs are located deeply enough that those found in the palm will react to the indirect stimulation. The second design's was ultimately chosen because of its inclusiveness and the practicality of the actuator locations.

The glove uses a total of eight actuators. The vibro-haptic actuators used for the device are similar to the vibrator in a cell phone. These actuators consist of a MOSFET and 56 k $\Omega$  resistor between the lead to a communal microcontroller and the power source (Fig. 19.10). The MOSFET facilitates the square waves sent from the microcontroller by managing the connection to the power source.

**Fig. 19.9** Design based on all four representations of PCs and mechanoreceptors mentioned previously, [18, 20, 21]. *Red dots* signify definite actuator placements. *Blue dots* represent locations which are variable



**Fig. 19.10** Detail of vibrational actuator electronics

At the beginning of assembling the actuators there was a wire directly soldered to the vibro-haptic actuator. When put under duress, the stresses at that juncture separated the internal circuitry in the main actuator unit. To rectify this weakness we replaced the wire with a conductive ribbon and glued it to the back of the vibrating actuator. This practice supplied extra support to the location and was repeated for the remaining actuators. Once the actuators were built, they were sewn to the glove in a temporary fashion so as to be easily relocated if necessary (Fig. 19.11).

### 19.3 Proposed Human Subject Testing

In order to demonstrate the feasibility of the cooperative SHM paradigm it is necessary to perform experiments using human subject. The purpose of human subject testing is necessary to demonstrate that it is feasible for humans to effectively use the vibro-haptic interface to correctly classify various responses (both linear and non-linear) of the above-mentioned surrogate three-story structure. It is important to note that to perform human subject testing researchers must coordinate with their Institutional Review Board (IRB).



**Fig. 19.11** Implementation of the glove



### 19.3.1 Proposed Procedure

Currently we are still coordinating with our IRB on the details of the human subject testing, but it can basically be described as follows. The testing procedure begins with data collection, storage and categorization of data collected from the test structure. For consistency, data used in testing will be per-recorded, and the same set of data must always be used to indicate a given set-up. Data is categorized according to which bumpers are and are not engaged. For each of the eight combinations of bumper engagement, a data structure containing the recorded accelerometer data is maintained. Each of these data structures constitutes an instance of a “test”. Tests are combined to create one “test regime”. For this research, only one test regime—containing all eight tests – is used, though in further research, more test regimes could be created, i.e., where the number of times one test occurs in the regime could vary.

Once the test regime has been created, the subject can be brought in for testing. The subject’s test session begins with familiarizing the human subject with the interface and the actuation patterns that may be encountered due to various structure responses. The subject is also shown the structure and given an explanation of how the system works. This step is referred to as training. Subjects are outfitted with the glove interface and allowed to make adjustments until comfortable. Once comfortable, a test regime is loaded into the testing software. For each test, the subject is informed what combination of bumper engagements is being used, and the corresponding test is used to actuate the glove. The full test regime will be used, exposing the subject to each possibility, allowing the subject to internalize the sensations caused by each bumper set up. Training is complete when the subject indicates that he or she feels prepared.

Upon completion of testing, the process to determine how well the subject has learned to feel the structure begins. Using Graphical User Interfaces (GUIs) – one for each the test subject, and the test administrator, the vibro-haptic interface is controlled and the subject allowed to input his or her diagnosis of bumper engagement. Figure 19.12 shows a representation of the GUI that will be presented to the human subjects. Data will be recorded indicating which bumpers they believe are engaged, the amount of time it takes the human subject to make a decision of which bumpers are engaged, and the number of repeats of any test case that they request. This data will be used to begin characterizing that accuracy and certainty of the human subjects.

## 19.4 Conclusions

This work introduces a new paradigm in for SHM that involves combining the intelligence and adaptively of humans with SHM distributed sensing systems. This paradigm is referred to as “cooperative SHM.” This paradigm is accomplished using haptic interfaces and hopes to capitalize on the well documented phenomenon of sensory substitution. Follow on work will focus on performing human subject testing in order to determine the efficacy of this paradigm.

**Fig. 19.12** Representative test GUI presented to the human subject



**Acknowledgements** Acknowledgements The authors are grateful for the support obtained to complete this work through the 2012 Los Alamos National Laboratory (LANL) Dynamic Summer School and its director Charles Farrar. They are also thankful to the LANL Human Subject Research Review Board (HSRRB) for their assistance and valuable input toward laying the foundation to eventually begin human subject testing. HSRRB project designation LANL 12-05 X.

## References

1. Farrar C, Duffey T, Doebling S, Nix D (1999) A statistical pattern recognition paradigm for vibration-based structural health monitoring. In 2nd international workshop on structural health monitoring, Stanford, 8–10 Sept 1999
2. Schwamb ME, Orosz JA, Carter JA, Welsh WF, Fischer DA, Torres G et al (2012) Planet Hunters: a transiting circumbinary planet in a quadruple star system. arXiv:1210.3612 [astro-ph.EP]
3. Kasparov G (2010) The chess master and the computer. *The New York Review of Books*. 11 Feb 2010
4. Melchner LV, Pallas S, Sur M (2000) Visual behaviour mediated by retinal projections directed to the auditory pathway. *Nature* 404:871–876
5. Sharma J, Angelucci A, Sur M (2000) Induction of visual orientation modules in auditory cortex. *Nature* 404:841–847
6. Bach-y-Rita P, Kercel SW (2003) Sensory substitution and the human-machine interface. *Trends Cogn Sci* 7(12):541–546
7. Bach-y-Rita P, Kaczmarek KA, Tyler M, Garcia-Lara J (1998) Form perception with a 49 point electrotactile stimulus array on the tongue: a technical note. *J Rehabil Res Dev* 35(4):427–430
8. Thaler L, Arnott S, Goodale MA (2011) Neural correlated of natural human echolocation in early and late blind echolocation experts. *PLOS One* 6: <http://dx.doi.org/10.1371/journal.pone.0020162>. May 2011
9. Clement J (2003) Imagistic simulation in scientific model construction. In: Proceedings of the twenty-fifth annual conference of the cognitive science society. Boston
10. The Literary Digest (1911) The machinist's sense of touch. *The Literary Digest* 28 Oct 1911 p 733

11. Van Erp JBF, Van Veen HAHC, Jansen C, Dobbins T (2005) Waypoint navigation with a vibrotactile belt. *ACM Trans Appl Percept* 2(2): 106–117
12. Nagel S, Carl C, Kringe T, Martin R, Konig P (2005) Beyond sensory substitution – learning the sixth sense. *J Neural Eng* 2(4):R13–R26
13. Yoon MJ, Yu KH (2006) Psychophysical experiment of vibrotactile pattern recognition at fingertip. In: SICE-ICASE international joint conference Busan
14. Figueiredo E, Park G, Figueiras J, Farrar C, Worden K (2009) Structural health monitoring algorithm comparisons using standard data sets. Los Alamos, Los Alamos National Laboratory, US Department of Energy, March 2009. Report No.: LA-14393
15. United States Government Anatomy of the human skin with English language labels. 2005–2009. <http://commons.wikimedia.org/wiki/File:Skin-IT.jpg>
16. Mahns DA, Perkins NM, Sahai V, Robinson L, Rowe MJ (2006) Vibrotactile frequency discrimination in human hairy skin. *J Neurophysiol* 95(3):1442–1450
17. Vallbo AB, Johansson RS (1984) Properties of cutaneous mechanoreceptors in the human hand related to touch sensation. *Hum Neurobiol* 3(1):3–14
18. Bear M, Connors B, Paradiso MA (2007) *Neuroscience: exploring the brain*. Lippincott Williams & Wilkins, Philadelphia
19. Myle K, Binseel M (2007) The tactile modality: a review of tactile sensitivity and human tactile interfaces. Army Research Laboratory, May 2007. Report No.: ARL-TR-4115
20. Johansson RS, Vallbo AB (1979) Tactile sensibility in the human hand: relative and absolute densities of four types of mechanoreceptive units in glabrous skin. *J Physiol* 286:283–300
21. Edin BB (2004) Quantitative analyses of dynamic strain sensitivity in human skin mechanoreceptors. *J Neurophysiol* 92(6):3233–3243
22. Gemperle F, Hirsh T, Goode A, Pearce J, Sieewiorek D, Smailigic A (2003) Wearable vibro-tactile display. Pittsburgh Carnegie Mellon University, Carnegie Mellon Wearable Group

# Chapter 20

## Technologies for Seismic Safety Management of Existing Health Facilities

C. Rainieri and G. Fabbrocino

**Abstract** Safety of health facilities is only partially related to the performance of primary structural members. Stiffness and ductility are relevant for life safety of occupants but they have limited influence on the resilience of the system. Thus, modern seismic codes provide strict requirements to structural and non-structural components. They are aimed at ensuring that the system remains fully operational in the case of frequent earthquakes. Electro-mechanical and medical equipments, tanks and distribution systems, heat, ventilation and air conditioning (HVAC) systems, elevators and power supply systems have a predominant position in the safety hierarchy over the mechanical performance of structural members. In the present paper the opportunities provided by state-of-the-art monitoring technologies for seismic safety management of existing health facilities are investigated. Attention is focused on the implementation of a methodology able to cover the needs of knowledge, storage and monitoring of crucial information and physical data by taking advantage of the most recent developments in sensing, data acquisition and processing. This is not a trivial task, since system resilience depends also on the ability of inspectors and managers to integrate theoretical evaluations and interpretation of field measurements.

**Keywords** Health facilities • Non-structural components • Operational limit state • Monitoring system • Seismic protection

### 20.1 Introduction

Health facilities are usually very complex systems. They perform a large number of functions: they provide health care but also function as office for the medical staff and administration, laboratories and warehouses. They are also strategic structures, which should remain fully operational after earthquakes.

Many hospitals worldwide and mainly in European regions exposed to medium or high seismic hazards, i.e. Italy, Greece and Turkey, are often built according to outdated codes of practice and they often do not fulfil the above-mentioned requirement. Thus, attention has been recently focused on their seismic safety at National and International level [1].

Hospitals play a fundamental role in the case of an earthquake, but they are also very vulnerable due to their complexity, occupancy level and the presence of specific equipments and installations. Vulnerability assessment requires consideration of both structural aspects and non-structural and administrative ones [1, 2]. As a consequence, the structure has to be able to resist the force of natural disasters and equipments and furnishing should remain undamaged, vital connections (water, electricity, medical gases, and so on) have to be in service and the personnel has to be able to provide medical assistance even in emergency conditions.

A “safe hospital” is a facility whose services remain accessible and functioning at maximum capacity and in the same infrastructure during and immediately after the impact of a natural hazard [1]. Actually, existing hospitals are rarely out of service after an earthquake because of structural damage. Functional breakdown is usually the reason for service interruption. Thus, an effective protection strategy has to ensure not only that hospitals remain standing in the case of an earthquake, but above all that they remain in service without interruption, in order to accomplish the following tasks [1]:

---

C. Rainieri (✉) • G. Fabbrocino  
Dipartimento di Bioscienze e Territorio, Structural and Geotechnical Dynamics Laboratory StreGa, University of Molise,  
Via Duca degli Abruzzi, 86039 Termoli, Italy  
e-mail: [carlo.rainieri@unimol.it](mailto:carlo.rainieri@unimol.it); [giovanni.fabbrocino@unimol.it](mailto:giovanni.fabbrocino@unimol.it)

- Protect the life of patients, visitors and hospital staff,
- Protect the investment in equipments and furnishing,
- Protect the performance of the health facility.

The definition of an operational limit state is critical in particular in the case of frequent earthquakes, when slight or no structural damage can be observed, but the health facility experiences service interruptions due to non-structural damage or damage to equipments and installations. A prompt fault detection of equipments and installations after a ground motion and near real time identification and localization of eventual structural damage are the main tasks in the development of “smart health facilities” (SHFs). The attention focused on the performance of equipments and installation is fundamental to assess also the indirect losses due to the loss of functions, that are often more relevant than those associated to structural damage.

Taking into account that the damage of critical equipments and installations, such as tanks, lifeline services and so on, might cause downtime in health facilities, different levels of acceptable damage can be defined based on the related consequences on the user community and the frequency of occurrence of such a damage level, in compliance with the concept of performance-based design. Thus, a thorough assessment of health facilities requires an integrated performance evaluation based on continuous monitoring of structural, non-structural and operational safety.

When earthquake is the main natural hazard in the geographic area of interest, a reliable seismic vulnerability assessment plays a primary role in the definition of the expected performance of the structure in the case of a seismic event. The vulnerability assessment of health facilities is currently carried out according to various methods depending on the objectives of the assessment and the availability of data and technology [3, 4]. From a general point of view, they can be classified as qualitative and quantitative methods. The former are usually used to analyze large building stocks and to prioritize interventions in hospitals while the latter are used for individual buildings requiring more detailed assessment and analyses.

Among the qualitative methods, score assignment methods and, in particular, rapid visual screening (RVS) procedures are often adopted. However, such methods suffer the subjectivity of the expert judgement. This drawback can be overcome by the implementation of effective monitoring strategies where relevant parameters related to the system response and environmental factors are continuously recorded and processed in order to get relevant information about the health status of the system itself. An integrated monitoring strategy, focused not only on the structural behaviour but also on equipments and installations by a proper choice of sensors and data processing strategies, provides significant information about the overall performance of the health facility both in operational conditions and in the case of extreme events such as earthquakes. The collected data and information lead to the formulation of a more objective judgement about the system. This result can be obtained through the integration of different sensing elements and data processing procedures, so that the combination of information and data coming from each monitored subsystem is able to provide, almost in real time, a scenario about the health conditions and performance of the facility. Eventually, the combination of effective monitoring strategies with control and early warning systems can improve the global safety of health facilities against hazardous events.

The advantage of development and implementation of SHFs is in the setting of a platform able to assist the management committee of the hospital in the prompt and effective maintenance of structure and equipment under operational conditions, and in decision making and emergency management in the case of seismic events, thus extending the lifespan of the facility. However, the continuous monitoring of structural and non-structural components requires the definition of a sustainable monitoring strategy in terms of sensor type and number, architecture of the monitoring system and computational burden associated to data acquisition and processing. The Structural Health Monitoring (SHM) system has to be robust and reliable, and its lifespan has to be comparable to that of the monitored facility. Durability requires additional efforts in the design of the monitoring system, related to the choice of the measurement chain and, above all, its organization in a way able to prevent downtime when single components may require replacement because out of order or obsolete. Moreover, in order to fulfil the objective of assisting the maintenance and management of the monitored infrastructure, ease of use of the monitoring system and report of a few intelligible information instead of large amounts of raw data are key requirements in the design and development of an SHF.

In the present paper criteria and methods adopted in the design of a sample SHF in a seismically prone area are investigated. Attention is focused on the sustainable implementation of an SHF able to cover the needs of knowledge, storage and monitoring of crucial information and physical data by taking advantage of the most recent developments in sensing, data acquisition and processing. Taking into account that a high percentage of public spending [5] is for specialized health personnel and sophisticated and costly equipment, it is critical that hospitals continue to work even in the case of an earthquake. This is not a trivial task, since functions and resilience of the system as a whole depend also on the ability of inspectors and managers to integrate theoretical evaluations with field measurements and their effective physical interpretation [6, 7].

## 20.2 Safety Issues in Health Facilities

Seismic protection of health facilities can take advantage of the recent advances in civionics [8] and in the development of smart structures and systems in order to provide information about their health state in an automated way. SHFs are based on the implementation of appropriate monitoring strategies consisting in the installation of a number of sensors on structural and non-structural components and in automated data processing procedures able to extract relevant information about their performance from the raw measurements.

The collected data and information provide a relevant contribution to risk reduction since effective management and maintenance strategies can be implemented in order to reduce vulnerability and enhance the overall performance of the facility. Disaster risk, defined as the probability that damages will overwhelm the ability of the affected community to respond, is in fact the combination of a hazard with vulnerability. The (natural or man-made) hazard, which is the probability that a potentially damaging phenomenon will occur, interacts with vulnerability, which is the likelihood that a community will be adversely affected by that hazard. While hazard can be of natural origin, vulnerability is always the result of human activities (planning, construction and development). Thus, different communities have different resilience to disasters occurring at their location and the extent and severity of damage is inversely proportional to the level of resilience. A comprehensive assessment of the risk in the case of a health facility starts from the identification of the hazard in the geographic area where it is located. This information is critical for performance evaluation and determination of safety levels in structural and non-structural components. Thus, an effective SHF requires also the collection of data about ground motions eventually occurring in the area.

On the other hand, the factors making health facilities vulnerable [2] have to be clearly identified. They can be summarized as follows:

- Complexity, related to the large number of functions accomplished in hospitals, ranging from health care to office and administration, laboratory, warehouse and so on;
- High level of occupancy 24 h a day and presence of medical equipment, potentially dangerous gases and life support equipment requiring continuous power supply;
- High level of dependence on public services and infrastructures (power supply, water, clinical gases, oxygen, fuel, communications), and critical supplies (medicines, splints, bandages, and so on);
- Presence of heavy medical equipment (X-ray machines, backup generators, autoclaves and other pieces of specialized equipment) which can be damaged as a result of intense ground motions;
- Presence of hazardous materials which can cause indirect losses or, at least, contamination if they spill or leak.

Issues related to structural safety, non-structural safety and safety based on functional capacity have to be therefore identified and analyzed.

Structural safety involves monitoring of structural components and materials and their response to hazards. The objective is the assessment of the performance of the structure under operational conditions, the identification of incipient damage and eventual degradation phenomena, and the assessment of the impact of earthquakes or other hazards on structural integrity and functional capacity. Vibration based techniques able to identify and locate structural damage [9] have a potential in the development of effective SHFs.

The failure of non-structural elements mainly endangers people and the contents of a building. The monitoring strategy has to focus the attention on the stability of non-structural elements (supports, anchors . . . ) and check whether equipment can function during and after an earthquake. In particular, the continuous observation and analysis of the performance of critical systems reduces downtimes for checks of equipments and networks after the impact of an earthquake, since eventual failures are automatically detected by the SHF. This leads also to an optimization of emergency management procedures, since economic and human resources can be entirely devoted to the maintenance of damaged systems only.

The information coming from processing of the data collected by different sensors deployed throughout the health facility plays a fundamental role not only in the definition of appropriate and effective maintenance actions, but also in the organization and optimization of the response of the personnel after an earthquake. Disaster preparedness of the staff can take advantage of the monitoring results to organize assistance in the early earthquake aftershock based on still working equipment and networks.

The above mentioned critical aspects and the opportunities provided by the implementation of an SHF point out how an effective reduction of the overall vulnerability of health facilities requires an integrated monitoring and management strategy which takes into account the different structural, non-structural and administrative components, their interaction and the related safety issues [2].



### 20.3 Criteria for Sustainable Implementation of Smart Health Facilities

An effective SHF requires the installation of an appropriate number of sensors, of different types and performance, and, above all, an efficient data processing system. The latter acquires sensor output, processes data and eventually provides an alarm. Thus, data processing, reduction and storage, sampling frequency and simultaneous sampling are the fundamental issues, especially with the use of a large number of installed sensors. However, it is worth pointing out how all installations must have also a minimum impact on functions in the hospital.

The different nature of structural and non-structural components requires different strategies for data acquisition and processing. Since there is no sensor able to fit the needs of every monitoring application, sensor choice has to take into account the nature and type of the monitored component and the objectives of monitoring. Sensor selection depends on the physical quantity of interest, and this varies depending on the nature of the component and the expected vulnerability issues. Protection of sensors, wires and connections is fundamental to ensure durability of the SHM system and data quality. For some types of sensors electromagnetic radiation (EMR) effects must be considered.

About the choice of sensors, they must be able to resolve the system response both in operational conditions and in the case of an earthquake. The type of sensor depends also on the monitoring requirements: if a global assessment based on a number of accelerometers deployed on the structure and vibration based damage detection algorithms can provide relevant information about the health state of the structure, different sensors and data processing strategies are required for non-structural elements. For instance, connections and anchorages of tanks, large medical devices (CAT scanners, X-ray machines) can be more effectively monitored by strain gauges, settlements of distribution systems by FBG sensors, losses in tanks and distribution systems by pressure measurements, while medical equipments sensitive to vibrations require acceleration measurements. A summary of typical safety issues in health facilities and of the most appropriate sensors for different monitoring objectives is reported in Table 20.1.

An integrated platform for seismic protection of health facilities should also take into account the following measures:

- Prevention during the years before an earthquake, through seismic design, strengthening of buildings, and the installation of earthquake early warning systems, seismic alarms and earthquake rapid response systems;
- Early Warning, represented by the measures which can be carried out whenever a relevant seismic event is detected by a seismic network such as the evacuation of buildings or shut-down of critical systems. The SEWS must be able to calculate in real-time the seismic parameters. Whenever a given threshold is exceeded, a warning signal must be transmitted to the interested receivers in order to take adequate countermeasures [10];
- Emergency management, represented by all actions to be taken in the early aftershock hours or whenever the structural conditions of critical buildings have to be assessed to ensure the safety of rescue and/or emergency functions inside the structure.

**Table 20.1** Sensor classes for different monitoring objectives and safety issues

Item	Monitoring objective	Sensors
Structural safety	Overall structural performance and health assessment	High sensitivity accelerometers
	Structural detailing (connections, joints . . . )	Strain gauges, displacement transducers, fiber optic sensors
Non-structural safety	Foundations (vulnerability to floods, differential settlement, liquefaction)	Fiber optic sensors,
	Connections and anchorages	Strain gauges, displacement transducers
	Large medical devices (CAT scanners, X-ray machines), medical equipments sensitive to vibrations	Accelerometers, displacement transducers
	Settlements of distribution systems	Fiber optic sensors
	Losses in tanks and distribution systems	Pressure sensors
	Antennas and lightning rods	Anemometers, corrosion sensors, accelerometers
Safety based on functional capacity	HVAC, pipes, connection, valves	Humidity sensors, fiber optic sensors, temperature sensors, pressure sensors, accelerometers
	Fire protection systems	Pressure sensors
	Alarm activation/deactivation	Accelerometers, displacement transducers
	Elevators	Seismic switches
Hazard	Valve shut off	Seismic switches
	Seismic hazard	Accelerometers, velocimeters, seismometers

In such a framework, the collected data and information are certainly useful to improve the knowledge about the health state and performance of the health facility over time. Thus, also management and maintenance interventions and investments can be addressed towards certain subsystems or installations according to a rational prioritization. However, the combination of monitoring plans with basic early warning and control strategies can further enhance the overall safety of the health facility. The information coming from sensors can be also used for the implementation of control strategies able to improve the overall safety in the case of an earthquake. This is the case, for instance, of lift: the information coming from accelerometers deployed on the structure and eventually from early warning system can be used to activate strategies for the immediate shutdown of elevator systems in the event of a potentially damaging earthquake. Shut-down of lifts and critical systems and closure of valves in the case of damage to distribution systems are other possible applications.

A SHF, able to diagnose its own faults and damage, represents also a primary tool for the reduction of the administrative and organizational vulnerability, acting on the preparedness of personnel in the event of an earthquake and helping in the management and maintenance of structural and non-structural elements over time. For instance, the possibility to have a scenario about the performance of structures and subsystems in a few minutes after the earthquake can help the staff in the emergency management and in the identification of the required interventions (for instance, replacement of components in distribution systems) to maintain the hospital fully operational. In this framework, the combination of monitoring plans with early warning strategies can provide additional level of seismic protections (shut-down of critical equipments, reduction of the risk of indirect losses related to the failure of tanks and distributions systems) at minor costs [11]. The continuous monitoring of the health state and performance of hospitals, including equipment and installations, can help in the formulation also of disaster mitigation plan and in the prioritization of investments for safety of people and goods. The importance rating of clinical and support services [2] can help in the definition of priorities in the implementation of the monitoring system in the presence of budget constraints. The development of a smart system, which analyzes data related to different subsystems (structure, equipment, installations and so on) and provides synthetic information about its overall performance and also eventual warnings in the case of damage or faults, can effectively take into account the critical nature and interdependence of the various processes, buildings and equipment.

For a near real-time response of the system, data must be collected, stored, assessed for validity and processed within a very short time. Sampling frequency has to be carefully chosen in order to acquire and retain an optimized amount of data. Along with filtering, this is an issue related to the data reduction and storage which cannot and should not be neglected. The problem of simultaneous sampling is easily solved when a single data logger is used, as data synchronization is governed by the switch rate of the data logger [12]. However, with the rapid increase in the number and type of installed sensors, modular and wireless architectures are also gaining in existence. If two or more loggers are used definite strategies have to be adopted in order to ensure a simultaneous sampling.

Sensing, power, communication and storage technologies are not the only issues while dealing with such systems. Raw data can provide only limited information about the health of a structure. Thus, data mining, signal processing and health assessment (damage detection and prognosis) algorithms have to be considered as well. The continuous progress in the field of damage detection is yielding algorithms that are able to identify the existence, location and extension of damage in structures on the basis of structural response measurements [13, 14].

Vibration based damage identification techniques represent promising tools for structural health assessment. The efforts of the scientific community in the field are leading to the development of effective methods for incipient damage detection and localization based on measurements of the structural response to ambient vibrations [9]. The development of automated output-only modal identification techniques [15, 16] has determined a renewed interest also towards modal based damage detection [9]. Other approaches are based on post-processing of the measurement data to detect anomalies directly from measurements (ARMA modelling, wavelet decomposition and so on). In both the cases, the trend is to use methods that are able to automate the detection process by taking advantage of the recent advances in information technology [17]. Apart from vibration-based methods, static data can be also effectively used for damage detection [18]. Recent developments in data mining and data fusion are exploiting the opportunities arising from the combination, into the same monitoring system, of information coming from different sensors and related to different physical variables. Thus, a number of tools are already available for an effective assessment of the structural safety of health facilities. However, as mentioned before, structural damage is not the main cause of failure of health facilities. Non-structural damage affecting critical equipments and installations is more often the cause of service interruptions.

Even if the failure of non-structural elements does not usually put the stability of a building at risk, it can endanger people and contents. In particular, critical equipment such as medical devices, tanks, adduction system, power supply systems and backup generators, heat, ventilation and air conditioning (HVAC) systems have a primary influence on the in-service conditions of health facilities. Earthquakes occurred in the past (Takachi-oki, Japan, 1968; San Fernando, USA, 1971; Nihonkai-Chubu, Japan, 1983; El Salvador, Salvador, 2001) have demonstrated [2] that the cause of service interruption and indirect losses due to contamination or out-of-service of health facilities is often the damage to installations (water,

steam, medical gases, fuel, air conditioning, piping) and equipment (medical equipment, furnishings, supplies, clinical files, pharmacy shelving, laboratory shelving). Even low magnitude events can affect the vital aspects of a hospital, that is to say those connected to its functions. For instance, experience has shown that the secondary effects caused by damage to non-structural elements can endanger people like structural damage: fire, explosions and leaks of chemical substances can be life-threatening. Damage to equipment and installations and interruption of services, therefore, can make a modern hospital virtually useless.

In order to protect investments in equipment and technological devices, advanced diagnostic tools and monitoring of critical parts such as joints and connections play a fundamental role in the prompt assessment of the functionality of health facilities after a seismic event. For instance, mechanical equipments are very sensitive to acceleration and monitoring of inertial or shaking effects on critical equipment and installations can provide useful information for the prompt assessment of their functionality. Advanced techniques for machine condition monitoring and fault diagnosis can provide objective data and information about the functionality of equipment and installations, and suggestions about the priority of eventual maintenance interventions. An extensive review of such techniques useful for the assessment of non-structural components such as equipment and installations (medical equipment, HVAC and so on) can be found elsewhere [19].

## 20.4 Conceptual Framework for Design and Implementation of a Pilot SHF in Central Italy

An appropriate choice of sensors and consideration of the main issues related to installation and data processing (maintenance of sensors, data volume and processing time) represent key issues for the implementation of effective SHFs, as sketched in Fig. 20.1. This illustrates the architecture adopted for the design of a pilot SHF. Its implementation is expected on a sample existing health facility built according to obsolete design codes in a seismically prone area in Central Italy. It is based on remote sensors wired to local data acquisition modules. These transmit the data to a centralized data acquisition system in wireless mode or via Ethernet. Local data processing for individual subsystem and components can be carried out by local servers. The role of the centralized data server is to aggregate, store and further process the data in order to provide a synthetic overview of the overall performance of the facility. As the number of sensors increases, the adoption of a modular architecture and of wireless sensing units leads also to a minimization of the impact of the monitoring system on the functions in the hospital. The presence of databases on the local and master servers simplify the replacement of components without changes in the overall architecture of the monitoring system, whose durability is therefore ensured.

The designed SHF system will be able to assess in near real time the health conditions of the structure by continuous tracking of natural frequencies and mode shapes and modal based damage detection algorithms. The automated extraction of

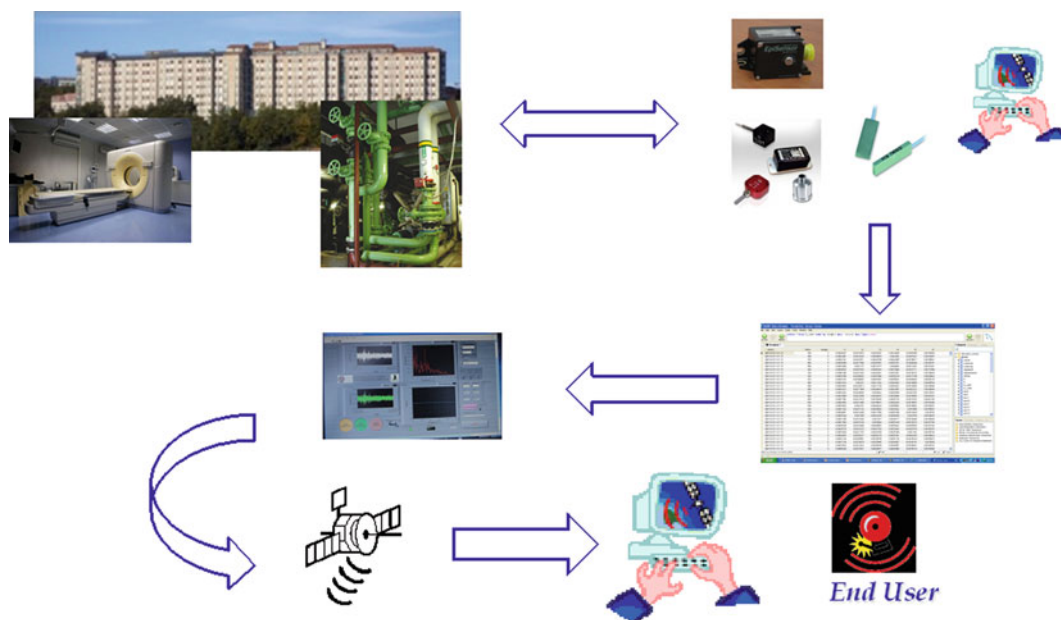


Fig. 20.1 Schematic architecture of the prototype SHF

the information about the dynamic properties of the structure from records of the structural response (in terms of acceleration) to the ambient excitation allows for a significant data reduction. In fact, only some days of raw data will be stored on the local database and cyclically deleted, while the estimated modal parameters will be permanently stored on the master server for health assessment and visualization, with significant savings in terms of storage volumes. The continuous monitoring of the modal parameters leads also to a knowledge enhancement about the dynamic behavior of the structure in operational conditions and a statistical characterization of the influence of environmental factors on the structural response. Whenever a seismic event occurs, a link with seismic stations installed over the territory allows for the identification of such events so that related data can be permanently stored. The information about seismic events plays a fundamental role in the characterization of the structural performance and response to ground motions, but it is relevant also to assess the performance and health status of equipment and other non-structural components when an earthquake strikes the facility. Appropriate local data processing procedures can be activated and the information provided by fault diagnosis and machine condition monitoring algorithms can be acquired by the master server in order to support decision making and emergency management. Adoption of local processing reduces the amount of data to be transmitted and this is particularly useful in the post-earthquake phase. However, redundant vectors for data transmission make the SHF more robust in the case of strong motions. The consequences of extreme events on data transmission systems have to be taken into account in particular when early warning and disaster management are primary objectives in the implementation of a SHF.

In summary, the integration of different sensors and continuous condition assessment procedures allows for a performance-based maintenance of health facilities and an assessment of both the short-term impact due to earthquakes and the long-term deterioration process due to physical aging and routine operation. Anomalies can be detected by continuously processing the incoming data. In the case of earthquake risk analysis, monitoring systems can be used to create a database from measurements taken during the life of the structure. In the pre-seismic event phase, these data can be analyzed to evaluate the ability of the building to withstand seismic events on the basis of tremors, such as those due to traffic or wind excitation, by updating the numerical model. At the same time, calibration of the available structural models can improve the ability of structural calculations to make reliable estimations of seismic performance, including the effect of quakes on equipment and installations according to simplified formulation or even the computation of floor spectra [5]. Finally, an in-depth knowledge about the seismic characteristics of the site (such as zone of the epicentre, seismicity, etc.) provides additional useful information. As the database builds over time, this analysis improves, and the detailed characterization of seismicity and structural behaviour allows more reliable predictions of the structural response and of the event that will occur, so decreasing the problem of a false alarm. The design of the prototype SHF is currently undergoing a detailed analysis for the identification of appropriate data acquisition solutions taking into account the characteristics of the monitored structure and the equipments and non-structural components located in the health facility. In fact, they have an influence on the choice of the sensors, since they determine the parameters and physical quantities of interest. Moreover, a detailed characterization of the seismic hazard of the area is in progress [20] and this will have an influence on the architecture of the monitoring system and the design choices for the implementation of a robust data acquisition, processing and transmission, taking into account the probability of extreme events in the area. The outcomes of the present study are preliminary and certainly not comprehensive. However, encouraging recommendations for future developments and experimental studies have been obtained and extensively discussed.

## 20.5 Conclusions

Safety of health facilities mainly depends on the resilience of the overall system rather than on the performance of primary structural members. Thus, stiffness and ductility, which are relevant design parameters, have limited impact on safety of occupants. For this reason, the modern seismic codes provide strict requirements to both structural and non-structural components. They are aimed at ensuring that the system remains fully operational in the case of frequent earthquakes. Electro-mechanical and medical equipments, tanks and distribution systems, heating, ventilation and air-conditioning systems, elevators and power supply systems have a predominant position in the safety hierarchy over the ordinary mechanical (strength and ductility) performance of structural members. Standardized approaches, criteria and indicators for a reliable assessment and management of existing facilities are needed. The present study has investigated the opportunities provided by a monitoring plan in the objective structural and non-structural characterization of existing hospitals. Attention has been focused on the analysis of the factors which make health facilities vulnerable and on the issues related to a rational and objective assessment of performance and health state of structural and non-structural components. This is not a trivial task, since functions and resilience of the system as a whole depend also on the ability of inspectors and managers to integrate theoretical evaluations with field measurements and their effective physical interpretation. In this context the

opportunities provided by the implementation of SHFs based on methodologies able to cover the needs of knowledge, storage and monitoring of crucial information and physical data by taking advantage of the most recent developments in sensing and data acquisition have been reviewed. The integration of different sensors and continuous condition assessment procedures allows for a performance-based maintenance of health facilities and an assessment of both the short-term impact due to earthquakes and the long-term deterioration process due to physical aging and routine operation. Anomalies can be detected by continuously processing the incoming data. Data driven experimental methods (in particular, vibration based methods) have been primarily considered to assess performance and health state of structural and non-structural systems. The outcomes of the study are definitely not comprehensive, but provide encouraging recommendations for future developments and experimental studies.

**Acknowledgements** Acknowledgments The present study is related to the activities issued by the ASREM Molise Director General Dr. Angelo Percopo on the complex of the P.O. Cardarelli in Campobasso. The Authors wish to thank Dr. Eng. G. Gallina and Dr. Arch. G. Getuli for their contribution in the context of the validation of available seismic assessment data of the above mentioned Health Facility and their valuable support in the definition of operational conditions of structural and non-structural components. In addition, collaboration with ReLUIIS Consortium research groups active in the framework of Line 2.2 Special Systems of the ReLuis-DPC Executive Project 2010–2013 “RELUIIS II”, rep. 823 is also gratefully acknowledged.

## References

1. Pan American Health Organization (2008) Hospital safety index – guide for evaluators. Pan American Health Organization, Washington, DC
2. World Health Organization – Regional Office for Europe (2006) Health facility seismic vulnerability evaluation – a handbook. World Health Organization – Regional Office for Europe, Copenhagen, Denmark
3. Trendafiloski GS (2003) GIS-oriented method for development of probabilistic earthquake scenarios. Institute of Earthquake Engineering and Engineering Seismology, Skopje
4. Lang K (2002) Seismic vulnerability of existing buildings. Institute of Structural Engineering, Swiss Federal Institute of Technology, Zurich, Switzerland
5. Ministero della Salute (2003) Raccomandazioni per il miglioramento della sicurezza sismica e della funzionalità degli ospedali, Rome
6. ATC 51–1 (2002) Recommended U.S. – Italy collaborative procedures for earthquake emergency response planning for hospitals in Italy. Applied Technology Council, Redwood City
7. ATC 51–2 (2003) Recommended U.S. – Italy collaborative guidelines for bracing and anchoring non-structural components in Italian hospitals. Applied Technology Council, Redwood City
8. Klowak C, Rivera E, Mufti A (2005) Implementation of civionics in a second generation steel-free bridge deck. Proc. SPIE 5767, Nondestructive Evaluation and Health Monitoring of Aerospace Materials, Composites, and Civil Infrastructure IV, 195, doi:10.1117/12.604903
9. Doebling SW, Farrar CR, Prime MB, Shevitz DW (1996) Damage identification and health monitoring of structural and mechanical systems from changes in their vibration characteristics: a literature review, Technical report LA-13070-MS, UC-900, Los Alamos National Laboratory, New Mexico
10. Salzano E, Garcia Agreda A, Di Carluccio A, Fabbrocino G (2009) Risk assessment and early warning systems for industrial facilities in seismic zones. *Reliab Eng Syst Saf* 94(10):1577–1584
11. Rainieri C, Fabbrocino G, Cosenza E (2010) Integrated seismic early warning and structural health monitoring of critical civil infrastructures in seismically prone areas. *Struct Health Monit An Int J* 10(3):291–308
12. McConnell KG, Reiley WF (1987) Strain-gage instrumentation and data analysis. In: Kobayashi AS (ed) *Handbook on experimental mechanics*. Prentice-Hall, Englewood Cliffs, pp 79–116
13. Fujino Y, Abe M (2001) Structural health monitoring in civil infrastructures and R & D of SHM of bridges at University of Tokyo. In: *Proceedings of the 3rd International Workshop Structural Health Monitoring: The Demands and Challenges*, 4337, Stanford, CA, USA, pp.61–79
14. Various Authors (2007) Structural health monitoring 2007 – quantification, validation and implementation. In: F-K Chang (ed) *Proceedings of the 6th international workshop on structural health monitoring*. Stanford University, Stanford
15. Rainieri C, Fabbrocino G (2010) Automated output-only dynamic identification of civil engineering structures. *Mech Syst Signal Process* 24(3):678–695
16. Rainieri C, Fabbrocino G, Cosenza E (2011) Near real-time tracking of dynamic properties for standalone structural health monitoring systems. *Mech Syst Signal Process* 25(8):3010–3026
17. Aktan AE, Ciloglu SK, Grimmelsman KA, Pan Q, Catbas FN (2005) Opportunities and challenges in health monitoring of constructed systems by modal analysis. In: *Proceedings of the international conference on experimental vibration analysis for civil engineering structures*. Bordeaux, France
18. Lanata F (2008) Statistical algorithms for damage detection using static and dynamic approaches. In: *Proceedings of the 4th European workshop on structural health monitoring*, Cracow, Poland, pp 1047–1054
19. Widodo A, Yang B-S (2007) Support vector machine in machine condition monitoring and fault diagnosis. *Mech Syst Signal Process* 21(6):2560–2574
20. Caccavale M, Convertito V, Mancini M, Fabbrocino G (2010) Seismic hazard disaggregation in the Molise region, Italy: the case study of Campobasso. In: *Proceedings of the 14th European conference on earthquake engineering*, paper 1684, Ohrid



# Chapter 21

## Wave-Induced Vibration Monitoring for Stability Assessment of Harbor Caisson

So-Young Lee, Thanh Canh Huynh, Han-Sam Yoon, Jeong-Tae Kim, and Sang-Hun Han

**Abstract** Up-to-date structural health monitoring (SHM) studies have been focused mostly on in-land structures such as bridge and building. Only a few research efforts have been made for harbor structures such as caisson-type breakwater. For stability assessment of harbor caisson structures, it is very essential to monitor vibration responses with limited accessibility, to analyze the vibration features, and to specify the sensitive motions with respect to damage in the caisson-foundation's interface. In this paper, a wireless sensing system for SHM of harbor caisson structures is presented. To achieve the objective, the following approaches were implemented. First, a wave-induced vibration sensing system was designed for global structural health monitoring. Second, global SHM methods which are suitable for damage monitoring of caisson structures were selected to alarm the occurrence of unwanted behaviors. Third, a SHM scheme was designed for the target structure by implementing the selected SHM methods. Operation logics of the SHM methods were programmed based on the concept of the wireless sensor network. Finally, the performance of the proposed system was globally evaluated for a field harbor caisson structure for which a series of tasks were experimentally performed by the wireless sensing system.

**Keywords** Wave-induced vibration • Stability assessment • Harbor caisson • Breakwater • Vibration monitoring

### 21.1 Introduction

Coastal structures are getting used to face more severe state of typhoon; thus, the safety of coastal structures becomes more significant against the storm waves. The safety can be monitored in a regular periodic or irregular time-scale, depending on the state of the target structures and also the occurrence of extreme loading events such as storm-surges or typhoons. The safety is usually done by structural health monitoring (SHM) to identify existing damages in the target structures, gravity-type or pile-type, and finally to make an assessment of their healthy status. In the gravity-type coastal structures, the damages can be classified into settlement, overturning, or sliding. Local defects such as scouring and disturbance in foundation can be also occurred and these defects tend to propagate into severer damages i.e., the global damages, such as partial settlement, under extreme wave forces. Thus, it is imperative to capture the local defects in time, at least just before these defects become a real threat.

Most coastal or harbor structures in South Korea have been constructed as gravity-type and recently, thanks to the advances in concrete and towing and laying technology, very large caissons, a gravity-type, became popular for constructing breakwaters, quays, etc. Considering the report [1, 2], significant damages of harbor caissons are mostly attributed to foundation-structure interface i.e., foundation mound. Goda and Takagi [3] and Takahashi et al. [4] also reported that sliding

---

S.-Y. Lee • T.C. Huynh • J.-T. Kim (✉)

Department of Ocean Engineering, Pukyong National University, 599-1, Daeyeon3-dong, Nam-gu, Busan 608-737, South Korea  
e-mail: [idis@pknu.ac.kr](mailto:idis@pknu.ac.kr)

H.-S. Yoon

Research Center for Ocean Industry and Development, Pukyong National University, 599-1, Daeyeon3-dong, Nam-gu, Busan 608-737, South Korea

S.-H. Han

Coastal Development & Ocean Energy Research Division, Korea Institute of Ocean Science and Technology, 787 Haean-ro, Sangnok-gu, Ansan-si, Gyeonggi-do 426-744, South Korea



at the foundation-structure interface is the primary damage of caissons. It is known that cavity in foundation mound or backfill makes harbor caissons weaker against extreme loads such as storm waves, mainly occurred from typhoon. Thus, SHM for gravel mounds for existing caisson structures is absolutely demanded.

Since as early as the 1980s, many researchers had studied SHM techniques in the field of civil engineering by mainly performing vibration-based damage monitoring of civil structures [5–9]. Also, many researchers have worked on developing damage detection methods such as the modal sensitivity method, modal flexibility method, genetic algorithm, neural network, etc. [10–15]. Related to the damage detection, sensor placement techniques have been studied and evaluated by applying to the tower structure [16, 17].

Up-to-date research studies, however, have focused mostly on inland structures but only few research efforts have been made to harbor structures, which include vibration response analyses of soil-structure or fluid-soil-structure interactions in harbor caisson structures [18, 19] and SHM of a cylinder caisson using fiber grating sensing technology [20]. Considering harbor caisson structures, there exist research needs to monitor vibration responses with limited access and to identify sensitive vibration methods of a row of caisson units with respect to damage in caisson's foundation and/or damage in caisson's interlocking members.

The demand to test full-scale structures has led structural engineers to develop new methods to perform such experiments i.e., input–output (forced vibration) and output-only (ambient vibration) modal identification methods. Since it is difficult to excite large and massive civil structures in a controlled manner, the performance of output-only modal identification tests became an alternative in the field of civil engineering. Bridge structures have been the representative target to verify the efficiency of output-only modal identification [21–25]. Also, other structures have been tested through the identification [26–29]. These studies show that ambient tests have been successfully applied to a number of large bridges, towers, storage tanks, and buildings. Thus, in this study, we applied vibration-based SHM on massive caisson structures that are not applicable to be excited by forced vibration. In other words, instead of using forced vibrations, we used water wave-induced vibrations for SHM, which was utilized by ambient vibration modal identification methods.

Output-only modal identification methods can be classified into two groups: parametric methods in time-domain and nonparametric methods that essentially developed in the frequency domain. The frequency domain methods are initiated by the construction of power spectral densities (PSDs) involving all of the measurement points in the test program. In this study, we also used PSDs and, consequently, correlation coefficient (CC) and lower control limit (LCL) to alarm the damaged states. Namely, the occurrence of damage was indicated when the standard deviation of CC values is beyond the bound of LCL. In addition, frequency domain decomposition (FDD) method was used to extract modal parameters such as natural frequency and mode shape. These modal parameters were used to determine a reference state and, accordingly, distinguish the healthy states of the target caissons.

Recent development in wireless smart sensor node (SSN) technologies has motivated various applications in the frequency domain-based SHM of massive engineering structures. So far, numerous field works have demonstrated that wireless smart sensors can be used to construct a reliable and accurate SHM system [30–35]. In addition to the relatively lower cost than wired SHM systems, one of the great advantages for using wireless sensors is that autonomous operations for SHM can be implemented by embedding advanced system technologies. In the study, we also proposed a vibration-based wireless sensing system comprising of an accelerometer, wireless data logger, wireless receiver, and laptop. Moreover, was developed an autonomous SHM scheme utilizing CC and modal parameter-based method, which were operation logics of the proposed SHM.

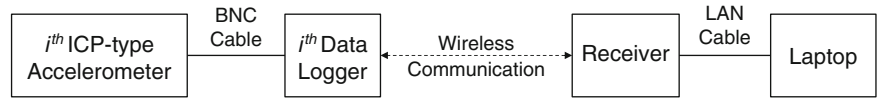
In summary, we present a wireless sensing system for structural health monitoring of harbor caisson structures. To achieve the objective, the following approaches were implemented. First, a wave-induced vibration sensing system was designed for global structural health monitoring. Second, global SHM methods which are suitable for damage monitoring of caisson structures were selected to alarm the occurrence of unwanted behaviors. Third, a SHM scheme was designed for the target structure by implementing the selected SHM methods. Operation logics of the SHM methods were programmed based on the concept of the wireless sensor network. Finally, the performance of the proposed system was globally evaluated for a field harbor caisson structure for which a series of tasks were experimentally performed by the wireless sensing system.

## 21.2 Wireless Monitoring System for Harbor Caisson Structure

### 21.2.1 Vibration-Based Wireless Sensing System

Figure 21.1 shows the proposed vibration-based wireless sensing system. One system comprised of accelerometers, wireless data loggers, a wireless receiver, and a laptop, as shown in Fig. 21.1. Rechargeable battery, which supplied electric power

**Fig. 21.1** Schematic of wireless vibration sensing system



to the data logger itself and to the accelerometer through the BNC cable was embedded in the data logger. Electric power for receiver was supplied by external portable battery. In the system, as shown in the figure, the  $i$ th accelerometers capture the signals and transport the captured to the  $i$ th data loggers by the BNC cables, then the transported signals were wirelessly transmitted to the receiver, and finally the signal arrived to the laptop via the LAN cable. To acquire the wave-induced, micro-vibration signals, we used PCB393B03 model for the accelerometers, which have the measurable range of  $\pm 0.5$  g and sensitivity of 10 V/g. In the wireless communication, 2.4 GHz Bluetooth of transmitting frequency was used to range its communication to 1.2 km. The wireless data loggers had a programmable low pass filter from 10 Hz to 1 kHz and resolution of 16 bits. Also, the available sampling frequency ranged from 1 Hz to 1 kHz and the accuracy of synchronization was in 10 ms.

The wireless sensing system utilized the vibration-based SHM methods – PSD-based method and modal parameter-based method. Moreover, an autonomous operation was carried out in the wireless sensing system by the operation logics based on correlation coefficient of power spectral density and modal parameter-based method. The brief introduction to the SHM methods and autonomous operation are briefly explained in the following sections.

## 21.2.2 Vibration-Based SHM Methods

### 21.2.2.1 Power Spectral Density-Based Method

Assume there are two acceleration signals,  $x(t)$  and  $y(t)$ , measured before and after a damaging episode, respectively. The corresponding power spectral densities (PSDs),  $S_{xx}$  and  $S_{yy}$ , are calculated from Welch's procedure as [36]:

$$S_{xx}(f) = \frac{1}{n_d T} \sum_{i=1}^{n_d} |X_i(f, T)|^2 \quad (21.1a)$$

$$S_{yy}(f) = \frac{1}{n_d T} \sum_{i=1}^{n_d} |Y_i(f, T)|^2 \quad (21.1b)$$

where  $X$  and  $Y$  are the frequency response transformed from correspondent acceleration signal;  $n_d$  is the number of divided segments; and  $T$  is the data length of divided segment.

The correlation coefficient (CC) of PSDs represents the linear identity between the two PSDs obtained before and after a damage event, as follows:

$$\rho_{XY} = \frac{E[S_{xx}S_{yy}] - \mu_{S_{xx}}\mu_{S_{yy}}}{\sigma_{S_{xx}}\sigma_{S_{yy}}} \quad (21.2)$$

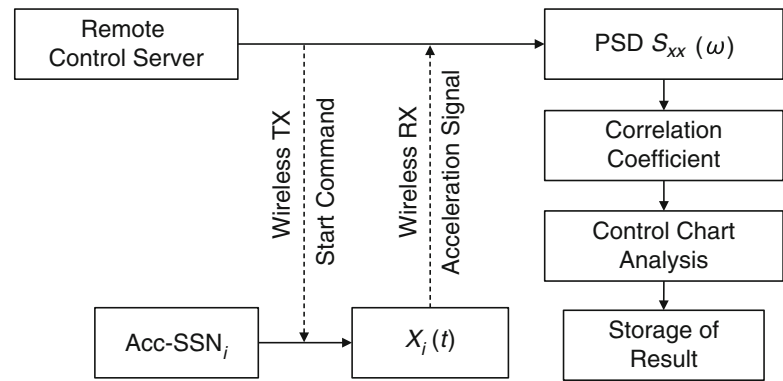
where  $E[\bullet]$  is the expectation operator, and  $\sigma_{S_{xx}}$  and  $\sigma_{S_{yy}}$  are the standard deviations of PSDs of acceleration signals measured before and after damaging episode, respectively. If any damage occurs in target structure, its acceleration responses would be affected and, consequently, the decrement of CC can be a warning sign of the presence of damage.

For damage alarming, control chart analysis is also performed to discriminate damage events from the CC values. The alarming threshold is determined by the lower control limit (LCL) as follows:

$$LCL_{\rho} = \mu_{\rho} - 3\sigma_{\rho} \quad (21.3)$$

where  $\mu_{\rho}$  and  $\sigma_{\rho}$  are the mean and the standard deviation of the CC values, respectively. The occurrence of damage is indicated when the CC values are beyond (i.e., less than) the bound of the LCL; otherwise, there is no indication of damage occurrence.

**Fig. 21.2** An autonomous SHM procedure for PSD-based method



### 21.2.2.2 Modal Parameter-Based Method

Frequency domain decomposition (FDD) method is used to extract modal parameters such as natural frequency and mode shape [37, 38]. The singular values of the PSD function matrix  $\mathbf{S}(\omega)$  are used to estimate the natural frequencies instead of the PSD functions themselves as follows:

$$\mathbf{S}(\omega) = \mathbf{U}(\omega)^T \boldsymbol{\Sigma}(\omega) \mathbf{V}(\omega) \quad (21.4)$$

where  $\boldsymbol{\Sigma}$  is the diagonal matrix consisting of the singular values ( $\sigma_i$ 's) and  $\mathbf{U}$  and  $\mathbf{V}$  are unitary matrices. Since  $\mathbf{S}(\omega)$  is symmetric,  $\mathbf{U}$  becomes equal to  $\mathbf{V}$ . In this FDD method, the natural frequencies can be determined from the peak frequencies of the singular value, and the mode shape from any of the column vectors of  $\mathbf{U}(\omega)$  at the corresponding peak frequencies. Generally the first singular value  $\sigma_1(\omega)$  among  $\sigma_i$ 's ( $i = 1, \dots, N$ ) is used to estimate the modal parameters except in some special cases such as with two or more identical excitations.

## 21.2.3 Autonomous SHM Scheme

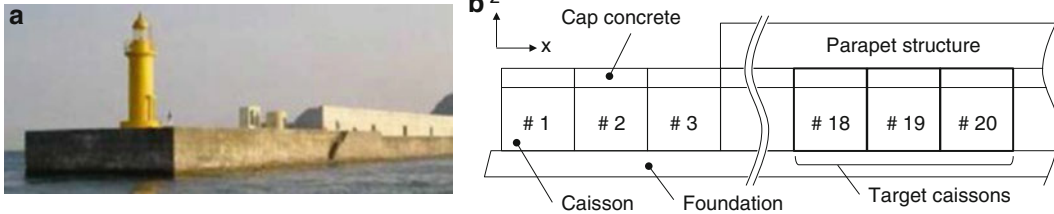
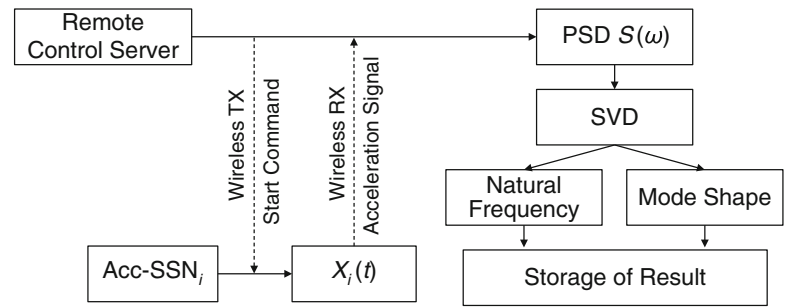
### 21.2.3.1 Power Spectral Density-Based Method

An autonomous SHM procedure for PSD-based method is designed as shown in Fig. 21.2. The detail procedure is as follows: (1) transmit “start command” by remote control server to the Acc-SSN (acceleration-based smart sensor node); (2) acquire acceleration signals and store the measurement data in the Acc-SSN; (3) transmit the acceleration signal by the Acc-SSN into the remote control server; (4) compute power spectral density in the remote control server using the embedded FFT algorithm; (5) calculate correlation coefficient in the remote control server; and (6) determine if damage is occurred by performing the control chart analysis.

### 21.2.3.2 Modal Parameter-Based Method

An autonomous SHM procedure for the modal parameter-based method is designed as shown in Fig. 21.3. The detail procedure is as follows: (1) transmit “start command” by remote control server to the Acc-SSN (acceleration-based smart sensor node); (2) acquire acceleration signals and store the measurement data in the Acc-SSN; (3) transmit the acceleration signal by the Acc-SSN into the remote control server; (4) compute power spectral density in the remote control server using the embedded FFT algorithm; and (5) calculate natural frequency and mode shape using singular value decomposition (SVD) in the remote control server.

**Fig. 21.3** An autonomous SHM procedure for modal parameter-based method



**Fig. 21.4** Oh-Ryuk-do breakwater and test layout of the structure. (a) Oh-Ryuk-do breakwater (b) Test layout

## 21.3 Field Evaluation

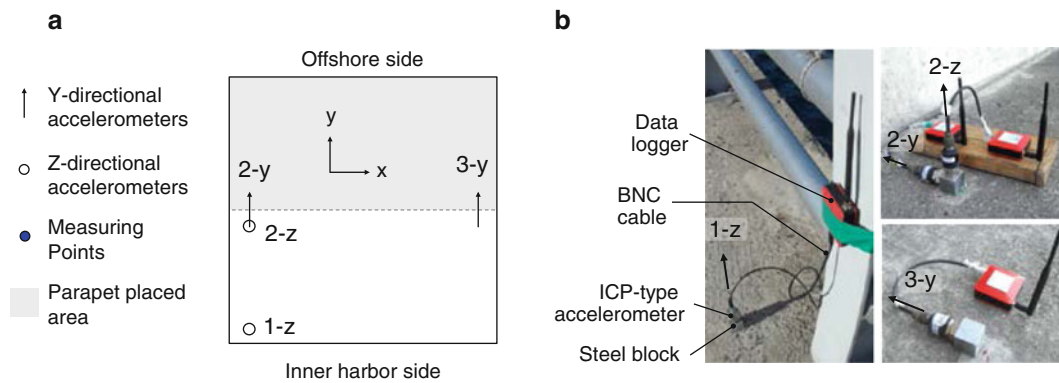
### 21.3.1 Target Caisson Structure

A real caisson-type breakwater locating in Busan, South Korea, Oh-Ryuk-do breakwater was selected to verify the applicability of the proposed vibration-based SHM technique. The breakwater consisted of 50 caissons and its total length was 1,004 m. Each caisson is covered by cap concrete to the height of 4 m. Parapet structure, which has 5.3 m height and 8.8 m width, is located above the caisson units except #1–3 and #48–50. The parapet structure increases the crest height of breakwater and gives higher calmness of harbor. All of the caissons were submerged in seawater and only their cap concretes were exposed in air. Three target structures, which have the same geometry with the parapet, were selected to compare the relative vibration responses by wireless vibration sensing system. Vibration tests were mainly performed on target caissons denoted by #18, #19, and #20 as shown in Fig. 21.4. The size of each caisson is 20 m (width) × 20 m (length) × 16.78 m (depth).

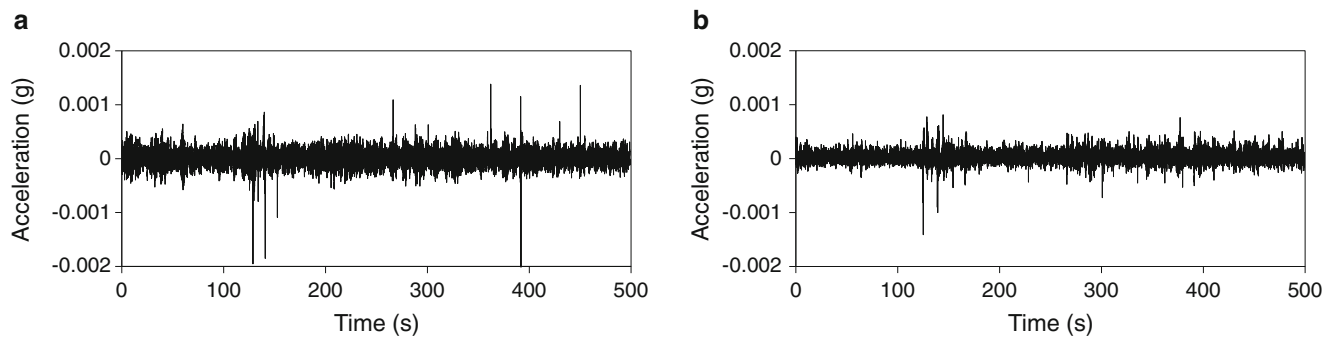
### 21.3.2 Wave-Induced Ambient Vibration Test

In general, it is not easy to acquire forced vibration responses from heavy structures like Oh-Ryuk-do breakwater. To get the response, we may need a tugboat, which was not a possible option in the test. Instead, we measured ambient vibration signals without using any artificial impact load by utilizing the fact that the caisson structures were under incident waves and wind loads.

The measurement was made by the wireless vibration sensing system as schematically shown in Fig. 21.1. As explained earlier, wireless vibration sensing system consisted of accelerometers, wireless data loggers, a wireless receiver, and a laptop. A system of 12 acceleration channels was employed to get the vibration responses of three target caisson units at the same time. Four channels were assigned to each caisson unit (#18, #19, and #20) along the direction of the wave incident ( $y$ -direction) and upward vertical direction ( $z$ -direction), as shown in Fig. 21.5a. The sensors are denoted by 2- $y$ , 3- $y$ , 1- $z$ , and 2- $z$ , respectively. Here the first notation (1, 2 or 3) indicates the location of the sensors and the second notation ( $y$  or  $z$ ) denotes the direction of acceleration. The orientation of sensors on the three caisson units was set as same as each other. Before installing the sensors in the pre-cast steel blocks, the surfaces of the top concrete caps were ground down. Figure 21.5b shows the component of local node and installed local node for three measuring points. Representative received



**Fig. 21.5** Schematic of vibration sensing system and installed sensing system (a) Schematic of vibration sensing system (b) Installed sensor for three measuring points



**Fig. 21.6** Acceleration signals obtained from sensor 2-y and 2-z of caisson #18. (a) Sensor 2-y (b) Sensor 2-z

signals, obtained from 2-y and 2-z of #18, were shown in Fig. 21.6. As shown, the acceleration of the sensor 2-y has a bigger acceleration level than that of sensor 2-z because the wave-induced, ambient vibration was the same direction as the y-axis.

### 21.3.3 Vibration-Based Damage Monitoring

For the three target caissons, damage monitoring was performed by the proposed methods. In the first step, six sets of acceleration measurements were acquired from each caisson and PSDs corresponding to the sets were calculated. The PSDs corresponding to the first set of each caisson were shown in Fig. 21.7, respectively. We can observe from Fig. 21.7 that there are two peaks in the frequency range from 0 to 6 Hz and the y-direction responses are clearer than the z-direction responses. This result comes from the incident wave motion along with the y-axis on the caisson response. The first peak locates at the fixed value of 1.51 Hz for all of the caissons while the second peak locates approximately at 2.5 Hz with the variances such as 2.69 Hz in #18, 2.47 Hz in #19, and 2.54 Hz in #20. The maximum difference of the second peak values is about 8 %, which means structural abnormality is sensitive to the second peak. In the second step, planar mode shapes (mode 1) were extracted to examine the relative motions between interfaces, as shown in Fig. 21.8. Frequency domain decomposition (FDD) algorithm [38] was used to extract the mode shapes corresponding to the first frequency 1.51 Hz. As shown, the relative motion of #19 is much larger than those of #18 and #20. Between #18 and #20, the relative motion of #18 is slightly smaller than that of #20; thus, the caisson #18 was selected as the reference and then the states of #19 and #20 were compared with that of the reference caisson. In the final step, CC values were calculated and, accordingly, LCL values were determined as shown in Fig. 21.9. This figure illustrates the relative gaps in the healthy states among the caissons. The correlation between #18 and #19 is bigger than that between #18 and #20, which means the healthy state of #19 is worse than that of #20. This observation becomes clearer in the results from 1-z and 3-y because the gaps between the caissons are extinct.

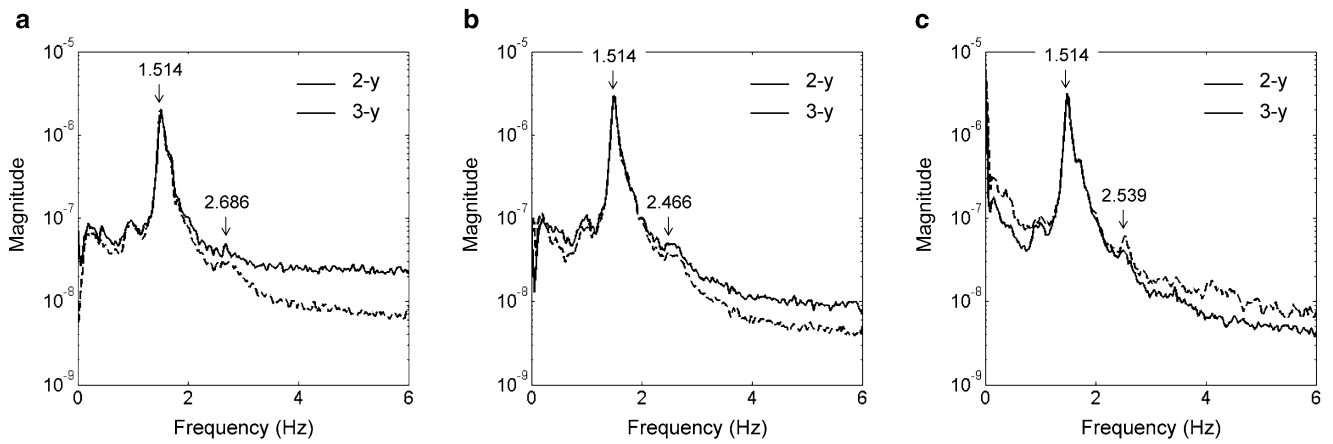


Fig. 21.7 Power spectral densities of caisson #18–20. (a) Caisson #18 (b) Caisson #19 (c) Caisson #20

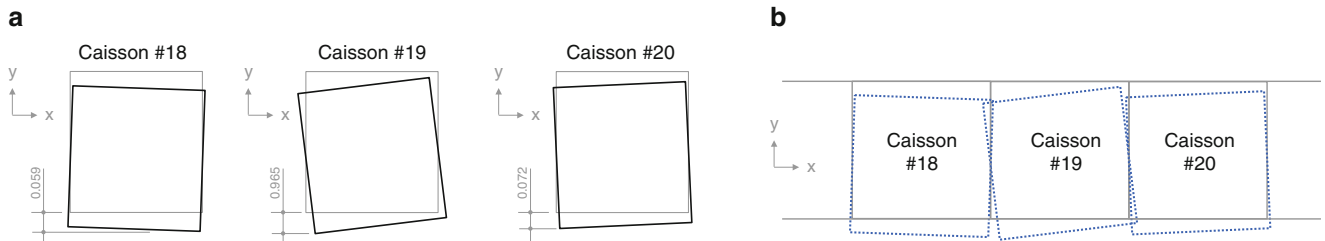


Fig. 21.8 Planar mode shapes of caissons #18–20 for mode 1 and their relative motion (a) Planar mode shape (b) Relative motion of three caissons

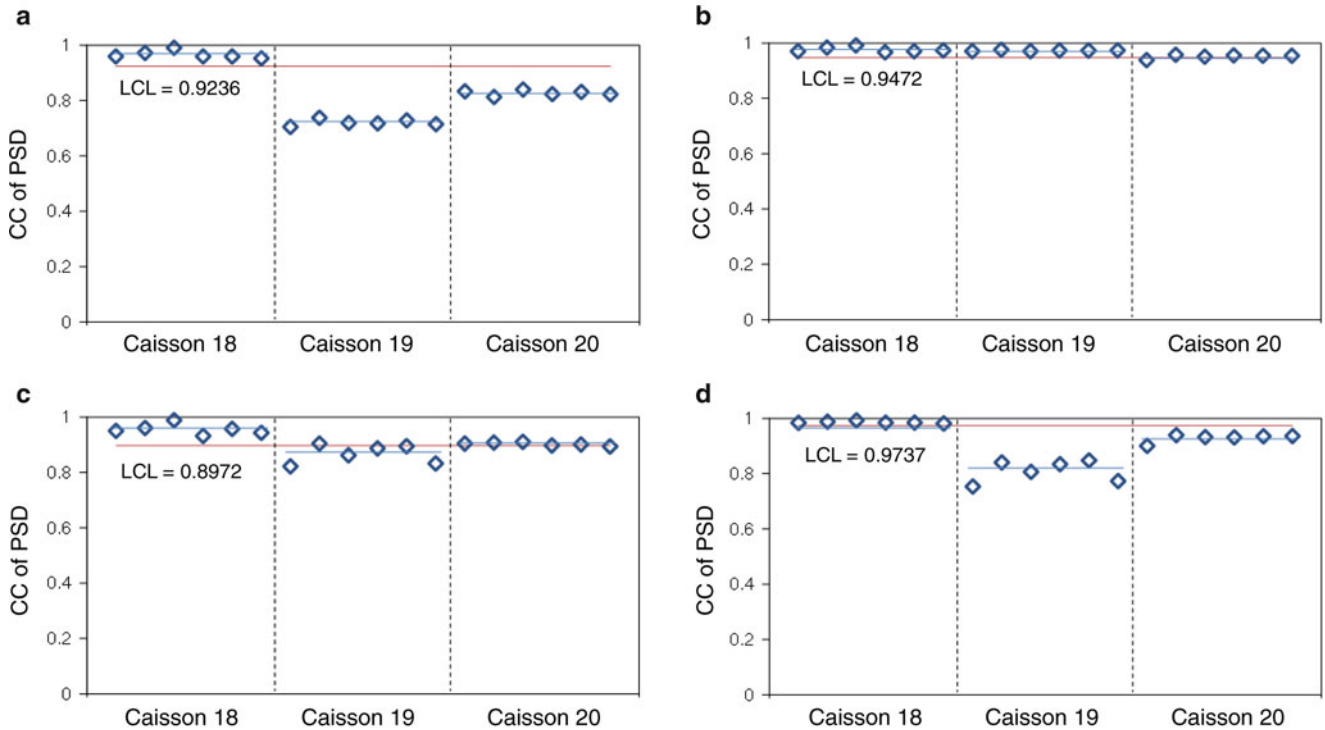


Fig. 21.9 Correlation coefficient of PSD for caissons #18–20. (a) Sensor 1-z (b) Sensor 2-y (c) Sensor 2-z (d) Sensor 3-y



## 21.4 Summary and Conclusions

In this study, a wireless sensing system for monitoring of the caisson structures of Oh-Ryuk-do breakwater was presented. The following approaches were implemented to achieve the objective. Firstly, a wave-induced vibration sensing system was designed for global structural health monitoring. Secondly, global SHM methods, utilizing correlation coefficient and modal parameters, were selected to alarm the occurrence of unwanted behaviors. Thirdly, autonomous SHM scheme, implementing correlation coefficient and modal parameter-based method, was designed for the target structure. Operation logics of the SHM methods were programmed based on the concept of the wireless sensor network. Finally, the performance of the proposed system was globally evaluated the caisson structures for which a series of tasks were experimentally performed by the wireless sensing system.

From the field test, we found the proposed wireless sensing system can make an assessment of the healthy states of the target caissons by implementing the value of correlation coefficient with respect to the bound of the lower control limit. For the implementation, we need to establish the reference state, which can be possibly identified by comparing the relative motions of the target caissons. It should be also noted here that the direction of accelerometer is quite significant to get a strong signal. In this study, we found the wave-induced, ambient vibration gave a strong signal when accelerometers were along with wave direction. Moreover, it is found that the clear peaks were established in the power spectral densities obtained from the sensors located in the y-direction. This fact supports the correlation coefficients extracted from the sensor 3-y, which distinguish the healthy states of the three caissons. However, the correlation coefficients from the sensor 1-z also gave a distinct assessment. It seems the sensor location is also an important factor to get a promising test result, along with the sensor orientation. Thus, the distributed sensor system should be addressed with promising damage detection methods, schemes, and wireless networks.

This study shows a successful wireless monitoring procedure for the harbor caisson structures. Thus, we believe that the proposed wireless SHM method and process provide invaluable information for designers, construction crews, and field engineers when they design, construct, and inspect caissons of breakwaters and quays, which are widely used in connection with men and goods transportation from the mainland to an island, and from a nation to other nations.

**Acknowledgements** Acknowledgements This work was supported by Basic Science Research Program through the National Research Foundation of Korea (NRF) funded by the Ministry of Education, Science and Technology (2011-0004253). The authors also would like to acknowledge the financial support of the project 'Development of inspection equipment technology for harbor facilities' funded by Korea Ministry of Land, Transportation, and Maritime Affairs.

## References

1. Committee of Coastal and Ocean Engineering (2003) Current extent of damage due to typhoon Maemi and its countermeasure, civil engineering. *Korean Soc Civil Eng* 21(10):28–38
2. Lee SY, Kim JT, Yi JH, Kang YK (2009) Structural health monitoring of harbor caisson-type structures using harmony search method. *J Ocean Eng Technol* 23(1):122–128
3. Goda Y, Takagi H (2000) A reliability design method of caisson breakwaters with optimal wave heights. *Coastal Eng J* 42:357–387
4. Takahashi S, Shimosako K, Kimura K, Suzuki K (2000) Typical failure of composite breakwaters in Japan. In: *Proceedings of 27th international conference on coastal engineering, Sydney*
5. Adams RD, Cawley P, Pye CJ, Stone BJ (1978) A vibration technique for non-destructively assessing the integrity of structures. *J Mech Eng Sci* 20(2):93–100
6. Stubbs N, Osegueda R (1990) Global non-destructive damage evaluation in solids. *Int J Anal Exp Modal Anal* 5(2):67–79
7. Doebling SW, Farrar CR, Prime MB (1998) A summary review of vibration-based damage identification method, the shock and vibration. *Digest* 30(2):91–105
8. Brownjohn JMW, Xia PQ, Hao H, Xia Y (2001) Civil structure condition assessment by FE model updating: methodology and case studies. *Finite Elem Anal Des* 37:761–775
9. Catbas FN, Gul M, Burkett J (2008) Conceptual damage-sensitive features for structural health monitoring: laboratory and field demonstrations. *J Mech Syst Signal Process* 22:1650–1669
10. Kim JT, Stubbs N (1995) Model-uncertainty impact and damage-detection accuracy in plate girder. *J Struct Eng* 121(10):1409–1417
11. Aktan AE, Farhey DN, Helmicki AJ, Brown DL, Hunt VJ, Lee KL, Levi A (1997) Structural identification for condition assessment: experimental arts. *J Struct Eng ASCE* 123(12):1674–1684
12. Levin RJ, Lieven NAJ (1998) Dynamic finite element model updating using simulated annealing and genetic algorithms. *Mech Syst Signal Process* 12(1):91–120
13. Yun CB, Bahng EY (2000) Substructural identification using neural networks. *Comput Struct* 77(1):41–52
14. Kim JT, Ryu YS, Cho HM, Stubbs N (2003) Damage identification in beam-type structures: frequency-based method vs mode-shape-based method. *Eng Struct* 25:57–67

15. Yun GJ, Ogorzalek KA, Dyke SJ, Song W (2009) A two-stage damage detection approach based on subset of damage parameters and genetic algorithms. *Smart Struct Syst* 5(1):1–21
16. Yi TH, Li HN, Gu M (2011) A new method for optimal selection of sensor location on a high-rise building using simplified finite element model. *Struct Eng Mech* 37(6):671–684
17. Yi TH, Li HN, Gu M (2012) Sensor placement for structural health monitoring of Canton tower. *Smart Struct Syst* 10(4–5):313–329
18. Yang Z, Elgamal A, Abdoun T, Lee CJ (2001) A numerical study of lateral spreading behind a caisson-type quay wall. In: *Proceeding of 4th international conference on recent advances in geotechnical earthquake engineering and soil dynamics and symposium, California*
19. Kim DK, Ryu HR, Seo HR, Chang SK (2005) Earthquake response characteristics of port structure according to exciting frequency components of earthquakes. *J Korean Soc Coastal Ocean Eng* 17(1):41–46
20. Chen Y, Zhou J (2012) Monitoring strain study of cylinder caisson based on fiber grating sensing technology. *Appl Mech Mater* 166–169: 1308–1311
21. Shama AA, Mander JB, Chen SS, Aref AJ (2001) Ambient vibration and seismic evaluation of a cantilever truss bridge. *Eng Struct* 23: 1281–1292
22. Ren WX, Peng XL (2005) Baseline finite element modeling of a large span cable-stayed bridge through field ambient vibration tests. *Comput Struct* 83:536–550
23. Lee JJ, Yun CB (2006) Damage diagnosis of steel girder bridges using ambient vibration data. *Eng Struct* 28:912–925
24. Gentile C, Gallino N (2008) Ambient vibration testing and structural evaluation of an historic suspension footbridge. *Adv Eng Software* 39:356–366
25. Siringoringo DM, Fujino Y (2008) System identification of suspension bridge from ambient vibration response. *Eng Struct* 30:462–477
26. Ivanović SS, Trifunac MD, Novikova EI, Gladkov AA, Todorovska MI (2000) Ambient vibration tests of a seven-story reinforced concrete building in Van Nuys, California, damaged by the 1994 Northridge earthquake. *Soil Dyn Earthquake Eng* 19:391–411
27. Yin T, Lam HF, Chow HM, Zhu HP (2009) Dynamic reduction-based structural damage detection of transmission tower utilizing ambient vibration data. *Eng Struct* 31:2009–2019
28. Amiri M, Sabbagh-Yazdi SR (2011) Ambient-vibration test and finite element modeling of tall liquid storage tanks. *Thin-Walled Struct* 49: 974–983
29. Osmancikli G, Uçak Ş, Turan FN, Türker T, Bayraktar A (2012) Investigation of restoration effects on the dynamic characteristics of the Hagia Sophia bell-tower by ambient vibration test. *Construct Build Mater* 29:564–572
30. Jang S, Jo H, Cho S, Mechitov K, Rice JA, Sim SH, Jung HJ, Yun CB, Spencer BF Jr, Agha G (2010) Structural health monitoring of a cable-stayed bridge using smart sensor technology: deployment and evaluation. *Smart Struct Syst* 6:7439–7459
31. Min J, Park S, Song BH, Yun CB (2010) Development of wireless sensor nodes for impedance-based structural health monitoring. *Smart Struct Syst* 6:678–709
32. Park JH, Kim JT, Hong DS, Mascarenas D, Lynch JP (2010) Autonomous smart sensor nodes for global and local damage detection of prestressed concrete bridges based on accelerations and impedance measurements. *Smart Struct Syst* 6:711–730
33. Wu J, Yuan S, Ji S, Zhou G, Wang Y, Wang Z (2010) Multi-agent system design and evaluation for collaborative wireless sensor network in large structure health monitoring. *Expert Syst Appl* 37:2028–2036
34. Yun GJ, Lee SG, Carletta J, Nagayama T (2011) Decentralized damage identification using wavelet signal analysis embedded on wireless smart sensors. *Eng Struct* 33:2162–2172
35. Ho DD, Lee PY, Nguyen KD, Hong DS, Lee SY, Kim JT, Shin SW, Yun CB, Shinozuka M (2012) Solar powered multi-scale sensor node on Imoete2 platform for hybrid SHM in cable-stayed bridge. *Smart Struct Syst* 9:145–164
36. Bendat JS, Piersol AG (2003) *Engineering applications of correlation and spectral analysis*. Wiley-Interscience, New York
37. Otte D, Van de Ponsele P, Leuridan J (1990) Operational shapes estimation as a function of dynamic loads. In: *Proceedings of the 8th international modal analysis conference*. Florida
38. Yi JH, Yun CB (2004) Comparative study on modal identification methods using output-only information. *Struct Eng Mech* 17(3–4):445–456

## Chapter 22

# Damage Assessment of a Beam Using Artificial Neural Networks and Antiresonant Frequencies

V. Meruane and J. Mahu

**Abstract** The main problem of damage assessment is how to ascertain the presence, location and severity of structural damage given the structure's dynamic characteristics. The most successful applications of vibration based damage assessment are model updating methods using global optimization algorithms. Nevertheless, these algorithms are very slow, and the damage assessment process is achieved through a costly and time-consuming inverse process. This is a problem for real-time health monitoring applications. Artificial Neural Networks (ANN) have been recently introduced as an alternative to model updating methods. Once a neural network has been properly trained, it can potentially detect, locate and quantify structural damage in a short period. Hence, it can be used for real-time damage assessment. The primary contribution of this research is the development of a real-time damage assessment algorithm using ANN and antiresonant frequencies. Antiresonant frequencies can be identified easier and more accurately than mode shapes and still provide the same information. An experimental beam with multiple damage scenarios is used to validate the approach.

**Keywords** Damage assessment • Artificial neural networks • Antiresonant frequencies • Real-time monitoring • Multi-layer perceptron

### 22.1 Introduction

Damage assessment must detect and characterize damage at the earliest possible stage and estimate how much time remains before maintenance is required, the structure fails, or it is no longer usable. Damage assessment has a tremendous potential for life-safety and/or economic benefits: it reduces the maintenance cost and increases the structure safety and reliability. It is a subject of large importance for several industry sectors as well as for the safety of citizens. It can be applied to civil engineering structures, such as buildings or bridges, to transport vehicles, such as airplanes, helicopters, trains, ships or cars, and to industrial equipment, such as mills, turbines, pumps, boilers, among others.

The main problem of damage assessment is how to ascertain the presence, location and severity of structural damage given the structure's dynamic characteristics. The most successful applications of vibration based damage assessment are model updating methods using global optimization algorithms [1–5]. Model updating is an inverse method to identify uncertain parameters of a numerical model, and it is usually formulated as an inverse optimization problem. In inverse damage detection, the algorithm uses the differences between models of the structure updated before and after the presence of damage to localize and determine the damage extend. The basic assumption is that damage can be directly related to a decrease of stiffness in the structure. Nevertheless, these algorithms are exceedingly slow, and the damage assessment process is achieved through a costly and time-consuming inverse process. This is a problem for real-time health monitoring applications. Recent studies have introduced Artificial Neural Networks (ANN) as an alternative to model updating in damage assessment [6–8]. A trained neural network can potentially detect, locate and quantify structural damage in a short period. Hence, it can be used for real-time damage assessment. Damage detection by means of ANN has the advantage that it is a general approach. Unlike many other damage detection methods, which are often developed for specific quantities [9–11], ANN can in principle be

---

V. Meruane (✉) • J. Mahu

Department of Mechanical Engineering, Universidad de Chile, Beauchef 850, Santiago, Chile  
e-mail: [vmeruane@ing.uchile.cl](mailto:vmeruane@ing.uchile.cl)

applied to any correlation coefficient that is sensitive to damage. Additionally, ANN can be used with structures that exhibit a non-linear response [12].

One of the main challenges in structural damage assessment is the selection of an appropriate measure of the system response, which is sufficiently sensitive to small damages. The fact that many measures have been studied over the past years, and continue to be investigated, with no consensus as to the optimum one, is a testament to the difficulty of the problem. This measure can be constructed in the time, frequency or modal domain. The last two are the most largely used. The idea of using frequency response functions (FRFs) directly to train neural networks has attracted many researchers. Among all the dynamic responses, the FRF is one of the easiest to obtain in real-time, as the in-situ measurement is straightforward. However, the number of spatial response locations and spectral lines is too large for neural network applications. The direct use of FRFs will lead to networks with a large number of input variables and connections, making them impractical. Hence, it becomes necessary to extract features from the FRFs, and use these features as inputs to the neural networks. Castelli and Revel [13] presented an algorithm to detect and locate structural damage based on laser vibrometry measurements and a neural network for data processing. They use features extracted from the frequency response functions as inputs to the neural network. The authors were able to use the same network to detect and locate damage in three different experimental structures. To reduce the number of input variables, Zang and Imregun [14] applied a principal component analysis (PCA) technique to the measured FRFs. The output of the neural network is the actual state of the structure: undamaged or damaged. The algorithm was able to distinguish with accuracy between the undamaged and damaged cases. Fang et al. [15] selected key spectral points around the resonance frequencies in the FRF data. These selected points are the inputs of a neural network while the outputs are the stiffness reduction factors. The algorithm showed a high accuracy in identifying damage of a simulated cantilever beam under different damage scenarios.

Recently, researchers have proposed the use of antiresonant frequencies [16]. Antiresonant frequencies correspond to the zeros (dips) of the FRFs; they are an attractive alternative because they can be determined easier and with less error than mode shapes, still providing the same information. Antiresonances can be derived from point frequency response functions (FRFs), where the response coordinate is the same as the excitation coordinate; or from transfer FRFs, where the response coordinate differs from the excitation coordinate. Point FRFs are preferred because matching problems arise when antiresonances from transfer FRFs are used. Moreover, the distribution of the transfer antiresonances can be significantly modified with small structural changes [16]. On the other hand, the procedure to obtain point FRFs differs from common modal testing, i.e. the excitation degree of freedom (DOF) is moved together with the response DOF. This may become not practical or too expensive. Meruane and Heylen [17] show that antiresonances are a good alternative to mode shapes in damage assessment. However, they stated that further research is needed in the identification of experimental antiresonances, and in the matching of experimental and numerical antiresonances. Antiresonances are an attractive alternative to mode shapes as input values of neural networks: the number of input variables is lower; they are less contaminated by noise and still offer the same information. Nevertheless, the use of antiresonances is still under development and the application of antiresonances to structural damage detection has not been fully investigated, mainly because the inverse optimization problem using antiresonances is particularly challenging and robust optimization algorithms are needed. However, this should not be a problem for methods based on neural networks.

### **22.1.1 Artificial Neural Networks**

An ANN is a data processing algorithm, which tries to emulate the processing scheme of the human brain [18]. An ANN is formed by “neurons” that are interconnected together to build a complex network. Knowledge is acquired by a learning process and stored in the inter-neuron connections, known as the “synaptic weights”. There are different types of network architectures, among them the Multilayer Perceptron (MLP) is the most frequently used. An MLP network consists of an array of input neurons, known as the input layer, an array of output neurons, known as the output layer and a number of hidden layers. Each neuron receives a weighted sum from the neurons in the preceding layer and provides an input to every neuron of the next layer.

A disadvantage of ANN is the need of large training sets. It is extremely difficult and time-consuming to produce large enough training data sets from experiments. An alternative to generate training samples is to use a numerical model of the structure. Castelli and Revel [13] showed that it is possible to produce correct damage predictions in an experimental structure using a neural network that was trained with samples generated by a finite element model. Nevertheless, this approach is highly dependent on the accuracy of the numerical model. There are two approaches to overcome this problem. The first is to update the numerical model using experimental data from the undamaged structure. However, even after updating there will still be differences between the numerical and experimental models. The second alternative is to define an input parameter that considers the initial errors in the numerical model, thus avoiding the need for an accurate numerical model. This is

achieved by using the data changes instead of their absolute value. The main assumption is that any change in the structure properties is caused by damage. Thus, any error in the undamaged model of the structure that is also present in the damaged model will be removed [19]. Lee et al. [20] showed that natural frequency changes due to structural damage in a system without modeling errors are approximated the same as those in a system with modeling error. Hence, changes in natural frequencies are less sensitive to modeling errors than the natural frequencies themselves. They demonstrated the applicability of a neural network trained with mode shape changes. Damage locations were estimated with reasonable accuracy, although false alarms are detected at several locations.

Simulated data derived from a numerical model is noise free, whereas measurements are never free from experimental noise. Noise in the measurements will cause the network to estimate parameters different from actual properties of the structure. A solution is to introduce artificial noise in the numerical data that is used to train the network. This process is known as data perturbation scheme [21]. Yun et al. [22] used a noise-injection learning algorithm and a data perturbation scheme. They implemented a neural network based damage assessment algorithm to detect damage in structural joints. Joints are modeled as semi-rigid connections using rotational springs. Accurate results are obtained in the cases of moderated noise. Sahin and Shenoii [23] trained a neural network with artificially added noise to detect single damage in beam-like composite laminates. The network has two outputs: the location and the amount of damage. They studied different combination of features extracted from resonant frequencies and mode shape curvatures, as inputs to the neural network. Their results show that feature selection plays a crucial role in the predictions accuracy.

The primary contribution of this research is the development of a real-time damage assessment algorithm using ANN and antiresonant frequencies. This study is restricted to antiresonant frequencies obtained from point FRFs. Although measuring point FRFs is time-consuming because the excitation point is moved together with the response location, it has several advantages for damage assessment:

- All antiresonances contain independent information since they correspond to the resonant frequencies of the system grounded at different degrees of freedom.
- For a given FRF, the number of antiresonant frequencies does not change from one damage scenario to the next. This is a valuable property if we need them to be inputs to a neural network.
- An antiresonant frequency lies always between two resonant frequencies. Hence, there is no doubt, whether a dip in an FRF is an antiresonant frequency or a minimum.

## 22.2 Neural Network for Damage Assessment

This study intends to train a neural network using antiresonant frequencies and determine its feasibility to assess experimental damage. Hence, it was decided to work with the simplest neural network that has been able to detect, locate and quantify structural damage. This is a multilayer perceptron (MLP) with three layers (input, hidden and output), as presented by Fang et al. [15]. The outputs of the network correspond to the damage indices of each element, while the inputs are the changes in antiresonant frequencies. The number of hidden nodes is defined after a sensitivity analysis for each application case.

### 22.2.1 Inputs

As was proposed by Lee et al. [20], the inputs to the neural network are defined as the changes in the modal parameters rather than their absolute value, with this approach, the network is less sensitive to errors in the baseline FE model.

Therefore, the inputs correspond to the experimental change in antiresonant frequencies with respect to the intact case:

$$x_{i \times n} = \frac{\omega_{r,i,n}^D - \omega_{r,i,n}^U}{\omega_{r,i,n}^U} \quad (22.1)$$

The superscripts  $D$  and  $U$  refer to undamaged and damaged respectively,  $\omega_{r,i,n}$  is the  $i$ th antiresonant frequency of the  $n$ th FRF.

To reduce the effects of experimental noise, simulated data is polluted with random noise. As proposed by Hjelmstad and Shin [21], each set of perturbed data is created by adding a uniformly distributed random noise to the numerical data:

$$\omega_{r,i,n} = \omega_{r,i,n} (1 + \xi) \quad (22.2)$$

where  $\xi$  is a uniform random number with a specified amplitude. The variance of the perturbing noise should be the same as the variance of the measurement noise.

### 22.2.2 Outputs

Damage indices are represented by elemental stiffness reduction factors,  $\beta_i$ , defined as the ratio between the stiffness reduction to the initial stiffness:

$$y_i = \beta_i \quad (22.3)$$

The stiffness matrix of the damaged structure,  $\mathbf{K}_d$ , is expressed as a sum of element matrices multiplied by reduction factors,

$$\mathbf{K}_d = \sum_i (1 - \beta_i) \mathbf{K}_i \quad (22.4)$$

The value  $\beta_i = 0$  indicates that the element is undamaged whereas  $0 < \beta_i \leq 1$  implies partial or complete damage.

### 22.2.3 Training and Validation Patterns

The distribution of the training patterns plays a crucial role in the success of a neural network. The relation between antiresonant frequencies and the different damage levels is not linear. In consequence, the network might not be able to interpolate. Fang et al. [15] recommends to use training patterns with evenly distributed damaged levels. Combining multiple damages into the training, increases the number of training patterns and a large number of training patterns could overwhelm the training procedure. In this study, training patterns were generated by considering up to two simultaneous damages, with nine damage levels evenly distributed between 0% and 80%. Hence, the total number of training patterns depends on the number of elements,  $N$ , as:

$$\text{Number of training patterns} = 9^2 \times C(N, 2) \quad (22.5)$$

where  $C(N,2)$  is the number of combinations of  $N$  elements taking 2 at a time.

The algorithm trains the network using the *early stopping technique* [24]. Here, two sets of data are used during training: a *training set* and a *validation set*. The training set is used for update the network weights and biases. The mean square error, evaluated on the validation set is monitored during training. When the validation error increases for six iterations, the algorithm stops the training. The weights of the network at the minimum validation error are the final weights.

The validation set is a group of patterns that must be different to the training patterns. To ensure the last condition, the training patterns were created with nine damage levels evenly distributed between 5% and 85%, considering up to two simultaneous damages. Note that the number of training patterns is equal to the number of validation patterns. This set of validation patterns are also used to check the network performance after training.

### 22.2.4 Measures of Network Performance

The performance of the network is measured by three indicators: the mean sizing error, damage missing error and false alarm error, as defined by Yun et al. [22]. The mean sizing error (MSE) is the average quantification error:

$$\text{MSE} = \frac{1}{NO} \sum_i |y_i - o_i| \quad (22.6)$$



where  $y_i$  and  $o_i$  are the estimated and desired output for node  $i$ , and  $NO$  is the number of output nodes. The damage missing error (DME) is given by,

$$DME = \frac{1}{NT} \sum_i \varepsilon_i^I, 0 \leq DME \leq 1 \tag{22.7}$$

where  $\varepsilon_i^I = 0$  if the  $i$ th damaged element is correctly detected and  $\varepsilon_i^I = 1$  if not.  $NT$  corresponds to the number of true damage locations. If  $DME = 0$ , all damage locations are correctly detected.

It is assumed that an element is detected as damaged if the estimated damage,  $y_i$ , is greater than a prescribed critical value  $\alpha_c$ . The critical damage level,  $\alpha_c$ , is defined equal to the average MSE. This is the minimum damage the network can reasonably assess.

The false alarm error (FAE) is defined as,

$$FAE = \frac{1}{NF} \sum_i \varepsilon_i^{II}, 0 \leq FAE \leq 1 \tag{22.8}$$

where  $\varepsilon_i^{II} = 0$  if the  $i$ th detected damage is truly damaged and  $\varepsilon_i^{II} = 1$  if not.  $NF$  is the number of predicted damage locations. If  $FAE = 0$ , all of the detected locations are actual damage locations. Identification and matching of antiresonant frequencies

### 22.3 Experimental Beam

The structure consists of a steel beam of rectangular cross-section. The dimensions of the beam are length 1m and section  $25 \times 10\text{mm}^2$ . As shown in Fig. 22.1, soft springs suspend the structure to simulate a “free-free” boundary condition.

A hammer excites the beam in four points distributed along the beam and an accelerometer measures the response at each excitation location. Both the excitation force and the measured responses are in the horizontal direction. In this direction, antiresonant frequencies are more sensitive to the experimental damage. Five antiresonant frequencies are identified at each of the four experimental FRFs.

The numerical model is built in Matlab with 2D beam elements. The model has 20 beam elements and 40 degrees of freedom, as shown in Fig. 22.2. Shadowed elements are possible locations of damage.

A model-updating algorithm updates the material and geometrical properties of the numerical model. After updating, the maximum difference between numerical and experimental antiresonances is 1.98%.

The structure is subjected to four different damage scenarios containing single and double cracks. Cracks are introduced to the structure by saw cuts of length  $l_c$ . Table 22.1 summarizes the different damage cases; it indicates the distance from the left-end to the cut, the corresponding element in the numerical model and the cut length.



Fig. 22.1 Experimental beam

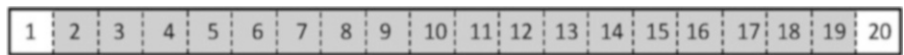
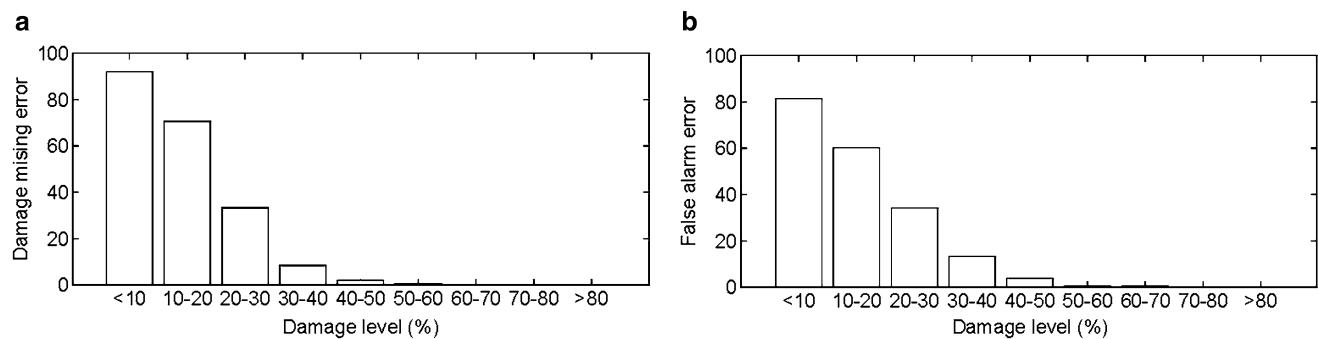


Fig. 22.2 Numerical model and element numbering

Table 22.1 Damage cases introduced to the beam

Case	Distance from the left end (mm)	Element number	Saw cut length (mm)	Distance from the left end (mm)	Element number	Saw cut length (mm)
1	315	7	5	–	–	–
2	635	13	10	–	–	–
3	303	7	5	640	13	10
4	360	8	5	810	17	15



**Fig. 22.3** Damage missing error (DME) and false alarm error (FAE) for different damage levels

### 22.3.1 Network Validation

The network parameters were selected after a sensitivity analysis. It was studied the effect of the number of hidden nodes, transfer functions and the training algorithm. The combination of parameters that provided the minimum validation error were selected. The network parameters are:

- Network: Three layers multi-layer perceptron
- Number of input nodes: 20
- Number of hidden nodes: 80
- Number of output nodes: 18
- Transfer function in the hidden layer: Logarithm sigmoid
- Transfer function in the output layer: Symmetric saturating linear
- Training method: Levenberg-Marquardt

Training and validation patterns were polluted with 1.5% of random noise. The mean sizing error obtained for the validation patterns is  $MSE = 1.53\%$ ; thus the network quantification accuracy is 98%. Figure 22.3 shows the damage missing error (DME) and false alarm error (FAE) separated by damage levels. The results of the DME indicate that the detection of damages with low severities is poor. In fact, near 90% of the damages with severities lower than 10%, and 70% of the damages with severities between 10% and 20%, are not detected. The algorithm can detect with confidence damages with severities larger than 40%; it correctly detects 99.5% of the damages with severities over 40%. The false alarm results indicate that most of the damages detected with levels lower than 10% are false damages (near 80%). The amount of false damage detection reduces with an increment of the level of damage; 99% of the damages detected with levels over 40% are true damages.

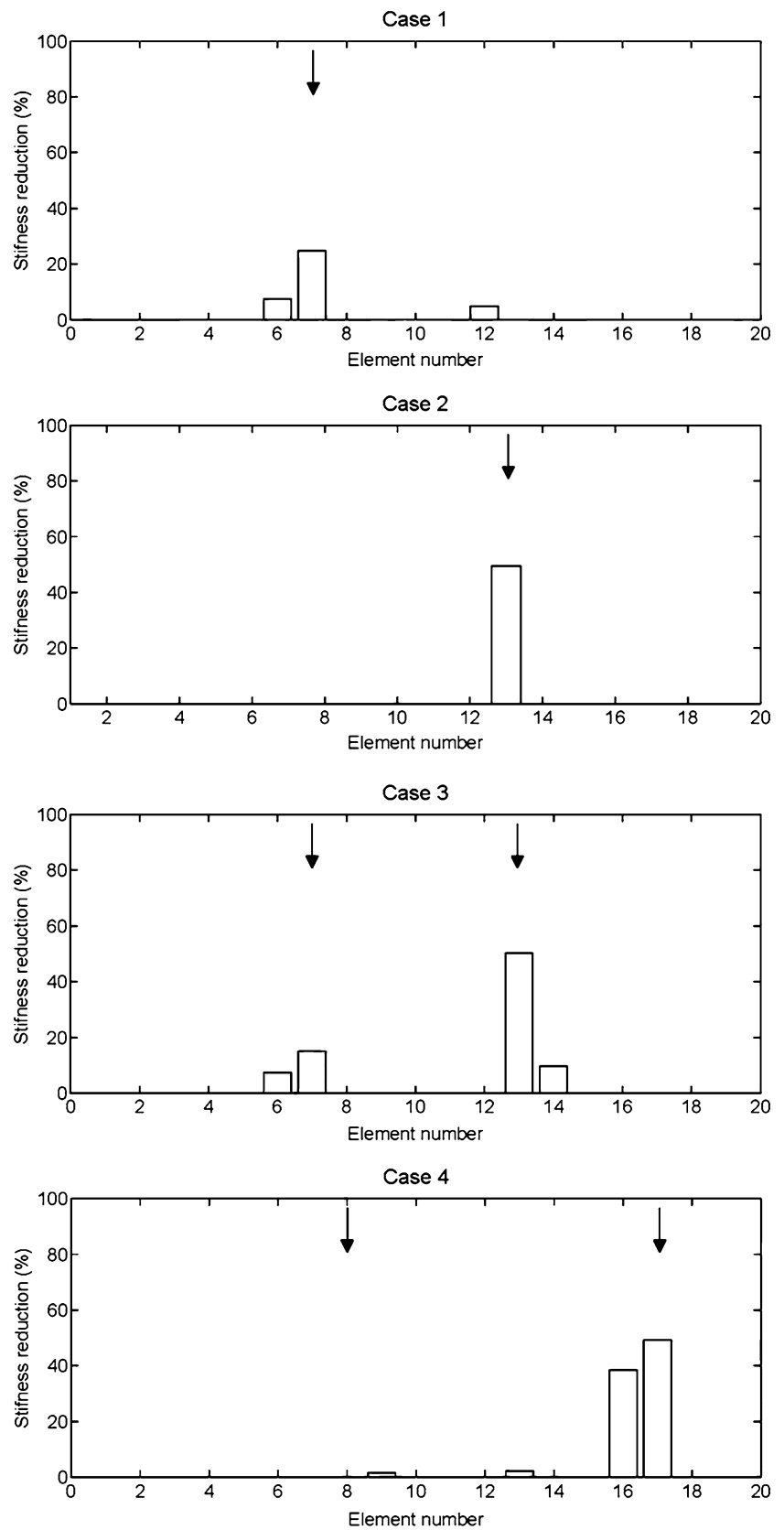
Figure 22.4 shows the results of the damage detected in the four experimental cases. An arrow indicates the actual damage location. In the first three cases, damage is correctly located, though a few false damages appear next to the actual locations. Nevertheless, the assumption that a crack only affects the stiffness of the corresponding element might not be always true. For instance, in the fourth case, the effect of the larger cut is represented better by a stiffness reduction of two elements rather than one. In the last case, the network does not detect the small crack in element eight. This is because the effect of the larger cut hides the effect of the smaller cut.

## 22.4 Conclusions

This article presents a new methodology to assess experimental damage using neural networks and antiresonant frequencies. A multilayer perceptron network was trained with data obtained from a numerical model and tested with experimental data. The study addresses the setting-up of the neural network parameters, thus providing guidelines to their selection in similar damage assessment problems. An experimental cases of a beam with multiple damage scenarios verify the algorithm.

The algorithm is successful in assessing the experimental damage. The damage detected has a close correspondence with the experimental damage in all cases. These results show that it is possible to locate and quantify structural damage using only antiresonant information obtained from point frequency response functions. Hence, antiresonant frequencies are an attractive feature to be used in damage assessment.

**Fig. 22.4** Experimental reduction of stiffness detected at each case



The present study shows that it is possible to assess experimental damage in real-time in a beam structure. Hence, it provides the possibility of continuously monitoring its condition. Nevertheless, according to the validation results, the algorithm has a minimum level of damage that can be assessed with confidence, which is 40%. These results can be improved using a larger training database, but it implies larger training times.

An area of further research is the use of antiresonant frequencies obtained from transfer frequency response functions, which are more sensitive to structural changes, but need more attention, especially when pairing experimental and numerical antiresonant frequencies.

**Acknowledgements** This research has been partially funded by Program U-INICIA VID 2011, grant U-INICIA 11/01, University of Chile and by the fondo nacional de desarrollo científico y tecnológico of the Chilean government, proyect Fondecyt iniciación 11110046.

## References

1. Meruane V, Heylen W (2010) Damage detection with parallel genetic algorithms and operational modes. *Struct Health Monit* 9(6):481–496
2. Meruane V, Heylen W (2011) An hybrid real genetic algorithm to detect structural damage using modal properties. *Mech Syst Signal Process* 25(5):1559–1573
3. Perera R, Torres R (2006) Structural damage detection via modal data with genetic algorithms. *J Struct Eng* 132(9):1491–1501
4. Kouchmeshky B, Aquino W, Bongard JC, Lipson H (2007) Co-evolutionary algorithm for structural damage identification using minimal physical testing. *Inter J Numer Methods Eng* 69(5):1085–1107
5. Teughels A, De Roeck G, Suykens JAK (2003) Global optimization by coupled local minimizers and its application to FE model updating. *Comput Struct* 81(24–25):2337–2351
6. González-Pérez C, Valdés-González J (2011) Identification of structural damage in a vehicular bridge using artificial neural networks. *Struct Health Monit* 10(1):33–48
7. Sahoo B, Maity D (2007) Damage assessment of structures using hybrid neuro-genetic algorithm. *Appl Soft Comput* 7(1):89–104
8. Arangio S, Beck JL (2012) Bayesian neural networks for bridge integrity assessment. *Struct Control Health Monit* 19(1):3–21
9. Messina A, Jones A, Williams E.J (1996) Damage detection and localisation using natural frequency changes. In: *Proceedings of the first conference on identification in engineering systems*. Swansea, pp 67–76
10. Lim RM, Edwins DJ (1990) Model updating using FRF data. In: *Proceedings of 15th international seminar on modal analysis*. Leuven, pp 141–163
11. Stubbs N, Kim JT, Topole K (1992) An efficient and robust algorithm for damage localization in offshore platforms. In: *Proceedings of the ASCE tenth structures congress*, San Antonio, pp 543–546
12. Masri SF, Smyth AW, Chassiakos AG, Caughey TK, Hunter NF (2000) Application of neural networks for detection of changes in nonlinear systems. *J Eng Mech* 126:666–676
13. Castellini P, Revel G (2000) An experimental technique for structural diagnostic based on laser vibrometry and neural networks. *Shock Vib* 7(6):381–397
14. Zang C, Imregun M (2001) Structural damage detection using artificial neural networks and measured FRF data reduced via principal component projection. *J Sound Vib* 242(5):813–827
15. Fang X, Luo H, Tang J (2005) Structural damage detection using neural network with learning rate improvement. *Comput Struct* 83(25–26):2150–2161
16. D'Ambrogio W, Fregolent A (2000) The use of antiresonances for robust model updating. *J Sound Vib* 236(2):227–243
17. Meruane V, Heylen W (2011) Structural damage assessment with antiresonances versus mode shapes using parallel genetic algorithms. *Struct Control Health Monit* 18(8):825–839
18. Arbib MA (2003) *The handbook of brain theory and neural networks*. Bradford Book, USA
19. Friswell MI, Penny JET, Garvey SD (1998) A combined genetic and eigensensitivity algorithm for the location of damage in structures. *Comput Struct* 69(5):547–556
20. Lee JJ, Lee JW, Yi JH, Yun CB, Jung HY (2005) Neural networks-based damage detection for bridges considering errors in baseline finite element models. *J Sound Vib* 280(3–5):555–578
21. Hjelmstad KD, Shin S (1997) Damage detection and assessment of structures from static response. *J Eng Mech* 123(6):568–576
22. Yun CB, Yi JH, Bahng EY (2001) Joint damage assessment of framed structures using a neural networks technique. *Eng Struct* 23(5):425–435
23. Sahin M, Sheno RA (2003) Vibration-based damage identification in beam-like composite laminates by using artificial neural networks. *Proc Inst Mech Eng Part C: J Mech Eng Sci* 217(6):661–676
24. Prechelt L (1998) Early stopping – but when? *Neural Network Tricks Trade* 1524(553):55–69

# Chapter 23

## Case Studies of Tools Used in Teaching Structural Dynamics

Kurt Veggeberg

**Abstract** This is an overview of case studies of the tools used in teaching structural dynamics and their development. A key feature was the requirement for hardware and software to be comprehensive for the application, but easy to use and affordable. One example includes the hardware and software used in ambient vibration monitoring and forced impact testing on the International Bridge Study. The other includes the use of ModalVIEW for a full modal analysis of a modified unmanned aerial vehicle (UAV) to better understand its flight characteristics and to help determine appropriate flight conditions for operation by the Unmanned Aircraft Systems Engineering (UASE) laboratory team at the University of North Dakota.

**Keywords** Modal analysis • Experimental modal analysis • ModalVIEW • LabVIEW • National instruments

### 23.1 Introduction

A desirable feature in teaching structural dynamics is for hardware and software tools to be comprehensive for the application, but easy to use and affordable. This is an overview of case studies where such tools were used. One example includes the hardware and software used in ambient vibration monitoring and forced impact testing on the International Bridge Study. The International Bridge Study was designed to demonstrate and document the best-practices in bridge technology integration and educate bridge inspectors, consultant, technology providers, and others. Drexel University conducted live load testing, forced impact testing and ambient vibration monitoring over the length of the study as well as completing the modeling both before and after testing. The other example includes the use of ModalVIEW to conduct a full modal analysis of a modified unmanned aerial vehicle (UAV) to better understand its flight characteristics and to help determine appropriate flight conditions for operation by the Unmanned Aircraft Systems Engineering (UASE) laboratory team at the University of North Dakota. ModalVIEW has an easy to understand interface for every step of the vibration testing process, from connecting the sensors to animating the structure with the mode shapes.

### 23.2 International Bridge Study Hardware and Software

National Instruments cRIO data acquisition system were used in testing the structural behavior of a bridge in the International Bridge Study (IBS) through ambient and forced excitation to calibrate and improve the accuracy of the bridge model to diagnose, perform prognosis, and design treatments to mitigate performance deficiencies of bridges [1].

The Intelligent Infrastructure Alliance (IIA), hosted by the Civil, Architectural & Environmental Engineering Department at Drexel University, is a university – government – industry partnership. The IIA was invited to participate in the International Bridge Study (IBS) with the goal of establishing the worldwide *best practices* for the integration and application of technology to diagnose, perform prognosis, and design treatments to mitigate performance deficiencies for a given bridge. As part of this program, a steel stringer bridge was selected in northern New Jersey for a round robin study conducted by

---

K. Veggeberg (✉)  
National Instruments, 11500 N. Mopac, Austin, 78759 TX, USA  
e-mail: [kurt.veggeberg@ni.com](mailto:kurt.veggeberg@ni.com)



**Fig. 23.1** US 202/NJ 23 Bridge used in international bridge study

teams from the United States, Europe and Asia. The primary objectives of the program included developing more accurate estimates of bridge structural health improve and disseminate knowledge of bridge performance, and to promote the safety, longevity and reliability of the United States highway transportation system (Fig. 23.1).

IIA conducted live load testing, forced impact testing and ambient vibration monitoring over the length of the study as well as completing the modeling both before and after testing. The selected bridge was considered to be representative of a large portion of bridges in form, material, age and span length. In this research, an integrated analytical/experimental strategy and an associated experimental tool was used for an objective evaluation of bridge condition to supplement visual inspection. Termed as rapid modal analysis, this test technique aims at reducing both the time and personnel required to produce estimates of bridge flexibility at strategic coordinates using spatially truncated measurement grids.

Given the concerns surrounding the vibration of the spans, a preliminary ambient vibration monitoring of the bridge was conducted during one of the site visits. This study consisted of recording 10 min of data from four accelerometers installed on the sidewalk of each span (so no traffic control was required). During a 10 min time window, ambient traffic was able to provide sufficient input and signal to noise ratios for all sensors, including those located at the boundaries, resulting in reliable modal parameter estimation.

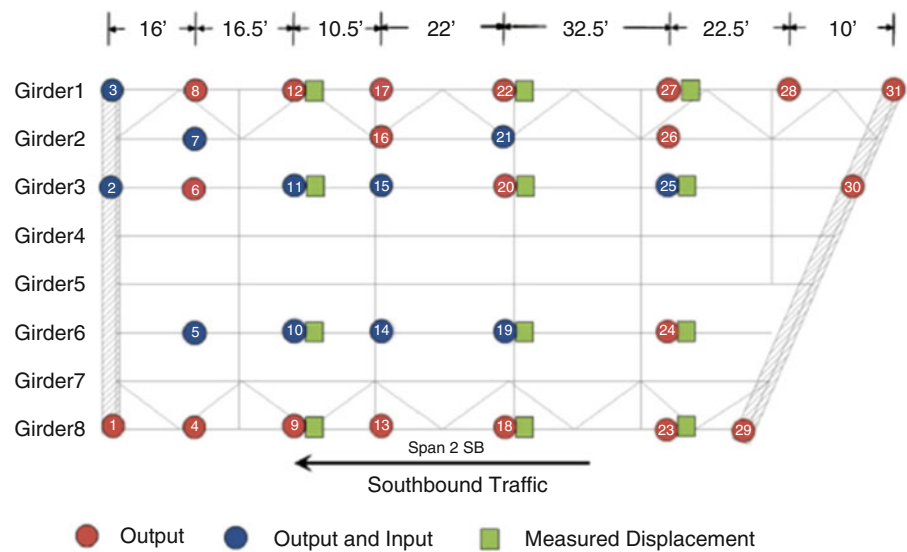
For the US 202/NJ 23 Bridge, the primary objective of the impact test was reliable estimation of modal parameters to allow for an effective model calibration. Using the modes (and their variations) estimated by the a priori model, a series of fixed sensor locations for both Span 2 NB and Span 2 SB were selected. The instrumentation plan aimed to provide regular and spatially well-distributed sensor number of sensors near nodal points of critical modes, and to select impact locations at maximum modal displacements of principal modes (Fig. 23.2).

Impact excitation was to be applied by drop hammer and sledgehammer. Natural frequencies derived from mode shapes from both types of the excitation tests and those derived from the ambient vibration test varied by less than 5%. This small difference demonstrates that each excitation method can produce consistent estimates of the damped natural frequencies. Each driving point location was impacted five times with the sledgehammer and three times with the drop hammer in order to average out the effects of extraneous inputs. Several clean impact response cycles are needed to obtain adequate FRFs. Since the Drexel drop hammer provided high force levels and a flat frequency spectrum, the results obtained during the drop hammer tests were selected for presentation.

The data acquisition system used for the forced (impact) vibration testing campaigns was provided by National Instruments and combined a CompactRIO chassis with eight NI 9234 dynamic signal acquisition modules used to read piezoelectric accelerometers programmed via LabVIEW. The entire data acquisition system was debugged while collecting time domain data under ambient excitation. The PCB 393A03 accelerometer was used since it has a significantly more robust connection design than common piezoelectric sensors designs that use the 10–32 microdot connection. All calibration factors were input to the test file, and each sensor was checked for proper operation. Prior to conducting the multi-reference impact testing on the top side of the structure, numerous ambient excitation time records were collected during normal operation of the structure. The ambient monitoring program provided valuable information about the natural frequencies and mode shapes of each structure under ambient conditions. The test control during impact testing was conducted from the topside of structure and the control laptop was connected to the data acquisition system on the ground via an Ethernet cable (Fig. 23.3).



**Fig. 23.2** Sensor locations for the span of bridge being tested



**Fig. 23.3** National instrument cRIO data acquisition system used for impact testing campaigns on bridge



The drop hammer used in this research was designed by the Drexel University team. An adjustable heavy, moving mass drops from an adjustable height and a PCB 200C50 load cell with a medium polyurethane impact tip (Model 084A32) provides an impact on the surface of the deck. Since the impact carriage bounces off the bridge deck, several impacts occur. The rebound control system aims to stop these multiple impacts and consists of a brake system activated by a control system that tracks the position of the impact carriage. The sensing/control system includes a National Instruments (NI) CompactRIO Data Acquisition system (cRIO DAQ) that interfaces with an Acuity AR700 laser distance gauge. The cRIO controller runs a NI LabVIEW Real-Time program that interfaces with the NI 9112 cRIO chassis, and a host PC that runs an interactive user interface. An NI 9205 analog input module reads distance measurement data from the laser, while an NI 9269 analog output module provides control signals to the mechanical control system (Fig. 23.4).

The motivation of this research was to explore the feasibility and reliability of a “rapid modal analysis” concept for bridge condition evaluation. The concept incorporates multi-input-multiple-output (MIMO) modal analysis of a bridge by controlled impact(s) at the critical coordinates of the superstructure while measuring the impact, as well as the transient acceleration responses of the superstructure. Although bridge modal analysis by impact has been demonstrated as a reliable tool for flexibility, its feasibility for widespread applications to bridges was not considered favorable due to the need to close the bridge for an extended period. On the other hand, the challenges of reliable bridge condition evaluation and the opportunity to adapt new tools, such as a falling weight deflectometer (FWD), justified further exploration for transforming MIMO modal analysis into a rapidly applicable method with only a short-duration (~15 min) traffic control. To build on this research and findings, additional work is recommended to develop and evaluate the implementation of the proposed rapid modal analysis tool.

**Fig. 23.4** Automated drop hammer system with rebound control designed by Drexel team



Available hardware (sensors, excitation devices and data acquisition hardware) as well as software including LabVIEW and ModalVIEW were used. There was no budget for additional equipment purchase which is typical in many academic applications.

Processing data on site was used as a data quality check and as a tool to provide useful insight to inform the design and execution of the impact test. Plot mode shapes help determine whether the shapes make sense physically. Seven possible modes were identified from 2 to 15 Hz. The conclusion was that rapid modal analysis methods complement full scale comprehensive testing techniques and are not intended to replace any of the validated and mature structural testing techniques presented in the literature.

### 23.3 ModalVIEW

ModalVIEW is a turn-key software solution offered by AB Signal required that has been used by a number of universities for education. These include Drexel University, the University of North Dakota, Penn State College of Engineering and others. After obtaining a set of time histories, it can animate the response of a structure's vibration behavior. ModalVIEW software was designed in LabVIEW by a former National Instruments (NI) software developer. ModalVIEW software supports direct acquisition from NI dynamic signal acquisition (DSA) hardware including PXI, PCI and USB to speed up the time needed to perform experimental measurements. ModalVIEW incorporates the steps required for modal testing and analysis. It supports frequency-based and order-based operational deflection shapes (ODS), experimental modal analysis (EMA) and operational modal analysis (OMA).

The software was an outgrowth of Modal Analysis Parameter Extraction LabVIEW VIs developed as a part of a toolkit. This consists of a set of algorithms used to identify the modal parameters of a structure (natural frequency, damping ratio, mode shapes). These algorithms are either used for experimental research or for operational on-line monitoring. These algorithms include Peak Picking, Least Square Complex Exponential Fit, Frequency Domain Polynomial Fit, Stochastic Subspace Identification, and FRF Synthesis. Each of these algorithms perform the same function of identifying the modal parameters, however, each are optimized for a specific test scenario [2].

### 23.4 Structural Analysis of a Small Unmanned Aircraft Using ModalVIEW and NI CompactDAQ

The Unmanned Aircraft Systems Engineering Laboratory at the University of North Dakota was interested in analyzing how adding wing pods changes the flight characteristics of a small unmanned aerial vehicle (UAV) used for flight testing

multiple payloads. They chose ModalVIEW and an NI CompactDAQ system that can measure up to 32 channels to extract and visualize the modal parameters of the aircraft with and without the added weight of wing pods to determine if they adversely affect flight performance. They chose this software because of its ease of use and perfect fit for the type of testing they are doing. A paper on this application, “Structural Analysis of the Effects of Wing Payload Pods on Small UAS,” was presented at SEM IMAC XXX in 2012 [3].

The Unmanned Aircraft Systems Engineering (UASE) laboratory team operates a Bruce Tharpe Engineering (BTE) Super Hauler UAV. They develop aircraft payloads up to 30 lb (14 kg) for intelligence, surveillance, and reconnaissance (ISR) missions, as well as airborne sense and avoid (ABSAA) systems. The Super Hauler is 10 ft long (3 m) and has a 12 ft (3.6 m) wingspan and a dry weight of 48 lb (22 kg). The aircraft’s behavior in its original configuration is well understood, but adding wing payload pods for future missions will change the aircraft’s structural and flight behavior.



The Super Hauler is custom designed to provide a large, unobstructed payload bay to mount multiple payloads for flight testing. This capability meets the needs of the previous payloads tested, but adding wing payload pods is necessary to conduct new missions and evaluate payloads for radar-related work. The wing payload pods will most often be used in pairs to equalize the wing loading and provide a symmetric load on the airframe. They will run the electrical and power connectors and wiring inside of the wing so they are out of the airflow. In this manner, the antenna systems inside the wing pods have an uninterrupted front-facing field of view.

The goal was to obtain a full modal analysis of the UAV to better understand its flight characteristics and the effect of the wing pods, and to help determine appropriate flight conditions for operation. This sort of testing has been done before on many different kinds of aircrafts, but it was hoped that their work will assist others that are testing small UAVs in a similar manner.

ModalVIEW and NI CompactDAQ hardware were used to create a plug-and-play system. ModalVIEW has an easy to understand interface for every step of the vibration testing process, from connecting the sensors to animating the structure with the mode shapes that were found.

They used experimental modal analysis to obtain structure modal parameters by measuring and analyzing the dynamic response of the structure when excited by a stimulus. ModalVIEW supports a variety of multiple-degree-of-freedom (MDOF) global fitting analysis methods and multiple-input, multiple-output (MIMO) polyreference experimental methods using impact hammers or shakers. It also has an animation tool that was used to visualize the aircraft’s mode shape.

The Super Hauler was isolated for analysis by placing it on bungee cords in a test rig so all the wheels were 1.25 in. off the ground, which simulates a free-free boundary condition for modal testing. A 5 lb weight was mounted on each wing to simulate the wing pods. To perform the analysis, the BTE Super Hauler was first instrumented with accelerometers in key locations. A mixture of PCB Piezotronics triaxial and uniaxial accelerometers were mounted directly on the aircraft’s outer skin. The accelerometers were connected to an NI cDAQ-9178 chassis containing eight NI 9234 dynamic signal acquisition (DSA) modules. The Super Hauler was excited with a PCB Piezotronics 086C03 impact hammer.



The NI CompactDAQ front end interfaced seamlessly with the ModalVIEW software for the analysis. Six impact tests were performed both with and without the simulated wing pods attached. Each of the tests consisted of impacting the Super Hauler at one of the nodes, measuring the frequency response, then obtaining the natural frequencies from the frequency response function (FRF) and animating the line model with the corresponding mode shapes. It was speculated that the first natural frequency without the pods doesn't have a match in the set with the pods because there isn't as much structural coupling between the wings and the fuselage.

In the mode shapes observed, the natural frequencies all shifted dramatically down with the addition of the wing pods. This was expected since a substantial amount of weight was added. The wing pods account for 20% of the total weight, and they have a fairly dramatic influence on the structural response. Although significant changes in frequencies were observed, none of the fundamental modes shifted out of the operational frequency range of the aircraft without the pods installed. Therefore, it is expected that changes in flight dynamics will not be a significant factor in flight performance.

Without Pods	With Pods	Description
12.4 Hz	-	Wing-tip bending only
27.0 Hz	10.8 Hz	Tail twisting only
27.6 Hz	12.54 Hz	Wing bending opposite tail bending
72.8 Hz	19.9 Hz	Wing bending and tail twisting
90.8 Hz	27.9 Hz	Mode 2 wing bending





## 23.5 Conclusions

A key feature in teaching is the requirement for hardware and software to be comprehensive for the application, but easy to use and affordable. The case studies here illustrate examples that can be useful for teaching experimental and analytical structural dynamics.

**Acknowledgements** Acknowledgements The author would like to thank John Prader of Pennoi Associates for the use of information from his PhD thesis from Drexel University and Kaci J. Lemmer and Willam H. Semke for information from their presentation at SEM IMAC 2012.

## References

1. Prader J (2012) Rapid impact modal testing for bridge flexibility: towards objective evaluation of structures, Ph.D. thesis, Drexel University May 2012. [http://www.di3.drexel.edu/w2/files/Prader\\_Thesis\\_2012.pdf](http://www.di3.drexel.edu/w2/files/Prader_Thesis_2012.pdf)
2. Modal Parameter Extraction LabVIEW VIs. National Instruments. <http://zone.ni.com/devzone/cda/epd/p/id/6121>
3. Lemler K, Semke W (2012) Structural analysis of the effects of wing payload Pods on small UAS. In: Topics in modal analysis II, volume 6 conference proceedings of the society for experimental mechanics series, vol 31, pp 515–523. DOI: 10.1007/978-1-4614-2419-2\_53, Springer New York

# Chapter 24

## “Structural System Testing and Model Correlation”: An Industry-University Collaborative Course in Structural Dynamics

Michael Todd, Dustin Harvey, David Gregg, Bill Fladung, Paul Blesloch, and Kevin Napolitano

**Abstract** The field of structural dynamics inevitably involves aspects of modeling (e.g., finite element approaches and related), testing (both planning and execution), signal processing, model parameter determination, and correlating model predictions to test results. While each of these topics exists in some form in United States university engineering curricula, very few curricula offer these topics in integrated groupings, and, to our knowledge, no single course exists that covers all these topics. This paper describes the structure and execution of a senior undergraduate elective course taught annually for the past 3 years in the Department of Structural Engineering at the University of California, San Diego (UCSD). This course was developed in a close collaboration between a university faculty member and local industry engineers at ATA Engineering Inc. (ATA), whose business largely consists of performing all aspects of design/modeling, testing, analysis, and model correlation/updates. The presentation will cover the specifics of the course curriculum and how the class is structured around performing the complete model/test/update paradigm on a test structure. The paper will share assessments of students who took the course and conclude with recommendations and observations about implementing such a class in an engineering curriculum.

**Keywords** Structural dynamics • Model updating • Model correlation • Vibration testing • Structural dynamics education

### 24.1 Introduction

Structural dynamics is a fundamental topic in all mechanical, aerospace, civil, structural, and even some biomedical/biomechanics undergraduate engineering curricula. Although not considered comprehensively within most structural dynamics courses, structural dynamics itself consists of modeling structures (e.g., with finite element, other numerical, or even analytical methods), designing structural dynamic tests, processing test data, identifying structural properties from the test data (system identification), and updating/correlating structural models to reflect the test data. An informal survey of United States undergraduate structural dynamics curricula in 2009 revealed no single course integrating all of these aspects. The famous dynamics programs at the University of Cincinnati (Profs. David Brown and Randy Allemang) and the University of Massachusetts at Lowell (Prof. Pete Avitabile) came the closest. However, they either consider each aspect in a separate course (but at the graduate level rather than undergraduate level) or rotate subsets of each aspect into a single course (e.g., have no testing component in 1 year’s offering, have no model updating in the next year’s offering, etc.). At the University of California San Diego, the structural dynamics curriculum in the Structural Engineering Department and the Mechanical and Aerospace Engineering Department historically has offered the common three-course core (i.e., required) sequence in classical “mechanics”: Statics, Dynamics (of rigid bodies), and Vibrations. Core courses were also taught in finite

---

M. Todd (✉) • D. Harvey  
Department of Structural Engineering, UC San Diego, 9500 Gilman Dr., La Jolla, CA, 2093 USA  
e-mail: [mdtodd@ucsd.edu](mailto:mdtodd@ucsd.edu); [dyharvey@ucsd.edu](mailto:dyharvey@ucsd.edu)

D. Gregg • B. Fladung • P. Blesloch • K. Napolitano  
ATA Engineering Inc., 11995 El Camino Real, Suite 200, San Diego, CA, 92130 USA  
e-mail: [david.gregg@ata-e.com](mailto:david.gregg@ata-e.com); [bfladung@ata-e.com](mailto:bfladung@ata-e.com); [paul.blesloch@ata-e.com](mailto:paul.blesloch@ata-e.com); [knapolitano@ata-e.com](mailto:knapolitano@ata-e.com)



element modeling, numerical methods, matrix structural analysis, and electronics (with an emphasis on simple voltage data acquisition in non-structural dynamics experiments), in addition, of course, to other core courses and electives not directly related to structural dynamics.

The department's Undergraduate Affairs Committee (which has been chaired by the first author of this paper, Prof. Michael Todd, for the last 10 years), is responsible for designing and implementing the undergraduate curriculum in Structural Engineering (and partly in Mechanical and Aerospace Engineering for shared courses). Discussions between this committee and the Structural Engineering Industrial Advisory Board revealed that the curriculum was not meeting some industry expectations in preparing its graduates. Graduates reasonably understood, in a "stovepipe" context, different aspects of how to model structures, how to test structures (at least statically), to a much lesser degree how to do system identification and its associated signal processing, and how to update or correlate models with test data. However, no student had ever undertaken a comprehensive project that integrated all of these tasks on a common structural system, which is exactly what industry is called to do by their customers. As a result of this shortcoming, ATA Engineering Inc., an engineering services company in San Diego whose primary capabilities are in structural design, analysis, and testing, partnered with Prof. Todd to design and teach a course that provided undergraduates with this relevant educational experience. This paper describes the resulting undergraduate senior-level elective course entitled "SE 168: Structural System Testing and Model Correlation," which has been co-taught by Prof. Todd and senior engineers from ATA for the past 3 years. The course is intended for senior students as a technical elective course; and the prerequisites for the course are undergraduate courses in dynamics, vibrations, finite element analysis, and MATLAB programming. The course is presently limited to 20 students due to equipment restrictions, although the department is evaluating whether it could become a core (required) course that would replace an existing core course in electronics taught in the Mechanical Engineering Department. This paper will present the content and syllabus of the course and a description of the test structure around which the entire course is organized, and conclude with evaluations of the course by the students who have taken it so far.

## 24.2 Course Description and Execution

The 10-week course meets 4 h per week (2 h lecture and 2 h lab) and is structured over three modules: "pretest," "test," and "posttest," which reflect the three fundamental, high-level portions of the complete curriculum. Instruction is divided between UCSD faculty and ATA engineers to provide students both academic depth and exposure to real-world engineering experience. The general syllabus content is shown below in Table 24.1.

**Table 24.1** Course syllabus and schedule

Week	Lecture topic	Laboratory topic	Instructor
1 (Pretest)	Multi-DOF vibrations review; obtaining mass, stiffness, and damping matrices; time-domain solution of multi-DOF systems review	MATLAB software review	UCSD
2 (Pretest)	Modal solution for multi-DOF systems, Fourier analysis, and FRF; comparison of spatial, modal, and response models	Finite element analysis modeling review; introduction to test structure	UCSD
3 (Pretest)	Finite element analysis review; model reduction techniques; unmeasured DOFs	Model reduction, DOF selection	ATA
4 (Pretest into Test)	Test hardware, data acquisition, and sensors; data acquisition issues	Introduction to experimental modal testing; data acquisition practice	ATA
5 (Test)	Digital signal processing I (FFT, aliasing, averaging, windowing)	Signal processing exercises	UCSD
6 (Test)	Digital signal processing II (spectral estimation, FRF estimation)	Boundary condition experimental test verification; signal processing exercises	UCSD
7 (Test)	Experimental modal analysis: excitation and data quality	Modal testing of structure	UCSD/ATA
8 (Test)	Experimental modal analysis: modal parameter extraction	Modal testing of structure	UCSD/ATA
9 (Posttest)	Model/test correlation	Parameter extraction and model correlation via boundary condition updating	ATA
10 (Posttest)	Model updating	Model updating project given blind test data	ATA

Fig. 24.1 Test structure relationships

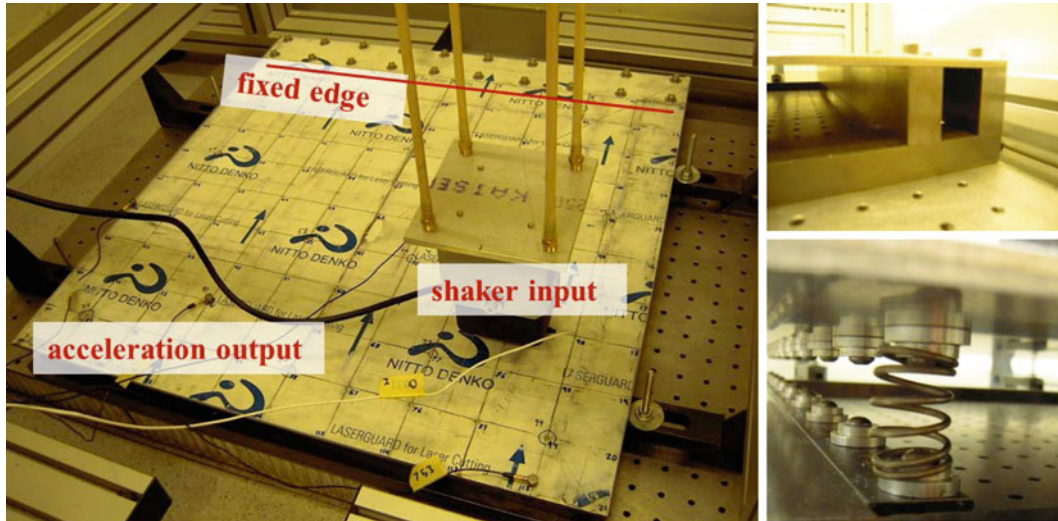
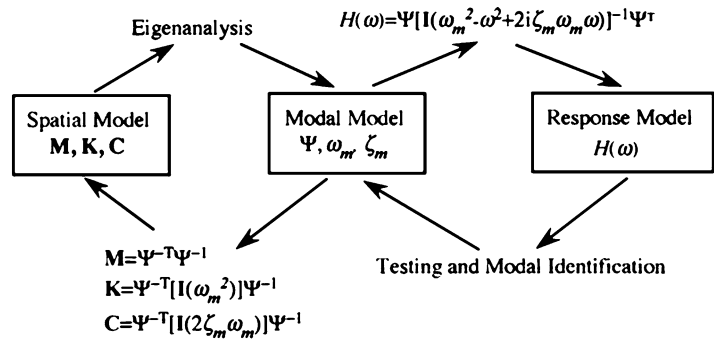


Fig. 24.2 Photographs of the test structure

As Table 24.1 shows, the first 4 weeks are dedicated to the pre-test topics of (1) review of general multi-degree-of-freedom time and frequency domain analytical modeling (impulse response and frequency response function) and solving the governing equations of motion; (2) a quick review of finite element analysis modeling; (3) finite element model reduction techniques (Guyan reduction, both static and dynamic condensation); and (4) methods to select test degrees of freedom and how to deal with unmeasured modes (forward and back expansion). The pretest module ends with an introduction to the data acquisition hardware needed for modal testing, with a focus on excitation methods (electrodynamics shakers and impactors), accelerometer measurements, and basic issues with data acquisition for vibration testing. The overarching principle is to ensure that students (1) fundamentally understand the relationships among the spatial, modal, and frequency response models of structures and can comfortably transfer information between them (Fig. 24.1); (2) know how to implement model expansion/reduction techniques with discrete structural spatial models for matching model to test; and (3) are aware of the basic concepts for planning a vibration test by selecting appropriate observable degrees of freedom and realize the consequences of certain choices..

The lecture topics are complemented by weekly laboratory sessions where the students directly use what they learned in lecture to develop relevant analysis code based in MATLAB. The laboratory sessions continuously build on the previous week’s topic(s); the code that the students develop over the course of the quarter grows to include more functionality (e.g., first model reduction/expansion, then extracting eigenproperties from system matrices, then signal processing/FRF estimation, then parameter estimation, and then finally model updating). In the pretest module, students primarily develop code to manipulate the mass, stiffness, and damping matrices for analytical eigenanalysis, model reduction/expansion, and degree-of-freedom selection for test preparation. The students take a first, in-class exam on pre-test module material in the third or fourth week.

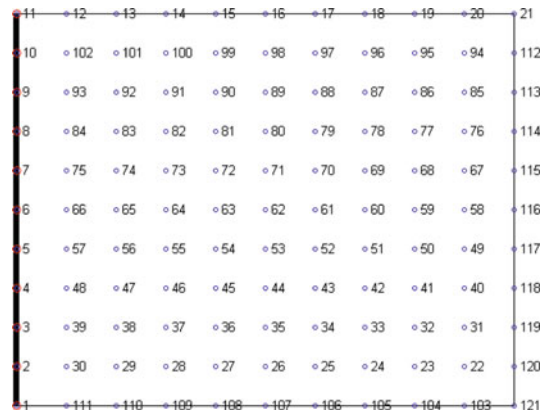
The modeling (and, ultimately, testing) is focused on a test structure provided to the students. The structure is a cantilevered plate that is fixed at one end with a series of bolted connections (Fig. 24.2). A detail of the double-bolted clamp is shown in the upper right of the figure. Additionally, fixtures were added to the free edge to support adding springs of various stiffness, as shown in the bottom right of the figure; these are used for final project test data, which is discussed later in this paper. In Lab 2 of the pre-test module, the students are given a finite element model of a free plate of the dimensions

**Fig. 24.3** Modal test checksheet students complete before testing

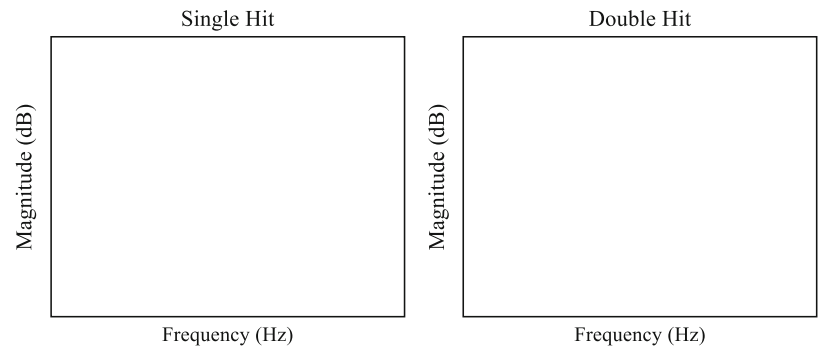
**SE168 Laboratory #4**  
**Due: during individual testing**

**Before starting your experimental data collection, complete this worksheet:**

1. Target modes #'s from FEM: \_\_\_\_\_
2. Target mode frequencies (Hz) from FEM: \_\_\_\_\_
3. Nyquist frequency (Hz): \_\_\_\_\_ Sampling frequency (Hz): \_\_\_\_\_
4. Roughly how long does the plate vibrate in a step relaxation (seconds)? \_\_\_\_\_
5. Sample length (seconds): \_\_\_\_\_ Sample length (samples): \_\_\_\_\_
6. Nodes in aset: \_\_\_\_\_
7. Reference node (excitation): \_\_\_\_\_
8. On the diagram below, circle your aset nodes and mark an X at the reference node.



9. Select a hammer tip to provide a flat spectrum in the range of interest and as little energy as possible elsewhere. Which tip did you choose? \_\_\_\_\_
10. In the boxes below, sketch the input spectrum for a good, single hit and for a double hit.



of this test structure, and they are asked to modify the model to add a clamped boundary condition that (ideally) models that boundary. After doing an eigenanalysis to test the code they wrote in Lab 1, the students write modal effective mass fraction code and use it to select target modes for a test they will perform. In Lab 3, they write code for modal assurance criteria (MAC), orthogonality, pseudo-orthogonality, Guyan reduction and back expansion, and ultimately for select test degrees-of-freedom to identify the target modes they selected in Lab 2. ATA makes its IMAT software available on a temporary educational license to the students enrolled in the course. This software, which is based on MATLAB, provides functionality for working with finite element models of structures and animating mode shapes

Week 4 of the course transitions from the pre-test module into the test module. In Lab 4, the students are provided a pre-lab checksheet (Fig. 24.3) that summarizes all of their test preparation on the structure. As Fig. 24.3 shows, the students report their target modal information, data acquisition sampling and record length requirements, target nodes (in a diagram, as shown), impact hammer reference node, and hammer choice, including a qualitative description of what a double-hit spectral response looks like (which should thus be rejected).

The students then individually sign up to perform their modal tests on the structure with their choices from the worksheet. They perform a single-input, multiple-output (SIMO) impact test with the hammer of their choice. They also perform a

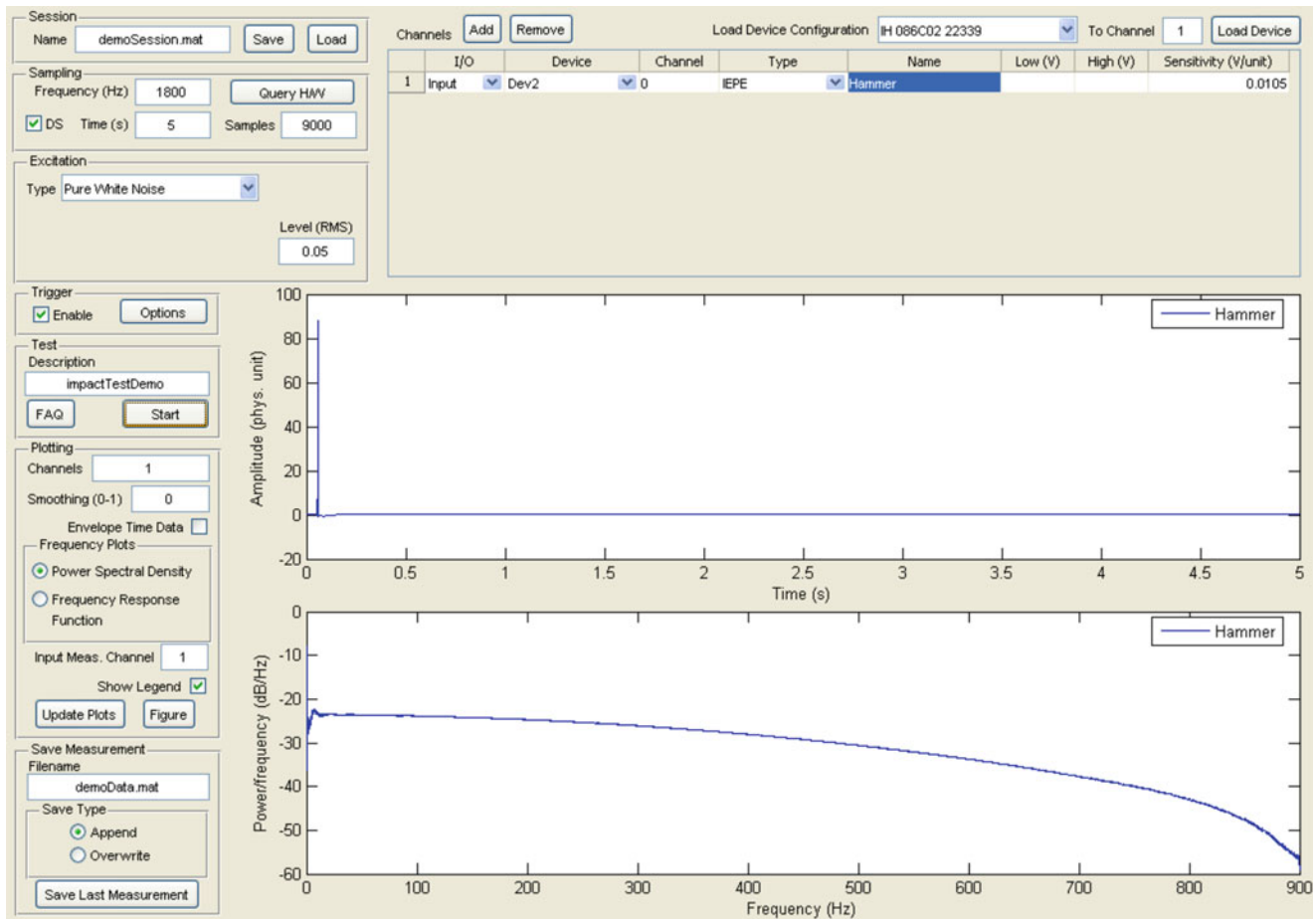


Fig. 24.4 Matlab-based data acquisition front end used in the course

random excitation test with the shaker at a predetermined drive point. The students receive a tutorial in the data acquisition software, which was written in MATLAB to interact with drivers for the National Instruments acquisition hardware; the MATLAB-based graphical user interface, written by the second author Dustin Harvey, is shown in Fig. 24.4. The software has a very user-friendly interface that allows maximum flexibility in choosing sampling rates, setting input/output locations, choosing excitation type, performing spectral and FRF estimations, and managing data. After modal testing, the test course module continues with initial data quality checks and fundamental signal processing, leading up to estimation of the frequency response function (FRF) from the measured data. The students take a second, in-class examination on the test module and some basic signal processing from the post-test module during the eighth or ninth week.

In Lab 5, the students write code to estimate spectral density functions and to study the effects of windowing and averaging (some randomly excited data from the structure is provided to them for this part of the lab exercise). With these skills honed, Lab 6 takes the students back to their own modal test data and requires them to write code to perform data quality checks and to process their own shaker and impact data into the spectral domain to obtain FRF estimates, which they then compare to their earlier finite element model predictions. From their estimates of FRF and other data quality checks, students are asked to choose either their shaker data or impact data for the remainder of the course and to defend their choice. In Lab 7, the students learn about modal parameter estimation via the rational fraction polynomial method (the only method chosen to teach in class due to its flexibility and ubiquity), and they actually extract modal parameters from the FRFs that were computed from their measured data in Lab 6.

The post-test module of the course begins at this point. The first main task presented in Lab 8 is for the students to update their finite element models to match the extracted modal parameters from their individual tests. The students are given some training on what parameters are most uncertain (e.g., geometric, stiffness, boundary) and are free to manipulate those model parameters in physically meaningful ways to do the model correlation. In general, all students are asked to employ elastic boundary conditions on their clamped end to reflect the lack of an “ideal” restrained rotation/deflection boundary. The

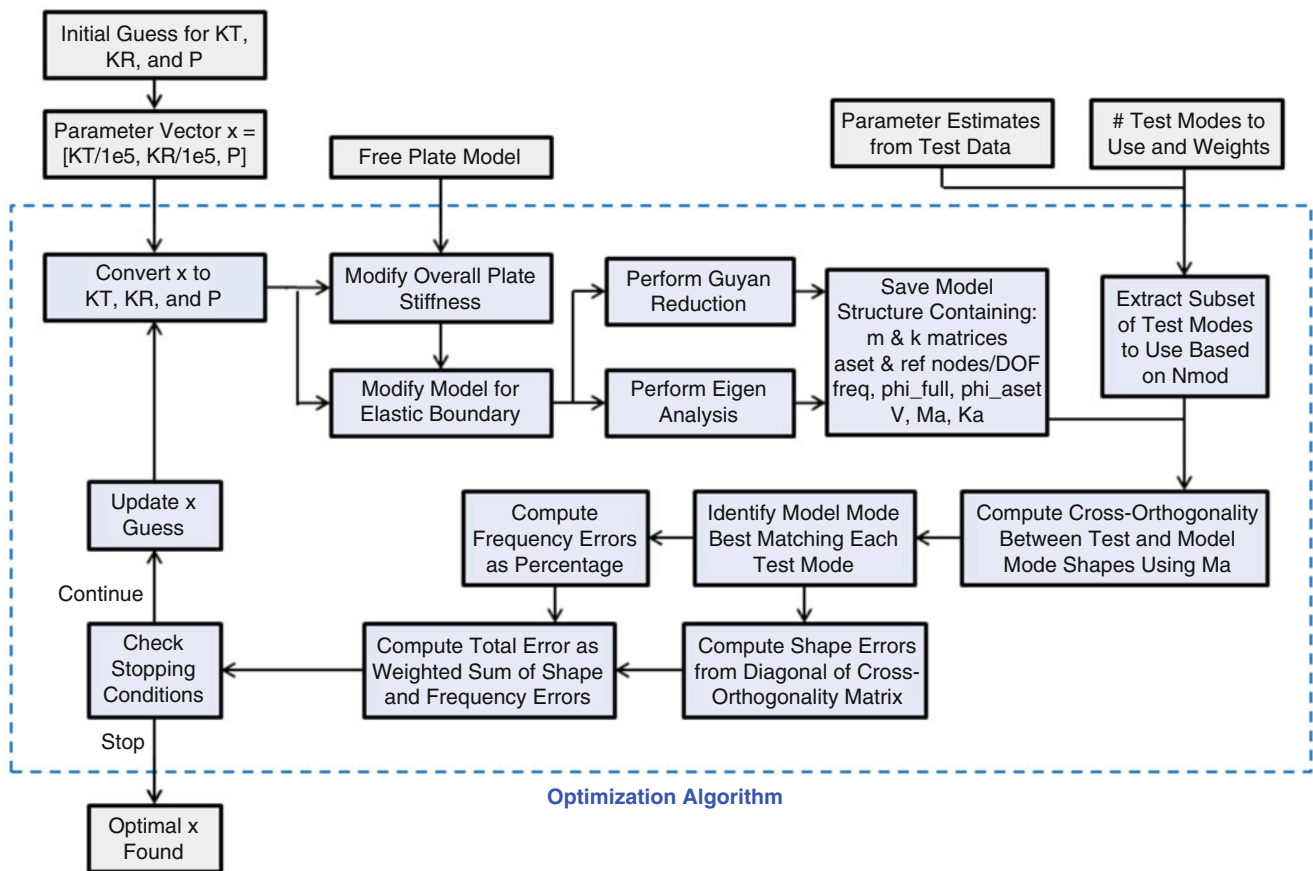


Fig. 24.5 Optimization flowchart taught in posttest module

optimization strategy with this variable set is shown in Fig. 24.5 below. The students are encouraged to experiment within the framework until satisfied with an optimal model, and in their reporting, the students must defend all choices made to optimize their models.

The second part of this final lab tests the students' ability to detect system changes from blind data. Using the springs mentioned previously, the instructors perform modal tests with various springs added along the free edge and provide the raw data sets, along with the relevant data acquisition parameters, to each student. Each test has a different stiffness change and spring location so that no student has exactly the same modified dynamic system. The students are then tasked to identify what changed in the structure, with the only specification that a spring of unknown stiffness (but in the range 1–500 lbf/in) was added somewhere along the free edge. Students are then asked, as a final examination, to prepare 10–15 min oral presentations demonstrating (1) how they updated their model to reflect the actual boundary condition, from the first part of the lab, and (2) how they identified the specific dynamic change to the plate, from the second part of the lab. In all cases, heavy emphasis is placed upon each student being able to defend his or her choices on the analyses performed and the conclusions reached.

### 24.3 Discussion and Conclusion

As described, the course continuously builds upon itself. The lecture material is strongly correlated with the week's laboratory exercises, and the previous week's laboratory exercises are almost always used in the subsequent week's exercises. The goal is to take students through the entire process of modeling a structure, using the model to design a structural test, performing the test, and updating the model in a meaningful way to reflect the test results. For simplicity and consistency, MATLAB is used throughout, even in the data acquisition process. In addition to directly complementing laboratory exercises, the lecture includes actual case studies and examples from the practicing engineers at ATA. This gives students actual "best practices" information, enhancing the course beyond what most undergraduate courses do.

Student assessments of the course have been overwhelmingly positive. Below is a representative sample of student comments:

This course has been a fantastic learning opportunity that I have been glad to be part of.

... loved the relationship between a class and professional engineering firm.

The course is a very practical course that combines many of the undergraduate theoretical class, taking the class really helps one to understand why courses like vibration and dynamics are useful in the real world. This class is definitely a lot more challenging than most undergraduate courses. Hopefully one day it will be a required class.

Overall every speaker did well as they tied together the course quite well. The repeats were good as they help reinforce basic concepts other lecturers already taught.

The only constructive criticism students have given over the years is that the level of programming skill in MATLAB assumed by the instructors is too high for many students. The department has recognized its problem in teaching programming skills in MATLAB, even though a dedicated sophomore course exists to do this, followed by two numerical methods courses that utilize MATLAB. The MATLAB programming skill level among students is, indeed, quite variable, and this class of comment seems valid. While the Structural Engineering Department will continue to investigate how better to train students in MATLAB programming skills, overall the academic-industry partnership has been a tremendous success in preparing structural and mechanical engineers with the skill sets needed to practice in the structural dynamics field. The department is also continuing to evaluate resource management and funding streams to increase available testing and computing equipment in order to determine whether the course should become a required core course instead of a technical elective.



# Chapter 25

## Visualizing Structural Vibrations Using Stroboscopic Light in a Novel Setup

Markus J. Hochrainer

**Abstract** The visualization of structural vibrations has always been a key technology when teaching vibration analysis. If the structural motion can be perceived directly without numerical simulation or extensive measurements, basic modal analysis concepts like mode shapes, natural frequencies or resonances and anti-resonances are intuitively understood. The application of stroboscopes has a long tradition in vibration analysis and is particularly well established in rotor dynamics. Nevertheless a cheap and simple to use device for the visualization of larger structures like e.g. car wings was missing. The application of several arrays of white light high power light emitting diodes together with a power electronic circuit resulted in an innovative and highly flexible distributed light source perfectly suited to visualize resonant vibrations of flexible structures in the mid frequency range. Furthermore, the effect of aliasing is demonstrated convincingly and the results can be compared qualitatively to experimental modal analysis. In combination with an electrodynamic shaker the setup has been applied successfully to visualize vibrations of parts of car bodies, tennis rackets, skis, piano or cello strings as well as plate and shell structures.

**Keywords** Modal visualization • Stroboscope • Mode shape • Operational deflection shape • Resonant vibrations

### 25.1 Introduction

Theoretical and experimental modal analysis is a demanding and complex scientific discipline and consequently it is important to attract the student's attention by a suitable combination of complementary teaching methods. If the confidence in numerical simulations and the virtual experiment is sufficient, almost any phenomenon might be explained and understood applying theoretical or numerical methods only. However, since vibrations are present in everyday life it is possible to explain many phenomena by investigating real effects on commonly used structures. In the low frequency range structural vibrations might be felt directly, medium or high frequencies often radiate acoustic emissions which can be heard. Unfortunately this direct perception contributes little to a fundamental insight. If, on the other side, it is possible to fully visualize the movement of a structure, the understanding will be increased tremendously. Furthermore, if it can be proven convincingly that theoretical predictions and real experiments do compare well, this raises confidence in the virtual experiment. These considerations were the driving force behind the development of the proposed setup which has shown to be a versatile tool for explaining and teaching vibration phenomena. It is still widely accepted to use large and strongly simplified structures with low natural frequencies to prove that theoretical predictions do compare well with experiments. Pendulum type structures, large helical springs, standing waves on water or large strings are commonly used to explain basic principles like natural frequencies and mode shapes. Also widespread are Caldrini plates to display node lines or the visual demonstration of sound wave patterns in Kundt's pipe filled with cork or polystyrene balls. All these experiments have in common that they are based on idealized elementary structures or substantial structural simplifications when compared to real systems, a drawback which is eliminated with the proposed application of stroboscopic light. The basic idea is to apply several arrays of high power light emitting diodes (LED) in a stroboscopic configuration to obtain a homogenous illumination level over the entire vibrating structure. At frequencies of more than 40 Hz the sequence of light flashes is perceived as comfortable and uniform light

---

M.J. Hochrainer (✉)  
University of Applied Sciences, 2700 Wiener, Neustadt, Austria  
e-mail: [markus.hochrainer@fhwn.ac.at](mailto:markus.hochrainer@fhwn.ac.at)

intensity by most observers. Assuming a harmonic motion of a relatively flexible structure with moderate to large vibration amplitudes an arbitrary frequency shift can be achieved by violating Shannon's sampling theorem. Consequently the original high frequency motion is mirrored about the sampling frequency rendering the visible alias frequency. Conversely, the actual mode shapes remain unaffected and the real structure seems to vibrate in slow motion. This strategy works for any structure as long as the vibration amplitudes are in the visible range. Laboratory experiments have been carried out using many technical, but also everyday life articles and the setup has become a valuable, quick and easy to use system for demonstrating different vibration modes and creating a feeling for modal relations.

## 25.2 Theoretical Background

Whenever a continuous process is discretized by taking equally spaced samples, the effect of aliasing has to be considered. In many film productions aliasing is the reason for car wheels turning forward and backward during an accelerated motion. In computer graphics and image processing a similar effect results from a finite spatial resolution, often observed as appearance of Moiré pattern. Aliasing is a frequently encountered and widely underestimated problem that can occur in all data acquisition processes whenever samples are taken from a continuous process, thereby corrupting the measured data by changing the signal or system information. In modal analysis it can be observed as both, spatial or temporal effect. Although generally undesired, it is exactly the effect of changing the frequency content of the observed motion by aliasing which the current application is based on.

From the theory of signal analysis it is well known that any discrete time signal corresponds to a periodic spectrum, and due to the symmetry (duality) of the Fourier transform (FT) any discrete spectrum has a corresponding periodic time signal [1]. If a continuous signal  $s(t)$  is discretized by impulse sampling at equally spaced time intervals  $\Delta t$  using the sampling frequency  $f_s = 1/\Delta t$ , the discrete time signal  $s_d(t)$  is obtained, see Fig. 25.1a, b.

Its spectrum  $S_d(f) = FT\{s_d(t)\}$  is continuous with the period  $f_s$  in frequency domain and proportional to the spectrum of the original continuous time signal  $S(f)$ , see Fig. 25.1c, d. Since the considered mechanical systems have lowpass characteristics and the excitation is limited in frequency as well, the highest signal frequency component of  $s(t)$  is denoted

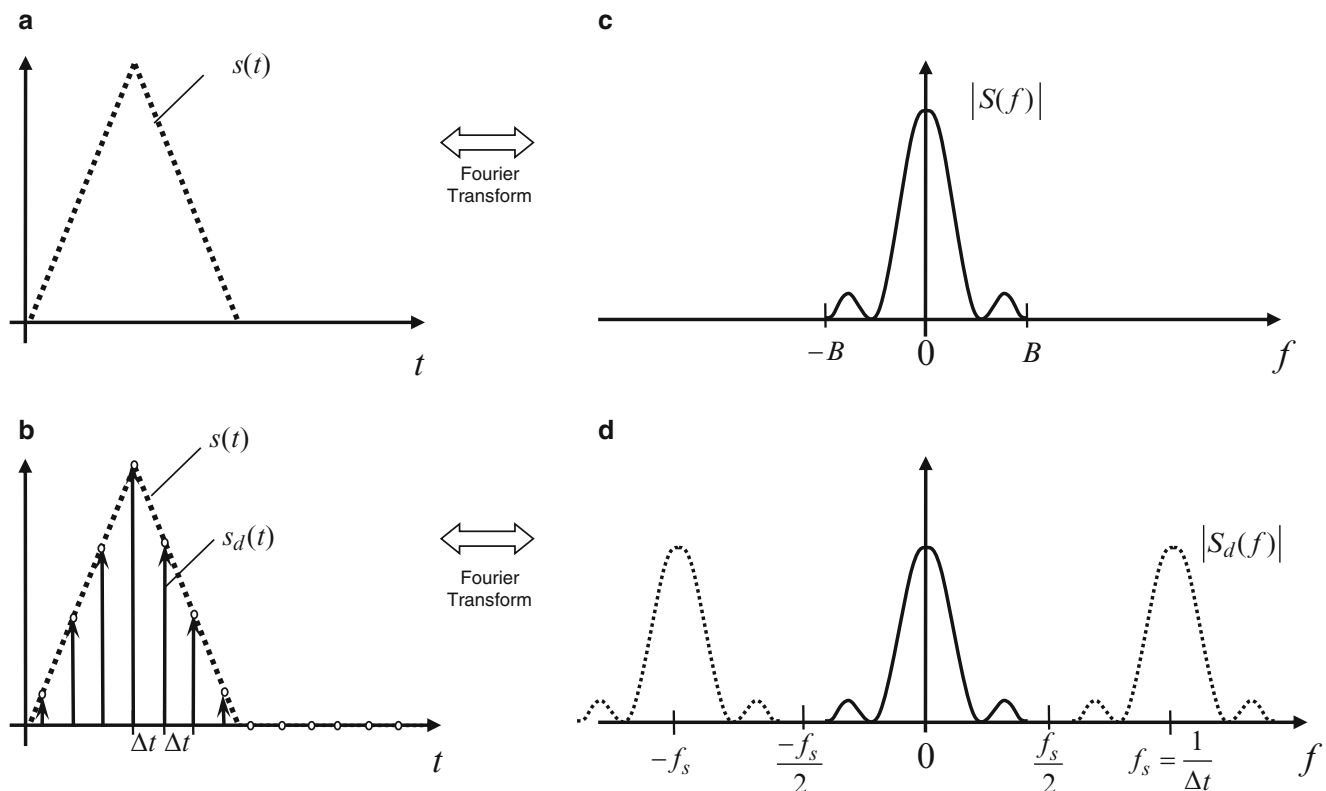


Fig. 25.1 Continuous and impulse sampled time signal with corresponding spectra

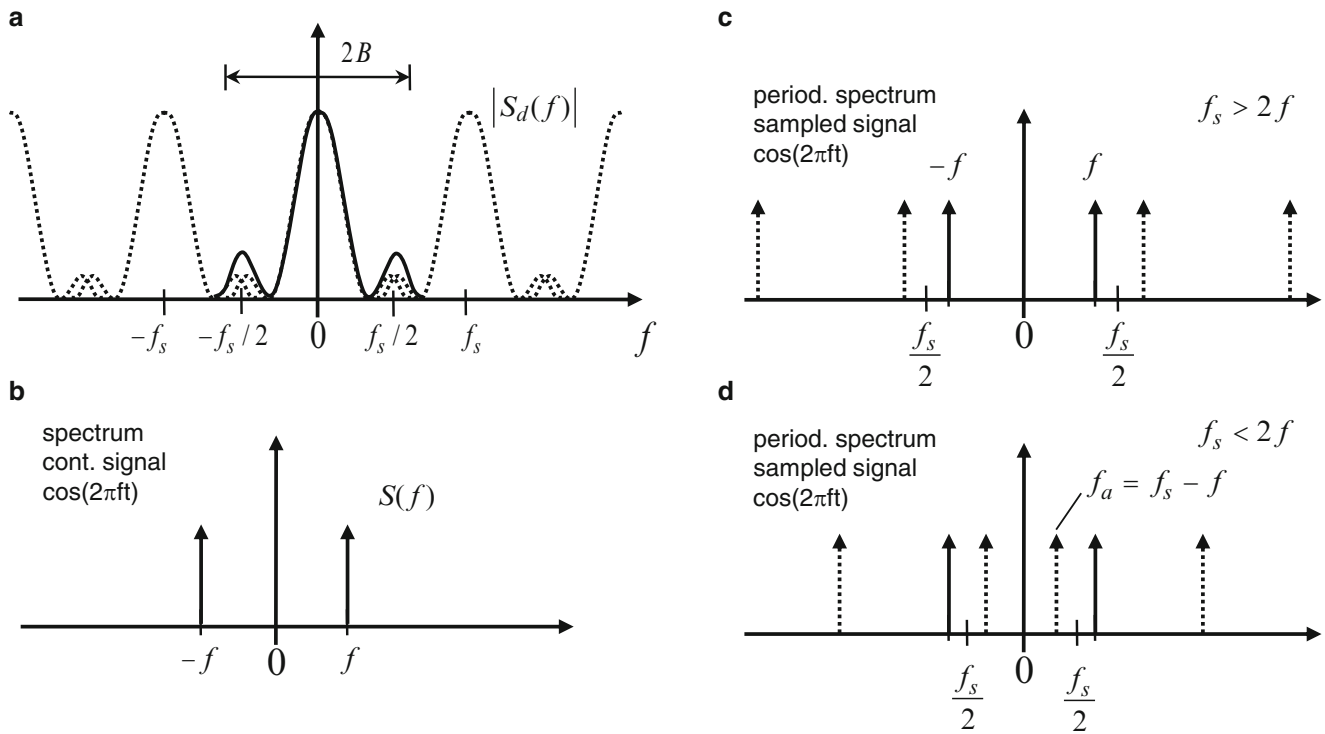


Fig. 25.2 Spectral degeneration by frequency folding

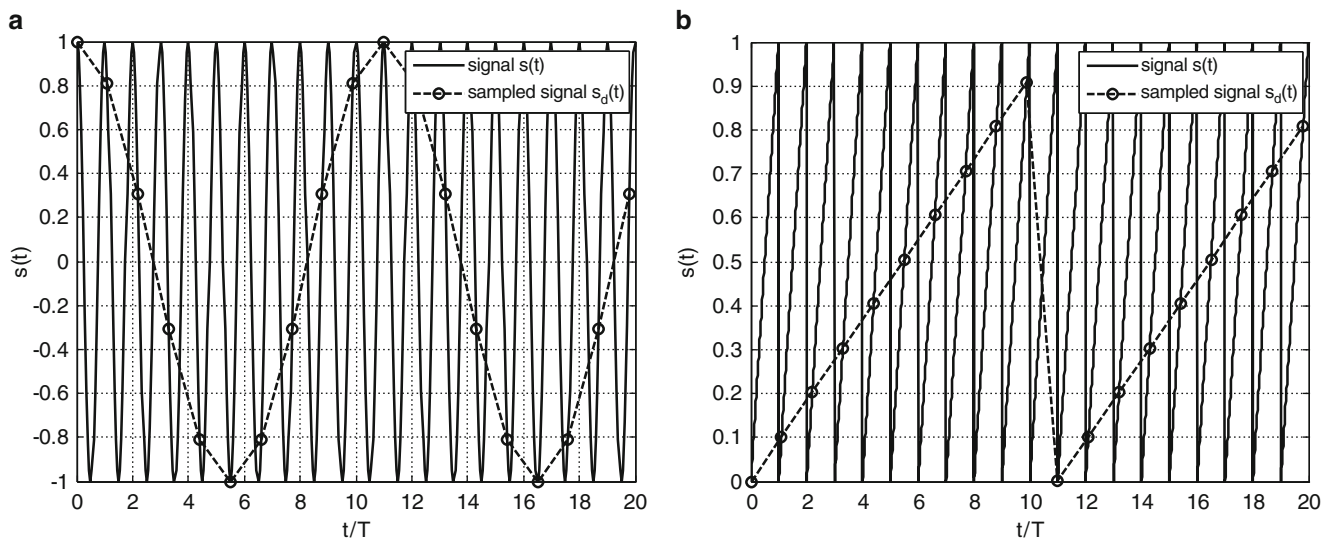
*B.* If properly sampled,  $S_d(f)$  contains periodic and well separated signal sections. If  $f_s$  is reduced the periodic sections will start to overlap. Since  $S_d(f)$  is the sum of all spectral images,  $S(f)$  and  $S_d(f)$  will start to differ in the fundamental frequency band  $-B \leq f < B$ , see Fig. 25.2a. Because of symmetry of real signals,  $|S_d(f)| = |S_d(-f)|$ , it becomes apparent from simple geometric interpretations that the resulting spectrum seems mirrored about  $f_s/2$ . Consequently high frequency components will appear in the fundamental frequency band thereby representing alias frequencies. This spectral degeneration, also known as frequency folding, can be avoided if the condition

$$f_s > 2B \tag{25.1}$$

holds. Equation 25.1 is known as the Nyquist-Shannon sampling theorem and represents a sufficient condition for exact reconstructability of the original time continuous signal  $s(t)$  from the sampled data  $s_d(t)$ . The Nyquist rate  $2B$  is a central property of a band limited signal, contrary to the Nyquist frequency  $f_s/2$  which results from the sampling system. The effect of undersampling can be best explained by considering the single frequency signal  $s(t) = \cos(2\pi ft)$ . For this signal the bandwidth is certainly limited by  $B = f$ , and the spectrum consists of two spectral lines at the frequencies  $\pm f$ . For the sampled signal this is also true as long as inequality (1) holds, but as soon as the sampling frequency is reduced below  $f_s < 2B$  the true spectrum and its periodic images overlap thereby forming a spectrum whose lowest and therefore predominant frequency is a result of the sampling process and does not exist in the original signal, see Fig. 25.2b, d.

The spectrum given in the fundamental frequency band of Fig. 25.2d corresponds to the alias signal  $s_a(t) = \cos(2\pi f_a t)$ ,  $f_a = f_s - f$ . Actually only  $s_a(t)$  is visible in the time domain, see Fig. 25.3a.

Although the frequency has changed the amplitude of  $s(t)$  and  $s_d(t)$  remain identical.  $f_a$  vanishes if  $f_s = f/n$ , and  $n = 1, 2, 3 \dots$ . The condition  $f_a = f_s - f = 0$  is frequently used to determine the angular frequency of rotating shafts. For periodic signals with the fundamental frequency  $f$  and several frequency components, the frequency folding still appears and can be analyzed by linear superposition. However, instead of using the time scaling theorem of the Fourier transform, the effect occurring is directly understood by looking at the time signal, see Fig. 25.3b. In fact any signal of period  $T = 1/f$  shows a scaling in the time domain and can be slowed down to almost zero if  $f_s \approx f/n$ . For  $f_s > f/n$  the signal is running forward, for  $f_s < f/n$  it seems to be running backward in time. Again, the amplitudes of the signal are generally not affected by the undersampling procedure. Because the aim is to visualize fast vibrations in slow motion only sampling frequencies of about  $f_s \approx f/n$  are of interest. If sampling is performed by stroboscopic light flashes and  $s(t)$  represents the displacement of an arbitrary point on a vibrating structure, the time scaling effect must occur for any point and thus the entire structure



**Fig. 25.3** Aliasing effect for harmonic and periodic signal

appears in slow motion. To ensure that the structural motion is visible, the peak displacements should be in the mm-range. This requires a strong excitation or the effect of a structural resonance. For this reason the setup is adequate to visualize resonant vibrations which are observed as the operating deflection shape (ODS) in case of single frequency excitation. If, furthermore, the structure's natural frequencies are well separated, the ODS are almost identical to the mode shapes. This unusual application demonstrates the fundamental influence of the sampling frequency on the result, particularly the need for applying a properly designed low pass and checking system frequencies before sampling the system response.

### 25.3 Technical Details and Practical Aspects

The LED stroboscope is a prototype which has been designed and built at the University of Applied Sciences in Wiener Neustadt. A total of 32 white high power light emitting diodes (3 W each) are arranged in four linear arrays of about 1 m length. Because of the significant heat production the LEDs are directly attached to a cooling body which additionally acts as supporting element. The cooling is a measure of precaution in case the light is switched on permanently. During normal stroboscope operation the LED's duty cycles is around 1–2% which requires no cooling. To achieve a constant homogenous illumination, the power supply offers four channels with linear constant current control. Each channel is connected to a standard BNC connector to control one array using standard TTL-signals. Although it is possible to operate the arrays independently, they are generally connected together and used in phase for best illumination of the test object. The power section is protected against external overvoltage up to 50 V and equipped with an internal protection against overheating.

Experiments have revealed that best visual effects are obtained if ambient and especially artificial light is reduced to a minimum. The higher the duty cycle, the better the illumination level, however, at the price of blurring the visual perception. Experience shows that, depending on the spectator, stroboscopic light flicker can cause discomfort and for this reason the author recommends to operate the system at frequencies higher than 40–50 Hz. This guarantees a perfect illusion of the slowly moving structure. However, it must be mentioned that flashing light might trigger epileptic seizures in people who suffer from photosensitive epilepsy, thus people watching the experiment must know about the effect applied. For best results the alias frequency should be around 1–2 Hz, ideally with maximum displacement amplitudes of more than 1–2 mm. If the structure has shiny or painted surfaces, the moving light reflections also clearly indicate the structural motion and thus contribute to a strong visual effect, even for much smaller displacements. Since switching of the electronic device is possible up to several kHz, it is possible to investigate local vibration effects as well as very small devices. In this situation magnifying optics might be necessary to observe the vibrations.

For appropriate excitation harmonic force or ground excitation is recommended, which is generally provided by an electrodynamic shaker. For light and almost undamped structures a simple alternative has proven to work satisfactorily: If a small strong permanent magnet is attached to a lightly damped test structure, a simple coil connected to a commercial audio amplifier under harmonic input can be used to excite the test structure's resonance. A similar but inverse setup can

be used if electrically conducting elements of string type have to be analyzed. A current-carrying conductor located in the homogenous field of a strong permanent magnet experiences an electric force proportional to the current and the magnetic field. This type of excitation is used to investigate vibration and wave phenomena on strings or excite stringed instruments in a realistic way, respectively.

### 25.4 Applications

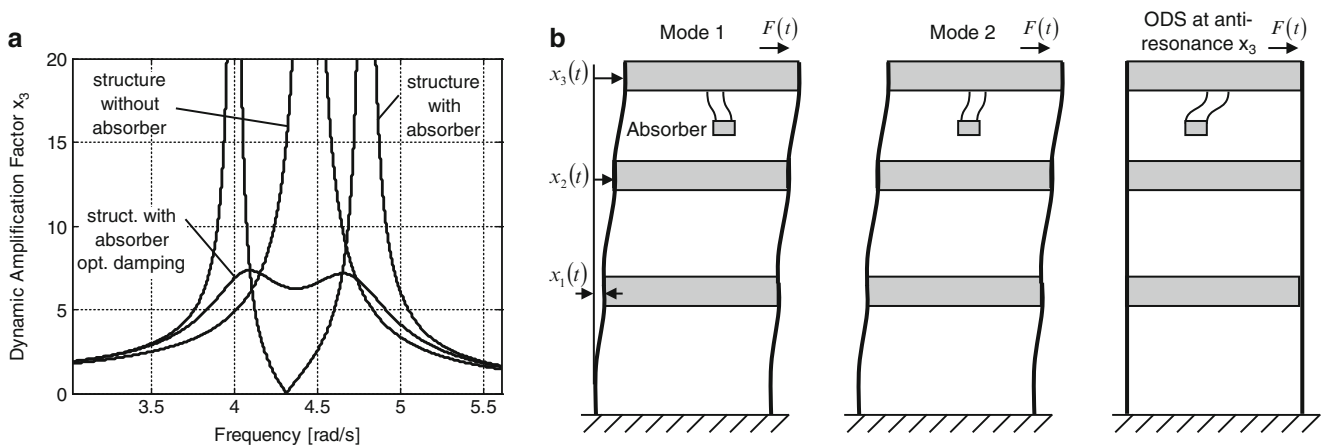
It must be pointed out clearly, that the presented system can never be used to replace vibration measurements or experimental modal analysis. However, it is a very simple and effective setup to visualize and understand some basic principles of modal analysis like modal decomposition and its corresponding deflection shapes, the effect of resonance peaks as well as anti-resonances, superposition, the influence of the modal constant and the effect of nodes and node lines. One major advantage of the setup is the possibility to apply it for the analysis of both, simple teaching experiments and complex structures. When using the stroboscope only estimates of the structural resonances are required, because varying the harmonic excitation frequency quickly renders the resonant vibrations which are often accompanied by acoustic emissions and a blurred view of the geometry. Using the stroboscope with a flash rate of 1 or 2 Hz above the resonance frequency  $f_j$  extracts the true structural displacements in slow motion, and the mode shape vector  $\Psi_j$  (precisely the ODS) is observed directly. Several different applications are discussed in the following paragraphs.

Cantilever beam: When studying a cantilever beam experimentally, the natural frequencies, the number and position of vibration nodes as well as the deflection shape is in perfect agreement with theoretical considerations for the lower vibration modes. Therefore, it is straightforward to explain the effect of a node with respect to structural vibration measurements or structural excitation. When looking at transfer functions in the modal superposition form, see e.g. [2, 3]

$$H_{pq}(j\omega) = \sum_{r=1}^N \frac{A_{pqr}}{j\omega - s_r} + \frac{A_{pqr}^*}{j\omega - s_r^*}, \quad A_{pqr} = Q_r \Psi_{pr} \Psi_{qr}, \quad (25.2)$$

with  $s_r$ ,  $Q_r$ ,  $\Psi_{nm}$  denoting the pole and modal scaling constant for each mode  $r$  and the elements of the modal shape matrix respectively, the influence of the modal constant (residual)  $A_{pqr}$  becomes apparent and can be proven experimentally by varying the excitation point. Of course the experienced practitioner knows about the danger of missing natural frequencies and mode shapes using single point excitations but when studying modal analysis the demonstration of this effect is crucial.

Anti-resonances: This important phenomenon, often applied in passive vibration absorption, can also be understood directly by simple visualization. When adding a vibration absorber to a structure and tuning it to a resonance  $f_j$  of the host structure the vibration amplitude vanishes, see e.g. [4], if damping is neglected. A close look at this effect reveals that the absorber adds a degree of freedom to the structure, thereby forming a pair of adjacent natural frequencies, see Fig. 25.4a.



**Fig. 25.4** (a) Frequency response of a structure with/without dynamic absorber. (b) Corresponding mode shape vectors and ODS at anti-resonance for a plane three story shear frame model with a dynamic absorber attached

Due to the phase shift at resonance both mode shapes vibrate in opposite direction and compensate each other at the tuning frequency  $f_j$ . However, from the inspection of the extended mode shape vector it is apparent that this compensation by modal superposition is only achieved for the host structure, see Fig. 25.4b for a plane three story shear frame model. Although the story displacements vanish, the absorber motion is amplified thereby generating the compensating forces. This perfect passive vibration absorption can only be achieved at the single frequency  $f_j$ . If the excitation frequency changes the absorbing effect decreases and even worse, another resonance phenomenon is obtained. This behavior can be avoided by adding viscous damping to the absorber which is common practice in wind- and earthquake engineering, see Fig. 25.4a.

Complex operation deflection shapes: When working e.g. with a shear frame laboratory model, complex ODS can be observed. They occur when the structural displacements are not in phase for harmonic forcing, giving the impression of traveling wave whereas real ODS appear as standing waves. This phenomenon results from the relative phase differences between adjacent modes which dominate the ODS.

Mass loading effect: When investigating with light structures it is frequently observed that the mass loading of the vibration transducer influences natural frequencies and mode shapes, an effect which can also be shown using the presented setup.

Complex structures: Out of the variety of ways to present modal concepts and phenomena, maybe the most impressive is the application to real structures whose modal deflection shapes cannot be derived intuitively. Amongst others are real size car wings and doors, skis, tennis rackets, blank CDs and other arbitrary shaped plate structures or loudspeaker membranes. Bending modes, torsional modes and even compression modes have been made visible directly. Some of the structures have also been analyzed numerically for qualitative comparison and it has turned out that confirming the computer results with real scale experiments contributes a lot to the understanding and confidence of modal analysis.

Transient vibrations: Experiments with transient processes, like free vibration, beating or mode jumping experiments, have not been convincing because the decay in absolute time is usually much too fast for visualization. Nevertheless, if a structure is excited periodically, e.g. with an impulse type of excitation, then a direct observation of the transient response is possible. This effect has been tested on a steel string of length  $L = 0.8$  m, rigidly fixed at both ends, with a fundamental frequency of  $f_0 = 48$  Hz. A suitable excitation is generated applying a strong current impulse  $i_0 \approx 30$  A to the string which is partly placed in the homogenous magnetic field of strong permanent magnet. The resulting force is close to an ideal impulse which induces traveling waves on the string. A periodic transient motion is obtained when repeating the impulsive excitation with frequency  $f_0$ . Flashing the stroboscope with  $f_s = f_0 + 1$  Hz displays the traveling wave in perfect accordance with the theoretical prediction. D'Alembert's solution (traveling wave approach) but equivalently Bernoulli's solution (modal decomposition) can be used to fully describe the propagating wave, see [2, 5]. The latter is given by

$$u(x, t) = \sum_{n=1}^{\infty} u_n \sin\left(\frac{n\pi x}{L}\right) \cos(2n\pi f_0 t), \quad (25.3)$$

where the coefficients  $u_n$  are defined by the initial displacement, and the string is released with no initial velocity. Since standing waves can be generated with the same setup, this simple experiment can be used to demonstrate that modes and waves are dual theories which, in this context, explain structural displacements for a specific forcing. From an engineer's perspective, however, the modal approach is characterized by its versatility, because the modes can be measured or calculated, in contrary to the wave approach where a closed form solution is required.

Rotordynamics: Although the application of stroboscopes has a long tradition in rotordynamics it is mainly used to determine the speed of a rotating shaft. Experiments on a simple small scale rotor test rig show that it is straightforward to visualize the forward whirling of a cantilever elastic shaft close to the critical speed. Consequently a similar result can be expected for the backward whirl if it is excited properly.

## 25.5 Conclusions

This work presents an experimental setup to visualize structural vibrations using LED based distributed stroboscopic light technology. The LED technology has turned out to be cheap, robust, fast, energy saving, flexible and easy to use. For the experimental setup 32 high power LEDs are arranged in four mobile arrays to homogeneously illuminate a test structure. For any periodic excitation the structural response appears in slow motion if the vibrational displacements are in the visible range and the flash frequency is chosen close to the excitation frequency. Several basic modal analysis concepts like mode shapes, natural frequencies or resonances and anti-resonances become apparent through direct observation. Furthermore, the results can be compared qualitatively to classical experimental modal analysis methods or computational results. The system has



been applied to a variety of structures including piano or cello strings, skis, tennis rackets, as well as plate and shell type structure of various sizes. For large structures the illumination and light intensity increased by simply adding further light arrays all operating in phase which allows observing local and global vibration modes at the same time.

**Acknowledgements** The author gratefully acknowledge DI (FH) Johann Leinweber and DI Helmut Frais-Kölbl, Dept. of Electrical Engineering, University of Applied Sciences, Wiener Neustadt, for their help in the development of the electrical part of the project and for various discussions of the experimental setup and the results.

## References

1. Oppenheim AV, Schafer RW, Buck JR (1999) Discrete-time signal processing, 2nd edn. Prentice-Hall, Upper Saddle River
2. Brandt A (2011) Noise and vibration analysis. John Wiley & Sons, Ltd., Chichester, UK
3. Ewins DJ (2000) Modal testing, theory, practice and application, 2nd edn. Research Studies Press Ltd., England
4. Den Hartog JP (1985) Mechanical vibrations. Dover Edition, Mineola, NY, USA
5. Elmore WC, Heald MA (1966) Physics of waves. McGraw-Hill Book Company, New York

# Chapter 26

## Analytical and Experimental Learning in a Vibrations Course at the University of Massachusetts Lowell

Pawan Pingle and Peter Avitabile

**Abstract** At the University of Massachusetts Lowell, Vibrations 22.550 is taught in a slightly different manner than traditional courses in other universities. The traditional single and multiple Degree of Freedom (DOF) systems are addressed along with transmissibility, isolation and related topics in the first half of the course. However, in the second half of the course, rather than explore continuous solutions, the course is focused on development of simplistic beam finite element discrete models along with experimental modal testing coupled with tuned absorber applications to detune critical modes of the structure. The structures studied have ranged from simplistic beams, tennis rackets, snowboards and similar equipment to wind turbine blades.

Recently, small wind turbine blades have been used in the course. Models are developed to address simplistic beam modeling of complicated varying blade cross section and conditions of free-free, built-in and mass perturbed boundary conditions. In addition, tuned mass absorbers are studied to reduce the response of particular modes of vibration, both analytically as well as experimentally. This paper discusses the course philosophy and presents some results of the student projects to drive home the necessary important theoretical concepts through an experiential learning process. Generally, the students have endorsed this approach because it firmly solidifies the theoretical concepts discussed in the course.

**Keywords** Educational • Vibrations • Teaching • Experimental • Analytical

### 26.1 Introduction

Teaching structural dynamics utilizing both analytical and experimental approaches in an undergraduate/graduate curriculum poses some unique challenges and unique opportunities. While “hard core theory” is critical to be included in all of the material delivered, there is a very important need to include experimental components to solidify the theory through practical examples. Students learn best with hands-on approaches that provide them the opportunity to see the “theory in action”. This helps to explain the theory as well as allow the students to more deeply understand and appreciate various aspects of structural dynamic modeling techniques and applications.

Reference [1] and [2] presented some approaches used at UMASS Lowell in the educational curriculum to assist students in firmly learning important and critical concepts in structural dynamic analysis using analytical and experimental approaches. This paper concentrates on presenting some detailed specific material related to the Vibrations course which is one course as part of the structural dynamics curriculum.

---

P. Pingle (✉) • P. Avitabile  
Structural Dynamics and Acoustic Systems Laboratory, University of Massachusetts Lowell,  
Lowell, MA 01854-2881, USA  
e-mail: [Pawan.Pingle@student.uml.edu](mailto:Pawan.Pingle@student.uml.edu); [peter.avitabile@uml.edu](mailto:peter.avitabile@uml.edu)

## 26.2 Vibrations

Typically, a Vibration course can be found in most ME programs. In order to provide undergraduate students with a diverse, broad background in the major tools needed to solve typical engineering problems involving vibrations, the traditional course was modified to include an assortment of tools that might be necessary to solve a wide assortment of typical problems encountered.

The foundation for this Vibrations ME course # 22.550 is laid in undergraduate Dynamic Systems ME course # 22.451. Basic concepts related to modeling of various systems, typically mechanical mass-spring-dashpot (MCK) systems are covered in the Dynamic Systems course. The basic core material related to single degree of freedom (SDOF), free and forced response, as well as sinusoidal excitations and arbitrary inputs that are presented in Vibrations 22.550, are continued in the same thought process as Dynamic Systems course. This type of teaching methodology is seen to be much more effective because students are already in sync with the course philosophy and the thought process required to master the Vibrations concepts. For instance the students already have knowledge of development of governing equations of motion of a typical SDOF/MDOF system, putting them in matrix form and solving them using various methodologies such as state-space technique through the course Dynamic Systems. Teaching advanced Vibrations concepts is hence possible in 22.550 Vibrations.

In Vibrations, typical base excitation, isolation and force transmission are presented. The traditional multiple degree of freedom (MDOF) systems presented for two DOF is included along with modal space representations, tuned absorbers and the related material. The course then extends into very simple finite element modeling techniques with simple beam and lumped mass representations to extend the SDOF and MDOF to be able to handle more realistic modeling situations. The introduction to experimental modal analysis is the logical extension of this material to complement the finite element modeling approaches. A brief introduction into random vibrations is included to help the students be able to understand how to apply the basic SDOF and MDOF theory as a building block to understand more complicated loading scenarios. Beyond this, the introduction of base excitation of MDOF systems leads directly into structural modeling applications including seismic analysis, shock analysis and response spectrum analyses.

While the theoretical foundations are presented in class, the importance of all the theory is amplified through the use of projects to solidify many different concepts. Several of the more important projects used in prior years are listed:

- Concepts of response for SDOF and MDOF systems are reinforced with projects that utilize MATLAB to determine the forced response of SDOF, MDOF and mode superposition and show the interrelationship of the different approaches. Also, where possible, Simulink models are utilized to form solutions to these problems along with closed form solution if available. In addition, a LabVIEW GUI allows for the easy identification of different free and forced response characteristics for a SDOF system which is used as part of class projects to help reinforce theoretical concepts.
- Development of MDOF equations by defining a project to build a seismic anchor to simulate a built-in condition is an “eye-opening assignment”. This forces the students to obtain a better grasp of the physical parameters needed to actually simulate such a severe constraint that typically is so easy to write analytically but extremely difficult to achieve in a real test situation.
- A finite element modeling project is assigned and each student is given a slightly different configuration that can be modeled with simple beams and lumped masses and simplistic support boundary conditions. A general problem is posed for the students to determine how system level response will change due to a rotating sinusoidal excitation when various parameters of the system are changed (such as mass of specific components, (Center of gravity) CG shift of certain components, support stiffness changes). The effects of number of elements, distribution of mass and other items must be addressed. In many cases, the students are asked to design tuned absorbers to de-tune a troublesome mode of the system. In earlier years, the students were given configurations such as vertical pumps, muffler configurations, valve/piping systems, heat exchanges, generator turbine sets, and various other typical industrial applications. All the models are presented in class to provide some meaningful discussion of modeling scenarios deployed and alternate mechanisms to possibly model the system.
- An experimental modal test is performed on a variety of simpler structures including application of tuned absorbers to see the effect of mode de-tuning. Structures have included simple beams, plates, and frames but have also included aluminum baseball bats, snowboards, tennis rackets, skis and racket ball rackets (with some equipment coming from wood, aluminum, composites and other constructions to see differences in resulting characteristics). In the evaluation of snowboards, six different commercial configurations were evaluated to observe the change characteristic shapes due to different construction configurations and resulting frequency patterns.

In past couple of years, the finite element models and experimental modal tests have concentrated on some smaller wind turbine blades (from an Ampair wind turbine) where a variety of models have been developed with a variety of different boundary conditions are studied along with the design of a tuned absorber. This is then further evaluated by performing experimental modal tests on the turbine blade as well as implementing the tuned absorber design to confirm the modal tuning. Six different turbine blades have been tested and evaluated by different groups from the class. The specific project requirements are identified next and the results discussed; note that a few different student project results are described in the appendices of this paper.

## 26.3 Finite Element Models

The finite element model project is shown in Fig. 26.1.

The students are required to develop a basic finite element model for the small wind turbine blade in MATLAB. Cross sectional characteristics are obtained from the solid model to identify cross section and area moment of inertia; only flapwise modes are to be considered and any out of plane geometry effects are not to be considered in order to keep the model simplistic.

The model is to be evaluated as a free-free system; additional models are developed to address the design of a mass loaded interface. A small rectangular block of approximately the same weight of the blade is used to perturb the attachment points with a mass loaded interface (Note that the mass is also added as an interface for attachment of the tuned absorber to the structure.)

Additional models need to be developed for the design of the tuned absorber to detune the first two modes of the blade.

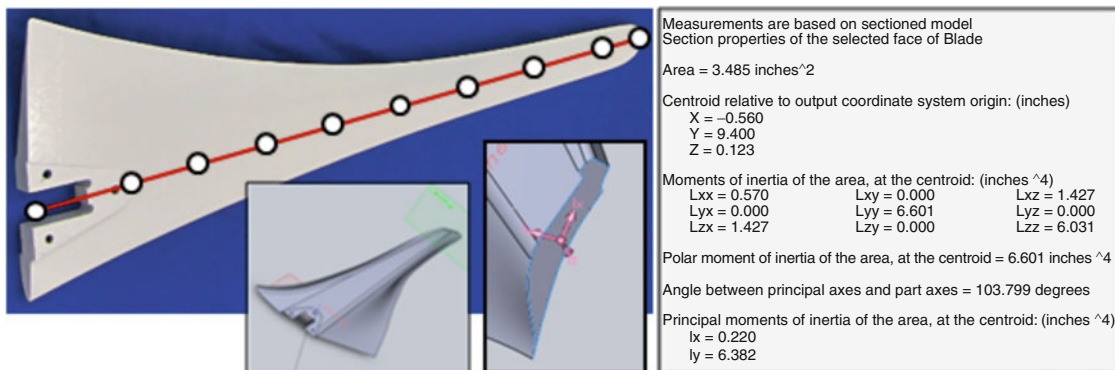
Students need to give consideration to the fact that the material properties are not clearly identified, that the attachment of the mass to the blade can be achieved in several different ways, that the blade cross section also has some twist due to the curvature of the blade as well as many other important factors. Students are expected to perform some type of mesh convergence to assure that the model is appropriate.

**VIBRATIONS - 22.550**

**HANDED-OUT MARCH 8, 2011**

**PROJECT GROUP: (two group members)**

**DUE MARCH 29, 2011**



A finite element model is to be developed for a free-free attachment and a mass attachment to simulate a relatively greater fixed boundary condition. The mass at the attachment point is an aluminum block that is 5" × 5" × 1" thick. Consider the effects of model refinement in your model and the effects of different approaches to approximate the attached mass.

In addition a tuned absorber is to be designed to detune the first mode and second mode of the system. Identify the first several modes of the blade. Identify the tuned absorber designed and the effect on the modes of the blade.

**Fig. 26.1** A typical finite element project at UMASS Lowell

**VIBRATIONS - 22.550**  
**HANDED-OUT MARCH 29, 2011**

**PROJECT GROUP: (two group members)**  
**DUE: MAY 10, 2011**

Vibration tests are to be performed for FEA models constructed for the analytical model. One test should be with the blade in a free-free condition. Another modal test needs to be performed to characterize the boundary condition modification used in the FEA models. In addition, modal tests need to be performed to identify how well the tuned absorber designed affected the modes of the blade.

Impact measurements are to be used to determine the frequency response function; the imaginary part of the FRF can be used to determine the modal coefficients and can be obtained using MEscope. Compare two frequency response functions and identify any change in the vibration characteristics observed.

**Fig. 26.2** A typical finite element project handout at UMASS Lowell

## **26.4 Experimental Modal Analysis**

The experimental modal analysis project is shown in Fig. 26.2.

The students are required to perform an experimental modal test for the free-free blade and the mass loaded blade to determine the frequencies and mode shapes for the blade in those two configurations. Traditional modal impact testing is performed with a stationary reference accelerometer placed on the blade. Reference locations for the experimental modal test are identified individually by each group. Data is imported into MEscope [3] and modal parameter estimation studies are performed.

## **26.5 Test/Analysis Correlation**

The results of the finite element model and experimental modal test are compared. There are some simplifying assumptions in the beam finite element model (such as lack of twist, element length and mass distribution) that tend to make the predicted frequencies higher than the actual configuration. In any event, the different blades are compared to each other and a MAC is computed among all the different test configurations (These results are reported in a separate IMAC paper [4] and are included here for illustration.)

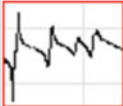
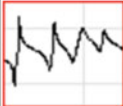

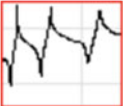
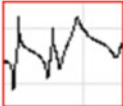
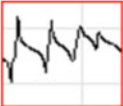
## **26.6 Tuned Absorber Applications**

The analytical model is used as the starting point for the design of the tuned absorber for general sizing. However, the experimental modal model is also used to predict the tuned absorber characteristics. Once attached, the effects of the tuned absorber can be clearly seen in the measured FRFs. While the analytical equations can be used for the prediction of the tuned absorber effect, there is so much more really learned and absorbed by the students with the live experimental tuned absorber study. The actual measurement is proof that the theoretical equations work.

## **26.7 Test/Test Correlation**

As part of one of the series of turbine blade tests performed in the Vibrations Class of 2011, an additional study was performed to compare all the test results and was presented in class as an extra educational learning experience. The main emphasis

**Table 26.1** First five natural frequencies of Ampair blades in flapwise direction tested in free free configuration

BLADE	#001	#002	#003	#004	#005	#006
MODE	Hz	Hz	Hz	Hz	Hz	Hz
1	40.2	42.6	45.1	41.0	40.7	40.3
2	119.9	127.4	132.5	120.5	122.0	122.1
3	183.2	191.3	194.3	187.2	181.1	193.9
4	225.7	245.0	251.5	240.1	N/A	235.6
5	303.3	319.6	323.8	N/A	306.5	319.4
Ref dof	pt 18	pt 18	pt 18	pt 20	pt 19	pt 18
Drive Pt FRF 300 Hz BW						

**Fig. 26.3** General test setup of blade in free free configuration



was in relation to variability that may result due to actual hardware differences. In addition, the results of the testing can be affected by the manner in which the test is conducted and the reference locations are selected. This helps to clearly identify that care needs to be exercised in the conduct of the test. Table 26.1 shows the results of the frequency comparison whereas Fig. 26.3 and Table 26.2 shows the MAC correlation for all the blades tested by the different groups.

## 26.8 Student Projects

The attached appendices to this paper contain some selected results for two projects related to the wind turbine blade project over the past 2 years. These results clearly show the student involvement in identifying the models, tests and overall results. In the Appendix “CN”, the results present the model developed and the tuned absorber designed followed by the testing performed and the implementation of the tuned absorber designed. This appendix is the summary of a typical project for the Vibrations class. In the Appendix “LD”, the results are similar to the previous appendix and are included to show a slightly different student group approach for the project and what was presented.

The third project shown is an extended project where the same concepts were deployed for the CX-100 wind turbine blade. In those studies actual boundary condition changes were studied and applied to actual data for the experimental configuration. In Appendix “JH”, the studies clearly show that the academic projects are very clearly extended to a very



**Table 26.2** MAC correlation values for six Ampair blades in flapwise direction tested in free free configuration

	Blade 1					Blade 2					Blade 3					Blade 4					Blade 5					Blade 6				
	1	2	3	4	5	1	2	3	4	5	1	2	3	4	5	1	2	3	4	5	1	2	3	4	5	1	2	3	4	5
Blade 1	1	100	0.9	2.7	10.3	7.1	99.5	2.5	0.9	6.9	2.3	99.8	0.6	6.5	15.0	12.7	99.7	1.7	2.1	13.1	99.3	3.9	0.1	1.4	99.1	2.6	0.5	5.4	0.5	
	2	0.9	100	2.6	3.4	3.0	0.5	99.1	2.6	3.8	0.8	1.3	99.5	3.0	1.5	0.7	0.9	98.9	3.3	0.8	0.3	97.2	4.9	0.4	0.7	99.2	1.3	1.1	0.4	
	3	2.7	2.6	100	7.5	13.3	1.9	2.1	97.5	2.5	5.0	2.1	1.8	98.5	4.4	10.1	1.9	2.9	99.2	2.1	1.5	0.6	96.3	4.2	3.4	1.9	95.3	0.0	5.3	
	4	10.3	3.4	7.5	100	8.7	9.6	2.7	8.6	97.5	3.1	8.5	4.7	10.2	95.8	10.1	9.0	4.6	8.9	95.7	10.3	2.1	7.6	3.3	8.1	3.9	7.9	91.7	2.2	
	5	7.1	3.0	13.3	8.7	100	5.5	2.8	12.7	4.5	95.1	5.7	3.1	16.8	4.8	96.1	5.5	4.1	13.2	3.9	6.6	2.7	12.2	93.4	6.7	2.7	13.7	1.3	92.1	
Blade 2	1	99.5	0.5	1.9	9.6	5.5	100	1.7	0.6	6.7	1.4	99.6	0.2	5.2	14.5	10.1	99.6	1.2	1.5	12.6	99.6	2.9	0.0	0.7	98.6	1.8	0.2	5.3	0.1	
	2	2.5	99.1	2.1	2.7	2.8	1.7	100	2.3	3.1	1.0	3.1	98.7	2.3	0.8	0.6	2.5	99.3	2.8	0.4	1.3	99.1	4.7	0.6	2.1	99.6	1.2	0.8	0.7	
	3	0.9	2.6	97.5	8.6	12.7	0.6	2.3	100	3.5	4.9	0.6	1.7	94.0	5.0	8.3	0.5	3.0	98.3	2.6	0.3	0.7	98.8	4.2	1.2	2.1	99.0	0.2	5.7	
	4	6.9	3.8	2.5	97.5	4.5	6.7	3.1	3.5	100	1.1	5.6	5.3	4.1	95.8	5.4	6.1	5.0	3.5	96.8	7.3	2.6	2.9	1.2	5.1	4.6	2.9	97.1	0.6	
	5	2.3	0.8	5.0	3.1	95.1	1.4	1.0	4.9	1.1	100	1.6	0.8	6.6	0.8	92.6	1.5	1.5	4.9	0.7	2.1	1.2	4.9	99.3	2.0	0.8	6.2	0.1	99.0	
Blade 3	1	99.8	1.3	2.1	8.5	5.7	99.6	3.1	0.6	5.6	1.6	100	0.9	5.4	13.1	10.8	99.8	2.3	1.6	11.4	99.3	4.5	0.0	0.9	99.1	3.2	0.3	4.4	0.2	
	2	0.6	99.5	1.8	4.7	3.1	0.2	98.7	1.7	5.3	0.8	0.9	100	2.3	2.4	0.9	0.5	99.1	2.4	1.7	0.1	97.3	3.7	0.5	0.4	99.0	0.7	2.1	0.5	
	3	6.5	3.0	98.5	10.2	16.6	5.2	2.3	94.0	4.1	6.6	5.4	2.3	100	7.0	13.8	5.1	3.3	97.3	4.0	4.6	0.7	91.7	5.4	7.6	2.2	90.5	0.4	6.4	
	4	15.0	1.5	4.4	95.8	4.8	14.5	0.8	5.0	95.8	0.8	13.1	2.4	7.0	100	6.4	13.7	2.0	5.1	99.2	15.0	0.4	3.6	0.8	12.4	1.5	4.1	92.9	0.3	
	5	12.7	0.7	10.1	10.1	96.1	10.1	0.6	8.3	5.4	92.6	10.8	0.9	13.8	6.4	100	10.6	1.4	9.5	5.6	11.8	0.6	7.6	90.9	12.2	0.5	9.2	2.2	88.0	
Blade 4	1	99.7	0.9	1.9	9.0	5.5	99.6	2.5	0.5	6.1	1.5	99.8	0.5	5.1	13.7	10.6	100	1.8	1.4	11.9	99.6	3.8	0.0	0.8	99.2	2.6	0.2	4.9	0.2	
	2	1.7	98.9	2.9	4.6	4.1	1.2	99.3	3.0	5.0	1.5	2.3	99.1	3.3	2.0	1.4	1.8	100	3.6	1.3	0.8	98.4	5.6	1.1	1.4	99.4	1.6	1.8	1.1	
	3	2.1	3.3	99.2	8.9	13.2	1.5	2.8	98.3	3.5	4.9	1.6	2.4	97.3	5.1	9.5	1.4	3.6	100	2.7	1.2	1.0	97.7	4.2	2.7	2.6	96.3	0.2	5.3	
	4	13.1	0.8	2.1	95.7	3.9	12.6	0.4	2.6	96.8	0.7	11.4	1.7	4.0	99.2	5.6	11.9	1.3	2.7	100	13.1	0.2	1.7	0.7	10.5	1.0	2.1	96.1	0.2	
	5																													
Blade 5	1	99.3	0.3	1.5	10.3	6.6	99.6	1.3	0.3	7.3	2.1	99.3	0.1	4.6	15.0	11.8	99.6	0.8	1.2	13.1	100	2.3	0.0	1.3	98.5	1.4	0.1	5.8	0.4	
	2	3.9	97.2	0.6	2.1	2.7	2.9	99.1	0.7	2.6	1.2	4.5	97.3	0.7	0.4	0.6	3.8	98.4	1.0	0.2	2.3	100	2.4	0.9	3.4	98.8	0.2	0.7	0.9	
	3	0.1	4.9	96.3	7.6	12.2	0.0	4.7	98.8	2.9	4.9	0.0	3.7	91.7	3.6	7.6	0.0	5.6	97.7	1.7	0.0	2.4	100	4.3	0.2	4.4	98.2	0.1	5.8	
	4																													
	5	1.4	0.4	4.2	3.3	93.4	0.7	0.6	4.2	1.2	99.3	0.9	0.5	5.4	0.8	90.9	0.8	1.1	4.2	0.7	1.3	0.9	4.3	100	1.2	0.5	5.6	0.1	99.0	
Blade 6	1	99.1	0.7	3.4	8.1	6.7	98.6	2.1	1.2	5.1	2.0	99.1	0.4	7.6	12.4	12.2	99.2	1.4	2.7	10.5	98.5	3.4	0.2	1.2	100	2.1	0.6	3.7	0.3	
	2	2.6	99.2	1.9	3.9	2.7	1.8	99.6	2.1	4.6	0.8	3.2	99.0	2.2	1.5	0.5	2.6	99.4	2.6	1.0	1.4	98.8	4.4	0.5	2.1	100	1.0	1.6	0.6	
	3	0.5	1.3	95.3	7.9	13.7	0.2	1.2	99.0	2.9	6.2	0.3	0.7	90.5	4.1	9.2	0.2	1.6	96.3	2.1	0.1	0.2	98.2	5.6	0.6	1.0	100	0.1	7.3	
	4	5.4	1.1	0.0	91.7	1.3	5.3	0.8	0.2	97.1	0.1	4.4	2.1	0.4	92.9	2.2	4.9	1.8	0.2	96.1	5.8	0.7	0.1	0.1	3.7	1.6	0.1	100	0.0	
	5	0.5	0.4	5.3	2.2	92.1	0.1	0.7	5.7	0.6	99.0	0.2	0.5	6.4	0.3	88.0	0.2	1.1	5.3	0.2	0.4	0.9	5.8	99.0	0.3	0.6	7.3	0.0	100	

(Notice that some groups did not find all the modes of the structure during test because of an inappropriate selection of reference point for the test; this is a useful outcome so that all the students understand that if care is not exercised then incorrect results can occur)

real-world evaluation. The results of this project address modeling, testing and evaluation of the actual test configuration and that the models developed are a very good mechanism to assess the overall test evaluation for the 9 m turbine blade project.

In all the projects performed over the years, the students are exposed to a more realistic engineering class of problems that enable them to understand that the course material has very significant and practical applications for real engineering problems. This is reinforced with realistic hardware assessment rather than academic exercises with no clear relevance to real world type applications.

### 26.9 Observations

Over the past 20 or more years, a variety of courses have been taught in the Structural Dynamic option at University of Massachusetts Lowell in the Mechanical Engineering Department. Vibrations, Structural Dynamic Modeling Techniques, Experimental Modal Analysis are the core courses of the program; the Vibrations course is the course described in more detail in this paper. All of these courses have been taught with the same basic philosophy – present basic material and drill home concepts and techniques through project-based work. These projects are, in cases of the more critical concepts and ideas, orally presented so that an open discussion can evolve where the students have to justify their approach, technique and results obtained. This forces a much greater student understanding of all the material presented (Tests are rarely given in any of these classes.) Student comments have always been very positive as to their overall understanding and comprehension of material presented – but the majority have always stated that the workload is significant in all of these classes. While at times some oral presentations have appeared as if a student is in front of a firing squad (from their perspective), the dialogue greatly assists the students to further query areas where they still feel not as strong in understanding the material as they may have liked to. The dialogue also helps in the overall evaluation of the student performance.

### 26.10 Summary

The curriculum in the Structural Dynamics and Acoustic Systems Laboratory in the Mechanical Engineering Department at the University of Massachusetts Lowell is heavily complemented with hands on projects to foster deeper student learning

and comprehension. This paper describes some of the concepts introduced and integrated into the curriculum with a heavy project based format. In particular, the Vibrations course is described in more detail in this paper.

## A.1 Appendix CN

### A.1.1 Vibrations Project Spring 2011

An Euler-Bernoulli beam finite element model was developed to model the flapwise modes of the Ampair wind turbine blade. Each node has two degrees of freedom, rotary and translation. The model was programmed in a series of MATLAB scripts. The cross sectional properties for the beam elements were extracted from a CAD model. A mesh convergence study was conducted using 9, 18 and 27 beam elements. The mode shapes and frequencies of each model were compared. There was a negligible difference between the 18 and 27 element models for lower order modes. The 18 element model was selected for the final model because the extra computation of the 27 element model did not yield significantly different or better results. The results of the convergence study are shown in Table CN-1. If higher order modes were of interest, the 27 element model would be used.

To model the blade in the free-free condition, the root was supported by soft translation and rotation springs, 2 lb/in and 2 lb/in/rad respectively. These soft springs provided enough boundary stiffness to make the rigid body frequencies non-zero, which more closely models the test configuration. An aluminum block was bolted to the root. Three techniques were used to model the additional mass. The first and simplest technique was to add a point mass to the translational degree of freedom closest the center of mass of the aluminum block. The issue with this technique is it does not account for the mass moment of inertia of the block. The next model used the same point mass but with a mass moment of inertia added to the rotary d.o.f. The technique used for the final model distributed the mass and mass moment of inertia of the block over three nodes. The area moment of inertia of the beam elements connecting these three nodes were also increased to account for the stiffness added by the block. The frequencies and mode shapes of the two models that accounted for the mass moment were very similar. Table CN-2 compares the frequencies of each of these methods.

Figure CN-1 overlays the shapes calculated using each method for Mode 1 and Mode 3.

The frequencies and modes shapes show the point mass model diverges from others at higher modes. These results show mass moment is important, especially for higher order modes.

A tuned absorber was designed to detune the first flexible mode of the blade. The mounting location and materials for the tuned absorber were specified. The absorber is attached at the root and is made of 10–32 threaded rod and steel masses. The length of the threaded rod and tuned absorber mass were the parameters that needed to be tuned. The tuned absorber mass was arbitrarily set to 10 % of the mass of the turbine blade. The length of the threaded rod was calculated such that the frequency of the tuned absorber was the same as the first flexible turbine mode. The tuned absorber was first implemented

**Table CN-1** Frequency results of mesh convergence study

Mode	Frequencies (Hz)		
	9 Beam elements	18 Beam elements	27 Beam elements
Rigid Body 1	0.17	0.17	0.17
Rigid Body 2	3.2	3.2	3.2
Flex. 1	100.9	98.8	100.2
Flex. 2	215.0	231.7	236.6
Flex. 3	392.1	411.8	424.8
Flex. 4	610.4	641.0	667.7

**Table CN-2** Frequency of different mass modeling methods

Mode	Frequencies (Hz)		
	Point mass	Point mass w/mass moment	Distributed mass
Rigid body 1	0.20	0.20	0.20
Rigid body 2	2.5	2.5	2.5
Flex. 1	47.4	46.4	46.5
Flex. 2	114.1	110.0	110.5
Flex. 3	205.6	193.1	196.1
Flex. 4	323.7	294.8	305.6

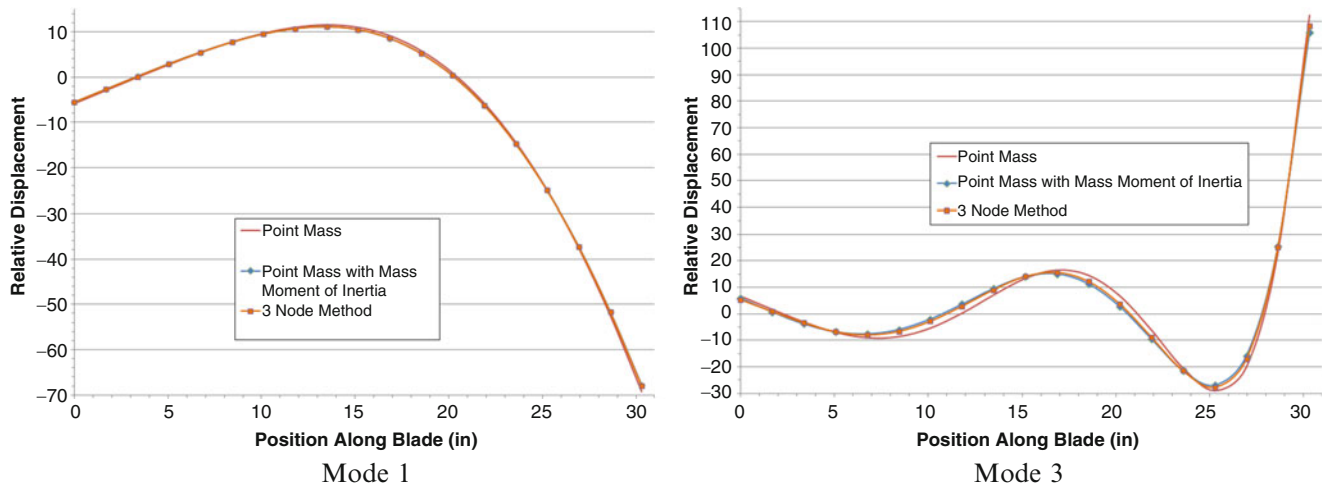
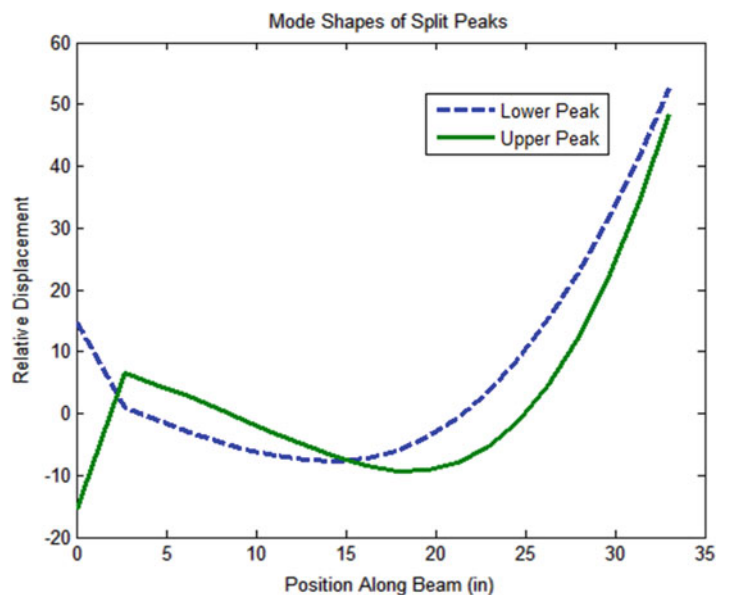


Fig. CN-1 Overlay of mode shapes from different mass modeling methods

Table CN-3 FEM frequencies of original mode one and split peaks

Peak	Frequency (Hz)
Lower split peak	40.1
Original 1st mode	46.8
Upper split peak	59.0

Fig. CN-2 Mode shapes of split peaks

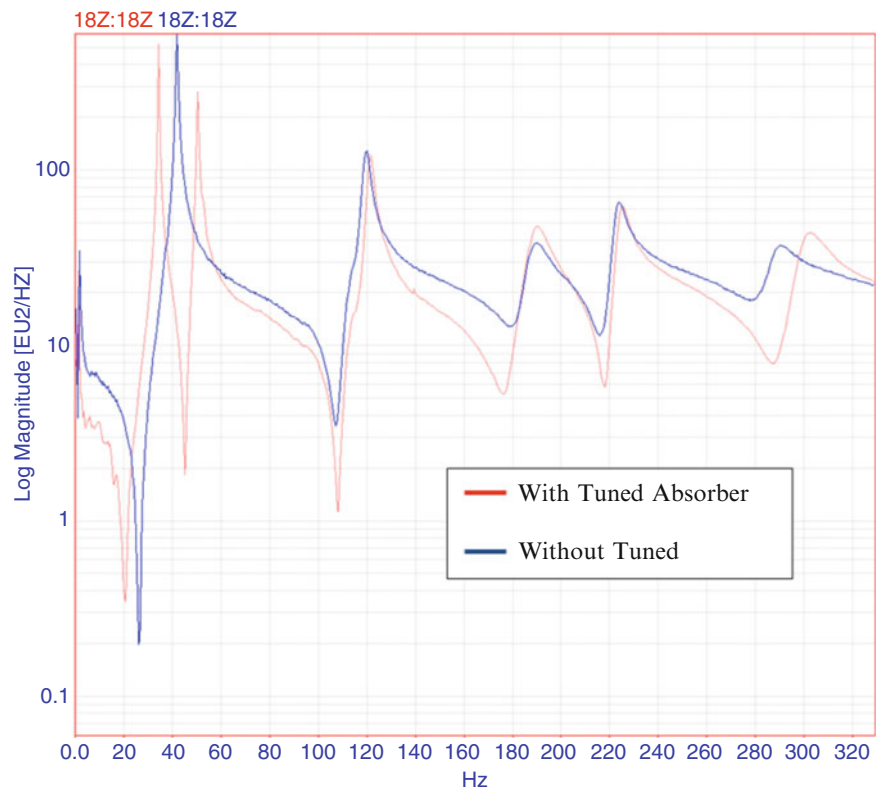


on the beam finite element model by adding another beam element and node to the root. Table CN-3 shows the original and split peak frequencies.

Figure CN-2 shows the mode shapes corresponding to the split peaks after the addition of the tuned absorber.

The mode shapes of the split peak are one mode with the blade and tuned absorber in phase and one when they are out of phase. A roving impact hammer modal test was conducted on the blade to measure the flapwise modes. The blade was tested with and without the aluminum block attached. Impacts were made at 20 locations. The reference accelerometer was located close to the tip and leading edge. The FRFs were curve fit in MEScope. The free-free condition was simulated by hanging the blade from the ceiling using bungee cords. The bungee cords were attached to the root. The analytical model predicted the first three natural frequencies to within 15 % of the experimental frequencies. The mode shapes were compared visually; there was fairly good correlation. With more time, the parameters of the model could be tuned to enhance correlation.

A modal test was conducted with and without the tuned absorber attached. The tuned absorber was optimized by slightly adjusting its frequency. This is done by threading the mass up and down until a “good” peak split is achieved. Figure CN-3 shows an overlay of the drive point FRF with and without the tuned absorber.

**Fig. CN-3** Effect of tuned absorber on drive point FRF**Table CN-4** Frequencies of original first mode and split peaks

Peak	Frequency (Hz)
Lower split peak	34.8
Original 1st mode	41.8
Upper split peak	51.2

After adding the tuned absorber, the first flexible mode is split into two peaks, resulting in an anti-resonance at the original first mode frequency. The tuned absorber also shifts the higher order modes up in frequency as expected. Table CN-4 lists the original first mode frequency and the two split peak frequencies.

These results show a specific mode at a specific frequency can be attenuated using a tuned absorber.

## A.2 Appendix LD

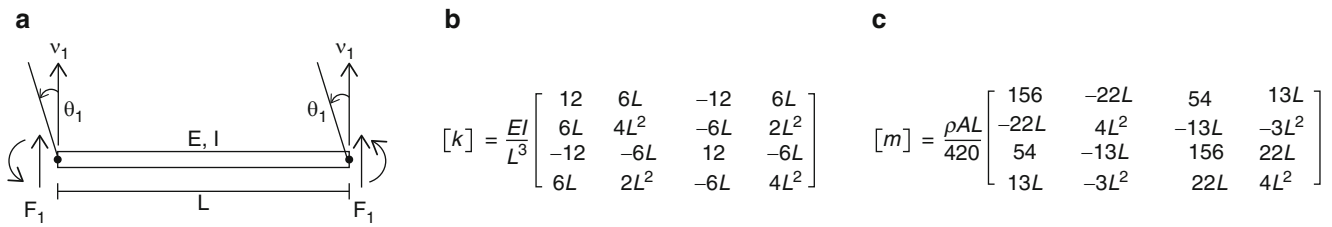
### A.2.1 Vibrations Project Spring 2012

A finite element model (FEM) was developed using MATLAB to predict the natural frequencies and mode shapes of a wind turbine blade. The FEM was created using a two noded planar beam elements. Each node on an element has a translational and a rotational degree of freedom as seen in Fig. LD-4a. The element is prescribed an elastic modulus ( $E$ ), area moment of inertia ( $I$ ), cross-sectional Area ( $A$ ), length ( $L$ ), and density ( $\rho$ ). These properties are then arranged in an element stiffness matrix and an element mass matrix identified as shown in Fig. LD-4b, c respectively.

To assemble the model, a global mass matrix and a global stiffness matrix must be calculated. This is done by merging the coincident nodes together which adds the elements of two different mass or stiffness matrices for corresponding degrees of freedom. An example assembly of a global stiffness matrix can be seen in Fig. LD-5.

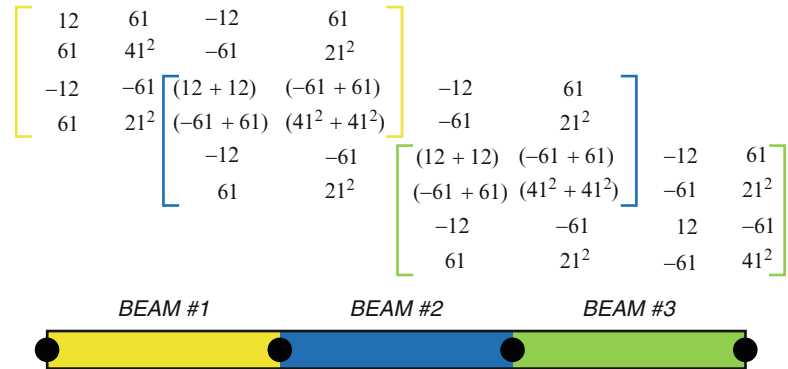
The wind turbine blade was discretized into eight elements for the finite element model. The elements were not of consistent length due to difficulty in defining unique cross sections (Fig. LD-6).

Two boundary conditions, free-free and mass perturbed, were studied. To replicate a free-free boundary condition in the FEM, no nodal rotations or translations were constrained. An aluminum block was added to the blade root while keeping nodal rotations and displacements unconstrained in order to simulate a mass perturbed boundary condition. The resulting

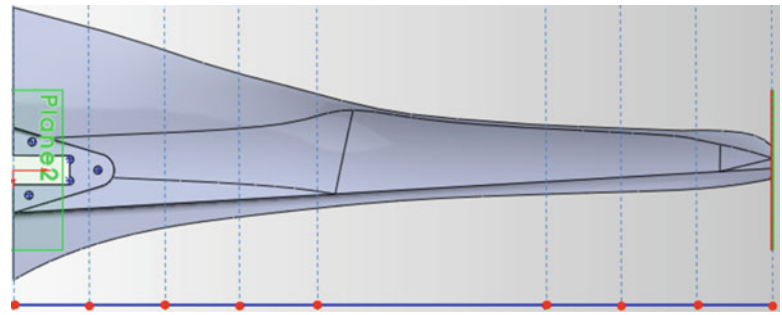


**Fig. LD-4** Schematic of (a) 1-D beam element with (b) stiffness and (c) mass matrices

**Fig. LD-5** Merging stiffness matrices for three beam elements



**Fig. LD-6** Discretization of wind turbine blade into eight elements



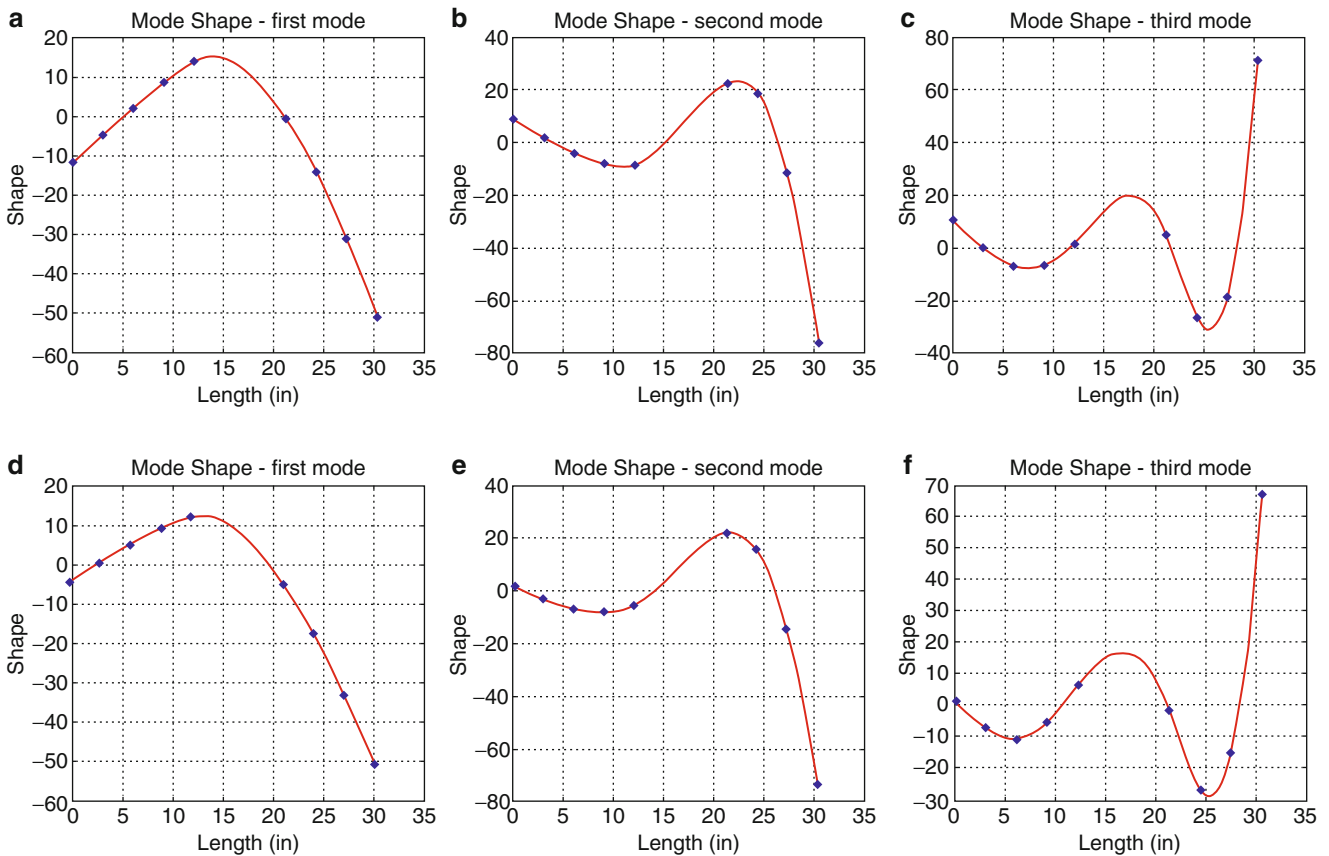
**Table LD-5** Natural frequencies for free-free and mass perturbed boundary conditions

Mode	Free-free BC Frequency (Hz)	Mass perturbed BC Frequency (Hz)	Percent difference (%)
1	37.9	32.9	13.2
2	114	107	6.14
3	222	201	9.46

natural frequencies for each model are listed in Table LD-5. Adding the aluminum block to the structure’s base decreased the natural frequencies of the system. This result was expected since the natural frequency is inversely proportional to the square root of the system’s mass; therefore, adding mass decreases the system’s frequencies.

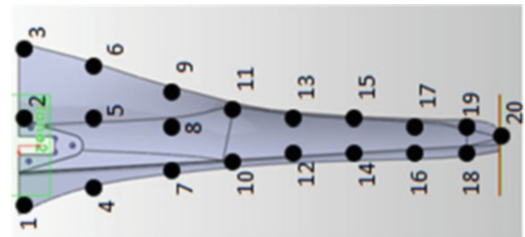
The mode shapes were also extracted from the finite element analysis. The first three mode shapes for the free-free boundary condition are presented in Fig. LD-7a–c. Likewise, the first three mode shapes for the mass perturbed boundary condition are presented in Fig. LD-7. The corresponding mode shapes for each boundary condition follow the same contour but the values differ slightly. The mode shapes for the free-free boundary condition have a maximum root displacement close to an amplitude of ten units relative to the undeformed position whereas the maximum root amplitude for the mass perturbed boundary condition is much less. The added mass at the blade root causes less displacement at the base and the larger the mass that is added to the base, the less motion the blade sees at the root. Adding root mass brings the system closer to a cantilever boundary condition.

Experimental modal impact testing was performed to determine the natural frequencies and the mode shapes of a wind turbine blade. The blade was suspended from the ceiling using bungee cords and was impacted at 20 different locations. The response was measured with an accelerometer mounted at location 18 indicated on Fig. LD-8. Each point was impacted five times and the results were averaged to ensure good coherence and repeatability of measurements.



**Fig. LD-7** Free-free BC mode shapes for the (a) first, (b) second, and (c) third natural frequencies and mass perturbed BC mode shapes for the (d) first, (e) second, and (f) third natural frequencies

**Fig. LD-8** Blade geometry and impact locations



**Table LD-6** Experimental and FEM natural frequencies

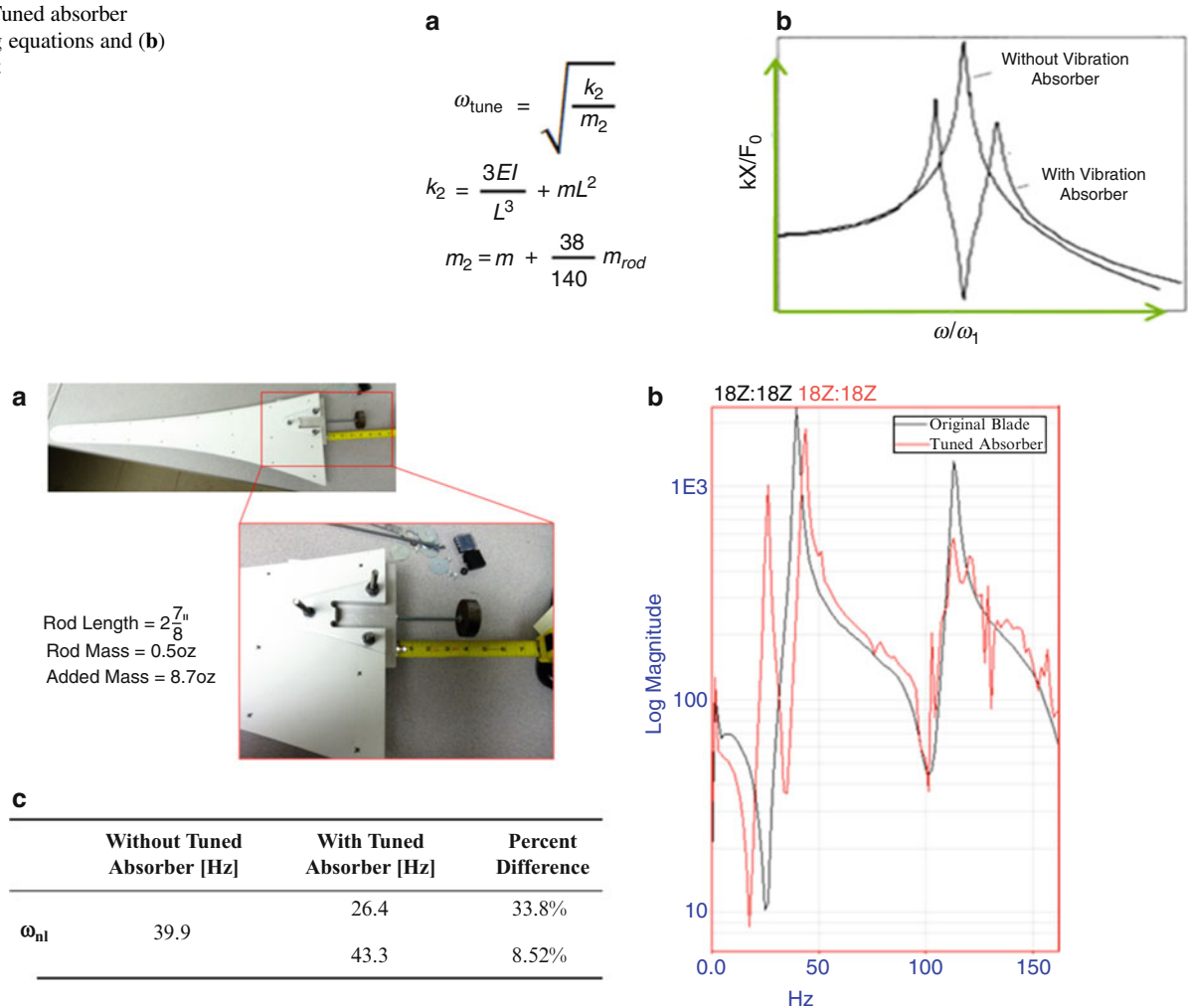
	Experimental (Hz)	FEM model (Hz)	Percent difference (%)
$\omega_{n1}$	43.2	37.9	12.4
$\omega_{n2}$	128	114	10.8
$\omega_{n3}$	194	222	14.4

The natural frequencies of the experiment are compared to the FEM in Table LD-6. The results differ within 15 % and there are several factors that could contribute to the error. The model boundary conditions were free-free whereas the test configuration simulated a free-free condition using bungee. Also, due to the complex nature of a composite turbine blade, the material properties and structure geometry were approximated in the model by beam elements with lumped masses. In the FEM, the properties were consistent throughout the entire beam element however, in reality, the geometry and material properties change significantly within the discretized sections. More elements should have been used to accurately model the complex structure.

A vibration absorber was designed to detune the first natural frequency of the system. A tuned absorber was generated by adding a mass-spring system to the test structure. The mass-spring system was modeled as a rod with a tip mass that is cantilevered from the root of the turbine blade. To detune the first mode of the system, the vibration absorber was designed



**Fig. LD-9** Tuned absorber (a) governing equations and (b) desired result



**Fig. LD-10** Tuned absorber (a) implementation, (b) graphical results, and (c) tabular results

to have a natural frequency equal to the first frequency of the blade. The tuned absorber was modeled using the equations presented in Fig. LD-9a. In these equations, the stiffness of the tuned absorber ( $k_2$ ) is determined by the stiffness of the rod added to the rotational inertia of the point mass. The mass ( $m_2$ ) is a combination of the tip mass and a lumped approximation of the rod mass. The cantilever rod length was chosen based on available hardware. Using these equations and setting the frequency of the vibration absorber ( $\omega_{\text{tune}}$ ) equal to the first natural frequency of the blade, the necessary tip mass was calculated. The desired result of the tuned absorber is a frequency split around the first natural frequency as illustrated in Fig. LD-9b.

The tuned absorber was implemented in the experiment by adding a cantilever rod with a tip mass to the root of the blade as shown in Fig. LD-10a. As expected, the addition of a tuned absorber split the first natural frequency as shown in Figs. LD-10 and LD-4b. The frequency split is quantitatively expressed in Figs. LD-10LD-4c.

## A.3 Appendix JH

### A.3.1 Some Considerations of Boundary Conditions in Dynamic Testing

The work presented here was a direct extension of a project done in Spring 2011 for UMass Lowell's Vibrations course. The project description included testing and modeling a simple aluminum beam with various boundary conditions to study the approximations that are often made to simulate a fixed-free boundary condition. After agreeable correlation results were



**Fig. JH-11** Test setup of entire blade as well as only tip section, both in free-free configurations

**Table JH-7** Comparison of model and test results for (a) entire blade and (b) tip section of blade

		Model – Full					Model – Section				
		1	2	3			1	2	3		
MAC		7.84 Hz	18.50 Hz	34.52 Hz	MAC		26.15 Hz	68.41 Hz	134.90 Hz		
Test – Full	1	7.76 Hz	99.85	53.12	17.09	Test – Section	1	26.85 Hz	99.70	25.64	39.15
	2	21.26 Hz	44.28	98.28	43.72		2	68.40 Hz	28.57	99.71	25.32
	3	31.34 Hz	20.59	57.42	98.85		3	123.37 Hz	39.74	36.4	98.82

achieved between experimental modal tests and planar beam models of the aluminum beam in several configurations, the same concepts and techniques were extended to characterize a more complex, realistic test subject – a 9 m wind turbine blade (For extensive details on this project, see [5].)

The subject for this study was an experimental 9 m wind turbine blade, the CX-100, as shown in Fig. JH-11. As seen, the blade was tested using impact excitation in a free-free configuration. Then the blade was cut into sections, and a 3 m tip section was also tested in a free-free configuration. This provided for comparisons to be made between test and model for the entire blade as well as the tip section where the majority of motion occurs, allowing for a more accurate assessment of a model.

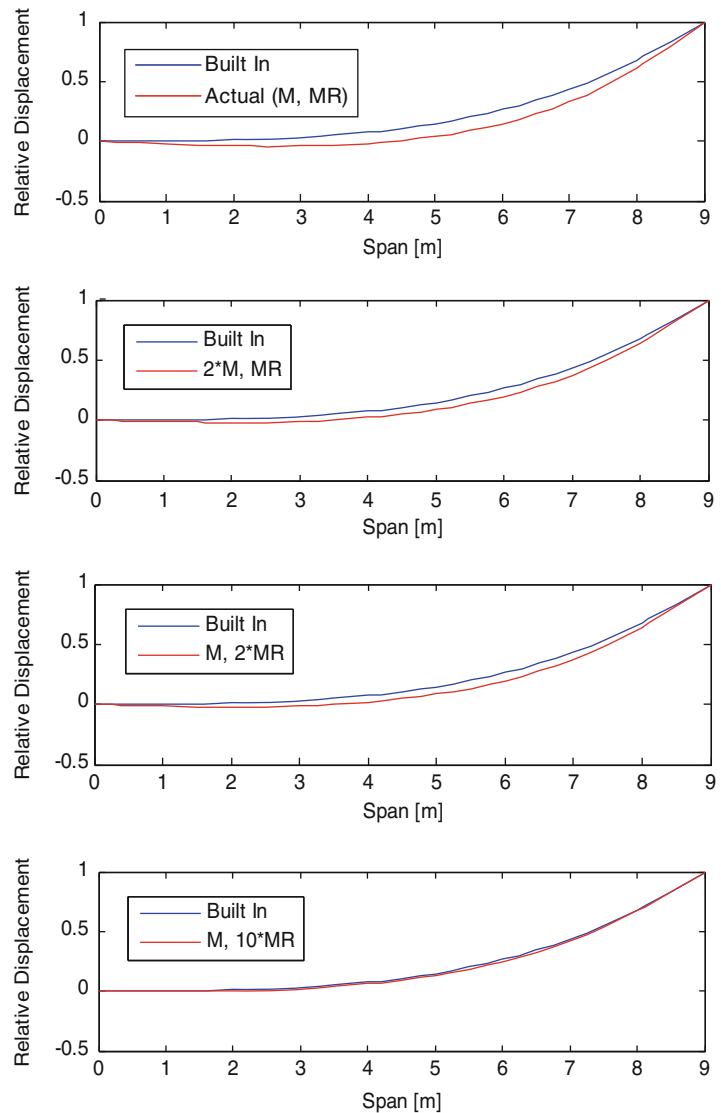
A simple planar beam model of the blade was created using MATLAB [6] with two DOF per node – one translation and one rotation. The material properties chosen for the beams were within the reasonable range of values for wind turbine blade properties, and the values were chosen such that the weights of the full and sectioned blade matched between model and physical measurements. A Modal Assurance Criterion (MAC) was performed to compare the model and test results for both the full and partial blade tests; the results of which can be seen in Table JH-7. As seen, the simplistic model provides an accurate representation of the blade's first three natural frequencies and mode shapes, excluding rigid body modes because those could not be experimentally measured with ease. The frequencies and shapes compare well for both the entire blade and the tip section of the blade, providing great support for the accuracy of the simplistic beam model.

With confidence in the model, a study was performed to observe the effect of adding a lumped mass at the root of the blade. Incremental masses were connected to the translational degree of freedom at the root for most cases. For the most substantial mass considered, 1,000 lbs, an approximate mass inertia was also added to the rotational degree of freedom at the root. For comparison, a built-in condition was obtained by attaching extremely stiff springs to the root of the blade. The analytical results for the first three flapwise bending modes are displayed in Table JH-8. The results exemplify the extreme necessity for rotational inertia to be included. When only a translational mass is attached to the root, the natural frequencies do not vary significantly from the free-free frequencies. When translation and rotation components are simultaneously added to the root, a major (expected) change in frequencies is observed. With both the translation and rotational mass, the frequency results are noticeably closer to the built-in case than any other approximation. This study demonstrates the need for not only high translational mass in a fixture, but also high mass moment of inertia of the fixture in the testing configuration.

An additional study was generated where the blade had a boundary condition more similar to a realistic test setup. As detailed in Ref. [5], the approximate mass and rotational mass effects of a real fixture were entered into this model. Although the fixture was very massive compared to the blade, Fig. JH-12a shows that there was still a difference between the curvature of the first mode shape of the blade with the assumed built-in condition and the realistic approximation. To further study the

**Table JH-8** Frequency results from modeling blade with various boundary conditions

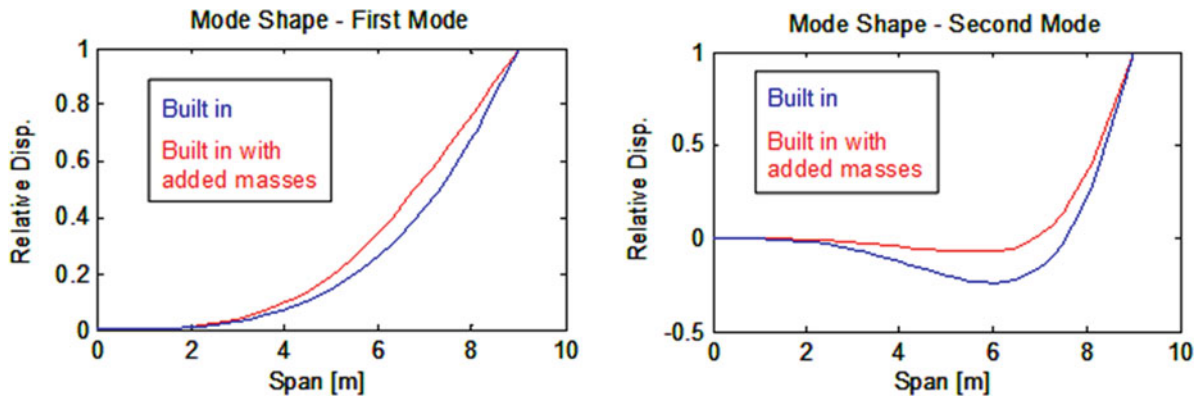
	Free-free (Hz)	250 lb mass (translation) (Hz)	500 lb mass (translation) (Hz)	1,000 lb mass (translation) (Hz)	1,000 lb mass with mass inertia (Hz)	Built-in (assumed)
Mode 1	7.84	7.45	7.35	7.28	4.60	4.36 Hz
Mode 2	18.50	17.67	17.48	17.36	12.05	11.76 Hz
Mode 3	34.52	33.21	32.95	32.77	24.63	24.35 Hz

**Fig. JH-12** Comparison of analytical first mode shape when attached to fixture with varying mass properties

necessity for appropriate mass characteristics of a fixture, the mass and rotational mass values of the fixture were varied as shown in the figure. There is a slight difference of curvature in the first mode of the realistic approximation and assumed built in configuration for all four approximations. This shows the difficulty to achieve a truly built in condition and also exemplifies the noticeable difference in curvature of mode shape that can be attributed to fixture approximations.

In the certification process for turbine blades, fatigue tests are performed with the blade mounted to a very large and massive fixture, such as the one shown in the test configuration in Fig. JH-13 that was made by the National Renewable Energy Laboratory. For conduct of the fatigue test, two saddles of substantial mass are utilized. Experimental modal tests were performed on the blade in the fixture with and without the added masses. The simple beam model was updated to include these masses at the appropriate locations, with results shown in Table JH-9. As supported by both modeling and test results, the frequencies of the first two modes shifted down significantly due to the addition of the two masses. Note that only the first two flapwise bending modes are studied because these are the modes of interest for fatigue studies. The simplistic planar beam model developed shows good correlation to the measured results.

**Fig. JH-13** CX-100 blade in NREL fixture with saddles for fatigue testing



**Fig. JH-14** First two flexible flapwise mode shapes of turbine blade with and without added masses determined from simplistic planar beam model

Not only will the addition of masses have an effect on natural frequencies of a test subject, but the mode shapes can have a noticeable change. The curvature of mode shapes is very important when studying stress and strain. The first two mode shapes of the simplistic planar model with and without added masses, as described previously, are shown in Fig. JH-14 where a substantial difference in curvature of the turbine blade is seen. Note that the tip displacements of the mode shapes were scaled to one for comparison purposes. Consideration must be given to this curvature difference when conducting the fatigue tests

**Table JH-9** Comparison of model and test results for clamped turbine blade with and without added masses

	Model Built-in (Hz)	Test On NREL fixture (Hz)	Model With added masses (Hz)	Test With saddles attached (Hz)
Mode 1	4.36	4.35	1.84	1.82
Mode 2	11.76	11.51	9.83	9.79

This work clearly shows that the attachment condition of a test subject can have a significant effect on the frequencies and, most importantly, the mode shapes identified. Care must be exercised to assure that the desired boundary condition is achieved otherwise the resulting frequencies and mode shapes may not adequately represent the intended dynamic interface. Consideration needs to be given to the effect of this curvature change when performing fatigue tests to assure this does not invalidate the intent of the test. Also, it is possible to accurately approximate a complex structure such as a wind turbine blade using a simple two dimensional beam model.

## References

1. Avitabile P, O'Callahan J (2007) Teaching structural dynamic modeling techniques in the UMASS Lowell modal analysis program. In: Proceedings of the twenty-fifth international modal analysis conference, Orlando, Feb 2007
2. Avitabile P (2007) An integrated undergraduate dynamic systems teaching approach using Response Under Basic Excitation (RUBE). In: Proceedings of the twenty-fifth international modal analysis conference, Orlando, Feb 2007
3. MEscope, Modal analysis software package. Vibrant Technology, Santa Cruz
4. Harvie J, Avitabile P (2012) Comparison of some wind turbine blade tests in various configurations. In: Proceedings of the 30th international modal analysis conference. Jacksonville, Feb 2012
5. Harvie J, Avitabile P (2012) Some considerations of boundary conditions in dynamic testing. In: Proceedings of the 30th international modal analysis conference. Jacksonville, Feb 2012
6. MATLAB – Matrix Analysis Software. The MathWorks, Inc., Natick

# Chapter 27

## Around the World in 80 Courses

David Ewins

**Abstract** This paper summarises the genesis and evolution over 30 years of a series of short courses on Analytical and Experimental Structural Dynamics. In total, more than 120 of these courses have been presented in more than 20 countries. In the early days, the courses were specifically focussed on teaching the basic techniques and applications of the then-new subject of Modal Testing (or Experimental Modal Analysis). Later came the need for more advanced and complex capabilities in some of the more demanding tasks, and especially in the more challenging applications to which the modal test results were to be subjected. The major changes in information technology that have taken place in this 30-year period have resulted in some significant changes in the style and content of the courses. Most recently, the ‘courses’ have turned more towards developing a full integration of the experimental, numerical and theoretical skills that combine to make the complete Structural Dynamicist – that rare individual who knows, above all, that solving problems in structural dynamics hinges on being able to ask the right questions. The answers can usually be found in text books and scientific papers. Not so the questions. Learning how to formulate these requires practice and experience and this is best passed on in courses.

**Keywords** Courses • Structural dynamics • Philosophy • Modal analysis • Education

### 27.1 Genesis

The ‘birth’ of Experimental Modal Analysis coincided with another phenomenon which has become very familiar to most engineers: that of the Short Course. Not surprisingly, then, short courses (1–5 days) on Modal Analysis or Modal Testing have become very popular and an effective way of bridging between the classical Vibrations courses taught to most undergraduates and the real world of actual engineering structures: namely, the need to measure how they vibrate and to predict and control such behaviour.

The particular suite of courses that are the subject of this paper grew out of research some 50 years ago which addressed the complexities of vibration of real engineering structures which, as is mostly the case, were actually an assembly of several components, often of disparate form and composition, that constituted machines vehicles or other structures. Specifically, interest was focussed on two industrial applications where vibration represented (and still does) a major concern as regards reliability and integrity of critical engineering products. One was machinery installed on board a ship (Fig. 27.1) where the transmission of vibration and sound throughout the vessel and thence radiated into the surrounding sea was a major concern and the other was concerned with the integrity of a store mounted on the side of helicopter (Fig. 27.2). In both these applications, some form of mathematical model was required in order to describe the various structural dynamic features in such a way as to be able to control them and thus to contain them within acceptable limits. In the period of those projects (the 1960–1970s), mathematical models were hard to come by, and very limited in capacity when created. As a result, it was more commonplace to rely on measured data to describe the required vibration properties, even though this is inaccurate and incomplete. At least it represented how the actual structure was really behaving. In effect, the methodology adopted in those

---

D. Ewins (✉)  
Bristol University and Imperial College London, SW7 2AZ, London, UK  
e-mail: [d.ewins@imperial.ac.uk](mailto:d.ewins@imperial.ac.uk)



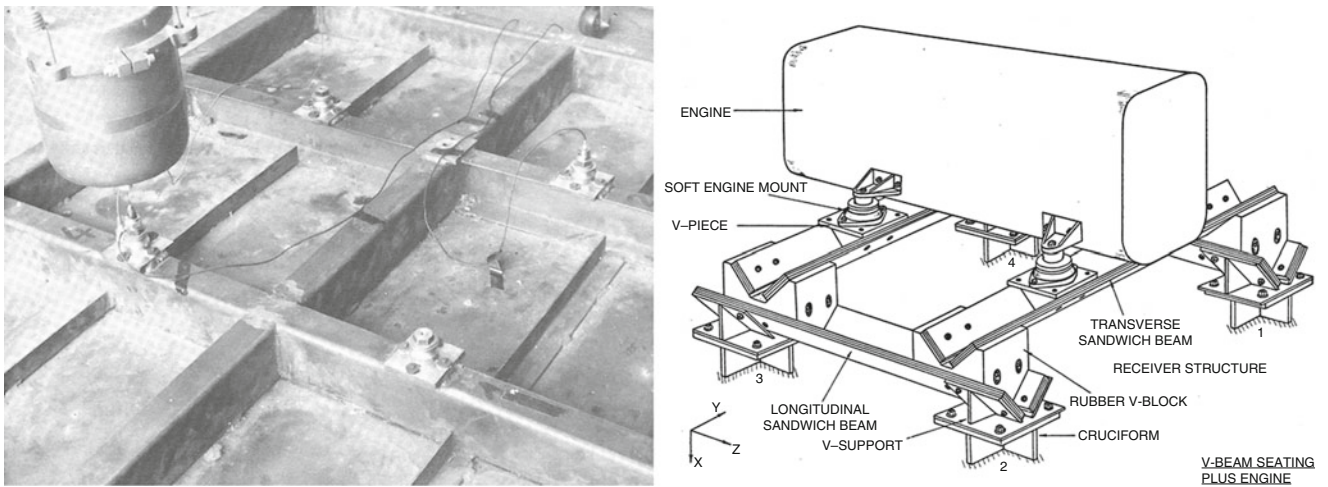


Fig. 27.1 Early attempts to analyse the dynamics of a highly complex structural assembly of shipboard equipment

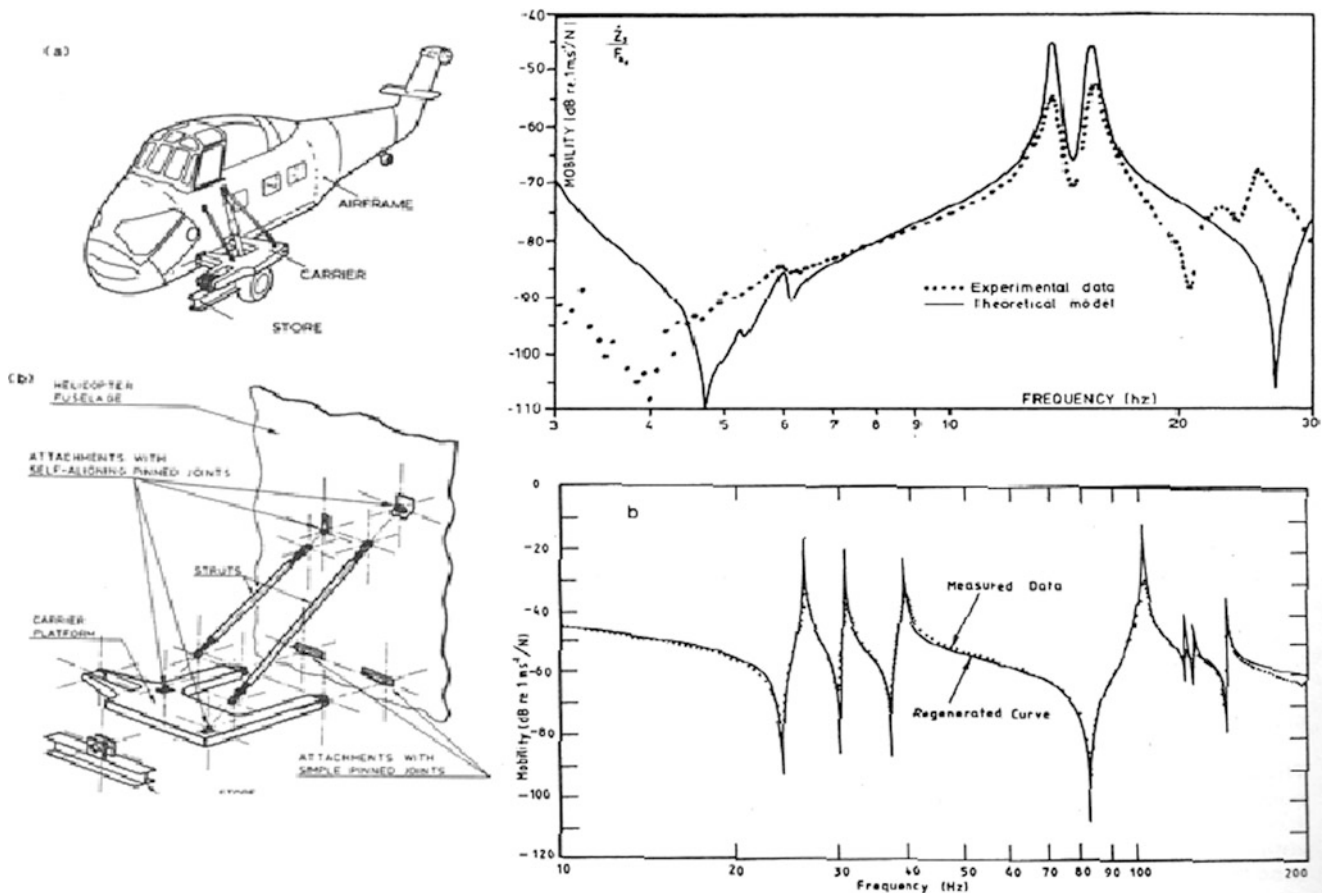


Fig. 27.2 Combined theoretical-experimental generated mode of helicopter dynamic response analysis

days was to construct simple mathematical models from theory wherever possible and to formulate mathematical models from measured data where the necessary theoretical descriptions were unavailable. This approach to the engineering needs, in effect, gave birth to modal testing, or experimental modal analysis that is so widely practiced today, although it was often referred to as the ‘impedance method’ approach rather than experimental modal analysis that quickly became the norm.

## 27.2 First-Generation Courses on Modal Testing

There was a need for courses that could combine the classical theoretical treatment of vibration of systems and structures, with the corresponding measurement techniques that were usually undertaken as they represented the only way of gaining any useful insight into the critical characteristics of many engineering structures. The first such offering by the author was presented in Shanghai, in 1982, unknowingly foretelling the international (“around the world”) nature of the many subsequent courses that have now been visited on some 20 countries spanning six of the seven continents. The first ‘deliberate’ Modal Testing course was given in the USA in 1983, followed by others the following year, also in the USA. The first course in the UK was not until 1985.

The history of the individual courses is not of interest here. Rather, the structure and format is relevant as it evolved through experience is perhaps worth mention because it became the foundation for teaching the subject today – three decades on. The main ingredients were: (i) Theory of SDOF and MDOF systems, with a strong emphasis on **both** the free vibration (modal) behaviour and the forced vibration (FRF) characteristics; (ii) Measurement and testing techniques, as applied to real engineering structures, and (iii) Analysis techniques, primarily for extracting useful information about the makeup of the structures based on measurements of its dynamic behaviour. These three key fundamental tools were supplemented by a synthesis process that sought to combine the theoretical and experimental descriptions of a structure’s dynamics into a single model, for subsequent use and, lastly, by a number of applications to which the assembled model can be put to the benefit of the designer or user of the structure(s) itself.

All this information was collected for presentation first as a book [1], whose chapters simply follow this list of five main themes, and as a typically 3-day course in which the subject matter is delivered, slice by slice (not chapter by chapter) in such a way that the interdependence of the different parts of the process of modelling, measurement and interpretation is emphasised. Typically, the sequence would be:

**Theory-1; Measurements-1; Theory-2; Measurements-2; Analysis-1; Theory-3; Analysis-2; Synthesis (Modelling); Applications; ..Advanced methods (as dictated by the persistent discrepancies between theory and practice) . . .**

. . . supplemented with demonstrations and exercises to illustrate the main points through practical examples. Suddenly, three days have passed!

## 27.3 Underlying Philosophy of Models for Structural Dynamics

As mentioned above, the destination of most of these studies was almost always the construction of some form of mathematical model that would allow the user to extend their knowledge of how the structure would vibrate under different circumstances – both under different loading (excitation) conditions and/or when selected physical changes had been made to the original structure by adding mass, or stiffness or damping, for example. It is appropriate now to describe what is meant by ‘mathematical model’, and in particular from the perspective of the teacher of the subject who wants to instil in the pupil the necessary understanding and philosophy of the concepts involved essential to understand the physics as well as the maths. In general, a mathematical model is defined by a set of equations which describe the dynamic behaviour of the subject structure. Not surprisingly, there is more than one type of model and three different versions are in regular use in structural dynamics: (i) Spatial, (ii) Response and (iii) Modal. A **spatial model** is one which describes the structure’s relevant properties in terms of their distribution in space: i.e. the geographic distribution of mass, stiffness and damping and the interconnections of these elements at and between junctions. It is what the structure ‘looks like’ and we can influence this directly by changing individual masses thicknesses, etc. etc. A **response model** is one which describes the structure’s dynamic properties in terms of set of response characteristics – most commonly, the FRF properties, but any other formal response characteristic will suffice. The response model describes how the structure ‘behaves’ in a response sense, and is a direct measure of the performance of the structure from a vibration perspective. The response is what we want to be able to predict and to control but we cannot adjust this quantity directly: we can only change the spatial model elements. So, the relationship between the spatial and the response models is what most structural dynamics analysis is all about. The third type of model is the **modal model**, a ‘virtual’ model which is an intermediate form sitting between the spatial and the response models and providing a very convenient means of communicating between these two ‘real’ models. These three models are illustrated in Fig. 27.3. The usual ‘Analysis’ activity in Structural Dynamics seeks to predict the response behaviour of the subject structure by defining its spatial model and solving the equations of motion to a given input excitation loading. The usual ‘Test’ activity consists of measuring response characteristics of a test structure and seeking to infer from these measurements the underlying spatial model properties with a view to changing these in order to bring about an improvement in the response behaviour. The modal model provides a very efficient way of communicating between these two primary models.

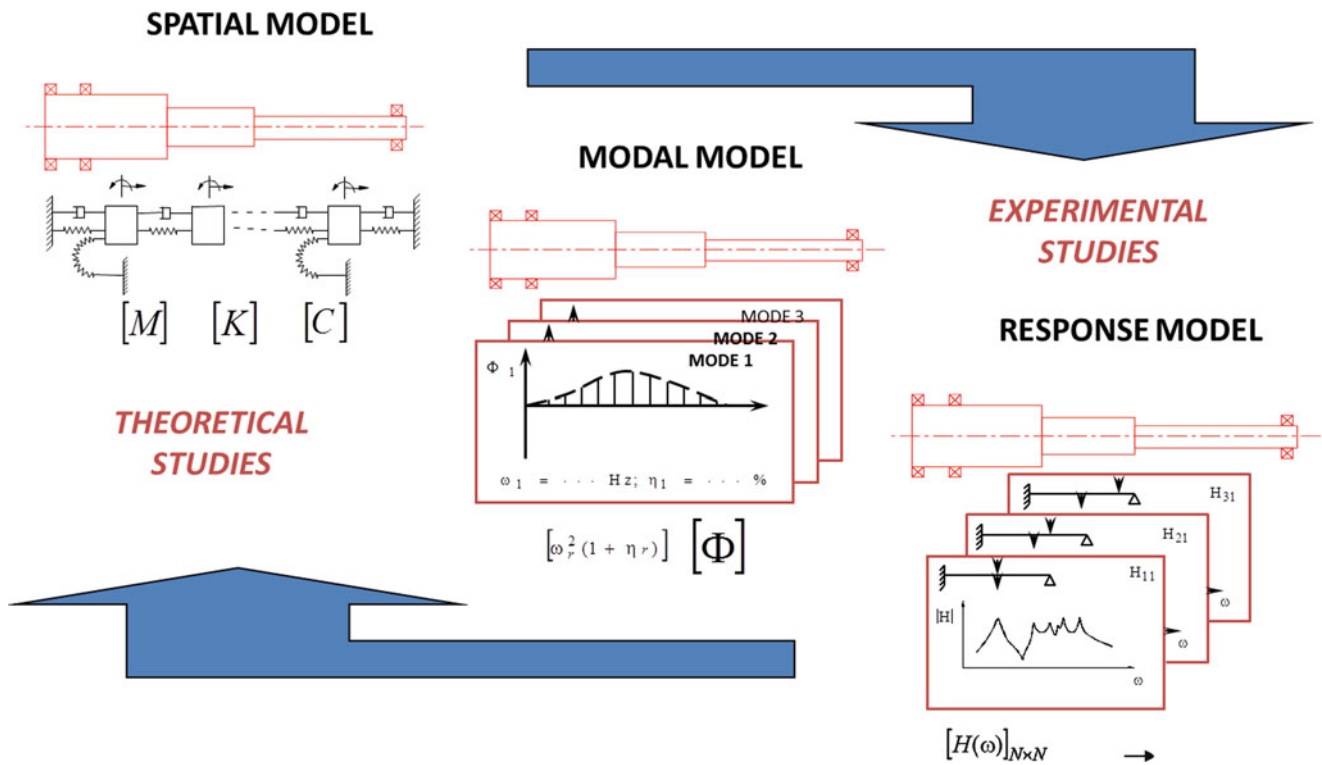


Fig. 27.3 Types of model used for structural dynamic studies

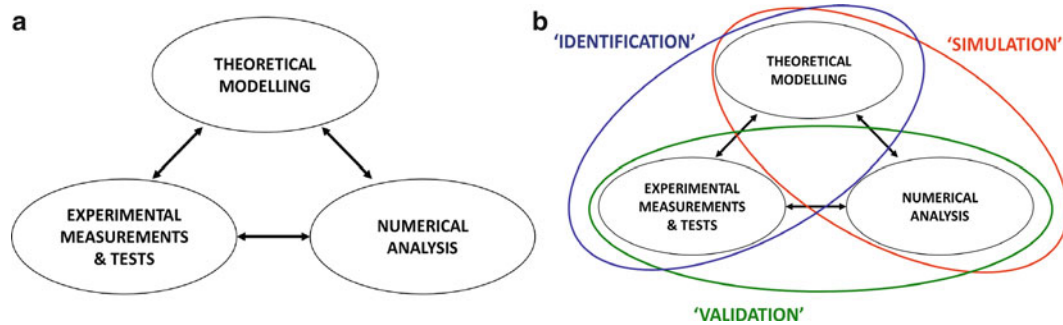
A full grasp of this underlying philosophy is essential to the student of structural dynamics who seeks to design and maintain machines, vehicles and structures which are subjected to dynamic loads.

## 27.4 Future Needs and Trends for Next-Generation Courses in Structural Dynamics

The preceding paragraphs describe the aims and the form of a suite of courses that have been delivered for more than 20 years. What next? The underlying subject matter that needs to be taught and (more importantly) learned has not changed much. There are some more advanced topics but essentially, the basics are still the same. Perhaps what is changing is the context in which the material needs to be taught (and learned). In fact, what started out as a course for Modal Testing (or EMA) has now evolved into one on the broader, and complete, subject of Structural Dynamics

The conventional wisdom is that what is needed is an improved modelling capability. We need better (more reliable, cheaper) models with which to design and to maintain through monitoring and diagnostics engineering products with greater reliability and resilience to the dynamic loads that are imposed on all machines and vehicles. At first sight, this approach suggests that the future is in ‘Analysis’ with less emphasis on ‘Test’. However, it is not as simple as that! There are three primary skills (tools) which are distinct but mutually interdependent: (i) Theoretical Modelling, (ii) Numerical Analysis and (iii) Experimental Measurement. Modern structural dynamics requires an integration of all three. Figure 27.4 shows the trio of basic skills. Alongside, Fig. 27.4 shows how the three basic skills are used in combinations to provide the technologies of (a) Simulation, (b) Identification and (c) Validation which together provide the capabilities required to address and resolve most structural dynamics problems encountered today. This construction is more complex than the simpler ‘Test’ versus ‘Analysis’ scenarios that are often cited, and is thought to be more realistic of the real situation. It is important here to note the central role played by experimental measurement activities.

In the identification process, *experiments* are the basis for observing, understanding and thereby modelling the increasingly complex physics that we need to describe in our models. At the other end of the design process, *tests* are the means of checking or ‘validating’ the predictions that are the result of simulations (modelling plus computation). Even later in the life cycle of these products, *measurements* are the basis for monitoring and diagnostics that will keep the products in effective service throughout their life. A full set of experimental procedures is shown in Fig. 27.5: clearly experimental methods will continue to play an essential role in structural dynamics and so need to be embedded in modern courses on the subject.



**Fig. 27.4** (a) The three basic skills required for structural dynamics studies and (b) the three main procedures that are carried out

### Experimental Procedures

- **Measurements:** quantification of physical parameters
- **Experiments:** use of measurements to observe (and then to understand and explain) physical phenomena
- **Tests:** use of measurements to prove or 'test' a theory (i.e. validation)
- **Trials:** use of measurements to demonstrate the overall performance of a machine or structure (e.g. Certification)
- **Monitoring/Diagnostics:** repeated measurement of selected parameters to detect changes in structural condition or differences between nominally identical structures

**Fig. 27.5** The different types of experimental measurement activities involved in structural dynamics

#### 27.4.1 Subtleties and the Questions

The future need is for *valid* models. 'Valid' means 'good enough' – not perfect, not too good, but good enough. This requires a definition of what is good enough followed by methods to test if a model is good enough and, if not, then to improve/update it so that it is good enough – i.e. how to **validate** it.

At this stage, it is important to consider more thoroughly the different types and sources of deficiency that determine whether a model is valid or not. There are essentially two types of deficiency to be considered. The first arises from the use of inaccurate data in the modelling procedure: incorrect values of the various parameters that comprise the model, perhaps resulting from errors in measured data or assumed data. The second, and more serious deficiency, is the omission of parameters that are relevant but which may be assumed to be unimportant or, simply, ignored. Such omissions can be of physical elements themselves, or the degree of complexity with which individual elements are described. A classic example of this latter situation is the oversimplification of a non-linear characteristic by a simple linear representation. A model which is deficient in this way, by incompleteness of the parameter set, is more seriously limited in its usefulness and cannot generally be validated. Both of these limitations – often referred to as Variability and Uncertainty – must be addressed and corrected. These are the subject of validation and verification, respectively.

These issues may seem to be subtleties, but they can differentiate between models which are fit for purpose – good enough – for the increasingly stringent demands placed on structural dynamics analysis today, and those which are not good enough. The means to answer these questions are to be found in the theoretical and experimental tools mentioned above. The ability to ask the right questions comes from experience and effective teaching of the subject. Verified? Validated? Uncertainty? Variability? Linear or Nonlinear?

### Reference

1. Ewins DJ (2000) Modal testing: theory, practice and application. Research Studies Press, Wiley, UK

# Chapter 28

## Review of a Pilot Internet System Dynamics Course

C.C. Claeys, S. Leuridan, D. Brown, and J. Connor

**Abstract** The University of Cincinnati has offered a Ph.D. level System Dynamics Course since the early 1980s. Originally, the course was concerned with experimental modeling aspects (impedance and modal modeling) and was complemented by a Fourier Analysis (Digital Signal Processing) and a Finite Element course sequence. In the 1990s, this course morphed from a lecture based course to a project based self study course with reduced formal lectures and more mentoring. The students in the course were broken up into groups of 3–5 students and they were required to use MATLAB to program the signal processing, parameter estimation and modeling algorithms. In 2006, this course was offered for the first time as an Internet Course to students at other universities and institutions. The main reason is that at any single site or university there are not enough students to justify offering such a course. This paper will review the progress of this effort.

**Keywords** Structural dynamics • Teaching • Online learning • Mentoring • Collaboration

### Acronyms

CMIF	Complex Mode Indicator Function
DSS	Digital Sensor System
DOF	Degree of Freedom
EMIF	Enhanced Mode Indicator Function
ERA	Eigenvalue Realization Algorithm
FEM	Finite Element Modeling
FFT	Fast Fourier Transform Algorithm
FRF	Frequency Response Function
GUI	Graphical User Interface
IMAC	International Modal Analysis Conference
IT	Information Technology
ITD	I Time Domain
JMAC	Japanese Modal Analysis Conference

---

C. Claeys (✉)

Department Mechanical Engineering, PMA, KU Leuven, Celestijnenlaan 300 B, B-3001 Heverlee, Belgium  
e-mail: [claus.claeys@mech.kuleuven.be](mailto:claus.claeys@mech.kuleuven.be)

S. Leuridan

Department Mechanical Engineering, Biomechanics Section, KU Leuven, Celestijnenlaan 300 B, B-3001 Heverlee, Belgium  
e-mail: [steven.leuridan@mech.kuleuven.be](mailto:steven.leuridan@mech.kuleuven.be)

D. Brown

Structural Dynamics Research Laboratory, University of Cincinnati, 2600 Clifton Avenue, Cincinnati, 45221 OH, USA  
e-mail: [david.l.brown@uc.edu](mailto:david.l.brown@uc.edu)

J. Connor

SPACEX, 1 Rocket Road, Hawthorne, 90250 CA, USA  
e-mail: [Jack.Connor@spacex.com](mailto:Jack.Connor@spacex.com)



MATLAB	Matrix Laboratory
MIMO	Multiple Input and Multiple Output
MRIT	Multiple Reference Impact Testing
NVH	Noise Vibration and Harshness
PC	Personal Computer
PTD	Polyreference Time Domain
RBNB	Ring Buffer Network Bus
SDA	System Dynamic Analysis
SVD	Singular Value Decomposition
UCSDRL	University of Cincinnati Structural Dynamics Laboratory
MPA	Universal Matrix Polynomial Approach
MPA	Universal Matrix Polynomial Approach
VITALNET	Virtual Instrumentation Test and Analysis Laboratory Network

## 28.1 Background

This is the second technical paper describing the Structural Dynamics Analysis (SDA) Internet Course. The [first paper was presented at the ISMA2012](#) conference held at the University of Leuven in Belgium. The University of Cincinnati and the University of Leuven Mechanical Engineering Departments have had a close collaborator relationship since the mid-1960s. Both universities have had a strong educational and research program in the areas of Vibrations, Structural Dynamics, and Acoustics. As a result, students from the Leuven program participate in the SDA Internet course. The two primary authors of the first paper were students from Leuven and the third author was the professor at the University of Cincinnati who directed the Internet Course. The ISMA paper was primarily concerned with looking at the course from the students prospective.

It included the historical background of the course and a general overview of the course, including the course syllabus. The course is a self learning course which means that the instructor acts more as a mentor than a teacher. A great deal of Internet course material is reference material associated with the prerequisite material normally required for students at the University of Cincinnati before they can register for the course. Much of the prerequisite material is also taught at most of the Universities that participated in the pilot program but the perspective is very often different. Therefore, much of the mentoring is targeted towards developing an understanding of the different perspectives.

The SDA sequence of courses evolved from a lecture based course with homework and exams for evaluation in a project-based course where the students were required to use MATLAB to develop software for processing measurement data into an impedance and/or modal model of a structural system. The modal model could be used to predict modifications to the system being analyzed and/or to update or validate a FEM model of the system. In other words, the student had to develop their own software to model several systems from measurements or from analytical data sets generated from lumped mass models. They could use commercial software to check or validate their results.

The project-based course forces the students to look at the course from a number of different prospects. They have to interact with other students in their own project group and with students from other project groups. The self learning portion of the course puts the major responsibility of the learning process directly on the student. They are advised to seek help from other students and faculty members in this process. The programming of the algorithms is an iterative process of debugging MATLAB code which causes students to review both the algorithms and the code. All of these interactions increase understanding and creates lasting knowledge.

## 28.2 MATLAB

In the mid to late 1980s, an Interpretive Programming Language (MATLAB) was developed at the University of New Mexico by Cleve Moler (C.S. Professor and co-author of LINPACK), who wrote MATLAB (Matrix Laboratory) as means for students to avoid writing their own codes and algorithms with languages like FORTRAN, which involves many cycles of compiling and debugging, but to use MATLAB.

An engineer, Jack Little, saw MATLAB demonstrated during a lecture by Cleve Moler at Stanford University and got permission to develop a C-version of MATLAB and added the functionality of m-files (stored programs) and many new



features and libraries. This resulted in the forming of a company called Mathworks to support and market the program. MATLAB became the engineering programming language of the 1990s. In fact, in many engineering schools MATLAB has become the programming language taught to freshman students that are not majoring in computer science.

In the late 1980s and early 1990s, MATLAB and the increasing power of personal computers made it possible for groups of students to program many of the computer algorithms for signal processing and parameter estimation in the period of just a few weeks. For example, in the SDA-I course; MATLAB is used to process analytically generated and experimentally measured data into Frequency Response Functions (FRFs) and/or Unit Impulse Response Functions (UIFs).

In the SDA II course the FRF and/or UFI measurements are used as input to modal parameters estimation algorithms that can estimate the Modal Parameters (eigenvalues, eigenvectors and modal scale factors) to generate a Modal Model of the system being analyzed.

In the SDA III course an Impedance Modeling Program and a Model Modeling Program can be developed to predict modification to the systems being analyzed using the measured FRFs (Impedance Modeling) and/or the Modal Model of the system generated in the SDA II Class.

In each of the three sections of the course, student groups of 3–5 students have 5 weeks to develop a program to process the data and to generate a presentation and report of their work. The grade for the student groups are based upon an in-class presentation and the final report for the group effort.

MATLAB is an interpretive language and the students are encouraged to avoid developing GIUs, but just to group all the input variables at the beginning of the program and simply change these lines of codes. Unless they are very experienced programmer they will spend too much of their time debugging their GUIs.

As mentioned in the previous section, one of the positive aspects of developing the MATLAB codes is that it forces the student to iterate between reviewing the algorithms they are programming and debugging the MATLAB codes to get satisfactory results. This iteration process forces the students to develop a better understanding of both the experimental processes and the underlining theory. Going over this process multiple time reinforce knowledge. They are required to process both analytically generated data sets where the answers are known and experimentally generated data set where the answers are unknown. The analytical data sets are designed to help them debug their MATLAB code.

The students are given several MATLAB program that allow them to animate their mode shapes and a universal file reader for converting input measurement data in a MATLAB data file. These programs were written by students that had taken the course and made available to students currently taking the course. If they have problems, the students in the course are encouraged to seek help from other students and faculty members who have knowledge of the course material.

The current version of MATLAB has a very good display and presentation capability and many of the students are fairly experienced at using these features, since MATLAB is currently used in many other courses at the undergraduate or graduate level. Since the groups have three to five students, historically, the use of MATLAB has not presented a big hurdle since in any given group one or two of the most experienced students will do most the coding. Historically, the biggest problem in programming has been in the bookkeeping associated with keeping track of transducer orientations and its impact on the modeling programs. As a result, the data sets are checked using a UCSDRL and/or a commercial software program before the students are given the data sets.

The final presentation and final report for the course sequence integrates the reports for SDA I and SDA II into the SDA III report.

One of the disadvantages of MATLAB is that it is a very high level programming language, making it very difficult to trouble shoot someone else's code, so the students are advised to generously comment their own computer code.

### 28.3 Internet

It was clear in the mid 1990s that advancements in the consumer market place were contributing to technologies which were to have a significant impact on the structural dynamics, vibration, acoustics and control areas. The PC revolution and the Internet were two of the more significant technologies.

In this paper we will profit from one of the big advantages of the internet by using hyperlinks, which allow for the downloading of relevant available reference material. Material we don't have permission to download will be added to the list of references in the bibliography at the end of the paper. It should be noted that [DigitalRights](#) and [DigitalRightsManagement](#) has to be addressed in copying, distributing or referencing information that is the intellectual property of other parties.

In the late 1990s and the early 2000s, several papers were submitted and presentations given concerning the impact of consumer technologies both on education and research. In 1999 Los Alamos National Laboratory organized and hosted a forum to discuss the future direction in the area of Structural Dynamics. This included an effort to define a number of Grand

Challenge projects in Structural Dynamics. These Grand Challenge projects were described in a [2001IMACPaper](#) and a [copyoftheemailattachment](#) that was sent to the committee that made the selections.

In a [2002conferencepaper](#) concerning the impact of the consumer market upon NVH was presented at the IMAC conference and in the IMAC technology center a [presentation](#) was shown on the impact of the consumer technology on education and research at the University of Cincinnati. This presentation was originally given at the JMAC conference in 2001 in Japan and later at a number of other universities and industries.

## 28.4 Internet Courses

Starting in the fall of 2004, the Mechanical Engineering Department at the University of Cincinnati started experimenting with use of the Internet for teaching and mentoring courses. In 2004 the University used video conferencing software for conducting Internet meetings with various Industries. Presentations, mentoring, software training, technical meetings, etc. were conducted between the university and the industries. It was clear that there was significant promise to use these emerging technologies for education, mentoring and consulting applications.

After Dr. Brown retired and became a Professor Emeritus, he continued to teach the SDA course sequence. He came to school for the classes, which met twice a week, but he often had office hours from his home where he used video conferencing software for mentoring or just meeting with the students. WEBEX was the software which was used in these early Internet-based meetings.

This effort continued into 2006 when the University starting teaching a pilot course for a new design course. The pilot course “Concurrent Product and Manufacturing Process Development (CPPD)-(20-MECH-639)” was being introduced into the curriculum.

There were two instructors involved in teaching the initial CPPD course. It involved 14 students. The course was taught in an electronic class room at the university. The students would meet in the class room and one of instructors would be in the class room hosting the WEBEX meeting and the other instructor was located in a local industry site in the Cincinnati area. Lectures were given using PowerPoint presentations and the students had copies of the presentation and copies of the course reference material. The course met three times a week for 10 weeks, including: two WEBEX meetings per week; and one question-answer session conducted at the university. The students actively participated in the development of the pilot course.

The SDA course was also taught in 2006–2007, with a group of students in the class room at the University plus a second group of students located at local industries. In this course GoToMeeting was used for the first time. [DetailsonGoToMeetingcanbefoundattheirwebsite](#) and in a [ISMA2012paper](#) which is the predecessor to this paper.

The first SDA course with students from other universities occurred in the 2008–2009 school year. The course was still taught in a class room at the University of Cincinnati but the students from other universities were taught over the Internet.

## 28.5 SDA Course Curriculum

In the [ISMA2012paper](#), a detailed description of the course and course syllabus is given. This paper only repeats the hyperlinks to the course syllabi. This paper will concentrate more on the technical material covered in each section of the course sequence and gives a more detailed example of the students’ efforts.

## 28.6 Course Syllabi Hyperlinks

---

<a href="#">Fourier-SDAI</a>	Fourier Transform Techniques and System Dynamics Analysis I
<a href="#">SDAII</a>	System Dynamics Analysis II
<a href="#">SDAIII</a>	System Dynamics Analysis III

---

## 28.7 SDA I Course

The theme of the SDA I course is Digital Signal Processing and it is offered to Ph.D. level graduate students who have transferred to the University of Cincinnati or are from other engineering departments at the University of Cincinnati which don't offer a DSP course. The course is taught in conjunction with Fourier Transform Techniques Class which is a dual level course (Undergraduate and graduate) and is a prerequisite for number of graduate courses including the Vib 2 and Vib 3 courses which are prerequisite courses for the SDA II and SDA III courses.

The lectures, home work problems, and mid-term exam are the same for the two courses. After the mid-term exam, the students are required to work on a project. They are arranged in groups of 3–5 students and assigned a common project. The project for the Fourier students is to process analytical data sets into measurements [power spectrums, cross power spectrums, Frequency Response Functions( $H_1$  and  $H_2$ ), Ordinary Coherence] from analytically generated data sets (time histories).

The SDA I students are required to collect a set of time histories measured on an UCSDRL structure (C-Plate) or for the Internet students a structure in their faculties. The C-Plate structure is an historical test structure; it is a very lightly damped circular structure which results in a large number of repeated eigenvalues. This is a simple but challenging structure due to "leakage" problems and the nearly repeated roots.

The students have to write a MATLAB program to process two different data sets into FRFs and Coherence measurements, using two different excitation methods. The first excitation method involves measurement of FRFs ( $H_1$ ,  $H_2$  and  $H_v$ ) and the multiple coherence function using a Multiple Input Multiple Output (MIMO) test. For this test, 30 accelerometers are mounted on the C-Plate, and three electromechanical exciters are attached to the structure. The second excitation method involves the Multiple Reference Impact Test (MRIT), using 30 accelerometers mounted on the structure and an impact hammer. Impacting occurs at the locations of the 30 accelerometers.

Using either the University of Cincinnati X-Modal software or commercial software, the data are processed into modal parameters. This gives the students a check on the quality of the data taken in the data acquisition cycle and gives them a preview of what they are expected to do in SDA II. In SDA II they are required to write their own program to process the FRF data into modal parameters.

## 28.8 C-Plate Test

The C-Plate is a historical testing structure located in the UCSDRL. It is permanently set up in the laboratory and used as a test structure for several of the structural dynamics oriented courses (Vib 3, SDA, FEM, etc.). Figure 28.1 shows a photo of the 2002 test setup. It was also used in the 2002 IMAC conference to demonstrate remote testing. The C-Plate was tested using the Internet from the IMAC Technology Center Booth. An [IMACpaper](#) was presented at the IMAC Conference that described this remote testing capability. The test was performed as a demonstration of the Digital Sensor System (DSS). The Digital Sensor System is a network appliance prototype. It has an IP address and can be operated remotely over the Internet. Up to 64 sensors can be connected together on a single cable, tremendously reducing the cabling cost and simplifying the test set-up.

A student was on call at the University to trouble shoot and correct communication problems for the remote test. Two to three shakers were used to excite the C-Plate and 30 accelerometers were mounted on the C-plate to monitor the motion. The [secondgenerationDSS](#) had four pure random noise sources, which could be used for excitation signals. Historically pure uncorrelated random signals were not used on lightly damped systems, due to the potential of "leakage errors". A number of specialized excitation signals were developed in the 1970s and 1980s which had "randomizing characteristics" to average out distortion errors due to non-linearities, but were a completely observed signal in order to reduce "leakage" errors (for example Burst Random, Periodic Random, etc.).

One of the techniques proposed in the late 1970s that could not be conveniently implemented because of memory limitations in the computers of the time was cyclic averaging. The DSS has enough internal memory to store long recorded time waveforms for the input and response channels. The long DSS time records can then be downloaded over the Internet and processed with MATLAB using cyclic averaging to obtain nearly leakage-free FRF measurements.

The students in SDA I are required to test the C-Plate, including setting up the test setup, calibration, etc., and to write a MIMO MATLAB program to estimate  $H_1$ ,  $H_2$  and  $H_v$  of the FRF matrix of the C-plate. These data are then processed using an existing reliable software package to check the quality of the data set. This data set is then archived and used as one of the data sets that will be processed into Modal Parameters in the SDA II Class.

**Fig. 28.1** C-Plate setup with two prototype first generation DSS systems shown



The students at the University of Cincinnati then performed a MRIT test of the C-Plate by impacting at all 30 points where the accelerometers were located. This generates a 30 by 30 number spectral line Frequency Response matrix. This data set is also checked and archived for processing in SDA II. It should be noted, since the MRIT requires impacting by the students, this test cannot be performed remotely over the Internet. However, the test can be monitored using web video cameras and the data file made available to students at other sites. Typical FRF measurements computed in the SDA I course will be shown in a report which documents the testing in SDA I and the parameter estimation in SDA II.

## 28.9 SDA II Course

The SDA II course concentrates on extracting modal parameters from measured Frequency Response Functions (FRFs), Unit Impulse Functions (UIF), free decays, Power Spectrums (PS), etc. for a given structure. Historically, this is the most challenging topic in the SDA course sequence. There has been extensive research since the early 1970s on developing parameter estimation algorithms. Many of these algorithms have resulted in an almost religious following.

A prerequisite for the SDA II course is an advanced vibration course (Vib 2), in which the vibrations of multiple degree of freedom systems are studied in detail and the eigenvalues and eigenvectors and modal scale factors of the equation of motions are formulated. At the beginning of the SDA II course, depending on the background of the students, a quick review of the Vib 2 course is presented. Mathematically, relationships between the responses of the multiple degree of freedom system and the input (Frequency Response Functions) to the system are derived and studied in detail. The influence of damping distributions are discussed (proportional and non-proportional damping models).

An [AdvancedParameterEstimationOverview](#) set of course notes were written for the SDA II course in the late 1980s and this set of notes is distributed on-line for the students. This set of notes summarizes many of the important mathematical relationships formulated in the University of Cincinnati's Vib 2 prerequisite course.

It also covers and summarizes most of the important parameter estimation algorithms, concepts, and developments in the 1970s through the 1980s. One of the biggest developments in the mid 1980s was the search for a way to unify the many parameter estimation procedures. This led to the formulation of the Unified Matrix Polynomial Approach (UMPA) by the late 1980s. The UMPA parameter estimation procedure could be used in the time, frequency or Laplace domain. The first real application of the UMPA parameter estimation procedure was in the late 1980s when a spatial sine testing method was developed as a modal testing procedure. A narrow frequency band frequency domain UMPA procedure was developed where an array of exciters could be used in a step sine testing procedure to sweep out the eigenvalues and eigenvectors of a test system. This method is described in a more detail in a more [recentpaperreviewingspatialtestingmethods](#):

At the end of this paper there are a number of additional references located in the [bibliography](#) describing the UMPA parameter estimation procedures.

The most current mathematical formulation of the UMPA Model is:

$$\sum_{i=0}^n [\alpha_i] \{X_{k+1}\} = \sum_{j=0}^m [\beta_j] \{f_{k+1}\} \quad \text{Time Domain}$$

$$\sum_{i=0}^n (S_k)^i [\alpha_i] \{X(S_k)\} = \sum_{j=0}^m (S_k)^j [\beta_j] \{F(S_k)\} \quad \text{Generalized Frequency Domain}$$

Where

---

$[\alpha_i]$	is the $i$ Coefficient Matrix of the response vector
$[\beta_j]$	is the $j$ Coefficient Matrix of input vector
$\{x_{k+i}\}$	is the response vector time domain
$\{f_{k+j}\}$	is the input vector time domain
$\{X(s_k)\}$	is the response vector frequency domain
$\{F(s_k)\}$	is the input vector frequency domain
k	is the equation index
I	is the response index
J	is the input index
s	is the generalize frequency variable

---

Using the UMPA procedure, it is possible to write a very small MATLAB script that will emulate nearly all of the current commercial time-domain algorithms. This is why the students are able to develop an emulation program in the 3–5 week period allocated in the SDA II course.

In the SDA II course, the students are required to use the time domain UMPA model to emulate the Complex Exponential Algorithm (CAE), Ibrahim Time Domain (ITD), Polyreference Time Domain (PTD), and the Eigenvalues Realization Algorithm (ERA). All of these algorithms can be emulated using the ERA algorithm, so the students are required to write a MATLAB ERA script and then use this script to emulate the other algorithms. They are then required to process one analytical data set (a 15 DOF system) and the two C-Plate data sets measured in the SDA I class into modal parameters (eigenvalues, eigenvectors and modal scale factor).

This basic process is demonstrated to the SDA class by emulating a single measurement using the ERA algorithm. This is one extreme of the emulation process since the ERA was developed to process MIMO data sets.

A [classroomdemonstration](#) of this process is shown in a short document which is available for download. This document includes a boiler plate MATLAB program which demonstrates a number of ways of generating the data matrices for the UMPA ERA algorithm which is used, in turn, to emulate the CEA algorithm. The document also contains a second MATLAB script of the standard formulation of the CEA algorithm. Furthermore the document also includes several other small MATLAB scripts which are standard display and data manipulation scripts useful in developing MATLAB scripts.

## 28.10 SDA II Project

The student groups are required to develop MATLAB software to extract modal parameters from analytical and measurement data sets of a component or systems' measured FRFs, free decays, power spectrums, etc. The analytical data sets are a 15DOF system, and two FRF measurements sets are taken on the C-Plate structures described in the previous section. In the following section, a brief review of results of this project will be shown. However, a much more detailed review will be shown in results extracted from some typical student reports. This includes several MATLAB scripts, for processing the data sets, and a more extensive review of the data taken in SDA I as well as the results generated in the SDA II course.

[OverviewofSDAIandSDAIIResults](#): This hyperlink is a more detailed write-up of the theory, and a look at typical student results.

## 28.11 SDA III

The main theme of the SDA III course is building dynamic system models directly from experimentally measured data. These models can be used to predict the influence of modifications to these systems and to validate or to update analytical



models of these systems. Modeling is the area which has been most impacted by the recent advancements in computer and networking technologies. The students are expected to build both an impedance model and a modal model of the systems measured and analyzed in the SDA I and SDA II courses.

Several other topics are covered in SDA III:

- Frequency Domain and spatial domain parameter estimations are reviewed and the students are required to program a simple narrow band [frequencyalgorithmEMIF](#), which has been useful for trouble shooting with MRIT testing methodologies.
- A review of [modalcompletionalgorithms](#) which are used to estimate missing DOFs. For example, in building a system model, rotational degrees of freedom and moments are often very important and these measurements are very difficult or impossible to estimate. These missing DOF's are estimated by interpolation from measured translational DOFs near the missing DOFs by assuming that the system behaves as a rigid body in the local region near the point of interest.
- Demonstration of using pole clustering to improve eigenvalue filtering, and to obtain statistical estimates of eigenvalues.

[OverviewoftheSDAIIICourse](#): This overview includes presentation of both impedance and modal modeling theory as well as the student results.

## 28.12 Discussion

### 28.12.1 Evaluation of the Current Course Format

A thorough understanding of the principles and methodologies in system dynamics is essential for many fields of study in mechanical engineering, from algorithm development for improved parameter estimation to the use of system dynamics as a tool in solving structural health monitoring challenges. System dynamics draws and integrates knowledge from many disciplines, such as signal processing and numerical modeling. Although most students at the Ph.D. level have seen some of the signal processing techniques and modeling methodologies in their Bachelor's and Master's courses, they were often not applied to mechanical problems, nor was the detail and depth always sufficient to be useful for their Ph.D. research. A Ph.D. level course giving an overview of how these topics and techniques interlink, can be generalized, and can be applied to mechanical systems is priceless for students starting their Ph.D. in this challenging field of research. A major problem, however, is that student groups at any institution are often far too small to justify this type of course. Another problem is that profound expertise on every aspect of system dynamics is not always present at every institution. An online course organized by experts in their fields and focusing on a thorough understanding of core concepts and core algorithms is a perfect solution to these problems.

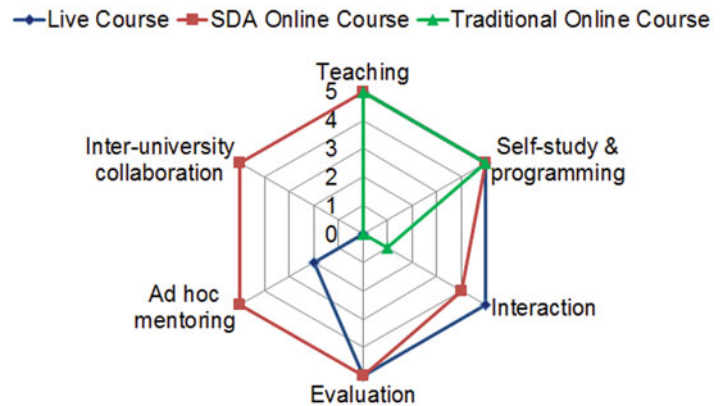
Key in making these online classes an efficient and compelling learning experience is the format that is used. A live course typically comprises four didactic steps: teaching; self-study and programming; evaluation; and interaction. Bringing these four steps to an online course experience is challenging, but nevertheless this was exactly the ambition of the online SDA course.

Being able to interact directly with and get feedback from the instructor has previously been proven to be of key importance in successful e-learning environments [1] and was also perceived as a big added value of the online SDA course. Other e-seminars that cover system dynamics and modal analysis can be found online from different universities (e.g. MIT OpenCourseWare), however access to faculty for these courses is, understandably, limited, ultimately hampering the learning experience and possibly discouraging students from following through the whole course. Besides feedback and interaction on the course content, the SDA course also allowed for ad hoc mentoring on topics the participants were working on. This was a big added value both for the students from academia as well as from industry. Due to the format of the course and the use of GoToMeeting and Dropbox, these mentoring sessions could be set up on short notice and probably more frequently even than in a live course environment.

The e-lectures at set times with peers from all over the world (the KU Leuven students followed the first part of the course with students from Michigan Technical University, University of Purdue and the experimental testing experts at SpaceX) provided for an exciting and vibrant atmosphere surrounding the course. Again the moments of interaction and questions from the different groups during the lectures proved to be of key importance in learning and understanding the material. Additionally, since different groups are often working on niche domains, the questions tend to be very specific, challenging the other participants to think along and come up with creative solutions. Working across different institutions has additional advantages as this creates communities of students working at a graduate level on topics related to the course



**Fig. 28.2** The didactic aspects and features typically offered in a live, traditional online and the SDA online course format. 5 indicates that the particular aspect is present and contributing to the learning experience in the respective course format



content. This opens up the possibility for new contacts and future collaborations. Achieving this in a live course environment is almost impossible (Fig. 28.2).

Efforts were also made to record and save the audio, video and chat logs of each session. This allowed the students to get back to the parts they didn't fully grasp during the first pass and proved to be a very valuable and helpful tool of the classes.

In spite of the numerous positive aspects of the online SDA course, the format suffers from some drawbacks as well. Student retention is a challenge. The KU Leuven group started out with 8 of which 4 finished the first two parts (SDA 1 & 2) and 2 sat through all 3 parts of the course. Results here seem to be different between different institutions, e.g. the group in Purdue finished the whole course with all students. When polled for reasons for quitting, time requirements of the course and content not exactly matching with research topic were given as the main arguments. These are points of action for future editions of the course and could be neutralized for example by condensing the course down to an intensive week-long format. An intensive concentration of the material in 1 week might allow students to grasp the overview of the whole course, but might hinder the learning process from writing and implementing the code themselves. To circumvent the second point of critique, an effort was made to indeed avoid topical dissonances and to select topics that were of prime interest to the students by allowing them to propose topics or problems they wanted clarification on besides the normal course content. This expects the tutor to take more of a consulting and mentoring role, which worked great for the SDA course, but is perhaps not something every tutor would want to do.

### 28.13 Future Improvements

The online SDA course can lay the foundation for a much **bigger online learning platform** centered around system dynamics and modal analysis in particular. Weird as it may seem, a comprehensive platform that explains and brings these topics together in an accessible way is not yet available on the internet, although there are some tutorials available that do an excellent job at explaining some of the fundamentals [2].

A first step toward such a platform can be to change the evaluation of the SDA-course from handing in a formal written report to summarizing the theory and their insights in the form of e.g. a **Wikibook**. This platform could, besides serving as an entry and overview point of the theory, also list the key references in the respective domains, avoiding the time-consuming effort for newcomers on the subject to work their way through the vast amount of literature available but giving them a good starting point instead.

As this field is as much about theory as it is about putting this theory into practice, the platform can also provide some of the key MATLAB-files that are developed during the SDA course. These go from simple data processing algorithms to full-fledged parameter estimation procedures and may even feature some animation programs as this often is a difficult hurdle for students to get past. Together these files should allow the students to get an in-depth understanding of what is behind the formulas and provide them with a toolbox that allows him/her to further explore and develop these algorithms.

The platform could be further extended in several ways. Forums can be coupled to the site to discuss topics and problems, perhaps even volunteer moderated by some of the key people in the field; monthly webinars can be organized and a tool to set up dedicated e-mentoring sessions can be provided so that dedicated topics can be treated. In order to improve the dissemination of the material, the lectures or webinars can be made available on widely known e-learning channels such as iTunes U. By doing this, a SDA Online research Community can be created, which can start of on existing platforms such as ResearchGATE.

An intricate part of modal analysis is the **experimental techniques**. These seem to be especially difficult for students entering the field. Theoretical information can be obtained; albeit this may take an effort, but learning the skills needed to perform proper experiments and data collection is often a huge hurdle. More often than not, experimental expertise is missing at the institutions. Being able to build this knowledge through the online SDA course would be of tremendous value for the students. This poses some difficulties however. Other e-learning courses have faced similar problems and progress is underway in the development of remote controllable labs [3]. It might be a challenging question to see how these concepts can be translated into a remote testing facility for performing system dynamics course work. An easier solution however would be to schedule for one session where the tutor shows how an experimental modal analysis is performed on a test structure at the tutor's lab while this is being videoed and commented by the tutor. Alternatively the course could evolve to a format where the different groups fly in for 1 week to work together on some experimental data acquisition and processing, using the algorithms developed during the SDA course. This could for example take place in the week before or after conferences such as ISMA or IMAC at a laboratory close to the conference.

The idea of a **physical get-together** of the student participants to the online course is however valuable even if this would not be coupled to a week of performing experimental work together. As a closure to the course it would be an opportune moment of discussing and getting to know the persons one has been working with over the course period. A conference would be an ideal venue for these get-togethers, maybe even allowing the participant to show the work they have been doing during the course and how they used the knowledge gained to move their own topics forward, perhaps even in a special session. This may provide starting Ph.D. students with an excellent forum to present their work to a knowledgeable audience for the first time. Conferences such as IMAC already have special sessions related to education in modal analysis and engineering in general, so perhaps hope would be justified for a session dedicated to the online SDA course or similar initiatives.

Another added value for the participating students would be that this course is certified by their home institutions. Although participants often get an ad hoc approval from their promoters that this course is suitable for their Ph.D. track, this is an aspect that cannot be overlooked in the e-learning environment.

## 28.14 Conclusions

Since 2006 the University of Cincinnati has offered a Ph.D. level System Dynamics Course as an Internet Course to students at other universities and institutions. The main reasons are that at any given site or university there are not enough students to justify offering a course or the profound expertise on every aspect of system dynamics and modal analysis is not always present.

The use of the GoToMeeting application allows voice and video over IP combined with screen-sharing. The big advantage of this format is that lectures transcend the one-way interaction such as in recorded lectures and that two-way interaction is possible. This is especially suitable for the SDA-course since it is based on teaching, self-study, programming and interaction.

The interactive format allows not only teaching, but creates space for discussion on technical topics, enabling the possibility to create new contacts and future collaborations. Also, if desired, the teacher can extend his role to mentor and consultant, helping the students with the specific problems they are struggling with.

With the growing trend towards specialization in all branches of science, this format of courses seems to be an ideal tool in sharing knowledge and creating bridges between different research groups.

## References

1. Hilton JL, Graham C, Rich P, Wiley D (2010) Using online technologies to extend a classroom to learners at a distance. *Dist Educ* 31(1):77–92
2. P. Avitable, <http://macl.caeds.eng.uml.edu/umlspace/mspace.html> (visited on 15.10.12)
3. Ku H, Ahfock T, Yusaf T (2011) Remote access laboratories in Australia and Europe. *Eur J Eng Educ* 36(3):253–268
4. Other references not used directly in this paper but which are consider as important references for students studying in the Structural Dynamics area are included below in the hyperlinked bibliography. The students can download this reference material in real time.
5. This bibliography is a Word Document which will make it easy to cut and paste selected references to be included in other documents.
6. **Note:** A [modified version of this paper](#) can be downloaded which means that the original paper can be updated periodically. For an archived conference reference document which will be used for historical purposes this is not an acceptable option but for course fare, this is an optimal option since it can evolve with the advancements of new concepts and technology.
7. [Bibliography](#)

# Chapter 29

## Using Random Response Input in Ibrahim Time Domain

Peter Olsen and Rune Brincker

**Abstract** In this paper the time domain technique Ibrahim Time Domain (ITD) is used to analyze random time data. ITD is known to be a technique for identification of output only systems. The traditional formulation of ITD is claimed to be limited, when identifying closely spaced modes, because of the technique being Single Input Multiple Output (SIMO). It has earlier been showed that when modifying ITD with Toeplitz matrix averaging. Identification of time data with closely spaced modes is improved. In the traditional formulation of ITD the time data has to be free decays or impulse response functions. In this article it is showed that when using the modified ITD random time data can be analyzed. The application of the technique is displayed by a case study, with simulations and experimental data.

**Keywords** Ibrahim time domain • Operational modal analysis • Random input • Time domain technique • Toeplitz matrix averaging

### 29.1 Introduction

In the process of identifying the modal parameters there are numerous applicable identification techniques. One possibility is to measure the input and the output signal and by means of these identify the modal parameters. These techniques are often quite complex and in many cases it can be quite difficult to obtain a usable input signal, with for example large structures. An alternative is the operational techniques where only the output signal is measured. Having the measured response there is the choice of using time domain or frequency domain techniques. The time domain identification techniques are an attractive alternative to frequency domain techniques because they prevent errors such as leakage, truncation and biased data.

Amongst several time domain techniques this paper focusses on ITD. ITD was one of the first identification theories, which were developed in the modal community. ITD was formulated by Sam Ibrahim in 1977 [1]. The original formulation of ITD is a SIMO technique and the input has to be in the form of free decays or impulse response functions. The random decrement technique makes it possible to use random input in ITD [2]. Being a SIMO technique the ITD technique has some difficulties with identifying closely spaced modes. In [3] it has been showed that a small modification in the formulation of traditional ITD makes it possible for the technique to use multiple input.

The modified ITD technique has only been used on free decays and proved very successful. In this paper the applicability of the modified ITD technique is extended by demonstrating the ability of identifying random response.

### 29.2 Theory

ITD uses measured time data to find the modal parameters. From the time data an eigenvalue problem is constructed. The modal parameters frequency damping ratio and mode shapes is estimated by solving the eigenvalue problem. The time data can be free decays or impulse functions which are the inverse of the structures transfer function. It is also possible to use random data either by processing the random time data by the random decrement technique or to use correlation functions.

---

P. Olsen (✉) • R. Brincker  
Department of Engineering, Aarhus University, Dalgas Avenue 2, 8000 Aarhus C, Denmark  
e-mail: [pto@iha.dk](mailto:pto@iha.dk); [rub@iha.dk](mailto:rub@iha.dk)

The basis of the ITD technique is that any free response or correlation function can be expressed as a linear combination of mode shapes and exponential decays.

$$y(t) = y(k\Delta t) = c_1 a_1 e^{\lambda_1 k \Delta t} + c_2 a_2 e^{\lambda_2 k \Delta t} + \dots = c_1 a_1 \mu^k + c_2 a_2 \mu^k + \dots \quad (29.1)$$

Where  $a_i$  are the mode shapes,  $\lambda_i$  are the continues poles,  $\mu_i$  are the discrete poles and  $c_i$  are the initial modal amplitudes defining the free decay at time zero. ITD uses three time shifts  $\Delta t_1$ ,  $\Delta t_2$  and  $\Delta t_3$  in the original formulation using the modern formulation of the classic ITD, this is shown in [3]. Setting up a block Hankel matrix containing the time data and the shifted time data in four block rows of the matrix.

$$\mathbf{H} = \begin{bmatrix} y(1) & y(2) & \dots & y(np-3) \\ y(2) & y(3) & \dots & y(np-2) \\ y(3) & y(4) & \dots & y(np-1) \\ y(4) & y(5) & \dots & y(np) \end{bmatrix} \quad (29.2)$$

$np$  is the number of points in the time data. This can be expressed by the mode shapes and the discrete poles as in (29.1).

$$\mathbf{H} = \begin{bmatrix} \mathbf{a}_1 & \mathbf{a}_2 & \dots \\ \mu_1 \mathbf{a}_1 & \mu_2 \mathbf{a}_2 & \dots \\ \mu_1^2 \mathbf{a}_1 & \mu_2^2 \mathbf{a}_2 & \dots \\ \mu_1^3 \mathbf{a}_1 & \mu_2^3 \mathbf{a}_2 & \dots \end{bmatrix} \begin{bmatrix} c_1 \mu_1^0 & c_1 \mu_1^1 & \dots & c_1 \mu_1^{np-3} \\ c_2 \mu_2^0 & c_2 \mu_2^1 & \dots & c_2 \mu_2^{np-2} \\ \vdots & \vdots & & \vdots \end{bmatrix} = \Psi \Lambda \quad (29.3)$$

$\Psi$  is a matrix holding the mode shapes in the columns. Splitting the block Hankel matrix in the middle, in an upper block matrix  $\mathbf{H}_1$  and a lower block matrix  $\mathbf{H}_2$ .

$$\mathbf{H}_1 = \Psi_1 \Lambda \quad (29.4)$$

Where  $\Psi_1$  is the upper part of  $\Psi$  given as.

$$\Psi_1 = \begin{bmatrix} \mathbf{a}_1 & \mathbf{a}_2 & \dots \\ \mu_1 \mathbf{a}_1 & \mu_2 \mathbf{a}_2 & \dots \end{bmatrix} \quad (29.5)$$

By (29.4)  $\mathbf{H}_2$  can be expressed as.

$$\mathbf{H}_2 = \Psi_1 [\mu_n]^2 \Lambda \quad (29.6)$$

$[\mu_n]$  is a diagonal matrix with the discrete poles in the diagonal. Considering (29.4) and (29.6)  $\Lambda$  can be eliminated, which results in.

$$\Psi_1^{-1} \mathbf{H}_1 = \Psi_1^{-1} [\mu_n]^{-2} \mathbf{H}_2 \quad (29.7)$$

By isolating  $\mathbf{H}_2$  (29.7) can be written as.

$$\Psi_1^{-1} [\mu_n]^2 \Psi_1 \mathbf{H}_1 = \mathbf{H}_2 \quad (29.8)$$

The system matrix is given by.

$$\mathbf{A} = \Psi_1^{-1} [\mu_n]^2 \Psi_1 \quad (29.9)$$

This results in the ITD equation for estimating the system matrix  $\mathbf{A}$  by inserting (29.9) in (29.8).

$$\mathbf{A} \mathbf{H}_1 = \mathbf{H}_2 \quad (29.10)$$

The traditional method of solving this over determined problem using ITD is by regression. So multiplying with  $\mathbf{H}_1^T$  from the right the square and normally full rank matrix  $\mathbf{H}_1\mathbf{H}_1^T$  is obtained. This matrix can be inverted.

$$\Psi_1^{-1} = [\mu_n]^{-2} \Psi_1^{-1} \mathbf{H}_2 \mathbf{H}_1^T (\mathbf{H}_1 \mathbf{H}_1^T)^{-1} \quad (29.11)$$

From (29.8) and (29.9) we find the system matrix A as

$$\mathbf{A}_1 = \mathbf{H}_2 \mathbf{H}_1^T (\mathbf{H}_1 \mathbf{H}_1^T)^{-1} \quad (29.12)$$

Similar operations can be done by multiplying with  $\mathbf{H}_2^T$  obtaining the square and normally full rank matrix  $\mathbf{H}_1\mathbf{H}_2^T$ , resulting in an alternative system matrix.

$$\mathbf{A}_2 = \mathbf{H}_2 \mathbf{H}_2^T (\mathbf{H}_1 \mathbf{H}_2^T)^{-1} \quad (29.13)$$

It is well known that the estimates for the system matrix  $\mathbf{A}_1$  and  $\mathbf{A}_2$  are weakly biased. But using an average estimate as for example the Double Least Squared estimate, this estimate is considered unbiased.

$$\mathbf{A} = \frac{(\mathbf{A}_1 + \mathbf{A}_2)}{2} \quad (29.14)$$

As mentioned earlier the traditional formulation of ITD is limited by being SIMO. Using the formulation proposed in [3] ITD can be modified to be multiple input multiple output (MIMO).

Considering two different free decays  $y_1(t)$  and  $y_2(t)$  setting up the Hankel matrix for each of the free decays and dividing the two Hankel matrices in an upper and lower block matrix.

$$\begin{aligned} \mathbf{H}_{11} &= \begin{bmatrix} y_1(1) & y_1(2) & \cdots & y_1(np-3) \\ y_1(2) & y_1(3) & \cdots & y_1(np-2) \end{bmatrix} & \mathbf{H}_{21} &= \begin{bmatrix} y_1(3) & y_1(4) & \cdots & y_1(np-1) \\ y_1(4) & y_1(5) & \cdots & y_1(np) \end{bmatrix} \\ \mathbf{H}_{12} &= \begin{bmatrix} y_2(1) & y_2(2) & \cdots & y_2(np-3) \\ y_2(2) & y_2(3) & \cdots & y_2(np-2) \end{bmatrix} & \mathbf{H}_{22} &= \begin{bmatrix} y_2(3) & y_2(4) & \cdots & y_2(np-1) \\ y_2(4) & y_2(5) & \cdots & y_2(np) \end{bmatrix} \end{aligned} \quad (29.15)$$

Realizing that the matrix product in (29.12) and (29.13)  $\mathbf{H}_{i,r} \mathbf{H}_{i,r}^T$ , where i denotes the upper or the lower block matrix and r denotes the number of free decay are toeplitz matrices which can be added together. Adding the toeplitz matrices and using (29.12), (29.13) and (29.14) results in a system matrix estimated from the two free decays. Solving the eigenvalue problem for the new system matrix results in the discrete poles and the modeshapes

In order to assess the quality of the estimated poles and mode shapes a fit of the correlation functions obtained from the physical data and a modal model from the estimated poles and mode shapes is used.

$$\mathbf{R}_y(k) = 2\pi \sum_{n=1}^{2N} \Gamma [\mu_n]^k \mathbf{A}^T \quad (29.16)$$

Where  $\mathbf{R}_y(k)$  is the correlation function matrix sampled at the discrete time shifts  $\tau = k\Delta t$ ,  $\Gamma = [\gamma_n]$  is a matrix containing the modal participation vectors,  $[\mu_n]^k$  is a diagonal matrix of the discrete poles and  $\mathbf{A}$  is the mode shapes.

The physical correlation functions are arranged in a single block Hankel matrix H and the discrete poles and mode shapes in the matrix M.

$$\mathbf{H} = 2\pi \Gamma \mathbf{M} \quad (29.17)$$

From (29.17) the modal participation vectors  $\gamma_n$  can be determined by regression. Noise modes often tend to have a low modal participation factor hereby the factor helps to determine which modes are physical modes. The relative modal participation factor is often used as measure and is given as

$$\pi_n = \frac{p_n^2}{\mathbf{p}^T \mathbf{p}} \quad (29.18)$$

$\mathbf{p}^T = [p_1 \ p_2 \ \dots]$  is a vector which contains the absolute value of the modal participation factor.

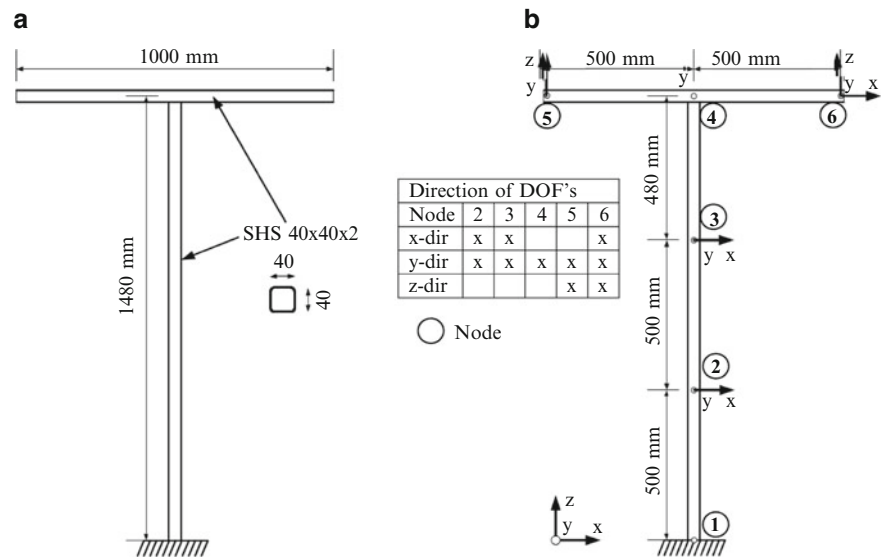
A measure for comparing two sets of modes shapes is the modal assurance criterion (MAC) [4], which is the correlation coefficient between the two modes.

$$MAC(\mathbf{a}_i, \mathbf{a}_j) = \frac{|\mathbf{a}_i^* \mathbf{a}_j|^2}{|\mathbf{a}_i^* \mathbf{a}_i| |\mathbf{a}_j^* \mathbf{a}_j|} \tag{29.19}$$

### 29.3 Case Study

To demonstrate the application of the modified ITD using random input a case study using a steel T-structure is presented. The T-structure is made of structural steel with cross sections of square hollow sections with the dimension 40x40x2 mm, two bars are welded together and fixed to a steel clamping table. The geometry and dimension of the T-structure is shown in Fig. 29.1. Times series are measured with accelerometers at node 2 to 6 for different degree of freedoms relative to the xyz coordinate system, see Fig. 29.1 for placement of nodes and degrees of freedom. The random excitation is achieved by means of a wire brush.

To identify the modal parameters of the T-structure an analysis with B&K’s software OMA [5] using the identification routine EFDD has been used. The measurements are taken at the node 2–6 in the direction shown in Fig. 29.1. Each measurement is recorded for 120 s with a sampling rate at 17,065 Hz. Natural frequencies, damping ratio are displayed in Table 29.1, associated mode shapes are shown in Fig.29.3 and a SVD plot for the identification is shown in Fig. 29.2. For clarity only the first 5 modes are taken in to account. The modes are distributed so the first and second mode are closely spaced and the third mode is torsional. It has been showed in [3], that the tradintional ITD has problems identifying closely spaced modes.

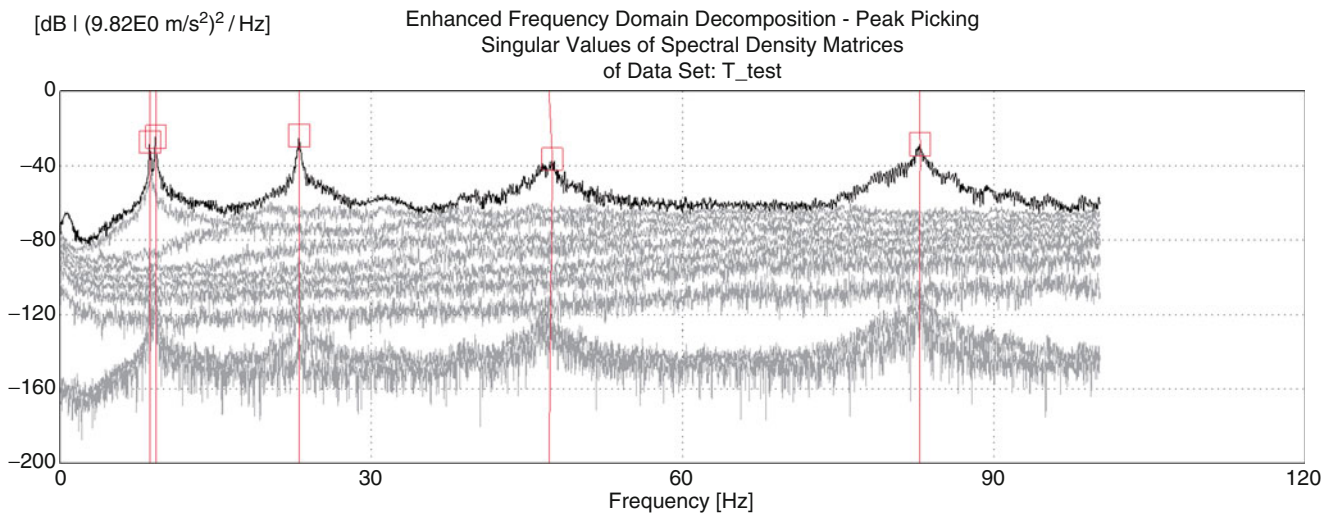


**Fig. 29.1** (a) Geometry of fixed welded steel T-structure (b) Placement of nodes and degree of freedom (DOF) for of square hollow cross section 40 × 40 × 2 mm the nodes

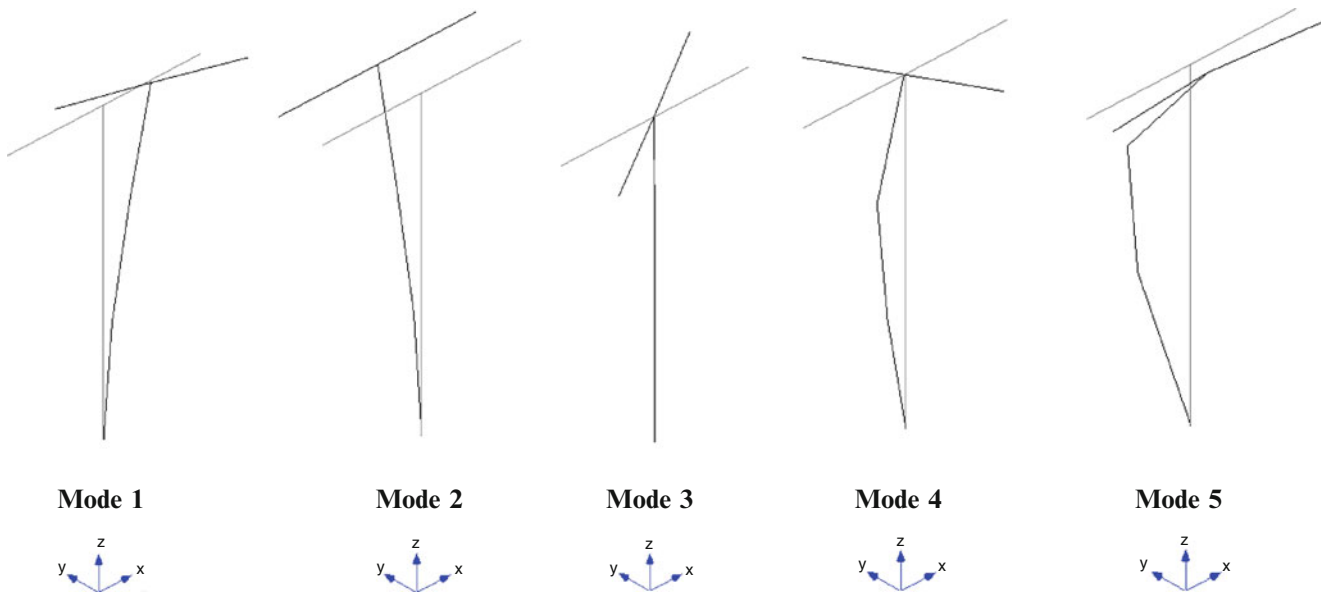
**Table 29.1** Natural frequencies and damping ratios for the T-structure estimated by the EFDD technique by the software B&K-Pulse-OMA [5]

	Mode 1	Mode 2	Mode 3	Mode 4	Mode 5
Natural frequency, $f_i$ (Hz)	8,6357	9,2066	23,0144	47,1008	82,7893
Damping ratio, $z$ (%)	0,36	0,40	0,36	1,65	0,39





**Fig. 29.2** SVD plot for the first five poles where B&K Pulse-OMA software [5] is used to estimate frequencies, mode shapes and damping ratio by the EFDD technique



**Fig. 29.3** Mode shapes for the first five modes. Mode 1 and mode 2 are the first translation modes in x and y direction. Mode 4 and mode 5 are the second translation modes. Mode 3 is the first rotational mode about the z direction

### 29.4 Simulation

To show that the modified ITD is unbiased several free decays are simulated exciting the structure by an initial load in each degree of freedom. The simulations with free decays are performed without noise and with noise corresponding to 1/100,000 and to 1/10,000 of the largest amplitude from the noise free signal. The identification is done with five free decays.

Simulations of the theoretical correlation function [6] using the modal parameters of the structure found in Table 29.1, with white noise as input. The simulation is performed by decreasing the number of modes used to simulate the response in order to find the estimate equal to the input modal parameters.

## 29.5 Experimental Result

Finally the modified ITD technique is used on the data from the measurements on the steel T-structure. Where the correlation functions of the measured signal is used as input in the modified ITD.

## 29.6 Conclusion

The aim of this paper was to use the modified Ibrahim time domain on a random signal. This has been done, firstly by using the modified technique on free decays, as in the traditional ITD. It is seen from the modal parameters and the MAC values for the case with no noise in Table 29.2 that the formulation of the modified ITD is unbiased. Adding noise to the free decay, the modal parameters differ from the input parameters. Secondly the modal parameters is estimated from the theoretical correlation functions by the modified ITD, from Table 29.3 it is seen when estimating 5 modes, the modal parameters differ from the input parameters and the number modes has to be reduced to 3 modes before the estimated poles is equal to the input. Finally the modified ITD is used on a measured signal with random input. From Table 29.4 the results show that the same modes are identified using the EFDD technique and the modified ITD technique and that the deviations are quite small on the modal parameters. Hereby concluding that the modified ITD technique can be used on random response using the correlation functions of the measured response as input.

**Table 29.2** Natural frequencies and damping ratios for the T-structure estimated by the Modified ITD technique, for a simulation with five free decays

Free decay, no noise	Mode 1	Mode 2	Mode 3	Mode 4	Mode 5
Natural frequency, $f_i$ (Hz)	8,6357	9,2066	23,0144	47,1008	82,7893
Damping ratio, $z$ (%)	0,36	0,40	0,36	1,65	0,39
MAC-value	1,0	1,0	1,0	1,0	1,0
Noise 1/100,000* $y_{\max}$	<b>Mode 1</b>	<b>Mode 2</b>	<b>Mode 3</b>	<b>Mode 4</b>	<b>Mode 5</b>
Natural frequency, $f_i$ (Hz)	8,6393	9,2446	23,0139	47,1010	82,7887
Damping ratio, $z$ (%)	0,36	0,39	0,36	1,65	0,39
Noise 1/10,000* $y_{\max}$	<b>Mode 1</b>	<b>Mode 2</b>	<b>Mode 3</b>	<b>Mode 4</b>	<b>Mode 5</b>
Natural frequency, $f_i$ (Hz)	8,6370	9,2066	–	47,1001	82,7891
Damping ratio, $z$ (%)	0,30	0,41	–	1,64	0,39

**Table 29.3** Natural frequencies and damping ratios for the T-structure estimated by the Modified ITD technique, for simulation of the theoretical correlation functions

5 modes	Mode 1	Mode 2	Mode 3	Mode 4	Mode 5
Natural frequency, $f_i$ (Hz)	8,6439	9,2263	23,0297	47,1000	82,7806
Damping ratio, $z$ (%)	0,35	0,38	0,35	1,65	0,38
4 modes	<b>Mode 1</b>	<b>Mode 2</b>	<b>Mode 3</b>	<b>Mode 4</b>	<b>Mode 5</b>
Natural frequency, $f_i$ (Hz)	8,6584	9,2066	23,0144	47,1008	–
Damping ratio, $z$ (%)	0,36	0,40	0,36	1,65	–
3 modes	<b>Mode 1</b>	<b>Mode 2</b>	<b>Mode 3</b>	<b>Mode 4</b>	<b>Mode 5</b>
Natural frequency, $f_i$ (Hz)	8,6357	9,2066	23,0144	–	–
Damping ratio, $z$ (%)	0,36	0,40	0,36	–	–
3 modes, with noise 1/100,000	<b>Mode 1</b>	<b>Mode 2</b>	<b>Mode 3</b>	<b>Mode 4</b>	<b>Mode 5</b>
Natural frequency, $f_i$ (Hz)	8,6498	9,2068	23,0153	–	–
Damping ratio, $z$ (%)	0,35	0,40	0,36	–	–

**Table 29.4** Natural frequencies and damping ratios for the T-structure, estimated by the modified ITD technique on real data Natural frequencies and damping ratios for the T-structure estimated by the EFDD technique by the software B&K-Pulse-OMA [5]

	Mode 1	Mode 2	Mode 3	Mode 4	Mode 5
Estimated by the EFDD technique					
Natural frequency, $f_i$ (Hz)	8,6376	9,1968	23,0141	46,9514	82,7840
Damping ratio, $z$ (%)	0,36	0,40	0,35	1,60	0,35
Estimated by the modified Ibrahim Time Domain technique					
Natural frequency, $f_i$ (Hz)	8,6454	9,1934	23,0145	47,0079	82,7859
Damping ratio, $z_i$ (%)	0,38	0,42	0,33	1,61	0,38
Relative modal participation factor, $\pi_i$ (–)	1.5	12	26	3	49

## References

1. Ibrahim SR, Mikulcik EC (1977) A method for the direct identification of vibration parameters from free response. *Shock Vib Bull* 47:183–196
2. Ibrahim SR (1977) Random decrement technique for modal identification of structures. *J Spacecraft Rockets* 14:696–700
3. Malekjafarian A, Brincker R, Ashory MR, Khatibi MM (2011) Identification of closely spaced modes using ibrahim time domain method. In: *Proceedings of the fourth international operational modal analysis conference*. Istanbul
4. Allemang R. J, Brown DL, (1982) A correlation coefficient for modal vector analysis. In: *Proceedings of the first modal analysis conference*. Orlando
5. Brüel & Kjaer (2012) Pulse – operational modal analysis vers. 5.3, SVS software
6. Brincker R, Zhang L (2009) Frequency domain decomposition revisited. In: *Proceedings of the third international operational modal analysis conference*. Porto Novo

# Chapter 30

## Modal Parameter Identification of New Design of Vertical Axis Wind Turbine

Prasad D. Chougule and Søren R.K. Nielsen

**Abstract** Vertical axis wind turbines have lower power efficiency than the horizontal axis wind turbines. However vertical axis wind turbines are proven to be economical and noise free on smaller scale. A new design of three bladed vertical axis wind turbine by using two airfoils in construction of each blade has been proposed to improve power efficiency. The purpose of two airfoils in blade design of vertical axis wind turbine is to create high lift which in turns gives higher power output. In such case the structural parameter identification is important to understand the system behavior due to its first kind of design before experimental analysis. Therefore a study is carried out to determine the natural frequency to avoid unstable state of the system due to rotational frequency of rotor. The present paper outlines a conceptual design of vertical axis wind turbine and a modal analysis by using Abaqus cae software. The study is limited to evaluate lowest fundamental modal frequencies and mode shapes of proposed wind turbine.

**Keywords** Vertical axis wind turbine • Multiple element airfoils • Modal analysis

### 30.1 Introduction

Various types of VAWTs have been suggested, most well-known of them is Darrieus VAWT which was invented in 1931 [3], Savonius type VAWT was invented in 1929 and the H-rotor type design, which came up after research activity carried out during 1970–1980 in UK. Recently, it has been documented that the Darrieus VAWTs can be alternative solution for small power production [4–6]. VAWT's are getting lot of importance due to its simplicity in construction and less noise. In general, Darrieus VAWT consist of three blades with straight, curved or spiral geometry to improve the efficiency. A review of such designs and techniques of VAWT are summarized by Bhutta et al. [2].

In current paper a new design of VAWT by using multiple airfoil element technology in which a blade is designed with two airfoils is proposed. The current work is in its initial phase of design. A testing of prototype is planned and it is aim of this work to perform free vibration analysis for determining parameters such as natural frequencies and mode shapes for proposed design to be used in an urban application.

This study is focused on numerical study using Abaqus cae [1] finite element software using its modeling features. A subspace method has been used to analyze the natural frequency while wind turbine mode shapes have been utilized because of their accuracy and faster solution. The paper represents preliminary results of modal analysis and detail study with more complexities of FE model will be implemented and validated with experimental work in future work.

In Sect. 30.2.1 the physical model and the FEM model is described in detail. Chapter 30.3 represents the results of modal analysis. The future work is very important and it is mentioned in Chap. 30.4. Finally, a work carried in this paper is summarized and conclusions drawn in Chap. 30.5.

---

P.D. Chougule • S.R.K. Nielsen  
Department of Civil Engineering, Aalborg University, Sohngaardsholmsvej 57, DK-9000 Aalborg, Denmark  
e-mail: [pdc@civil.aau.dk](mailto:pdc@civil.aau.dk); [srkn@civil.aau.dk](mailto:srkn@civil.aau.dk)

## 30.2 Material and Method

### 30.2.1 Physical Model

A VAWT proposed in this work consists of a Double airfoil blade design which is constructed by a main and a slat airfoil. The working principle of double airfoil is based on multiple element airfoil technology and is explained in detail in [7]. In designing double airfoil, the position of the slat airfoil is important due its effect of delaying the stall angle of airfoil to develop high lift. Therefore, the position of trailing edge TE of slat airfoil and orientation of slat airfoil are very important design parameters. The position and orientation of a slat airfoil with respect to the main airfoil is expressed by three parameters. The first two parameters describes the position of the TE of the slat airfoil along the local x-direction ( $x_{TE}$ ) and along local y-direction ( $y_{TE}$ ), respectively. The third parameter is the slat angle ( $\beta$ ), which represents the orientation of a slat airfoil and is the angle between the chord length of a slat airfoil ( $c_s$ ) and the local x-direction and is positive in nose up direction. These three parameters are shown in Fig. 30.1.

A 3D modeling is done in Abaqus cae environment, Fig. 30.2 shows the vertical axis wind turbine with double airfoil blade design proposed in this study.

It consists of three blades mounted vertically on a rotating shaft and in this study we are interested only in rotor modal parameters hence VAWT is mounted on fix base. The blade material is a fiber glass reinforced plastic and whole structure is of structural steel with square sections and pipes. The blade has aerodynamic shape with constant cross section and is assumed to be solid structure. Overall size of the model is 1.5 m diameter and 1.25 m height in which blades are 1 m length.

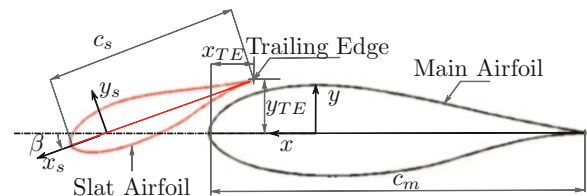


Fig. 30.1 Double airfoil

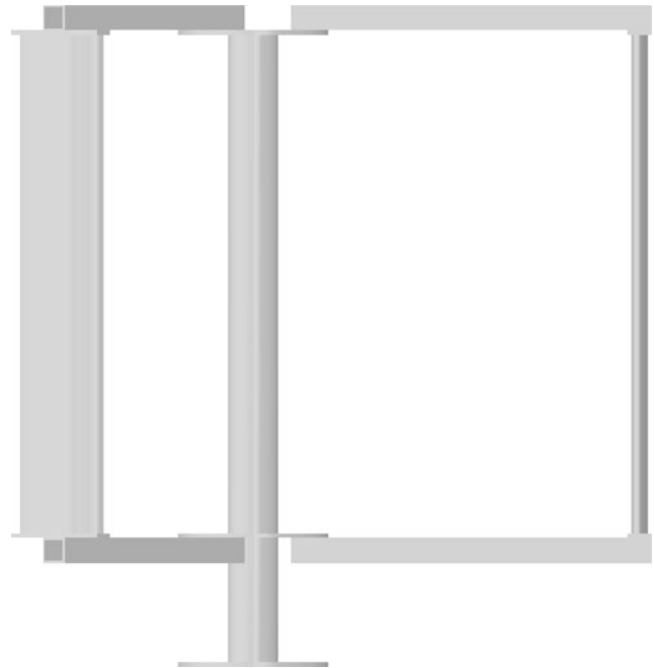
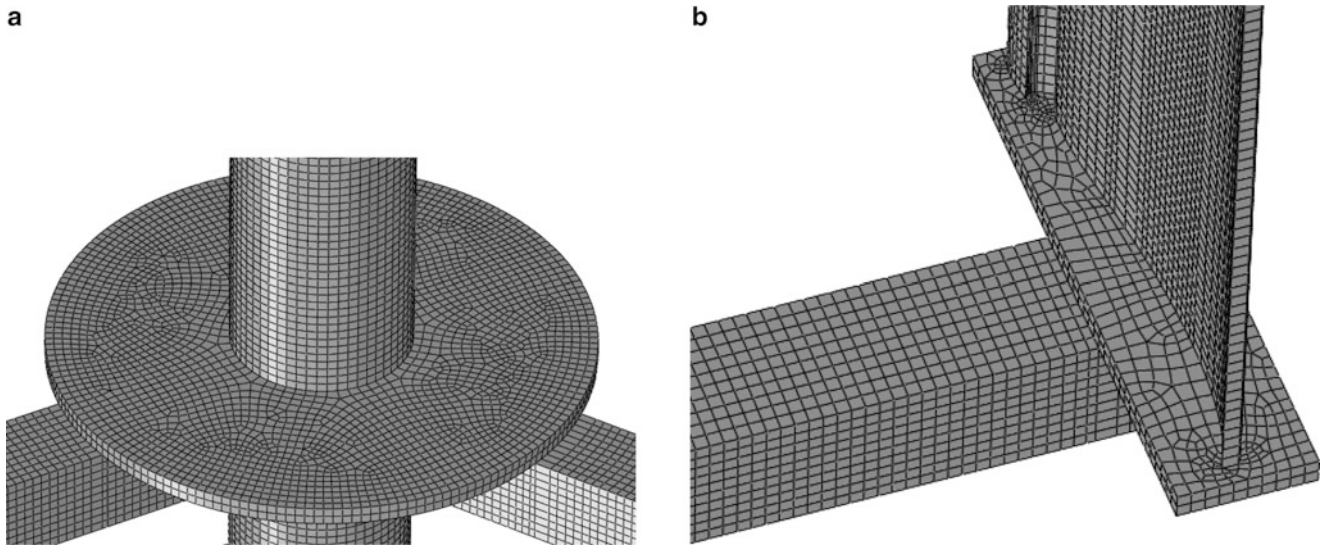


Fig. 30.2 Vertical axis wind turbine



**Fig. 30.3** Finite-element mesh. (a) Mesh at rotor shaft. (b) Mesh at blade connection

### 30.2.2 FEM Model

The commercial finite-element method (FEM) package Abaqus cae is used to model the VAWT using solid continuum finite elements. eight-node brick elements with quadratic spatial interpolation of the displacement are adopted with global mesh size of 5 mm. The mesh size is chosen based on the geometrical size of smallest part of rotor structure. The global mesh is created in such a way that the changes in the geometry is approximately aligned since it lowest fundamental frequencies are focus of this study. Figure 30.3 shows the mesh of the VAWT

All structural elements are merged by retaining the geometry of each structural element and then global mesh is created. Later on properties are assigned to the each structural element. The bottom of the end plate is constrained in all degrees of freedom.

The proposed VAWT consists of a steel structure to hold the blades made up of fiber glass reinforced plastic. In reality blades are fiber composites having two directional lay-up to provide structural strength. In this study it is focused on overall structural modes of the proposed VAWT therefore blades are assigned with solid element with a homogeneous and isotropic properties. The structure of proposed VAWT is made from square sections and pipes and also assigned with a homogeneous and isotropic properties to avoid complications in FE model and perform quick analysis.

The material is regarded as a linear elastic with a Young's modulus  $E_s = 2 \text{ GPa}$ , a Poisson ratio of  $\nu_s = 0.30$  and a mass density  $\rho_s = 7,800 \text{ kg/m}^3$ . The blades are assigned with linear elastic fiber reinforced plastic material with Young's modulus  $E_b = 1.81 \text{ GPa}$ , a poisson ratio  $\nu_b = 0.50$  and a mass density  $\rho_b = 1,800 \text{ kg/m}^3$ . Subscripts  $s$  and  $b$  represents steel structure and blade structure respectively.

## 30.3 Modal Analysis

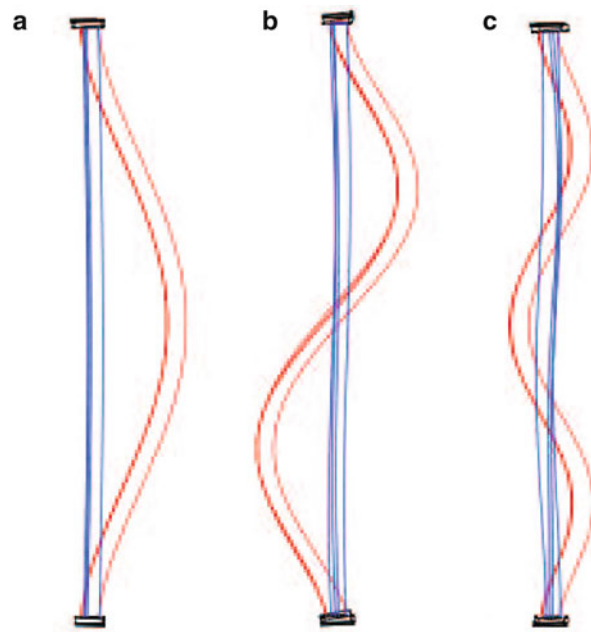
The fundamental Eigen frequencies and the corresponding Eigen modes are determined for proposed VAWT model as described in Chap. 30.2. The subspace solver implemented in Abaqus cae is applied for the structural analysis and 100 modes below 20 Hz frequency are requested with 300 maximum integrations to avoid computational errors. In this study lowest fundamental modes are of interest hence the modes are examined one by one in order to identify the required modes. The Eigen modes and the corresponding Eigen frequencies of the proposed wind turbine are extracted. Figure 30.4 shows the accumulated number of modes appearing below a given frequency in the interval from 0 to 20 Hz.

Figure 30.4 shows the first three independent modes of the slat blade. It is to be noted that in Figs. 30.4 and 30.5 the blue color represents the main blade and red color represents a slat blade.

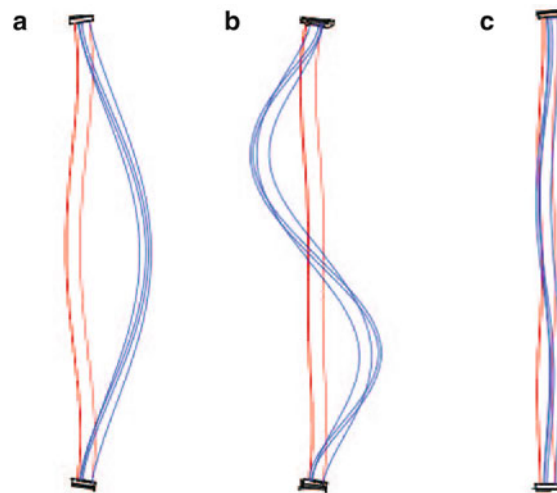
Figure 30.5 shows the first three independent modes of the main blade



**Fig. 30.4** Mode shapes of slat blade. (a) First mode at 0.60 Hz  
(b) Second mode at 1.63 Hz  
(c) Third mode at 3.24 Hz



**Fig. 30.5** Mode shapes of main blade. (a) First mode at 0.88 Hz.  
(b) Second mode at 2.86 Hz.  
(c) Third mode at 3.90 Hz



### 30.4 Conclusion

A modal analysis has been performed for proposed VAWT design in the present paper to determine modal frequencies and mode shapes. The investigations are based on the primary design of proposed VAWT. The VAWT structure being modeled was made up of blade structure and supporting structure of two different materials. FE model was utilized to perform modal analysis by linear perturbation implemented in the commercial FE code Abaqus. The FE model was simplified to make analysis quicker to determine modal frequency and corresponding mode shapes for proposed VAWT quantitatively.

It is found from the mode shapes that the location of slat airfoil with respect to the main airfoil is the critical due to modal behavior of the slat blade. It is important to make slat blade more rigid to avoid large displacements because it could be possible that the slat blade might penetrate the main blade since both blades are mounted very close to each other due to necessity of new blade design.

## 30.5 Future Work

The present study was performed to quantitatively determine the modal frequencies and corresponding mode shape by simplified geometry and assuming solid elements. It is very important to model blade structure as shell element due to airfoil shape of the blades. secondly it is needed to implement composite blade structure which will give more precise estimate of the modal frequencies.

Structural damping is not implemented in both rotor structure and blade structure. Since blade structure is flexible it will introduce aerodynamic damping in the blade structure which is critical for slat blade which will introduce uncontrollable rotor vibrations. A simple blade testing can be performed to determine modal frequencies experimentally to validate the FEM model. It is planned to make testing of proposed VAWT to determine the performance of new design of blades alongside modal frequencies will be determined from experiment.

**Acknowledgements** The SYSWIND project (project no. 238325) funded by the Marie Curie Actions is acknowledged for the financial support under the grant Seventh Framework Programme for Research and Technological Development of the EU.

## References

1. ABAQUS Analysis. User's manual version 6.10. Dassault Systèmes Simulia Corp., Providence
2. Bhutta MMA, Hayat N, Fahrooq AU, Ali Z, Jamil ShR, Hussian Z (2008) Evaluation of different turbine concepts for wind power. *Renew Sustain Energy Rev* 12:1419–1434
3. Darrieus GJM (1931) Turbine having its rotating shaft transverse to the flow of the current. United States Patent Office, Patent No. 1835018, 1931
4. Eriksson S, Bernhoff H, Leijon M (2008) Evaluation of different turbine concepts for wind power. *Renew Sustain Energy Rev* 12:1419–1434
5. Kjellin J, Bulow F, Eriksson S, Deglaire P, Leijon M, Bernhoff H (2011) Power coefficient measurement on a 12 kw straight bladed vertical axis wind turbine. *Renew Energy* 36:3050–3053
6. Muller G, Jentsch MF, Stoddart E (2009) Vertical axis resistance type wind turbines for use in buildings. *Renew Energy* 34:1407–1412
7. Smith AMO (1975) Hight lift aerodynamics. *J Aircr* 12(6):501–530

# Chapter 31

## Predicting Dynamic Strain on Wind Turbine Blade Using Digital Image Correlation Techniques in Conjunction with Analytical Expansion Methodologies

Jennifer Carr, Javad Baqersad, Christopher Niezrecki, Peter Avitabile, and Micheal Slattery

**Abstract** Wind turbine blades are often subjected to static and dynamic testing to identify the performance levels of the blades. In general, strain gages are employed to capture strain data at discrete points. Recent advances in digital image correlation (DIC) and digital photogrammetry have allowed for new opportunities for blade inspection and structural health monitoring. DIC allows for imaging techniques to measure displacement values at various points on the structure. This displacement data is then used in conjunction with a finite element model to apply modal expansion techniques to obtain displacement values at each finite element degree of freedom for each time step of dynamic transient data. This technique is used to predict strain values at any point on the structure. This paper presents results obtained from dynamic testing at limited measurement locations to predict the full field dynamic strain for two structures evaluated. A major benefit to this approach is that strain values can be found at locations that are not in the measurement field of view, including on surfaces that are contained within the structure.

**Keywords** Wind turbine blade • Digital image correlation • 3D point tracking • Modal expansion • Dynamic strain

### 31.1 Introduction

Generally, wind turbine blades are subjected to static and dynamic tests to validate the structural configuration. These tests include both load and fatigue tests. During testing, the blades are instrumented with strain gages, which are located at discrete points. As a result, the strain information from the tests is only available at these points, rather than full-field.

In a previous set of papers, the advantages of using digital image correlation in wind turbine blade applications were shown [1, 2]. Full-field strain was measured using DIC techniques first on a cantilevered aluminum beam, and then on a Southwest Windpower turbine blade. Both static and dynamic tests were performed. The DIC results were compared to traditional strain gages mounted on the structures. The DIC results correlated well to the strain gages.

The work in this paper focuses on predicting full-field strain results on a wind turbine blade, including on surfaces not measured, using digital image correlation techniques and modal expansion techniques. Dynamic tests were performed and analyzed. The test configuration is described and the measurements from conventional strain gages are compared to the DIC technique to validate the method and show the advantages of the full-field approach.

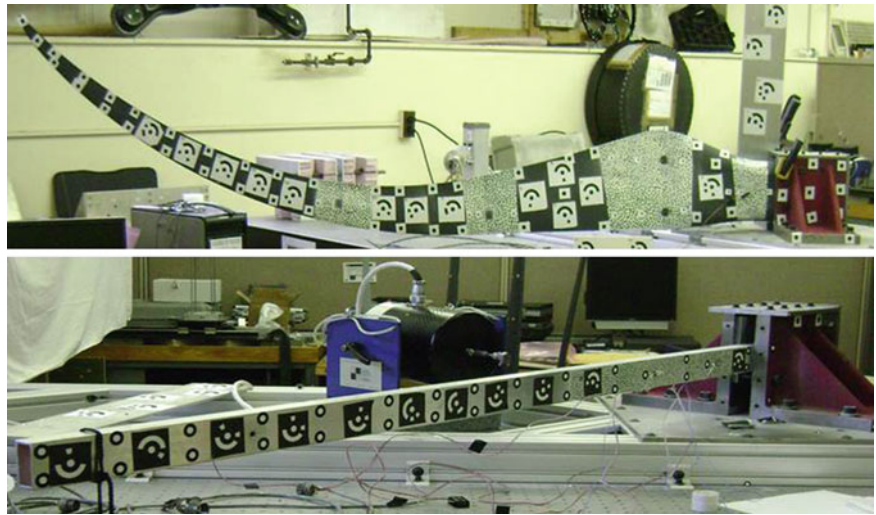
In preparation for the testing of an actual wind turbine blade, a simple beam-like structure was used for the validation of the test set-up and methodology (see Fig. 31.1). The beam is very easy to characterize from both a test and model standpoint and the results provide more credibility for the proposed approach. Both the static and dynamic testing results measured using strain gages and DIC techniques are presented and analyzed.

---

J. Carr (✉) • J. Baqersad • C. Niezrecki • P. Avitabile  
Structural Dynamics and Acoustic Systems Laboratory, University of Massachusetts Lowell, One University Avenue,  
Lowell, MA 01854, USA  
e-mail: [jennifer.carr17@gmail.com](mailto:jennifer.carr17@gmail.com)

M. Slattery  
Southwest Windpower, 1801 W. Route 66, Flagstaff, AZ 86001, USA

**Fig. 31.1** Test setup for turbine blade (*top*) and aluminum beam (*bottom*)



## 31.2 Theoretical Background

For this work two significant techniques are utilized, namely, Digital Image Correlation and Model Reduction/Expansion techniques. These are described next.

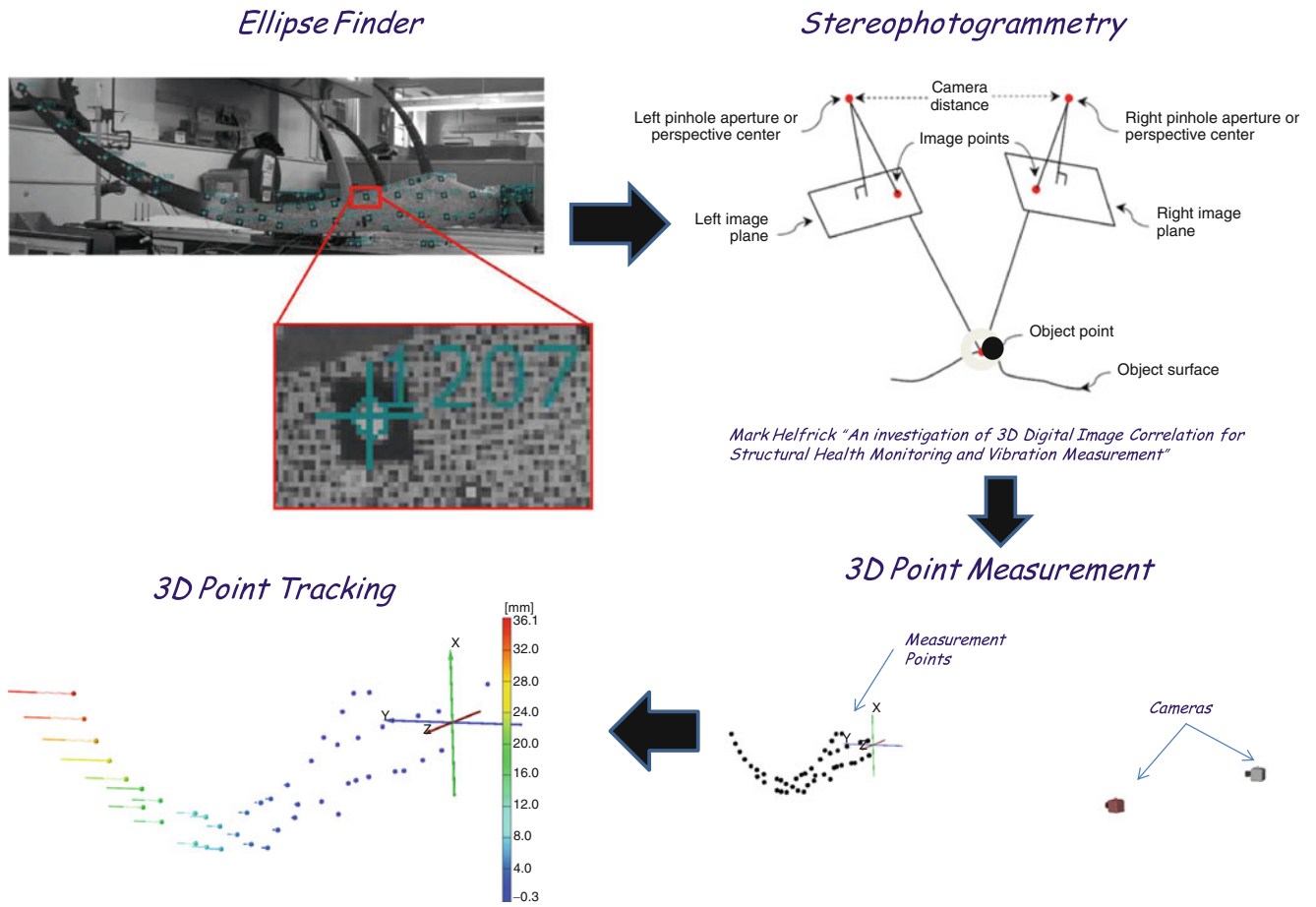
### 31.2.1 Digital Image Correlation

Digital Image Correlation and 3D Dynamic Point Tracking are measurement techniques that employ stereophotogrammetry to locate three-dimensional coordinates of a structure and tracking methods to determine the displacements of those points. The work presented in this paper was performed using Pontos™ Dynamic 3D Analysis Software.

To utilize the Pontos software, the structure of interest first must be prepared by placing black and white points (optical targets) on the surface of the structure at the desired measurement locations. Then two high-speed cameras are positioned and calibrated to determine their position in space relative to each other. An ellipse-finder algorithm was used to find, number, and determine the location of the measurement points in space. Throughout the test the cameras take a series of images at a defined frequency. For each image, the ellipse-finder identifies the points, and these points are tracked from image to image. Stereophotogrammetry determines the 3D coordinates of the points through the images taken by the two cameras. The cameras identify a common point on each image. A line-of-sight can be constructed from the camera locations to the point on the object. Because the position of the cameras were determined through the calibration process, the intersection of the line-of-sight beams can be determined through triangulation, which gives the 3D coordinates of the points. Displacement measurements can be made based on changes in coordinates between the images. An overview of the DIC measurement process is shown in Fig. 31.2. Through the use of the DIC software, the deformation and motion of a complex structure can be captured with this non-contact technique.

### 31.2.2 Modal Reduction/Expansion Techniques

Model reduction is necessary in order to develop expansion approaches for modal data for the unmeasured translational DOF (degree of freedom) as well as for rotational DOF. For this work the expansion is needed for augmenting the limited set of real-time operating data to provide a full field displacement solution. The reduction techniques are the basis of the expansion discussed in this work. These techniques have been presented in earlier work cited in the references; only summarizing equations are presented below. Several model reduction methods have commonly been used for expansion of measured data but the SEREP (System Equivalent Reduction-Expansion Process) [3] technique is used for this work. For any reduction/expansion process, the relationship between the full set of degrees of freedom and a reduced set of degrees of freedom can be written as



**Fig. 31.2** 3D dynamic point tracking measurement overview

$$\{X_n\} = [T]\{X_a\} \tag{31.1}$$

The transformation matrix [T] is used to project the full mass and stiffness matrices to a smaller size. The reduced matrices can be formulated as

$$[M_a] = [T]^T [M_n] [T] \tag{31.2}$$

$$[K_a] = [T]^T [K_n] [T] \tag{31.3}$$

For the specific work in this paper, the SEREP method has been used for the expansion of mode shapes. The SEREP produces reduced matrices for mass and stiffness that yield the exact frequencies and mode shapes as those obtained from the eigensolution of the full size matrix. The SEREP transformation is formed as

$$[T_U] = [U_n] [U_a]^g \tag{31.4}$$

The SEREP transformation is developed with analytical mode shapes for the structure (but can also be evaluated using measured modal vectors as done in Chipman’s work [4] and Pingle’s work [5]). Equation 31.1 is used for expansion of measured real-time operating data [RTO<sub>a</sub>] to the full space of the finite element model [ERTO<sub>n</sub>] and is written as

$$[ERTO_n] = [T] [RTO_a] \tag{31.5}$$

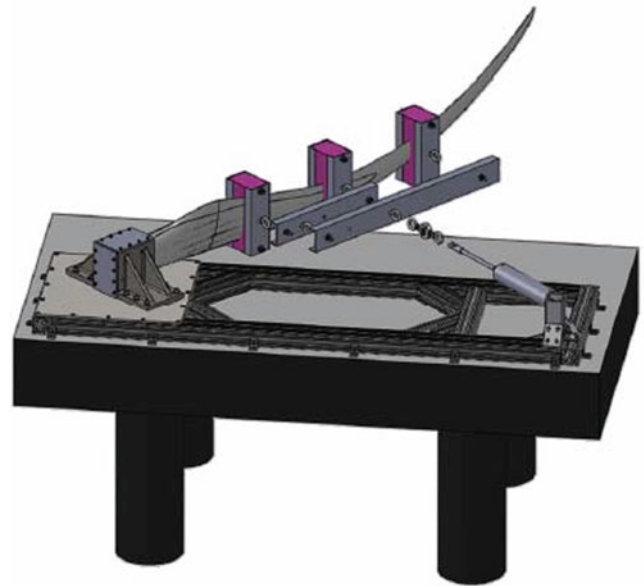
The transformation matrix, [T], can be one of the commonly used matrices used but SEREP is utilized for all the work presented herein.

### 31.3 Structure Description

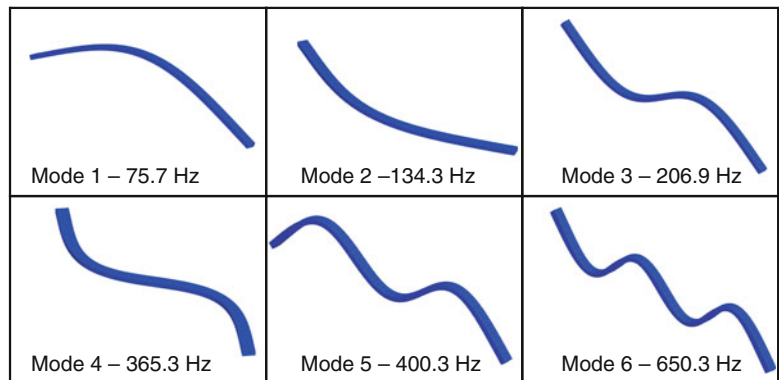
Two structures were evaluated as part of this work – a simple cantilever beam type structure and a Southwest Windpower Turbine Blade. Testing and analysis was first performed on a 5-ft long aluminum beam as a simpler structure to demonstrate the methodology. The cross-section of the beam was a rectangular tube with dimensions of 1-in. by 2-in. and a thickness of 1/8-in. The beam was clamped in a fixture specifically designed for testing a wind turbine blade. More details of the test rig are described in Ref. [6]. The beam is very easy to characterize from both a test and model standpoint and the results provide more credibility for the proposed approach. Following the testing of the beam, a small wind turbine blade, provided by Southwest Windpower, was tested using the same techniques. Figure 31.3 shows an overview of the test setup.

### 31.4 Model Description

To perform the modal expansion for predicting strain on all surfaces of the structure, finite element models of the beam and blade were created and validated through correlation to mode shapes. The 1/8" thick tubular beam FE model was defined using plate elements; the model consisted of 1,260 nodes and 1,248 elements with appropriate material properties for the structure. The frequencies and flexible mode shapes obtained from the finite element model in the free-free configuration are shown in Fig. 31.4.



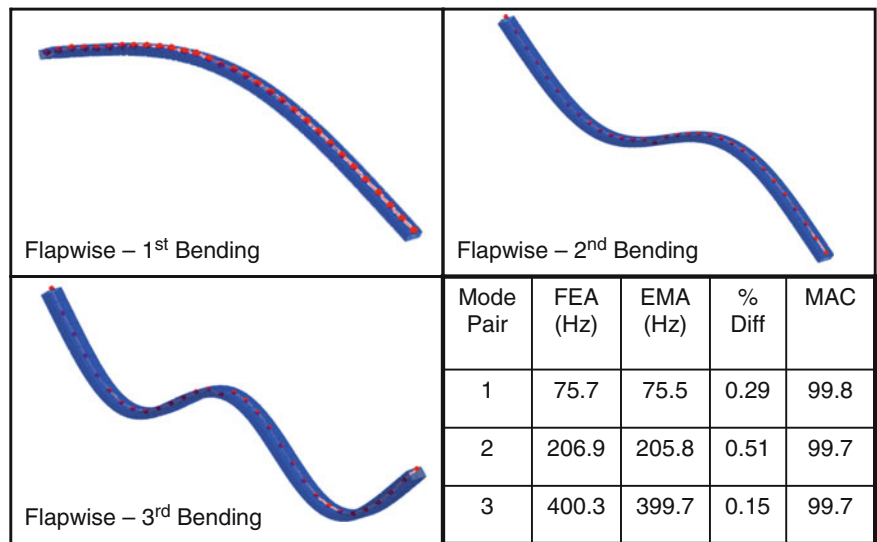
**Fig. 31.3** Test rig including the mounting fixture, turbine blade, whiffle tree, and pneumatic actuator



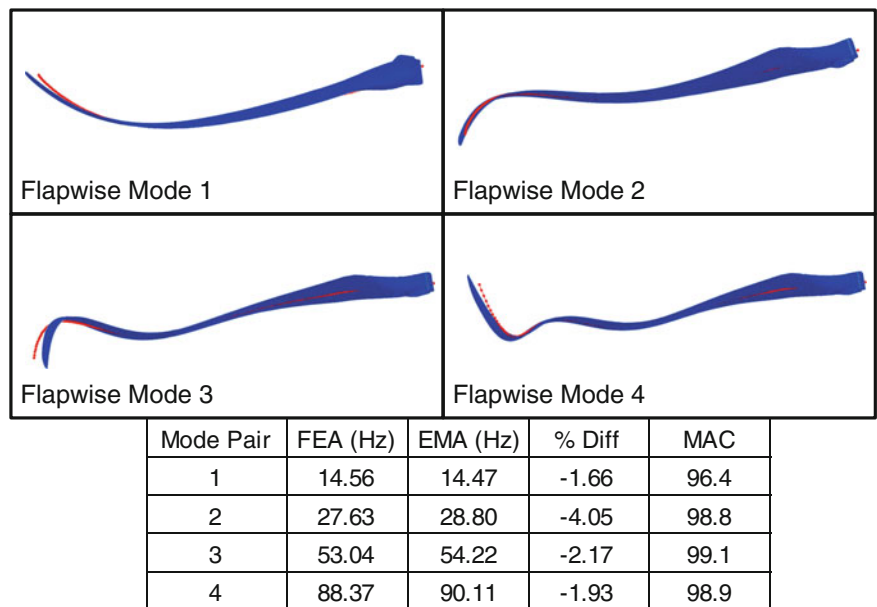
**Fig. 31.4** Beam finite element model free-free mode shapes



**Fig. 31.5** Correlation of free-free test to beam model



**Fig. 31.6** Correlation of free-free test to blade model



The finite element model was initially validated with a simple free-free modal test. Only the modes in the flapwise direction were of interest, so a uniaxial accelerometer was used to measure motion in the flapwise direction. The first three flapwise modes were measured and correlated to the model. This correlation is shown in Fig. 31.5. The natural frequencies were all within 0.5 % and the minimum MAC value was 99.7.

A finite element model of the wind turbine blade was created using solid elements. The process in developing this model is described in Ref. [7]; the model consisted of 56,299 nodes and 29,648 elements. Figure 31.6 shows a correlation of the finite element modes to free-free modal testing. Once again, only the flapwise modes were correlated, as those were the modes of interest.

## 31.5 Testing Performed

### 31.5.1 Beam Testing

The first tests were performed on the aluminum beam to validate the technique. (For the complete evaluation of the techniques proposed, the beam was subjected to static tests, sinusoidal dynamic tests and pluck tests. However, for this paper only the sinusoidal dynamic tests are presented here; the other tests are still under development and will be the subject of future publications.)

Dynamic testing was performed on the beam using a shaker with a discrete sine input at the first natural frequency of the system (determined to be 14.8Hz through modal testing). Displacement measurements from the DIC were recorded at 29 points. These displacements were then expanded to all nodes of the finite element model using the first mode from the FE model with SEREP expansion technique. These expanded displacements were applied to the FE model to determine the strain. The results of the shaker test are shown in Fig. 31.7. For the shaker testing, the peak values of strain compare very well.

### 31.5.2 Blade Testing

Following the preliminary testing on the beam, similar tests were performed on the wind turbine blade. (Again, for the complete evaluation of the techniques proposed, the blade will be subjected to static tests, sinusoidal dynamic tests and pluck tests. However, for this paper only the sinusoidal dynamic tests are presented; the other tests are still under development and will be the subject of future publications.) The first test was the shaker test with a discrete sine input near the first system natural frequency (determined to be 5.6 Hz through modal testing). This test was performed first due to the simplicity of expanding data when primarily only one mode is excited. The strain results are shown in Fig. 31.8. The top image in the figure depicts the predicted strain field from the expanded displacements applied to the finite element model, with red indicating the areas of highest strain. From this model, the predicted strain was compared to strain gages mounted to the blade at three points. These results compare very well overall.

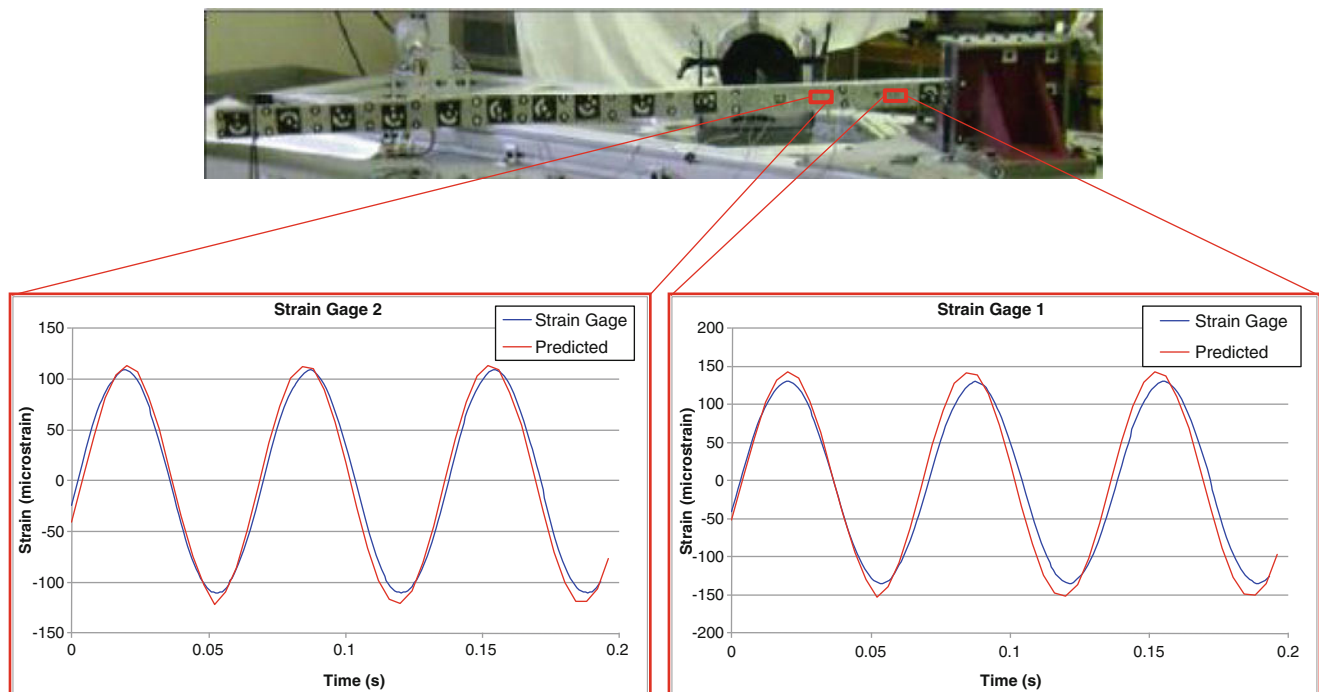
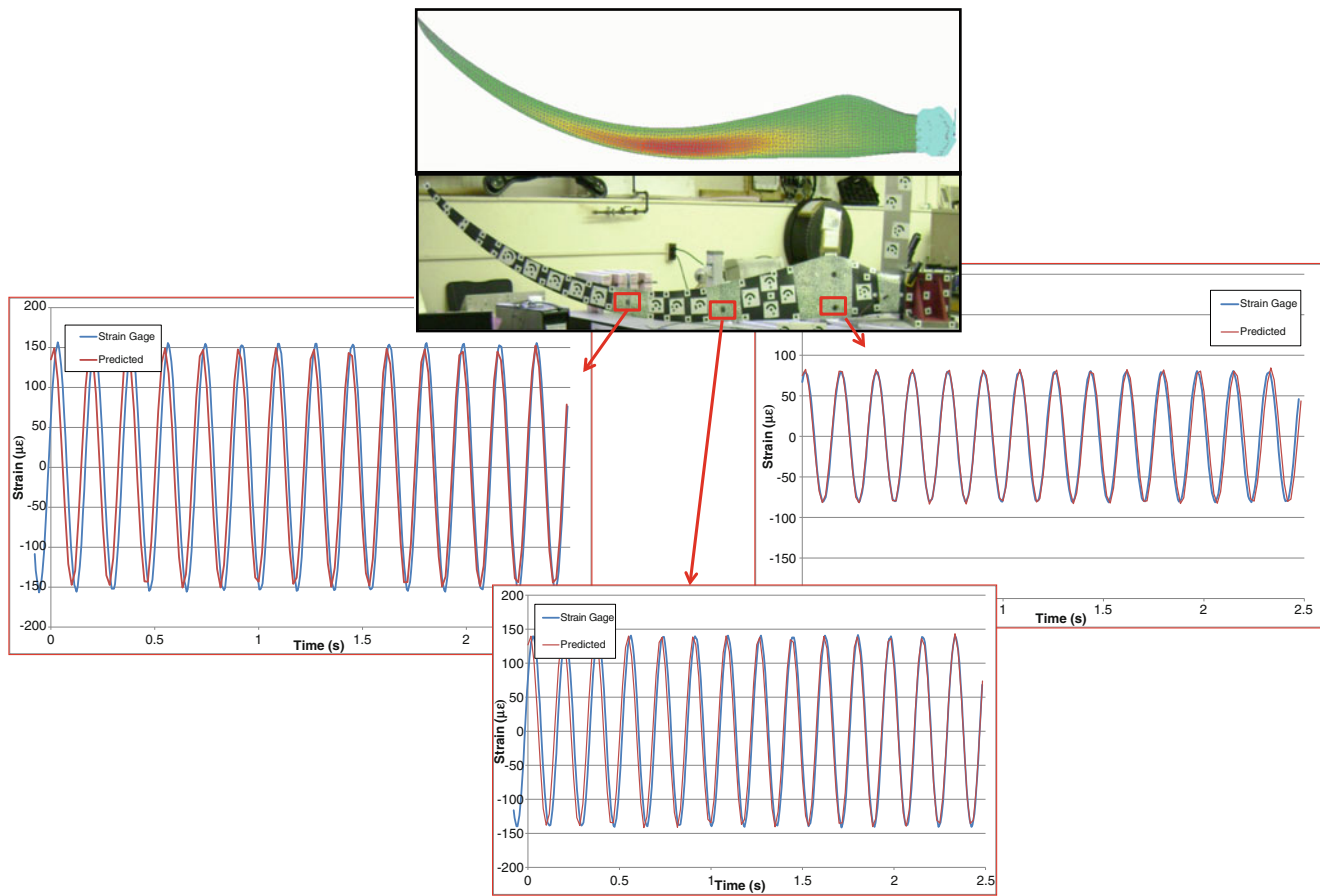


Fig. 31.7 Shaker excitation of a box beam comparing experimental and modal expansion results



**Fig. 31.8** Shaker excitation of a blade comparing experimental and modal expansion results

## 31.6 Conclusion

Static and dynamic measurements for wind turbine blades are generally required for validation and certification procedures, which usually record strain measurements using strain gages at discrete points. Digital image correlation and dynamic point tracking have been used for making full-field surface measurements of displacement and strain in many applications and is currently being explored for measurement on turbine blades. For this work, a method of predicting full-field strain on all surfaces using digital image correlation and modal expansion techniques was explored. Preliminary tests were performed on a cantilevered aluminum box beam to validate the technique. Dynamic tests were performed as part of this work. For the two structures evaluated, a simple cantilevered beam and a Southwest Windpower Turbine Blade, dynamic strain was measured and compared to expanded data from a limited set of measurement locations to obtain full field strain information. For both structures very good results were obtained thereby proving the adequacy of the proposed methodology.

**Acknowledgements** Some of the work presented herein was partially funded by NSF Civil, Mechanical and Manufacturing Innovation (CMMI) Grant No. 0900543 entitled “Dynamic Stress–Strain Prediction of Vibrating Structures in Operation”. Any opinions, findings, and conclusions or recommendations expressed in this material are those of the authors and do not necessarily reflect the views of the particular funding agency. The authors are grateful for the support obtained.

The test rig used in all testing found in this paper was a direct result of the effort of a Capstone Design Team during the Spring Semester of 2011. Jennifer Carr, Samuel Dyas, Matthew Ertos, Jack LoPiccolo, Christopher Nonis, and Joseph Romano were responsible for the design and fabrication of the test rig and development of test plans and procedures for operating the test rig. Their efforts were substantial and very much appreciated.

Southwest Windpower supplied several blades and CAD models and provided consultation related to this work. Their time and support and materials are greatly appreciated.

## References

1. Carr J, Baqersad J, Avitabile P, Niezrecki C (2011) Dynamic stress-strain on turbine blade using digital image correlation techniques. Part 1 – Static load and calibration. In: Proceedings of the IMAC-XXX, Jacksonville, 30 Jan–2 Feb 2011
2. Carr J, Baqersad J, Avitabile P, Niezrecki C (2011) Dynamic stress-strain on turbine blade using digital image correlation techniques. Part 2 – Dynamic measurements. In: Proceedings of the IMAC-XXX, Jacksonville, 30 Jan–2 Feb 2011
3. O'Callahan JC, Avitabile P, Riemer R (1989) System equivalent reduction expansion process. In: Seventh international modal analysis conference, Las Vegas, Feb 1989
4. Chipman C (2009) Expansion of real time operating data. Master's thesis, University of Massachusetts Lowell, May 2009
5. Pingle P (2010) Prediction of full-field dynamic stress-strain from limited sets of measured displacement data. Doctoral thesis, University of Massachusetts Lowell, Aug 2010
6. Carr J, Dyas S, Ertos M, LoPiccolo J, Nonis C, Romano J (2011) Static and dynamic testing of a 7-ft wind turbine blade. University of Massachusetts Lowell, James B. Francis College of Engineering, Department of Mechanical Engineering, Capstone design, 6 May 2011
7. LoPiccolo J, Carr J, Niezrecki C, Avitabile P (2011) Validation of a finite element model used for dynamic stress-strain prediction. In: Proceedings of the IMAC-XXX, Jacksonville, 30 Jan–2 Feb 2011

# Chapter 32

## Dynamic Characterization of a Free-Free Wind Turbine Blade Assembly

Javad Baqersad, Christopher Niezrecki, Peter Avitabile, and Micheal Slattery

**Abstract** Accurate prediction of full-field dynamic stress–strain of rotating structures is needed (e.g. wind turbines or helicopter rotors) during operation for condition based monitoring and damage prognosis. In order to perform a dynamic stress–strain prediction of a wind turbine using empirical data, a validated numerical model is required. To understand the dynamic properties and develop a validated finite element model of a 3-bladed wind turbine, an experimental modal test has been conducted and is reported in this paper. Impact hammer modal testing was performed with three wind turbine blades mounted to a hub while supported in a free-free configuration to determine the assembly’s resonant frequencies and mode shapes. The results reveal several closely spaced modes present within the turbine assembly. Furthermore, some experimentally derived modes of the multi-blade system can be predicted by determining the modes of an individual blade supported in a cantilevered boundary condition.

**Keywords** Modal analysis • Wind turbine • Multi-blade • Experimental modal

### 32.1 Introduction

Wind energy is known as a promising source of clean and renewable energy that helps to offset greenhouse gas emissions. Wind turbines have grown significantly in size as the need for more consumable energy increases and it is predicted that these machines will continue to grow in the decades to come. However, as the size of these machines scales to meet energy demands, wind turbines are subjected to a combination of increased static and dynamic loading that has an impact on their performance, efficiency, and reliability. The increased loading makes the need for structural health monitoring and damage prognosis of these sizable machines more important. Additionally, a comprehensive understanding of the dynamics of wind turbines is usually an integral part of many health monitoring algorithms. Therefore, the dynamics of wind turbine has been extensively studied using theoretical approaches in recent years. In order to have accurate theoretical models, the models need to be validated and/or updated using experimental measurements.

Experimental set-ups to perform the modal analysis of a single blade can be readily conducted in either a laboratory or a blade test facility. Thus, numerous researchers have performed experimental modal analysis on single blades of wind turbines [1–6]. Furthermore, the dynamics of assemblies of blades connected to supports such as towers or fuselages have been measured by using accelerometers [7], piezoelectric sensors [8, 9], laser Doppler vibrometers [10], and photogrammetric cameras [11–17]. However, few studies in the literature can be found that experimentally model the dynamics of a multi-blade system in a known boundary condition such as free-free or cantilevered configuration. The free-free configuration is desirable because it provides valuable information about the dynamics of an assembly of blades without any external constraints, is repeatable, and is a boundary condition that is easy to create in a laboratory setting.

---

J. Baqersad • C. Niezrecki (✉) • P. Avitabile  
Structural Dynamics and Acoustic Systems Laboratory, One University Avenue, Lowell, MA 01854, USA  
e-mail: [Javad\\_Baqersad@student.uml.edu](mailto:Javad_Baqersad@student.uml.edu); [Christopher\\_Niezrecki@uml.edu](mailto:Christopher_Niezrecki@uml.edu); [Peter\\_Avitabile@uml.edu](mailto:Peter_Avitabile@uml.edu)

M. Slattery  
Southwest Windpower, 1801 W. Route 66, Flagstaff, AZ 86001, USA  
e-mail: [Micheal.Slattery@windenergy.com](mailto:Micheal.Slattery@windenergy.com)

The current paper reports the results obtained and lesson learned during an experimental modal test of a multi-blade wind turbine placed in a free-free configuration. The study aims to improve the understanding of the dynamic characteristics of multi-blade systems using experimental measurements obtained only from a single blade test placed in a cantilevered boundary condition.

## 32.2 Model Description

Experimental modal analysis is an approach for identifying the modal parameters of structures using a combination of input and output measurements. For an impact hammer experimental modal test, an impact force is applied to a structure and the response of the structure is measured at several locations using accelerometers. Frequency response functions (FRFs) are calculated to identify modal parameters of the structure. Free-free modal testing is a practical and readily available approach to study the dynamic characteristics of a small-scale multi-blade wind turbine.

Three blades of Southwest Windpower Skystream 4.7 were mounted to a central hub while supported in a free-free configuration. The 2.3 m blades were made of a composite/plastic material. The hub included an aluminum component and a steel plate that were connected using 12 steel bolts. In order to minimize the inconsistencies that can be caused by the variability of the supports and owing to the high stiffness of the roots of the blades and the hub compared to the tip of the blades, the multi-blade wind turbine was supported by using several bungee cords connected to the hub. A photograph of the test set-up is shown in Fig. 32.1.

The number of sensors and their locations were selected by using a finite element model of the multi-blade wind turbine. By performing an eigensolution on the numerical model in a free-free boundary condition, FE mode shapes were extracted. Using the FE model, an appropriate set of sensor locations was selected so that all the modes of interest could be identified.

The origin of the coordinate system for the turbine is centered at the center of the hub where the x and z axes are located in the rotating plane and z points toward the tip of Blade 1 (see Fig. 32.2). The y axis refers to the transverse displacement of the blade (i.e. the out-of-plane or flapwise direction).

Because extracting both flapwise and edgewise modes were desirable, triaxial accelerometers were selected for the measurement. A 60-channel LMS data acquisition system was used to record the response of the structure and the input force. Due to high flexibility of the tips of the blades, force impacts were made closer to the hub, near the middle of each blade. Twelve accelerometers were mounted per blade distributed at locations over all three blades of the turbine. The limitations in the number of available accelerometers and the available channels of the data acquisition system did not allow all the measurement to be carried out in a single set-up of accelerometers. Therefore, the test was performed on three separate set-ups; however, this requires extra consideration to mass loading which is discussed further. In the first

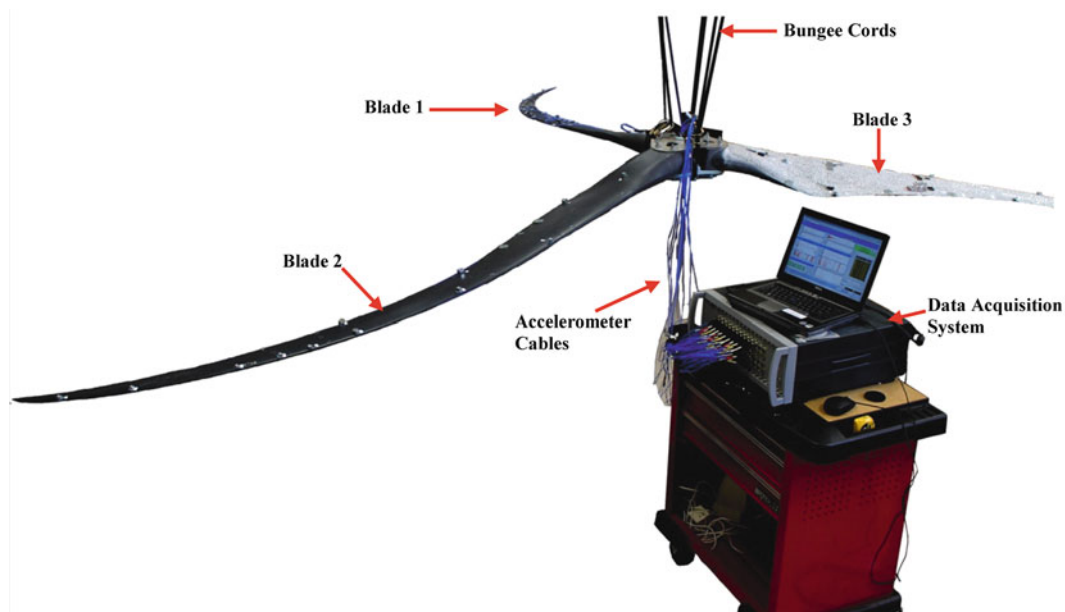
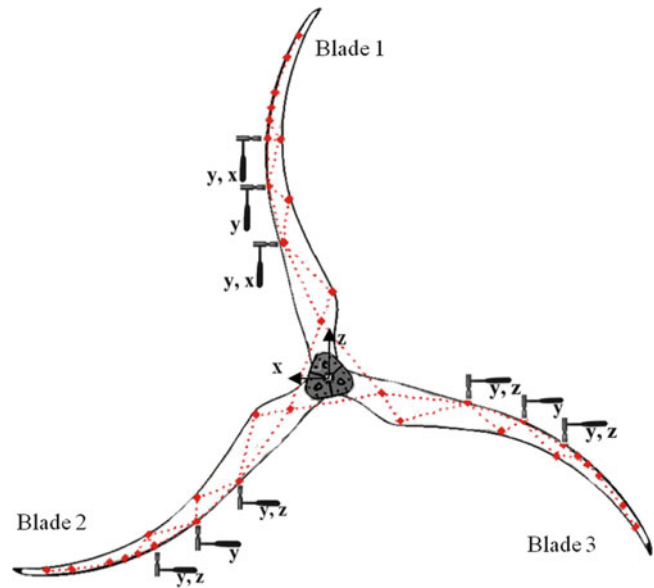


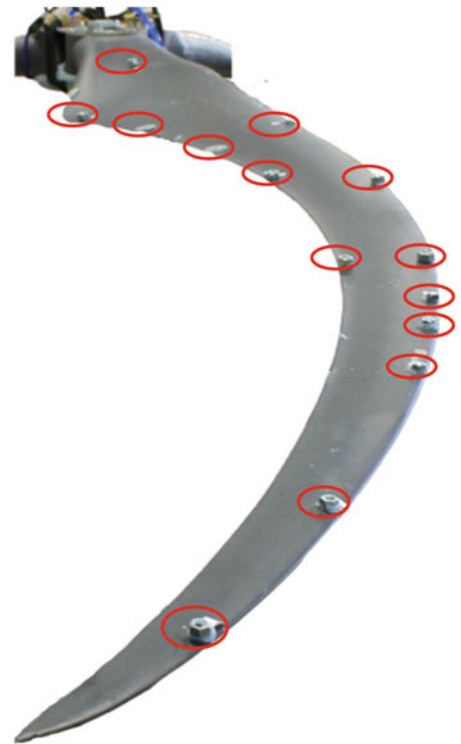
Fig. 32.1 Modal impact hammer test set up on the three-bladed assembly using a free-free configuration



**Fig. 32.2** Thirty-six accelerometer locations (*red dots*) and 15 impact locations with the force impact orientation directed either along y-axis (out-of-plane) or along either the x-axis or z axis (in-plane)



**Fig. 32.3** A photograph of dummy masses on one of the blades



set-up, all the accelerometers were installed on Blade 1. The impact hammer excited the turbine at nine different locations in the out-of-plane direction and at six locations in the in-plane direction. The response of the turbine to the impacts was measured by using 12 triaxial accelerometers mounted to Blade 1 ( $12 \times 3 = 36$  channels). Then, the accelerometers were moved to Blade 2 and the 15 impacts were repeated. Finally, the accelerometers were moved to Blade 3 and the 15 impact tests were repeated again. Therefore, the test included measurements of the vibration when the blades were impacted at 15 separate locations/orientations (each with five averages). A drawing of the accelerometer and impact locations with associated orientation is shown in Fig. 32.2.

To compensate for the removal of accelerometers, dummy masses were installed to emulate the weight of the removed accelerometers. When the accelerometers are mounted to one blade, a set of dummy masses were used on the accelerometer locations of the other two blades (see Fig. 32.3). In order to lower the mass loading effects, lighter accelerometers were used

at the points near the tip of the blades. (The use of dummy masses on this type of lightweight blade structure is critical to the success of measuring and extracting useful mode shapes. If these compensation masses are not used then there would be a significant mass loading effect and the frequency response functions used in the modal extraction process would be not of sufficient quality to extract accurate mode shapes.)

### 32.3 Cases Studied

#### 32.3.1 Case 1: Experimental Measurement Using a Low Frequency Bandwidth

An experimental modal test was performed on the multi-blade wind turbine. For this part of the test, a frequency bandwidth of 128 Hz (with 1,024 spectral lines) was used. The acquisition system recorded the response of the structure due to the impact of a hammer (with a rubber tip) for 8 s. In order to find resonant frequencies of the assembly, a LMS PolyMAX [18] stability diagram was used. As can be seen in the stability diagram shown in Fig. 32.4, there are several closely spaced modes in FRFs of the multi-blade turbine. The stability diagram generated some distinct stable poles and others that were not as easy to discern. This is likely caused by the shifting in the sensors from one test to the next as the dummy masses

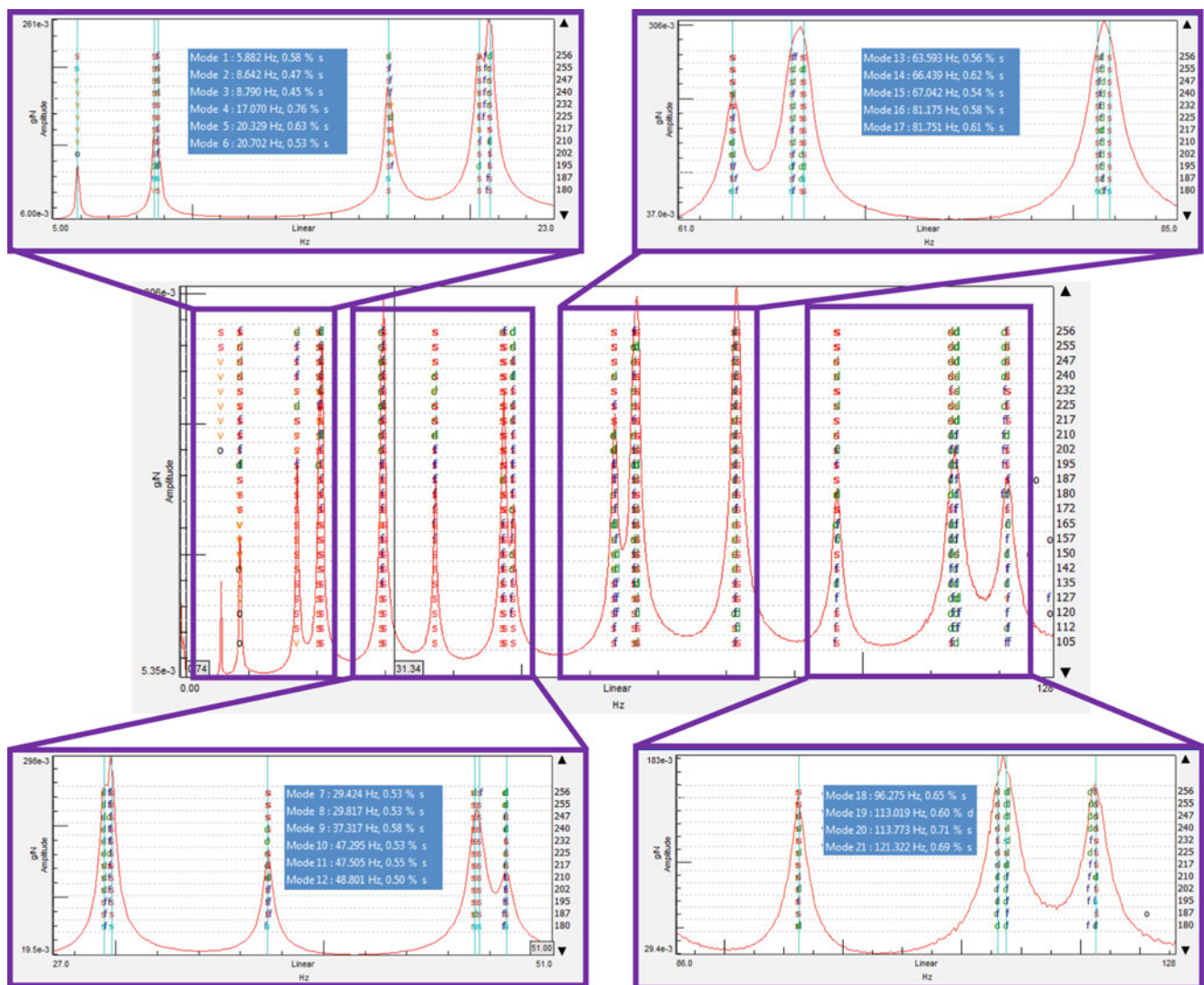


Fig. 32.4 The stability diagram for all the measured FRFs of in Case 1

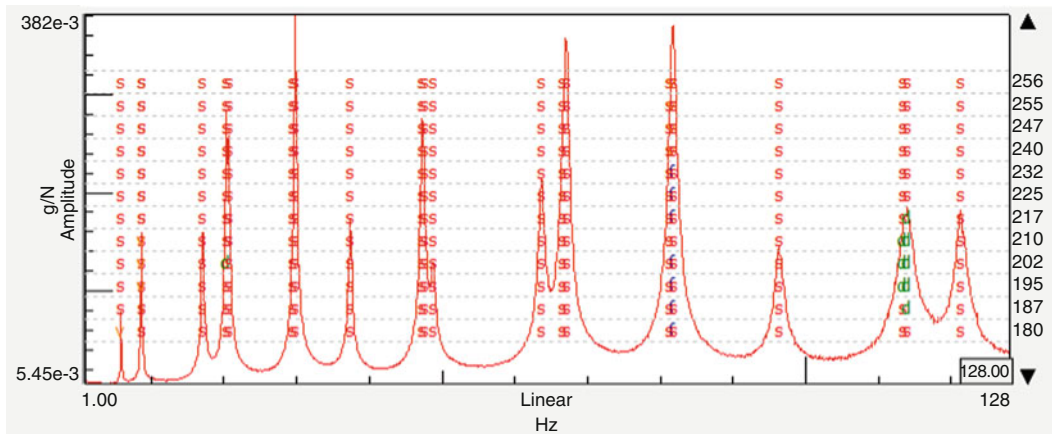


Fig. 32.5 The stability diagram for the FRF for a single set-up with accelerometers located only on Blade 1

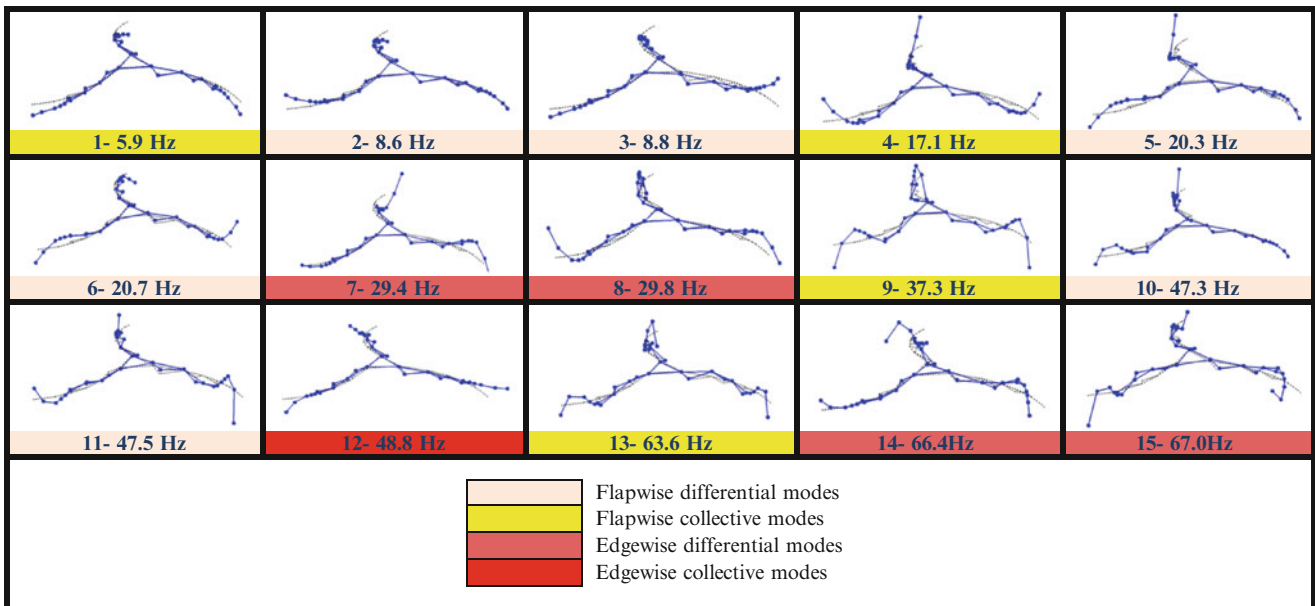


Fig. 32.6 The mode shapes of the multi-blade turbine in a free-free configuration (for interpretation of the references to color in this figure and other figures and tables, the reader is referred to the electronic version of the paper)

are moved, therefore generating the equivalent modes at slightly different frequencies between tests. It is not possible to perfectly replicate the spatial mass distribution with dummy masses. The discrepancies are caused by the moving masses or mass differences that affect higher frequency modes more than the lower order modes.

In order to identify the true location of the stable poles that reveal the correct number of mode shapes, the data was reprocessed for each of the three individual blade set ups. The stability diagrams for the individual tests were used to better understand the diagram when data for all the three blade tests were included. An example of a stability diagram for a single set up is shown in Fig. 32.5. Once the exact number of modes was determined, the stability diagram of all the collected FRFs in Fig. 32.4 was used for obtaining the natural frequencies and mode shapes of the system.

The first 15 mode shapes of the multi-blade turbine with their associated resonant frequencies are shown in Fig. 32.6. It should be noted not all of the first six rigid body modes of the system are not shown here. The modes of the multi-blade turbine are categorized as flapwise and edgewise modes. In another classification, each mode of a turbine can be called either a collective mode or differential mode. The collective modes are those in which all the blades have similar deflection and the same phase, while in differential modes, either the deflections are not similar or are not in the same phase. The first and fourth modes, for instance, are collective flapwise modes. Likewise, mode 12 is a collective edgewise mode. The higher order natural frequencies could be identified but the mode shapes are not shown here due to lack of sufficient spatial distribution

**Table 32.1** The auto-MAC comparison of mode shapes extracted in Case 1

Freq. (Hz)	1	2	3	4	5	6	7	8	9	10	11	12	13	14	15
1 5.9	100	0	0	20	0	0	0	0	5	0	0	0	9	0	0
2 8.6	0	100	0	0	16	3	1	14	0	5	1	0	0	1	4
3 8.8	0	0	100	0	3	16	15	1	0	1	6	0	0	3	1
4 17.1	20	0	0	100	0	1	0	0	41	0	0	0	5	0	0
5 20.3	0	16	3	0	100	0	1	1	0	35	1	1	0	1	0
6 20.7	0	3	16	1	0	100	1	1	0	1	35	0	0	0	1
7 29.4	0	1	15	0	1	1	100	0	0	1	3	0	0	14	1
8 29.8	0	14	1	0	1	1	0	100	0	1	1	0	0	0	16
9 37.3	5	0	0	41	0	0	0	0	100	0	0	0	17	1	0
10 47.3	0	5	1	0	35	1	1	1	0	100	2	0	1	0	0
11 47.5	0	1	6	0	1	35	3	1	0	2	100	0	0	0	0
12 48.8	0	0	0	0	1	0	0	0	0	0	0	100	2	0	0
13 63.6	9	0	0	5	0	0	0	0	17	1	0	2	100	0	0
14 66.4	0	1	3	0	1	0	14	0	1	0	0	0	0	100	0
15 67.0	0	4	1	0	0	1	1	16	0	0	0	0	0	0	100

of the accelerometers on each of the blades; more accelerometer measurements are needed to sufficiently describe the higher order modes.

In order to verify the validity of the extracted mode shapes, an auto-modal assurance criterion (MAC) calculation was performed on the results (see Table 32.1). Most of the off-diagonal terms in auto-MAC table are negligible. However some flapwise mode-pairs with higher levels reveal some off-diagonal correlation (4–9, 5–10, 6–11). These off-diagonal terms are not necessarily a concern for these studies.

### 32.3.2 Case 2: Experimental Measurement Using a Higher Frequency Bandwidth

In the second case, a modal testing was performed on the 3-bladed wind turbine with a higher frequency span. To excite modes with higher frequencies, an impact hammer with a hard tip was used. In this measurement, special attention was paid to precisely compensate the moving-mass of the accelerometers. As can be seen in Fig. 32.7, there are fewer discrepancies in the stability diagram of this experiment compared to the stability diagram shown in Fig. 32.4. However, still there are some effects of moving-mass at the higher frequency ranges.

It should be noted that due to the hard hammer tip which was used in this case, the low order natural frequencies were not excited significantly, that causes some difficulties in extracting those modes by using the stability diagram. In order to extract the low frequency modes of the blades, a separate curve was fitted to the first three modes. The rest of the modes were extracted using second curve-fitting procedure. The auto-MAC of the second test and the MAC comparison between the first and second tests were very similar to the auto-MAC in Fig. 32.6 and are not shown here.

## 32.4 Discussion of Results

The results of the study showed the natural frequencies and mode shapes of a 3-bladed wind turbine. In order to improve the understanding of the dynamics of a multi-blade system, theoretical models can be used to help explain the experimental results obtained in this paper. The current work focuses on the experimental measurement of a wind turbine blade. A companion paper by Baqersad et al. [19] presents a theoretical model of a wind turbine and correlations of the wind turbine to subcomponents with different boundary conditions.

Natural frequencies of a cantilevered individual blade test of a Skystream 4.7 was previously determined using one-dimensional accelerometers and modal impact hammer testing [20]. The results are shown in Table 32.2. This previous test was focused on flapwise modes and only the flapwise deformations of the mode shapes were extracted. One-dimensional accelerometers, however, could find the flapwise and edgewise resonant frequencies. Therefore, the resonant frequencies of the previous measurement (see Table 32.2) were used in the current study but the mode shapes of the single blade could not



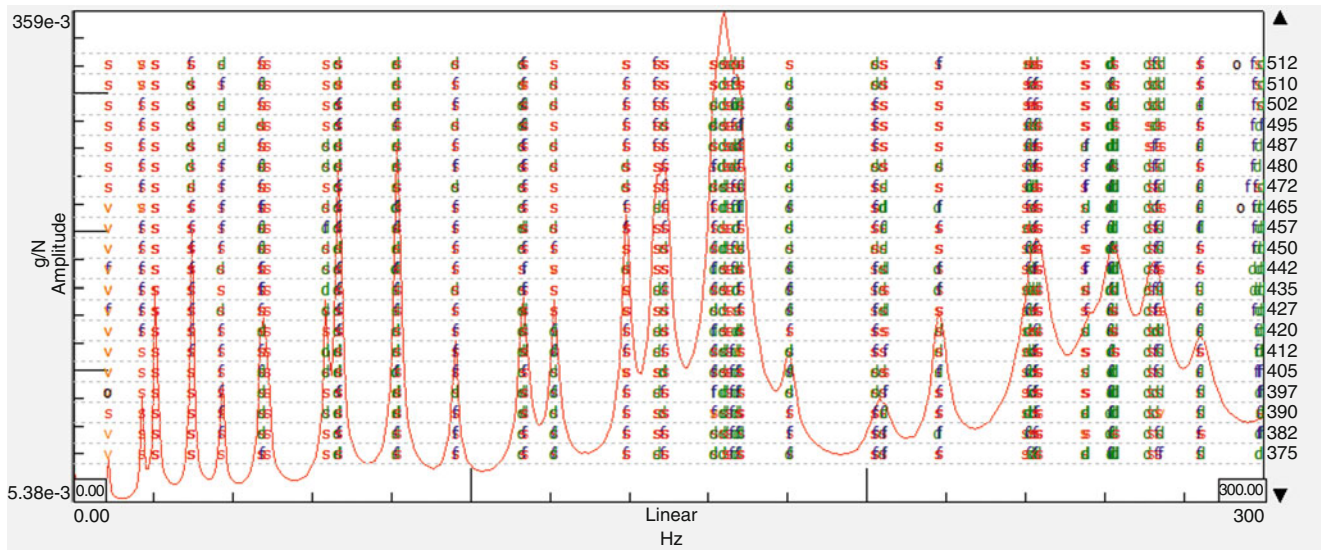


Fig. 32.7 The stability diagram for Case 2

Table 32.2 Resonant frequencies of a Skystream 4.7 blade in a cantilevered boundary condition [20]

Mode	Frequency
1	5.7
2	17.0
3	27.0
4	38.4
5	60.9
6	69.9
7	101.4

Flapwise modes of the cantilevered blade (each leads to a collective mode of the turbine)  
 Edgewise modes of the cantilevered blade (each leads to two differential modes of the turbine)

Table 32.3 Flapwise resonant frequencies of the turbine in a free-free boundary condition measured in Case 1

Mode	Frequency (Hz)
1	-
2	-
3	5.9
4	8.6
5	8.8
6	17.1
7	20.3
8	20.7
9	37.3
10	47.3
11	47.5
12	63.6
13	81.2
14	81.8
15	96.3
16	113.0
17	113.8
18	-

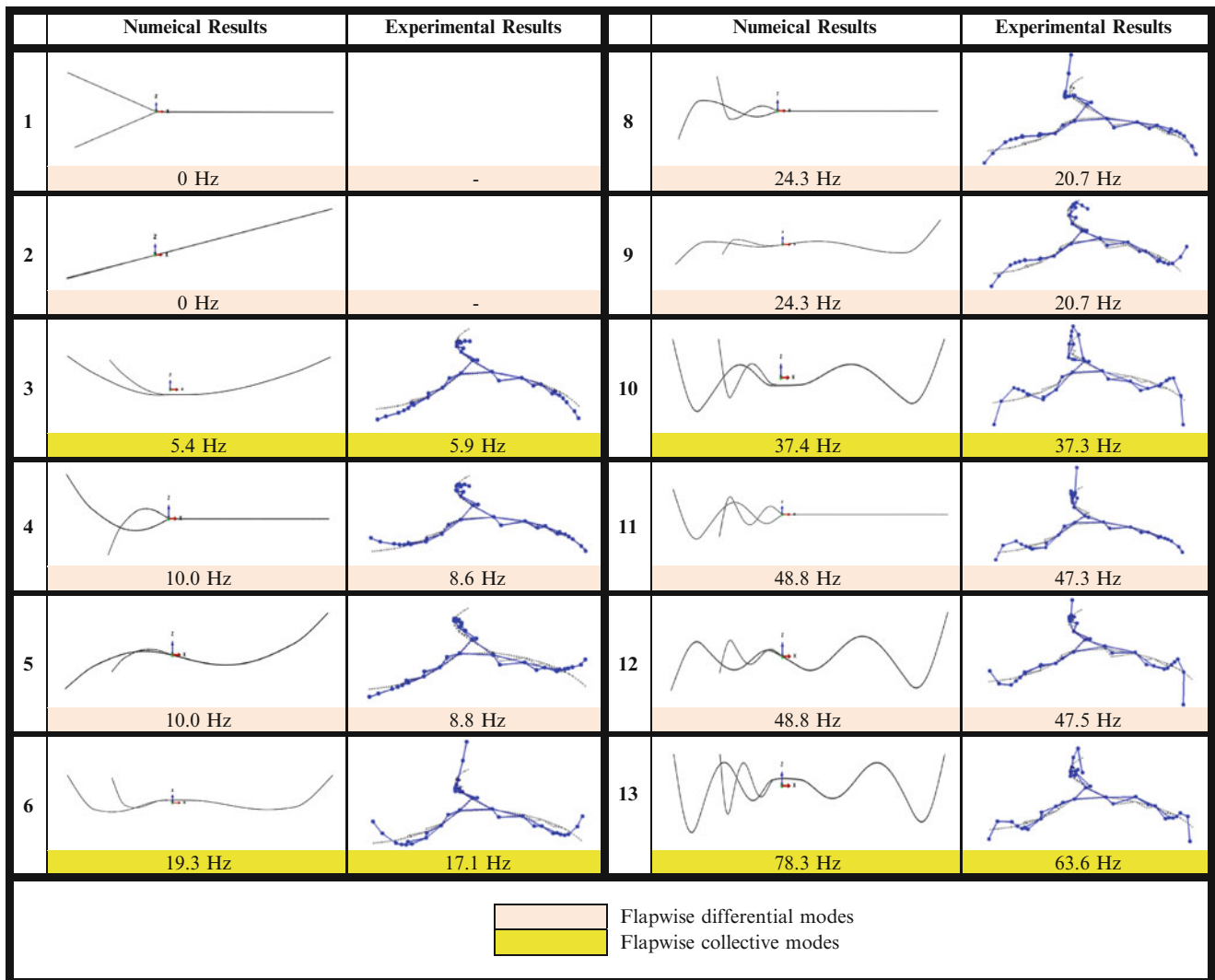
Flapwise differential modes  
 Flapwise collective modes  
 Edgewise differential modes  
 Edgewise collective modes

be used to correlate the shapes of the single blade to mode shapes of a blade in the turbine; the accelerometer measurement points were located at different locations for these two separate tests.

Both edgewise and flapwise modes of a 3-bladed wind turbine can be classified in groups of three modes; one collective and two differential modes. A set of three modes of the multi-blade turbine are related to a single mode of an individual blade tested in a cantilevered boundary condition. Therefore, the experimental flapwise and edgewise modes of the multi-blade wind turbine are classified in groups of three in Tables 32.3 and 32.4 respectively. It should be mentioned that the first

**Table 32.4** Edgewise resonant frequencies of the turbine in a free-free boundary condition measured in Case 1

Mode	Frequency (Hz)
1	-
2	29.4
3	29.8
4	48.8
5	66.4
6	67.0
7	121.3
8	-
9	-



**Fig. 32.8** Flapwise mode shapes and natural frequencies of the numerical model [19] compared to the experimental modes measured in Case 1

two modes in the flap direction (shown in Table 32.3) and first mode in the edge-wise direction (shown in Table 32.4) refer to rotational rigid body modes; the three other translational rigid body modes are not shown.

The results of Table 32.3 shows that a flapwise collective mode happens at a frequency close to the natural frequency of a cantilevered individual blade, as was expected. This fact can be verified by comparing the frequencies of modes 3, 6, 9, 12, and 15 of Table 32.3 with flapwise modes of the individual blade in Table 32.2. However, for the edgewise modes, two modes occur at frequencies close to the frequency of an individual cantilever blade. This fact can be seen by comparing the edgewise modes 2, 3, 5, 6 of the multi blade turbine (shown in Table 32.4) and the two edgewise modes of the cantilever individual blade in Table 32.2.



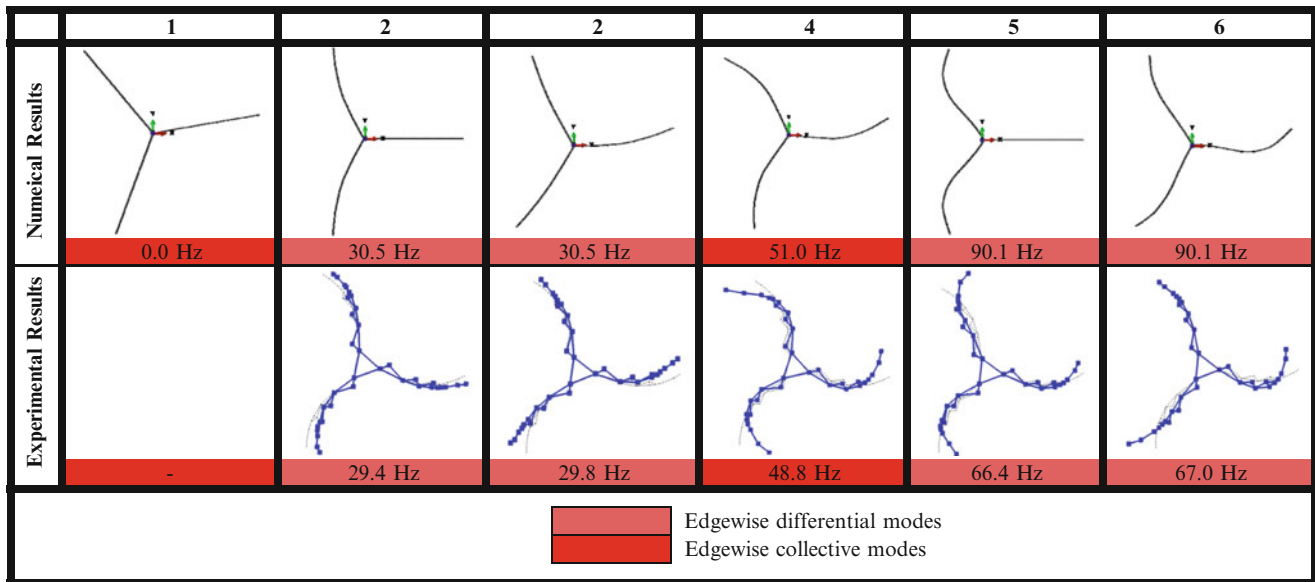


Fig. 32.9 Edgewise mode shapes and natural frequencies of the numerical model [19] compared to the experimental modes measured in Case 1

The flapwise modes shapes and natural frequencies of the theoretical model and the experimental model of Case 1 are compared in Fig. 32.8 (the two first rigid body modes were not extracted in Case 1). As can be seen, the experimental mode shapes are similar to the mode shapes that were extracted using a finite element beam model. However, the theoretical model shows higher natural frequencies because the finite element model tends to be stiffer than the blade.

Figure 32.9 compares the edgewise mode shapes and natural frequencies of the FE model to the experimental model. The comparison shows a similarity between the mode shapes of the two models. Because the theoretical model of the blades tends to be very stiffer in edge direction than the real blade, the natural frequencies of the beam element model are higher than experimental model.

## 32.5 Conclusion

Several different single and multi-blade experimental modal data sets were evaluated in this work. The results show that there are several very closely spaced modes, as expected, which are referred to as the collective and differential modes of the multi-blade system. Due to the closeness of the modes and the light-weight nature of the turbine blade, care must be exercised in using distributed dummy masses along with the roving accelerometers to prevent serious distortion of the measured frequency response functions due to mass loading effects. Comparisons were made between the single blade test results and the multi-blade test results to show some of the similarities and differences between the two different test configurations; this can be useful in distinguishing some of the modes of the final system multi-blade configuration based on single blade experimental results.

**Acknowledgements** The authors gratefully appreciate the financial support for this work provided by the National Science Foundation (Grant No. CMMI-0900534) and also the U.S. Army Research Office (Nanomanufacturing of Multifunctional Sensors, Award Number: W911NF-07-2-0081). Any opinions, findings, and conclusions or recommendations expressed in this material are those of the authors and do not necessarily reflect the views of NSF or ARO.

## References

1. Paquette J, Laird D, Griffith DT, Rip L (2006) Modeling and testing of 9 m research blades. In: 44th AIAA aerospace sciences meeting, Reno, NV, pp 14569–14581
2. Ye Z, Ma H, Bao N, Chen Y, Ding K (2001) Structure dynamic analysis of a horizontal axis wind turbine system using a modal analysis method. *Wind Eng* 25:237–248

3. Lopiccolo J, Carr J, Niezrecki C, Avitabile P, Slattery M (2012) Validation of a finite element model used for dynamic stress-strain prediction. In: 30th IMAC, a conference on structural dynamics. Jacksonville, FL, pp 205–214
4. Deines K, Marinone T, Schultz R, Farinholt K, Park G (2011) Modal analysis and SHM investigation of Cx-100 wind turbine blade. In: 29th IMAC, a conference on structural dynamics. Jacksonville, FL, pp 413–438
5. Marinone T, Leblanc B, Harvie J, Niezrecki C, Avitabile P (2012) Modal testing of 9 M Cx-100 turbine blades. In: 30th IMAC, a conference on structural dynamics. Jacksonville, FL, pp 351–358
6. Harvie J, Avitabile P (2012) Comparison of some wind turbine blade tests in various configurations. In: 30th IMAC, a conference on structural dynamics. Jacksonville, FL, pp 73–79
7. White JR, Adams DE, Rumsey MA (2010) Theoretical analysis of acceleration measurements in a model of an operating wind turbine. Active and passive smart structures and integrated systems, Proceedings of SPIE, San Diego, CA
8. Coronado R, Gonzales E, Jennings A, Leyden K, Min J, Duron Z (2012) Dynamic characterization of an operational whisper 500 wind turbine, 2011/12 LANL Wind Turbine Clinic Report, Los Alamos National Laboratory, Los Alamos, New Mexico
9. Rinker J, Russell A, Jahiu V, Wornick H, Peck N, Reade L (2011) Dynamic characterization of an operational whisper 500 wind turbine, 2011/12 LANL Wind Turbine Clinic Final Report, Los Alamos National Laboratory, Los Alamos, New Mexico
10. Yang S, Allen MS (2012) Output-only modal analysis using continuous-scan laser Doppler vibrometry and application to a 20 Kw wind turbine. *Mech Syst Signal Process* 31:228–245
11. Warren C, Niezrecki C, Avitabile P (2011) Determination of wind turbine operating deflection shapes using full-field 3D point-tracking. In: 29th IMAC, a conference on structural dynamics. Jacksonville, FL, pp 217–226
12. Warren C, Niezrecki C, Avitabile P (2011) Optical non-contacting vibration measurement of rotating turbine blades II. In: 28th IMAC, a conference on structural dynamics. Jacksonville, FL, pp 39–44
13. Paulsen US, Schmidt T, Erne O (2010) Developments in large wind turbine modal analysis using point tracking videogrammetry. In: 28th IMAC, a conference on structural dynamics. Jacksonville, FL, pp 187–198
14. Ozbek M, Rixen DJ, Erne O, Sanow G (2010) Feasibility of monitoring large wind turbines using photogrammetry. *Energy* 35:4802–4811
15. Lundstrom T, Baqersad J, Niezrecki C, Avitabile P (2012) Using high-speed stereophotogrammetry techniques to extract shape information from wind turbine/rotor operating data. In: 30th IMAC, a conference on structural dynamics. Jacksonville, FL, pp 269–275
16. Lundstrom T, Baqersad J, Niezrecki C (2013) Using high-speed stereophotogrammetry to collect operating data on a helicopter. In: 31st IMAC, a conference on structural dynamics. Garden Grove, CA
17. Helfrick MN, Pingle P, Niezrecki C, Avitabile P (2009) Optical non-contacting vibration measurement of rotating turbine blades. In: 27th conference and exposition on structural dynamics, IMAC XXVII Jacksonville, FL
18. LMS International (2009) Lms Test.Lab 10a. Leuven
19. Baqersad J, Niezrecki C, Avitabile P (2013) Effects of boundary condition on the structural dynamics of wind turbine blades. In: 31st IMAC, a conference on structural dynamics. Garden Grove, CA
20. Carr J, Dyas S, Ertsoy M, Lopiccolo J, Nonis C, Romano J (2011) Static and dynamic testing of a 7-ft wind turbine blade. Capstone design report, Department of Mechanical Engineering, University of Massachusetts Lowell, Lowell, MA

## Chapter 33

# Harmonic Analysis on a Lévy Plate and Its Application to Fatigue Analysis

Nam-Gyu Park, Jung-Min Suh, and Kyeong-Lak Jeon

**Abstract** This paper discusses a harmonic response estimation method on the Lévy plate with two opposite edges simply supported and the other two edges having free boundary conditions. Then, the harmonic response is processed to evaluate fatigue damage. Since the equation of motion of the plate is not self-adjoint, the modes are not orthogonal to each other on the structure domain. Noting that the Lévy plate can be expressed using one term sinusoidal function that is orthogonal to other sinusoidal functions, this paper suggested the calculation method that is equivalent to finding a least square error minimization solution of the finite number of algebraic equations. Example problems subjected to a distributed area loading and a distributed line loading are defined and their solutions are provided. The solutions are compared to those of the commercial code, ANSYS. The plate motion due to high frequency vibration can be seen in the nuclear fuels subjected to highly turbulent coolant flow. The dominant exciting frequency is dependent on the coolant velocity and Strouhal number, a dimensionless number describing oscillating flow mechanism. This paper also discusses fatigue damage considering the high frequency vibration using the Dirlik equation.

**Keywords** Harmonic response • Lévy plate • Fatigue • Nuclear fuel • Least-square error

### 33.1 Introduction

The study on plate vibrations has been almost established through Euler, Bernoulli, Navier, Levy, Kirchhoff, and Love [1, 2], and the theories provide direct solutions or a guidance for lots of practical problems. Kirchhoff is the first researcher who introduced the equation of motion of a plate based on the principle of variation [2], and it is verified that his hypothesis can provide almost exact solutions when the length of a plate is 20 times larger than the thickness [3].

One can analyze structural dynamic characteristics or determine effective design parameters based on the responses of a structure subjected to external forces. Therefore response analysis is critical to structural design, and Lee etc. [4] studied the vibration isolating method by applying design sensitivity analysis on a plate. Doyle developed Timoshenko spectrum beam element using Fourier transform, and laid solid foundation on the structural response analysis with spectrum element method. Kulla [5] derived the dynamic stiffness of a beam using Euler-Bernoulli spectrum beam element. One of the most useful response analysis is the mode superposition method that the dynamic equation can be simplified using the orthogonal property of the modes. On the other hand, the orthogonality of the plate modes is not valid for all boundary conditions, thus the applicability of the mode superposition is limited. Navier [1] proposed a solution using trigonometric functions for the plate that has all the boundaries are simply supported. It is known that the solutions of the plate with two opposite edges simply supported are Levy type solutions. Since the solutions can be applicable to many practical areas, lots of research results have been published. For an example, the buckling and eigenvalue problem for the plate with multiple supports was studied by Xiang [6, 7]. Marynowsky discussed the stability of the moving viscoelastic plate, and Lellep [8] provided an eigenvalue solution for the plate with a crack.

Mechanical structures frequently accompany with reciprocating power generator, thus a dominant frequency component can be seen when the structure is operating at a constant speed. In this case, the dynamic behavior can be estimated using

---

N.-G. Park (✉) • J.-M. Suh • K.-L. Jeon  
R&D Center, KEPCO Nuclear Fuel, 493 Deokjin-dog Yusong-gu, Daejeon 305-353, Republic of Korea  
e-mail: [nkpark@knfc.co.kr](mailto:nkpark@knfc.co.kr)

harmonic analysis. For a plate with arbitrary boundary conditions, its modes are not orthogonal to each other. For harmonic analysis, therefore, one rarely obtains analytic solution except a few simple cases. This paper dealt with harmonic response of the Lévy plate that two opposite edges are simply supported and the other two edges free boundary. The plate that has such boundary conditions does not have the modes satisfying orthogonal condition. This paper introduced linear algebraic equations to find the harmonic response of the plate. The plate in the work is a simplified version of a nuclear fuel component. Since the component is subjected to flow induced vibration for a long time, it is vulnerable to fatigue damage. Thus the solution is utilized to estimate fatigue damage.

### 33.2 Equation of Motion and Boundary Conditions

Figure 33.1 shows the schematic representation of the target structure. Two opposite sides are simply supported and the other two edges are free. It is assumed that the plate is uniform and homogeneous, and if rotary inertia is negligible, the equation of the motion can be written

$$D\nabla^4 w + \rho h \ddot{w} = p(x, y)f(t). \quad (33.1)$$

Where  $\rho$ ,  $h$ , and  $w$  denotes the plate density, thickness, and z-directional motion, respectively. The right-hand-side of (33.1) means external dynamic load varying as a function of time and space.  $\nabla^2$  denotes Laplace operator, and  $\ddot{w}$  denotes second-order differentiation with respect to time.  $D$  denotes flexural rigidity  $\left(\frac{Eh^3}{12(1-\nu^2)}\right)$  of the plate with Young's modulus ( $E$ ) and Poisson's ratio ( $\nu$ ). The boundary condition in Fig. 33.1 means that displacement and moment must be 0 in the free edges, and shear force and moment must be 0 in the simply supported edges. Since the z-directional displacement,  $w$ , can be expressed as  $W(x, y)q(t)$ , one can write the above mentioned boundary conditions,

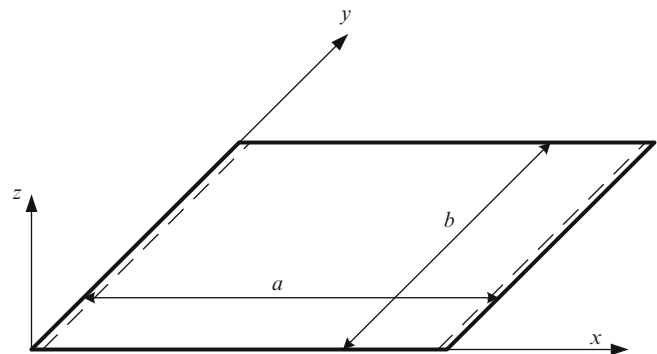
$$\begin{aligned} W(0, y) = 0, \quad \frac{\partial^2 W(0, y)}{\partial x^2} + \nu \frac{\partial^2 W(0, y)}{\partial y^2} &= 0 \\ W(a, y) = 0, \quad \frac{\partial^2 W(a, y)}{\partial x^2} + \nu \frac{\partial^2 W(a, y)}{\partial y^2} &= 0 \end{aligned} \quad (33.2a)$$

$$\begin{aligned} \frac{\partial^2 W(x, 0)}{\partial y^2} + \nu \frac{\partial^2 W(x, 0)}{\partial x^2} = 0, \quad \frac{\partial^3 W(x, 0)}{\partial y^3} + (2-\nu) \frac{\partial^3 W(x, 0)}{\partial y \partial x^2} &= 0 \\ \frac{\partial^2 W(x, b)}{\partial y^2} + \nu \frac{\partial^2 W(x, b)}{\partial x^2} = 0, \quad \frac{\partial^3 W(x, b)}{\partial y^3} + (2-\nu) \frac{\partial^3 W(x, b)}{\partial y \partial x^2} &= 0 \end{aligned} \quad (33.2b)$$

One can obtain the response of the structure using the modes,

$$W_{mn}(x, y) = Y_n(y) \sin \frac{m\pi}{a} x. \quad (33.3)$$

Equation (33.3) satisfies the boundary condition, (33.2a). With (33.3), we can estimate the structure response using modal superposition method. Therefore, one can write the response,



**Fig. 33.1** Lévy plate; two sides are simply supported ( $x=0$ ,  $x=a$ ) and the other two sides are free

$$w = \sum_{m=1}^{\infty} \sum_{n=1}^{\infty} q_{mn}(t) Y_n(y) \sin \frac{m\pi}{a} x. \quad (33.4)$$

Where,  $q$  means time varying contribution factor for each mode. When all modes are orthogonal to each other, by inserting (33.4) into (33.1), one can obtain ordinary differential equations.

### 33.3 Approximate Harmonic Solution

One can see a specific frequency component when a structure is under normal stationary operation. In that case, the time dependent external force,  $f(t)$ , is expressed as harmonic force. Therefore, (33.4) turns to

$$w = \sum_{m=1}^{\infty} \sum_{n=1}^{\infty} Q_{mn} e^{j\omega t} Y_n(y) \sin \frac{m\pi}{a} x. \quad (33.5)$$

On the other hand,  $y$ -directional modes,  $Y(y)$ , that satisfying (33.2) can be written [19]

$$Y(y) = \begin{cases} A \cosh \frac{r_1}{b} y + B \sinh \frac{r_1}{b} y + C \cos \frac{r_2}{b} y + D \sin \frac{r_2}{b} y, & \text{if } K_n \geq 1, \text{ where } r_1 = \frac{b}{a} m\pi \sqrt{K_n + 1}, r_2 = \frac{b}{a} m\pi \sqrt{K_n - 1} \\ A \cosh \frac{r_1}{b} y + B \sinh \frac{r_1}{b} y + C \cosh \frac{r_2}{b} y + D \sinh \frac{r_2}{b} y, & \text{if } K_n < 1, \text{ where } r_1 = \frac{b}{a} m\pi \sqrt{K_n + 1}, r_2 = \frac{b}{a} m\pi \sqrt{1 - K_n} \end{cases} \quad (33.6)$$

Where, A, B, C, and D denote coefficients for each term.  $K_n$  is defined as,

$$K_n = \omega_{mn} a^2 \sqrt{\frac{\rho h}{D}} / (m\pi)^2 \quad (33.7)$$

After substituting (33.5) to (33.1), multiplying the sine function for both side, and integrating along the  $x$ -axis, one can obtain the final equation

$$\frac{Eh^3}{12(1-\nu^2)} \frac{a}{2} \sum_{n=1}^{\infty} Q_{kn} \left[ Y_n(y) \left( \frac{k\pi}{a} \right)^4 - 2 \frac{\partial^2 Y_n(y)}{\partial y^2} \left( \frac{k\pi}{a} \right)^2 + \frac{\partial^4 Y_n(y)}{\partial y^4} \right] - \rho h \omega^2 \frac{a}{2} \sum_{n=1}^{\infty} Q_{kn} Y_n(y) = \int_0^a \left( p(x, y) \sin \frac{k\pi}{a} x \right) dx \quad (33.8)$$

Since the  $y$ -directional modes are not orthogonal to each other, (33.8) cannot be simplified anymore. Noting that (33.8) must be satisfied for all frequencies, one can induce algebraic equations along  $y$ -directional points

$$\begin{bmatrix} C_{k11} & C_{k12} & \cdots & C_{k1n} \\ C_{k21} & C_{k22} & \cdots & C_{k2n} \\ \vdots & \vdots & \ddots & \vdots \\ C_{kr1} & C_{kr2} & \cdots & C_{krn} \end{bmatrix} \begin{Bmatrix} Q_{k1} \\ Q_{k2} \\ \vdots \\ Q_{kn} \end{Bmatrix} = \begin{Bmatrix} f_1 \\ f_2 \\ \vdots \\ f_n \end{Bmatrix}. \quad (33.9)$$

Where, a component in the left-hand-side matrix is

$$C_{kij} = \frac{Eh^3}{12(1-\nu^2)} \frac{a}{2} \left[ Y_j(y_i) \left( \frac{k\pi}{a} \right)^4 - 2 \frac{\partial^2 Y_j(y_i)}{\partial y^2} \left( \frac{k\pi}{a} \right)^2 + \frac{\partial^4 Y_j(y_i)}{\partial y^4} \right] - \rho h \omega^2 \frac{a}{2} Y_j(y_i). \quad (33.10)$$

And, the forcing function in the right-hand-side is

$$f_i = \int_0^a \left( p(x, y_i) \sin \frac{k\pi}{a} x \right) dx \quad (33.11)$$

The solution in (33.9) is the coefficient in (33.5), then the harmonic solution can be identified. It should be noted that precision of the solution is dependent on the identified coefficient. When the number of equation is greater than the unknowns, a reliable least-square solution can be found. When a specific mode’s contribution is dominant, the solution could have significant uncertainty due to the rank-deficient coefficient matrix in (33.9). Therefore, it is desirable to construct the coefficient matrix such that the every equation comes from the evenly selected positions along y-direction.

### 33.4 Verification Examples

#### 33.4.1 Uniform Harmonic Excitation on the Entire Area

A spacer grid assembly, one component in a nuclear fuel, maintains lateral position between the rods, and it is fabricated using lots of thin straps. The strap thickness varies with the type of a grid assembly, but it is less than 0.5 mm. In this example, a protective grid with 0.2667 mm thickness is chosen. The protective grid is located just above the fuel assembly bottom nozzle, thus, the grid is directly exposed to the turbulent coolant flow. When the coolant flow passes over the protective grid strap, vortex-induced vibration can be seen. Although the grid has complex configuration, for simplicity, a portion of the grid strap is considered in this example. That is, a strap in one cell is used to verify the suggested method. The target structure size is 10.67 mm × 2.54 mm, and has the material properties of stainless steel. The protective grid structure is actually made from nickel alloy, but it is assumed that it consists of stainless steel straps. The structure’s boundary conditions are same to those in Fig. 33.1, and the natural frequencies are listed in Table 33.1.

Coolant flow in the fuel assembly is very fast, and vortex-induced vibration causes high frequency vibration on the strap. More than a 1,000 Hz frequency component can be seen, thus the sinusoidal force with 1.8 kHz frequency and 50 N amplitude is applied on the strap. Thus, the excitation force can be written

$$f_i = \frac{50a}{m\pi} (1 - \cos m\pi). \tag{33.12}$$

Since (33.12) equals to zero when  $m$  is even number, the corresponding mode does not contribute to the response. Table 33.2 shows each mode’s contribution factor; the even number contribution factor is relatively smaller than that of the odd number as shown in the first column ( $n = 1$ ). The cases, when  $n$  is greater than 1, correspond to skew-symmetric torsion modes, and their contribution is quite negligible. Operating deflection shape at the frequency is delineated in Fig. 33.2. The most dominant mode is the 3-rd mode shape, since the excitation frequency is close to the 3-rd natural frequency in the first column in Table 33.1. As shown in Fig. 33.3, harmonic response at the center point shows that the estimated solution is comparable to that from commercial software, ANSYS.

As the number of equation increases, the solution converges as shown in Fig. 33.4. When the number of equation is 10, the difference is less than 1% comparing to that of the case with 500 equations.

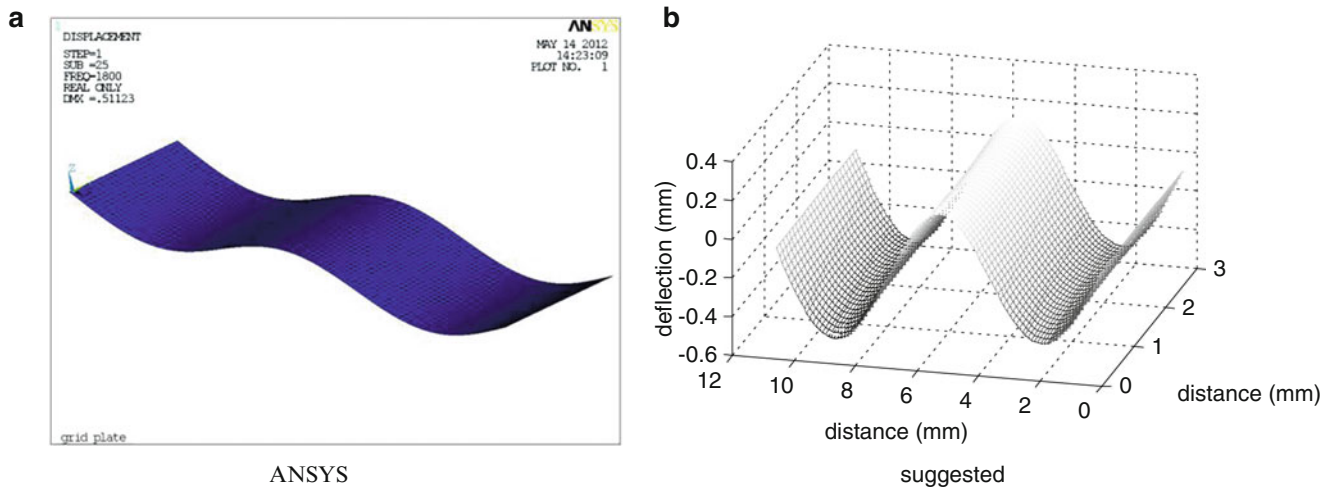
**Table 33.1** The plate natural frequencies in Hz (present/ANSYS)

m \ n	1	2	3
1	174/174	1,013/1,013	7,588/7,587
2	700/701	2,119/2,120	8,466/8,465
3	1,587/1,588	3,399/3,400	9,819/9,817
4	2,839/2,840	4,913/4,916	11,559/11,559
5	4,450/4,456	6,707/6,712	13,637/13,637

**Table 33.2** Weighting factor(Q) at 1.8 kHz excitation

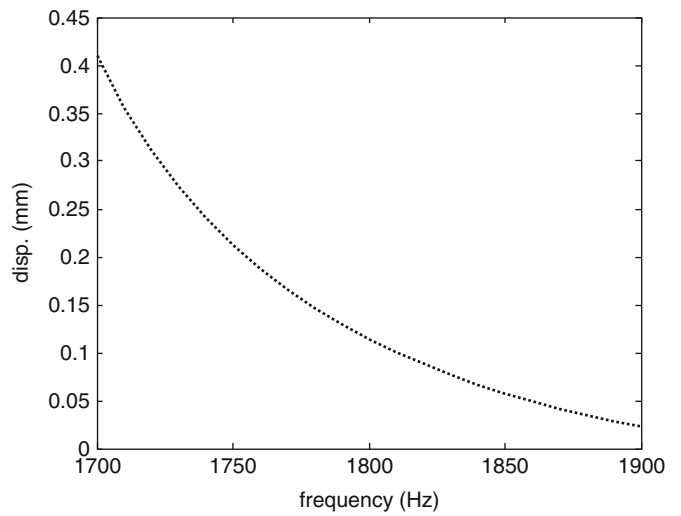
m \ n	1	2	3
1	-0.0210	0.0000	-0.0001
2	0.0041	0.0000	0.0000
3	-0.0499	0.0001	-0.0001
4	0.0005	0.0000	0.0000
5	0.0018	0.0000	0.0000



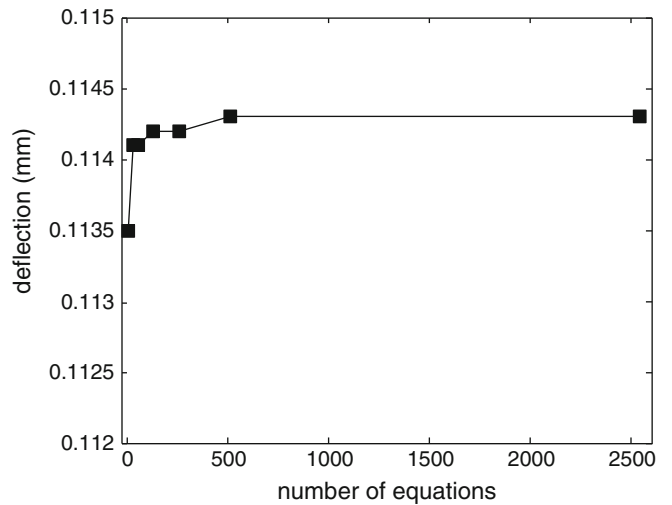


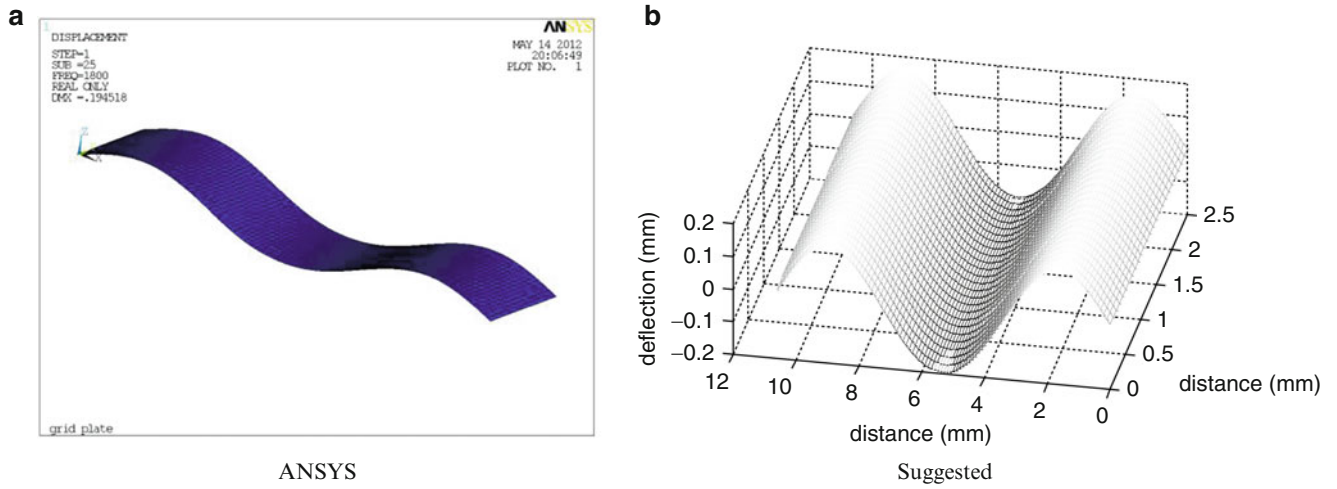
**Fig. 33.2** Operating deflections subjected to 1.8 kHz uniform distributed load. (a) ANSYS. (b) Suggested

**Fig. 33.3** Harmonic response at the center node (*solid*: ANSYS, *dotted*: suggested)



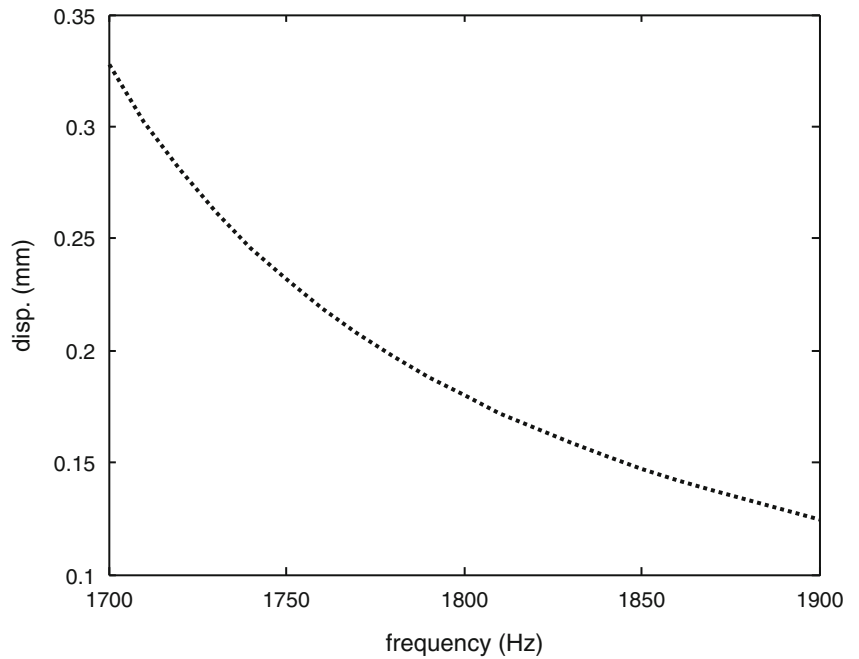
**Fig. 33.4** Variation of the deflection with respect to number of equations





**Fig. 33.5** Operating deflections subjected to 1.8 kHz uniform line load. (a) ANSYS. (b) Suggested

**Fig. 33.6** Harmonic response at the center node (solid: ANSYS, dotted: suggested)



### 33.4.2 Harmonic Excitation Along a Line

When a line load is active along a line at  $x = x^*$ , (33.11) turns to

$$f_i = p(x^*, y_i) \sin \frac{m\pi x^*}{a}. \tag{33.13}$$

Figure 33.5 shows the deflected shape when the line load with the amplitude, 50 N/mm, is oscillating at 1.8 kHz. The line load is applied along the central line in the y-direction. Therefore, the odd number modes in the x-direction should be dominant. Figure 33.6 is the frequency response at the center point, and the solution in this case is quite comparable to that of ANSYS

### 33.4.3 Remarks on the Limiting Case

It must be noted that the accuracy of the method is dependent on the external load. That is, since the finite number of equation is built including the force, a discontinuous line load or a point load causes solution with error. For the limiting cases, the right hand side of (33.9) consist of zeros corresponding to the region that is not subjected any external force. For example, when the line load is applied along a free boundary, (33.9) becomes

$$\begin{bmatrix} C_{k11} & C_{k12} & \cdots & C_{k1n} \\ C_{k21} & C_{k22} & \cdots & C_{k2n} \\ \vdots & \vdots & \ddots & \vdots \\ C_{kr1} & C_{kr2} & \cdots & C_{krn} \end{bmatrix} \begin{Bmatrix} Q_{k1} \\ Q_{k2} \\ \vdots \\ Q_{kn} \end{Bmatrix} = \begin{Bmatrix} 0 \\ \vdots \\ 0 \\ f_n \end{Bmatrix} \quad (33.14)$$

Therefore, the norm of the external force does not change while the norm of the coefficient matrix becomes large as the number of equation increases. The solution is dependent on the number of equations, and it is not unique.

The suggested method works well when an area load is applied on the whole domain. Considering that the body in water is exposed to entire area loading condition, the method will be applicable for that case.

## 33.5 Stress Estimation and Application for Fatigue Analysis

Fatigue analysis requires alternating stress or strain amplitude. Based on the developed method, alternating stress is estimated. From the displacement–strain relationship, strain can be written as

$$\varepsilon_{xx} = -z \frac{\partial^2 w}{\partial x^2}, \quad \varepsilon_{yy} = -z \frac{\partial^2 w}{\partial y^2}, \quad \gamma_{xy} = -2z \frac{\partial^2 w}{\partial x \partial y} \quad (33.15)$$

It is noted that (33.15) is reasonable when the rotations of transverse normal are negligible. Since the rotation is rarely seen in the target structure, (33.15) is applicable. The successive second derivative of the mid plane displacement can be calculate when the displacement filed is identified. When every stress component is calculated, we can compute principal stress intensities.

Since the calculates stress is dynamically varying, it is useful to introduce frequency domain fatigue analysis methodology [9]. Fatigue analysis in the frequency domain requires power spectral density function. The stress power spectrum is proportional to the calculated stress at each frequency. Dirlik developed an empirical closed form expression for the spectral density of rainflow amplitude based on extensive Monte Carlo simulations of stress amplitude [9]. With the stress spectrum, one can estimate the service life through Dirlik's methodology.

## 33.6 Summary and Conclusions

This work discussed harmonic response estimation in the Lévy plate with the specific boundary conditions. The solution of the finite number of equations provides weighting factor for every mode, thus displacement filed can be estimated. Since the orthogonal modes are not available for the problem, the suggested method is quite useful to obtain an approximate solution. Limiting cases are studied, and it is noted that the suggested method is limited to the case when area load is applied on the entire domain.

One can calculate fatigue stress spectrum using the approximate displacement field, and principal stress intensities are useful to estimate fatigue life. Since the amplitude of the turbulent forcing function is not available, one needs to identify the forcing function. It is expected that the fatigue life estimation is possible using the method when the forcing function is provided.

## References

1. Venstel E, Krauthammer T (2001) Thin plates and shells. Marcel Dekker, New York
2. Yu YY (1996) Vibrations of elastic plates. Springer, New York
3. Lee KH, Lim GT, Wang CM (2002) Thick levy plates re-visited. *Int J Solids Struct* 39(127):144
4. Lee JH, Lee KH (1996) The reduction of harmonic dynamic response of plate structure using continuum design sensitivity analysis. *Trans Korean Soc Noise Vib Eng* 6(1):27–34
5. Kulla PH (1997) High precision finite elements. *Finite Elem Anal Des* 26:997–114
6. Xiang Y, Zhao YB, Wei GW (2002) Lévy solutions for vibration of multi-span rectangular plates. *Int J Mech Sci* 44:1195–1218
7. Xiang Y, Wei GW (2004) Exact solutions for buckling and vibration of stepped rectangular Mindlin plates. *Int J Solids Struct* 41:279–294
8. Lellep J, Kägo E (2011) Vibrations of elastic stretched strips with cracks. *Int J Mech* 5(1):27–34
9. Lee YL, Pan J, Hathaway R, Barkey M (2005) Fatigue testing and analysis. Elsevier, Boston

# Chapter 34

## Vibration Level Assessment of Nuclear Power Plant Powerhouse Hall

G.G. Boldyrev and A.A. Zhivaev

**Abstract** This paper presents the results of vibration acceleration measurements of building structures as a result of equipment operation in NPP powerhouse hall.

Acceleration measurements were carried out at foundation column support or at different points of turbine foundation plate by means of three-dimensional accelerometer and RefTek 130 recorder.

As a result of these measurements the spectrograms used for steady-state response visualization of building structures were obtained, harmonics were identified and maps of harmonic source location as well as vibration level range were compiled.

Assessment of measurements conducted has shown the followings: spectral distribution of responses changes with time in a minor way, which means steady-state effect caused by vibration sources. Many of harmonics were recorded at each response; these were identified by means of suggested automatic search algorithm. The overall picture of identified harmonics shows clearly harmonic frequencies from 25 to 225 Hz at turbine vibration frequency of 25 Hz.

**Keywords** Vvibration assessment • Nuclear power plant • Harmonics identification • Spectrogram • Acceleration deviation maps

### 34.1 Introduction

This paper presents the results of vibration acceleration measurements of building structures as a result of equipment operation in NPP powerhouse hall of Balakovo Nuclear Power Plant (Russia).

The following tasks were completed in this study:

1. Oscillation's acceleration of bearing columns made of steel was measured at the bottom level of machinery plant.
2. Oscillation's acceleration was measured at different points of turbo-generator foundation plate.
3. Spectrograms were obtained to visualize the response of the structure.
4. Harmonic oscillations were identified and the harmonic diagram was obtained.
5. The maps of oscillation range and the sources of harmonic were obtained.

### 34.2 The Equipment of Powerhouse Hall

Powerhouse hall is constructed like a steel rack consisting of three parts: powerhouse hall, deaerator shop and pipeline service shop. The dimensions of the powerhouse hall are the following:  $127 \times 45$  m; the bottom of the roof truss is marked at the level of +35, 50 m. A turbine-generator set and additional equipment are located in powerhouse hall. The deaerator shop is placed along the powerhouse hall and has the following dimensions:  $127 \times 12$  m; the bottom of the roof truss is marked at the level of +42,00 m.

---

G.G. Boldyrev (✉) • A.A. Zhivaev  
Penza State University of Architecture and Construction, Penza, Russia  
e-mail: [g-boldyrev@geoteck.ru](mailto:g-boldyrev@geoteck.ru); [zhivaev@geoteck.ru](mailto:zhivaev@geoteck.ru)

### 34.3 Measurement Points of Oscillation Acceleration

Measurements of oscillation acceleration were carried out by means of tri-axis accelerometer produced by the company RefTek 131B-01/3 [1]. Signal recording was done by 6-channel seismic recorder RefTek 130-01. The sampling frequency was 500 Hz. In the Fig. 34.1 are shown the points of measurement carried out at the bottom of the columns of powerhouse hall.

For each point observed the measurements of oscillation acceleration were carried out as orthogonal triaxial oriented (three measuring point) or as uniaxial measurements (one measuring point). At the same time oscillation acceleration were measured at two points on the foundation plate of turbine. Acceleration sensors were rigid located to the columns by means of a screw-clamp and through embedded parts to the foundation plate.

### 34.4 Measurement Analysis Methods

A block diagram in the Fig. 34.2 presents the procedure applied for analysis of measurements results. Signals, recorded by sensors, were cleared of a drift. Afterwards a selection was carried out of the data files obtained for each sensor for further processing.

Vibrations, recorded by each sensor, is a total vibrations induced by different oscillation sources, which behavior can be permanent, alternating or impulse. As a result some alternating or impulsive points of structure oscillations may occur. The following methods were used to take into consideration exposures mentioned above:

1. To obtain spectral-response characteristics Fourier transformation were applied [2].
2. To visualize stationary of an oscillation development a spectral recording was carried out.
3. To identify harmonics of signals the harmonic identification method was used [3].
4. To visualize images formed by different criteria the maps of distribution for calculated criteria in plan of powerhouse hall were used.

The current vibration level was estimated by means of criteria distribution map. By criterion should be understood to mean some test feature – in this paper it is oscillation amplitude or location of sources of harmonic oscillations.

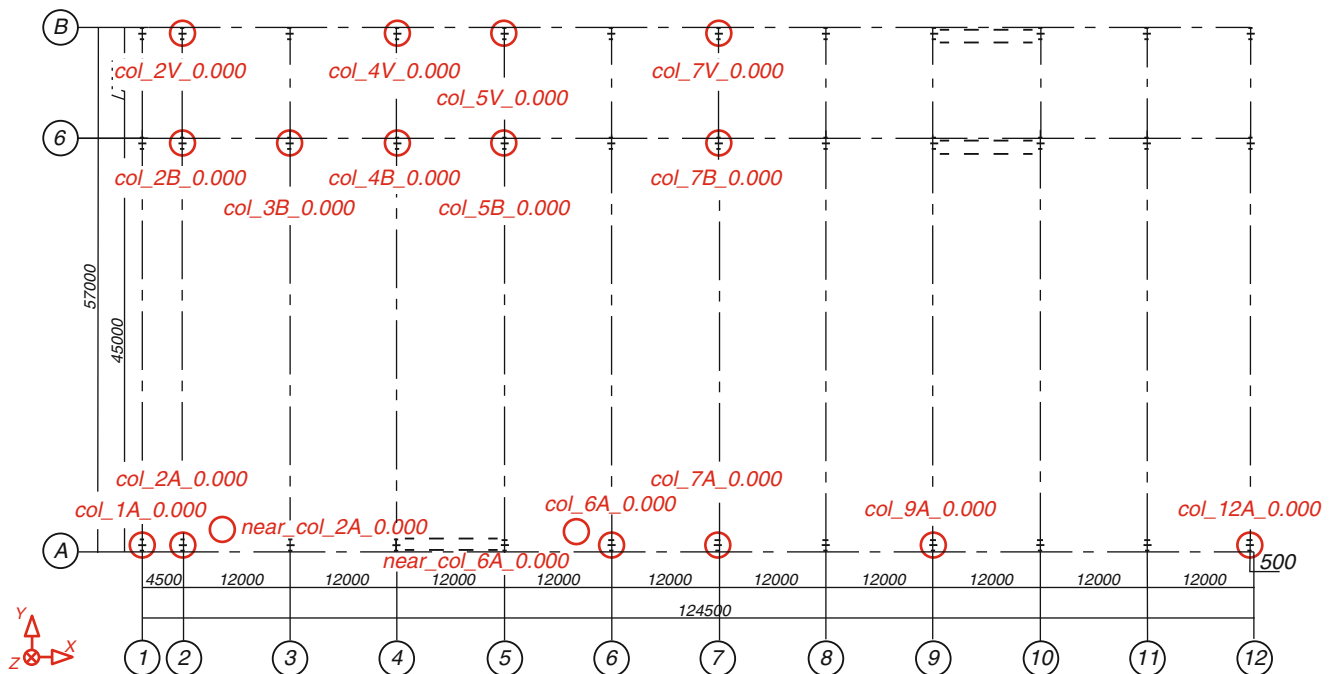


Fig. 34.1 Plan of measurement point location



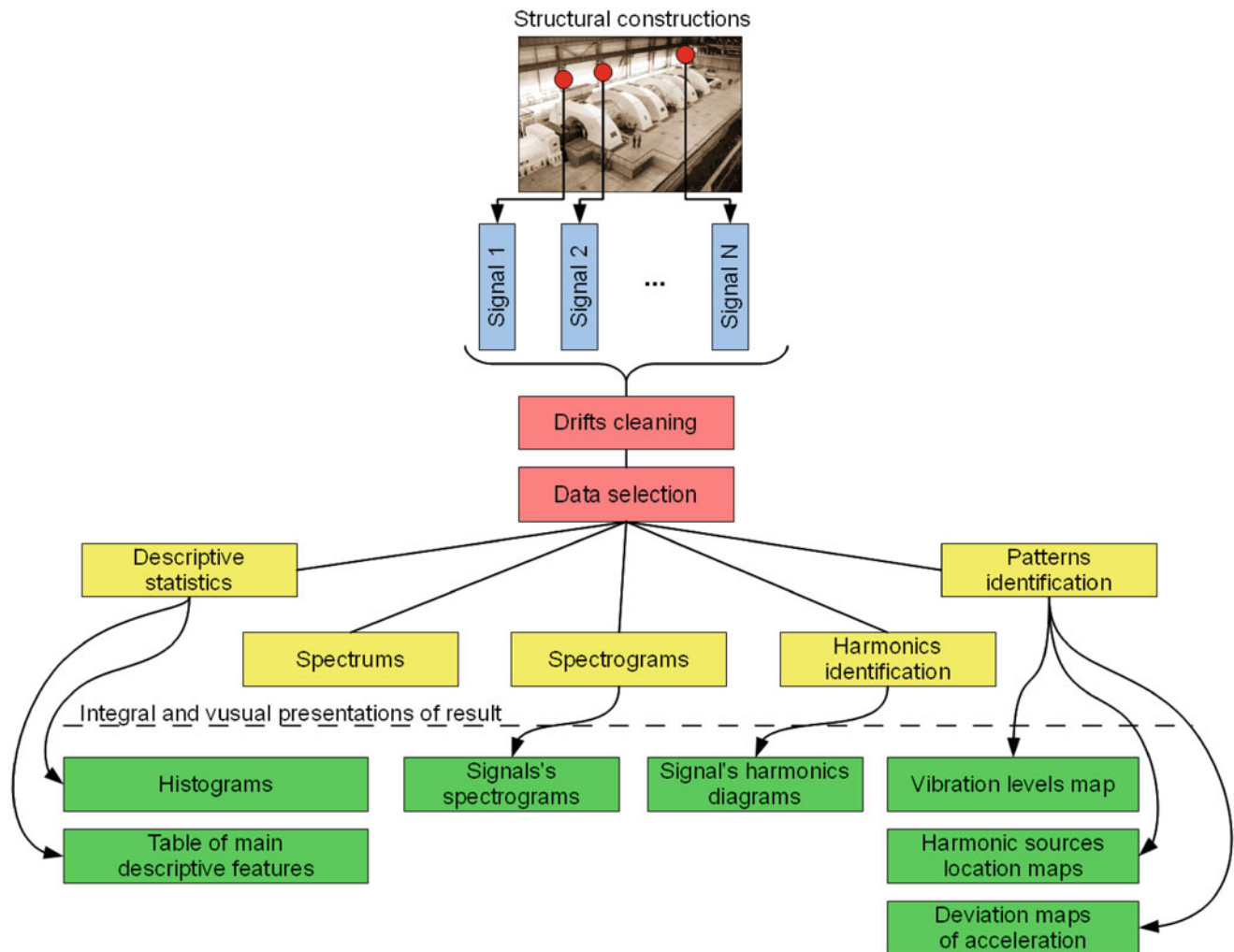


Fig. 34.2 Diagram of measurement data analysis

### 34.5 Calculation of Spectral Frequency-Time Characteristics

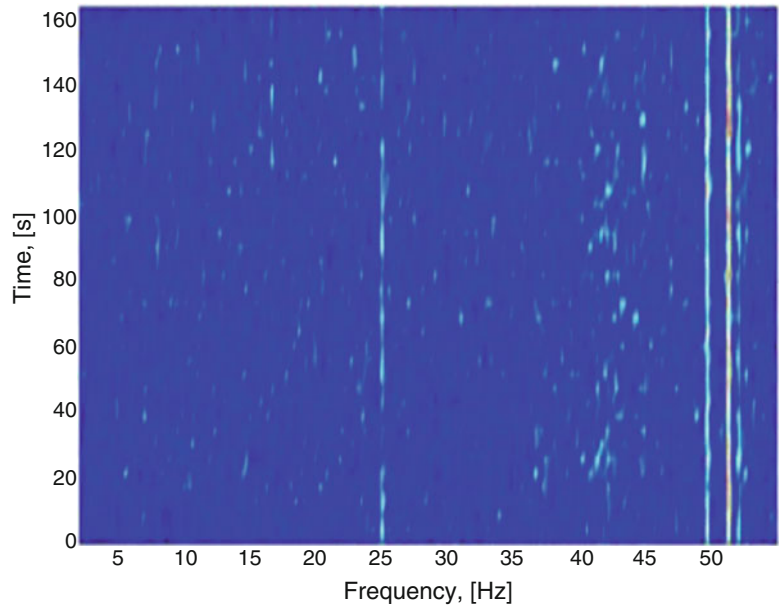
It is necessary to obtain sufficient volume of data in order to identify the most harmonics. In case spectral distribution changes in a minor way over period of time, it is sufficient to obtain a small amount of data to analyze harmonic. Otherwise this amount of data should be enlarged according to changes in spectral distribution over a period of time.

Convenient tool to visualize changes of spectral distribution over a period of time is spectrogram. Spectrogram is a time-varying spectral representation that shows how the spectral density of a signal varies with time. Spectrograms presented in this paper were obtained by means of STFT method [2].

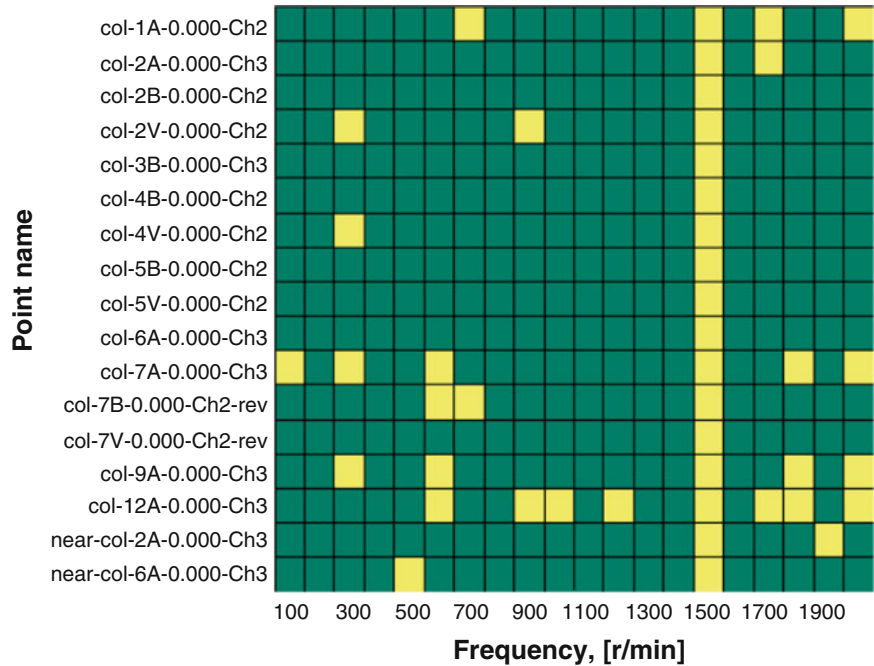
In the Fig. 34.3 it is shown an example of a typical spectrogram, which was drawn for a period of 163.4 c (ten data series constructed due to 8,192 points at the report rate of 500 Hz) for the column : col-2V-0.000-Ch1 (Fig. 34.1). All amplitudes of spectrogram were normalized through division into maximum value in order to obtain maximum amplitude, which equals to 1.

Data are noisy, but pulse-spike amplitudes could be seen at the frequencies of 25 Hz, 50 Hz and which are close to 50 Hz. Spectral division changes in a minor way.

**Fig. 34.3** Typical spectrogram of structure response

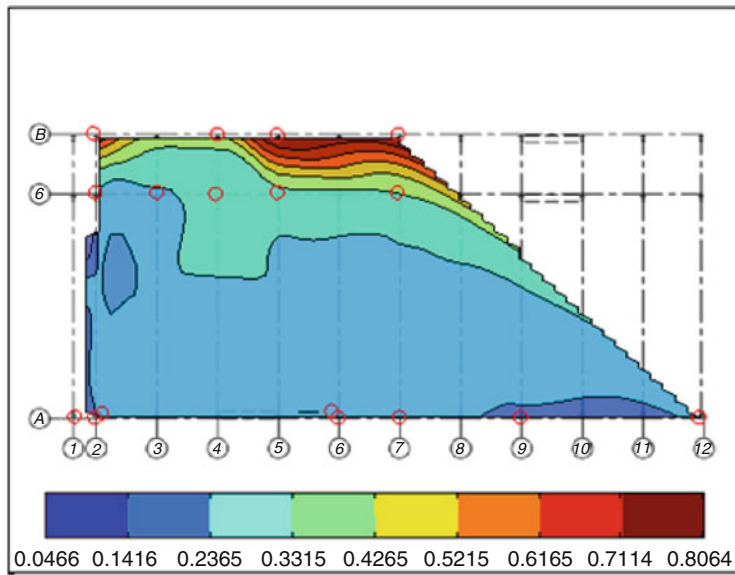


**Fig. 34.4** Frequencies of harmonic vibration sources identified along the axis X



### 34.6 Harmonic Identification Results

A method of procedure for harmonic identification was developed by the authors and applied for all responses of this structure. Five accesses each consisting out of 4,096 data were carried out for each point to identify harmonics. To make data submission more convenient the harmonics identified as to each response were aggregated with an accuracy of 100 r/min (1.67 Hz). The cumulative diagram of the harmonics identified for all observed points is presented in the Fig. 34.4, where an occurrence of a harmonic for the frequency specified is drawn in white. In the Fig. 34.4 we can see for the majority of signals well-defined harmonics at the frequency of 25 Hz, which are a multiple of 25–50, 75, 100, 125, 150, 175, 200, and 225 Hz. It is probably due to the following fact: the turbine, which rotation frequency is 25 Hz, is based on a plate and supplies vibrations to all structures nearby the turbine plate.



Point name	Accel [m/s <sup>2</sup> ]
col-1A-0.000-Ch2	0.0539
col-2A-0.000-Ch3	0.0699
col-2B-0.000-Ch2	0.1637
col-2V-0.000-Ch2	0.7608
col-3B-0.000-Ch3	0.1463
col-4B-0.000-Ch2	0.2167
col-4V-0.000-Ch2	0.3627
col-5B-0.000-Ch2	0.2360
col-5V-0.000-Ch2	0.7602
col-6A-0.000-Ch3	0.0934
col-7A-0.000-Ch3	0.0918
col-7B-0.000-Ch2-rev	0.2571
col-7V-0.000-Ch2-rev	0.8064
col-9A-0.000-Ch3	0.0466
col-12A-0.000-Ch3	0.0922
near-col-2A-0.000-Ch3	0.0763
near-col-6A-0.000-Ch3	0.0666

Fig. 34.5 Deviation map of column acceleration identified along the axis X

The composition of harmonic vibration sources of powerhouse hall is well known. However by means of the method introduced were identified the vibration sources with the rotation frequencies given in Fig. 34.4.

As it is seen in the Fig. 34.4 the most common sources with the rotation frequencies of 600 r/min is appearing four times, whereas the frequency of 1,500 r/min (25 Hz, turbine and possibly other sources) is appearing in all cases except of two signals and the frequency of 1,800 r/min (930 Hz) – is presented three times. An example of the harmonic sources location map with corresponding rotation frequencies is shown below in the Fig. 34.7.

### 34.7 Acceleration Deviation Maps

As far as the response division was close to normal, the most appropriate measure of deviation can be triplicate rate of standard deviation value  $\sigma$ . This deviation value guarantees that the data obtained will be within the range  $[\bar{x} - 3\sigma; \bar{x} + 3\sigma]$  ( $\bar{x}$  - standard deviation) with a probability of 99.7%.

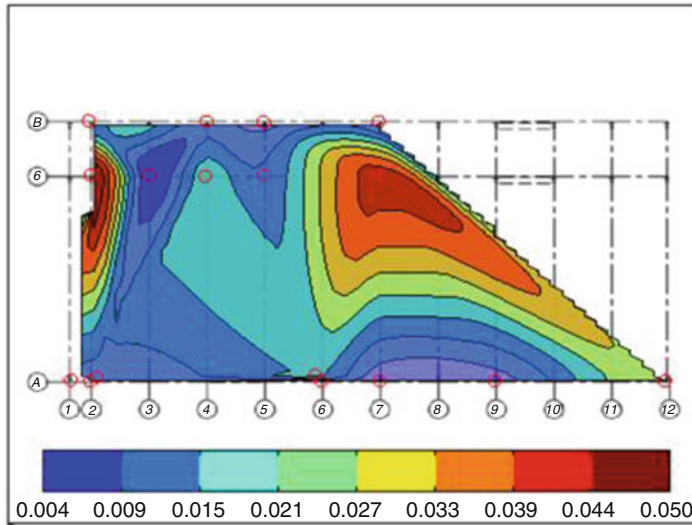
Acceleration deviation maps were made separately for each direction of measurements, one of these is shown in the Fig. 34.5, where the acceleration deviation is presented leftwards and the corresponding vector of information is given in the table rightwards. The analysis has shown that the largest acceleration deviations correspond to points of column oscillations induced in lateral direction. The largest deviation along the X-axis is 0.8064 m/s<sup>2</sup> (col-7V-0.000-Ch2-rev), along the Y-axis – 1.4033 m/s<sup>2</sup> (col-5V-0.000-Ch3), along the Z-axis – 0.2038 m/s<sup>2</sup> (col-5V-0.000-Ch1).

### 34.8 Acceleration Amplitude Maps

The maps of acceleration amplitude were made for frequencies, where the largest amplitudes of acceleration were identified: 25, 50 Hz. An example of acceleration amplitude map at the frequency of 25 Hz is shown in Fig. 34.6.

The largest acceleration amplitude along the X-axis is 0.0503 m/s<sup>2</sup> (col-2B-0.000-Ch2), along the Y-axis – 0.0173 m/s<sup>2</sup> (col-7A-0.000-Ch2), along the Z-axis – 0.0299 m/s<sup>2</sup> (near-col-2A-0.000-Ch2).

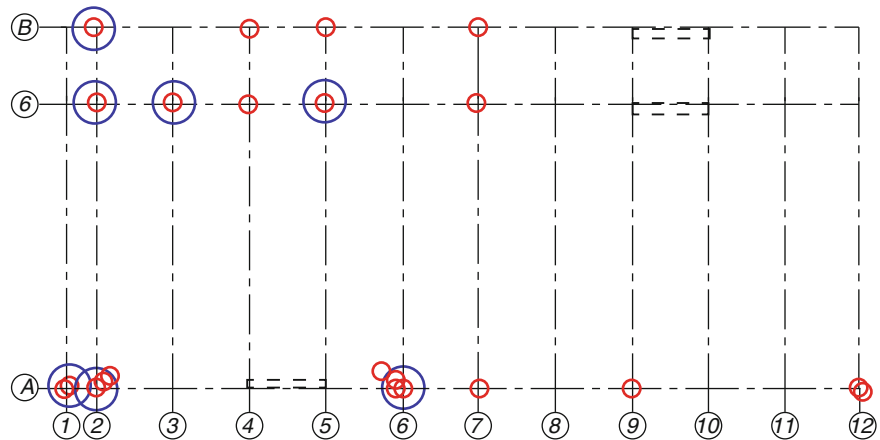
For vertical oscillations at the frequency of 25 Hz it is established that the amplitude for column points of turbine service plate near-col-6A-0.000-Ch2 near-col-2A-0.000-Ch2 is well above then for the columns of transverse frame of powerhouse hall. This probably related to the fact that these points are located on the columns, which are more closely connected to load-bearing elements of turbine.



Point name	Accel [m/s <sup>2</sup> ]
col-1A-0.000-Ch2	0.0036
col-2A-0.000-Ch3	0.0114
col-2B-0.000-Ch2	0.0503
col-2V-0.000-Ch2	0.0087
col-3B-0.000-Ch3	0.0051
col-4B-0.000-Ch2	0.0223
col-4V-0.000-Ch2	0.0113
col-5B-0.000-Ch2	0.0151
col-5V-0.000-Ch2	0.0065
col-6A-0.000-Ch3	0.0113
col-7A-0.000-Ch3	0.0059
col-7B-0.000-Ch2-rev	0.0417
col-7V-0.000-Ch2-rev	0.0050
col-9A-0.000-Ch3	0.0067
col-12A-0.000-Ch3	0.0270
near-col-2A-0.000-Ch3	0.0125
near-col-6A-0.000-Ch3	0.0201

**Fig. 34.6** The amplitude map of column acceleration measured along the X axis

**Fig. 34.7** Harmonic sources location map at the frequency 10 Hz



For the frequency of 50 Hz the largest acceleration amplitude along the X-axis is 0.0094 m/s<sup>2</sup> (col-7V-0.000-Ch2-rev), along the Y-axis – 0.0094 m/s<sup>2</sup> (col-6A-0.000-Ch2), along the Z-axis – 0.0081 m/s<sup>2</sup> (near-col-6A-0.000-Ch2).

### 34.9 Harmonic Sources Location Maps

Harmonic sources location maps were made for the mostly well-defined frequencies: 10 Hz (600 r/min); 25 Hz(1,500 r/min); 30 Hz (1,800 r/min). In Fig. 34.7 the measurement points are shown in bold, whereas locations of harmonic oscillations are circled. Sources were identified according to the measurement data obtained unidirectional.

The affecting frequency of 10 Hz (1,500 r/min) were identified in each measurement points, which probably means that turbine affects all the structures. For the frequencies of 15 Hz (600 r/min) and 30 Hz (1,800 r/min) the sources were identified only for some measurement points, this implies that the harmonic sources with the frequencies given are located locally.

## 34.10 Conclusions

Joint accelerations of columns and turbine plate were measured in this paper. For most of structure points oscillations are induced by different sources of exposure and dominant harmonics were fixed only for some directions of measurement points.

Maximum of accelerations (triplicate standard deviation) were identified for col-5V-0.000-Ch3 and col-7V-0.000-Ch3-rev (acceleration along the Y-axis) at the rate of 1.4 and 1.14 m/s<sup>2</sup>.

Spectral distribution of responses changes slightly over period of time; this implies that the impact of vibration sources is of stationary nature.

Multiple harmonics were fixed in each response and identified by means of suggested method of harmonics automated search. When analyzing the overall picture of harmonic identification, harmonic frequencies of 5, 10, 25, 30, 33 Hz are well defined.

## References

1. <http://reftek.com/products/index.htm>
2. Oppenheim AV, Schafer RW, Buck JR (1999) Discrete-time signal processing. Prentice Hall, Upper Saddle River, 870 p
3. Andersen P, Brincker R, Ventura C, Cantieni R (2008) Modal estimation of civil structures subject to ambient and harmonic excitation. In: Proceedings of the 26th international modal analysis conference (IMAC), Orlando, 8 p

# Chapter 35

## Study on the Band Structure of Trigonal Chiral Structures

Shiyin Xu, Xiuchang Huang, and Hongxing Hua

**Abstract** The Bloch theorem and finite element technique are applied to investigate the bandgap property of trigonal chiral cellular, which is illustrated through band diagrams. The finite element model is developed to validate the results. Vibration transmission displays significant attenuation for the frequency located in the band gap. The distribution of the band gap is determined by the geometry of the unit cell and can be tuned to specific frequency range. Attention is devoted to the dependence of phase speed and group velocity on frequency and direction, which provides important information about anisotropic wave behavior of the structure and shows existence of preferential directions of propagation and energy flow. The research outcomes will lay a solid theoretical base for the designing of chiral isolation structures.

**Keywords** Trichiral structure • Bloch theorem • Dispersion behavior • Band gap • Layered gradient structure

### 35.1 Introduction

Honeycomb structures, whose properties are determined by the topology and spatial arrangement of the unit cell, are extensively used in project field due to its light-weight, high-strength and excellent designable. The chiral topology was proposed by Wojciechowski firstly in 1989 [1]. Because of its unique geometry and performance, chiral lattice becomes a focus among the honeycomb structures. Prall validated that chiral tessellations lead to in-plane negative Poisson's ratio theoretically and experimentally [2]. Alderson calculated Young's modulus and Poisson's ration of several kinds of chiral lattice and studied their deformation mechanism by FE model as well [3]. Lorato estimated the elastic properties along the thickness direction by analytical method, FE method and experimental research respectively [4]. Scarpa's research showed that hexachiral honeycomb has better buckling strength compared with the hexagonal one [5]. According to other studies [6–8], the chiral structure, owning excellent static performance, combines large deflection deformation and large shear stiffness. Meanwhile, due to the designable characteristic offered by the unique configuration, the dynamic behaviour of the chiral structure can be optimized without the modification of the total weight.

On the other hand, wave propagation in the periodic structure, especially the bandgap characteristics, has attracted widespread attention. The impedance mismatch generated by periodic discontinuities in geometry within the structure causes destructive wave interference phenomena over specified frequency bands called “stop-bands” or “bandgaps” [9]. Phani analysed the behaviour of wave propagation in several kinds of plane lattice to compare their bandgap property [10]. Tee and Spadoni studied the wave propagation in the tetrachiral and hexachiral lattice respectively [11, 12]. These chiral lattices exhibit stop-band in higher frequency and further research indicated the influence of the geometry of the unit cell on the bandgap. Based on the idea of localized resonant structures, Liu fabricated a novel chiral metamaterial featuring remarkable vibration isolation over the range of low frequency [13].

The current work describes the wave propagation characteristics of trichiral honeycombs from a numerical point of view. The pass-stop band of trichiral honeycombs is compared with the results of the hexachiral structure. Attention is devoted to

---

S. Xu (✉) • X. Huang • H. Hua

State Key Laboratory of Mechanical System and Vibration, Shanghai Jiao Tong University, Shanghai 200240, China  
e-mail: xushiyin0628@sjtu.edu.cn; xchhuang@sjtu.edu.cn; hhx@sjtu.edu.cn



the similarity between two kinds of chiral cellular in geometry and the influence of combining these two structures on the bandgap. The directionality of the wave propagation in the trichiral lattice is discussed through the contours of the phase and group velocities.

## 35.2 Geometries of the Chiral Lattice

### 35.2.1 Unit Cell's Geometry Characteristics

The schematic of the trichiral honeycomb is illustrated in Fig. 35.1, composed of a periodic array of nodes connected by ligaments tangentially. According to the number of ligaments attached to each node, the chiral honeycomb can be classified into three types: trichiral, tetrachiral and hexachiral. Attaching adjacent nodes on opposite sides of the connecting ligament produces the chiral honeycomb, whereas attaching the nodes on the same side of the connecting ligament creates the antichiral honeycomb [3]. In Fig. 35.1,  $r$  and  $l$  are the node radius and the ligament length respectively, while  $R$  denotes the distance between the center of nodes.  $\theta$  and  $\beta$  respectively represent the angle between the centerline of two neighboring nodes and the angle between the centerline and the ligament. The geometry of the trichiral unit cell is determined through formula as follows:

$$\sin \beta = \frac{2r}{R}, \tan \beta = \frac{2r}{R}, \sin \theta = \frac{R/2}{R}, \cos \beta = \frac{L}{R} \quad (35.1)$$

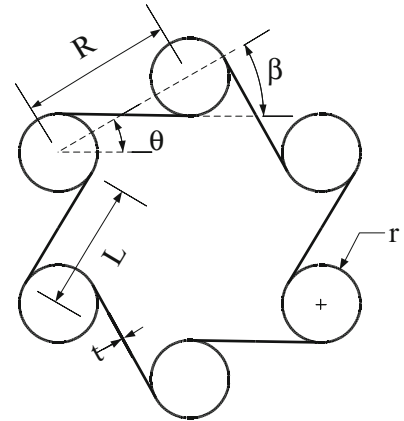
According to (35.1),  $\theta = 30^\circ$ . The trichiral lattice is much different from other chiral structures in structural properties. It owns the advantage of lighter weight due to the fewer nodes and ligaments. Meanwhile, it's Poisson ratio is always positive, which is caused by its unique deformation mechanism.

### 35.2.2 Lattice Vectors

As depicted in Fig. 35.2, chiral lattice is composed of several unit cells that are lined up repeatedly in periodic direction and the schematic of unit cell is highlighted by dashed lines in the figure. Lattice vectors  $\mathbf{e}_i$  are used to define the periodicity of the lattice, while the location of a unit cell in the lattice is determined by the linear combination of the lattice vector  $n_1\mathbf{e}_1 + n_2\mathbf{e}_2$ . The lattice vectors of the trichiral can be expressed as follows:

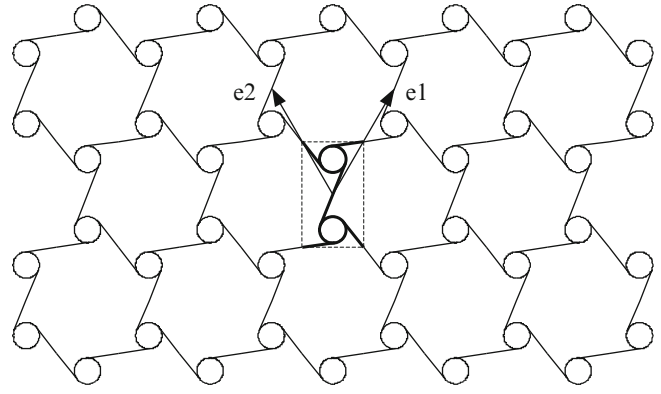
$$\mathbf{e}_1 = \{R \cos \theta, R \sin \theta\}^T = \left\{ \frac{\sqrt{3}}{2}R, \frac{1}{2}R \right\}^T, \mathbf{e}_2 = \{-R \cos \theta, R \sin \theta\}^T = \left\{ -\frac{\sqrt{3}}{2}R, \frac{1}{2}R \right\}^T \quad (35.2)$$

When the unit cell at  $(0,0)$  is the reference, the location of point P in the unit cell  $(n_1, n_2)$  can be represented as  $\mathbf{p}_P(n_1, n_2) = \mathbf{r}_P + n_1\mathbf{e}_1 + n_2\mathbf{e}_2$ , where  $\mathbf{r}_P$  donates the location of the point corresponding to P in the reference cell.



**Fig. 35.1** Geometry of the trichiral lattice

**Fig. 35.2** Schematic of unit cell and the lattice vectors



### 35.3 Unit Cell Analysis of Wave Propagation in 2-D Trichiral Lattices

Based on Bloch theorem, the amplitude variation of the propagation wave is independent of the cell location in the periodic structure. The wave propagation behaviour of the periodic can be identified through the analysis of the reference cell, where the displacement of P can be written as follows:

$$\mathbf{q}(\mathbf{r}_P) = \mathbf{q}_{P0} e^{i(\omega t - \mathbf{k} \cdot \mathbf{r}_P)} \quad (35.3)$$

In the equation,  $\mathbf{q}_{P0}$  is the wave amplitude and  $\mathbf{k}$  is the wave vector. Then the displacement of point Q at cell  $(n_1, n_2)$  corresponding to P can be expressed as:

$$\mathbf{q}(\mathbf{r}) = \mathbf{q}(\mathbf{r}_P) e^{i\mathbf{k}(\mathbf{r} - \mathbf{r}_P)} = \mathbf{q}(\mathbf{r}_P) e^{n_1 k_1 + n_2 k_2} \quad (35.4)$$

Application of the FE procedure finds the model of the unit cell and yields its equation of motion:

$$(\mathbf{K} - \omega^2 \mathbf{M}) \mathbf{q} = \mathbf{F} \quad (35.5)$$

where  $\mathbf{K}$  and  $\mathbf{M}$  are the global stiffness and mass matrix of the unit cell, while  $\mathbf{q}$  and  $\mathbf{F}$  are the generalized nodal displacement and force vector that can be expressed as follows:

$$\mathbf{F} = \{\mathbf{F}_{LB} \ \mathbf{F}_{LT} \ \mathbf{F}_{RT} \ \mathbf{F}_{RB} \ \mathbf{F}_I\}^T, \quad \mathbf{q} = \{\mathbf{q}_{LB} \ \mathbf{q}_{LT} \ \mathbf{q}_{RT} \ \mathbf{q}_{RB} \ \mathbf{q}_I\}^T \quad (35.6)$$

In (35.6), the subscripts  $LB, LT, RB, RT, L, R$  represent the nodes on the boundary of the cell and the subscript  $I$  represents the internal node. According to Bloch theorem, the displacement and force vectors of the node on the boundary are mutually related and can be expressed as:

$$\begin{aligned} \mathbf{F}_{RT} &= -\mathbf{F}_{LB} e^{k_1}, \quad \mathbf{F}_{LT} = -\mathbf{F}_{RB} e^{k_2}, \\ \mathbf{q}_{RT} &= \mathbf{q}_{LB} e^{k_1}, \quad \mathbf{q}_{LT} = \mathbf{q}_{RB} e^{k_2}, \end{aligned} \quad (35.7)$$

Equation 35.7 can be rewritten in the matrix form as:

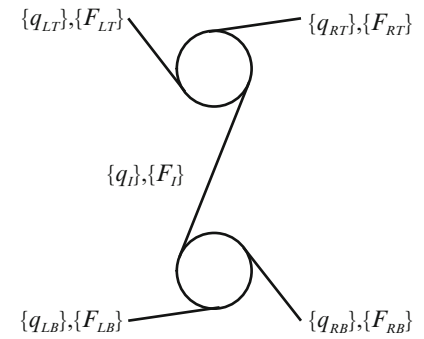
$$\mathbf{F} = \mathbf{T}_F \mathbf{F}_r, \quad \mathbf{q} = \mathbf{T}_u \mathbf{q}_r \quad (35.8)$$

where the subscript  $r$  represents the reduced vector  $\mathbf{q}_r = \{\mathbf{q}_{LB}, \mathbf{q}_{RB}, \mathbf{q}_B, \mathbf{q}_I\}$ .  $\mathbf{T}_u$  and  $\mathbf{T}_F^T$ , having the relationship  $\mathbf{T}_u = \mathbf{T}_F^T$ , are the corresponding reduction matrix. Substituting (35.8) into (35.5) and then left multiplying  $\mathbf{T}_u^H$  to obtain the reduced equation:

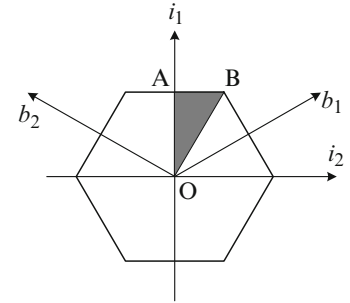
$$[\mathbf{K}_r(k_1, k_2) - \omega^2 \mathbf{M}_r(k_1, k_2)] \mathbf{q}_r = 0 \quad (35.9)$$

where  $\mathbf{K}_r$  and  $\mathbf{M}_r$ , the function of wavenumber  $\mathbf{k}$ , are reduced stiffness and mass matrices respectively. The natural frequency  $\omega$ , corresponding to certain wavenumber, can be obtained by the eigensolution of (35.9).  $\omega = \omega(k_1, k_2)$  donates the

**Fig. 35.3** Internal and boundary DOFs of unit cell



**Fig. 35.4** Brillouin zone and irreducible Brillouin zone



dispersion surface, which has the same number of the eigensolution. If the dispersion surfaces don't overlap each other, the corresponding frequency band is the forbidden zone of the lattice, where the wave propagation can't occur and the structure vibration will be suppressed significantly. The scope of  $\mathbf{k}$  is determined by irreducible Brillouin zones as depicted in Figs. 35.3 and 35.4 by shadow region. The natural frequency corresponding to the wavenumber within the irreducible Brillouin zone will fall into the range determined by the wavenumber along the boundary O-A-B-O.

## 35.4 Numerical Simulation

### 35.4.1 Band Diagrams

The method, presented in the previous section, is exploited to calculate the band of the trichiral lattice. The steel is selected to simulate the unit cell, whose geometric parameters are  $L = 0.1$  m and  $t = 0.002$  m. Figure 35.5 shows the band of the unit cell, where the shade region donates the stop band of the lattice. Figure 35.5a presents the dispersion curves of the unit cell when  $r = 0.02$  m and there are two board stop bands over the range of [294, 845 Hz] and [1,088, 1,845 Hz]. The dispersion curves, when  $r = 0.045$  m, are shown in Fig. 35.5b. In contrast, the band structure of these two lattices changes drastically. It can be noticed that the curves appear to be more compact in arrangement and the location and the extension of the bandgap change accordingly. We can find that the larger the node radius is, the lower frequency the bandgap locates. The results expose the variation of the band structure under various node radius and provide a qualitative description of the strong influence of the configurational parameter on the dispersion characteristics.

The modes of the cell are shown in Fig. 35.6, associated with the dispersion curves and calculated at vertex O, A and B. They can be categorized into several groups as follows: the rigid mode of the unit cell, the bending mode of the ligament, the rotary mode of the node and the circumferential mode of the node. The first two modes at point O associates with rigid motion of the cell; the third mode at point A, associates with the flexural motion of the ligament, is caused by the translation of the node, which corresponds to the initial frequency of the first bandgap; the seventh and eighth modes at point B and point A, corresponding to the second and third bandgaps respectively, are the circumferential modes of the node. It proves that the modes of the unit cell are related to the distribution of the bandgap, which can be used to optimize the geometry of the unit cell.

The FE model of trichiral honeycomb, whose geometry parameter is the same as the one in Fig. 35.5b, is founded to verify the occurrence of the bandgap estimated in the previous section. There are 5 cells in vertical direction and 12 ones in

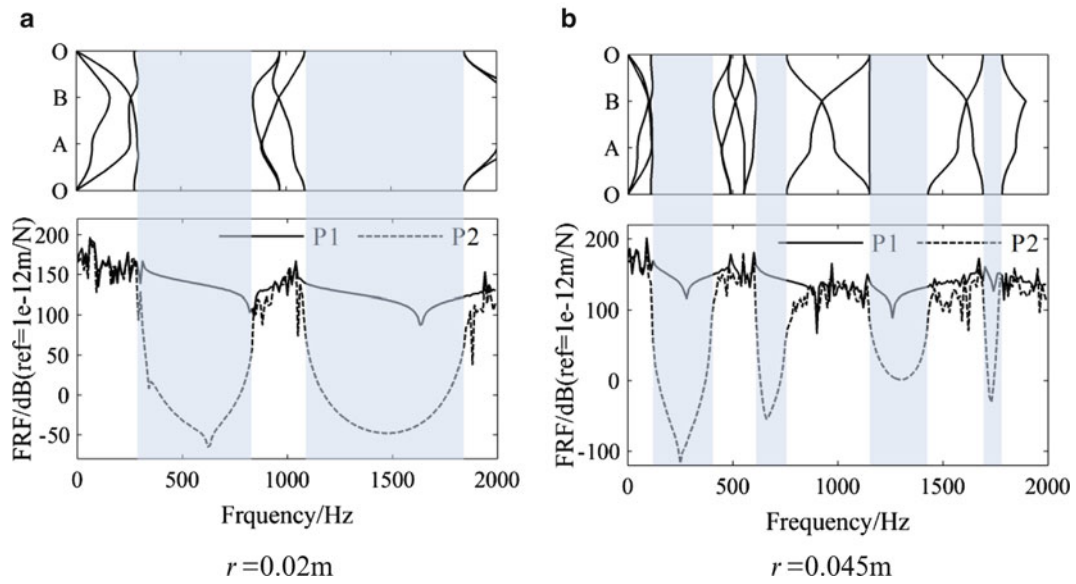
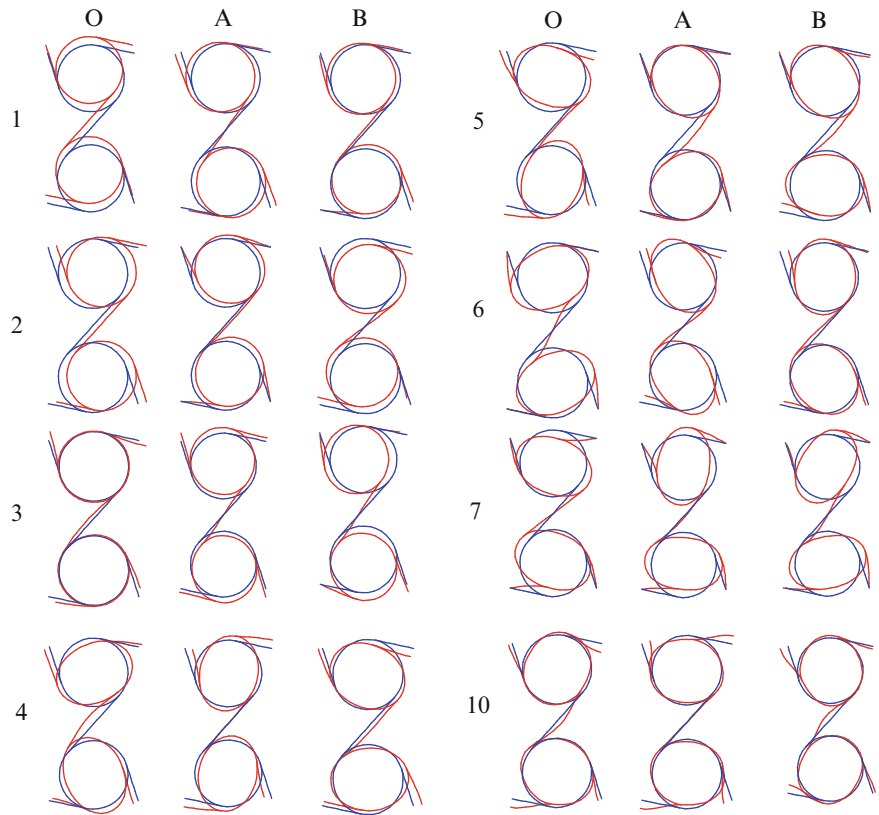
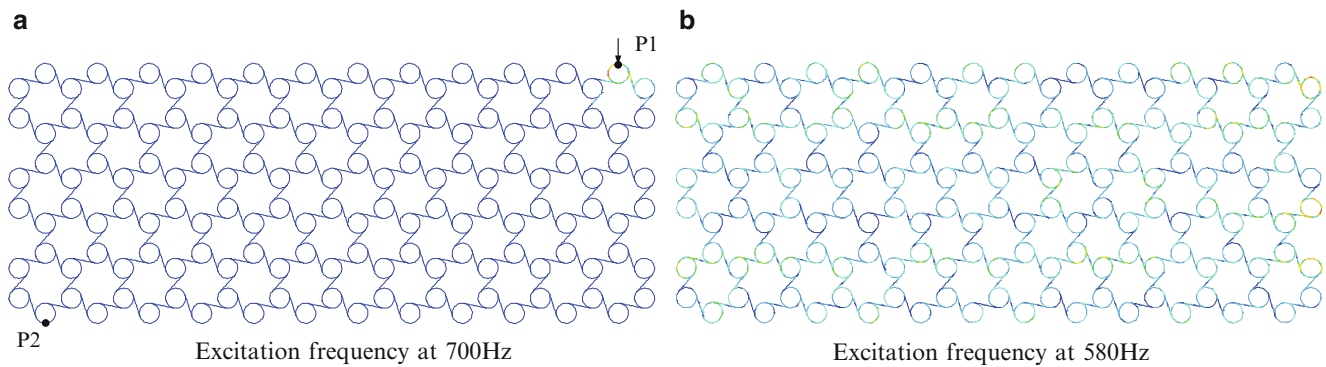


Fig. 35.5 Band diagrams and frequency response of unit cell. (a)  $r = 0.02\text{ m}$ . (b)  $r = 0.045\text{ m}$

Fig. 35.6 Wave modes of the chiral unit cell

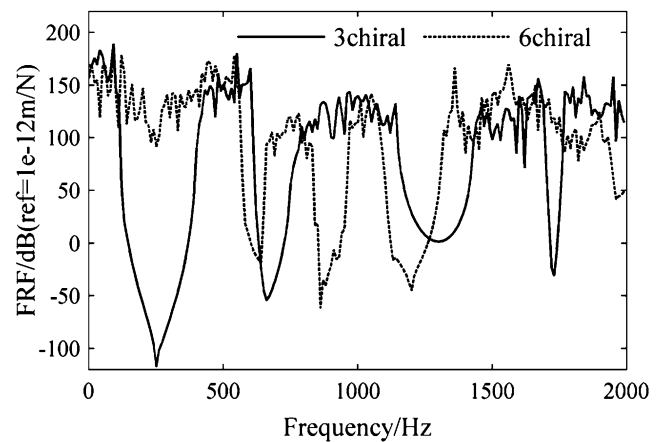


horizontal, and the free boundary condition is considered. A harmonic unit load is applied at point P1 vertically (Fig. 35.7) and the range of excitation frequency is 1–2,000 Hz covering the first four bandgap of the unit cell. The frequency response curve of the lattice (Fig. 35.5), evaluated via the displacement at P1 and P2, can be used to analyse the vibration transmission characteristics. The result clearly displays the presence of the bandgap by the shade region, where the response at P2 has attenuation significantly. It is indicated the feature of the trichiral with vibration reduction and the validity of the proposed method.



**Fig. 35.7** Deformation map of the finite periodic chiral lattice. (a) Excitation frequency at 700 Hz. (b) Excitation frequency at 580 Hz

**Fig. 35.8** Frequency response of two kinds of lattices



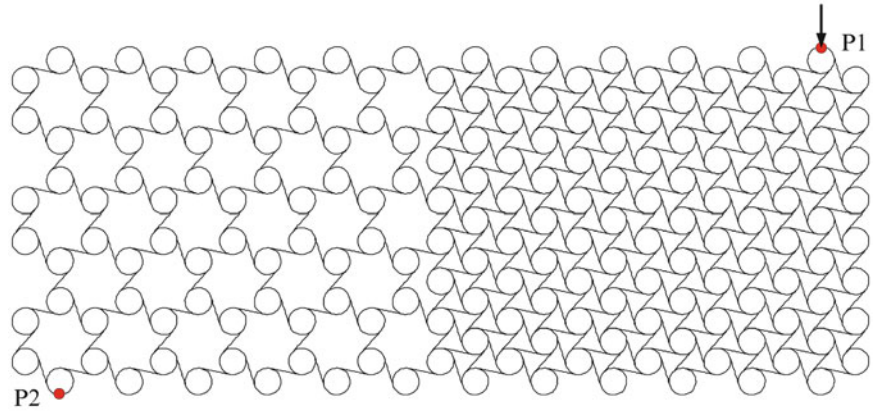
The deformation of the chiral lattice under the vertical load is portrayed in Fig. 35.7. When the excitation frequency is 700 Hz, lying in the scope of the bandgap, the main deformation is limited at the area close to the exciting point and decays along the direction of the periodicity. When the excitation frequency is 580 Hz, out of the scope of the bandgap, the homogeneous deformation occurs.

### 35.4.2 Comparison Between Trichiral and Hexachiral Lattice

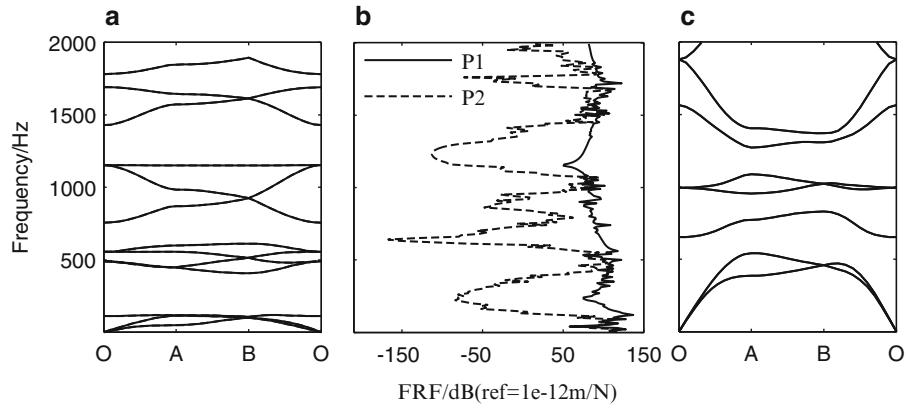
To yield a deep insight of the bandgap property of the chiral structure, a comparison between the tetrachiral and hexachiral lattice is conducted. The trichiral and hexachiral lattices have comparability in the band structure, which can be attributed to the structural similarity. The frequency spectrum of two lattices is displayed in Fig. 35.8, where the solid line and dash line represent the curve of the trichiral and hexachiral lattice respectively. It is obvious that both of the lattices can play the role of suppressing the vibration response over the frequency range of [600, 670 Hz] and [1,150, 1,370 Hz], while the trichiral lattice features a lower bandgap in the range of [150, 450 Hz] compared with the hexachiral one.

A novel hybrid lattice, utilizes trichiral lattice in the left side and contains hexachiral lattice in the right side, is proposed (Fig. 35.9). A harmonic unit load is applied at point P1 vertically and the frequency spectrum of the lattice, shown in Fig. 35.10, is evaluated via the displacement at P1 and P2. For the sake of comparison, the band diagram of the trichiral and hexachiral lattice are also given as reference in the figure. With the hybrid configuration, it is worth noting that the vibration suppression areas are achieved by the sum of the bandgap of the trichiral and the hexachiral lattice, leads to the vibration reduction over a wider frequency range. On the other hand, the proposed lattice is more lighter than the hexachiral, which caters to the requirement of the engineering application.

**Fig. 35.9** Schematic of hybrid structure



**Fig. 35.10** (a) Band diagram of the trichiral honeycomb, (b) frequency response of the hybrid honeycomb and (c) band diagram of the hexachiral honeycomb



### 35.4.3 Phase and Group Velocities

The phase and group velocities, derived from the contours of the dispersion surfaces, can be exerted to evaluate the direction of wave propagation in the lattice. The phase velocity, donates the rate at which the phase of the wave propagates in the structure, can be given in terms of wave’s angular frequency and wavenumber as:

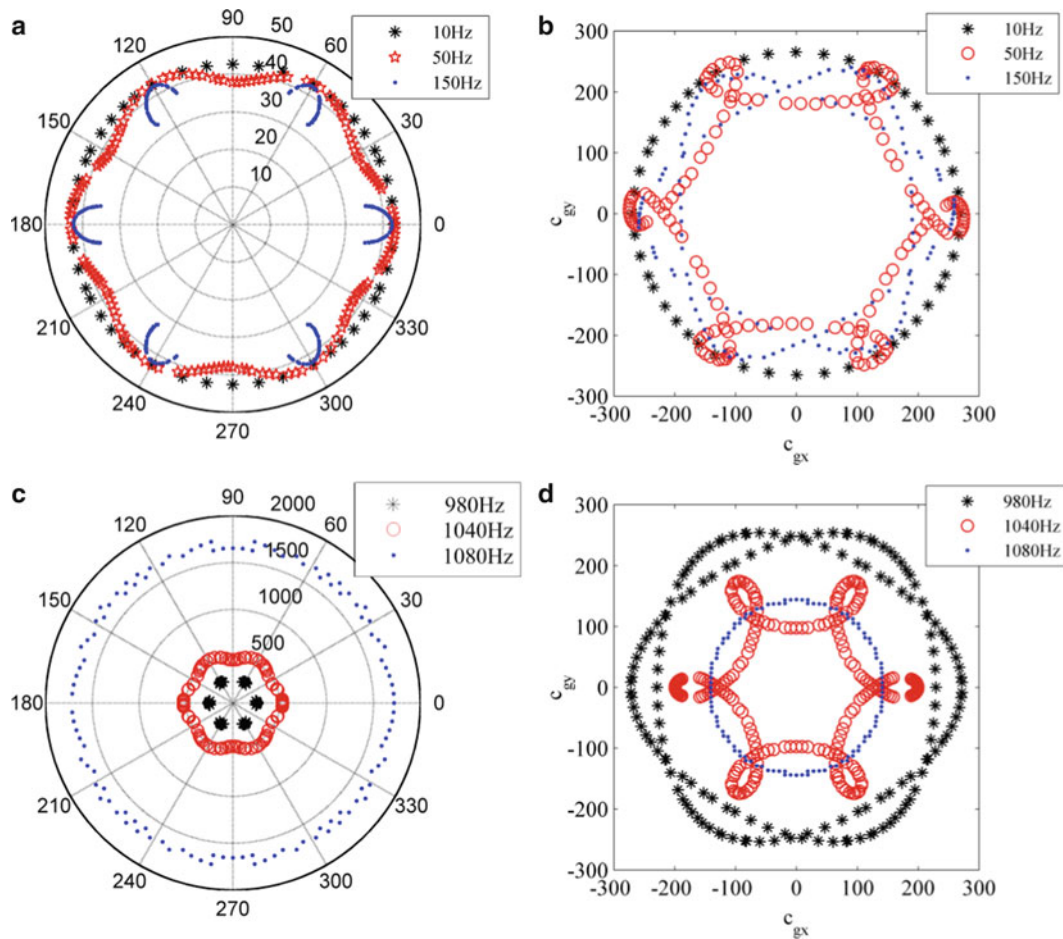
$$\mathbf{c}_{ph} = \frac{\omega}{k} \mathbf{u}, \tag{35.10}$$

where  $k = |\mathbf{k}|$  and  $\mathbf{u}$  is the unit vector in the direction of the wave vector. The group velocity represents the propagation velocity of the vibrational energy in the undamp structure, which can be expressed as follows:

$$\mathbf{c}_g = \left( \frac{\partial \omega}{\partial \xi_1}, \frac{\partial \omega}{\partial \xi_2} \right)^T \tag{35.11}$$

A FE model of unit cell is founded to calculate the phase and group velocities of the trichiral lattice, whose dimensions are the same as those in Fig. 35.5a. The results at different frequencies of interest for the first mode are compared in Fig. 35.11a to verify the dependence of directionality on the frequency. From the figure, we can notice that at lower frequencies the contours of the phase velocity can be regarded as a circle, which indicates that the directions of wave propagation vary from 0 to 360 and there is no preferential direction at this frequency. With the increase of the frequency, the anisotropy of the contours become more and more obvious which exposes the main directions of the wave propagation. It is worth noting that the magnitude of the phase velocity tends to decrease as the frequency increases. The results of the group velocity, shown in Fig. 35.11b, are in consistent with phase velocity in directionality. The contours shape of the phase and group velocities are almost identical at low frequency. While the group velocity is confined to six directions at high frequency, which reveals the energy concentration along specific directions.





**Fig. 35.11** Phase and group velocities of the first mode (a, b) and sixth mode (c, d)

In comparison, the phase and the group velocity corresponding to the sixth mode are depicted in Fig. 35.11c, d. It should be noted that the curves display the anisotropy at lower frequency and gradually become isotropy as frequency increases, which are opposite to the presented results. The modal order has a significant influence in the variation of the directionality of the trichiral lattice.

### 35.5 Conclusion

In this work, the wave propagation in trichiral lattice is analysed by means of the Bloch theorem incorporating with finite element method. The simulation results confirm the isolation characteristic of the considered lattice and the validation of the method. The comparison between the trichiral and hexachiral lattice is provided in the geometry and the band structure, from which we can notice that the trichiral lattices have the features of low-frequency bandgap and light weight. The mixed lattice, consists of these two structures, can suppress the vibration response over a wider frequency range, which is the superposition of the bandgap of individual lattice. The strongly anisotropy behavior of the lattice at high frequency, investigated by means of the contours of the phase and group velocities, demonstrates the directionality of wave propagation.

**Acknowledgements** The authors gratefully acknowledge the support for this work by the National Natural Science Foundation of China (NSFC) under grant No. 11172173.

## References

1. Wojciechowski KW (1989) Two-dimensional isotropic system with a negative poisson ratio. *Phys Lett A* 137(1–2):60–64
2. Prall D, Lakes R (1997) Properties of a chiral honeycomb with a poisson's ratio of  $-1$ . *Int J Mech Sci* 39(3):305–314
3. Alderson A, Alderson KL, Attard D et al (2010) Elastic constants of 3-, 4- and 6-connected chiral and anti-chiral honeycombs subject to uniaxial in-plane loading. *Compos Sci Technol* 70(7):1042–1048
4. Lorato A, Innocenti P, Scarpa F et al (2010) The transverse elastic properties of chiral honeycombs. *Compos Sci Technol* 70(7):1057–1063
5. Scarpa F, Blain S, Lew T et al (2007) Elastic buckling of hexagonal chiral cell honeycombs. *Compos Part A Appl Sci Manuf* 38(2):280–289
6. Spadoni A, Ruzzene M (2007) Numerical and experimental analysis of the static compliance of chiral truss-core airfoils. *J Mech Mater Struct* 2(5):965–981
7. Spadoni A, Ruzzene M (2006) Structural and acoustic behavior of chiral truss-core beams. *J Vibr Acoust* 128(5):616–626
8. Spadoni A, Ruzzene M, Scarpa F (2006) Dynamic response of chiral truss-core assemblies. *J Intell Mater Syst Struct* 17(11):941–952
9. Gonella S, Ruzzene M (2008) Analysis of in-plane wave propagation in hexagonal and re-entrant lattices. *J Sound Vibr* 312(1–2):125–139
10. Phani AS, Woodhouse J, Fleck NA (2006) Wave propagation in two-dimensional periodic lattices. *J Acoust Soc Am* 119(4):1995–2005
11. Spadoni A, Ruzzene M, Gonella S et al (2009) Phononic properties of hexagonal chiral lattices. *Wave Motion* 46(7):435–450
12. Tee KF, Spadoni A, Scarpa F et al (2010) Wave propagation in auxetic tetrachiral honeycombs. *J Vibr Acoust* 132(3):0310071–0310078
13. Liu XN, Hu GK, Sun CT et al (2011) Wave propagation characterization and design of two-dimensional elastic chiral metamaterial. *J Sound Vibr* 330(11):2536–2553

# Chapter 36

## FEM Sensitivity Vector Basis for Measured Mode Expansion

Robert N. Coppelino

**Abstract** Expansion of measured mode vectors (or operating deflection shapes) from sensor to FEM degrees of freedom requires utilization of theoretical FEM shape vectors. The most often used shape vectors are based on (a) the Guyan reduction (static condensation) transformation, and (b) FEM theoretical mode shapes. Accuracy of such expansions is severely limited by the fact that the vector expansion is derived from a specific baseline FEM. This paper introduces an expansion transformation based on FEM sensitivity vectors that have been employed for the past decade in FEM parametric sensitivity and FEM-test reconciliation analyses. Since the sensitivity vector based expansion spans a wide parametric uncertainty space, it accurately reconstructs the full order FEM modes, regardless of actual unknown system parameters. A simple illustrative example is provided to demonstrate performance of the currently used and sensitivity based mode expansion strategies. A series of practical applications of the new strategy are cited.

**Keywords** FEM • Sensitivity • Residuals • Mode expansion

### 36.1 Introduction

An accurate and efficient method for computation of structural dynamic modal frequency and mode shape sensitivities due to variation of physical stiffness and parameters was published at IMAC XXIX [1]. At the heart of the method is the formation of residual vectors that describe the distributed effect of both stiffness and mass deviations with respect to the baseline system's modes. The combined set of baseline modes and residual vectors (robust trial vectors) define a transformation matrix which is used to form a greatly reduced order sensitivity model that accurately tracks changes in system modes and natural frequencies driven by large stiffness and mass variations. This technique was successfully applied to effect reconciliation of an International Space Station component's finite element model with modal test data as early as 2001 [2]. An extended application of sensitivity analysis was published in IMAC XXX [3] focusing on efficient estimation of system dynamic response variations (accelerations, displacements, strains and stresses) due to stiffness and mass uncertainties.

The present paper introduces a technique for expansion of measured operating deflection or laboratory modal test data employing robust trial vectors. This technique requires (a) a detailed system finite element model for the measured system used to define an appropriate set of robust trial vectors from sensitivity analyses, and (b) measured system deflection data at a sufficient number of locations to reconstruct the remaining deflections. Utilization of the robust trial vector set provides the capability to accurately expand measured operating deflection data with much fewer trial vectors than required when baseline system modes are employed as the trial vector set. Expansion of operating deflection data to FEM degrees of freedom using the robust trial vector set follows operations defined by the SEREP procedure [4].

Practical application of the robust trial vector expansion technique for operating deflection analysis must include utilization of additional data analysis and system identification techniques including (a) output-only modal parameter estimation, e.g., randomdec analysis [5, 6], (b) FEM reconciliation analysis [1, 3], and (c) nonlinear system identification procedures [7].

---

R.N. Coppelino (✉)  
Measurement Analysis Corporation, 23850 Madison Street, Torrance, CA 90505, USA  
e-mail: [bobcoppelino@mindspring.com](mailto:bobcoppelino@mindspring.com)

## 36.2 Nomenclature

Variable	Definition	Equation	Variable	Definition	Equation
$[M_O]$	Baseline FEM mass matrix	1	$[m_O]$	Generalized baseline FEM mass	6
$[K_O]$	Baseline FEM stiffness matrix	1	$[\Delta k_i]$	Generalized FEM sensitivity stiffness	6
N	Number of independent sensitivities	1	$[\Delta m_i]$	Generalized FEM sensitivity mass	6
$[\Delta M]_i$	Mass sensitivity matrix	1	$[\phi]$	Generalized modal matrix	5
$[\Delta K]_i$	Stiffness sensitivity matrix	1	$[\bar{\Phi}_A]$	Trial vector set measured partition	8
$p_i$	Sensitivity scale factor	1	$[\bar{\Phi}_O]$	Trial vector set “other” partition	8
$\{u\}$	Displacement vector	1	$[\Phi_{ODS}]$	Measured operating deflection shapes	9
$[\Phi_{OL}]$	Baseline FEM modes (lowest)	2	$[q]$	Generalized displacement matrix	9
$[\lambda_{OL}]$	Baseline FEM eigenvalues (lowest)	2	$[R]$	Residual error matrix	10
$[\Phi_{iL}]$	FEM sensitivity modes (lowest)	3	$[W]$	Weighting matrix	10
$[\lambda_{iL}]$	FEM sensitivity eigenvalues (lowest)	3	$[\Phi_{ODS,FEM}]$	Expanded operating deflection shapes	11
$[\Psi]$	Redundant trial vector set	4	$[OR]$	Orthogonality matrix	12
$[\bar{\Phi}_{OL}]$	Linearly independent trial vector set	Appendix	$[COR]$	Cross-orthogonality matrix	12
$[k_O]$	Generalized baseline FEM stiffness	6	Note: Additional variables in <a href="#">Appendix</a> are not defined in this table		

## 36.3 Sensitivity Vectors and Measured Mode Expansion

Low frequency mode sensitivity was the primary focus of Ref.[1]. The matrix equation set describing free vibration of a baseline or altered undamped system is

$$\left[ M_0 + \sum_{i=1}^N p_i \cdot \Delta M_i \right] \{\ddot{u}\} + \left[ K_0 + \sum_{i=1}^N p_i \cdot \Delta K_i \right] \{u\} = \{0\} \quad (36.1)$$

When all “ $p_i$ ” are null, the system is “baseline”. Attention shall be limited to sensitivities due to stiffness and mass changes.

The low frequency undamped modes of the baseline system are solutions of the eigenvalue problem

$$[K_O] [\Phi_{OL}] - [M_O] [\Phi_{OL}] [\lambda_{OL}] = [0] \quad (36.2)$$

Definition of residual vectors describing parametric variations in (36.1) is accomplished utilizing the lowest frequency mode shapes of the baseline structure as well as the lowest mode shapes associated with each independent alteration of the structure

$$[K_O + \bar{p}_i \Delta K_i] [\Phi_{iL}] - [M_O + \bar{p}_i \Delta M_i] [\Phi_{iL}] [\lambda_{iL}] = [0] \quad (\text{for } i = 1, \dots, N), \quad (36.3)$$

where  $\bar{p}_i$  is a finite (rather than infinitesimal parametric perturbation). An initial set of trial vectors that redundantly encompass all low frequency altered system mode shapes is

$$[\Psi] = [\Phi_{1L} \Phi_{2L} \dots \Phi_{NL}] \quad (36.4)$$

The redundant set of trial vectors is reduced to a linearly independent “modal” set,  $[\bar{\Phi}_{OL}]$ , by following the methodology described in [Appendix](#).  $[\bar{\Phi}_{OL}]$  is the trial vector set (sensitivity vectors) to be used for expansion of measured operating deflection shapes.

It is of interest to note that the resulting approximate generalized sensitivity model (that may be employed in a more complete system identification exercise) is

$$\left[ k_O + \sum_{i=1}^N p_i [\Delta k_i] \right] [\varphi] - \left[ m_O + \sum_{i=1}^N p_i [\Delta m_i] \right] [\varphi] [\lambda] = [0], \quad (36.5)$$

where the reduced stiffness and mass matrix components are

$$[k_O] = [\bar{\Phi}_{OL}^T K_O \bar{\Phi}_{OL}], \quad [m_O] = [\bar{\Phi}_{OL}^T M_O \bar{\Phi}_{OL}], \quad [\Delta k_i] = [\bar{\Phi}_{OL}^T \Delta K_i \bar{\Phi}_{OL}], \quad [\Delta m_i] = [\bar{\Phi}_{OL}^T \Delta M_i \bar{\Phi}_{OL}] \quad (36.6)$$

The low frequency physical modes for the altered dynamic system are recovered using the relationship

$$[\Phi_L] = [\bar{\Phi}_{OL}] [\varphi] \quad (36.7)$$

### 36.4 Serep Expansion Using Sensitivity Vectors

Estimation of FEM order operating deflection shapes, using the above defined sensitivity vectors, follows the basic SEREP procedure, which is outlined herein. The first SEREP step involves partitioning the sensitivity vectors into “measured” and “other” displacement partitions,

$$[\bar{\Phi}_{OL}] = \begin{bmatrix} \bar{\Phi}_A \\ \bar{\Phi}_O \end{bmatrix} = \begin{bmatrix} \text{“measured”} \\ \text{“other”} \end{bmatrix} \quad (36.8)$$

The relationship between measured operating deflections,  $[\Phi_{ODS}]$ , and the “measured” displacement partition is

$$[\Phi_{ODS}] = [\bar{\Phi}_A] [q] + [R] \quad (36.9)$$

where  $[R]$  is the residual error matrix. Employing weighted least-squares analysis, the generalized displacements,  $[q]$ , are estimated as

$$[q] = [\bar{\Phi}_A^T W \bar{\Phi}_A]^{-1} [\bar{\Phi}_A^T W \Phi_{ODS}] \quad (36.10)$$

A convenient choice of the weighting matrix,  $[W]$ , may be the Guyan reduced FEM mass matrix [8]. Otherwise, an intuitive mass weighting or identity matrix (non-weighted least squares option) may be utilized. In all situations, the overall quality of the least-squares fit is judged based on the residual error matrix,  $[R]$ .

The expanded operating deflection shapes are finally

$$[\Phi_{ODS.FEM}] = [\bar{\Phi}_{OL}] [q] \quad (36.11)$$

### 36.5 Illustrative Example: Segmented Beam

A four segment beam, illustrated below in Fig. 36.1, is used as an illustrative example (described by a 73 grid point FEM) to demonstrate the measured mode expansion procedure.

Beam sections 1–3 each have flexural stiffness,  $EI = 1.473 \times 10^8$ , and mass per unit length,  $\rho A = 0.00122$ . Beam section 4, a small appendage, has flexural stiffness,  $EI = 7.363 \times 10^6$ , and mass per unit length,  $\rho A = 0.0122$ . The reference rotational bending stiffness values for the sensitive interfaces are  $\Delta K_1 = \Delta K_2 = \Delta K_3 = 10^7$ . Note that the first stiffness is intended to represent the beam’s foundation, and the other two rotational stiffnesses represent interior joints.

Modes associated with four different combinations of local rotational bending stiffness parameters are calculated as follows:

1. Baseline model:  $p_1 = 5, p_2 = p_3 = 10$  (stiff interior joints)
2. Sensitivity model 1:  $p_1 = 5, p_2 = 3, p_3 = 1$  (soft interior joints)
3. Sensitivity model 2:  $p_1 = 5, p_2 = 1, p_3 = 3$  (soft interior joints)
4. Simulated test data:  $p_1 = 5, p_2 = 0.50, p_3 = 0.25$

The computed modal frequencies associated with the above noted combinations of parameters are shown below in Table 36.1.

It is of interest to note the baseline model and simulated modes shapes illustrated below in Fig. 36.2.

Note that the second and third modes of the simulated test model are characterized by abrupt changes in slope due to the “soft” joints, which contrast the smooth changes in the baseline model, which has stiff joints. The modes associated with the two sensitivity cases (not shown) also are characterized by abrupt changes in slope due to “soft” joint combinations.

In order to simulate measured operating deflection shapes, lateral deflections at the five grid points denoted in Fig. 36.3 were selected.

Trial vectors for expansion of five simulated operating deflection shapes were generated using the following strategies:

1. Five baseline system (stiff joints) modes (classic SEREP application)
2. Guyan expansion using the baseline model stiffness (stiff joints)
3. Seven trial vectors consisting of five baseline modes and two residual vectors from sensitivity cases (see Appendix)

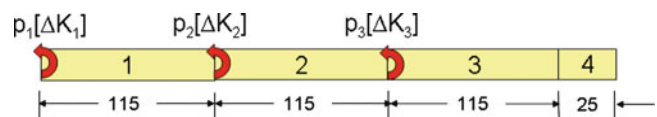
Modal expansions resulting from the above three trial vector sets are illustrated in Fig. 36.4 for the second and third measured test modes (operating deflection shapes). It is clear in these results that the trial vectors associated with sensitivity analyses produce features that express the abrupt slope changes that the two other trial vector sets cannot express.

A more precise numerical assessment of the three modal expansion strategies is realized by calculation of (a) orthogonality matrices among expanded modes, and (b) cross-orthogonality matrices between “exact” and expanded modes. The orthogonality and cross-orthogonality relationships are:

$$[OR] = [\Phi_{ODS,FEM}]^T [M_O] [\Phi_{ODS,FEM}], \quad [COR] = [\Phi_{ODS,FEM}]^T [M_O] [\Phi_{ODS}] \tag{36.12}$$

where  $[\Phi_{ODS,FEM}]$  is defined in (36.11), and  $[\Phi_{ODS}]$  is the set of exactly computed (simulated) modes. The orthogonality and cross-orthogonality matrices are provided below.

The modal expansion comparisons with “exact” modal vectors illustrated in Fig. 36.4 and Table 36.2 clearly indicate that utilization of sensitivity based trial vectors provide superior fidelity for the SEREP expansion process. This is attributed



**Fig. 36.1** Illustrative example four segment beam

**Table 36.1** Segmented beam modal frequencies

Mode	Modal frequency (Hz)			
	Baseline	Sensitivity 1	Sensitivity 2	“Test”
1	1.339	1.269	1.156	0.987
2	8.980	6.829	7.137	4.602
3	23.815	17.709	18.786	11.228
4	49.584	49.450	49.496	49.367
5	59.229	57.353	57.336	55.642



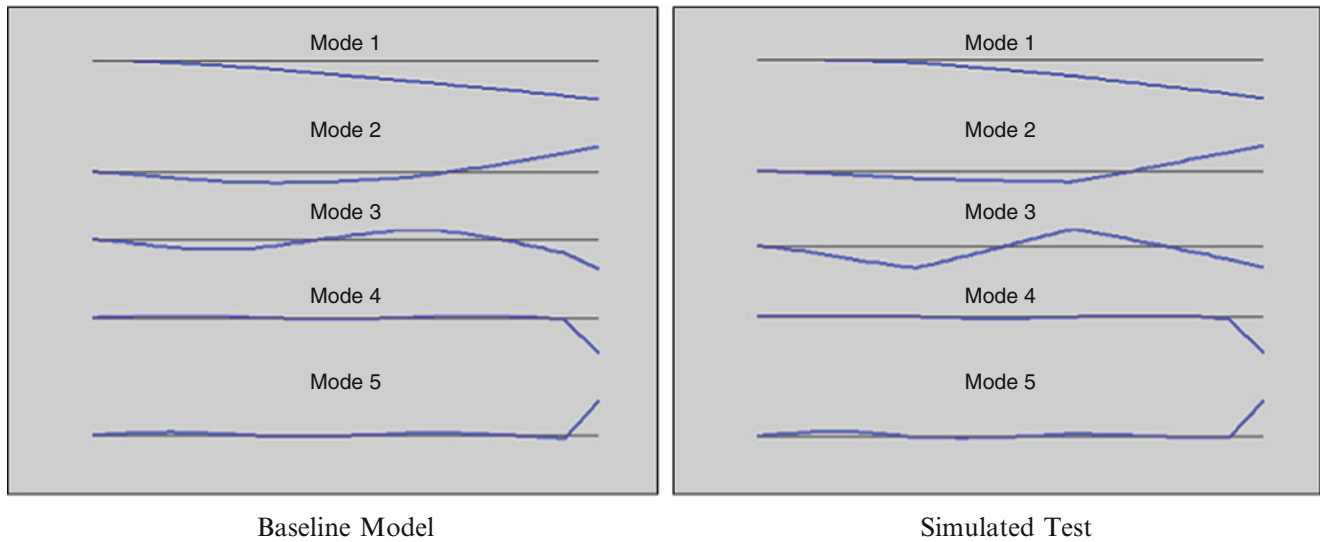


Fig. 36.2 Baselines model and simulated test modes

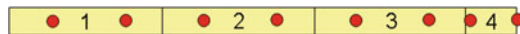


Fig. 36.3 Measured lateral deflection locations

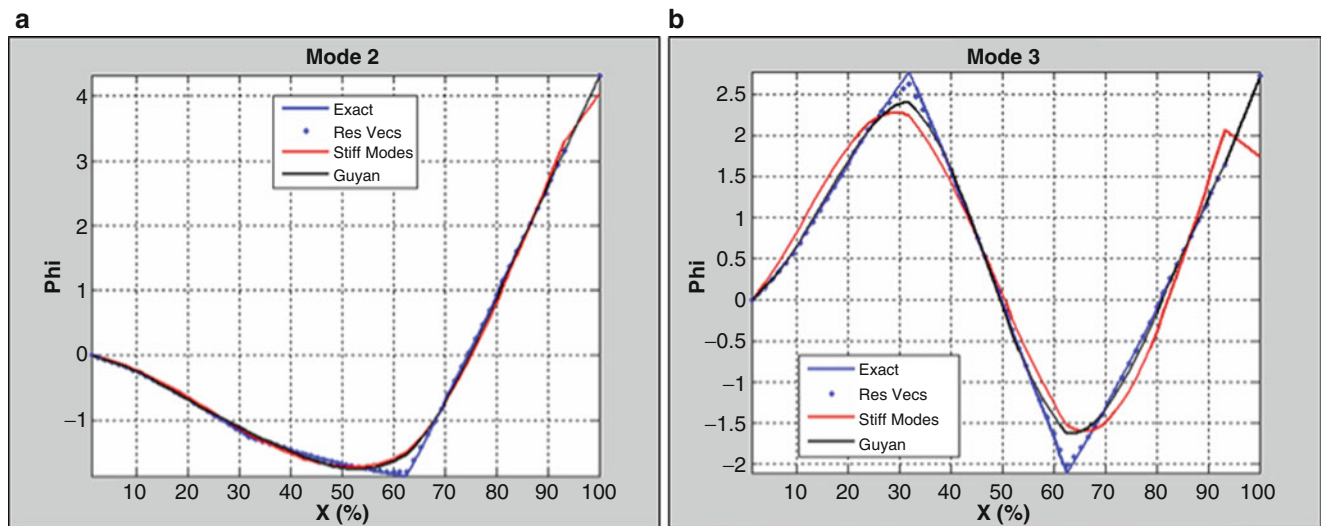


Fig. 36.4 Modal expansions for the second and measured modes (operating deflection shapes)

to the fact that the sensitivity based residual vectors possess the (abrupt slope change) features required to reconstruct the behavior of the “softened” joints.

### 36.6 Concluding Remarks

This paper introduced an expansion transformation based on FEM sensitivity vectors that have been employed for the past decade in FEM parametric sensitivity and FEM-test reconciliation analyses. Since the sensitivity vector based expansion spans a wide parametric uncertainty space, it has been shown to accurately reconstruct the full order FEM modes, regardless of actual unknown system parameters, with a simple multi-cell beam structure. The accuracy of the newly introduced

**Table 36.2** Orthogonality and cross-orthogonality matrices for expanded operating deflection shapes

		[OR] for Expanded Modal Vectors							[COR] with respect to Exact Modes				
Sensitivity Vectors (SEREP)		100	0	0	0	0	Sensitivity Vectors (SEREP)		100	0	0	0	0
		0	100	0	0	0			0	100	0	0	0
		0	0	100	0	0			0	0	100	0	1
		0	0	0	100	0			0	0	0	100	0
		0	0	0	0	100			0	0	0	0	100
Stiff Modes (SEREP)		100	-1	1	0	1	Stiff Modes (SEREP)		100	-1	1	0	1
		-1	100	3	-1	3			0	100	2	-1	3
		1	3	100	1	-11			0	2	99	1	-9
		0	-1	1	100	2			0	0	1	100	1
		1	3	-11	2	100			0	2	-6	1	96
Guyan Expansion		100	-1	1	0	1	Guyan Expansion		100	-1	1	0	1
		-1	100	3	-1	3			0	100	2	-1	2
		1	3	100	1	-8			0	2	100	1	-6
		0	-1	1	100	1			0	0	1	100	1
		1	3	-8	1	100			0	1	-3	0	99

expansion transformation was shown to be of superior accuracy to (a) baseline FEM trial vectors and (b) a Guyan transformation derived from the baseline FEM stiffness matrix.

The sensitivity based expansion transformation represents a valuable new tool for practical applications of operating deflection analysis. A number of possible implementations, in combination with other technical tools include:

1. Localization of structural damage based on operating deflection shape expansions for further diagnostic measurements.
2. Enhanced output-only modal parameter estimation that combines features of linear system modal analysis tools (e.g., randomdec) and the operating deflection shape expansion (provided the system appears to behave linearly).
3. FEM reconciliation analysis using system identification tools combined with the operating deflection shape expansion (provided the system appears to behave linearly).
4. Utilization of the operating deflection shape expansion to generate concise dynamic models that include nonlinear joints for efficient system identification of measured systems (that appear to behave nonlinearly).

## A.1 Appendix

### A.1.1 General Procedure for Generating Residual Vector Sets

Consider the general task of relating an arbitrary set of trial vectors,  $[\Psi]$ , to a set of the lowest frequency system modes,  $[\Phi_{OL}]$ , of an undamped dynamic system

$$[K_O][\Phi_{OL}] - [M_O][\Phi_{OL}][\lambda_{OL}] = [0] \quad \text{where, } [\Phi_{OL}^T M_O \Phi_{OL}] = [I], [\Phi_{OL}^T K_O \Phi_{OL}] = [\lambda_{OL}] \quad (36.13)$$

In addition, the stiffness matrix is related to the low and high frequency modes according to

$$[K_O] = [M_O \Phi_{OL}][\lambda_{OL}][\Phi_{OL}^T M_O] + [M_O \Phi_{OH}][\lambda_{OH}][\Phi_{OH}^T M_O] \quad (36.14)$$

The set of trial vectors is the sum of (a) a linear combination of system modes,  $[\Phi_{OL}]$  and (b) residual vectors,  $[\Psi_R]$

$$[\Psi] = [\Phi_{OL}][Q] + [\Psi_R] \quad (36.15)$$

Employing weighted least squares, and enforcing orthogonality of the residuals with respect to the system modes,

$$[\Phi_{OL}^T K_O \Psi] = [\Phi_{OL}^T K_O \Phi_{OL}] [Q] + [\Phi_{OL}^T K_O \Psi_R] \quad (36.16)$$

which results in,

$$[Q] = [\Phi_{OL}^T K_O \Phi_{OL}]^{-1} [\Phi_{OL}^T K_O \Psi] \quad (36.17)$$

Thus the residual vectors are,

$$[\Psi_R] = [\Psi] - [\Phi_{OL}] [\Phi_{OL}^T K_O \Phi_{OL}]^{-1} [\Phi_{OL}^T K_O \Psi] = [\Psi] - [\Phi_{OL}] [\lambda_{OL}]^{-1} [\Phi_{OL}^T K_O \Psi] \quad (36.18)$$

Due to the assumption in (36.15), the residual vectors are orthogonal with respect to the stiffness matrix as well as the mass matrix, as shown below:

$$[\Phi_{OL}^T M_O \Psi_R] = [\Phi_{OL}^T M_O \Psi] - [\Phi_{OL}^T M_O \Phi_{OL}] [\lambda_{OL}]^{-1} [\Phi_{OL}^T K_O \Psi] = [\Phi_{OL}^T M_O \Psi] - [\lambda_{OL}]^{-1} [\Phi_{OL}^T K_O \Psi] \quad (36.19)$$

Substituting (36.14) into the above results in

$$\begin{aligned} [\Phi_{OL}^T M_O \Psi_R] &= [\Phi_{OL}^T M_O \Psi] - [\lambda_{OL}]^{-1} \left[ [\Phi_{OL}^T M_O \Phi_{OL}] [\lambda_{OL}] [\Phi_{OL}^T M_O] + [\Phi_{OL}^T M_O \Phi_{OH}] [\lambda_{OH}] [\Phi_{OH}^T M_O] \right] \Psi \\ [\Phi_{OL}^T M_O \Psi_R] &= [\Phi_{OL}^T M_O \Psi] - [\lambda_{OL}]^{-1} [\lambda_{OL}] [\Phi_{OL}^T M_O] \Psi \equiv [0] \end{aligned} \quad (36.20)$$

It can also be proven that mathematically equivalent residual vectors may be derived using the mass matrix as a weighting matrix,

$$[\Psi_R] = [\Psi] - [\Phi_{OL}] [\Phi_{OL}^T M_O \Phi_{OL}]^{-1} [\Phi_{OL}^T M_O \Psi] = [\Psi] - [\Phi_{OL} \Phi_{OL}^T M_O \Psi] \quad (36.21)$$

While the residual vectors are orthogonal to the low frequency modes, they are not necessarily linearly independent of one another. A reduced order linearly independent residual vector set, however, may be estimated using singular value decomposition. This is accomplished by solving the following algebraic eigenvalue problem,

$$[A] = [\Psi_R^T M_O \Psi_R], [A] [\varphi_\rho] = [\varphi_\rho] [\lambda_\rho], \lambda_{\rho 1} \geq \lambda_{\rho 2} \geq \lambda_{\rho 3} \geq \dots \quad (36.22)$$

A suitable cut-off criterion, noted below, that has been employed over the past ten years with good success in defining the suitable reduced trial vector set, is

$$\frac{\lambda_{\rho N}}{\lambda_{\rho 1}} \leq 10^{-5}. \quad (36.23)$$

The set of linearly independent residual vectors and an augmented trial vector set, respectively, are defined as

$$[\Psi'_R] = [\Psi_R] [\varphi_\rho] \text{ and } [\bar{\Psi}_{OL}] = [\Phi_{OL} \Psi'_R] \quad (36.24)$$

Finally, a mutually orthogonal trial vector set may be defined based on the complete (not truncated) solution of the following reduced eigenvalue problem:

$$[\bar{\Psi}_{OL}^T K_O \bar{\Psi}_{OL}] [\psi] - [\bar{\Psi}_{OL}^T M_O \bar{\Psi}_{OL}] [\psi] [\lambda_\psi] = [0], \quad (36.25)$$

where

$$[\bar{\Phi}_{OL}] = [\bar{\Psi}_{OL}] [\psi] \quad (36.26)$$

## References

1. Coppelino R (2002) International space station P5 modal survey: test planning through FEM reconciliation. In: Proceedings of the 20th international modal analysis (IMAC) conference, Los Angeles, CA USA, Feb 2002
2. Coppelino R (2011) Sensitivity method for uncertainty and reconciliation analysis. In: Proceedings of the 29th international modal analysis (IMAC) conference, Jacksonville, FL USA, Feb 2011
3. Coppelino R (2012) FEM sensitivity technique for dynamic response uncertainty analyses. In: Proceedings of the 30th international modal analysis conference, Garden Grove, CA USA, Feb 2012
4. O'Callahan J, Avitable P, Riemer R (1989) System equivalent reduction expansion process (SEREP). In: Proceedings of the 7th international modal analysis conference, Las Vegas, NV USA, Feb 1989
5. Ibrahim SR (1977) Random decrement technique for modal identification of structures. *J Spacecraft Rockets* 14(11):696–700
6. Coppelino R (2003) Efficient and enhanced options for experimental mode identification. In: Proceedings of the 21st international modal analysis (IMAC) conference, Kissimmee, FL USA, Feb 2003
7. Bendat JS, Palo PA, Coppelino RN (1995) Identification of physical parameters with memory in nonlinear systems. *Int J Non Linear Mech* 30(6):841–860
8. Guyan RJ (1965) Reduction of stiffness and mass matrices. *AIAA J* 3(2):380

# Chapter 37

## Estimation of Unmeasured DOF's on a Scaled Model of a 4-Storey Building

Anders Skafte and Rune Brincker

**Abstract** This paper presents how a linear transformation between two set of mode shapes can be used to predict and expand the measured response of a structure. The method is known as the Local Correspondence Principle and states that a set of mode shapes can be described as another set of mode shapes, as long as there only exists a minor difference between the two set of mode shapes. This is often the case when comparing mode shapes obtained from experiments on a structure with mode shapes from a finite element of the same structure.

The method is validated by tests performed on a scaled model of a 4-storey building made of aluminum bars and plates bolted together. The first part of the validation shows how the experimental mode shapes can be expanded, using a combination of the finite element mode shapes. The second part of the validation focus on how the measured response can be calculated in a large amount of DOF's using the expanded mode shapes.

**Keywords** Expansion • Mode shapes • Transformation • Finite element • Operational modal analysis

### 37.1 Introduction

The advantage of using the Local Correspondence [LC] Principle [1] is that it provides a very precise expansion of the experimental mode shapes using a relatively simple algorithm. The simplicity makes it easy to compute, and results can be extracted instantly.

The general formulation of the LC Principle is valid for any two sets of eigenvectors which are alike. However in this article there is focused on experimentally obtained mode shapes, and mode shapes from an Finite Element [FE] model. The experimentally obtained mode shapes has the advantage of being the *true* mode shapes of the structure, disregarding noise from the measurements and the identification algorithm. The disadvantage is that we often only know the experimental mode shape coordinates in a limited amount of Degrees Of Freedom [DOF].

If we were able to construct an FE model of the structure with mode shapes that aligned precisely with the experimental mode shapes, we wouldn't have the problem of using expansion methods. But this is hardly never the case even with very simple structures. The FE mode shapes will always vary from the experimental mode shapes, even with a very good FE model. The advantage of the FE mode shapes is that we can compute them in as many DOF's as wanted.

When using this expansion method the trick is to find the transformation matrix  $T$  that combines the experimentally obtained mode shapes with the FE mode shapes. The transformation matrix can then be multiplied by the full FE mode shape matrix, to create a new set of expanded mode shapes. In that way the preciseness of the experimental mode shapes is combined with large amount of data given by the FE mode shapes, to create an expanded set of mode shapes that fits the structure.

---

A. Skafte (✉) • R. Brincker  
Department of Engineering, Aarhus University, Finlandsgade 22, Aarhus N, 8200 Denmark  
e-mail: [ask@iha.dk](mailto:ask@iha.dk); [rub@ib.sdu.dk](mailto:rub@ib.sdu.dk)

## 37.2 Theory

The idea behind the LC Principle originates from the eigenvector sensitivity equations [2]. These equations are deduced mathematically by observing complete systems, where the number of modes coincides with the number of DOF's – which is never the case in reality. But when the change in mode shape is considered small, it can be shown that the mode shape sensitivity for a given mode is only depending on the mode shapes close by in terms of frequency.

The basic equation of the LC Principle can be written as:

$$A = B T \quad (37.1)$$

Where  $A$  indicates the experimental mode shape matrix,  $B$  indicates a set of FE mode shapes, and  $T$  indicates the transformation matrix.

With subscript “ $a$ ” indicating “active” DOF's as where sensors have been placed on the model, (37.1) can be rearranged to the following.

$$\hat{T} = B_a^\dagger A_a \quad (37.2)$$

Where  $B_a$  indicates a subset of FE modes with DOF's coinciding with the points on the structure where sensors have been placed.  $\dagger$  indicates the pseudo inverse and  $\hat{\phantom{x}}$  indicates an estimate.

Once an estimate of the transformation matrix is found, an estimate of the expanded mode shapes is quickly found:

$$\hat{A} = B \hat{T} \quad (37.3)$$

Where  $B$  this time contain all the DOF's in the FE model.

It is important to notice that (37.2) tells us that  $B_a$  can't hold more modes than DOF's since it then can't be inverted. There is no analytical solution to how many FE modes  $B_a$  should contain in order to get the most accurate expansion – this has to be done as an iterative process.

The expansion of the mode shapes is the key to expand the measured response. This is done using the classical theory from modal dynamics that the response of a structure can be described as a linear combination of the structures mode shapes and its modal coordinates.

$$y = A q \quad (37.4)$$

Once the experimental mode shapes are determined, an estimate of the modal coordinates can be found.

$$\hat{q} = A_a^\dagger y_a \quad (37.5)$$

Finally the response can be expanded by multiplying the expanded set of mode shapes with the estimate of the modal coordinates.

$$\hat{y} = \hat{A} \hat{q} \quad (37.6)$$

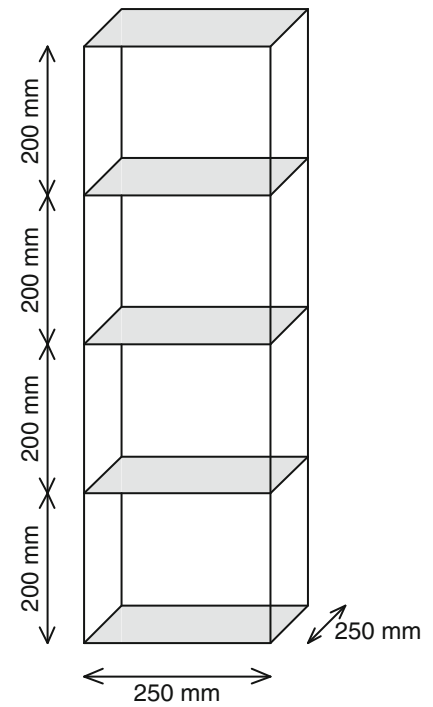
It is important to note that even though the response is only measured in one direction (for example measurements on a plate) the estimated response can be found in all three directions for each DOF. Likewise the rotational response can be found in all three directions of each DOF. This is due to the uniqueness of the modal coordinates. To do this all six degrees of freedom have to be included in FE mode shape  $B$  in (37.3).

## 37.3 Test Setup and Experimental Mode Shapes

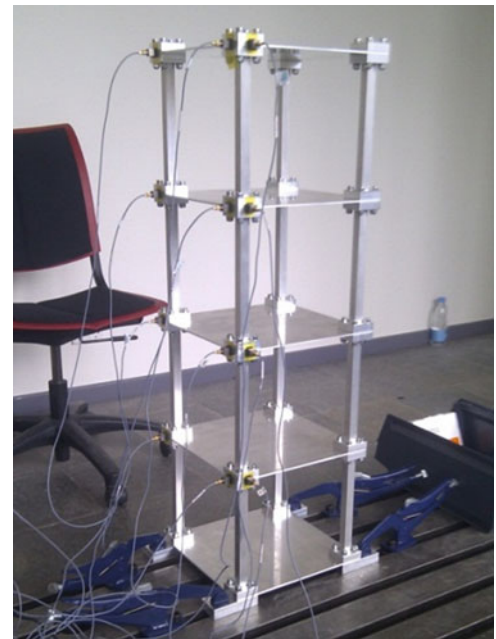
To validate the theory tests were performed on a scaled model of a 4-storey building. Each storey measure 200 mm in height giving the structure a total height of 800 mm. The slabs are made of 3 mm aluminum plates, and measure 250 × 250 mm. The columns are quadratic aluminum bars with a cross-section measuring 15 × 15 mm. Each joint are bolted together, and the base of the structure was bolted to a fixed plane (Figs. 37.1 and 37.2).



**Fig. 37.1** 3D sketch of the test structure



**Fig. 37.2** Picture of the test structure



To measure the response the structure was mounted with 12 accelerometers. Three accelerometers were placed at each slab (except at the bottom) – two measuring in y-direction and one measuring in x-direction. The accelerometers used for these tests were Brüel & Kjaer 4508-B-002 (Fig. 37.3).

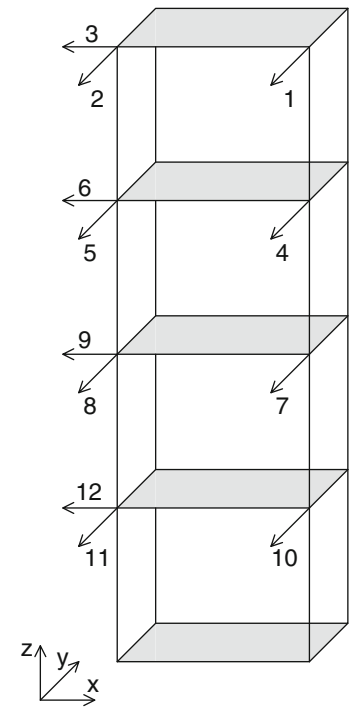
Due to initial testing the sampling frequency was set to 2,048 Hz, to ensure that all modes of importance could be estimated through Operational Modal Analysis [OMA]. The recording time was set to 60 s which is approximately 1,000 times the lowest period (1st natural frequency is 18.4 Hz).

Load was applied to structure simply by scratching with a sharp object, to ensure that a stochastic response was achieved.

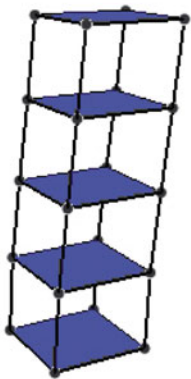
The experimental mode shapes are extracted using the Frequency Domain Decomposition [FDD] technique [3]. The software used in these tests is ARTEMIS [4].

Figure 37.4 illustrates the first nine experimental mode shapes.

**Fig. 37.3** Placement of accelerometers



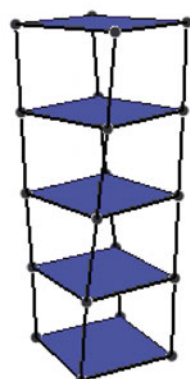
1<sup>st</sup> mode:



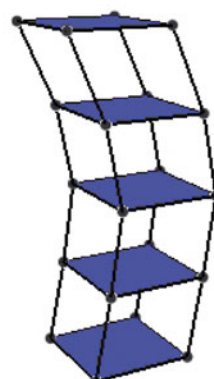
2<sup>nd</sup> mode:



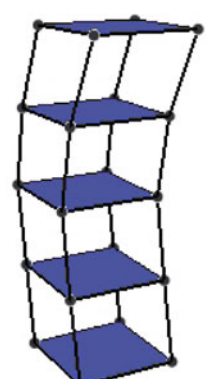
3<sup>rd</sup> mode:



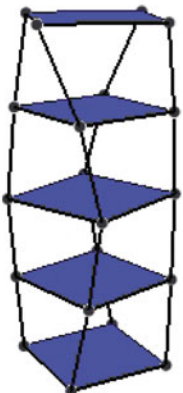
4<sup>th</sup> mode:



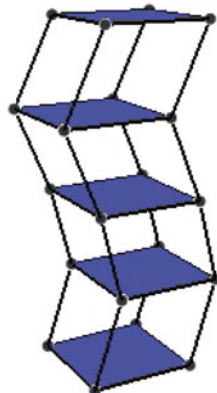
5<sup>th</sup> mode:



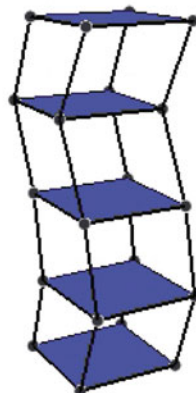
6<sup>th</sup> mode:



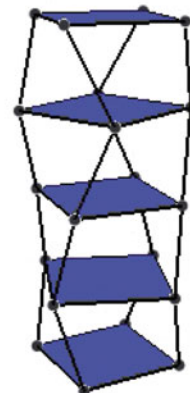
7<sup>th</sup> mode:



8<sup>th</sup> mode:



9<sup>th</sup> mode:



**Fig. 37.4** First nine experimental mode shapes

In the expansion there is only focused on the part of the response created from the first nine modes, which is why only nine experimental modes have been identified.

### 37.4 Finite Element Model

A finite element model was created using Patran/Nastran [5]. The model consists off bars and slabs of the same dimensions as the physical model, and with material parameters given as:

Density:	$\rho = 2,550 \text{ kg/m}^3$
Youngs modulus:	$E = 70,000 \text{ MPa}$
Possions ratio:	$\nu = 0.35$
Shear modulus:	$G = 26,000 \text{ MPa}$

All joints are modeled as rigid, and four fixed supports have been placed at the bottom nodes of the first four bars. Each bar has been divided into five elements and each slab into 25 elements, making it a total of 244 nodes in the model (Fig. 37.5).

Twelve mode shapes (four bending in each direction, and four torsional) were extracted from the model, and used in the expansion.

### 37.5 Expansion and Results

When doing the expansion it is necessary to identify all the modes that contribute to the response. Since only nine modes were identified, the response has been lowpass filtered with a cut-off frequency just above the 9th mode. The lowpass filtered response is used as reference in the results below.

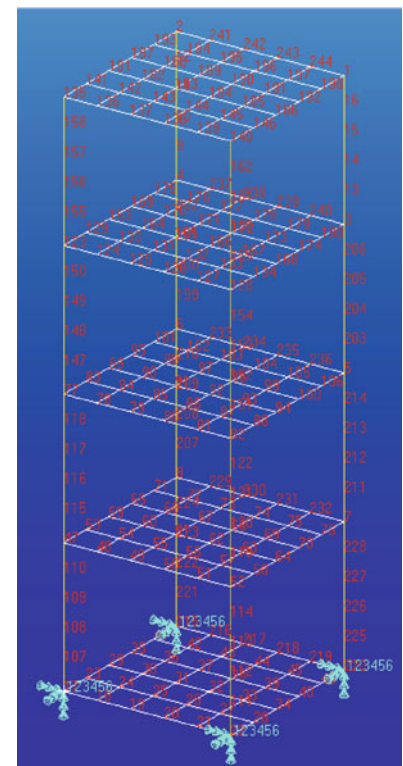
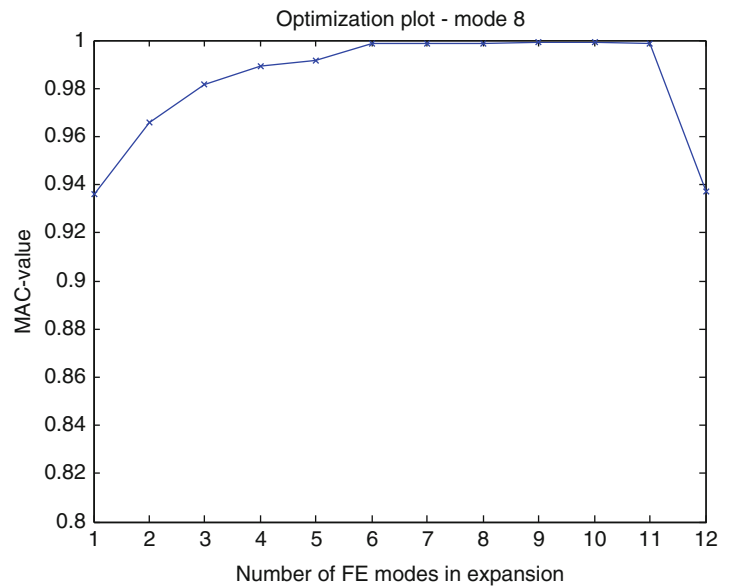


Fig. 37.5 Finite element model

**Fig. 37.6** MAC-value between the 8th measured- and estimation mode shape, as a function of the number of FE modes used in the estimation



The expansion of the response to unmeasured DOF's is performed in three steps. First the mode shapes are expanded using (37.2) and (37.3). Then the measured response is decomposed into modal coordinates using (37.5). And finally the response is expanded into unmeasured DOF's by multiplying the expanded mode shapes with the modal coordinates, (37.6).

In order to expand the mode shapes it is necessary to divide all the known DOF's from the experimental mode shapes into two sets – “estimated” DOF's and “predicted”. The trick is to find the order and number of FE modes in (37.2) that results in the highest MAC-value between the experimental mode and the estimated mode. If all the measured DOF's were used in (37.2) and (37.3), the MAC-value [6] would be 1 when the matrix  $\mathbf{B}_a$  holds as many modes as DOF's. But the fit would only be perfect for the measured DOF's. All the unmeasured DOF's would be far from their true value.

By dividing the known DOF's into “estimated” and “predicted”, one set can be used in the expansion and the other can be used to measure the fit of the expansion.

Figure 37.6 shows the optimization plot for the 8th mode. The initial MAC-value between the measured mode and corresponding FE mode is a little less than 0.94. When the expanded mode is created as a combination of eight FE modes, the MAC-value rises to almost 1.

Then the modal coordinates are the estimated using (37.5). When an estimate of the expanded mode shapes and the modal coordinates are found, the response can be expanded by multiplying the two. Figure 37.7 shows the error between the measured (lowpass-filtered) response and the expanded response.

The error is calculated using (37.7):

$$\mathit{error}_i = \frac{\sigma_{(y_i - \hat{y}_i)}}{\sigma_{y_i}} \quad (37.7)$$

Where  $\sigma$  indicates the standard deviation.

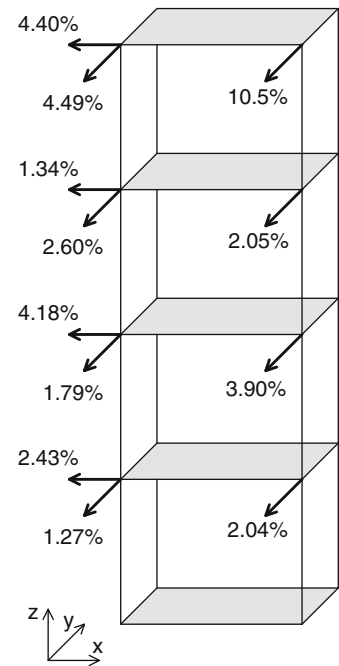
The errors are presented in Fig. 37.7.

Except for channel 1, the estimated responses all show errors between 1% and 5% when compared with the bandpassed measured signal (Fig. 37.8).

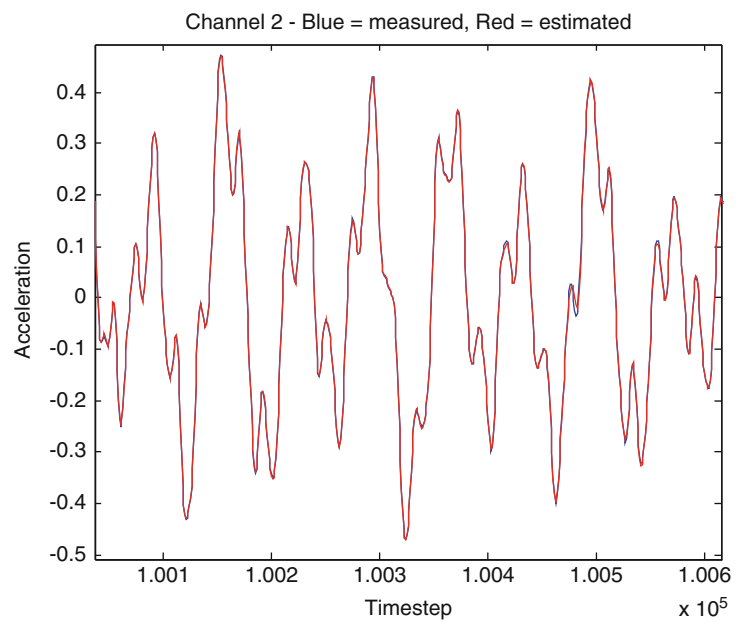
## 37.6 Conclusion

A technique for estimating the response in unknown DOFs has been presented. The technique uses an expansion of the mode shapes through a linear combination of experimentally obtained mode shapes, and mode shapes from a finite element model. The technique has been tested on a scaled model of a 4-storey building showing high level of accuracy between the measured- and estimated response.

**Fig. 37.7** Errors between measured and estimated response



**Fig. 37.8** Measured and estimated response



## References

1. Brincker R, Skafta A, López-Aenlle M, Sestieri A, D'Ambrogio W, Canteli A. A local correspondence principle for mode shapes in structural dynamics (to be published)
2. Nelson RB (1976) Simplified calculation of eigenvector derivatives. *AIAA J* 14(9):1201–1205
3. Brincker R, Zhang LM, Andersen P (2001) Modal identification of output-only systems using frequency domain decomposition. *Smart Mater Struct* 10(3):441–445
4. Operational modal analysis, release 5.3 – Structural Vibration Solution A/S
5. Patran/Nastran 2012 – MSC Software
6. Allemang RJ, Brown D (1982) A correlation coefficient for modal vector analysis. In: *Proceedings of IMAC I, SEM, Orlando*, pp 110–116

# Chapter 38

## Estimation of Rotational Degrees of Freedom by EMA and FEM Mode Shapes

A. Sestieri, W. D'Ambrogio, R. Brincker, A. Skaftø, and A. Culla

**Abstract** In this paper a new technique is presented to estimate the rotational degrees of freedom of a flexural structure, using only a limited number of sensors that measure the translational DoFs of the system. A set of flexural mode shapes in a limited number of nodes is obtained by modal testing, while a different set of approximated mode is calculated by a Finite Element Model (FEM) at all the nodes and degrees of freedom of the structure. The technique is based on the classical assumption that the response can be determined by a linear combination of the structure's mode shapes. The structure's mode shapes are approximated by using the local correspondence principle for mode shapes, i.e. by using an optimally selected set of finite element mode shapes as Ritz vectors for the true mode shapes. This allows to obtain the rotational response at unmeasured DoFs. The technique is validated by comparing predicted and experimental results.

**Keywords** Experimental mode shapes • FE mode shapes • Rotational DoFs • Expansion

### 38.1 Introduction

Rotational DoFs are generally involved in substructuring applications aimed to predict the dynamic behavior of coupled subsystems characterized by flexural behavior. In fact, neglecting rotational DoFs, an important part of compatibility and equilibrium conditions at the joint are lost, and the obtained results become meaningless.

Several techniques have been devised to estimate rotational FRFs from measurement of translational FRFs: they range from the use of T-blocks [1] to the use of finite differences [2, 3]. Other techniques are aimed at directly obtaining rotational FRFs using particular transducers [4]. Some more literature about experimental devices to obtain rotational FRFs is listed in [5], where a number of expansion techniques are proposed as a valid alternative to either unsatisfactory or expensive rotational FRF measurements. Notwithstanding several years have passed, the situation is more or less the same, and the requirement for efficient expansion techniques capable of estimating FRFs or mode shapes at rotational DoFs is very strong.

In this paper a new technique is introduced to estimate unmeasured degrees of freedom of a flexural structure, with particular emphasis to rotational DoFs. The method is based on the Local Correspondence (LC) Principle, presented in [6, 7] to estimate a linear transformation between mode shapes identified by experimental modal analysis (EMA) and modes from a Finite Element model. The technique is validated by comparing experimental results with those determined by both this new technique and SEREP expansion [8]. This comparison seems to be especially appropriate because, under particular conditions, both LC and SEREP provide very similar results.

---

A. Sestieri • A. Culla (✉)

Dipartimento di Ingegneria Meccanica e Aerospaziale, Università di Roma La Sapienza, Via Eudossiana 18, I 00184 Rome, Italy  
e-mail: [antonio.culla@uniroma1.it](mailto:antonio.culla@uniroma1.it)

W. D'Ambrogio

Dipartimento di Ingegneria Industriale e dell'Informazione e di Economia, Università dell'Aquila,  
Via G. Gronchi, 18 - I-67100, L'Aquila (AQ), Italy  
e-mail: [walter.dambrogio@univaq.it](mailto:walter.dambrogio@univaq.it)

R. Brincker • A. Skaftø

Department of Engineering, Aarhus University, Nordre Ringgade 1 - DK-8000 Aarhus C, Denmark  
e-mail: [rub@ib.sdu.dk](mailto:rub@ib.sdu.dk); [ask@iha.dk](mailto:ask@iha.dk)



## 38.2 Theory

In modal analysis theory, the eigenvectors, or mode shapes, of an  $N$ -DoF system form a basis in the  $N$ -dimensional vector space, i.e. any  $N$ -dimensional vector can be expressed as a linear combination of the eigenvectors. This is also known as the expansion theorem. For instance, it is possible to consider as a basis the set of mode shapes deriving from an FE model, organized in the modal matrix  $[\Psi]_{\text{FE, complete}}$ , where any column represents a different eigenvector  $\{\psi\}_{\text{FE}, r}$ ,  $r = 1, \dots, N$ . Therefore, any  $N$ -dimensional vector  $\{\psi\}$  can be expressed as:

$$\{\psi\} = [\Psi]_{\text{FE, complete}} \{t\} \quad (38.1)$$

where the  $N$ -dimensional vector  $\{t\}$ , containing the linear combination coefficients, is given by:

$$\{t\} = [\Psi]_{\text{FE, complete}}^{-1} \{\psi\} \quad (38.2)$$

because  $[\Psi]_{\text{FE, complete}}$  is a square  $N \times N$  non-singular matrix (the eigenvectors form a basis in the  $N$ -dimensional space).

If  $m < N$  eigenvectors are considered, Eq. (38.1) holds approximately and is rewritten:

$$\{\psi\} \cong [\Psi]_{\text{FE}} \{\hat{t}\} \quad (38.3)$$

where  $[\Psi]_{\text{FE}}$  is now an incomplete ( $N \times m$ ) modal matrix, and  $\{\hat{t}\}$  is given by:

$$[\hat{t}] = [\Psi]_{\text{FE}}^+ \{\psi\} \quad (38.4)$$

being  $[\Psi]_{\text{FE}}^+ = ([\Psi]_{\text{FE}}^T [\Psi]_{\text{FE}})^{-1} [\Psi]_{\text{FE}}^T$  the pseudo-inverse of the  $N \times m$  matrix  $[\Psi]_{\text{FE}}$ , with  $N > m$ .

Equation (38.3) can also be applied to a reduced set of  $n < N$  DoFs, e.g. those measured in a modal test. In this case, it is possible to consider an  $n$ -dimensional vector  $\{\psi\}_{\text{X}, r}$  corresponding to an identified mode shape, and to write:

$$\{\psi\}_{\text{X}, r} \cong [\Psi]_{\text{FE, ex}} \{\hat{t}\} \quad (38.5)$$

where the subscript, ex, indicates that the DoFs selected from the FE mode shapes correspond to those of the identified modes shape, so that  $[\Psi]_{\text{FE, ex}}$  is an  $n \times m$  matrix. If  $n \geq m$ ,  $\{\hat{t}\}$  is given by:

$$\{\hat{t}\} = [\Psi]_{\text{FE, ex}}^+ \{\psi\}_{\text{X}, r} \quad (38.6)$$

being  $[\Psi]_{\text{FE, ex}}^+ = ([\Psi]_{\text{FE, ex}}^T [\Psi]_{\text{FE, ex}})^{-1} [\Psi]_{\text{FE, ex}}^T$ . (Note that  $[\Psi]_{\text{FE, ex}}^+ = [\Psi]_{\text{FE, ex}}^{-1}$  if  $n = m$ .)

Equation (38.5) can be also rewritten as:

$$\{\hat{\psi}\}_{\text{X}, r} = [\Psi]_{\text{FE, ex}} \{\hat{t}\} \quad (38.7)$$

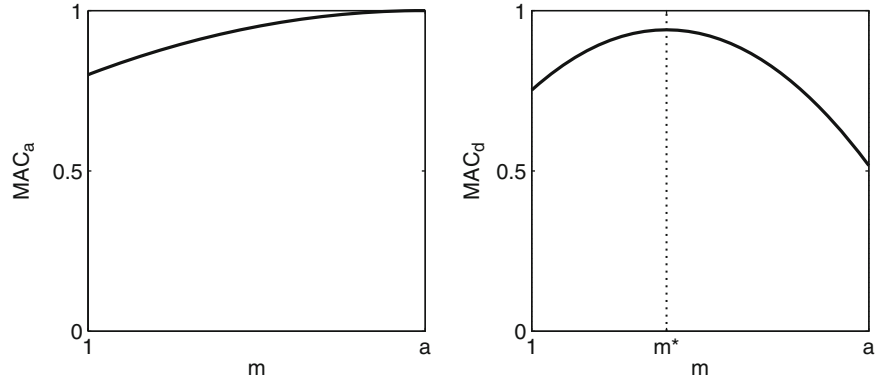
where  $\{\hat{\psi}\}_{\text{X}, r}$  represents an estimate of  $\{\psi\}_{\text{X}, r}$ . (This can be seen as a smoothing technique for experimental mode shapes.)

In [6] it is shown that the mode shapes in the incomplete modal matrix should be selected so as their frequencies be the closest to the frequency of the identified mode shape. This is called the Local Correspondence Principle. In [9] a similar issue was raised, concerning the correlation between an experimental modal vector and a subspace spanned by several FE modal vectors.

Once the vector of linear combination coefficients  $\{\hat{t}\}$  has been determined, it can be multiplied by  $[\Psi]_{\text{FE}}$ , i.e. the FE mode shape matrix at the full set of DoFs, to expand the experimental mode shape at the full set of DoFs, including rotational DoFs whenever they are included in the FE model, as for beam and shell elements:

$$\{\hat{\psi}\}_{\text{X - full}, r} = [\Psi]_{\text{FE}} \{\hat{t}\} \quad (38.8)$$

**Fig. 38.1** MAC performed on the active DoFs (*left*) and deleted DoFs (*right*) by increasing  $m$  from 1 to  $a$



### 38.2.1 Smart Selection of Mode Shapes Based on the Local Correspondence Principle

The accuracy of the estimates provided by Eqs. (38.7) and (38.8) depends on several factors such as:

- The accuracy of the FE model;
- How many ( $m$ ) and which modes shapes are retained in the incomplete FE modal matrix;
- How many ( $n$ ) and which DoFs are measured in the modal test.

Actually, if  $n = m$ , i.e. if the number of retained modes is equal to the number of measured DoFs, Eq. (38.7) provides exactly the experimental mode shape  $\{\psi\}_{X,r}$ . Furthermore, the accuracy of the expansion provided by Eq. (38.8) is difficult to assess since the involved DoFs are not measured.

The problem of finding how many and which FE mode shapes have to be retained to obtain the best fit for any given experimental mode is addressed in [6, 7]. The trick is to partition the measured DoFs in two sets, the a-set of ‘active’ DoFs and the d-set of ‘deleted’ DoFs, so that a given identified mode is written as:

$$\{\psi\}_{X,r} = \begin{Bmatrix} \{\psi\}_{Xa,r} \\ \{\psi\}_{Xd,r} \end{Bmatrix} \quad (38.9)$$

The deleted DoFs are used as reference, to assess the quality of the mode shape expansion. The active DoFs are used in the computation of the expanded mode shape. Therefore Eq. (38.6) is applied to the a-set, provided that  $m \leq a$ , where  $a$  is the number of DoFs in the a-set. It is obtained:

$$\{\hat{t}\} = [\Psi]_{FE,a}^+ \{\psi\}_{Xa,r} \quad (38.10)$$

The value of  $\{\hat{t}\}$  provided by Eq. (38.10) is used to estimate the identified mode shape both at the a-set and at the d-set of DoFs:

$$\{\hat{\psi}\}_{Xa,r} = [\Psi]_{FE,a} \{\hat{t}\} \quad \{\hat{\psi}\}_{Xd,r} = [\Psi]_{FE,d} \{\hat{t}\} \quad (38.11)$$

The accuracy of the estimate can be assessed by considering the Modal Assurance Criterion (MAC) [10] among estimated and identified eigenvectors at active and deleted DoFs:

$$MAC_a = \frac{\left( \{\hat{\psi}\}_{Xa,r}^H \{\psi\}_{Xa,r} \right)^2}{\left( \{\hat{\psi}\}_{Xa,r}^H \{\hat{\psi}\}_{Xa,r} \right) \left( \{\psi\}_{Xa,r}^H \{\psi\}_{Xa,r} \right)} \quad MAC_d = \frac{\left( \{\hat{\psi}\}_{Xd,r}^H \{\psi\}_{Xd,r} \right)^2}{\left( \{\hat{\psi}\}_{Xd,r}^H \{\hat{\psi}\}_{Xd,r} \right) \left( \{\psi\}_{Xd,r}^H \{\psi\}_{Xd,r} \right)} \quad (38.12)$$

where the superscript  $H$  stands for the conjugate transpose.

The procedure leading to the computation of  $MAC_a$  and  $MAC_d$  can be repeated by varying the number  $m$  of retained modes, e.g. by increasing  $m$  from 1 to  $a$ . Whilst  $MAC_a$  monotonically increases with  $m$  until it becomes equal to 1 for  $m = a$ ,  $MAC_d$  usually does not reaches its maximum for  $m = a$  (Fig. 38.1).

Strategies to select how to increase  $m$ , that is which mode shape should be added to  $[\Psi]_{\text{FE}}$  at each step, are currently under investigation. At the same time, strategies to efficiently partition the measured set of DoFs into active and deleted DoFs are being investigated as well.

The value  $m^*$  at which  $MAC_d$  is maximum represents the optimum. The corresponding  $\{\hat{t}\}^*$  is then used to expand experimental mode shapes at any desired DoF, eventually including rotational DoFs:

$$\{\hat{\psi}\}_{X-\text{full},r} = [\Psi]_{\text{FE}} \{\hat{t}\}^* \quad (38.13)$$

The procedure can be repeated to expand all the identified modes. At the end, an optimal set of expanded mode shapes is obtained. Using the expanded mode shapes, the FRF matrix at the full set of DoFs can be expressed as:

$$[H(j\omega)] = \sum_r \frac{\{\hat{\psi}\}_{X-\text{full},r} \{\hat{\psi}\}_{X-\text{full},r}^T}{m_r (\omega_r^2 - \omega^2 + j\eta_r \omega_r^2)} \quad (38.14)$$

where  $\omega_r$ ,  $\eta_r$  and  $m_r$  are the natural frequency, loss factor (having assumed to use structural damping) and modal mass of the  $r$ -th mode shape. If identified mode shapes are scaled to unit modal mass, it is  $m_r = 1$  for any  $r$ .

It is now appropriate to compare the results obtained using the proposed smart mode expansion technique based on the Local Correspondence Principle with results obtained using other DoF expansion techniques (e.g Guyan expansion, dynamic expansion, SEREP). Among them, SEREP [8] is specifically considered here since it is also based on a set of FE mode shapes and, under particular conditions, it provides the same results as the mode expansion technique.

### 38.2.2 SEREP Expansion

SEREP is conceived as a DoF expansion procedure where the expanded modes are a linear combination of a selected set of FE modes. Using this procedure, an expanded mode shape is written as:

$$\{\hat{\psi}\}_{X-\text{full},r} = [T] \{\psi\}_{Xa,r} \quad (38.15)$$

where the transformation matrix  $[T]$  is given by:

$$[T] = [\Psi]_{\text{FE}} [\Psi]_{\text{FE},a}^+ \quad (38.16)$$

By substituting Eq. (38.16) into Eq. (38.15) one obtains:

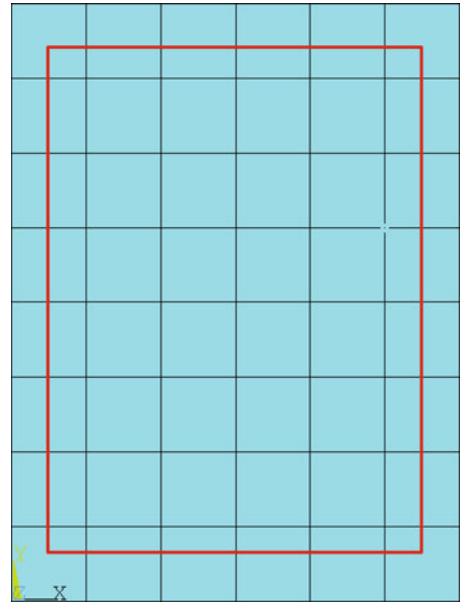
$$\{\hat{\psi}\}_{X-\text{full},r} = [\Psi]_{\text{FE}} [\Psi]_{\text{FE},a}^+ \{\psi\}_{Xa,r} \quad (38.17)$$

By recalling Eq. (38.10) it is easy to realize that the expanded mode shape obtained using SEREP is very similar to the one provided by the mode expansion technique. Actually, they are exactly the same if the set of FE mode shapes that is used to obtain the expanded mode shape contains all the initially selected mode shapes, i.e. it is not reduced by optimization. Therefore, SEREP expansion can be seen as a suboptimal solution to the considered expansion problem.

## 38.3 Application

The interest here is mainly addressed to estimate the rotational DoFs of an aluminum plate of size  $300 \times 400 \times 3$  mm. The plate is initially modeled by finite elements to calculate its natural frequencies and mode shapes. Subsequently, experiments are performed to determine the frequency response functions used to identify natural frequencies and mode shapes.

**Fig. 38.2** Finite element mesh of the plate



### 38.3.1 FEM Reference Model

The finite element model consists of 63 nodes and 48 shell elements. Each element is  $50 \times 50$  mm, has 4 nodes and 6 degrees of freedom per node. Figure 38.2 shows the finite element mesh and the considered reference frame. The nodes considered for further comparison with experimental results are those shown within the red rectangle in Fig. 38.2.

The results obtained by this analysis, to be used for expansion, are the first nine elastic modes in the frequency range 0–500 Hz. The first six mode shapes are shown in Fig. 38.3. The mode shapes are calculated on the full set of 210 degrees of freedom, including rotational DoFs.

### 38.3.2 Experimental Results

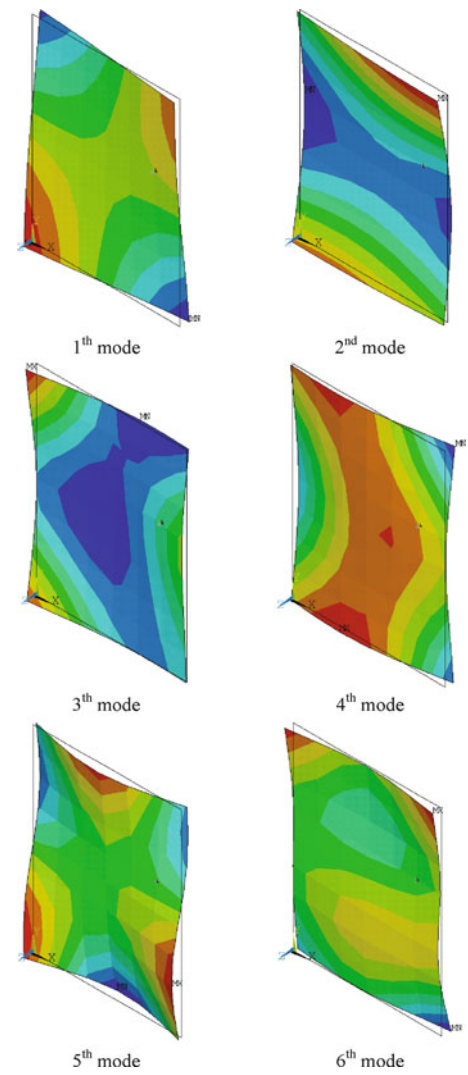
The experiments are performed on the plate suspended by a soft rubber band to simulate free boundary conditions (Fig. 38.4a). The plate is excited using the hammer impact technique, and the drive point is shown in Fig. 38.4a. The acceleration along  $z$  direction is measured at all the 35 nodes. To estimate the rotational accelerations at node 24 (see Fig. 38.4b), three accelerometers along  $x$  direction and three along  $y$  direction are placed at a relative distance of 20 mm. These measurements allow to calculate by central finite difference the derivative of the flexural acceleration [2, 3], which provide an estimate of rotational accelerations around  $x$  and  $y$  axes.

Accelerations and force are used to determine FRFs (inertances), from which eight natural frequencies, structural dampings, and mode shapes are identified by a curve fitting technique. Figure 38.5 shows the comparison between measured and fitted FRF at DoF 24z.

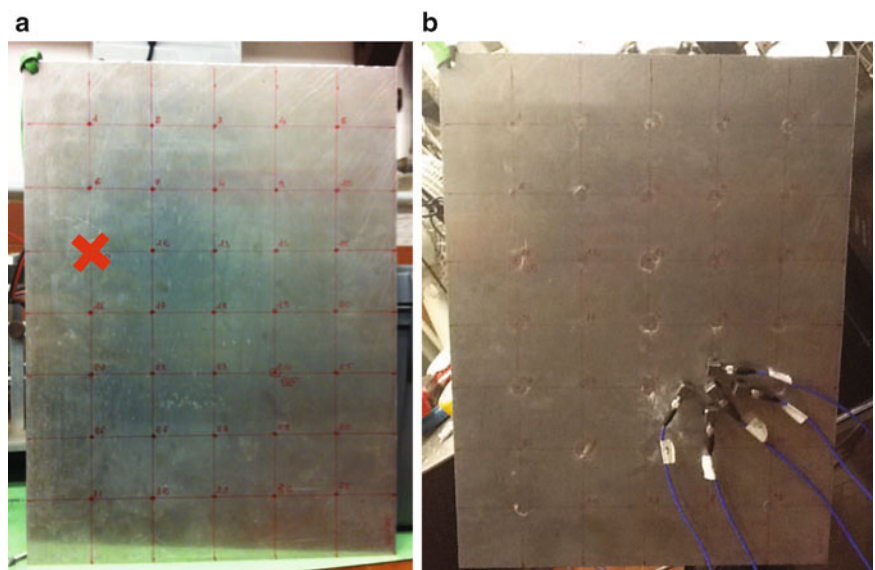
### 38.3.3 Numerical Results

The smart mode expansion technique based on the Local Correspondence Principle (LC) is carried out by taking into account a set of 34 active DoFs over 35 measured DoFs every time: the deleted DoF is roved over the whole set. The results of LC are compared with the results of SEREP technique and with the measured FRFs.

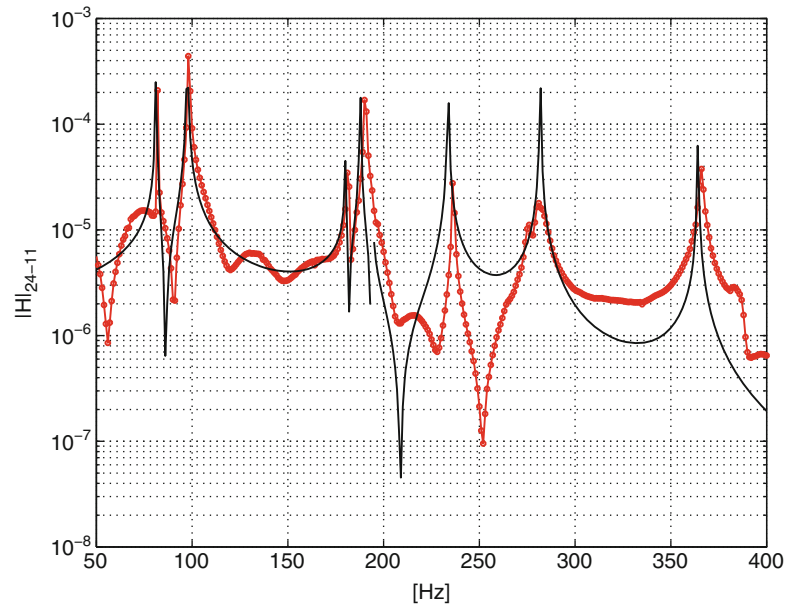
**Fig. 38.3** The first six elastic modes of the FE model



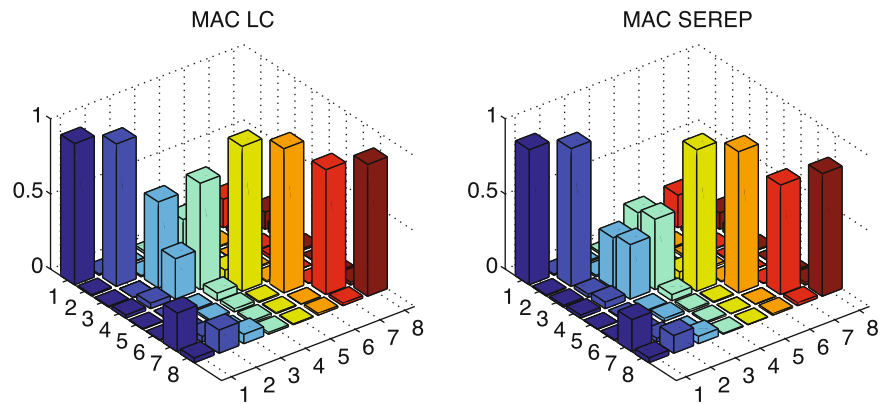
**Fig. 38.4** Experimental setup: (a) the suspended plate and the drive point, (b) accelerometers placed to calculate the rotational accelerations



**Fig. 38.5** Comparison between measured ( $\text{---}\circ\text{---}$ ) and fitted ( $\text{---}$ ) FRF  $|H|_{24z-11z}$



**Fig. 38.6** MAC between the identified mode shapes and the expanded mode shapes: LC vs. SEREP



In Fig. 38.6 the MAC between the identified mode shapes and the expanded mode shapes using the LC technique (left) and SEREP (right) is shown. It can be noticed that the LC technique provides better results, especially for modes 3 and 4, and also for mode 7. This demonstrates the effectiveness of the smart mode expansion technique compared to SEREP.

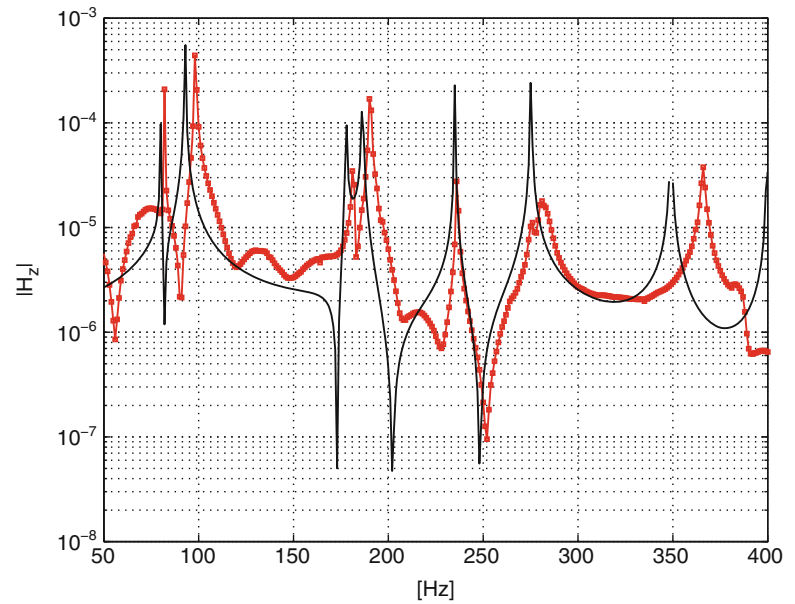
In Fig. 38.7 the experimental FRF  $|H|_{24z-11z}$  is compared with the corresponding FRF obtained from the FE model. In Fig. 38.8 the same experimental FRF is compared with the one given by expression (38.14) using expanded mode shapes obtained using both LC and SEREP. No particular difference can be noticed in the synthesized FRFs. Both match the experimental FRF fairly well, and definitely better than the FRF obtained from the FE model.

In Fig. 38.9 the experimentally derived FRF  $|H|_{24\vartheta_x-11z}$  is compared with the corresponding FRF obtained from the FE model. It should be noticed that the experimentally derived rotational FRF shows a certain amount of scatter probably due to the procedure used to estimate such rotational FRFs (finite differences). In Fig. 38.10 the same experimental FRF is compared with the one given by expression (38.14) using expanded mode shapes obtained using both LC and SEREP. Now, some difference between LC synthesized and SEREP synthesized FRF is noticed, especially at one antiresonance. Both match the experimental FRF better than the FRF obtained from the FE model, especially in the frequency range up to 200 Hz.

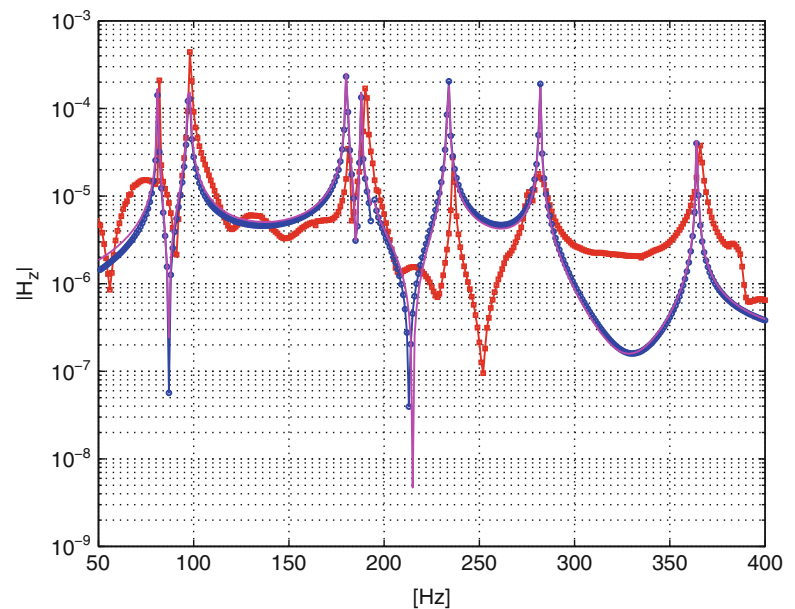
In Fig. 38.11 the experimentally derived FRF  $|H|_{24\vartheta_y,-11z}$  is compared with the corresponding FRF obtained from the FE model. Again, some amount of scatter is noticed. In Fig. 38.12 the same experimental FRF is compared with the one obtained



**Fig. 38.7**  $|H|_{24z-11z}$ : measured (—○—) vs. FEM (—)



**Fig. 38.8**  $|H|_{24z-11z}$ : measured (—○—) vs. LC (—○—) and SEREP (—)

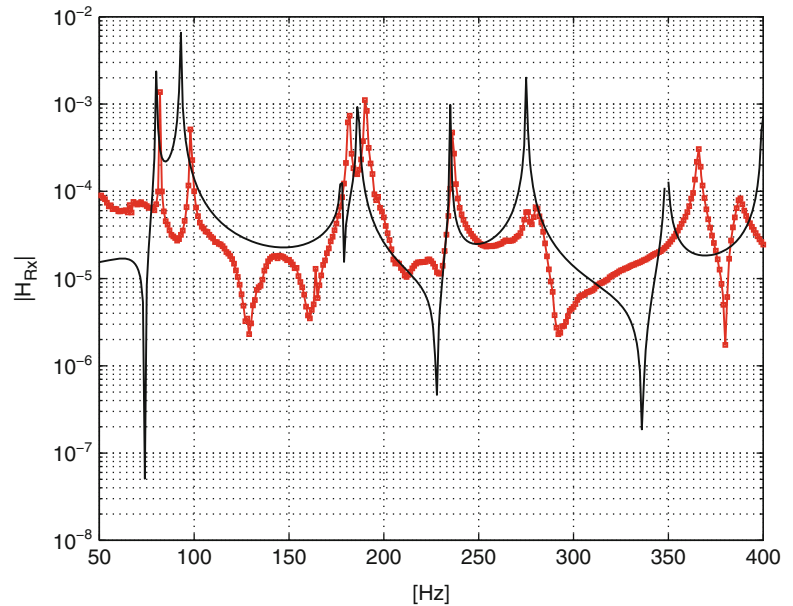


from expression (38.14) using expanded mode shapes obtained using both LC and SEREP. Now, some difference between LC synthesized and SEREP synthesized FRF is noticed, especially at one antiresonance. Both match the experimental FRF better than the FRF obtained from the FE model, except at the resonance immediately above 100 Hz.

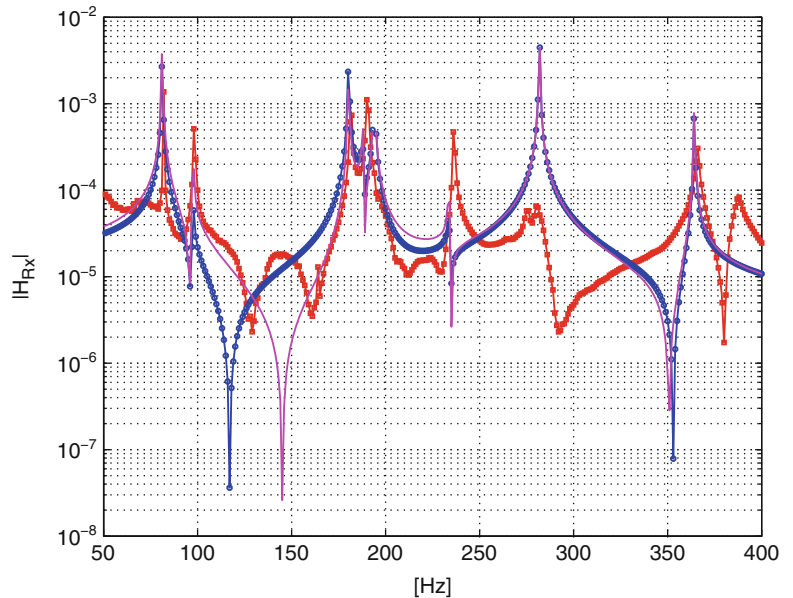
## 38.4 Conclusions

This work is an application of the Local Correspondence (LC) Principle developed to estimate unmeasured DoFs in a structure using only a limited amount of sensors. Specifically, here the technique is used to determine rotational mode shapes and related FRFs. The method is based on the classical assumption that the response can be determined by a linear combination of the structure's mode shapes. The FE mode shapes are then combined using a linear transformation to match the experimentally obtained mode shapes, thus creating a new set of modes having a large amount of DoFs.

**Fig. 38.9**  $|H|_{24\theta_x-11z}$ : measured (—○—) vs. FEM (—)



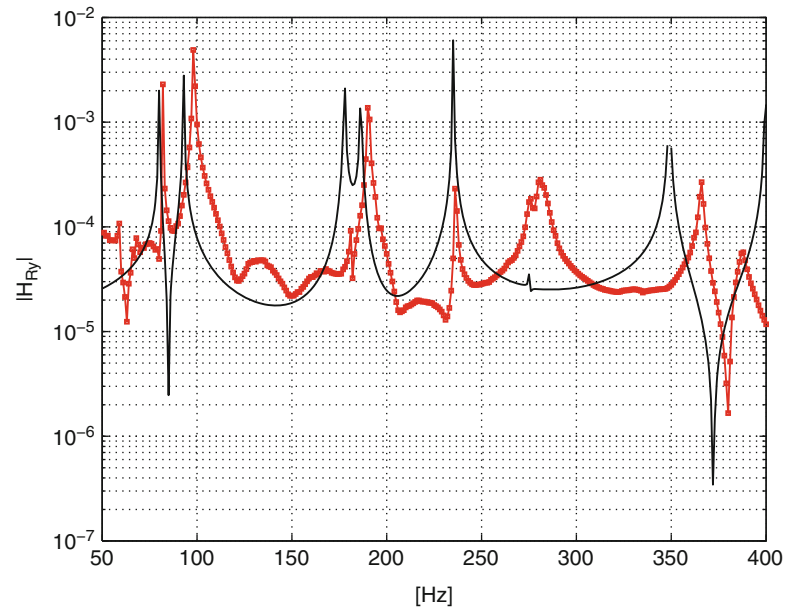
**Fig. 38.10**  $|H|_{24\theta_x-11z}$ : measured (—○—) vs. LC (—○—) and SEREP (—)



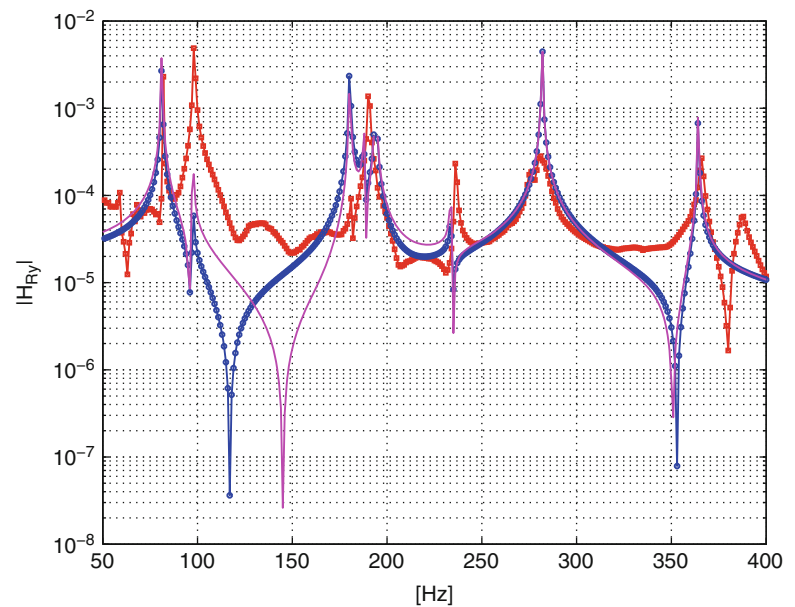
The method is applied on a simple rectangular plate. A set of flexural mode shapes in a limited number of nodes is obtained by modal testing, while a different set of modes is calculated by a Finite Element Model (FEM) at all the nodes and DOFs of the structure. The results provided by the LC technique are compared with experimental results and with results of SEREP expansion. Although both LC and SEREP provide similar results, it is still difficult to assess how well they can estimate the rotational DOFs. In fact, the rotational DOFs experimentally presented here are not directly measured but rather reconstructed by a finite difference scheme of translational DOFs along close measurement points. On the other side, the FE Model used here is not sufficiently accurate to provide reliable values of rotation for comparison and an updated FE model could be used. In any case, a challenging test would be to use the rotational FRFs in substructuring applications.

**Acknowledgements** This research is supported by grants from University of Rome La Sapienza and University of L'Aquila.

**Fig. 38.11**  $|H|_{24\theta_y-11z}$ :  
measured (—○—) vs. FEM  
(—)



**Fig. 38.12**  $|H|_{24\theta_y-11z}$ :  
measured (—○—) vs. LC  
(—○—) and SEREP (—)



## References

1. Ewins DJ, Gleeson PT (1975) Experimental determination of multidirectional mobility data for beams. *Shock Vib Bull* 45:153–173
2. Sattinger SS (1980) A method for experimentally determining rotational mobilities of structures. *Shock Vib Bull* 50:17–27
3. Sestieri A, Salvini P, D'Ambrogio W (1991) Reducing scatter from derived rotational data to determine the frequency response function of connected structures. *Mech Syst Signal Process* 5(1):25–44
4. Bello M, Sestieri A, D'Ambrogio W, La Gala F (2003) Development of PZT's as rotational transducers. *Mech Syst Signal Process* 17(5): 1069–1081
5. D'Ambrogio W, Sestieri A (2004) A unified approach to substructuring and structural modification problems. *Shock Vib* 11(3–4):295–310
6. Brincker R, Skaftø A, Lpez-Aenlle M, Sestieri A, D'Ambrogio W, Canteli A (2012) A local correspondence principle for mode shapes in structural dynamics. *Mech Syst Signal Process*

7. Skaftø A, Brincker R (2012) Estimation of unmeasured dof's using the local correspondence principle. In: Caicedo JM, Catbas FN, Cunha A, Racic V, Reynolds P, Salyards K, Proulx T (eds) Topics on the dynamics of civil structures, vol 1. Volume 26 of conference proceedings of the society for experimental mechanics series. Springer, New York, pp 265–271. doi:10.1007/978-1-4614-2413-0\_26
8. O'Callahan J, Avitabile P, Riemer R (1989) System equivalent reduction expansion process. Proceedings 7th IMAC, Las Vegas, pp 29–37
9. D'Ambrogio W, Fregolent A (2003) Higher order MAC for the correlation of close and multiple modes. Mech Syst Signal Process 17(3): 599–610
10. Allemang RL, Brown DJ (1982) A correlation coefficient for modal vector analysis. Proceedings of the 1st International Modal Analysis Conference, November 8-10, Orlando, FL USA, Society for Experimental Mechanics, Inc., Bethel, CT USA, pp. 110–116

# Chapter 39

## Real-Time Dynamic Stress Response Estimation at Critical Locations of Instrumented Structures Embedded in Random Fields

Eric M. Hernandez and Kalil Erazo

**Abstract** The use of output feedback as a means to monitor stresses at critical locations in instrumented structures has been the subject of recent work by researchers in the field of vibration based structural health monitoring. In the present paper we propose an model-based state estimator that can be implemented as a modified finite element model of the system subjected to corrective forces proportional to the measurements. The proposed estimator is able to explicitly account for the non-white nature of loads by using knowledge of the power spectral density of the process. The proposed estimator is successfully implemented in a controlled laboratory environment under various loading scenarios.

**Keywords** Estimation • Kalman filter • Observers • Finite element models • Structural health monitoring

### 39.1 Introduction

In many engineering applications ranging from fatigue monitoring of structural or mechanical systems [1–3] to estimating heart kinematics [4], optimal estimation of unmeasurable quantities is essential. In fatigue analysis, for example, the estimated stress time histories can be used as inputs to damage functions and consequently be used to estimate the failure risk due to cyclic loads [1]. If measurements of the system's response at a number of measurable locations are available, it follows that one can attempt to estimate or reconstruct the unmeasurable quantities from the measured ones. The collection of computational methods used to perform this interpolation fall under two categories: static data interpolation methods and methods based on control theory that explicitly account for the dynamic relationship between the measurements, measurement noise, disturbances and the quantities of interest (QoI).

Traditionally static data interpolation methods provide acceptable results for systems where the response is governed only by a few modes of vibration. For complex large-scale systems where the dynamic response is governed by many modes and(or) the excitations are broadband, static interpolation methods typically fail to provide accurate results [5, 6].

An alternative approach is a family of methods based on estimation and control theory, known as observers. One of the most celebrated of these methods is the Kalman filter, a Bayesian estimation algorithm which allows for optimal estimation (in the Euclidean sense) of the state trajectory of a linear system on the basis of a state-space model of the system and noise-contaminated measurements [7]. The fundamental assumption in Kalman filtering is that disturbances and noise are white Gaussian stationary random processes. Currently in most of the applications some version of the Kalman filter is used to perform response time history reconstruction, but only systems with few degrees of freedom are considered, mainly due to the computational difficulties that arise when implementing on very large systems [2, 8].

In addition to the implementation issues, theoretical issues have also been raised related to the consistency of first order observers when applied to second order symmetric systems; especially loss of symmetry, definiteness and the fact that first order observers might yield an estimate of the state that does not correspond to the physical state sought, i.e. it does not

---

E.M. Hernandez (✉)

Assistant Professor, University of Vermont, 33 Colchester Ave., 301 Votey Hall, Burlington, VT 05401, USA  
e-mail: [eric.hernandez@uvm.edu](mailto:eric.hernandez@uvm.edu)

K. Erazo

Graduate Student, University of Vermont, 301 Votey Hall, 33 Colchester Ave., 201 Perkins Hall, Burlington, VT 05405, USA  
e-mail: [kerazo@uvm.edu](mailto:kerazo@uvm.edu)

conserve internal consistency between certain variables such as the fact that the estimated velocities must be derivatives of the estimated displacement. This was demonstrated by Balas [9] and Hernandez [10], who concluded that unless certain restrictions are placed on the observer formulation these inconsistencies will occur and could lead to estimation errors. Observers that satisfy this requirement are called natural observers, because they maintain the second order structure of the underlying system whose state is trying to estimate. It can be shown that the KF is not a natural second order observer [10].

In the present paper a natural observer developed by Hernandez [10], with the additional feature that it can be realizable as a second order finite element model (FEM), is implemented to estimate the strain time histories in a cantilever beam. The proposed observer resembles the KF in accuracy, but with the capability of direct implementation as a modified finite element model of the system of interest. By taking the estimation problem to a finite element model we are exploiting the computational power of current FEM solvers and reducing the computational difficulty in comparison with most estimation techniques [10].

A brief introduction to the theory behind the proposed methodology is presented in the first section. This is followed by a section describing the results from the laboratory experiment. The proposed method was compared to the modal interpolation technique, the Luenberger observer and the Kalman filter. The results show that the proposed FEM based observer performs very similar to the Kalman filter and outperforms all other methods.

## 39.2 Theoretical Background

The proposed estimator is applicable to systems whose dynamic response can be closely estimated by the following matrix ordinary differential equation:

$$M\ddot{q} + C_d\dot{q} + Kq = b_1u + b_2w(t) \quad (39.1)$$

where  $M = M^T > 0 \in R^{N \times N}$  is the mass matrix,  $C_d = C_d^T > 0 \in R^{N \times N}$  is the damping matrix and  $K = K^T > 0 \in R^{N \times N}$  is the stiffness matrix. The vector  $q(t) \in R^{N \times 1}$  is the displacement vector of the  $N$  degrees of freedom of the system,  $b_1 \in R^{N \times r}$  defines the spatial distribution of the measured excitation  $u(t) \in R^{r \times 1}$  and  $b_2 \in R^{N \times l}$  defines the spatial distribution of the unmeasured excitation  $w(t) \in R^{l \times 1}$ . By defining the state vector  $x^T(t) = [q^T(t) \quad \dot{q}^T(t)]$  Eq. (39.1) can be written in first order form as

$$\dot{x}(t) = A_c x(t) + B_1 u(t) + B_2 w(t) \quad (39.2)$$

where the matrices  $A_c$ ,  $B_1$  and  $B_2$  are given by

$$A_c = \begin{bmatrix} 0 & I \\ -M^{-1}K & -M^{-1}C_d \end{bmatrix} \quad (39.3)$$

$$B_1 = \begin{bmatrix} 0 \\ M^{-1}b_1 \end{bmatrix} \quad B_2 = \begin{bmatrix} 0 \\ M^{-1}b_2 \end{bmatrix} \quad (39.4)$$

Measurements  $y(t)$  of global structural response are assumed contaminated by additive Gaussian white noise  $v(t)$  with zero mean and linearly related to the state vector  $x(t)$  and input vector  $u(t)$  such that

$$y(t) = Cx(t) + Du(t) + v(t) \quad (39.5)$$

where for acceleration measurements  $C = c_2[-M^{-1}K \quad -M^{-1}C_d]$  and  $D = c_2M^{-1}b_2$ . For velocity measurements  $C = c_2[0 \quad I]$  and for displacement measurements  $C = c_2[I \quad 0]$ . The output distribution matrix  $c_2 \in R^{m \times N}$  is a Boolean matrix such that every row contains a single non-zero entry in a column corresponding to the measured degree of freedom and  $m$  is the number of measurements.

In general the state estimate provided by any observer can be written in first order state-space form as

$$\dot{\hat{x}}(t) = A_c \hat{x}(t) + B_1 u(t) + G[y(t) - C \hat{x}(t)] \quad (39.6a)$$

$$= (A_c - GC) \hat{x}(t) + B_1 u(t) + Gy(t) \quad (39.6b)$$

where  $\hat{x}$  represents the state estimate. As can be seen from Eq. (39.6b), the observer state estimate is the response of the system subject to excitations consisting of the weighted difference between measured response and model response



estimates. The gain matrix  $G$  is the essence of observer design and it is selected based on the minimization of a user defined function of the state error  $e(t) = x(t) - \hat{x}(t)$  given by

$$\dot{e}(t) = (A - GC)e(t) + (B_2 - GD)w(t) - Gv(t) \quad (39.7)$$

In the Kalman filter formulation it is assumed that the unmeasured excitations and measurement noise are realizations of white Gaussian random processes with zero mean and known covariance matrix. The objective function is the trace of the state error covariance matrix.

The proposed observer was originally derived in [10] and for velocity measurements it is given by

$$M\ddot{\hat{q}}(t) + (C_D + MG_2c_2)\dot{\hat{q}}(t) + K\hat{q}(t) = MG_2\dot{q}_m(t) \quad (39.8)$$

where

$$G_2 = M^{-1}c_2^T E \quad (39.9)$$

and  $E$  is selected as the matrix that minimizes the trace of the following integral, namely the trace of the state error covariance matrix

$$J = Tr \int_{-\infty}^{+\infty} \Phi_{ee}(\omega) d\omega \quad (39.10)$$

where

$$\Phi_{ee}(\omega) = H_o \Phi_{ww} H_o^* + H_o c_2^T G_2 \Phi_{vv} G_2^T c_2^T H_o^* + H_o \Phi_{wv} G_2 c_2 H_o^* \quad (39.11)$$

and

$$H_o = (-M\omega^2 + (C_D + c_2^T G_2 c_2) i \omega + K)^{-1} \quad (39.12)$$

The matrices  $\Phi_{ww}$ ,  $\Phi_{vv}$ ,  $\Phi_{wv}$  are the power spectral density of the unmeasured input, measurement noise and the cross-spectral density between unmeasured input and measurement noise. As can be seen from Eq. (39.8) the proposed FEM based estimator can be implemented as modified version of the original FEM of the system with added dampers and driven by corrective forces which are linear combination of the measurements.

Finally, the estimate for stress time histories are obtained by

$$\hat{\sigma}(t) = T\hat{q}(t) \quad (39.13)$$

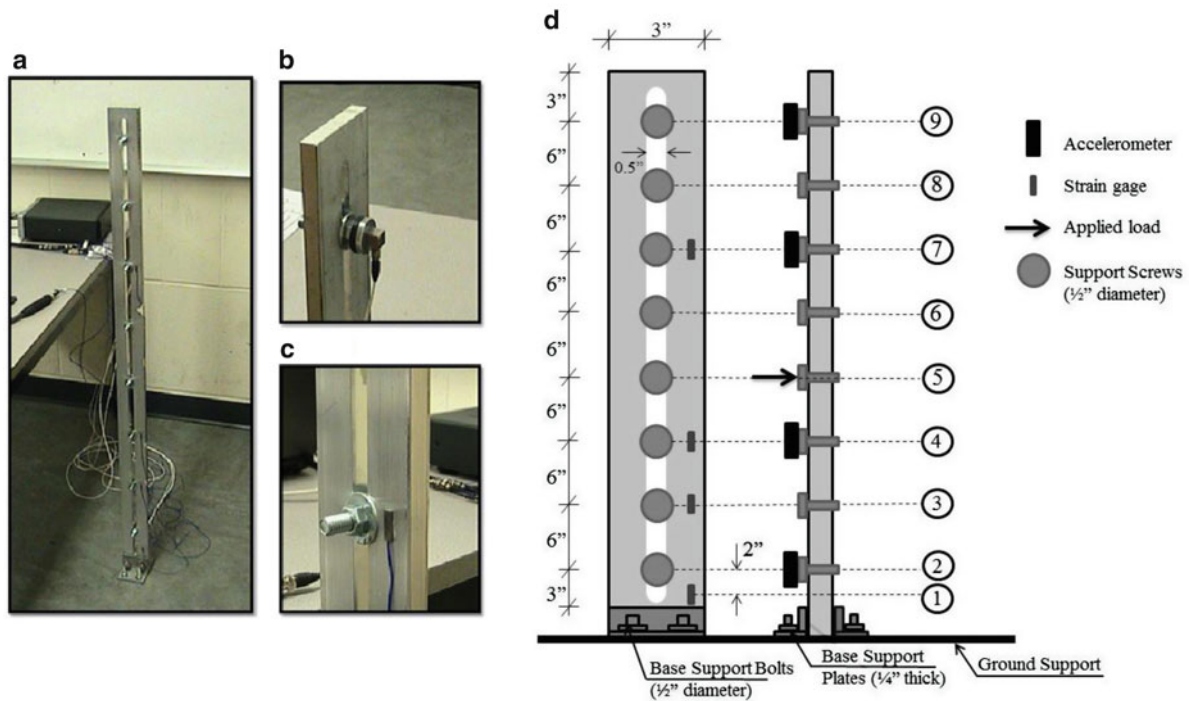
where the linear transformation  $T$  maps the estimated displacement to the desired internal stress.

It is important to note that it is theoretically possible to formulate the estimator based on displacement or acceleration measurements and this is shown in [10]. In the case of displacement measurements, the physical interpretation of the resulting observer is a modified system with grounded springs added at the measured degrees of freedom and corrective forces applied collocated with the measurements and proportional to the measurements and to the added springs. In the case of acceleration measurements, the resulting observer is a modified system with added masses and corrective forces collocated with the measurements and proportional to the added masses and the measurements. In this paper, we focus on velocity feedback mainly because the resulting estimator possesses the same fundamental undamped frequencies and mode shapes as the system. This results in an estimator with lower estimation error than in the cases of displacement and acceleration feedback in which the frequencies of the estimator have been distorted by adding springs or masses.

### 39.3 Experiment and Procedure

This section describes the experiments conducted in order to assess the estimation capabilities of the proposed FEM based observer. It is worth noting that the capabilities of the observer have already been verified in a simulation environment[3], however the results presented herein constitute the first experiments to assess its accuracy in a real structure. An aluminum cantilever beam with dimensions as shown in Fig. 39.1 was used for the experiments. Based on free vibration data the fundamental frequency of the beam was identified at 6.4 Hz and the damping ratio at approximately 0.0013.

The cantilever is instrumented with four accelerometers (PCB 333B30) and four strain sensors (PCB 740B02). A photograph of the experimental setup is shown in Fig. 39.1. The data was recorded using the LMS Scadas Mobile Data



**Fig. 39.1** Aluminium cantilever beam experiment; (a) Experiment, (b) Accelerometer mounting, (c) Strain sensor mounting, (d) Experiment setup

Acquisition System at a sampling frequency of 16 kHz. For the purposes of this experiment, only accelerometers in locations (4) and (9) are used as feedback for the estimator, the rest are only used for comparison purposes.

The strain at positions (1), (3), (4) and (7) were estimated using the measured accelerations at positions (4) and (9). Two different tests were carried out: (i) a banded white noise generated using an electrodynamic shaker (TMS2060E) and (ii) an impact load generated using a modal impact hammer (PCB086C03). The modal hammer excitation was applied at position (5), while the banded white noise was applied at position (3).

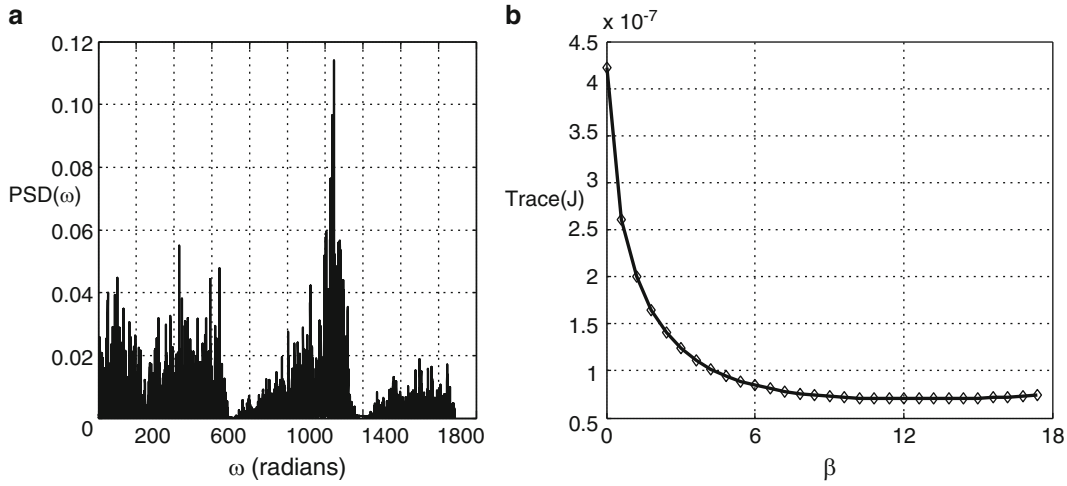
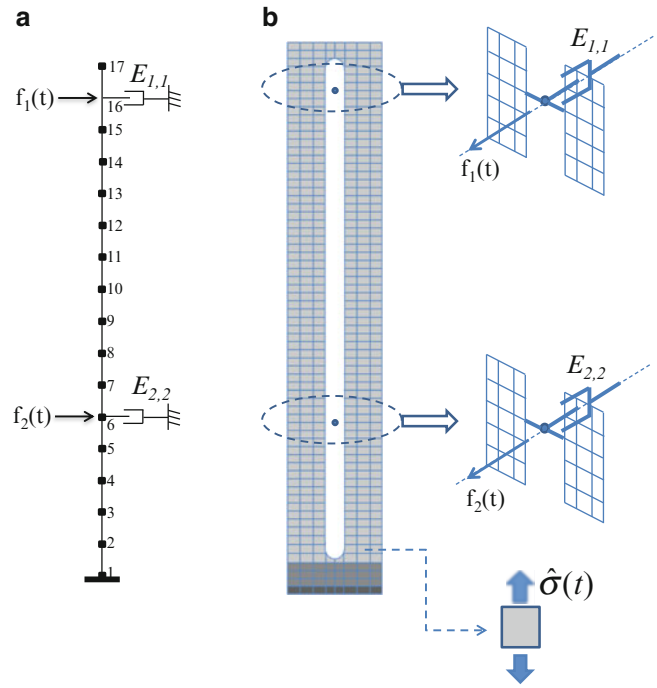
As mentioned previously, estimation from four different methods were compared: the proposed FEM based observer, the Kalman filter, Luenberger observer and modal interpolation. As a reference we have also computed the FEM model response to the measured excitation, we refer to this estimate as the open loop.

### 39.3.1 FEM Based Observer

To implement the proposed observer we begin by setting a FEM model of the system and proceed to minimize Eq. 39.3 in order to determine the optimal value of the added dampers and proportionality constant that will scale the measurements. Figure 39.2 shows the simplified FEM used to formulate and solve Eq. 39.3 and the more refined FEM used to actually implement the proposed observer. The model on Fig 39.2a contains only 16 elements and 32 DoF, while the more refined model on Fig 39.2a has 477 elements and 11,448 DoF. Note that the added dampers and driving forces are the same for both models and thus the proposed methodology allows for the flexibility of increasing or refining the model resolution without having to solve for the feedback gain repeatedly on increasingly larger models.

Figure 39.3b depicts the shape of  $J(\beta)$  and a minimum can be found and used to formulate the proposed FEM observer. The measurement noise power spectral density matrix used in the optimization was  $\Phi_{vv} = 5.42 \times 10^{-7} I_{2 \times 2}$  and the disturbance power spectral density  $\Phi_{ww} = 5.4 \times 10^{-3}$ . It is worth emphasizing that the power spectral density of the load actually delivered through the shaker (Fig. 39.3a) is significantly different from the one selected to perform the optimization, this indicates the robustness of the proposed method to errors in the description of the disturbances and noise characteristics. From Fig. 39.3b we found that  $\beta^* = 13.5$ . This plot also indicates that there is a relatively wide range of values of  $\beta$  for which the proposed method provides almost equal accuracy, this also is indicative of some inherent robustness. It was shown in [10] that the curvature of  $J(\beta)$  increases with increasing ratio of intensity between measurement noise and disturbance.

**Fig. 39.2** (a) Simplified FEM used to perform the minimization and (b) FEM used to perform the estimation



**Fig. 39.3** (a) Power spectral density of delivered load through shaker (b) Shape of optimization function for  $\beta$  in Eq. 39.3

**Kalman Filter**

To formulate a Kalman filter for this problem three matrices are necessary: the covariance matrix of the initial condition error, the measurement noise covariance and the disturbance covariance matrix [11]. We selected the initial condition covariance matrix as zero. Since the Kalman filter is implemented in discrete time, the noise and disturbance covariance matrices in discrete time can be approximated as a function of the spectral density matrices as [11].

$$R = R_o / \Delta t \tag{39.14}$$

$$Q = \int_0^{\Delta t} e^{A_c \Delta t} B_1 Q_o B_1^T (e^{A_c \Delta t})^T dt \approx B_1 Q_o B_1^T \Delta t \tag{39.15}$$

where for the present experiment  $R_o = 5.42 \times 10^{-7} I_{2 \times 2} \delta_o$  and  $Q_o = 5.42 \times 10^{-3} \delta_o$  are the continuous noise and disturbance correlation matrices for the equivalent Gaussian white noise processes.

**Table 39.1** Comparison of estimation accuracy between different methods for the hammer test

	$\  RE \ _2$	$\  RE \ _\infty$
Model-based observer	0.41	0.89
Kalman filter	0.29	1.29
Luenberger observer	0.58	1.52
Modal interpolation	1.09	1.62
Open-loop model	1.88	2.19

### 39.3.2 Luenberger Observer

In the case of the Luenberger observer, the only information needed to formulate the observer is the position of the poles of the closed loop system, i.e.  $A - GC$ . For this experiment we set all the poles as  $\lambda_{cl} = 0.95\lambda_{ol}$ , where  $\lambda_{cl}$  are the poles of the closed loop system and  $\lambda_{ol}$  are poles of the open loop system (the original FEM model of the beam). Since we are using constant modal damping, all poles of the closed loop system will lie in a circle centered at the origin in the complex plane.

### 39.3.3 Modal Interpolation

To implement the modal interpolation approach, we used the shape of the first two undamped modes of the FEM model shown in Fig. 39.2a. This selection was based upon observation of the dynamic response at the accelerometer locations (4) and (9) and noticing that the two modes with highest contribution to the dynamic response had natural frequencies of 6.4 and 40.0 Hz.

## 39.4 Results and Discussion

In this section we present the results from the two tests carried out, one with a band limited excitation delivered through a shaker and the other, an impulsive load delivered using an impact modal hammer, both tests had a duration of 8 s.

### 39.4.1 Impact Modal Hammer Test Results

The following table presents a summary of the Euclidean and infinity norms of the relative error (RE) for the different methods at strain location (1)(Table 39.1).

where the relative error is the time series defined by

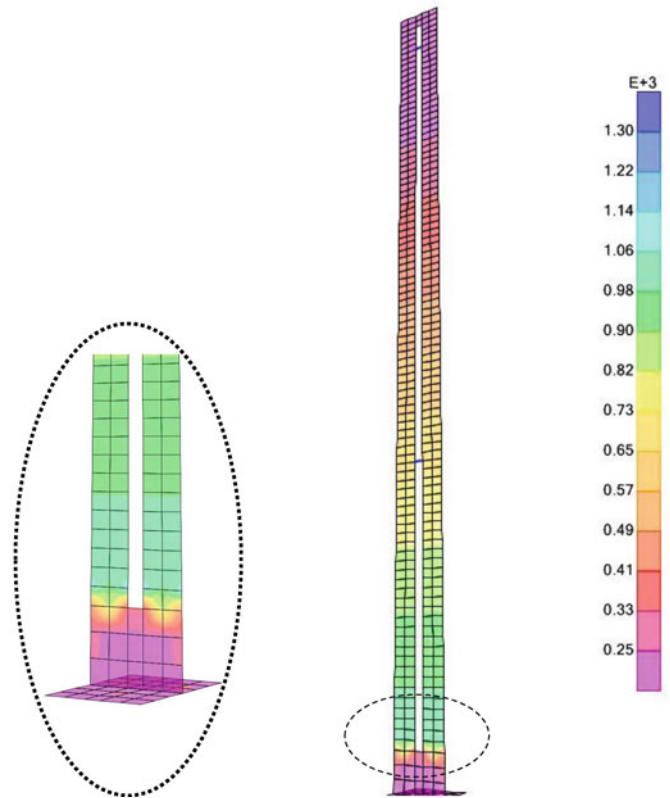
$$RE(t) = \frac{|Measurement(t) - Estimate(t)|}{\| Measurement \|_2} \quad (39.16)$$

### 39.4.2 Shaker Test Results

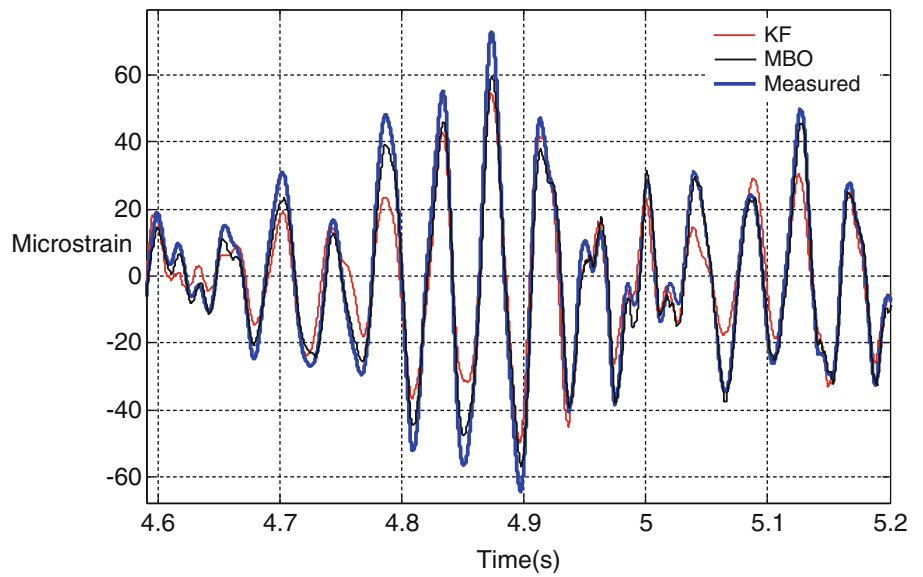
In this section we present the results obtained from the shaker excitation. Figure 39.4 shows the stress contour at the time of maximum stress in the critical location near the fixed support. A close-up of the estimated stress contour at the critical location near the base is also shown. Figure 39.5 depicts a time window of approximately half a second where the maximum strains were measured. The estimates from the proposed observer, the Kalman filter and the measured response are compared. As can be seen the proposed observer outperforms the Kalman filter in estimation accuracy.

The following table presents a summary of the Euclidean and infinity norms of the relative error (RE) for the different methods at strain location (1) (Table 39.2).

**Fig. 39.4** Superficial stress contour at time of maximum stress at critical location in cantilever estimated using proposed FEM based observer



**Fig. 39.5** Kalman filter and proposed FEM based estimator versus measured strain



**Table 39.2** Comparison of estimation accuracy between different methods for the shaker test

	$\ RE\ _2$	$\ RE\ _\infty$
Model-based observer	0.25	0.30
Kalman filter	0.46	0.44
Luenberger observer	0.47	0.67
Modal interpolation	1.13	1.07
Open-loop model	0.59	0.55

## 39.5 Conclusion

The results demonstrate the performance of the proposed model based estimator for various load cases. The results show the capability of the proposed algorithm to track the measured response of unmeasured quantities. Two major advantages of the method can be pointed out. First, its capability of handling high order systems by working directly in a finite element model, and secondly, all unmeasurable responses that can be extracted from the FEM are readily available from the estimator.

## References

1. Bolotin V (1999) *Mechanics of fatigue*. CRC, Boca Raton
2. Papadimitriou C, Fritzen CP, Kraemer P, Ntotsios E (2011) Fatigue predictions in entire body of metallic structures from a limited number of vibration sensors using kalman filtering. *J Struct Control Health Monit* 18(5):554–573
3. Hernandez EM, Bernal D, Caracoglia L (2012) On-line monitoring of wind induced stresses and fatigue damage in instrumented structures. *Struct Control Health Monit*. doi:10.1002/stc.1536
4. Liu H (2007) State-space analysis of cardiac motion with biomechanical constraints. *IEEE Trans Image Process* 16(4):901–917
5. Bernal D, Nasser A (2009) Schemes for reconstructing the seismic response of instrumented buildings. In: SMIP seminar on seismological and engineering implications of recent strong motion data. Los Angeles, CA, pp 23–38
6. Hernandez EM, Bernal D (2008) State estimation in structural systems with model uncertainties. *ASCE J Eng Mech* 134, 3:252–258
7. Kalman RE (1960) A new approach to linear filtering and prediction problem. *J Basic Eng Trans ASME* 82:35–45
8. Mendel J (1971) Computational requirements for a discrete kalman filter. *IEEE Trans Autom Control* 16(6):748–758
9. Balas MJ (1998) Do all linear flexible structures have convergent second-order observers? *AIAA J Guid Control Dyn* 4:2319–2323
10. Hernandez EM (2011) A natural observer for optimal state estimation in second order linear structural systems. *Mech Syst Signal Process* 25:2938–2947
11. Grewal M, Andrews A (1998) *Kalman filtering, theory and practice using MATLAB*. Wiley, New Jersey



# Chapter 40

## Strain Estimation in a Glass Beam Using Operational Modal Analysis

Manuel L. Aenlle, Anders Skafte, Pelayo Fernández, and Rune Brincker

**Abstract** A potential application of operational modal analysis is the prediction of strain or stress time histories which, on the other hand, are one of the most important sources of uncertainty in fatigue design and remaining fatigue life calculations. This is due to the difficulty of estimating the stiffness, mass and damping properties with accuracy, as well as the use of simplified loading models.

In this work, it is proposed a methodology to estimate the strain or stress time histories at any point of a beam, which need the strain mode shapes, expanded using a finite element model and the modal coordinates of the responses, which contain the information corresponding to the damping and the natural frequencies. Experimental tests were carried out on a monolithic glass beam to study the accuracy obtained in the strain mode shapes.

**Keywords** Operational modal analysis • Strains • Strain mode shapes • Modal assurance criterion • Glass elements

### 40.1 Introduction

Operational modal analysis (OMA) is a technique with many potential applications in civil structures [1, 2] and mechanical systems [3]. OMA makes use of the natural or operating loads to excite the structure and the modal tests can be performed with the structure in operation subject to natural or operational loads [4].

Experimental modal analysis has been widely used in the past to validate finite element models, model updating, health monitoring, structural modification, damage detection, etc. In this paper it is proposed a methodology to estimate strains or stresses in any arbitrary point of the structure, which combines a numerical model, previously updated using the modal parameters identified by OMA and the acceleration time histories recorded at several points of the structure. With this methodology, the only information needed from the finite element model is the strain mode shapes whereas the information corresponding to natural frequencies and damping are contained in the modal coordinates which are estimated from the experimental responses [5, 6].

This paper only deals with the estimation of the strain mode shapes. The accuracy in the estimation of strain mode shapes has been studied by experimental tests carried out on a monolithic glass beam. Several accelerometers were used to measure the responses whereas some strain gauges were attached to identify the strain mode shapes by operational modal analysis. The strain mode shapes from the strain gauges are compared with those derived from the mode shapes identified from the accelerations and expanded using a finite element model.

---

M.L. Aenlle (✉) • P. Fernández  
Department of Construction and Manufacturing Engineering, University of Oviedo,  
Campus de Gijón s/n. Ed. Oeste. Bloque 7, Gijón, 33203 Spain  
e-mail: [aenlle@uniovi.es](mailto:aenlle@uniovi.es); [fernandezpelayo@uniovi.es](mailto:fernandezpelayo@uniovi.es)

A. Skafte • R. Brincker  
Department of Engineering, Aarhus University, Edison Building, Finlandsgade 22, Aarhus N, 8200 Denmark  
e-mail: [ask@iha.dk](mailto:ask@iha.dk); [rub@iha.dk](mailto:rub@iha.dk)

## 40.2 Theory

The methodology proposed in this paper is particularized to a plane Euler-Bernoulli beam.

For an Euler-Bernoulli beam (see Fig. 40.1) the bending moment and the curvature are related by the equation:

$$EI_z \frac{d^2 y}{dx^2} = M_z \quad (40.1)$$

where E is the Young's modulus,  $I_z$  is the second moment of the cross section about z axis, y is the vertical displacement and  $M_z$  is the bending moment.

The stress can be calculated by means of the Navier's Law equation, i.e.:

$$\sigma(x) = \frac{M_z}{I_z} \cdot h \quad (40.2)$$

where h is the beam thickness.

If (40.1) and (40.2) are combined, a relation between the strain and the curvature is obtained by:

$$\varepsilon(x) = h \cdot \frac{d^2 y}{dx^2} \quad (40.3)$$

On the other hand, if a finite element model is used, the displacement in any arbitrary point of an element (see Fig. 40.2) is given by [7]:

$$y(x) = N_e \cdot u_e \quad (40.4)$$

where  $N_e(x)$  and  $u_e$  are vectors containing the shape functions and the nodal displacements, respectively.

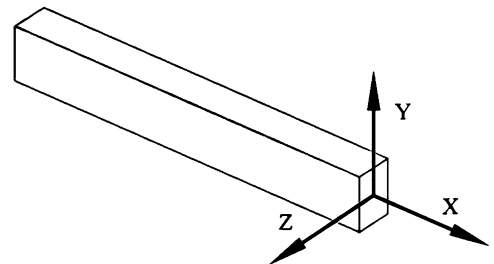
If (40.4) is combined with (40.3), the following expression is inferred:

$$\varepsilon(x, t) = N''_e(x) \cdot u_e(t) h \quad (40.5)$$

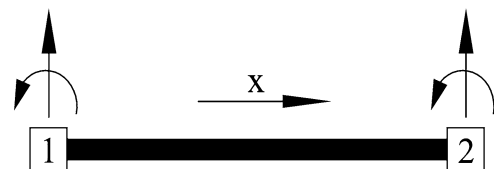
Using modal-superposition [8], the vector  $u_e(t)$ , corresponding to each element, can be expressed in terms of mode shapes,  $\Phi_e$ , and the modal coordinates,  $q(t)$ , as follows [5, 6]:

$$u_e(t) = \phi_e \cdot q(t) \quad (40.6)$$

where  $\phi_e$  is a matrix containing the components of mode shapes at the DOF's of the element.



**Fig. 40.1** Example of Euler-Bernoulli beam



**Fig. 40.2** Linear beam element

Finally, if (40.6) is substituted in (40.5), the strains at any point of the beam element can be calculated by means of the expression:

$$\varepsilon(x, t) = N''_e(x) \cdot \phi_e \cdot q(t) \cdot h \quad (40.7)$$

In (40.7) two main terms can be identified: the modal coordinates,  $q(t)$ , and the strain mode shapes:

$$\phi_\varepsilon(x) = \phi''_e(x) = N_e(x)'' \cdot \phi_e \quad (40.8)$$

which are estimated using the shape functions and the components of the updated mode shapes at the DOF's of the element.

## 40.2.1 Steps

### 40.2.1.1 Finite Element Model

The first stage of the proposed method is to assemble a numerical model [7]. This step can be avoided if the mode shapes can be fitted using analytical functions, splines, etc.

### 40.2.1.2 Modal Parameters

A modal identification is performed to obtain the natural frequencies,  $f_{\text{exp}}$ , and mode shapes,  $\Phi_{\text{exp}}$ , of the structure. The identification may be performed by e.g. Stochastic Subspace Identification (SSI) [9], or Frequency Domain Decomposition (FDD) [10]. The FDD is used in this paper as implemented in the ARTEMIS Extractor software. The FDD is based on calculation of Spectral Density Matrices of the measured data series by discrete Fourier transformation. For each frequency line the Spectral Density Matrix is decomposed into auto spectral functions corresponding to a single degree of freedom system (SDOF) [10].

### 40.2.1.3 Modal Scaling

An important disadvantage of OMA is that not all modal parameters can be estimated [5, 11]. Since the forces are unknown, the mode shapes can not be mass normalized and only the un-scaled mode shapes can be obtained for each mode. However, the procedure proposed in this paper can be used with both mass normalized or arbitrary scaled mode shapes. If mass normalized mode shapes are used, the scaling factors can be estimated by the mass change method [5, 11] which consists of modifying the dynamic behaviour of the structure adding masses in the points of the structure where the mode shapes are known and performing repeated modal tests on both the original and the perturbed structure

### 40.2.1.4 Model Up-Dating and Modal Expansion of the Mode Shapes

In this stage, the finite element model is updated using the experimental modal parameters estimated with OMA [12]. After updating, a transformation matrix  $T$  is obtained from:

$$\phi_{\text{exp}}^m = \phi_{FE}^m \cdot T \quad (40.9)$$

where subscripts ' $_{\text{exp}}$ ' and ' $_{FE}$ ' indicates experimental and numerical mode shapes, respectively, and superscript ' $^m$ ' indicates measured DOF's. In expression (40.9), the experimental mode shapes are assumed to be a linear combination of the numerical mode shapes [12]. Then, the experimental mode shapes are expanded to the unmeasured degrees of freedom by the expression:

$$\phi_{\text{exp}}^{um} = \phi_{FE}^{um} \cdot T \quad (40.10)$$

where superscript 'um' indicates unmeasured DOF's. The same procedure has to be followed in case of un-scaled mode shapes.

#### 40.2.1.5 Modal Coordinates

The experimental displacement modal coordinates,  $q_{exp}(t)$ , have to be calculated from the measured acceleration,  $\ddot{u}_{exp}(t)$ . The acceleration modal coordinates,  $\ddot{q}_{exp}(t)$ , are firstly obtained by means of the expression:

$$\ddot{q}_{exp}(t) = \phi_{exp}^{-1} \cdot \ddot{u}_{exp}(t) \quad (40.11)$$

where  $\ddot{u}_{exp}(t)$  is the measured acceleration and  $\phi_{exp}$  is the experimental mode shape matrix. Then, the displacement coordinates,  $q(t)$ , are estimated by a double integration of  $\ddot{q}_{exp}(t)$ . In this work a double integration in the frequency domain was used as follows:

$$q_{exp}(\omega) = -\frac{\ddot{q}_{exp}(\omega)}{\omega^2} \quad (40.12)$$

and the corresponding modal coordinates in the time domain can be obtained by inverse Fourier Transform.

If un-scaled mode shapes,  $\psi$ , are used, the scaling factors are needed. The mass normalized,  $\phi$ , and the un-scaled mode shapes,  $\psi$ , are related by:

$$\phi = \psi \cdot \alpha \quad (40.13)$$

where  $\alpha$  is a diagonal matrix containing the scaling factors.

If (40.13) is substituted in (40.6), it results in:

$$u_e(t) = \psi_e \cdot \alpha \cdot q(t) \quad (40.14)$$

or, alternatively:

$$u_e(t) = \psi_e \cdot q^*(t) \quad (40.15)$$

where  $q^*(t)$  is denoted here as pseudo modal coordinate, which is estimated by means of the expression:

$$\ddot{q}_{exp}^*(t) = \psi_{exp}^{-1} \cdot \ddot{u}_{exp}(t) \quad (40.16)$$

#### 40.2.1.6 Strain Estimation

Finally, combining (40.5), (40.6) and (40.11), the strains can be determined by the equation:

$$\varepsilon(x, t) = N''_e(x) \cdot \phi_e \cdot q_{exp}(t) \cdot h \quad (40.17)$$

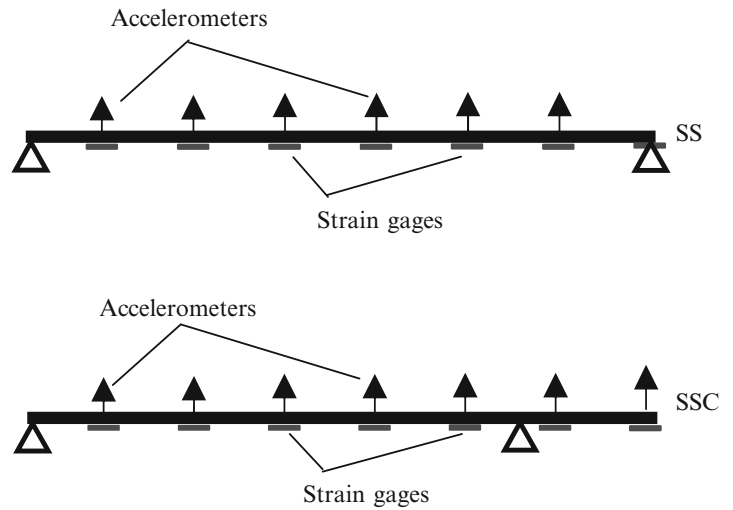
for the case of mass normalized mode shapes. In the case of un-scaled mode shapes, (40.5), (40.15) and (40.16) give:

$$\varepsilon(x, t) = N''_e(x) \cdot \psi_e \cdot q_{exp}^*(t) \cdot h \quad (40.18)$$

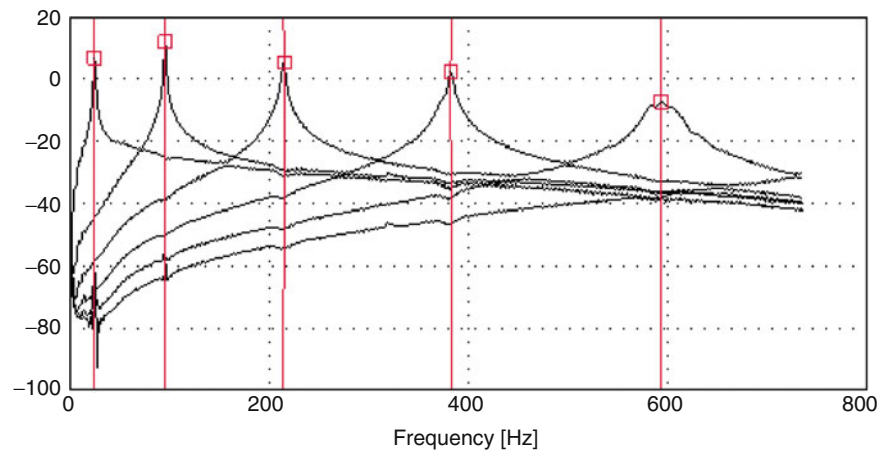
### 40.3 Experimental Tests

A monolithic glass beam was used to perform the tests (see Fig. 40.3). The beam was 1 m long, showing a  $100 \times 10$  mm rectangular section. Two support configurations were considered in the investigation: simply supported (SS) and simply supported with a cantilever (SSC). A finite element model was assembled in ABAQUS to obtain a set of mode shapes, using linear beam elements (Fig. 40.2).

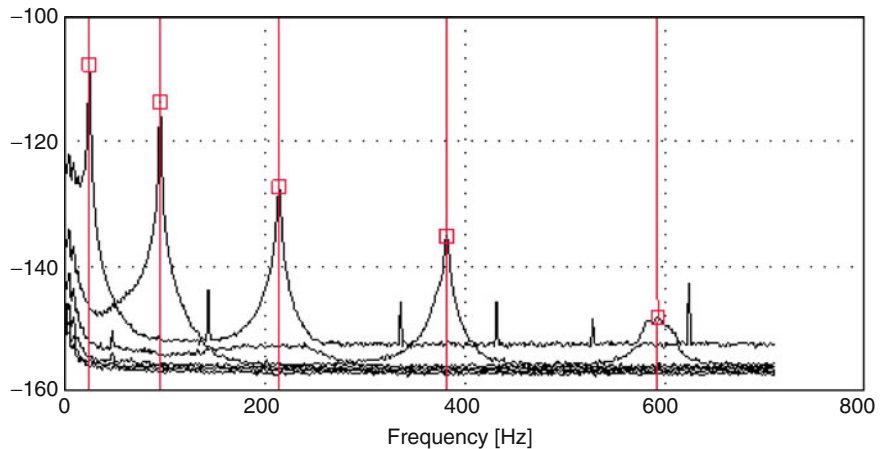
**Fig. 40.3** Accelerometers and strain gage configuration



**Fig. 40.4** Modes identified from the accelerometers in SS configuration by EFDD



**Fig. 40.5** Modes identified from the strain gages in SS configuration by EFDD



### 40.3.1 Operational Modal Analysis

The beam was excited applying hits with a small piece of wood along the beam trying to reproduce a stationary broad banded load. The responses were measured using accelerometers with a sensitivity of 100 mv/g, weighing 5 g and located as shown in Fig. 40.3. The tests were carried out using a sampling frequency of 2,000 Hz during a period of approximately 4 min. Seven 350  $\Omega$  strain gauges were also attached (Fig. 40.3) to obtain the strain mode shapes by OMA.

**Table 40.1** Natural frequencies [Hz]

MODE		1	2	3	4	5
SS	Accelerometers	25.22	96	214.7	382.6	593.2
	Strain gauges	25.23	96	214.7	382.7	592.3
SSC	Accelerometers	36.1	104.4	187.9	368.5	620.7
	Strain gauges	36.1	104.3	187.9	368.5	621.9

**Table 40.2** MAC between the numerical and the experimental models

	SS (accelerometers)			SSC (accelerometers)		
Numerical	0.9998	0.0000	0.0001	0.9980	0.0561	0.0207
Model	0.0001	0.9994	0.0001	0.0754	0.9990	0.0941
	0.0002	0.0003	0.9986	0.0569	0.1294	0.9831

**Table 40.3** MAC in the strain mode shapes

	SS (accelerometers)			SSC (accelerometers)		
Strain gauges	0.9827	0.0007	0.0079	0.9478	0.0001	0.0163
	0.0002	0.9507	0.0011	0.0002	0.9757	0.0072
	0.0001	0.0005	0.9191	0.0005	0.0044	0.9831

The modal parameters were identified by Enhanced Frequency Domain Decomposition (EFDD) [10]. The normalized singular values are presented in Figs. 40.4 and 40.5. The first five natural frequencies, for both support configurations, are shown in Table 40.1.

The Modal Assurance Criterion (MAC) between the numerical and the experimental modes is presented in Table 40.2.

### 40.3.2 Results

In Fig. 40.6 are presented the first three strain mode shapes of the simply supported configuration (SS) obtained using (40.9) and (40.10), together with those obtained by modal identification of the strain gauges. The finite element model was not updated as there was a good agreement between the experimental and the numerical mode shapes (see Table 40.2). It can be observed that there is a good agreement between the results provided by both methods, except at the borders of the beam.

If linear beam elements (C1) are used in the finite element model, the continuity in the deflection and the rotation is guaranteed. However, there is a lack of continuity in the curvature across inter-element boundaries. In this work, the curvature has been smoothed at each node averaging the curvatures corresponding to each element connected at the node. However, this technique cannot be applied at the borders of the beam, reason by which the largest error appears in these positions. In Table 40.3 is presented the MAC between the strain mode shapes obtained by both methods. If the strain mode shapes components at the borders are not considered, a good agreement is achieved (see Table 40.4) and the MAC improves significantly.

In Fig. 40.7 the results for the simply supported with cantilever configuration (SSC) are presented. Again, a good agreement exists between the results of both methods. With respect to the MAC, presented in Tables 40.3 and 40.4, the same conclusions as for the SS configuration can be established.

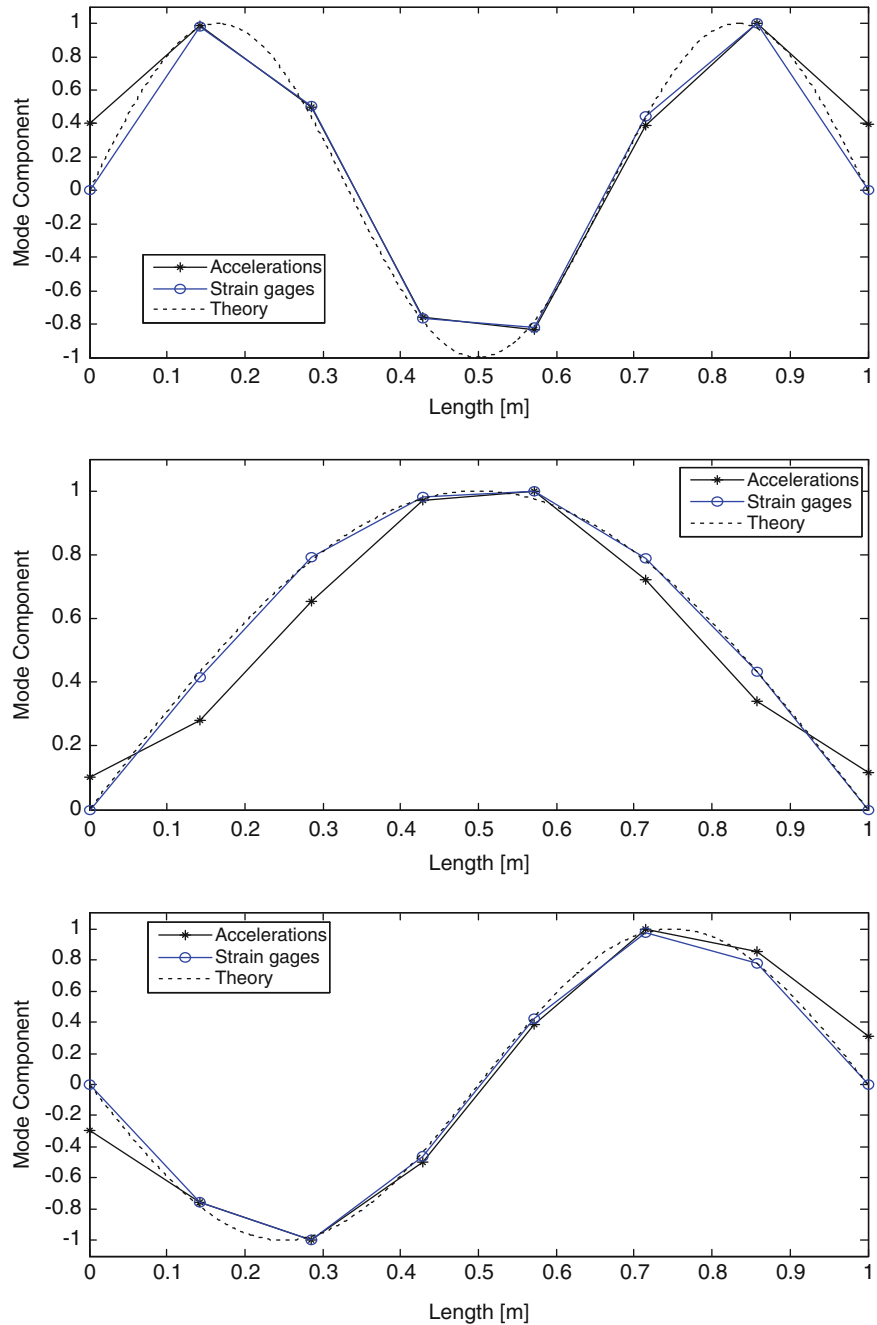
## 40.4 Conclusions

- A methodology to estimate strains at any arbitrary point of a structure, which combines a numerical model, previously updated using the modal parameters identified by OMA, and the acceleration time histories recorded at several points of the structure, is proposed. The methodology only needs the strain mode shapes and the modal coordinates estimated from the experimental responses.
- The accuracy obtained with this technique in the strain mode shapes has been investigated performing experimental tests on a monolithic glass beam using different support configurations. The results show the difficulty of estimating the strain mode shapes at the borders of the beam with accuracy. However, a good precision has been obtained for all the modes in the rest of the points of the beam.

**Acknowledgements** The economic support given by the Spanish Ministry of Science and Innovation through the project BIA 2011-28380-C02-01 is gratefully appreciated.



**Fig. 40.6** Strain mode shapes for the first three modes in SS configuration



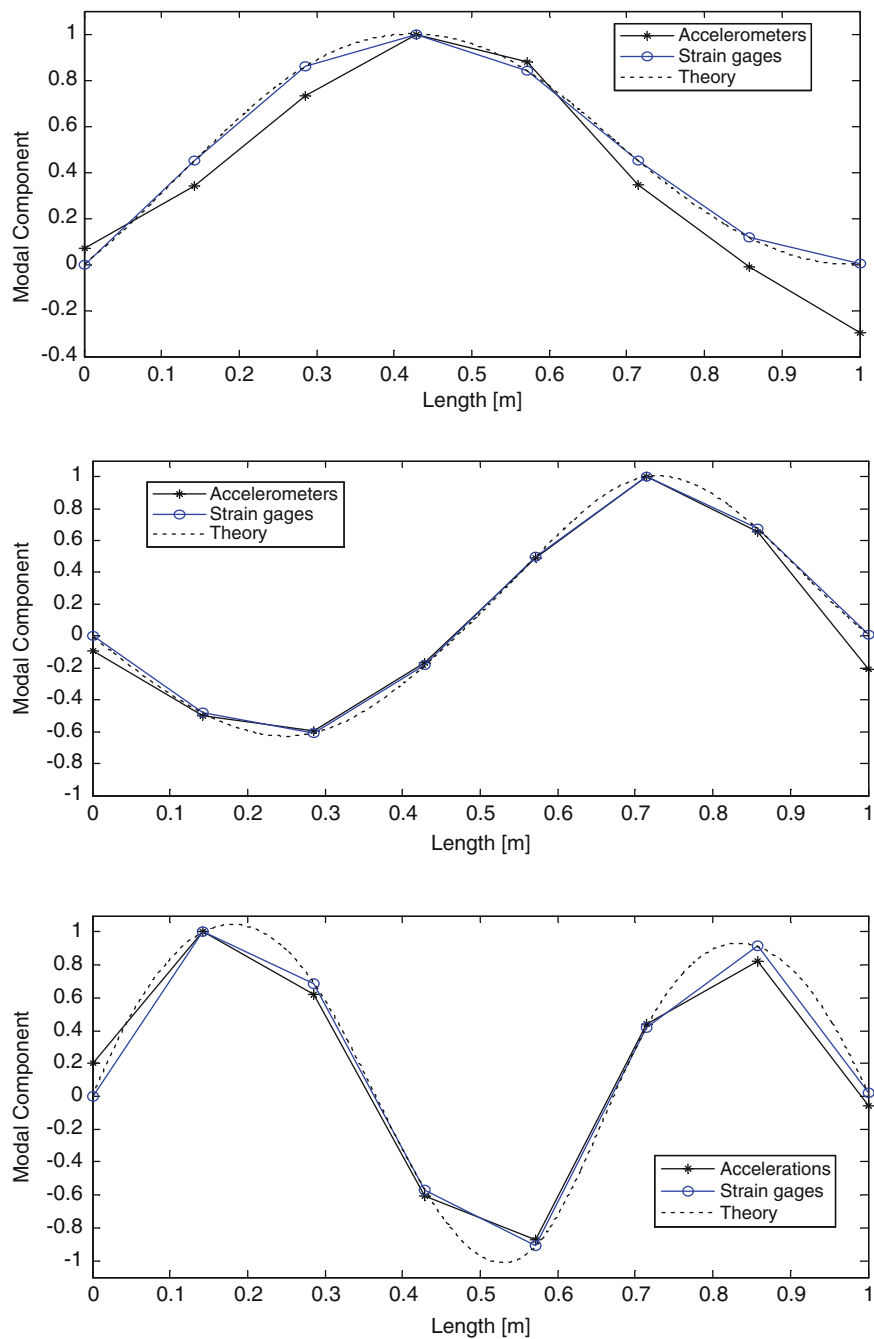
**Table 40.4** MAC in the strain mode shapes when border points are not considered

	SS (accelerometers)			SSC (accelerometers)		
Strain gauges	0.9902	0.0007	0.0079	0.9822	0.0001	0.0164
	0.0002	0.9997	0.0011	0.0002	0.9995	0.0071
	0.0001	0.0006	0.9992	0.0005	0.0044	0.9967

**References**

1. Cantieni R (2005) Experimental methods used in system identification of civil engineering structures. In: Proceedings of the international operational modal analysis conference (IOMAC), Copenhagen, pp 249–260
2. Cunha A, Caetano E (2005) From input-output to output-only modal identification of civil engineering. In: Proceedings of the international operational modal analysis conference (IOMAC), Copenhagen, pp 11–27
3. Møller N, Brincker R, Herlufsen H, Andersen P (2001) Modal testing of mechanical structures subject to operational excitation forces. In: Proceedings of the 19th international modal analysis conference (IMAC), Kissimmee, pp 262–269

**Fig. 40.7** Strain mode shapes for the first three modes in SSC configuration



4. Brincker R, Ventura C, Andersen P (2003) Why output-only modal testing is a desirable tool for a wide range of practical applications. In: Proceedings of the international modal analysis conference (IMAC) XXI, Kissimmee, Florida, paper 265
5. Pelayo F (2010) Scaling factors and strains estimation in structures by means of operational modal analysis. Ph.D., University of Oviedo
6. Fernández P, Aenlle ML, Brincker R, Fernández-Canteli A (2009) Stress estimation in structures using operational modal analysis. In: 3th international operational modal analysis conference (IOMAC), Portonovo
7. Zienkiewicz OC, Taylor RL (2005) The finite element method for solid and structural mechanics, 6th edn. Elsevier, Oxford
8. Clough RW, Penzien J (1993) Dynamics of structures, 2nd edn. McGraw-Hill, New York
9. Van Overschee P, De Moor B (1996) Subspace identification for linear systems: theory, implementation, applications. Kluwer Academic, Dordrecht
10. Brincker R, Zhang L, Andersen P (2001) Output-only modal analysis by frequency domain decomposition. Smart Mater Struct 10:441–445
11. López-Aenlle M, Fernández P, Brincker R, Fernández-Canteli A (2010) Scaling-factor estimation using an optimized mass-change strategy. Mech Syst Signal Process 24:1260–1273
12. Friswell MI, Mottershead JE (1995) Finite element model updating in structural dynamics. Kluwer Academic, Dordrecht

# Chapter 41

## Pressure Measurement Sensor for Jointed Structures

G. Chevallier, H. Festjens, F. Renaud, and J.-L. Dion

**Abstract** The talk will deal with measurements of normal loads in assembled structures. A new sensor has been developed to measure the distribution of the normal force in a bolted joint. This sensor is piezoelectric and is associated to an electronic device for carrying out a static measurement. Moreover, the electrode of the sensor is shaped in order to make possible the measurement of a detailed normal stress field. Furthermore, preliminary results of the study of the vibrations are presented.

**Keywords** Jointed structures • Piezoelectricity • Pressure sensor • Modal analysis • Contact

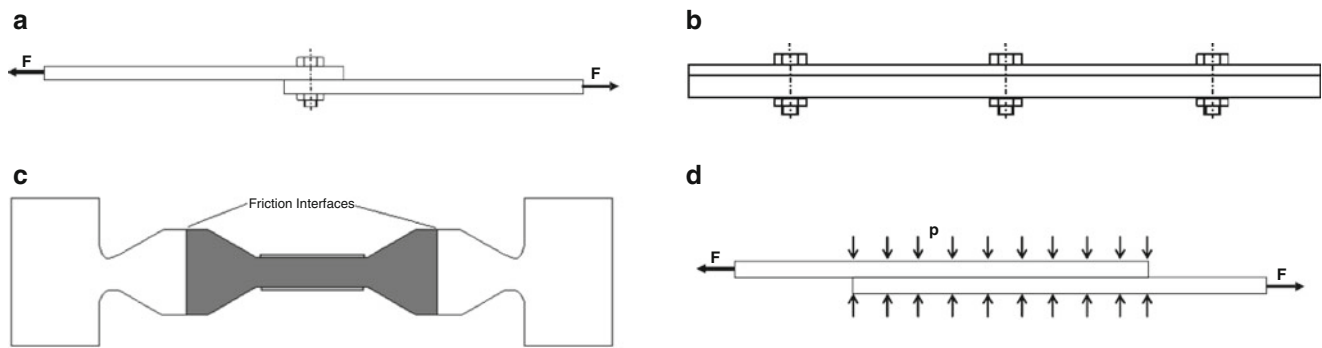
### 41.1 Introduction

In the field of structure assemblies, the problem of vibration-damping remains a great challenge. Simulation tools (Computer Aided Design and Finite Element Method) are currently being used to predict the mass and stiffness matrices with precision. Damping is traditionally affected by an error which can sometimes exceed 100 % and consequently the vibration levels are very hard to predict. Interfaces (welded points, bolted joints or rivets) influence the dynamics of these structures, specifically in the prediction of the damping. Several studies were carried out to understand and to define the mechanism of energy losses (EL) in jointed structures. Few testing devices among the most famous are presented on Fig. 41.1: clamped beams with a longitudinal interface, see Goodman et al. [1] (see Fig. 41.1b), sandwich beams loaded with a pure transverse force, see Metherell et al. [2] (see Fig. 41.1c) or lap joints, see Earles [3], beam elements screwed together, see Esteban et al. [4] (see Fig. 41.1a). In such devices, the contact pressure between the parts is very difficult to know. Moreover the contact pressure is non uniformly distributed over the surface and can depend on the vibration motion. More recently, Peyret et al. [5] and [6] have proposed a new test bench, see Fig. 41.1c. The latter ensures that the normal stress is not time-dependent and is uniformly distributed over the contact surface.

In order to predict the EL in the contact interfaces, one can compute the energy dissipation during the vibration motion, see for example [7] or [8]. The work of Caignot et al. [9] shows that it is possible to predict the damping thanks to a Finite Element simulation with contact and friction non-linearity. In order to improve this kind of simulation, it is necessary to measure the stress fields in the region of the contact. The purpose of this talk is to deal with a piezoelectric sensor dedicated to the measurement of the normal stresses in the contact interface. To achieve this goal, the authors have considered a testing device based on the same geometry than the one presented by Foltete et al. [10]. The latter is very close to the one presented on Fig. 41.1b. One of the parts is constituted with a  $d_{33}$  piezoelectric patch; the other one is a sheet of steel. Both are assembled together with bolts. The next section details the measurement principle. The third one presents some perspectives in terms of vibration damping.

---

G. Chevallier (✉) • H. Festjens • F. Renaud • J.-L. Dion  
ISMEP LISMMA, 3 rue Fernand Hainaut, 93407 Saint- Ouen Cedex, France  
e-mail: [gael.chevallier@supmeca.fr](mailto:gael.chevallier@supmeca.fr); [jean-luc.dion@supmeca.fr](mailto:jean-luc.dion@supmeca.fr)



**Fig. 41.1** Different kinds of benchmark. (a) Beam element screwed together with a single bolt. (b) Beam elements screwed together over the length. (c) New testing device proposed by Peyret et al. [5] and [6]. (d) Lap joint loaded with pure shear forces

## 41.2 Measurement Principle

As it was said in the introduction, the testing device is constituted with two beams assembled with bolts. In order to measure the contact-stress field over the interface, one of the parts is made with a piezoceramic **PI 255** provided by *PI Piezoceramics*. The other one is made of steel, see Fig. 41.2.

### 41.2.1 Geometry and physics

The manufacturers of piezos are able to provide thin patches. Here, the width of our patches is equal to 2 mm. Moreover for this structure, the whole structure has to be thin in order to study low frequency vibrations. Both parts are linked with three bolted joints to obtain a quite homogeneous contact stress field. The width of the sheet of steel is equal to 0.5 mm in order to be as conformable as possible. All the dimensions are summarized on Fig. 41.3.

To simulate the behavior of the sensor, we used finite element computations. Firstly, the patches are simulated alone with a pressure applied on the contact area, see Fig. 41.3 right. The  $S_{33}$  stress is plotted on Fig. 41.4, the associated voltage is plotted on the left. However, it is not possible to obtain a stress field as detailed as the one of Fig. 41.3 because of the presence of an electrode on the surface of the patch. This electrode constrains the voltage to be homogeneous on all the surface, see Fig. 41.5. The electrode acts as a filter which averages the electrical potentials on the surface. Nevertheless, it is possible to have a good representation of the stress field by making an *electrode shaping* on the surface. For this, we cut the electrode area in smaller areas on which the electric potential is uniform, see Fig. 41.5 right.

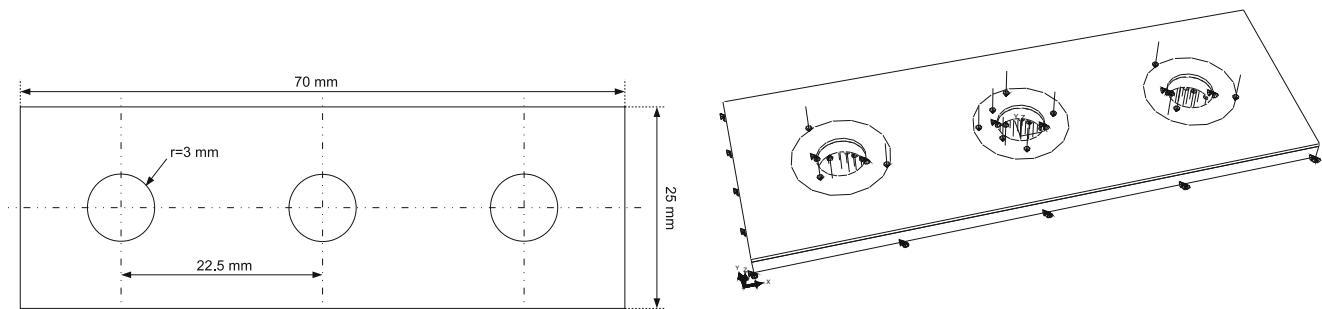
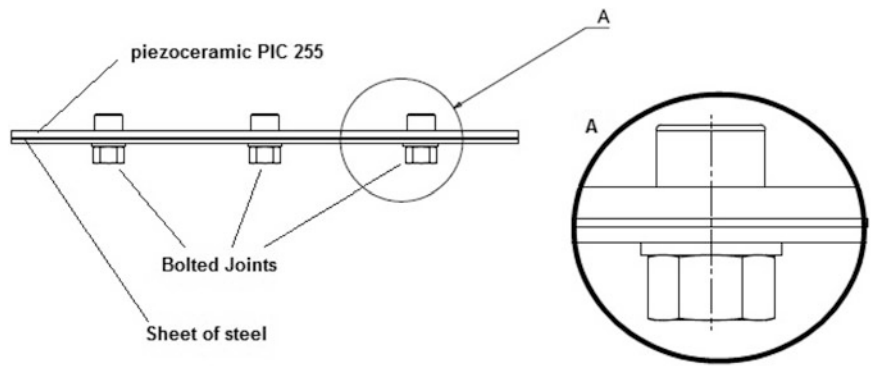
### 41.2.2 Static Measurement

The measurement of static deformations using piezoceramics is an engineering challenge. A piezo electric strain gauge is generating an electric charge proportional to the strain. This charge will dissipate in a relatively short period of time due to the electric resistance of the data acquisition electronic devices. Smart Material has developed an electronic device: the store & hold technique which transfers the generated charge to a high-end, leakage free capacitor, while the charge proportional voltage across the capacitance can be measured with a special designed high impedance operational amplifier. This guarantees constant output signals over up to 3 min without any significant drift (Figs. 41.6 and 41.7).

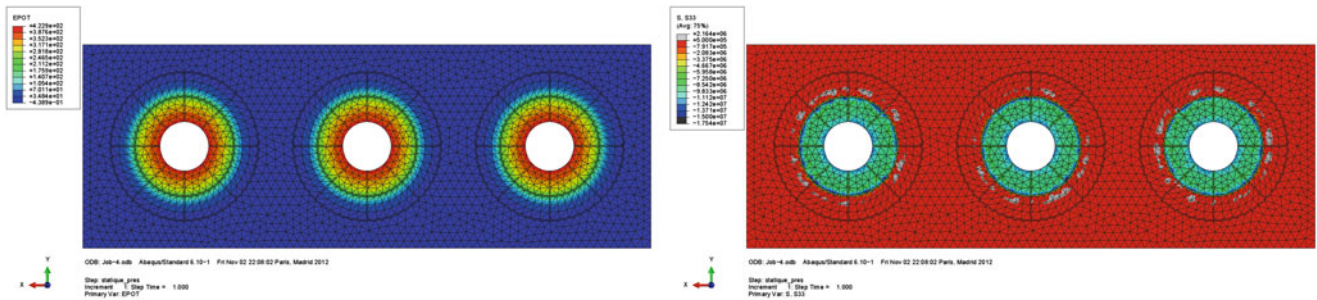
## 41.3 Vibrations

To calculate the vibration damping, we first calculate the contact stress field. This calculation will be updated by the measurements of the voltage which are in progress in our laboratory. Then we will apply the displacement field of each mode, see Fig. 41.8, as a loading of the structures. Using the Masing rules, see [7], we will simulate the energy dissipated by friction in the contact surfaces under the normal stresses that we have previously determined.

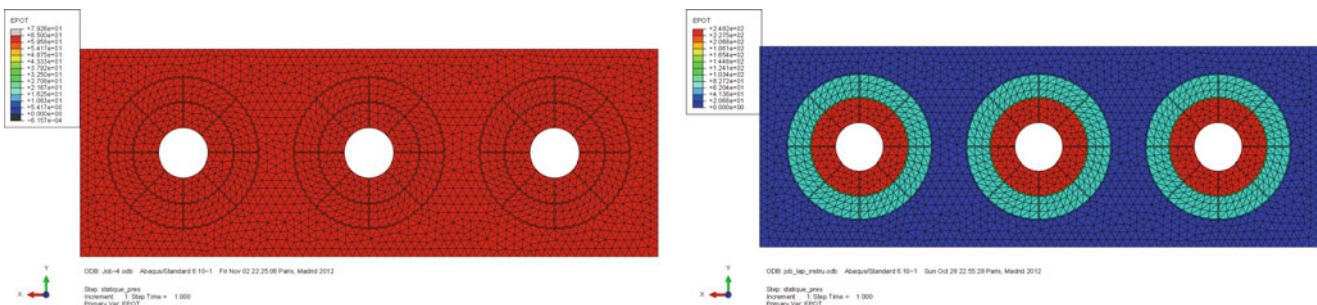
**Fig. 41.2** Schema of the testing device with the different parts and the details of a bolted joint



**Fig. 41.3** Load case: clamped edges on the ceramic (*bottom*) and pressure to take into account the bolts (*top*)

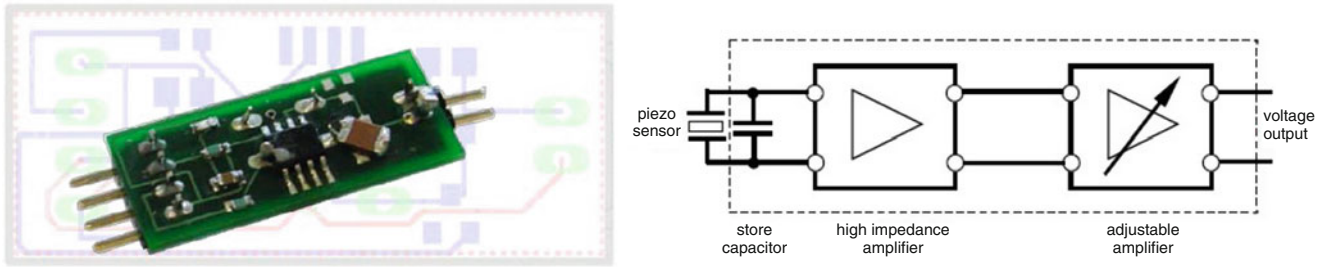


**Fig. 41.4** *Left*: Electric voltage field over the face of the ceramic part. *Right*:  $S_{33}$  Stress field



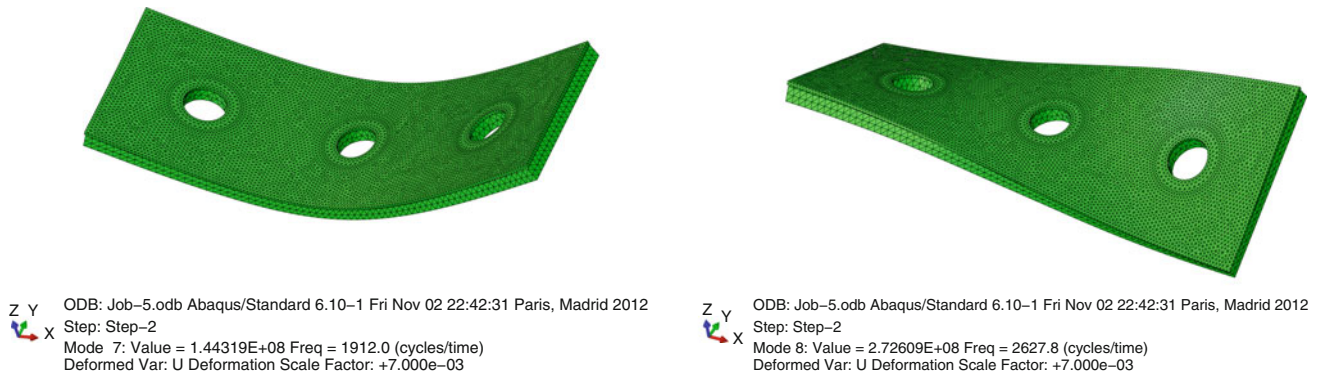
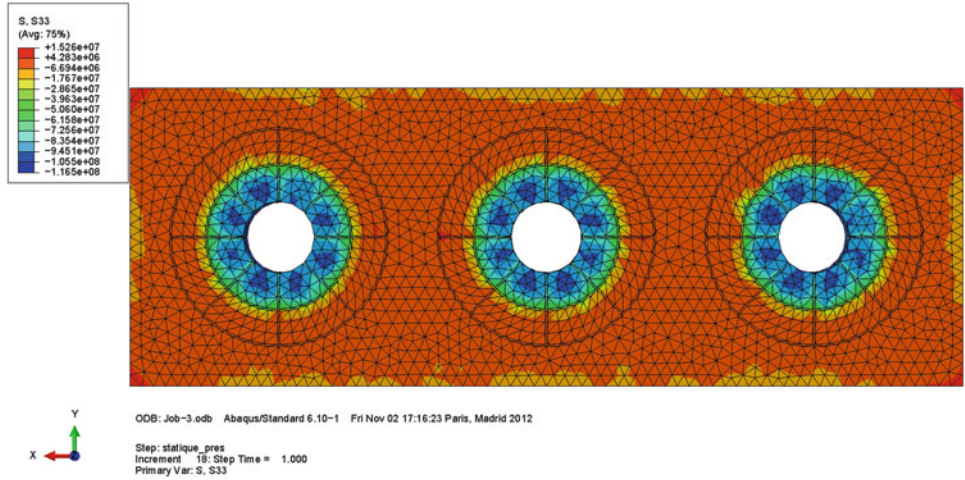
**Fig. 41.5** Electric voltage field over the face of the ceramic part. *Left*: with one electrode over the surface. *Right*: with electrode shaping





**Fig. 41.6** Picture and schema of the electronic device used as a memory for static measurement

**Fig. 41.7**  $S_{33}$  stresses computed thanks to a non-linear static simulation



**Fig. 41.8** First vibrations modes. *Left*: bending mode, 1,900 Hz. *Right*: torsion mode, 2,620 Hz

### 41.4 Conclusion

In this talk, we present the principles of a new sensor which allows to measure the normal stresses in an assembly. It is based on the use of piezoelectric materials polarized along their thickness. To be efficient, this sensor has to be machined in order to obtain a very specific electrode shape. Moreover, an electronic device is used to perform measurement in static.

### Appendix: Piezoelectric Materials

This section summarizes the datas provided by PI and the datas that are used for finite element simulation.



## Manufacturer Datas

The manufacturers provide incomplete and inhomogeneous datas. The following summarizes the datas given by PI :

- Density  
 $\rho = 7,800 \text{ kg/m}^3$
- Strain piezoelectric constants  
 $d_{31} = -180 \cdot 10^{-12} \text{ C/N}$   $d_{33} = 400 \cdot 10^{-12} \text{ C/N}$   $d_{15} = 550 \cdot 10^{-12} \text{ C/N}$
- Dielectric constants  
 $\epsilon_{33}^T = 1750\epsilon_0$   $\epsilon_{11}^T = 1650\epsilon_0$   $\epsilon_0 = 8.854 \cdot 10^{12} \text{ F/m}$
- Elastic compliance at constant electric field  
 $S_{11}^E = 16.1 \cdot 10^{-12} \text{ m}^2/\text{N}$   $S_{33}^E = 20.7 \cdot 10^{-12} \text{ m}^2/\text{N}$
- Material coupling factor (IEEE definition, see [11])  
 $k_{31} = 0.35$   $k_{33} = 0.69$   
 $k_{15} = 0.66$   $k_p = 0.62$

## ABAQUS Datas

Parameters are given for an assumed  $p$  thickness polarized piezoceramic material in the coordinate frame  $R_0$ .

- Density  
 $\rho = 7,800 \text{ kg/m}^3$
- Strain piezoelectric constants  
$$d = \begin{bmatrix} 0 & 0 & 0 & 0 & d_{15} & 0 \\ 0 & 0 & 0 & 0 & 0 & d_{15} \\ d_{31} & d_{31} & d_{33} & 0 & 0 & 0 \end{bmatrix}$$
 where all the parameters are given by PI
- Elastic compliance at constant electric field  
$$S^E = \begin{bmatrix} S_{11}^E & S_{12}^E & S_{12}^E & & & \\ S_{12}^E & S_{11}^E & S_{13}^E & & & \\ S_{12}^E & S_{13}^E & S_{33}^E & & & \\ & & & S_{55}^E & & \\ 0 & & & S_{55}^E & & \\ & & & & S_{66}^E & \end{bmatrix}$$
 with  $S_{55}^E = \frac{d_{15}^2}{\epsilon_{11}^T k_{15}^2}$   
 $S_{12}^E = -S_{11}^E + 2 \frac{d_{31}^2}{\epsilon_{33}^T k_p^2}$   
 $S_{13}^E = -\nu_{13}^E S_{11}^E$   
 $S_{66}^E = 2(S_{11}^E - S_{12}^E)$
- Engineering constants at constant electric field  
 $E_i = 1/S_{pp}^E$  for  $i = \{1, 2, 3\}$  and  $p = \{1, 2, 3\}$   
 $G_{ij} = 1/S_{pp}^E$  for  $i = \{2, 1, 1\}, j = \{3, 3, 2\}$  and  $p = \{4, 5, 6\}$
- Dielectric constants  
 $e = d(S^E)^{-1}$  and  $\epsilon^S = \epsilon^T - de^t$   
 $\epsilon_{11}^S = 0.8245 \cdot 10^{-9} \text{ m/F}$   $\epsilon_{33}^S = 0.7122 \cdot 10^{-9} \text{ m/F}$

## References

1. Goodman LE, Klumpp JH (1956) Analysis of slip damping with reference to turbine blade vibration. Journal of Applied Mechanics, Am Soc Mech Eng Appl Mech Div **23**, pp. 421
2. Metherell A, Diller S (1968) Instantaneous energy dissipation rate in a lap joint-uniform clamping pressure. Am Soc Mech Eng J Appl Mech **35**:123–128
3. Earles SWE (1966) Theoretical estimation of the frictional energy dissipation in a simple lap joint. J Mech Eng Sci **8**:207–214
4. Esteban J, Rogers CA (2000) On the damping effect due to bolted junctions in space structures subjected to pyro-shock. Comput Struct **75**:347–359

5. Dion J-L, Chevallier G, Peyret N (2012) Improvement of measurement techniques for damping induced by micro sliding. *Mech Syst Signal Process.* **34**(1–2):106–115. <http://dx.doi.org/0000> doi:0000.
6. Peyret N, Dion J-L, Chevallier G, Argoul P (2010) Micro-slip induced damping in planar contact under constant and uniform normal stress. *Int J Appl Mech* 02:281. <http://dx.doi.org/10.1142/S1758825110000597> doi:10.1142/S1758825110000597.
7. Festjens H, Chevallier G, Dion J-L (2012) A numerical quasi-static method for the identification of frictional dissipation in bolted joints. In: ASME IDETC, Chicago
8. Chen W, Deng X (2005) Structural damping caused by micro-slip along frictional interfaces. *Int J Mech Sci* 47:1191–1211
9. Caignot A, Ladeveze P, Neron D, Gallo VL, Romeuf T (2007) Prediction by virtual testing of damping in the spatial structures. In: Proc Colloque national en calcul de structures
10. Foltete E, Heller L (2005) Identification experimentale de l'amortissement modal non-linaire dans des poutres boulonnees. In: Premier congres conception et modelisation des systemes mecaniques
11. <http://ieeexplore.ieee.org/lpdocs/epic03/wrapper.htm?arnumber=26560176-1987> – IEEE standard on piezoelectricity, Tech. rep. (1988). <http://ieeexplore.ieee.org/lpdocs/epic03/wrapper.htm?arnumber=26560>

# Chapter 42

## Modal Analysis of Machine Tools Using a Single Laser Beam Device

Christian Brecher, Stephan Bäumlér, and Alexander Guralnik

**Abstract** Two main vibration measurement principles are dominating the modal analysis. These are laser vibrometers used as three-beam scanning devices for open surfaces as in the automotive and aerospace industries and three-axial accelerometers used in cases, where laser vibrometers are not applicable due to difficulties with the line-of-sight, very big sizes of tested structures, particularly high 3D precision requirements or simply due to the high costs. In our paper ‘Modal Testing using Tracking-Interferometers’ at IMAC XXX we presented a method and a measurement device for simultaneous 3D vibration measurement using a single laser beam.

This paper introduces the now fully implemented and partly automated testing method using this technique and device for experimental modal analyses. We describe the vibration measurement as well as geometry measurement the latter used to set-up the animation model for complex structures. We proceed with a detailed planning of the measurement procedure taking the example of our demonstrator machine. Finally we discuss our research on some main limitations and uncertainties of the system particularly the dynamic limitation of reflector mounting.

**Keywords** Modal analysis • Vibration • Optical measurement • Tracking-Interferometer • Laser tracker

### 42.1 Introduction

Despite ‘the rapid growth in the use and capacity of computing power [...], the need of experimental measurement is as compelling as ever’ [1]. Most commonly experimental data are used for comparison or adjustment of finite element or analytical models. Particularly the continuous improvement of virtual prototypes is needed to precisely predict the effects of modifications to engineering structures.

Depending on the structure size and form as well as the time and the experimenter’s financial constraints modal analysis is carried out either by 3D scanning laser vibrometers or three-axial accelerometers. The scanning vibrometers uses three laser beams to aim a dense grid of measurement points. The measurement is contactless and rapidly covers big surfaces. On the other hand the angles between the beams are important to the 3D measurement accuracy of the in-plane movement. This way the required broad corridor of undisturbed sight limits the use of 3D-vibrometers to open surfaces in automobile or aerospace industries [2]. Recently the use of infrared lasers in vibrometers extended their application towards civil structures [3]. Three-axial accelerometers are mostly used in experimental set-ups, where the structures are partially housed, have to be repeatedly measured from different sides or when simply cost constrains exclude the use of scanning vibrometers [4–6]. Moreover, some research works conclude to achieve better results with accelerometers [7]. On the other hand measuring with a few accelerometers requires much longer time if the number of points increases.

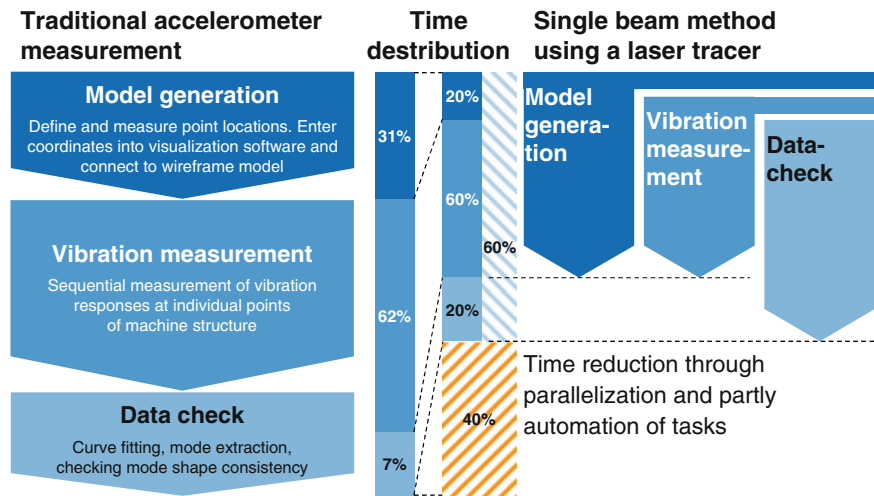
For research needs and in our industrial services the Laboratory of Machine Tools and Production Engineering conducts experimental modal analysis on machine tools and other production equipment. Particularly in case of investigation at chop floors the investigation subject is usually well housed corresponding to industrial security standards and there are very harsh time constrains, because the machine is unavailable for production during investigation time. Additionally, CAD-data is not provided to the investigator for secrecy reason, so the geometric model has to be measured on site.

---

C. Brecher • S. Bäumlér • A. Guralnik (✉)

Laboratory for Machine Tools and Production Engineering (WZL), RWTH Aachen University, Steinbachstr. 19, Aachen, 52074, Germany  
e-mail: [c.brecher@wzl.rwth-aachen.de](mailto:c.brecher@wzl.rwth-aachen.de); [s.baessler@wzl.rwth-aachen.de](mailto:s.baessler@wzl.rwth-aachen.de); [a.guralnik@wzl.rwth-aachen.de](mailto:a.guralnik@wzl.rwth-aachen.de)

**Fig. 42.1** Comparison of traditional accelerometer measurement and single beam method for modal analysis



For these reasons experimental modal analysis at machine tools is carried out using accelerometers. The testing consist of the three steps carried out on site as shown in Fig. 42.1 on the left hand side, geometric model generation, vibration measurement and data check [8], followed up by more profound analysis off site [5], where time is somewhat less crucial. The figure equally shows approximate time distribution. The geometric model generation amounts to approximately one third of the entire investigation time on site. The resulting model is used to visualize the measured structure and is usually very inaccurate in terms of geometric precision. Within vibration measurement, that accounts to two thirds of the time the most time consuming and error-prone activity is the reorientation of the accelerometers. This becomes clear in the vibration mode visualization, when single nodes seem to move in a whole different direction from the rest of the structure. The usual noise on the chop floor, which makes communication difficult and the big size of machine tools, which sometimes requires climbing on the structures, slow down the whole measurement procedure.

At IMAC XXX [8] we presented a new measurement method for modal testing based on a single laser beam device that allows three dimensional measurement. We subsequently developed the method along with the measurement equipment [6, 9]. This paper concentrates on strategy planning that allows to quickly measure all structural points of interest in terms of geometric location and vibration response. With this procedure we aim to reduce the measurement time by 40% as shown in Fig. 42.1. The time reduction is mainly due to parallelization of model generation and vibration measurement as well as partly automation of both tasks. In the end, we discuss reflector take-off limitation at high vibration levels.

## 42.2 Vibration Measurement Using the Single Beam Method

To reduce the line of sight problem the three dimensional vibration and geometry measurement can be conducted using a single laser beam and an optical target. The optical target is shown in Fig. 42.2b. This so called corner reflector reflects any incoming beam towards its source but with a lateral shift. The in-beam movement of the reflector can be measured with a laser interferometer, the lateral shift is measured with a position sensing device, a particular kind of a photodiode. Both devices are depicted in Fig. 42.2a. It can be shown mathematically that in beam and lateral movement do not have significant crosstalk and the reflector rotation does not influence any of those latter two [8].

The lasertracer as shown in the sketch set up in Fig. 42.2c is an interferometer mounted on two rotational axes. It comprises a two dimensional position sensing device that allow the device to sense lateral shifts of the laser beam and hence to track the target. The set up in Fig. 42.2 was designed for frequency response measurements of a machining center from different directions. The lasertracer is mounted on a platform and moved around the machine in the illustrated way. The necessary angle information needed for coordinate transformation is depicted directly from the tracer's rotary encoders. The graphs in Fig. 42.2d show the machine's vibration response in x-direction. Moving from  $0^\circ$  to  $90^\circ$  the measurement turn from purely position sensing device measurements through mixed forms to interferometric measurements. Interferometric measurements are of a much better quality, resulting in a higher coherence, but even the measurement at  $0^\circ$  shows all important resonances and seems to be suitable for the later curve fitting and mode extraction. Basically the graphs are conform to each-other. A profound analysis and detailed benchmark against traditional devices for vibration measurement, accelerometer, uniaxial laser vibrometer and inductive displacement sensor has been presented in [6].

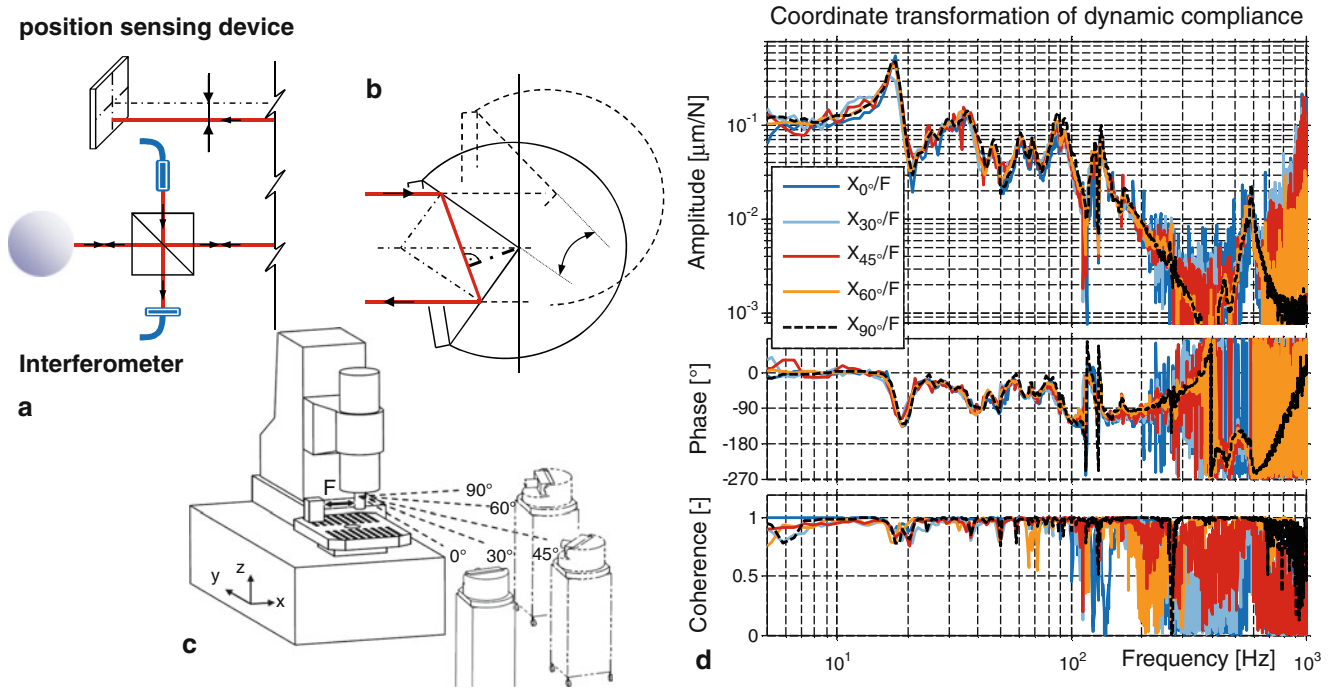


Fig. 42.2 Principles of the single beam vibration measurement using a lasertracer

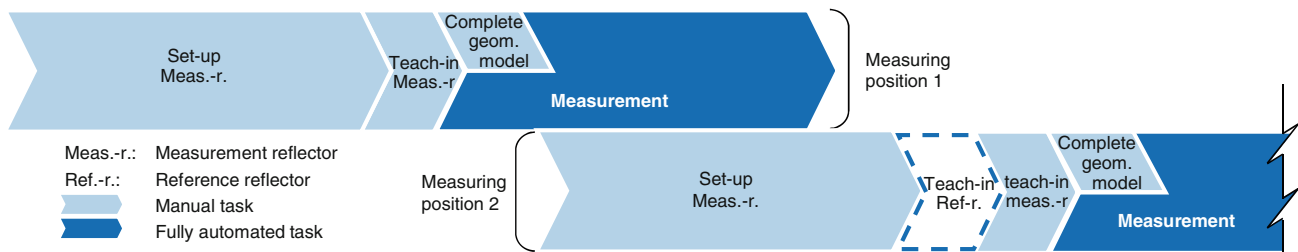


Fig. 42.3 General measurement proceeding for single-beam method modal testing of a machining center

### 42.3 Measurement Strategy Using a Lasertracer

The lasertracer can be controlled in its two axes using a simple joystick. As soon as a target is roughly aimed it can be centered automatically with the help of the tracer’s position sensing device. With the information of the two rotatory encoders and the absolute distance measurement unit the tracer measures the location of a reflector in space and automatically process its coordinates to the modal analysis program particularly to the user interface. The user does not enter coordinates but only connects the points to a wireframe.

Figure 42.3 shows the strategy to conduct a modal analysis for a partly housed machine tool. We use a set of reference reflectors and two sets of measuring reflectors. The reference reflectors are distributed around the machine on the chop floor walls or other structures at points that are visible from many different measurement positions of the tracer. The first set of measuring reflectors is attached to the machine structure within the view field of the tracer at its first measuring position. The position of every point is taught-in by the operator, who aims the reflectors with the joystick. The point coordinates are immediately available to the geometric model. During the tracer automatically measures vibrations of reflectors one by one, the operator completes the geometric model by connecting the points to a wire-frame. Still during the automatic measurement the second set of reflectors is attached to the machine within the view filed of the second measurement position of the tracer. One can discuss that working on the machine structure would influence measured frequency response functions. According to our expertise even a person standing on the machine bed does not measurably influence dynamic properties of a medium sized machine tool.

After displacing the lasertracer to a new position reference reflectors are taught in first to determine the tracer's new position and orientation relatively to previous measurement positions. Than a coordinate transformation can be carried out, so all measurements – geometric and vibration – use a common global coordinate system. The automated measurement cycle restarts as described before.

#### 42.4 Example of Measurement Strategy for a Demonstrator Machining Center

To demonstrate the approach of modal testing using the single beam method we build a showroom consisting of a modified lasertracer and a miniaturized machine tool. The CAD-model is presented in Fig. 42.4. The demonstrator was designed as a medium sized machining center scaled down by 1:3. The resulting height of the demonstrator is of approximately 800 mm corresponding to real size heights of 2,400 mm. The crucial point of the single beam method measurement is the line of sight, so the model housing has been designed to meet requirements of a demonstrator as well as to correspond to real machine tool housing. For this machine tool four measurement positions and four reference reflectors are a sufficient set up for the entire modal test.

Reference reflectors are placed in a way that they are visible from at least three measurement positions. This requirement can be met pretty easily, too. The analysis of the geometric evaluation would show pretty good conditions for coordinate transformation. The measurement beams from each of the measurement positions towards the reference reflectors are far from being parallel and the measurement positions are clearly out of plane defined by three reference reflectors.

Machine tools usually have one or two windows faced to the operator. The windows are mounted on doors that are used for manual tool changes or any other kind of manual involvement of the operator. A view through such a slid open door is shown in Fig. 42.4a. From here a big part of the machine's side can be covered. The other side of the machine is covered from the opposite side. In absence of a door on the opposite side the housing may be easily removed, if measurements through open doors do not to cover enough measurement points. There is usually a large door in a machine tool that is used for loading and unloading work pieces. A look through this door is shown in Fig. 42.4c. From here a large part of the machine including parts of the rear bed can be measured. Finally many machines have doors on the back side which are used for maintenance but can be opened for modal analysis as well. From this view the whole back side auf the machine including the bed can be measured (Fig. 42.4d).

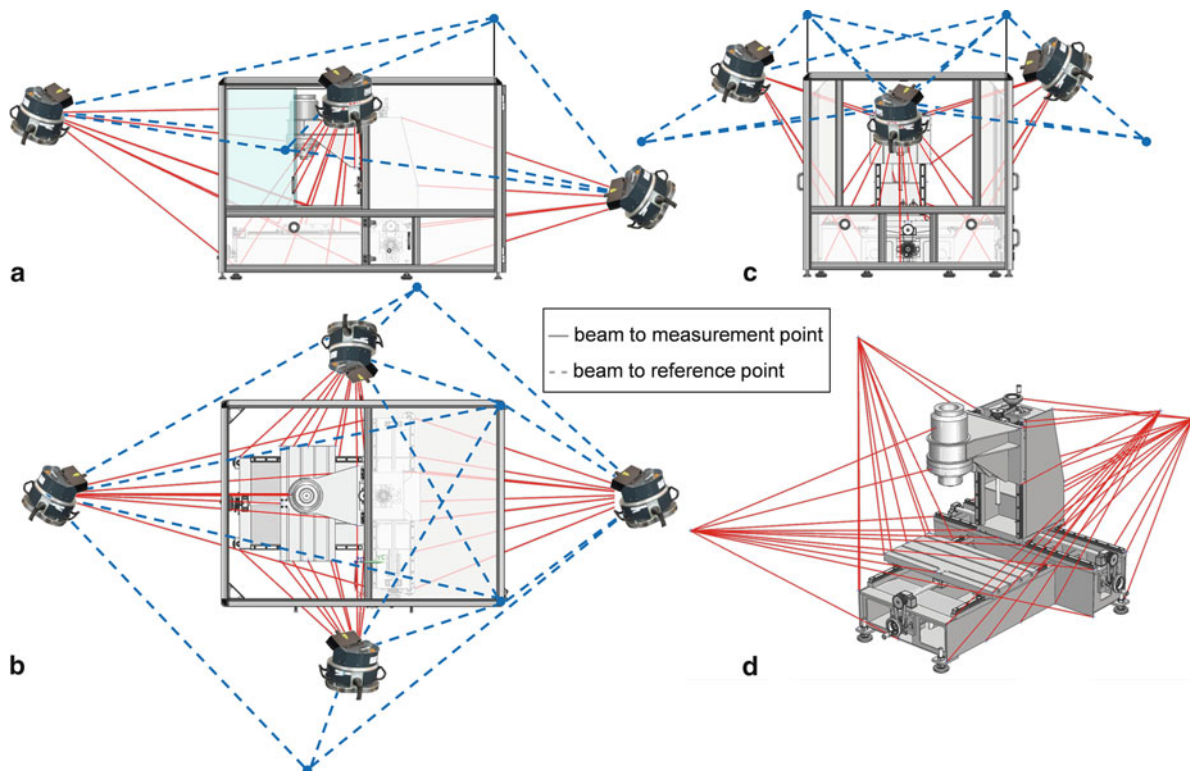


Fig. 42.4 Strategy planning for the single beam method modal testing of the demonstrator machine tool



## 42.5 Consideration on Mounting Stability

There is an important limitation to the maximum measurable displacement. At a critical acceleration the target mass cannot be held by the magnet anymore and the reflector starts taking-off of the nest. This maximum acceleration is mainly determined by the mass of the reflector and the magnet force and can be calculated analytically. Therefore we measured reflector masses and the peak force when manually pulling the reflector out of the nest. Figure 42.5a shows analytical calculations and the measured take-off amplitude over frequency.

The corresponding experimental set up is shown in Fig. 42.5b. A high voltage piezo stack actuator of big length is mounted into a membrane guide device. This device guaranties a linear movement. The vibration is measured using a laser vibrometer. At distinct frequencies one slowly changes the amplitude and observes target vibrations. The displacement time signal reveals a strong non-sinusoidal shape, once the target starts taking-off of the nest. The time-frequency waterfall plot shows a continuous raise of the displacement amplitude. When the take-off amplitude is reached the main amplitude line breaks down first and starts growing from a lower level. Noticeably, the second harmonic jumps up exactly in the point of take-off. We drew hence the main amplitude line against second harmonic and got a very sharp indicator of the take-off amplitude.

The distinct points of the experimental graph in Fig. 42.5b have been taken from these ‘main frequency – second harmonic’ – plots. The experimental results show a very good correlation to the calculated data. The somewhat lower amplitudes in experimental plots might be explicable by imperfect forms and reflector body compliance that might act as a spring.

Concerning the quantitative evaluation of measured amplitudes, according to our expertise vibration levels of machine tools in modal testing remain at least a factor of 10 under the measured values for the 1.5" reflector. Though reflector take-off is not a limiting issue in modal testing of machine tools, it might need to be taken into account in other applications.

## 42.6 Conclusion

This paper deals with the single beam 3D-vibration measurement method for modal testing of machine tools. We explained the principle of 3D simultaneous vibration measurement with one single laser beam. Some measurement results of a machine tool are shown along with coordinate transformation of dynamic compliancy measurements. The measurement strategy is described generally first and then applied to plan the measurement of a demonstrator machine. It is shown that only four different measurement positions and only four reference points are sufficient for the entire modal analysis. Considering measurement uncertainties and limitations the problem of reflector take-off of the nest at higher accelerations has been addressed. Analytical calculations and experimental results of the take-off amplitudes correspond well with amplitudes being

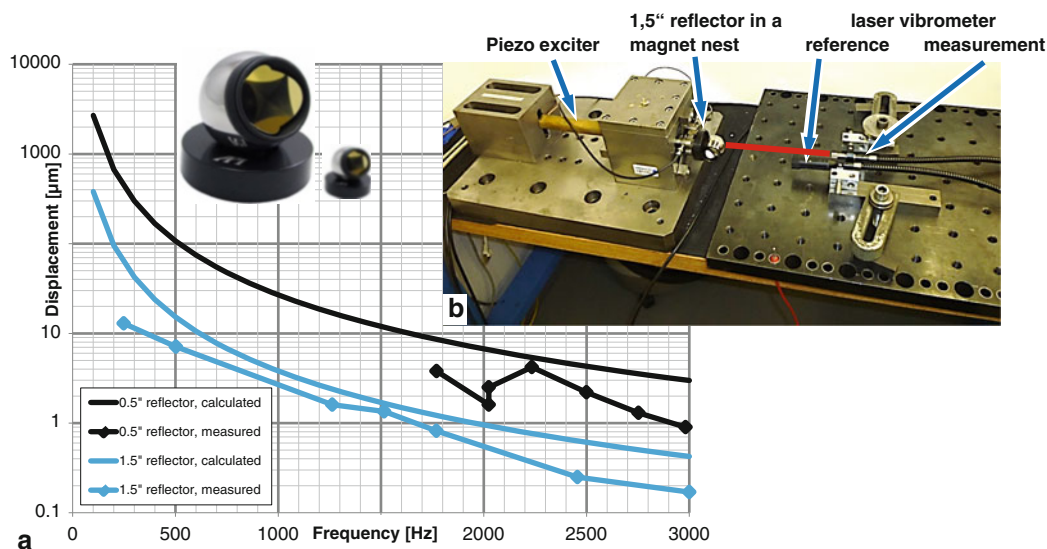


Fig. 42.5 Take-off frequency-displacement plot and experimental set-up

much higher than any that are reached during modal testing of machine tools. Though the take-off phenomenon might have to be considered in different applications. In our following research works we aim to apply our developed method to different machine tool and to compare performance to traditional accelerometer measurements.

**Acknowledgements** This research work is carried out in the project 'DynaTrac' funded by the German Federal Ministry of Education and Research (BMBF) within the Framework Concept 'Research for Tomorrow's Production' and managed by the Project Management Agency Forschungszentrum Karlsruhe, Production and Manufacturing Technologies Division (PTKA-PFT). The authors highly appreciate the support by our project partners Heiko Paluszek and Daniel Berk from sigma3D GmbH and Heinrich I. Schwenke and Mark Wissmann from ETALON AG.

## References

1. Ewins DJ (2000) Modal resting, theory, practice and application. Research Studies, Baldock
2. Oliver DE (2009) Tutorial: 3D scanning vibrometry for structural dynamics measurements. In: Presentation at the IMAC-XXVII: conference and exposition on structural dynamics, Orlando, 9-12 Feb. [http://www.sem.org/PDF/Oliver\\_3D%20Scanning%20Vibrometry.pdf](http://www.sem.org/PDF/Oliver_3D%20Scanning%20Vibrometry.pdf). Accessed 20 Apr 2011
3. Dräbenstedt A, Sauer J, Rembe C (2012) Remote-sensing vibrometry at 1550 nm wavelength. In: 10th international conference on vibration measurements by laser and noncontact techniques – AIVELA, AIP conference proceedings, vol 1457, Ancona, Italy, pp 113–121
4. Brecher C, Manoharan D, Ladra U, Köpken HG (2010) Chatter suppression with an active workpiece holder. *Prod Eng Res Dev* 4:239–245
5. Brecher C, Weck M (2006) *Werkzeugmaschinen, Vol 5. Messtechnische Untersuchung und Beurteilung, dynamische Stabilität*. Springer, Berlin
6. Brecher C, Guralnik A, Bäuml S (2012) Measurement of structure dynamics using a tracking-interferometer. *Prod Eng Res Dev* 6(1):89–96
7. Pingle P, Sailhamer J, Avitabile P (2009) Comparison of 3D laser vibrometer and accelerometer frequency measurements. Presentation at the IMAC-XXVII: conference and exposition on structural dynamics, Orlando, 9–12 Feb
8. Brecher C, Bäuml S, Wissmann M, Guralnik A (2012) Modal testing using tracking-interferometers. In: Allemang R, De Clerck J, Niezrecki C, Blough JR (eds) *Proceedings of the SEM IMAC XXX conference*, vol 6, Jacksonville, pp 311-320
9. Brecher C, Guralnik A, Bäuml S (2012) Simultaneous 3D-vibration measurement using a single laser beam device. In: 10th international conference on vibration measurements by laser and noncontact techniques – AIVELA, AIP conference proceedings, vol 1457, Ancona, Italy, pp 105–112

# Chapter 43

## Valvetrain Motion Measurements in Firing Conditions by Laser Doppler Vibrometer

P. Castellini, P. Chiariotti, M. Martarelli, and E.P. Tomasini

**Abstract** A methodology for the measurement of the valve kinematics in a high performance IC engine in firing condition is described in this paper. The method is based on the use of an In-plane Laser Doppler Vibrometer pointing on the valve stem through a transparent window on the engine inlet duct. The main advantages and drawbacks of the technique are discussed through the paper as well as guidelines for proper test settings. Results obtained are illustrated, they highlighting the potentials of the proposed technique to monitor valvetrain motion in operating conditions.

**Keywords** Valvetrain kinematic • Laser Doppler Vibrometer • Engine testing • Desmodromic distribution • Non-contact measurements

### 43.1 Introduction

The internal combustion engine (IC) is still evolving despite the strong impact alternative solutions like electric motor have been having during the last decades.

The development trend is concentrated on downsizing, where the reduction of engine displacement corresponds to a significant increase in efficiency and power obtained with a more extreme setting.

The motorsport world (especially the one of motorcycles) goes to the same direction, even though oriented to tire management and motricity. However, drivability of such “extreme” motors can be an issue, which designers try to solve with a smarter management of engine parameters.

Within those strategies, valvetrain management represents a valid option for engine optimization, and great attention has been put in finding a valid methodology for an accurate measurement of valvetrain kinematics. Keeres et al. [1] presented an overview about the most common measurement techniques used to fulfill that task. The most traditional approaches based on accelerometers and LVDTs, widely described in [2], have been substituted since the 1980s with the emerging technology of Laser Doppler Vibrometry (LDV).

Single-point and differential LDV were used in motored cylinder heads [3, 4] to support the motor development. Some commercial products were also almost specifically developed for the application on valvetrain [5, 6]. It should be reminded in fact that “common” LDV are usually limited to a maximum measurable speed of 10 m/s (even much less for digitally decoded systems), and this is frequently not enough in high performances engine.

Performances of LDVs when exploited to assess the valve kinematics were also analyzed in a recent paper [7], where specific signal processing techniques for the detection of drop-outs on the vibrometer signal were also presented.

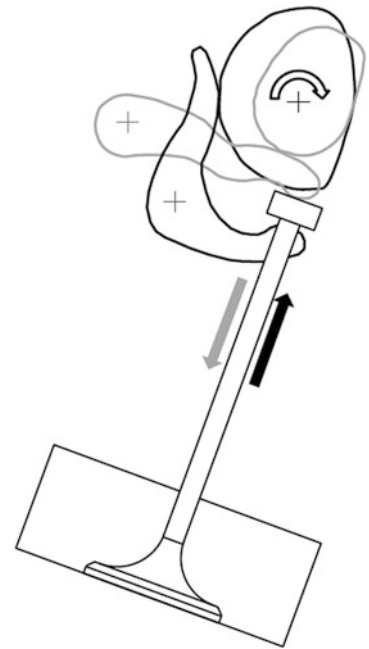
It should be remarked, however, that the air flow inside the cylinder influences the overall behavior of the engine itself. Some experiments have been done in the past for obtaining a more realistic analysis of the complete engine, like for instance

---

P. Castellini (✉) • P. Chiariotti • E.P. Tomasini  
Università Politecnica delle Marche, Via Brecce Bianche, Ancona 60131, Italy  
e-mail: [p.castellini@univpm.it](mailto:p.castellini@univpm.it); [p.chiariotti@univpm.it](mailto:p.chiariotti@univpm.it); [ep.tomasini@univpm.it](mailto:ep.tomasini@univpm.it)

M. Martarelli  
Università degli Studi e-Campus, Via Isimbardi, Novedrate (CO), Italy  
e-mail: [milena.martarelli@unicampus.it](mailto:milena.martarelli@unicampus.it)

**Fig. 43.1** Desmodromic distribution configuration



blowing up the air in order to reproduce the cylinder flow and simultaneously measuring the fluid velocity field by Laser Doppler Anemometry [8, 9].

In any case, these approaches cannot substitute the analysis in real fired conditions, since gas exchanges, thermal effects and firing vibrations of the engine cannot be simulated accurately.

Whenever the final goal is the fine adjustment of the engine, these parameters cannot be neglected, because very often they influences the overall behavior more than the difference between the desired and actual valve opening/closing operations.

This paper describes a measurement procedure to measure the valvetrain kinematics of a high performances and high revolution engine in firing conditions. Tests were conducted on a Ducati Testastretta engine (revolution regime up to 13,000 rpm), featured by a desmodromic transmission. Desmodromic systems (Fig. 43.1) are characterized by a couple of cams, the first (represented in gray in Fig. 43.1) managing the valve opening, the second (black) driving the valve closing. That solution substitutes the elastic (or pneumatic) system used in conventional set-ups allowing both quite high revs and full control of valve timing. On the other hand, desmodromic is a “non-elastic” system, in which actual valve motion and vibrations are determined by backlash and actual rigidity of the cam-leverage system. Transitions between opening and closing, i.e. between the contact with the first and the second cam, can also be critical, determining a jump of the valve.

## 43.2 Experimental Set-Up

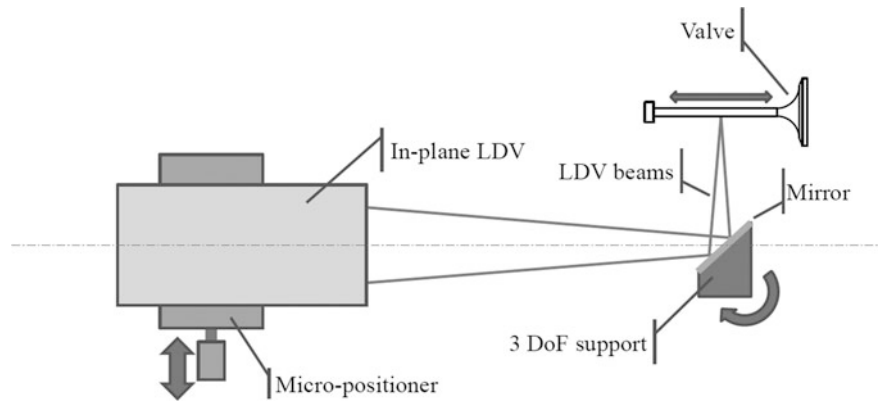
### 43.2.1 Test Bench

The tests were performed on an engine test stand, commonly used to develop, characterize and test engines. The facility allows a full control of the engine for operation at different regimes and conditions: several physical variables of the engine are monitored by a set of sensors and data acquisition systems, moreover dedicated actuators control the engine state.

The sensors measure several physical variables of interest:

- Crankshaft torque and angular velocity;
- Intake air and fuel consumption rates;
- Atmospheric conditions (temperature, pressure, humidity . . . );
- Air-fuel ratio for the intake mixture, detected using an exhaust gas oxygen sensor;
- Environment pollutant concentrations in the exhaust gas, such as carbon monoxide, different configurations of hydrocarbons and nitrogen oxides, sulfur dioxide, and particulate matter;
- Temperatures and gas pressures.

**Fig. 43.2** Test set-up for valve kinematics measurement



### 43.2.2 Valvetrain Kinematics Measurement Method

The valvetrain kinematics measurement procedure described in the paper is based on the use of an In-Plane Laser Doppler Vibrometer (model LSV-060-F/OFV-3300 Polytec [10]). This type of sensor presents some interesting features suitable for the specific application:

1. Very large velocity range ( $-70 \div 100$  m/s);
2. High frequency range ( $0.5 \div 10$  kHz);
3. Possibility of measuring surface velocity in the orthogonal direction to the optical axis of the vibrometer (it requiring lateral optical access);
4. Accuracy of 0.5 % of reading.

The valve motion was observed focusing the laser beams on the valve stem from the side. The vibrometer head was placed on a micrometric stage that allows precise movement (in order to guarantee a fine positioning of the LDV), while the laser beams were folded by a highly reflecting mirror, installed on a three degree-of-freedom micrometric support as sketched in Fig. 43.2.

The powerfulness of performing such measurement with an in-plane vibrometer is linked to the optical non-contact nature of the vibrometer itself. However, for obtaining high quality measurement data, several experimental aspects must be carefully considered:

1. Optical behavior of the valve stem surface;
 

In LDVs the optical behavior of the surface on which the laser beams (or beam) operate is of crucial importance in order to guarantee a correct measurement of the velocity. The most cooperative surface should diffuse light, scattering it back to the interferometer.

The surface of the valve stem cannot in general be treated using retro-reflecting tapes or paintings, because of the operating temperature of the engine. In the presented experiment, stem surface were not treated because their finishing guaranteed a good scattering.
2. Optical window:
 

An optical access must be drilled in the engine head in order to allow the laser beams to reach the valve stem. The hole should be large enough to avoid interference phenomena between the engine and the two laser beams; however it should not be too large, that in order to exclude significant changes to the fluids circuits (cooling, lubricant, inlet air) which could modify the correct behavior of the engine.

That holding, a small pipe equipped with an optical window (showing good transparency and very high flatness) was inserted for both sealing the circuits (mainly the cooling one) and avoiding connection between the external environment and the engine inlet through the optical access.
3. Laser-valve alignment:
 

Any LDVs measure only the component of the velocity in its direction of sensitivity, and therefore valve axis and vibrometer axis must be accurately aligned in terms of directions. Moreover, in-plane systems have a very small depth-of-field. Valve surface position must be located with respect the measuring volume with an error lower than 0.1 mm.
4. Engine head motion/vibration:
 

The LDV measures the valve velocity with respect to the laser head: this includes not only the motion of the valve with respect to the engine head, but also engine head movement itself. In order to quantify this last contribution and,

eventually, compensate it, an additional sensor must be installed. This sensor should be able to measure the motion in the same direction of sensitivity and measure in the same coordinate system of the LDV. The easiest solution consists in placing an accelerometer on the engine carter.

#### 5. LDV head vibration:

Since LDVs measure the relative motion between the laser head and the target, it is necessary the former to be installed in a stationary reference system, that in order to isolate the target motion. That results in the necessity of either monitoring the vibration of the base where vibrometer is placed, or insulating the LDV from the base itself, in order to avoid:

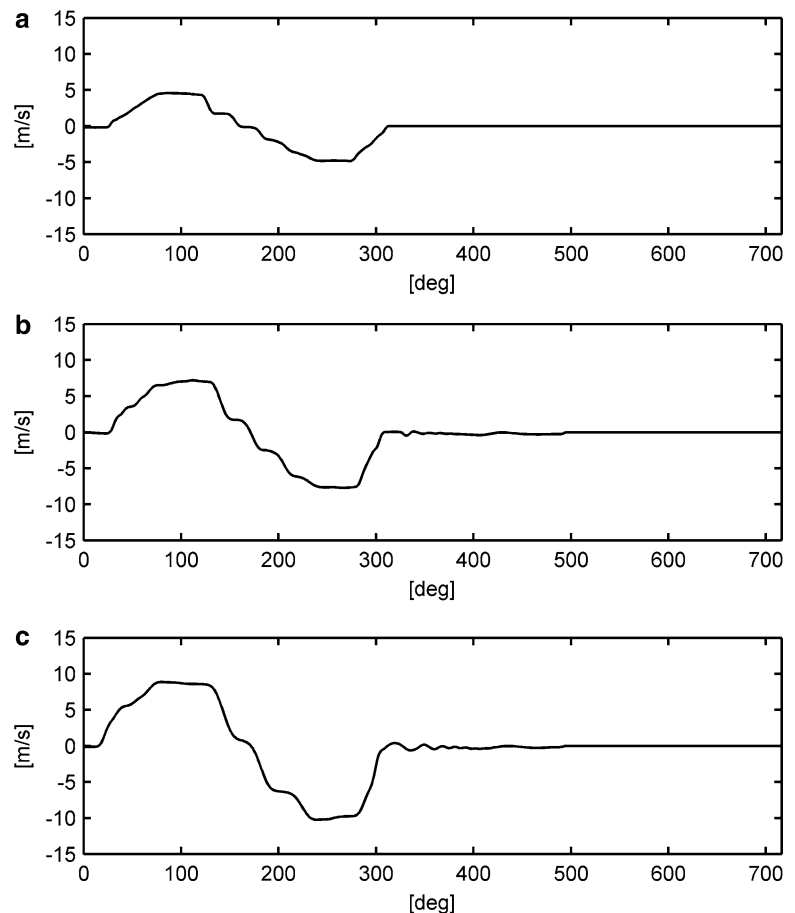
- The measured signal be a vector combination of vibrometer and target velocities along the sensitivity direction of the LDV;
- Transversal motions of the laser beam which can induce inaccuracy in laser positioning, drop-outs due to speckle motions, modulation phenomena due to motions superposition [11], change of beam focus due to change of the measurement distance;
- Rotation of the laser head which produces large displacements of the laser spot.

### 43.3 Results

The signal recorded by the in-plane vibrometer was averaged over several revolutions, in order to lower the spoiling effect of noise, since the engine speed could be considered stationary. A total amount of 320 averages was performed for each velocity regime, it ranging from 4,900 to 13,000 rpm.

More generally it should be said that the velocity signal of the valve can be processed both in time and in angle domain, using the shaft position to resample the acquired time domain signal: angle domain is generally preferred when dealing with engine data.

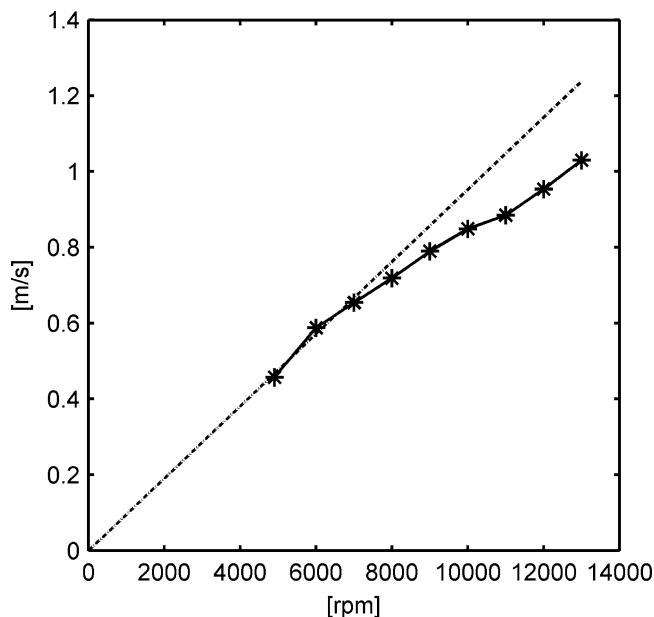
Figure 43.3 shows the valve velocity evolution in the angle domain for three different engine regimes (6,000, 9,000, 12,000 rpm). The maximum velocity, as expected, changes significantly at different rpms. The general trend, e.g. the



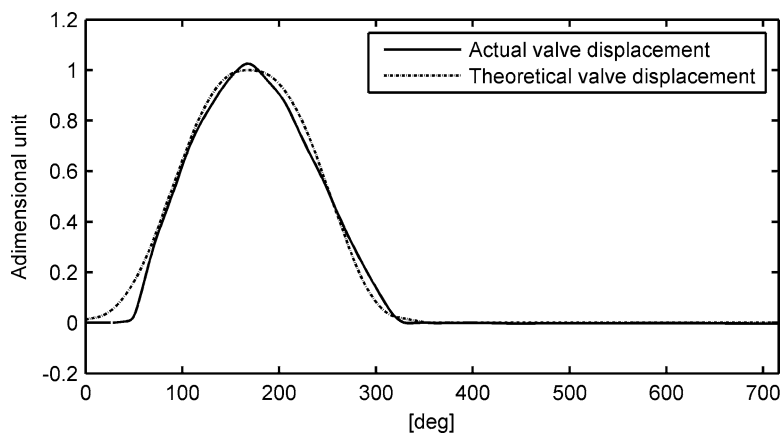
**Fig. 43.3** Velocity time history (average) at different engine rpm: (a) 6,000 rpm, (b) 9,000 rpm, (c) 12,000 rpm



**Fig. 43.4** Maximum velocity at different engine rpm



**Fig. 43.5** Valve aperture obtained by integration @6,000 rpm



typical trapezoidal shape of valvetrain in desmodromic engines, remains the same despite the increase in rpm. Small scale oscillations induced by valve vibrations and backlash between the two cams are also visible at higher regimes.

Figure 43.4 reports the comparison of the maximum valve linear velocity with respect to the engine regime. The velocity increases as the rpm does: however, it can be noticed that the trend is not linear like would happen in case of constant valve aperture. This is an expectable behavior considering the limits in stiffness of the valvetrain in desmo engines. When the regime increases the valve should accelerate more and more in order to guarantee the desired aperture in a shorter time cycle. Increased acceleration needs increased force from the cam, but the actual stiffness of the mechanism does not allow the reaching of the expected kinematic values.

It is also interesting to integrate the velocity signal in order to obtain the valve aperture versus the shaft angle. An example of aperture profile is given for the engine working at 6,000 rpm in Fig. 43.5, where the actual valve displacement and the theoretical one are compared. A good matching between the two curves is clearly visible, that further proving the In-plane LDV can successfully measure the valvetrain kinematics also when the engine is in firing conditions.

## 43.4 Conclusions

A measurement procedure for the assessment of the valve velocity of an engine in firing conditions has been described in this paper. The procedure is based on the use of a non-contact optical sensor, the in-plane Laser Doppler Vibrometer, which is sensitive to the vibration velocity orthogonal to the optical axis of the vibrometer itself. The exploitability and potentials

of the In-plane LDV with respect to standard transducers (accelerometers, LVDTs . . . ) has been discussed. The In-plane vibrometer needs to be used with particular care in order to get consistent results: it is always mandatory to consider all the issue linked to the optical nature of the sensor, as the need either for an optical access or a good surface scattering. Relative motions between the target and the laser head should also be considered in order to be able to separate pseudo-vibrations (e.g. vibrations which are due to laser head than to the target) from real motions of the target.

The technique was successfully use exploited on a Ducati Testastretta engine in firing conditions. Results presented in the paper proved the In-plane LDV can be an extremely powerful sensor for monitoring the actual kinematics of valvetrain on engine in extreme working conditions (e.g. firing and high revs).

**Acknowledgements** The authors want to acknowledge Dr. Andrea Sassaroli from Ducati Motor Holding for the interesting technical discussions about Testastretta engine and Desmodromic distribution.

## References

1. Kerres R, Schwarz D, Bach M, Fuoss K et al (2012) Overview of measurement technology for valve lift and rotation on motored and fired engines. *SAE Int J Engines* 5(2):197–206. doi:[10.4271/2012-01-0159](https://doi.org/10.4271/2012-01-0159)
2. Norton RL (2002) *Cam design and manufacturing handbook*. Industrial Press, New York
3. Paone N, Santolini C, Tomasini EP (1994) Application of a laser Doppler vibrometer to evaluate engine poppet valve kinematics, XII IMAC, Hawaii, Proceedings of the IMAC XII conference, Honolulu, USA
4. Carlini A, Rivola A, Dalpiaz G, Maggiore A (2002) Valve motion measurements on motorbike cylinder heads using high-speed laser vibrometer. In: Proceedings of SPIE. Fifth international conference on vibration measurements by laser techniques: advances and applications. Ancona, Italy, vol 4827, pp 564–574
5. Polytec Gmbh, Application Note VIB-C-03. Waldbronn, Germany
6. Kerres R. Measuring with lasers: optimizing valvetrain dynamics at Porsche Engineering, InFocus 2/2011, Polytec Gmbh. Waldbronn, Germany
7. Hosek P. Algorithm for signal drop-out recognition in IC engine valve kinematics signal measured by laser Doppler vibrometer, *J Optics Laser Technol*. doi:[10.1016/j.optlastec.2011.09.034](https://doi.org/10.1016/j.optlastec.2011.09.034)
8. Paone N, Santolini C, Tomasini EP (1994) Simultaneous measurement of inlet flow and valve motion in internal combustion engines by laser Doppler techniques. In: 7th international symposium an applications of laser techniques to fluid mechanics, Lisbon
9. Gasparetti M, Paone N, Tomasini EP (1996) Laser Doppler techniques for the combined measurement of inlet flow and valve motion in IC engines. *Meas Sci Technol* 7:576–591
10. Polytec Gmbh, OFV-3300/LSV-060 user's guide. Waldbronn, Germany
11. Revel GM, Castellini P, Chiariotti P, Tomasini EP, Cenedese F, Perazzolo A (2011) Laser vibrometry vibration measurements on vehicle cabins in running conditions: helicopter mock-up application. *Optical Eng* 50:101502

# Chapter 44

## Using High-Speed Stereophotogrammetry to Collect Operating Data on a Robinson R44 Helicopter

Troy Lundstrom, Javad Baqersad, and Christopher Niezrecki

**Abstract** Stereophotogrammetry in conjunction with three-dimensional point tracking (3DPT) algorithms has proven to be a highly robust measurement technique when used to perform dynamic measurements on small, rotating systems. This measurement technique can be scaled up to much larger systems and has several desirable features for helicopter and wind turbine measurement applications that include: (1) it is non-contact and doesn't require the use of roll rings or slip rings for signal transmission, (2) the applied measurement targets have a negligible effect on the aerodynamics, mass or stiffness of the structure, and (3) position data can be readily collected on many hundreds of points over what is capable using conventional multi-channel data acquisition systems and transducers. A field test was conducted in which operating data was collected on the main rotor of a Robinson R44 helicopter in both grounded and hovering operating conditions. The first part of this work describes the experimental setup and data acquisition process of the test performed and the second part of this work presents some of the results including blade dynamics and extracted operating deflection shape information for a Robinson R44 Helicopter.

**Keywords** Stereophotogrammetry • Operational modal analysis • Helicopter rotor dynamics • Rigid body correction • Harmonic content

### 44.1 Introduction

As a non-contacting measurement technique, stereophotogrammetry lends itself to the measurement of the operational dynamics of large, rotating systems because it avoids the cabling difficulties of wired transducers and can be easily scaled up to larger systems by increasing the size of the targets applied to the surfaces of the structure. Stereophotogrammetry also offers the ability to collect dynamic measurements in 3D on many more points on a structure, more easily, than compared to a typical multi-channel transducer data acquisition (DAQ) system.

The primary challenge when making photogrammetry measurements of rotating structures involves the large angular rotations that result when a turbine or rotor is spinning. To appropriately extract the small vibratory structural motion from the large rigid body movements and interpret the effects of the harmonics is not trivial. Helfrick et al. [1] proposed a method to use low speed cameras for measuring vibrations in rotating structures. High-speed cameras were used by Warren et al. [2, 3] to measure vibrations in a small scale rotating wind turbine but only a few operating deflection shapes could be determined. Lundstrom et al. [4] showed that appropriate rigid body correction (RBC) for a rotating structure, a sufficient number of points that are stationary with respect to each other needs to be used. In another work by Lundstrom et al. [5], operating deflection shapes of a wind turbine-like structure were extracted by applying RBC using the nodes of the non-rotating mode shapes in conjunction with a harmonic filter to the 3DPT measured data. A robust method for point tracking in rotating structures is suggested by Kaploe et al. [6].

One of the first works to use stereophotogrammetry for large wind turbines was performed by Paulsen et al. [7, 8]. The stereophotogrammetric measurement technique has been used to collect dynamic operating data on large wind turbines

---

T. Lundstrom • J. Baqersad • C. Niezrecki (✉)

Structural Dynamics and Acoustic Systems Laboratory, Department of Mechanical Engineering, University of Massachusetts Lowell, One University Ave, Lowell, MA 01854, USA  
e-mail: [troy.lundstrom@gmail.com](mailto:troy.lundstrom@gmail.com); [javad\\_baqersad@student.uml.edu](mailto:javad_baqersad@student.uml.edu); [Christopher.Niezrecki@uml.edu](mailto:Christopher.Niezrecki@uml.edu)

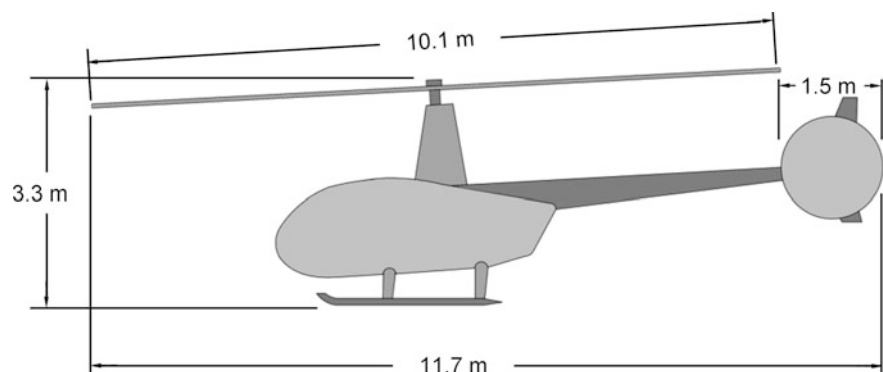
including the measurement of the dynamic behavior of a 500 kW wind turbine during an emergency stop from 24 to 0 rpm. Following their work, Ozbek et al. [9–12] measured the displacement of retro-reflective optical targets on a 2.5 MW Nordex N80 wind turbine with an 80-m tower height and rotor diameter. Within their work the researchers describe the efforts to sufficiently illuminate this large structure and collect stereophotogrammetric operating data. The structure was illuminated with high-power light emitting diode (LED) strobe lights synchronized with the camera pair by a central computer. The papers also describe the domination of harmonic components in the measured dynamics hindering modal parameter estimation from power spectra.

3DPT has also been used for measurement of vibrations in helicopter rotors. Lawson [13] measured the vibrations of a small-scale flexible, rotating, blade assembly for helicopters. Several experiments have been performed in which stereophotogrammetry was applied to the dynamic measurement of helicopter rotors. In 2001, a wind tunnel test was performed in the Large Low-Speed Facility of the Dutch-German wind tunnel on a 4 m, four-bladed rotor system; the stereophotogrammetry system utilized four cameras. Flapwise, edgewise and torsional data was collected on all four blades of the rotor [14–16]. The work also describes efforts to properly determine the rotor center of rotation and transformation of the coordinate system from the wind tunnel coordinate system to a more convenient rotor coordinate system. Following the German-Dutch wind tunnel measurement, another full-scale test on a helicopter was performed by NASA at the National Full-Scale Aerodynamic Complex (NFAC) at NASA Ames Research Center in Moffet Field, California [17]. Their paper describes the procedure and results for the second of three stereophotogrammetry tests on a UH-60A four-bladed rotor system. The use of retro-reflective targets on the “instrumentation pod” located above the rotor hub simplified their rigid body correction and mode extraction. The researchers could extract five operating shapes of blades in that test. The full-scale stereophotogrammetric helicopter test presented in this work was performed in the field (outside) with sunlight as the primary source of illumination. In addition, only a single pair of high-speed cameras was used in the data acquisition and the blades of the main rotor were realistically loaded as the helicopter hovered. A more detailed discussion of the test setup and the results can be found in [18].

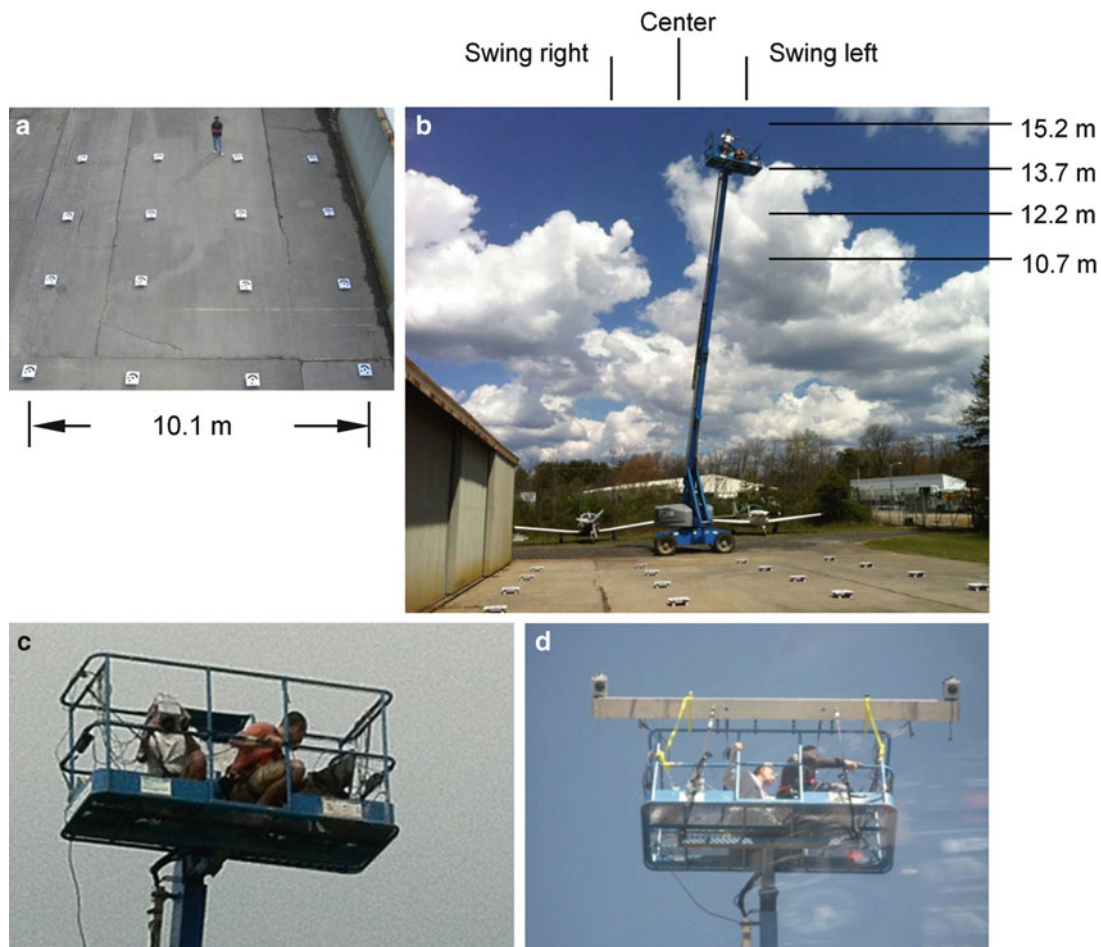
## 44.2 Experimental Setup and Procedure

The full-scale test article was a Robinson R44 helicopter with a 10.1-m diameter main rotor. According to the R44 pilot’s operating handbook [19], the main rotor tip speed is 215 m/s at 102% of the operating rate. With a main rotor circumference of 31.7 m, the rotational frequency of the main rotor is 6.8 Hz. Optical data was to be acquired with a pair of Photron SA2 FASTCAM high-speed cameras controlled by a portable laptop workstation. This frequency rate raised several concerns regarding performing the full-scale field test using only natural sunlight. Several pretests were performed with a model helicopter to insure the adequacy of natural sunlight to properly illuminate the structure and to determine a proper shutter time to minimize blurring at the rotor extents. A shutter time of 1/8,000 s was selected for the full-scale helicopter test. The Robinson R44 Raven helicopter used in this experiment can be seen in Fig. 44.1.

Several pieces of custom equipment were developed for this test including a 3.7-m camera bar, a series of 7.4E-2-m diameter vinyl targets to temporarily adhere to the helicopter blades to track the motion of the blades and a series of coded targets to perform a large-scale calibration prior to data acquisition. Images of the large-scale calibration can be seen in Fig. 44.2.

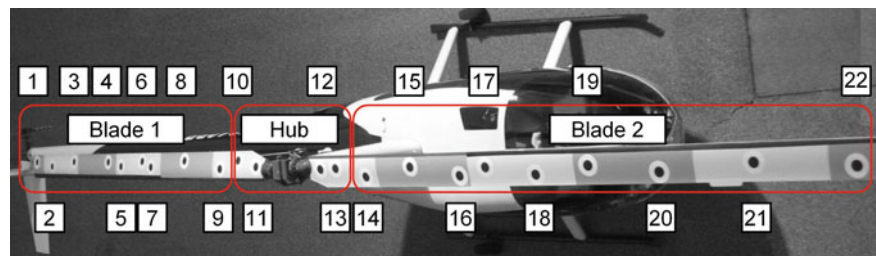


**Fig. 44.1** A schematic of Robinson R44 Raven helicopter with dimensions obtained from the Raven pilot’s operating handbook [19]



**Fig. 44.2** Large-scale calibration procedure for full-scale helicopter test showing (a) coded target array with Javad Baqersad shown as a scale reference; (b) positions for the boom lift platform for calibration; (c) calibration picture acquisition from the platform (T. Lundstrom and C. Niezrecki); (d) camera bar and high-speed cameras mounted to boom lift

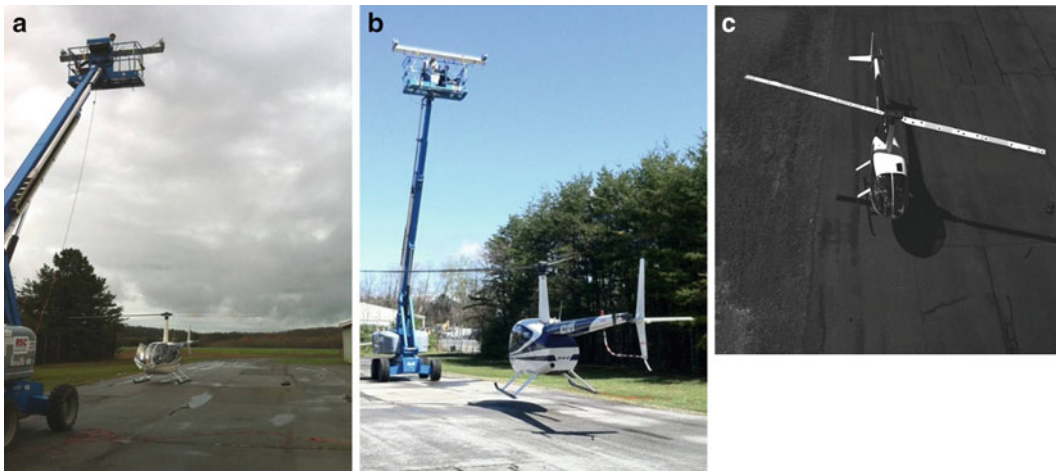
**Fig. 44.3** Rotor measurement point labels and measurement point subset labels



The large-scale calibration shown in Fig. 44.2 was performed with a Genie S60 boom lift. The 16 coded targets were mounted to the tarmac in a square,  $4 \times 4$  array with 10.1-m sides as shown in Fig. 44.2a and a series of pictures were taken with the high-speed cameras at different elevations and orientations as shown in Fig. 44.2b, c. Measurements were taken between several targets to scale the calibration. A detailed description of the calibration procedure can be found in [18].

A series of 22 uncoded vinyl targets were mounted to the top surface of the helicopter main rotor in the configuration shown in Fig. 44.3. The targets were evenly distributed across the blades to see both flexing and twisting operating deflection shapes (ODS). Figure 44.3 also shows the subsets of uncoded targets (blade 1, hub, blade 2) used to examine the rotor dynamics with and without rigid body correction (RBC). Subsequent rigid body corrections performed on this data utilized the “hub” measurement points to track/remove rotor rigid body motion. ODSs were determined without the application of RBC.





**Fig. 44.4** Operational data acquisition with (a) the helicopter on the ground; (b) the helicopter hovering (picture taken in front of boom lift); (c) the helicopter hovering (picture taken from above main rotor)

Five operational data sets were collected for the main rotor of the Robinson R44 helicopter. Two data sets were collected with the helicopter grounded at 50% (3.4 Hz idle rotation rate) and 102% (6.9 Hz operating rotation rate) operating speeds. A pair of high-speed cameras was lifted diagonally above the main rotor of the helicopter with the boom lift to achieve a working distance of approximately 12 m. The height of the cameras above the ground was approximately 14 m. Data was acquired for both operating frequencies with a camera sample rate of 250 frames per second (fps), with a 1/8,000 s shutter time, but only the 6.9 Hz data set will be discussed in this paper.

Three additional data sets were collected above and below the helicopter with the helicopter hovering above the ground. Two data sets were acquired from above the main rotor and a final data set was acquired below the helicopter, unfortunately, the high-speed cameras lost calibration during the acquisition of the fifth data set; the fifth data set will not be discussed in this paper. The data acquisition for the grounded and hover data sets can be seen in Fig. 44.4.

### 44.3 Initial Data Processing

Only three data sets {full-speed grounded, hover 1 ( $f_s = 1,080$  fps) and hover 2 ( $f_s = 250$  fps)}, will be presented in this work as the quality of these data surpassed that of the other two data sets. The description of the initial processing procedure follows.

The series of photo pairs for the three data sets were imported into PONTOS<sup>TM</sup> [20] with the calibration file and appropriate settings for the ellipse quality, ellipse radius and maximum allowable intersection error to allow the software find all 22 measurement points in all data stages. The values for these parameters for the three helicopter tests is shown in Table 44.1.

Prior to performing any additional processing, the  $X$ ,  $Y$ ,  $Z$  coordinates for all analysis points for all data stages were exported as an ASCII file for each of the five PONTOS<sup>TM</sup> projects. Initially, the orientations/positions of the global coordinate systems are arbitrary relative to the measurement points. To effectively process all data, the center of rotation and a best-fit swept rotor plane was established. The center of rotation was calculated as the centroid of the point clouds using the maximum number of integer main rotor rotations that occurred in each data set. The composite point clouds for the three data sets were also used to determine the best fit plane through which the rotor swept for each data set. A singular value decomposition (SVD) was performed to determine the principal coordinates of each composite point cloud yielding best-fit coordinate systems for each data set. The SVD can be calculated according to:

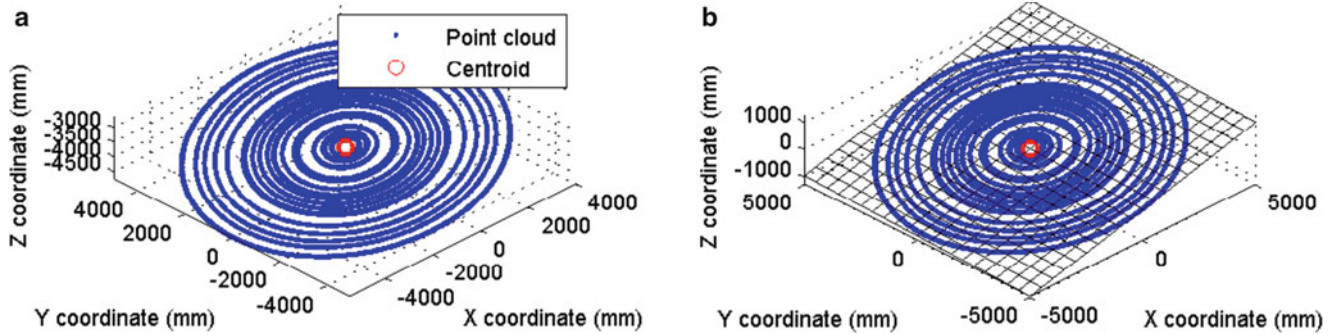
$$A = UEV^T, \quad (44.1)$$

where  $U$  and  $V$  are orthogonal matrices and  $E$  is a diagonal matrix of singular values. The eigenvectors of  $AA^T$  are the columns of  $U$  and the eigenvectors of  $A^T A$  are the columns of  $V$ . The third row of the  $V$  matrix is a unit vector normal to the best-fit plane of each point cloud. Using:



**Table 44.1** Parameter values for three helicopter tests

	Max. intersection error (pixels)	Min. radius (pixels)	Ellipse qual. (pixels)
Full-speed, grounded	0.70–0.80	2.0	0.30
First hover, $f_s = 250$ fps	1.00	2.0	0.30
Second hover, $f_s = 1,080$ fps	0.80–0.90	1.8	0.30



**Fig. 44.5** (a) Raw, full-speed, grounded point cloud and centroid; (b) full-speed, grounded best-fit swept plane, centroid coincident with global origin

**Table 44.2** Center of rotation coordinates and best-fit plane unit vector for three data sets

	Center of rotation (mm)			Best-fit plane unit vector (mm)		
	$X$	$Y$	$Z$	$i$	$j$	$k$
Full-speed, grounded	-744.3	29.7	-3,655.5	-0.217	0.029	0.976
First hover, $f_s = 250$ fps	122.0	-287.5	-2,964.5	-0.216	-0.101	0.971
Second hover, $f_s = 1,080$ fps	-25.4	-101.3	10.3	-0.005	0.147	-0.989

$$V = \begin{bmatrix} u_i & v_i & w_i \\ u_j & v_j & w_j \\ u_k & v_k & w_k \end{bmatrix}, \tag{44.2}$$

The equation for the best-fit plane can be written according to:

$$Z_{bfp} = -\frac{w_i}{w_k}X - \frac{w_j}{w_k}Y. \tag{44.3}$$

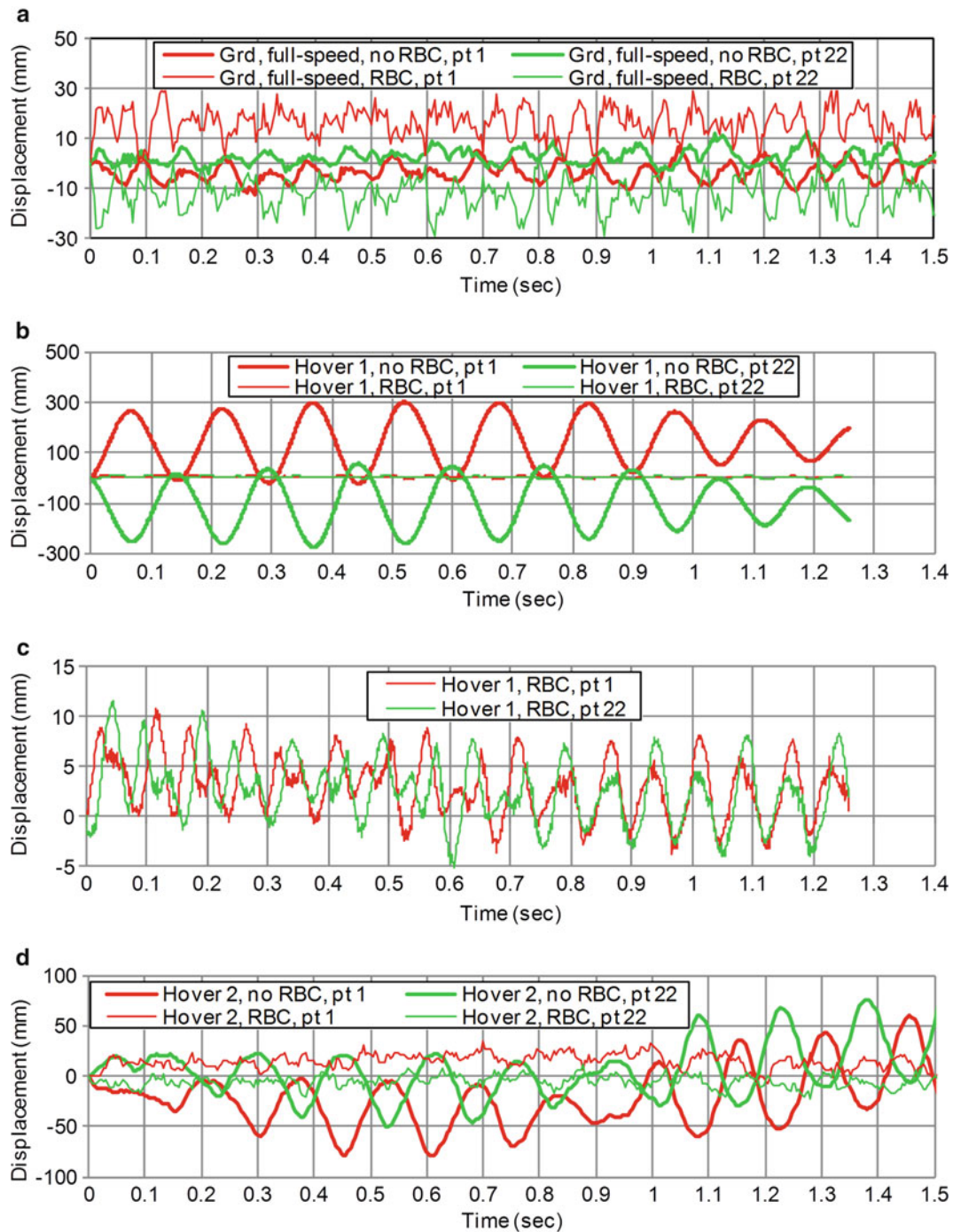
Equation 44.2 was used to plot the best-fit planes for all three data sets. The center of rotation and best-fit plane for the full-speed, grounded test can be seen in Fig. 44.5. Similar plots/calculations were performed for the remaining two data sets.

The calculated centers of rotation and best-fit swept plane unit vectors for the three data sets can be seen in Table 44.2.

The center of rotation coordinates and best-fit plane unit vectors were used to perform coordinate system transformations in PONTOS™. This coordinate system transformation helps to reduce the dominance of the fundamental harmonic in measured data by reducing the misalignment between the rotor axis of rotation and the global  $Z$  axis. A description of the preliminary results for the three data sets processed follows.

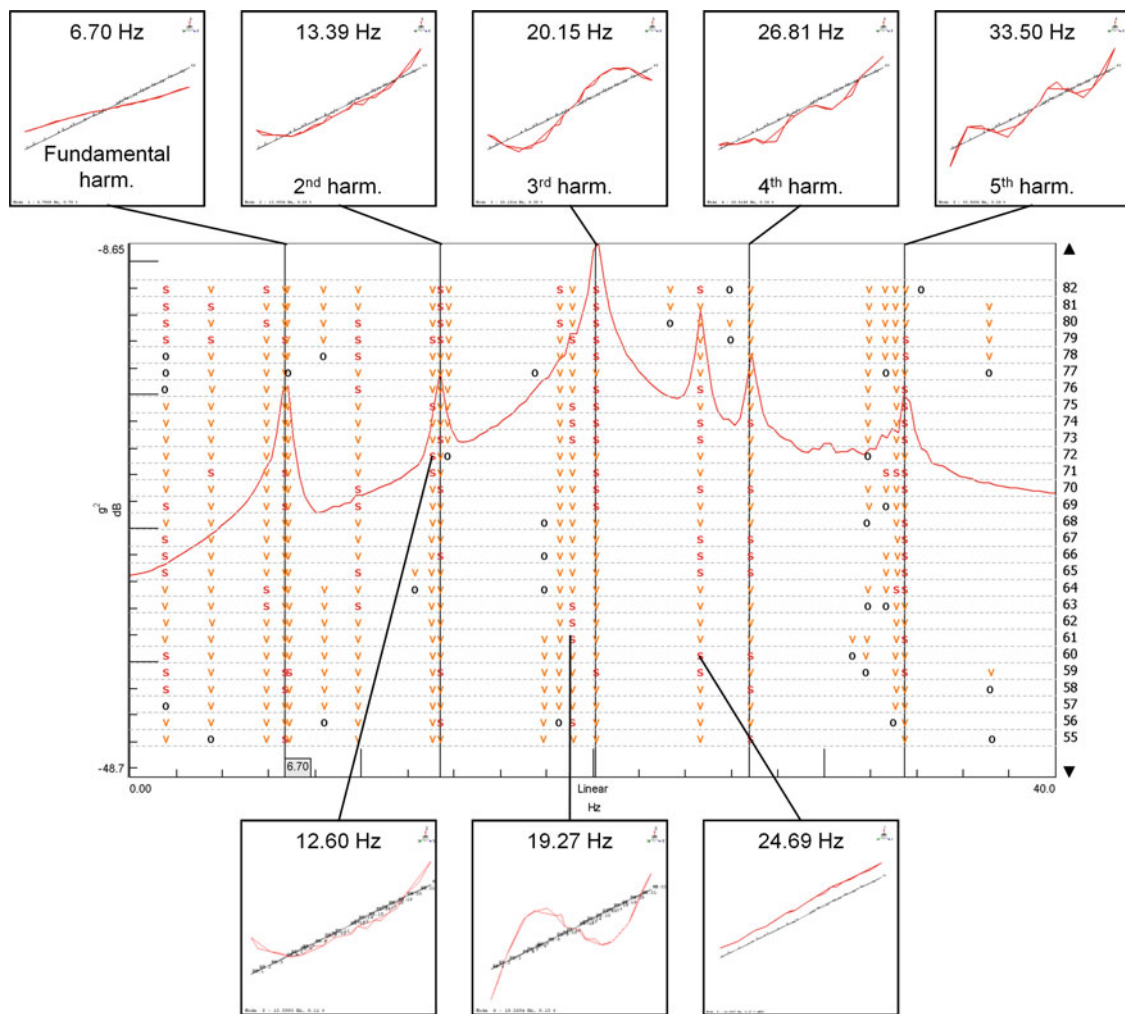
### 44.4 Experimental Results

Prior to the calculation of power spectra and extraction of ODSs, the operating data for the grounded, full speed and first and second hover tests was processed in PONTOS™ to track the motion of the optical targets in three dimensions, perform coordinate transformation, and process several data sets with rigid body correction to better observe the flexible motion of the rotor blades with respect to the hub. Several plots can be seen in Fig. 44.6 showing rotor tips displacements versus time for three data sets processed with and without rigid body correction. The sampling frequency is listed for the first and second hover tests.



**Fig. 44.6** (a) Grounded, full-speed with and without RBC for point 1 and point 22; (b) first hover ( $f_s = 1,080$  fps) with and without RBC for point 1 and point 22; (c) expanded view of first hover with RBC for point 1 and point 22; (d) second hover ( $f_s = 250$  fps) with and without RBC for point 1 and point 22

From Fig. 44.6a, the fundamental harmonic is not readily apparent in the “no RBC” plots for tip points 1 and 22 as the helicopter was grounded and the main rotor exhibited only small rigid body movements. The application of RBC to the full-speed, grounded data set resulted in some amplitude attenuation. The “no RBC” displacement-time traces in Fig. 44.6b, d exhibit well-defined fundamental harmonics; these harmonics appear to change amplitude over time as the main rotor moves during the helicopter hover. As shown in Fig. 44.6c, d, the application of RBC using the rotor hub to track the rotor motion resulted in significant attenuation of the fundamental harmonic.



**Fig. 44.7** Stability diagram for the full-speed, grounded test with ODSs at harmonic and non-harmonic poles

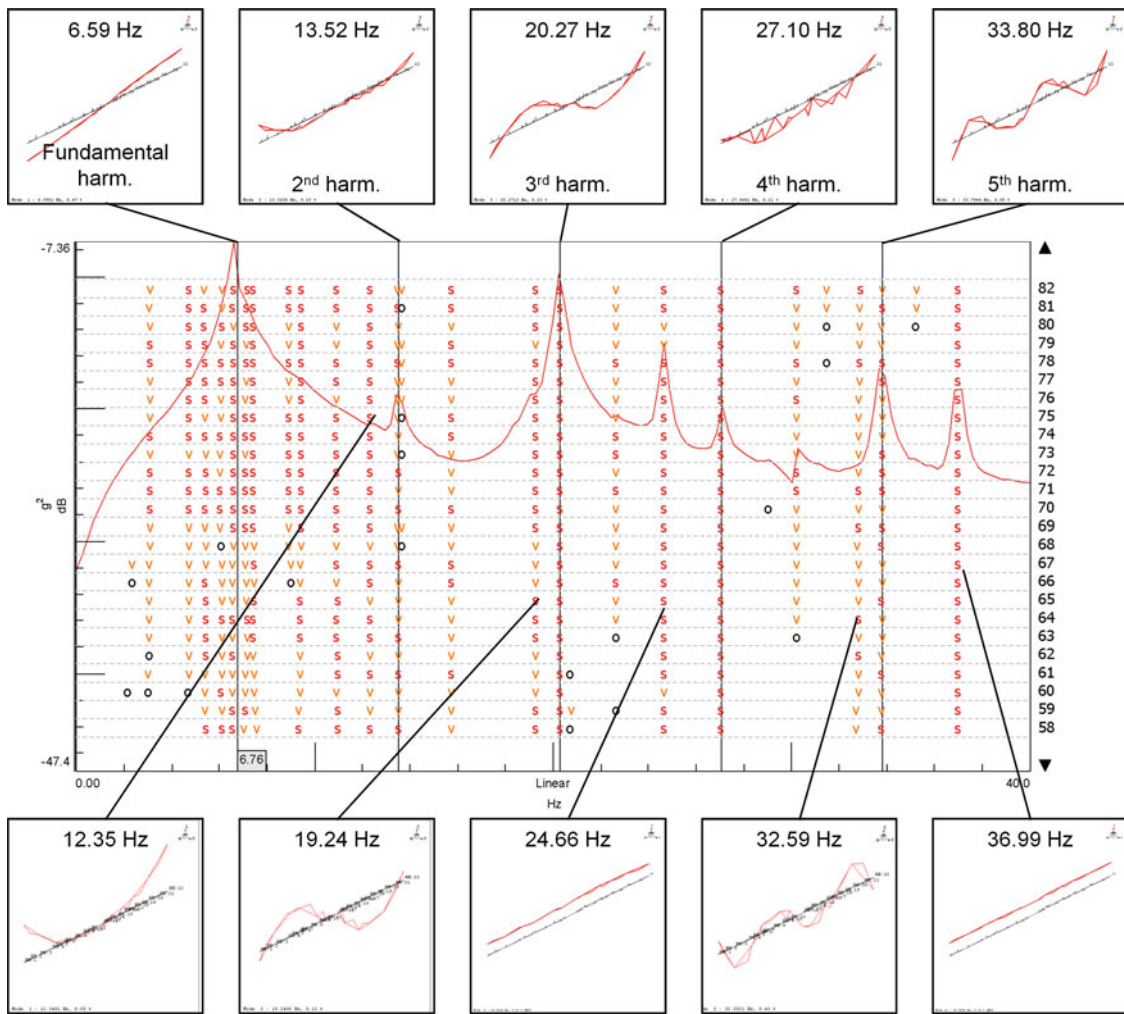
The displacement-time data for the full-speed grounded and second hover tests ( $f_s = 250$  fps) was passed through a 40 Hz low pass filter and double differentiated to yield acceleration-time data. The data was converted to Type 58 Universal File Format (UFF) for further processing within LMS Test.Lab 10A. Crosspower spectra were calculated and Operational POLYMAX was used to estimate modal parameters at stable poles. Tip points 1 and 22 were used as references. The stability diagram and extracted ODSs for the full-speed, hover test is shown in Fig. 44.7. Only data with 250 fps sampling rates were used to yield sufficient frequency resolutions (maximum frame count of 1,361).

As shown in Fig. 44.7, ODSs were initially extracted for the first five harmonic frequencies. Clearly, the data was dominated by harmonic content. Stable poles can also be seen at non-harmonic frequencies; three poles were extracted at 12.60, 19.27 and 24.69 Hz independently from the harmonic poles shown above the stability diagram in Fig. 44.7. At this point it is unclear whether the two flexible (12.60 and 19.27 Hz), non-harmonic poles are true ODSs/frequencies of the helicopter rotor at full-speed. Currently, the stable pole at 24.69 Hz exhibiting rigid body motion is not fully understood and requires further study.

The stability diagram and extracted ODSs for the second hover test ( $f_s = 250$  fps) is shown in Fig. 44.8.

Similar to that shown in Fig. 44.7, stable poles were readily found as shown in Fig. 44.8 for the first five harmonic frequencies. In addition, stable poles could also be seen at several non-harmonic frequencies including: 12.35, 19.24, 24.66, 32.59 and 36.99 Hz. Currently, the stable poles at 24.66 and 36.99 Hz exhibiting primarily rigid body motion are not fully understood and require further study.





**Fig. 44.8** Stability diagram for second hover test ( $f_s = 250$  fps) with ODSs at harmonic and non-harmonic frequencies

**Table 44.3** Modal assurance criterion (MAC) comparison and percent frequency difference between full-speed, grounded and second hover ( $f_s = 250$  fps) tests

Full-speed grounded (Hz)	Second hover test ( $f_s = 250$ fps) (Hz)	MAC	Percent freq. diff. (%)
12.60	12.35	0.64	-1.98
19.27	19.24	0.79	-0.16
24.69	24.66	0.97	-0.12

A shape and frequency comparison between three, non-harmonic ODSs between the full-speed, grounded and second hover tests can be seen in Table 44.3.

As shown in Table 44.3, the shape similarity (MAC) between the 12.60 and 12.35 Hz poles was fairly low at 0.64. In contrast, the remaining two shapes exhibited high similarity with MAC values of 0.79 and 0.97, respectively. In addition, the frequencies for the three, non-harmonic pole comparisons are nearly identical.

Much of the difficulty encountered in the estimation of modal parameters at non-harmonic stable poles was due to the dominance of high-amplitude harmonic content in the operating data. In addition, as stereophotogrammetry remains static with respect to the measured structure in contrast to measurement transducers mounted directly to the surface of the structure, the quality of the measurement is highly dependent on the selection of a convenient coordinate system and prior work has shown that the application of RBC can artificially constrain the structure being measured distorting extracted ODSs [5, 18, 21].

## 44.5 Future Work

To further process operating data from the helicopter, a modal impact test should be performed to determine the resonant frequencies and shapes for the structure without rotational effects. In addition, high amplitude harmonic content was present in the helicopter operating data and this made the extraction of operating deflection shapes quite difficult. Future work will include the collection of operating data from the helicopter main rotor at a number of operating frequencies including a static modal impact test. In addition, the exploration/development of a robust harmonic filter may improve the ODS extraction results for rotation systems. Several harmonic filtration techniques have already been developed by Groover et al. [22], Peeters et al. [23] and Randall et al. [24].

## 44.6 Conclusion

Operating data was successfully collected from the main rotor of a Robinson R44 helicopter in both grounded and hovering states using stereophotogrammetry techniques. A technique was presented to determine the center of rotation and perform coordinate transformation on the displacement data to present the flapwise displacement data most effectively. Displacement-time data was present for the rotor tip points with and without the application of RBC showing the attenuation of much of the fundamental harmonic for three data sets. Several non-harmonic ODSs were extracted from operational power spectra calculated from acceleration data.

**Acknowledgements** The authors gratefully appreciate the financial support for this work provided by the U.S. Army Research Office Nanomanufacturing of Multifunctional Sensors Ref. Award Number: W911NF-07-2-0081 and the National Science Foundation under Grant No. 0900534, entitled “Dynamic Stress–Strain Prediction of Vibrating Structures in Operation”. Any opinions, findings, and conclusions or recommendations expressed in this material are those of the authors and do not necessarily reflect the views of the National Science Foundation or Army Research Office. The research team is indebted to Stephen Booth of STB Enterprises for providing access to and piloting the helicopter.

## References

1. Helfrick MN, Pingle P, Niezrecki C, Avitabile P (2009) Optical non-contacting vibration measurement of rotating turbine blades. In: 27th conference and exposition on structural dynamics, IMAC XXVII, Jacksonville, FL
2. Warren C, Niezrecki C, Avitabile P (2011) Determination of wind turbine operating deflection shapes using full-field 3D point-tracking. In: 29th IMAC, a conference on structural dynamics. Jacksonville, FL, pp 217–226
3. Warren C, Niezrecki C, Avitabile P (2011) Optical non-contacting vibration measurement of rotating turbine blades II. In: 28th IMAC, a conference on structural dynamics. Jacksonville, FL, pp 39–44
4. Lundstrom T, Niezrecki C, Avitabile P (2011) Rigid body correction using 3D digital photogrammetry for rotating structures. In: SEM annual conference on experimental and applied mechanics. Uncasville, CT, pp 307–321
5. Lundstrom T, Baqersad J, Niezrecki C, Avitabile P (2012) Using high-speed stereophotogrammetry techniques to extract shape information from wind turbine/rotor operating data. In: 30th IMAC, a conference on structural dynamics. Jacksonville, FL, pp 269–275
6. Kalpoe D, Khoshelham K, Gorte B (2011) Vibration measurement of a model wind turbine using high speed photogrammetry. In: Videometrics, range imaging, and applications XI: proceedings, Munich
7. Paulsen US, Erne O, Moeller T, Sanow G, Schmidt T (2009) Wind turbine operational and emergency stop measurements using point tracking videogrammetry. In: Proceedings of the 2009 SEM annual conference and exposition, Albuquerque
8. Paulsen US, Schmidt T, Erne O (2010) Developments in large wind turbine modal analysis using point tracking videogrammetry. In: 28th IMAC, a conference on structural dynamics. Jacksonville, FL, pp 187–198
9. Ozbek M, Rixen DJ (2011) Optical measurements and operational modal analysis on a large wind turbine: lessons learned. In: 29th IMAC, a conference on structural dynamics Jacksonville, FL, pp 257–276
10. Ozbek M, Rixen DJ, Erne O, Sanow G (2010) Feasibility of monitoring large wind turbines using photogrammetry. 35(12):4802–4811
11. Ozbek M, Mengt F, Rixen DJ, Van Tooren MJL (2011) Identification of the dynamics of large wind turbines by using photogrammetry. In: 28th IMAC, a conference on structural dynamics. Jacksonville, FL, pp 351–359
12. Özbek M, Rixen DJ (2012) Operational modal analysis of a 2.5 MW wind turbine using optical measurement techniques and strain gauges. *Wind Energy*. doi:10.1002/we.1493
13. Lawson M (2011) Measurement of deformation of rotating blades using digital image correlation. University of Texas, Austin
14. Schneider O (2005) Analysis of SPR measurements from HART II. *Aerospace Sci Technol* 9:409–420
15. Schneider O, Van Der Wall BG, Pengel K (2003) HART II blade motion measured by stereo pattern recognition (SPR). In: American Helicopter Society 59th annual forum. Phoenix, AZ
16. Schneider O, Van Der Wall BG (2003) Final analysis of HART II blade deflection measurement. In: Twenty-ninth European rotorcraft forum. Friedrichshafen, Germany

17. Olson L, Barrows D, Abrego A, Burner A (2010) Blade deflection measurements of a full-scale UH-60A rotor system. In: 2010 AHS specialists' conference on aeromechanics
18. Lundstrom T (2012) Dynamic measurement and analysis of large-scale rotating systems using stereophotogrammetry. M.Sc. thesis, University of Massachusetts Lowell, Lowell
19. Robinson Helicopter Company (2002) R44 II pilot's operating handbook. Robinson Helicopter, Torrance
20. PONTOS v6.2 user manual (2009) GOM mbH, Mittelweg 7-8, 38106 Braunschweig, Germany
21. Lundstrom T, Niezrecki C, Avitabile P (2011) Appropriate rigid body correction for analyzing the dynamics of rotating structures using 3D digital photogrammetry. In: Proceedings of the 8th international workshop on structural health monitoring, Stanford, 13–15 Sept 2011
22. Groover C, Trethewey M, Maynard K, Lebold S (2005) Removal of order domain content in rotating equipment signals by double resampling. *Mech Syst Signal Process* 19(3):483–500
23. Peeters B, Cornelius B, Jannsens K, Van der Auweraer H (2007) Removing disturbing harmonics in operational modal analysis. In: Proceedings of IOMAC 2007, Copenhagen
24. Randall R, Sawalhi N (2011) A new method for separating discrete components from a signal. *Sound Vibr* 45(5):6–9



# Chapter 45

## Principles of Image Processing and Feature Recognition Applied to Full-Field Measurements

John E. Mottershead and Weizhuo Wang

**Abstract** Recent advances in measurement techniques such as digital image correlation (DIC) allow full-field maps (images) of vibration shapes or strain to be obtained easily. This generally results in the acquisition of large volumes of highly redundant data. Fortunately, image decomposition offers feasible techniques for data condensation while retaining essential information. The selection, or construction, of decomposition basis (kernel) functions is essential to data reduction and has been shown to produce descriptions of the full-field image capable of accurate reproduction of the original data, very efficiently. Image descriptors are robust to measurement noise. Classical orthogonal kernel functions include Fourier series, wavelets and Legendre, Zernike and Tchebichef polynomials, defined on either rectangular or circular domains. In practice full-field measurements of the engineering components are usually non-planar within irregular domains, so that the classical kernel functions are not immediately applicable. This problem may be addressed using a methodology based on adaptive geometric moment descriptors (AGMD) as will be demonstrated in a series of illustrative examples. Model updating from full-field measurements and modal testing in the shape-feature domain are enabled with attendant advantages of the full-field data over measurements taken with a limited number of sensors at discrete locations.

**Keywords** Image decomposition • Full-field measurement • Moment descriptor • Surface parameterization • Pattern recognition

### 45.1 Introduction

The availability of non-contact optical sensing techniques enables full-field measurement for mechanical systems. These techniques include digital image/volume correlation (DIC [1–3]/DVC [4–6]), automated photoelasticity [7–9], electronic speckle pattern interferometry (ESPI) [10, 11] and thermoelastic stress analysis (TSA) [12, 13]. However, the measured data by such systems are usually very large and highly information redundant. It is possible to apply image processing techniques [14–16] to extract useful information from the raw full-field data.

The majority of full-field measurement techniques capture the surface responses of the test structure and the obtained data may be expressed as functions of two spatial coordinates, e.g.  $x$ - and  $y$ -coordinates. 2D image decomposition is one of the popular approaches to extract shape features [17]. In principle, a 2D shape may be expressed as a linear combination of a set of 2D elementary (also called basis or kernel) decomposition functions. The combination coefficients are usually called shape features. Numerous kernel functions have been applied for image decomposition. These functions include Fourier functions [17], windowed Fourier functions (such as the short-time Fourier transform (STFT) [17]), wavelets [14–16, 18], ridgelets [19], curvelets [20, 21], contourlets [22], brushlets [23] and the family of polynomials [24–32]

The overall procedure of shape decomposition is shown in Fig. 45.1. The first step in shape decomposition is to select suitable kernel functions for the problem at hand. Some preliminary judgements can usually be made to assist the selection,

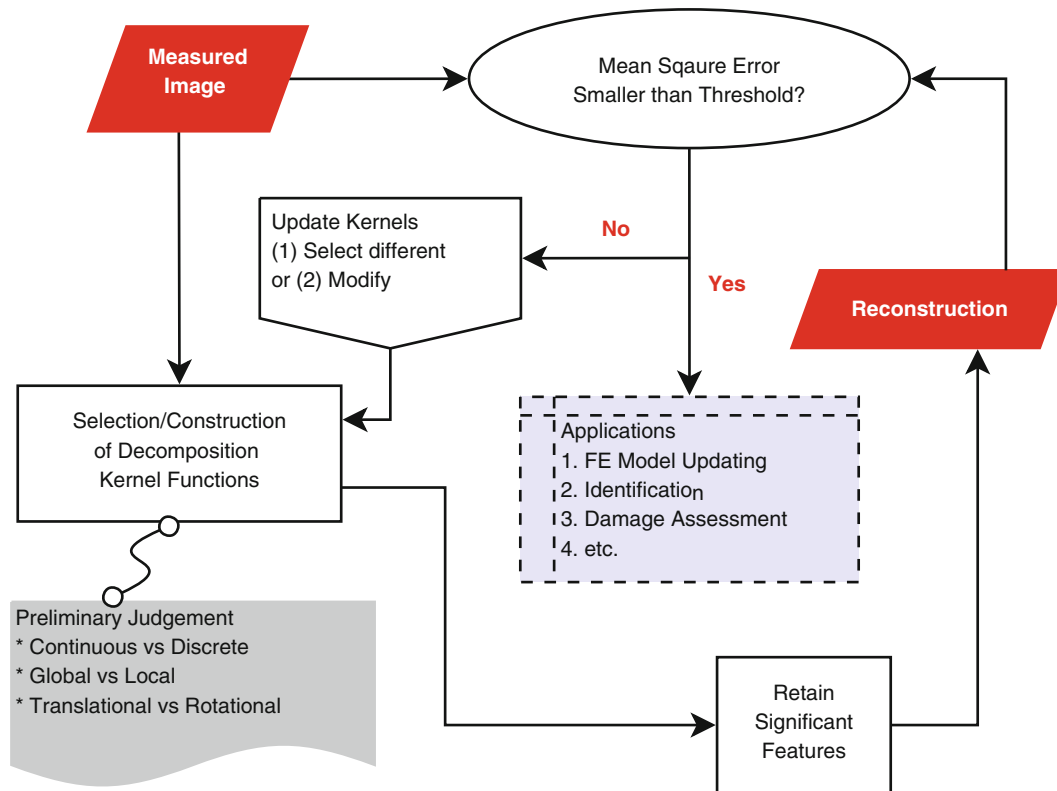
---

J.E. Mottershead (✉)

School of Engineering, University of Liverpool Liverpool, L69 3GH, UK  
e-mail: [j.e.mottershead@liv.ac.uk](mailto:j.e.mottershead@liv.ac.uk)

W. Wang

School of Engineering, Manchester Metropolitan University, Manchester M1 5GDK  
e-mail: [W.Wang@mmu.ac.uk](mailto:W.Wang@mmu.ac.uk)



**Fig. 45.1** Flowchart of shape (displacement/strain) decomposition

such as whether the measurements are continuous or discrete, or whether global or local features of the image are of primary interest. The choice of different kernel functions will determine the order of the reconstructed image necessary to replicate the measurement to within a chosen tolerance. Measures of dissimilarity, such as the mean square error (MSE), or of similarity such as Pearson's correlation coefficient (PCC) may be used for the truncation of shape features. If the MSE is smaller than a pre-defined threshold or the PCC is close enough to unity, the shape features may be applied in further analysis such as FE model updating, identification and damage detection etc. If the reconstruction is deficient, then alternative decomposition kernel functions may be selected; or modification of the existing kernel functions may be carried out to improve performance. Pearson's correlation coefficient may be used to assess which of a number of candidate sets of kernel functions will reproduce a measured image to desired accuracy with the smallest number of shape-descriptor terms.

The shape feature extraction kernels discussed above are analytical functions defined on regular domains e.g. on a circle or a square. In real engineering problems full-field measured domains are most probably irregular and the surfaces are non-planar. To be able to apply image analysis additional techniques are needed. For example, it is possible to map the measured domain to the definition domain of the analytic functions via coordinate transformation. Surface parameterisation [33, 34] provides a set of practical tools for coordinate transformation. On the other hand, construction of kernel functions adaptively based on the full-field measured domain can be highly effective. Gram-Schmidt orthogonalisation (GSO) and principal component analysis (PCA) [35] are two feasible approaches. Detailed discussions of constructing feature extraction kernel functions is provided in case studies described later. Appropriate selection or construction of kernel functions usually produces effective and succinct shape features [36–38]. Further structural analysis of full-field images may then be carried out by using the shape features, e.g. application of shape features for finite element model updating, modal identification and non-linearity detection etc.

The paper is arranged as follows. The theory of full-field data decomposition is presented in Sect. 45.2. Three case studies are demonstrated in Sect. 45.3: (1) Simulated composite panel with localised strain-field disturbances caused by delamination, using Krawtchouk moment descriptors. (2) Experimental quasi-static strain maps of a test piece with a central circular hole under tensile loading, using adaptive Zernike kernel functions. (3) Surface parameterisation of a car bonnet with irregular boundaries and curved surfaces using surface parameterisation and Gram-Schmidt orthogonalisation for the experimental determination of full-field vibration mode shapes. Various conclusions on the image processing of full-field strain and displacement measurements are presented in Sect. 45.4.

## 45.2 Shape Decomposition

Let  $\mathcal{S}(\mathbf{x}, \zeta)$  denote the full-field strain/displacement data. It may be expressed as a linear combination of elementary waveforms  $\phi_i(\bullet)$  (called kernel or basis functions) as

$$\mathcal{S}(\mathbf{x}, \zeta) = \sum_{i=1}^{\infty} \alpha_i \phi_i(\mathbf{x}, \zeta) \quad (45.1)$$

where  $\alpha_i$  are the combination coefficients,  $\mathbf{x} \in \{\text{measured surface domain}\}$  denotes the spatial coordinates and  $\zeta$  is the temporal parameter. For spatially discrete full-field data, (45.1) may be expressed in matrix form as

$$\mathbf{s}(\zeta) = \mathcal{D}\alpha(\zeta) = \sum_i \alpha_i(\zeta) \boldsymbol{\phi}_i \quad (45.2)$$

where  $\mathbf{s} \in \mathbb{R}^{\mathcal{P} \times 1}$  is the discrete full-field data organised in vector format with  $\mathcal{P}$  dimensions,  $\boldsymbol{\phi}_i \in \mathbb{R}^{\mathcal{P} \times 1}$  are discrete kernel functions,  $\mathcal{D} = \{\boldsymbol{\phi}_1, \boldsymbol{\phi}_2, \dots\}$  denotes the collection of kernel functions – usually called a dictionary [39],  $\boldsymbol{\alpha} \in \mathbb{R}^{\mathcal{Q} \times 1}$  are the decomposition coefficients – usually called shape features.

For data compression, it is desired that a good approximation of  $\mathbf{s}$  is achieved by only a small number of components in  $\boldsymbol{\alpha}$ , expressed as

$$\mathbf{s} = \sum_{i=1}^{\mathcal{M}} \alpha_i \boldsymbol{\phi}_i + \boldsymbol{\epsilon}^{(\mathcal{M})} \quad (45.3)$$

where  $\mathcal{M}$  is a positive integer,  $\boldsymbol{\epsilon}^{(\mathcal{M})}$  is the approximation error. The objective of an efficient decomposition is to determine sufficiently small number of  $\mathcal{M}$  subject to  $\|\boldsymbol{\epsilon}^{(\mathcal{M})}\|_2 < T_a$  where  $T_a$  is a pre-specified threshold.

Decomposition of a collection of data  $\mathbf{S} \equiv [\dots s_j \dots]$  may be expressed as

$$\mathbf{S} = \mathcal{D}\mathbf{A} \quad (45.4)$$

where  $\mathbf{A} \equiv [\dots \boldsymbol{\alpha}_j \dots]$  are the vectors of decomposition coefficients corresponding to the individual signals in  $\mathbf{S}$ . Analogous to (45.3), the  $\mathcal{M}$ -term approximation of the signals may be determined by the following objective function with a pre-specified threshold  $T_{\mathcal{I}_M}$  as

$$\|\mathbf{S} - \mathcal{D}_{\mathcal{I}_M} \mathbf{A}_{\mathcal{I}_M}\|_F < T_{\mathcal{I}_M} \quad (45.5)$$

where  $\mathcal{D}_{\mathcal{I}_M}$  is the column-submatrix of  $\mathcal{D}$  for the collection of indices in  $\mathcal{I}_M$ .  $\mathbf{A}_{\mathcal{I}_M}$  is the row-submatrix of  $\mathbf{A}$  indexed by  $\mathcal{I}_M$  and  $\|\mathbf{B}\|_F = \sqrt{\sum_{i,j} |b_{i,j}|^2}$  denotes the Frobenius norm.

### 45.2.1 Orthogonal Decomposition

Orthogonal decomposition is a common way to determine the shape features. The decomposition coefficient  $\alpha_i$  may be evaluated by inner product of the shape pattern  $\mathcal{S}(\mathbf{x}, \zeta)$  and the  $i$ th kernel function  $\phi_i(\mathbf{x}, \zeta)$ , expressed as,

$$\alpha_i = \int_{\mathbf{x} \in \Omega} \mathcal{S}(\mathbf{x}, \zeta) \phi_i^*(\mathbf{x}, \zeta) d\mathbf{x} \quad (45.6)$$

where  $\Omega$  is the measured domain. The discrete version is written as,

$$\boldsymbol{\alpha} = \mathcal{D}^H \mathbf{s} \quad (45.7)$$

where  $H$  denotes the Hermitian transpose.

**Table 45.1** Useful shape decomposition kernel functions

		Global		Local
Continuous		Legendre [28] and Fourier [40] Zernike [28] Fourier-Mellin [41]	Gegenbauer [24] Gaussian-Hermite [25]	Continuous wavelets
				lets family: (e.g. contourlet [22], ridgelet [19], curvelet [20, 21], brushlet [23], bandelet [42] etc.)
Discrete	<i>Uniform lattice</i>	Tchebichef [27]	Hahn [30]	Discrete wavelet, Krawtchouk [29]
	<i>Non-uniform lattice</i>	Racah [32] and dual Hahn [31]		

**Table 45.2** Definition domain and parameters of different orthogonal polynomials

Name	Notation	Domain	Parameters	Order
Legendre	$p_n(x)$	$x \in [-1, 1]$	—	$n \in \{0, 1, 2, \dots\}$
Zernike	$V_{n,m}(\rho, \vartheta)$	$0 \leq \rho \leq 1; \vartheta \in [0, 2\pi]$	—	$n \in \{0, 1, 2, \dots\}; m \in \{1, 2, 3, \dots\};$ $n -  m  \text{ even},  m  < n$
Hahn	$H_n(s; \alpha, \beta, N)$	$s \in \{1, 2, \dots, N\}$	$\alpha > -1 \ \& \ \beta > -1$ or $\alpha < -N \ \& \ \beta < -N$	$n \in \{0, 1, \dots, N-1\}$
Tchebichef	$T_n(s; N)$	$s \in \{1, 2, \dots, N\}$	—	$n \in \{0, 1, \dots, N-1\}$
Krawtchouk	$K_n(s; p, N)$	$s \in \{1, 2, \dots, N\}$	$0 < p < 1$	$n \in \{0, 1, \dots, N-1\}$

### 45.2.2 Classical Orthogonal Kernel Functions

Analytic orthogonal functions are the classical kernels used in image decomposition. Table 45.1 lists a number of popular decomposition kernel functions. Different categorisation may be defined as shown in Table 45.1. According to the definition domain, the orthogonal kernel functions may be classified as continuous or discrete. Sensitivity to local or global features is another classification criteria. Most of the kernel functions are defined in the Cartesian coordinate system. Two special kernel functions in Table 45.1 (in *italic*) are defined in the polar coordinate system which are suitable for cyclically symmetric shape feature extraction.

Mathematical expression of several kernel functions are given in the following. Parameters and orthogonal domains of the given kernel functions are listed in Table 45.2. The Legendre and Zernike polynomials are among the earliest kernel functions for orthogonal moment descriptors [28].

- Legendre polynomials;

The 2D Legendre polynomials may be defined as,

$$P_{n,m}(x, y) = p_n(x)p_m(y) \quad (45.8)$$

which is the Cartesian product of two 1D Legendre polynomials – expressed as

$$p_n(x) = \frac{1}{2^n} \sum_{k=0}^{\lfloor \frac{n}{2} \rfloor} \frac{(-1)^k (2n-2k)!}{k!(n-k)!(n-2k)!} x^{n-2k} \quad (45.9)$$

where  $\lfloor \cdot \rfloor$  is the floor operator,  $\bullet!$  is the factorial operator and  $n, m, k \in \{0, 1, 2, \dots\}$ .

- Zernike polynomials;

The Zernike polynomials defined in polar coordinate system within a circle with unitary radius may be written as

$$V_i \equiv V_{n,m}(x, y) \equiv V_{n,m}(\rho, \vartheta) = R_{n,m}(\rho) e^{im\vartheta} \quad (45.10)$$

where  $\rho$  is the radial coordinate,  $\vartheta$  is the phase angle,  $i = \sqrt{-1}$  and

$$R_{n,m} = \sum_{s=0}^{(n-|m|)/2} (-s)^s \frac{(n-s)!}{s! \binom{n+|m|}{s}! \binom{n-|m|}{s}!} \rho^{n-2s} \quad (45.11)$$

where the polynomial orders  $n$  and  $m$  are given in Table 45.2.

### 45.2.3 Discrete Orthogonal Polynomials

Numerical errors inevitably arise in the processing of digital (discrete-point) images using continuous kernel functions, typically Legendre and Zernike polynomials. The use of discrete orthogonal polynomials is then generally preferable since the digitisation of continuous analytical functions is then avoided.

Discrete orthogonal polynomials may be defined in the form of hypergeometric functions as [43]

$$Q \equiv {}_rF_s \left( \begin{matrix} a_1, a_2, \dots, a_r \\ b_1, b_2, \dots, b_s \end{matrix} \middle| z \right) = \sum_{k=0}^{\infty} \frac{(a_1)_k (a_2)_k \dots (a_r)_k}{(b_1)_k (b_2)_k \dots (b_s)_k} \frac{z^k}{k!} \quad (45.12)$$

where  $(\bullet)_k$  is the Pochhammer symbol.

The Hahn polynomials [43] may be defined as

$$H_n(s; \alpha, \beta, N) = {}_3F_2 \left( \begin{matrix} -n, & n + \alpha + \beta + 1, & -s \\ \alpha + 1, & -N \end{matrix} \middle| 1 \right) \quad (45.13)$$

where  $\alpha > -1$  &  $\beta > -1$  or  $\alpha < -N$  &  $\beta < -N$  are two parameters. The Tchebichef polynomial  $T_n(s)$  is a special case of the Hahn polynomial when  $\alpha = \beta = 0$ . i.e.

$$T_n(s; N) = {}_3F_2 \left( \begin{matrix} -n, & -s, & 1 + n \\ 1, & -N \end{matrix} \middle| 1 \right) \quad (45.14)$$

Another special case of Hahn polynomials, known as the Krawtchouk polynomial  $K_n(s)$ , may be defined as [32]

$$\begin{aligned} K_n(s; p, N) &\equiv \lim_{t \rightarrow \infty} H_n(s; \alpha(p, t), \beta(p, t), N) \\ &= \lim_{t \rightarrow \infty} H_n(s; pt, (1-p)t, N) \\ &= {}_2F_1 \left( \begin{matrix} -n, & -s \\ -N \end{matrix} \middle| \frac{1}{p} \right) \end{aligned} \quad (45.15)$$

where  $0 < p < 1$  is the position parameter. Tchebichef and Krawtchouk polynomials are suitable for recognising global and local image features respectively.

### 45.2.4 Construction of Kernel Functions

Analytic orthogonal kernel functions are defined on simple regular domains. However, real engineering structures are generally irregular with curved surfaces, so that image decomposition requires rather special treatment. 3D curved surfaces are essentially two-manifolds and 2D analytical functions may be defined on two curvilinear coordinates of the measurement surface. Surface parameterisation is the technique used to determine the curvilinear coordinates. The mapping from a 3D surface to a 2D parametric domain is called *isometric* if it is arc length preserving, *conformal* if it is angle preserving or *authalic* if it is area preserving [33, 34]. The full-field measured domain consists of discrete grids. Triangularisation may be used to connect the grid points, thereby forming a surface. Surface parameterisation is then carried out based on the discrete triangularised surface.

**Fig. 45.2** Discrete surface parameterisation: (a) triangular mesh of Nefertiti's face; (b) discrete conformal mapping to a fixed circular boundary; (c) discrete conformal mapping with free boundary conditions (Neumann)

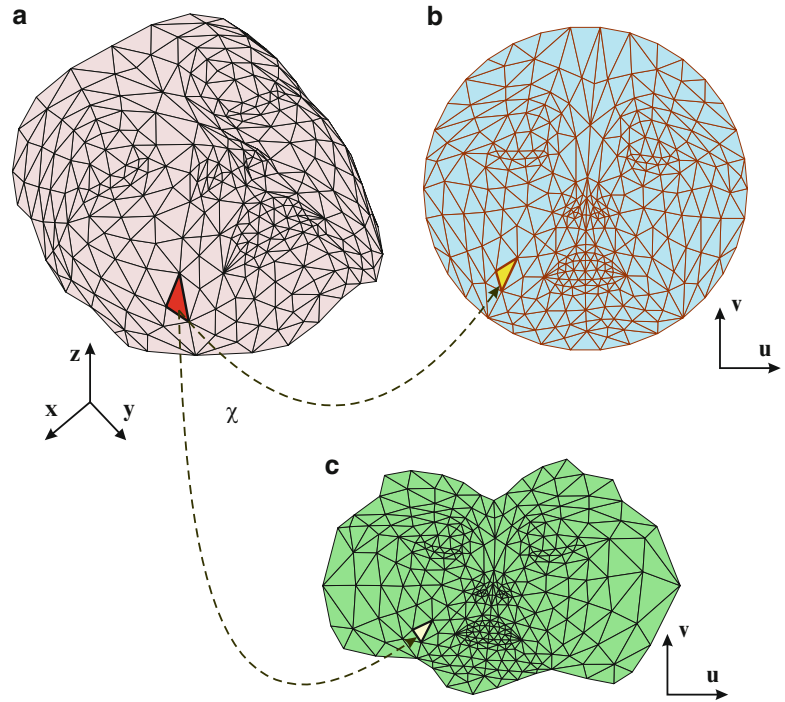


Figure 45.2 illustrates a simple example (Nefertiti's face) of discrete surface parameterisation. A operation  $\chi$  maps the triangles in  $\{x, y, z\}$  space (Fig. 45.2a) to the triangles in the  $\{u, v\}$  parametric domain (Fig. 45.2b). A distortion measure (e.g. the Dirichlet energy [34]) between the pairs of triangles may be written as,

$$\mathbb{E}_D = \frac{1}{2} \int_{triangle\ domain} |\nabla \chi(\mathbf{x})|^2 d\mathbf{x} \quad (45.16)$$

Then the objective of the mapping is to minimise the measure  $\mathbb{E}_D$ , which may be obtained by solving the following equations

$$\frac{\partial \mathbb{E}_D}{\partial \mathbf{u}_i} = \mathbf{0} \quad (45.17)$$

where  $\mathbf{u}_i \equiv \{u, v\}_{i,i=1,\dots,N}$  are the grids coordinates in the parametric domain.

In addition to distortion, there are a number of other conditions should be considered. As listed in Fig. 45.3, the conditions include *boundary conditions* (fixed or free), *bijectivity* (invertible or not) and *complexity* (linear or nonlinear) [34]. The mapping result shown in Fig. 45.2b is the discrete conformal mapping with circular boundary and in Fig. 45.2c is the discrete conformal mapping with free boundary condition.

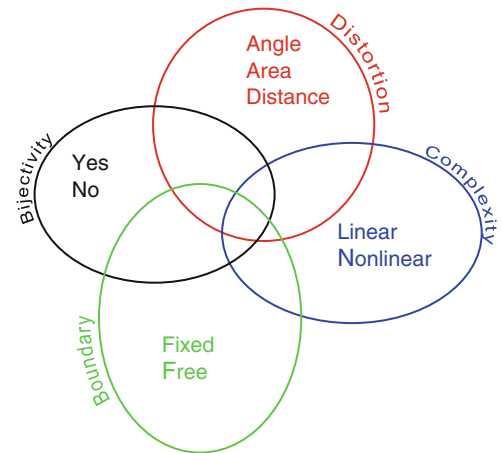
The kernel functions may be defined on the obtained parametric coordinates  $(u, v)$ . Gram-Schmidt orthogonalisation may then be employed to recover orthogonality over the measured domain.

### 45.2.5 Sparse Representation

The kernel functions discussed above are complete or truncated sets of orthogonal bases. The use of overcomplete basis functions has attracted increasing attention since the 1990s [44] and representation of the data is then said to be sparse (when the dictionary  $\mathcal{D}$  is overcomplete), such as by the combination of Fourier kernel functions and wavelets. Then the kernel functions are not necessarily orthogonal to each other. In this case, the solution for  $\boldsymbol{\alpha}$  in (45.2) is not unique any more. A number of well-known algorithms, e.g. Method of Frames [45], Basis Pursuit [46], Best Orthogonal Basis [47], Matching Pursuit [39], have been proposed and tested to find optimal solutions. Sparse representation is most advantageous [44] in



**Fig. 45.3** Discrete surface mapping conditions



applications that involve data compression or denoising. Sparse representation might have great potential for application in data compression for full-field measurement but is beyond the scope of this paper.

### 45.3 Case Studies

In this section, four case studies are presented. The full-field data considered includes strain maps under quasi-static loading and full-field displacement patterns in steady-state vibration. The geometric shapes of the specimens range from rectangular flat surfaces to irregular curved panels. Shape feature extraction involves the selection or construction of analytic basis functions and the obtained shape features show effectiveness and succinctness in representing the full-field data.

#### 45.3.1 Composite Panel with Delamination Using the Krawtchouk Moment

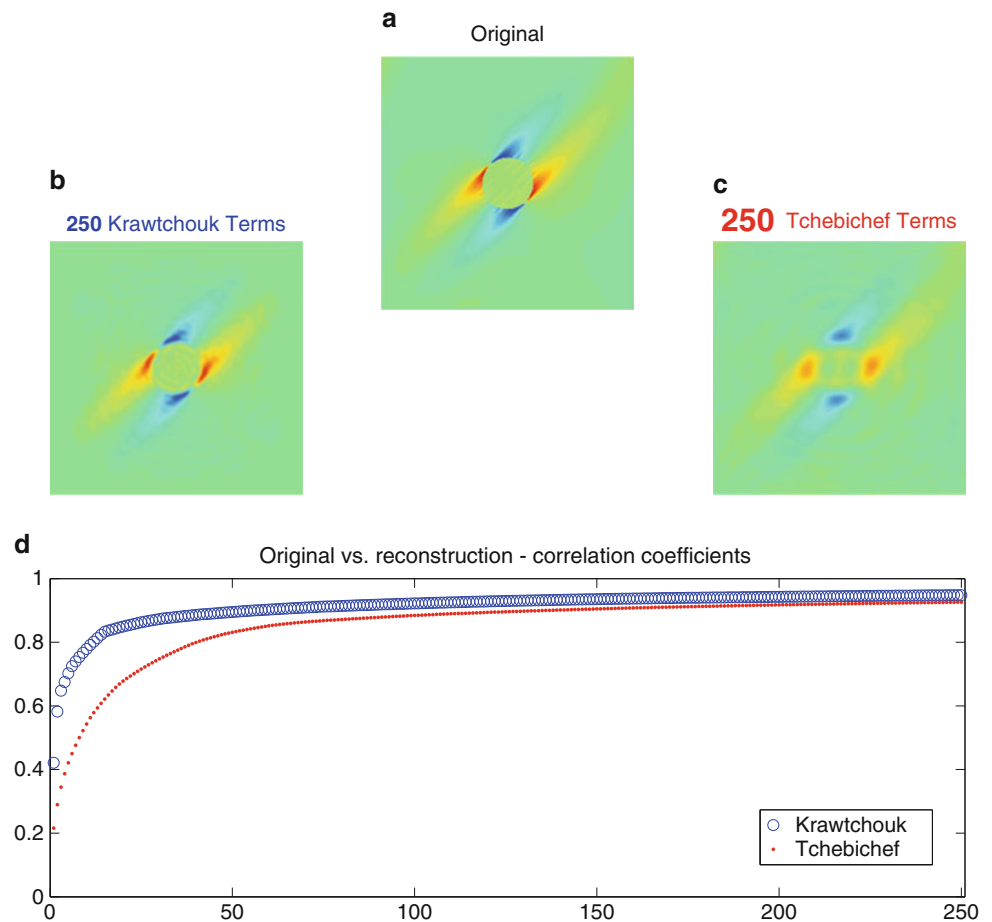
In this section, the surface strain map of a simulated carbon fibre composite panel is considered. The panel,  $1,000 \times 1,000$  mm in dimension, consists eight plies of fibre in the directions  $(45^\circ, -45^\circ, 45^\circ, -45^\circ, 45^\circ, -45^\circ, 45^\circ, -45^\circ)$ . A circular delamination region between the 3rd and 4th fibre plies is assumed to be located at the centre of the panel. The FE model consists of  $200 \times 200 = 40,000$  elements. The principal strain map of the specimen under tensile loading is shown in Fig. 45.4a. It is seen that the most important strain pattern appears around the delamination region due to the stress concentration caused by the delamination itself. The number of data points is 40,000, which may be condensed by image decomposition without significant loss of information.

The Krawtchouk (sensitive to local shape features) and the Tchebichef (generally suitable for global shape features) moment descriptors were adopted. The reconstructed strain patterns using the Krawtchouk (KMD) and the Tchebichef moment descriptors (TMD) based on 250 shape feature terms are shown in Fig. 45.4b, c respectively. It is clear that the KMD outperforms the TMD. The asymptotic curves of the Pearson correlation coefficients between the reconstructed images with the original map are shown in Fig. 45.4d. The curve with circular markers is the convergent correlation coefficients with increasing number of KMDs included to the reconstruction whilst the dotted curve is the convergence using TMDs. It is seen that the KMD performs quantitatively better than the TMD in this case of local stain field disturbance caused by the delamination.

#### 45.3.2 Zernike Moment Descriptor

The Zernike moment descriptor (ZMD) is ideal for image recognition on circular domains, for example the vibration mode shapes of plane circular discs with degenerate eigenvalues were studied by Wang et al. [36]. The same degenerate mode was recognised from the ZMD amplitudes and the angular orientation from the phase of the ZMDs. The ZMD kernels are also

**Fig. 45.4** Strain map reconstruction from Krawtchouk moments and Tchebichef moments



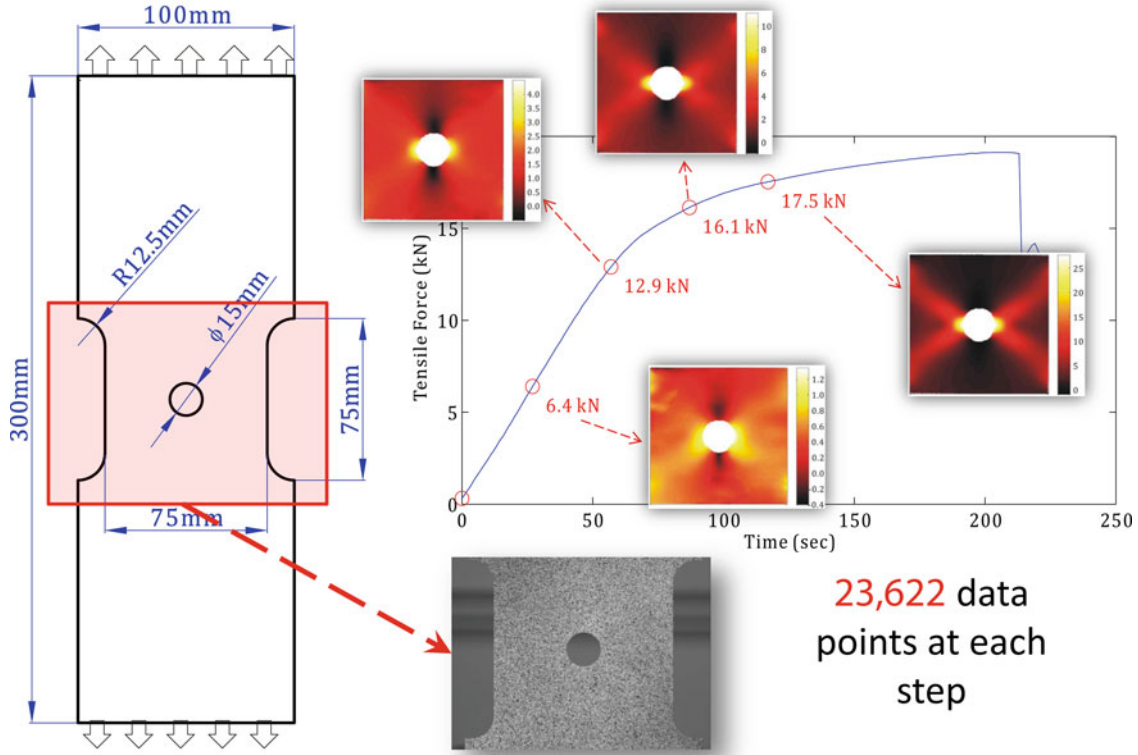
useful for the decomposition of cyclically symmetric displacement or strain fields, which can then be described using a small number of shape features. This generally requires transformation and weighting of the Zernike kernels as explained in the following description of the Adaptive Zernike Moment Descriptor (AZMD). In this particular analysis the quasi static strain map of a square plate with a circular hole in the centre was measured using a DIC system. The full-field strain map with more than 23k data points was reconstructed efficiently using only 15 terms of the AZMD.

#### *Adaptive Zernike Moment Descriptor – Strain Map*

The use of Zernike polynomials is only valid if the definition domain of the shape is the unit circle. To extend the application of ZMD to non-circular domains, modification of the circular ZMD may be carried out to match the actual domain being considered. The modified version is denoted as the AZMD (adaptive ZMD) in this paper.

In this section, the full-field strain distribution on the surface of a test specimen, a thin square plate with a central circular hole, under uniform tensile loading at top and bottom edges is measured by a DIC system. The drawing of the test specimen is shown on the left hand side in Fig. 45.5. The right hand side of Fig. 45.5 shows the curve of the loading history along which four samples (6.4, 12.9, 16.1 and 17.5 kN respectively) are taken. Full-field measurements are captured by a DIC system. The obtained principal strain distributions of the four samples are shown in Fig. 45.5 as well. Each of the strain maps consist of 23,622 data points. The critical regions on the strain maps appears around the central hole and is cyclically symmetric. It is desirable to condense the full-field strain map to form shape feature terms, much fewer than 23,622 data points, without losing significant shape information.

To better capture the strain map of this specific specimen, three operations are made to modify the circular Zernike polynomials. The operations include tailoring the definition domain and transformation and weighting of the radial functions. These procedures are illustrated in Fig. 45.6. The strain map is shown in the middle of the figure. Two particular circular Zernike polynomials (ZP) number 14 and 26 show approximate similarity to the strain map as shown in Fig. 45.6a. The first modification is to ‘cut’ the Zernike polynomials to fit the measured domain of the specimen. After tailoring, the ‘hot-spots’ of the 14th and 26th ZPs shown in Fig. 45.6b are not close enough to the central hole as the strain map shows. It is possible to ‘squeeze’ the adaptive kernels so that the ‘hot-spots’ of the 14th and 26th ZPs are moved towards the central hole.



**Fig. 45.5** Tensile test specimen (*thin square plate with central hole*) using digital image correlation. Loading history is plotted along with four samples

This second modification step is carried out by transforming the coordinates of the radial function as

$$R'_{n,m}(\rho) \equiv R_{n,m}(\rho') = R_{n,m}(\rho^v) \quad (45.18)$$

where  $v \in \mathbb{R}$  and  $0 < v < 1$ ,  $R_{n,m}(\bullet)$  is defined in (45.11).

The coordinate-transformed 14th and 26th ZPs are shown in Fig. 45.6c. Compared to the strain map, the pattern appearing around the outer edges of the transformed 14th and 26th ZPs is too strong. A decaying weighting function is applied to the radial function to erase edge effects and may be expressed as,

$$R_{n,m}^w(\rho, t) \equiv w(\rho, t) R'_{n,m}(\rho) = \rho^t R'_{n,m}(\rho), \quad t \in \mathbb{R}^- \quad (45.19)$$

The weighted version of the 14th and 26th ZPs are shown in Fig. 45.6d. Finally, the tailored, transformed and weighted ZPs are orthogonalised by the Gram-Schmidt approach. It is possible to optimise the coordinate transformation parameter and weighting function parameter for better AZMDs. Details may be found in [37].

An AZMD spectrum, i.e. the projection of a FE strain map onto the orthonormal space constructed by the modified ZPs, is shown in Fig. 45.7. It is seen that the data is concentrated in a small number of AZMD. The modified ZPs corresponding to the first few greatest AZMD are shown in the figure as well. Retaining the most significant terms of the AZMD is sufficient to describe the original strain map. The reconstructed strain map by 15 terms of the AZMD is shown in Fig. 45.7. It is difficult to identify any difference between the original and the reconstructed strain map by visual comparison. Table 45.3 lists the Pearson correlation coefficients between the original strain maps from the four loading samples and the corresponding reconstructed maps from 15 terms of AZMD. All the coefficients in the table are greater than 98 % which indicates that the AZMD is an efficient and succinct shape descriptor for these strain maps. i.e. 15 terms of AZMD encapsulate almost all of the shape information of 23,622 data points. Further analysis using the efficient AZMDs for FE Model updating may be found in [37].

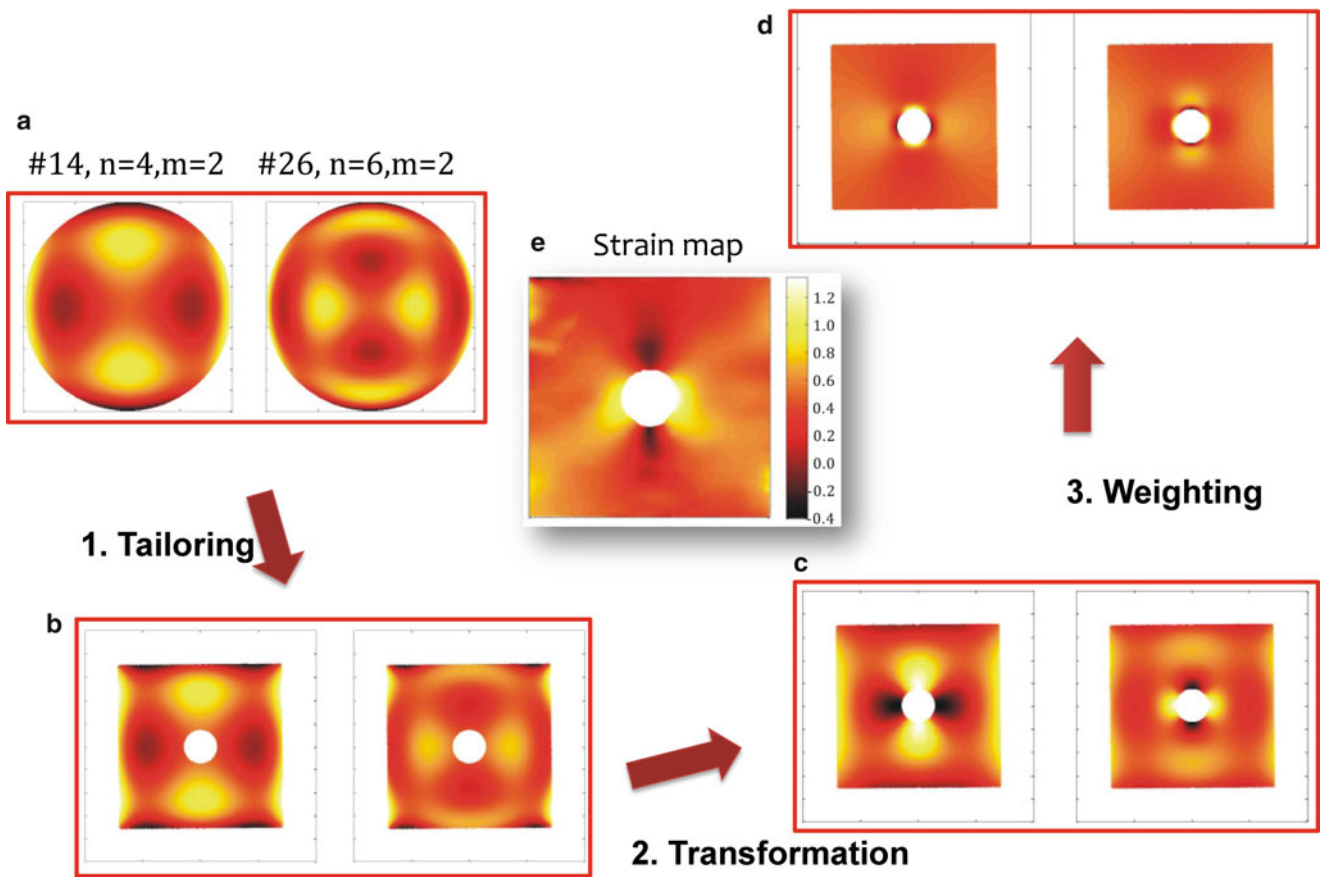


Fig. 45.6 Construction of adaptive Zernike kernel functions

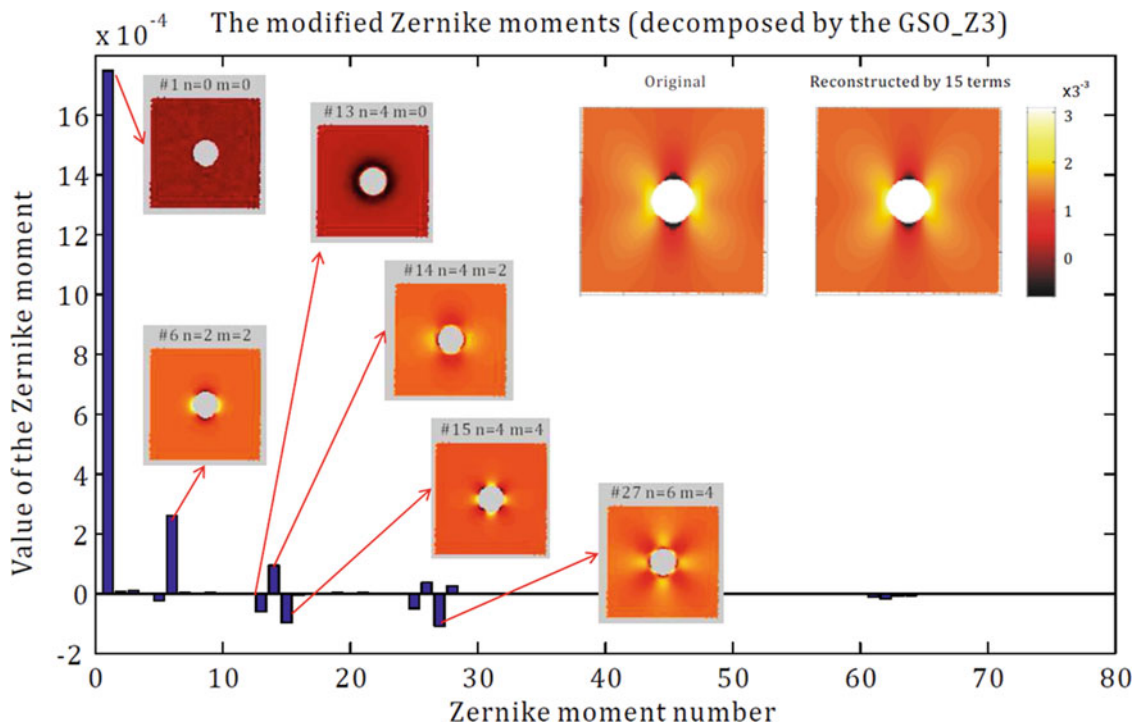
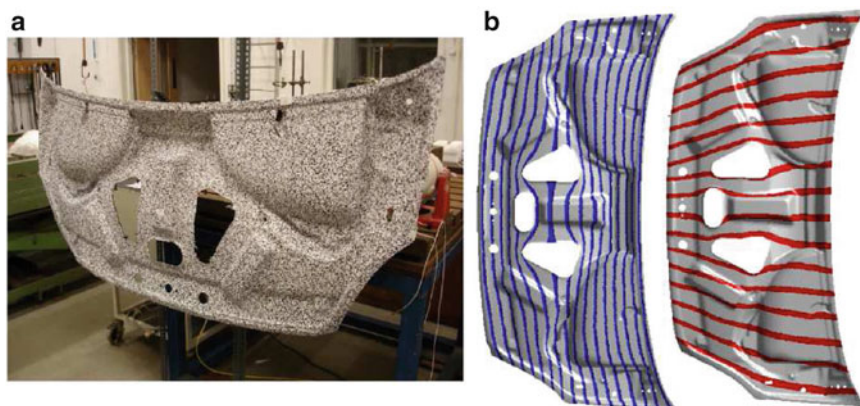


Fig. 45.7 Modified Zernike shape descriptors of a full-field strain map. The DIC measured strain map with more than 22 k data points is reconstructed by 15 terms of shape descriptors

**Table 45.3** Pearson correlation coefficients between the original measured strain maps and the reconstructed strain maps from 15 terms of AZMDs

Loading (kN)	Pearson correlation coefficients
6.4	98%
12.9	99%
16.1	99%
17.5	98%

**Fig. 45.8** (a) Test specimen – a car bonnet covered with speckle pattern paper; (b) surface parameterisation of the bonnet surface, the lines are the curvilinear coordinates of the two surface parameters ( $u, v$ )



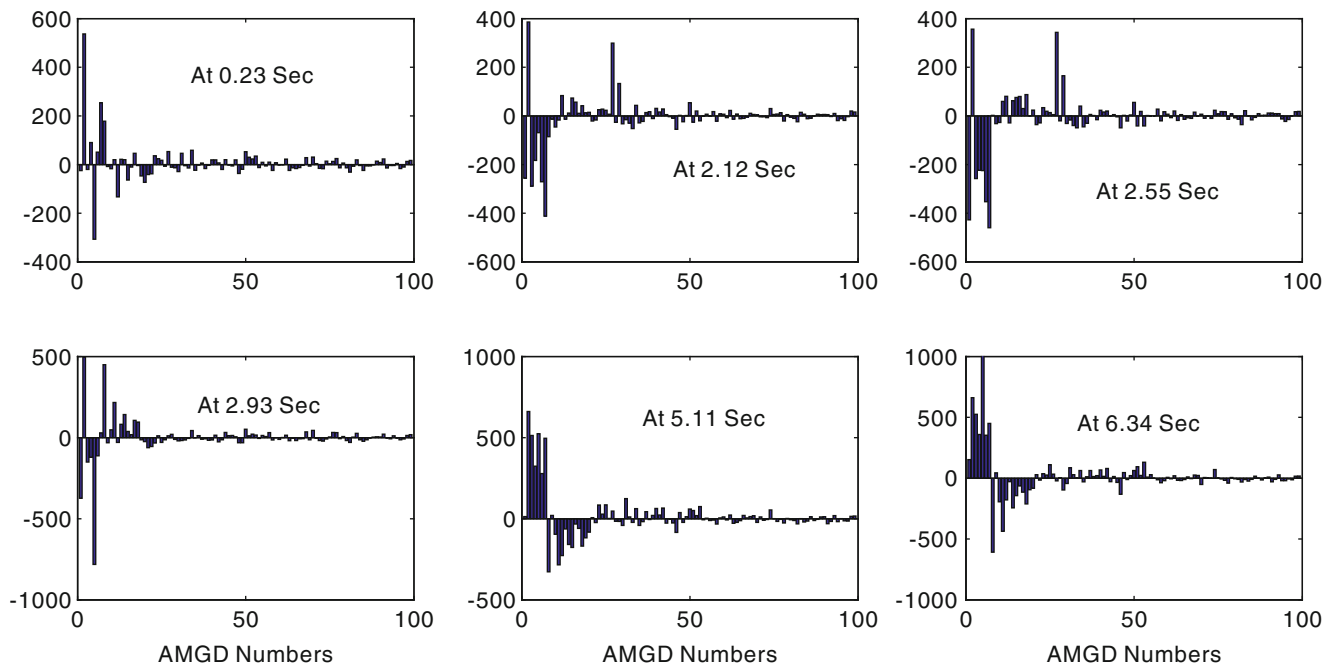
### 45.3.3 Adaptive Geometric Moment Descriptor

Vibration measurement of a car bonnet was carried out using a DIC system as shown in Fig. 45.8a. The bonnet was suspended by two elastic chords to simulate free boundary conditions and single frequency excitation was applied at 32 Hz, close to a predetermined natural frequency, using an electromagnetic shaker. Steady state vibration of the bonnet was measured by the DIC system at a camera speed of 300 fps so that 2,000 temporal steps were measured in total. At each of the measured steps, approximately 2,080 spatial data points are evaluated and orthogonal image decomposition was applied to condense the data. The bonnet has a complex, non-flat surface with irregular boundaries requiring surface parameterisation for mapping to a planar surface and Gram-Schmidt orthogonalisation for the construction of kernel functions. In this case study, discrete conformal parameterisation with fixed boundary method was applied. Results of the mapping are presented in Fig. 45.8b where the iso-curvilinear-coordinate lines obtained from the surface parameterisation are shown. Therefore, the decomposition kernel functions and the bonnet deflections were defined on the domain of the surface parametric coordinates – denoted by  $(u, v)$ . Two-dimensional monomials were defined as the kernel functions – expressed as,

$$g_{n,m}(u, v) \equiv u^n v^m \quad (45.20)$$

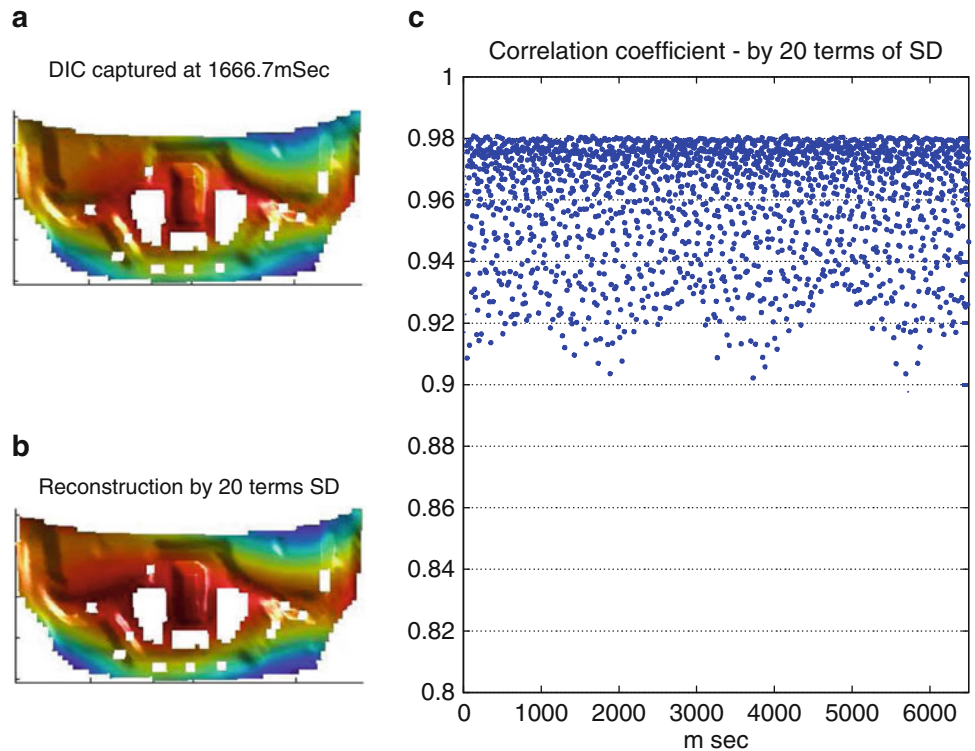
where  $n, m \in \{0, 1, \dots\}$  are monomial orders and  $u, v$  are the parametric coordinates defined on the bonnet surface. The Gram-Schmidt orthogonalisation approach was applied to (45.20) to determine the orthonormal kernel functions – denoted as  $g_{n,m}^{GSO}(u, v)$ . The shape features determined by kernel functions  $g_{n,m}^{GSO}(u, v)$  are known as the adaptive geometric moment descriptors (AGMD). The AGMDs of the transient displacement at 6 temporal samples are shown in Fig. 45.9. The orders are  $n \in [0, 1, \dots, 10]$  and  $m \in [0, 1, \dots, 8]$ , respectively. There are a small number of significant AGMDs mainly concentrated in the lower orders. These were retained to reconstruct the measured vibration shape. Pearson correlation coefficients between the 2,000 point DIC measurement and the reconstruction from 20 AGMD terms are shown in Fig. 45.10c. All the correlation coefficients are greater than 90 % and most are close to 98 %. One pair of the original and reconstructed deflection patterns is illustrated in Fig. 45.10a, b. It is seen that the reconstructed pattern is a smoothed version of the original deflection pattern with good similarity. Thus, the full-field measured vibration data (>2,000 data points) may be effectively condensed to a small number of shape features (20 AGMDs). Further analysis, including full-field modal identification of the car bonnet using AGMDs is elaborated by [36].





**Fig. 45.9** Adaptive geometric moment descriptors at six measured instants

**Fig. 45.10** (a) Transient deflection of the bonnet at a time instant; (b) reconstructed deflection pattern using 20 AGMD terms; (c) Pearson’s correlation coefficients between the original and the reconstructed shape patterns for all measured steps



### 45.4 Conclusions

The application of optical techniques enables non-contact full-field measurement in experimental mechanics. To utilise highly information-redundant full-field data, image decomposition approaches are introduced to extract features that are both effective and succinct in representing the raw data accurately with a small number of terms. The selection of decomposition



kernels from analytic functions is intuitive but limited to regular domains such as rectangles and circles. However, the surfaces of engineering structures are generally curved and their domains are irregular. They require special treatment using surface parameterisation for mapping to planar surfaces and Gram-Schmidt orthogonalisation for the construction of kernel functions on domains with irregular boundaries. Further structural analysis, including finite element model updating, modal testing, non-linearity detection and uncertainty analysis may then be carried out by using the obtained shape features. The proposed approach has been elaborated in a number of case studies.

**Acknowledgements** The authors wish to acknowledge the support of EC FP7 project ADVISE (Advanced Dynamic Validations using Integrated Simulation and Experimentation) – grant no. 218595. Several figures and tables were reprinted from references [37] and [38] with permission from Elsevier. Several figures and tables were reprinted from: W. Wang and J.E. Mottershead, Adaptive moment descriptors for full-field strain and displacement measurements, *Journal of Strain Analysis in Engineering Design*, 48(1), 2013, 16–35 (published by SAGE)

## References

1. Sutton MA, Cheng Mingqi, Peters WH, Chao YJ, McNeill SR (1986) Application of an optimized digital correlation method to planar deformation analysis. *Image Vis Comput* 4(3):143–150
2. Sutton MA, Wolters WF, Peters WH, Ranson WF, McNeill SR (1983) Determination of displacements using an improved digital correlation method. *Image Vis Comput* 1(3):133–139
3. Tiwari V, Sutton MA, McNeill SR, Shaowen Xu, Xiaomin Deng, Fourney WL, Bretall D (2009) Application of 3D image correlation for full-field transient plate deformation measurements during blast loading. *Int J Impact Eng* 36(6):862–874
4. Bay BK, Smith TS, Fyhrie DP, Saad M (1999) Digital volume correlation: three-dimensional strain mapping using X-ray tomography. *Exp Mech* 39(3):217–226
5. Bay BK (2008) Methods and applications of digital volume correlation. *J Strain Anal Eng Des* 43(8):745–760
6. Forsberg F, Sjo M, Mooser R, Hack E, Wyss P (2010) Full three-dimensional strain measurements on wood exposed to three-point bending: analysis by use of digital volume correlation applied to synchrotron radiation micro-computed tomography image data. *Strain* 46:47–60
7. Nurse AD, Patterson ES (1990) Photoelastic technique to predict the direction of edge crack extension using blunt cracks. *Int J Mech Sci* 32:253–264
8. Patterson EA, Wang ZF (1991) Towards full field automated photoelastic analysis of complex components. *Strain* 27(2):49–53
9. Patterson EA (1988) Automated photoelastic analysis. *Strain* 24(1):15–20
10. Pedrini G, Osten W, Gusev ME (2006) High-speed digital holographic interferometry for vibration measurement. *Appl Opt* 45(15):3456
11. Whelan MP, Albrecht D, Hack E, Patterson EA (2008) Calibration of a speckle interferometry full-field strain measurement system. *Strain* 44(2):180–190
12. Dulieu-Barton JM, Stanley P (1998) Development and applications of thermoelastic stress analysis. *J Strain Anal Eng Des* 33(2):93–104
13. Pitarresi G, Patterson EA (2003) A review of the general theory of thermoelastic stress analysis. *J Strain Anal Eng Des* 38:405–417
14. Antonini M, Barlaud M, Mathieu P, Daubechies I (1992) Image coding using wavelet transform. *IEEE Trans Image Process* 1(2):205–220
15. Daubechies I (1992) Ten lectures on wavelets. SIAM: Society for Industrial and Applied Mathematics, Philadelphia
16. Mallat SG, Hwang WL (1992) Singularity detection and processing with wavelets. *IEEE Trans Info Theory* 38(2):617–643
17. Proakis JG, Manolakis KK (2006) Digital signal processing, principles, algorithms, and applications. Prentice Hall, Upper Saddle River
18. Donoho DL, Vetterli M, DeVore RA, Daubechies I (1998) Data compression and harmonic analysis. *IEEE Trans Info Theory* 44(6):2435–2476
19. Candès EJ, Donoho DL (1999) Ridgelets: a key to higher-dimensional intermittency? *Philos Trans R Soc A Math Phys Eng Sci* 357(1760):2495–2509
20. Candès EJ, Donoho DL (1999) Curvelets: a surprisingly effective nonadaptive representation for objects with edges. In: Schumaker LL et al (eds) *Curves and surfaces*. Vanderbilt University Press, Nashville, pp 1–10
21. Candès EJ, Donoho DL (2004) New tight frames of curvelets and optimal representations of objects with piecewise  $C^2$  singularities. *Commun Pure Appl Math* 57(2):219–266
22. Do MN, Vetterli M (2005) The contourlet transform: an efficient directional multiresolution image representation. *IEEE Trans Image Process* 14(12):2091–2106
23. Meyer FG, Coifman RR (1997) Brushlets: a tool for directional image analysis and image compression. *Appl Comput Harmon Anal* 187(4):147–187
24. Hosny KM (2011) Image representation using accurate orthogonal Gegenbauer moments. *Pattern Recognit Lett* 32:795–804
25. Hosny KM (2012) Fast computation of accurate Gaussian-Hermite moments for image processing applications. *Digit Signal Process* 1:1–10
26. Ming-Kuei Hu (1962) Visual pattern recognition by moment invariants. *IEEE Trans Info Theory* 8(2):179–187
27. Mukundan R, Ong SH, Lee PA (2001) Image analysis by Tchebichef moments. *IEEE Trans Image Process* 10(9):1357–1364
28. Teague MR (1980) Image analysis via the general theory of moments. *J Opt Soc Am* 70(8):920
29. Pew-Thian Yap, Paramesran R, Seng-Huat Ong (2003) Image analysis by Krawtchouk moments. *IEEE Trans Image Process* 12(11):1367–1377
30. Pew-Thian Yap, Paramesran R, Seng-Huat Ong (2007) Image analysis using Hahn moments. *IEEE Trans Pattern Anal Mach Intell* 29(11):2057–2062
31. Hongqing Zhu, Huazhong Shu, Jian Zhou, Limin Luo, Coatrieux JL (2007) Image analysis by discrete orthogonal dual Hahn moments. *Pattern Recognit Lett* 28(13):1688–1704
32. Zhu H, Shu H, Liang J, Luo L, Coatrieux J (2007) Image analysis by discrete orthogonal Racah moments. *Signal Process* 87(4):687–708
33. Desbrun M, Meyer M, Alliez P (2002) Intrinsic parameterizations of surface meshes. *Comput Graph Forum* 21:209–218

34. Floater MS, Hormann K (2005) Surface parameterization: a tutorial and survey. In: Dodgson NA, Floater MS, Sabin MA (eds) *Advances in multiresolution for geometric modelling*. Springer, Heidelberg, pp 157–186
35. Jolliffe IT (2002) *Principal component analysis*, 2nd edn. Springer, New York
36. Weizhuo Wang, Mottershead JE, Mares C (2009) Mode-shape recognition and finite element model updating using the Zernike moment descriptor. *Mech Syst Signal Process* 23(7):2088–2112
37. Weizhuo Wang, Mottershead JE, Sebastian CM, Patterson EA (2011) Shape features and finite element model updating from full-field strain data. *Int J Solids Struct* 48(11–12):1644–1657
38. Weizhuo Wang, Mottershead JE, Siebert T, Pipino A (2012) Frequency response functions of shape features from full-field vibration measurements using digital image correlation. *Mech Syst Signal Process* 28:333–347
39. Mallat SG, Zhang Z (1993) Matching pursuits with time-frequency dictionaries. *IEEE Trans Signal Process* 41(12):3397–3415
40. Persoon E, King-Sun Fu (1977) Shape discrimination using fourier descriptors. *IEEE Trans Syst Man Cybern* 7(3):170–179
41. Yunlong Sheng, Lixin Shen (1994) Orthogonal Fourier-Mellin moments for invariant pattern recognition. *JOSA A* 11(6):1748–1757
42. Le E, Mallat SG (2005) Sparse geometric image representations with bandelets. *IEEE Trans Image Process* 14(4):423–438
43. Koekoek R, Swarttouw RF (1998) The Askey-scheme of hypergeometric orthogonal polynomials and its q-analogue. Technical report No. 98-17
44. Rubinstein R, Bruckstein AM, Elad M (2010) Dictionaries for sparse representation modeling. *Proc IEEE* 98(6):1045–1057
45. Daubechies I (1988) Time-frequency localization operators: a geometric phase space approach. *IEEE Trans Info Theory* 34(4):605–612
46. Chen SS, Donoho DL, Saunders MA (1998) Atomic decomposition by basis pursuit. *SIAM J Sci Comput* 20(1):33
47. Coifman RR, Wickerhauser MV (1992) Entropy-based algorithms for best basis selection. *IEEE Trans Info Theory* 38(2):713–718

# Chapter 46

## Model Updating Using Shape Descriptors from Full-Field Images

Weizhuo Wang, John E. Mottershead, Eann Patterson, Thorsten Siebert, and Alexander Ihle

**Abstract** The comparison of structural responses (natural frequencies, mode shapes or strain maps) between predictions and measurements is an important step in finite element (FE) model updating. Full-field measurement techniques such as digital image correlation (DIC) provide detailed, global displacement data. It is necessary to compress huge amounts of full-field data before implementing the comparison procedures. Image decomposition using orthogonal kernel functions is one of the most common approaches. Appropriate selection or construction of the kernels generates shape feature terms capable of accurate image reproduction. Thus, the discrepancies between data and FE predictions may be assessed by using distance measures between the shape feature vectors. Two examples of model updating using shape features are described. In the first example vibration mode shapes of a composite panel from a structure to be deployed in outer space are measured by a DIC system. FE model updating is carried out using natural frequencies and Tchebichef moment descriptors. In the second example a square plate with a circular hole subject to a uniaxial tensile load is considered. Model updating of nonlinear elasto-plastic material properties is carried out using modified Zernike moment descriptors.

**Keywords** Finite model updating • Shape features • Digital image correlation • Image decomposition • Moment descriptors

### 46.1 Introduction

Finite element (FE) analysis is one of the most powerful numerical approaches for solving engineering problems. However, errors (numerical and modeling [1, 2]) are inevitable due to the nature of the FE method. It is crucial to validate FE predictions using measured responses. The emergence of optical sensing technologies [3–6] makes full-field validation possible. The validation process involves data comparison. The full-field measured data are usually noisy and information redundant. It is necessary to compress the full-field data while retaining the most important information in the form of ‘shape features’. Wang et al. [7, 8] investigated a number of techniques to compare the full-field mode shapes based on shape features obtained by integral transformation e.g., the wavelet transform. It is found that appropriate selection or construction of transform kernels usually produces efficient and succinct shape features. Detailed discussions of shape feature extraction based on functional decomposition may be found in [9] (IMAC XXXI paper 422) or [10]. The full-field mode shape comparisons of thousands or even millions of data points can then be transformed into a measure of distance between the shape feature vectors with only small number of terms. The model validation approach may then be carried out by comparing shape features rather than

---

W. Wang  
School of Engineering, Manchester Metropolitan University, Manchester, UK

J.E. Mottershead (✉) • E. Patterson  
School of Engineering, University of Liverpool, Liverpool, UK  
e-mail: [j.e.mottershead@liv.ac.uk](mailto:j.e.mottershead@liv.ac.uk)

T. Siebert  
Dantec Dynamics GmbH, Ulm, Germany

A. Ihle  
High Performance Space Structure Systems GmbH, Munich, Germany

raw data. Discrepancies of shape features between FE prediction and full-field measurement might be good indicators for FE model parameterization and updating. Inverse methods may then be employed to correct the FE model iteratively [11, 12].

The general form of iterative model updating approach is discussed in Sect. 46.2. Two case studies of updating using shape features from full-field measurement are presented in Sects. 46.3 and 46.4 respectively. Conclusions are drawn in Sect. 46.5.

## 46.2 Iterative Model Updating

The iterative updating equation with weighting matrices for output vector and parameters may be expressed as [2],

$$\boldsymbol{\theta}_{(i+1)} = \boldsymbol{\theta}_{(i)} + \left[ \mathbf{G}_{(i)}^T \mathbf{W}_{\varepsilon\varepsilon} \mathbf{G}_{(i)} + \mathbf{W}_{\theta\theta} \right]^{-1} \left\{ \mathbf{G}_{(i)}^T \mathbf{W}_{\varepsilon\varepsilon} \{ \mathbf{x}_{(m)} - \mathbf{x}_{(i)} \} - \mathbf{W}_{\theta\theta} \{ \boldsymbol{\theta}_{(i)} - \boldsymbol{\theta}_{(0)} \} \right\} \quad (46.1)$$

where  $\boldsymbol{\theta}_{(i+1)}$  and  $\boldsymbol{\theta}_{(i)}$  are  $p \times 1$  vectors of structural modification parameters at the current and next iterations;  $\mathbf{x}_{(m)}$  and  $\mathbf{x}_{(i)}$  denote the  $q \times 1$  responses of measured and predicted output vectors (consisting of, e.g. natural frequencies, strain, displacement or shape features etc.) at the current iteration;  $\mathbf{W}_{\varepsilon\varepsilon}$  is the weighting matrix for the errors of output vectors;  $\mathbf{W}_{\theta\theta}$  is the weighting matrix for the parameters;  $\mathbf{G}_{(i)}$  is the sensitivity matrix at the current iteration, written as

$$\mathbf{G}_{(i)} = \left[ \frac{\partial x_k}{\partial \theta_\ell} \right]_{\theta=\theta_{(j)}}; k = 1, 2, \dots, q; \ell = 1, 2, \dots, p \quad (46.2)$$

It is usual to apply scaling so that the prediction errors are divided by the prediction and the parameter errors are divided by the initial values of the parameters. Thus the sensitivity equation may be expressed as,

$$\begin{bmatrix} \frac{\partial x_1}{\partial \theta_1} \frac{\theta_{(0),1}}{x_{(0),1}} & \dots & \frac{\partial x_1}{\partial \theta_\ell} \frac{\theta_{(0),\ell}}{x_{(0),\ell}} & \dots & \frac{\partial x_1}{\partial \theta_p} \frac{\theta_{(0),p}}{x_{(0),p}} \\ \vdots & & \vdots & & \vdots \\ \frac{\partial x_k}{\partial \theta_1} \frac{\theta_{(0),1}}{x_{(0),k}} & \dots & \frac{\partial x_k}{\partial \theta_\ell} \frac{\theta_{(0),\ell}}{x_{(0),k}} & \dots & \frac{\partial x_k}{\partial \theta_p} \frac{\theta_{(0),p}}{x_{(0),k}} \\ \vdots & & \vdots & & \vdots \\ \frac{\partial x_q}{\partial \theta_1} \frac{\theta_{(0),1}}{x_{(0),q}} & \dots & \frac{\partial x_q}{\partial \theta_\ell} \frac{\theta_{(0),\ell}}{x_{(0),q}} & \dots & \frac{\partial x_q}{\partial \theta_p} \frac{\theta_{(0),p}}{x_{(0),q}} \end{bmatrix}_{(j)} \begin{bmatrix} \frac{\delta \theta_1}{\theta_{(0),1}} \\ \vdots \\ \frac{\delta \theta_\ell}{\theta_{(0),\ell}} \\ \vdots \\ \frac{\delta \theta_p}{\theta_{(0),p}} \end{bmatrix}_{(j)} = \begin{bmatrix} \frac{\delta x_1}{x_{(0),1}} \\ \vdots \\ \frac{\delta x_k}{x_{(0),k}} \\ \vdots \\ \frac{\delta x_q}{x_{(0),q}} \end{bmatrix}_{(j)} \quad (46.3)$$

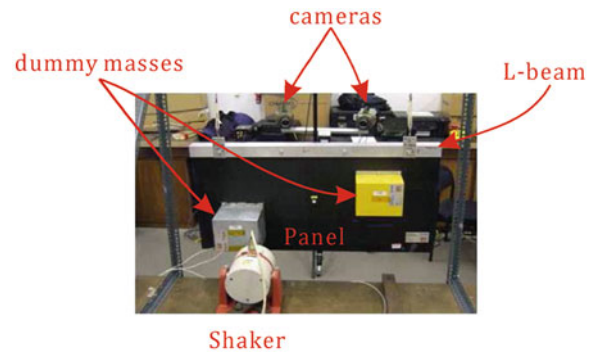
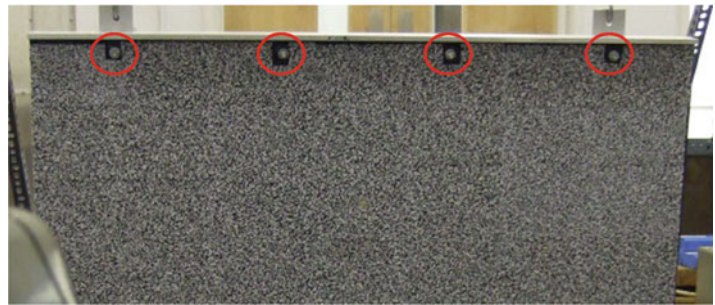
where  $\boldsymbol{\theta}_{(0)} = \{ \theta_{(0),1}, \dots, \theta_{(0),\ell}, \dots, \theta_{(0),p} \}^T$  and  $\mathbf{x}_{(0)} = \{ x_{(0),1}, \dots, x_{(0),k}, \dots, x_{(0),q} \}^T$  are the initial unknown parameter and prediction vectors respectively.

## 46.3 Updating A Composite Panel Using Features of Mode Shapes

### 46.3.1 Vibration Mode Shape Measurement Using DIC

In this case study, full-field vibration mode shapes of a composite sandwich panel were captured by using the Dantec Dynamics 3D High-Speed Image Correlation System (Q-450: the number of pixels was  $1,280 \times 800$ , the frame rate was 2.500/s and the exposure time was  $300 \mu\text{s}$ ). The panel with dimensions of  $1,000 \times 500 \times 25$  mm was connected with an L-shaped aluminium beam by four bolted joints as shown in Fig. 46.1. In order to capture effective images for the DIC algorithm, papers with speckle patterns were pasted on one side of the panel surface as shown in Fig. 46.2. It was checked that the additional paper did not change the modal-test results. Two dummy-mass boxes may be attached to the other side of the panel as shown. Thus two cases are defined. The first case denoted as  $P_{ND}$  is the panel without the two dummy mass boxes. The other one,  $P_{WD}$ , is the case including the masses.

The first few natural frequencies for both cases  $P_{ND}$  and  $P_{WD}$  were initially determined by accelerometers using a hammer test. Full-field measurements were then obtained by using the DIC system with cyclic excitations at natural frequencies 124.6 Hz (mode 1), 331.9 Hz (mode 3) and 473.6 Hz (mode 5) for case  $P_{ND}$  and 103.9 Hz (mode 1) and 134.2 Hz (mode 2) for case  $P_{WD}$ . Steady-state displacement patterns at cyclic excitations are recorded as full-field mode shapes.

**Fig. 46.1** Test configuration**Fig. 46.2** Speckle pattern stuck on the panel surface (*circles highlight the four bolted joints*)**Table 46.1** DIC mode shapes correlation coefficients between original and reconstructed images

Mode shapes	The greatest terms retained	Correlation coefficients
$P_{ND}$ mode 1	2	99.7%
$P_{ND}$ mode 3	5	99.7%
$P_{ND}$ mode 5	9	99.5%
$P_{WD}$ mode 1	5	99.2%
$P_{WD}$ mode 2	7	99.4%

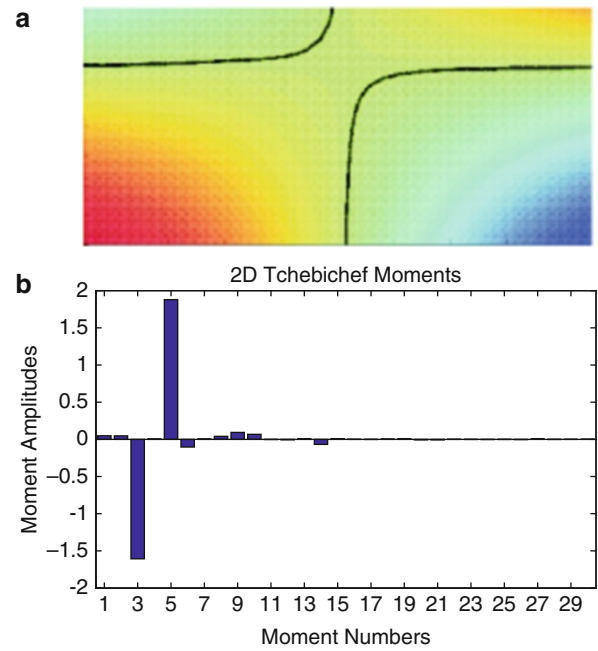
### 46.3.2 Construction of Shape Features

The three obtained mode shapes for panel  $P_{ND}$  are shown in Figs. 46.3a, 46.4a and 46.5a respectively. Each of these full-field mode shapes consists more than 1,000 data points. The Tchebichef moment descriptor was applied to extract features from the full-field mode shapes. Figures 46.3b, 46.4b and 46.5b show the Tchebichef features corresponding to the mode shapes. The first two mode shapes of the panel  $P_{WD}$  with dummy masses are shown in Fig. 46.6. The corresponding Tchebichef shape features are displayed in the figure as well. It is seen that only a small number of the Tchebichef moments are significant. Retaining a small number of the most significant Tchebichef features is seen to be sufficient to describe the mode shapes. The correlation coefficients between the measured mode shape and the reconstruction by the first few greatest Tchebichef features are close to unity as listed in Table 46.1. Similarly, the full-field mode shapes of the panel with dummy mass ( $P_{WD}$ ) may be effectively represented by Tchebichef features. Therefore, it is seen that full field vibration mode shapes with  $10^3 \sim 10^4$  points can be effectively represented by only  $10^0$  Tchebichef-feature terms.

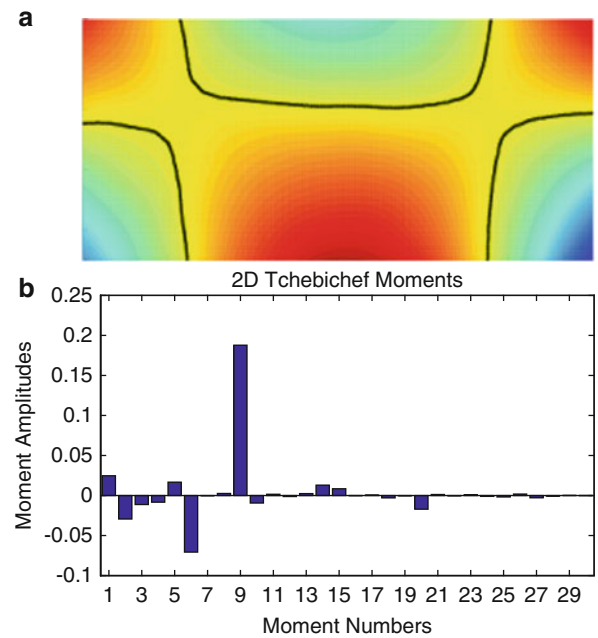
### 46.3.3 Comparison of Feature Vectors

Finite element models for cases  $P_{ND}$  and  $P_{WD}$  were constructed as shown in Fig. 46.7a, b. The four bolted joints that connect the L-shaped aluminium beam and the sandwich composite panel were modelled as rigid connections and one leg of the L-beam was coplanar with the panel (see Fig. 46.7c). Full-field analytical mode shapes were obtained from nodal displacements and element shape functions. The Tchebichef feature vectors for the finite element mode shapes were obtained

**Fig. 46.3** Mode shape and the Tchebichef moments of DIC measurement mode 1 –  $P_{ND}$



**Fig. 46.4** Mode shape and the Tchebichef moments of DIC measurement mode 3 –  $P_{ND}$

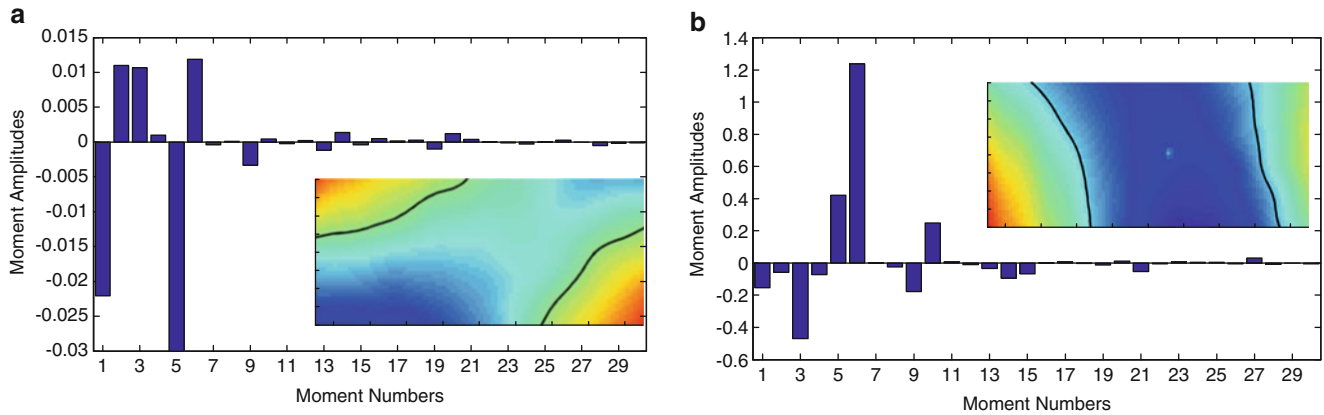
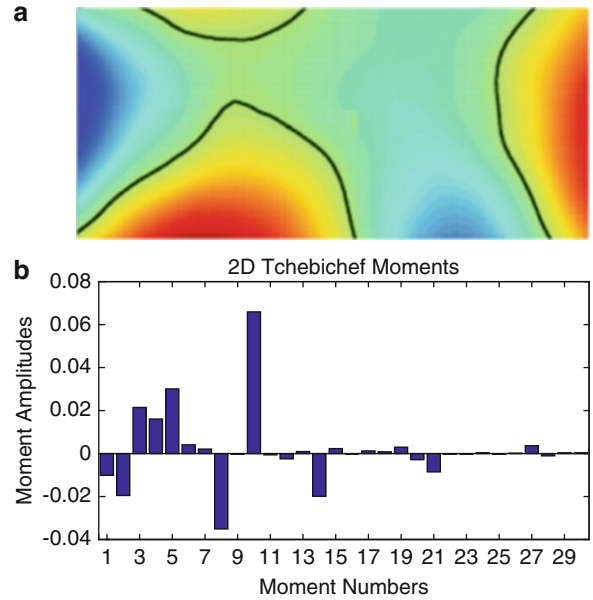


by the same procedures as described previously for the full-field DIC measurement. Figure 46.8 shows the auto correlation matrix of the Tchebichef feature vectors for the FE mode shapes of the panel without dummy masses  $P_{ND}$ . It is clear that this matrix is close to the identity matrix, as it is supposed to be.

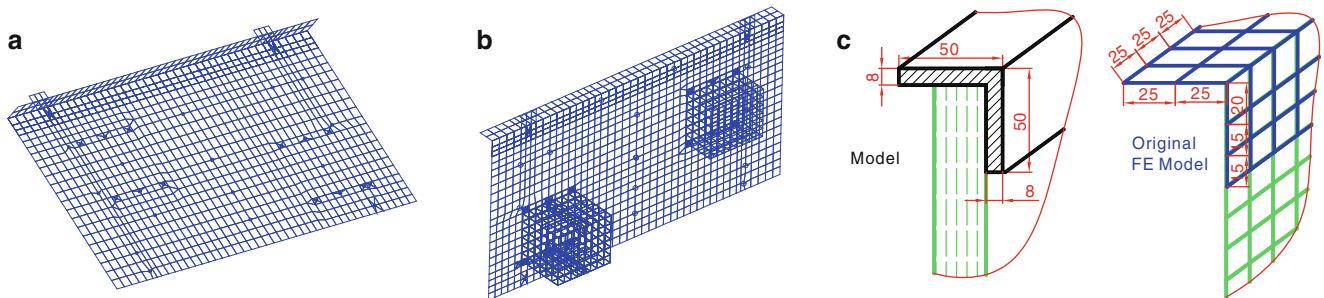
To validate the finite element models based on full field mode shapes, the FE Tchebichef feature vectors are compared with the DIC measured feature vectors as shown in Fig. 46.9a, b for the composite panel with and without dummy masses respectively. Cosine distances between vectors were employed. The closer the cosine distance is to unity the more similar are the shapes. It is seen that the first two DIC modes correlate well with the FE modes. However, the FE mode 5 of  $P_{ND}$  is slightly different from the DIC measured mode 5 (473.2 Hz) as indicated by the 0.75 cosine distance shown in the figure. It is possible to correct the FE model by the iterative updating procedure using the Tchebichef features.



**Fig. 46.5** Mode shape and the Tchebichef moments of DIC measurement mode 5 –  $P_{ND}$



**Fig. 46.6** Mode shapes and the Techbichef descriptors of the panel with dummy masses from DIC measurement, (a) mode 1, (b) mode 2

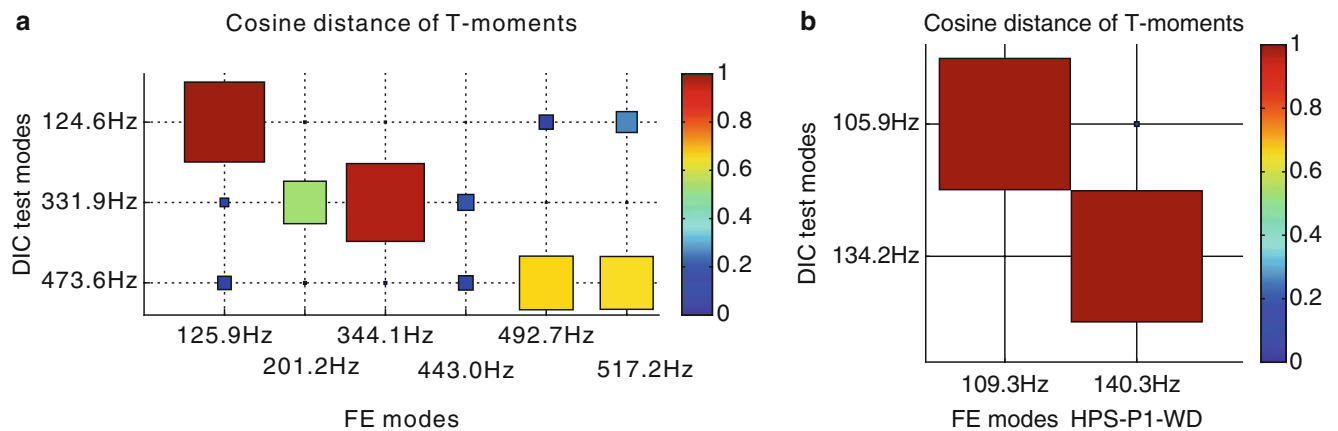
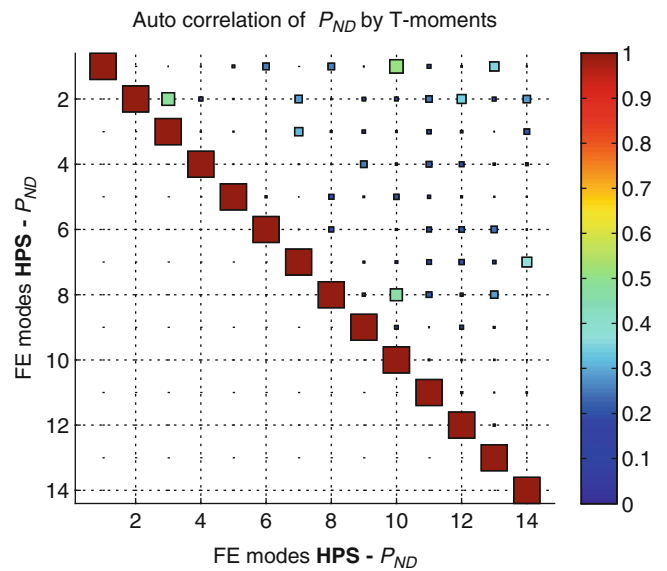


**Fig. 46.7** Finite element meshes of the panel and dummy masses. (a) Case  $P_{ND}$ ; (b) case  $P_{WD}$ ; (c) cross-section dimensions of the L-beam and the panel

### 46.3.4 Model Modification and Parameterization

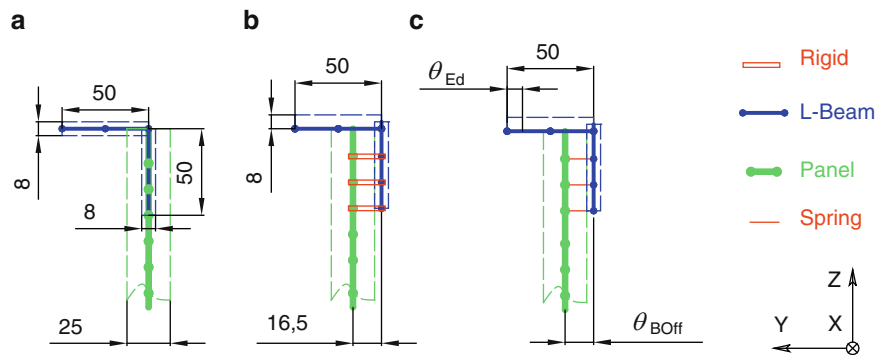
For model updating, it is crucial to identify the factors that cause the discrepancy. Constraints, material properties and geometric dimensions are usually the most important aspects to be considered. For this particular FE model, a number of possible modifications, as shown in Fig. 46.10, including finite element offset nodes, changes to the cross-section of the L-beam, and spring connections to represent the four bolted joints between the L-beam and composite panel will be considered.

**Fig. 46.8** Auto correlation of mode shapes for case  $P_{ND}$  based on the Tchebichef moment descriptors



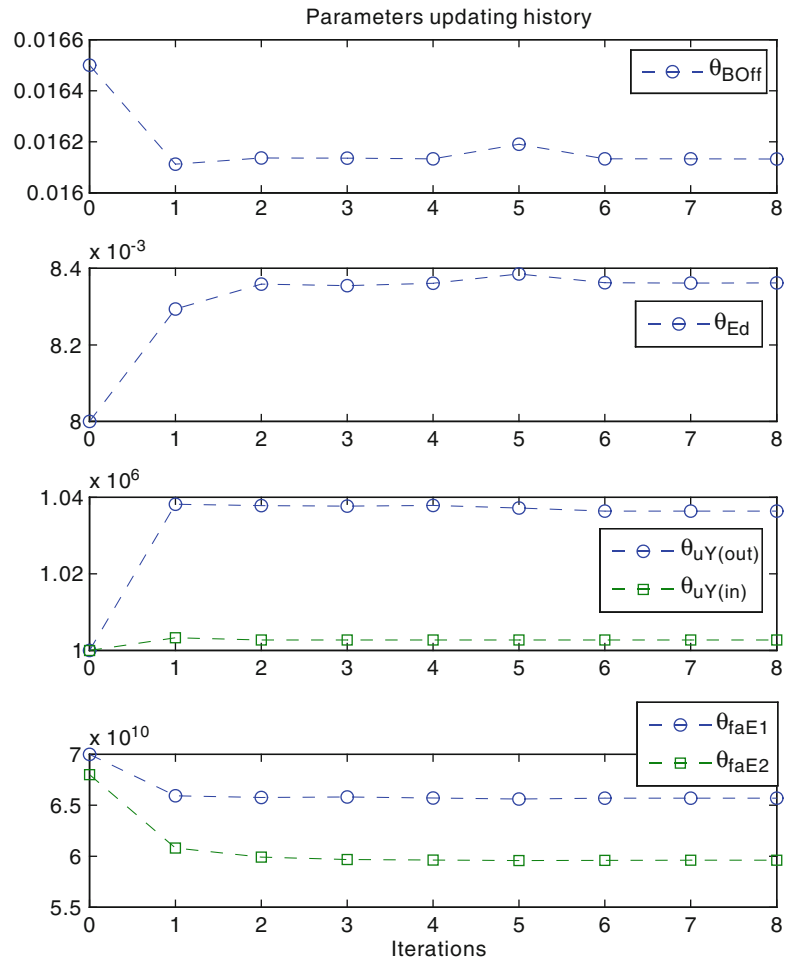
**Fig. 46.9** Cosine distances of the Tchebichef feature vectors of FE mode shapes and the DIC measurement. (a) Cases  $P_{ND}$ ; (b)  $P_{WD}$

**Fig. 46.10** Modification and parameterisation of the FE model



Thus, modifications of the FE model are defined as: Offset  $\theta_{BOff}$  of the L-beam from the panel as shown in Fig. 46.10c; cut short the top edge  $\theta_{Ed}$  of the L-beam to cancel out the overlapped effect at the corner; since the facing sheet of the composite is an orthotropic material, it is possible to parameterise the Young's modulus,  $\theta_{faE1}$  and  $\theta_{faE2}$  along the orthogonal directions '1' and '2' respectively. A further modification of the bolted-joints connection is considered. The complete rigid connections between the nodes of the L-beam and the panel are modified as translational spring connections along the Y-axis and rigid

**Fig. 46.11** Parameter updating history using shape features only



constraints for X- and Z-axes as shown in Fig. 46.10c. Therefore, a parameter  $\theta_{uY}$  represents the bolted-joint connections by spring stiffnesses, with each spring having the same value.

The modifications are summarized as,

- L-beam offset (with X- and Z-directional rigid connection);
- Cut short the top edge of the L-beam;
- Material properties of the panel facing sheet;
- Spring connection stiffnesses – inner and outer.

Therefore, the parameters for the present updating process are

$$\boldsymbol{\theta} = \{ \theta_{BOff} \ \theta_{Ed} \ \theta_{uY(out)} \ \theta_{uY(in)} \ \theta_{faE1} \ \theta_{faE2} \}^T \quad (46.4)$$

which may be substituted to (46.1) as input. Only the shape features are considered as output of this updating process – denoted as  $\mathbf{x}^{SF}$  and including only the few most important Tchebichef moments is necessary.

### 46.3.5 Updated Results

The iterative updating process converged and the histories of the parameters are shown in Fig. 46.11. Natural frequencies and mode shapes of the updated model are compared with the measurements and listed in Table 46.2. As shown in the table, the mean natural frequency error is reduced to 1.94% (from 4.97% originally) with 2.59% standard deviation whilst the mode shapes 1, 3 and 5 remain highly similar, with the three cosine distances all greater than 0.958.

**Table 46.2** Model modification and updating

	Test	Original FE model		UP(SF only)		
		Hz	Relative error (%)	Hz	Relative error (%)	Hz
Natural frequencies	1	(125.9)	0.01	(125.9)	1.10	(127.3)
	2	(195.1)	3.16	(201.2)	-2.45	(190.3)
	3	(328.8)	4.66	(344.1)	0.11	(329.1)
	4	(428.5)	3.38	(443.0)	5.56	(452.4)
	5	(472.1)	4.37	(492.7)	3.83	(490.2)
	6	(507.5)	1.90	(517.2)	1.96	(517.5)
	7	(660.4)	-1.70	(649.2)	0.17	(661.5)
	8	(700.2)	5.61	(739.5)	0.72	(705.3)
	9	(864.0)	-9.28	(783.8)	-2.84	(839.5)
	10	(905.2)	15.61	(1,046.4)	-0.68	(899.0)
	absMean	4.97		1.94		
	std	6.26		2.59		
Shape		Cosine distance		Cosine distance		
	DIC vs. FE mode1	0.994		0.996		
	DIC vs. FE mode3	0.972		0.958		
	DIC vs. FE mode5	0.752		0.958		
Parameters		Converged to				
	$\theta_{\text{BOff}}(m)$			0.0161		
	$\theta_{\text{Ed}}(m)$			0.0084		
	$\theta_{\text{uy(out)}}(N/m)$			1.035E + 06		
	$\theta_{\text{uy(in)}}(N/m)$			1.003E + 06		
	$\theta_{\text{faE1}}(\text{Pa})$			6.549E + 10		
	$\theta_{\text{faE2}}(\text{Pa})$			5.955E + 10		

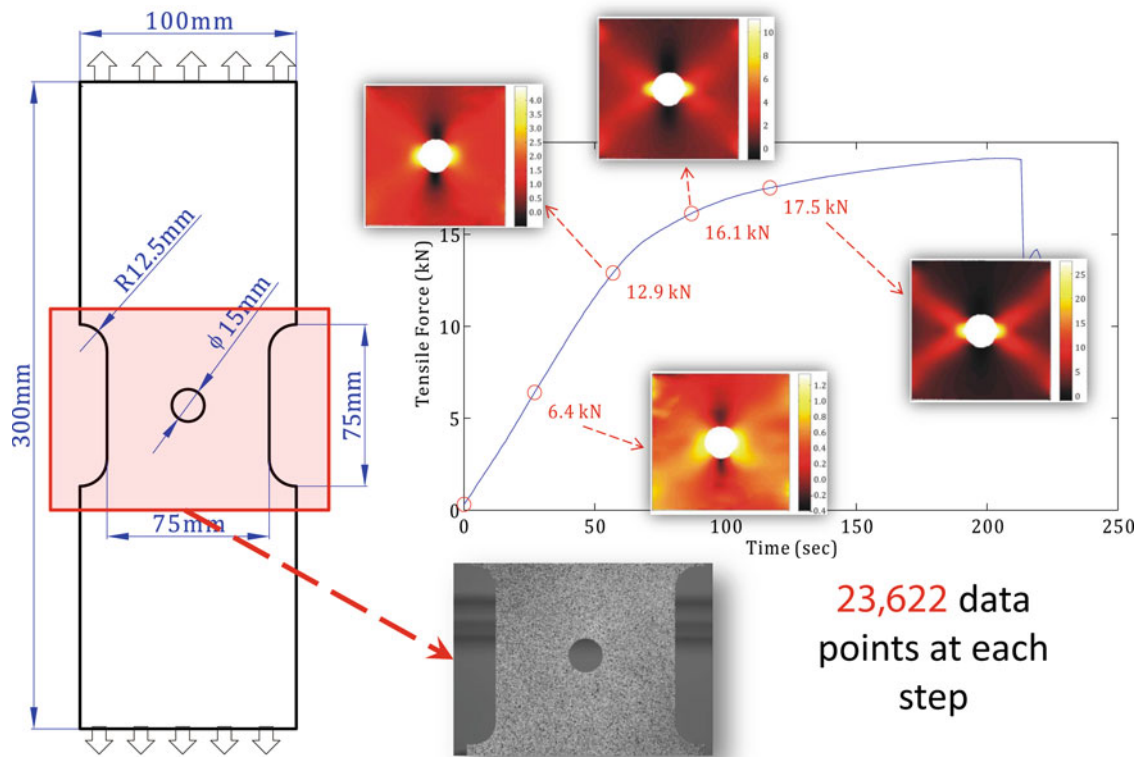
**Table 46.3** Natural frequency comparisons for the panel with dummy masses

	IABG test	FE $P_{WD}$ Original model		FE $P_{WD}$ Updated model		
		Hz	Relative error (%)	Hz	Relative error (%)	Hz
Natural frequencies	1	(106.2)	2.9	(109.3)	-0.3	(105.9)
	2	(134.2)	4.6	(140.3)	-2.0	(131.5)
	3	(215.9)	5.6	(227.9)	2.3	(220.9)
	4	(268.7)	5.1	(282.3)	-1.8	(263.9)
	5	(362.9)	1.4	(368.1)	-3.5	(350.2)
	6	(401.2)	5.0	(421.4)	0.3	(402.5)
	7	(538.1)	9.2	(587.5)	3.5	(557.0)
	8	(568.0)	9.8	(623.9)	5.6	(599.9)
	9	(652.7)	10.2	(719.0)	3.5	(675.2)
	10	(727.5)	12.4	(817.6)	4.4	(759.6)
	absMean	7.03		2.99		
	std	3.51		3.11		

Also, the natural frequency errors between the original FE model and measurements for case  $P_{WD}$ , i.e. two dummy masses attached to the panel, are shown in Table 46.3. It is seen that the natural frequency predictions of  $P_{WD}$  are enhanced significantly when using the updated FE panel. The mean of the absolute relative error for the first 10 modes was reduced from 7.03% (with 3.51% standard deviation) to 2.99% (with 3.11% standard deviation).

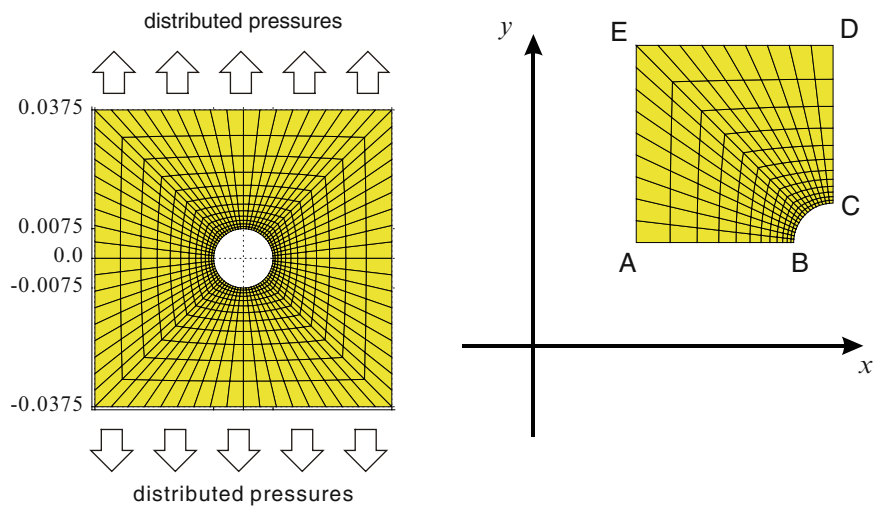
#### 46.4 Updating Elasto-plastic Material Properties Using Shape Features

In this section, the full-field strain distribution on the surface of a test specimen, a thin square plate with a central circular hole, under uniform tensile loading at the top and bottom edges is measured by a DIC system (Istra 4D, Dantec Dynamics, Ulm, Germany). The drawing of the test specimen is shown on the left hand side in Fig. 46.12. The right hand side of Fig. 46.12



**Fig. 46.12** Tensile test specimen (thin square plate with central hole) using digital image correlation. Loading history is plotted along with four samples

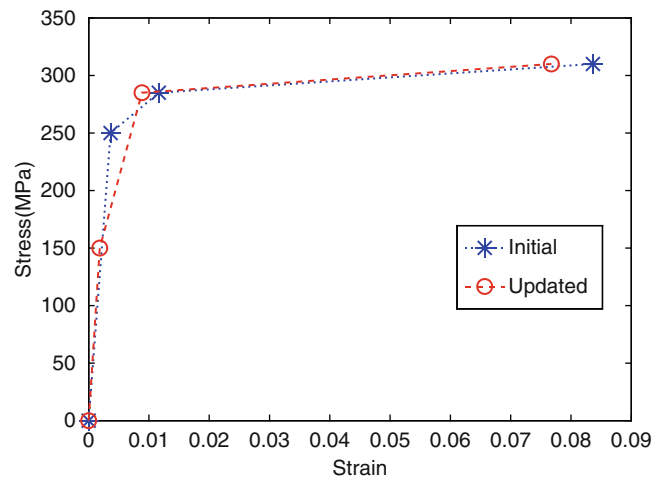
**Fig. 46.13** Finite element mesh for a square plate with circular a hole representing the central portion of the specimen in Fig. 46.12



shows the curve of the loading history along which four samples (6.4, 12.9, 16.1 and 17.5 kN respectively) are taken. The obtained principal strain distributions of the four samples are shown in Fig. 46.12 as well. Each of the strain maps consist of 23,622 data points. The critical regions on the strain maps appears around the central hole and is cyclically symmetric. It is desirable to condense the full-field strain map to form shape feature terms, much fewer than 23,622 data points, without losing significant shape information. Detailed discussions on applying the adaptive Zernike moment descriptor to extract succinct and efficient shape features from the full-field strain maps may be found in [9] (paper number 422) or [11].

A FE model as show in Fig. 46.13 was constructed to simulate the tensile test of the specimen. It is possible to update the FE model by using the efficient adaptive Zernike moment descriptors. The parameters to be updated are the material properties that define the elastic–plastic stress/strain curve and the geometric dimensions of the specimen. Specifically, the

**Fig. 46.14** Elasto-plastic material property curve (nominal and updated)



parameters are the Young's modulus, which determines the linear stress/strain curve in the elastic range, yield stress, the plastic strain at 285 and 310 MPa, which partially define the stress/strain curve in the plastic range in the form of linear segments, and the thickness of the plate

For this aluminium specimen, the machining of the circular hole may have induced a heat affected zone in which the material properties might be different from the nominal values. Therefore, the parameters for the present updating process are

$$\theta = \{ E \ \sigma_{y0} \ \epsilon_1 \ \epsilon_m \ T_p \}^T \quad (46.5)$$

where  $E$  represents the Young's modulus,  $\sigma_{y0}$  initial yield stress,  $\epsilon_1$  plastic strain corresponding to 285 MPa,  $\epsilon_m$  the plastic strain corresponding to the ultimate stress (310 MPa) and  $T_p$  the thickness of the plate.

The initial values of these parameters are

$$\theta_{(0)} = \{ 69 \text{ GPa} \ 250 \text{ MPa} \ 0.008 \text{ m/m} \ 0.075 \text{ m/m} \ 1 \text{ mm} \}^T$$

The nominal stress/strain curve for the FE model is shown in Fig. 46.14 as the blue dotted line labelled with asterisks.

Using (46.1) all the five parameters converged after 15 iterations as shown in Fig. 46.15 and the updated stress/strain curve for the FE model is shown in Fig. 46.14 as the red dotted line labelled with circles. It can be seen that the main discrepancy in the material model was the region in the vicinity of the initial yielding. The improvement in ZMD values due to model updating is evident in Fig. 46.16.

## 46.5 Conclusions

The availability of optical experimental measurement systems offer the possibility of performing detailed comparisons and validation of data from numerical models. The challenge arising from this is to carry out meaningful and useful quantitative comparisons when the data sets from experiment and modelling possibly contain  $10^5$  or  $10^6$  data values. It is demonstrated here that pattern recognition techniques enable an effective and efficient way to characterise the full-field measurements. Finite element model updating was also successfully carried out based on a small number of shape features. This approach represents a quantifiable route to validation and a means to provide confidence in modelling results

**Acknowledgements** The authors wish to acknowledge the support of EC FP7 project ADVISE (Advanced Dynamic Validations using Integrated Simulation and Experimentation); grant no. 218595. Several figures and tables were reprinted from Refs. [11] and [12] with permission from Elsevier.



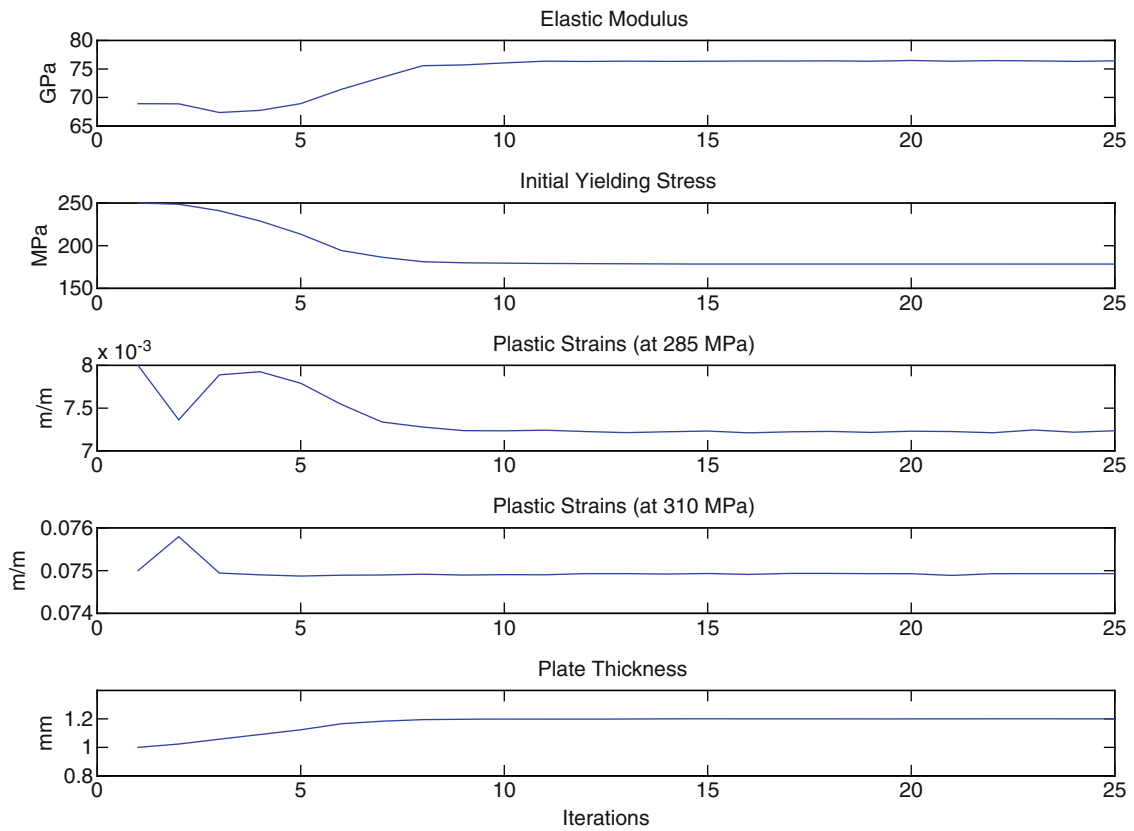
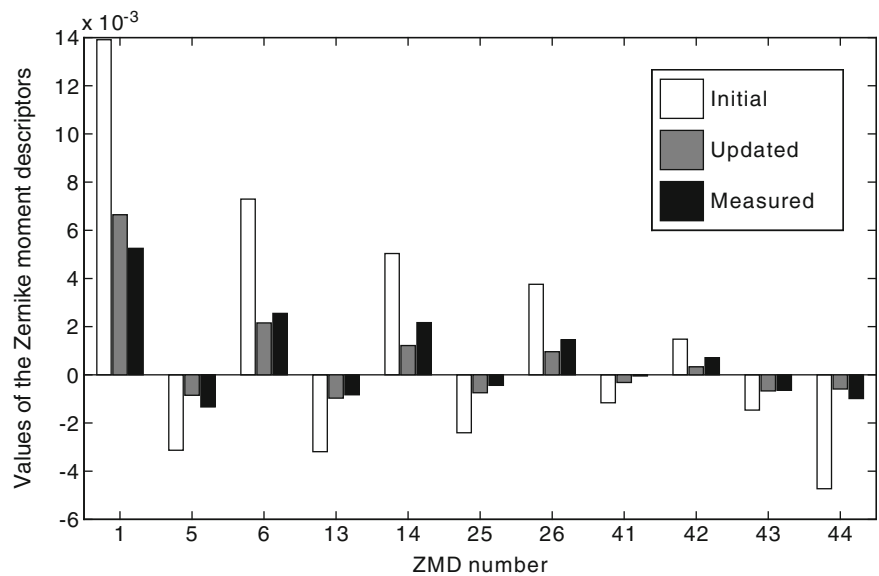


Fig. 46.15 Parameter updating history

Fig. 46.16 ZMDs before and after model updating



## References

1. Mottershead JE, Friswell MI (1993) Model updating in structural dynamics: a survey. *J Sound Vib* 167(2):347–375
2. Friswell MI, Mottershead JE (1995) *Finite element model updating in structural dynamics*. Kluwer Academic, Dordrecht
3. Stanbridge AB, Martarelli M, Ewins DJ (2004) Measuring area vibration mode shapes with a continuous-scan LDV. *Measurement* 35(2): 181–189

4. Sutton MA, Orteu J-J, Schreier H (2009) Image correlation for shape, motion and deformation measurements. SpringerLink, New York
5. Siebert T, Wood R, Splitthof K (2009) High speed image correlation for vibration analysis. *J Phys Conf Ser* 181(1):012064
6. Whelan MP, Hack E, Siebert T, Burguete RL, Patterson EA, Saleem Q (2005) On the calibration of optical full-field strain measurement systems. *Applied mechanics and materials*, Southampton, pp 397–402
7. Wang W, Mottershead JE, Mares C (2009) Mode-shape recognition and finite element model updating using the Zernike moment descriptor. *Mech Syst Signal Process* 23(7):2088–2112
8. Wang W, Mottershead JE, Mares C (2009) Vibration mode shape recognition using image processing. *J Sound Vib* 326(3–5):909–938
9. Mottershead JE, Wang W (2013) Principles of image processing and feature recognition applied to full-field measurements. In: *IMAC XXXI*, Garden Grove
10. Wang W, Mottershead JE (2013) Adaptive moment descriptors for full-field strain and displacement measurements. *J Strain Anal Eng Des.* 48(1):16–35
11. Wang W, Mottershead JE, Sebastian CM, Patterson EA (2011) Shape features and finite element model updating from full-field strain data. *Int J Solids Struct* 48(11–12):1644–1657
12. Wang W, Mottershead JE, Ihle A, Siebert T, Schubach HR (2011) Finite element model updating from full-field vibration measurement using digital image correlation. *J Sound Vib* 330(8):1599–1620

# Chapter 47

## Shape-Descriptor Frequency Response Functions and Modal Analysis

John E. Mottershead, Weizhuo Wang, Thorsten Siebert, and Andrea Pipino

**Abstract** Modal identification is carried out in the shape-feature domain using full-field data from a DIC system. The methodology is illustrated using a car bonnet of 3D irregular shape typical of many engineering structures. The full-field measured data are highly redundant, but the application of image processing using functional transformation enables the extraction of a small number of shape features without any significant loss of information from the raw DIC data. Surface parameterization is applied to ‘flatten’ the 3D surface to form a 2D planar domain. An adaptive geometric moment descriptor (AGMD), defined on surface parametric space, is used to extract shape features from a series of full-field transient responses under pseudo-random excitation. Approximately 14 thousand data points of raw DIC measurement are represented by 20 shape features terms at each time step. Shape-descriptor frequency response functions (SD-FRFs) of the response field and the loading field are derived. The usual modal identification procedure is applied to determine the natural frequencies, damping factors and Eigen-shape-feature vectors from the SD-FRF. Natural frequencies and mode shapes from a finite element (FE) model are correlated with the experimental data using the cosine distance between the shape feature vectors with 20 terms.

**Keywords** Frequency response function • Modal identification • Digital image correlation • Full-field vibration measurement • 3D signal processing

### 47.1 Introduction

The conventional modal testing approach involves the use of point-wise accelerometer measurements. This approach has a number of limitations namely (1) the addition of mass – especially evident for light weight structures; (2) it is difficult to measure high temperature components; (3) it is difficult to measure spinning structures; and (4) optimizing the number and location sensors is not straightforward [1–3]. Optical sensing techniques such as scanning laser Doppler vibrometry (SLDV) [4], digital speckle shearography (DSI), electronic speckle pattern interferometry (ESPI) [5, 6] and digital image correlation (DIC) [7] enable full-field non-contact measurements [8] and may overcome the limitations in the conventional approach. However, the amounts of data captured by the optical sensing systems are usually very large – especially in the case of full-field dynamic measurement when employing high speed cameras. It is desired to compress the full-field data into reasonably small amount of attributes (or shape features) without sacrificing significantly the fidelity of the raw data. Orthogonal decomposition is one of the popular ways to extract succinct and efficient shape features. Detailed discussion of image decomposition may be found in another IMAC XXXI paper (number 422 [9]) or [10]. Given that efficient shape

---

J.E. Mottershead (✉)

Centre for Engineering Dynamics, University of Liverpool, Liverpool L69 3GH, UK  
e-mail: [j.e.mottershead@liv.ac.uk](mailto:j.e.mottershead@liv.ac.uk)

W. Wang

School of Engineering, Manchester Metropolitan University, Manchester M1 5GD, UK

T. Siebert

Dantec Dynamics GmbH, Kaessbohrer Str. 18, Ulm, D 89077 Germany

A. Pipino

Centro Ricerche Fiat, Torino, Italy

features were obtained from appropriate orthogonal decomposition, further analysis e.g. model updating, material properties identification, damage assessment etc may then be carried out based on the condensed shape feature information.

In this paper, modal identification is carried out using shape features from full-field vibration measurements. Frequency response functions of shape features (SF-FRF) are derived. It is found that the SF-FRF may be expressed mathematically in a similar style to the conventional receptance FRF. Furthermore, classical FRF estimation and curve fitting techniques may be applied to identify natural frequencies, damping factors and ‘eigen-shape-feature-vectors’ from the shape features of the full-field data. The whole process is elaborated by a case study on a Fiat car bonnet. Some brief background of shape decomposition is given in Sect. 47.2. Construction of the adaptive geometric moment descriptor is discussed in Sect. 47.3. In Sect. 47.4, the SF-FRF is derived. The case study is illustrated in Sect. 47.5. Finally conclusions are presented in Sect. 47.6.

## 47.2 Transient Shape Decomposition

Generally, the full-field transient response  $W(\tilde{\mathbf{n}}, t)$  may be expressed as linear combination of as

$$W(\tilde{\mathbf{n}}, t) = \sum_{\ell=1}^{\infty} S_{\ell}(t) \mathfrak{K}_{\ell}(\tilde{\mathbf{n}}) \quad (47.1)$$

where  $\mathfrak{K}_{\ell}(\tilde{\mathbf{n}})_{\ell=1,2,\dots,\infty}$  are the set of transformation kernels and  $*$  denotes the complex conjugate;  $\Omega(\tilde{\mathbf{n}})$  denotes the spatial domain of definition (measured surface domain in this case);  $\tilde{\mathbf{n}}$  is the spatial coordinates and  $t$  denotes time; the combination coefficients  $s_{\ell}(t)$  are usually called shape features. Equation (47.1) is often approximated by retaining only the most significant terms

$$W(\tilde{\mathbf{n}}) \approx \tilde{W}(\tilde{\mathbf{n}}, t) = \sum_{\ell=1}^{\mathcal{M}} s_{\ell}(t) \mathfrak{K}_{\ell}(\tilde{\mathbf{n}}) \quad (47.2)$$

The maximum number of shape feature terms  $\mathcal{M}$  to retain may be determined by asymptotic analysis when comparing  $W(\tilde{\mathbf{n}}, t)$  and  $\tilde{W}(\tilde{\mathbf{n}}, t)$  [11]. The shape features  $s_{\ell}(t)$  may be determined by

$$s_{\ell}(t) = \int_{\Omega(\tilde{\mathbf{n}})} \mathfrak{K}_{\ell}^*(\tilde{\mathbf{n}}) W(\tilde{\mathbf{n}}, t) d\tilde{\mathbf{n}} \quad (47.3)$$

provided that the kernel functions are orthonormally defined.

The 3D DIC measures the surface response which is essentially defined on 2-manifold. In this case, the shape features defined in (47.3) may be expressed in the form of first kind of surface integration as

$$s_{\ell}(t) = \int_{Q(x,y,z)} W(\mathbf{x}, t) \mathfrak{K}_{\ell}(\mathbf{x}) ds \quad (47.4)$$

where  $\mathbf{x} \equiv \{x, y, z\}$  and  $Q$  denotes the 3D surface;  $ds$  denotes the infinitesimal surface area. Equation (47.4) may be written in parametric form

$$s_{\ell}(t) = \int_{\Omega} W(\mathbf{x}(u, v), t) \mathfrak{K}_{\ell}(\mathbf{x}(u, v)) \frac{\partial \mathbf{x}}{\partial u} \times \frac{\partial \mathbf{x}}{\partial v} du dv \quad (47.5)$$

## 47.3 Adaptive Geometric Moment Descriptor

A generic approach of determining the shape features from 3D DIC measurement was proposed [12]. It may be divided into two steps: namely (1) surface parameterization – to determine the 2-parametric-coordinates from 3D surfaces; and (2) orthogonal kernel function construction using Gram-Schmidt orthogonalization. The geometric moment descriptor (GMD) as proposed by Hu (1962) adapts two-dimensional monomials  $u^p v^q$ ,  $u, v \in \mathbb{R}$ ,  $p, q \in \mathbb{N}$ , for planar domain as the kernel functions. This is extended to parametric domain for 3D surface by the authors [12] and denoted as adaptive geometric

moment descriptor (AGMD). Detailed discussion of surface parameterization of AGMD construction may be found in another IMAC XXXI paper (number 422 [9]) or [10, 12].

## 47.4 Modal Identification Using Full-Field Shape Features

To identify the modal properties of the bonnet using the full-field shape features, the full-field excitation (analogously to (47.1)) may be written as

$$f(\tilde{\mathbf{n}}, t) = \sum_{n=1}^{\infty} p_n(t) \mathfrak{R}_n(\tilde{\mathbf{n}}) \approx \sum_{n=1}^{\mathcal{M}} p_n(t) \mathfrak{R}_n(\tilde{\mathbf{n}}) \quad (47.6)$$

where  $p_n(t)$  denotes the shape features of the field excitation pattern, which may be acoustic wave or point-wise shaker excitation. Similar to (47.5) shape features of the excitation may be determined by orthogonal transformation in parametric form as

$$p_n(t) = \int_{\Omega} f(\mathbf{x}(u, v), t) \mathfrak{R}_\ell(\mathbf{x}(u, v)) \frac{\partial \mathbf{x}}{\partial u} \times \frac{\partial \mathbf{x}}{\partial v} du dv \quad (47.7)$$

For the case of point-wise shaker the excitation field may be expressed as

$$f(\mathbf{x}(u, v), t) = \delta(\mathbf{x} - \mathbf{X}_L) F(t) \quad (47.8)$$

where  $\delta(\bullet)$  is the Dirac delta function,  $\mathbf{X}_L$  is the position where the shaker is applied and  $F(t)$  is the discrete force as a function to time. Thus, (47.7) may be expressed as

$$p_n(t) = C_n^L F(t) \quad (47.9)$$

where  $C_n^L$  is the value of the  $n^{\text{th}}$  kernel function evaluated at point  $\mathbf{X}_L$ .

### 47.4.1 Frequency Response Functions of Shape Descriptors

The full-field displacement response of (47.2) and excitation of (47.6) may be expressed in the frequency domain by conducting the Fourier transform, expressed respectively as

$$\mathcal{W}(\tilde{\mathbf{n}}, \omega) \approx \tilde{\mathcal{W}}(\tilde{\mathbf{n}}, \omega) = \sum_{\ell=1}^{\mathcal{M}} \mathcal{S}_\ell(\omega) \mathfrak{R}_\ell(\tilde{\mathbf{n}}) \quad (47.10)$$

and

$$\mathcal{F}(\tilde{\mathbf{n}}, \omega) = \sum_{n=1}^{\infty} \mathcal{P}_n(\omega) \mathfrak{R}_n(\tilde{\mathbf{n}}) \approx \sum_{n=1}^{\mathcal{M}} \mathcal{P}_n(\omega) \mathfrak{R}_n(\tilde{\mathbf{n}}) \quad (47.11)$$

where  $\mathcal{S}_\ell(\omega)$  and  $\mathcal{P}_n(\omega)$  are the shape features of displacement and excitation in frequency domain respectively. For a discrete data set, e.g. the DIC measured grid, (47.10) may be written as

$$\mathbf{W} \equiv \{W_i\}_{\mathcal{N} \times 1} = [\mathcal{K}_\ell^i]_{\mathcal{N} \times \mathcal{M}} \{\mathcal{S}_\ell\}_{\mathcal{M} \times 1} \equiv \mathcal{K} \mathcal{S} \quad (47.12)$$

where  $\mathcal{K}_\ell^i$  is the  $\ell^{\text{th}}$  shape kernel function evaluated at point  $\mathbb{X}_{i,i=1,\dots,\mathcal{N}}$  and  $\mathcal{S}_\ell$  is the  $\ell^{\text{th}}$  shape feature. The equivalent forces applied at the discrete points  $\mathbb{X}_i$  may be written in the form

$$F_i = \int_{\mu_{\mathbb{X}_i}} \mathcal{F}(\tilde{\mathbf{n}}) d\tilde{\mathbf{n}} \cong \mu_{\mathbb{X}_i} \mathcal{F}(\mathbb{X}_i) \approx \mu_{\mathbb{X}_i} \sum_{n=1}^{\mathcal{M}} \mathcal{P}_n(\omega) \mathfrak{R}_n(\mathbb{X}_i) \quad (47.13)$$

where the generalized distributed loading  $\mathcal{F}(\tilde{\mathbf{n}})$  is considered to act over a region  $\mu_{\mathbb{X}_i}$  that includes the point  $\mathbb{X}_i$ . Equation (47.13) may be expressed in matrix form so that

$$\mathbf{F} \equiv \{F_i\}_{\mathcal{N} \times 1} = [\mu_i]_{\mathcal{N} \times \mathcal{N}} [\mathcal{K}_\ell^i]_{\mathcal{N} \times \mathcal{M}} \{\mathcal{P}_n\}_{\mathcal{M} \times 1} \equiv {}^T \mathcal{K} \mathcal{P} \quad (47.14)$$

where  $[\mu_i]$  is a diagonal matrix whose terms represent the measures of the vicinity of the points  $\mathbb{X}_{i,i=1,\dots,\mathcal{N}}$ .

It is possible to assemble (47.13) and (47.14) according to the definition of receptance, i.e.  $\mathbf{W} = \boldsymbol{\alpha}(\omega)\mathbf{F}$ , and leads to

$$\mathcal{K} \mathcal{S} = \boldsymbol{\alpha}(\omega) \boldsymbol{\mu} \mathcal{K} \mathcal{P} \quad (47.15)$$

where is the displacement/force frequency response function. Equation (47.15) may further be expressed as [12]

$$\mathcal{S} = \boldsymbol{\beta}(\omega) \mathcal{P} \quad (47.16)$$

where  $\boldsymbol{\beta}(\omega)$  is shape-descriptor frequency response function (SD-FRF), defined as

$$[\beta_{\ell,n}(\omega)] \equiv \boldsymbol{\beta}(\omega) \equiv \mathcal{K}^T \boldsymbol{\mu} \boldsymbol{\alpha}(\omega) \boldsymbol{\mu} \mathcal{K} = \mathcal{K}^T \boldsymbol{\mu}^T \boldsymbol{\alpha}(\omega) \boldsymbol{\mu} \mathcal{K} \equiv \dot{\mathcal{K}}^T \boldsymbol{\alpha}(\omega) \dot{\mathcal{K}} \quad (47.17)$$

For instance, the SD-FRF of a proportionally damped system becomes

$$\begin{aligned} \beta_{\ell,n}(\omega) &= \sum_{j,k} \dot{\mathcal{K}}_j^\ell \alpha_{jk}(\omega) \dot{\mathcal{K}}_k^n \\ &= \sum_{j,k} \dot{\mathcal{K}}_j^\ell \left( \sum_{r=1}^{\mathcal{N}} \frac{\phi_{rj} \phi_{rk}}{\omega_r^2 - \omega^2 + i\omega_r^2 \eta_r} \right) \dot{\mathcal{K}}_k^n \\ &= \sum_{r=1}^{\mathcal{N}} \frac{\left( \sum_j \dot{\mathcal{K}}_j^\ell \phi_{rj} \right) \left( \sum_k \dot{\mathcal{K}}_k^n \phi_{rk} \right)}{\omega_r^2 - \omega^2 + i\omega_r^2 \eta_r} \\ &= \sum_{r=1}^{\mathcal{N}} \frac{\varrho_{r\ell} \varrho_{rn}}{\omega_r^2 - \omega^2 + i\omega_r^2 \eta_r} \end{aligned} \quad (47.18)$$

where  $\omega_r$ ,  $\eta_r$  and  $\phi_{rj} \phi_{rk}$  are the  $r^{\text{th}}$  natural frequency, damping factor and modal constant, respectively;  $\varrho_{r\bullet} = \sum_k \dot{\mathcal{K}}_k^\bullet \phi_{rk} \cong \int_{\Omega(\tilde{\mathbf{n}})} \mathcal{W}_r(\tilde{\mathbf{n}}) \mathfrak{R}_\bullet(\tilde{\mathbf{n}}) d\tilde{\mathbf{n}}$  denotes the  $\bullet^{\text{th}}$  shape feature of the  $r^{\text{th}}$  mode shape  $\mathcal{W}_r(\tilde{\mathbf{n}})$ .

#### 47.4.2 Modal Identification from SD-FRFs

As defined in (47.16), (47.17) and (47.18), the SD-FRF has exactly the same format as the well-known receptance FRF. The only difference is that the residue of receptance is the product between two mode-shape components and the residue of the SD-FRF is the product between two shape descriptors of the mode shape. Therefore, the well-developed modal parameter extraction methods are applicable to identify the SD-FRF model.

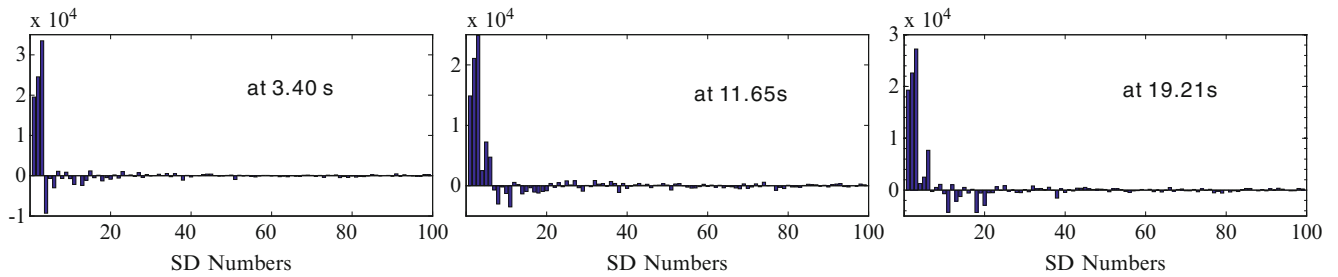
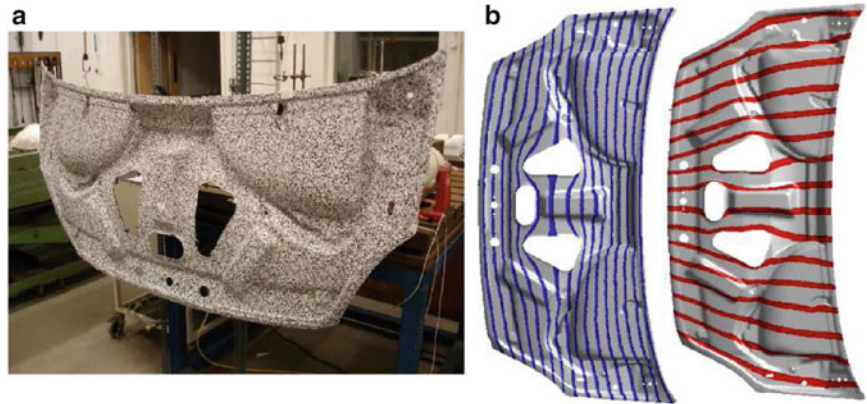
### 47.5 Case Study: Modal Testing of a Car Bonnet Using SD-FRF

#### 47.5.1 3D DIC Measurement

A Fiat car bonnet manufactured from fibre reinforced thermoplastic composite material (polyamide (PA)) as shown in Fig. 47.1a was approximately  $1.8 \times 0.8$  m in overall dimensions and its thickness was nominally 3 mm. Free-free boundary conditions were simulated by suspending the bonnet from elastic chords. Pseudo-random force loading from 0 to 128 Hz was presented to the bonnet by means of a shaker. A pair of high speed charge-coupled device (CCD) cameras were applied to capture the stereographic images. The capturing frame rate was set to 300 Hz and the size of individual frames was 1280



**Fig. 47.1** (a) Test specimen – a car bonnet covered with speckle pattern paper; (b) surface parameterisation of the bonnet surface, the lines are the curvilinear coordinate lines of the two surface parameters ( $u, v$ )



**Fig. 47.2** Spectrum of adaptive geometric moment descriptors from the DIC measured responses (at three random steps)

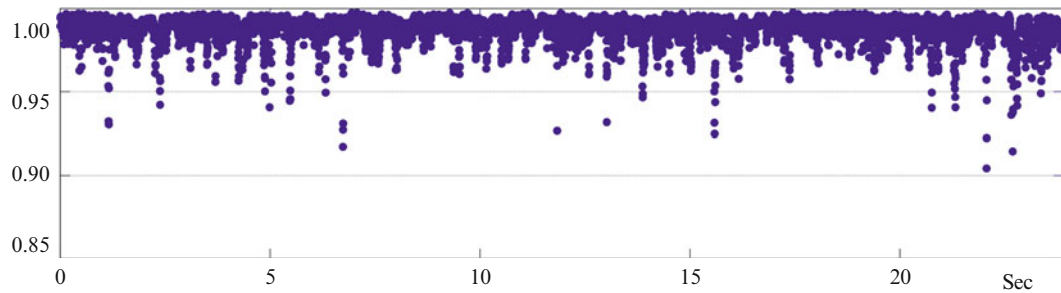
$\times 800$  pixels. This low frame rate does not require very short exposure times. High intensity illumination for the whole area with exposure times of about 0.6 ms was used. 7,200 pairs of images were collected in 24 s for displacement evaluation using DIC software Dantec Dynamics Istra 4D V4.

### 47.5.2 Surface Parameterization

The complex 3D bonnet surface is a 2-manifold in topological space. Mapping the bonnet surface from 3D space  $Q(x, y, z)$  to a 2D planar parametric domain  $\Omega(u, v)$  isomorphically enables the utilization of well-developed image decomposition techniques defined on planar domains. In this case study, the *discrete conformal parameterization* [14] is adopted to parameterize the bonnet surface. The objective is to determine a piecewise mapping  $\chi : Q(x, y, z) \rightarrow \Omega(u, v)$ , which minimizes an angular distortion measure subject to the Dirichlet boundary condition. The obtained parameterization are shown in Fig. 47.1b. The lines plotted on the bonnet are the iso-coordinate lines of the parameters  $u$  and  $v$ , respectively.

### 47.5.3 AGMD

The obtained adaptive geometric moment descriptors of four samples from the 7,200 steps of measured responses are shown in Fig. 47.4. Totally 99 terms of shape descriptor ( $p = 0$  to 10,  $q = 0$  to 8 are the orders considered for the monomials) are shown in each step. It is seen from Fig. 47.4 that only a few lower order shape descriptors are significant. It may be possible to discard the insignificant terms. Comparison between the original displacement patterns and the reconstructed ones using the 20 most significant shape descriptors throughout all the 7,200 measurement steps is shown in Fig. 47.3. It is clear that all the reconstructed and original shapes are correlated to more than 90% agreement and most of the steps greater than 97%. Therefore, the constructed shape features are succinct and efficient because the redundant full-field measurement (14,158 data-points evaluated by the DIC system for each step) is well represented by the small number of the adaptive geometric moment descriptors (Fig. 47.2).



**Fig. 47.3** Correlation coefficient between the original shapes and their reconstruction from the 20 most significant terms of the shape descriptors for all the 7,200 captured steps

#### 47.5.4 SD-FRF Estimation and Modal Identification

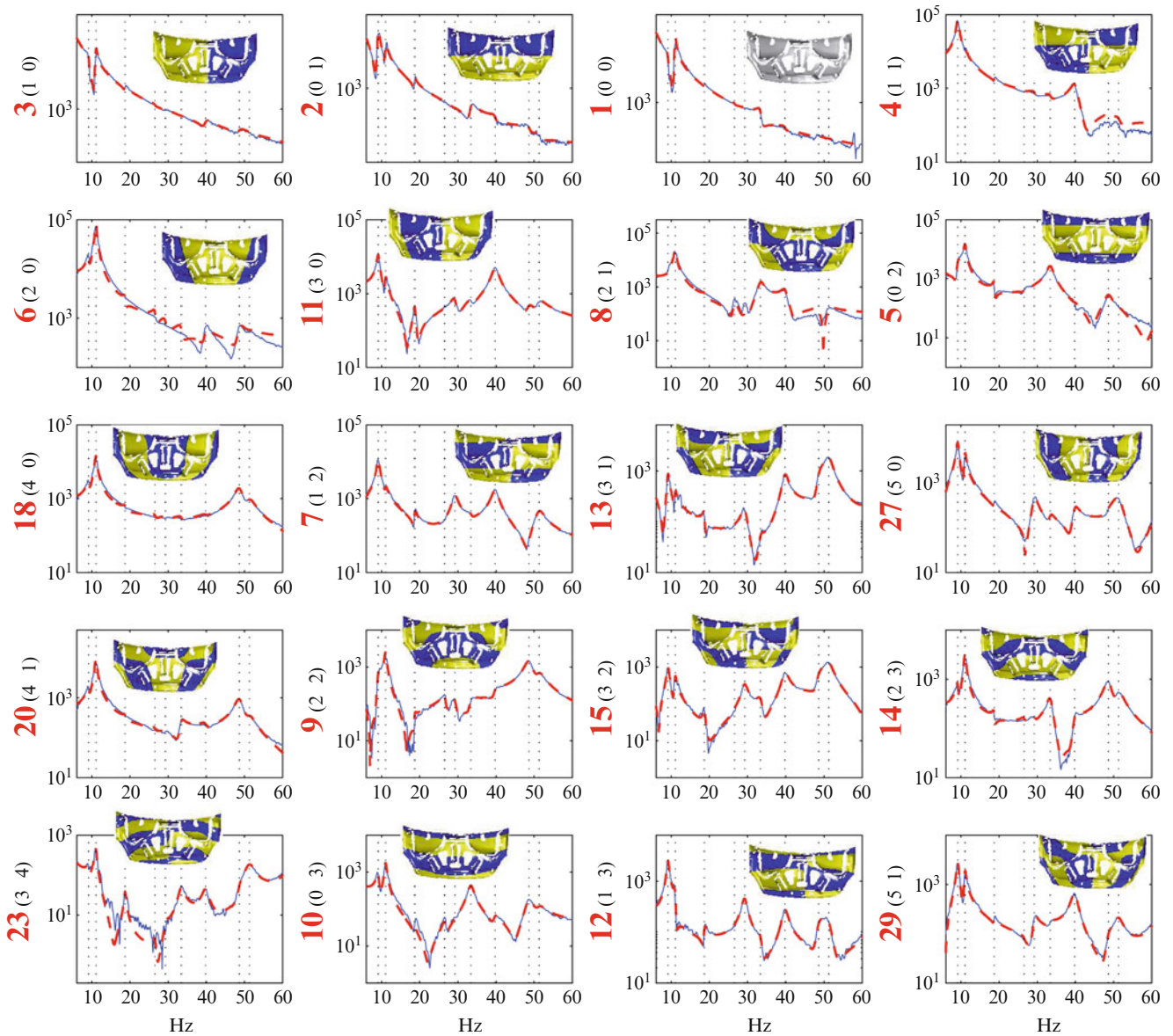
The experimental SD-FRF was estimated by Welch's averaged periodogram method [15]. The amplitudes of the SD-FRF are shown as blue solid lines in Fig. 47.4, which was obtained by retaining the 20 most significant shape features of the displacement response, as discussed previously and with excellent correlation as indicated in Fig. 47.3. The corresponding kernel functions are also shown in the sub-figures. Modal properties were then extracted by the general nonlinear least-squares curve-fit approach [16]. The fitted curves are shown in Fig. 47.4 with red dashed lines, which are closely fitted from 6 to 80 Hz. The identified natural frequencies and damping factors are listed in Table 47.1. The FE predicted natural frequencies are also shown in the table.

#### 47.5.5 Comparison with FE Model

Figure 47.5a shows the reconstructed mode shapes in binary color map from the Eigen-shape-feature vectors (20 SDs  $\times$  11 Modes). The corresponding FE mode shapes are shown in Fig. 47.5b. The similarities of the two sets of mode shapes are quite evident. The only difference is that DIC-measured mode 3 is not predicted by the FE model. Thus, it is seen that the 20 retained shape feature terms are sufficient for describing the full-field responses of the car bonnet. Mode shape results of similar clarity are unlikely to be obtained by using 20 accelerometers. It is possible to carry out a quantitative comparison of FE and DIC mode shapes based on shape feature vectors. It is not necessary to match the FE nodes to the measurement grids by interpolation as conventional methods do because the shape features are obtained by integration over the domain. The cosine distances between the shape-feature vectors of FE mode shapes and the Eigen-shape-feature vectors identified from SD-FRF are shown in Fig. 47.6. It is seen that FE model agrees very well with the first eleven measured mode shapes except for the third mode, which the FE model fails to predict and is irrelevant to the performance of the SD representation of full-field vibration data.

### 47.6 Conclusions

The high-speed 3D DIC technique enables full-field vibration measurement. Image decomposition was adopted to extract succinct and efficient shape features from full-field measurements. Thus, information redundant full-field data may then be effectively expressed by reasonably small amount of shape feature terms. Frequency response functions of shape features were also derived. Vibration measurement using 3D DIC system on a car bonnet was conducted. Random excitation was considered. Full-field transient vibration measurements were transformed into shape features by using the adaptive geometric moment descriptors. Experimental SF-FRF was estimated from the obtained adaptive geometric moment descriptors. Classical curve fitting techniques were adapted for identification. Natural frequencies, modal damping coefficients and eigen-shape-feature vectors were successfully identified from the estimated SF-FRF. Mode shapes were reconstructed from the identified eigen-shape-feature vectors and compared with the FE mode shapes.



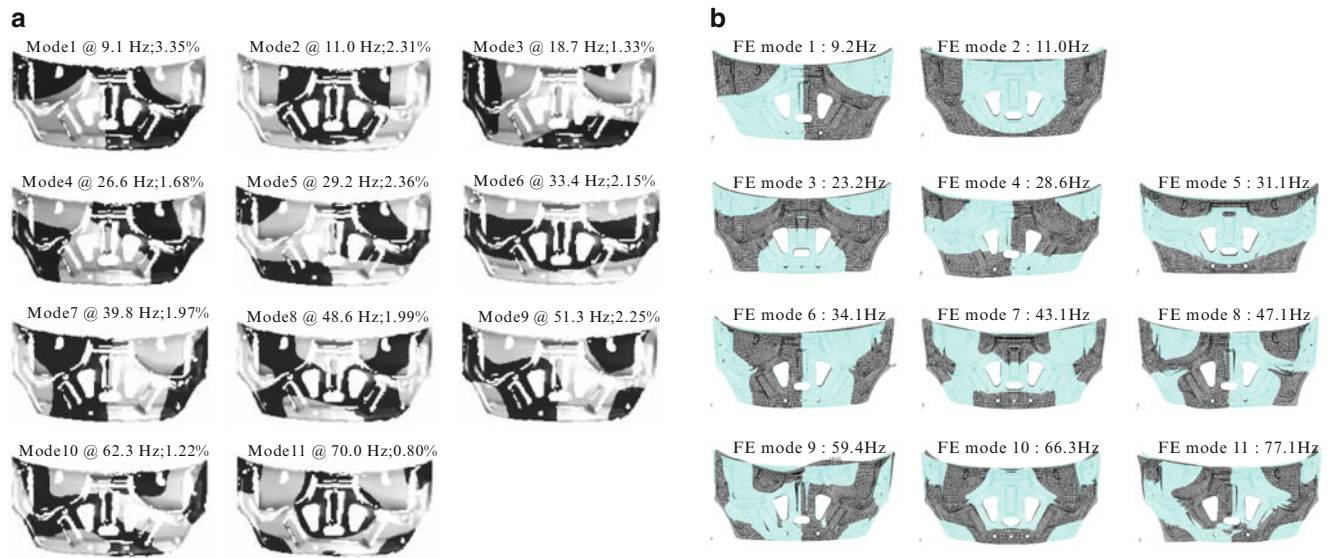
**Fig. 47.4** Amplitudes of frequency response function of the 20 most significant shape features (blue solid and red dashed lines represent tested and fitted by non-linear least squares approach ([16]), respectively); the corresponding shape kernel functions defined on the surface parametric space are shown on the sub-figures as well

To summarize, there are numerous benefits of using shape feature extraction techniques to handle the full-field measurement: (1) succinctness and efficiency; (2) noise robustness; (3) it is also possible to determine the frequency response function of any point on the bonnet by assigning its coordinate to the kernel functions of the retained shape feature terms. The method is applicable to general field excitation, such as acoustic, magnetic or pressurized air excitation.

**Acknowledgements** The authors wish to acknowledge the support of EU FP7 through project ADVISE (Advanced Dynamic Validations using Integrated Simulation and Experimentation); grant no. 218595

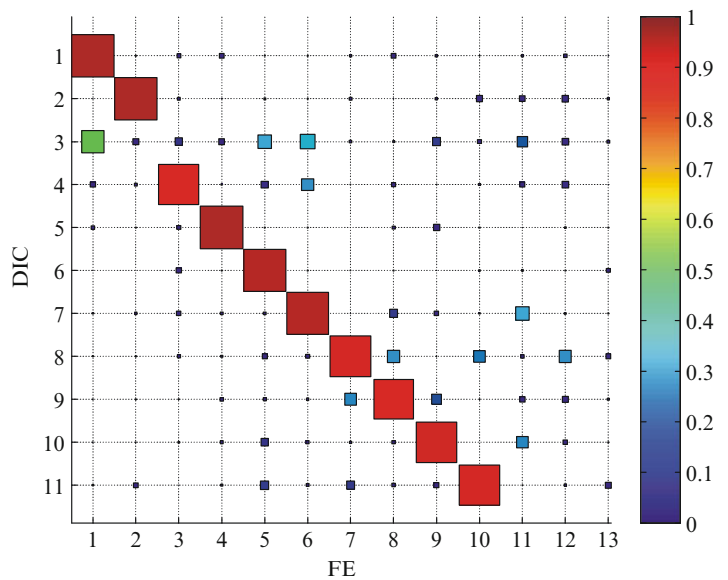
**Table 47.1** Natural frequencies of the CRF bonnet

Mode	FE: MSC.Nastran	DIC: SD-FRF	
	Normal mode (Hz)	Freq. (Hz)	Damp. (%)
1	9.2	9.1	3.35
2	11.0	11.0	2.31
3	—	18.7	1.33
4	23.2	26.6	1.68
5	28.6	29.2	2.36
6	31.1	33.4	2.15
7	34.1	39.8	1.97
8	43.1	48.6	1.99
9	47.1	51.3	2.25
10	59.4	62.3	1.22
11	66.3	70.0	0.80



**Fig. 47.5** Mode shapes; (a) Reconstructed from identified Eigen-shape-feature-vectors in binary color map; (b) Finite element mode shapes

**Fig. 47.6** Cosine distance between the DIC-measured eigen-shape-feature-vectors (20 terms) and the FE prediction (calculated from the domain in Fig. 47.5b)



## References

1. Kammer D (2005) Sensor set expansion for modal vibration testing. *Mech Syst Signal Process* 19(4):700–713
2. Schedlinski C, Link M (1996) An approach to optimal pick-up and exciter placement. In: *Proceedings of the 14th international modal analysis conference*, Dearborn, pp 376–382
3. Bonisoli E, Delprete C, Rosso C (2009) Proposal of a modal-geometrical-based master nodes selection criterion in modal analysis. *Mech Syst Signal Process* 23(3): 606–620
4. Stanbridge AB, Martarelli M, Ewins DJ (2004) Measuring area vibration mode shapes with a continuous-scan LDV. *Measurement* 35(2): 181–189
5. Huntley JM (1998) Automated fringe pattern analysis in experimental mechanics: a review. *J Strain Anal Eng Des* 33(2): 105–125
6. Powell RL, Stetson KA (1965) Interferometric vibration analysis by wavefront reconstruction. *J Opt Soc Am* 55(12): 1593
7. Sutton MA, Orteu J-J, Schreier H (2009) *Image correlation for shape, motion and deformation measurements*. Springer, New York.
8. Schmidt T, Tyson J, Galanulis K (2003) Full-field dynamic displacement and strain measurement using advanced 3D image correlation photogrammetry: Part I. *Exp Tech* 27(3): 47–50
9. Mottershead JE, Wang W (2013) Principles of image processing and feature recognition applied to full-field measurements. In: *IMAC XXXI*, Garden Grove
10. Wang W, Mottershead JE (2012) Adaptive moment descriptors for full-field strain and displacement measurements. *J Strain Anal Eng Des*
11. Wang W, Mottershead JE, Sebastian CM, Patterson EA, (2011) Shape features and finite element model updating from full-field strain data. *Int J Solid Struct* 48(11–12): 1644–1657
12. Wang W, Mottershead JE, Siebert T, Pipino A (2012) Frequency response functions of shape features from full-field vibration measurements using digital image correlation. *Mech Syst Signal Process* 28: 333–347
13. Hu M-K (1962) Visual pattern recognition by moment invariants. *IEEE Trans Info Theory* 8(2): 179–187
14. Desbrun M, Meyer M, Alliez P (2002) Intrinsic parameterizations of surface meshes. *Comput Graph Forum*, Wiley Online Library 21: 209–218
15. Welch P (1967) The use of fast Fourier transform for the estimation of power spectra: a method based on time averaging over short, modified periodograms. *IEEE Trans Audio Electroacoustics* 15(2): 70–73
16. Ewins DJ (2000) *Modal testing: theory, practice, and application*. Research Studies Press, Philadelphia



# Chapter 48

## Dynamic Simulation of the Lunar Landing Using Flexible Multibody Dynamics Model

Huinam Rhee, Sang Jin Park, Tae Sung Kim, Yong Ha Kim, Chang Ho Kim, Jae Hyuk Im, and Do-Soon Hwang

**Abstract** Flexible multibody dynamic model of the lunar lander was developed in this research. Dynamic stiffness and damping properties of lunar soil and shock absorber are included in the model. Various moon landing simulations were performed for different friction characteristics between the lander and soil, and also for various landing velocities and slope angles of the lunar surface on the landing stability.

**Keywords** Lunar lander • Flexible multibody dynamics • Dynamic simulation • Landing stability • Tip-over

### 48.1 Introduction

The lunar lander is designed so that its structural integrity is maintained under the influence of static and dynamic loadings during landing process, and no tip-over takes place. Since 1960s there have been many studies on this matter especially for Apollo series program [1]. Nowadays commercial multibody dynamic simulation computer programs are available, therefore, it is recommended to utilize multibody dynamics to simulate the landing behavior of the lunar lander. Three dimensional multibody dynamic model was developed in author's previous research [2] in which a rigid body model was developed, that is, all bodies were assumed rigid. In this paper a flexible multibody dynamic model of a lunar lander rather than the rigid body model is developed.

### 48.2 Multibody Dynamic Modeling of the Lunar Lander

Figure 48.1 shows the design feature of the lunar lander considered in this paper. It includes the lander body and the landing gear assembly which consists of center and side struts, footpads and honeycomb-type shock absorbers.

The multibody dynamic model developed in this research considered the lumped mass model of the main body, the nonlinear spring-damper model of the shock absorber, contact properties between the lander and lunar soil, friction between the lander and lunar soil, inclination angle of the landing spot, horizon and vertical landing speeds, etc. Center and side struts are modeled as flexible bodies, which includes a few of important modes of the components using modal analysis results while previous research used a rigid body model [2].

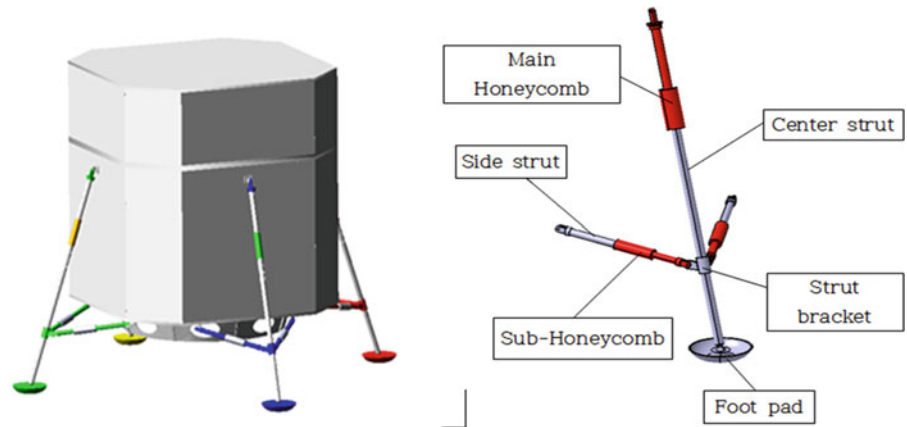
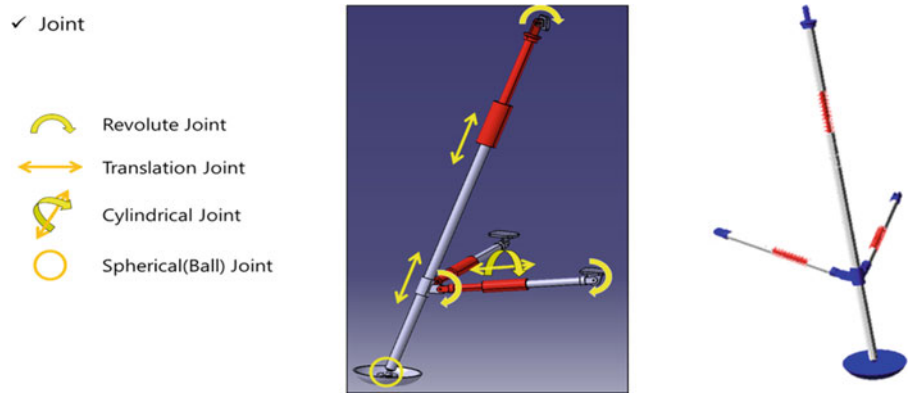
The connection parts between center struts and main body are modeled as revolute joints as shown in Fig. 48.2 [2]. The honeycomb and strut are connected by a sliding joint. The landing gear model includes flexible parts for center and side struts because they can provide some flexibility while impacts occur between lunar surface and footpads. Number of modes included in the flexible model was determined by parametric studies using models with different modes. Using the flexible multibody dynamic model more realistic results could be obtained about tip-over characteristics during landing.

---

H. Rhee (✉) • S.J. Park • T.S. Kim • Y.H. Kim  
Suncheon National University, 150 Maegok-dong, Suncheon, Chonnam 540-742, South Korea  
e-mail: [hnrhee@suncheon.ac.kr](mailto:hnrhee@suncheon.ac.kr)

C.H. Kim • J.H. Im • D.-S. Hwang  
Korea Aerospace Research Institute, 169-84, Kwahak-ro, Yuseong-ku 305-806, South Korea



**Fig. 48.1** Lunar lander**Fig. 48.2** Modeling of various joints and flexible landing gear

The force-displacement relationship of the shock absorber as shown in Fig. 48.3 was obtained by experiments and modeled by a nonlinear spring and damper element [2].

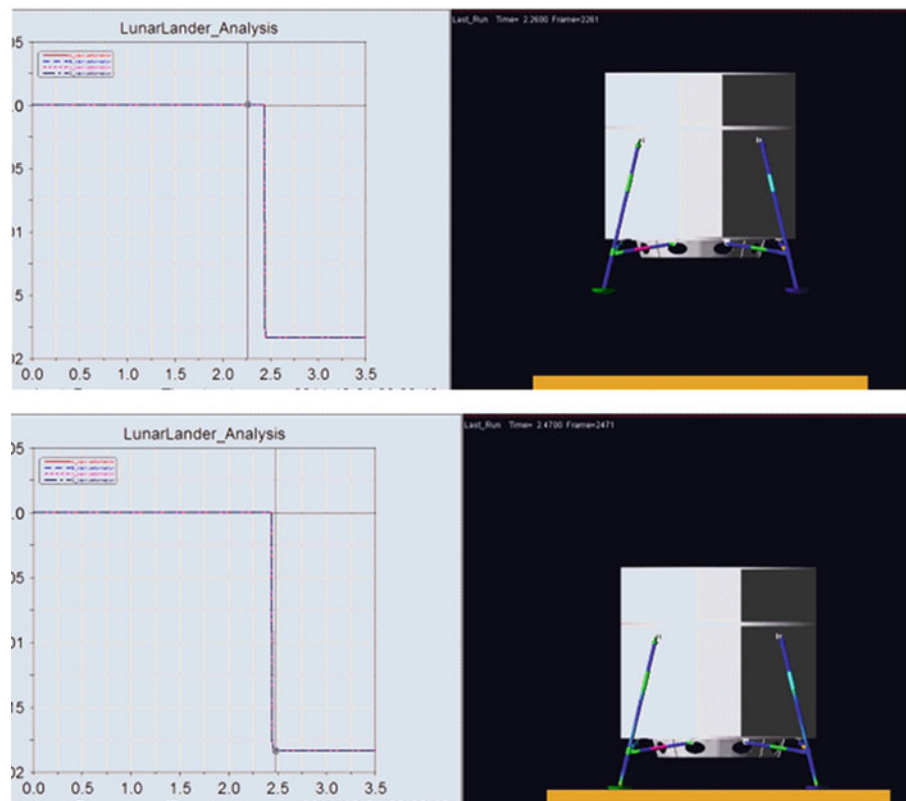
The soil properties of lunar surface have been considered in the contact element between footpads and the lunar surface based on the same method in the previous research [2]. The stiffness and damping properties of the lunar surface was determined by parametric simulation. It was difficult to determine the damping coefficient of the lunar surface, which was not clearly defined in any reference. Therefore, it was adjusted to produce reasonable contact force and penetration data according to the experimental data.

### 48.3 Landing Simulation

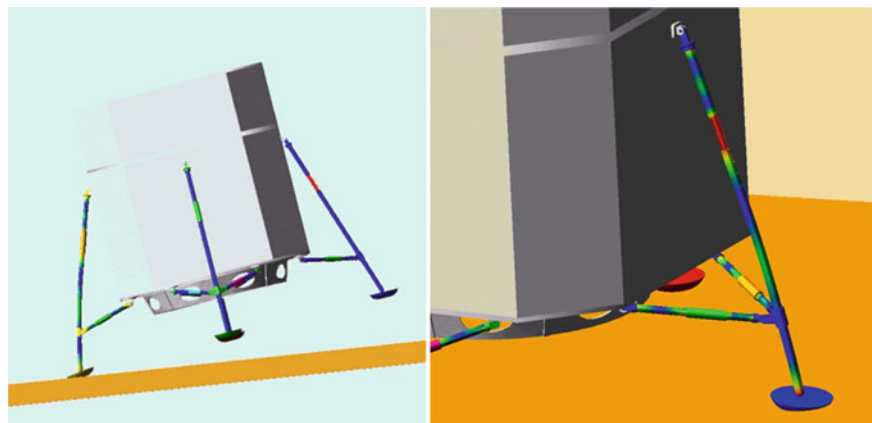
Dynamic simulation of the lunar lander were performed with the developed multibody dynamics model for various cases: vertical landing and landing with non-zero horizontal velocity on the flat or inclined surface. The coefficients of friction between lunar surface and the footpads can be varied to know the effect of friction on the stability.

Figure 48.3 shows examples of shock absorber deformation during vertical landing on the flat surface. The nonlinear spring-damper model of the shock absorber proved to be reasonably working. Figure 48.4 represents an example of bending deformation of the landing gear. Bending of the struts has an influence on the tip-over characteristics: in some cases negative effects and in some other cases positive effects. It depends on the surface inclination angle, coefficient of friction between lunar surface and the footpads, and landing velocity. In Fig. 48.4 stresses can also be obtained in which flexible models have an advantage compared to rigid body models. Figure 48.5 shows an example of detailed information from landing simulation. The amount of shock absorber deformation, force on the shock absorber, contact force on the foot pads, and penetration depth into the lunar surface are shown for the case of 1 m/s landing speed and 6° inclination angle. Figure 48.6 represents an example of tip-over during landing. The tip-over characteristics depends on various parameters, i.e., location of center of mass, moment of inertia, inclination angle of the landing surface, landing velocity, static and dynamic coefficients of friction, etc.

**Fig. 48.3** Vertical landing simulation: shock absorber deformation

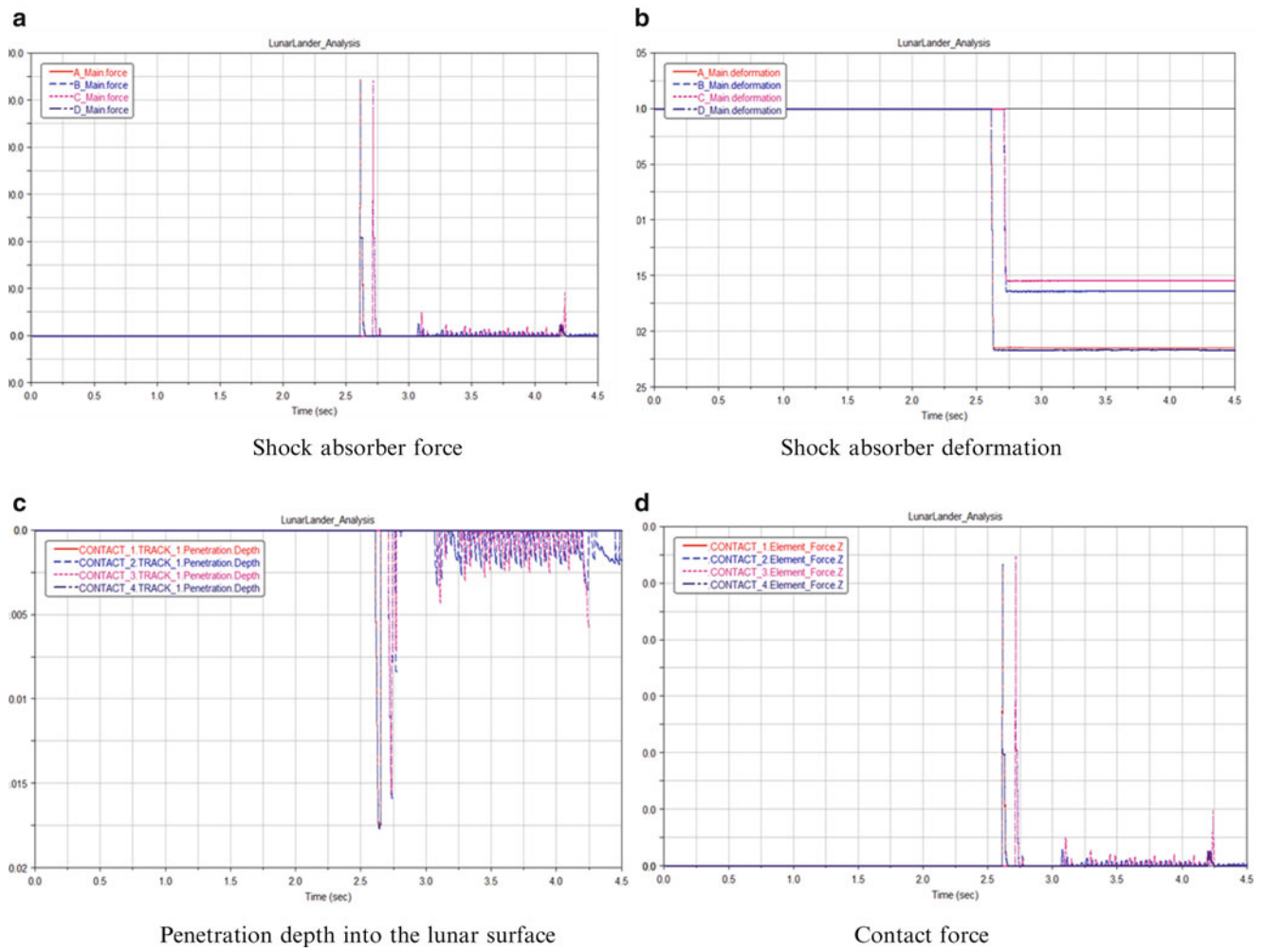


**Fig. 48.4** Bending deformation of landing gear



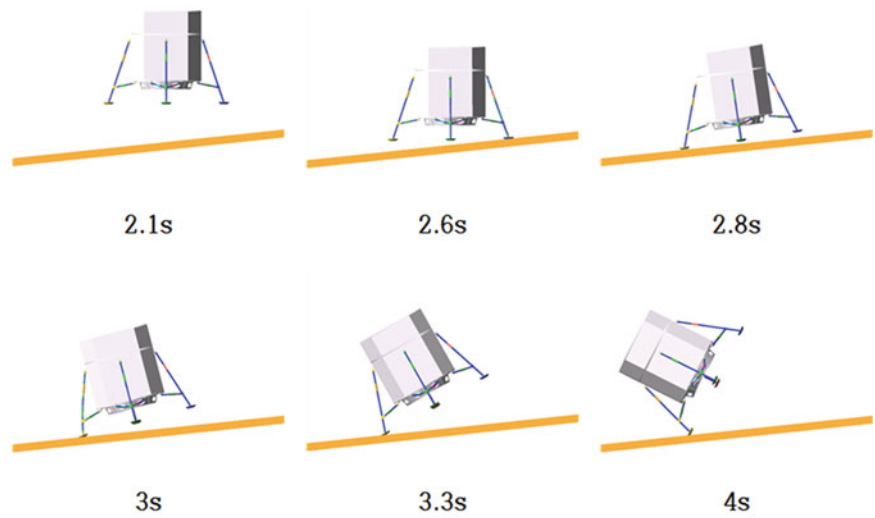
## 48.4 Conclusions

In this research flexible multibody dynamic modeling of the lunar lander was developed and dynamic landing simulation were performed. The lander model includes dynamic soil properties of the moon as well as the lander structure including nonlinear spring-damper characteristics of the shock absorber. Using the flexible multibody dynamic model various kinds of moon landing simulation can be performed with various characteristics of the friction between the lander and the soil. The effect of the landing velocities and inclination angle of the landing area on the tip-over characteristics during landing can be easily predicted using the developed model. The flexible model can predict more realistic dynamic behavior compared to the rigid body model. Flexible multibody dynamic simulation can be a very useful tool to improve the landing performance of the lunar lander.



**Fig. 48.5** Example of detailed information from landing simulation (a) Shock absorber force (b) Shock absorber deformation (c) Penetration depth into the lunar surface (d) Contact force

**Fig. 48.6** Example of the tip-over simulation



## References

1. Rogers WF (1972) Apollo experience report – lunar module landing gear subsystem. Manned Spacecraft Center, National Aeronautics and Space Exploration, Houston
2. Huinam Rheet al (2012) Multibody dynamic simulation of the lunar landing. IMAC

# Chapter 49

## A New Approach for a Train Axle Telemetry System

M. Bassetti, F. Braghin, F. Castelli-Dezza, and M.M. Maglio

**Abstract** The application of a telemetry system for train axle fatigue monitoring is analyzed in this paper. Monitoring of the axle bending deformation at critical points is of great importance for both high speed and freight trains. The fatigue life of the axle may be significantly reduced due to accidental peak loads. Commonly used telemetry systems require special pick-ups for transmitting electrical power to the electronics placed on the rotating axle and for transferring back sensor signals. Inductive power transfer is performed through a high frequency magnetic field linking a rotating winding. Sensor signals are modulated on top of the power signal and transferred at an even higher frequency to be immune to the inductive magnetic field. In this paper a new approach for an inductive power transfer system, completely decoupled from the transfer of sensor signals, is analyzed. The layout of the energy transmission system has been simplified with respect to traditional telemetry systems and its efficiency is increased. Also the immunity of the measurements against the power magnetic field, the distance of the power head and all the electrical noise induced results have been improved. The combination of a simple power induction system, a fast data processing unit and a low power RF data transmission system lead to an easy and reliable telemetry system for train axle monitoring.

**Keywords** Telemetry • Train axle • Fatigue monitoring • Rainflow • RF transmission

### 49.1 Introduction

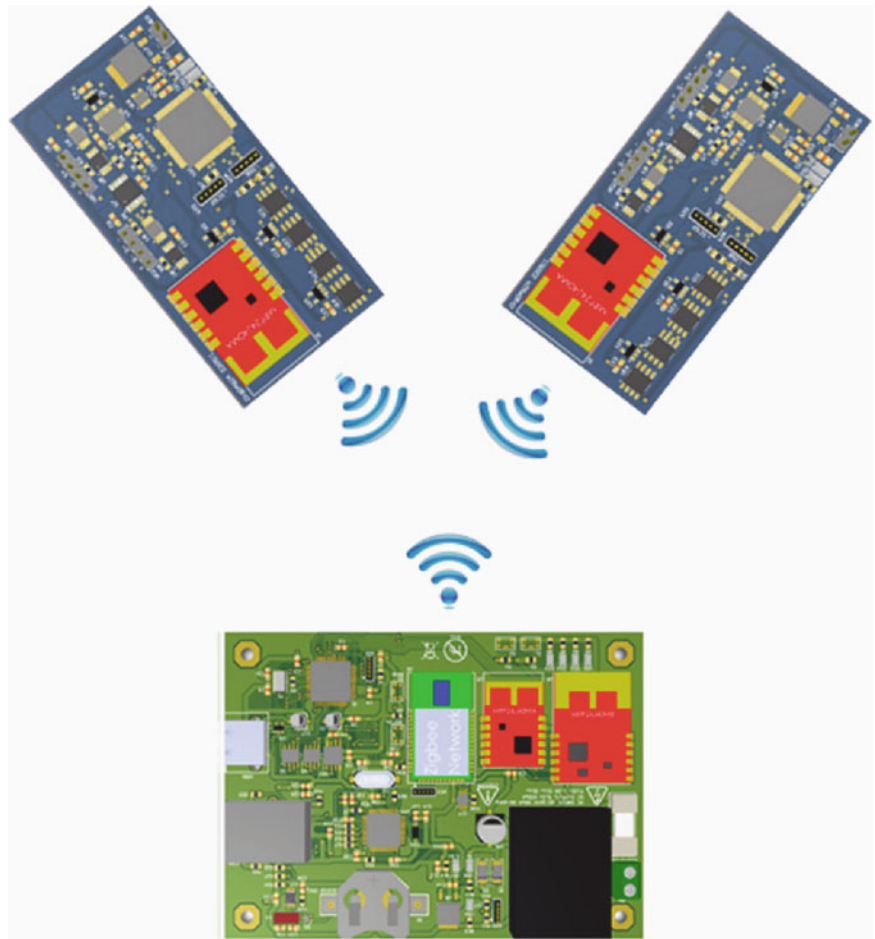
In railway applications, telemetry systems are usually used for the measurement of wheel-rail contact forces during homologation tests [1] and/or for track monitoring [2]. A new application is the use of use of telemetry systems for the monitoring of critical railway components. Among these, railway axles have a very special role as shown in some of the most catastrophic railway accidents (e.g. Viareggio accident). Since railway axles are subjected to flexural bending fatigue while rotating and fatigue life is greatly affected by the occurrence of exceptional loads [3], a continuous monitoring system able to measure strains at critical points, thus experimentally determining the load spectrum, would greatly improve safety.

For this purpose, a rugged telemetry system has been developed. Obviously, to be applicable as a continuous monitoring system for railway axles, its service life should be longer than that of the axle on which it is mounted. Moreover, since no batteries exist that are able to last such long periods (more than 20 years) and to withstand 250 g of centrifugal acceleration (for high speed train axles), a battery-less telemetry system is required. Preliminary tests were carried out on an axle fatigue test bench to assess whether the main requirements, especially in terms of energy consumption and mechanical survivability of the board to such high accelerations, were met.

---

M. Bassetti (✉) • F. Braghin • F. Castelli-Dezza • M.M. Maglio  
Department of Mechanics, Politecnico di Milano, Via La Masa 1, Milan 20156, Italy  
e-mail: [marco.bassetti@polimi.it](mailto:marco.bassetti@polimi.it); [francesco.braghin@polimi.it](mailto:francesco.braghin@polimi.it); [francesco.castellidezza@polimi.it](mailto:francesco.castellidezza@polimi.it); [matteo.maglio@polimi.it](mailto:matteo.maglio@polimi.it)

**Fig. 49.1** Chassis board communicating with two axle boards



## 49.2 The Telemetry System

The telemetry project has been developed making two different kind of boards. The first typology of board (Axle Board) is dedicated to acquire strain from the axle, calculate the rainflow algorithm and send data through a wireless communication link. The second typology of board (Chassis Board) is designed to collect data from axle boards and to store them. The projects has been designed to work into railways and other ragged environment. In order to satisfy these requirements, all of the following environment points have been analyzed.

- Working temperature from  $-40\text{ }^{\circ}\text{C}$  to  $+120\text{ }^{\circ}\text{C}$ .
- Accelerations up to 650 g, considering an axle with a diameter equal to 100 mm and a rotational speed of 40 Hz.
- Impulsive accelerations up to 2,000 g.
- Mechanical dimensions less or equal to  $15 \times 60 \times 40\text{ mm}$ .
- Maintenance free PCB board construction.
- Working period of 30 years or more.

To be able to satisfy all of these requirements, a custom telemetry system has been developed at the Department of Mechanics at Politecnico di Milano. Figure 49.1 shows a communication scheme of this new axle telemetry system. Every axle board is able to communicate with the chassis board and vice-versa. Moreover, every axle board is able to be configured by the chassis board, without the need of any cable. In order to ménage the communication between the boards, a star typology configuration has been implemented. Thanks to the star configuration, every single board is detected as an independent node within the wireless sensor network. Hence the chassis board is able to establish a communication link with every axle board irrespective of the other axle boards. This is a great advantage because allows to have this telemetry system more flexible and more modular. A maximum number of 256 can be connected through the same wireless network.



### 49.3 Axle Board

The axle board has been designed in order to measure strain produced within the train axle. The specifications required for this boards are described as follow:

- ADC converter up to 16bit, equal to 0,061  $\mu\epsilon$  of resolution.
- Signal sample-rate up to 1,000 Hz
- Maximum stain up to  $\pm 2,000 \mu\epsilon$ , equal to  $\pm 412$  MPa.
- Thirty seconds time-history with strain threshold value.
- $80 \times 80$  rainflow matrix array, with resolution of  $80 \mu\epsilon$ , equal to 5 MPa.
- Wireless communication features, with a low-power interface.

In order to provide all of these requirements, a micro-controller based board has been developed. Every feature has been integrated onboard and every component has been chosen to limit the power consumption.

#### 49.3.1 Bridge Amplification

The Cauchy strain  $\epsilon$  is the ratio between the deformation  $\Delta L$  of a body when subjected to a force normalized with respect to its initial dimension  $L$ :

$$\epsilon = \frac{\Delta L}{L} \quad (49.1)$$

It can be either positive (tensile) or negative (compressive). Since strain values are usually very small, they are often expressed in micro-strain i.e.  $\epsilon \cdot 10^{-6}$  or  $\mu\epsilon$ . There are various methods for measuring strains: mechanical, optical, acoustical and electrical methods. Some of these, however, do not provide high accuracy while others require too expensive or delicate instrumentation. The use of electrical methods to measure strain is, so far, the cheapest and most practical way. Capacitance and inductance gages have been constructed but vibration sensitivity, mounting difficulties and circuit complexity make them difficult to apply and use. Also piezoelectric sensors can be used to measure strain as, due to a material deformation, a quite high voltage is generated at its terminals but these sensors are fragile and not suitable for static measurements. Resistive gauges are therefore the most widely used. Even for this type of sensors, different solutions were investigated. Carbon-resistor strain gages and the semiconductor strain gages showed high sensitivity to temperature variations. Thus, bonded resistance strain gage are today the most widely used sensors to measure strains. They are made of a very thin wire, or metallic foil, bonded to a thin insulating layer called carrier matrix that must be firmly bonded to the specimen's surface with strong adhesive. The carrier matrix has two important functions: it provided the electrical insulation between the conductor and the specimen and it transmits the proper heat quantity to dissipate. It has been proven that the electrical resistance of the sensor varies linearly with the strain and the sensor's output is only moderately affected by temperature changes and suitable for static and dynamic measurements. Thanks to the printed board technology, very thin foils are achievable, thus leading to very compact gages (with length between 0.2 and 100 mm), and their cost is very small. Gages resistance values are usually in the 30–3,000  $\Omega$  range with the 120–350  $\Omega$  as the mostly used values.

The measure of the resistance change as a function of strain is the so-called gage factor (GF) defined as

$$GF = \frac{\Delta R}{R_G} \bigg/ \frac{\Delta L}{L} = \frac{\Delta R}{R_G} / \epsilon \quad (49.2)$$

where  $\Delta R$  is the change in the resistance and  $R_G$  is the resistance of the gage at no strain. It is a dimensionless quantity that indicated the sensitivity of the strain gauge: the larger the gage factor, the higher its sensitivity. Note that strain gauges are also sensitive to transverse strains since winding have a small part normal to the main direction of the gauge. To minimize this cross-sensitivity, the small part of the winding normal to the main direction of the gauge can be made of special alloys having low resistivity. Moreover, corrections can be made for the transverse strain in the data analysis phase. In order to measure the very small resistance variation that typically occur on railway axles (strains are typically small), a Wheatstone bridge circuit is usually adopted. In order to measure the signal coming from the Wheatstone bridge, the circuit shown in Fig. 49.2 has been designed.

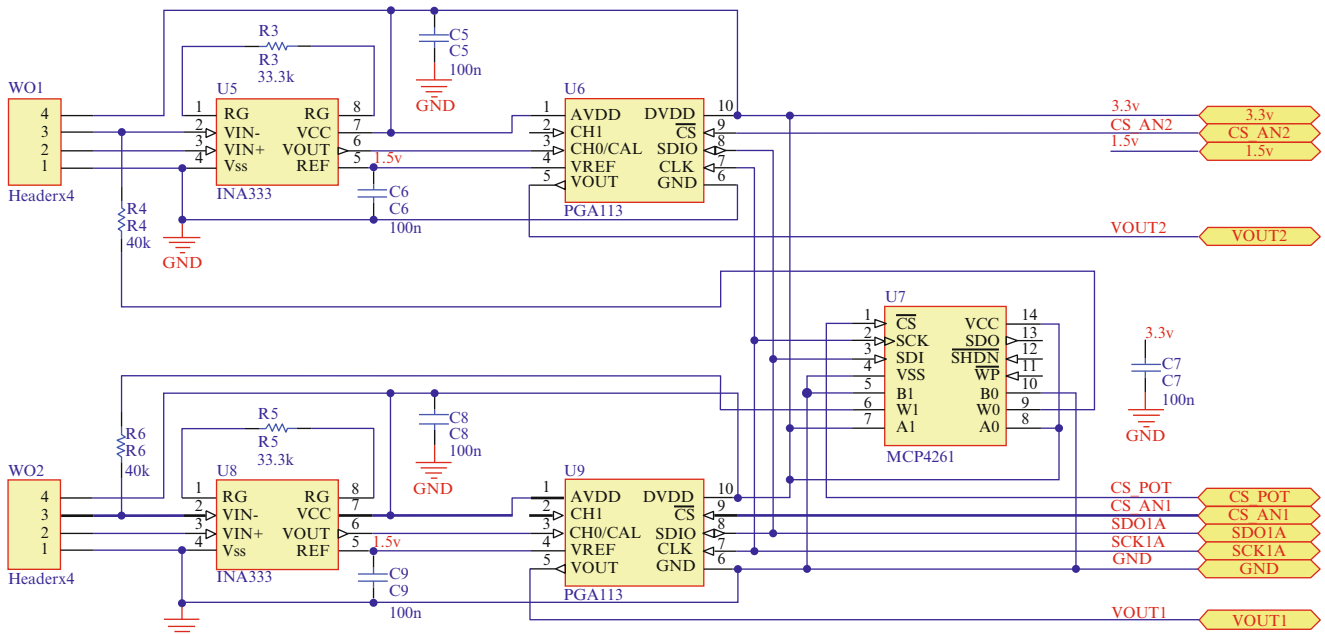


Fig. 49.2 The dual-channel strain gauge amplifier

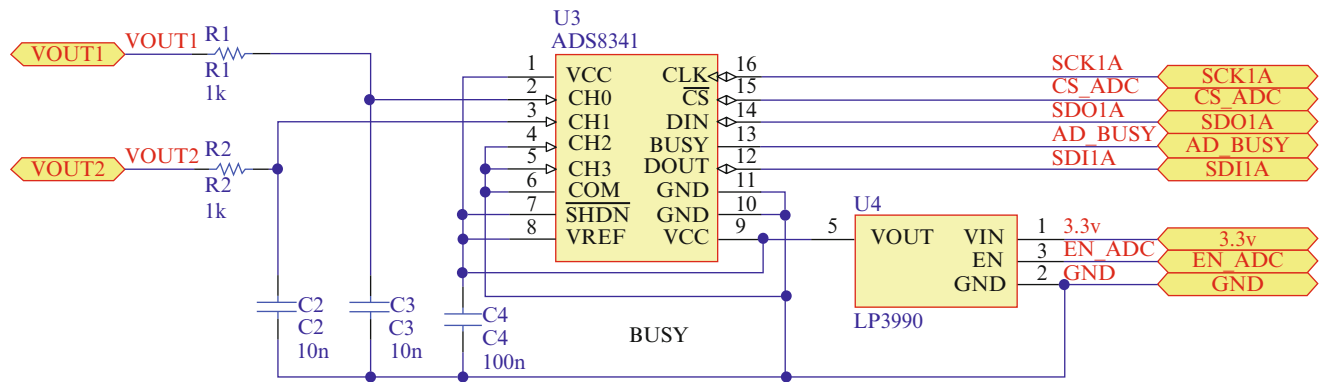


Fig. 49.3 ADC with its own power supply manager

The circuit is able to amplify two different bridges, each with its own gain and offset compensation. This could be useful for measuring strains at two different points along the axle. A Texas Instruments INA333 low-noise zero-drift amplifier has been used as fixed gain pre-amplifier:

$$G = 1 + \frac{100K\Omega}{R_5} = 4 \tag{49.3}$$

The following amplification stage has been designed to be configurable from the firmware. A Texas Instruments PGA113 programmable zero-drift low-noise amplifier has been used. This amplifier has a Rail-to-Rail Input/Output, an offset of 25 mV and a gain error of 0.1% max ( $G \leq 32$ ). Thanks to the SPI interface, the micro-controller is able to adjust the gain to fit the axle strain in the best way. The gain can vary from 2 to 200; hence the total gain can vary from 8 to 800. To be able to compensate a bridge imbalance, a MCP4261 has been placed into the board too. This SPI digital potentiometer is able to compensate up to 100% of imbalance, reducing the need of external and expensive calibration resistors. Figure 49.3 shows the ADC acquisition sub-system. This is a Texas Instruments ADS8341 four-channel multiplexed SAR ADC, with a sampler rate up to 100 kHz in single channel mode, and up to 50 kHz in dual channel mode.

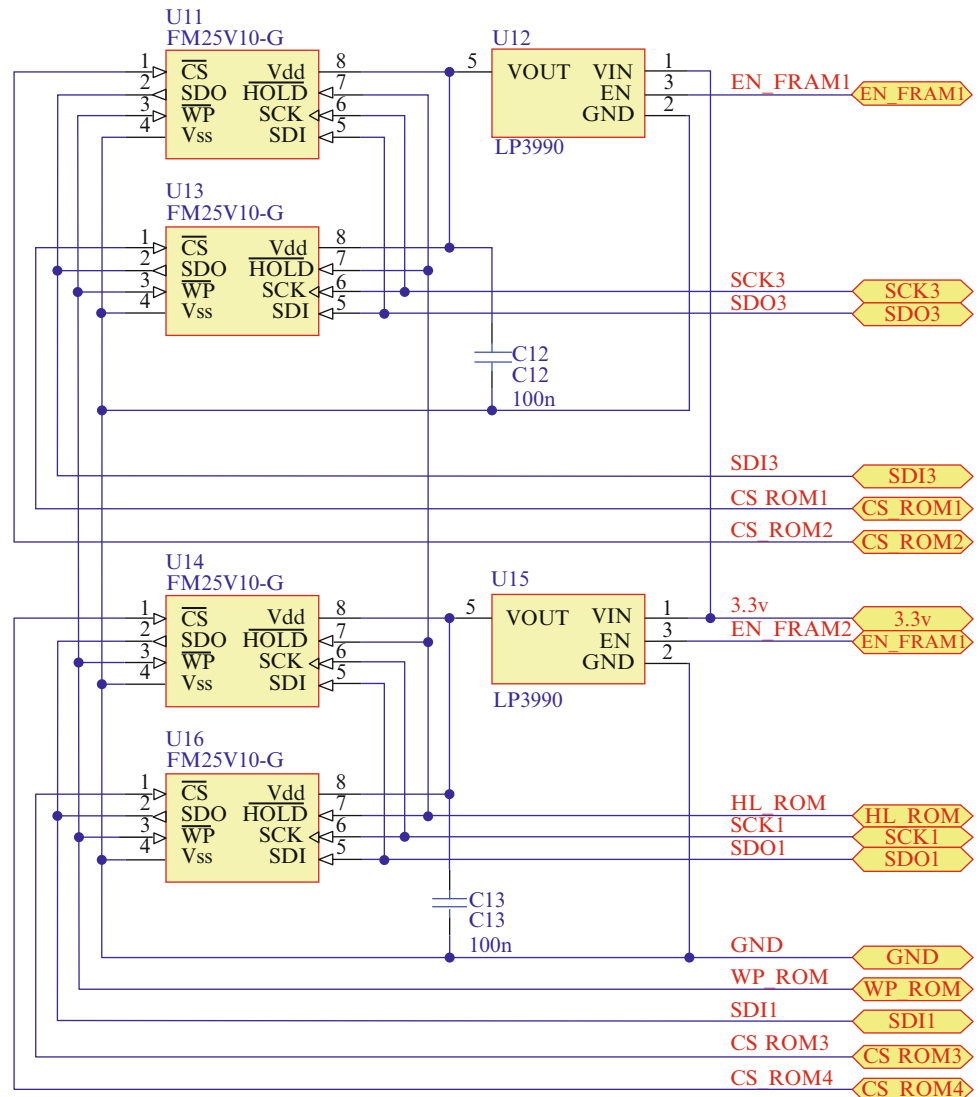
The acquired signal is sampled and hold by the ADS8341 and sent to the micro-controller at the frequency of 1 kHz.

### 49.4 FRAM

The axle telemetry system has been designed to store the strain data onboard. Thus, two ferromagnetic Ramtron FM25V10 RAMs with size equal to 1 Mb were adopted. Their main characteristics are that they guarantee up to 10 years of data retention without any supply and  $10^{14}$  read/write cycles. Two different modules are required to increment the throughput between the microcontroller and the ADC. As shown in Fig. 49.4, each RAM module has been connected with each SPI communication bus. This guarantees the maximum data rate without any data collision problem. Every memory is filled by a double buffer structure every 60 s. Hence, with this storage data rate, we can monitor the axle for a time equal to  $10^{14}$  min, i.e. more or less 190 million years. Considering an  $80 \times 80$  rainfall matrix and a 40 bit representation for each cell of the rainfall matrix, is it possible to monitor up to  $2^{40} = 1.1 \cdot 10^{12} \text{cycles} = 2969 \cdot 10^6 \text{km}$ . Due to the fact that a train axle has an expected life of about  $20 \cdot 10^6 \text{km}$ , the number of cycles stored by the axle board is considered sufficient.

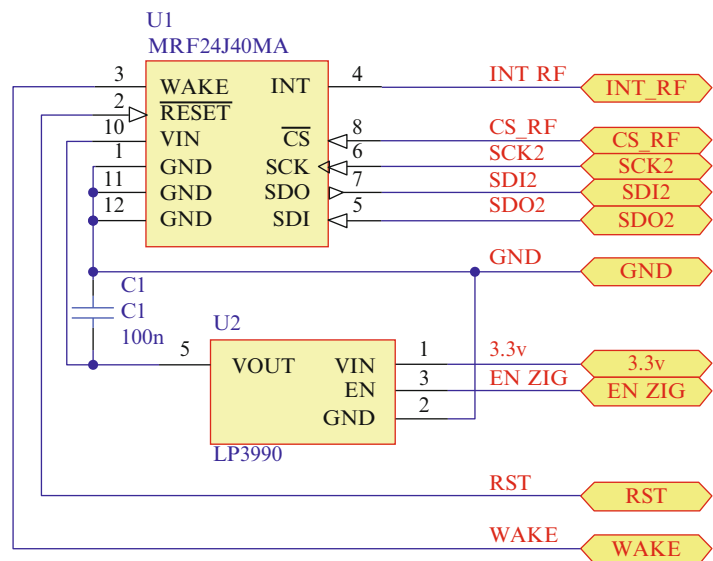
#### 49.4.1 Wireless Communication Module

In order to provide a wireless communication, a RF module from Microchip Electronic has been installed onboard. This is a MRF24J40MA 2.4GHz RF module suitable for both Mi-Wi and Zigbee protocol. Due to the fact that in this application



**Fig. 49.4** Fram modules. Each memory block is connected to a separated SPI bus

**Fig. 49.5** RF module with power manager



a standard communication protocol is not strictly required, a customized Mi-Wi protocol implementation has been used. This customization allows to have an higher throughput data-rate (up to 250 kbps without overhead). The wireless module is useful also for set the axle board parameters and to run a board self test. Figure 49.5 shows the wireless communication module used on axle board.

#### 49.4.2 CPU

The micro-controller used for this board is a Microchip Technology PIC32MX795F512L. This microcontroller is a low power 32bit RISC machine. This controller is able to manage all the internal and external peripherals. Moreover, thanks to its four SPI buses, every external device (i.e. FRAM, ADC, RF module) has its own communication bus towards the micro-controller. This is fundamental to data reliability and data throughput. CPU scheme is shown in Fig. 49.6.

### 49.5 Chassis Board

The chassis board has been designed to allow both connections from all axle boards (if more than one are present on the train) and to store data. The data collected from the axle boards are stored on a USB key, ready to be analyzed when needed. The chassis board is able to send all the collected data through an Ethernet data link too. The micro-controller used for the chassis board, is the same used for the axle boards. This fact has permitted to minimize time overhead during the development and the debugging process. Moreover, this family of micro-controller can easily handle a USB stack for data storage, a TCP/IP stack for Ethernet data link and a Mi-Wi stack for wireless communication concurrently. Due to the fact that is board is placed inside the train chassis, it has not special power supply request.

### 49.6 Power Supply

Unlike the chassis board, the axle board has a tight power supply management. Every component placed on the board has been selected for both performances and low power consumption. Thanks to this approach, we have been able to obtain an high performance and low power board. Anyway we have investigated also different sources for power supply in order to maximize the life of the whole system. The first method the has been implemented is based on a rotating shaft mounted on the train axle. As explained in [4], very good results in terms of power efficiency and reliability are expected. The quality of

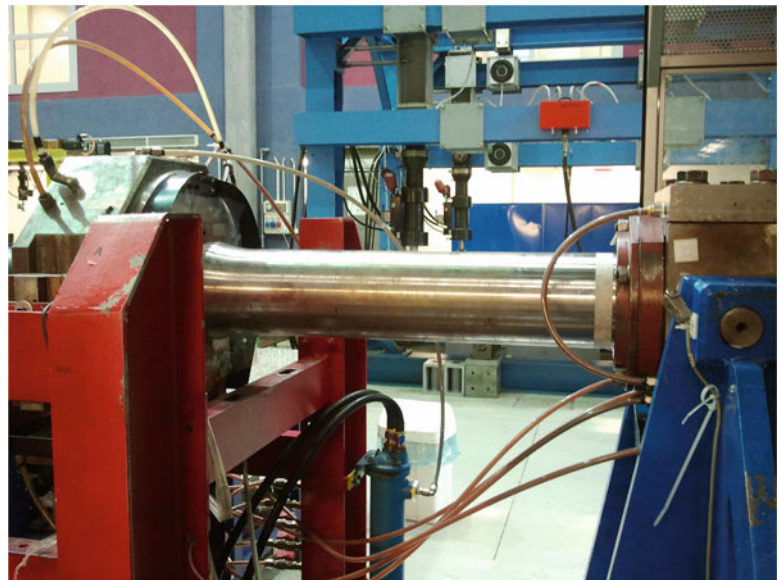




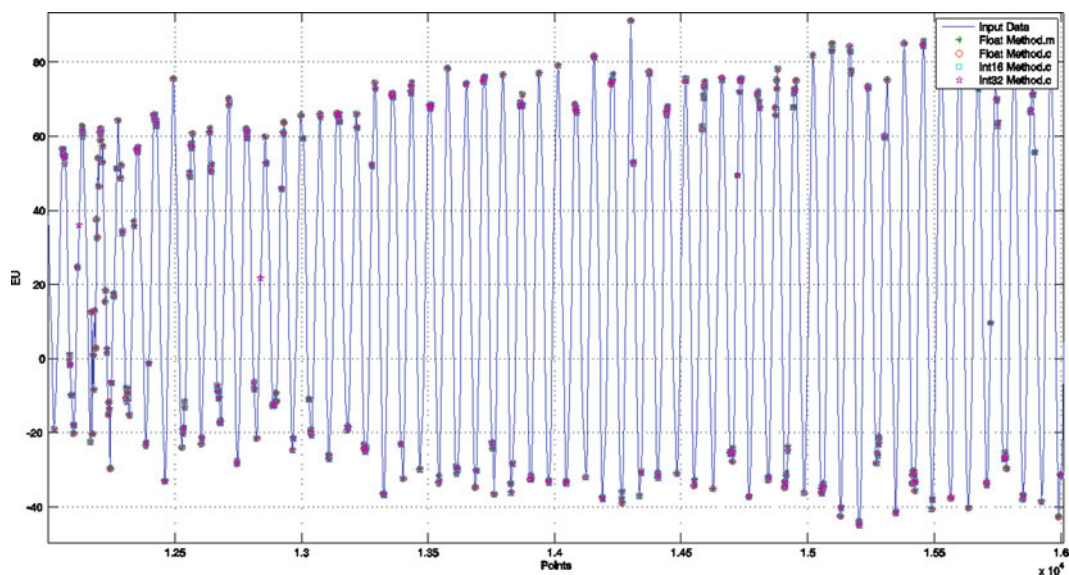
## 49.7 Preliminary Tests

Preliminary tests have been performed at Department of Mechanics at Politecnico di Milano. An axle fatigue test bench has been used for this purpose, and a sinusoidal force pattern has been used. As shown in Fig. 49.7, the test bench as an hydraulic actuator. It is able to apply a force up to 200 MPa at the center of the axle during its rotation. This allows to apply a flexural strength force to be measured by the axle board presented in this paper.

As shown in Fig. 49.8, a flexural strength force has been measured by the axle board. An history of four million points has been use to compare the rainflow algorithm. The first algorithm tested has been written in Matlab using double variables. Then the same input data-set has been analyzed by an algorithm written with Microsoft C++ compiler using double precision variables. Further steps have been performed, using firstly 32-bits integer variables and then 16-bits integer variables. The great advantage of using 16-bits integer variables rather than double precision variables, is a less occupancy of CPU ram and Flash program memory. Moreover, the required dimension for FRAM and the RF data throughput is a quarter when using a 16-bits integer variables. In Fig. 49.9 all of the different configurations are shown. It is clear how 16-bits integer variables allows to reach the same results as double precision variable, but with a significant enhancement regarding code

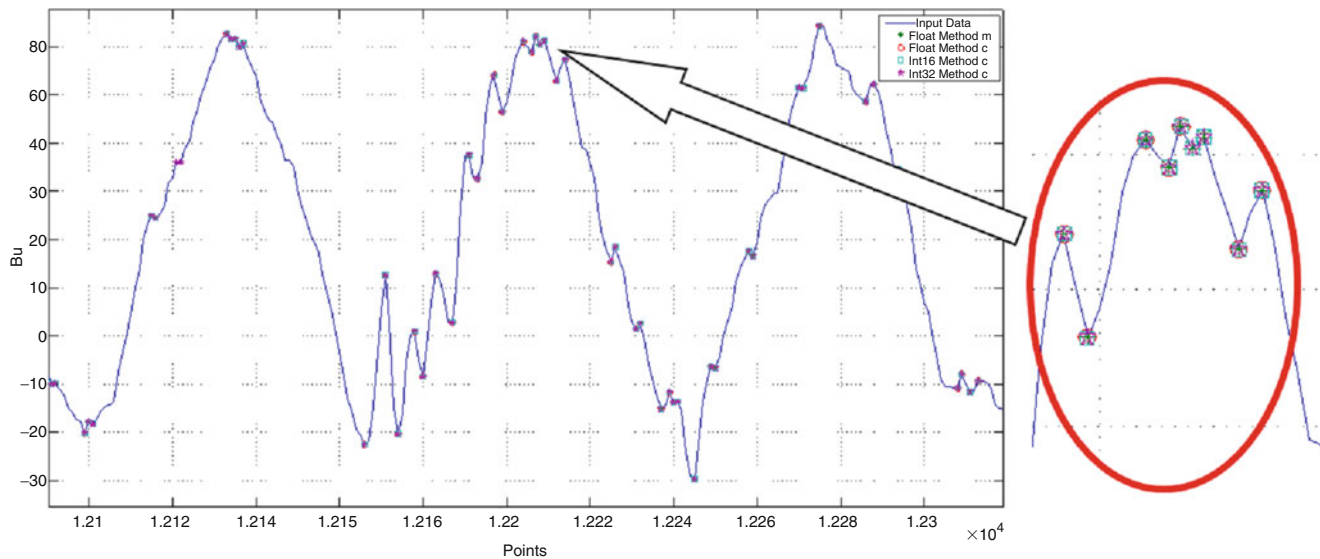


**Fig. 49.7** Axle fatigue bench installed at Department of Mechanics



**Fig. 49.8** A flexural strength acquire by the telemetry axle board





**Fig. 49.9** A comparison between different rainflow algorithm used

efficiency and power consumption. Laboratory tests has shown that a 100 kB data history has been transferred by the RF link in 12 s using a 16-bits variable, and in 42 s using double precision variables. The RF protocol does not allows to reduce the necessary transmission overhead.

## 49.8 Conclusions

In the present paper it is shown that the combination of a simple power induction system, a fast data processing unit and a low power RF data transmission system lead to an easy and reliable telemetry system for train axle monitoring. Preliminary tests have been carried out on an axle fatigue test bench to assess whether the main requirements, especially in terms of energy consumption and mechanical survivability of the board to such high accelerations, were met.

## References

1. Diana G, Resta F, Braghin F, Boccione M, Di Gialleonardo E, Crosio P (2012) Methodology for the calibration of dynamometric wheel-sets for the measurement of the wheel-rail contact forces. *Ingegneria Ferroviaria* 67(1):9–21
2. dos Santos JLA, de Araújo RCC, Filho ACL, Belo FA, de Lima JAG (2011) Telemetric system for monitoring and automation of railroad networks. *Transport Plann Tech* 34(6):593–603
3. Alfi S, Braghin F, Bruni S (2008) Numerical and experimental evaluation of extreme wheel-rail loads for improved wheelset design. *Vehicle Syst Dynam* 46(suppl1):431–444
4. Bassetti M, Braghin F, Castelli-Dezza F, Iacchetti MF, Maglio MM (2012) Energy transfer on rotating shafts using PM-printed winding machine. In: *Proceedings of the XXth international conference on electrical machines (ICEM'2012)*. Marseille, France

# Chapter 50

## Triaxial Multi-range MEMS Accelerometer Nodes for Railways Applications

M. Bassetti, F. Braghin, G. Cazzulani, and F. Castelli-Dezza

**Abstract** For the homologation of railway vehicles, standards ([1, 2]) require the measurement of wheel-rail contact forces as well as the accelerometric monitoring of all bogies along the train. Moreover, also carbody accelerations are usually measured for assessing passenger comfort. Obviously, measuring ranges of accelerometer mounted on axle boxes, bogies and carbodies are significantly different and require different types of accelerometer. Besides the measuring range, also other requirements are important for this type of application: accelerometers have to be rugged, easy-to-configure, low-noise and sealed and, due to the possibility of having long cables (long distances between the measuring point and the acquisition system), measured signals have to be pre-amplified at the measuring point. Weight and dimensions, instead, are of less importance. In the present paper, a low cost, sealed, rugged, easy-to-configure, low-noise, amplified triaxial multi-range MEMS based accelerometer for railway applications is designed, produced, calibrated and tested on a freight train. Acceleration ranges,  $\pm 2$ ,  $\pm 16$  and  $\pm 40$  g, along the three axis can be adjusted interactively and independently and the output can be set either to digital or to analog (with compensation of the cable length). In the paper the design of the acceleration nodes both from the electronic and mechanical point of view is presented. The results of the calibration and of the experimentation are also shown.

**Keywords** MEMS • Accelerometer • Sensors • Railway • Homologation

### 50.1 Introduction

Railway vibrations are induced by track irregularity [3] as well as wheel and rail defects [4], and may affect vehicle stability [5] and passengers' comfort [6]. It is therefore of great importance to monitor the vibratory behavior of railway vehicles. This can be done either by directly measure accelerations at different point on the vehicle (as prescribed by the standards) or by using innovative measuring systems such as FBGs [7]. Note that the same measuring setup can be used for monitoring the track behavior [8, 9]. The present paper focuses on railway vehicle monitoring through accelerometers.

As stated in the standards, lateral “accelerations at the bogie . . . allow an assessment of running safety on a simplified basis. Furthermore they allow the monitoring of the running behaviour of vehicles. The running characteristics of the vehicles of a test train, for example, can be monitored if the vehicles are not equipped for the measurement of forces between wheel and rail” [2]. Moreover, lateral and vertical “accelerations in the vehicle body . . . are used for the simplified assessment of running safety” [2]. Finally, also accelerations at the axle are sometimes “used for non-bogie vehicles if no forces are measured” [2]. Thus, for the homologation of railway vehicles, several accelerometers with quite different measuring ranges, depending on the direction of measurement (lateral or vertical) as well as on the point of application of the accelerometer (axle box, bogie or carbody), are required. This implies that railway homologation laboratories have the need of acquiring numerous low-noise accelerometers as well as of re-calibrating them periodically. Now imagine to have a general purpose low noise accelerometer for railway homologation applications with ranges that could be adjusted independently along the

---

M. Bassetti (✉) • F. Braghin • G. Cazzulani • F. Castelli-Dezza  
Department of Mechanical Engineering, Politecnico di Milano, Via La Masa 1, 20156 Milan, Italy  
e-mail: [marco.bassetti@polimi.it](mailto:marco.bassetti@polimi.it); [francesco.braghin@polimi.it](mailto:francesco.braghin@polimi.it); [gabriele.cazzulani@polimi.it](mailto:gabriele.cazzulani@polimi.it); [francesco.castellidezza@polimi.it](mailto:francesco.castellidezza@polimi.it)

three directions. This would significantly reduce the required stock of accelerometers, since the same accelerometer could be mounted anywhere on the train, as well as greatly facilitate the installation, since the accelerometer could be oriented as best fits the position.

Besides the requirement of having a general purpose low noise accelerometer with independently adjustable ranges along the three axis (with the possibility of easily reconfiguring these ranges), basic requirements for railway applications are that the accelerometer should be able to measure constant accelerations (at least on the carbody) and it should be rugged and sealed (in order to be mounted on axle-boxes and bogies). Finally, the acquisition system is typically installed inside the carbody while the measuring points may be quite far away from where the acquisition system is (it can happen that accelerations on bogies different from those of the wagon on which the acquisition system is installed are acquired). Thus, long cables are required. To compensate for the voltage dropout of such possibly long cables, various solutions are available: digital mode, current mode and voltage mode with voltage dropout compensation. For railway applications, instead, weight and dimensions of the accelerometer are less important.

According to these requirements an innovative low cost, sealed, rugged, easy-to-configure, low-noise, amplified triaxial multi-range MEMS based accelerometer for railway applications is designed, produced, calibrated and tested on a freight train.

## 50.2 Design of the Accelerometer Node

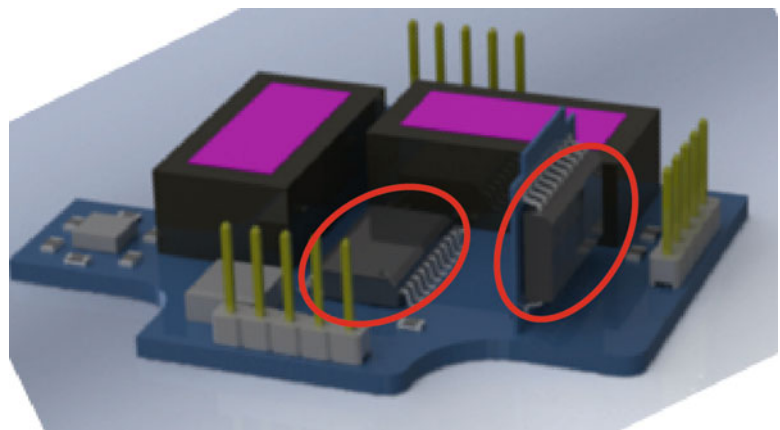
The accelerometer node has four built in bi/triaxial MEMS accelerometers with three different sensibilities, one low noise differential amplifier for each MEMS channel, internal regulated power supply and a sensibility switch. The two triaxial  $\pm 2$  and  $\pm 16$  g MEMS accelerometers are produced by Analog Devices® (ADXL327 and ADXL326 model) while the two biaxial  $\pm 40$  g MEMS accelerometers are produced by Freescale Semiconductor® (MMA3201KEG model).

The MEMS accelerometers by Analog Devices are capacitive, thus allowing to measure accelerations from DC up to 1,600 Hz along both X and Y axes and up to 550 Hz along Z axis, can survive to shocks up to 10,000 g and have an analog output. Both sensors have a very compact package ( $4 \text{ mm} \times 4 \text{ mm} \times 1.45 \text{ mm}$ ), have an offset versus temperature of  $\pm 1 \text{ mg}/^\circ\text{C}$  and a noise density of  $300 \mu\text{g}$  along all three axes. All signals from ADXL327 and ADXL326 are low-pass filtered with a first order Butterworth filter having cut-off frequency equal to:

$$f_{-3dB} = \frac{1}{2\pi RC_{x,y,z}} \quad (50.1)$$

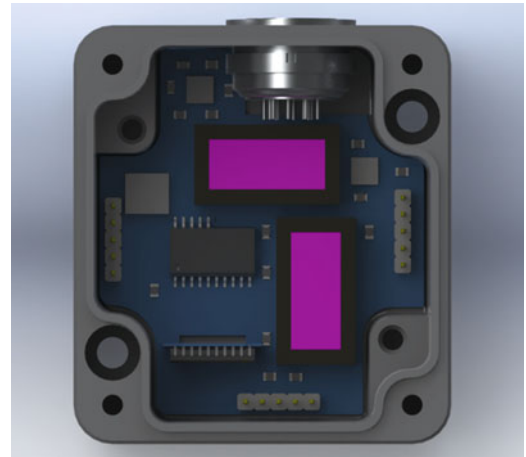
being  $C_{x,y,z}$  equal to 10 nF and R equal to 32 k $\Omega$ . Thus, the cut-off frequency along all three axis is equal to 495 Hz.

The MEMS accelerometers by Freescale Semiconductor are 2-axis capacitive sensors with integrated temperature compensation, analog output and low-pass fourth order Bessel filter with cut-off frequency equal to 400 Hz. Bessel analog filters are characterized by almost constant group delay over the entire pass-band thus preserving the wave shape of filtered signals. The MMA3201KEG has a noise density of 2.2 mg along both axes. In order to measure accelerations along three axes, two sensors have been installed on the PCB, one with base parallel to the PCB and one with base normal to the PCB (Fig. 50.1). The mounting of the MEMS accelerometers is such that there is a redundancy along Y-axis.

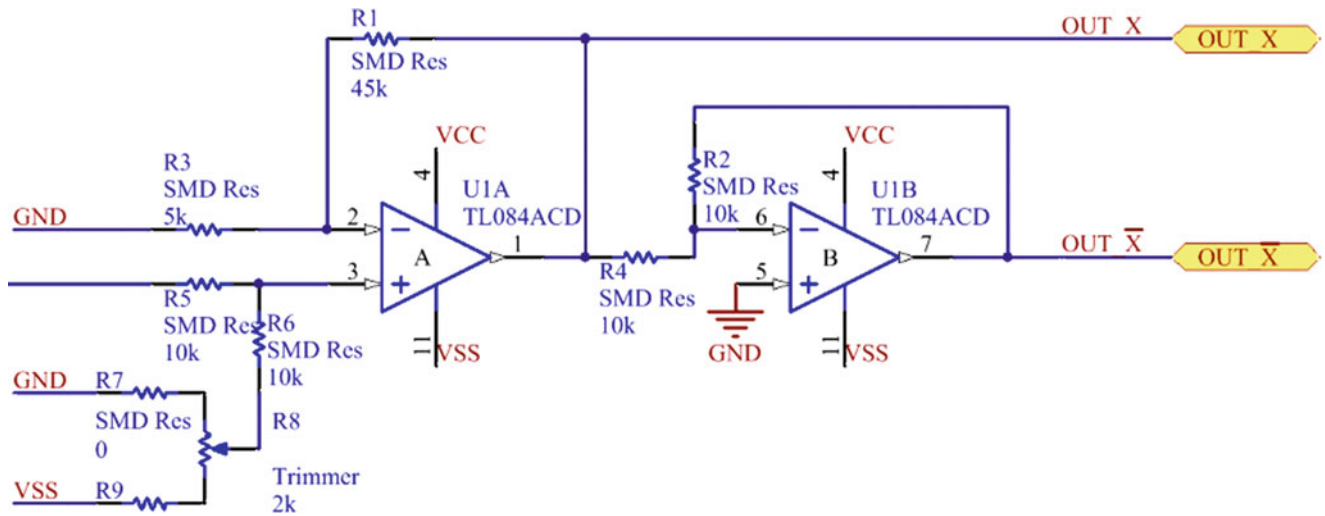
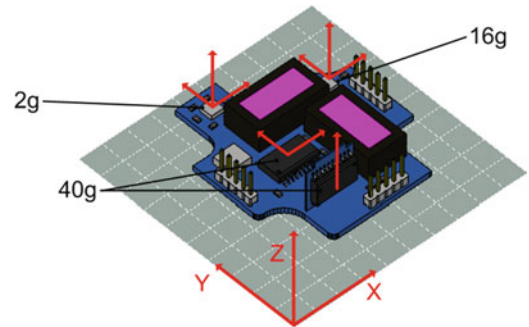


**Fig. 50.1** Layout of the 2-axis Freescale Semiconductor® MMA3201KEG accelerometers

**Fig. 50.2** Lower PCB inside the aluminum case



**Fig. 50.3** Orientation of the sensors on the lower PCB



**Fig. 50.4** Electronic scheme of the differential output amplifier

To maintain a compact size, without giving up integration or features, two separated PCBs, installed inside an IP68 aluminum case, have been used. On the lower PCB (Fig. 50.2), rigidly connected to the base of the aluminum case, all accelerometers as well as the power supplies are mounted (Fig. 50.3). This guarantees the highest possible bandwidth of the accelerometer node.

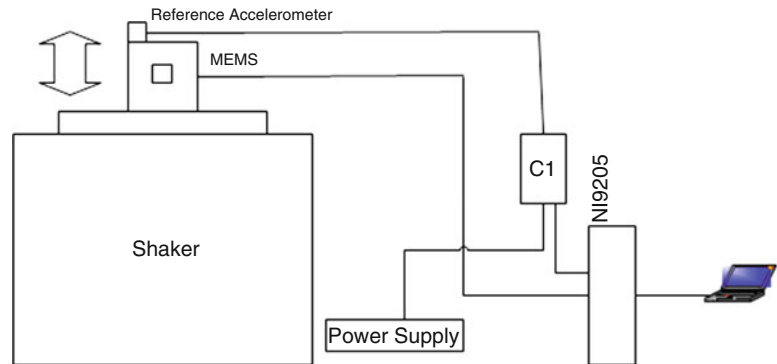
The second PCB includes the sensibility switch and the differential output amplifier. The sensibility switch allows selecting the measuring range for each axis independently. The gain for each channel is fixed, and, as shown in Fig. 50.4, it is equal to:

$$G = 1 + \frac{R_1}{R_3} \quad (50.2)$$

i.e. it is equal to 10. To fine adjust the offset of the amplified signals, three trimmers have been placed onboard. The second stage of the operational amplifier acts as a unitary gain inverter, providing the differential output. The output signal is proportional to the measured acceleration and is limited to  $\pm 10$  V. Three 16bit ADC converters are also mounted on the second PCB thus allowing to digitalize the measured accelerations for the digital mode.

### 50.3 Calibration of the Accelerometer Node

After the design phase, the accelerometer node has been calibrated. In order to estimate the frequency response function, a back-to-back calibration method has been applied: a Brüel & Kjær DeltaTron 4,508 reference accelerometer has been placed contiguous to the sensor to be tested. Both the reference accelerometer and the accelerometer node have been rigidly constrained to an Unholtz-Dickie Corp. SA15-S452-PB electrodynamic shaker (Fig. 50.6) through an aluminum block (approx. 100 mm  $\times$  100 mm  $\times$  100 mm) and submitted to sweep sine accelerations (generated by an Agilent 33220A function generator) along all three axes. The reference and node accelerations (analog mode) have been acquired at 5,120 Hz through a National Instruments NI9205 acquisition board (Fig. 50.5).



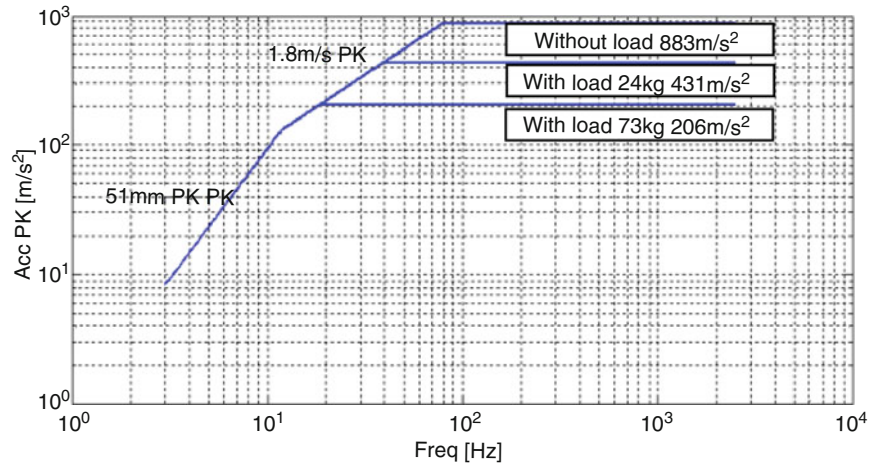
**Fig. 50.5** Acquisition scheme adopted for the calibration of acceleration nodes



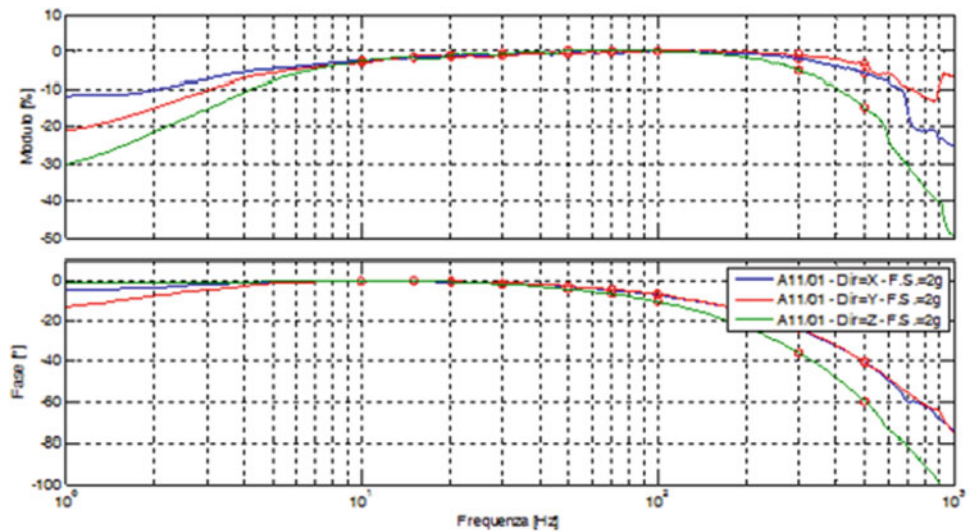
**Fig. 50.6** Unholtz-Dickie Corp. SA15-S452-PB electrodynamic shaker



**Fig. 50.7** Maximum acceleration achievable through Unholtz-Dickie Corp. SA15-S452-PB electrodynamic shaker



**Fig. 50.8** Transfer function  $H_1$  for A11 accelerometer node, set to  $\pm 2$  g, along all three directions



The adopted shaker is able to drive excitations up to 100 g at 100 Hz. At lower frequencies, the maximum acceleration is limited by the maximum displacement of the magnet (54 mm) as shown in Figs. 50.6 and 50.7.

The reference Brüel & Kjær accelerometer adopted has the following specifications:

- Reference sensibility (@159.2 Hz, 20 m/s<sup>2</sup> RMS): 98.3 mV/g
- Bandwidth (+/-4 %): 5–9,000 Hz
- Bandwidth (+/-2 %): 20–6,000 Hz
- Measure range: +/-50 g

A sweep signal from 0.1 to 1 kHz at three different levels of acceleration ( $\pm 1.5$ ,  $\pm 4$  and  $\pm 4.5$  g), corresponding to the three measuring scales ( $\pm 2$ ,  $\pm 16$  and  $\pm 40$  g), has been applied along all three axes. For each test, the transfer function  $H_1 = P_{xy}/P_{xx}$  between reference and node accelerations has been evaluated,  $P_{xy}$  being the cross power spectral density between the input signal (reference acceleration) and the measured output (node acceleration) and  $P_{xx}$  represents the power spectral density of the input signal. As an example, Fig. 50.8 shows the transfer function  $H_1$  for A11 accelerometer node, set to  $\pm 2$  g, along all three directions. The module diagram has been calculated as percentage deviation from the reference accelerometer at 100 Hz while the phase diagram has been calculated as a phase shift with respect to the phase of the reference accelerometer at 10 Hz.



## 50.4 In-line Tests of the Accelerometer Node

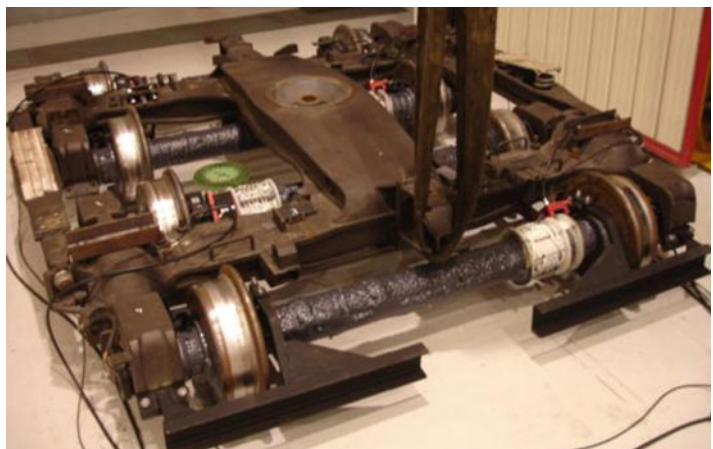
Accelerometer nodes have been used for homologation tests of Saadkms freight wagons (Fig. 50.9). These wagons are characterized by very small radius wheels (380 mm), by a loading level over top-rail equal to 450 mm (thus being called “low floor wagons” or “ultra low floor wagons”) and by a payload equal to 44 t. The small wheel radius, combined with the high payload, generates high wheel-rail contact pressures that lead to increased rolling contact fatigue and wear [10]. To avoid these phenomena, each wagon is equipped with two bogies and each bogie is equipped with four wheelsets (Fig. 50.10). To improve curving performances, wheelsets are coupled two by two through a semi-bogie that is connected to the bogie through rubber elements.

In order to carry out homologation tests, acceleration nodes were placed:

- One accelerometer on the left semi-bogie connecting the first and second wheelsets in correspondence of the connection with the bogie
- One accelerometer on the bogie in correspondence of the connection with the left semi-bogie connecting the first and second wheelsets
- One accelerometer on the bogie in correspondence of the connection with the left semi-bogie connecting the third and fourth wheelsets
- One accelerometer on the bogie in correspondence of the connection with the left semi-bogie connecting the fifth and sixth wheelsets
- One accelerometer on the bogie in correspondence of the connection with the left semi-bogie connecting the seventh and eighth wheelsets
- One accelerometer at the center of the wagon in correspondence of the connection with the front bogie (Fig. 50.11)
- One accelerometer at the center of the wagon in correspondence of the connection with the rear bogie

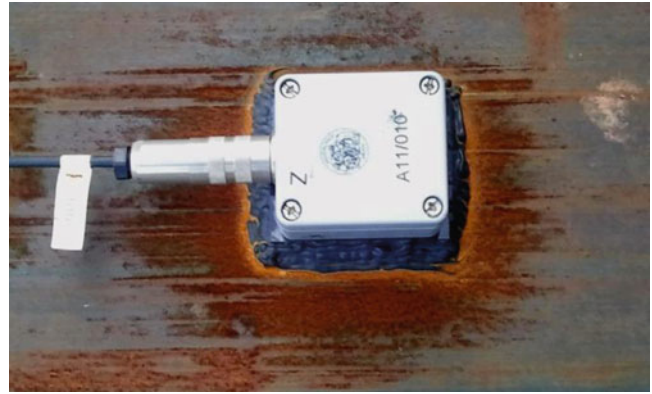


**Fig. 50.9** Saadkms freight wagon

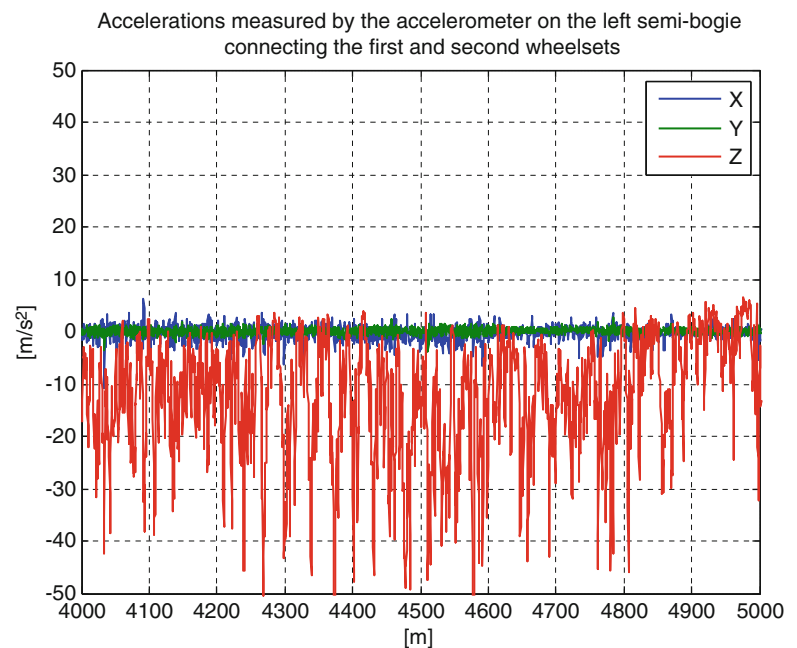


**Fig. 50.10** Saadkms bogie

**Fig. 50.11** Accelerometer node placed at the center of the wagon in correspondence of the connection with the front bogie



**Fig. 50.12** Accelerations measured by the accelerometer on the left semi-bogie connecting the first and second wheelsets while running at 90 km/h along a straight track followed by a right and left hand curve



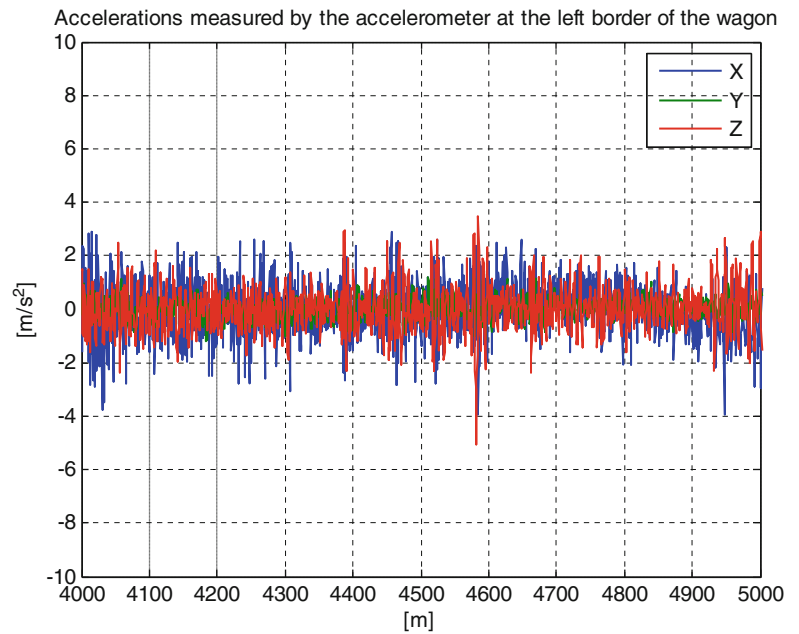
- One accelerometer at the left border of the wagon in correspondence of the connection with the front bogie

Besides acceleration channels, several other quantities were measured, from wheel-rail contact forces on the first four wheelsets to relative displacements of the semi-bogie/bogie with respect to the wagon. Tests were performed along the Italian homologation track (from Florence to Arezzo and to Empoli) as well as on switches and crossings to assess the curving performances of the considered wagon. As an example, Fig. 50.12 shows the accelerations measured by the accelerometer on the left semi-bogie connecting the first and second wheelsets in correspondence of the connection with the bogie while running at 90 km/h along a straight track followed by a right and left hand curve of 500 m radius with a super-elevation of 100 mm. Figure 50.13, instead, shows the accelerations measured by the accelerometer at the left border of the wagon in correspondence of the connection with the front bogie while running along the same track. The constant contribution associated to gravity has been removed and all signals are low pass filtered at 40 Hz with a fourth order Butterworth filter.

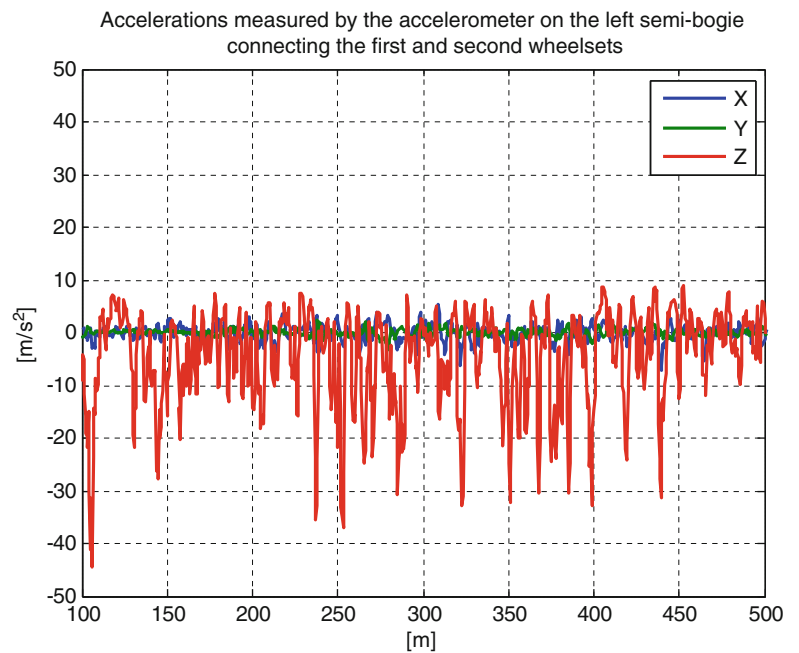
From Fig. 50.12 it can be clearly seen that the left semi-bogie experiences high vertical accelerations (higher than 5 g) and there is a dominant frequency of about 1 Hz (25 m of wavelength) associated to a vertical resonance of the semi-bogie with respect to the bogie. Figure 50.13, instead, shows much lower accelerations and there is no dominant frequency. Right hand curve entrance and right hand curve exit – left hand curve entrance can be seen at 4,380 and 4,580 m.

Figures 50.14 and 50.15, instead, show the accelerations measured by the same accelerometers considered in the previous figures while running over a double crossing of 170 m radius at 30 km/h.

**Fig. 50.13** Accelerations measured by the accelerometer at the left border of the wagon while running at 90 km/h along a straight track followed by a right and left hand curve

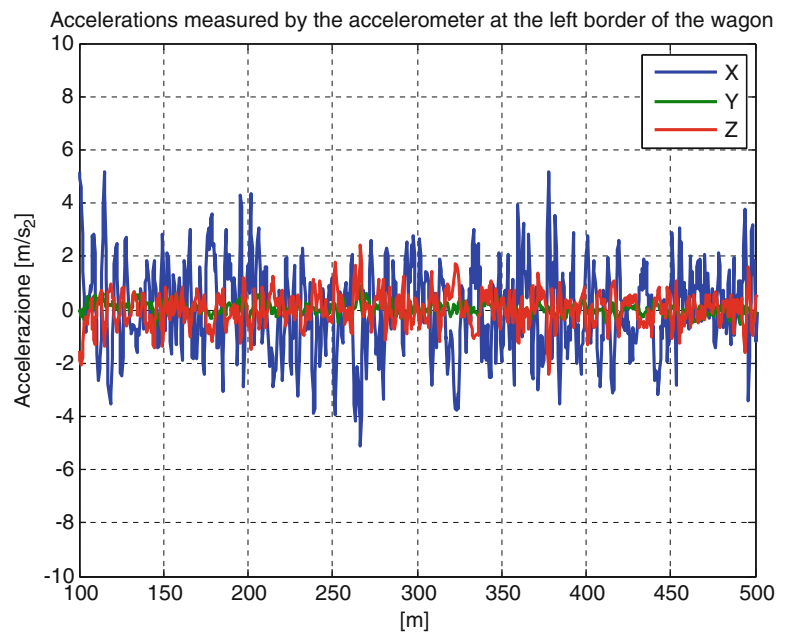


**Fig. 50.14** Accelerations measured by the accelerometer on the left semi-bogie connecting the first and second wheelsets while running at 30 km/h over a double crossing of 170 m radius



On crossings, a higher longitudinal acceleration along the longitudinal direction than along the vertical and lateral directions of the accelerometer node at the left border of the wagon can be observed. This is due to the high irregularity present on crossings [11].

**Fig. 50.15** Accelerations measured by the accelerometer at the left border of the wagon while running at 30 km/h over a double crossing of 170 m radius



## 50.5 Conclusions

A low cost, sealed, rugged, easy-to-configure, low-noise, amplified triaxial multi-range MEMS based accelerometer node for railway applications has been designed, produced, calibrated and used for the homologation of a freight train. It is shown that the use of such accelerometer node greatly facilitates the measurement setup. Further improvements will be implemented in order to be re-configure the measuring ranges as well as the offset of the accelerometer nodes via software instead of acting on deep switches and on trimmers as it is presently.

## References

1. Fiche UIC 518 (2005) Testing and approval of railway vehicles from the point of view of their dynamic behaviour – Safety –Track fatigue – Ride quality
2. EN 14363 (2005) Railway applications – Testing for the acceptance of running characteristics of railway vehicles – Testing of running behaviour and stationary tests
3. Cheli F, Corradi R (2011) On rail vehicle vibrations induced by track unevenness: analysis of the excitation mechanism. *J Sound Vib* 330(15):3744–3765
4. Alfi S, Braghin F, Bruni S (2008) Numerical and experimental evaluation of extreme wheel-rail loads for improved wheelset design. *Veh Syst Dyn* 46(1):431–444
5. Braghin F, Bruni S, Alfi S (2006) Critical velocity of railway vehicles. In: Proceedings of the mini conference on vehicle system dynamics, identification and anomalies. Budapest, Hungary, pp 143–152
6. Cohen B, Dai M, Ogorodnikov D, Laurens J, Raphan T, Müller P, Athanasios A, Edmaier J, Grossenbacher T, Stadtmüller K, Brugger U, Hauser G, Straumann D (2011) Motion sickness on tilting trains. *FASEB J* 25(11):3765–3774
7. Barreda A, Molina T, Valero E, Recuero S (2010) Use of fiber optic sensors for measurement railway vibrations. In: Proceedings of SPIE: the international society for optical engineering, vol. 7653. Porto, Portugal
8. Weston PF, Ling CS, Roberts C, Goodman CJ, Li P, Goodall RM (2007) Monitoring vertical track irregularity from in-service railway vehicles. In: Proceedings of the institution of mechanical engineers, Part F: Journal of Rail and Rapid Transit 221(1):75–88
9. Braghin F, Bruni S, Collina A (2009) Prediction of structure-borne vibrations induced in a large structure by train passage. In: Proceedings of the 12th international conference on civil, structural and environmental engineering computing. Stirlingshire, UK
10. Braghin F, Bruni S, Dwyer-Joyce R, Lewis R (2004) A fast and reliable algorithm for the estimation of railway wheel wear. In: Proceedings of the mini conference on vehicle system dynamics, identification and anomalies. Budapest, Hungary, pp 201–208
11. Di Gialleonardo E, Braghin F, Bruni S (2012) The influence of track modelling options on the simulation of rail vehicle dynamics. *J Sound Vib* 331(19):4246–4258

# Chapter 51

## Acoustical Excitation for Damping Estimation in Rotating Machinery

Bram Vervisch, Michael Monte, Kurt Stockman, and Mia Loccufier

**Abstract** In experimental modal analysis a structure is excited with a force in order to estimate the frequency response function. Typically, this force is generated by a shaker or a hammer impact. Both methods have proven their usefulness, but have some well-known disadvantages. A main disadvantage of the shaker is that it has to be fixed to the structure whereas with a hammer it is not possible to excite a specific frequency. To overcome these disadvantages, alternative non-contact methods can be used. There are several non-contact techniques, i.e. pressurized air, laser, acoustics, etc. By using acoustics as an excitation technique it is easy to select an excitation signal going from random noise to a simple sine. Also the equipment to produce the acoustic excitation is rather cheap. However, the state of the art does not offer a straightforward technique to estimate the excitation force, making it difficult for applications such as experimental modal analysis. In this research, acoustic excitation is compared with hammer excitation to estimate the frequency response function of two shafts. Especially a method to validate the force induced by the acoustics is derived. The final purpose of this research is to estimate the damping properties of rotating machinery.

**Keywords** Rotordynamics • Damping estimation • Non-contact excitation • Acoustics • Frequency response function

### 51.1 Introduction

In rotating machinery, damping plays an important role in the stability analysis [1]. If the bearings do not provide sufficient damping, a rotor can become unstable due to the presence of its internal damping, because the latter can excite instead of dissipate vibrational energy [2]. Several theoretical models have been investigated to estimate the stability threshold speed above which no stable operation is possible [3–5]. In order to validate these models, experimental methods are necessary. Non-contact excitation and measurement techniques are required because the system is rotating.

Excitation with an electrodynamic shaker has proven its usefulness in experimental modal analysis. With a shaker, several excitation signals such as random noise or simple sines are possible. Furthermore, the excitation force and the acceleration can be measured accurately by using an impedance head [6]. The shaker can also be used on a rotating shaft by applying the force on an existing or a dedicated bearing [7]. This bearing, however, not only introduces mass loading, but also adds extra damping, making it inefficient for accurate damping estimation. With a hammer impact, this drawback can be avoided. Nevertheless, there are also some significant disadvantages when using this technique [8]. For one thing, repeatability is a

---

B. Vervisch (✉) • M. Monte • K. Stockman  
Department of Electromechanical Engineering, Technical University of West-Flanders,  
Graaf Karel de Goedelaan 5,  
B-8500, Kortrijk, Belgium

Department of Electrical Engineering, Systems and Automation, University of Ghent,  
Technologiepark 914, B-9052, Zwijnaarde, Gent, Belgium  
e-mail: [bram.vervisch@howest.be](mailto:bram.vervisch@howest.be); [michael.monte@howest.be](mailto:michael.monte@howest.be); [kurt.stockman@howest.be](mailto:kurt.stockman@howest.be)

M. Loccufier  
Department of Electrical Engineering, Systems and Automation, University of Ghent, Technologiepark 914,  
B-9052, Zwijnaarde, Gent, Belgium  
e-mail: [mia.loccufier@ugent.be](mailto:mia.loccufier@ugent.be)



concern that becomes even a bigger problem when the system is rotating. Also, there is still the possibility of damaging the system and only one type of excitation, namely impact, is possible.

Therefore, non-contact excitation techniques become important. These techniques are mainly pressurized air [9, 10], laser [11], and acoustics [12]. Laser excitation can only be used if very small forces are needed. Pressurized air can produce higher forces, but has a limited bandwidth due to by the minimum pulse duration. With acoustic excitation, the forces are also small, but high enough to get a measurable displacement. Moreover, any kind of excitation signal can be used. However, it is difficult to measure the excitation force caused by the acoustic pressure. Therefore, acoustic excitation is used mostly in operational modal analysis, where the excitation force does not have to be known [12, 13]. Nevertheless, if the goal is to estimate the damping accurately, it is preferable to know the excitation force. In this research an effort is made to estimate the force caused by the acoustic excitation.

In Sect. 51.2, the acoustic excitation is explained for the application of shaft excitation. Subsequently, in Sect. 51.3, acoustic excitation is used to measure one frequency response function, or FRF, of two non-rotating shafts: one shaft supported by two wires in the nodes of the first free mode approximating a free-free beam and a second shaft on rolling element bearings. Section 51.4 proposes a calibration procedure for the estimation of the force produced by the acoustic pressure.

## 51.2 Acoustic Excitation

Acoustic excitation is a technique that has some specific advantages in comparison with traditional techniques such as hammer and shaker excitation. Besides being non-contact, the choice of the excitation signal is arbitrary making parameters such as bandwidth easy to deal with. In Table 51.1 some of the main characteristics of traditional and newer techniques are summed up.

### 51.2.1 Force by Acoustic Excitation

In this research acoustic excitation is used to excite a cylindrical shaft with a length-diameter ratio of 100. Because the shaft is chosen to be thin, small excitation forces will result in a measurable displacement. While hammer or shaker excitation can be assumed to be single-point, acoustic pressure produces multiple-point excitation. Nevertheless, it can be shown that modal parameter estimation is similar [8]. The forces acting on the shaft can be calculated by integrating the acoustic pressure over the surface exposed to the pressure. However, the calculation of the acoustic pressure is far from straightforward and can be calculated with an exact knowledge of the source (sound power, directivity, ...) by using numerical techniques [14]. Without this knowledge, the state of the art does not provide direct technique to calculate the force. Here, a simplified estimation of the force is made, by measuring the pressure at a certain distance and assuming that this pressure is equal on the whole surface of the shaft.

The source is an Atlas Sound PD60A compression driver. These kind of drivers are used in multiple purpose high power horns. In Table 51.2, the specifications taken from the datasheet are shown. The construction of the driver (Fig. 51.2) allows the assumption of plane wave propagation if considered near to the source. Therefore, the shaft will always be placed at a 2 mm distance, in the near field, for low frequencies. At this distance, the force equals the measured sound pressure multiplied

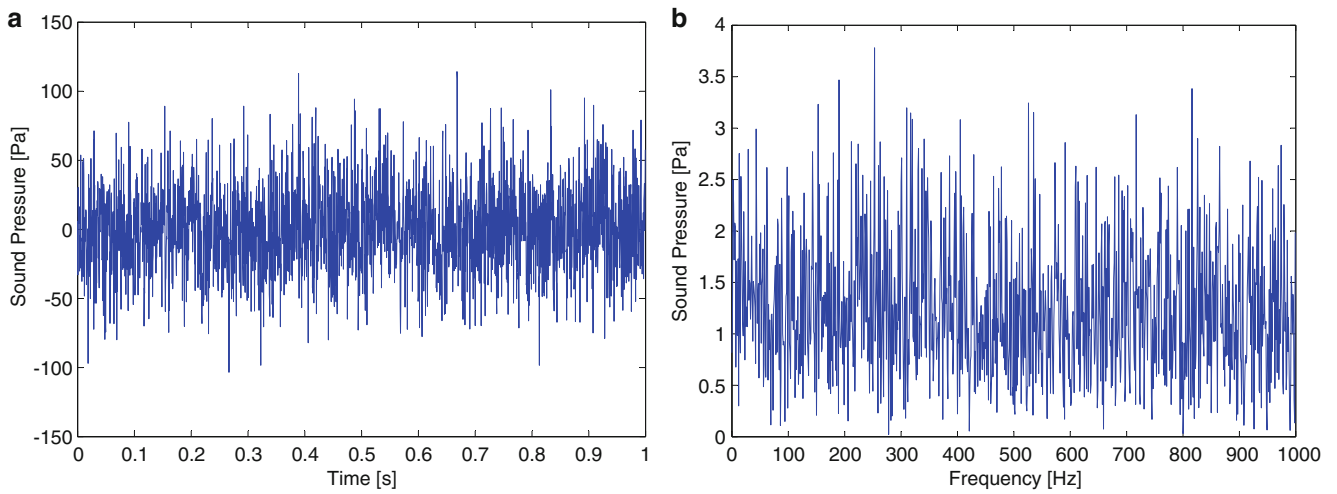
**Table 51.1** Comparison of excitation techniques

Excitation technique	Contact/non-contact	Force range (N)	Excitation signal	Repeatability
Elektrodynamik shaker	Contact	8–1,800	Arbitrary	Fair
Hammer	Contact	5–45,000	Impact	Poor
Laser	Non-contact	$<5 \times 10^{-4}$	Impact	Fair
Pressurized air	Non-contact	$<0.6$	Impact	Fair
Acoustics	Non-contact	$<5 \times 10^{-2}$	Arbitrary	Fair

**Table 51.2** Specifications of the Atlas Sound PD60A taken from the datasheet

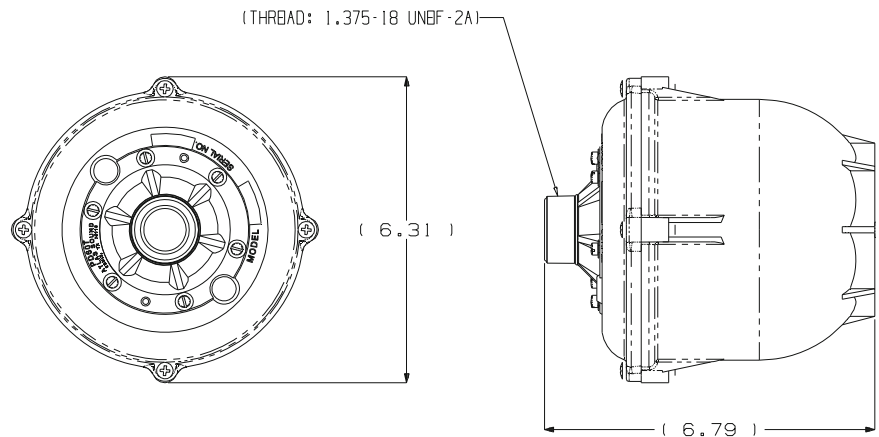
Power rating	Plane wave freq. response	Low freq. limit @ full power	Sound level
60 W	100–3,700 Hz ( $\pm 5$ dB)	300 Hz	Sound level 112.7 (avg)





**Fig. 51.1** Sound Pressure of Gaussian white noise with a sample frequency of 2,000 Hz in time and frequency domain. (a) Sound pressure in time domain. (b) Sound pressure in frequency domain

**Fig. 51.2** Drawing of the Atlas Sound PD60A (dimensions in inch)



by the exposed surface:

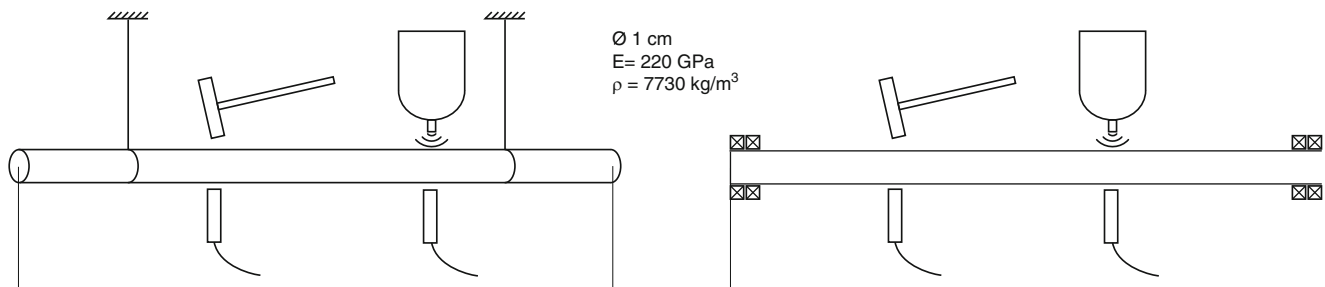
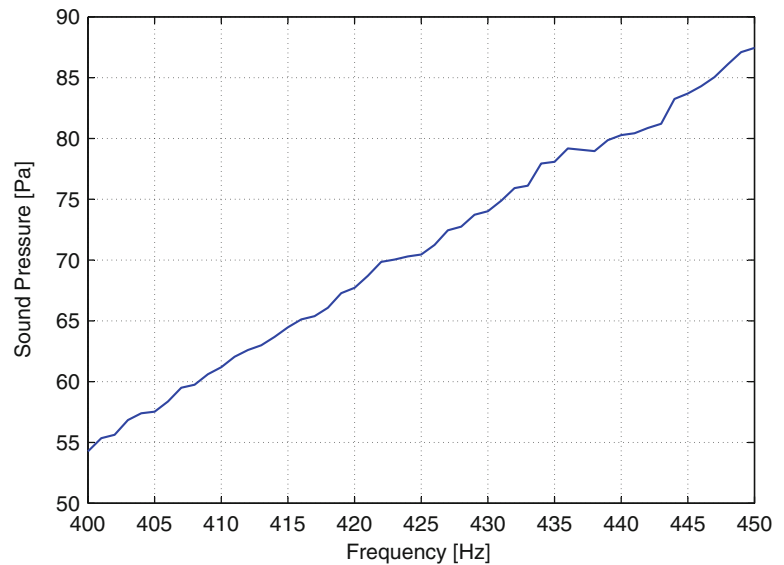
$$F_{acoustic} = P_{acoustic} \frac{\pi d l_{exposed}}{2} \tag{51.1}$$

with  $P_{acoustic}$  the pressure measured at two millimeter from the source,  $d$  the shaft diameter and  $l_{exposed}$  the length of the shaft part exposed to the pressure. This last parameter, by assuming plane wave propagation, equals the diameter of the tube where the sound leaves the source. The amplifier is a Saigor 100, a regular consumer amplifier. In order to get the same pressure in the different measurements, the amplification is kept the same during the whole experiment.

### 51.2.2 Excitation Signal

With acoustical excitation, different excitation signals are possible. Multi-sine, random noise and even pulses can be imposed to the system. However, by having a relatively small acoustic force, all combined signals divide the force over the frequency band. This can be seen in Fig. 51.1a, b where the sound pressure is shown for Gaussian white noise in the time domain and frequency domain. To use the acoustic source at full power, a stepped sine is imposed. While this method is time consuming, it leads to accurate results.

**Fig. 51.3** Sound pressure of the source measured at a distance of 2 mm for a fixed setting of the amplifier



**Fig. 51.4** Impact and acoustic excitation of a free-free shaft and a shaft on bearings

## 51.3 Shaft Experiments

### 51.3.1 Sound Pressure of the Source

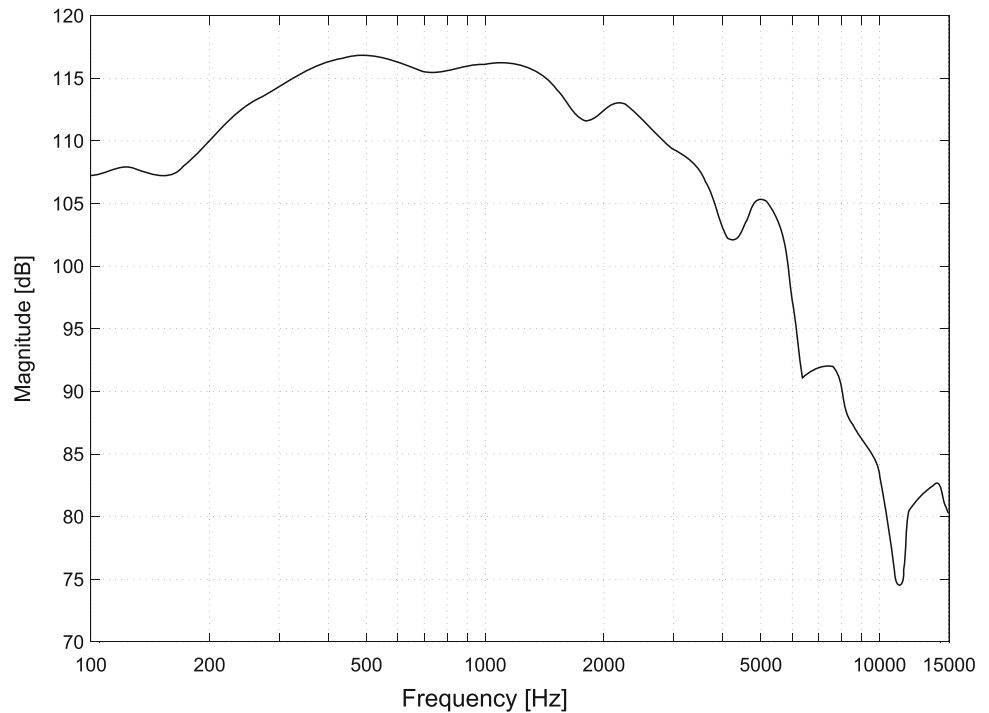
The pressure of the source is measured with a microphone PCB 130D20 in front of the source. The amplifier level is calibrated in a way that the pressure has an amplitude of 54.27 Pa for a 400 Hz sine. Because the source can produce the highest power in an 400–500 Hz range (Fig. 51.5), the pressure is measured from 400 to 450 Hz, with a resolution of 1 Hz. The results are depicted in Fig. 51.3. It can be seen that there is a slight rise in the pressure when the frequency increases, which also corresponds to the trend in Fig. 51.5.

### 51.3.2 Free-Free Shaft

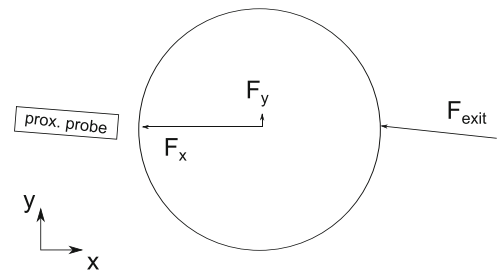
As a proof of concept, the acoustic excitation technique is applied on a shaft in a free-free configuration. This configuration is accomplished by suspending the shaft on two wires in the nodes of the first free mode. The FRF is measured while exciting and measuring at the same location, 0.425 m from the left side. The shaft is in steel CF53 with a density of  $7,730 \text{ kg/m}^3$  and a Young modulus of  $2.2 \times 10^{11} \text{ Pa}$ . The diameter is 0.010 m and the length 1.00 m. At first the shaft is excited by a hammer to get a reference FRF. Secondly the shaft is excited with the sound source at exactly the same place (Fig. 51.4). The displacement is measured by using eddy current probes in order to eliminate the mass-loading of the sensors.

By assuming that the force can be calculated by (51.1) and taking the pressures of Fig. 51.3, the frequency response of the shaft can be calculated directly from displacement measurements. The comparison between the hammer excitation and the acoustic excitation is shown in Fig. 51.9a. For the hammer excitation, no window is used on the measurements, to avoid

**Fig. 51.5** PD-60A Plane Wave Tube Response taken from the datasheet



**Fig. 51.6** Deviation of the excitation force and displacement measurements leading two double resonance frequencies



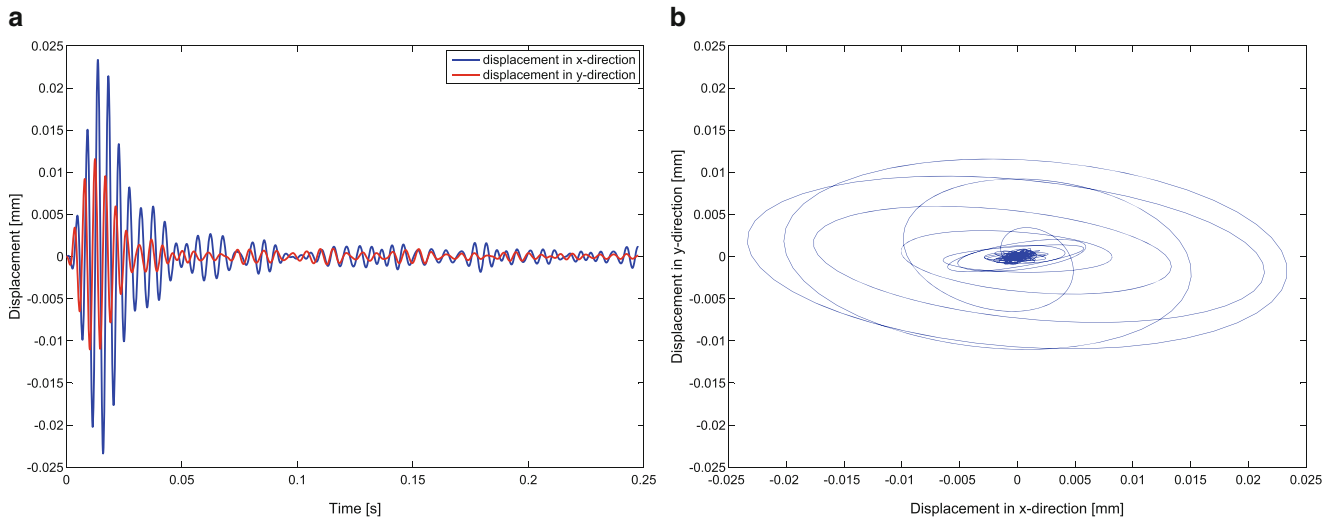
amplitude loss. Also, the FRF of the hammer impact is the result of averaging five FRF's. Both FRF's agree quite well, even with the simplified force estimation. Moreover, if the damping factor of the shaft is calculated with a simple peak-amplitude method [15], both damping factors are the same, i.e. 0.0013. The resonance frequency is 423 Hz and corresponds to the fourth free mode. It deviates slightly from the theoretical expected value of 411 Hz.

### 51.3.3 Shaft on Bearings

The same technique as in the free-free shaft is used for a shaft on bearings (Figs. 51.4 and 51.7). The shaft is also in steel CF53 with a density of  $7,730 \text{ kg/m}^3$  and a Young modulus of  $2.2 \times 10^{11} \text{ Pa}$ . The diameter is 0.010 m and the length 1.14 m. The shaft is placed on angular contact high precision bearings. Although clamped boundary conditions are intended, a result inbetween clamping and supporting is obtained. Also, it should be noted that the stiffness properties of this configuration are not exactly the same for both directions in a chosen  $x$ - $y$  coordinate system and the shape of the shaft surface implies excitation in both directions, as illustrated in Fig. 51.6. Because the proximity probe can never be put exactly in one direction, both movements are measured. Two resonance frequencies close to each other can be expected. To validate this phenomenon, a measurement is made with hammer excitation and proximity probes in both directions and exciting in the  $x$ -direction. In Fig. 51.8a, both displacements, filtered with a bandpass filter between 400 and 450 Hz, are plotted. Both displacements start in phase but have a slightly different frequency. This results in a trajectory depicted in Fig. 51.8b. In this trajectory it is clear that the shaft does not only move in the  $x$ -direction, but has a small movement in the  $y$ -direction too.



**Fig. 51.7** Drawing of the shaft on bearings

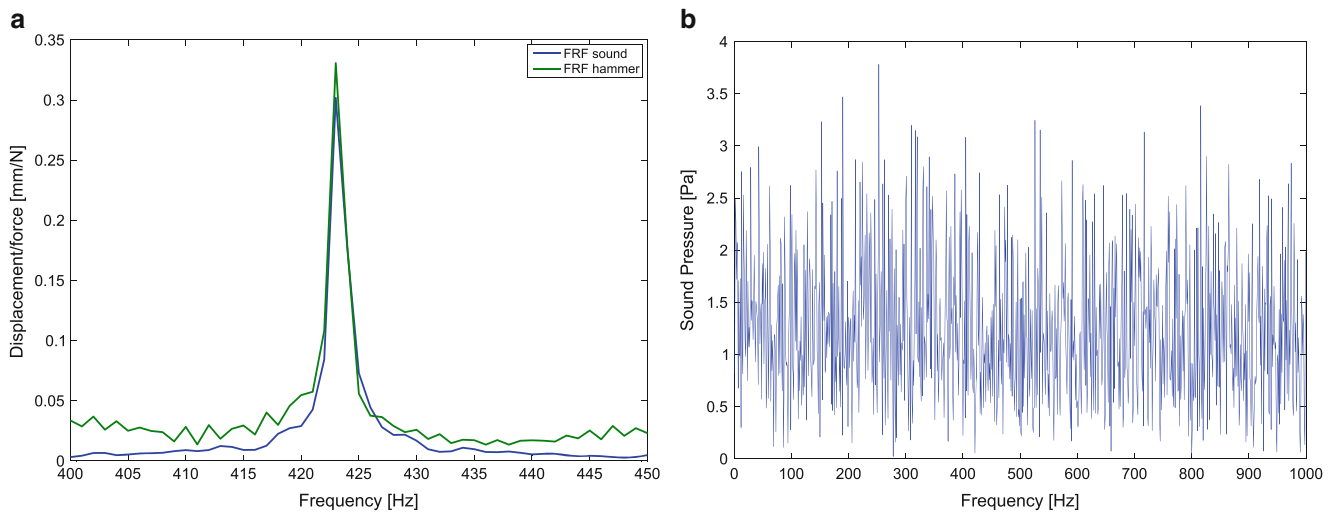


**Fig. 51.8** Displacement of the shaft with hammer excitation for frequencies between 400 and 450 Hz. (a) Displacement as a function of time. (b) Trajectory of displacements

For a clamped shaft, a resonance frequency of 483 Hz, corresponding to the fifth mode, is theoretically calculated. Because ideal clamping is not accomplished, a lower frequency can be expected. As can be seen in Fig. 51.9b, the FRF meets the expectation. The FRF measured with hammer impact indicates that there are two resonance frequencies close to each other, i.e. 424 and 439 Hz. The one with acoustic excitation is slightly different, having two resonance frequencies of 423 and 439 Hz. By using the peak-amplitude method on these measurements, the hammer impact technique leads to respectively a damping factor of 0.0040 and 0.0035 and the acoustic excitation leads to both 0.0045. These differences should be interpreted carefully. Firstly, the force is estimated with a simplified method. Secondly, the frequency resolution is only 1 Hz, resulting in an error on the absolute peak, i.e. picket fence effect [16]. Thirdly, and most importantly, with the hammer impact technique it is not possible to hit the shaft every time on exactly the same place. This means that, the five separate FRF's that are measured and averaged, can deviate depending on the hit. With acoustic excitation, the position of the source with respect to the shaft does not change. Therefore, acoustic excitation assures repeatability.

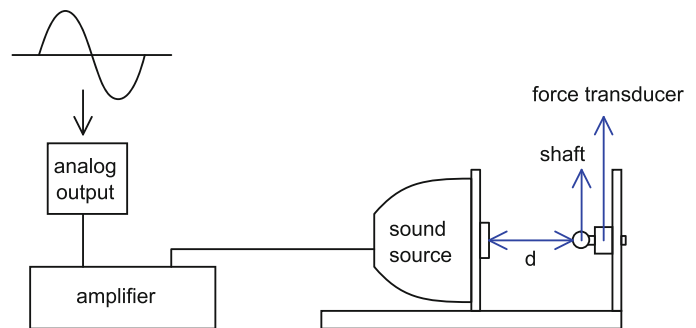
## 51.4 Calibration Procedure

Because of the difficulty to estimate the excitation force theoretically, a calibration procedure is proposed, to increase the accuracy of the results. Figure 51.10 shows the test setup. A sound source and a shaft sample are mounted on a variable distance. The samples are bolted to a force transducer. The sample shafts have a varying length so that the influence of the force on the length of the shaft can be verified. If the length of these samples is small, they can be assumed to be rigid for low frequencies. A thorough testing set which will yield calibration charts will be included in future work.



**Fig. 51.9** FRF's with acoustic vs. hammer excitation for frequencies between 400 and 450 Hz. (a) FRF's of the free shaft. (b) FRF's of the shaft on bearings

**Fig. 51.10** Setup for calibration procedure



## 51.5 Conclusions

Acoustic excitation is a non-contact excitation technique that can be used to measure frequency response functions of shafts. By using this technique, the shaft is excited by a force which equals the pressure integrated over the surface of the shaft. Different kinds of excitation signals can be used. However, if multi-sine signals are used, the force is divided over the different frequencies, resulting in a lower force per frequency. In comparison to hammer impact, acoustic excitation leads to an exactly reproducible force, while hammer impact depends on the hit. In this research a simplified estimation of the excitation force is made by multiplying the acoustic pressure, measured by a microphone, with the excited surface. The method is validated by measuring a frequency response function of a shaft supported by two wires at the nodes of the first free mode and a shaft on bearings and comparing it to the hammer impact. For both shafts, the method leads to acceptable results, and gives similar damping factors when calculated with a peak-amplitude method. However, if an exact damping measurement is necessary, the simplified force estimation will not suffice. Therefore, a calibration procedure is proposed. Furthermore, the method has some practical drawbacks. By using the stepped-sine, it is rather time-consuming compared to the hammer impact. On top of that, the high acoustic pressure require the executor to wear hearing protection. Hence, Acoustic excitation is advisable when non-contact excitation is required, for example in rotordynamics and when effects of mass loading and other influences are of a particular concern. In future work, besides the calibration procedure, numerical techniques can be used to estimate the pressure of the source. Also, other sources, with a better frequency response for lower frequencies can be used. If higher power can be accomplished, combined signals such as noise can be evaluated.

## References

1. Vervisch B, Stockman K, Loccufer M (2012) Sensitivity of the stability threshold in linearized rotordynamics. In: ISMA conference, Leuven 2012
2. Kandil MA (2004) On rotor internal damping instability. PhD thesis, Imperial College London
3. Forrai L (2000) Instability due to internal damping of symmetrical rotor-bearing systems. *JCAM* 1(2):137–147
4. Forrai L (2000) A finite element model for stability analysis of symmetrical rotor systems with internal damping. *JCAM* 1(1):37–47
5. Genta G, Amati N (2010) Hysteretic damping in rotordynamics: an equivalent formulation. *J Sound Vib* 329(22):4772–4784
6. Peres MA, Bono RW, Brown DL (2010) Practical aspects of shaker measurements for modal testing, pp 2539–2550. [processvibration.com](http://processvibration.com)
7. Bucher I, Ewins DJ (2001) Modal analysis and testing of rotating structures. *Philos Trans R Soc A* 359(1778):61–96
8. Wu J, Moslehy FA (1995) On modal testing using speaker for excitation. *IMAC XIII proc* (7):24–29
9. Vanlanduit S, Daerden F, Guillaume P (2007) Experimental modal testing using pressurized air excitation. *J Sound Vib* 299(1–2):83–98
10. Farshidi R, Trieu D, Park SS, Freiheit T (2010) Non-contact experimental modal analysis using air excitation and a microphone array. *Measurement* 43(6):755–765
11. Castellini P (2004) Measurement of vibrational modal parameters using laser pulse excitation techniques. *Measurement* 35(2):163–179
12. Xu YF, Zhu WD (2011) Rotating machinery, structural health monitoring, shock and vibration, vol 5. Springer, New York, pp 359–374
13. Herlufsen H, Møller N (2002) Operational modal analysis of a wind turbine wing using acoustical excitation.  *Brüel & Kjaer Application Note BO0500-11*, (1):1–8
14. Fahy FJ (1987) Sound and structural vibration: radiation, transmission and response. Academic Press, London
15. Ewins DJ (2000) Modal testing: theory, practice and application. Mechanical engineering research studies: engineering dynamics series. Wiley, Hertfordshire
16. Randall RB (1987) Frequency Analysis. Briel & Kjaer, Glostrup



# Chapter 52

## Numerical Simulations on the Performance of Passive Mitigation Under Blast Wave Loading

Oruba Rabie, Yahia M. Al-Smadi, and Eric Wolff

**Abstract** The current work, which is largely exploratory in nature, involves blast wave travelling within a matrix of piles or columns. The fluid structure interactions reach a maximum peak of vibration at a particular set of input parameters. Therefore, possible damage, which affects vibration structural integrity and reliability, may occur. The presented numerical blast tests will accompany the introduction of new structural design concepts associated with mitigation details. Reliable and robust analysis (ANSYS and LS-DYNA) software will be used to complete 3D finite element model and conduct numerical testing.

**Keywords** Blast • Mitigation • CFRP • RC column • Retrofits

### Nomenclature

$A_c$	Cross sectional area of concrete
$\alpha$	Decay coefficient
$A_{st}$	Cross sectional area of reinforcing steel
$E_c$	Concrete modulus of elasticity
$E_f$	FRP modulus of elasticity
$E_s$	Steel modulus of elasticity
$f'_c$	Concrete compressive strength
$f_{fu}$	Ultimate tensile strength of CFRP
$f_y$	Yield strength of steel
$I_g$	Gross moment of inertia
$I_{se}$	Moment of inertia of steel about centroidal axis of cross section
$P_o$	Maximum reflected pressure
$P_{so}$	Peak side-on overpressure
$P_f$	Fiber density
$\rho_s$	Steel density
$\rho_{RC}$	Reinforced concrete density
$R$	Standoff distance
$W$	Mass of the explosive charge
$Z$	Scaled distance of the explosive charge

---

O. Rabie

Department of Civil and Environmental Engineering, New Jersey Institute of Technology, Newark, NJ 07102, USA  
e-mail: [onr2@njit.edu](mailto:onr2@njit.edu)

Y.M. Al-Smadi (✉)

AECOM, 20 Exchange Pl, New York, NY 10005, USA  
e-mail: [yahia.alsmadi@njit.edu](mailto:yahia.alsmadi@njit.edu)

E. Wolff

Fyfe Company LLC, 8,380 Miralani Drive, San Diego, CA 92126, USA  
e-mail: [ericw@fyfeco.com](mailto:ericw@fyfeco.com)

## 52.1 Introduction

The collapse of the Twin Towers of the World Trade Center in 2001 has inspired engineers and developers to study the stability of structural systems subjected to bombs and blasting in addition to conventional applied loads of self-weight, live load and unconventional loadings from major hurricane and earthquake. Consequently, development of blast resisting techniques for existing structures which have not been designed for explosions have become one of the main issues in the structural design field. One of these cost-effective techniques is strengthening the structural members that support the building with carbon fiber reinforced polymer composites (CFRP).

Fiber reinforced polymer FRP composites are now being utilized instead of steel due to their higher strengths, better corrosion resistance and greater ease of transportation and handling. The method can be applied quickly and is non-intrusive so it does not intrude into the buildings floor space [1]. It will also be shown in this study that it provides a dramatic increase in the ability of a structure to resist blast by increasing the structural strength and reducing possible deflection. Also, the apparent high purchase cost of FRP composites compared to other materials has previously been cited as a disadvantage for this technique. However, a direct comparison on a unit price basis may not be appropriate. Including installation and transportation in the cost comparison FRPs can often compete with conventional materials. If the comparisons include through-life costs FRPs can be advantageous [2].

Researchers have studied different available fiber reinforced polymers composites that can be used to strengthen structural members. Muszynski et al. [3] reported explosive tests on reinforced concrete RC columns strengthened with glass fiber reinforced polymers GFRP and CFRP. Unfortunately, during these tests a previously tested wall became detached and collided with the retrofitted columns, shearing the top and bottom. This spoiled test was blamed on a higher than predicted pressure from the explosive. Teng and Lam [4] conducted an experimental study on FRP-confined concrete in elliptical columns. Test results which indicated that although the confining FRP becomes increasingly less effective as the circular section becomes more elliptical, substantial strength gains from FRP confinement can still be achieved even for strongly elliptical sections. Based on the test results, a simple compressive strength model for FRP-confined concrete in elliptical columns was proposed, in which the effect of the section shape was taken into account by a shape factor.

Mutalib and Hao [5] performed numerical simulations using LS-DYNA to construct Pressure-Impulse diagrams for FRP strengthened RC columns to provide correlations between the damage levels of FRP strengthened RC columns and blast loading. Numerical solution was compared with test results and verified.

However, limited numerical research has been conducted on the blast-resistance of reinforced concrete columns strengthened with CFRP. In this study, a numerical analysis is performed for a typical square reinforced concrete column strengthened with CFRP and compared with unstrengthened column when subjected to the same blast load. Different combinations of explosive charge mass and standoff distance from the column under study has been taken to draw a solid conclusion on the effect of CFRP when used to increase column blast resistance.

## 52.2 Blast Simulation

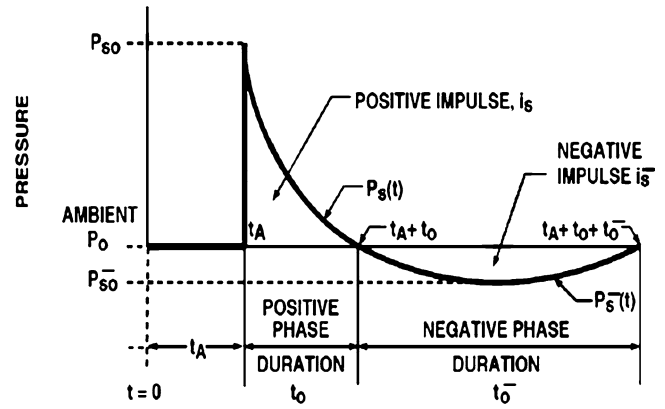
The characteristics of air blast waves are mainly affected by the physical properties of the explosion source. The typical pressure–time history of an airblast is shown in (Fig. 52.1). At the arrival time  $t_A$  following the detonation, pressure suddenly increases over the ambient pressure,  $P_o$  to a peak value of overpressure,  $P_{so}$  then decays exponentially. Following this there is a negative suction pressure at the point with a much lower intensity, but longer duration than the positive phase pressure. The impulse is the area under the P-t curve.

The P-t curve depends on the mass of the explosive charge  $W$  and its standoff distance  $R$  that are both related to the scaled distance  $Z$  as follows:

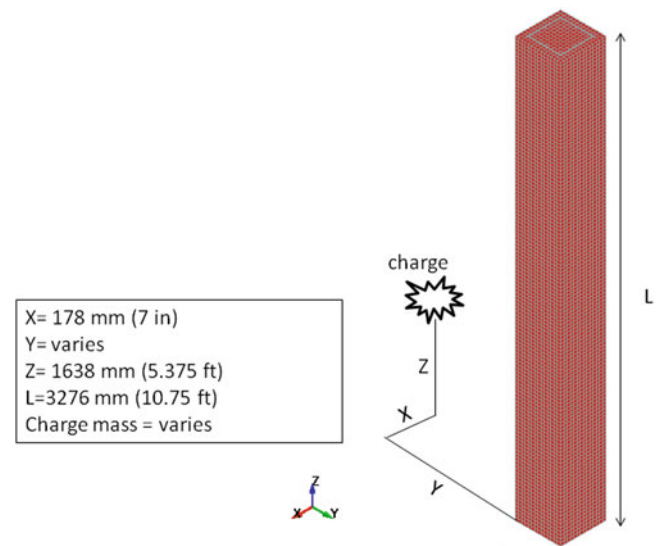
$$Z = \frac{R}{W^{1/3}} \quad (52.1)$$

Different charge masses were used in this study, ranging from 22.67 kg (50 lbs) to 4,989.5 kg (11,000 lbs), each was applied to a  $356 \times 356$  mm ( $14'' \times 14''$ ) RC column and located at a standoff distance that varies from 3.05 to 21.34 m (10–70 ft). Pressure–time history curves, displacement and impulse curves were then compared and discussed in an effort to find the effect of CFRP addition to a square reinforced concrete column. Column height is 3,276 mm, with all translational and rotational degrees of freedom fixed at both ends. Solid elements were cubical of 25.4 mm edge length. Location of explosive charge is shown in (Fig. 52.2).

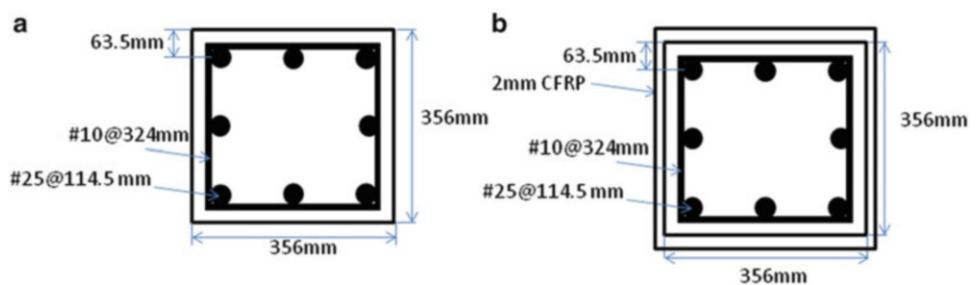
**Fig. 52.1** Typical pressure–time history of an airburst in free air



**Fig. 52.2** Explosive charge location



**Fig. 52.3** (a) Unretrofitted RC column cross-section and reinforcement, (b) Retrofitted RC column cross-section and reinforcement



The explicit software LS-DYNA was used to carry out the analysis for the fix-fix column shown in (Fig. 52.3) under different explosive charge masses ranging from 22.67 to 4,989.5 kg and different standoff distances ranges from 3.05 to 21.34 m. Each blast event scenario was carried out twice for each column, one for unretrofitted case and the other for retrofitted column with Tyfo® SCH wraps of 2 mm thickness applied vertically to the column.

Half of the model was analyzed with symmetric condition applied in the Y-Z plane to reduce the computational time. Solid elements (SOLID164) of 25.4 mm cube edge length were used to model the concrete column. Beam elements (BEAM161) were used to model reinforcement bars and stirrups. The column surface facing the blast was modeled using shell elements (SHELL163), and same shell elements were used to model CFRP. The material type 159 called MAT\_CSCM\_CONCRETE was used to model the concrete, MAT\_PLASTIC\_KINEMATIC was used to model the steel and MAT\_LAMINATED\_COMPOSITE\_FABRIC was used to model TYFO wraps. Material properties of concrete, steel and CFRP are all shown in Tables 52.1, 52.2 and 52.3 respectively. Analysis was done at 0.5 msec time-step and termination time was set to 50 msec.

**Table 52.1** Concrete properties

$f'_c$ MPa	$E_c$ MPa	$\rho_c$ kg/m <sup>3</sup>	$I_g$ mm <sup>4</sup>	$A_c$ mm <sup>2</sup>
38.7	29238.4	2,400	$1.3385 \times 10^9$	126,736

**Table 52.2** Reinforcement steel properties

$f_y$ MPa	$E_s$ MPa	$\rho_s$ kg/m <sup>3</sup>	$I_{se}$ mm <sup>4</sup>	$A_{st}$ mm <sup>2</sup>
462	200,000	7,850	349,683	4,072

**Table 52.3** Tyfo® SCH material properties

$f_{tu}$ MPa	$E_f$ GPa	$\rho_f$ kg/m <sup>3</sup>	Elongation at break	Thickness mm
834	82,000	1,740	1 %	2

**Table 52.4** Blast event scenarios used to perform numerical simulations

Charge mass (kg)	Standoff distance (mm)	Maximum deflection (mm)		Displacement drop (mm)
		FRP	RC	
22.68	3.35	5.37	7.90	2.54
22.68	4.57	3.38	4.98	1.60
45.36	3.66	8.42	13.30	4.88
68.04	3.66	12.56	20.66	8.10
68.04	4.88	7.64	12.30	4.65
68.04	6.10	7.64	8.51	0.87
90.72	3.05	28.82	43.19	14.37
113.40	3.05	40.27	59.80	19.53
136.08	3.05	56.31	77.15	20.84
907.18	18.29	6.62	13.31	6.69
2267.96	18.29	19.38	43.70	24.32
3628.74	18.29	46.73	89.76	43.02
4082.33	21.34	30.21	66.88	36.67
4989.51	21.34	45.81	92.31	46.50

Bonding FRP reinforcement to the tension face of a concrete flexural member with fibers oriented along the length of the member will provide an increase in flexural strength [6]. However, it was found in this study that introducing CFRP composites to the column will have a higher effect on increasing flexural strength (minimize displacement) if the explosive charge is placed farther. The reason for this, is that the flexural behavior of the column is more likely to occur for far-field explosions, while for close-in explosives shear failure is more likely to happen, i.e. the column will not deflect under the blast pressure but will shear at the top or bottom of column causing a brittle failure. Maximum displacement for each blast event scenario is listed in Table 52.4.

A case of 113.40 kg charge mass and 3.05 m standoff is taken to study the effect of wrapping the reinforced concrete column with CFRP. The pressure–time history curve  $p(t)$  is shown in (Fig. 52.4) where time of arrival  $t_a$  is 1.01 msec, positive phase duration  $t_0$  is 2.037 msec and maximum reflected pressure  $P_0$  is 24.83 MPa (3,602 psi). Pressure–time relationship shown in (Fig. 52.1) is given in (52.2).

$$p(t) = P_0 \left[ 1 - \frac{(t - t_a)}{t_0} \right] \cdot \exp\left(-\frac{t - t_a}{\alpha}\right) \quad (52.2)$$

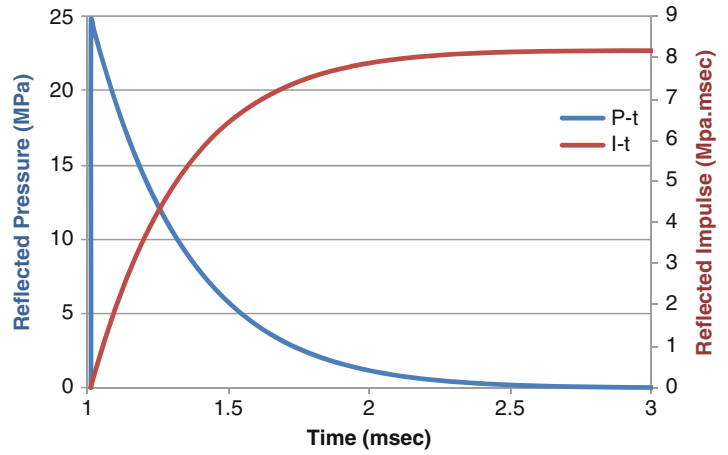
where  $\alpha$  equals 0.292.

Figure 52.4 shows the pressure–time history and the impulse–time history curves that were found using Conventional Weapons Effects ConWep for the blast loading scenario of 113.40 kg and 3.05 m standoff. The pressure–time curve shown is based on (52.2) given previously, and the impulse–time history curve is the area under the  $p$ - $t$  curve.

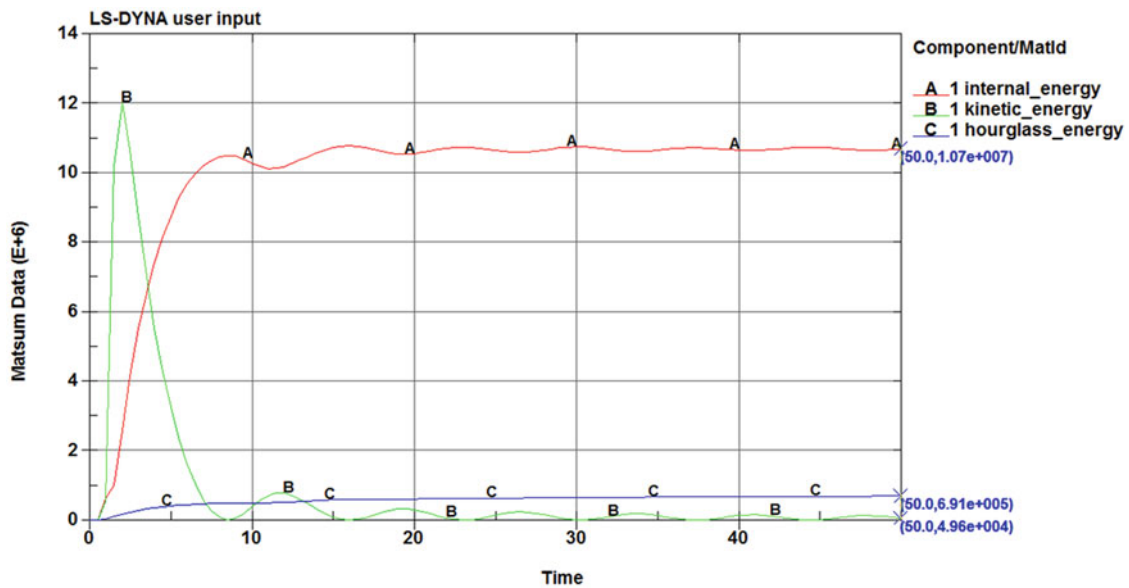
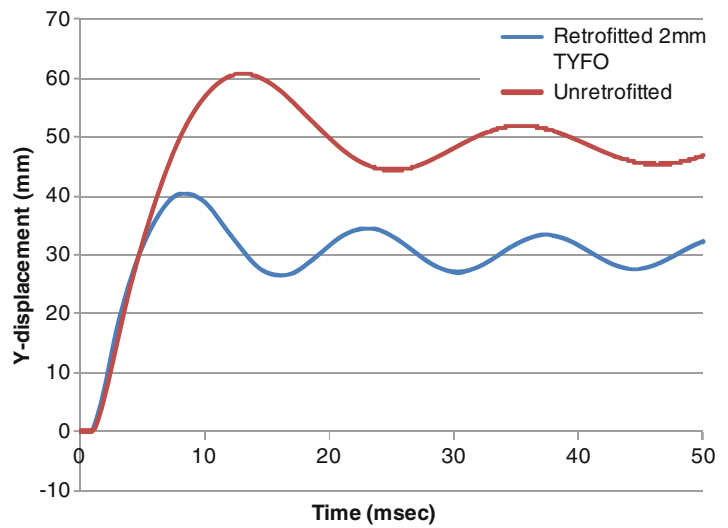
Displacement time history curve for the retrofitted and unretrofitted RC column are shown in (Fig. 52.5). The figure illustrates the drop in the displacement peak value from 59.80 to 40.2 mm when using 2 mm layer of TYFO wraps.

The energy time history for the simulation is shown in (Fig. 52.6). In order to eliminate the zero energy hourglass modes, additional artificial stiffness was introduced into the system. One way to quantify the amount of this added stiffness is through the hourglass energy. Ideally, the hourglass energy should be less than 10 % of the internal energy. The energy time history shows that the hourglass energy is very low. For the entire simulation the hourglass energy was less than 5 % of the internal energy.

**Fig. 52.4** ConWep pressure-time and Impulse-time history diagrams for a charge weight of 113.4 kg TNT and a standoff distance of 3.05 m

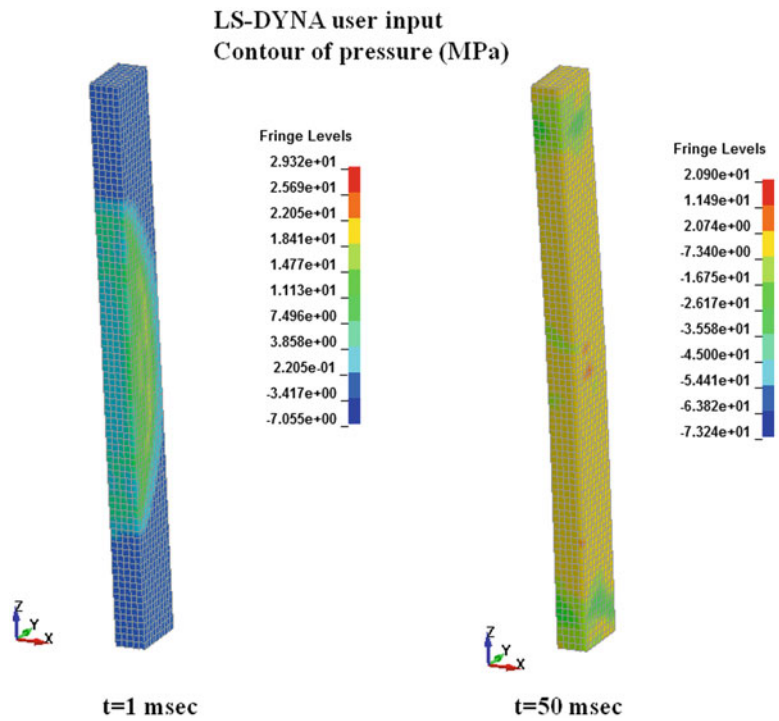


**Fig. 52.5** LS-DYNA y-displacement at midheight of retrofitted and unretrofitted 356 × 356 mm RC column subjected to 113.4 kg charge mass placed at 3.05 m



**Fig. 52.6** LS-DYNA energy profile of a 356 × 356 mm RC column subjected to 113.4 kg charge mass placed at 3.05 m

**Fig. 52.7** LS-DYNA pressure contour at the beginning and end of the blast loading phase (113.4 kg charge mass at 3.05 m)



**Fig. 52.8** LS-DYNA y- velocity at midheight of retrofitted and unretrofitted 356 × 356 mm RC column subjected to 113.4 kg charge mass placed at 3.05 m

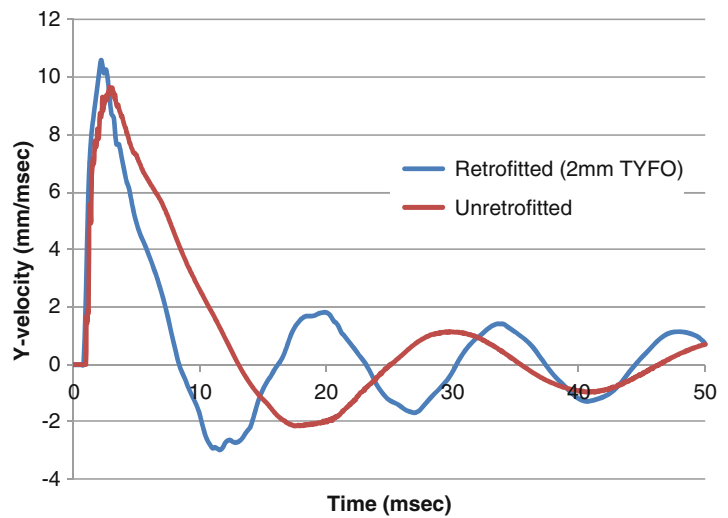


Figure 52.7 shows the pressure contour at the beginning and the end of the blast loading phase, the maximum reflected pressure was found to equal 29.32 MPa which is 17 % higher than CONWEP calculated pressure. Velocity time history profile is shown in (Fig. 52.8). It can be shown that there was no appreciable difference between FRP wrapped and unwrapped RC column.

### 52.3 Conclusion

In this paper, the numerical results are used to study the effect of strengthening reinforced concrete columns with one layer of Tyfo<sup>®</sup> SCH using the FEA software LS-DYNA. Twenty-eight hypothetical blast events were simulated and maximum displacement results were then compared.



Results found illustrate that the CFRP composite won't be of an effect on strengthening a reinforced concrete column if the latter is subjected to a close-in explosive charge. While, this effect will start to take place as the charge is placed farther. However, this behavior may change if thicker CFRP layer is used.

## References

1. Buchan PA, Chen JF (2007) Blast resistance of FRP composites and polymer strengthened concrete and masonry structures – A state-of-the-art review. *Compos B* 38:509–522
2. Concrete Society (2004) Design guidance for strengthening concrete structures using fiber composite materials, 2nd edn. TR 55, Berkshire
3. Muszynski LC, Purcell MR (2003) Composite reinforcement to strengthen existing concrete structures against air blast. *J Compos Constr ASCE* 7:93–97
4. Teng JG, Lam L (2002) Compressive behavior of carbon fiber reinforced polymer-confined concrete in elliptical columns. *J Struct Eng ASCE* 128:1535–1543
5. Mutalib AA, Hao H (2011) Development of P-I diagrams for FRP strengthened RC columns. *Int J Impact Eng* 38:290–304
6. ACI Committee 440 (2002) Guide for the design and construction of externally bonded FRP systems for strengthening concrete structures (ACI 440.2R-02). American Concrete Institute, Farmington Hills, Mich

# Chapter 53

## Finite Element Model Updating Using the Shadow Hybrid Monte Carlo Technique

I. Boulkaibet, L. Mthembu, T. Marwala, M.I. Friswell, and S. Adhikari

**Abstract** Recent research in the field of Finite Element Model (FEM) updating has advocated the benefits of adopting Bayesian analysis techniques. These techniques are well suited to dealing with the uncertainties associated with complex systems. However, Bayesian formulations require the evaluation of the Posterior Distribution Function (pdf) which may not be available in analytical form. This is the case in FEM updating. In such cases sampling methods can provide good approximations of the Posterior distribution when implemented in the Bayesian context. In this paper, we propose the use of the Shadow Hybrid Monte Carlo (SHMC) technique for the problem of determining the most probable FEM updating parameters for the given data. SHMC is based on Hybrid Monte Carlo (HMC) and designed to improve sampling by allowing for larger system sizes and time steps. The accuracy and efficiency of this sampling method is tested on the updating of a structural beam models.

**Keywords** Bayesian • Sampling • Finite Element Model updating • Markov Chain Monte Carlo • Hybrid Monte Carlo method • Shadow Hybrid Monte Carlo

### 53.1 Introduction

Finite Element Models (FEMs) are well-known numerical methods used to provide approximate solutions for complex engineering problems [1, 2]. The FEM method is recognised as a powerful method for computing displacements, stresses and strains in structures under a set of loads. However, the FEM results degrade with the complexity of the modelled system where the obtained FEM results for the complex systems are different from those obtained from experiments [3, 4]. These differences can be seen as an outcome of the modelling errors and the uncertainties associated with the process of constructing the FEM of a structure. Therefore, the models obtained from the FEM method need to be updated to match the measured data. In recent years, Bayesian model updating techniques have shown promising results in systems identification research [4–7].

The Bayesian approach is a useful method for complex uncertain systems, where it possesses the ability to characterize the uncertainties of these systems. The Bayesian approach is used to update the uncertain parameters of the FEM. This can be done by representing these parameters as random vectors with a joint probability density function (pdf). This density function is known as the posterior distribution function. The use of Bayesian techniques becomes useful when an analytical solution to this function, the posterior (pdf), is not available. This is often the case because of the high dimensionality of the parameter search space. In these situations, a Markov Chain Monte Carlo (MCMC) simulation method will provide the only practical solution [4, 6, 7].

In this paper, the Shadow Hybrid Monte Carlo (SHMC) [8] is implemented for its ability to sample the posterior (pdf) of FEM updating parameters. The SHMC is based on the HMC method but it uses an accurate approximation of the modified

---

I. Boulkaibet (✉) • L. Mthembu • T. Marwala

The Centre For Intelligent System Modelling (CISM), Electrical and Electronics Engineering Department, University of Johannesburg, 524, Auckland Park 2006, Johannesburg, South Africa

e-mail: [iboulkaibet@student.uj.ac.za](mailto:iboulkaibet@student.uj.ac.za)

M.I. Friswell • S. Adhikari

College of Engineering, Swansea University, Singleton Park, Swansea, SA2 8PP, United Kingdom

Hamiltonian, the Shadow Hamiltonian, to sample through the phase space in an efficient way. The shadow Hamiltonian is exactly conserved by an augmented numerical integrator that has been proposed in [9, 10]. The SHMC samples a non-canonical distribution defined by high order approximations to the shadow Hamiltonian, which greatly increases the acceptance rate of the method. This method is tested by updating a structural beam model. The efficiency, reliability and limitations of the SHMC technique are investigated when a Bayesian approach is implemented on an FEM updating problem.

In the next section, the finite element model background is presented. In Sect. 53.3, an introduction to the Bayesian framework is introduced where the posterior distribution of the uncertain parameters of the FEM are presented. Section 53.4 introduces the HMC technique. Section 53.5 introduces the SHMC technique which is used to predict the posterior distribution. Section 53.6 presents the construction of the Shadow Hamiltonian function. Section 53.7 presents an implementation of Bayesian FEM updating on a steel beam. Section 53.8 presents the second implementation of on H-beam structure. Finally, the Sect. 53.9 concludes the paper.

## 53.2 Finite Element Model Background

In finite element modelling, an  $N$  degree of freedom dynamic structure may be described by the matrix equation of motion [7, 11]

$$\mathbf{M}\ddot{\mathbf{x}}(t) + \mathbf{C}\dot{\mathbf{x}}(t) + \mathbf{K}\mathbf{x}(t) = \mathbf{f}(t), \quad (53.1)$$

where  $\mathbf{M}$ ,  $\mathbf{C}$  and  $\mathbf{K}$  are the mass, damping and stiffness matrices of size  $N \times N$ ,  $\mathbf{x}(t)$  is the vector of  $N$  degrees of freedom and  $\mathbf{f}(t)$  is the vector of loads applied to the structure. In the case that no external forces are applied to the structure and if the damping terms are neglected ( $\mathbf{C} \sim 0$ ), the dynamic equation may be written in the modal domain (natural frequencies and mode shapes) where the error vector for the  $i$ th mode is obtained from

$$\left[ -(\omega_i^m)^2 \mathbf{M} + \mathbf{K} \right] \phi_i^m = \boldsymbol{\varepsilon}_i \quad (53.2)$$

$\omega_i^m$  is the  $i$ th measured natural frequency,  $\phi_i^m$  is the  $i$ th measured mode shape vector and  $\boldsymbol{\varepsilon}_i$  is the  $i$ th error vector. In (53.2), the error vector  $\boldsymbol{\varepsilon}_i$  is equal to 0 if the system matrices  $\mathbf{M}$  and  $\mathbf{K}$  correspond to the modal properties ( $\omega_i^m$  and  $\phi_i^m$ ). However,  $\boldsymbol{\varepsilon}_i$  is a non-zero vector if the system matrices obtained analytically from the finite element model do not match the measured modal properties  $\omega_i^m$  and  $\phi_i^m$ .

## 53.3 Bayesian Inferences

In order to update the mathematical models, the uncertain parameters have to be identified. Bayes theorem offers this possibility, and uncertain parameters can be determined from the measurements [4, 7, 12]. In this work, the Bayesian method is used to solve the FEM updating problem in the modal domain. Bayesian approaches are governed by Bayes rule [7, 12]:

$$P(\mathbf{E}|D) \propto P(D|\mathbf{E})P(\mathbf{E}) \quad (53.3)$$

where  $\mathbf{E}$  represent the vector of updating parameters and the mass  $\mathbf{M}$  and stiffness  $\mathbf{K}$  matrices are functions of the updating parameters  $\mathbf{E}$ . The quantity  $P(\mathbf{E})$ , known as the prior probability distribution, is a function of the updating parameters in the absence of the data.  $D$  is the measured modal properties; the natural frequencies  $\omega_i$  and mode shapes  $\phi_i$ . The quantity  $P(\mathbf{E}|D)$  is the posterior probability distribution function of the parameters in the presence of the data  $D$ .  $P(D|\mathbf{E})$  is the likelihood probability distribution function [4, 12, 13].

The likelihood distribution can be seen as the probability of the modal measurements in the presence of uncertain parameters [7]. This function can be defined as the normalized exponent of the error function that represents the differences between the measured and the analytic frequencies. It can be written as

$$P(D|\mathbf{E}) = \frac{1}{\left(\frac{2\pi}{\beta}\right)^{N_m/2} \prod_{i=1}^{N_m} \omega_i^m} \exp\left(-\beta \sum_i^{N_m} \left(\frac{\omega_i^m - \omega_i}{\omega_i^m}\right)^2\right) \quad (53.4)$$

where  $\beta$  is a constant,  $N_m$  is the number of measured modes and  $\omega_i$  is the  $i$ th analytical frequency.

The prior pdf represents the prior knowledge of the updating parameters  $\mathbf{E}$  [7], and quantifies the uncertainty of the parameters  $\mathbf{E}$ . In this paper, some parameters are updated more intensely than others. For example, in structural systems, parameters next to joints should be updated more intensely than for those corresponding to smooth surface areas far from joints. The prior probability distribution function for parameters  $\mathbf{E}$  is assumed to be Gaussian and is given by [13, 14]

$$P(\mathbf{E}) = \frac{1}{(2\pi)^{Q/2} \prod_{i=1}^Q \frac{1}{\sqrt{\alpha_i}}} \exp\left(-\sum_i^Q \frac{\alpha_i}{2} \|\mathbf{E}\|^2\right) \quad (53.5)$$

where  $Q$  is the number of groups of parameters to be updated, and  $\alpha_i$  is the coefficient of the prior pdf for the  $i$ th group of updating parameters. The notation  $\|\cdot\|$  denotes the Euclidean norm of  $\cdot$ . In (53.5), if  $\alpha_i$  is constant for all of the updating parameters, then the updated parameters will be of the same order of magnitude. Equation 53.5 may be viewed as a regularization parameter [7, 13, 15]. In (53.5), Gaussian priors are conveniently chosen because many natural processes tend to have a Gaussian distribution.

The posterior distribution function of the parameters  $\mathbf{E}$  given the observed data  $D$  is denoted as  $P(\mathbf{E}|D)$  and is obtained by applying Bayes' theorem as represented in (53.3). The distribution  $P(\mathbf{E}|D)$  is calculated by substituting (53.4) and (53.5) into (53.3) to give

$$P(\mathbf{E}|D) = \frac{1}{Z_s(\alpha, \beta)} \exp\left(-\beta \sum_i^{N_m} \left(\frac{\omega_i^m - \omega_i}{\omega_i^m}\right)^2 - \sum_i^Q \frac{\alpha_i}{2} \|\mathbf{E}\|^2\right) \quad (53.6)$$

where

$$Z_s(\alpha, \beta) = \left(\frac{2\pi}{\beta}\right)^{N_m/2} \prod_{i=1}^{N_m} \omega_i^m (2\pi)^{Q/2} \prod_{i=1}^Q \frac{1}{\sqrt{\alpha_i}} \quad (53.7)$$

In most cases, the analytical form of the Posterior (pdf) solution may not available which is often the case because of the complexity of the systems as well as the high dimensionality of the parameter search space. In these situations, the sampling methods will provide the only practical solution. Sampling techniques can simplify the Bayesian inference by providing a set of random samples from posterior distribution [6, 7, 12, 13, 16]. In case that  $Y$  is the observation of certain parameters at different discrete time instants; the total Probability theorem provides the probabilistic information for the prediction of the future responses  $Y$  at different time instants. Consider the following integral,

$$P(Y|D) = \int P(Y|\mathbf{E}) P(\mathbf{E}|D) d[\mathbf{E}] \quad (53.8)$$

Equation 53.8 depends on the posterior distribution function. The dimension of the updating parameters makes it very difficult to obtain an analytical solution. Therefore, sampling techniques, such as Markov Chain Monte Carlo (MCMC) methods are employed to predict the updating parameter distribution and subsequently to predict the modal properties. Given a set of  $N_s$  random parameter vector drawn from a pdf  $P(\mathbf{E}|D)$ , the expectation value of any observed function  $Y$  can be easily estimated.

The integral in (53.8) can be solved using sampling algorithms [6, 12, 17, 18]. These algorithms are used to generate a sequence of vectors  $\{\mathbf{E}_1, \mathbf{E}_2, \dots, \mathbf{E}_{N_s}\}$  where  $N_s$  is the number of samples and these vectors can be used to form a Markov chain. This generated vector is then used to predict the form of the posterior distribution function  $P(\mathbf{E}|D)$ . The integral in (53.8) can be approximated as

$$\tilde{Y} \cong \frac{1}{N_s} \sum_{i=1}^{N_s} G(\mathbf{E}_i) \quad (53.9)$$

where  $G$  is a function that depends on the updated parameters  $\mathbf{E}_i$ . As an example, if  $\mathbf{G} = \mathbf{E}$  then  $\tilde{Y}$  becomes the expected value of  $\mathbf{E}$ . Generally,  $\tilde{Y}$  is the vector that contains the modal properties and  $N_s$  is the number of retained states. In this paper, the SHMC method is used to sample from the posterior pdf.

### 53.4 The Hybrid Monte Carlo Method

The Hybrid Monte Carlo method, known as the Hamiltonian Markov Chain method, is considered as a powerful sampling method for solving higher-dimensional complex problems [6, 12, 18]. The HMC combines a Molecular Dynamic (MD) trajectory with a Monte Carlo (MC) rejection step [7, 13]. In HMC, a dynamical system is considered in which auxiliary variables, called momentum,  $\mathbf{p} \in R^N$ , are introduced. The updated vector entries in the posterior pdf are treated as displacements. The total energy (Hamiltonian function) of the new dynamical system is defined by  $H(\mathbf{E}, \mathbf{p}) = V(\mathbf{E}) + W(\mathbf{p})$ , where the potential energy is defined by  $V(\mathbf{E}) = -\ln(P(\mathbf{E}|D))$  and the kinetic energy  $W(\mathbf{p}) = \mathbf{p}^T \mathbf{M}^{-1} \mathbf{p} / 2$  depends only on  $\mathbf{p}$  and some chosen positive definite matrix  $\mathbf{M} \in R^{N \times N}$ . Now, we consider the joint distribution of the Hamiltonian function which can be written in the form:  $f(\mathbf{E}, \mathbf{p}) = K \exp(-H(\mathbf{E}, \mathbf{p}))$  where  $K$  is normalization constant. It is easy to see that  $f(\mathbf{E}, \mathbf{p})$  can be rewritten as  $f(\mathbf{E}, \mathbf{p}) = K \exp(-V(\mathbf{E})) \cdot \exp(-W(\mathbf{p}))$  or  $f(\mathbf{E}, \mathbf{p}) = K \cdot P(\mathbf{E}|D) \cdot \exp(-\mathbf{p}^T \mathbf{M}^{-1} \mathbf{p} / 2)$ . Clearly, sampling  $\mathbf{E}$  the posterior distribution can be obtained by sampling  $(\mathbf{E}, \mathbf{p})$  from the joint distribution  $f(\mathbf{E}, \mathbf{p})$  noticing that  $E$  and  $p$  are independent according to  $f(\mathbf{E}, \mathbf{p})$ .

Using Hamilton's equations, the evolution of  $(\mathbf{E}, \mathbf{p})$  through time  $t$  and time step  $\delta t$  is given by the following leapfrog algorithm [6, 7]

$$\mathbf{p}\left(t + \frac{\delta t}{2}\right) = \mathbf{p}(t) - \frac{\delta t}{2} \nabla V[\mathbf{E}(t)] \quad (53.10)$$

$$\mathbf{E}(t + \delta t) = \mathbf{E}(t) + \delta t \mathbf{M}^{-1} \mathbf{p}\left(t + \frac{\delta t}{2}\right) \quad (53.11)$$

$$\mathbf{p}(t + \delta t) = \mathbf{p}\left(t + \frac{\delta t}{2}\right) - \frac{\delta t}{2} \nabla V[\mathbf{E}(t + \delta t)] \quad (53.12)$$

where  $\nabla V$  is obtained numerically by finite difference as

$$\frac{\partial V}{\partial E_i} = \frac{V(\mathbf{E} + \nabla h) - V(\mathbf{E} - \nabla h)}{2h \nabla_i} \quad (53.13)$$

$\nabla = [\nabla_1, \nabla_2, \dots, \nabla_N]$  is the perturbation vector and  $h$  is a scalar which dictates the size of the perturbation of  $\mathbf{E}$ . After each iteration of (53.10), (53.11), and (53.12), the resulting candidate state is accepted or rejected according to the Metropolis criterion based on the value of the Hamiltonian  $H(\mathbf{E}, \mathbf{p})$ . Thus, if  $(\mathbf{E}, \mathbf{p})$  is the initial state and  $(\mathbf{E}^*, \mathbf{p}^*)$  is the state after the equations above have been updated, then this candidate state is accepted with probability  $\min(1, \exp\{H(\mathbf{E}, \mathbf{p}) - H(\mathbf{E}^*, \mathbf{p}^*)\})$ . The obtained vector  $\mathbf{E}$  will be used for the next iteration. The algorithm stopping criterion is defined by the number of  $\mathbf{E}$  samples ( $N_s$ ). The HMC algorithm can be summarized as following:

1. An initial value  $\mathbf{E}_0$  is used to initiate the algorithm.
2. Initiate  $\mathbf{p}_0$  such that  $\mathbf{p}_0 \sim N(0, M)$
3. Initiate the leapfrog algorithm with  $(\mathbf{E}, \mathbf{p})$  and run the algorithm for  $L$  time steps to obtain  $(\mathbf{E}^*, \mathbf{p}^*)$ .
4. Update the FEM to obtain the new analytic frequencies and then compute  $H(\mathbf{E}^*, \mathbf{p}^*)$ .
5. Accept  $(\mathbf{E}^*, \mathbf{p}^*)$  with probability  $\min(1, \exp\{H(\mathbf{E}, \mathbf{p}) - H(\mathbf{E}^*, \mathbf{p}^*)\})$ .

Repeat steps (53.3), (53.4), and (53.5) to get  $N_s$  samples.

The performance of the HMC method degrades when the time step  $\delta t$  and the updated vector dimension grow, since the errors in the Hamiltonian increase causing an extremely high sampling rejection rate.

### 53.5 The Shadow Hybrid Monte Carlo Method

The SHMC is considered as a generalization of HMC where the main idea of the SHMC is to use an accurate modified Hamiltonian approximation to sample in all of phase space rather than configuration space alone [8]. This can eliminate the HMC inconvenient caused by a large time step  $\delta t$  and the updated vector dimension. Consider  $\tilde{\rho}(\mathbf{E}, \mathbf{p})$  a target density function for SHMC, where:

$$\tilde{\rho}(\mathbf{E}, \mathbf{p}) \propto \exp(-\tilde{H}(\mathbf{E}, \mathbf{p})), \quad (53.14)$$

$$\tilde{H}(\mathbf{E}, \mathbf{p}) = \max(H(\mathbf{E}, \mathbf{p}), H_{[2k]}(\mathbf{E}, \mathbf{p}) - c). \quad (53.15)$$

where  $H_{[2k]}(\mathbf{E}, \mathbf{p})$  is the highly accurate shadow Hamiltonian defined in Sect. 53.6.  $c$  is an arbitrary constant that allows  $H_{[2k]}(\mathbf{E}, \mathbf{p})$  to depart from  $\tilde{H}(\mathbf{E}, \mathbf{p})$ . It is assumed that  $\tilde{H}(\mathbf{E}, R\mathbf{p}) = \tilde{H}(\mathbf{E}, \mathbf{p})$ . In SHMC, a new set of momentum  $\mathbf{p}$  are generated from a Gaussian distribution function  $N(0, \mathbf{M})$ . However, this momentum vector is accepted or rejected according to the Metropolis acceptance-rejection step. This step is repeated until a new momentum vector is accepted. Choosing the right parameter  $c$  reduces the number of attempts required to get the new momentum vector. Next, the system is integrated using an MD step [8]. The SHMC algorithm can be summarized as following [8]:

1. Initial value  $\mathbf{E}_0$ .
2. Repeat for  $N_s$  samples.

#### MC step

- (a) Generate  $\mathbf{p}$  such that  $\mathbf{p} \sim N(0, \mathbf{M})$
- (b) Accept with probability  $\min(1, \exp\{H(\mathbf{E}, \mathbf{p}) - (H_{[2k]}(\mathbf{E}, \mathbf{p}) - c)\})$ ,
- (c) Repeat until a new  $\mathbf{p}$  is accepted

#### MD step

- (a) Initiate the extended leapfrog algorithm with  $(\mathbf{E}, \mathbf{p})$  and run the algorithm for  $L$  time step to obtain  $(\mathbf{E}^*, \mathbf{p}^*)$
- (b) Update the FEM to obtain the new analytic frequencies and then compute  $\tilde{H}(\mathbf{E}^*, \mathbf{p}^*)$
- (c) Accept  $(\mathbf{E}^*, \mathbf{p}^*)$  with probability  $\min(1, \exp\{\tilde{H}(\mathbf{E}, \mathbf{p}) - \tilde{H}(\mathbf{E}^*, \mathbf{p}^*)\})$ .

SHMC's parameter  $c$  appears in the both MC and MD steps where it has a very significant effect on the simulation [8]. For a large positive  $c$ , SHMC is equivalent to HMC with a different set of momentum, and the acceptance rate of the MD step decreases as well as it increases that of the MC step. Conversely, a large negative  $c$  increases the acceptance rate of the MD step and decreases the acceptance rate of the MC step. In this paper, the value of  $c$  is chosen proportional to the average difference between the Hamiltonian and the shadow Hamiltonian. Finally, in order to calculate balanced values of the mean, the results must be reweighted. This can be done by using  $\rho(\mathbf{E}, \mathbf{p}) / \tilde{H}(\mathbf{E}, \mathbf{p})$  before evaluating the averages. The average of an observable  $B$  is giving by  $B = \frac{\sum_{i=1}^{N_s} B_i a_i}{\sum_{i=1}^{N_s} a_i}$ , where  $a_i = \frac{\exp(-H(\mathbf{E}, \mathbf{p}))}{\exp(-\tilde{H}(\mathbf{E}, \mathbf{p}))}$  [13].

## 53.6 Construction of the Shadow Hamiltonian

The effects of discretization error in the numerical solution of a system of differential equations could be analysed by examining the “modified equations” of this system [9, 10]. These equations are exactly satisfied by the (approximate) discrete solution [9, 19, 20]. The modified equations are defed by an asymptotic expansion in powers of the discretization parameter. Nonetheless, if the expansion is suitably truncated, the resulting modified equations have a solution which is remarkably close to the discrete solution. This could be the case for Hamiltonian systems. The modified integrator is Hamiltonian if and only if the integrator is symplectic [8, 9]. The integrator is symplectic if  $\partial_y \varphi(\mathbf{y})^T \mathbf{J} \partial_y \varphi(\mathbf{y}) \equiv \mathbf{J}$ , where  $\mathbf{y} = \varphi(\mathbf{y})$  is a numerical integrator and  $\mathbf{J} = \begin{bmatrix} 0 & \mathbf{I} \\ -\mathbf{I} & 0 \end{bmatrix}$ . There is also evidence that the numerical solution of symplectic integrators stays close to the solution of a modified Hamiltonian  $H^{\delta t}(\mathbf{E}, \mathbf{p})$  for very long times [8, 9]. Skeel and Hardy [9] show how to compute an accurate approximation to the modified Hamiltonian integrated by symplectic integrators based on splitting. The goal is to compute

$$H_{[2k]}(\mathbf{E}, \mathbf{p}) = H^{\delta t}(\mathbf{E}, \mathbf{p}) + \mathcal{O}(\delta t^{2k}) \quad (53.16)$$

where  $H_{[2k]}(\mathbf{E}, \mathbf{p})$  is a shadow Hamiltonian of order  $2k$ . The construction adds a new position variable and a conjugate momentum variable  $\beta$  to obtain an extended Hamiltonian  $\tilde{H}(\mathbf{y})$ ,  $\mathbf{y} = [\mathbf{E}^T, \alpha, \mathbf{p}^T, \beta]^T$  and  $\alpha = 1$ , which is homogeneous of order 2. For this Hamiltonian  $\tilde{H}(\mathbf{y}) = \frac{1}{2} \mathbf{y}^T \mathbf{J} \mathbf{y}$ . An approximation to  $\mathbf{y}$  is formed using the numerical solution of the extended Hamiltonian system  $\tilde{H}(\mathbf{y})$ . The resulting shadow Hamiltonian approximation satisfies (53.16).



The shadow Hamiltonian is a combination of trajectory information, that is,  $k$  copies of available positions and momenta generated by the MD integration, and an extra degree of freedom  $\beta$  that is propagated along with the momenta. By construction  $H_{[2k]}(\mathbf{E}, \mathbf{p})$  is exact for quadratic Hamiltonians, which is useful, because harmonic motion dominates applications such as MD. For more details see [8–10]. Formulae for the 4th and 8th shadow Hamiltonians,  $k = 2$  and  $k = 4$  respectively [9, 10], are

$$H_{[4]}(\mathbf{E}, \mathbf{p}) = \mathbf{A}_{10} - \frac{1}{6}\mathbf{A}_{12} \quad (53.17)$$

$$H_{[8]}(\mathbf{E}, \mathbf{p}) = \mathbf{A}_{10} - \frac{2}{7}\mathbf{A}_{12} - \frac{19}{210}\mathbf{A}_{14} + \frac{5}{42}\mathbf{A}_{30} + \frac{13}{105}\mathbf{A}_{32} - \frac{1}{140}\mathbf{A}_{34} \quad (53.18)$$

where the  $\mathbf{A}_{ij}$  are defined as

$$\mathbf{A}_{ij} = \begin{cases} \mu\delta^i \mathbf{E} \cdot \delta^j \mathbf{p} - \delta^j \mathbf{E} \cdot \mu\delta^i \mathbf{p} - \mu\delta^i \beta & : j = 0 \\ \mu\delta^i \mathbf{E} \cdot \delta^j \mathbf{p} - \delta^j \mathbf{E} \cdot \mu\delta^i \mathbf{p} & : j \neq 0 \end{cases} \quad (53.19)$$

and  $\delta\mathbf{E}$  represents the central difference of vector  $\mathbf{E}$  defined by  $\delta\mathbf{E} = \mathbf{E}^{\frac{1}{2}} - \mathbf{E}^{-\frac{1}{2}}$ , and the averaging operator  $\mu\mathbf{E}$  is similarly defined by  $\mu\mathbf{E} = 1/2(\mathbf{E}^{\frac{1}{2}} + \mathbf{E}^{-\frac{1}{2}})$ . To evaluate the leapfrog algorithm, we again use (53.10), (53.11) and (53.12), and we include the term  $\beta$ , where  $\beta$  is evaluated according to

$$\beta(t+1) = \beta(t) + \delta t \cdot (\mathbf{E}(t) \cdot \nabla V[\mathbf{E}(t)] - 2V(t)) \quad (53.20)$$

In this paper, the SHMC method is investigated on the updating of structural beam models. The first example is a simple cantilever beam. The second example is an unsymmetric H-shaped aluminium structure. The results of this method will be compared with those obtained by using an HMC method.

### 53.7 A Cantilever Beam Example

An experimental cantilever steel beam is updated based on the measurements of Kraaij [21]. The beam has the following dimensions: length 500 mm, width 60 mm and thickness 10 mm.  $E = 2.1 \times 10^{11}$  N/m<sup>2</sup>,  $\nu = 0.3$  and  $\rho = 7850$  kg/m<sup>3</sup> (Fig. 53.1).

Three accelerometers were used in the experiment, which were all located 490 mm from the clamped end. This location was chosen because the response at this point is large [21]. Each accelerometer has a mass of 40 g; the middle accelerometer is of type 303A3, the outer accelerometers are of type 303A2 (see [21] for more details of the experimental set-up). To test the proposed updating methods, the beam was modelled using Version 6.3 of the Structural Dynamics Toolbox SDR<sup>®</sup> for MATLAB. The beam was divided into 50 Euler–Bernoulli beam elements and excited at various positions. The measured natural frequencies of interest of this structure are: 31.9, 197.9, 553, 1082.2 and 1781.5 Hz. In this investigation, the moments of inertia and the section areas are updated. This is done by associating an area moment of inertia,  $I_x$ , and an area,  $A_x$ , to each group of 25 elements of the beam (this will reduce the number of the parameters to be updated to four parameters). The updated parameters vector is thus  $\mathbf{E} = \{I_{x1}, I_{x2}, A_{x1}, A_{x2}\}$ .

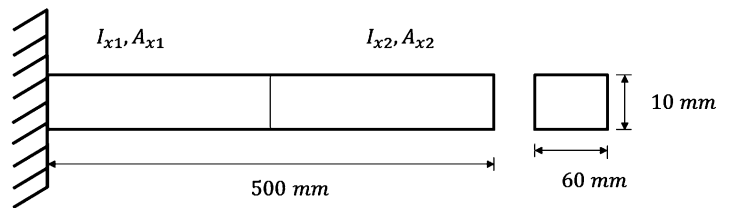


Fig. 53.1 The cantilever beam structure

**Table 53.1** Initial and updated parameters using HMC, and 4th and 8th order SHMC

	Initial E	E vector, HMC method	E vector, SHMC4 method	E vector, SHMC8 method
$I_{x1}$	$5 \times 10^{-9}$	$6.16 \times 10^{-9}$	$6.17 \times 10^{-9}$	$6.16 \times 10^{-9}$
$I_{x2}$	$5 \times 10^{-9}$	$5.36 \times 10^{-9}$	$5.36 \times 10^{-9}$	$5.35 \times 10^{-9}$
$A_{x1}$	$6 \times 10^{-4}$	$7.32 \times 10^{-4}$	$7.32 \times 10^{-4}$	$7.33 \times 10^{-4}$
$A_{x2}$	$6 \times 10^{-4}$	$6.91 \times 10^{-4}$	$6.92 \times 10^{-4}$	$6.89 \times 10^{-4}$

**Table 53.2** Natural frequencies and errors when HMC, and 4th and 8th order SHMC are used to update the FEM

Modes	Measured frequency (Hz)	Initial FEM frequency (Hz)	Frequencies HMC method		Frequencies SHMC4 method		Frequencies SHMC8 method		
			Error (%)	(Hz)	Error (%)	(Hz)	Error (%)	(Hz)	
1	31.9	30.6	4.11	31.8	0.3	31.81	0.29	31.83	0.23
2	197.9	196	1.01	195.0	1.46	195.0	1.46	195.0	1.46
3	553	556.4	0.61	550.5	0.45	550.5	0.45	550.4	0.47
4	1082.2	1157.3	6.94	1087.4	0.48	1087.4	0.48	1087.3	0.47
5	1781.5	1835.0	3.01	1812.5	1.74	1812.4	1.74	1812.2	1.72

### 53.7.1 The Cantilever Simulation

The constant  $\beta$  in (53.6), the posterior distribution function, is set to 1, and all coefficients  $\alpha_i$  are set equal to  $\frac{1}{\sigma_i^2}$ , where  $\sigma_i^2$  is the variance of the parameter  $E_i$ . Since the updating parameter vector contains area moments of inertia and section areas, the  $\sigma_i$  vector is defined as  $\sigma = [5 \times 10^{-10}, 5 \times 10^{-10}, 5 \times 10^{-5}, 5 \times 10^{-5}]$ . The Young's modulus is set to  $2.1 \times 10^{11}$  N/m<sup>2</sup>. The updating parameters  $E_i$  are bounded by maximum values equal to  $[6.5 \times 10^{-9}, 6.5 \times 10^{-9}, 7.5 \times 10^{-4}, 7.5 \times 10^{-4}]$  and minimum values equal to  $[4 \times 10^{-9}, 4 \times 10^{-9}, 5 \times 10^{-4}, 5 \times 10^{-4}]$ . The number of samples  $N_s$  is set to 10,000, the time step is set to  $0.004s$  and the  $c$  is set to 0.01. The FEM updated simulation results using the proposed methods are presented in Tables 53.1 and 53.2.

Table 53.1 shows that the HMC, 4th and 8th order SHMC techniques update all of vector parameters and give results that are close to the mean value (the initial values). The updated vector for both HMC and 4th order SHMC are very close, while the 8th order SHMC results were slightly different. The time step,  $\delta t = 0.004s$ , helps to maintain a good acceptance sampling rate for both HMC and SHMC (99.9%). Choosing a different time step may reduce the acceptance sampling rate for the HMC method, and this can significantly affect the results obtained.

Table 53.2 shows the output errors of the different FEM models. The results show that the updated FEM natural frequencies are better than the initial FEM for both methods: HMC and SHMC. The 4th order SHMC and HMC give similar frequencies. Moreover, the 8th order SHMC provides results that are very close to HMC and 4th order SHMC where the HMC and 8th order SHMC algorithms give identical results except for the first and the fifth natural frequencies. The error between the first measured natural frequency and that of the initial model was 4.11 %. With the HMC method implementation, this error was reduced to 0.3 % and by implementing the 8th order SHMC it was reduced to 0.23 %. The same comment can be made for the fifth natural frequency. Both SHMC and HMC methods converge fast (almost the first 200 iterations during the simulation). However, a different time step might decrease the acceptance sampling rate which will significantly affect the convergence of the HMC method. On the other hand, the SHMC can provide a good acceptance rate despite the changes of the time step. The constant  $c$  introduced in (53.15) has a very important role in the SHMC method. Choosing a positive large value of  $c$ , compared to the Hamiltonian function value, might make the methods similar with different momentum sets. Choosing a very small value of  $c$  might decrease the acceptance rate and this will affect both the results and convergence rate. The value of  $c$  used in this simulation was an average value which allowed us to start from the Hamiltonian function (the modified Hamiltonian equal the original one at the first iteration) and helped to achieve an acceptance rate of 99.9 % for the SHMC method.

In general, a conclusion about the most efficient method, between HMC and SHMC, is difficult to make by using only one example. For this reason, another updating exercise is performed, where the area moments of inertia and cross-section area of an H-shaped aluminium structure are updated and the results obtained are discussed in Sect. 53.8.

### 53.8 Unsymmetric H-shaped Structure

The unsymmetric H-shaped aluminium structure is shown in Fig. 53.2. The structure was divided into 12 elements and each was modelled as an Euler-Bernoulli beam. The structure was excited at the position indicated by the double arrow in Fig. 53.2, and the acceleration was measured at 15 different positions. The structure was excited using an electromagnetic shaker and the response was measured using an accelerometer and a set of 15 frequency-response functions were calculated [4].

A roving accelerometer was used to measure the response, see [4] for more information about the experiment. The measured natural frequencies are: 53.9, 117.3, 208.4, 253.0 and 445.0 Hz. In this implementation, the moments of inertia and the section areas (as shown in Fig. 53.3) are updated. The updated parameter vector is  $\mathbf{E} = \{I_{x1}, I_{x2}, I_{x3}, A_{x1}, A_{x2}, A_{x3}\}$ .

#### 53.8.1 H-shaped Structure Simulation

The constant  $\beta$  of the posterior distribution is set equal 10, and all coefficients  $\alpha_i$  are set equal to  $\frac{1}{\sigma_i^2}$ , where  $\sigma_i^2$  is the variance of the parameter  $E_i$ . Since the updating parameter vector contains area moments of inertia and section areas, the vector of  $\sigma_i$  is defined as  $\sigma = [5 \times 10^{-9}, 5 \times 10^{-9}, 5 \times 10^{-9}, 5 \times 10^{-5}, 5 \times 10^{-5}, 5 \times 10^{-5}]$ . The Young's modulus is set to  $7.2 \times 10^{10}$  N/m<sup>2</sup>. The updating parameters  $E_i$  are bounded by maximum values equal to  $[3.73 \times 10^{-8}, 3.73 \times 10^{-8}, 3.73 \times 10^{-8}, 4.16 \times 10^{-4}, 4.16 \times 10^{-4}, 4.16 \times 10^{-4}]$  and minimum values equal to  $[1.73 \times 10^{-8}, 1.73 \times 10^{-8}, 1.73 \times 10^{-8}, 2 \times 10^{-4}, 2.16 \times 10^{-4}, 2.16 \times 10^{-4}]$ . The number of samples  $N_s$  is set to 1,000, the time step is set to 0.0045 s and the constant  $c = 0.001$ . The results are given in Tables 53.3 and 53.4.

Table 53.3 presents the initial value, and the mean value, of the vector  $\mathbf{E}$ , as well as the updated values obtained by each method. The HMC, and the 4th and 8th order SHMC techniques update all of the parameters successfully. The first three updated parameters, i.e. the moments of inertia, are close to the mean values for both the HMC and SHMC techniques. On

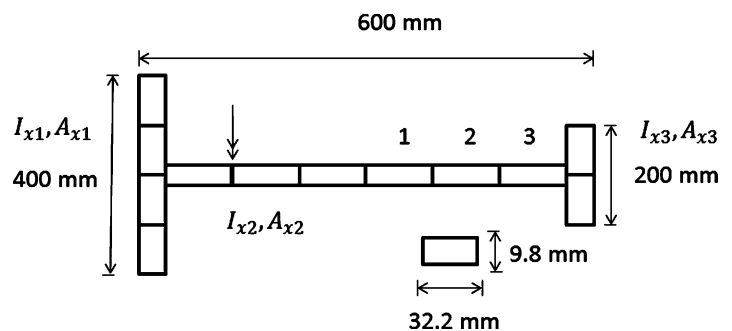


Fig. 53.2 The H-shaped aluminium structure

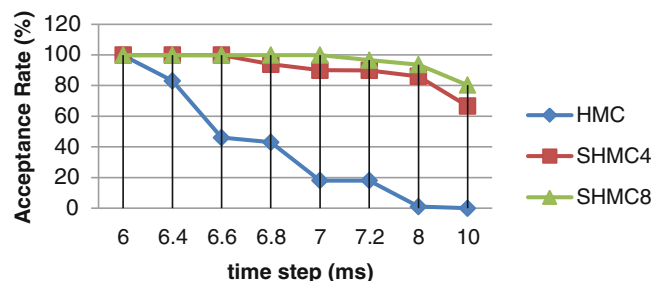


Fig. 53.3 The acceptance rate obtained for different time steps using HMC and SHMC (4th and 8th order)

Table 53.3 Initial and updated parameters using HMC, and 4th and 8th order SHMC

	Initial $\mathbf{E}$	$\mathbf{E}$ vector, HMC method	$\mathbf{E}$ vector, SHMC4 method	$\mathbf{E}$ vector, SHMC8 method
$I_{x1}$	$2.73 \times 10^{-8}$	$2.21 \times 10^{-8}$	$2.18 \times 10^{-8}$	$2.24 \times 10^{-8}$
$I_{x2}$	$2.73 \times 10^{-8}$	$2.6 \times 10^{-8}$	$2.49 \times 10^{-8}$	$2.52 \times 10^{-8}$
$I_{x3}$	$2.73 \times 10^{-8}$	$2.9 \times 10^{-8}$	$2.96 \times 10^{-8}$	$2.94 \times 10^{-8}$
$A_{x1}$	$3.16 \times 10^{-4}$	$4.0 \times 10^{-4}$	$4.05 \times 10^{-4}$	$4.04 \times 10^{-4}$
$A_{x2}$	$3.16 \times 10^{-4}$	$2.3 \times 10^{-4}$	$2.46 \times 10^{-4}$	$2.41 \times 10^{-4}$
$A_{x3}$	$3.16 \times 10^{-4}$	$2.4 \times 10^{-4}$	$2.25 \times 10^{-4}$	$2.29 \times 10^{-4}$

**Table 53.4** Natural frequencies and errors when HMC, and SHMC of orders 4 and 8, are used to update the parameters

Mode	Measured frequency (Hz)	Initial frequency (Hz)	Frequencies HMC method		Frequencies SHMC4 method		Frequencies SHMC8 method		
			Error (%)	(Hz)	Error (%)	(Hz)	Error (%)	(Hz)	Error (%)
1	53.9	51.40	4.63	52.93	1.8	52.94	1.79	53.05	1.58
2	117.3	116.61	0.59	118.82	1.3	118.23	0.79	118.7	1.2
3	208.4	201.27	3.42	208.81	0.2	207.91	0.23	208.61	0.1
4	253.0	247.42	2.59	253.41	0.16	253.84	0.06	253.91	0.03
5	445	390.33	12.28	444.13	0.2	443.0	0.45	443.22	0.40

the other hand, these methods gave significant variations to the rest of the parameters. In general, the updated vector obtained from HMC, 4th order SHMC and 8th order SHMC are different from each other and this because of the used value of the constant ( $c = 0.001$  helps to achieve a good acceptance rate for the SHMC method). Using the said time step provides a very good acceptance sampling rate for both HMC and SHMC (99.9%).

Table 53.4 shows the errors and the FEM updated frequencies. The results show that the updated FEM natural frequencies, for both the HMC and SHMC, are better than the initial FEM. The 4th and 8th order SHMC give better results than the HMC. The 8th order SHMC provides a smaller error compared to both HMC and 4th order SHMC. The error between the first measured natural frequency and that of the initial model was 4.63 %. With the HMC method implementation, this error was reduced to 1.8 % and by implementing the 8th order SHMC it was reduced to 1.58 %. The same comment can be made for the third and the fourth natural frequencies. The 4th order SHMC method provides better results than the HMC (see Table 53.4). Both methods, HMC and SHMC, converge fast and they almost have the same convergence rate (the algorithms start converging in the first 300 iterations during the simulation).

The time step,  $\delta t = 0.004s$ , provides a good acceptance sampling rate for both methods: HMC and SHMC (99.9%). Choosing a different time step may reduce the acceptance sampling rate for the HMC method. This can significantly affect the results obtained as well as the convergence rate. Figure 53.3 plots the acceptance rate for a different time steps (from 0.006 to 0.01 s). In HMC methods, the acceptance sampling rate starts decreasing from the time step 0.006 s (99.7 %) and continues to decrease until it reaches 0 % (no updated values for  $E$  vector) at time step 0.01 s. On the other hand, the SHMC method kept a good acceptance rate. At time step 0.006 s both 4th and 8th order SHMC have an acceptance rate equal to 99.9 %. The 4th order SHMC keeps this value (99.9 %) for time step  $\delta t = 0.0064s$  and  $\delta t = 0.0066s$  and starts decreasing from  $\delta t = 0.0068s$  (93.9 %) to reach an acceptance rate equal to 66 % at time step  $\delta t = 0.01s$ . However, the 8th order SHMC keeps the acceptance rate equal to 99.9 % for larger time steps (until  $\delta t = 0.007s$ ). The acceptance sampling rate for the 8th order SHMC reduces to 80.3 % at time step  $\delta t = 0.01s$ .

## 53.9 Conclusion

In this paper Bayesian FEM methods are used to update a cantilever beam and an H-shaped beam structure. To evaluate the posterior distribution function, two Markov Chain Monte Carlo (MCMC) sampling techniques have been implemented; the Shadow Hybrid Monte Carlo method (SHMC) and the Hybrid Monte Carlo (HMC) technique. In the first simulation the HMC and SHMC techniques gave almost the same results. In addition, both methods converged fast for the given time steps. A large time step might weaken this property for the HMC method. In the second simulation the 8th order SHMC method gave better results than both the 4th order SHMC and HMC. Moreover, the SHMC method provides samples with a large step time which is not the case with the HMC method where the sampling rate decreases when the time step increases. Further work will consider the differences between the above methods and other variations of the Hamiltonian Monte Carlo method.

## References

1. Onãte E (2009) Structural analysis with the finite element method. Linear statics, vol 1, Basis and solids. Springer, London
2. Rao SS (2004) The finite element method in engineering, 4th edn. Elsevier Butterworth Heinemann, Burlington
3. Friswell MI, Mottershead JE (1995) Finite element model updating in structural dynamics. Kluwer, Academic, Boston
4. Marwala T (2010) Finite element model updating using computational intelligence techniques. Springer, London
5. Yuen KV (2010) Bayesian methods for structural dynamics and civil engineering. Wiley, New York

6. Cheung SH, Beck JL (2009) Bayesian model updating using Hybrid Monte Carlo simulation with application to structural dynamic models with many uncertain parameters. *J Eng Mech* 135(4):243–255
7. Boulkaibet I, Marwala T, Mthembu L, Friswell MI, Adhikari S (2012) Sampling techniques in Bayesian finite element model updating. *Proc Soc Exp Mech* 29:75–83
8. Izaguirre JA, Hampton SS, Comput J (2004) Shadow Hybrid Monte Carlo: an efficient propagator in phase space of macromolecules. *J Comput Phys* 200:581–604
9. Skeel RD, Hardy DJ (2001) Practical construction of modified Hamiltonians. *SIAM J Sci Comput* 23(4):1172–1188
10. Engle RD, Skeel RD, Drees M (2005) Monitoring energy drift with shadow Hamiltonians. *J Comput Phys* 206:432–452
11. Ewins DJ (1984) *Modal testing: theory and practice*. Research Studies, Letchworth
12. Bishop CM (2006) *Pattern recognition and machine learning*. Springer, New York
13. Marwala T, Sibisi S (2005) Finite element model updating using Bayesian approach. In: *Proceedings of the international modal analysis conference*, Orlando, ISBN: 0-912053-89-5
14. Bishop CM (1995) *Neural networks for pattern recognition*. Oxford University Press, Oxford
15. Vapnik VN (1995) *The nature of statistical learning theory*. Springer, New York
16. Ching J, Leu SS (2009) Bayesian updating of reliability of civil infrastructure facilities based on condition-state data and fault-tree model. *Reliab Eng Syst Saf* 94(12):1962–1974
17. Neal RM (2000) *Slice sampling*, technical report, no. 2005, Department of Statistics, University of Toronto
18. Hanson KM (2001) Markov Chain Monte Carlo posterior sampling with the Hamiltonian method. *Proc SPIE* 4322:456–467
19. Creutz M (1988) Global Monte Carlo algorithms for many-fermion systems. *Phys Rev D* 38:1228–1238
20. Kennedy AD, Pendleton B (1991) Acceptances and autocorrelations in hybrid Monte Carlo. *Nucl Phys B Proc Suppl* 20:118–121
21. Kraaij CS (2007) *Model updating of a ‘clamped’-free beam system using FEMTOOLS*. Technische Universiteit Eindhoven, Eindhoven, Netherlands

# Chapter 54

## Pseudo Velocity Shock Data Analysis Calculations Using Octave

Howard A. Gaberson

**Abstract** Octave [1] is a GNU licensed free signal processing program that does all our basic shock data calculations and plotting. It's more clumsy than Matlab [2], but it's free. I have adjusted my Matlab programs to run on it, and have enough done for a paper on how to do it. The paper will give you a big start in doing shock data analysis on your own. I've always felt less than helpful giving papers on how to do shock analyses, knowing that the user needs a two thousand dollar program to use the material. This changes the game entirely. This paper shows how to use Octave to do all the basic shock data analysis calculations and plotting. Once you can do analysis for yourself, you gain understanding of data analysis. It will give you a start and enough confidence to see that you can learn it. I will give out my programs, which you can use as is, or change to better suit your needs.

**Keywords** Shock analysis • Shock spectrum • SRS (shock response spectrum) • PVSS (pseudo velocity shock spectrum) • FFT (fast Fourier transform) • Fourier transforms • Matlab • Octave • Shock signal analysis

### 54.1 Introduction

I have been fascinated with digitized shock and vibration signals since 1969. It's just extremely interesting, and makes a lot of the seemingly useless math come alive and solves problems. I've been using this expensive digital signal arithmetic program, Matlab, since the early 90s. I learned a little Fortran in graduate school, and started using it to calculate shock spectra in the early 70s. What I can do now, in my last years, is try and show what interested me and give some ideas for people to try. I'm sure the calculation possibilities will continue to offer opportunity.

I think the obstacle of the high cost of Matlab for routine signal arithmetic may prevent many potential innovators from learning the ideas, and they are not very difficult. This free program Octave may be enough to do it, so in this paper I want to teach/show some basic shock analysis calculations normally done with Matlab but here done with Octave so you can try them out. Maybe I can attract a subgroup to develop this further and then we can make it easier for all to learn. Knowing how to do the calculation yourself develops a relationship with the signal arithmetic. You can call it math, but I want you to see that we're talking about just a few concepts: add, subtract, multiply, divide, and raise to powers; on long lists of numbers, while keeping track of where we are. So let's start doing some simple shock analysis digital signal analysis.

I'd like you to learn how to calculate something on your own. For example the pseudo velocity shock spectrum (PVSS) and how to integrate the shock and plot it. Then go to my program that I used for the calculation and plotting, and convince yourself that I am doing it correctly. A difficult job is to download Octave and get comfortable with it. I'll try and explain that next. Maybe the paper could be described as part elementary amateur programming; so let's go through some of the steps of shock data analysis.

---

H.A. Gaberson (✉)  
234 Corsicana Dr, Oxnard, CA 93036, USA  
e-mail: [hagaberson@att.net](mailto:hagaberson@att.net)



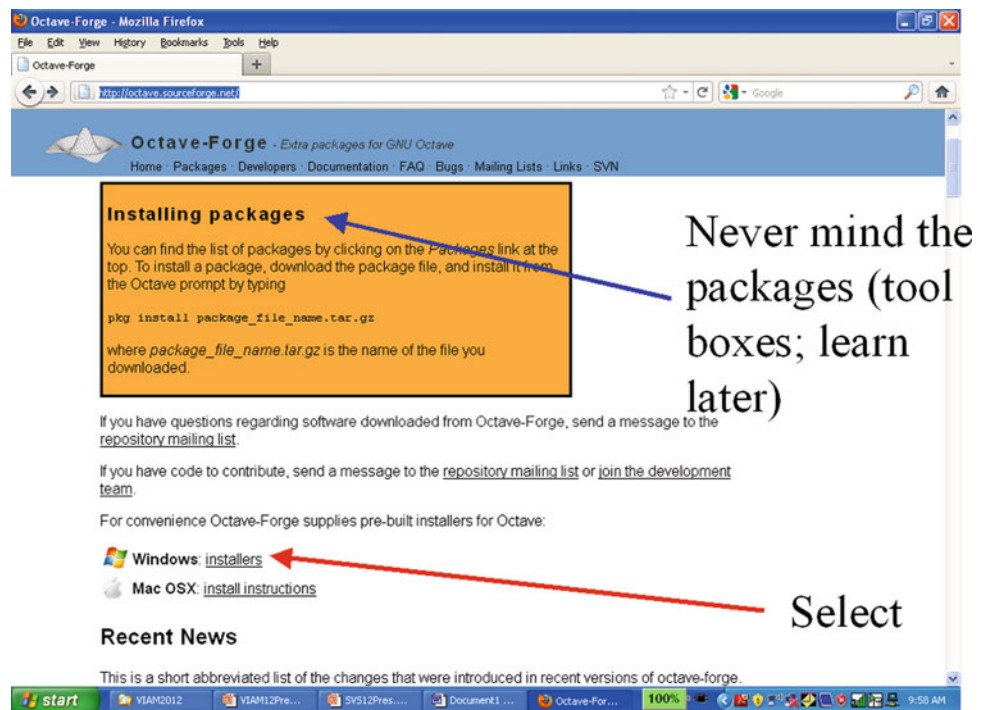
## 54.2 Version to Use

There is a potentially very helpful GUI (Graphical User Interface), for Octave called GUI Octave. It permits more direct Windows plotting, and cut and paste of script portions for faster programming. The version of GUI Octave available when I wrote this is 1.5.4 and can be downloaded; I had too much trouble with this to try and explain it. I depend on the diary to keep track of what I've done and this GUI Octave has trouble and loads the diary with too much extra annotation. Octave 4.6.1 is the latest Octave version, but I had trouble downloading that. Instead of a single program with an ".exe" extension, it has a sequence of confusing instructions involving several downloads prior to trying to install. There is a new GUI Octave version for this new Octave. I tried earlier versions that installed simply; both 3.4.3 and 3.2.4. This early version 3.2.4 is the only one able to print at  $45^\circ$  which we need for the four coordinate paper and decided to work with it. After you learn this simple Octave 3.2.4, you can teach yourself the newer versions. Colleges are being forced to use Octave due to the high cost of Matlab, so there is a great deal a material available. By internet searching I found several manuals. I even found a movie of a math teacher showing his class how to download Octave 3.2.4. That helped convince me to use version 3.2.4.

## 54.3 Down Loading Octave

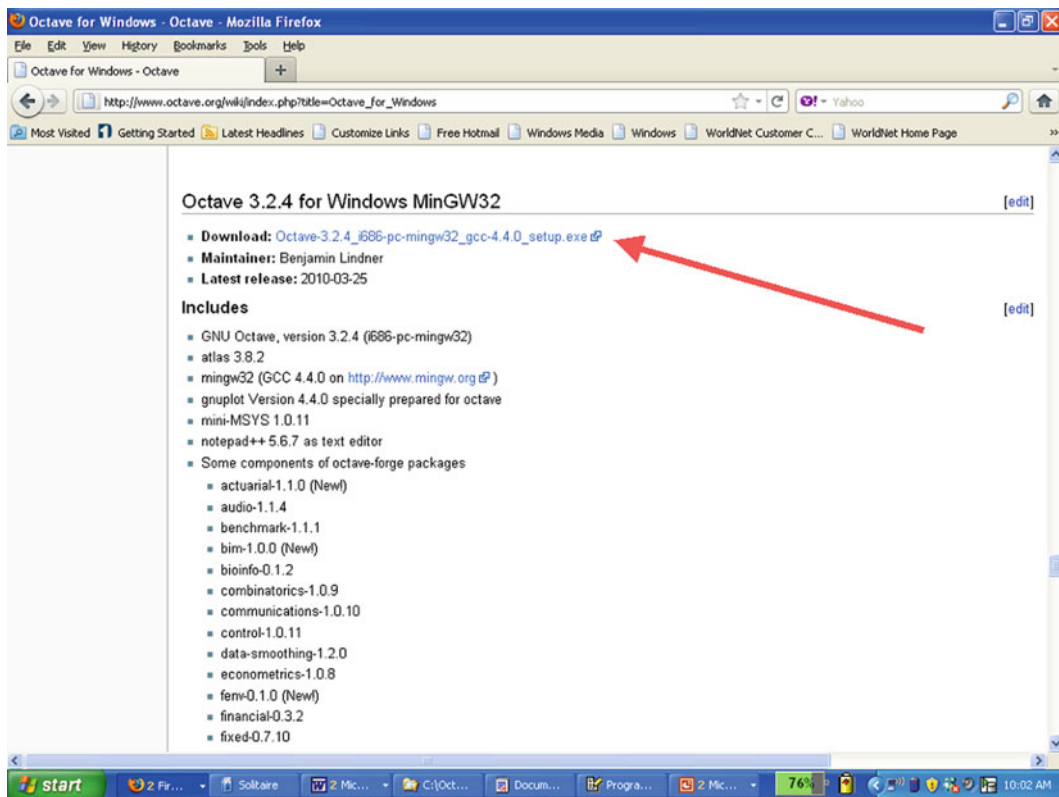
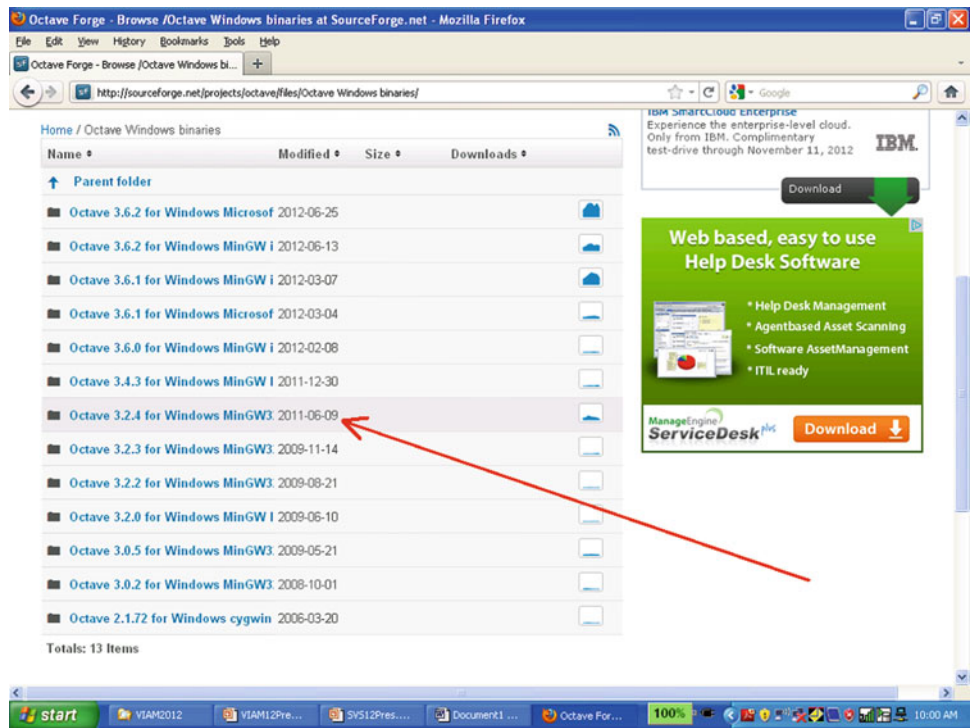
Friends advised me that 'Source Forge' [3] is a safe site to download from, and that's what I used.

Figure 54.1 came from <http://octave.sourceforge.net>. I clicked on Windows Installers and this took me to Fig. 54.2. In the screen of Fig. 54.2. I clicked on Octave 3.2.4. which took me to the screen shown in Fig. 54.3. The red arrow shows where to click to download Octave 3.2.4. After it download, it asked if I wanted to save the ".exe" file and I said yes and copied it on two different flash drives before I clicked on it in my computer to install it. Figure 54.4, is a print screen of Windows Explorer showing the folders and files set up by installing Octave 3.2.4. We get 11 folders and 4 files that are Octave 3.2.4 with the shortcut on the desktop and are ready to go. Clicking on our new Octave desktop icon opens Octave and we see the box or screen of Fig. 54.5. This is a dos or command screen; I remember working on the similar black dos screens from early versions of Matlab. You can't cut, copy, and paste into here and the mouse doesn't work in here. To command Octave you must type each command or write a series of instructions in the editor, save them as a script, and run the script. We'll see this many times but that gets us far enough to learn by starting to use it.



**Fig. 54.1** This is the screen I used to find a windows installer

**Fig. 54.2** The screen showed many Octave versions are available. I selected and clicked on Octave 3.2.4



**Fig. 54.3** I clicked on Download 3.2.4, (at the red arrow) and since that is a “.exe” file it downloaded that

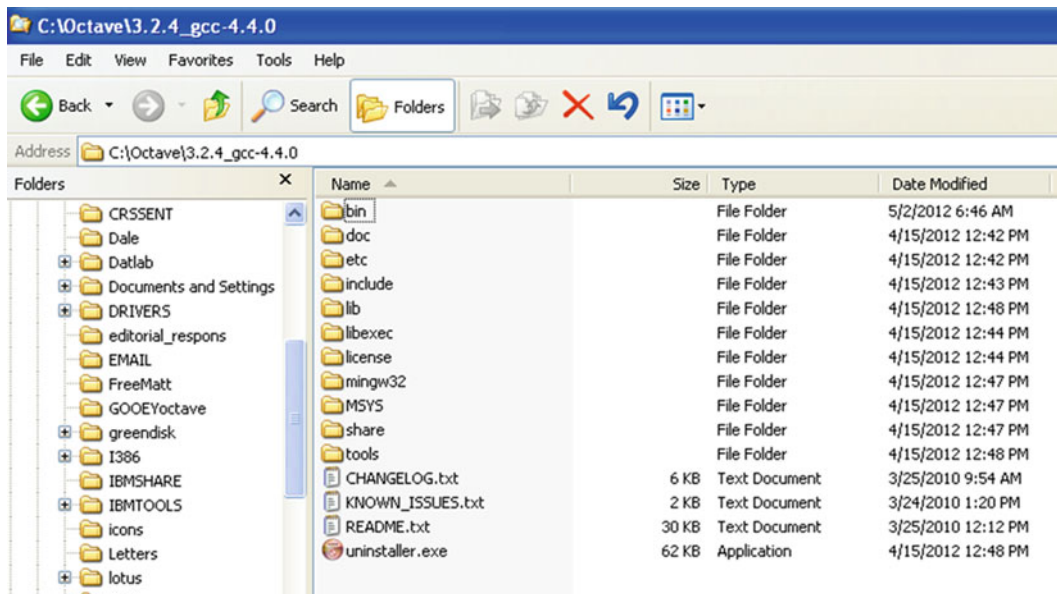


Fig. 54.4 This is the directory structure the installer sets up for Octave 3.2.4. Bin is where a lot of our action is saved, for example the diaries

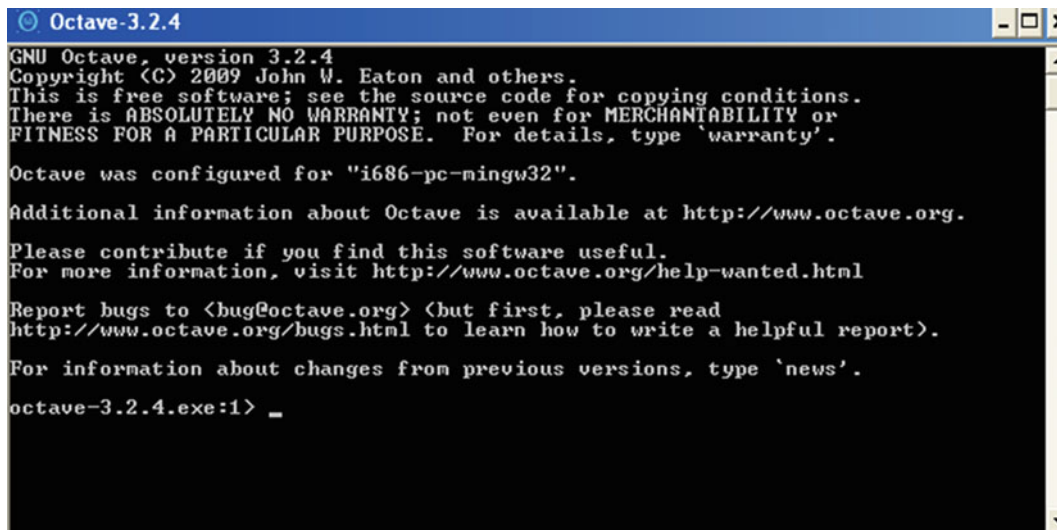


Fig. 54.5 This is the opening Octave 3.2.4 screen

## 54.4 Shock Data Analysis Preliminaries

In this paper I'm going to assume we have a means to get a copy of the digitized data, and I'm going to try and explain how you can do the shock signal analysis calculations on your laptop with Octave 3.2.4. I'm hoping this is understandable enough so that you can try out everything I discuss. Shock data analysis is mainly data handling, editing, maybe filtering, plotting, integration, and shock spectrum calculation. SRS (Shock Response Spectrum, means the absolute acceleration shock spectrum) calculation is the most widely used of the shock evaluation technologies. I have shown that it's not the best way to look at shock and that the PVSS is far better [4, 5, 6]. I use about 10 short programs for shock analysis and I'll explain many of those here and how to use them in Octave.

## 54.5 Editor

You have to use an ascii editing program to modify `pvssz.m`, `fourcp.m`, and `timhist3.m`, and to write short scripts and programs. You will also need the editor to modify ascii data with comment identifiers (%). I think you can use notepad, but it may not accept the `.m` extension, or allow you to turn the line numbers on and off. When Octave finds an error, it will tell you its line number. Octave includes an editor that most people use, but I don't use it. I use and suggest PFE32. You can get a copy by going to Google and searching on PFE, and downloading it from what looks like a reliable site. It's freeware.

## 54.6 Housekeeping

What I always do to keep track of things is open each session of Octave or Matlab with the command "diary 050306o" for today's date. That date means 05 for 2005, 03 for March, and 06 for the 6th of March; the little 'o' means it's an Octave diary. The diary records what I've done that day in a file called 050306 in Matlab's "work" directory and in Octave's "c:\Octave\3.2.4\_gcc-4.4\bin" directory. (Newer Matlab releases store diaries in different places.) By so doing, I have a record of everything I've done since 1994. Also a good idea I try to make myself do, has been to annotate every plot I print with the date in this same format, over in a corner someplace. With this I can go back to the corresponding diary to see how I made the plot. Right now I intend to keep using my old Release 12 Matlab, but I want to learn enough Octave to help people who want to try shock analysis without spending the sizable cost of Matlab.

I suggest you also append a date to each copy of `pvss` you modify: make it `pvss050306.m` so you keep the one I sent as a back up in case you lose it. I assume you have a folder where you keep your Matlab scripts or program files. For this paper and lessons I am using a folder called Shocko.

## 54.7 Digitizing and Aliasing

To process shock signals in a computer, they must be digitized. Just prior to digitizing, the analog transducer signal must be analog filtered to avoid aliasing. Although many problems arise in trying to assure no aliasing occurs, we will assume the files we work on are properly digitized data. Shannon's sampling theorem [7] states that a signal is adequately sampled if it is sampled at a rate at least twice the highest frequency present in the signal. By frequency content he means that the Fourier transform is zero beyond the maximum frequency present, and this condition is essential in his proof. A signal that is adequately sampled is completely defined for all points even those between the samples; per Claude: "one and only one function can pass through those points and be band limited." A signal digitized without analog antialiasing has been essentially destroyed. Any little spike or spurious high frequency squiggle, can be folded into the data and totally corrupt the digitized signal. Insist on good antialiasing. We're going to work on signals that are adequately digitized.

## 54.8 Programs Used

I use about ten programs for shock data analysis and have modified and testes more than half of them in Octave 3.2.4. Only slight changes are needed to get them to run. The programs I'll discuss here are listed below. I have them in a folder called Shocko which I'll be happy to send you.

---

1.	<code>ASRSo.m</code>	Calculate and plot SRS and APVSS using zeros for residual. [3]
2.	<code>fourcp1o.m</code>	Print four coordinate grid over PVSS plot and set axis limits 0.1 10,000 Hz
2b	<code>fourcp1100o.m</code>	Print four coordinate grid over PVSS plot and set axis limits 1 100,000 Hz
7a	<code>PVposnego.m</code>	Calculate and plot the positive and negative PVSS
7.	<code>pvsszo.m</code>	Calculate and plot PVSS using zeros for residual
8.	<code>rvsso.m</code>	Calculate and plot RVSS using zeros for residual
10.	<code>timhis3o.m</code>	Integrate and plot acceleration into velocity and displacement, in three subplots, one below the other

---

## 54.9 Lesson One: Load and Plot Some Text Data

Octave and Matlab expect and accept numerical data in ascii format as a matrix of numbers. Every column has the same number of numbers and every row has the same number of numbers, even if some are zero. Thus a column of 1,000 numbers is fine by itself. If the file name has any three letter extension other than “\*.mat”, Octave expects it to be a text or ascii matrix of numbers. If it has a “.mat” extension, the same applies except it is written in a more compressed Octave and Matlab format. A “%” causes everything on the remainder of that line to be ignored. Thus if your data file has a lot of important info in the header section, you can leave all that in the file by beginning each header line with a “%”. Just below in Table 54.1, I have printed the first 15 lines of a shock data file called “mohamedgunfire.txt”. Notice the % preceding the first line which is header material to be ignored. I have 14 rows and 2 columns of numbers in this example. On the second line, the second column value seems shifted; it’s not as far as Octave is concerned.

Now, in Table 54.2, I’ll show a diary portion of what I did and how Octave responded as I loaded the text file called mohamedgunfire.txt into Octave and plotted the data. I’ll describe what is going on in the comments that follow.

Line 1 is a title I added later to label the diary. Line 2 sets the path to include c:\shock\Shocko. It is saying make the path what you have now and add c:\shock\Shocko. Notice the needed apostrophes. Now I can use any data or programs in Shocko as well as what Octave has available. On line 3 I loaded mohamedgunfire.txt. Notice the 15 characters of boilerplate Octave puts in front of the second 4 in line 3; that’s almost always there. On line 5, I executed the ‘whos’ command and its results show in line 12. It says it has mohamedgunfire which has 16,384 rows and two columns of data values, or numbers. On line 16, I named the time ttt (which is a column of numbers we call a vector) and set it equal to every row (the colon) and the first column of mohamedgunfire. (By the way, the semi colon at the end of the line tells Octave not to print. In this case that would be 16,384 lines of time values, a big mess.) On line 17, I calculate the sampling rate by thinking as follows: there are 16,383 spaces between the first sample and the last sample. I take the number of spaces and divide it by the time between the first sample and the last sample. This gives the answer, 8,192 on line 18. It printed the answer because I didn’t put a semi colon at the end of line 17. On line 20 I named the acceleration YYDD; it’s a vector of every row of mohamedgunfire and the second column. In this case the colon means every row. On line 21, I plotted YYDD with a line width of 1, and in color ‘k’ which is black, with a grid, and it shows up on the screen in a box labeled Fig. 54.1. Then on lines 22, 23, and 24 I added axis labels and a title. Notice the apostrophes, and what I have to enclose in apostrophes. On line 25, I annotate the plot at coordinates 10,000, and –30, with the date. Then on line 26, I print the figure as a png file, labeling it ‘121007figone.png’. Octave places it in c:\Octave\3.2.4\_gcc-4.4\bin, and calls it 121007figone.png. I then go into Word under insert/ picture/ From File/ and find that folder and insert that picture into here as Fig. 54.6, below.

In line 28, I use the ‘axis’ command to expand the x axis to show the coarseness of sampled data as shown in Fig. 54.7. The axis command expects the lower and higher x coordinates followed by the lowest and highest y coordinates. In line 29, I annotate the plot with a sentence, and in line 30, I print it and name it 121009figone.png. It is amazing to see the coarseness of the digitizing sampled data that has been anti-aliased to 2.56 times the highest frequency present. In that form it’s not too good for shock spectrum analysis and I have a way to fix that, but that’s another lesson and another paper [8]. In line 32 I quit the session, and there you have a first lesson in shock data analysis with Octave.

**Table 54.1** The first 15 lines of a shock data file called “mohamedgunfire.txt”

%Time (s)	Accel (g)
0	0.4589
0.000122	0.4644
0.000244	0.4453
0.000366	0.4603
0.000488	0.455
0.00061	0.4477
0.000732	0.4508
0.000854	0.4539
0.000977	0.4627
0.001099	0.4437
0.001221	0.4503
0.001343	0.4484
0.001465	0.465
0.001587	0.4391



**Table 54.2** A diary portion that shows loading text file “mohamedgunfire.txt” into Octave and plotted it

---

```

1 DIARY 121007o
2 octave-3.2.4.exe:3> path(path, '\shock\Shocko')
3 octave-3.2.4.exe:4> load mohamedgunfire.txt
4 warning: load: file found in load path
5 octave-3.2.4.exe:5> whos
6 Variables in the current scope:
7
8 Attr Name Size Bytes Class
9 =====
10 ans 1x11 92 cell
11 mohamedgunfire 16384x2 262144 double
12
13 Total is 32779 elements using 262236 bytes
14 octave-3.2.4.exe:6> % 16,384 rows, and 2 columns; assume col 1 is time
15 octave-3.2.4.exe:6> %Calculate fs
16 octave-3.2.4.exe:6> ttt=mohamedgunfire(:,1);
17 octave-3.2.4.exe:8> fs=16383/(ttt(16384)-ttt(1))
18 fs = 8192.0
19 octave-3.2.4.exe:9> %That sounds correct.
20 octave-3.2.4.exe:9> YYDD=mohamedgunfire(:,2);
21 octave-3.2.4.exe:10> plot(YYDD,'linewidth',1,'k'),grid
22 octave-3.2.4.exe:11> ylabel('Acceleration, g','fontsize',16)
23 octave-3.2.4.exe:12> xlabel('Index','fontsize',16)
24 octave-3.2.4.exe:13> title('Mohameds gunfire','FontSize',16)
25 octave-3.2.4.exe:14> text(10000,30,'121009')
26 octave-3.2.4.exe:15> print('121007figone.png')
27 warning: implicit conversion from matrix to string
28 octave-3.2.4.exe:16> axis([3289 3353 -40 40])
29 octave-3.2.4.exe:17> text(3300,-30,'x axis expanded to show detail','fontsize',16)
30 octave-3.2.4.exe:18> print('121025figone.png')
31 warning: implicit conversion from matrix to string
32 octave-3.2.4.exe:19> quit

```

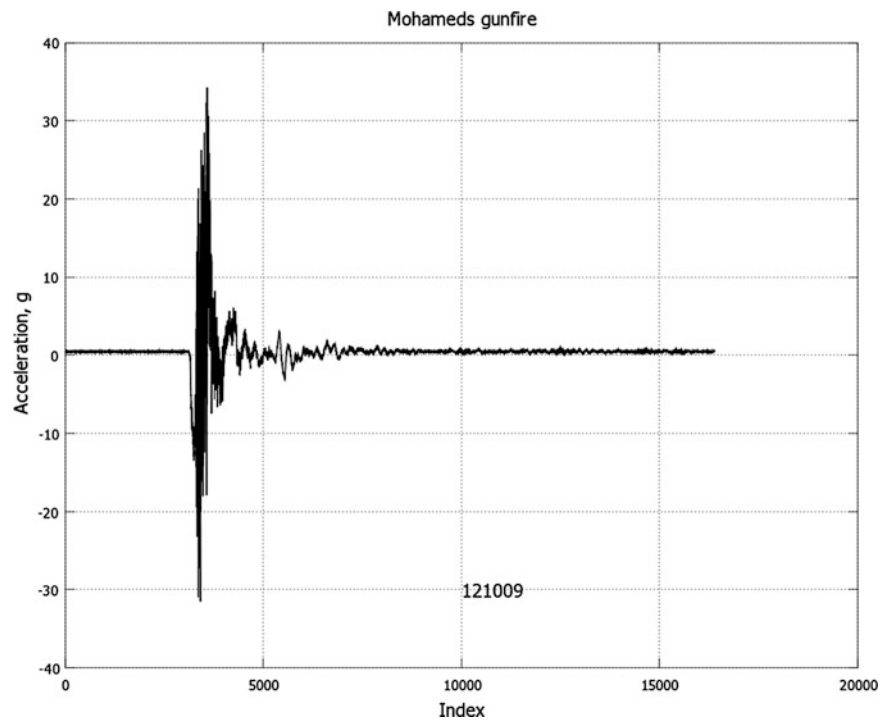
---

## 54.10 Lesson 2: Load, Edit, Integrate and Plot Shock Data and then Calculate and Plot the Pseudo Velocity Shock Spectrum

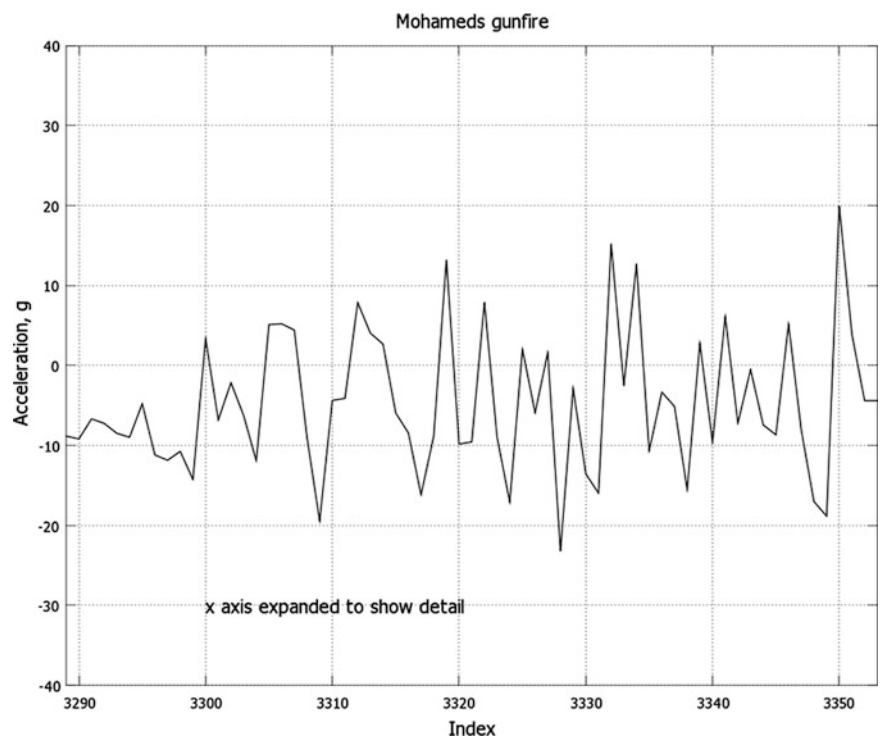
For this lesson we will work with Anderson’s pyroshock data which I have placed in Shocko in mat format. In Table 54.3, I’ll print another diary portion so we can go through the preparation of the data for the calculation of the pseudo velocity shock spectrum (PVSS). You can open Octave, and PFE, and put Shocko in your path and work along with me. In line 3, we set the path, and we have already turned on the diary with a command like diary 121025. In line 4, we load Anderson and we don’t need any extension because it is a “\*.mat” file. In line 6 we command “whos” and lines 7 and 9 show we have an “fs” and a vector ‘y’ which is 32,768 rows and one column. I type fs in line 10 and it tells me the value is 250,000 samples per second. In line 11, I plot ‘y’. I have a little three line script in Shocko called Scriptb121009.m that prints the labels and the title. I’ll print it below as Table 54.4. In line 13, I type ‘grid’ to add a grid. In line 14 at coordinates: 10,000, and –2,000, I insert the date 121009. In line 15 I print the figure as a ‘\*.png’ file named ‘121009figthree.png’ and Octave puts it over in ‘c:\Octave\3.2.4\_gcc-4.4\bin’, where I have Word insert it in this document. as Fig. 54.8.



**Fig. 54.6** This is the plot of the data file mohamedgunfire.txt, as received. It is plotted versus the index of the data value



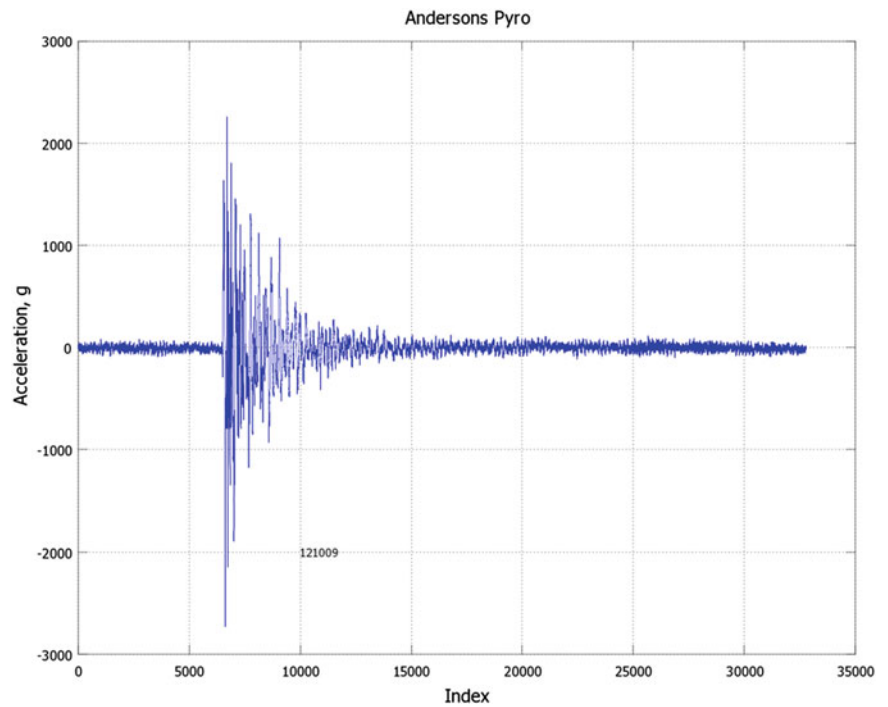
**Fig. 54.7** This is a plot of file mohamedgunfire.txt, with the time or index expanded as shown



### 54.11 Timhis3o.m and the PVSS

We'll now use my program timhis3o.m and I have printed it as Table 54.5, below so I can explain how you use it. Program timhis3o.m requires a sample rate, fs and an acceleration file in g named YYDD to be in the workspace. In Table 54.3, line 17, I make YYDD=y, and fs is already there. Then I go into timhis3o.m in the editor and put in an appropriate title in line 13. (I open timhis3o.m in PFE to do this.) I run it once to find a good spot for the date and insert it in line 14; notice the first two

**Fig. 54.8** This is a plot of Anderson's pyroshock data, acceleration versus index



values in the parentheses following text are the coordinates of the start of the text. The figure appears on the screen; I find it satisfactory and print it in line 19. I inserted that picture into this Word document as Fig. 54.10. In line 22, I type 'figure', to open a blank Fig. 54.2 keeping the figure we have just plotted available as Fig. 54.1. The leader portion downward sloping velocity in Fig. 54.9, shows we have a negative mean value in the leader. Now we'll calculate the mean value of the leader, and subtract that from the file, YYDD.

### 54.12 Determine Mean of the Leader and Subtract It

In line 24, I plot YYDD with a thicker line ('linewidth',1) and black (the k). The comma and 'grid' puts a grids on the plot. I use a little three line script, "ascript121028a.m" for labels and title shown in Table 54.6, and stored in Shocko. Now I use the axis command in line 25, several times (not shown in the diary) to locate a good ending point for the leader and finally select 6,475. In line 28 I print it and insert it into here as Fig. 54.10. In line 29 I use the mean function to calculate the leadermean to be  $-5.5265$ . And in line 32 I subtract it from every value of YYDD. In line 33 I open another figure, and in line 34 I run timhis3o.m on this new YYDD, after inserting the title shown in Fig. 54.11 in line 13 of timhis3o.m. Notice now we have no slope in the velocity leader, but we end up with a ridiculous final velocity of about 200 ips.

### 54.13 Remove the Leader, Truncate the Data, and Remove the Mean from the Final Data to Be Analyzed

Next I want to remove the leader and truncate the data. Certainly I would like to know from test notes if it is possible that a displacement of 12 in. actually occurred, and if it is also reasonable that a velocity of 240 ips occurred 10 ms after the event. Without additional information, I'll assume that the high velocity at 0.12 s in Fig. 54.12, is unimportant or random wondering and truncate the data at 0.034 s. I do that in the diary of Table 54.3 and will discuss that now. By examining

**Table 54.3** A diary showing editing, integration, plotting, and pseudo velocity shock spectrum analysis

---

```

1 DIARY 121025oCombo (in IMAC13)
2 Diary makeup to use to explain Anderdson analysis
3 octave-3.2.4.exe:3> path(path,'\shock\Shocko')
4 octave-3.2.4.exe:4> load Anderson
5 warning: load: file found in load path
6 octave-3.2.4.exe:5> whos
7 Variables in the current scope:
8 fs 1x1 8 double
9 y 32768x1 262144 double
10 octave-3.2.4.exe:6> fs = 250000
11 octave-3.2.4.exe:7> plot(y)
12 octave-3.2.4.exe:8> Scriptb121009 % (little 3 line program for labels and title)
13 octave-3.2.4.exe:9> grid
14 octave-3.2.4.exe:10> text(10000,-2000,'121009')
15 octave-3.2.4.exe:11> print('121009figthree.png')
16 octave-3.2.4.exe:12> %since it knows fs, I name y YYDD and run timhis3o
17 octave-3.2.4.exe:12> YYDD=y;
18 octave-3.2.4.exe:13> timhis3o;%I had put title in timhis3o.m
19 octave-3.2.4.exe:14> print('121009figfour.png')
22 octave-3.2.4.exe:10> figure
23 octave-3.2.4.exe:11> %Remove leader mean; plot to find leader end
24 octave-3.2.4.exe:11> plot(YYDD,'linewidth',1,'k'),grid
25 octave-3.2.4.exe:14> ascript121028a
26 octave-3.2.4.exe:15> axis([6460 6510 -3000 3000])
27 octave-3.2.4.exe:16> %have leader end at 6475
28 octave-3.2.4.exe:17> print('121028figone.png')
29 octave-3.2.4.exe:18> leadermean=mean(YYDD(1:6475))
30 leadermean = -5.5265
31 octave-3.2.4.exe:19> %Subtract this from YYDD
32 octave-3.2.4.exe:19> YYDD=YYDD-leadermean;
33 octave-3.2.4.exe:20> figure
34 octave-3.2.4.exe:21> timhis3o
35 octave-3.2.4.exe:22> print('121010figthree.png')
36 octave-3.2.4.exe:7> %Decide to end data at 15000, and remove leader
37 octave-3.2.4.exe:7> YYDDnew=YYDD(6475:15000);
38 octave-3.2.4.exe:8> clear YYDD YYD YY tt
39 octave-3.2.4.exe:9> YYDD=YYDDnew;
40 octave-3.2.4.exe:10> %mod timhis3o for title
41 octave-3.2.4.exe:10> timhis3o
42 octave-3.2.4.exe:11> size(YYDD) = 8526
43 octave-3.2.4.exe:12> YYD(8526) = 51.799
44 octave-3.2.4.exe:13> %Final vel = 51.8 ips; maybe not too bad
45 octave-3.2.4.exe:13> print('121010figfour.png')
46 octave-3.2.4.exe:14> %Remove mean
47 octave-3.2.4.exe:14> YYDD=YYDD-mean(YYDD);
48 octave-3.2.4.exe:15> figure
49 octave-3.2.4.exe:16> timhis3o
50 octave-3.2.4.exe:17> print('121010figfive.png')
51 warning: implicit conversion from matrix to string
52 octave-3.2.4.exe:18> fs
53 fs = 250000
54 octave-3.2.4.exe:19> figure
55 octave-3.2.4.exe:21> pvsszo121010
56 octave-3.2.4.exe:22> hold on
59 octave-3.2.4.exe:25> fourcp1100o
60 octave-3.2.4.exe:26> hold on
62 octave-3.2.4.exe:28> title('Anderson 5% damped PVSS, 121010')
63 octave-3.2.4.exe:29> print('121010figsix.png')

```

---

**Table 54.4** Script121009.m

---

```

1 %Scriptb121009
2 ylabel('Acceleration, g','fontsize',16)
3 xlabel('Index','fontsize',16)
4 title('Andersons Pyro','FontSize',16)

```

---

**Table 54.5** timhis3o.m A program to integrate and plot shock data

---

```

1 %timhis3o.m 111208 Timhist3 for Octave
2 %To accomplish the subplot(111) command I use in Matlab, I open a figure after the plot
3 %Shock acceleration time history and its two integrals plotted as three subplots.
4 %Program expects file YYDD of accelerations in g and sample rate fs in workspace.
5 %It forms a time vector, tt.
6 %After running and plotting, YYD in ips, and YY in inches, remain in the workspace.
7 %You must change title
8 G=386.087 ;
9 tt=(1:length(YYDD))/fs;
10 subplot(3,1,1)
11 plot(tt,YYDD,'linewidth',1,'k'),grid
12 ylabel('Acceleration, g','color','k','FontSize',16)
13 title('Time History of Andersons Pyro, 121010','color','k','FontSize',16);%*****
14 text(.1,1500,'121010');%insert date in figure***** find location by trial
15 yydd=G*YYDD;
16 h=1/fs;
17 YYD=h*cumtrapz(yydd)
18 subplot(3,1,2)
19 plot(tt,YYD,'linewidth',1,'k'),grid
20 subplot(3,1,2)
21 ylabel('Velocity, ips','color','k','FontSize',16)
22 subplot(3,1,3)
23 YY=h*cumtrapz(YYD);
24 plot(tt,YY,'linewidth',1,'k'),grid
25 subplot(3,1,3)
26 ylabel('Displacement, in','color','k','FontSize',16)
27 subplot(3,1,3)
28 xlabel('Time, seconds','color','k','FontSize',16)
29 %figure

```

---

**Table 54.6** aScript121028a.m

---

```

1 %ascript121028a.m
2 ylabel('Acceleration, g','fontsize',16);
3 xlabel('Index','fontsize',16);
4 title('Estimate Anderson leader ends at 6475','fontsize',16)

```

---

Fig. 54.9, I arbitrarily decide to truncate the data at an index of 15,000. So in line 37 I take the values of the data from the end of the leader at 6,475 to index 15,000 and call this segment YDDnew. Now notice this: timhis3o.m retains four vectors in the workspace; these are YYDD (the acceleration in g), YYD (the velocity in ips), YY (the displacement in inches), and tt (the time in seconds). Because the new segment of data we will work on is shorter, these longer vectors will not get completely over written, so I clear them in line 38. In line 39 I set YYDD equal to the new no leader truncated portion of our data, YYDDnew. I change the title in timhis3o.m, and run timhis3o.m again in line 41. In line 42 I check the size of the truncated data and find it is 8,526 values long. I want to know the final velocity so in line 43 I get the value of the velocity, YYD, at index 8,526 and find it is 51.8 ips. I print the figure in line 45, and insert it in here as Fig. 54.12.

Finally I don't like to analyze data that has a final velocity [8]. I feel that if the final velocity is not zero, the shock is not over. So, if it is at all reasonable, I find a way to zero the final velocity, and a very simple, not too offensive way is to remove the mean of the final acceleration data. The algorithms assume the velocity starts at zero, so if the mean value of the acceleration is zero, the velocity has to end up at zero. So in line 47, I remove the mean. In line 48 I open a new figure, and put a suitable title in timhis3o.m and run timhis3o.m again in line 49. I print it in line 50 and insert it in here as Fig. 54.13. That's it. We're finally ready for the PVSS.

I will get rid of it by removing the mean

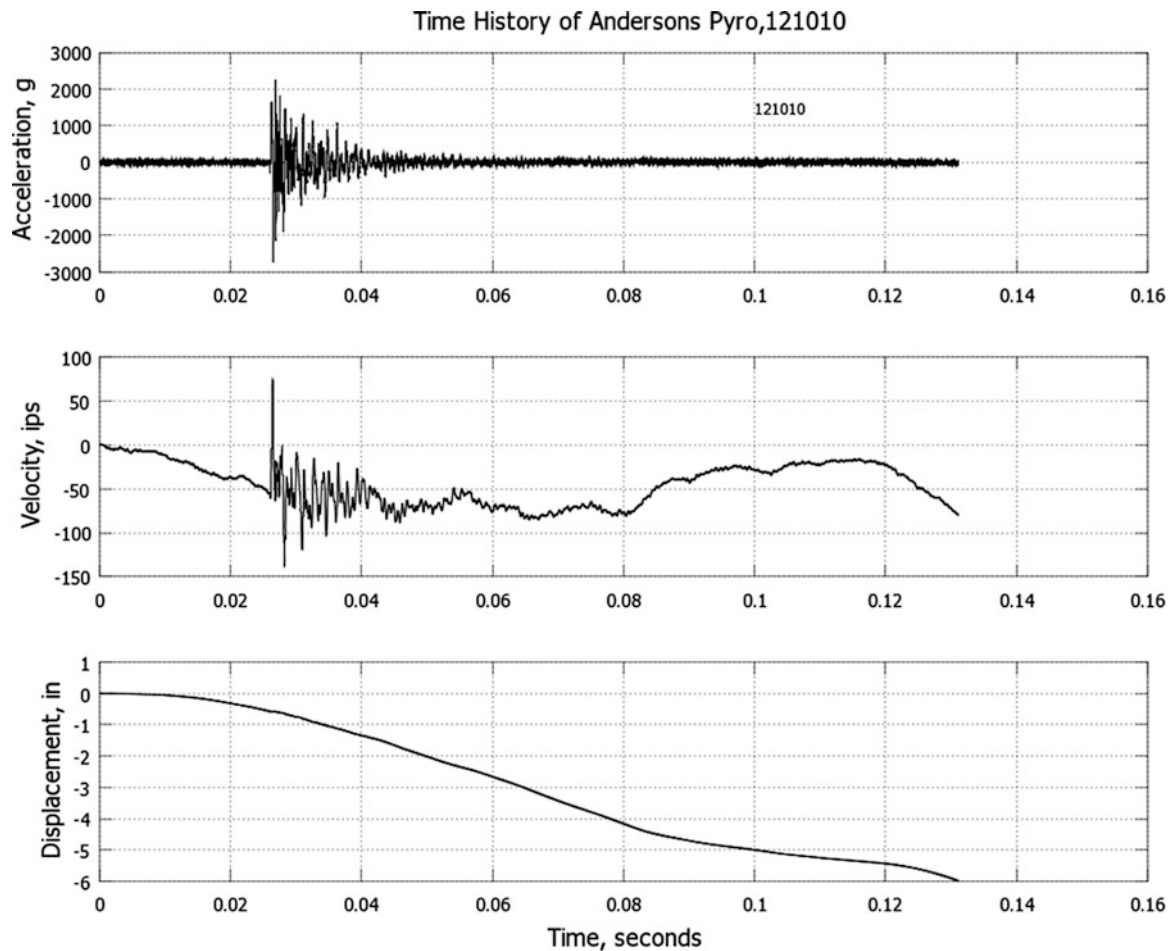


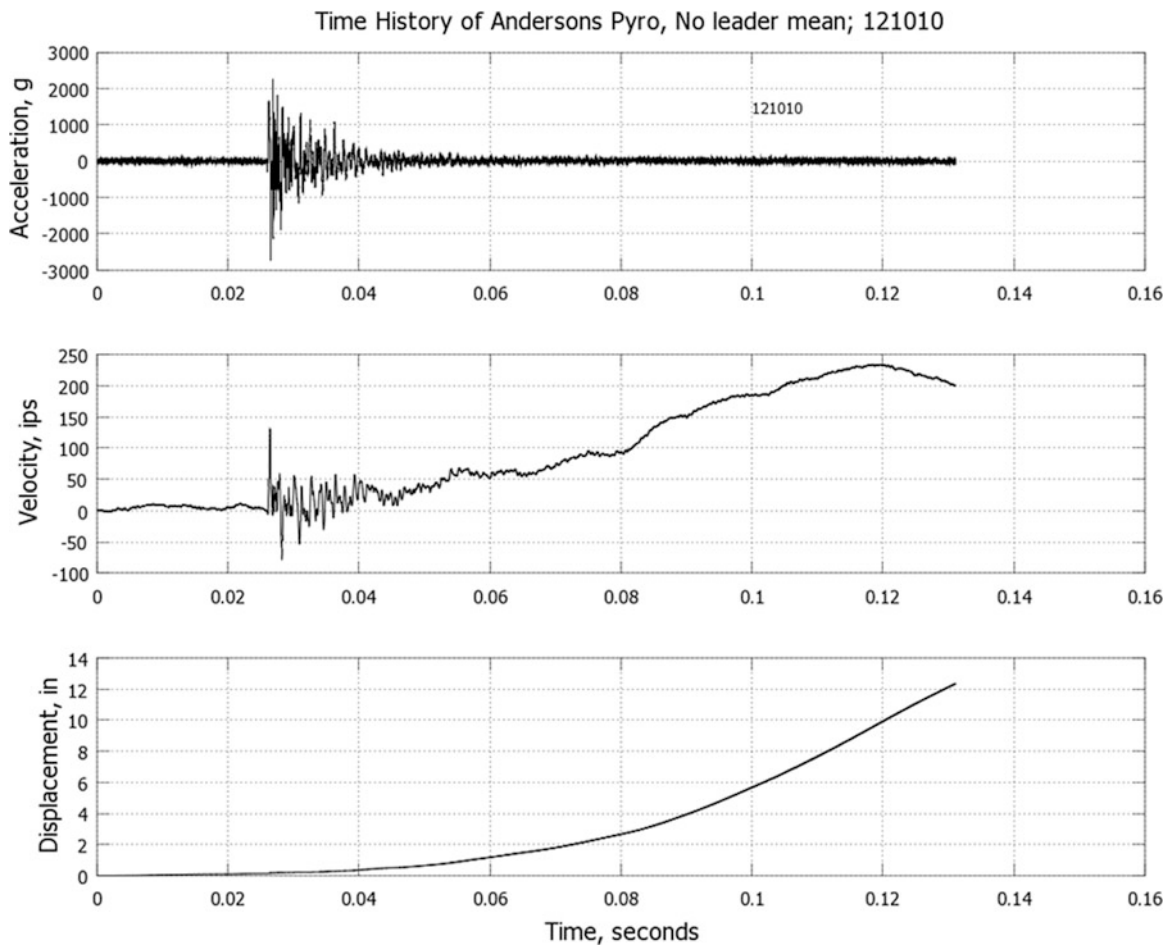
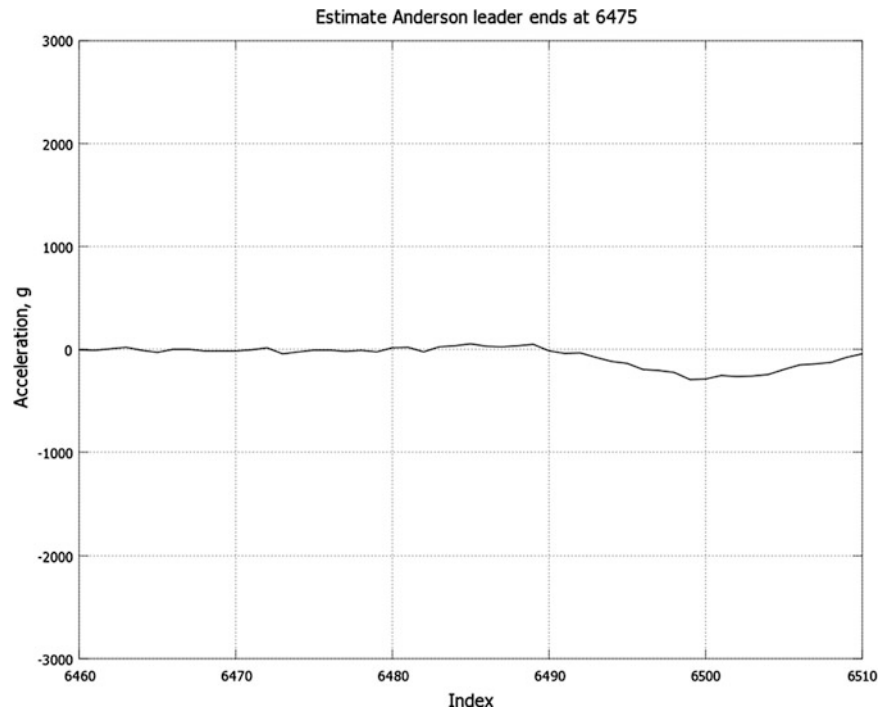
Fig. 54.9 Anderson's pyro shock and its two integrals, as received

#### 54.14 Calculate and Plot the PVSS

Calculating the PVSS is anticlimactic along side the editing and plotting needed to get ready, but let's finish. I forgot the sample rate so in line 52, I type 'fs' and in line 53, and Octave answers 250,000 samples per second. I open another figure in line 54. I open a copy of pvsszo.m in PFE and save it in Shocko as pvsszo121010.m. I go into the program in PFE and set the sample rate to 250,000, the high frequency limit, fhigh, to 25,000, and the low frequency limit, flow, to 1 Hz. There is an underflow problem if you try to calculate to a frequency less than  $720,000/fs$ , which is stated in the program. I check to see that the damping ratio is 5 % and save the pvss121010.m. In line 55 I run pvss121010, and in a minute or so, the log log plot appears in the figure box. I type "hold on" in line 56, and in line 59, I type fourcp11000 to draw the 4CP on the plot. Be patient; it takes this version of Octave a minute or so to draw the 4CP. The "hold on" command prevents erasing figure contents when you add to an existing figure. In line 62, I give it a title, and in line 63, I print it as "121010figsix.png", and then go back to Word and insert that picture here as Fig. 54.14.

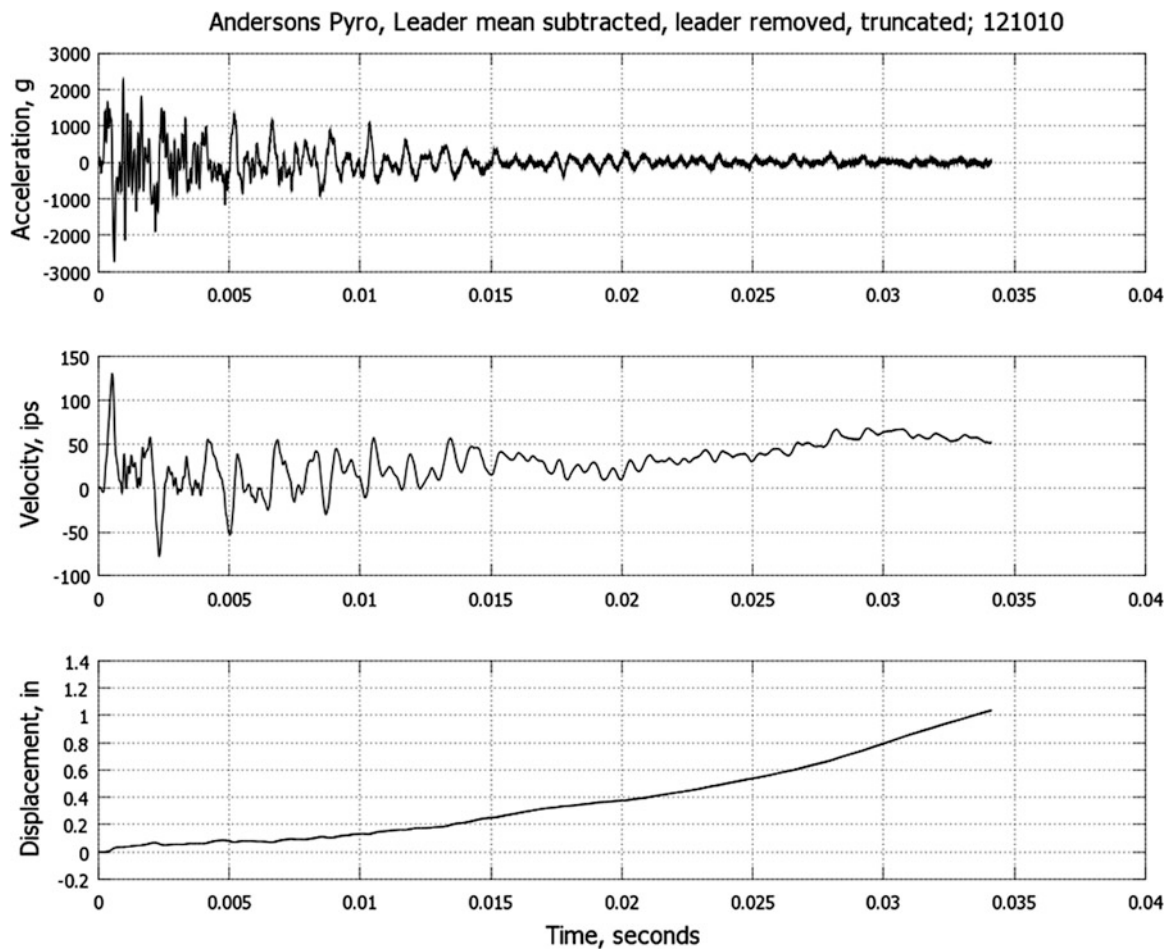
What we see in the PVSS of Fig. 54.14 is that the shock is severe (over 200 ips) in the 800–1,500 Hz frequency range. Gaberson [6] and that it is moderately severe (over 100 ips) in the 600–2,500 Hz range. The peak acceleration is just under 3,000 g. (This is the high frequency asymptote looking at the acceleration scale.) The peak shock displacement is about 0.15 in. (This is the low frequency asymptote viewed on the displacement scale) [4, 5]. I also think Octave does an acceptable job of drawing the four coordinate paper (4CP). This should be enough to convince you that you can do shock data analysis with Octave.

**Fig. 54.10** This figure shows an expanded x-axis used in trial and error with the axis command to estimate the leader ending index of 6,475



**Fig. 54.11** This is Anderson's pyro time history after subtracting the mean of the leader from every value of the data





**Fig. 54.12** Notice final velocity is 53.8 ips, and this is what I want to remove

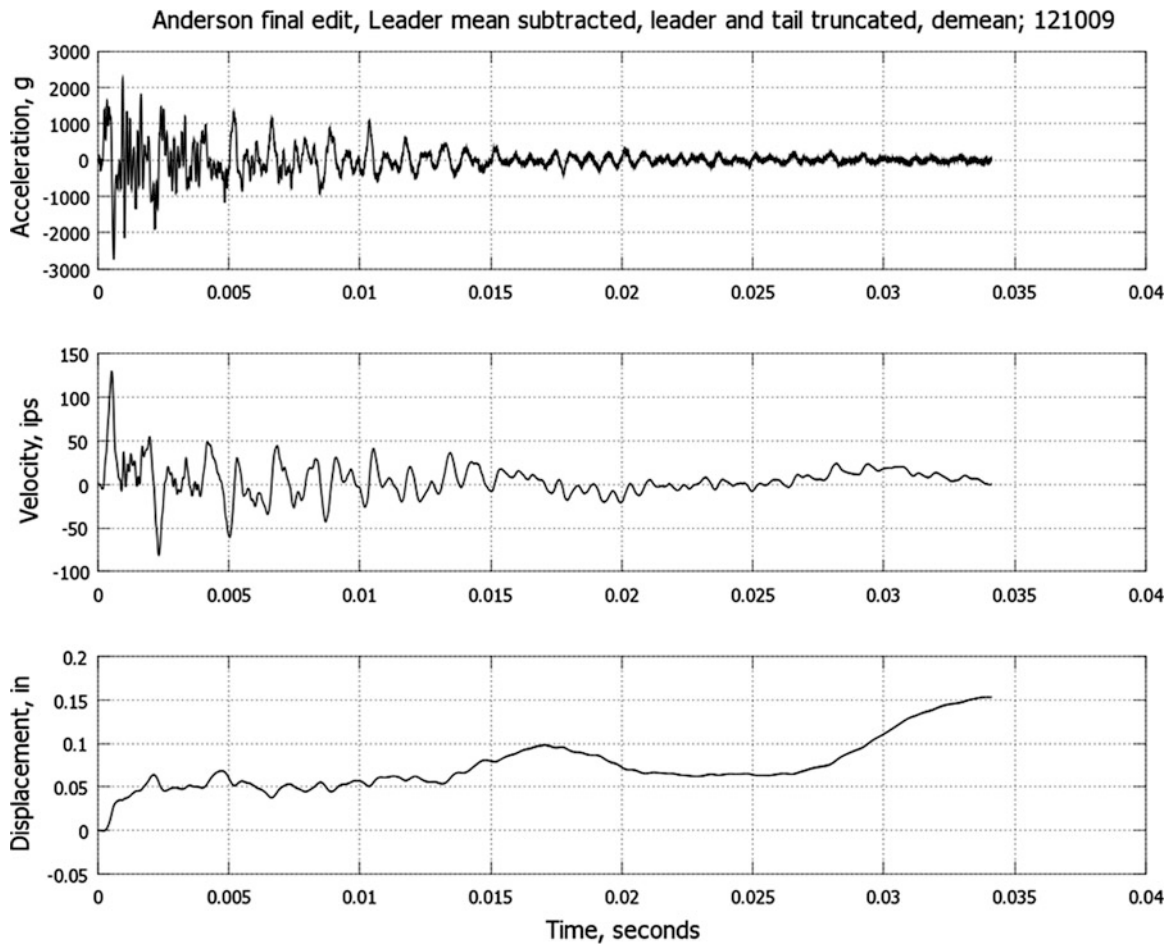
## 54.15 Conclusions

That's it. I've presented a first lesson in doing shock data signal processing on a general purpose signal analysis program with Matlab and Octave. It's disappointing how little I can get done in one paper. I hope it's a tempting start and I can entice some of you to try it. Cost is no longer an excuse. I didn't try to write a manual; this is different. I don't know if this type of instruction is useful, but I wanted to try it and see. I've told you how to do it. J.P. Den Hartog, my professor, once told me: to learn something, find a smart person who knows how to do it. Watch what he does. Then "ape" him. I'm smart in this area; one of the good ones. This is what I do.

I explained how I downloaded Octave and I showed you step by step how to do many editing operations. I carefully calculated the PVSS and overlaid four coordinate paper over the plot. I went over inserting the results in to Word.

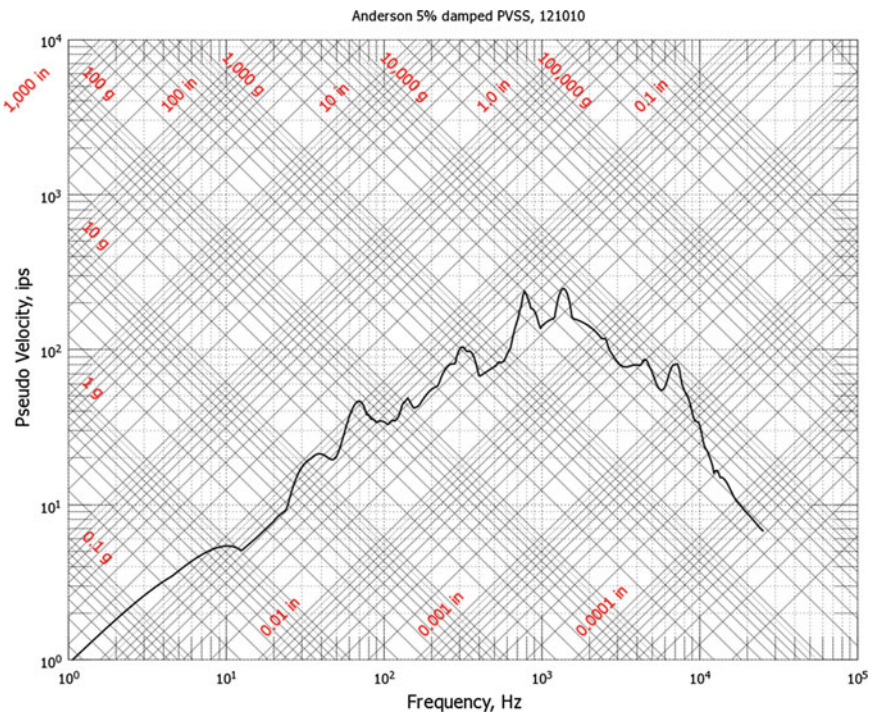
I have tried to talk you into taking some time and downloading Octave and trying out some simple good shock data. I showed you how to input the data, plot it up and see what you have. I've gone into detail on how we edit and set up the time history for zero final velocity and pseudo velocity analysis. Email me for the folder Shocko and give it a try.

Maybe all I accomplished was to take apart and explain plotting, integration, and calculating a useful PVSS. If so, do that. The paper tries to give a start. It goes into the simplest yet most important of our operations, integrating and the PVSS, which is easy for the computer to do. When you get comfortable, go over my past papers and try those methods. If you have questions, contact me.



**Fig. 54.13** This is the final edited file to be analyzed by the PVSS program. Its final velocity is zero, and it has a maximum displacement of about 0.15 in.

**Fig. 54.14** The PVSS (Pseudo Velocity Shock Spectrum) of Anderson's pyro shock



## References

1. Eaton JW, others (2009) GNU Octave, version 3.2.4. <http://www.octave.org>
2. Matlab for Windows, Version 6 (2000) High performance numeric computation and visualization software, The MathWorks, 3 Apple Hill Drive, Natick, 01760
3. <http://octaveSourceforge.net>
4. Gaberson HA (2007) Pseudo velocity shock spectrum rules for analysis of mechanical shock. In: Proceedings of IMAC XXV, Orlando. Society of Experimental Mechanics, Bethel, p 367. [www.sem.org](http://www.sem.org)
5. Gaberson HA (2007) Pseudo velocity shock spectrum rules and concepts. In: Proceeding of the annual meeting of the mechanical failure prevention technology society, Virginia Beach, VA USA. [www.mfpt.org](http://www.mfpt.org), 19 April 2007
6. Gaberson HA (2010) Shock severity estimation. In: Shock and vibration symposium proceedings, available from HI-TEST Laboratories, Arvonnia
7. Shannon CE (1949) Communication in the presence of noise. *Inst Radio Eng* 37:10–21
8. Gaberson HA (2007) Proceeding of IMAC09 “Pseudo velocity shock spectrum analysis data editing”, Society of Experimental Mechanics, Bethel, p 367. [www.sem.org](http://www.sem.org)

# Chapter 55

## Analysis and Dynamic Characterization of a Resonant Plate for Shock Testing

Richard Hsieh, R. Max Moore, Sydney Sroka, James Lake, Christopher Stull, and Peter Avitabile

**Abstract** Satellite hardware subjected to pyroshock events during launch must pass one or more qualification tests to ensure proper function during operation in space. This research involves the dynamic characterization of a resonant plate that is used to perform qualification tests. The goal is to develop an analytical model that accurately predicts the shock response spectra (SRS) for a variety of configurations of the resonant plate. Experimental shock data is collected to analyze the system's variability. Experimental modal tests are performed to determine the system's mode shapes, natural frequencies, and damping. A finite element model is constructed to predict higher frequency mode shapes for use in the analytical model. The modal superposition technique is then employed to solve for acceleration time responses at specific locations on the plate which allow for the calculation of SRS at each point. The paper concludes by discussing multiple case studies that analyze the effects of key parameters on the analytical model's predicted SRS.

**Keywords** Shock testing • Modal analysis • Shock response spectrum • Modal superposition

### Nomenclature

SDOF Single-degree-of-freedom oscillator describes a system with one natural frequency and one mode shape  
MDOF Multiple-degree-of-freedom (MDOF) system describes a system with more than one natural frequency and mode shape  
FRF Frequency response function is used to describe the amplitude of response of a structure as a function of the excitation frequency

---

R. Hsieh (✉)

Department of Engineering, Harvey Mudd College, Claremont, USA  
e-mail: [rhsieh@g.hmc.edu](mailto:rhsieh@g.hmc.edu)

R.M. Moore

Department of Mechanical Engineering, University of California, Riverside, USA  
e-mail: [rmoor006@ucr.edu](mailto:rmoor006@ucr.edu)

S. Sroka

Department of Structural Engineering, University of California, San Diego, USA  
e-mail: [sgsroka@gmail.com](mailto:sgsroka@gmail.com)

J. Lake

Intelligence and Space Research Division (ISR-5), Los Alamos National Laboratory, Los Alamos, USA  
e-mail: [lake@lanl.gov](mailto:lake@lanl.gov)

C. Stull

Applied Engineering and Technology Division (AET-6), Los Alamos National Laboratory, Los Alamos, USA  
e-mail: [stull@lanl.gov](mailto:stull@lanl.gov)

P. Avitabile

Structural Dynamics and Acoustic Systems Laboratory, University of Massachusetts, Lowell, USA  
e-mail: [Peter.Avitabile@uml.edu](mailto:Peter.Avitabile@uml.edu)

- SRS** Shock response spectrum (or spectra) is used to describe the amplitude of response of a structure by exciting an array of SDOF oscillators with a prescribed damping with the acceleration time response collected from the structure. Unlike the FRF, the SRS omits phase information and is most applicable for very high amplitude, very high frequency content, transient excitations
- MAC** Modal assurance criteria refers to a metric that describes the congruency of two mode shapes. Two mode shapes which are exact scalar multiples of each other have a MAC value of 1, and two mode shapes that are exactly orthogonal have a MAC value of 0

## 55.1 Introduction

### 55.1.1 Background

The Intelligence and Space Research Division (ISR) at Los Alamos National Laboratory (LANL) is responsible for the design and fabrication of sensors destined for use in space. The sensors are attached to satellites where they collect valuable information pertaining to national security. During service, the devices encounter random vibration, thermal, and shock conditions that could potentially lead to malfunction. A common type of shock to which the sensors are subjected is called pyroshock, which results from exploding structural elements (e.g. bolts) during launch. To reduce the probability of failure, NASA has created standards that must be met in order to qualify a component for launch. The shock response spectrum (SRS) is the standard criterion used to measure pyroshock conditions, and is thus an important metric for the testing and qualification of many sensors deployed by ISR.

Formerly, each qualification test was conducted with a custom experimental fixture, designed to produce the SRS relevant to a specific test specimen's service conditions. Designing a fixture for a particular test specimen undergoing a specific mechanical excitation is both cost and time intensive, thus motivating the development of adjustable fixtures. Sandia National Laboratories experimented with several such tunable structures. An electro-dynamic shaker produces an accurate load, but the frequency and amplitude bandwidths usually cannot accommodate the high frequency, high amplitude excitation characteristic of a pyroshock [1]. Using either the actual or a mock structure with live ordnances provided confident measurements and response data, but the procedure became overwhelmingly cost intensive [2].

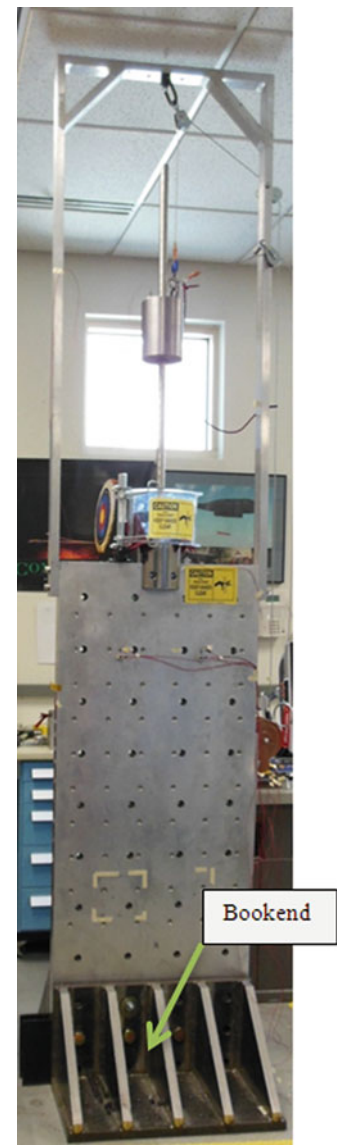
A mechanical impact was explored as an alternative to live ordnances, and could effectively deliver the desired SRS for many components located at a sufficient distance from the pyrotechnic [2]. A mechanical excitation with a metal-to-metal impact was determined to be an extremely cost effective technique, though the systems generally require significant manipulation which was guided mostly by trial-and-error. Researchers also explored resonant fixtures of two different geometries: a resonant bar and a resonant beam. The resonant beam was abandoned after calculations revealed that the beam fixture was unable to accommodate test specimens outside a narrow geometrical range. The resultant test structure at Sandia National Laboratories was a resonant bar system, designed to absorb the transient load and deliver the excitation to the test specimen. Additional masses and damping agents were also utilized to manipulate the pulse width to produce the desired excitation [2].

Based on the design at Sandia National Laboratories, engineers in ISR-5 have developed a resonant plate to simulate the conditions of a pyroshock. The fixture shown in Fig. 55.1 consists of a vertical, aluminum plate with multiple attachment points for component mounting, and is designed to accommodate a variety of masses and geometries. A cylindrical, stainless steel mass (or "slug") is released from a variable height and dropped vertically onto the top of the plate to simulate the magnitude and frequency content from a pyroshock. A test specimen is affixed to a mounting block that is attached to the aluminum plate. The desired SRS can be produced at the attachment points by adjusting the mounting block location, the drop height of the slug, and the amount of damping material (e.g. felt pads) at the point of impact.

### 55.1.2 Motivation

The resonate plate's dynamics can change significantly, based on the geometry, mass, and position of the mounting block location. This variability in the dynamics makes testing largely trial-and-error for targeting the required SRS. A better understanding of these dynamics and how the mounting configuration affects the SRS would allow for more efficient testing.

**Fig. 55.1** Shock test fixture in ISR-5 at LANL clamped at the base with a bookend structure



## 55.2 Methodology

The main goal of the project was to obtain SRS predictions for various test plate configurations. A thorough dynamic analysis of the plate would allow for SRS predictions from an analytical model. To achieve an accurate analytical simulation, many factors were considered, such as modal characteristics, boundary conditions, experimental variability, and damping. To investigate these factors, the project was separated into four parts: experimental shock testing, modal analysis, finite element (FE) modeling, and the development of the analytical model. A flow diagram of the overall process is illustrated in Fig. 55.2. The first part of the project involved FE modeling and experimental modal analysis to determine the plate's mode shapes, natural frequencies, and damping. The data collected from the FE modeling and experimental modal analyses were used to calibrate the analytical shock model. Experimental SRS data were also collected and analyzed to refine the analytical model. The subsequent sections will discuss in further detail the theoretical background, experimental shock testing, finite element modeling, experimental modal analysis, and analytical model.



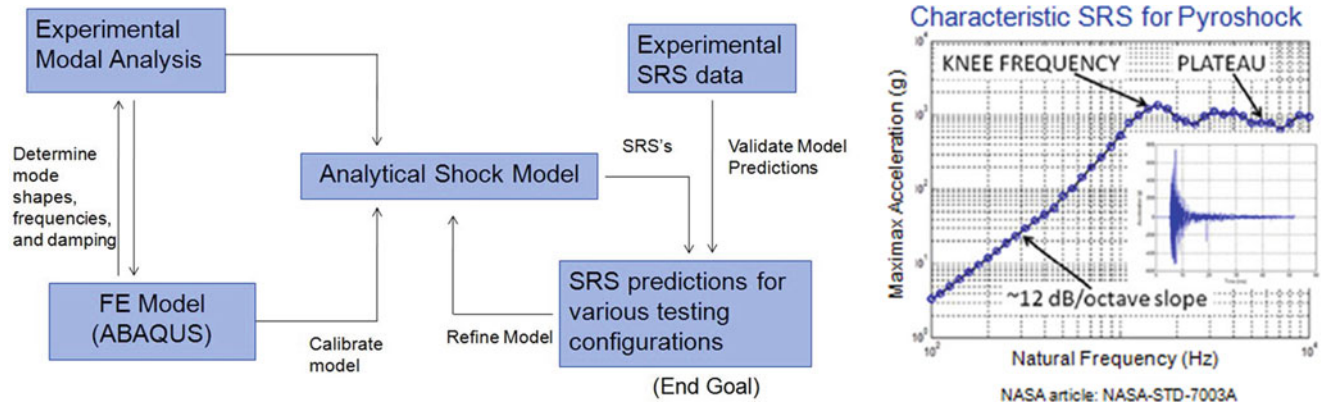


Fig. 55.2 Flow chart of project methodology

## 55.3 Theoretical Background

This section contains background information relevant to the shock response spectrum, analytical model, and numerical model. It briefly describes the theory motivating these concepts, which are explained in more detail in Ref. [5].

### 55.3.1 Shock Response Spectrum

Shock, defined as a large amplitude, high frequency, transient excitation, is best characterized with a shock response spectrum (SRS). The SRS can be calculated for displacement, velocity, or acceleration [3]. For the purposes of this research, the absolute magnitude of the acceleration is most relevant. The SRS is calculated by defining a discrete number of single-degree-of-freedom (SDOF) oscillators per octave, over a given frequency range. Each oscillator has a prescribed damping value that contributes significantly to the amplitude of the resultant curve. Each oscillator is subjected to either a force time history or, in the case of this paper, an acceleration time history. The curve represented by the maximum absolute acceleration (i.e. that which occurs during the first cycle) is plotted along an abscissa of natural frequencies corresponding to the SDOF oscillators.

A shock test fixture exhibits a characteristic “knee” at a dominant resonant frequency. A typical SRS is shown on the right side of Fig. 55.2. The particular SRS that a customer provides to the operator is typically accompanied by a  $\pm 6$  dB error bound.

### 55.3.2 Modal Superposition Technique

The response of the fixture can be easily obtained using the mode superposition approach. The basic theory behind this approach is summarized next. The equations of motion for a multi-degree-of-freedom (MDOF) system can be written as

$$[M]\{\ddot{x}\} + [C]\{\dot{x}\} + [K]\{x\} = \{F(t)\}, \quad (55.1)$$

where  $[M]$  is the global mass matrix,  $[C]$  is the global damping matrix,  $[K]$  is the global stiffness matrix,  $\{F(t)\}$  is the vector of forces applied, and  $\{x\}$  is the set of physical coordinates of the system. These equations are of size  $N \times N$ , where  $N$  corresponds to the number of degrees-of-freedom (DOF) of the system.

A generalized eigenvalue problem for the undamped system can be obtained using

$$([K] - \lambda_i[M])\{x\} = \{0\}, \quad (55.2)$$

where the eigenvalues  $\lambda_i$  correspond to the squares of the natural frequencies  $\omega_i$  of the system and the eigenvectors  $\{u_i\}$  correspond to the mode shapes of the system. The eigenvectors can be arranged in column-fashion to construct a modal

matrix  $[U]$  that is used to decouple the MDOF equations of motion. This involves applying a coordinate transformation that transforms the system from its physical coordinates  $\{x\}$  to modal space  $\{p\}$  using

$$\{x\} = [U]\{p\}. \quad (55.3)$$

The modal superposition technique exploits the orthogonality of mode shapes, which assumes that  $[U]$  is normalized to unit modal mass such that the modal mass matrix  $[\bar{M}]$  is the identity matrix and the modal stiffness matrix  $[\bar{K}]$  is a diagonal matrix of the squares of the natural frequencies, given as

$$[U]^T[M][U] = [\bar{M}] = [I] \quad (55.4)$$

and

$$[U]^T[K][U] = [\bar{K}] = \begin{bmatrix} \ddots & & & \\ & \omega_i^2 & & \\ & & \ddots & \\ & & & \ddots \end{bmatrix}. \quad (55.5)$$

Substituting (55.3) into (55.1) and pre-multiplying by  $[U]^T$  gives

$$\begin{bmatrix} \ddots & & & \\ & \bar{M} & & \\ & & \ddots & \\ & & & \ddots \end{bmatrix} \{\ddot{p}\} + \begin{bmatrix} \ddots & & & \\ & \bar{C} & & \\ & & \ddots & \\ & & & \ddots \end{bmatrix} \{\dot{p}\} + \begin{bmatrix} \ddots & & & \\ & \bar{K} & & \\ & & \ddots & \\ & & & \ddots \end{bmatrix} \{p\} = [U]^T \{F(t)\}. \quad (55.6)$$

Here it is assumed that  $[C]$  is proportional to  $[M]$  and  $[K]$  (i.e.  $[C] = \alpha[M] + \beta[K]$ , where  $\alpha$  and  $\beta$  are constants). Note that the coupled MDOF equations of motion are now decoupled into multiple SDOF oscillators as shown in (55.6). The right hand side of (55.6) is of great importance as it describes how the force applied in physical space is distributed to each mode of the system in modal space. Once the response is computed in modal space, the solutions can be transformed back to the physical coordinates of the system using (55.3).

It is important to note that generally not all of the eigenvalues and eigenvectors of the system are available. This implies that for a  $N$ -DOF system, there may only be  $M$  modes of vibration available, resulting in a modal matrix  $[U]$  of size  $N \times M$ . As a result, once the system is transformed to modal space, the equations of motion will be of size  $M \times M$  and are generally smaller in dimension than the physical matrices describing the system.

### 55.3.3 Newmark Direct Integration Technique

In this work, the Newmark Method [4] is used to perform the direct integration of the equations of motion for the modal space solution. From the known initial conditions for displacement and velocity, the initial acceleration vector is computed using the equations of motion and the applied force vector as

$$\{\ddot{x}_0\} = [M]^{-1} (\{F_0\} - [C]\{\dot{x}_0\} - [K]\{x_0\}), \quad (55.7)$$

where  $\{\ddot{x}_0\}$ ,  $\{\dot{x}_0\}$ , and  $\{x_0\}$  are the initial acceleration, velocity, and displacement vectors, respectively, and  $\{F_0\}$  is the initial force vector. Choosing an appropriate  $\Delta t$ ,  $\alpha$ , and  $\beta$ , the displacement vector is

$$\begin{aligned} c\{x_{i+1}\} &= \left[ \frac{1}{\alpha(\Delta t)^2}[M] + \frac{\beta}{\alpha(\Delta t)}[C] + [K] \right]^{-2} \\ &\times \left\{ \{F_{i+1}\} + [M] \left( \frac{1}{\alpha(\Delta t)^2} \{x_i\} + \frac{1}{\alpha(\Delta t)} \{\dot{x}_i\} + \left( \frac{1}{2\alpha} - 1 \right) \{\ddot{x}_i\} \right) + [C] \left( \frac{\beta}{\alpha(\Delta t)} \{x_i\} + \left( \frac{\beta}{\alpha} - 1 \right) \{\dot{x}_i\} + \left( \frac{\beta}{\alpha} - 2 \right) \frac{\Delta t}{2} \{\ddot{x}_i\} \right) \right\}. \end{aligned} \quad (55.8)$$

The values chosen for  $\alpha$  and  $\beta$  were  $\frac{1}{4}$  and  $\frac{1}{2}$ , respectively. This assumes constant acceleration and that the integration process is unconditionally stable for any time step. However, the time step should be chosen such that the highest frequency involved in the system response can be characterized properly to avoid numerical damping in the solution. The time step should be chosen to be at least ten times smaller than the period of the highest frequency component involved in the system response. (The time step used for the analytical cases studied in this work was  $9.7656\text{E-}6$  s.)

Following the displacement vector calculation, the acceleration and velocity vectors are computed for the next time step using

$$\{\ddot{x}_{i+1}\} = \frac{1}{\alpha(\Delta t)^2} (\{x_{i+1}\} - \{x_i\}) - \frac{1}{\alpha(\Delta t)} \{\dot{x}_i\} - \left(\frac{1}{2\alpha} - 1\right) \{\ddot{x}_i\} \quad (55.9)$$

and

$$\{\dot{x}_{i+1}\} = \{\dot{x}_i\} + (1 - \beta)\Delta t\{\ddot{x}_i\} + \beta\Delta t\{\ddot{x}_{i+1}\}. \quad (55.10)$$

This process is repeated at each time step for the duration of the time over which the solution is desired.

### 55.3.4 Structural Dynamic Modification

The modal superposition technique provides a basis for a computationally efficient method of extracting the modal characteristics of a system. However, as additional structural elements are attached, the characteristic modal data changes. Rather than reverting to the full set of physical equations to identify structural changes, a structural dynamic modification technique [5] can be employed to greatly reduce the set of equations describing the system (generally, FE models are quite large and multiple perturbations of these models can be computationally costly). This structural dynamic modification method projects the physical system into modal space through the modal matrix  $[U]$  of the unmodified system. A modal space solution then provides a system of equations that are significantly reduced in size from the physical system, which can be solved more efficiently.

Consider changes to the system mass or stiffness matrices,  $[\Delta\bar{M}_{12}]$  or  $[\Delta\bar{K}_{12}]$ . These modifications can be projected to modal space and a new set of modal equations result, which are given by

$$\left\{ \left[ \begin{array}{ccc} \ddots & & \\ & \bar{M}_1 & \\ & & \ddots \end{array} \right] + [\Delta\bar{M}_{12}] \right\} \{\ddot{p}_1\} + \left\{ \left[ \begin{array}{ccc} \ddots & & \\ & \bar{K}_1 & \\ & & \ddots \end{array} \right] + [\Delta\bar{K}_{12}] \right\} \{p_1\} = \{0\} \quad (55.11)$$

where

$$[\Delta\bar{M}_{12}] = [U_1]^T [\Delta M_{12}] [U_1]$$

and

$$[\Delta\bar{K}_{12}] = [U_1]^T [\Delta K_{12}] [U_1].$$

It should be noted that even though the unmodified modal matrices  $[\bar{M}_1]$  and  $[\bar{K}_1]$  are diagonal,  $[\Delta\bar{M}_{12}]$  and  $[\Delta\bar{K}_{12}]$  are not. Therefore, once the modifications are added, the modal space equations of motion are no longer decoupled. However, a new eigenvalue problem can be solved, which yields new eigenvalues and eigenvectors that can be used to construct another modal matrix  $[U_{12}]$ . This new matrix then provides a new coordinate transformation as given by

$$\{p_1\} = [U_{12}]\{p_2\}. \quad (55.12)$$

Using this transformation and applying the same modal superposition technique described earlier, the equations of motion can once again be decoupled as

$$\begin{bmatrix} \ddots & & \\ & \bar{M}_2 & \\ & & \ddots \end{bmatrix} \{\ddot{p}_2\} + \begin{bmatrix} \ddots & & \\ & \bar{K}_2 & \\ & & \ddots \end{bmatrix} \{p_2\} = \{0\}. \tag{55.13}$$

These decoupled equations can then be solved in modal space and the resulting solutions can be transformed back to the physical coordinates of the system using

$$\{x\} = [U_1][U_{12}]\{p_2\}. \tag{55.14}$$

### 55.4 Experimental Shock Testing

Preliminary experimental testing was performed on the SRS test fixture. Conducting experimental shock tests not only contributed to the assembly of a lookup table, but also provided greater insight into the underlying dynamics and variability that govern the system. The instrumentation included two uniaxial accelerometers and two triaxial accelerometers, all of which have sensitivities of approximately 1 mV/g. One uniaxial accelerometer was mounted to the top of the stainless steel slug and used to estimate the force applied. The other uniaxial accelerometer was mounted very close to the point of impact on the top of the plate. The two triaxial accelerometers were moved around nine test points on the plate. The data acquisition system was set for a sampling rate of 102,400 Hz, a total acquisition time of 0.64 s, and a useful bandwidth of output of up to 40 kHz.

Shock tests were performed with different sensor and mounting block configurations to study the hysteresis and symmetry of the system. To study the variability inherent to the test fixture, several drop tests were performed with two different boundary conditions and identical sensor configurations. The first boundary condition involves the plate being loosely bolted to the bookends with a rubber pad on each side of the plate, separating it from the bookend (see Fig. 55.1). The second boundary condition involves the plate being tightly bolted to the bookend without insulating the base of the plate with rubber. The loosely bolted boundary condition exhibits significantly more variability compared to the tightly bolted boundary condition, as shown in Figs. 55.3 and 55.4. These results suggest that the fixture should be tested in a configuration that is tightly bolted to reduce the amount of variability in the SRS.

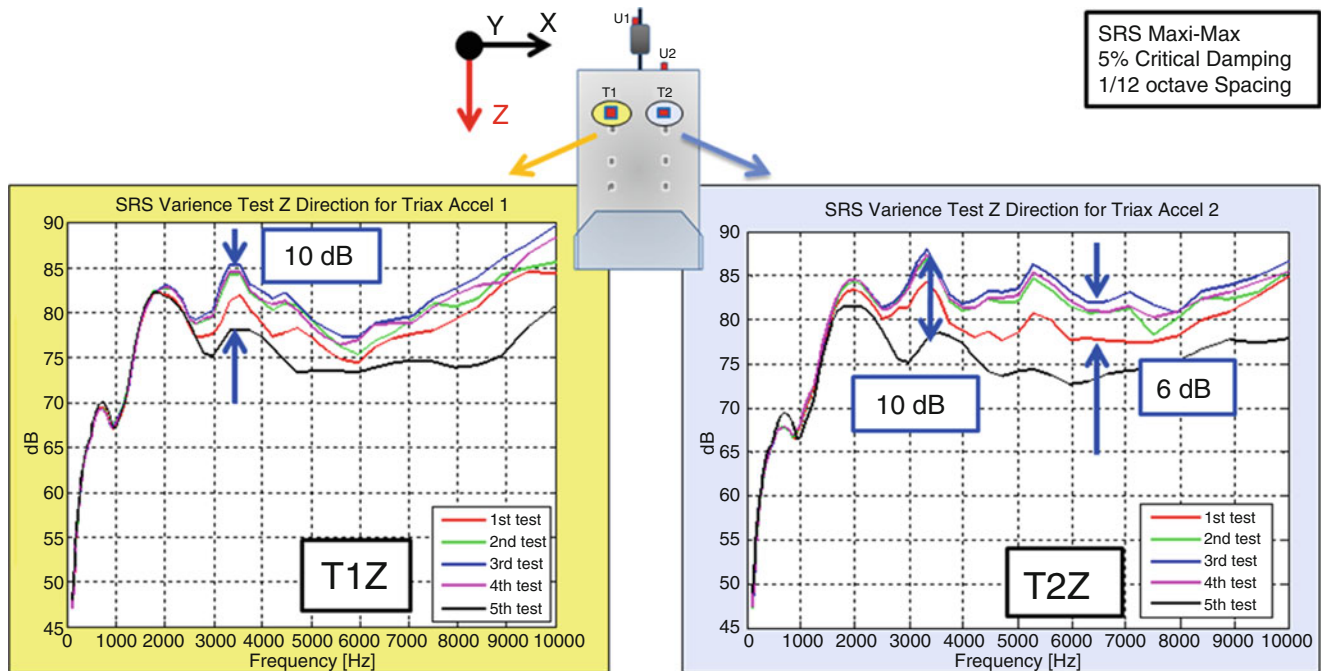
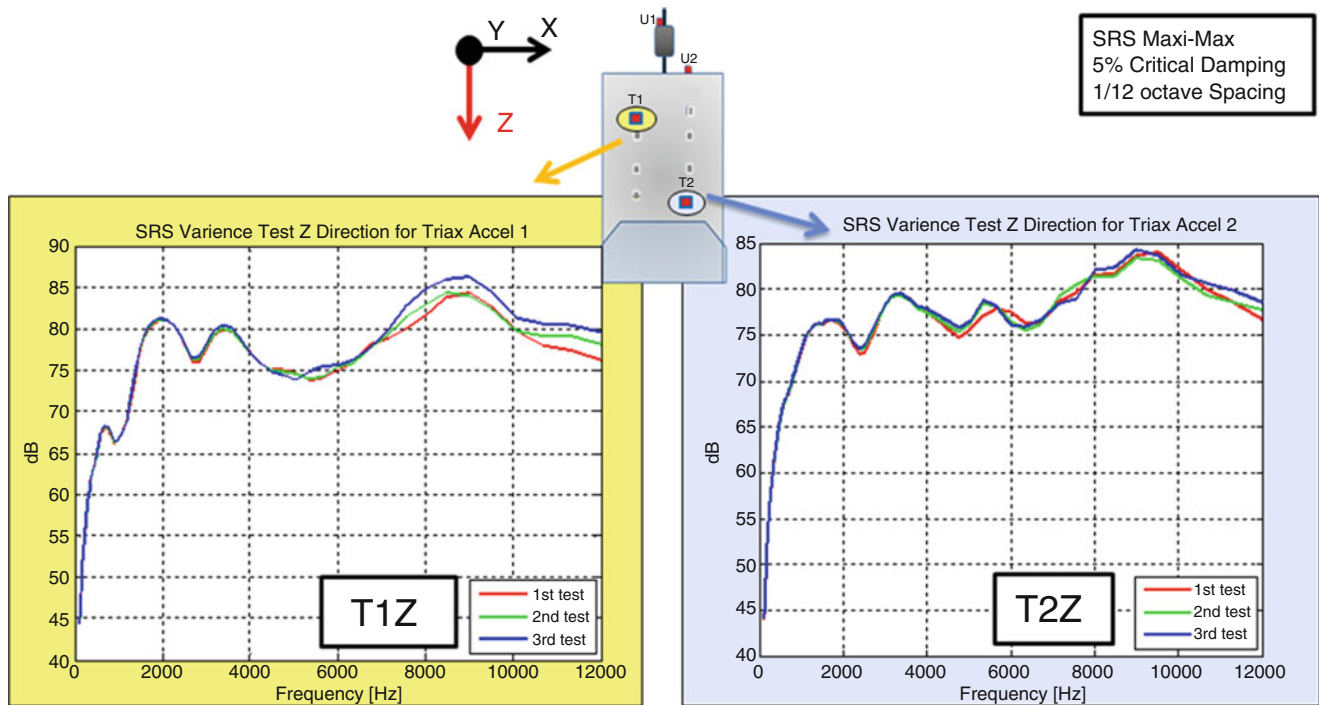


Fig. 55.3 Loosely bolted boundary condition variance test



**Fig. 55.4** Tightly bolted boundary condition variance test

To study the symmetry of the system, two triaxial accelerometers were positioned at equal distances away from the point of impact and the corresponding SRS from each of the three orthogonal directions was overlaid, as shown in Fig. 55.5.

Approximating the system response as symmetric about the vertical midline is reasonable up to about 4,000 Hz for the  $z$  direction, but for the very high frequencies, there are discrepancies between the left and right measurements that contribute approximately 5 dB of variability. Symmetry between the left and right side is less consistent for the other two axial directions. Variability in the  $z$  direction is more consistent because the impact is parallel to the  $z$  axis, i.e. the direction of force applied is the same as the direction of measurement.

To study the way the mounting block changes the SRS, a block was mounted to four test positions on the left side of the plate as shown in Fig. 55.6. One triaxial accelerometer on the right was kept horizontally level with the block and matched the measurement location from the bare plate shock tests. The other triaxial accelerometer was placed on the mounting block to estimate the SRS delivered to a test specimen. The transducer on the block revealed that the introduction of the mounting block's inertia is substantial enough that studying the plate alone would insufficiently describe the predicted SRS. The triaxial accelerometer mounted next to the mounting block varied by about 5 dB between the two shock tests. A more detailed study needs to be conducted to describe the amount of influence the block imposes on points further away from the attachment location and to describe the spectra delivered close to the base.

## 55.5 Finite Element Model

To calculate and extract the plate's mode shapes and corresponding natural frequencies, a finite element (FE) model was constructed using the commercially available software system, Abaqus. The model separated the structure into three main assemblies: the plate, the slug, and the upper structure. The plate, slug, and upper structure were modeled using linear hexagonal shell elements, linear tetragonal solid elements, and linear beam elements, respectively. A rendering of the FE model is shown in Fig. 55.7. The model was constrained using two sets of boundary conditions for the top and bottom: (a) top, free and bottom, free and (b) top, free and bottom, fixed. The interface between the slug and plate, principally the layer of felt capable of modifying the pulse width of the excitation, was not considered in this study. To determine the significance of the upper structure's inertial loading on the plate, a solution was calculated with and without the upper structure attachment. Mode shapes and natural frequencies were calculated using a Lanczos numerical eigensolution for a frequency range of 5–10,000 Hz. A mesh refinement study was also conducted.



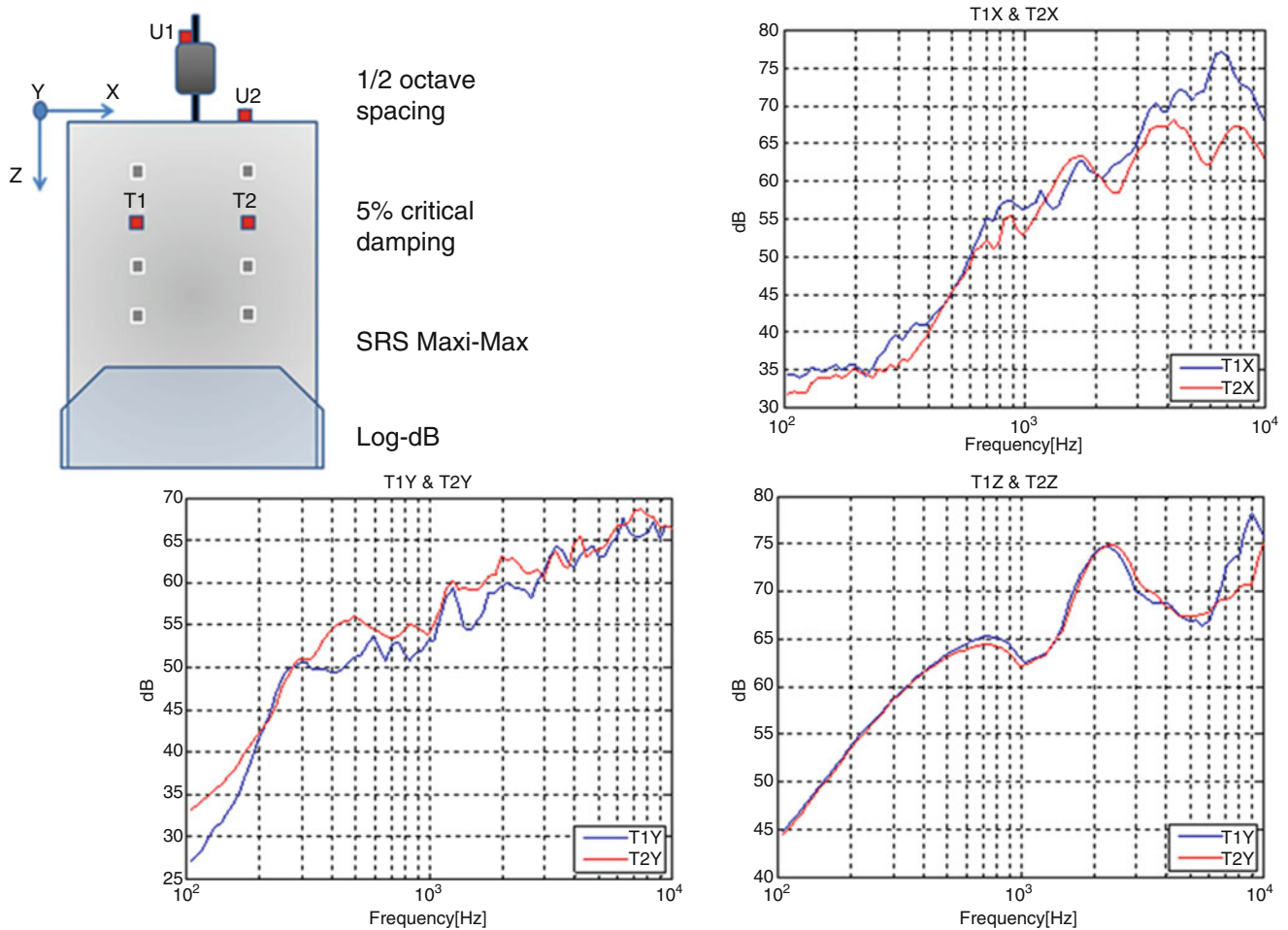


Fig. 55.5 Symmetry study with a log-dB with four configurations progressing down the plate with two tri-axial accelerometers

## 55.6 Experimental Modal Analysis

The experimental modal analysis portion of this research was used to determine whether the boundary conditions employed in the finite element model were reasonable. Three modal tests were conducted with the parameters specified in Table 55.1. The structure was impacted at 28 points as shown in Fig. 55.8. Three reference accelerometers, highlighted in red, green, and blue in Fig. 55.8, measured accelerations in the directions specified in the figure. The accelerometers were attached to the structure with wax, and the locations of the accelerometers did not change throughout all three modal tests. The sensitivity of the accelerometer highlighted in green was approximately 10 mV/g while the other two accelerometers had sensitivities close to 100 mV/g. The data acquisition system VibPilot, which interfaced with the M&P software package, was set to collect data at a sample rate appropriate for the particular test being conducted. The coherence was monitored for anomalies throughout the five impacts per node. The coherence was usually lower toward the fixed end, which is both closer to the bookends and farther away from the accelerometers. The acceleration time history of the hammer was monitored for double hits that may contaminate the data. For either very poor coherence or a substantial double hit, the acquisition was stopped and the impact test of the point was restarted. The points for which coherence did not improve or where a double hit could not be avoided were recorded.

The frequency response functions were loaded into the software ME'scope for curve fitting to extract experimental modes of vibration. The magnitude of the motion in the upper structure far exceeded that of the plate for most mode shapes. The damping values extracted from all of the tests suggest that there was more damping present in the lower frequency modes as compared to the higher frequency modes.



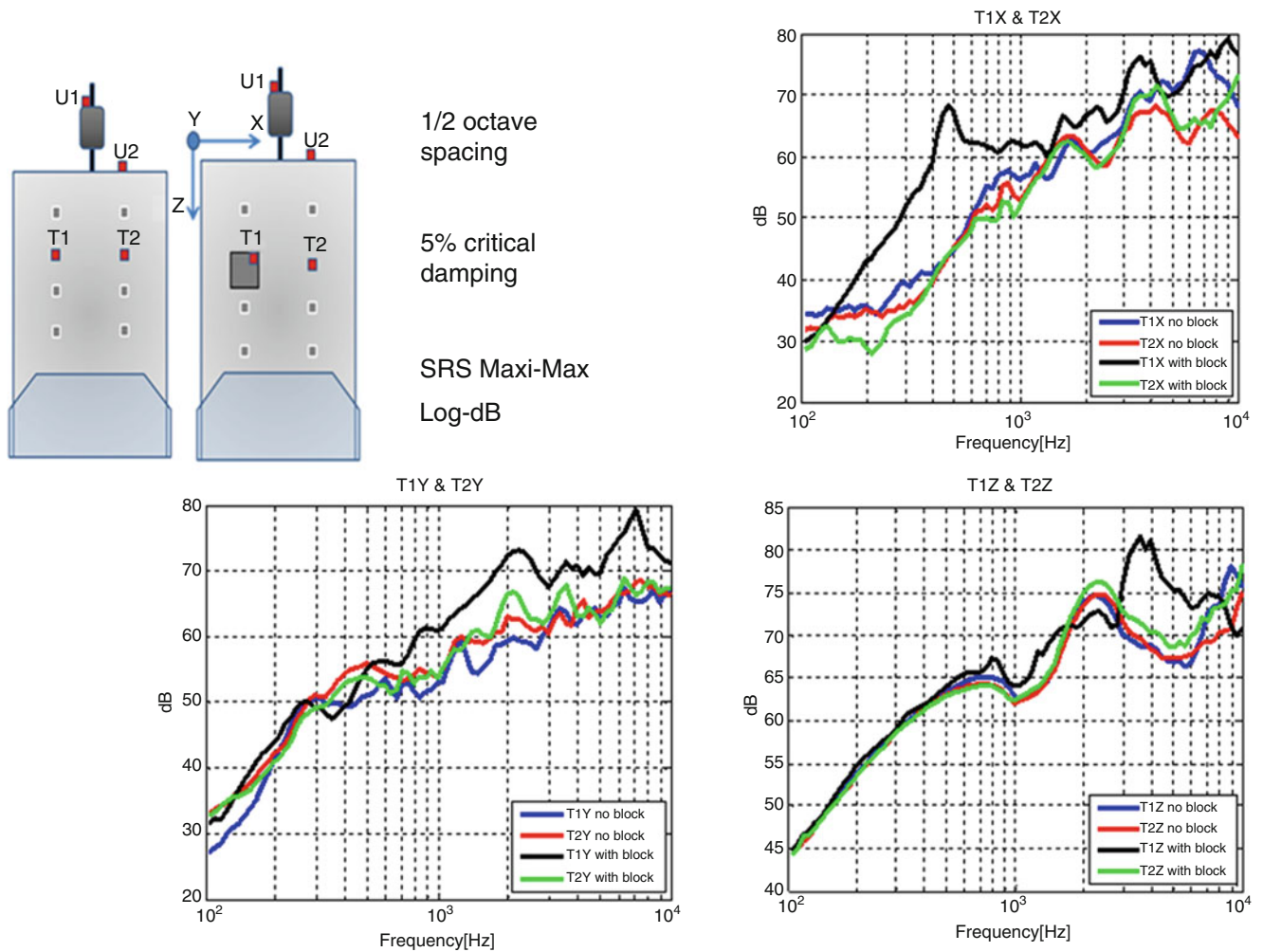


Fig. 55.6 Comparison of SRS with and without attaching mounting block

## 55.7 Correlation

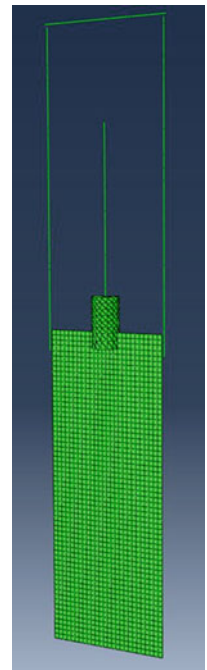
The mode shapes extracted from ME'scope were compared to those calculated by the finite element model in Abaqus using a Modal Assurance Criteria (MAC). Because the primary efforts of this research focused on the prediction of the SRS, a more detailed modal analysis needs to be conducted in order to attain better correlation between the experimental and finite element mode shapes. However, a few of the fundamental plate modes (i.e. first bending, first torsion, and second bending) are shown in Fig. 55.9 as examples of well-correlated mode shapes.

## 55.8 Analytical Model

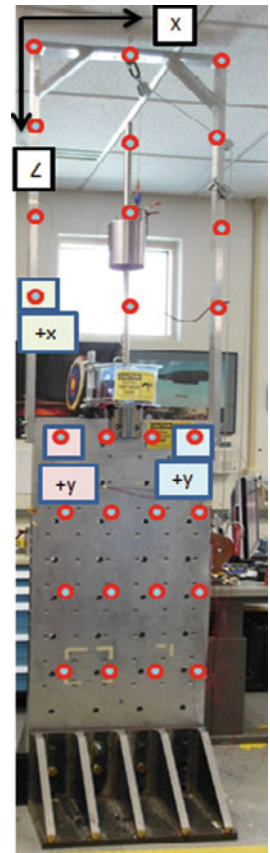
The analytical shock model employs the modal superposition technique and the Newmark time integration method to predict the SRS of the shock plate by using mode shapes extracted from the FE model. This provided an analytical means of studying how different parameters of the plate affect its SRS without the need of running multiple operational tests.

From the FE model, 30 points were selected which correspond to 30 locations on the shock test plate where the SRS is of interest.  $M$  modes of vibration that span the frequency range of interest for the SRS calculations (0–10 kHz in this case) were chosen. This resulted in a modal matrix  $[U]$  of dimension  $30 \times M$ . Furthermore, the FE model provided mode shapes that

**Fig. 55.7** Rendering of finite element model



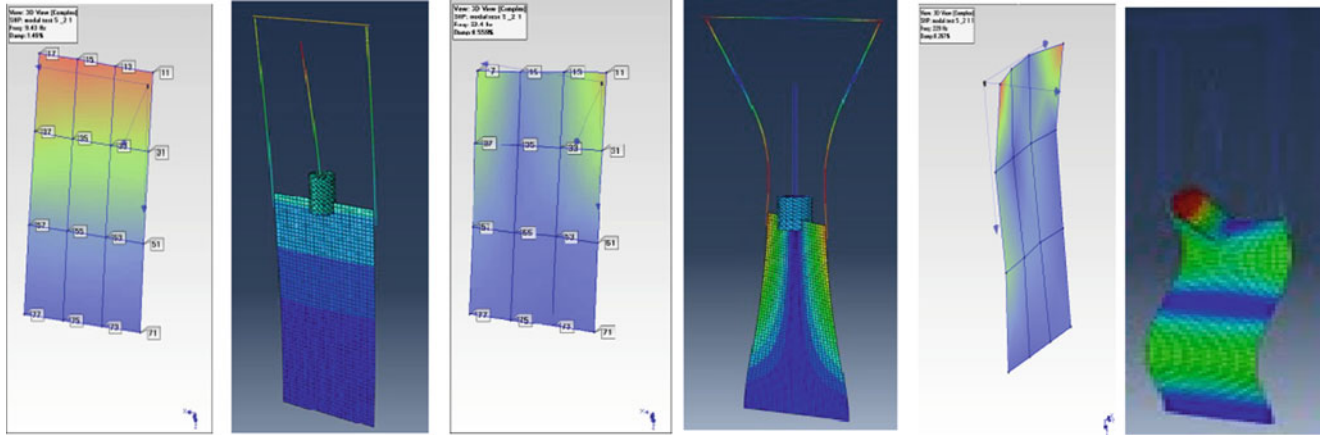
**Fig. 55.8** Impact points (*red circles*) and accelerometers (*green, red, and blue Rectangles*)



were normalized to unit modal mass such that the modal mass matrix  $[\bar{M}]$  was the identity matrix and the modal stiffness matrix  $[\bar{K}]$  was a diagonal matrix of the natural frequencies squared. The damping of the shock plate was not adequately quantified or studied, so a constant damping ratio  $\xi$  was assumed for every mode in this preliminary analysis such that the modal damping matrix  $[\bar{C}]$  was a diagonal matrix of  $2\xi\omega_i$  given as

**Table 55.1** Modal test setup parameters

Modal test	Boundary condition	Excitation range of the modal hammer [Hz]	Sample rate of DAQ [Hz]
1	Loosely bolted	<400	6,400
2	Tightly bolted	<400	6,400
3	Tightly bolted	200–5,000	16,384

**Fig. 55.9** From left to right: first bending at approximately 9.7 Hz MAC value of 0.9610. First torsion at approximately 87.5 Hz with a MAC value of 0.9150. Second bending at approximately 243 Hz with a MAC value of 0.9759

$$[\bar{C}] = \begin{bmatrix} \ddots & & & \\ & 2\xi\omega_i & & \\ & & \ddots & \\ & & & \ddots \end{bmatrix} \quad (55.15)$$

Once the system matrices were assembled, the acceleration time histories of each of the 30 points from the FE model were solved for in modal space. Ultimately, these responses were transformed back to the physical coordinates of the system, where the SRS was calculated.

## 55.9 Case Studies

Several studies were performed to better understand the overall effects of several variables on the SRS prediction. These were:

- Effects of varying the number of modes employed in modal superposition technique;
- Influence of the upper structure;
- Influence of the variability of the natural frequencies of the test fixture;
- Effects of assumed damping;
- Effects of varying location on plate;

and are presented next.

### 55.9.1 Effects of Varying the Number of Modes Employed in Modal Superposition Technique

The analytical model was used to identify the effects of varying the number of modes employed in the modal superposition technique and its subsequent effect on the SRS. The results in Fig. 55.10 show that as higher frequency modes are included in the modal space calculation, the SRS captures higher frequency peaks. The data suggest that to have an accurate SRS, the

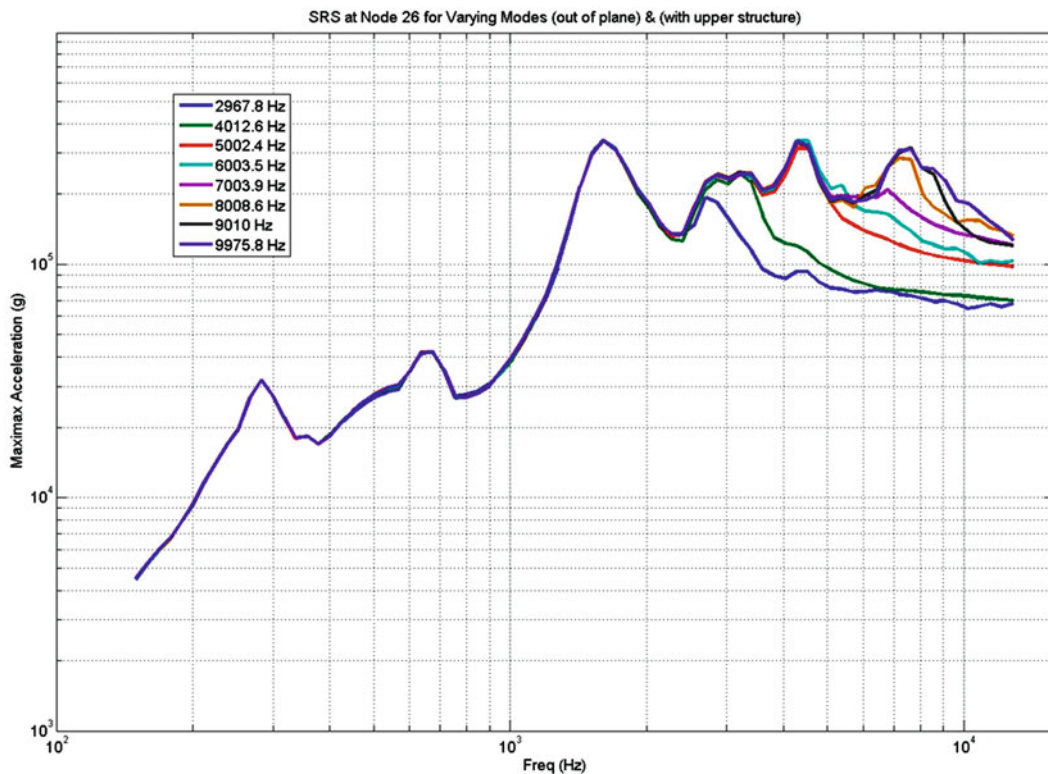


Fig. 55.10 SRS's for varying modes

highest mode shape used in the modal matrix should be at least 1,500 Hz greater than the desired frequency. The SRS in Fig. 55.10 that have fewer modes in the modal matrix tend to roll off earlier than the SRS with more modes. The effects of the higher frequency residual modes, beyond the test frequency range of interest, clearly have an effect on the SRS and need to be included in order to compute the appropriate SRS for the desired test frequency range of interest. Failure to include a sufficient number of modes beyond the desired test frequency range will result in an incorrect SRS.

### 55.9.2 Influence of the Upper Structure

A study was performed to investigate the effects that the upper structure of the shock test fixture has on the SRS.

For the case where the upper structure is not considered, the modes of vibration of the test fixture without the upper structure are extracted from the FE model and utilized in the analytical model for SRS calculation. The FE model predicts approximately 150 modes in the range interest (0–10 kHz) for the SRS calculation. On the other hand, for the case where the upper structure is considered, the FE model predicts approximately 330 modes in the 0–10 kHz range. This significant increase in the number of modes of vibration is due to the fact that the upper structure itself has dynamic characteristics that introduce additional modes of vibration into the test fixture.

As shown in Fig. 55.11, the presence of the upper structure had an effect on the SRS. Even though the general shape of the SRS does not show significant deviation, the overall amplitude, especially in the high frequency range beyond 700 Hz, decreases when the upper structure is included in the analysis. The upper structure can be thought of as a tuned mass damper that suppresses the response of the shock plate at various frequencies. In the frequency domain, some of the resonant peaks of the test fixture without the upper structure are redistributed by the presence of the upper structure. This result manifests itself in the plots, as the peaks of the SRS with the upper structure are shifted slightly (e.g. around 700 and 2,000 Hz).

Considering the fact that the SRS of interest in this project include a  $\pm 6$  dB band, the presence of the upper structure may not have a significant effect on the results. Particularly in the higher frequency range (as opposed to the low frequency range below approximately 700 Hz), the deviations in the amplitude of SRS are small and within an acceptable level of variability.

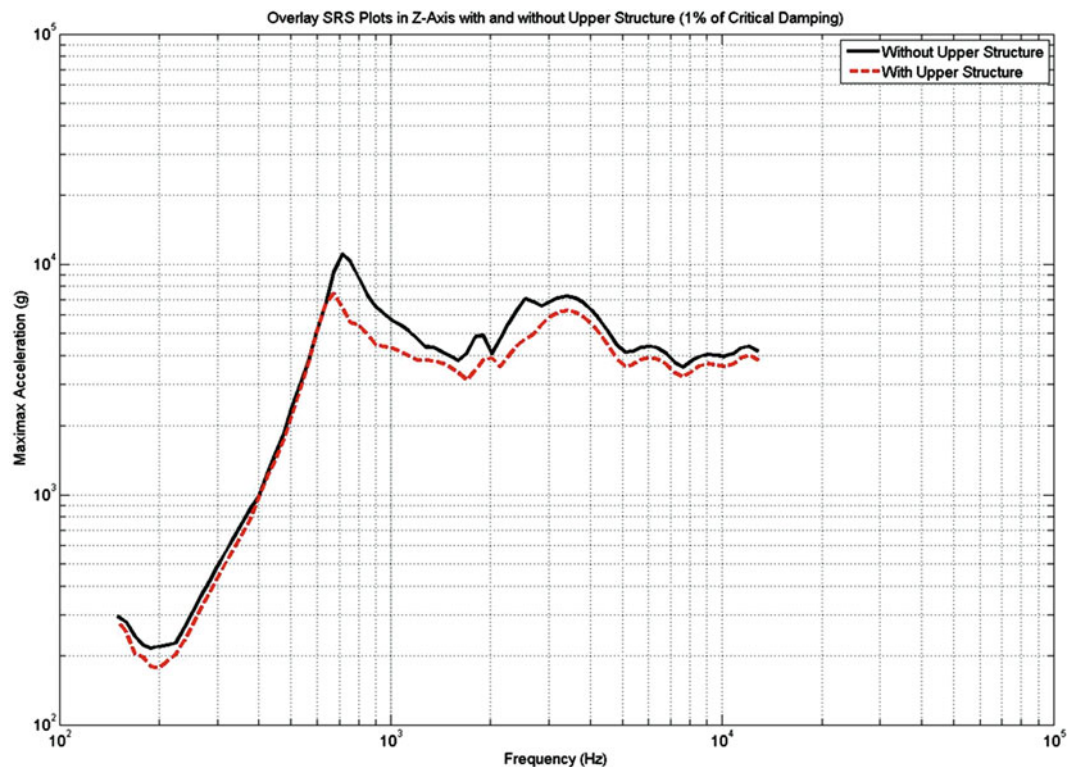


Fig. 55.11 SRS overlay plot demonstrating the influence of the upper structure

### 55.9.3 Influence of Variability of Natural Frequencies on the Test Fixture

A study was performed to investigate how perturbations in the natural frequencies of the test fixture affect the SRS. This is done to evaluate how discrepancies between the natural frequencies predicted by the FE model and those from the experimental modal analyses affect the SRS of the system.

For this study, perturbations are limited to  $\pm 8\%$ ,  $\pm 10\%$ ,  $\pm 15\%$ , and  $\pm 20\%$  of the nominal natural frequencies predicted by the FE model. Random percent increases or decreases are generated using a pseudorandom number generator in MATLAB and multiplied by each natural frequency extracted from the FE model.

As can be seen in Fig. 55.12, for a  $\pm 8\%$  and  $\pm 10\%$  frequency variation, the SRS does not exhibit a significant deviation from the nominal case. Both cases preserve the same general shape of the original SRS and exhibit peaks at approximately the same frequency locations, 650 and 3,500 Hz. There are slight deviations present in the SRS due to frequency variations; however, the SRS of interest in this project includes a  $\pm 6$  dB band. As a result, the discrepancies in SRS resulting from up to a 10% frequency variation are still within acceptable range.

On the other hand, as shown in Fig. 55.13, for a  $\pm 15\%$  and  $\pm 20\%$  frequency variation, the SRS begins to show significant changes from the nominal case. The overall shapes of the SRS no longer follow closely with each other and the location of the peaks has shifted. Clearly, a perturbation in the natural frequency of the system by over  $\pm 15\%$  has a significant effect on the SRS.

As a result of these studies, it can be conjectured that slight discrepancies between the predicted and actual natural frequencies may not cause a significant change in the SRS. This provides confidence that even though the experimental natural frequencies and FE model natural frequencies did not correlate perfectly, as long as the discrepancies are within  $\pm 10\%$ , the deviations may still be acceptable.



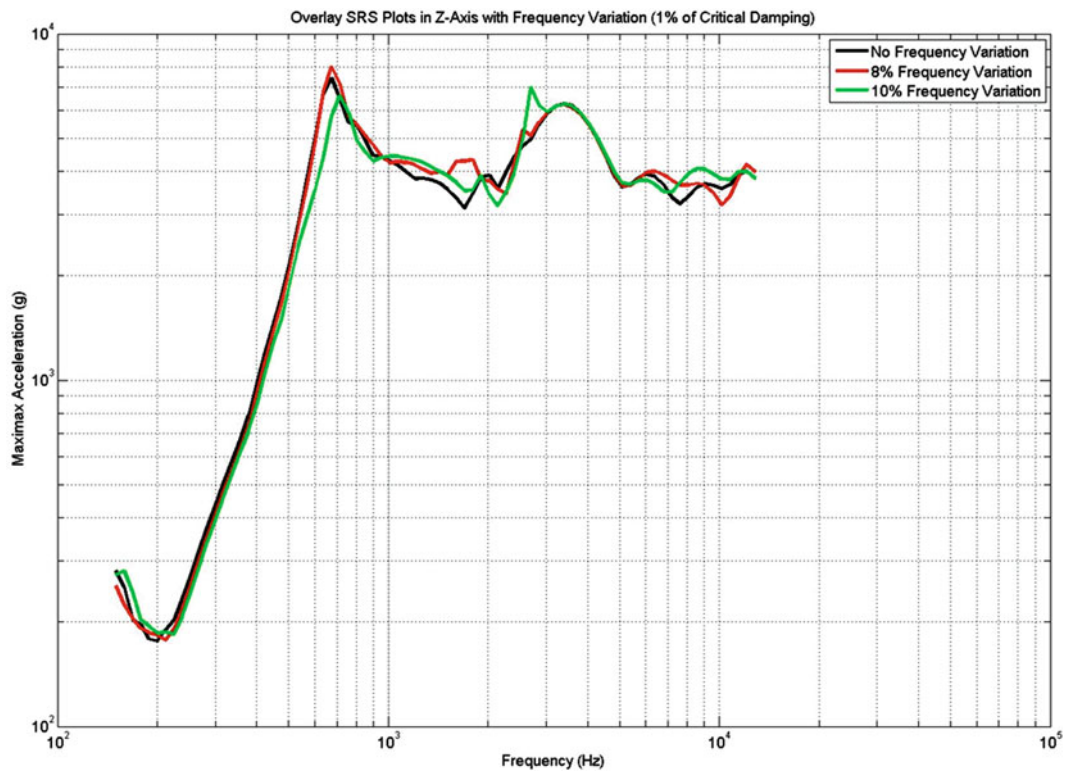


Fig. 55.12 SRS plot demonstrating influence of small variation in natural frequency

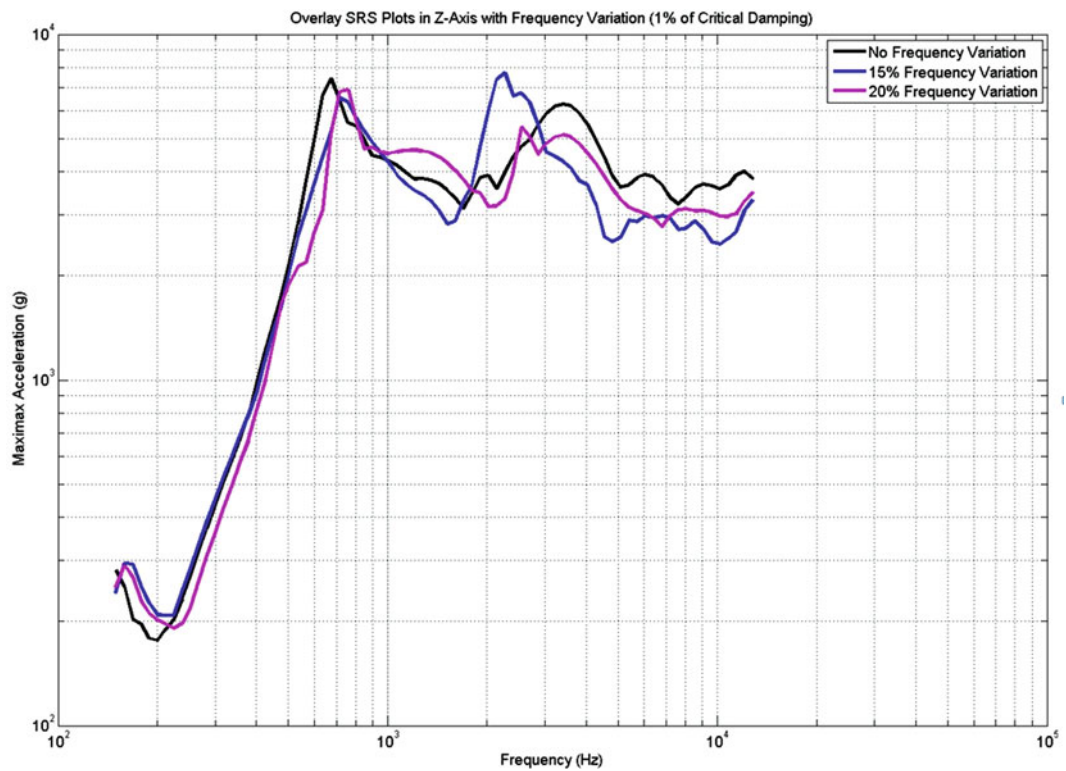


Fig. 55.13 SRS plot demonstrating the influence of large variation in natural frequency



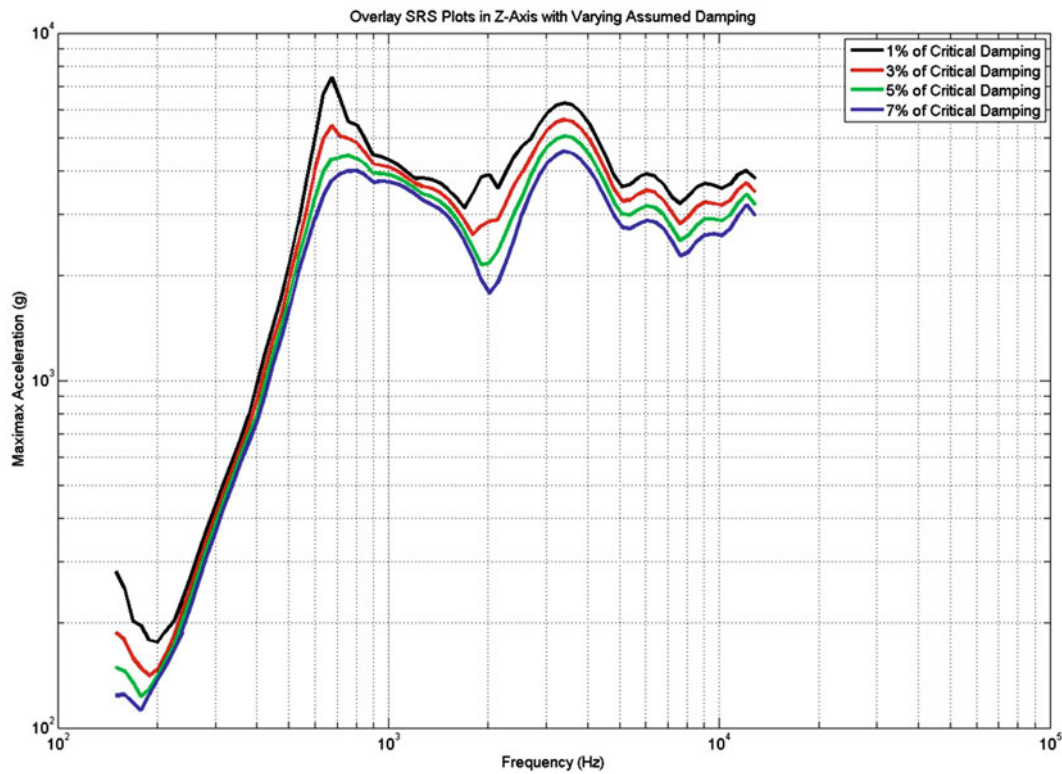


Fig. 55.14 SRS plot demonstrating the influence of assumed damping

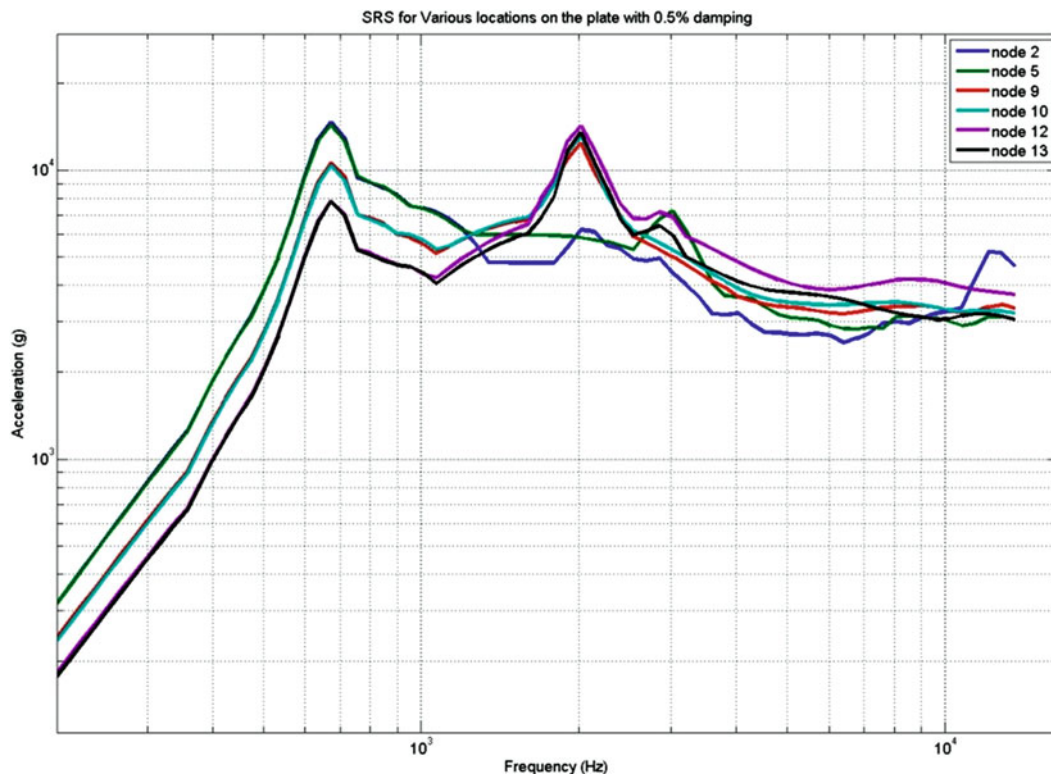
#### 55.9.4 Effects of Assumed Damping

Recall that since the actual damping of the shock plate was not studied in detail, a constant damping ratio was assumed for every mode in the analytical model during this preliminary analysis. Thus, a study was performed to investigate how varying the assumed damping ratios affect the SRS.

As can be seen in Fig. 55.14, the effect of varying the assumed damping ratios shows a clear trend. As the amount of damping increases, the overall amplitude of the SRS decreases. This result is reasonable since damping acts as a means of suppressing the response of the system. Thus, a higher damping ratio results in lower responses due to a shock input and subsequently lower amplitudes in the SRS.

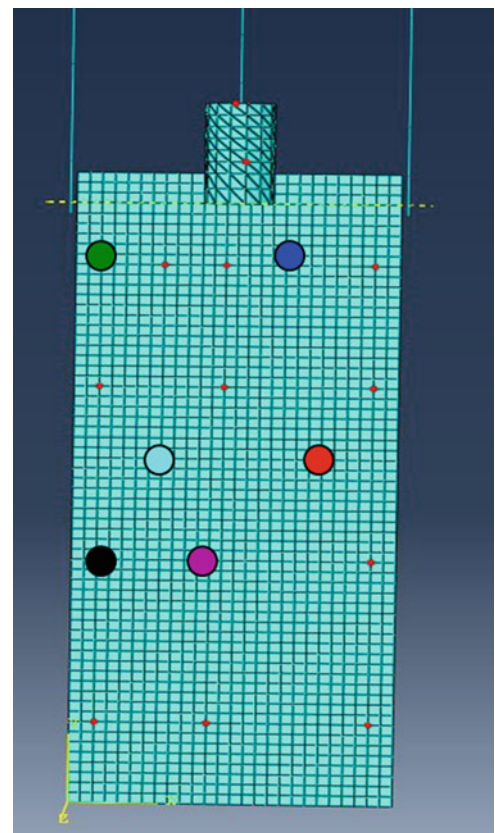
#### 55.9.5 Effects of Varying Location on Plate

Figure 55.15 shows the SRS plots for different node locations on the plate. The plots were made using the analytical model with an assumed damping of 0.5%. Mode shapes and frequencies were calculated using the FE model from 0 to 10,000 Hz. The noticeable features are the ramp from 0 to 700 Hz and the fairly consistent plateau around 4,000 g's. There are three peaks at around 670, 2,016, and 2,900 Hz that range from 6,000 to 10,500 g's. Figure 55.16 shows the nodes corresponding to the peaks shown in the SRS plots. The mode shapes at a certain frequency dictate the amplitude response for the SRS. Notice how the position of the node affects the amplitude of the response for each of the peaks. For example, the mode shape for 670 Hz shows the highest vertical displacement near the top of the plate. Correspondingly, the two nodes nearest to the top of the plate are the green and blue nodes in Fig. 55.16, which have the highest amplitude for the peak near 670 Hz as shown in Fig. 55.15. As the analytical model becomes more accurate, specific modes shapes can be targeted to reduce or amplify a certain region of the SRS. It should be noted that if variable damping were used, the frequencies ranging from 2,000 to 10,000 Hz would be shifted higher, creating a more even plateau and as a result the first peak around 670 Hz would be lowered in amplitude due to higher damping in that frequency range.



**Fig. 55.15** SRS plot demonstrating the influence of nodal location

**Fig. 55.16** Corresponding point locations on plate



## 55.10 Experimental and Analytical Srs Comparison

One of the most important results from the case studies is the effect that damping has on the plate's SRS. For the case studies presented in this report, damping is assumed to be constant throughout all the frequencies. Clearly, this assumption of constant damping throughout the structure is inappropriate for a more accurate analytical model of the structure. Figure 55.17 shows an overlay of the analytical SRS prediction to the corresponding experimental result. The general trend of the analytical model is similar to that of a characteristic pyroshock, but the specific peaks and slope do not match well.

Based on the information learned from the case studies, the main reason for the discrepancy between the analytical model and the actual plate is the assumed damping. Experimental modal analysis data show that the damping of the structure is not constant. Instead, damping is higher at lower frequencies and lower at higher frequencies. By including variable damping in the analytical model, the authors expect that the predictions will become more accurate.

## 55.11 Conclusion

This work presented the study of the design, test, and analysis of a new shock testing machine that will allow for more efficient shock testing. The work focused on several different aspects of the shock test machine evaluation, including finite element model development, experimental modal testing, experimental shock testing, and the development of a modal-based, analytical shock response model. The project incorporated the aforementioned features to obtain a methodology for evaluating the machine under a variety of conditions. While not all aspects of the shock machine were completely evaluated in this 7 week effort, a sufficient number of preliminary tests and preliminary analyses were performed to substantiate the design of the shock machine and warrant additional, more detailed studies to further refine the overall design of the machine and further development of the analytical shock response model formulated.

For the work presented, a very simple, modal-based, shock response model was developed utilizing pieces of the FE model in order to quickly and efficiently set up the shock test machine to predict SRS levels to identify appropriate locations for mounting items for SRS testing. Several key assessments presented in the paper regarding damping assumptions, dynamic

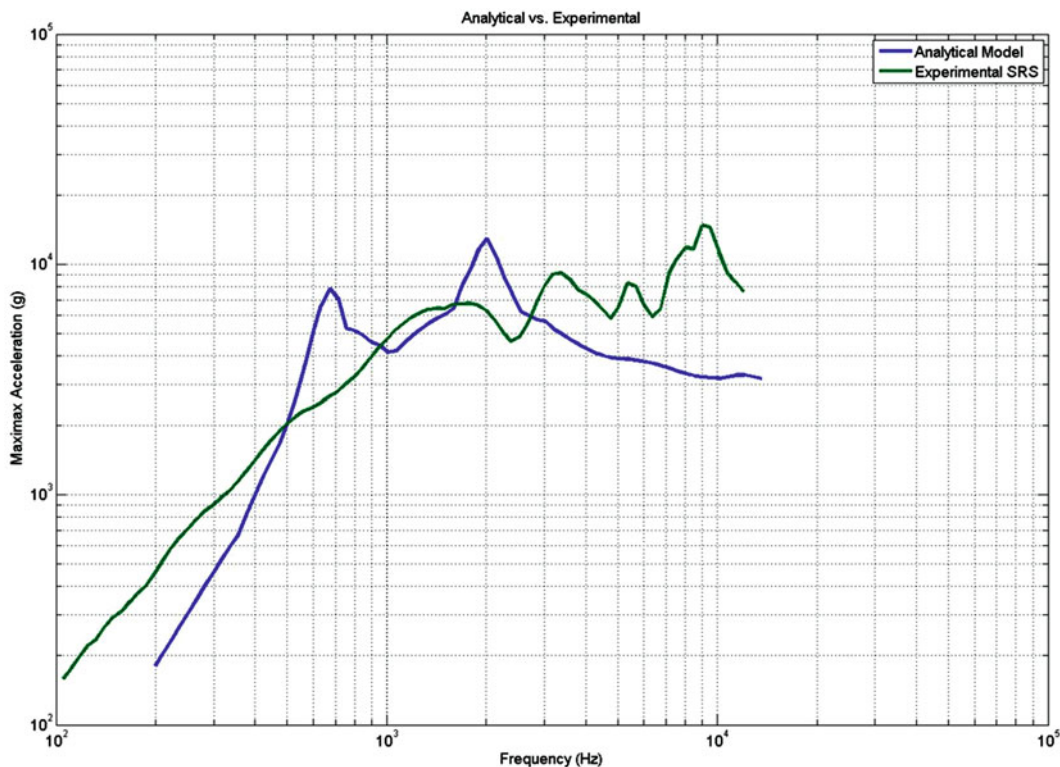


Fig. 55.17 SRS plot of analytical model versus experimental results

variability, influence of ancillary equipment, spatial response distribution, and other key factors, all show that the design of the machine produces useful results, considering the simplicity of the design. Further work needs to be performed to further tune all aspects of work addressed in this paper as well as augment the shock response model to include a moveable mounting mass for a more versatile shock machine. These future extensions of the shock response model will likely include structural dynamic modification approaches to allow for very simple adjustments of the shock response model and mitigate the need for an extremely detailed finite element model.

All the preliminary assessments described in this paper provide strong justification for extended, more in-depth studies to further develop the shock test machine, as well as the shock response model for the identification of appropriate parameters to set up a suitable SRS test to customer specifications.

**Acknowledgements** The team would like to acknowledge the software used during the research: MATLAB, Abaqus and ME'scope. Also, the team would like to thank the Los Alamos Dynamics Summer School, which provided the project and funding for the research. Lastly, the team would like to thank the three mentors Peter Avitabile, Jim Lake, and Chris Stull for their invaluable guidance.

## References

1. Davie NT, Bateman VI (1997) Pyroshock simulation for satellite components using a tunable resonant fixture – phase 2. Sandia National Laboratories, Albuquerque
2. Piersol AG (2010) Harris' shock and vibration handbook. Ch18 test criteria and specifications. Ed. N.p.: McGraw Hill, New York, [www.knovel.com](http://www.knovel.com)
3. Rubin S, Ahlin K (2010) Harris' shock and vibration handbook. Ch20 shock data analysis. Ed. N.p.: McGraw Hill, New York. [www.knovel.com](http://www.knovel.com)
4. Rao S (2004) Mechanical vibrations, 4th edn. Prentice Hall, New Jersey, pp 834–843
5. Avitabile P (2002) Twenty years of structural dynamics modification – a review. In: Proceedings of the twentieth international modal analysis conference, Los Angeles, California

# Chapter 56

## Resonances of Compact Tapered Inhomogeneous Axially Loaded Shafts

Arnaldo J. Mazzei and Richard A. Scott

**Abstract** An important technical area is the bending of shafts subjected to an axial load. These shafts could be tapered and made of materials with spatially varying properties (Functionally Graded Material – FGM). Previously the transverse vibrations of such shafts were investigated by the authors assuming the shafts had large slenderness ratios so that Euler-Bernoulli theory could be employed. Here compact shafts are treated necessitating the use of Timoshenko beam theory. For constant axial load case analysis of the effects of both FGMs and tapering on frequencies, the value of the compressive load is chosen to be 80% of the smallest critical (buckling) value for the shafts considered. The equations of motion give rise to two coupled differential equations with variable coefficients. These equations in general do not have analytic solutions and numerical methods must be employed (here using MAPLE<sup>®</sup>) to find the natural frequencies. MAPLE<sup>®</sup>'s built-in solver for two-point boundary value problems does not directly provide the eigenvalues. The strategy used is to solve a harmonically forced motion problem. On varying the excitation frequency and observing the mid-span deflection the resonance frequency can be found noting where a change in sign occurs. For example, results for FGM cylindrical and tapered shafts show that for a compact cylindrical beam the resonant frequency obtained differs from the Euler-Bernoulli prediction by 11%, and for a tapered beam by 12%, indicating that the effects of compactness can be significant. Since Timoshenko theory requires a value for the shear coefficient, which is not readily available for FGM beams, a sensitivity study is conducted in order to access the effect of the value on the results. Some effects of axial load variations on frequencies are also presented.

**Keywords** FGM • Tapered shafts • Non-homogeneous shafts • Shaft resonances • Timoshenko beam

### Nomenclature

$A$	Area of the shaft cross section ( $A_0$ initial value of shaft cross sectional area)
$a, m, n, \lambda$	Real arbitrary constants
$E$	Young's modulus ( $E_0$ , Young's modulus initial value for non-homogenous material)
$G$	Shear modulus
$k$	Shear coefficient
$M$	Bending moment
$q$	External force per unit length acting on the shaft
$f_1, f_2, f_3, f_4$	Non-dimensional functions for material/geometrical properties
$I$	Area moment of inertia of the shaft cross section ( $I_0$ initial value of shaft area moment of inertia)
$L$	Length of shaft
$P$	Compressive axial force acting on the shaft

---

A.J. Mazzei (✉)

Department of Mechanical Engineering, C. S. Mott Engineering and Science Center, Kettering University,  
1700 University Avenue, Flint, MI, 48504 USA  
e-mail: [amazzei@kettering.edu](mailto:amazzei@kettering.edu)

R.A. Scott

Department of Mechanical Engineering, University of Michigan, G044 W. E. Lay Automotive Laboratory,  
1231 Beal Avenue, Ann Arbor, MI, 48109 USA



$R$	Cylindrical shaft radius
$R_1, R_2$	Conical shaft radii
$s$	Numerical parameter ( $\sqrt{3}/(\alpha^2 + \alpha + 1)$ )
$t$	Time
$V$	Shear force
$w$	Shaft displacement in the $y$ direction
$Y$	Non-dimensional shaft displacement in the vertical direction
$x, y, z$	Inertial reference system (coordinates $x, y, z$ )
$x$	Shaft's axial coordinate
$\alpha$	Numerical parameter ( $R_1/R_2$ )
$\alpha_0, \beta_0, Q, \gamma_0, \zeta_0$	Non-dimensional numerical parameters
$\gamma$	Shear strain
$\theta$	Rotational angle of the shaft's cross section
$\nu$	Non-dimensional frequency
$\xi$	Non-dimensional spatial coordinate
$\rho$	Mass density ( $\rho_0$ , density initial value for non-homogenous material)
$\tau$	Non-dimensional time
$\nu$	Poisson's ratio
$\Omega$	Frequency of the shaft
$\Omega_0$	Reference frequency – first bending frequency of a homogeneous shaft

## 56.1 Introduction

This work is a continuation of an earlier investigation by the authors (see Ref. [1]) on the vibration of axially loaded cylindrical and tapered shafts made of FGMs. In the former work the shafts were slender and Euler-Bernoulli theory, in which shear effects are neglected, could be employed. Here non-slender shafts are treated and Timoshenko beam theory must be used.

As noted in Ref. [1], “one strategy to avoid shaft resonances is to shift natural frequencies outside operational ranges”. This could be possibly achieved by employing FGMs.

Also, tapered shafts have a wide range of applications. The interest here is to investigate the effect of FGMs on the frequencies of these when the slenderness ratio (effective length of a column/least radius of gyration) is small. A somewhat novel feature is the assessment of the effect of the influence of the axial load on the frequencies.

Results for transverse vibrations of FGM beams (with material properties varying in the thickness direction) containing an open edge crack and employing Timoshenko beam theory were given by Ke et al. [2]. It was found that the natural frequencies decreased as the crack depth increased and beams with smaller slenderness ratio were more sensitive to the edge crack.

An approach for calculating exact frequencies of homogeneous Timoshenko beams with varying cross-sections is given by Eisenberger in Ref. [3]. Frequencies were calculated via a dynamic stiffness matrix approach and compared to known results of beams with various taper ratios.

Vibrations of Timoshenko beams with varying cross sections subjected to both axial and tangential loads were studied by Esmailzadeh and Ohadi [4]. Results for the natural frequencies were obtained applying the Frobenius method for several cases including the effect of non-uniformity, end masses and axial and tangential forces. (Note that a study on the vibrations of materially and geometrically non-uniform beams was conducted by Kerczek [5].)

Results for motions of axially loaded Timoshenko beams can also be found in Saito and Otomi [6] and Banerjee and Kennedy [7].

Here the modeling leads to a pair of coupled differential equations with variable coefficients. In general these equations do not have analytic solutions and numerical methods must be employed. In this work MAPLE<sup>®</sup>'s two-point boundary value solver is employed for a pin-pin beam.



## 56.2 Modeling

The development here follows previous works on axially loaded beams by Bishop and Price [8] and Esmailzadeh and Ohadi [4]. The equations of motion for a shaft in bending under axial load can be derived via a Newton-Euler approach applied to a differential element of the beam at its deformed configuration (see Fig. 56.1). The element is assumed to be rotated by an angle  $\theta$  due to bending and by an additional angle  $\gamma$  due to shear. The transverse deflection  $w$  is related to these angles by:

$$\frac{\partial w}{\partial x} = \theta + \gamma, \quad (56.1)$$

i.e., the slope of the neutral axis is due both to bending and shear effects. Figure 56.1 shows the shear forces and bending moments, as well as the axial forces. Note that the axial forces are assumed to act perpendicular to the shear forces following a model given in Ref. [4] (see also follower force models given in Refs. [6, 9, 10]). On the right side of the element the axial force is offset by the shear deformation, whereas the direction of the shear force is not affected by the shear strain  $\gamma$ .

Summation of forces about the  $y$  axis leads to:

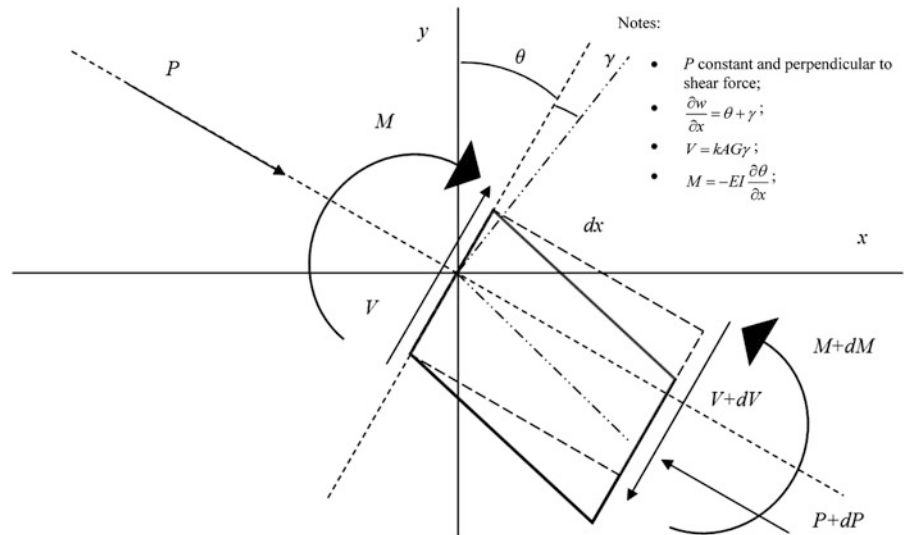
$$-\rho(x)A(x)dx \frac{\partial^2 w(x,t)}{\partial t^2} = V \cos \theta - (V + dV) \cos \theta - P \sin \theta + (P + dP) \sin \theta - q(x)dx \quad (56.2)$$

Balancing moments about the  $z$  axis gives:

$$-\rho(x)I(x)dx \frac{\partial^2 \theta(x,t)}{\partial t^2} = -M + (M + dM) - (V + dV) \frac{dx}{\cos \theta} - (P + dP) \frac{dx}{\cos \theta} \tan \gamma \quad (56.3)$$

Assuming small angles and constant axial load  $P$ , (56.2) and (56.3) can be written as:

$$\begin{aligned} \rho(x)A(x)dx \frac{\partial^2 w(x,t)}{\partial t^2} - \frac{\partial V}{\partial x} dx + P \frac{\partial \theta}{\partial x} dx - q(x)dx &= 0 \\ \rho(x)I(x)dx \frac{\partial^2 \theta(x,t)}{\partial t^2} + \frac{\partial M}{\partial x} dx - V dx - P \gamma dx &= 0 \end{aligned} \quad (56.4)$$



**Fig. 56.1** Beam differential element

Using a linearized curvature model the bending moment is taken to given by  $M = -EI \frac{\partial \theta}{\partial x}$ . Employing this relationship and substituting (56.1), one can rewrite (56.4) as:

$$\begin{aligned} \rho(x)A(x)\frac{\partial^2 w(x,t)}{\partial t^2} &= q(x) + \frac{\partial}{\partial x} \left[ kA(x)G(x) \left( \frac{\partial w(x,t)}{\partial x} - \theta(x,t) \right) \right] - P \frac{\partial \theta(x,t)}{\partial x} \\ \rho(x)I(x)\frac{\partial^2 \theta(x,t)}{\partial t^2} &= \frac{\partial}{\partial x} \left[ E(x)I(x) \left( \frac{\partial \theta(x,t)}{\partial x} \right) \right] + (P + kA(x)G(x)) \left( \frac{\partial w(x,t)}{\partial x} - \theta(x,t) \right) \end{aligned} \quad (56.5)$$

In (56.5), following the Timoshenko model, the shear force was assumed to be given by:  $V = kA(x)G(x)\gamma$ , where  $k$  is the so-called ‘‘shear coefficient’’ (see [11]). In classical terms the coefficient relates the maximum shear stress to the average value in the cross section of the beam. Note that in the case of tapered shafts and FGMs, such a calculation cannot be readily done since a model for the stress is lacking. Several strategies are possible. One could find accurate solutions to the Euler-Bernoulli version of the equations, using finite-difference schemes, and choose the value of  $k$  to match basic frequencies. Such an approach would require extensive computations and here a sensitivity study is employed in which the effect of different  $k$  values on the results is analyzed and their significance assessed.

No assumption was made for the material type in the derivation of equations (56.5), thus it can be either homogeneous or non-homogeneous. Here both types are considered and the non-homogeneous material utilized is a FGM (see, for example, Ref. [12]).

The proposed approach is to compare shafts of different materials and different profiles (cylindrical and tapered). If comparing shafts of same length, these are taken to have the same volume. This assumption leads to the following relations for the cross-sectional areas and area moments of inertia:

$$A(x) = A_0 s^4 \left[ \alpha + (1 - \alpha) \frac{x}{L} \right]^4, \quad I(x) = I_0 s^4 \left[ \alpha + (1 - \alpha) \frac{x}{L} \right]^4 \quad (56.6)$$

where  $\alpha$  is the ratio between the smallest to the largest radius of the tapered shaft:

$$\alpha = R_1 / R_2 \quad \text{and} \quad s = \sqrt{\frac{3}{(\alpha^2 + \alpha + 1)}} \quad (56.7)$$

### 56.2.1 Non-homogeneous Material

In the following the material is taken to be functionally graded and to follow the description given by Chiu and Erdogan [13]. It is assumed to be isotropic and non-homogeneous with properties given by:

$$E(x) = E_0 \left( a \frac{x}{L} + 1 \right)^m, \quad \rho(x) = \rho_0 \left( a \frac{x}{L} + 1 \right)^n \quad (56.8)$$

where  $a$ ,  $m$  and  $n$  are arbitrary real constants with  $a > -1$ .  $E_0$  and  $\rho_0$  are the Young’s modulus and mass density at  $x = 0$ .

Non-dimensional versions of equations (56.5) are developed next. By taking  $\tau = \Omega_0 t$ ,  $\nu = \frac{\Omega}{\Omega_0}$ ,  $\xi = \frac{x}{L}$ ,  $Y = \frac{w}{L}$ ,  $I(x) = I_0 s^4 [\alpha + (1 - \alpha)\xi]^4 = I_0 f_2(\xi)$ ,  $A(x) = A_0 s^4 [\alpha + (1 - \alpha)\xi]^4 = f_4(\xi)$ ,  $E(x) = E_0 (a\xi + 1)^m = E_0 f_1(\xi)$ ,  $G(x) = E(x) (1 / (2(1 + \nu))) = E_0 f_1(\xi) (2(1 + \nu))^{-1} = G_0 f_1(\xi)$ ,  $\rho(x) = \rho_0 (a\xi + 1)^n = \rho_0 f_3(\xi)$  and substituting into (56.5) one obtains:

$$\begin{aligned} f_3(\xi) f_4(\xi) \frac{\partial^2 Y(\xi, \tau)}{\partial \tau^2} &= Q(\xi) + \alpha_0 \frac{\partial}{\partial \xi} \left( f_4(\xi) f_1(\xi) \left( \frac{\partial Y(\xi, \tau)}{\partial \xi} - \theta(\xi, \tau) \right) \right) - \beta_0 \frac{\partial \theta(\xi, \tau)}{\partial \xi} \\ f_3(\xi) f_2(\xi) \frac{\partial^2 \theta(\xi, \tau)}{\partial \tau^2} &= \gamma_0 \frac{\partial}{\partial \xi} \left( f_1(\xi) f_2(\xi) \frac{\partial \theta(\xi, \tau)}{\partial \xi} \right) + \varsigma_0 (\beta_0 + \alpha_0 f_4(\xi) f_1(\xi)) \left( \frac{\partial Y(\xi, \tau)}{\partial \xi} - \theta(\xi, \tau) \right) \end{aligned} \quad (56.9)$$

where  $Q(\xi) = \frac{q(x)}{\rho_0 \Omega_0^2 A_0 L}$ ,  $\alpha_0 = \frac{k G_0}{\rho_0 \Omega_0^2 L^2}$ ,  $\beta_0 = \frac{P}{\rho_0 \Omega_0^2 A_0 L^2}$ ,  $\gamma_0 = \frac{E_0}{\rho_0 \Omega_0^2 L^2}$ ,  $\varsigma_0 = \frac{L^2 A_0}{I_0}$  and  $\Omega_0$  is a reference frequency (first bending frequency of a pin-pin cylindrical shaft made of aluminum).

**Table 56.1** Material properties for Al/SiC FGM

	Aluminum/silicon carbide
$E_0(GPa)$	105.197
$\rho_0(kg/m^3)$	2710.000
$a$	1.14568
$m$	1.00000
$n$	0.17611
$\nu$	0.33

Assuming free vibrations and no distributed loading ( $Q(\xi) = 0$ ), one can take  $Y(\xi, \tau) = U(\xi) \exp(i\nu\tau)$  and  $\theta(\xi, \tau) = \phi(\xi) \exp(i\nu\tau)$ , then:

$$f_3 f_4 \nu^2 U - \beta_0 \frac{d\phi}{d\xi} + \alpha_0 \frac{d}{d\xi} \left( f_4 f_1 \left( \frac{dU}{d\xi} - \phi \right) \right) = 0$$

$$f_3 f_2 \nu^2 \phi + \gamma_0 \frac{d}{d\xi} \left( f_1 f_2 \frac{d\phi}{d\xi} \right) + \zeta_0 (\beta_0 + \alpha_0 f_4 f_1) \left( \frac{dU}{d\xi} - \phi \right) = 0 \quad (56.10)$$

Given the properties of the FGM and (56.6), i.e.,  $f_1(\xi)$ ,  $f_3(\xi)$ ,  $f_2(\xi)$  and  $f_4(\xi)$ , numerical solutions for (56.10) can be attempted and subsequent results can be compared for different shafts.

The FGM utilized for the examples is a composite made from aluminum and silicon carbide (Al/SiC). The properties of the material are given in Table 56.1 and are taken from Ref. [13].

Note that in this model Poisson's ratio is taken to be a constant.

### 56.3 Numerical Results

The numerical values used in the simulations are the following ones:  $L = 0.896$  m,  $R = 0.034950$  m. Aluminum properties are:  $E = 0.71E11$  N/m<sup>2</sup>,  $\rho = 2710$  Kg/m<sup>3</sup> and steel properties are:  $E = 2.10E11$  N/m<sup>2</sup>,  $\rho = 7850$  Kg/m<sup>3</sup>. The exact value of the first bending frequency of a homogeneous aluminum shaft with these dimensions can be calculated from  $\Omega_0 = \frac{\pi^2}{L^2} \sqrt{\frac{EI}{\rho A}} \cong 175$  Hz (see, for example, [14]). The shear coefficient is initially taken to be  $k = \frac{6(1+\nu)}{7+6\nu} = 0.8886$  (as given in [11]).

The influences of the FGM, and profiles, on the first bending frequency are investigated next. In the following numerical simulations the values for the compressive load are chosen to be 80% of the smallest critical (buckling) value for all the shafts considered (approximately 6.0E5 N, see [1] for details).

Equation 56.10 are solved subjected to pin-pin boundary conditions. In non-dimensional form these are:

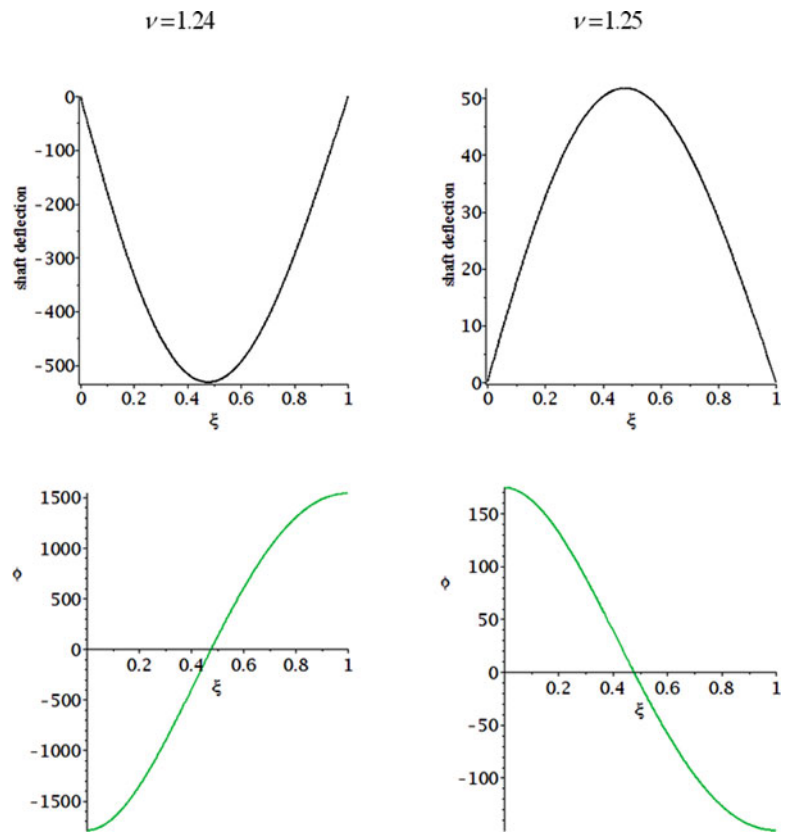
$$U(\xi)|_{\xi=0} = 0, \quad U(\xi)|_{\xi=1} = 0, \quad \frac{d\phi}{d\xi} \Big|_{\xi=0} = 0 \quad \text{and} \quad \frac{d\phi}{d\xi} \Big|_{\xi=1} = 0$$

The equations, in general, do not have analytic solutions. A problem is encountered here in that the "built-in" MAPLE<sup>®</sup> eigenvalue solver gives only the trivial solution. The strategy employed is the following: use is made of MAPLE<sup>®</sup>'s two-point boundary value solver to solve a forced motion problem. It consists of assuming a constant value for the forcing function and varying the forcing frequency. By observing the mid-span deflection, the resonant frequency can be found on noting where an abrupt change in sign occurs. Note that higher modes could be obtained by extending the search range.

For a pure aluminum cylindrical shaft an analytical solution involving the forcing frequency can be found. In Ref. [1], which contains an extended discussion on the subject, this resonance is shown to be  $\nu = 0.65$  (non-dimensional frequency corresponds to approximately 113.75 Hz). In that work the authors showed that the numerical method described above led to the same result for the frequency. The approach was conducted by assuming a value of 1 for the external forcing and varying  $\nu$ . A similar procedure is used in the following.

For example, Fig. 56.2 shows the deflections and angles of rotation for a cylindrical Al/SiC shaft (length =  $L$ ) for  $\nu = 1.24$  and 1.25, respectively. Resonance is seen to occur at  $\nu = 1.25$ .

**Fig. 56.2** Aluminum/silicon carbide cylindrical shaft deflections for  $\nu = 1.24$  and 1.25 respectively



**Table 56.2** Frequency variation based on beam modeling as a function of length for Al

Cylindrical shafts	First resonance frequency "Timoshenko model"	First resonance frequency "Euler-Bernoulli model"	Length
Aluminum	0.65	0.65	L
03.36% difference	0.89	0.92	L/2
11.35% difference	0.88	0.98	L/4

**Table 56.3** Frequency variation based on beam modeling as a function of length for an Al/SiC cylindrical shaft

Cylindrical shafts	First resonance frequency: "Timoshenko model"	First resonance frequency "Euler-Bernoulli model"	Length
Al/SiC	1.25	1.26	L
02.92% difference	1.37	1.41	L/2
11.54% difference	1.30	1.45	L/4

Utilizing the approach, resonances were found for three distinct homogenous shaft lengths. For comparison purposes, frequencies for the same shafts utilizing a simpler Euler-Bernoulli approach were also calculated (see [1]). Results are shown in Table 56.2. It is seen that as the slenderness ratio decreases the difference between values calculated by the two approaches increases. Note that in the case where the length was reduced by 50% the frequency decreased by 3.36% and in the case where the length was about 25% of the original, the frequency decreased by 11.35%. This demonstrates the need to use the "Timoshenko approach" when dealing with small slenderness ratios (in [15], for example, "long" shafts made of Aluminum Alloy 2014 have slenderness ratios larger than 55).

Table 56.3 shows similar comparison results as in Table 56.2 but, in this case, the results are for FGM shafts. As in the case of aluminum shafts, the Al/SiC frequency differences between models increase as the slenderness ratio decreases. For a reduction in shaft length of 50% the difference is 2.92% and for a reduction of 75% the difference is 11.54%. Therefore it can be seen that, for both homogeneous and non-homogeneous materials, differences can be substantial and the more appropriate model when dealing with "short" shafts is the one given by (56.5).

It should be noted that the previous results were obtained using a fixed value for the shear coefficient (and could depend on the value). Here a sensitivity study is conducted to find how its variation impacts the shaft's resonances. In the following the

**Table 56.4** Frequency variation as a function of shear coefficient for a short cylindrical Al/SiC shaft

Cylindrical shafts Al/SiC	First resonance frequency	Second resonance frequency	k
	1.28	4.15	0.750
	1.29	4.25	0.847
	1.30	4.25	0.889
	1.30	4.25	0.90
	1.34	4.55	1.50

**Table 56.5** Frequency variation based on beam modeling as a function of length for a tapered Al/SiC shaft

Tapered shafts ( $\alpha = 0.5$ ) Al/SiC	First resonance frequency "Timoshenko model"	First resonance frequency "Euler-Bernoulli model"	Length
	1.02	1.03	L
03.33% difference	1.20	1.24	L/2
12.17% difference	1.15	1.29	L/4

**Table 56.6** Frequency variation as a function of shear coefficient for a short tapered Al/SiC shaft

Tapered shafts ( $\alpha = 0.5$ ) Al/SiC	First resonance frequency	Second resonance frequency	k
	1.13	4.05	0.750
	1.14	4.15	0.847
	1.15	4.15	0.889
	1.15	4.15	0.90
	1.19	4.45	1.50

**Table 56.7** Frequency variation as a function of axial load and length for a tapered Al/SiC shaft

Tapered shafts ( $\alpha = 0.5$ )			
Al/SiC – 1st resonance	F = 6.0E5 N	F = 3.0E5 N	F = 0
L	1.02	1.17	1.30
L/2	1.20	1.23	1.27
L/4	1.15	1.16	1.16

first four values for the shear coefficient are taken from Ref. [11] and the last one is an assumed "large" value for investigation purposes. Table 56.4 shows the variation of the first and second resonant frequencies as a function of the shear coefficient for a short (L/4) cylindrical FGM shaft. Note that if the shear factor increases by 100% the first frequency increases by 4.7% and the second by 9.6%. Based on these results the comparison values given in Table 56.2 and Table 56.3 can be taken to be fairly accurate (from the maximum to the minimum value of  $k$  the first frequency only changes about 5%).

Next Table 56.5 shows frequency comparisons for the case of a tapered Al/SiC shaft. Once again it is seen that as the slenderness ratio decreases the frequency values predict by the two models stray apart. Here for a shaft 50% shorter the "Timoshenko approach" led to a frequency value which is 3.33% smaller than the value given by the "Euler-Bernoulli" approach. For a shaft which is 75% shorter the difference is 12.17%. As in the cylindrical case, short tapered non-homogenous shafts are better modeled using (56.5).

To test for dependency of the tapered results on the shear coefficient, the sensitivity analysis was conducted for a short FGM tapered shaft. Results are given in Table 56.6 and show that in this case if the shear coefficient is allowed to vary 100%, the first frequency increases by 5.3% and the second by 9.9%. It is seen that the effect can be more pronounced on higher frequencies, but, as far as the first one is concerned, the variation is small (5% for the "large" value of the coefficient and less for the values given in the literature).

Based on these results the comparison values given above can be taken as accurate and, in the following, the value of 0.889 (as given in [11]) is used for the coefficient.

In the preceding a constant value of 6.0E5 N was assumed for the axial load. This value was calculated by the authors in a previous work ([1]), using an Euler-Bernoulli model including an axial load, and corresponds to 80% of the smallest critical buckling load for the shafts considered in the work. It is of interest to understand the effect of the axial load on the frequencies of the shafts.

For example, Table 56.7 shows this effect for the Al/SiC tapered shaft. The loads considered are 100%, 50% and 0% of the value previously assumed. The frequencies were obtained for the lengths considered before. Note that the influence of the load is larger as the slenderness ratio increases. For the "short" shaft the load variation almost had no influence on the

frequency (0.9% increase when the load is set to zero). On the other hand, for the “long” shaft, the frequency increases by 27.5% when the load is set to zero. The dependency of these results on the shear coefficient is small. For the “short” shaft, using a value of 1.5, increases the first frequency by 2.6% when the load is 50% and 3.4% when the load is 0. For the values given in the literature these effects would be smaller.

## 56.4 Conclusions

It is seen that, for either homogeneous or non-homogenous material shafts, the slenderness ratio is important in determining a suitable model for calculating resonances. For short shafts the developed approach is more suitable for modeling and can give more accurate values for the frequencies.

As noted in a previous work of the authors utilizing long shafts and an “Euler-Bernoulli approach”, tapering leads to lower natural frequencies in both homogeneous and FGM cases. Here this is again observed for short shafts modeled using the “Timoshenko approach”.

It was found that the frequency results dependency on the shear coefficient is small, of the order of 5% for the fundamental one.

Also, the influence of the axial force on the frequency is less pronounced as the slenderness ratio decreases. For example, for a short tapered FGM shaft the maximum variation found was of the order of 3%.

## References

- Mazzei AJ, Scott RA (2012) On the effects of non-homogeneous materials on the vibrations and static stability of tapered shafts. *J Vib Control*. <http://jvc.sagepub.com/content/early/2012/02/22/1077546312438429.abstract>
- Ke L-L, Yang J, Kitipornchai S, Xiang Y (2009) Flexural vibration and elastic buckling of a cracked Timoshenko beam made of functionally graded materials. *Mech Adv Mater Struct* 16(6):488–502, <http://dx.doi.org/10.1080/15376490902781175>
- Eisenberger M (1995) Dynamic stiffness matrix for variable cross-section Timoshenko beams. *Commun Numer Methods Eng* 11(6):507–513, <http://dx.doi.org/10.1002/cnm.1640110605>
- Esmailzadeh E, Ohadi AR (2000) Vibration and stability analysis of non-uniform Timoshenko beams under axial and distributed tangential loads. *J Sound Vib* 236(3):443–456, <http://www.sciencedirect.com/science/article/pii/S0022460X00929997>
- Kerczek CH v (2012) <http://imechanica.org/node/11678>
- Saito H, Otomi K (1979) Vibration and stability of elastically supported beams carrying an attached mass under axial and tangential loads. *J Sound Vib* 62(2):257–266
- Banerjee JR, Kennedy D (1985) Response of an axially loaded Timoshenko beam to random loads. *J Sound Vib* 101(4):481–487
- Bishop RED, Price WG (1978) The vibration characteristics of a beam with an axial force. *J Sound Vib* 59(2):237–244
- Irie T, Yamada G, Takahashi I (1980) Vibration and stability of a non-uniform Timoshenko beam subjected to a follower force. *J Sound Vib* 70(4):503–512, <http://www.sciencedirect.com/science/article/pii/0022460X8090320X>
- Kounadis AN, Katsikadelis JT (1979) Coupling effects on a cantilever subjected to a follower force. *J Sound Vib* 62(1):131–139, <http://www.sciencedirect.com/science/article/pii/0022460X79905625>
- Cowper GR (1966) The shear coefficient in Timoshenko’s beam theory. *J Appl Mech* 33(2):335–340. <http://link.aip.org/link/?AMJ/33/335/1>, <http://dx.doi.org/10.1115/1.3625046>
- Miyamoto Y, Kaysser WA, Rabin BH, Kawasaki A, Ford RG (1999) *Functionally graded materials: design, processing and applications*, 1st edn. Springer, London
- Chiu TC, Erdogan F (1999) One-dimensional wave propagation in a functionally graded elastic medium. *J Sound Vib* 222(3):453–487, <http://www.sciencedirect.com/science/article/pii/S0022460X9892065X>
- Weaver W Jr, Timoshenko SP, Young DH (1990) *Vibration problems in engineering*, 5th edn. Wiley, New York
- Efunda (1999) [http://www.efunda.com/formulae/solid\\_mechanics/columns/intro.cfm](http://www.efunda.com/formulae/solid_mechanics/columns/intro.cfm)



# Chapter 57

## Modelling Friction in a Nonlinear Dynamic System via Bayesian Inference

P.L. Green and K. Worden

**Abstract** This work is concerned with the system identification of a real nonlinear system with Duffing-type and friction nonlinearities. With friction being a complex nonlinear phenomenon for which a variety of models have been developed, the identification problem investigated in this paper is one of model selection as well as parameter estimation. Consequently, through the comparison of experimental results with the output of various digital simulations the parameters of several different friction models (Coulomb, hyperbolic tangent and LuGre) are estimated using Bayesian inference in conjunction with Markov Chain Monte-Carlo methods. The performance of each model is then analysed using the Deviance Information Criterion which rewards the ability of the model to replicate the experimental behavior while penalising model complexity. The potential benefits of tackling model selection and parameter estimation problems using a Bayesian framework are discussed.

**Keywords** Nonlinear system identification • Bayesian • Markov chain Monte Carlo • Friction • Duffing

### 57.1 Introduction

This paper details the system identification of a real dynamic system with Duffing-type and friction nonlinearities. The modelling of friction in dynamic systems can be problematic because, as a result of its complex nature, there are many different friction models available in the literature. Consequently, the system identification of friction affected systems involves *model selection* as well as *parameter estimation*. Parameter estimation refers to the fact that, for any model, one must estimate the set of parameters which lead to the best match between model and experiment. The second part of the problem, model selection, arises in scenarios where several different models are available for investigation such that one has to infer which model is the most suitable for a particular problem. It should be noted that the nonlinear system studied in this paper has already been analysed using a deterministic identification approach in [1] but that the work in this article utilises a probabilistic, Bayesian approach.

At this point it is convenient to denote a certain model structure as  $\mathcal{M}_i$ ,  $\theta$  as the vector of parameters for that particular model and  $\mathcal{D}$  as some data describing the response of the real system. In the case detailed within this paper  $\mathcal{D}$  consists of an input  $\mathbf{y} = \{y(t), y(t + \Delta t), y(t + 2\Delta t), \dots\}$  and a measured response  $\mathbf{z} = \{z(t), z(t + \Delta t), z(t + 2\Delta t), \dots\}$ . Both  $\mathbf{y}$  and  $\mathbf{z}$  were measured experimentally at time intervals of  $\Delta t$ . Using a Bayesian framework, the parameter estimation problem can be written as follows:

$$P(\theta|\mathcal{D}, \mathcal{M}) = \frac{P(\mathcal{D}|\theta, \mathcal{M})P(\theta|\mathcal{M})}{P(\mathcal{D}|\mathcal{M})} \quad (57.1)$$

where the probability of realising some experimental data given a set of parameter values and model structure is given by  $P(\mathcal{D}|\theta, \mathcal{M})$  (termed the likelihood) and ones prior belief in the parameter values of model structure  $\mathcal{M}$  before the data  $\mathcal{D}$  was known is  $P(\mathcal{D}|\mathcal{M})$  (termed the prior). Consequently, for a specific model structure  $\mathcal{M}$ , evaluating  $P(\theta|\mathcal{D}, \mathcal{M})$  (termed the posterior) in equation (57.1) allows one to realise a probability density function for each parameter in the vector  $\theta$ .

---

P.L. Green (✉) • K. Worden  
Sheffield University, Sheffield, UK  
e-mail: [mep09plg@shef.ac.uk](mailto:mep09plg@shef.ac.uk); [k.worden@shef.ac.uk](mailto:k.worden@shef.ac.uk)

The denominator in Eq. (57.1) is termed the evidence and is used to normalise the posterior such that, being a probability distribution, it has an area of one. As a result, the evidence can be written as:

$$P(\mathcal{D}|\mathcal{M}) = \int_{-\infty}^{\infty} P(\mathcal{D}|\boldsymbol{\theta}, \mathcal{M})P(\boldsymbol{\theta}|\mathcal{M})d\boldsymbol{\theta}. \quad (57.2)$$

For a scenario where different model structures are available, the probability that the model  $\mathcal{M}_i$  is suitable given the data  $\mathcal{D}$  can also be written using Bayes rule:

$$P(\mathcal{M}_i|\mathcal{D}) = \frac{P(\mathcal{D}|\mathcal{M}_i)P(\mathcal{M}_i)}{P(\mathcal{D})} \quad (57.3)$$

thus allowing one to write the *relative* probability of two different models, given data  $\mathcal{D}$ , as:

$$\frac{P(\mathcal{M}_i|\mathcal{D})}{P(\mathcal{M}_j|\mathcal{D})} = \frac{P(\mathcal{D}|\mathcal{M}_i)P(\mathcal{M}_i)}{P(\mathcal{D}|\mathcal{M}_j)P(\mathcal{M}_j)} \quad (57.4)$$

where  $P(\mathcal{M}_i)$  and  $P(\mathcal{M}_j)$  represent ones prior beliefs in the suitability of each model (typically set equal to one another) and  $P(\mathcal{D}|\mathcal{M})$  is as defined in Eq. (57.2). Equation (57.4), which is referred to as Bayes factor, allows one to compare the suitability of different models relative to one another. Unfortunately, unless a small number of parameters are used, the multidimensional nature of the integral in Eq. (57.2) makes Bayes factor difficult to evaluate. While it has been suggested that this integral can be approximated using a Laplace approximation [2], recent work by Worden and Hensman [3] showed that, in the context of nonlinear dynamics, the problem of model selection can be tackled via a relatively simple model selection indicator termed the Deviance Information Criterion (originally proposed in [4]).

Before describing the Deviance Information Criterion (DIC) it is convenient to first define the deviance:

$$D(\boldsymbol{\theta}) = -2 \ln P(\mathcal{D}|\boldsymbol{\theta}) \quad (57.5)$$

where, as stated previously,  $P(\mathcal{D}|\boldsymbol{\theta})$  is the likelihood. The deviance is simply a measure of how well the model fits the data which, given that a Gaussian likelihood is used in this work (see Sect. 57.4.1), is proportional to the least squares difference between model and experiment. The DIC is then defined as:

$$\text{DIC} = 2E[D(\boldsymbol{\theta})] - D(\hat{\boldsymbol{\theta}}). \quad (57.6)$$

where

$$E[D(\boldsymbol{\theta})] = \int P(\boldsymbol{\theta}|\mathcal{D}, \mathcal{M})D(\boldsymbol{\theta})d\boldsymbol{\theta} \quad (57.7)$$

and

$$\hat{\boldsymbol{\theta}} = E[P(\boldsymbol{\theta}|\mathcal{D}, \mathcal{M})] = \int P(\boldsymbol{\theta}|\mathcal{D}, \mathcal{M})\boldsymbol{\theta}d\boldsymbol{\theta} \quad (57.8)$$

such that  $\hat{\boldsymbol{\theta}}$  represents the ‘best’ parameter estimate for model  $\mathcal{M}$ . The DIC is a model selection indicator which rewards the ability of the model to replicate the experimental data while penalising model complexity – for a more detailed discussion of the DIC the book [5] is recommended. Essentially, the lower the DIC, the more favorable the model. An approach for estimating  $E[D(\boldsymbol{\theta})]$  and  $D(\hat{\boldsymbol{\theta}})$  using Markov Chain Monte-Carlo (MCMC) methods is detailed in Sect. 57.4.2 of this work.

## 57.2 Nonlinear System

A schematic of the nonlinear system investigated in this paper is shown in Fig. 57.1. The ‘centre magnet’ is positioned such that it is free to slide along an aluminium rod via a set of linear bearings. The ‘outer magnets’ are positioned such that their poles oppose that of the centre magnet thus creating a magnetic restoring force on the centre magnet. Originally developed in the context of nonlinear energy harvesting, it is known that this restoring force can be closely approximated using a linear and cubic stiffness term (as is found in the hardening spring Duffing oscillator)[6]. A signal generator was used in conjunction with a PID controller to create a band limited white noise acceleration excitation. For a more detailed discussion of this experiment (which was also developed in the context of energy harvesting) the reader is directed towards Ref. [7].

### 57.3 Model

Defining  $z$  as the relative displacement between the shaker base and the centre magnet (such that  $z = x - y$ ), the equation of motion of the system shown in Fig. 57.1 is:

$$m\ddot{z} + c\dot{z} + kz + k_3z^3 + F = -m\ddot{y} - mg \quad (57.9)$$

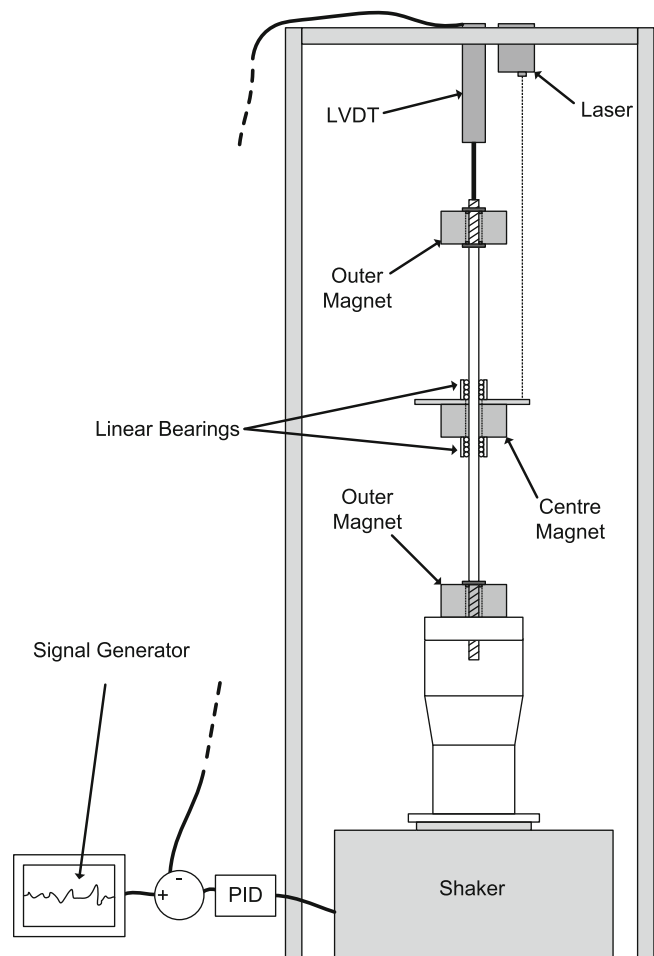
where  $m$  is the mass of the centre magnet,  $c$  is viscous damping,  $k$  is linear stiffness,  $k_3$  is nonlinear stiffness,  $g$  is the force due to gravity and  $F$  represents the force as a result of friction between the linear bearings and the aluminium rod. As mentioned previously, several different friction models were investigated – a description of which is given in the following sections.

#### 57.3.1 Coulomb

Using the Coulomb damping model, the force on the centre magnet as a result of friction is given by:

$$F = F_d \operatorname{sgn}(\dot{z}) \quad (57.10)$$

where  $F_d$  is a constant to be determined and  $\operatorname{sgn}$  represents the Signum function. While this model is relatively simple, difficulties can arise as a result of the discontinuity when  $\dot{z} = 0$ .



**Fig. 57.1** Schematic of experimental apparatus

### 57.3.2 Hyperbolic Tangent

The force due to friction according to the hyperbolic tangent model is given by:

$$F = F_d \tanh(\beta \dot{z}) \quad (57.11)$$

where  $F_d$  and  $\beta$  are constants to be determined. While the hyperbolic tangent model requires an extra parameter, it has the advantage that, by setting  $\beta$  to a relatively large value, it can approximate the Coulomb damping model without the presence of a discontinuity at  $\dot{z} = 0$ .

### 57.3.3 LuGre

The LuGre model [8] is based on the assumption that the interaction between two surfaces can be modelled as that of rigid bodies which make contact via a set of randomly distributed ‘bristles’. The average displacement of the bristles is modelled using:

$$\dot{\Theta} = \dot{z} - \frac{|\dot{z}|}{g(\dot{z})} \Theta \quad (57.12)$$

where  $\Theta$  is the average bristle displacement and  $g(\dot{z})$  is a function which is chosen depending on the material properties of the system. The friction force exerted on the mass is given by:

$$F = \sigma_0 \Theta + \sigma_1 \dot{\Theta} \quad (57.13)$$

where  $\sigma_0$  and  $\sigma_1$  are parameters to be found. One of the advantages of the LuGre model is its ability to account for the Stribeck effect (the phenomenon that, at low velocities, friction force decreases with increasing velocity). To account for the Stribeck effect the function  $g(\dot{z})$  will be defined as:

$$\sigma_0 g(\dot{z}) = F_c + (F_s - F_c) \exp\left(-(\dot{z}/\dot{z}_s)^2\right) \quad (57.14)$$

where  $F_s$  represents stiction force,  $F_c$  is the Coulomb friction level and  $\dot{z}_s$  is the Stribeck velocity. While this model requires the identification of five parameters ( $\sigma_0$ ,  $\sigma_1$ ,  $F_c$ ,  $F_s$  and  $\dot{z}_s$ ) it accounts for the majority of phenomenon associated with friction (friction lag, spring-like behavior in stiction and varying break-away force). This is discussed more in [8].

## 57.4 Bayesian Inference

### 57.4.1 Prior and Likelihood

Before inferring the posterior distribution in Eq. (57.1) one must first define the prior and likelihood functions. With regards to the likelihood, it is assumed that any errors in the measured signals are a consequence of measurement noise and that this noise has a Gaussian distribution. Consequently, if one were to measure one measurement point  $z$ , the likelihood is assumed to be:

$$P(\mathcal{D}|\boldsymbol{\theta}, \mathcal{M}) = \frac{1}{\sqrt{2\pi}\sigma} \exp\left(-\frac{1}{2\sigma^2}(z - \hat{z}(\boldsymbol{\theta}))^2\right) \quad (57.15)$$

where  $\hat{z}$  is the model output and  $\sigma$  is the variance of the measurement noise. This has the property that it is maximised when one has estimated the ‘best’ parameter vector  $\boldsymbol{\theta}$  as well as the correct noise variance  $\sigma$ . As a result, the noise variance can be included as one of the parameters to be identified. For the case where one has measured  $N$  different measurement points the likelihood is:

$$P(\mathcal{D}|\boldsymbol{\theta}, \mathcal{M}) = \prod_{i=1}^N \frac{1}{\sqrt{2\pi}\sigma} \exp\left(-\frac{1}{2\sigma^2}(z_i - \hat{z}_i(\boldsymbol{\theta}))^2\right) \quad (57.16)$$

$$= \left( \frac{1}{\sqrt{2\pi}\sigma} \right)^N \exp \left( -\frac{1}{2\sigma^2} J(\theta) \right) \quad (57.17)$$

where

$$J(\theta) = \sum_{i=1}^N (z_i - \hat{z}_i(\theta))^2. \quad (57.18)$$

The prior distribution for each parameter was chosen to be uniform between certain limits. As it was known that none of the parameters could be negative, the lower bound of each distribution was set equal to zero. The higher bound was chosen such that it was a factor of 1,000 larger than the best parameter estimates realised in [1]. While this may not seem like a particularly informative choice, it is important to note that in cases where large amounts of experimental data are available (30s of data sampled at 1,500 Hz in this case) then the likelihood will dominate the prior. This has an intuitive quality as it suggests that the more test data one has available, the less that one has to rely on their previous knowledge of the problem.

### 57.4.2 Markov Chain Monte-Carlo

As was stated previously, the evidence term in Eq. (57.1) is difficult to compute. Consequently, it is more common to sample from a distribution proportional to the posterior using a MCMC method such that the resulting histograms are approximations of the marginalised parameter distributions.

In this case the Metropolis algorithm was utilised – it is assumed that the reader is familiar with this method (for a detailed explanation of this and other Monte Carlo methods Ref. [9] is recommended). In the following examples each Markov chain was initiated from the best parameter estimates realised in [1]. A hyper-dimensional Gaussian proposal density was chosen whose covariance matrix was chosen manually such that the resulting Markov chain had a reasonably high acceptance ratio while avoiding random walk behavior (as this explores the parameter space relatively slowly [9]). While there are MCMC methods available which are designed such that random walk behavior is avoided (many of which are described in [10]), their application to this problem will be the focus of future work.

Using the successive parameter vectors realised by the MCMC algorithm (written as  $\{\theta^{(1)}, \theta^{(2)}, \dots, \theta^{(N)}\}$ ) then, the optimum parameter vector  $\hat{\theta}$  can be approximated by:

$$\hat{\theta} \approx \frac{1}{N} \sum_{i=1}^N \theta^{(i)} \quad (57.19)$$

while the expected deviance can be approximated by:

$$E[D(\theta)] \approx \frac{1}{N} \sum_{i=1}^N D(\theta^{(i)}) \quad (57.20)$$

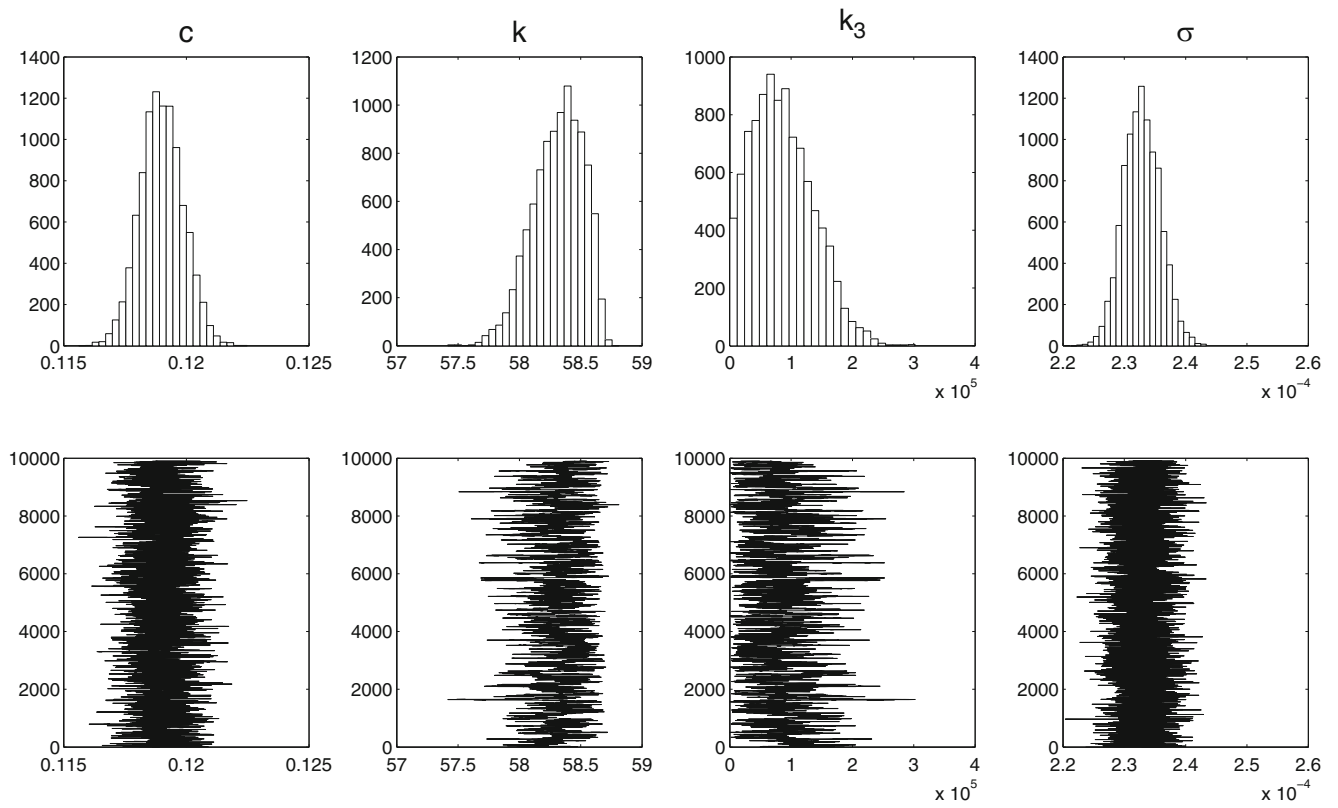
thus allowing one to approximate a value of the DIC (Eq. (57.6)).

## 57.5 Results

In all of the following cases, 100,000 iterations of the Metropolis algorithm was used. After removal of the ‘burn in’ period every tenth point of the Markov chain was sampled to increase the independence of subsequent samples from one another. The resulting downsampled Markov chains are shown in all of the subsequent figures.

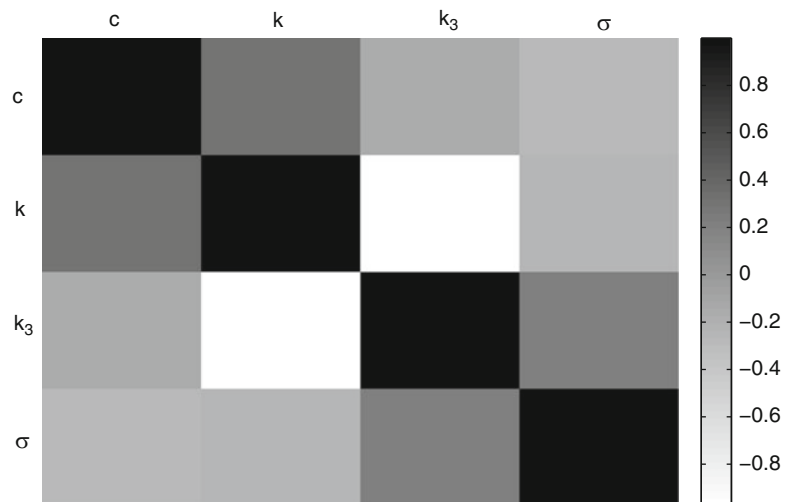
### 57.5.1 Viscous

Initially, the simulated response of the system with no friction model was investigated (such that all mechanical losses were modelled using a viscous damper). Figure 57.2 shows the resulting approximations of the parameter probability density



**Fig. 57.2** Parameter distributions for viscous damping model

**Fig. 57.3** Covariance matrix for viscous damping model



functions. It is interesting to note that there appears to be a dependence between the linear and nonlinear stiffness terms ( $k$  and  $k_3$ ). Indeed, one of the advantages of using an MCMC method is that, by calculating the covariance of the resulting chains, one can form an approximation of the parameter covariance matrix. This is shown (normalised) in Fig. 57.3 where one can see that there is a negative correlation between  $k$  and  $k_3$ . This is to be expected as it is known that approximation of the hardening-spring Duffing oscillator by equivalent linearisation is achieved via an increase in linear stiffness (see [11] for more details).



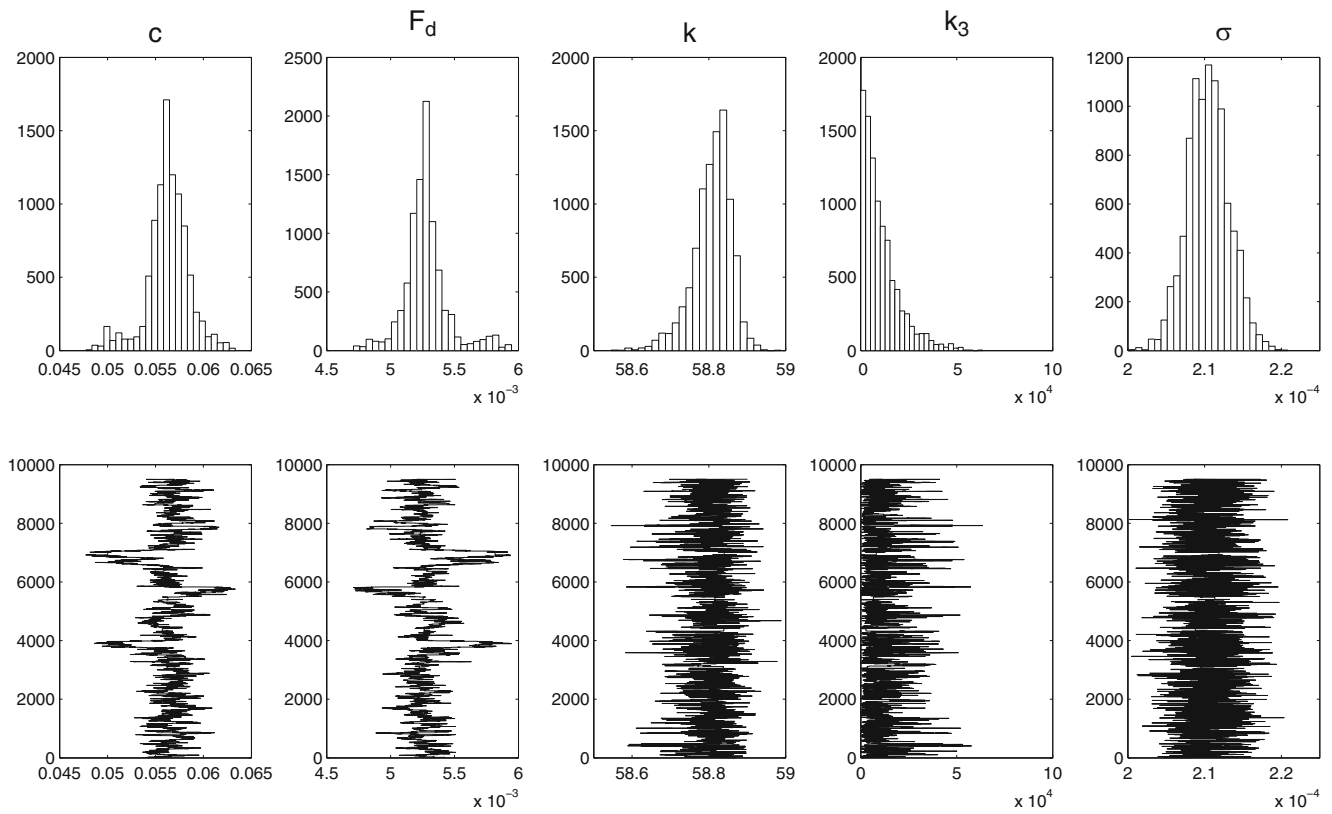
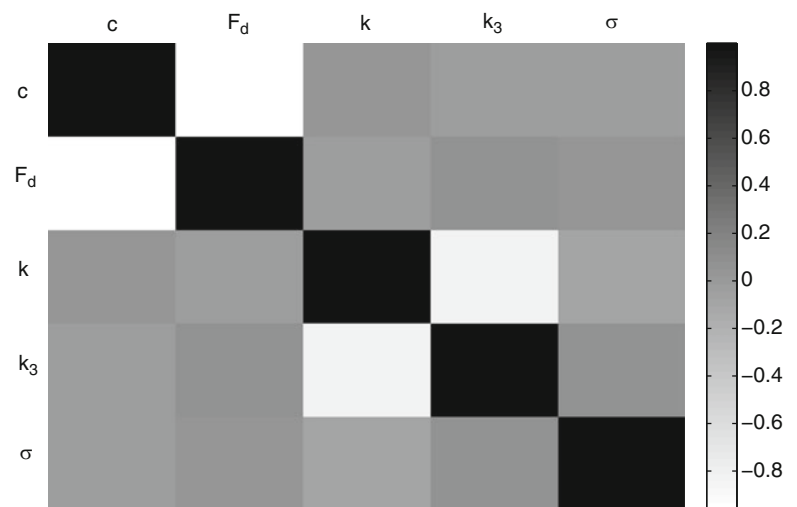


Fig. 57.4 Parameter distributions for Coulomb damping model

Fig. 57.5 Covariance matrix for Coulomb damping model



### 57.5.2 Coulomb

The approximate parameter distributions for the Coulomb damping model are shown in Fig. 57.4. It is interesting to note that, at some points, the chain jumps to relatively low values of viscous damping while simultaneously jumping to higher values of Coulomb damping. This is confirmed by a strong negative correlation between  $c$  and  $F_d$  in the covariance matrix (Fig. 57.5). This can be explained the fact that viscous and Coulomb damping are both representing loss mechanisms such that, to achieve a good match between simulation and experiment, when the energy lost through one mechanism is reduced the energy loss through the other mechanism must be increased to compensate. As well as this, it is evident that there is still a negative correlation between the linear and nonlinear stiffness terms.

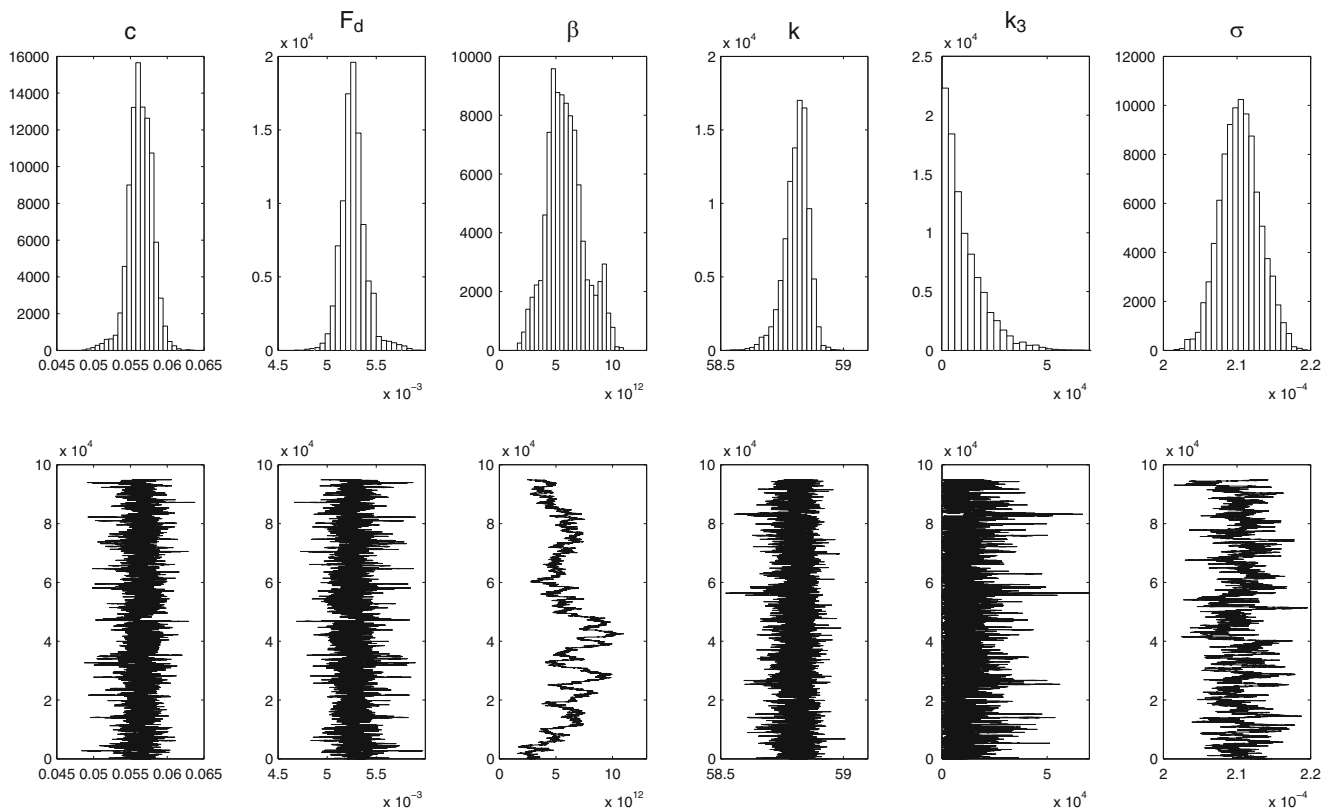


Fig. 57.6 Parameter distributions for hyperbolic tangent model

### 57.5.3 Hyperbolic Tangent

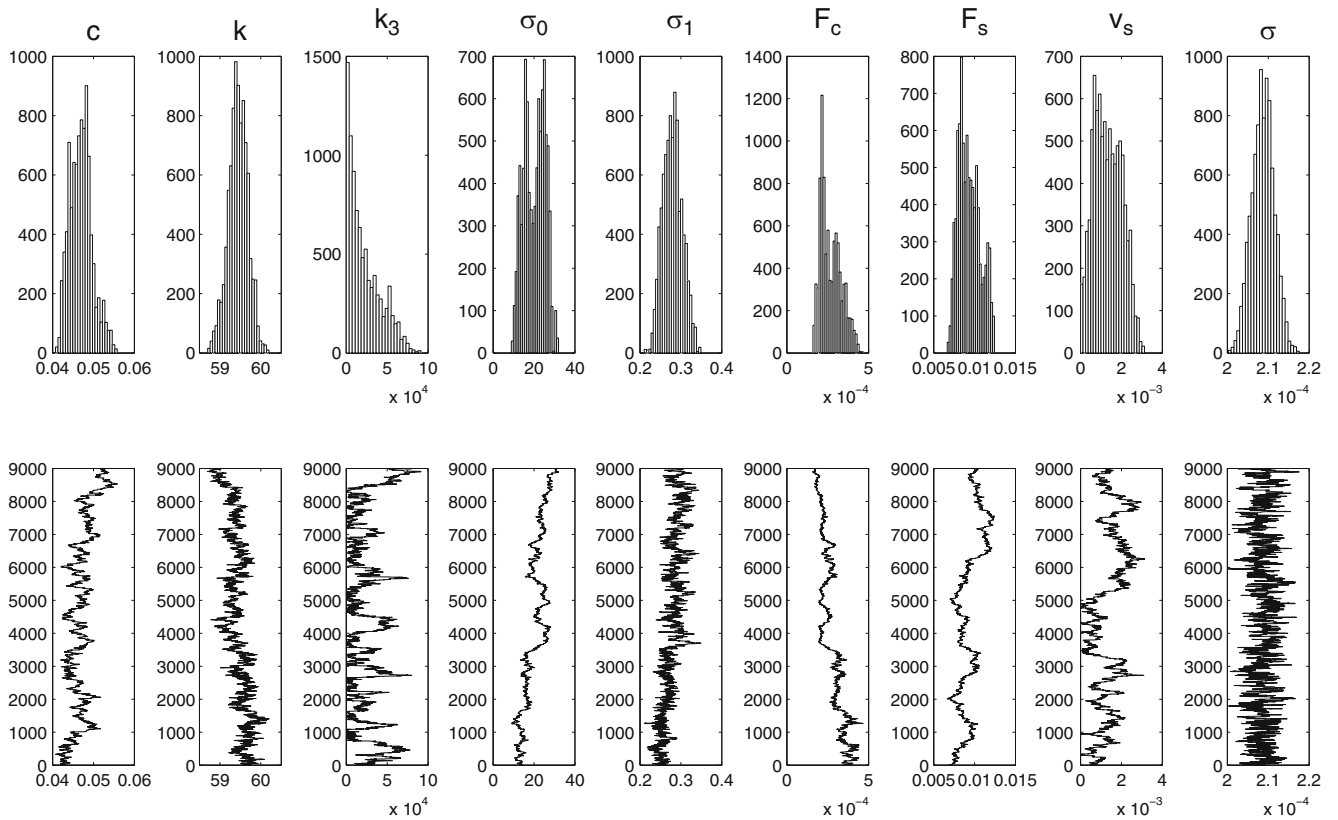
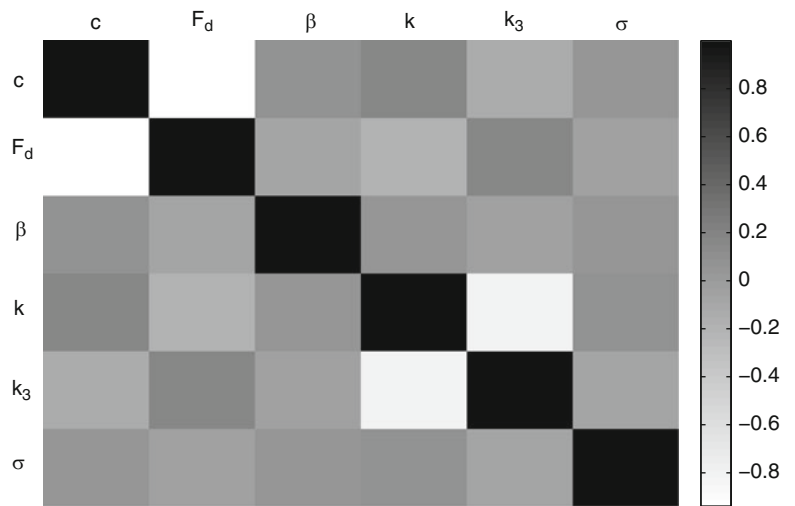
Figure 57.6 shows the parameter distributions for the hyperbolic tangent model. It is interesting to note that the chain representing values of  $\beta$  does not appear to be stationary but looks to be exhibiting random walk behavior. This was found to occur despite giving the proposal density of  $\beta$  a large variance – indeed in Fig. 57.6 it can be seen that the range of values covered by the chain is very large ( $\approx 5 \times 10^{12}$ ). This reveals two very important aspects about the real system. Firstly, the optimum value of  $\beta$  is very large. This means that the simulation matches the experimental behavior best if the hyperbolic tangent model is forming a close approximation to the Coulomb damping model. Secondly, the fact that random walk behavior occurs despite a large proposal density variance indicates that the response of the model is not *sensitive* to large changes in  $\beta$ . As long as  $\beta$  is large enough to allow a close approximation of Coulomb damping then its exact magnitude is of little significance. This type of information is valuable in a scenario where one is conducting a sensitivity analysis as it allows one to save computation time by holding parameters with little effect on the model constant.

With regards to the covariance matrix, once again it can be seen that there is a negative correlation between viscous damping and Coulomb damping; and linear stiffness and nonlinear stiffness (Fig. 57.7).

### 57.5.4 LuGre

Finally, Fig. 57.8 shows the parameter histograms for the LuGre model. It is clear from Fig. 57.8 that some of the Markov chains do not appear to be stationary ( $\sigma_0$  for example). This could be for two reasons. Firstly, it is possible that the proposal density covariance matrix was chosen such that some regions of the parameter space are being explored very slowly. Secondly, it could be that the parameter in question is a *nuisance parameter* – it has very little effect on the ability of the

**Fig. 57.7** Covariance matrix for hyperbolic tangent model



**Fig. 57.8** Parameter distributions for LuGre model

model to replicate the experiment. Unfortunately, one of the disadvantages of using the Metropolis algorithm in this scenario is the fact that manually tuning the transition probability density function (PDF) covariance matrix can be difficult, especially for models with parameters whose physical significance may not be obvious. Consequently, without further investigation it is not clear whether the nonstationary Markov chains shown in Fig. 57.8 are as a result of the model possessing nuisance parameters or of a poorly chosen transition PDF covariance matrix. Overcoming this difficulty through the use of different MCMC methods is left as a topic of future work.

## 57.6 Model Comparison

The normalised mean-square error was used to quantify the difference between the model and experimental response:

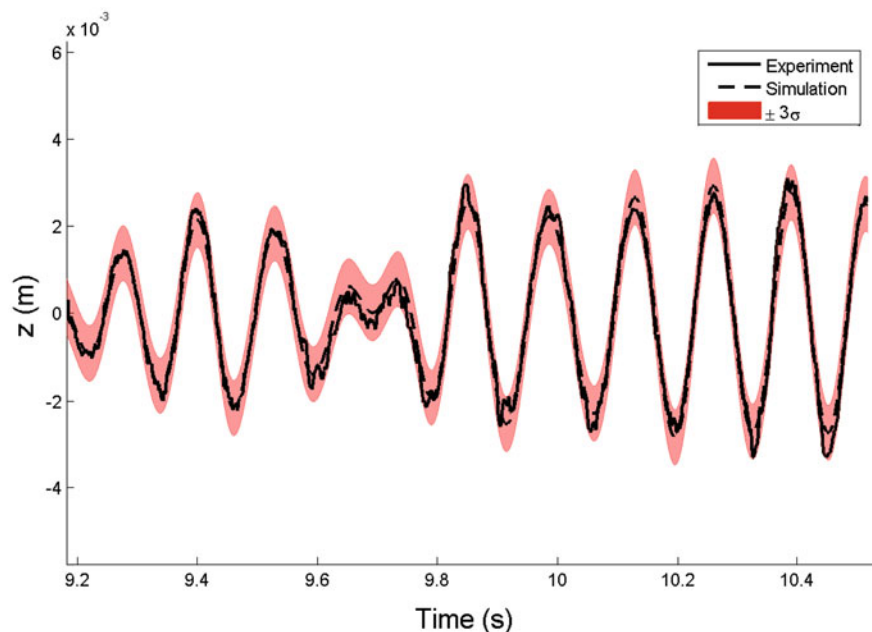
$$\begin{aligned} \text{NMSE} &= \frac{100}{N\sigma_z^2} J(\boldsymbol{\theta}) \\ &= \frac{100}{N\sigma_z^2} \sum_{i=1}^N (z_i - \hat{z}_i(\boldsymbol{\theta}))^2. \end{aligned} \quad (57.21)$$

This has the property that, if the model simply replicated the mean value of the experimental results then  $\text{NMSE} = 100$ . From experience it is known that  $\text{NMSE} < 5$  can be considered a good match between model and experiment. Table 57.1 shows the NMSE and DIC for each of the friction models. The DIC for the LuGre model is not shown here because, as discussed previously, some of the Markov chains did not appear to have become stationary. The viscous damping model has the largest NMSE and DIC values out of all the models investigated. This indicates that the improved model performance that is achieved through the inclusion of friction effects outweighs the increase in model complexity. The NMSE of the Coulomb and hyperbolic tangent models are very similar because, as was stated previously, the parameters of the hyperbolic tangent were such that it formed a close approximation to the Coulomb damping model. It is interesting to observe that the hyperbolic tangent model actually has a lower value of DIC than the Coulomb model even though it delivered a very similar NMSE while requiring an additional parameter. This may be because Table 57.1 is in fact showing *approximations* of the DIC (realised using the samples from the Metropolis algorithm). This is something which will be investigated in future work.

Figure 57.9 demonstrates the quality of the match between the Coulomb damping model the experiment time histories. The bounds of the shaded area are  $\pm 3\sigma$  from the model response  $\hat{z}(\boldsymbol{\theta})$ . Consequently, the shaded region represents the maximum difference that one would expect to see between model and experiment as a result of measurement noise (predicted to a 99.7% confidence level).

**Table 57.1** Normalised mean-square error and deviance information criterion for each friction model

Model	NMSE	DIC
Viscous	5.835	$-5.8357 \times 10^5$
Coulomb	2.792	$-6.2875 \times 10^5$
Hyperbolic tangent	2.793	$-6.2882 \times 10^5$



**Fig. 57.9** Experiment and simulation time histories using ‘best’ parameter estimates for the Coulomb damping

## 57.7 Conclusions

This paper is concerned with the development of a physical law based model of a nonlinear friction affected system using Bayesian system identification methods. With friction being a complex nonlinear phenomenon for which many mathematical models are available, the identification problem involves model selection as well as parameter estimation. Several friction models (Coulomb, hyperbolic tangent and LuGre) are compared using the Deviance Information Criteria – a measure which penalises model complexity while rewarding model fidelity. As well as this, it is shown that parameter estimation using a Bayesian framework can also reveal important aspects with regards to the parameter interactions of each model. Future work will be directed towards investigating whether other, more complex, Markov-Chain Monte Carlo algorithms can be used within a Bayesian framework to aid in the identification of nuisance parameters.

## References

1. Green PL, Worden K, Atallah K, Sims ND (2012) The modelling of friction in a randomly excited energy harvester. In: Proceedings of ISMA 2012, conference on noise and vibration engineering, Leuven, 20–22 Sept 2010
2. Beck JL, Katafygiotis LS (1998) Updating models and their uncertainties. I: bayesian statistical framework. *J Eng Mech* 124(4):455–461
3. Worden K, Hensman JJ (2012) Parameter estimation and model selection for a class of hysteretic systems using bayesian inference. *Mech Syst Signal Process* 32:153–169
4. Spiegelhalter DJ, Best NG, Carlin BP, Van Der Linde A (2002) Bayesian measures of model complexity and fit. *J R Stat Soc B* 64(4):583–616
5. Gelman A, Carlin JB, Stern HS, Rubin DB (2003) Bayesian data analysis. Chapman and Hall/CRC, Boca Raton/Fla
6. Mann BP, Sims ND (2009) Energy harvesting from the nonlinear oscillations of magnetic levitation. *J Sound Vib* 319(1–2):515–530
7. Green PL, Worden K, Atallah K, Sims ND (2012) The benefits of duffing-type nonlinearities and electrical optimisation of a mono-stable energy harvester under white gaussian excitations. *J Sound Vib* 331(20):4504–4517
8. De Wit CC, Olsson H, Astrom KJ, Lischinsky P (1995) New model for control of systems with friction. *IEEE Trans Autom Control* 40(3): 419–425
9. MacKay DJC (2003) Information theory, inference, and learning algorithms. Cambridge University Press, Cambridge
10. Neal RM (1993) Probabilistic inference using markov chain monte carlo methods, 1993
11. Worden K, Tomlinson GR (2000) Nonlinearity in structural dynamics: detection, identification and modelling. Taylor and Francis, IOP Publishing Ltd, London

# Chapter 58

## Optimum Load for Energy Harvesting with Non-linear Oscillators

A. Cammarano, A. Gonzalez-Buelga, S.A. Neild, D.J. Wagg, S.G. Burrow, and D.J. Inman

**Abstract** A viable way to increase the band-width of a vibration-based energy harvester is exploiting the frequency response of non-linear oscillators. In the literature there are several works on resonating energy harvesters featuring non-linear oscillators. In the majority of these works, the harvester powers purely resistive loads. Given the complex behaviour of non-linear energy harvesters, it is difficult to identify the optimum load for these kind of devices. The aim of this work is to find the optimal load for a non-linear energy harvester in the case of purely resistive loads. The work, following the analysis of a non-linear energy harvesting with hardening compliance, introduces a methodology based on numerical continuation which can be used to find the optimum load once the characteristics of device as well as the excitation is known.

**Keywords** Energy harvesting • Non-linear dynamics • Optimization • Continuation • Electrical load

### 58.1 Introduction

The advance of modern electronics and the decrease in their power demand has enabled a wide range of new wireless applications such as distributed sensor networks [1]. In this scenario, the possibility of powering these systems by harvesting energy from the environment has become a viable alternative to the use of batteries. Power-autonomous systems powered by ambient energy have been reported in several works in literature (see for example [1, 2]), while potential new applications continue to emerge.

The ability to harvest ambient energy depends largely on the application and in particular on the form and level of energy available. In previous works these and other authors presented some devices able to harvest energy from vibrations [3–5]. In particular, the device presented in [4, 5] uses high permeability magnetic materials which gives the device a highly non-linear compliance characteristic. The use of such material enables high magnetic loading of the transduction mechanism: magnetic loading is a measure of the utilization of the magnetic materials and a high value (i.e. high flux density) is desirable since it improves the efficiency for a given electro-mechanical coupling coefficient by minimizing the effect of certain parasitic loss mechanisms (e.g. coil resistance) and results in a smaller transducer for a given power.

Incorporating high permeability materials into the armature and stator structure produces reluctance forces which sum with the mechanical compliance to produce a non-linear characteristic. Vibration-based energy harvesters utilising linear oscillators only provide useful levels of output power when excited at their mechanical resonance. The resonance bandwidth is generally narrow and thus the harvester must be carefully tuned to the input frequency [6–10]. Non-linear oscillators are well known to exhibit a wider bandwidth and hence it may be possible to exploit this feature to maximize the harvestable energy where the source vibrations vary in frequency over time. Several authors have explored the advantages of non-linear oscillators for energy harvesting [5, 11–13], and demonstrated the potential benefits of this technology.

Unlike the linear energy harvesters, the modelling and the simulation of these devices is more complicated, making it difficult to find the set of optimal parameters (mechanical and electrical) which enables maximum energy generation. In this work an initial attempt to find the optimum load for an energy harvester featuring a hardening spring is shown. The method introduced is general and although applied to one parameter, can be easily extended to the other parameters.

---

A. Cammarano (✉) • A. Gonzalez-Buelga • S.A. Neild • D.J. Wagg • S.G. Burrow • D.J. Inman  
University of Bristol, Bristol, UK  
e-mail: [andrea.cammarano@bristol.ac.uk](mailto:andrea.cammarano@bristol.ac.uk)



In the next section, a short description of the load optimization for linear energy harvesting is provided. Insights of the effect of the load on the behaviour of the mechanical oscillator is also given together with some considerations on the optimum value of resistance. These considerations will be used both as a comparison for the non-linear case and as a useful tool to better understand the concept of optimum load.

In the following sections the main difference between the linear and the non-linear case are evidenced and a new method for investigating the optimum parameters is introduced. A discussion of the results follows and the potential of the method to investigate other parameters is highlighted.

## 58.2 Optimum Resistance: Linear

The concept of energy harvesting from vibrations relies on the fact that the energy of the primary structure can be transferred to a transducer, which converts it into electric energy. For this purpose an oscillator tuned to the frequency of excitation can be used. In other words a linear energy harvester can be thought of as a base-excited oscillator with an extra internal component which represents the interaction of the moving mass with the electromagnetic field (see Fig. 58.1). This simplified model is described by

$$m\ddot{x} + c\dot{x} + kx = -m\ddot{y} + F_e, \quad (58.1)$$

where  $m$  is the mass of the oscillator,  $c$  is the mechanical damping,  $k$  the stiffness of the spring. The device is base excited: the variable  $x$  measures the relative distance between the harvester mass and the base and  $y$  is the displacement of the moving base relative to inertial reference frame. The force  $F_e$  represents the electric force reflected back on the mass of the harvester. The electromagnetic force depends on the current induced in the coil by the movement of mass and can be written as follows

$$F_e = -\theta i. \quad (58.2)$$

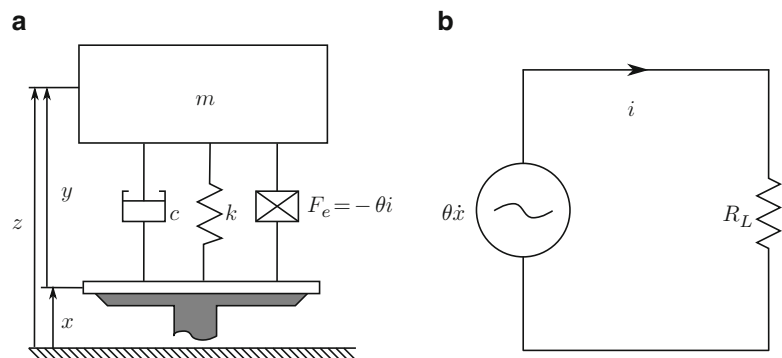
where  $\theta$  is a proportional constant called *electromechanical constant*. If the terminals of the coil are not connected to any circuit, ideally no current can pass through the coil and a tension proportional to the velocity of the coil is measured  $v = \theta\dot{x}$ . When the coil is connected to a purely resistive load, the value of  $i$  can be evaluated by using Kirchhoff's second law,

$$\theta\dot{x} = R_L i. \quad (58.3)$$

Using Eqs. 58.2 and 58.3, it is possible to relate the electromagnetic force to the velocity of the harvester mass. The expression obtained, substituted in Eq. 58.1 leads to

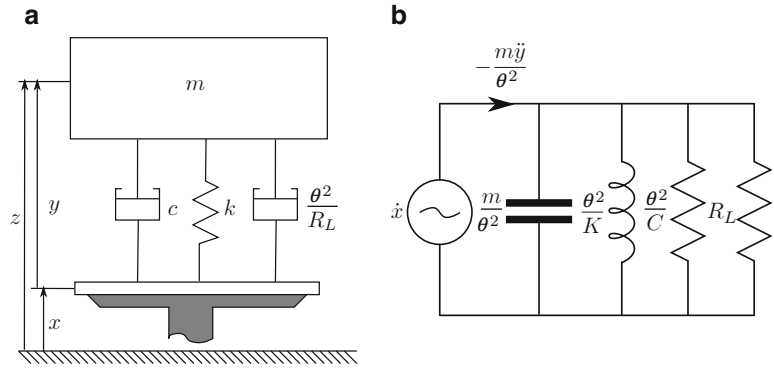
$$m\ddot{x} + \left(c + \frac{\theta^2}{R_L}\right)\dot{x} + kx = -m\ddot{y}. \quad (58.4)$$

By inspection of Eq. 58.4, it can be seen that the electromagnetic interaction, in this simple case, is perceived as a damping force from the harvester mass. Figure 58.2a represents the schematic of the system as an equivalent mechanical oscillator with two dampers in series. Using the *mobility analogy* on this system it can be shown that the circuit in Fig. 58.2b is the electrical equivalent to Fig. 58.2a. In the analogy the current circulating in the circuit is proportional to the force applied to



**Fig. 58.1** Schematic of a linear energy harvester powering a purely resistive load

**Fig. 58.2** Mechanical (a) and electrical (b) analogy of the energy harvester with a purely resistive load



the system and the voltage generated is proportional to the velocity. Applying Thevenin's theorem to the circuit it can be proved that the maximum energy dissipated in the load is obtained when the value of  $R_L$  is equal to  $\theta^2/c$ . This same result can be obtained analytically applying the Fourier transform to Eq. 58.4.

$$\left(m\omega^2 + \left(c + \frac{\theta^2}{R_L}\right)j\omega + k\right)X(\omega) = m\omega^2Y(\omega). \quad (58.5)$$

Finding the value of  $X(\omega)$  from Eq. 58.5 and substituting into Eq. 58.3 the Fourier transform of the current can be obtained. The average of the power dissipated in the load in a cycle can be evaluated as

$$P = \frac{1}{2}R_L I^2 = \frac{(\theta m \omega^3 |Y(\omega)|)^2}{R_L \left[ (k - m\omega^2)^2 + \left(c + \frac{\theta^2}{R_L}\right)\omega^2 \right]}. \quad (58.6)$$

The value of  $R_L$  which allows for the power in the load to reach its maximum can be found using the Fermat's theorem on the stationary points for n-dimensional functions

$$\left\{ \frac{\partial P}{\partial R_L}, \frac{\partial P}{\partial \omega} \right\} = \mathbf{0} \quad \Leftrightarrow \quad \left\{ R_L = \frac{\theta^2}{c}, \omega = \sqrt{\frac{k}{m}} \right\}, \quad (58.7)$$

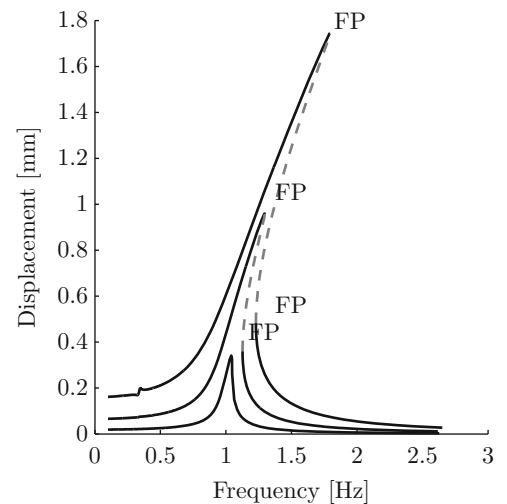
which means that the energy harvester gives the maximum power to the load if operated at its natural frequency and that the losses in the electrical resistance and in the mechanical damping have to be equal. A more exhaustive discussion about the optimum load for linear energy harvesters can be found in [14]. This result has the important implication that if the natural frequency of the harvester does not match the frequency of excitation the power conveyed to the load is very limited. For this reason many researchers have tried to extend the frequency range of operability of the harvester by increasing the bandwidth over which high amplitude oscillations occur.

### 58.3 Optimum Resistance: Non-linear

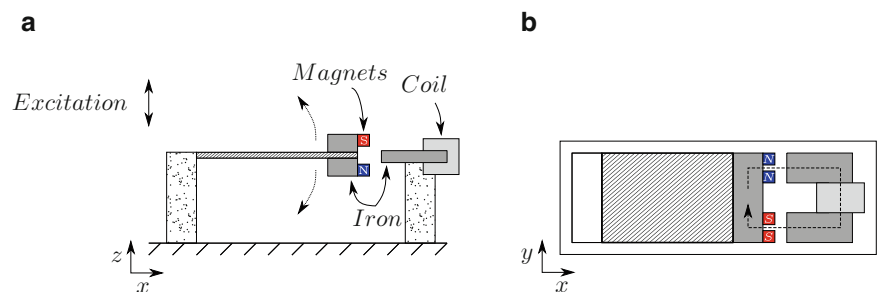
As previously mentioned, one method to expand the operational bandwidth is to exploit the behaviour of non-linear oscillators. In fact, non-linear oscillators have the capability to respond with high amplitude oscillations over a wider range of frequencies, as showed in [4, 5]. To find the optimum resistance, the procedure used for the linear case cannot be used and approximated methods become necessary.

Besides the difficulties in finding the optimum value of resistance, when the oscillator is non-linear there is a more important problem: what is optimum for a non-linear energy harvester? The losses (both electrical and mechanical) on a linear oscillator effect only the transmissibility and only have a marginal effect on the resonant frequency of the oscillator. The effect of the losses in non-linear harvesters is far more dramatic. Not only the height and the position of the peak is influenced but its shape and its stability is affected as well. Moreover, changing the level of excitation, the frequency response (see Fig. 58.3) of the system changes as well: as a consequence the optimum resistance is a function of the forcing term also. This means that different optimum loads exist for different level of excitations.

**Fig. 58.3** Effect of the level of excitation on the frequency response of the non-linear oscillator



**Fig. 58.4** Schematic of the non-linear harvester: lateral (a) and top view (b). The dashed line in figure is representative of the magnetic flux [3]



In this work a method based on numerical continuation is proposed. The method is described in the following section and its application to a non-linear energy harvester with a hardening spring is shown. A schematic of the energy harvester used in the application is shown in Fig. 58.4. The device is made of a cantilever beam with an harvester mass at the tip. The harvester mass is also the armature of an electromagnetic transducer: it is made of two bars of iron and four magnets. When the beam oscillates, the magnets moves in respect with the iron core which passes through the coil (see Fig. 58.4) and the magnetic circuit is closed. This happens twice during a full oscillation of the beam. The magnet polarity is such that the direction of the magnetic flux is reversed between the first and the second time the magnetic circuit is closed. For more details see [5].

The force between the magnets mounted on the armature and the iron stator depends on the relative distance between the two components. It has been proved experimentally that this force is in phase with the displacement and can be approximated with a cubic polynomial. The differential equation which describes the system can be written as follows

$$m\ddot{x} + \left(c + \frac{\theta^2}{R_L}\right)\dot{x} + kx + k_{nl}x^3 = -m\ddot{y}. \quad (58.8)$$

This equation is very similar to Eq. 58.4, except that the spring characteristics presents an extra non-linear term. The effect of this term can be observed in Fig. 58.3, where it can be seen that unlike the linear case, the peak of the frequency response presents a folding and, when amplitude of excitation is high enough, one side of the peak becomes unstable and two folding points appear. In this region, for a fixed value of frequency and amplitude of excitation, three limit cycles exists: two stable and one unstable. The initial condition determines which of the two stable limit cycles the system will be attracted to. Since the voltage produced by the harvester depends linearly on the velocity, high amplitude oscillations are to be preferred. For low level excitation, the response of the system is very close to the response of the linear system and the non-linear term can be neglected here: the considerations made for the linear system still hold. When the level of excitation is higher and the unstable branch of the response appears, it can be observed that the maximum amplitude of oscillation is very close to the folding point. Therefore, for the sake of simplicity, in the method shown in the next section, the maximum amplitude of oscillation will be approximated with the folding point.

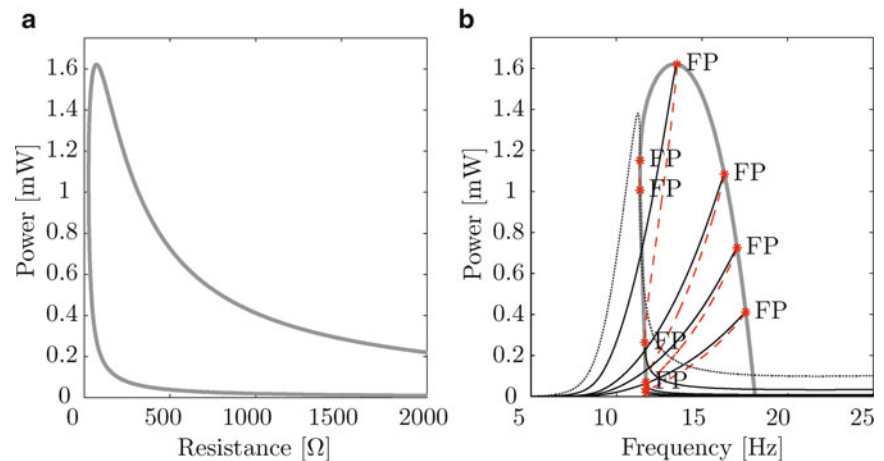
## 58.4 Continuation Method

The optimization method presented in this section is based on numerical continuation and it has been performed with the software Auto07P [15]. Numerical continuation is a numerical method used to investigate the response and bifurcations of a non-linear system. Specifically, solution branches are traced out in a predictor-corrector manner as the system parameters are changed (e.g., the forcing frequency). By tracking the solutions of a system in this manner, it is possible to track the evolution of the solution as the load resistance changes, and so determine how the power dissipated in the resistive load is affected. Numerical continuation has been successfully applied to a wide range of different ordinary differential equations, but to our knowledge, this technique has never been applied to vibration-based energy harvesters.

Auto07P is a software which implements the continuation technique and allows one to continue periodic orbits. In the case of periodic orbits, an initial solution has to be provided. The initial solution has been computed by integration of the differential equation with the *ode45* routine provided by Matlab. The resistance for the first integration has been set to 1 M $\Omega$  to simulate a condition of open-circuit.

The evolution of this periodic orbit is then evaluated with Auto07P as the frequency changes. The curves obtained are shown in Fig. 58.3. When the amplitude of excitation is the higher, the response clearly shows two folding points. As previously discussed, in this case, the highest amplitude of oscillation occurs very close to the first folding point. On the other hand, the maximum power is expected to occur in the region where the maximum level of oscillation is reached. Following these considerations, the folding point is continued considering the resistance as free parameter (that is the parameter which is changed during the continuation). For each value of resistance the power dissipated in the load is computed and shown in Fig. 58.5. In particular Fig. 58.5a shows the power estimation for all the values of resistance considered. It can be seen that for each resistance two values of power are found: one is relative to the lower folding point the other to the higher folding point. For resistance values lower than 24  $\Omega$  no solution is found: this is due to the fact that the resistance is very low and therefore the damping very high. That oscillator is heavily damped and the oscillation becomes so small that the contribution of the non-linear term to the frequency response remains negligible. For values of resistance close to the 24  $\Omega$  the folding point and the maximum of the peak move apart and the error between the power evaluated at the folding point and the maximum power increases. Figure 58.5b shows the frequency-power curves for different values of resistance. The peak on the left (dotted in figure) has been computed using a value of  $R_L$  equal to 26  $\Omega$ .

As the resistance increases the system becomes less damped and the amplitude of the oscillation increases. The folding point moves toward the maximum of the response and the maximum power occurs very close to this point. In all the other curves no appreciable difference can be seen between the maximum power and the power estimated at the folding point. If the resistance increases above the optimum value, the amplitude of oscillation does not increase indefinitely because it is limited by the mechanical damping. On the other hand the resistance is increasing and since the power can be evaluated as  $P = 1/2 V^2/R_L$ , the power available for the load decreases. Physically this is due to the fact that the value of the current circulating in the circuit is lower, which also explains why the mechanical system is becomes less affected by the electromagnetic force.



**Fig. 58.5** Dependency of the power on the resistance (a): the maximum value of power is reached for  $R_L = 71 \Omega$ . Power vs frequency plot for different values of resistances (b): the grey lines is the envelope of the position of the folding points

## 58.5 Conclusion and Future Work

This work investigates the optimum load for energy harvesters. After a brief recap of the techniques available to find the optimum resistive load for a linear energy harvester, a method to extend the concept of optimum load to non-linear energy harvesters has been shown. The motivation for this work is the increasing research on non-linear energy harvesters. The use of non-linearity in these generators is becoming more and more popular, thank to their natural capability to respond with high amplitude oscillations in a wider range of frequencies than their linear counterpart.

The method suggested in this paper is based on the numerical continuation of the differential equation which describes the behaviour of the harvester. Due to the complexity of the problem the use of a few simplification are made. Nevertheless, for the type of harvester considered, the optimum resistive load was successfully computed and the accuracy of the results have been proved to be quite high. Therefore the method is believed to be suitable to provide a good estimation of the optimum load.

The results have been shown just for a purely resistive load but other, more complex type of loads can be considered as well. In fact it is intention of the author to extend the study to reactive and non-linear loads as well, in the attempt to simulate more realistic scenarios.

The authors wish to acknowledge the support of the Engineering and Physical Sciences Research Council (EPSRC) for supporting this work through grant EP/J008532/1

## References

1. Beeby S (2008) Self-powered autonomous wireless sensor node using vibration energy harvesting. *Meas Sci Technol* 19(125202):125202
2. Roundy S, Wright PK (2004) A piezoelectric vibration based generator for wireless electronics. *Smart Mater Struct* 13(5):1131–1142
3. Cammarano A, Burrow SG, Barton DAW (2010) An energy harvester with bistable compliance characteristics. In: *ASME IDETC/CIE 2010*, Montreal, Canada
4. Burrow SG, Clare LR (2007) A resonant generator with non-linear compliance for energy harvesting in high vibrational environments. In: *IEMDC, Electrical Machines and Drives Conference, 2007*, Antalya, Turkey, 1:715–720
5. Cammarano A, Burrow SG, Barton DAW (2011) Modelling and experimental characterization of an energy harvester with bi-stable compliance characteristics. *Proc Inst Mech Eng I* 225(4):475–484
6. Williams CB, Yates RB (1996) Analysis of a micro-electric generator for microsystems. *Sens Actuator* 52(1–3):8–11
7. Williams MS, Blakeborough A (2001) Laboratory testing of structures under dynamic loads: an introductory review. *Philos Trans* 359: 1651–1669
8. Baker J, Roundy S, Wright P (2005) Alternative geometries for increasing power density in vibration energy scavenging for wireless sensor networks. In: *3rd international energy conversion engineering conference*, San Francisco, pp 1–12
9. Stephen NG (2006) On energy harvesting from ambient vibration. *J Sound Vib* 293(1–2):409–425
10. Renno JM, Daqaq MF, Inman DJ (2009) On the optimal energy harvesting from a vibration source. *J Sound Vib*, 320(1–2):386–405
11. Mann BP, Sims ND (2009) Energy harvesting from the nonlinear oscillations of magnetic levitation. *J Sound Vib*, 319(1–2):515–530
12. Stanton SC, McGehee CC, Mann BP (2010) Nonlinear dynamics for broadband energy harvesting: investigation of a bistable piezoelectric inertial generator. *Phys D* 239(10):640–653
13. Cottone F, Vocca H, Gammaitoni L (2009) Nonlinear energy harvesting. *Phys Rev Lett* 102(8):080601
14. Cammarano A, Burrow SG, Barton DAW, Carrella A, Clare LR (2010) Tuning a resonant energy harvester using a generalized electrical load. *Smart Mater Struct* 19:055003
15. Doedel EJ, Champneys AR, Fairgrieve TF, Kuznetsov YA, Sandstede B, Wang X *Auto 97: continuation and bifurcation software for ordinary differential equations (with homcont)*. <http://cmvl.cs.concordia.ca/auto/#documentation>

# Chapter 59

## Harvesting of Ambient Floor Vibration Energy Utilizing Micro-Electrical Mechanical Devices

Joshua A. Schultz and Christopher H. Raebel

**Abstract** Recent advances in device fabrication and energy harvesting technology combined with an increasing need for sustainable energy generation have encouraged the development of the micro-electro-mechanical (MEMS) energy harvesting model for floor vibrations presented herein. By calibrating arrays of MEMS energy harvesters in resonance with floor vibrations, building occupants become sustainable energy sources. Optimization of these harvesters to frequency ranges of floor vibrations, subsequent synchronization of harvester location to occupant flow and improved electromechanical modeling may result in an efficient, passive power source for low-demand applications independent of external environmental conditions.

A model of a floor-harvester system is developed, utilizing ambient floor vibration to excite MEMS energy harvesters via harmonic base translation. These devices then convert the mechanical vibrations to electrical power. Design considerations for piezoelectric-based energy harvesters inspired by MEMS-scale arrays are investigated. Single degree of freedom and distributed beam parameter electromechanical models are employed to predict performance, by optimization of resonant frequencies from measured low-level ambient vibrations. A simplified analytical expression for a frequency correction factor accounting for shear deformation and rotatory inertia effects is derived in terms of fundamental system parameters. Floor and energy harvesting device models are validated by comparison to experimental results and numerical modeling, respectively.

**Keywords** Energy harvesting • Floor vibration • Timoshenko beam • Resonance • MDOF model

### 59.1 Introduction

Floor systems constructed using concrete slab cast on form or composite deck supported by steel joists, beams and girders are commonly used in commercial buildings. Floor systems such as these have historically been prone to occupant-induced vibrations, often due to walking. Floor vibration acceptability standards exist [1], often stipulating maximum levels of acceleration for satisfactory designs.

Recent advances in micro-electro-mechanical systems (MEMS) have shown promise when considering ways to harvest low frequency and/or ambient vibrations for energy generation [2–4]. Since most current research focuses on energy harvesting at either the microscopic (i.e., microsensors) [2–4] or macroscopic (i.e., whole building) [5, 6] scale, the focus of this paper seeks to address energy harvesting at the intermediate scale (i.e., floor plenum space) by performing dynamic analysis of beam-type energy harvester devices that may be used to harvest the vibration generated due to floor vibrations from occupant activity or mechanical vibration for use with low power sustainable energy applications. Since many of the existing analytical models are SDOF or MDOF systems based on lumped parameter systems [2, 3, 5, 6], and in an effort to

---

J.A. Schultz (✉)

Department of Civil and Environmental Engineering, Marquette University, Milwaukee, WI 53233, USA

e-mail: [joshua.schultz@outlook.com](mailto:joshua.schultz@outlook.com)

C.H. Raebel

Department of Civil and Architectural Engineering and Construction Management, Milwaukee School of Engineering,

Milwaukee, WI 53202, USA

e-mail: [raebel@msoe.edu](mailto:raebel@msoe.edu)



more accurately model the interaction between floor vibration (i.e., support excitation) and energy harvester response, the harvester device is modeled as a continuous system from which an analytical expression for a frequency correction factor is derived. The simplified analytical expression for the correction factor is determined solely in terms of device parameters (material and geometry) to permit ready application of the frequency correction to SDOF models to facilitate new device designs at the intermediate scale. While significant research has gone into energy harvesting device design, the current research focuses on the frequency response in terms of general system parameters for beam-type devices. By developing a correction factor using Timoshenko beam theory and calibrating the frequency ranges to those of a ‘typical’ floor, this model seeks to facilitate further development of new energy harvesting devices by simplifying the frequency analysis.

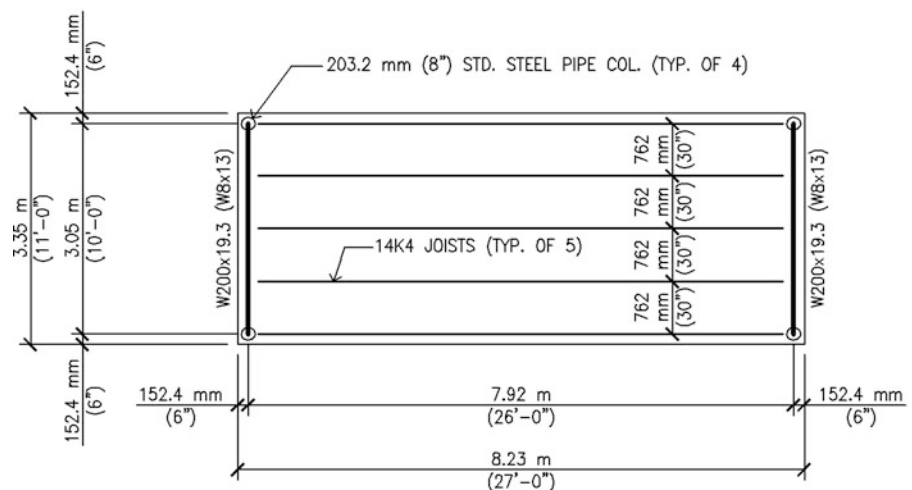
Dynamic analysis of energy harvesting techniques of MEMS devices are combined with ambient environmental floor vibrations to: (1) provide a new analytical model which incorporates shear deformation and rotatory inertia (i.e., “Timoshenko” effects) for development and optimization of energy harvesters, (2) use the model to investigate dynamic response of energy harvesters based on harmonic excitation from floor vibration to determine frequency and spatial response of energy harvesting devices and (3) serve as a feasibility study and initial investigation into frequency optimization of energy harvester devices taking into account the requirements associated with limits of floor serviceability and the frequency limits of current energy harvester designs.

An experimental floor is used as the subject of the investigation, partly because its vibration characteristics have already been determined [7] but more due to its susceptibility to occupant induced vibrations, allowing for the study to focus on the optimization of energy harvester dynamics with the (experimentally and numerically) determined dynamics of the floor system.

## 59.2 Description of the Experimental Floor

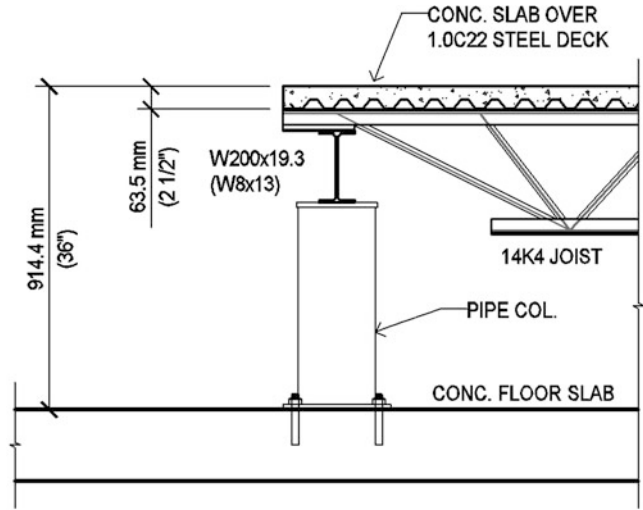
The subject of analysis is an experimental floor designed to be susceptible to walking vibrations. The floor under consideration has been used for past research, including the development of an experimental protocol for vibration assessment [8]. The past research was successful in determining modal parameters such as frequencies, damping ratios and mode shapes.

The experimental floor system, illustrated in plan view in Fig. 59.1, consists of a 63.5 mm (2-1/2 in.) thick floor slab comprised of concrete over 25.4 mm (1 in.) deep type “C” form deck. The deck was screwed to 14 K4 open web steel joists spaced at 762 mm (30 in.) center to center with a 8.23 m (27 ft.) total length. The open web steel joists are supported by W200 × 19.3 (W8 × 13) steel beams with a distance of 3.05 m (10 ft.) from center to center of supports. Standard 203.2 mm (8 in.) diameter pipe columns support the beams, and the pipe columns are anchored to a concrete slab-on-grade. Figure 59.2 shows a section cut through the W200 × 19.3 (W8 × 13) steel beam, illustrating the relationship between the deck, steel joist, steel beam and column.



**Fig. 59.1** Plan of experimental floor

**Fig. 59.2** Section cut through W200 × 19.3 (W8 × 13) beam



### 59.3 Floor Model

The floor system may be modeled mathematically using a lumped-parameter model possessing “m” modal (normal) and “n” spatial coordinates [9]. This type of model is convenient when attempting to target vibration modes for energy harvesting. The general form of this model is

$$M^* \ddot{Z} + C^* \dot{Z} + K^* Z = \Psi^T F(t) \tag{59.1}$$

$$\dot{Y} = \Psi \dot{Z}; \quad Y = \Psi Z \tag{59.2}$$

where  $\ddot{Z}$ ,  $\dot{Z}$ ,  $Z$  are the modal acceleration, velocity and displacement vectors, respectively, each containing  $m$  elements;  $m$  is the number of orthogonal modes of vibration included in the model;  $\dot{Y}$ ,  $Y$  are the spatial velocity and displacement vectors, respectively, each containing  $n$  elements;  $n$  is the number of spatial coordinates included in the model; and  $F(t)$  is the input force vector containing  $n$  elements.

$$\Psi = \begin{bmatrix} \Psi_{11} & \Psi_{12} & \cdots & \Psi_{1m} \\ \Psi_{21} & \Psi_{22} & \cdots & \Psi_{2m} \\ \vdots & \vdots & \ddots & \vdots \\ \Psi_{n1} & \Psi_{n2} & \cdots & \Psi_{nm} \end{bmatrix} = \begin{bmatrix} \Psi_1 \\ \Psi_2 \\ \vdots \\ \Psi_n \end{bmatrix} = \text{modal transformation matrix} \tag{59.3}$$

$$M^* = \begin{bmatrix} 1 & 0 & \cdots & 0 \\ 0 & 1 & \cdots & 0 \\ \vdots & \vdots & \ddots & \vdots \\ 0 & 0 & \cdots & 1 \end{bmatrix}_{m \times m} = \text{modal mass matrix} \tag{59.4}$$

$$C^* = \begin{bmatrix} 2\zeta_1\omega_1 & 0 & \cdots & 0 \\ 0 & 2\zeta_2\omega_2 & \cdots & 0 \\ \vdots & \vdots & \ddots & \vdots \\ 0 & 0 & \cdots & 2\zeta_m\omega_m \end{bmatrix} = \text{modal damping matrix} \tag{59.5}$$

where  $\zeta_i$  is the modal damping coefficient for the  $i$ th mode and  $\omega_i$  is the circular natural frequency for the  $i$ th mode.

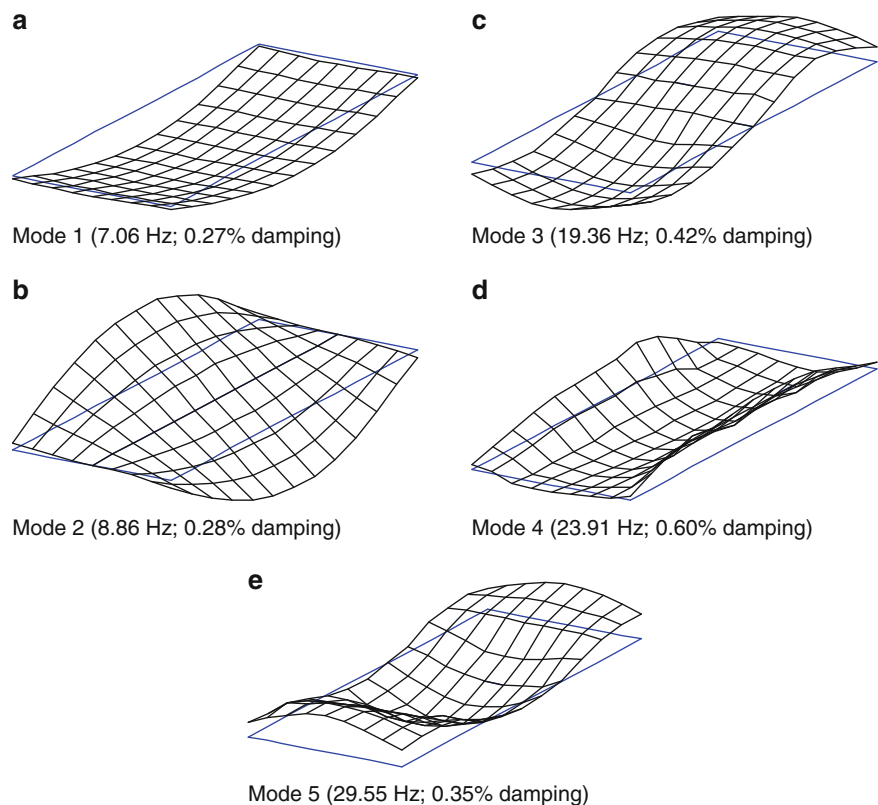
$$K^* = \begin{bmatrix} \omega_1^2 & 0 & \cdots & 0 \\ 0 & \omega_2^2 & \cdots & 0 \\ \vdots & \vdots & \ddots & \vdots \\ 0 & 0 & \cdots & \omega_m^2 \end{bmatrix} = \text{modal stiffness matrix} \quad (59.6)$$

The model above illustrates that the parameters required in the analysis of a specific floor system are the circular natural frequencies ( $\omega_i$ ), the modal damping coefficients ( $\zeta_i$ ) and the modal transformation matrix ( $\Psi$ ) for a prescribed number of vibration modes and spatial coordinates.

Walking produces an excitation that has frequency content in multiples of the step frequency, and dynamic load factors for walking are described by Pernica [10]. High modes of vibration do not significantly participate in the vibration response, so the effort shall be focused on the first few modes of vibration. Furthermore, lower frequency vibration modes dominate the dynamic response of the floor system [7], so effort shall be focused within the frequency range less than 30 Hz. Recent advances in MEMS technology has made the harvesting of vibrations with primarily low-frequency content possible [2–4, 11].

## 59.4 Modal Properties of the Floor System

Modal properties of the experimental floor system were extracted as part of a prior research initiative [7]. Normalized mode shapes are shown in Fig. 59.3, and the magnitudes of frequency and damping as a percent of critical are shown. The frequencies and damping ratios were measured from a 30 Hz chirp excitation generated from a mechanical shaker. This is noted because other excitation types produced very similar results, yet slight differences were observed.



**Fig. 59.3** Normalized mode shapes for modes 1–5

## 59.5 Mathematical Model of MEMS Energy Harvester

Since many recent energy harvesting devices employ cantilever beam and/or bridge configurations [12], this research focuses on the case of a cantilever beam with the analogous bridge configuration being readily addressed by a change in boundary conditions (BCs). Establishing an intelligent mathematical representation of these energy harvesting devices requires certain assumptions. The preceding devices are generalized as a continuous beam system which includes rotatory inertia ( $r$ ) and shear deformation ( $s$ ) (i.e., “Timoshenko” parameters). In addition, the following assumptions are applied:

1. The energy harvester cantilever beam is homogeneous and made of a material that is linear elastic and isotropic. Thus, when applied to silicon – an anisotropic material – care must be taken in utilizing the appropriate elastic moduli in the isotropic model. In addition, the beam is assumed to be of rectangular cross section and prismatic, i.e., the cross section is uniform along the beam length.
2. The slope of the deformed beam centerline is much smaller than unity.
3. The beam has a condition of perfect fixity (i.e., zero displacement and bending slope) at one end.
4. The loading is harmonic and applied in-plane, resulting in only in-plane flexural/shear deformation. Similarly, for any free-vibration cases considered, only vibrations involving in-plane flexural/shear deformation are considered.
5. Since the excitation is the imposed motion from the floor at a resonant mode, the assumption of harmonic load is deemed appropriate and of the form of a harmonic support translation.
6. Damping in the floor system is taken into account in the determination of the dynamic floor response. For this study, the energy harvester is assumed to have no inherent losses (i.e., an undamped system).

The well-known second and fourth order partial differential equations (PDE) of beam motion can be readily obtained by following the methodology employed by both Kruszewski [13] and Huang [14], which were based on the original contributions of Timoshenko [15, 16]. Solutions to these PDE’s can be sought in the following separable forms:

$$\bar{v} = \bar{V}(\xi) e^{i\tau} \quad (59.7)$$

$$\varphi = \Phi(\xi) e^{i\tau}. \quad (59.8)$$

Application of (59.7) and (59.8) to the PDEs results in second- and fourth-order ordinary differential equations (ODE) and concomitant BCs, where ( )’ indicates a spatial derivative with respect to  $\xi$ :

$$\bar{V}'' + \lambda^4 s^2 \bar{V} - \Phi' = 0, \quad (59.9)$$

$$s^2 \Phi'' - (1 - \lambda^4 r^2 s^2) \Phi + \bar{V}' = 0, \quad (59.10)$$

$$\bar{V}'''' + \lambda^4 (r^2 + s^2) \bar{V}'' - \lambda^4 (1 - \lambda^4 r^2 s^2) \bar{V} = 0, \quad (59.11)$$

$$\Phi'''' + \lambda^4 (r^2 + s^2) \Phi'' - \lambda^4 (1 - \lambda^4 r^2 s^2) \Phi = 0, \quad (59.12)$$

where  $\bar{v} \equiv v/L$  is the dimensionless beam displacement,  $v$  is displacement in the  $y$ -direction,  $L$  is beam length,  $\bar{V}$  is the amplitude of the total beam displacement,  $\xi = x/L$  is dimensionless spatial coordinate,  $x$  is coordinate along  $L$ ,  $\tau \equiv \omega t$  is the dimensionless time, and  $\Phi$  is the amplitude of the rotation of the beam cross-section. The Timoshenko parameters are defined as

$$r^2 \equiv \frac{I}{AL^2} \equiv \text{rotational inertia parameter} = \frac{1}{12} \left(\frac{b}{L}\right)^2 \text{ for a rectangular cross section,}$$

and

$$s^2 \equiv \frac{EI}{kAGL^2} \equiv \text{shear deformation parameter} = \frac{1}{12} \left(\frac{b}{L}\right)^2 \left(\frac{E}{kG}\right) \text{ for a rectangular cross section,}$$

where  $A$  is beam cross section ( $h \times b$ ),  $b$  is beam width,  $h$  is beam thickness,  $y$  is the coordinate along  $b$ ,  $E$  is the modulus of elasticity,  $I$  is the second moment of area,  $G$  is the shear modulus, and  $k$  is the shear coefficient. The dimensionless frequency parameter is given as  $\lambda^4 \equiv \frac{\omega_b^2 \bar{m}_b L^4}{EI} \equiv \text{dimensionless frequency parameter} = \omega_b^2 \left(\frac{12\rho_b L^4}{Eb^2}\right)$  for a rectangular cross section,

where  $\omega_b$  is the beam circular frequency,  $\rho_b$  is the beam mass density ( $\rho_b = 2,330 \text{ kg/m}^3$  for silicon) and  $\bar{m}_b$  is mass per unit length of beam. For the problems of interest herein, the dimensionless forms of the relevant BCs at the supported end ( $\xi = 0$ ) result in

$$\bar{V}(0) = \bar{V}_0, \quad (59.13)$$

$$\Phi(0) = 0, \quad (59.14)$$

where (59.13) and (59.14) correspond, respectively, to the total displacement being equal to the amplitude of the imposed support translation and the rotation angle being equal to zero (i.e., a perfectly clamped beam). The former BC is inspired by the harmonic transverse excitation method imparted according to the modal response of the floor response, where  $\bar{V}_0$  is the amplitude of the floor vibration [17].

The dimensionless forms of the relevant BCs at the tip ( $\xi = 1$ ) of the cantilever beam (see, e.g., Huang [14]) result in

$$\Phi'(1) = 0, \quad (59.15)$$

$$\bar{V}'(1) - \Phi(1) = 0. \quad (59.16)$$

Assuming a harmonic form of solution, we use standard methods to solve the boundary value problem (BVP) described by (59.9) through (59.16) analogous to the method provided by Huang [14]. Imposing the BCs on the general solution form results in the following linear algebraic system:

$$[e] \{C^*\} = \{f\} \quad (59.17)$$

where

$$[e] = \begin{bmatrix} 1 & 0 & 1 & 0 \\ 0 & \frac{n_1^2 + k_3}{n_1} & 0 & -\frac{n_3^2 + k_3}{in_3} \\ \frac{[n_1^2 + k_3] C(n_1)}{s^2} & \frac{[n_1^2 + k_3] S(n_1)}{n_1} & \frac{[n_3^2 + k_3] c(in_3)}{s^2} & \frac{[n_3^2 + k_3] s(in_3)}{in_3} \\ \frac{1}{s^2} \left[ n_1 - \frac{n_1^2 + k_3}{n_1} \right] S(n_1) & \frac{1}{s^2} \left[ n_1 - \frac{n_1^2 + k_3}{n_1} \right] C(n_1) & \frac{1}{s^2} \left[ -in_3 - \frac{n_3^2 + k_3}{in_3} \right] s(in_3) & \frac{1}{s^2} \left[ in_3 - \frac{n_3^2 + k_3}{-in_3} \right] c(in_3) \end{bmatrix} \quad (59.18)$$

$$\{C^*\} = \begin{bmatrix} C_1/\bar{V}_0 \\ C_2/\bar{V}_0 \\ C_3/\bar{V} \\ C_4/\bar{V}_0 \end{bmatrix} = \begin{bmatrix} C_1^* \\ C_2^* \\ C_3^* \\ C_4^* \end{bmatrix}, \quad (59.19)$$

$$\{f\} = \begin{bmatrix} 1 \\ 0 \\ 0 \\ 0 \end{bmatrix}. \quad (59.20)$$

The frequency-dependent roots of the characteristic equation,  $n_1$  and  $n_3$ , are and defined as

$$n_1 = + \left[ \left( \frac{1}{2} \right) \left( -k_1 \pm \sqrt{k_1^2 - 4k_2} \right) \right]^{\frac{1}{2}}, \quad (59.21)$$

where  $k_1 = k_1(\lambda) = \lambda^4 (r^2 + s^2)$  and  $k_2 = k_2(\lambda) = -\lambda^4 \{1 - r^2 s^2 \lambda^4\}$ .

The coefficients,  $C_i^*$ ,  $i = 1, 2, 3, 4$ , depend on  $r$ ,  $s$  and  $\lambda$  and are obtained by solving (59.17). These constants may then be used to obtain the solution in terms of total displacement as follows:

$$\bar{V}(\xi) = \bar{V}_0 [C_1^* C(n_1 \xi) + C_2^* S(n_1 \xi) + C_3^* c(in_3 \xi) + C_4^* s(in_3 \xi)]. \quad (59.22)$$

Similarly, the form for  $\Phi(\xi)$  becomes

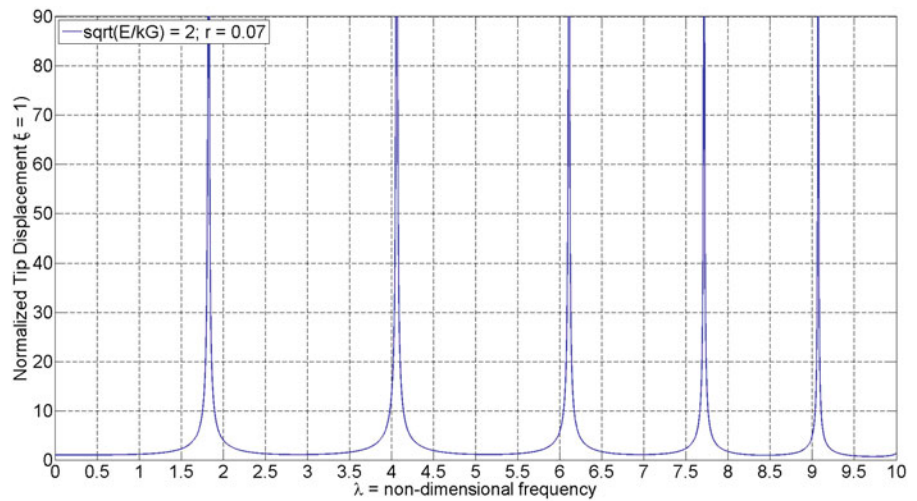
$$\Phi(\xi) = \bar{V}_0 [C_1^{*'} C(n_1 \xi) + C_2^{*'} S(n_1 \xi) + C_3^{*'} c(in_3 \xi) + C_4^{*'} s(in_3 \xi)]. \tag{59.23}$$

The tip response is obtained by evaluating the above equations at  $\xi = 1$ .

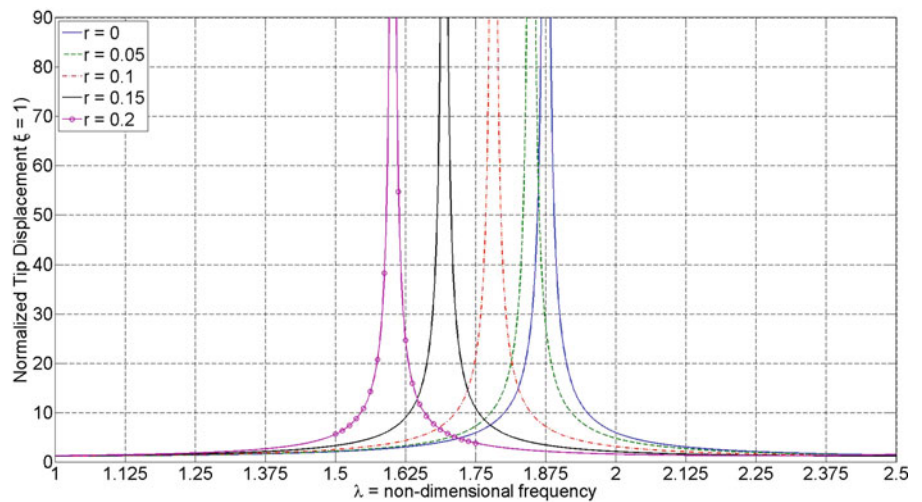
### 59.6 Vibrational Response and Frequency Results

The frequency response spectra for the energy harvesting devices are obtained by plotting the tip response of the total displacement according to (59.22) over a range of excitation (i.e., floor vibration) frequencies. Figure 59.4 shows the first five dimensionless resonant frequencies,  $\lambda_{res}$ , for  $b/L = 0.2425$  and  $e \equiv \sqrt{E/kG} = 2$ . Note that this model employs the elastic constants  $E$  and  $G$ ; however, silicon and other materials commonly used in energy harvesters are anisotropic. Accordingly, sufficient care must be exercised in selecting the correct values for the elastic moduli. The value for  $e = 2$  is obtained for common value for silicon, by taking the corresponding  $E_x$  and  $G_{xy}$  for standard (100) silicon oriented with axis along [110] (i.e., assuming  $E = 169$  Gpa (24,500 ksi),  $G = 50.9$  Gpa (7,380 ksi) and  $k = 5/6$ ) [18].

Figure 59.5 shows the impact of geometry  $b/L$  (via the  $r$  term) on the resonant frequency. Increases in  $r$  result in decreases in the resonant frequency compared to that predicted using Euler-Bernoulli theory. A similar trend is observed for increases in  $e$ , although not shown for conciseness.



**Fig. 59.4** Plot of the frequency response spectrum of normalized tip displacement for  $\lambda \in [0, 6]$ ,  $\sqrt{E/kG} = 2$  and  $r = 0.07$  for resonant frequencies 1–5



**Fig. 59.5** Plot of the frequency response spectrum of normalized tip displacement for  $\lambda \in [1, 2.5]$ ,  $\sqrt{E/kG} = 2$  and  $r = (0, 0.05, 0.10, 0.15, 0.20)$



The frequency of the energy harvesting device is obtained by applying the definition of the dimensionless frequency,  $\lambda$ , to the results from (59.22) as shown in Fig. 59.4. For example, by using the Timoshenko beam theory and assuming material properties of pure silicon,  $e = 2$  and a geometry of  $r = 0.07$  (i.e.,  $b/L = 0.2425$ ) the fundamental resonant frequency is  $\lambda_{\text{res}} = 1.8258$  which is 6% lower than the frequency obtained using Euler-Bernoulli theory. The non-dimensional frequency,  $\lambda_{\text{res}} = 1.8258$ , can easily be rewritten as  $f_{\text{res}} = 31.6$  Hz. Thus, the device described by  $e = 3$  and  $r = 0.07$  had a fundamental resonant frequency that corresponds to the fifth resonant mode of the floor system as well as the lower limit of current experimental devices [2–4, 11].

## 59.7 Simplified Analytical Expression for Resonant Frequency Ratio

Previous theoretical investigations of lateral-mode Timoshenko beams [15, 16, 19] have presented resonant frequency results in terms of a ratio of Timoshenko to Euler-Bernoulli resonant frequencies. Recent work by Schultz [19] shows that the dependence of the quality factor ( $Q$ ) on frequency dependent viscous-fluid damping ( $\zeta$ ) and the Timoshenko parameters ( $r$  and  $s$ ) is relatively straightforward. These observations provide motivation for pursuing a simplified analytical expression for the resonant frequency of an undamped system as a function of the Timoshenko parameters. Such an expression would be advantageous since it would provide a correction factor for the resonant frequency explicitly in terms of fundamental system parameters without resorting to the implementation of the relatively complicated BVP solutions presented by Schultz [19]. This correction factor can be applied to SDOF or MDOF analysis to adjust for the Timoshenko effects. Therefore, such an analytical expression has been derived for the ranges of  $r = [0, 0.2]$  and  $e = [0, 3]$ , since these ranges span most cases of practical interest for energy harvesting devices of cantilever beam (fixed-free) and bridge (fixed-fixed) configuration. The frequency ratio ( $f_{\text{ratio}} = \omega_{\text{TB}}/\omega_{\text{EB}}$ ) is plotted against the Timoshenko parameters as shown in Fig. 59.6.

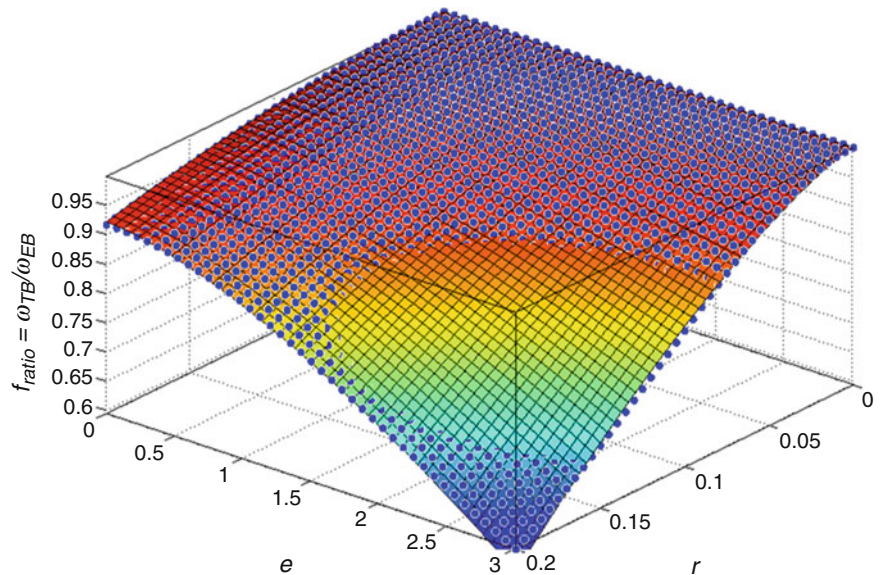
Using a least squares fitting method and imposing limiting conditions on the surface in Fig. 59.6 results in an analytical expression for  $f_{\text{ratio}}$ :

$$f_{\text{ratio}} \approx 1 - 1.788r^{1.95} - 0.571r^{1.34}e^{1.56}, \quad (59.24)$$

or, in terms of the fundamental system parameters (taking  $k = 5/6$ ),

$$f_{\text{ratio}} \approx 1 - 0.1585 \left(\frac{b}{L}\right)^{1.95} - 0.1246 \left(\frac{b}{L}\right)^{1.34} \left(\frac{E}{G}\right)^{0.78}. \quad (59.25)$$

The accuracy of the results over the practical range of values (and possibly beyond) is excellent. More specifically, the maximum percent difference between the analytical  $f_{\text{ratio}}$  results and the exact results of the continuous Timoshenko beam



**Fig. 59.6** Plot of the theoretical resonant frequency ratio,  $f_{\text{ratio}}$ , and the best-fit surface for  $\zeta = 0$  over the ranges  $\sqrt{E/kG} \in [0, 3]$  and  $r \in [0, 0.2]$

model is 2.8% (occurring at  $r = 0.2$  and  $e = 3$ ) over the ranges  $r = [0, 0.2]$  and  $e = [0, 3]$ . Over the range of  $e = [0, 2]$  the percent difference of the analytical model falls to within 1% of the continuous beam model.

## 59.8 Floor-Harvester System

Harvesting floor vibrations due to human activity comes with challenges. Structural engineers consider serviceability as part of the design and strive to minimize perceptible vibrations. Design strategies typically include avoidance of the frequency range of the human body and limitation of accelerations to acceptable levels. For example, in an office occupancy, designers will keep acceleration ratios below 0.5% of the acceleration of gravity. By doing so, the floor system is deemed acceptable [1]. This does not mean that vibrations are nonexistent, it simply means the vibrations have been minimized to the point where they are no longer annoying to most occupants.

The “annoying” vibration range falls around 7 Hz. Thus, structural engineers often avoid designing a floor system with a fundamental natural frequency close to the 7 Hz range. Even so, one can see from the results of the experimental floor system that several modes exist in the range less than 30 Hz and the MEMS device may be tailored to a particular mode of floor vibration. However, challenges may still exist due to the fact that the fundamental frequency of the floor system will be the lowest (1–10 Hz) and have the most participation (usually over 90%) whereas the higher frequencies (30 Hz) are the easiest to harvest, but have the lowest participation factor. It would be ideal if the energy harvesting devices were designed with resonant frequencies within the 1–10 Hz range.

While there has been an increasing number of developments in designing and fabricating energy harvesters [20, 21], to the authors knowledge, the development of low frequency (1–30 Hz) energy harvesting devices for intermediate scale (i.e., meters rather than nano- or micro- or millimeters) remains inchoate. An important exception to this is a recent a low-frequency energy harvester prototype utilizing MEMS technology as developed by Gu [11]. This device was able to harvest frequencies in the range of 30 Hz and is scaled in centimeters. The floor-harvester system explored herein is intended to provide a baseline model for frequency optimization of devices designed to fit within the plenum space (i.e., centimeter – meter scale).

## 59.9 Conclusions

This paper discussed the potential for harvesting energy from vibrations due to human activities on steel-framed floor systems. An experimental floor with several measurable modes of vibration within the frequency range of 0–30 Hz was used as the specimen for the study. A continuous Timoshenko beam model was used to obtain a relatively simple frequency correction factor that can be applied to Euler-Bernoulli models and SDOF/MDOF models to account for the effects of shear deformation and rotatory inertia.

For the case of a uniform cantilever-based harvesting device, it is observed that device geometry which necessitates application of Timoshenko beam theory also results in higher resonant frequencies. As a result, it was found that for the geometry which resulted in the lowest practical resonant frequency of 30 Hz (corresponding to the fifth resonant frequency of the floor and the lowest threshold of current energy harvesting devices) the Timoshenko effects account for a 6% difference from the frequency results according to Euler-Bernoulli theory. Thus, for geometry  $b/L < 0.24$ , the Timoshenko effects may be negligible. However, for larger  $b/L$  ratios the Timoshenko effects may be significant and can be accounted for by employing the frequency correction factor derived herein.

It was shown that harvesting energy from low frequency (30 Hz) floor vibration is possible and may become practical using existing MEMS based energy harvesters as examples for development of larger scale devices. Although the output power realized from the current model of floor-harvester vibration is low, ongoing research suggests that it is reasonable to expect the power output to scale up with harvester size, resulting in a sufficient source for low power demand applications such as LED lighting. Implementation of a system would provide a sustainable power source for such demands.

This research initiative is currently ongoing. In addition to using the floor-harvester model for optimization of device geometry for frequency, the authors are optimizing device geometry to limit deflection within plenum restrictions. These studies will provide the geometry for subsequent device manufacture and testing. Moreover, the initial results indicate that lower device resonant frequencies may require the addition of a tip mass and/or damping mechanism. Accordingly, the model is being extended to the case of a cantilever with additional tip mass and frequency dependent damping.

**Acknowledgements** The prior research performed on the experimental floor system was supported in part by National Science Foundation Grant No. CMS-9900099. The authors wish to acknowledge the work completed by the principal investigator of that research initiative, Dr. Linda Hanagan.

## References

1. Murray TM, Allen DE, Ungar EE (1997) Floor vibrations due to human activity. AISC Steel Design Guide #11. American Institute of Steel Construction, Chicago
2. Miller LM, Halverson E, Dong T, Wright PK (2011) Modeling and experimental verification of low-frequency MEMS energy harvesting from ambient vibrations. *J Micromech Microeng* 21(1), 13pp, IOP Publishing
3. Galchev T, Kim H, Najafi K (2001) Micro power generator for harvesting low-frequency and nonperiodic vibrations. *J Micromech Syst IEEE* 24(4):852–866
4. Beeby SP, Torah RN, Tudor MJ, Glynne-Jones P, O'Donnell T, Saha CR, Roy S (2007) A micro electromagnetic generator for vibration energy harvesting. *J Micromech Microeng* 17(1):1257–1265, IOP Publishing
5. Tang X, Zuo L (2012) Vibration energy harvested from random force and motion excitations. *Smart Mater Struct* 21(1), 9pp, IOP Publishing
6. Cassidy IL, Scruggs JT, Behrens S (2011) Design of electromagnetic energy harvesters for large-scale structural vibration applications. *Proc SPIE* 7977(1), 11p
7. Raebel CH (2000) Development of an experimental protocol for floor vibration assessment. Master's thesis, The Pennsylvania State University, University Park
8. Raebel CH, Hanagan LM, Trethewey MW (2001) Development of an experimental protocol for floor vibration assessment. In: Proceedings of IMAC-XIX: a conference on structural dynamics, Society for Experimental Mechanics, Bethel, 5–8 Feb 2001, pp 1126–1132
9. Hanagan LM, Murray TM (1997) Active control approach for reducing floor vibrations. *J Struct Eng* 123(11):1497–1505, ASCE
10. Pernica G (1990) Dynamic load factors for pedestrian movements and rhythmic exercises. *Can Acoustics* 18(2):3–18
11. Gu L (2011) Low-frequency piezoelectric energy harvesting prototype suitable for the MEMS implementation. *Microelectron J* 42(2):277–282
12. Kim HS, Kim JH, Kim J (2011) A Review of piezoelectric harvesting based on vibration. *Int J Precis Eng Manuf* 12(6):1129–1141, KSPE and Springer
13. Kruszewski E (1949) Effect of transverse shear and rotatory inertia on the natural frequency of a uniform beam. National Advisory Committee for Aeronautics Technical Note 1909, Langley Aeronautical Laboratory, Langley
14. Huang T (1961) The effect of rotatory inertia and of shear deformation on the frequency and normal mode equations of uniform beams with simple end conditions. *J Appl Mech* 28:579–584
15. Timoshenko S (1921) On the correction for shear of the differential equation for transverse vibrations of prismatic bars. *The London, Edinburgh and Dublin Philosophical Magazine and Journal of Science* 41:744–746
16. Timoshenko S (1922) On the transverse vibrations of bars of uniform cross sections. *The London, Edinburgh and Dublin Philosophical Magazine and Journal of Science* 43:125–131
17. Schultz J, Raebel CH (2012) MEMS energy harvesting of ambient floor vibrations as sustainable power source. In: Proceedings, annual green energy summit, Milwaukee, 7 Mar 2012
18. Hopcroft M, Nix W, Kenny T (2010) What is the young's modulus of silicon? *J Microelectromech Syst* 19:229–238
19. Schultz J (2012) Lateral-mode vibration of microcantilever-based sensors in viscous fluids using Timoshenko beam theory. Doctoral dissertation, Marquette University, Milwaukee
20. Lui H, Lee C, Kobayashi T, Tay TC, Quann C (2012) A new S-shaped MEMS PZT cantilever for energy harvesting from low frequency vibrations below 30Hz. *Microsystems Technology*, Springer, Technical Paper, 10p
21. Beeby SP, Tudor MJ, White NM (2006) Review article: energy harvesting vibration sources for microsystem applications. *Meas Sci Technol* 17(1):R175–R195, IOP Publishing

# Chapter 60

## Robust Optimization of Magneto-Mechanical Energy Harvesters for Shoes

Stefano Tornincasa, Maurizio Repetto, Elvio Bonisoli, and Francesco Di Monaco

**Abstract** Powering a remote wireless sensor is a challenging task if batteries are not suitable or enough capacious and their substitution is not feasible. A remote wireless sensor can be placed inside a shoe with the aim to collect and transmit data to evaluate and track the performance of an athlete. The primary energy source is the impact between the shoes and the ground while walking or running. The harvester has been designed by means of a multi-physics optimization based on an integrated electromagnetic-mechanical simulator. Thus an automated optimization of the device with respect to volume constraints, magnets dimensions, induction coils placement and size have been performed to increase the average power extracted from the device at different walking speeds. Finally, prototypes of the optimal configurations demonstrate the predicted performance and a more than satisfactory agreement is evinced.

**Keywords** Electromagnetic generator • Energy scavenger • Optimization • Magneto-mechanical • Shoe mounted device

### 60.1 Introduction

Energy harvesting is the only solution to power a remote wireless sensor if it is not possible to use batteries or to supply it through wires. This kind of device usually collects energy using the electromagnetic, electrostatic or piezoelectric effect [1–3].

Magneto-mechanical energy harvesters usually consist in one or more magnets in relative motion in respect to one or more coils. Two main topological families of solutions exist. In the first one [4, 5] a moving mass (that can either be the magnet or the coil) is suspended by a cantilever beam that acts as a spring. The second family is the one of the so-called linear generator in which one or more moving magnets slide into a guide around which are winded one or more coils. The elastic characteristic is usually given by a mechanical spring [6, 7] or by the interaction between the moving magnet and one or more fixed magnets [8–13].

To harvest energy from walking, and use it to power a shoe mounted remote sensor, several strategies have been proposed using piezoelectric or electromagnetic transducers. These strategies usually exploit the deformation of the shoe during the walk or the impulsive excitation due to the impact with the ground. If the power source is the deformation of the shoe a possible strategy is to use a piezoelectric polymer film in the sole [14, 15]. To exploit the impact with the ground a resonating system is usually used. A typical device is composed by a seismic mass placed at the free end of a piezoelectric cantilever [16, 17]. Another possible solution is to place a magneto-mechanic linear generator in the shoe. This kind of generator is usually placed with the axis in the foot direction. Carroll and Duffy [18] propose a device with two repulsing magnets sliding in a single coiled guide, Wang et al. [19] propose a magnet assembly sliding in a multiple coils guide. Other possible solutions are a rotary generator activated by an arm that extends under the sole [20] and a generator exploiting the flow of liquid metal between two pumps placed in the front and in the rear of the sole [21].

---

S. Tornincasa • E. Bonisoli (✉) • F. Di Monaco

Department of Management and Production Engineering, Politecnico di Torino, Corso Duca degli Abruzzi 24, 10129 Torino, Italy  
e-mail: [stefano.tornincasa@polito.it](mailto:stefano.tornincasa@polito.it); [elvio.bonisoli@polito.it](mailto:elvio.bonisoli@polito.it); [francesco.dimonaco@polito.it](mailto:francesco.dimonaco@polito.it)

M. Repetto

Department of Energy, Politecnico di Torino, Corso Duca degli Abruzzi 24, 10129 Torino, Italy  
e-mail: [maurizio.repetto@polito.it](mailto:maurizio.repetto@polito.it)

In the following sections an electromagnetic linear generator designed to be placed in the heel of a sport shoe is presented. Differently from the solutions reported in literature the axis of the generator is placed vertically in respect to the ground. An optimization strategy of the device components is proposed to increase the energy harvested while respecting the volume constraints of the device.

## 60.2 Device Model and Simulation

The device, whose main components are shown in Fig. 60.1, is basically a base excited one degree of freedom spring-mass-damper system. A rare-earth permanent magnet acts as a seismic mass oscillating in a guide suspended between two helical springs. Electromotive forces created by the permanent magnet motion are collected on two external coils representing a damper from the mechanical point of view. The coils are wound in opposite direction so that their electromotive force is summed. The mass is excited by the acceleration peak when the foot hits the ground while walking or running and the damper and the spring are tuned to terminate the mass dynamic before the subsequent pulse occurs.

A complete Matlab/Simulink model was made to study the dynamic behavior of the device. Starting from the geometrical dimensions all the operative parameters (mass, springs, motion amplitude, dimensions of coils, number of turns in coils) are calculated. Through an automatic FEM model the flux linkage as a function of the magnet position is calculated. Then the system is simulated using a proper acceleration profile to excite the device. The Simulink model layout is shown in Fig. 60.2. A full description of the simulation model is available in previous articles [9, 10].

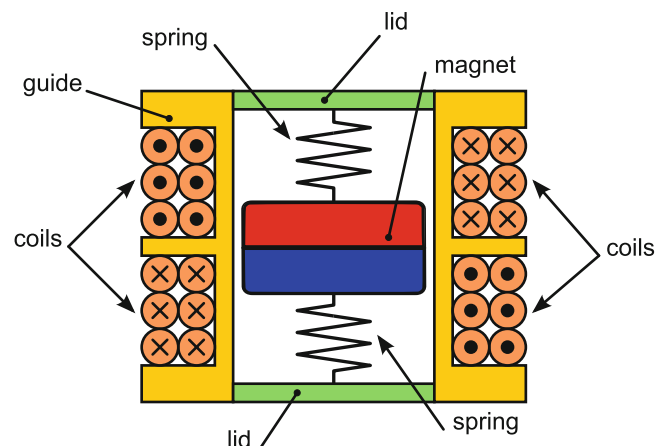
Several prototypes of the energy harvester have been built and tested to validate the simulation model. Both sine sweeps with different acceleration amplitudes and heel-strikes in different operative conditions (running or walking) have been reproduced on an acceleration controlled shaker. A good agreement has been found between simulated and experimental results as shown in Fig. 60.3.

In Fig. 60.3a is shown a 5 min direct sweep from 60 to 160 Hz with a constant acceleration amplitude of 5 g and frequency increasing linearly. The nonlinearity close to the resonance is due to the interaction with the end-strokes. In Fig. 60.3b is shown the voltage output of a step simulated on a shaker.

## 60.3 Optimization Problem

The purpose of the optimization algorithm is to maximize the extracted power at different walking speed. The degrees of freedom of the optimization are the main geometrical parameters of the harvester and the stiffness of the spring. For each parameter sample, the automated optimization scheme is based on:

- The creation of consistent model complying with overall constraints;
- The updating of a 3D CAD model, the evaluation of magneto-static field and map interactions;
- The updating of the parameters in a block-oriented model;
- The simulation on actual heel-strike acceleration source;
- Finally the evaluation of actual electrical power on adapted load.



**Fig. 60.1** Energy harvester layout

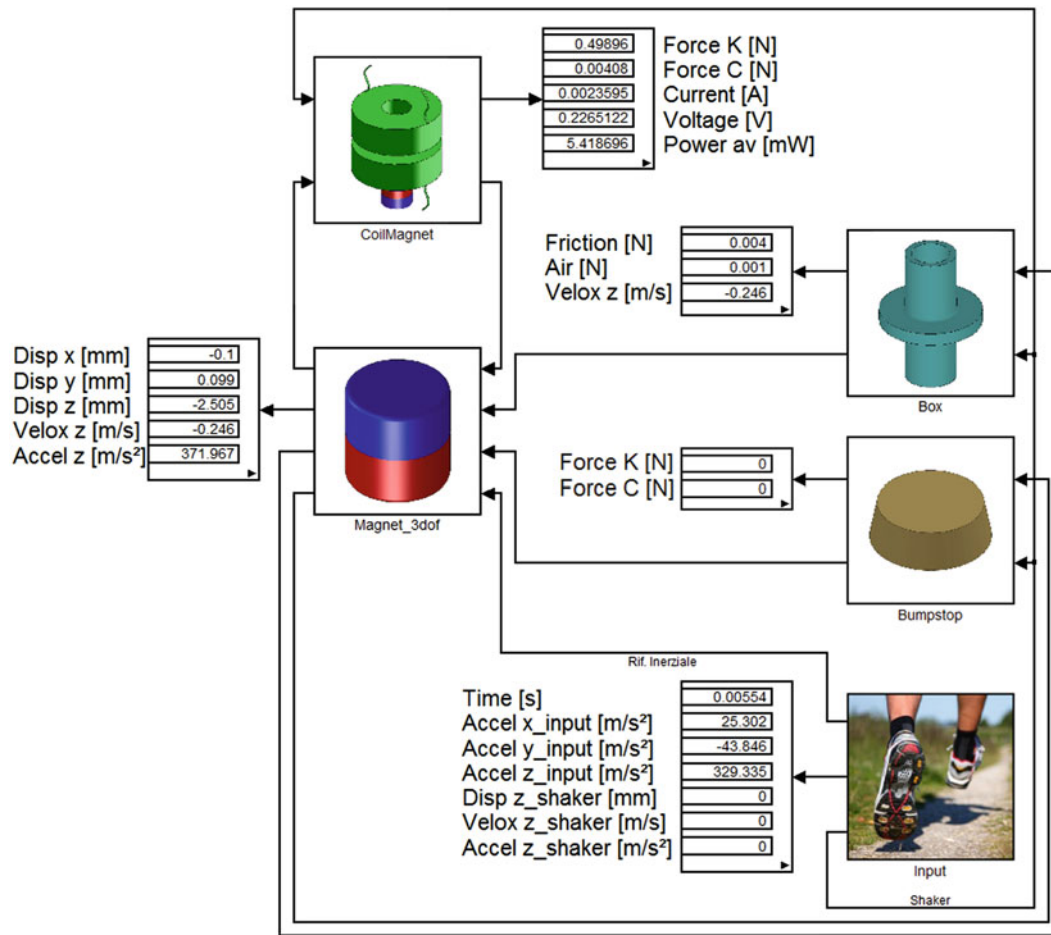


Fig. 60.2 Simulink model layout

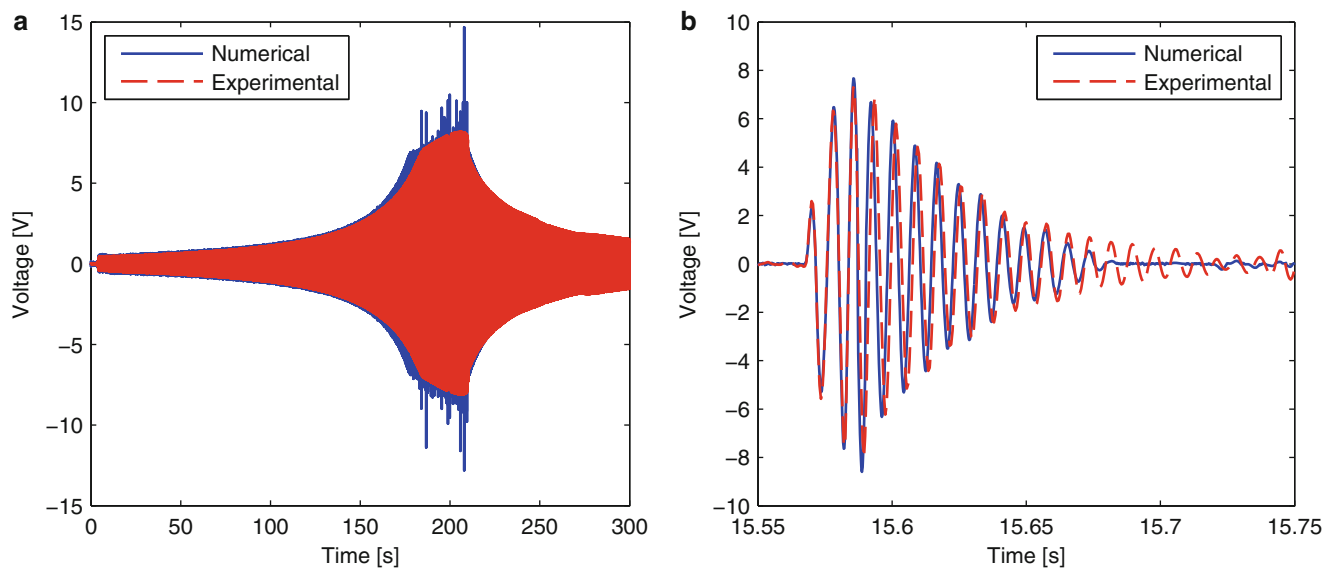
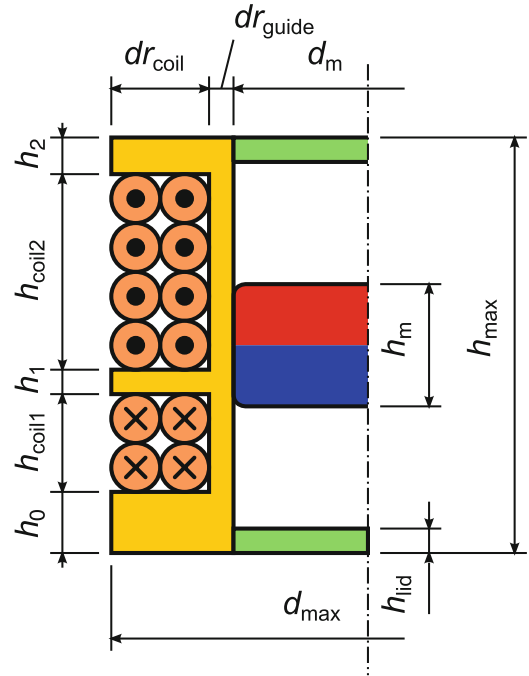


Fig. 60.3 Numerical/experimental comparison of the voltage output for sine sweep (a) and simulated heel-strike (b)



**Table 60.1** Optimization parameters

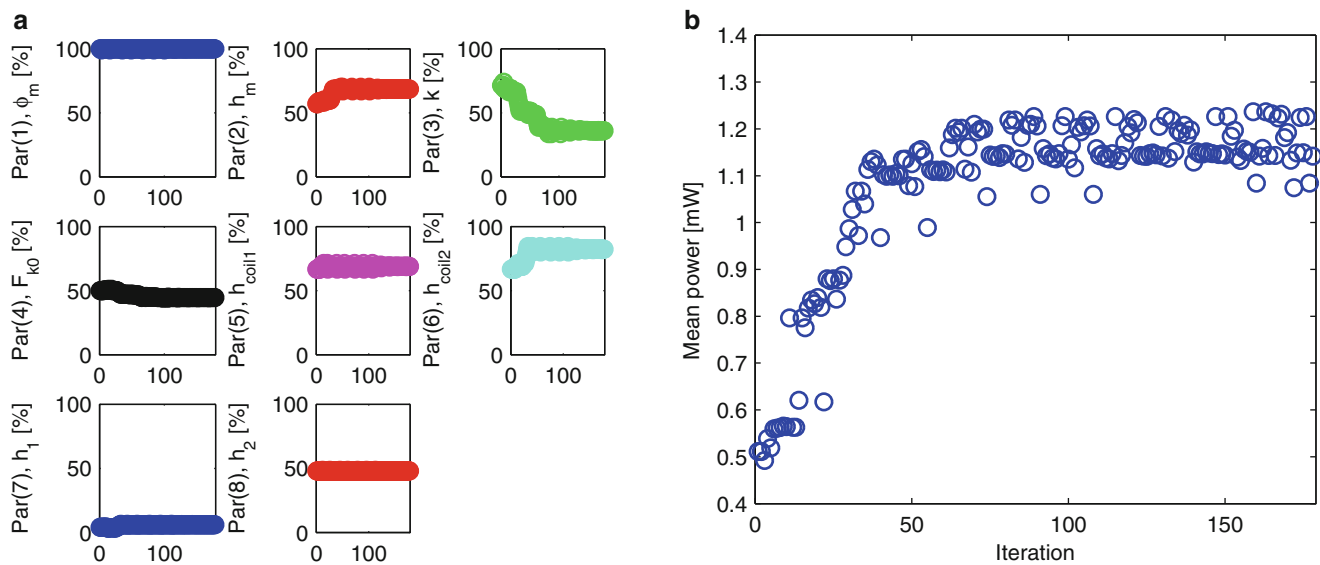
Parameter	Parameter number	Lower bound	Upper bound
Floating magnet diameter $d_m$ [mm]	Par(1)	5	15
Floating magnet height $h_m$ [mm]	Par(2)	1	8
Stiffness $k$ [N/m]	Par(3)	1,000	5,000
Spring offset $F_{k0}$ [N]	Par(4)	-10	+10
Coil 1 height $h_{coil1}$ [mm]	Par(5)	1	5
Coil 2 height $h_{coil2}$ [mm]	Par(6)	1	5
Coil gap $h_1$ [mm]	Par(7)	0.3	3
Coil gap $h_2$ [mm]	Par(8)	0.3	3

**Fig. 60.4** Geometrical parameters

Volume and aspect ratio constraints are imposed according to the available space in the heel of the shoe. Table 60.1 shows the degrees of freedom and bounds of the optimization. The meaning of the geometrical degrees of freedom is emphasized in Fig. 60.4.

It is necessary to remark that not all the parameters labeled in Fig. 60.4 can be optimized since some of them are not fully independent or it is not necessary to optimize them to know their optimal value. In fact  $h_{hid}$  and  $dr_{guide}$  have to be as small as possible,  $dr_{coil}$  is a consequence of  $d_m$  and  $h_3$  is a consequence of  $h_2$ ,  $h_{coil1}$ ,  $h_1$  and  $h_{coil2}$ . About the spring it has been chosen to optimize the equivalent stiffness of the two springs ( $k$ ) and the static force when the magnet is centered ( $F_{k0}$ ) instead of the springs geometrical parameters that are calculated in a subsequent step.

The computational cost of the objective function evaluation is not negligible: for a given acceleration profile the simulation of 1 s of physical time requires about 1 min of CPU time. Moreover, in order to take account of the step variability, a recorded acceleration of about 20 s is considered. Thus a 0th order deterministic technique has been used. Pattern Search algorithm [22] is a well know search scheme that has been extensively used in the automated optimization environment. Its main characteristics regard the search along coordinate directions in the optimization variable space and the operative definition of a preferred line search (“the pattern”) which often results in a fast motion of the search toward regions of high objective function values. As all other deterministic algorithms, its results guarantee to be globally optimal only in case of convex objective function landscapes, while the search can be trapped in local minima or maxima if they are present. In these cases the search results are dependent on its starting point. As a matter of fact, for computationally intensive direct problems, Pattern Search could be a first approach to test the objective function landscape especially if used with a multi-starting strategy that allows an exploration of different parts of the device feasibility space.



**Fig. 60.5** Evolution of parameters (a) and objective function (b)

## 60.4 Optimization Results

Figure 60.5 shows the evolution of the parameters and objective function. A consistent improvement of the performance is found mainly due to the tuning of the elastic characteristic. Moreover the magnetic mass is increased by the extension of the magnet height, reducing the available stroke. The upper-coil length is also slightly increased. The simulation result emphasized the fact that initial device did not exploit all the available length of the stroke. The problem is fixed by softening its elastic characteristic and increasing the magnet height.

## 60.5 Conclusion

Energy harvesting could be considered an emerging technique to supply remotely placed sensors wireless connected. The research activity on the optimal design of this kind of devices is world-wide active due to the innovative character of the application. The research highlights how the integrated analysis of the whole energy conversion chain is necessary to get a reliable estimate of the harvester device. In the paper the optimization of the complex design of an electro-mechanical harvesting device with practical and physical constraints has been demonstrated to be effective by means of a multi-physics tool based on an integrated electromagnetic-mechanical simulator. It has been simulated an increasing performance in the average power extracted from the device with respect to the first prototypes involved in the numerical-experimental validation. Therefore a next experimental phase of validation of these results on new prototypes is forecast.

**Acknowledgements** This work was performed under a research project with STMicroelectronics. The authors would like to thank Dr. Alessandro Gasparini, Dr. Stefano Ramorini and Dr. Alberto Cattani from STMicroelectronics for their enthusiasm and driving force in the project.

## References

1. Paradiso JA, Stamer T (2005) Energy scavenging for mobile and wireless electronics. *IEEE Pervasive Comput* 4(1):18–27. doi:[10.1109/MPRV.2005.9](https://doi.org/10.1109/MPRV.2005.9)
2. Mitcheson PD, Yeatman EM, Rao GK, Holmes AS, Green TC (2008) Energy harvesting from human and machine motion for wireless electronic devices. *Proc IEEE* 96(9):1457–1486. doi:[10.1109/JPROC.2008.927494](https://doi.org/10.1109/JPROC.2008.927494)
3. Priya S, Inman DJ (2009) *Energy harvesting technologies*. Springer, New York. ISBN 978-0-387-76463-4
4. Hatipoglu G, Ürei H (2010) FR4-based electromagnetic energy harvester for wireless sensor nodes. *Smart Mater Struct* 19(1). doi:[10.1088/0964-1726/19/1/015022](https://doi.org/10.1088/0964-1726/19/1/015022)

5. Marin A, Bressers S, Priya S (2011) Multiple cell configuration electromagnetic vibration energy harvester. *J Phys D Appl Phys* 44(29). doi:[10.1088/0022-3727/44/29/295501](https://doi.org/10.1088/0022-3727/44/29/295501)
6. Elvin NG, Elvin AA (2011) An experimentally validated electromagnetic energy harvester. *J Sound Vib* 330(10):2314–2324. doi:[10.1016/J.JSV.2010.11.024](https://doi.org/10.1016/J.JSV.2010.11.024)
7. Cepnik C, Radler O, Rosenbaum S, Ströhlhla T, Wallrabe U (2011) Effective optimization of electromagnetic energy harvesters through direct computation of the electromagnetic coupling. *Sens Actuator A Phys* 167(2):416–421. doi:[10.1016/J.SNA.2011.01.023](https://doi.org/10.1016/J.SNA.2011.01.023)
8. Mann BP, Sims ND (2009) Energy harvesting from the nonlinear oscillations of magnetic levitation. *J Sound Vib* 319(1–2):515–530. doi:[10.1016/j.jsv.2008.06.011](https://doi.org/10.1016/j.jsv.2008.06.011)
9. Bonisoli E, Canova A, Freschi F, Moos S, Repetto M, Tornincasa S (2010) Dynamic simulation of an electromechanical energy scavenging device. *IEEE Trans Magn* 46(8):2856–2859. doi:[10.1109/TMAG.2010.2044156](https://doi.org/10.1109/TMAG.2010.2044156)
10. Tornincasa S, Bonisoli E, Di Monaco F, Moos S, Repetto M, Freschi F (2011) Nonlinear dynamics of an electro-mechanical energy scavenger. In: *Modal analysis topics*, vol 3. Springer, New York, pp 339–349. doi:[10.1007/978-1-4419-9299-4\\_30](https://doi.org/10.1007/978-1-4419-9299-4_30)
11. Bonisoli E, Rosso C, Di Monaco F (2012) Nonlinear testing and models comparison of magneto-mechanical energy scavengers. In: *Topics in modal analysis*, vol 6. Springer, New York, pp 63–69. doi:[10.1007/978-1-4614-2419-2\\_7](https://doi.org/10.1007/978-1-4614-2419-2_7)
12. Tornincasa S, Repetto M, Bonisoli E, Di Monaco F (2012) Optimization of magneto-mechanical energy scavenger for automotive tire. *J Intell Mater Syst Struct* 23(18):2055–2064. doi:[10.1177/1045389X11430741](https://doi.org/10.1177/1045389X11430741)
13. Tornincasa S, Repetto M, Bonisoli E, Di Monaco F (2012) Energy harvester for vehicle tires: nonlinear dynamics and experimental outcomes. *J Intell Mater Syst Struct* 23(1):3–13. doi:[10.1177/1045389X11430739](https://doi.org/10.1177/1045389X11430739)
14. Rocha JG, Gonçalves LM, Rocha PF, Silva MP, Lanceros-Méndez S (2010) Energy harvesting from piezoelectric materials fully integrated in footwear. *IEEE Trans Ind Electron* 57(3):813–819. doi:[10.1109/TIE.2009.2028360](https://doi.org/10.1109/TIE.2009.2028360)
15. Shenck NS, Paradiso JA (2001) Energy scavenging with shoe-mounted piezoelectrics. *IEEE Micro* 21(3):30–42. doi:[10.1109/40.928763](https://doi.org/10.1109/40.928763)
16. Li WG, He S, Yu S (2010) Improving power density of a cantilever piezoelectric power harvester through a curved L-shaped proof mass. *IEEE Trans Ind Electron* 57(3):868–876. doi:[10.1109/TIE.2009.2030761](https://doi.org/10.1109/TIE.2009.2030761)
17. Moro L, Benasciutti D (2010) Harvested power and sensitivity analysis of vibrating shoe-mounted piezoelectric cantilevers. *Smart Mater Struct* 19(11). doi:[10.1088/0964-1726/19/11/115011](https://doi.org/10.1088/0964-1726/19/11/115011)
18. Carroll D, Duffy M (2012) Modelling, design, and testing of an electromagnetic power generator optimized for integration into shoes. *J Syst Control Eng* 226(2):256–270. doi:[10.1177/0959651811411406](https://doi.org/10.1177/0959651811411406)
19. Wang C, Miao D, Luk PC, Shen J, Xu C, Shi D (2010) A shoe-equipped linear generator for energy harvesting. In: *Proceedings of the 2010 IEEE international conference on sustainable energy technologies*. doi:[10.1109/ICSET.2010.5684934](https://doi.org/10.1109/ICSET.2010.5684934)
20. Baghebani R, Ashoorirad M (2009) A power generating system for mobile electronic devices using human walking motion. In: *Proceedings of the second international conference on computer and electrical engineering*, vol 2, pp 385–388. doi:[10.1109/ICCEE.2009.58](https://doi.org/10.1109/ICCEE.2009.58)
21. Dai D, Liu J, Zhou Y (2012) Harvesting biomechanical energy in the walking by shoe based on liquid metal magnetohydrodynamics. *Front Energy* 6(2):112–121. doi:[10.1007/S11708-012-0186-X](https://doi.org/10.1007/S11708-012-0186-X)
22. Hooke R, Jeeves TA (1961) Direct search solution of numerical and statistic problems. *J ACM* 8(2):212–229. doi:[10.1145/321062.321069](https://doi.org/10.1145/321062.321069)

# Chapter 61

## Optimization of an Energy Harvester Coupled to a Vibrating Membrane

Levent Beker, H. Nevzat Özgüven, and Haluk Külâh

**Abstract** Resonant energy harvesters are generally designed for the operating frequency of the host structure. However, when the flexibility and mass parameters of the host structure are comparable to those of the energy harvester, mounting an energy harvester on the host structure may change the vibration characteristics of the host structure considerably. In this study, modeling and optimization of an energy harvester coupled to a vibrating membrane are presented to show the effect of dynamic coupling on maximum voltage output of the energy harvester. First, the optimum design parameters of an energy harvester are calculated to obtain maximum voltage output from piezoelectric material for a given excitation at a specified frequency by considering the dynamics of the energy harvester only. Then, by using the finite element (FE) models of the membrane and the energy harvester, coupled analysis is made and design parameters are optimized to obtain maximum voltage output from piezoelectric material. Finally, the voltage output results from two optimization approaches are compared and it is observed that maximum voltage obtained by considering the coupling effects is several times higher than the voltage output obtained from the energy harvester designed traditionally. The study shows that disregarding the host structure that energy harvesters are mounted in optimization stage may prevent us to find the optimum design parameters.

**Keywords** Energy harvester • Coupling • Optimization

### 61.1 Introduction

Self-powered microsystems are needed for many emerging sensor applications. Recently, advances in integrated circuit (IC) manufacturing and low power circuit design techniques have reduced the power requirements of electronic devices to the order of microwatts. By use of energy harvesters, it is possible to minimize or eliminate the dependence of low power electronic sensors on external power sources or batteries. Among various sources for energy harvesting applications, vibration is more advantageous due to its abundance. Vibration can be found in applications including household goods (fridges, washing machines, etc.), industrial plant equipment, moving structures such as automobiles, airplanes and structures such as buildings and bridges [1]. Kinetic energy of vibrations can be converted to electrical power using three principles; piezoelectric [2], electromagnetic [3] and electrostatic [4]. Among these principles, piezoelectric received greatest attention due to high power density and ease of application [2].

Micro scale piezoelectric energy harvesters can be fabricated using microelectromechanical systems (MEMS) fabrication techniques. This allows micro piezoelectric energy harvesters to be implemented into many applications, such as structural health monitoring systems and wireless sensor networks. General tendency in literature is to design a resonant energy

---

L. Beker • H. Külâh

Micro and Nanotechnology Graduate Program, Middle East Technical University, 06800 Ankara, Turkey

L. Beker (✉) • H. Külâh

METU-MEMS Research Center, Middle East Technical University, 06800 Ankara, Turkey

e-mail: lbeker@mems.metu.edu.tr

H.N. Özgüven

Department of Mechanical Engineering, Middle East Technical University, 06800 Ankara, Turkey

H. Külâh

Department of Electrical and Electronics Engineering, Middle East Technical University, 06800 Ankara, Turkey

harvester by considering the operating frequency of the host structure. Although this approach would work in many cases, if the flexibility and mass parameters of the host structure are comparable to those of the energy harvester, coupling of an energy harvester might change the vibration characteristics of the system considerably. The aim of this paper is to investigate the difference between the optimization results for the cases where coupling effects are considered and excluded in the optimization analysis, and to show the enhancement of the voltage output when coupling effects are considered.

## 61.2 Coupled System

Figure 61.1 shows the considered system, which is a 5 mm by 5 mm and 0.8 mm thick energy harvester. Structural material of the energy harvester is silicon, which is the case for most MEMS structures. The piezoelectric material (PZT-5A) is bonded to the top of the silicon fixed-free beam, which has a tip mass at the free end. Energy harvester is bonded rigidly to a membrane, which has diameter of 10 mm, thickness of 75  $\mu\text{m}$  and has its first natural frequency at 1 kHz.

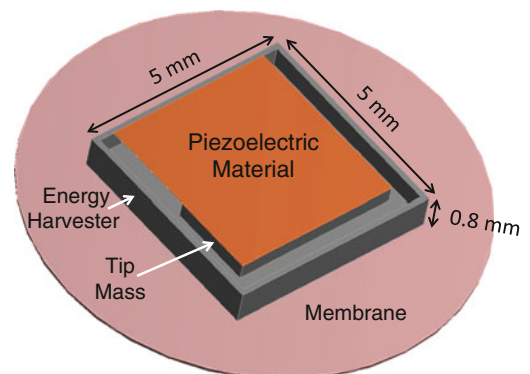
Several methods are used to model piezoelectric energy harvesters, such as single-degree-of-freedom (SDOF), continuous system and FE modeling. Advantages and disadvantages of these methods are discussed in references [2] and [5]. In this paper FE modeling is preferred due to the layered structure of the cantilever beam, anisotropic nature of piezoelectric material, high tip mass-to-beam length and width-to-length ratios. The membrane model is also developed using FE modeling, and natural frequency results are compared with those of the continuous system approach.

### 61.2.1 2D and 3D FE Models of Membrane

Vibration characteristics of membranes are widely studied in literature. Both continuous system models and FE models can be used to determine natural frequencies and mode shapes of membrane structures. Usually 2D elements are used in FE models for modeling thin structures. However, since we need to model a coupled system composed of a membrane and an energy harvester, which is modeled as a 3D solid structure, a proper 3D FE membrane model is required. Therefore, as a first step a 3D membrane model is developed. The model developed is compared with 2D FE model and continuous system model. Ansys FE program is used throughout the study.

For 3D membrane structure, SOLSH190 element suitable for analyzing thin structures is used [6]. Vibration analysis is made to obtain the natural frequencies of the prestressed membrane. In this analysis, prior to modal analysis, membrane is stretched from its boundary by simply giving a predetermined displacement. It is observed that in order to obtain the first mode at 1 kHz with 10 mm diameter and 75  $\mu\text{m}$  thick membrane, 20.6  $\mu\text{m}$  stretching in radial direction is required. A similar analysis is applied to the same membrane modeled using 2D SHELL181 element.

In order to verify 3D FE model developed, a continuous system model is used. However, the well-known equation for natural frequencies of circular membranes includes tension term instead of displacement term, which is used during FE model development. Therefore, an alternative form of the well-known equation is derived by relating tension components to applied stretching displacement. In order to relate tension components to displacement General Hooke's Law is used in cylindrical coordinates:



**Fig. 61.1** Energy harvester attached to the membrane

**Table 61.1** Comparison of natural frequencies of circular membrane obtained using continuous system model with those of 2D and 3D FE models

	CSM <sup>a</sup>	2D FEM	3D FEM	% 3D error
$\omega_{10}$	973.86	974.52	1000.10	2.68
$\omega_{11}$	1551.82	1552.38	1612.32	3.90
$\omega_{12}$	2079.89	2079.05	2181.51	4.89
$\omega_{20}$	2235.40	2234.74	2370.82	6.06

<sup>a</sup>Continuous system model

**Table 61.2** Material properties of silicon, PZT-5A and membrane used in simulations

(100) Silicon				PZT-5A				Membrane						
$E_x$	169	GPa	$\nu_{yz}$	0.36	–	$s_{11}^E$	16.4	$\text{pm}^2/\text{N}$	$d_{31}$	–171	$\text{pm}/\text{V}$	E	33	MPa
$E_y$	169		$\nu_{zx}$	0.28		$s_{12}^E$	–5.7		$d_{33}$	374		$\nu$	0.3	–
$E_z$	130		$\nu_{xy}$	0.06		$s_{13}^E$	–7.2		$d_{15}$	584		$\rho$	1,200	$\text{kg}/\text{m}^3$
$G_{yz}$	79.6		$\rho$	2,329	$\text{kg}/\text{m}^3$	$s_{33}^E$	18.8		$\varepsilon_{11}^T/\varepsilon_0$	1,730	–			
$G_{zx}$	79.6					$s_{55}^E$	47.5		$\varepsilon_{33}^T/\varepsilon_0$	1,700				
$G_{xy}$	50.9					$s_{66}^E$	44.3		$\rho$	7,750	$\text{kg}/\text{m}^3$			

$$\begin{Bmatrix} \sigma_{rr} \\ \sigma_{\theta\theta} \\ \sigma_{zz} \end{Bmatrix} = \frac{2G}{1-2\nu} \begin{bmatrix} 1-\nu & \nu & \nu \\ \nu & 1-\nu & \nu \\ \nu & \nu & 1-\nu \end{bmatrix} \begin{Bmatrix} \varepsilon_{rr} \\ \varepsilon_{\theta\theta} \\ \varepsilon_{zz} \end{Bmatrix} \quad (61.1)$$

where  $\sigma_{rr}$ ,  $\sigma_{\theta\theta}$ ,  $\sigma_{zz}$ ,  $\varepsilon_{rr}$ ,  $\varepsilon_{\theta\theta}$  and  $\varepsilon_{zz}$  represent stress and strain in radial, angular and axial directions respectively,  $\nu$  represents Poisson's ratio and  $G$  represents shear modulus. If we assume that there is no twisting due to uniform stretching from boundary,  $\varepsilon_{\theta\theta}$  becomes equal to  $\varepsilon_{rr}$  at the boundary of the membrane which is simply ratio of stretching displacement  $x_0$  to membrane radius  $a$ . Furthermore, since the circular membrane is stretched from its boundary in radial direction,  $\sigma_{zz}$  will be zero and (61.1) can be solved easily. As a result, after relating  $G$  with Young's modulus,  $E$ , and  $\nu$  using conversion formulas for isotropic materials, stress components  $\sigma_{rr}$  and  $\sigma_{\theta\theta}$  at the membrane boundary can be obtained as follows:

$$\sigma_{rr} = \sigma_{\theta\theta} = \frac{x_0 E}{a(1-\nu)} \quad (61.2)$$

Then, tension  $T$  can be written as multiplication of  $\sigma_{rr}$  with  $h$ , where  $h$  is the membrane thickness, and the natural frequency of the circular membrane as a function of stretching displacement  $x_0$  can be obtained as follows:

$$\omega_n = \frac{\lambda_n}{2\pi} \sqrt{\frac{x_0 E}{a^3 \rho(1-\nu)}} \quad (61.3)$$

Here,  $\lambda_n$  denotes eigenvalue of the  $n$ th mode and  $\rho$  denotes density per unit volume. Comparison of the evaluated natural frequencies using (61.3) and by FE analysis using 2D and 3D models are given in Table 61.1. It is observed that 2D FEM results are almost equal to continuous system model results (errors are less than 0.1%). Errors obtained using 3D FE model are considerably higher than those obtained with a 2D model. However, due to the reason explained above, 3D FE model is used in this study as the percentage error in the fundamental frequency is only about 2%.

### 61.2.2 FE Model of Energy Harvester

Energy harvester is composed of silicon and piezoelectric material. As most of the reported micro energy harvesters, proposed model has a large tip mass to decrease the natural frequency of the cantilever beam with such a small length. The piezoelectric material is bonded around the anchor and is to be exposed to maximum stress to obtain maximum voltage. Silicon cantilever beam and 5 mm by 5 mm square casing are modeled as a single volume which can be fabricated through standard MEMS processes such as silicon deep reactive etching (DRIE) [7]. PZT-5A is used as a piezoelectric material which can be modeled anisotropically using SOLID226 element with option 1001. Silicon is modeled as an orthotropic material [8]. Further details can be found in authors' previous study [5]. Material constants of silicon, PZT-5A, and membrane are given in Table 61.2.



### 61.3 Optimization

For the optimization procedure, first order method is used. This method uses a penalty function to find optimum variable set. Gradients of the variables are calculated in order to determine a search direction; thus, each iteration is composed of subiterations that include search directions and gradient calculations. Two different cases are studied to observe the effect of coupling. In the first approach, optimization analysis is made by considering the dynamics of the energy harvester only. For the latter approach, dynamics of both the energy harvester and the membrane are considered during optimization analysis. Harmonic vibration analysis is conducted in both cases with a given excitation frequency of 1 kHz. Some of the parameters such as beam thickness and tip mass thickness are kept constant due to fabrication limitations.

#### 61.3.1 Optimization of Energy Harvester Alone

The optimum parameters of the energy harvester are calculated by taking an excitation at 1 kHz applied to the bottom surface of the case of the energy harvester (Fig. 61.2a). This routine starts with parameter initialization and proceeds with harmonic vibration analysis at 1 kHz. At the end of the analysis, maximum voltage on the piezoelectric material is recorded as  $V_{max}$ . Optimization process terminates if the objective function converges to a value and cannot obtain better results for the given tolerance value. Design variables and system constants are given in Table 61.3.

#### 61.3.2 Optimization of Energy Harvester Coupled to Membrane

For this case, FE model of the energy harvester bonded rigidly to the membrane is used as described in Sect. 61.2.1. Main difference between this procedure and the previous is that the energy harvester is not excited directly but the pressure excites the bottom surface of the membrane at 1 kHz, as it is the case in real applications (Fig. 61.3). Design variables, system constants (Table 61.3) and objective of the optimization procedure are the same as the previous case.

Optimization results of the systems considered are given in Table 61.4. It is observed that the design variables obtained from the first optimization, where only the dynamics of the energy harvester is considered, give the first natural frequency of the energy harvester as 1005.9 Hz. This is an expected result for the energy harvester, which is directly excited with frequency of 1 kHz, since the first mode is expected to be at the operating frequency. Moreover, it is observed that decreasing the tolerance value specified for the convergence in optimization results in harvester with a natural frequency closer to 1 kHz. On the other hand, optimization results for the coupled system yield the first natural frequency of the coupled system as 778.4 Hz, while the 4th mode of is at 1012.5 Hz. Corresponding mode shapes of the energy harvester and the coupled system are given in Fig. 61.4.

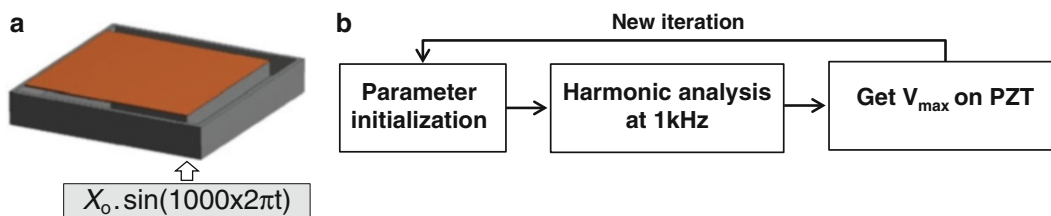
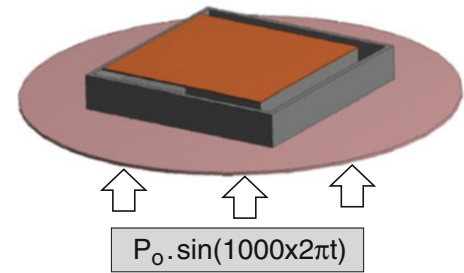


Fig. 61.2 (a) Representation of harmonic vibration analysis (b) Optimization procedure

Table 61.3 Design variables and system constants used in optimization process

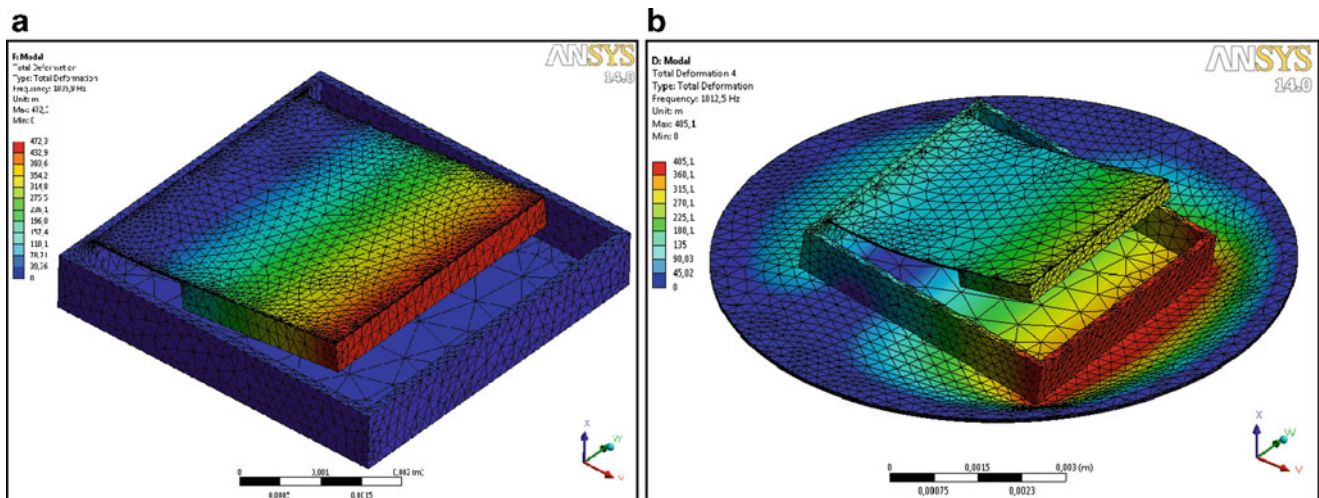
	Parameter	Min	Max	Unit
Variables	Beam length	2	4.25	mm
	PZT thickness	10	50	$\mu\text{m}$
	Tip mass length	0.2	3.5	mm
Constants	Beam thickness	20		$\mu\text{m}$
	Beam width	4		mm
	Tip mass thickness	300		mm

**Fig. 61.3** Representation of harmonic vibration analysis conducted on energy harvester coupled to membrane



**Table 61.4** Optimization results and natural frequencies of optimized harvesters (Opt. 1: optimization of the energy harvester only; Opt. 2: optimization of the coupled system)

Design variable	Opt. 1	Opt. 2	Unit
Beam length	3.92	4.25	mm
PZT thickness	18	20	$\mu\text{m}$
Tip mass length	2.65	2.04	mm
Natural freq. of harvester	1005.9	778.4	Hz

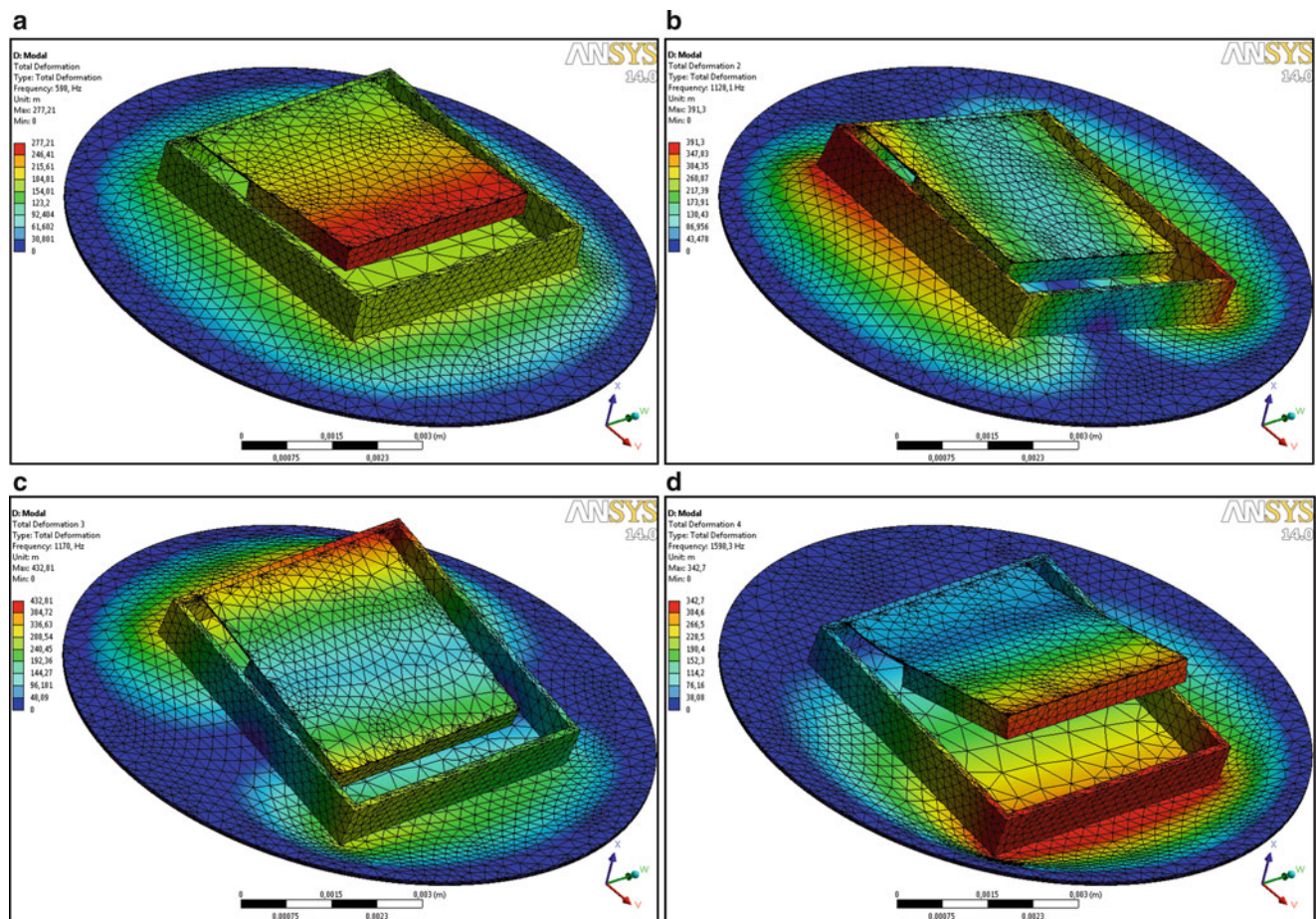


**Fig. 61.4** Mode shapes of (a) energy harvester alone (1st mode at 1005.9 Hz) (b) coupled system (4th mode at 1012.5 Hz)

### 61.3.3 Comparison of the Optimization Results

In order to compare the two approaches, optimum design parameters obtained from the two approaches are used to calculate the voltage generated for a pressure excitation of 20 Pa at 1 kHz when energy harvester is bonded to the membrane as in the real situation. Pressure excitation is applied to the membrane and a constant damping ratio of 0.018 is used in the simulations [9]. Harmonic vibration analysis is made first by using the energy harvester dimensions found from the first optimization (Opt. 1). The first four modes of the system are shown in Fig 61.5. The natural frequencies at these modes are found as 598, 1128.1, 1,170 and 1590.3 Hz (Fig. 61.5).

Harmonic vibration analysis results showed that the system shown in Fig. 61.5, which does not have any of its modes at 1 kHz, can generate a maximum voltage of 0.23 V if the membrane is excited with a pressure of 20 Pa at 1 kHz. The same approach is followed to find the voltage output when the second energy harvester (Opt. 2) is used. It is observed that 4th mode of the coupled structure has a resonance at 1012.5 Hz, and the maximum voltage of 1.45 V can be generated using the same excitation and damping ratio parameters. It can be seen that the enhancement of the voltage arise from the fact that when second energy harvester (Opt. 2) is mounted to the membrane, the coupled system is vibrating at almost its natural frequency when an excitation at 1 kHz is applied. Furthermore, the corresponding mode is not an arbitrary mode but is the one at which the maximum relative displacement between the tip of the beam and its base is obtained.



**Fig. 61.5** First four mode shapes of coupled system when energy harvester with 1005.9 Hz natural frequency is bonded to membrane (a) 1st mode at 598 Hz (b) 2nd mode at 1128.1 Hz (c) 3rd mode at 1,170 Hz and (d) 4th mode at 1590.3 Hz

## 61.4 Conclusion

Vibration energy harvesters are mostly designed and optimized separately from the host structure. The operating frequency of the host structure is taken as the excitation frequency of the energy harvester and the optimum parameters are calculated considering the dynamics of the energy harvester only. This approach can be justified for the cases where the mass of the energy harvester is negligible relative to the host structure. However, when flexible and low mass structures such as membranes are used as host structures, the effect of the energy harvester on the vibration of the host structure may not be negligible. In this case, coupled vibrations of the host structure and the energy harvester should be considered in the computation of the optimal design parameters for the energy harvester. In this study, we focused on a special application where a micro energy harvester is attached to a membrane. Modeling attempts begin by developing an appropriate model of the membrane structure. Although 2D FE membrane models are very accurate, a 3D FE membrane model is used in this analysis, in order to integrate the membrane model with the 3D solid model of the energy harvester. Optimum design parameters of the energy harvester are calculated first in a traditional way, by considering energy harvester only, and then by using the coupled membrane-energy harvester system. The design parameters found from these two approaches differ from each other about 10–23%. Although the first resonance frequency of the harvester designed using coupled system approach is quite different from the excitation frequency (778.4 vs. 1,000 Hz), under operating conditions the coupled system has its 4th resonance frequency very close to the excitation frequency. Furthermore, the maximum relative displacement of the tip mass of the harvester with respect to its base occurs at this mode. The performances of both of the energy harvesters are compared by calculating the maximum voltage outputs obtained for a given harmonic pressure excitation at 1 kHz when mounted to the membrane. It is observed that, although the design parameters differ 23% at the most, maximum voltage generated by the energy harvester designed considering coupling effect is 6.2 times of the voltage generated by the energy

harvester designed without considering the coupling effect at optimization stage. Then, it is concluded that coupling effects should be considered in designing a resonant energy harvester, when the flexibility and mass parameters of the host structure are comparable to those of energy harvester.

## References

1. Beeby SP, Tudor MJ, White NM (2006) Energy harvesting vibration sources for microsystems applications. *Meas Sci Technol* 17(12):175–195
2. Ertürk A, Inmann DJ (2011) *Piezoelectric energy harvesting*, Wiley, Hoboken, NJ USA
3. Sari İ, Balkan T, Külah H (2010) An electromagnetic micro power generator for low frequency environmental vibrations based on the frequency-up conversion technique. *J Microelectromech Syst* 19(1):14–27
4. Roundy S (2003) Energy scavenging for wireless sensor nodes with a focus on vibration to electricity conversion. Ph.D. thesis, University of California, Berkeley
5. Beker L, Muhtaroglu A, Özgüven HN, Külah H (2012) Finite element modeling of MEMS piezoelectric energy harvester. In: *Proceedings of nanotech modeling and simulation of microsystems*, vol 2, Santa Clara, pp 633–636
6. ANSYS® Release 14.0, *Elements Reference Guide*, ANSYS, Inc.
7. Aktakka E, Peterson RL, Najafi K (2010) A CMOS-compatible piezoelectric vibration energy scavenger based on the integration of bulk PZT films on silicon. In: *IEEE international electron devices meeting*, pp 31.5.1–31.5.4
8. Hopcroft MA, Nix WD, Kenny TW (2010) What's young's modulus of silicon? *J Microelectromech Syst* 19(2):229–238
9. Zorlu Ö, Topal ET, Külah H (2011) A vibration-based electromagnetic energy harvester using mechanical frequency up-conversion method. *IEEE Sens J* 11(2):481–488



# Chapter 62

## Experimental Localization of Small Damages Using Modal Filters

G. Tondreau and A. Deraemaeker

**Abstract** This work investigates the experimental application of a damage localization technique based on local modal filters on a small clamped-free steel plate equipped with eight piezoelectric (PVDFs) sensors, and excited with a PZT patch. A small damage responsible of a small shift of the eigenfrequencies (less than 4%) is introduced at different locations by fixing a stiffener. By following the guidelines established in previous numerical studies, the modal filters are applied on three local filters in order to locate damage, and a new feature extraction procedure is proposed. Univariate control charts are used to locate automatically all the damage positions correctly. The very nice results obtained with this first experimental application of modal filters based on strains show the real interest of this very simple method for output-only non-model based automated damage localization of real structures.

**Keywords** Structural health monitoring • Experimental damage localization • Piezoelectric sensors • Modal filters

### 62.1 Introduction

Structural health monitoring has gained a particular attention since more than 20 years to assess the health of structures [4]. Recently, a very simple non-model based output-only method using modal filters has been developed for damage detection [1]. By considering strain measurements as well as control charts [7], the idea has next been extended successfully to automated damage localization in many numerical studies [10]. However, with the exception of the experimental study led by Mendrok et al. using accelerations [6], the modal filters technique using strain sensors to locate damages has never been tested experimentally so far. This paper aims at presenting for the first time an experimental application of the modal filters with strain measurements by following the guidelines proposed by the authors in previous numerical studies. The structure investigated is a clamped-free steel beam, covered with eight PVDFs sensors. A small damage is introduced by fixing a stiffener at different positions, and can be automatically located with the proposed method. The results are very promising, and show in particular that PVDFs sensors seem to be very interesting for the application of modal filters to locate damages on real structures.

### 62.2 Damage Localization Using Local Filters

Consider a structure equipped with a large network of  $n$  sensors. In order to proceed to a data reduction, one can combine sensors responses  $y_k(t)$  to form a single output response with a linear combiner by applying Eq. (62.1):

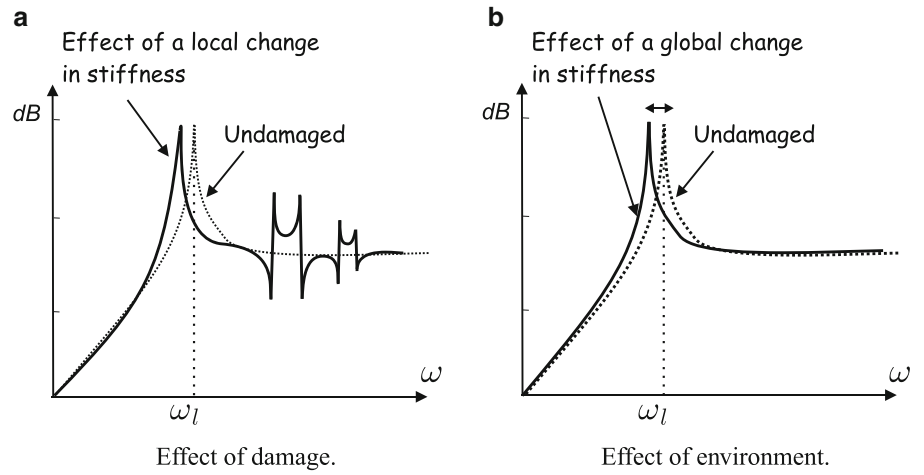
$$g(t) = \sum_{k=1}^n \alpha_k y_k(t) \quad (62.1)$$

---

G. Tondreau (✉) · A. Deraemaeker

ULB, Building Architecture and Town Planning (BATir), avenue F.D. Roosevelt 50, B-1050, Brussels, Belgium  
e-mail: [gilles.tondreau@ulb.ac.be](mailto:gilles.tondreau@ulb.ac.be); [aderaema@ulb.ac.be](mailto:aderaema@ulb.ac.be)

**Fig. 62.1** Modal filter tuned on mode  $l$ . (a) Effect of damage. (b) Effect of environment



The idea behind modal filtering is to choose coefficients  $\alpha_k$  in Eq. (62.1) in such a way that they are orthogonal to all the modes of the structure in a frequency band of interest, except mode  $l$ .

These coefficients are the solution of Eq. (62.2):

$$[C]^T \{\alpha\} = \{e_l\} \quad (62.2)$$

where  $\{e_l\}^T = (0 \dots 1 \dots 0)^T$  is a vector with all entries equal to 0 except entry  $l$  (corresponding to the eigenfrequency on which the modal filter is tuned) which is equal to 1, and  $[C]$  is the rectangular matrix of modal output gain. One can obtain  $\{\alpha\}$  by applying the widely used Moore-Penrose pseudo-inverse of  $[C]^T$ :

$$\{\alpha\} = ([C]^T)^\dagger \{e_l\} \quad (62.3)$$

However, the rank of matrix  $[C]^T$  is rarely full in practice, so that the previous approach is not adequate. More explanation on the rank deficiency can be found in [10]. The alternative adopted by the authors to regularize the inversion of  $[C]^T$  consists of applying a singular value decomposition (SVD) of  $[C]^T$ :

$$[C]^T = [U][S][V]^T, \quad (62.4)$$

with  $[S] = \text{diag}(\sigma_i)$ .

If  $u_i$  and  $v_i$  are the columns of the unitary matrices  $[U]$  and  $[V]$ , the solution of Eq. (62.2) is given by

$$\{\alpha\} = \{\alpha_1 \dots \alpha_n\}^T = \left( \sum_{i=1}^r \frac{1}{\sigma_i} u_i v_i^T \right) \{e_l\} \quad (62.5)$$

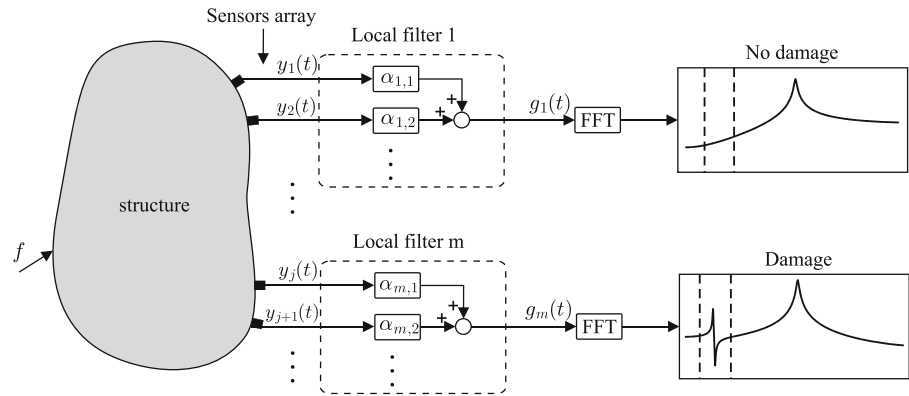
The calculation of coefficients  $\{\alpha\}$  is governed by two parameters which are the number of modes  $nm$  taken into account in  $[C]$  ( $nm$  is limited to the number of sensors), and the number of singular values  $r$  to solve Eq. (62.5) ( $2 \leq r \leq nm$ ). Previous works pointed out that the filtering is the most efficient if only two mode shapes ( $nm = 2$ ) are taken into account (both in numerical [10] and experimental tests.)

When damage occurs, the orthogonality condition (62.2) is not satisfied anymore. When looking at the Fourier transform of  $g(t)$ , or at its power spectral density (PSD), this results in spurious peaks near other natural frequencies than  $l$ . This principle has already been studied in [1] and [2] for damage detection, using acceleration measurements. It also has the advantage to distinguish global effects from local effects (see Fig. 62.1).

The extension of the previous idea to damage localization is straightforward. The network of  $n$  sensors is divided in  $m$  spatial filters, and the modal filters coefficients  $\{\alpha\}$  are computed so that they are orthogonal to the projection of all mode shapes on the sensors of each local filter, except mode  $l$ . Therefore, monitoring independently each local filter allows to locate the damage in a particular local filter by checking the appearance of a spurious peak in the filtered frequency response, as depicted in Fig. 62.2.



**Fig. 62.2** Principle of damage localization using local filters



The efficiency of the method relies on the assumption according to which the change of the mode shape due to a small damage is concentrated in the close vicinity of the damage. Such a property has been observed with curvatures in beam-like structures in [8], and it has been generalized to any kind of structures by considering strain measurements more recently, both numerically [3] and experimentally [5].

### 62.3 Statistical Approach for an Automated Damage Localization

In order to quantify the growth of a spurious peak, it is necessary to define an indicator in the frequency band of interest (around the  $i$ th eigenfrequency if the  $i$ th mode shape is filtered). This indicator should be sensitive to the shape of the function (appearance of spurious peak), but not to its level (change of the level of the excitation). Previous works considered an indicator called peak indicator [10, 11], but recent researches pointed out that this indicator presents some drawbacks. On the other hand, using the moment of order 4 which quantifies the flattening of a probability density function is a very interesting alternative. Because the signals are acquired at discrete time intervals, the PSD of  $g(t)$  is also obtained at discrete frequency points. If we note  $s_1, \dots, s_n$  the  $n$  discrete amplitudes of the filtered frequency response in the bandwidth  $\omega_a - \omega_b$  and  $P(s)$  the estimate of the corresponding probability density function, the estimate of the moment of order 4 of that function reads:

$$m_4 = \frac{1}{n} \sum_i (s_i - \bar{s})^4, \quad (62.6)$$

where  $\bar{s}$  is the mean value of  $s_i$  in the frequency band  $\omega_a - \omega_b$ . Figure 62.3 illustrates how a spurious peak can be detected and quantified by looking at  $m_4$ .

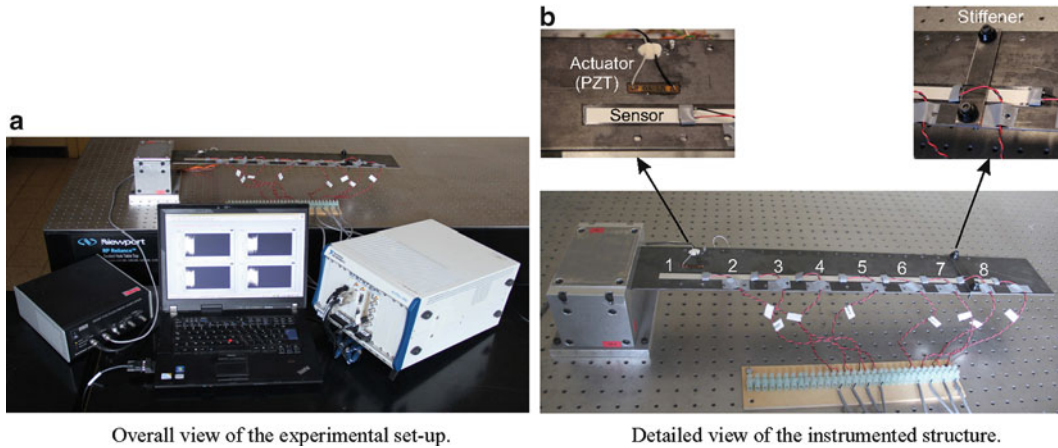
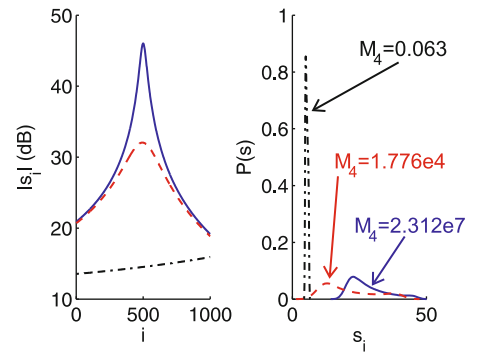
In the present work, we will focus on the appearance of spurious peaks around only one eigenfrequency for each local filter. Because the structure is considered to be excited by random excitations, we will deal with random features  $m_4$ . These features will have to be monitored in order to detect when they are shifted from their in-control values (values of  $m_4$  in the undamaged state). Control charts [7] are very efficient for these shifts detection. Control charts plot the feature as a function of the sample number. When operating conditions change, the feature will fall outside control limits (lower or upper limit) which are computed from samples when the conditions are assumed to be in control. Different types of control charts can be applied, but it has been found in previous studies that the individual control charts which focuses on the shifts of mean values is the most adequate. Finally, because of numerical issues not detailed here, the control chart is applied on  $\sqrt[8]{m_4}$  instead of  $m_4$ .

## 62.4 Experimental Application on a Small Scale Set-Up

### 62.4.1 Case Study Description

Figure 62.4 shows an overview of the experimental set-up.

**Fig. 62.3** Example of a spurious peak growth (*left*) and the effect on the estimate of the corresponding probability density function (*right*)



**Fig. 62.4** Experimental set-up. (a) Overall view of the experimental set-up. (b) Detailed view of the instrumented structure

**Table 62.1** Damage scenarios

Case	Samples	Location of damage (sensor)	Location of damage (local filter)
1	1 to 1,000	None	None
2	1,001 to 1,250	3	[1:4] and [3:6]
3	1,251 to 1,500	4	[1:4] and [3:6]
4	1,501 to 1,750	8	[5:8]

The structure consists in a  $100 \times 670 \times 3$  mm clamped-free steel plate. One PZT actuator is used to excite the structure, and eight  $13 \times 60 \text{ mm} \times 50 \mu\text{m}$  low-cost PVDFs sensors have been fixed with double-coated tape. These sensors are numbered from the clamped edge of the plate, and cover continuously the structure along its length. A National Instrument PXIe-1082 data acquisition system is used to measure the eight voltages from the PVDFs at the same time. The PZT actuator is driven with a band-limited white noise between 0 and 50 Hz generated by the PXI, and powered by a MIDE high voltage amplifier. In all cases, the measurements last for 30 s and the sampling frequency is 1,600 Hz. Finally, many threaded holes have been drilled all along the plate, so that a  $100 \times 20 \times 3$  mm stiffener can be fixed over any sensor to simulate a small (removable) damage.

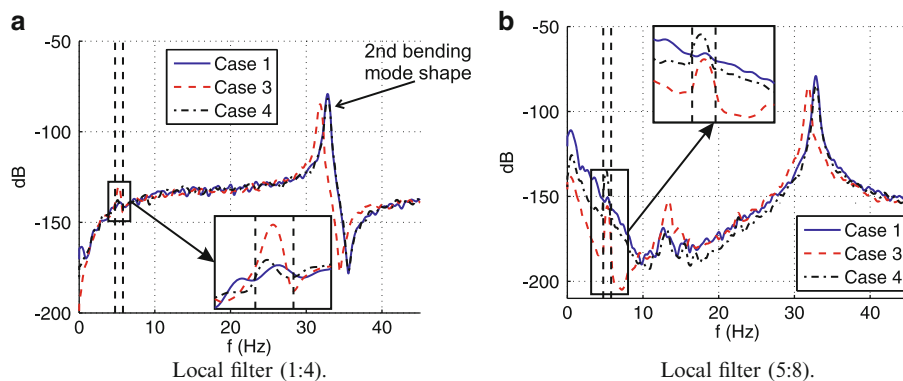
Because of the limited number of sensors, it has been chosen to consider three local filters of four sensors, with an overlap of two sensors: sensors 1–4, 3–6 and 5–8. We will investigate the damage scenarios given in Table 62.1, which also shows the local filters covering the damage.

### 62.4.2 Undamaged Structure

Using the *Macec Toolbox* in *Matlab* which applies the stochastic subspace identification method [9], we have been able to identify correctly the two first undamaged bending mode shapes  $\Phi_1$  ( $f_1 = 5.27$  Hz) and  $\Phi_2$  ( $f_2 = 32.51$  Hz). Since it has

**Table 62.2** Changes of eigenfrequencies due to damage

Case	$\Delta f_1$ (%)	$\Delta f_2$ (%)
2	0.08	1.83
3	0.40	3.09
4	3.41	<0.01

**Fig. 62.5** Examples of undamaged and damaged aged filtered frequency responses. (a) Local filter (1:4). (b) Local filter (5:8)

been demonstrated in several numerical and experimental studies that the effect of a damage is more local for low order mode shapes, it has been chosen to only consider modal filters tuned on  $\Phi_2$  and to check the appearance of spurious peaks around  $f_1$  for each local filter.

### 62.4.3 Damaged Structure

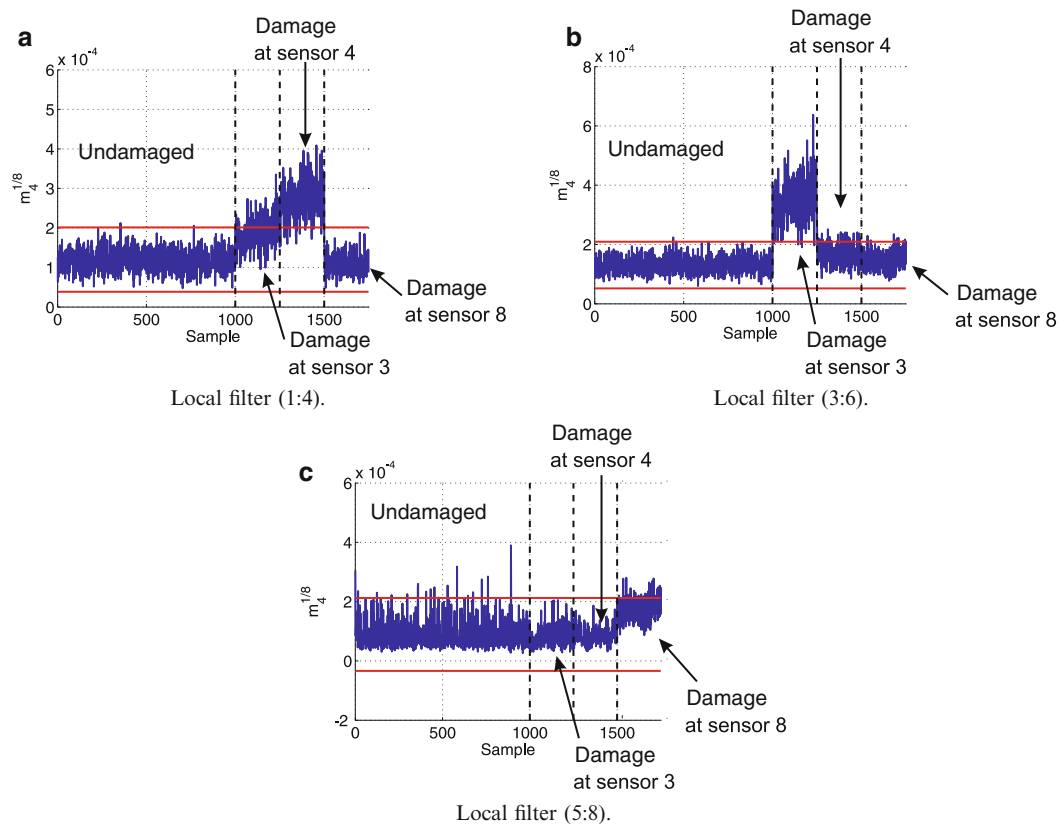
For the different damage scenarios, the eigenfrequencies as well as the mode shapes have been reidentified, in order to quantify the impact of the damage simulated by adding the small stiffener. It has been observed that the effect of the stiffener on the mode shape is local, as a real damage does. It has also been concluded that adding the stiffener can be interpreted as introducing a small damage, since the change of eigenfrequencies is small (see Table 62.2).

Figure 62.5 compares the filtered frequency responses of local filters [1:4] and [5:8] for case 1, 3 and 4. The frequency band in which the feature  $m_4$  is computed is shown with the two vertical dashed lines. It corresponds to the first undamaged eigenfrequency  $f_1 \pm 10\%$ .

As it can be seen, the filtering is quite nice, since the peak around the first eigenfrequency is efficiently filtered. Figure 62.5a shows clearly the possibility of locating damages with local filter. Indeed, the local filter [1:4] presents a spurious peak for damage scenario 3 (stiffener over sensor 4) but not for damage scenario 4 (stiffener over sensor 8). For local filter [5:8], the damage localization seems more tricky. This is in particular due to the fact that the level of the sensor responses decreases at the free extremity of the plate, which tends to increase the sensitivity of the filtered frequency responses to environmental effects.

### 62.4.4 Automated Damage Localization

In order to automate the damage localization, we apply individual control charts on each local filter separately. The control limits are computed by considering the first 750 undamaged samples during which the structure is assumed to be undamaged. The control limits are computed by considering a confidence interval of  $\pm 3\sigma$  around the mean (undamaged) value of  $\sqrt[8]{m_4}$ . Hence, 99.73% of the values of the features will fall in this interval if there is no change of the state. On the other hand, if less than 99.73% features fall in the confidence interval, we will assume that a damage appeared in the local filter. In this case study, it has been arbitrarily considered that the damage is located when less than 90% of the features fall in the confidence interval to avoid too frequent false alarms.



**Fig. 62.6** Individual control charts (control limits represented with the *horizontal red lines*). (a) Local filter (1:4). (b) Local filter (3:6). (c) Local filter (5:8)

**Table 62.3** Percentage of in-control features

Local filter	Case 1 (%)	Case 2 (%)	Case 3 (%)	Case 4 (%)
[1:4]	99.8	<b>68</b>	<b>8</b>	100
[3:6]	99.7	<b>2.8</b>	<b>84.4</b>	95.6
[5:8]	97.9	100	100	<b>79.6</b>

Figure 62.6 illustrates the application of the individual control charts for each local filter, while Table 62.3 summarizes the percentage of in-control features.<sup>1</sup>

It is clear from Table 62.3 that all the damage cases have been correctly located. Indeed, all the percentages smaller than 90% (in bold) corresponds to the real damage location (see Table 62.1). The interest of overlapping the local filters is also clearly illustrated. Indeed, damage at sensor 3 is better detected in filter [3:6] than in filter [1:4], while damage at sensor 4 is better detected in filter [1:4] than in filter [3:6].

## 62.5 Conclusion

In this paper a very simple output-only non-model based method using modal filters has been applied experimentally. Considering a small network of eight PVDFs sensors, it has been possible to locate correctly a small damage introduced by fixing a small stiffener at different positions. The success of the proposed technique for automated damage localization is due to a shrewd choice of the physical quantities to measure (strains), to the adequate definition of the new feature proposed ( $m_4$ ), to a local approach enhancing the effect of the damage, as well as to the control charts. Future researches will focus

<sup>1</sup>The percentage for case 1 is based on 1,000 samples, while it is based on 250 samples for the other cases.

on bigger experimental set-ups by considering ambient vibrations excitation, as well as environmental effects. Finally, the location of real damages (fatigue cracks in steel structures) will be assessed. The final aim is to check whether the method can be applied in-situ on real structures, beyond experiments in laboratories.

**Acknowledgements** The authors would like to thank Gilles Vanhooren for manufacturing the experimental set-up. This study has been supported by the FNRS-FRIA grant (Belgium).

## References

1. Deraemaeker A, Preumont A (2006) Vibration based damage detection using large array sensors and spatial filters. *Mech Syst Signal Process* 20:1615–1630
2. Deraemaeker A, Reynders E, De Roeck G, Kullaa J (2008) Vibration-based structural health monitoring using output-only measurements under changing environment. *Mech Syst Signal Process* 22:34–56
3. Deraemaeker A (2010) On the use of dynamic strains and curvatures for vibration based damage localization. In: *Proceedings of the fifth european workshop on structural health monitoring, Sorrento, 28 June–4 July 2010*, pp 835–840
4. Doebling SW, Farrar C, Prime MB (1998) A summary review of vibration-based damage identification methods. *Shock Vib Dig* 30:91–105
5. Gu Y, Tong L, Tan P (2011) Surface strain distribution method for delamination detection using piezoelectric actuators and sensors. In: *Proceedings of the 9th international conference on damage assessment of structures, Oxford, 11–13 July 2011*
6. Mendrok K, Uhl T (2010) Experimental verification of the damage localization procedure based on modal filtering. *Struct Health Monit Int J* 20:1615–1630
7. Montgomery DC (2009) *Statistical quality control: a modern introduction*. Wiley, New York
8. Pandey AK, Biswas M, Sammam MM (1991) Damage detection from changes in curvature mode shapes. *J Sound Vib* 145:321–332
9. Reynders E, De Roeck G (2008) Reference-based combined deterministic-stochastic subspace identification for experimental and operational modal analysis. *Mech Syst Signal Process* 22:617–637
10. Tondreau G, Deraemaeker A. Local modal filters for automated data-based damage localization using ambient vibrations. *Mechanical Systems and Signal Processing* (Accepted for publication)
11. Tondreau G, Deraemaeker A, Papatheou E (2011) Experimental damage detection using modal filters on an aircraft wing. In: *Proceedings of eurodyn2011, Leuven, 4–6 July 2011*, pp 2083–2089

# Chapter 63

## Output Only Structural Identification with Minimal Instrumentation

Suparno Mukhopadhyay, Raimondo Betti, and Hilmi Lus

**Abstract** It is of interest to the modal testing and structural health monitoring community to be able to identify the mass and stiffness parameters of a system from its vibration response measurements. However, incomplete instrumentation of the monitored system, and the more general ambient vibration situations, result in measured mode shapes which are incomplete and not normalized. In this paper, we consider the problem of mode shape expansion, normalization, and subsequent physical parameter identification, for shear-type structural systems with output-only (ambient vibration) measurements. It is shown that only two sensors, located at the first and last degrees of freedom of the system, are sufficient for parametric identification of the system. A mode shape expansion – physical parameter identification algorithm, starting from the incomplete modal parameters identified using a stochastic subspace based method, is discussed. The algorithm incorporates the information available from the structural topology of the physical system in terms of its modal parameters. The advantage of the algorithm lies in its ability to obtain a reliably accurate identification using the minimal necessary instrumentation, and the minimal necessary a-priori information about the system. The efficiency of the proposed algorithm is finally validated through numerical simulations of ambient vibration experiments on a 7 story shear-type structure, including the effect of white/colored measurement noise.

**Keywords** Parametric identification • Output-only data • Structural topology • Mode shape expansion • Minimal instrumentation

### 63.1 Introduction

As evidenced by the vast literature in modal analysis, system identification and structural health monitoring, in vibration-based structural identification, measured structural responses are often used to obtain structural modal parameters by employing various system identification techniques [1]. These experimentally obtained modal parameters may then be used for identifying the physical parameters, i.e. mass and stiffness matrices of the structural system, using orthogonality conditions. However, owing to incomplete instrumentation of the structure, the experimental mode shapes are available, in general, only at the instrumented degrees of freedom (DOFs). Thus, it is often necessary to expand the incomplete experimental mode shapes from the observed to the unobserved DOFs. Additionally, in many cases of vibration based health monitoring, it is not feasible to perform an experimental modal analysis consisting of planned forced vibration experiments. Instead, one has to perform the identification using ambient vibration response data, under normal operational conditions of the structure, i.e. operational modal analysis. In these situations, often referred to as output-only situations, the input force data is not available, and consequently determining the mass scaling (normalization) of the identified mode shapes becomes an additional issue.

---

S. Mukhopadhyay (✉) • R. Betti

Department of Civil Engineering and Engineering Mechanics, Columbia University, New York, NY 10027, USA  
e-mail: [sm3315@columbia.edu](mailto:sm3315@columbia.edu); [betti@civil.columbia.edu](mailto:betti@civil.columbia.edu)

H. Lus

Department of Civil Engineering, Bogazici University, Bebek, Istanbul 34342, Turkey  
e-mail: [hilmilus@boun.edu.tr](mailto:hilmilus@boun.edu.tr)



In this paper, we attempt to develop a robust algorithm for the identification of the mass and stiffness parameters of shear-type structural systems. The primary objective of the identification algorithm is to solve the inverse problem given the realistic constraints of incomplete instrumentation and the usually feasible ambient vibration testing condition. In the course of developing this algorithm, we also attempt to establish the minimal instrumentation set-up necessary for such systems under output-only situations. Moreover, to address the mode shape normalization issue, we attempt to use the minimal possible a-priori information about the system.

The proposed algorithm involves first identifying the complete (in terms of modes) set of modal parameters at the sensor locations using the recently developed subspace identification technique, the Enhanced Canonical Correlation Analysis (ECCA) [2, 3]. Following this a mode shape expansion is performed, expanding the ECCA identified incomplete mode shapes from the observed to the unobserved DOFs. The proposed mode shape expansion algorithm also inherently normalizes the mode shapes, such that at the end of the expansion process we get a mode shape matrix which is proportional through a scalar constant with the true mass normalized mode shape matrix of the system. For structural damage detection purposes, one can compare these proportional mode shapes with the corresponding mode shapes obtained from a previous healthy state of the structure/an analytical model of the healthy structure [4]. However, for model updating/validation purposes one needs to estimate the mass and stiffness parameters of the system, and consequently needs to estimate the scalar constant of proportionality. The proposed algorithm performs this estimation using only one a-priori knowledge about the system. Finally, the mass and stiffness matrices of the system are obtained using the modal orthogonality relations. The efficiency of the proposed method in physical parameter identification is validated via numerical simulations of ambient vibration testing of a 7-DOF shear type structure. Additionally, the robustness of the proposed method to the inevitable presence of measurement noise is also evaluated in the numerical simulations, by polluting the measured acceleration responses from the 7-DOF system using white/colored Gaussian noise.

### 63.2 Formulation of M-K Identification Methodology

Suppose we have an  $N$ -DOF classically damped shear type system whose response acceleration under ambient vibration we are measuring using  $N_s$  number of sensors located at DOFs  $s_i \in \{s_1, s_2, \dots, s_{N_s}\} \subset \{1, 2, \dots, N\}$ . Our objective is to develop a methodology for the identification of the mass,  $\mathbf{M}$ , and stiffness,  $\mathbf{K}$ , matrices of the system, and consequently the element masses and stiffnesses, using the measured output data with minimal instrumentation, i.e. with minimum allowable  $N_s$ . For a shear type system the  $\mathbf{M}$  and  $\mathbf{K}$  matrices have the form:

$$\mathbf{M} = \begin{bmatrix} m_1 & & 0 \\ & m_2 & \\ & & \ddots \\ 0 & & & m_N \end{bmatrix}; \quad \mathbf{K} = \begin{bmatrix} k_1 + k_2 & -k_2 & & & 0 \\ -k_2 & k_2 + k_3 & -k_3 & & \\ & \ddots & \ddots & \ddots & \\ & & -k_{N-1} & k_{N-1} + k_N & -k_N \\ 0 & & & -k_N & k_N \end{bmatrix} \quad (63.1)$$

where  $m_i$  and  $k_i$  are the  $i$ th floor mass and the  $i$ th story stiffness, respectively. These matrices are related with the system's eigenvalues and mode shapes through the generalized eigenvalue problem

$$\mathbf{KV} = \mathbf{MVA} \quad (63.2)$$

where  $\mathbf{\Lambda}$  and  $\mathbf{V}$  are the eigenvalue and mode shape matrices, respectively.

$$\mathbf{\Lambda} = \begin{bmatrix} \lambda_1 & & 0 \\ & \lambda_2 & \\ & & \ddots \\ 0 & & & \lambda_N \end{bmatrix} = \begin{bmatrix} \omega_1^2 & & 0 \\ & \omega_2^2 & \\ & & \ddots \\ 0 & & & \omega_N^2 \end{bmatrix}; \quad \mathbf{V} = [\mathbf{v}_1 \ \mathbf{v}_2 \ \dots \ \mathbf{v}_N] = \begin{bmatrix} v_{1,1} & v_{2,1} & \dots & v_{N,1} \\ v_{1,2} & v_{2,2} & \dots & v_{N,2} \\ \vdots & \vdots & \dots & \vdots \\ v_{1,N} & v_{2,N} & \dots & v_{N,N} \end{bmatrix} \quad (63.3)$$

where  $\lambda_i$ ,  $\omega_i$  and  $\mathbf{v}_i$  denote the  $i$ th modal eigenvalue, frequency and mode shape, respectively, while  $v_{i,j}$  denotes the  $j$ th component, corresponding to the  $j$ th physical coordinate, of the  $i$ th mode shape. Additionally, if  $\mathbf{V}$  is mass normalized, then the  $\mathbf{M}$  and  $\mathbf{K}$  matrices satisfy the modal orthogonality relations, and can consequently be estimated as:

$$\mathbf{V}^T \mathbf{M} \mathbf{V} = \mathbf{I} \Rightarrow \mathbf{M} = (\mathbf{V} \mathbf{V}^T)^{-1}; \mathbf{V}^T \mathbf{K} \mathbf{V} = \mathbf{\Lambda} \Rightarrow \mathbf{K} = \mathbf{V}^{-T} \mathbf{\Lambda} \mathbf{V}^{-1} \quad (63.4)$$

The identification method that we propose in this paper involves a two-step procedure, with the complete mass normalized modal information being obtained in the first step, and then the modal orthogonality relations of (63.4) being used to obtain the system's  $\mathbf{M}$  and  $\mathbf{K}$  matrices.

Although, (63.4) requires a complete mass normalized  $\mathbf{V}$ , owing to incomplete instrumentation ( $N_s < N$ ) of the structure, the measured mode shapes are available, in general, only at the instrumented  $N_s$  DOFs. Thus, it is necessary to expand these incomplete mode shapes from the observed to the unobserved DOFs, and also to make these mode shapes mass normalized. Furthermore, not all instrumentation set-ups may give sufficient information for the expansion of the mode shapes from the observed to the unobserved degrees of freedom. It is thus also necessary that we know what the minimal  $N_s$  requirement is and which physical DOFs should be instrumented, so that we can get the necessary information for estimating the unmeasured rows of  $\mathbf{V}$ . In the following discussions we address this issue of minimal instrumentation, and develop a mode shape expansion procedure for such an instrumentation setup.

Furthermore, since we only have the output measurements, and since the system under consideration is shear type, we need to know 1 system information (e.g. the total mass of the system), in order to correctly identify the system. In absence of that information we will only be able to identify a proportional system, which differs from the true system by a scalar constant of proportionality. Thus, in the proposed method, we first identify a proportional system, and then use our knowledge of the system to find the factor of proportionality, and scale the proportional system accordingly to get the true system. Here onwards, unless otherwise stated,  $\mathbf{V}^*$  and  $\mathbf{V}$  will denote the proportional and true mass normalized mode shape matrices, respectively, with  $\mathbf{V} = \beta \mathbf{V}^*$ , where  $\beta$  is the scalar factor of proportionality.

### 63.2.1 Estimation of $\mathbf{\Lambda}$ and $\mathbf{V}^*$

In the identification of the modal parameters, we first need to use an output only system identification procedure to realize a mathematical model of the system and identify its modal parameters at the measured DOFs. In this paper, for this purpose we use the recently developed ECCA [2, 3], a technique within the stochastic subspace identification (SSI) framework which has shown great promise for effectively determining the model order by highlighting true structural modes against numerical/noise modes when analyzing field measurements. We also assume that the measured responses obtained from the ambient vibration of the system are rich enough so that all the structural modes are identified at the  $N_s$  instrumented DOFs, i.e. using ECCA we estimate the full  $N \times N$  diagonal  $\mathbf{\Lambda}$  and a  $N_s \times N$  non-mass normalized mode shape matrix. In this step, using ECCA, we can also estimate all the  $N$  modal damping ratios, i.e.  $\zeta_i \forall i \in \{1, 2, \dots, N\}$ , although these are not necessary in the proposed  $\mathbf{M}$  and  $\mathbf{K}$  identification algorithm.

Our next objective is to estimate the complete  $\mathbf{V}^*$  matrix. Since,  $\mathbf{V}^*$  can be any matrix proportional to  $\mathbf{V}$ , we choose  $\mathbf{V}^*$  such that its first element is equal to 1. We next proceed to determine the remaining  $N^2 - 1$  elements of  $\mathbf{V}^*$ . To this end, we first derive two sets of equations involving the unknown elements in  $\mathbf{V}^*$ .

#### 63.2.1.1 Equations from Structural Topology

The first set of equations is derived from the structural topology of a shear type system, namely the nature of the mass  $\mathbf{M}$  and flexibility  $\mathbf{F}$  matrices. Let us first consider the  $\mathbf{M}$  matrix. Since we are trying to obtain the mass normalized mode shapes, and since  $\mathbf{M}$ , and thus  $\mathbf{M}^{-1}$ , are diagonal, from the mass orthogonality of (63.4), we get that the rows of  $\mathbf{V}^*$  are orthogonal to each other, i.e.

$$\sum_{i=1}^N v_{i,j}^* v_{i,k}^* = 0 \quad \forall j \in \{1, 2, \dots, N-1\}, k \in \{j+1, j+2, \dots, N\} \quad (63.5)$$

which gives us  $N \times (N-1)/2$  quadratic equations in terms of the elements of  $\mathbf{V}^*$ . Now let us consider the flexibility matrix of a shear type system, which has the form:

$$\mathbf{F} = \begin{bmatrix} \sum_{i=1}^1 \frac{1}{k_i} & \sum_{i=1}^1 \frac{1}{k_i} & \cdots & \sum_{i=1}^1 \frac{1}{k_i} \\ \sum_{i=1}^1 \frac{1}{k_i} & \sum_{i=1}^2 \frac{1}{k_i} & \cdots & \sum_{i=1}^2 \frac{1}{k_i} \\ \vdots & \vdots & \cdots & \vdots \\ \sum_{i=1}^1 \frac{1}{k_i} & \sum_{i=1}^2 \frac{1}{k_i} & \cdots & \sum_{i=1}^N \frac{1}{k_i} \end{bmatrix} \quad (63.6)$$

Using this nature of the  $\mathbf{F}$  matrix in the stiffness orthogonality of (63.4), we get an additional  $N \times (N-1)/2$  quadratic equations in the elements of  $\mathbf{V}^*$ :

$$\sum_{i=1}^N \frac{v_{i,j}^* v_{i,k}^*}{\lambda_i} - \sum_{i=1}^N \frac{v_{i,j}^{*2}}{\lambda_i} = 0 \quad \forall j \in \{1, 2, \dots, N-1\}, k \in \{j+1, j+2, \dots, N\} \quad (63.7)$$

Combining (63.5) and (63.7), we thus get a total of  $N \times (N-1)$  quadratic equations, which we store in a  $((N^2 - N) \times 1)$  dimensional vector of nonlinear functions as:

$$\mathbf{g}_a = \left\{ \begin{array}{l} \sum_{i=1}^N v_{i,j}^* v_{i,k}^* \\ \sum_{i=1}^N \frac{v_{i,j}^* v_{i,k}^*}{\lambda_i} - \sum_{i=1}^N \frac{v_{i,j}^{*2}}{\lambda_i} \end{array} \right\}_{\substack{j \in \{1, 2, \dots, N-1\}, \\ k \in \{j+1, j+2, \dots, N\}}} = \mathbf{0}_{(N^2-N) \times 1} \quad (63.8)$$

### 63.2.1.2 Equations from Measured Mode Shape Components

Since, we have a total of  $N^2 - 1$  unknowns in  $\mathbf{V}^*$ , which we want to estimate, and since we have a total of  $N^2 - N$  equations from structural topology relating these unknowns, we still need  $(N-1)$  more equations in order to estimate the complete  $\mathbf{V}^*$ . Now, in [5] it was shown that a shear-type system with a collocated actuator-sensor pair located at DOF 1 or  $N$ , i.e. with input-output data available at DOFs 1 or  $N$ , is globally identifiable. In terms of the mode shape matrix, this translates to the statement that with a knowledge of either the 1st or the  $N$ th row of  $\mathbf{V}$ , we will be able to estimate uniquely the remaining rows of  $\mathbf{V}$  by solving (63.8). In other words, different choices of the 1st or the  $N$ th row of  $\mathbf{V}$  will give different shear type systems on solving the  $N \times (N-1)$  equations of (63.8). It is worth noting that, knowing either the 1st or the  $N$ th row of  $\mathbf{V}$ , means having  $N$  additional information, each information corresponding to a different mode. This will imply that the extra  $(N-1)$  equations necessary in the output only case should correspond to different modes as well. Since we already have made the assumption that  $v_{1,1}^* = 1$ , the extra  $N-1$  information should thus correspond to the modes 2 to  $N$ , i.e. any additional information about mode 1 cannot be used as one of the necessary  $(N-1)$  equations. Furthermore, noting that in (63.8), the only parameters which are being obtained from the measurements are the  $N \lambda_i$ 's, and that these  $\lambda_i$ 's can be obtained from a single sensor's "rich" measurement, the necessary extra  $N-1$  equations should come from additional information given by any additional sensor. So the question now is, how much additional information does any additional sensor give us?

Let us suppose that the first sensor is located at the DOF 1, i.e. at the first floor. So any additional sensor, say located at DOF  $k$ , will give us  $N$  numbers, and thus  $N$  equations, of the form:

$$\begin{aligned} \alpha_{i,k} &= \frac{v_{i,k}^*}{v_{i,1}^*} = \frac{\phi_{i,k}}{\phi_{i,1}} \quad \forall i \in \{1, 2, \dots, N\} \\ \Rightarrow v_{i,k}^* - v_{i,1}^* \alpha_{i,k} &= 0 \quad \forall i \in \{1, 2, \dots, N\} \end{aligned} \quad (63.9)$$

where  $\phi_{i,k}$  is the non-normalized  $i$ th mode shape's component obtained from the  $k$ th sensor's measurement by ECCA. Amongst these  $N$  equations, the first equation,  $v_{i,k}^* = \alpha_{i,k} v_{i,1}^*$ , is about mode 1, and thus cannot serve as one of the necessary  $(N-1)$  equations. The question then becomes, whether the rest of the  $(N-1)$  equations, i.e. for  $i \in \{2, 3, \dots, N\}$  in (63.9), convey independent information, and thus may be used as the necessary extra  $(N-1)$  equations for the estimation of complete  $\mathbf{V}^*$ ? Since, these  $(N-1)$  equations will convey  $(N-1)$  independent information, if and only if the  $(N-1)$   $\alpha_{i,k}$ 's, for  $i \in \{2, 3, \dots, N\}$ , are independent of each other, what we would essentially want to know is whether these  $(N-1)$   $\alpha_{i,k}$ 's, are

independent for any location of the additional sensor, i.e. for any DOF  $k$ . In other words, we would like to know whether for any DOF  $k$ , knowing some of the  $\alpha_{i,k}$ 's can give us the rest of the  $\alpha_{i,k}$ 's, for  $i \in \{2, 3, \dots, N\}$ . To that end, let us write:

$$\mathbf{A} = \mathbf{M}^{-1}\mathbf{K} = \begin{bmatrix} a_{1,1} & a_{1,2} & & & 0 \\ a_{2,1} & a_{2,2} & a_{2,3} & & \\ & \ddots & \ddots & \ddots & \\ & & a_{N-1,N-2} & a_{N-1,N-1} & a_{N-1,N} \\ 0 & & & a_{N,N-1} & a_{N,N} \end{bmatrix} \quad (63.10)$$

Then, for any mode  $i$ , the eigenvalue problem can be written as:

$$\begin{bmatrix} a_{1,1} - \lambda_i & a_{1,2} & & & 0 \\ a_{2,1} & a_{2,2} - \lambda_i & a_{2,3} & & \\ & \ddots & \ddots & \ddots & \\ & & a_{N-1,N-2} & a_{N-1,N-1} - \lambda_i & a_{N-1,N} \\ 0 & & & a_{N,N-1} & a_{N,N} - \lambda_i \end{bmatrix} \begin{Bmatrix} 1 \\ \alpha_{i,2} \\ \vdots \\ \alpha_{i,N-1} \\ \alpha_{i,N} \end{Bmatrix} = \mathbf{0}_{N \times 1} \quad (63.11)$$

Suppose that the additional sensor is located at the second floor, i.e.  $k = 2$ . Then, considering the first row of (63.11), we get:

$$\frac{\alpha_{1,2} - \alpha_{i,2}}{\lambda_1 - \lambda_i} = \frac{1}{a_{1,2}} = c_1 \quad \forall i \in \{2, 3, \dots, N\} \quad (63.12)$$

where  $c_1$  is a constant. In (63.12), if we know any one of the  $\alpha_{i,2}$ 's, for  $i \in \{2, 3, \dots, N\}$ , and knowing  $\alpha_{1,2}$  and all  $\lambda_i$ 's, we can solve for  $c_1$ , and then for the rest of the  $(N - 2)$   $\alpha_{i,2}$ 's. Thus, an additional sensor at DOF  $k = 2$  gives only one independent  $\alpha_{i,2}$ , in addition to  $\alpha_{1,2}$ , and thus only one independent equation.

Now suppose that the additional sensor is located at the third floor, i.e.  $k = 3$ . Then, using the second row of (63.11), followed by some algebraic manipulations, we get:

$$\begin{aligned} \frac{\alpha_{1,3} - \alpha_{i,3}}{\lambda_1 - \lambda_i} - \frac{c_1}{a_{2,3}} \lambda_i &= \frac{\alpha_{1,2} - c_1 a_{2,2}}{a_{2,3}} \\ \Rightarrow \frac{\alpha_{1,3} - \alpha_{i,3}}{\lambda_1 - \lambda_i} + c_2 \lambda_i &= c_3 \quad \forall i \in \{2, 3, \dots, N\} \end{aligned} \quad (63.13)$$

where  $c_2$  and  $c_3$  are constants. In (63.13), if we know any two of the  $\alpha_{i,3}$ 's, for  $i \in \{2, 3, \dots, N\}$ , and knowing  $\alpha_{1,3}$  and all  $\lambda_i$ 's, we can solve for  $c_2$  and  $c_3$ , and then for the rest of the  $(N - 3)$   $\alpha_{i,3}$ 's. Thus, an additional sensor at DOF  $k = 3$  gives only two independent  $\alpha_{i,3}$ 's, in addition to  $\alpha_{1,3}$ , and thus only two independent equations. Using mathematical induction, it can similarly be shown that, for the additional sensor located at any DOF  $k = k^*$ , from the  $(k^* - 1)$ th row of (63.11) we can obtain an expression of the form:

$$\frac{\alpha_{1,k^*} - \alpha_{i,k^*}}{\lambda_1 - \lambda_i} + \sum_{j=1}^{k^*-2} c_{k^*,j} \lambda_i^j = d_{k^*} \quad \forall i \in \{2, 3, \dots, N\} \quad (63.14)$$

where  $d_{k^*}$  and all  $c_{k^*,j}$ 's are constants. Knowing any  $(k^* - 1)$  of the  $\alpha_{i,k^*}$ 's, in addition to  $\alpha_{1,k^*}$ , we can solve for these  $(k^* - 1)$  constants. Thus, for the additional sensor placed at any DOF  $k = k^*$ , we will have  $(k^* - 1)$  independent  $\alpha_{i,k^*}$ 's, in addition to  $\alpha_{1,k^*}$ , and thus  $(k^* - 1)$  extra independent equations. Since we need a total of  $(N - 1)$  such equations, along with the  $N^2 - N$  equations of (63.8), in order to estimate the complete  $\mathbf{V}^*$ , the additional sensor must thus be located at DOF  $N$ , i.e. at the top floor. Therefore, we conclude (1) that the minimum number of sensors required for the identification of the complete  $\mathbf{V}^*$  using output-only data is equal to 2, which is independent of the total number of DOFs of the shear type system, and (2) that these two sensors should be located at the first and the last DOFs, i.e. at the first and the top floors.

Satisfying the above minimal sensor requirement, and using the ECCA identified mode shape components,  $\phi_{i,l}$  and  $\phi_{i,N}$  for  $i \in \{2, 3, \dots, N\}$ , we thus get a set of  $(N - 1)$  linear equations in the elements of  $\mathbf{V}^*$  from (63.9), which we store in a  $((N - 1) \times 1)$  dimensional vector of linear functions as:

$$\mathbf{g}_b = \{v_{i,N}^* - v_{i,1}^* \alpha_{i,N}\}_{i \in \{2, 3, \dots, N\}} = \left\{ v_{i,N}^* - v_{i,1}^* \frac{\phi_{i,N}}{\phi_{i,1}} \right\}_{i \in \{2, 3, \dots, N\}} = \mathbf{0}_{(N-1) \times 1} \quad (63.15)$$

### 63.2.1.3 Solution Using a Modified Newton–Raphson Method

We can combine the two sets of equations, i.e. the  $(N^2 - N)$  nonlinear equations from the structural topology, (63.8), with the  $(N - 1)$  linear equations from the measured mode shape components, (63.15), and solve the resulting  $(N^2 - 1)$  equations for the  $(N^2 - 1)$  unknown elements of  $\mathbf{V}^*$  using any nonlinear equation solver. In this paper we use the damped Newton–Raphson method to solve these equations. We first store all the unknowns in a vector,  $\mathbf{x}$ , i.e., with  $v_{1,1}^*$  arbitrarily assumed to be 1,

$$\mathbf{x} = \left\{ v_{1,2}^* \cdots v_{1,N}^* \ v_{2,1}^* \ v_{2,2}^* \cdots v_{N,N}^* \right\}^T \quad (63.16)$$

Note that, although (63.8) and (63.15) appear to be a homogenous system with their right hand sides being zero vectors, the assumption of  $v_{1,1}^* = 1$  makes them a non-homogenous system of equations. The unknowns are now iteratively estimated, the estimate of  $\mathbf{x}$  in the  $k$ th iteration being:

$$\mathbf{x}^k = \mathbf{x}^{k-1} - \gamma^k [\mathbf{J}^{k-1}]^+ \mathbf{g}^{k-1} \quad (63.17)$$

where,

$$\mathbf{J}^{k-1} = \left. \frac{\partial \mathbf{g}}{\partial \mathbf{x}} \right|_{\mathbf{x}=\mathbf{x}^{k-1}} \quad (63.18a)$$

$$\mathbf{g}^{k-1} = \mathbf{g}|_{\mathbf{x}=\mathbf{x}^{k-1}} \quad (63.18b)$$

$$\mathbf{g} = \begin{Bmatrix} \mathbf{g}_a \\ \mathbf{g}_b \end{Bmatrix} \quad (63.18c)$$

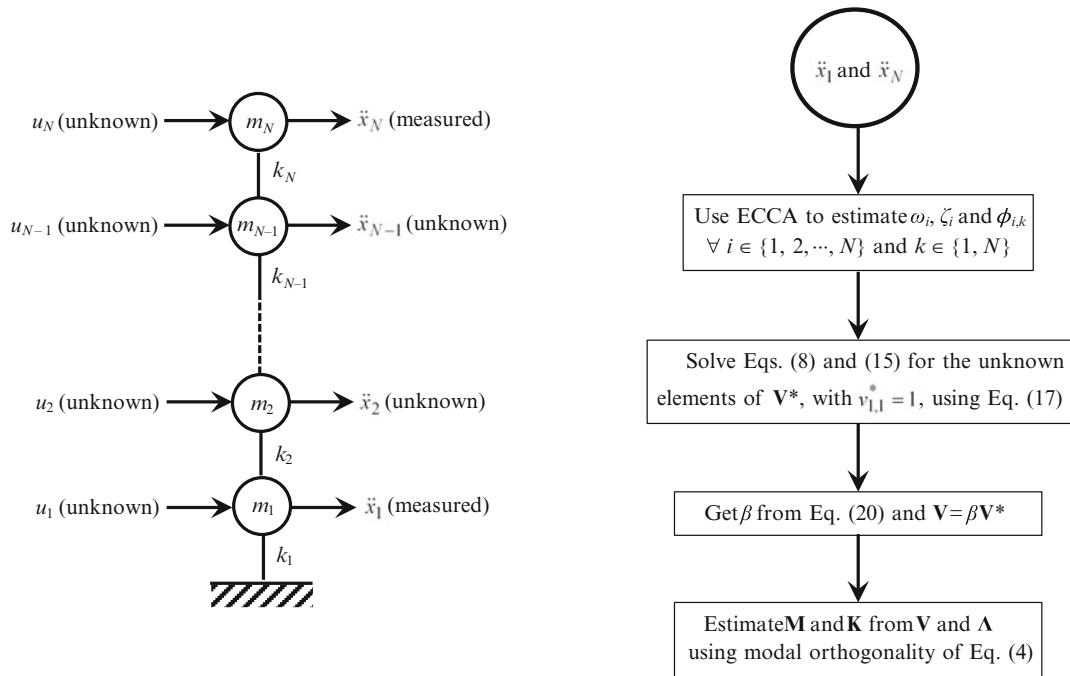
and the damping parameter  $\gamma^k$  is a scalar which is found by solving the constrained optimization problem:

$$\gamma^k = \arg \min_{\varepsilon < \gamma < 1} \left\| \mathbf{g} \left( \mathbf{x}^{k-1} - \gamma [\mathbf{J}^{k-1}]^+ \mathbf{g}^{k-1} \right) \right\| \quad (63.19)$$

where  $\|\cdot\|$  represents the Euclidean norm of the concerned vector argument, and  $\varepsilon$  is an arbitrarily chosen very small positive number. The starting point for the Newton–Raphson method is obtained by solving the eigenvalue problem for any arbitrary known  $N$ -DOF shear-type system (e.g. with say  $\mathbf{M} = \mathbf{I}$ , and a constant story stiffness  $k_i$  of 10, as has been adopted in the simulations in this paper) and taking the elements of the resultant eigenvector matrix as the elements of  $\mathbf{x}$  for the 1st iteration. Although a random non-zero assumption for the starting point would also suffice, the starting point selection followed in this paper is found to lead to a more controlled convergence of the Newton–Raphson iterations, as in this way we incorporate the expected nature of the mode shapes of a shear-type system in our initial guess of  $\mathbf{x}$ . The convergence criterion can be set in the conventional ways, e.g. through a maximum number of iterations and/or through a tolerance on the Euclidean norm of the error  $\|\mathbf{g}^k\|$ , etc.

## 63.2.2 Scaling of $\mathbf{V}^*$ for Estimation of $\mathbf{M}$ and $\mathbf{K}$

In Sect. 63.2.1 we first estimate the complete  $\mathbf{\Lambda}$  through ECCA, and then the complete  $\mathbf{V}^*$ , which is proportional to the true  $\mathbf{V}$  as  $\mathbf{V} = \beta \mathbf{V}^*$ . It is important to note that, if our sole purpose is structural damage detection, then at this stage itself, we can use the proportional mode shapes in  $\mathbf{V}^*$  in an appropriate damage detection algorithm, such as the one developed in [4]. However, if our objective is to estimate the true  $\mathbf{M}$  and  $\mathbf{K}$  matrices, as in model updating/validation exercises, then we need to estimate the scaling factor  $\beta$  using some known system information. In this paper we assume that the total system mass, i.e. sum of all the floor masses, is known. The advantage of such an assumption is that, while each floor mass can



**Fig. 63.1** Flowchart representation of proposed  $\mathbf{M}$ - $\mathbf{K}$  identification algorithm using response acceleration measurements from DOFs 1 and  $N$  only

be approximately estimated from an engineering drawing of the structure, the estimation errors for the various floors can be assumed to have a cancelling effect with each other, thereby making the accumulated estimation error in the total system mass relatively smaller than the approximation errors in the individual floor masses. Denoting this known total mass as  $M_T$ , the scalar factor of proportionality is then estimated as:

$$\beta = \left( \frac{1}{M_T} \sum_{k=1}^N m_k^* \right)^{1/2} \quad (63.20)$$

where

$$m_k^* = \left( \sum_{i=1}^N (v_{i,k}^*)^2 \right)^{-1} \quad (63.21)$$

Once we thus estimate  $\beta$ , we can then obtain the complete mode shape matrix  $\mathbf{V} = \beta \mathbf{V}^*$ , and then estimate the system's  $\mathbf{M}$  and  $\mathbf{K}$  matrices using the orthogonality relations of (63.4). Figure 63.1 summarizes through a flowchart the different steps involved in the proposed identification algorithm.

### 63.3 Numerical Validation

To verify the performance of the proposed algorithm, Monte Carlo simulations are performed in this section using a 7-DOF shear type structure for the following five different cases:

1. Undamped system; No measurement noise
2. Damped system; No measurement noise
3. Damped system; Type 1 measurement noise
4. Damped system; Type 2 measurement noise
5. Damped system; Type 3 measurement noise



**Table 63.1** Statistics of estimation errors in modal parameters ( $\omega$ ,  $\zeta$ ,  $\mathbf{V}$ )

Case	Frequency ( $\omega$ )			Damping ratio ( $\zeta$ )			MAC		COMAC	
	$\mu_{e\omega}$	$\sigma_{e\omega}$	Normality	$\mu_{e\zeta}$	$\sigma_{e\zeta}$	Normality	$\mu_{eMAC}$	$\sigma_{eMAC}$	$\mu_{eCOMAC}$	$\sigma_{eCOMAC}$
1	0.0006	0.0108	6/7	–	–	–	$4.24 \times 10^{-7}$	$3.81 \times 10^{-7}$	$2.43 \times 10^{-7}$	$2.13 \times 10^{-7}$
2	0.1716	0.6381	7/7	2.4288	12.5601	7/7	0.0057	0.0062	0.0028	0.0030
3	0.1787	0.6654	7/7	1.8579	13.1452	7/7	0.0055	0.0062	0.0029	0.0030
4	0.1757	0.6372	7/7	2.4655	12.5619	7/7	0.0057	0.0062	0.0028	0.0030
5	0.0767	0.6465	7/7	2.1553	12.2689	7/7	0.0056	0.0061	0.0027	0.0031

**Table 63.2** Statistics of estimation errors in floor masses and story stiffnesses

Case	Floor mass ( $m$ )			Story stiffness ( $k$ )		
	$\mu_{em}$	$\sigma_{em}$	Normality	$\mu_{ek}$	$\sigma_{ek}$	Normality
1	0.0047	0.0403	7/7	0.0025	0.0296	7/7
2	0.1560	2.0195	7/7	0.3262	1.5151	7/7
3	0.0905	1.9868	7/7	0.3895	1.7385	7/7
4	0.1607	2.0190	7/7	0.3302	1.5156	7/7
5	0.1976	1.8404	7/7	0.2559	1.8795	6/7

The lumped floor masses of the system are taken as  $m_i = 2,500$  kg  $\forall i \in \{1, 2, \dots, 6\}$ , and  $m_7 = 2,000$  kg, and the story (spring) stiffnesses are taken as  $k_i = 5 \times 10^6$  N/m  $\forall i \in \{1, 2, \dots, 7\}$ . For damped systems, modal damping is assumed, with  $\zeta_j = 0.05$   $\forall j \in \{1, 2, \dots, 7\}$ . Finally, in order to see the performance of the proposed algorithm in the presence of measurement noise, in the last three cases the true acceleration responses are polluted by adding different types of zero-mean Gaussian noise sequences, with Type 1 being white noise, Type 2 being band-passed white noise with a pass-band of  $[0.15, 0.55]$  of Nyquist, and Type 3 being band-stopped white noise with a stop-band of  $[0.15, 0.55]$  of Nyquist. The added noise sequences are scaled to have root-mean-square (RMS) values equal to 10% of the RMS of the corresponding true response signals.

For each of the five cases, 100 simulations for identifying the system parameters are run, with the input forces, applied at every floor, in the different simulations constituting of different sets of white noise sequences albeit coming from the same Gaussian distribution. The statistics of the errors in the estimated parameters, relative to the true values of the corresponding parameters, are then calculated using the estimation errors from the 100 simulations. Tables 63.1 and 63.2 show these error statistics for the different parameters in each of the five cases. These statistics are calculated in the following way. For any parameter  $\theta_i \forall i \in \{1, 2, \dots, 7\}$ , let  $\theta_i$  denote the true value and  $\hat{\theta}_{i,k}$  denote the value estimated in the  $k$ th simulation. Then the percentage error in  $\theta_i$  can be written as:

$$e\theta_{i,k} = \frac{\hat{\theta}_{i,k} - \theta_i}{\theta_i} \times 100 \quad \forall i \in \{1, 2, \dots, 7\}, k \in \{1, 2, \dots, 100\} \quad (63.22)$$

The sample mean and standard deviation of  $e\theta_i$  can then be calculated as:

$$\mu_{e\theta_i} = E[e\theta_i] = \frac{\sum_{k=1}^{100} e\theta_{i,k}}{100}; \quad \sigma_{e\theta_i} = (\text{Var}[e\theta_i])^{1/2} = \left( \frac{\sum_{k=1}^{100} e\theta_{i,k}^2 - 100\mu_{e\theta_i}^2}{99} \right)^{1/2} \quad (63.23)$$

The statistics listed in Tables 63.1 and 63.2 are the maximum values, with respect to index  $i \in \{1, 2, \dots, 7\}$ , of these sample means and standard deviations:

$$\mu_{e\theta} = \max_i (\mu_{e\theta_i}); \quad \sigma_{e\theta} = \max_i (\sigma_{e\theta_i}) \quad (63.24)$$

To quantify the errors in the identified complete  $\mathbf{V}$  matrices, we use the deviations from 1 of the Modal Assurance Criterion (MAC) [6], calculated for each mode, and the Coordinate Modal Assurance Criterion (COMAC) [7], calculated for each DOF, i.e.  $eMAC = 1 - MAC$  and  $eCOMAC = 1 - COMAC$ , respectively. Thus, the different parameters considered as  $\theta$  in Tables 63.1 and 63.2 are,  $\theta = \{\omega, \zeta, MAC, COMAC, m, k\}$ , with the true values of MAC and COMAC being 1.

In Tables 63.1 and 63.2, we also provide the results of a test for normality of the estimation errors in the different parameters, i.e. whether the distribution of the estimation errors, obtained from the 100 simulations, is a normal distribution or not. The Anderson Darling test [8] is used to test the normality of the estimation errors, with a significance level of 1%. The significance level of 1% denotes that the probability of incorrectly rejecting the null hypothesis, which in this case is that the estimation error is normally distributed, is 0.01. Since for any parameter  $\theta$  we have seven values, i.e.  $\theta_i \forall i \in \{1, 2, \dots, 7\}$ , the results of this test for the various parameters are presented in a fractional form. For example a fraction of 5/7 for the parameter  $\theta$  indicates that the estimation errors in 5 out of the 7  $\theta_i$ 's are normally distributed according to the Anderson Darling test. Note that, since MAC and COMAC are bounded between 0 and 1, eMAC and eCOMAC will have a bounded and consequently non-normal distribution. Thus, the Anderson Darling test is not carried out for eMAC and eCOMAC.

From the error statistics in Tables 63.1 and 63.2, it is evident that the proposed algorithm performs reliably well in estimating the complete  $\mathbf{V}$  matrix, as well as the lumped floor masses and story stiffnesses. In fact, even when the measurements are corrupted by 10% Gaussian noise, white or colored, the estimation errors in the mass and stiffness parameters are much lower than 1% in the mean sense, and have standard deviations around 2% or less. Also, the mean errors in estimation being close to zero, excepting for the modal damping ratios, indicates that there is no bias in the estimation. Finally, in most cases the estimation errors are normally distributed, which indicates that their distributions can be described through their means and standard deviations alone.

## 63.4 Conclusions

In this paper, an algorithm is developed for identifying the physical parameters (lumped masses and spring stiffnesses) of shear-type systems using ambient vibration response data. The proposed algorithm first identifies the complete set of modal parameters at the sensor locations using a subspace identification technique, ECCA. To overcome the limitation of incomplete instrumentation, a mode shape expansion method is developed which expands the ECCA identified incomplete mode shapes from the observed to the unobserved structural DOFs. The proposed expansion technique utilizes the information available from the structural topology of the system, as well as the information provided by the ratios of the non-normalized measured mode shape components identified through ECCA. The resulting equations are solved using a modified Newton–Raphson procedure to obtain the complete mode shape matrix. It is also shown that only two sensors, located at the first and last DOFs of the system, are sufficient for obtaining the complete mode shape matrix, and thus, this corresponds to the minimal necessary instrumentation set-up for shear-type systems in operational modal analysis.

The complete mode shape matrix obtained using the proposed expansion algorithm is however proportional to the true mass normalized mode shape matrix of the system through a scalar constant. The estimation of this scalar constant of proportionality, for output-only situations, necessitates the use of a-priori information about the system. In the proposed algorithm we need only one such a-priori information, which we assume to be the total mass of the system.

Once the scalar constant of proportionality is determined using the known system information, we scale the identified proportional mode shape matrix to the true mass normalized mode shape matrix of the system. Then using modal orthogonality, we obtain the mass and stiffness matrices of the system. These estimated physical matrices can be considered to represent the updated model of the system, defining its current state/condition, and can be used for model validation, damage detection, as well as for the verification of retrofitting operations.

The algorithm proposed in this paper has three main advantages: (1) its capability of identification using output-only data, and consequently its applicability to vibration-based structural identification in the operational (ambient) modal analysis framework, (2) its ability to obtain reliably accurate estimates of the system's physical parameters under the constraints of minimal instrumentation, and minimal available a-priori information about the system, and (3) its robustness in the presence of significant white/colored measurement noise, as evidenced from the numerical simulations involving the 7 story shear-type structure. However, we still need to account for the situation with unobserved modes, i.e. unidentified eigenvalues, and missing columns in the ECCA identified mode shape matrix, owing to some structural modes being weakly excited. Furthermore, other instrumentation set-ups should also be considered, since it may not be possible to instrument both the first and last DOFs in every situation. Finally, while the proposed identification algorithm is focused on a shear-type system, we need to extend/modify the algorithm to suit other structural systems as well.

## References

1. Doebling SW, Farrar CR, Prime MB, Shevitz DW (1996) Damage identification and health monitoring of structural and mechanical systems from changes in their vibration characteristics: a literature review. Technical report LA-13070-MS, Los Alamos National Laboratory, Los Alamos
2. Hong AL (2010) Model order determination in stochastic subspace identification for civil infrastructure systems. Ph.D. thesis, Columbia University, New York
3. Hong AL, Ubertini F, Betti R (2011) Wind Analysis of a suspension bridge: identification and finite-element model simulation. *J Struct Eng* 137:133–142
4. Balsamo L, Mukhopadhyay S, Betti R, Lus H (2013) Damage detection using flexibility proportional modal assurance criterion. In: Proceedings of the 31st International Modal Analysis Conference, Garden Grove
5. Franco G, Betti R, Longman RW (2006) On the uniqueness of solutions for the identification of linear structural systems. *J Appl Mech* 73: 153–162
6. Allemang RJ, Brown DL (1982) A correlation coefficient for modal vector analysis. In: Proceedings of the 1st International Modal Analysis Conference, Kissimmee, pp 110–116
7. Lieven NAJ, Ewins DJ (1988) Spatial correlation of mode shapes, the Coordinate Modal Assurance Criterion (COMAC). In: Proceedings of the 6th International Modal Analysis Conference, Bethel, pp 690–695
8. Stephens MA (1974) EDF statistics for goodness of fit and some comparisons. *J Am Stat Assoc* 69:730–737

# Chapter 64

## Simulation of Guided Wave Interaction with Defects in Rope Structures

Stefan Bischoff and Lothar Gaul

**Abstract** Ultrasonic waves travel in rope structures over long distances as guided waves, allowing for effective Structural Health Monitoring. In order to localize and characterize defects, an exact knowledge of the propagation, reflection, and transmission properties of the ultrasonic waves is required. These properties can be obtained using the Finite Element Method by modeling a segment of the periodic waveguide with a periodicity condition. The solution of the corresponding eigenvalue problem leads to all propagating modes of the waveguide as well as non-propagating modes.

The Boundary Element Method is used in combination with the Finite Element Method for characterizing the wave propagation. The mode conversion at discontinuities, such as cracks or notches, can be subsequently described by reflection and transmission coefficients. The simulation results are the corresponding coefficients as a function of frequency and enable the selection of adequate modes for effective defect detection. Additionally, it is demonstrated that along with the localization of cracks, conclusions about the crack geometry can be made with the help of reflection and transmission coefficients. The reliability and numerical accuracy of the simulation results are verified by transient FE simulations.

**Keywords** Structural health monitoring • Guided wave propagation • Crack detection • Boundary elements • Scattering coefficients

### 64.1 Introduction

Engineering structures are subject to deterioration due to aging, affected by environmental influences. In addition, manufacturing defects can also cause structural damages. All in all, these factors may restrict the intended service life of those structures. Non-destructive evaluation techniques estimate expiration of material and detect and characterize defects. Furthermore, regular monitoring allows for estimation of the residual life cycle [3].

New Structural Health Monitoring (SHM) methods target multi-wire cable structures, such as overhead transmission lines or stay cables of suspension bridges. Both types are subject to wind-induced vibrations, temperature changes, static loads, aging and corrosion. Failure of multi-wire cables begins with cracks in individual wires [11] and can eventually lead to a fracture of an entire multi-wire cable and e.g. power outages for important sectors, as described by Azevedo and Cescon [1]. Regular sight inspection from ground and by helicopter is the common way to detect damages in cable structures. This expensive practice can also be hazardous and is limited to the detection of flaws on the surface wires. Various schemes for automated monitoring are developed to overcome these drawbacks. Vibration based methods can be used to detect failure in cables [8]. This well-known technique is based upon the fact that structural damages generally causes a decrease in structural stiffness and therefore a shift of eigenfrequencies.

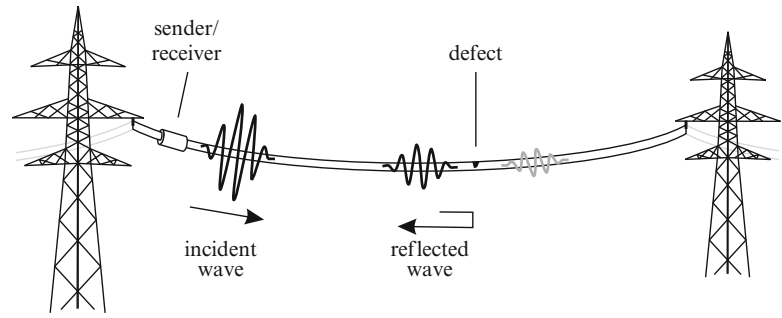
In the following, an ultrasound wave-based approach for damage detection in cable structures, as depicted in Fig. 64.1, is presented. Ultrasonic waves are excited in the monitored multi-wire cable and partially reflected and transmitted at discontinuities. Reflections are measured by a sensor, and damage detection algorithms evaluate whether a defect exists.

---

S. Bischoff (✉) • L. Gaul

Institute of Applied and Experimental Mechanics, University of Stuttgart, Pfaffenwaldring 9, D-70550, Stuttgart, Germany  
e-mail: [bischoff@iam.uni-stuttgart.de](mailto:bischoff@iam.uni-stuttgart.de); [gaul@iam.uni-stuttgart.de](mailto:gaul@iam.uni-stuttgart.de)

**Fig. 64.1** Scheme of guided ultrasonic wave SHM concept: transducer induces waves in overhead transmission lines. Generated waves are partially reflected at defects



In this article, a combination of the Boundary Element Method (BEM) and the Waveguide Finite Element Method (WFEM) is used in order to study scattering phenomena at arbitrarily shaped discontinuities with various depth and sharpness. After a brief introduction of guided wave propagation in cylindrical waveguides, a theoretical background on WFEM and BEM is given. In the next part, the interaction of guided waves with discontinuities is covered [6]. The third section includes numerically calculated scattering coefficients as functions of type of incident wave, of the geometry of discontinuity and of frequency. Based on these coefficients, mode sensitivity and the inverse problem of defect classification is analyzed. Conclusions complete this article.

## 64.2 Wave Propagation in Rope Structures

Rope structures act as waveguides if the length of the rope is significantly larger than the radius and the wavelength of the transmitted wave is larger compared to the radius.

In general, guided waves may propagate inside the structure with displacement and stress fields of the form

$$\mathbf{u}(\mathbf{x}, t) = \hat{\mathbf{u}}(x_1, x_2) e^{j(kx_3 - \omega t)} \quad \text{and} \quad (64.1)$$

$$\boldsymbol{\sigma}(\mathbf{x}, t) = \hat{\boldsymbol{\sigma}}(x_1, x_2) e^{j(kx_3 - \omega t)} \quad (64.2)$$

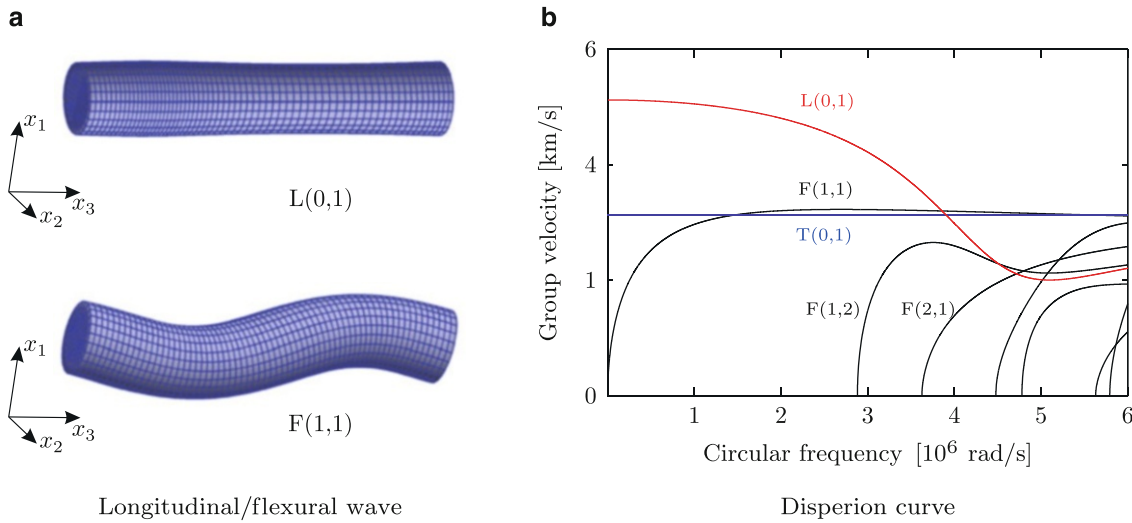
with the circular wavenumber  $k$  and the angular frequency  $\omega$ . The characteristic mode shapes are described by displacement and stress fields,  $\hat{\mathbf{u}}(x_1, x_2)$  and  $\hat{\boldsymbol{\sigma}}(x_1, x_2)$ , respectively.

Considering cylindrical rope structures one can distinguish between three types of guided wave modes: longitudinal (L), flexural (F) and torsional modes. Within each one of these types, there are an infinite number of modes. The longitudinal and flexural wave motion are displayed in Fig. 64.2a for a frequency of  $f = 200$  kHz. Moreover, Fig. 64.2b displays the dispersion relation, i.e. group velocity as a function of frequency.

## 64.3 Interaction with Discontinuities

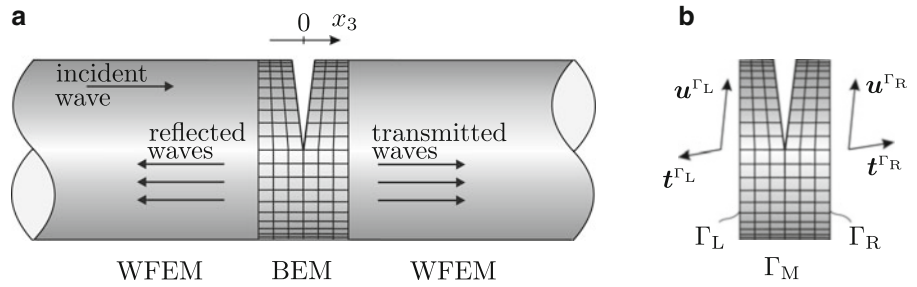
If an incident wave encounters a discontinuity, all possible propagating and non-propagating modes may be reflected and transmitted. Scaling the corresponding amplitudes of the scattered waves by the amplitude of the incident wave results in reflection and transmission coefficients. These coefficients depend on the geometry of the discontinuity, the type of incident wave, and frequency.

In the following a combination of the Boundary Element Method and the Waveguide Finite Element Method is used in order to study scattering phenomena of guided waves at arbitrarily shaped discontinuities.



**Fig. 64.2** (a) Deformation of rope structures carrying the fundamental longitudinal and flexural mode and (b) dispersion curve for a cylindrical aluminum alloy waveguide with radius 2 mm

**Fig. 64.3** Incident, reflected and transmitted wave fields in a waveguide with discontinuity (a) and corresponding free-body diagram (b)



### 64.3.1 Waveguide Finite Element Method

Wave solutions in cylindrical waveguides may be found by a method called the Waveguide Finite Element Method [9]. Based on a finite element model, one can describe the dynamics of a section  $s$  of the waveguide. Applying periodicity conditions, continuity of displacements and equilibrium of forces at the cross-section between sections  $s$  and  $s + 1$ , lead to a linear eigenvalue problem.

With eigenvalues and eigenvectors, the guided wave propagation characteristics such as wavenumbers  $k$  and mode shapes for displacement and stress fields,  $\hat{u}_i$  and  $\hat{\sigma}_i$ , respectively, can be derived. On the basis of wavenumbers, guided waves can be classified as propagating and non-propagating modes.

### 64.3.2 Elastodynamic Boundary Element Formulation

The elastodynamic boundary integral equation of a boundary model including the cracked region, as shown in Fig. 64.3a, be derived from Cauchy's equation of motion through a weighted residual statement [4] as follows

$$c_{ij}(\xi)u_j(\xi) = \int_{\Gamma} (u_{ij}^*(x, \xi) t_j(x) - t_{ij}^*(x, \xi) u_j(x)) d\Gamma, \xi \in \Gamma, \quad (64.3)$$

where  $c_{ij}$  displays the free term coefficient,  $u_j$  and  $t_j$  denote displacements and tractions on the boundary  $\Gamma$ , respectively, and  $u_{ij}^*$  and  $t_{ij}^*$  represent fundamental solutions for the time-harmonic state [2]. Furthermore, it is advantageous to use matrix notation in the subsequent formulations. For an approximation of the geometry, the boundary is divided into  $E$  quadratic boundary elements. With  $M$  nodes in element  $e$ , the shape of  $\mathbf{u}(x)$  and  $\mathbf{t}(x)$  are interpolated using shape functions  $\Phi$  by



$$\mathbf{u}^e(x) = \sum_{n=1}^M \Phi_n(x) \mathbf{u}_n^e \quad \text{and} \quad \mathbf{t}^e(x) = \sum_{n=1}^M \Phi_n(x) \mathbf{t}_n^e \quad (64.4)$$

respectively, where  $\mathbf{u}_n^e$  and  $\mathbf{t}_n^e$  are  $[3 \times 1]$  column vectors and  $\Phi_n = \text{diag}[\phi_n \ \phi_n \ \phi_n]$  is a diagonal matrix with the dimension of  $[3 \times 3]$ . Due to the discretization, the boundary integrals in Eq. (64.3) are evaluated element-wise,

$$\mathbf{C}(\xi) \mathbf{u}(\xi) + \sum_{e=1}^E \sum_{n=1}^M \left[ \int_{\Gamma_e} \mathbf{t}^* \Phi_n d\Gamma \right] \mathbf{u}_n^e = \sum_{e=1}^E \sum_{n=1}^M \left[ \int_{\Gamma_e} \mathbf{u}^* \Phi_n d\Gamma \right] \mathbf{t}_n^e. \quad (64.5)$$

By numbering all global nodes consecutively, one can replace the double summation over the elements  $e = 1, \dots, E$  and local element nodes  $n = 1, \dots, M$  by one summation over all  $N$  global nodes. Placing the load point  $\xi$  on the boundary node  $l$ , Eq. (64.5) can be written as

$$\mathbf{C}_l \mathbf{u}_l + \sum_{n=1}^N \mathbf{H}_{ln} \mathbf{u}_n = \sum_{n=1}^N \mathbf{G}_{ln} \mathbf{t}_n \quad (64.6)$$

with

$$\mathbf{H}_{ln} = \int_{\Gamma_{n,e}} \mathbf{t}^* \Phi_n d\Gamma \quad \text{and} \quad \mathbf{G}_{ln} = \int_{\Gamma_{n,e}} \mathbf{u}^* \Phi_n d\Gamma, \quad (64.7)$$

where  $\Gamma_{n,e}$  represents the elements  $e$  containing the common node  $n$ . Using the collocation method, where the load point  $\xi$  is located sequentially at all nodes of the discretization, Eq. (64.6) can be written in matrix form

$$\mathbf{H} \mathbf{u} = \mathbf{G} \mathbf{t} \quad \text{with} \quad \mathbf{H} = \begin{bmatrix} \mathbf{H}_{ln}(n \neq l) \\ \mathbf{C}_l + \mathbf{H}_{ln}(n = l) \end{bmatrix} \quad \text{and} \quad \mathbf{G} = \mathbf{G}_{ln}, \quad (64.8)$$

where  $\mathbf{u}$  and  $\mathbf{t}$  are the boundary displacement and traction vectors on the boundary  $\Gamma$ . The matrices  $\mathbf{H}$  and  $\mathbf{G}$  contain the boundary integral terms of the traction and displacement fundamental solutions.

While regular integrals can be evaluated using standard Gaussian quadrature formulas, special procedures have to be used to integrate singular and weakly singular integrals. Weak singularities are observed in the diagonal terms in  $\mathbf{G}$ -matrix and solved by regularising the transformation to polar coordinates [7].

The evaluation of singular integrals in diagonal terms of the  $\mathbf{H}$ -matrix is carried out by means of traction-free rigid body motion used for elastostatic singular integration in combination with regular Gaussian quadrature [5].

### 64.3.3 Modeling of Defects in Cylindrical Waveguides

In the following the interaction of guided waves in cylindrical waveguides with arbitrarily shaped cracks is analyzed. In general, a single guided wave at a discontinuity may lead to scattered propagating waves of different types. In addition, evanescent waves, decaying rapidly over distance, arise near the discontinuity. This process is known as mode conversion.

According to Fig 64.3b, reflected and transmitted fields on the left and right cross-section,  $\Gamma_L$  and  $\Gamma_R$  respectively, can be superposed to express the resulting displacement fields

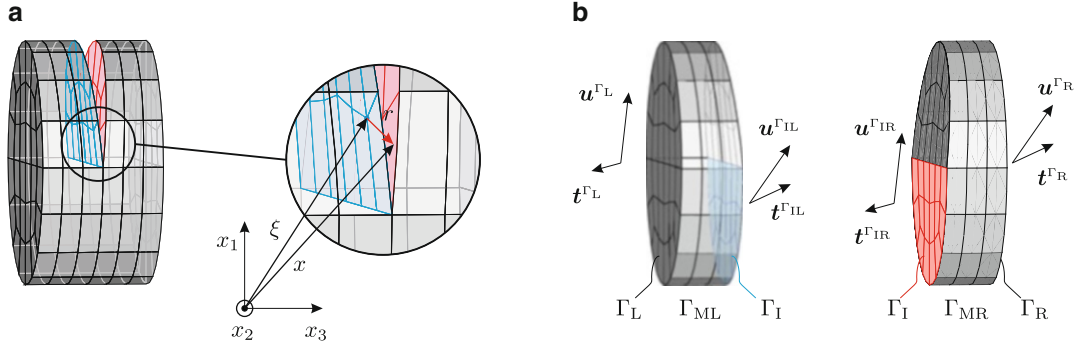
$$\mathbf{u}^{\Gamma_L} = \hat{\mathbf{u}}_{\text{inc}} + \mathbf{U}_{\text{refl}} \mathbf{r}_{\text{refl}} \quad \text{and} \quad (64.9)$$

$$\mathbf{u}^{\Gamma_R} = \mathbf{U}_{\text{trans}} \mathbf{r}_{\text{trans}} \quad (64.10)$$

with

$$\mathbf{U}_{\text{refl}} = [\hat{\mathbf{u}}^1 e^{-ik_1 x_3} \ \hat{\mathbf{u}}^2 e^{-ik_2 x_3} \ \dots \ \hat{\mathbf{u}}^n e^{-ik_n x_3}] \quad \text{and} \quad (64.11)$$

$$\mathbf{U}_{\text{trans}} = [\hat{\mathbf{u}}^1 e^{ik_1 x_3} \ \hat{\mathbf{u}}^2 e^{ik_2 x_3} \ \dots \ \hat{\mathbf{u}}^m e^{ik_m x_3}] \quad (64.12)$$



**Fig. 64.4** Boundary element discretization of waveguide segment (a) and corresponding substructures with conforming meshes at the interface (b)

The matrix  $\mathbf{U}_{\text{refl}}$  consists of all propagating modes which travel to the left and all evanescent modes which decay to the left. Accordingly,  $\mathbf{U}_{\text{trans}}$  is assembled from right going propagation modes and evanescent modes decaying to the right. The infinite series of evanescent modes is truncated to obtain a matrix of finite dimension, only evanescent modes with lowest imaginary part of their respective wavenumber are considered.

Using Cauchy's stress theorem  $\mathbf{t} = \boldsymbol{\sigma} \cdot \mathbf{n}$  with normal vectors  $\mathbf{n}^{\Gamma_L} = -\mathbf{e}_3$  and  $\mathbf{n}^{\Gamma_R} = \mathbf{e}_3$ , the tractions  $\mathbf{t}^{\Gamma_L}$  and  $\mathbf{t}^{\Gamma_R}$  can be expressed in matrix form as

$$\mathbf{t}^{\Gamma_L} = -\hat{\mathbf{t}}_{\text{inc}} - \mathbf{T}_{\text{refl}} \mathbf{r}_{\text{refl}} \quad \text{and} \quad (64.13)$$

$$\mathbf{t}^{\Gamma_R} = \mathbf{T}_{\text{trans}} \mathbf{r}_{\text{trans}} \quad (64.14)$$

with

$$\mathbf{T}_{\text{refl}} = \left[ \hat{\mathbf{t}}^1 e^{-ik_1 x_3} \quad \hat{\mathbf{t}}^2 e^{-ik_2 x_3} \quad \dots \quad \hat{\mathbf{t}}^n e^{-ik_n x_3} \right] \quad \text{and} \quad (64.15)$$

$$\mathbf{T}_{\text{trans}} = \left[ \hat{\mathbf{t}}^1 e^{ik_1 x_3} \quad \hat{\mathbf{t}}^2 e^{ik_2 x_3} \quad \dots \quad \hat{\mathbf{t}}^m e^{ik_m x_3} \right]. \quad (64.16)$$

Reflection and transmission coefficients are referred to as  $\mathbf{r}_{\text{refl}}$  and  $\mathbf{r}_{\text{trans}}$ .

As depicted in Fig 64.4a, the nodes of opposite boundary elements in vicinity of the crack tip are close to each other. Therefore, quasi-singular integrals occur due to a vanishingly small Euclidian distance  $r$  defined by  $r = |x - \xi|$ . In this case, the integrand being still regular has a pronounced peak for  $r \ll 1$ , which requires an approximation with a high-order polynomial. In order to avoid such time-consuming procedures, the boundary model is partitioned into substructures and interfaces so that no singularity has to be considered anymore [10]. Furthermore, Eq. (64.8) still holds for each single substructure,

$$\mathbf{H}_k \mathbf{u} = \mathbf{G}_k \mathbf{t} \quad (k = 1, 2, \dots, K), \quad (64.17)$$

where  $K = 2$  is the number of substructures. Partitioning with respect to the cylindrical surfaces (including the cracked surfaces),  $\Gamma_{ML}$  and  $\Gamma_{MR}$ , the interfaces,  $\Gamma_{IL}$  and  $\Gamma_{IR}$ , as well as the left and right cross-section,  $\Gamma_L$  and  $\Gamma_R$ , lead to

$$\begin{bmatrix} \mathbf{H}_1^{\Gamma_L} & \mathbf{H}_1^{\Gamma_{ML}} & \mathbf{H}_1^{\Gamma_{IL}} \end{bmatrix} \begin{bmatrix} \mathbf{u}^{\Gamma_L} \\ \mathbf{u}^{\Gamma_{ML}} \\ \mathbf{u}^{\Gamma_{IL}} \end{bmatrix} = \begin{bmatrix} \mathbf{G}_1^{\Gamma_L} & \mathbf{G}_1^{\Gamma_{ML}} & \mathbf{G}_1^{\Gamma_{IL}} \end{bmatrix} \begin{bmatrix} \mathbf{t}^{\Gamma_L} \\ \mathbf{t}^{\Gamma_{ML}} \\ \mathbf{t}^{\Gamma_{IL}} \end{bmatrix}, \quad (64.18)$$

$$\begin{bmatrix} \mathbf{H}_2^{\Gamma_{IR}} & \mathbf{H}_2^{\Gamma_{MR}} & \mathbf{H}_2^{\Gamma_R} \end{bmatrix} \begin{bmatrix} \mathbf{u}^{\Gamma_{IR}} \\ \mathbf{u}^{\Gamma_{MR}} \\ \mathbf{u}^{\Gamma_R} \end{bmatrix} = \begin{bmatrix} \mathbf{G}_2^{\Gamma_{IR}} & \mathbf{G}_2^{\Gamma_{MR}} & \mathbf{G}_2^{\Gamma_R} \end{bmatrix} \begin{bmatrix} \mathbf{t}^{\Gamma_{IR}} \\ \mathbf{t}^{\Gamma_{MR}} \\ \mathbf{t}^{\Gamma_R} \end{bmatrix}. \quad (64.19)$$

By applying continuity and equilibrium conditions,  $\mathbf{u}^{\Gamma_{IL}} = \mathbf{u}^{\Gamma_{IR}} = \mathbf{u}^{\Gamma_I}$  and  $\mathbf{t}^{\Gamma_{IL}} = -\mathbf{t}^{\Gamma_{IR}} = \mathbf{t}^{\Gamma_I}$ , coupling of the substructures is achieved

$$\begin{bmatrix} \mathbf{H}_1^{\Gamma_L} & \mathbf{H}_1^{\Gamma_{ML}} & \mathbf{H}_1^{\Gamma_{IL}} & \mathbf{0} & \mathbf{0} \\ \mathbf{0} & \mathbf{0} & \mathbf{H}_2^{\Gamma_{IR}} & \mathbf{H}_2^{\Gamma_{MR}} & \mathbf{H}_2^{\Gamma_R} \end{bmatrix} \begin{bmatrix} \mathbf{u}^{\Gamma_L} \\ \mathbf{u}^{\Gamma_{ML}} \\ \mathbf{u}^{\Gamma_I} \\ \mathbf{u}^{\Gamma_{MR}} \\ \mathbf{u}^{\Gamma_R} \end{bmatrix} = \begin{bmatrix} \mathbf{G}_1^{\Gamma_L} & \mathbf{G}_1^{\Gamma_{ML}} & \mathbf{G}_1^{\Gamma_{IL}} & \mathbf{0} & \mathbf{0} \\ \mathbf{0} & \mathbf{0} & -\mathbf{G}_2^{\Gamma_{IR}} & \mathbf{G}_2^{\Gamma_{MR}} & \mathbf{G}_2^{\Gamma_R} \end{bmatrix} \begin{bmatrix} \mathbf{t}^{\Gamma_L} \\ \mathbf{t}^{\Gamma_{ML}} \\ \mathbf{t}^{\Gamma_I} \\ \mathbf{t}^{\Gamma_{MR}} \\ \mathbf{t}^{\Gamma_R} \end{bmatrix}. \quad (64.20)$$

Furthermore, displacement and traction fields at the interface  $\Gamma_1$  can be expressed as

$$\mathbf{u}^{\Gamma_1} = \mathbf{U}_{\text{trans}}^I \mathbf{r}_{\text{trans}} \quad \text{with} \quad \mathbf{U}_{\text{trans}}^I = [\hat{\mathbf{u}}^1 \hat{\mathbf{u}}^2 \dots \hat{\mathbf{u}}^m] \quad (64.21)$$

and

$$\mathbf{t}^{\Gamma_1} = \mathbf{T}_{\text{trans}}^I \mathbf{r}_{\text{trans}} \quad \text{with} \quad \mathbf{T}_{\text{trans}}^I = [\hat{\mathbf{t}}^1 \hat{\mathbf{t}}^2 \dots \hat{\mathbf{t}}^m]. \quad (64.22)$$

By combining Eqs. (64.9) and (64.13), (64.10) and (64.14) as well as (64.21) and (64.22), one obtains constitutive relations between displacement and traction vectors in the cross-sections  $\Gamma_L$ ,  $\Gamma_R$  and  $\Gamma_I$ ,

$$\mathbf{t}^{\Gamma_L} = -\hat{\mathbf{t}}_{\text{inc}} - \mathbf{T}_{\text{refl}}(\mathbf{U}_{\text{refl}})^{-1}(\mathbf{u}^{\Gamma_L} - \hat{\mathbf{u}}_{\text{inc}}), \quad (64.23)$$

$$\mathbf{t}^{\Gamma_R} = \mathbf{T}_{\text{trans}}(\mathbf{U}_{\text{trans}})^{-1} \mathbf{u}^{\Gamma_R}, \quad (64.24)$$

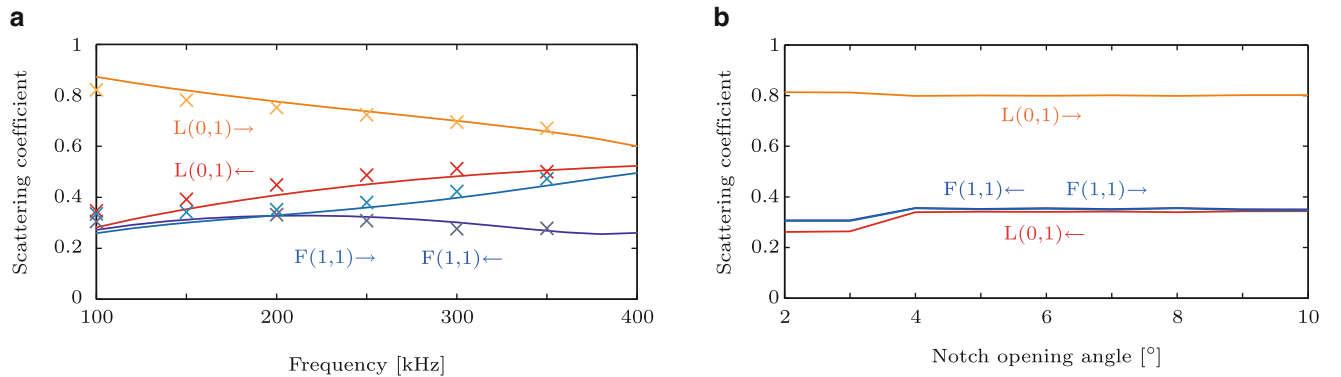
$$\mathbf{t}^{\Gamma_I} = \mathbf{T}_{\text{trans}}^I(\mathbf{U}_{\text{trans}}^I)^{-1} \mathbf{u}^{\Gamma_I}. \quad (64.25)$$

Inserting these constitutive relations as well as Neumann boundary conditions for a traction-free cylinder and for the free surface at the crack,  $\mathbf{t}^{\Gamma_{ML}} = \mathbf{t}^{\Gamma_{MR}} = \mathbf{0}$ , into Eq. (64.20) and solving for the unknown displacements  $\{\mathbf{u}^{\Gamma_L}, \mathbf{u}^{\Gamma_R}\}$ , one receives a system of linear equations in the form of  $\mathbf{A}\mathbf{u} = \mathbf{b}$  [6]. The unknown reflection and transmission coefficients can now be calculated under the assumption of Eqs. (64.9) and (64.10) by solving the linear, overdetermined system of equation in a least-squares sense. The accuracy of the solution is evaluated by an energy balance: the sum of the energy of the scattered waves has to be equal to the energy of the incident wave.

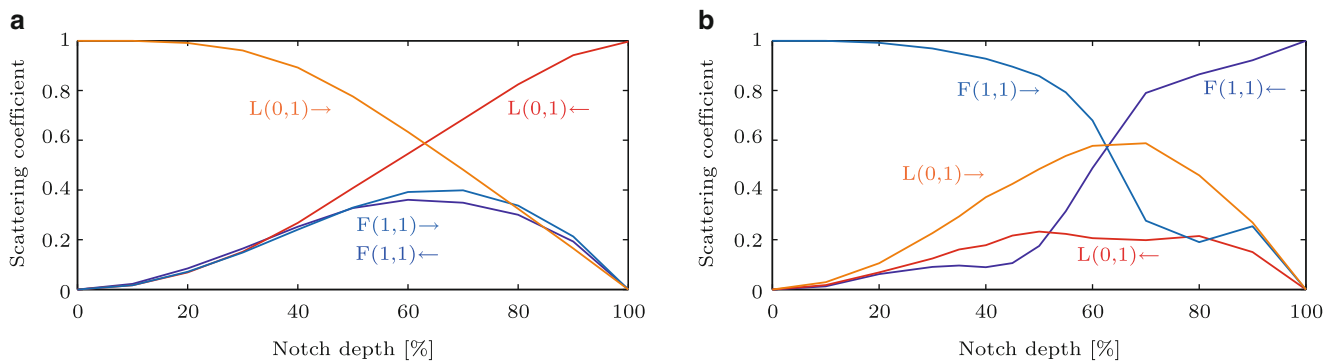
## 64.4 Results

Scattering coefficients calculated with the previously described procedure based on boundary elements is applied to evaluate reflection and transmission coefficients for arbitrarily shaped discontinuities depending on frequency, notch opening angle, notch size and type of incident wave. The obtained results allow for identification of suitable wave types and frequencies for Structural Health Monitoring applications.

Results for a 50% notch with an opening angle of  $6^\circ$  for frequencies from 100 kHz to 400 kHz are shown in Fig. 64.5a. Figure 64.5b depicts the sensitivity of an incident L(0,1) wave at a frequency of  $f = 200$  kHz to variable notch opening angle.



**Fig. 64.5** Reflection and transmission coefficients for (a) incident L(0,1) wave hitting a 50% notch with an opening angle of  $6^\circ$  in cylindrical waveguide. ← denotes reflected, → denotes transmitted propagation modes. (b) incident L(0,1) wave at  $f = 200$  kHz for variable notch opening angle. Numerical results based on boundary elements are plotted as *solid lines* and transient FE results are marked by  $\times$



**Fig. 64.6** Reflection and transmission coefficients for (a) incident L(0,1) and (b) incident F(1,1) wave at  $f = 200$  kHz for variable notch depth respectively. ← denotes reflected, → denotes transmitted propagation modes

Due to the moderate influence of the opening angle to the scattering coefficients for an angle up to  $10^\circ$ , a statement based on measured wave signals about the opening angle is complicated.

The influence of the notch size on scattering coefficients is subject of further investigations. Reflection and transmission coefficients are calculated for an incident L(0,1) wave and an incident F(1,1) wave at a frequency of  $f = 200$  kHz respectively. Results are shown in Fig. 64.6. One can recognize that the amplitudes of the transmitted and reflected longitudinal waves for an incident L(0,1) wave feature approximately linear behavior for notch sizes between 30 and 90%. This may be advantageous if measured wave signals in a monitored structure are used for quantification of defect size.

The numerical results are verified with transient Finite Element simulations for various frequencies using a hanning windowed sinusoidal burst as excitation signal. Reflection and transmission coefficients, shown in Fig. 64.5a as crosses, are calculated from the amplitudes of the scattered waves. A good agreement between WFEM-BEM and transient FE results is observed.

## 64.5 Conclusions

This research confirms that guided ultrasonic waves are a suitable tool for Structural Health Monitoring of rope structures in civil engineering applications. Nevertheless, guided wave propagation in coupled rope structures shows complex behavior, and many aspects have to be considered in order to develop a feasible damage detection concept. Issues, such as dispersive nature of guided waves in cylinders and interaction of waves with defects of various geometries were examined in this article. A detailed description of modeling and simulation was provided.

## References

1. Azevedo F, Cescon T (2002) Failure analysis of aluminum cable steel reinforced (acsr) conductor of the transmission line crossing the parana river. *Eng Fail Anal* 9(6):645–664
2. Brebbia C, Dominguez J (1992) *Boundary elements: an introductory course*. Wit, Southampton
3. Chang FK (ed) (1997) *Structural health monitoring: current status and perspectives*. Technomic, Chicago
4. Gaul L, Schanz M (1999) A comparative study of three boundary element approaches to calculate the transient response of viscoelastic solids with unbounded domains. *Comput Methods Appl Mech Eng* 179(1–2):111–123
5. Gaul L, Kögl M, Wagner M (2003) *Boundary element methods for engineers and scientists*. Springer, Berlin
6. Gaul L, Sprenger H, Schaal C, Bischoff S (2012) Structural health monitoring of cylindrical structures using guided ultrasonic waves. *Acta Mech* 223:1–12
7. Lachat JC, Watson JO (1976) Effective numerical treatment of boundary integral equations: a formulation for three-dimensional elastostatics. *Int J Numer Methods Eng* 10(10):991–1005
8. Lepidi M, Gattulli V, Vestroni F (2007) Static and dynamic response of elastic suspended cables with damage. *Int J Solids Struct* 44(25–26):8194–8212
9. Mace BR, Duhamel D, Brennan MJ, Hinke L (2005) Finite element prediction of wave motion in structural waveguides. *J Acoust Soc Am* 117(5):2835–2843
10. Mews H, Kuhn G (1988) An effective numerical stress intensity factor calculation with no crack discretization. *Int J Fract* 38:61–76
11. Siegert D, Brevet P (2005) Fatigue of stay cables inside end fittings: high frequencies of wind induced vibrations. *Bull Int Organ Study Endur Ropes* 89:43–51

# Chapter 65

## Estimation of Modal Parameters Confidence Intervals: A Simple Numerical Example

Elisa Bosco, Ankit Chiplunkar, and Joseph Morlier

**Abstract** Structural dynamic testing is concerned with estimation of system properties i.e. modal parameters. Modal parameters are extracted from measured data that are subjected to variability. Therefore these parameters when extracted from different data samples can be assumed to be random variables, which can be represented in terms of mean and standard deviation. These levels of variability can be quite important in areas of study such as damage identification given the relative insensitivity of the modal parameters to many types of system damage. This work aims at investigating how two different statistical techniques can estimate the confidence intervals on global modal parameters (natural frequencies and damping ratios), estimated by two different methods of modal extraction, on simulated data (corrupted by different levels of noise). Bootstrap and jackknifing techniques will be used on both time (LSCE) and frequency (UMPA) domain SIMO estimators. This will lead to a comparison of the capabilities of each technique to estimate the statistical properties of the modal parameters. Finally ongoing works on local modal parameters (i.e. mode shapes) estimation will be presented through the use of virtual FRFs constructed from surrogate modeling of the FRFs sets.

**Keywords** Modal parameters • LSCE • UMPA • Confidence intervals • Virtual FRFs

### 65.1 Introduction

When speaking of vibration-based damage detection methods it must be known that a simple measure of the vibration responses (and excitation) of the structure is not sufficient to guarantee the confidence in the model extracted. In fact the variability in such a response has to be quantified by estimating the uncertainties in the identified modal parameters [1–3]. Methods such as the bootstrap and the jackknife are useful to assign measures of accuracy to sample estimate. Whereas, the Least Square Complex Exponential (LSCE) and the Unified Matrix Polynomial Approach (UMPA) are two techniques of modal extraction, one uses time domain analysis whereas the other uses frequency domain analysis respectively to carry out modal parameter extraction procedure. Both are fed with the Frequency Response Function's (FRFs), of the system. This paper will deal with extraction of modal parameters for Single Input Multiple Output (SIMO) systems. Responses are measured at each degree of freedom of the structure and then these responses are converted into respective FRFs. The whole procedure right from experiment to extraction of FRF is assumed to be a black box. Our only inputs are the FRFs and statistical analyses that are performed on these methods.

---

E. Bosco • A. Chiplunkar • J. Morlier (✉)  
Université de Toulouse, ICA, ISAE, 10 av. Edouard Belin, BP54032, 31055 Toulouse, France  
e-mail: [elisa.bosco@isae.fr](mailto:elisa.bosco@isae.fr); [ankit.chiplunkar@isae.fr](mailto:ankit.chiplunkar@isae.fr); [joseph.morlier@isae.fr](mailto:joseph.morlier@isae.fr)

## 65.2 Theoretical Background

### 65.2.1 Modal Extraction

#### 65.2.1.1 LSCE

The Least Square Complex Exponential is a time a domain modal analysis method. It explores the relationship between the IRF, Impulse Response Function, of a Multi Degree of Freedom (MDOF) system and its complex poles and residues through a complex exponential [4]. We use in this paper the algorithm given by Kouroussis [5]. By establishing the analytical links between the state of each discrete output and the inputs, we can construct an autoregressive model. The solution of this model leads to the establishment of a polynomial whose roots are the complex roots of the system. Having estimated the roots (alias the natural frequencies and damping ratios), the residues can be derived from the AR model for mode shapes estimation. When disposing of data in frequency domain, the IRF can be derived from the inverse Fourier transform of an FRF. The IRF is sampled at a series of equally spaced time intervals:

$$h_{ij}(t) = \sum_{k=1}^{2N} (A_{ij})_r e^{s_r k t} \rightarrow h_k = \sum_{k=1}^{2N} (A_{ij})_r z_r^k \quad (k = 0, 1, \dots, 2N), \quad z_r^k = e^{s_r k \Delta} \quad (65.1)$$

The next step is to estimate the roots and residues from the samples of the IRF data. The  $z_r$  are the roots of a polynomial with real coefficients.

$$\beta_0 + \beta_1 z_r + \beta_2 z_r^2 + \dots + \beta_{2N-1} z_r^{2N-1} + \beta_{2N} z_r^{2N-1} = 0 \quad (65.2)$$

Taking  $2N$  sets of  $2N$  samples a linear matrix equation is formed and the coefficients of the polynomial are drawn. With the known coefficients the  $z_r$  roots are found. These roots are related to the system complex natural frequencies  $s_r$ . Since the complex natural frequencies  $s_r$  are determined by the undamped natural frequencies  $\omega_r$  and damping ratios  $\xi_r$ .

#### 65.2.1.2 UMPA

The Unified Matrix Polynomial Approach (UMPA) is a culmination of commonly used modal parameter estimation algorithms within a single educational framework [6]. It is a frequency domain MDOF method for extracting the modal parameters of a system. To understand its formulation, the polynomial model used for frequency response functions is considered and it is written for a general MIMO case:

$$\sum_{k=0}^m [\alpha_k] (j\omega)^k [H(\omega)] = \sum_{k=0}^{m-2} [\beta_k] (j\omega)^k \quad (65.3)$$

This method in the frequency domain is the AutoRegressive with eXogenous inputs (ARX(m,n)), a model that corresponds to the AutoRegressive (AR) model in time domain for the case of free decay or impulse response data. The general matrix polynomial concept recognizes that both time and frequency domain models generate functionally similar matrix polynomial models. This model, which describes both domains, is thus termed as Unified Matrix Polynomial Approach (UMPA). When the order of the denominator  $m$  is less or equal to 2 we speak of low order algorithms. They generate first or second order matrix coefficient polynomials.

$$[\alpha_2] (j\omega_i)^2 + [\alpha_1] (j\omega_i) + [\alpha_0] [H(\omega_i)] = [\beta_1] (j\omega_i) + [\beta_0] \quad \text{if } m = 2 \quad (65.4)$$

The basic equation so obtained can be rewritten for several frequencies and the matrix polynomial coefficients can be obtained after normalization (in the case of  $m = 2$ , normalizing respect to  $[\alpha_2]$ ).

$$[[\alpha_0] \quad [\alpha_1] \quad [\beta_0] \quad [\beta_1]]_{N_o \cdot 4N_i} \begin{bmatrix} (j\omega_i)^0 [H(\omega_i)] \\ (j\omega_i)^1 [H(\omega_i)] \\ -(j\omega_i)^0 [I] \\ -(j\omega_i)^1 [I] \end{bmatrix}_{4N_o \cdot N_i} = -(j\omega_i)^0 [H(\omega_i)]_{N_o \cdot N_i} \quad (65.5)$$



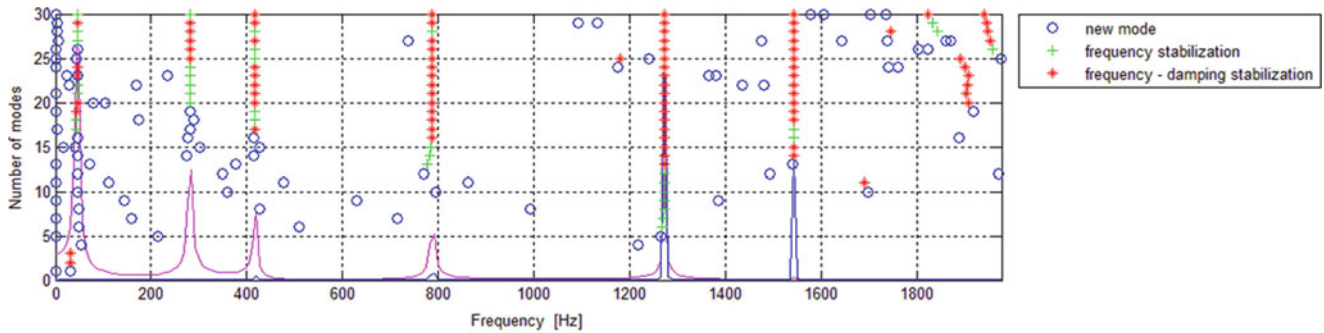


Fig. 65.1 Stabilization diagram for no-noise

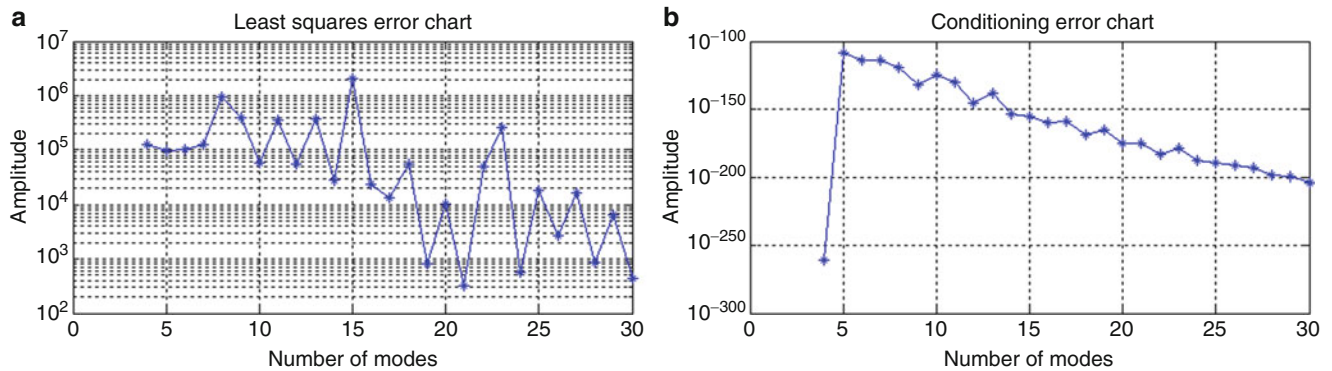


Fig. 65.2 Error chart (a) and conditioning number (b) for no-noise

The modal parameters are extracted from the companion matrix, which is formed with the polynomial coefficients.

High order models have  $m > 2$  and are usually necessary when spatial domain is under-sampled. In this case the matrix of coefficients  $[\alpha_k]$  is going to be  $N_i \times N_i$  and  $[\beta_k]$  is going to be  $N_i \times N_o$  when  $N_i < N_o$ . Evaluating the equation at a number of frequencies generates an over-determined set of equations which are solved for the coefficients  $[\alpha]$  and  $[\beta]$ . The  $[\alpha]$  coefficients are then used to form the companion matrix from which the system poles will be drawn.

### 65.2.2 Stabilization Diagram

Now the major concern while running any statistical analysis is the fact that we cannot pick and choose frequencies at our own pace. Since the number of iterations to be run to get to a stable enough mean value can be huge, an automatic modal frequency extraction mechanism should be implemented in our code. For this purpose time tested method of stabilization diagrams were chosen. One such stabilization diagram can be seen in Fig. 65.1. This diagram was run for simulated FRFs talked about in Sect. 65.3 of this paper.

In Fig. 65.2 above the x-axis denotes the value of the frequency; the Y axis denotes order of the denominator polynomial. We can see here that for every increase in the order of polynomial new modes are being introduced many of which are computation modes without any physical significance. But here and there we can see converging lines marked in red and green. They denote the frequencies occurring repeatedly and if two frequencies fall in a particular range with each other we assume them to be same frequency (here the margin is 2%). Similarly, when damping values also start converging for two already converged frequencies we have a good estimate of damping values as well (here the damping margin is 5%). The remaining two figures denote the error and the conditioning number of the system.

### 65.2.3 *Methods for the Estimation*

It was stated that the bootstrap and the jackknife are useful to assign measures of accuracy to sample estimate. These two methods are both based on the idea that if the original sample is reasonably representative of the population, then resampling from that sample should look pretty much like drawing new fresh samples [7].

#### 65.2.3.1 **Bootstrap**

This method was introduced in the late 70s by B. Efron. The main clue behind it is to construct a number of re-samples of the observed data set each of which is obtained by random sampling with replacement from the original dataset. Therefore the FRFs for a particular DoF are selected at random and with replacement. A single FRF sample may be used more than once in the ensemble average while others may not be included: this is nothing but a random weighting of the sample FRFs. In fact nor assumptions on the distribution of the identified parameters neither assumptions about the form of the input or response are made. More over this method can represent both bias and random errors. Concerning the bias, the one introduced during the estimation of the FRF cannot be captured.

Let  $x = \{x_1, x_2, \dots, x_n\}$  be the original sample. The objective is to compute a function of the data  $\hat{\theta}(x)$  which estimates some parameter  $\theta$  of the model. The bootstrap re-sample of the original sample  $x$  is  $\hat{x} = \{\hat{x}_1, \hat{x}_2, \dots, \hat{x}_n\}$  where each  $\hat{x}_i$  is drawn independently with replacement and with equal probability from the original sample  $x$ .

To be noted that, in the process of random selection, the bootstrap method requires that each individual FRF shall be stored for each measurement DoF.

#### 65.2.3.2 **Jackknife**

This technique, like a pocket Swiss knife, can be used as a quick replacement tool for a lot of sophisticates and specific tools. First developed by Quenouille and then expanded by J. Tukey in the late 50s, the jackknife procedure is a cross-validation technique to estimate the bias and variance of an estimator. It is a “leave out” iterative process, which can be applied, like the bootstrap to any statistic that is a function of  $n$  independent and identically distributed variables. It is relevant that this assumption were respected otherwise this method will lead to underestimation of the variance. In this process each element is, in turn, dropped from the sample and the parameter of interest is estimated from this smaller sample. This estimation is called a partial estimate (or also a jackknife replication).

Let  $x = \{x_1, x_2, \dots, x_n\}$  be the original sample. Again the objective is to compute a function of the data  $\hat{\theta}(x)$  which estimates some parameter  $\theta$  of the model. The jackknife will generate  $n$  re-samples of size  $n-1$  by leaving out one observation at a time. The jackknife sample is  $x^{-i} = \{x_1, \dots, x_{i-1}, x_{i+1}, \dots, x_n\}$ .

To be noted that this method works correctly only for statistics, which are linear functions of the parameters, in this case the bias error is eliminated by subtraction.

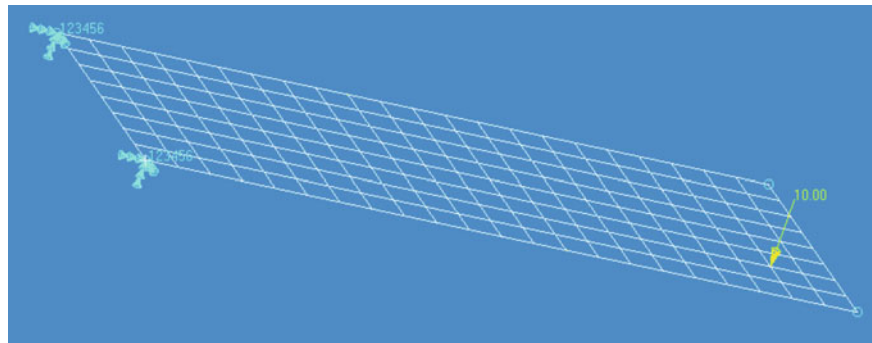
## 65.3 **Numerical Results**

These numerical results are an extension of previous SISO works on modal parameter estimation [8]. To test the two modal extraction procedures we have generated a set of 33 FRFs in a Single Input Multiple Output (SIMO) system with 33 Degrees Of Freedom's (DOF's). Later four different levels of white noise, with Signal to Noise Ratio (SNR) equal to no noise, 10, 50, and 100 were added to the 33 FRFs one by one. Now, the statistical sets for running the jackknife and bootstrap codes were run on these four noise sets and the two different modal extraction codes (LSCE and UMPA) were run on all the four cases of noise.

### 65.3.1 *Simulation Model*

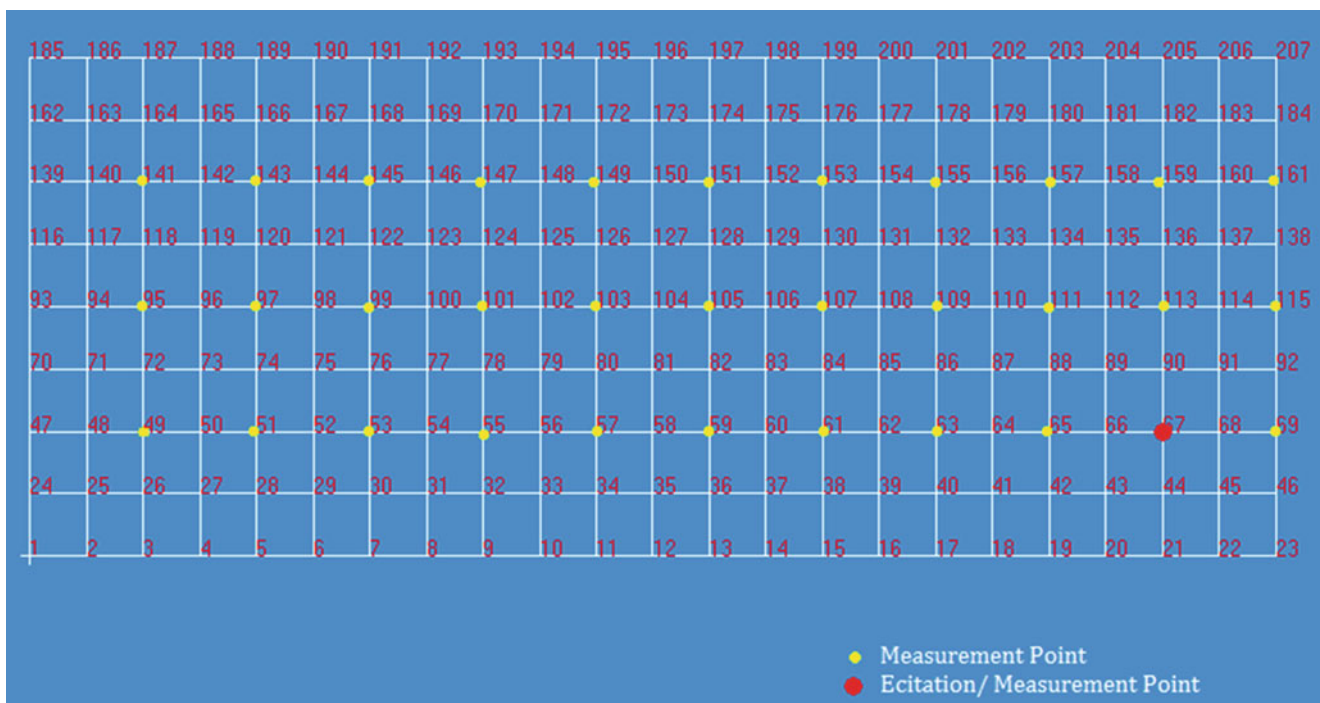
A simple thin plate, clamped at one side, was modeled in NASTRAN and excited in a manner to extract torsional modes as well as the bending modes (Fig. 65.3).

**Fig. 65.3** Geometry, BCs and load of the studied plate



**Table 65.1** Geometry and material properties for the plate under study

Geometry		Material properties	
Length [mm]	240	Young modulus [MPa]	210,000
Width [mm]	50	Poisson modulus [-]	0.3
Thickness [mm]	3.12	Density [ $\frac{\text{kg}}{\text{mm}^3}$ ]	$7.85 \cdot 10^{-6}$



**Fig. 65.4** Grid of 33 measurement points and one single excitation point (SIMO model)

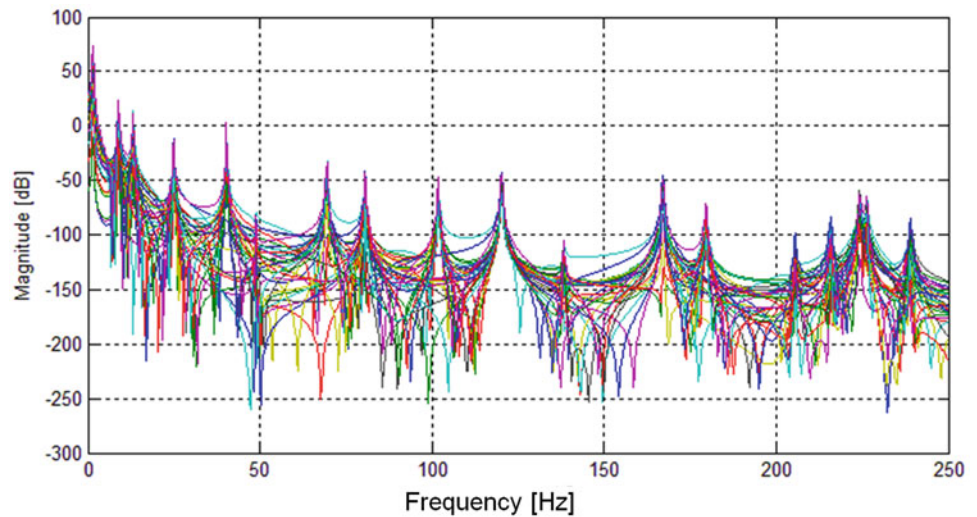
The model plate is meshed to the accuracy such that near stable modal frequencies were attained. In order to verify this, the modes extracted by Nastran itself are compared to the analytical ones (first three bending modes). The geometry and the material properties are listed in Table 65.1.

To have a further check the same values are compared with the ones extracted by LSCE and UMPA, without adding noise, as shown in Then 33 nodal points are chosen from the simulation model as seen in Fig. 65.4 and FRFs of these nodes are extracted from NATRAN.

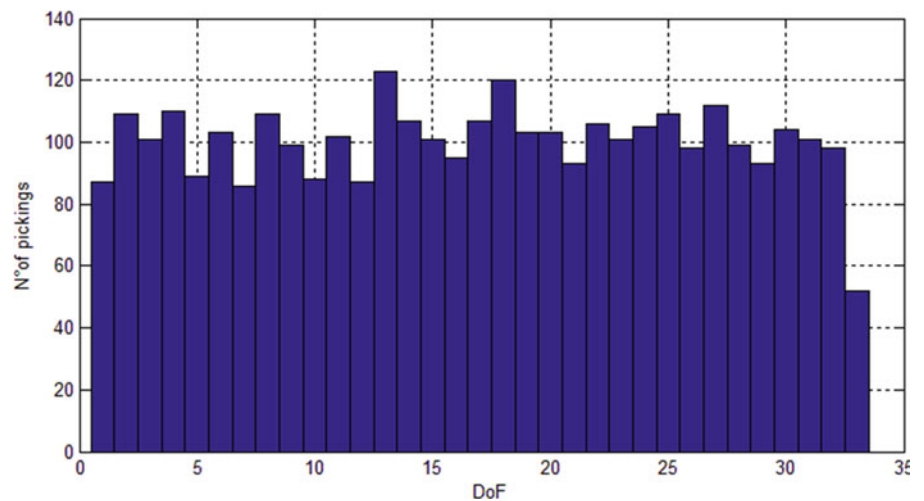
Finally, we have the required FRFs, which can serve as an input into our methods. The Fig. 65.5 below shows a typical example of FRFs set used for estimating the modal parameters.

The analysis was run in the frequency range [0 – 7, 900 Hz]. All the tables that follow will report just the first six modes extracted for reasons of conciseness.

**Fig. 65.5** Results of the harmonic analysis of the plate with random excitation



**Fig. 65.6** Bootstrap histogram



### 65.3.2 Comparison Between Bootstrap and Jackknife

The first comparison will be done on the two statistical devices used here in our paper on the extraction of confidence interval. The main difference between two statistical models is that where, bootstrap method pays importance to one particular FRF; the jackknife method removes one particular FRF and removes the influence of that FRF. Using replacement of bootstrap it is possible to see that over 1 iteration the 33 random FRF picked out of the original set may leave out some DoF but when repeating this process for a hundred times for instance, it is easy to see that all DoF have been picked a similar number of times (Fig. 65.6).

The modal parameter extraction is repeated a 100 times on a 100 of statistically independent population of data. This is one of the reason of the low level of standard deviation: the variability of the output features is reduced by the high number of iterations.

The jackknife method is run a number of times equal to the number of DoF, each time an FRF is excluded from the computation of the modal parameters. In Table 65.2 the two statistical methods are compared.

As shown in above diagram no reasonable comparison can be made for the two different modal confidence criterion methods just by looking at their mean frequency values. A more informed inference can be extracted after comparing the confidence interval but for no-noise case the standard deviations of these values are so minimal that even they cannot lead to a reasonable conclusion.

**Table 65.2** Comparison of BS and JK results for simulation without noise

No. modes	$\omega_n$ [Hz]	$\omega_{n\text{-mean}}$ [Hz]			
		BS	JK	BS	JK
	FEM	LSCE	LSCE	UMPA	UMPA
1	45.05	45.06	45.06	45.08	45.10
2	281.32	281.32	281.32	281.27	278.50
3	416.58	416.58	416.58	416.53	416.57
5	787.17	787.17	787.17	787.17	787.14

**Table 65.3** Comparison of frequency estimation and confidence intervals for different SNR

No. mode	$\omega_{n\text{-mean}}$ [Hz]			Standard deviation $\sigma_{\omega n}$ [Hz]		
	SNR = 10	SNR = 50	SNR = 100	SNR = 10	SNR = 50	SNR = 100
1	44.77	45.03	44.92	4.57E-02	1.48E-02	4.48E-03
2	285.54	281.40	281.35	7.92E-01	1.89E-02	6.58E-03
3	419.25	416.49	416.77	1.89E-01	1.99E-02	8.13E-03
4	787.56	787.24	787.18	4.44E-02	4.66E-03	5.44E-04
5	1273.74	1272.74	1272.72	4.12E-02	5.99E-03	1.15E-03

No. mode	$\omega_{n\text{-mean}}$ [Hz]			$\sigma_{\omega}$ [Hz]		
	SNR = 10	SNR = 50	SNR = 100	SNR = 10	SNR = 50	SNR = 100
1	45.05	44.99	44.98	2.25E-02	2.98E-02	6.77E-02
2	281.65	281.38	279.37	9.15E-02	8.75E-02	2.18E-01
3	416.47	416.54	416.67	1.03E-01	6.09E-02	2.98E-04
4	787.02	787.15	776.36	7.53E-02	1.61E-02	9.45E-03
5	1272.91	1272.73	1513.30	5.78E-01	4.58E-04	9.10E-03

**Table 65.4** Typical results of frequency and damping ratio estimation for BS analysis with medium noise

No. modes	SNR = 50 (Medium noise) Bootstrap analysis					
	$\omega_{n\text{-mean}}$ [Hz]			$\zeta_{\text{mean}}$ [-]		
	FEM	LSCE	UMPA	FEM	LSCE	UMPA
1	45.05	45.03	44.99	0.10	0.10	0.08
2	281.32	281.40	281.38	0.10	0.10	0.12
3	416.58	416.49	416.54	0.10	0.10	0.09
5	1272.73	1272.74	1272.73	0.10	0.10	0.10

### 65.3.3 Comparison Between Various Noises

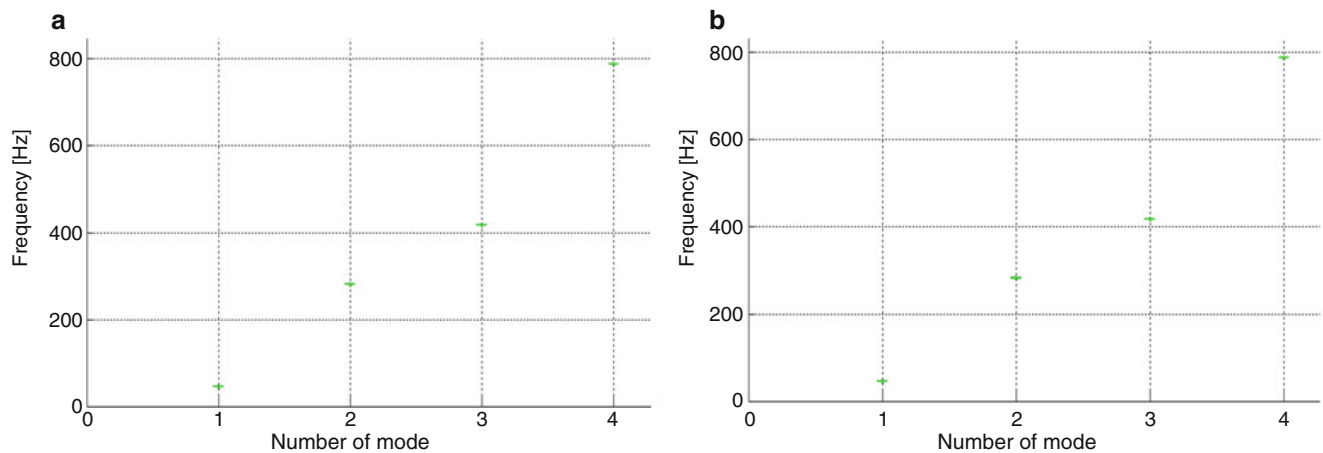
Finally, we have a comparison of effects of various types of noise on the modal parameter extraction. Gaussian white noise was added to the FRFs. Noises from the range of SNR 10, SNR 50 and SNR 100 were added with SNR 10 being the highest level of noise and SNR 100 being the lowest. The Table 65.3 shows the effect of noise on the modal parameters calculated through bootstrap method in the LSCE and UMPA computations.

The effect of addition of noise on the standard deviation of the frequencies is pretty evident, which shows lower confidence for higher values of noise. While the results are quite obvious we can have an idea of the amount of noise in our experiment upon looking at the standard deviation of frequencies. This kind of results is produced when experiments are performed on a same specimen but at different times. The amount of standard deviation can easily determine reliability of a particular experimental setup.

### 65.3.4 Comparison Between UMPA and LSCE

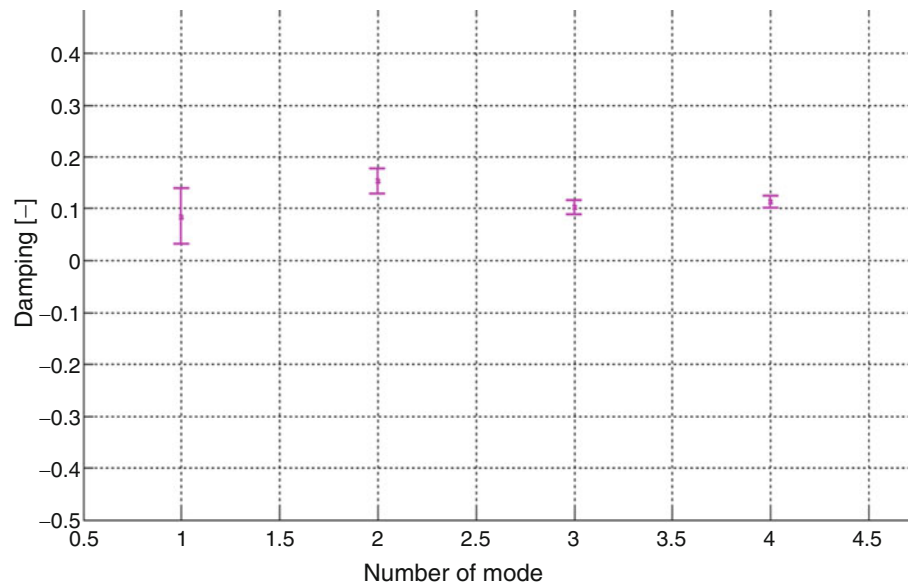
The last comparison will be done on the two methods of modal extraction used UMPA and LSCE. The major difference between the two is that where one uses time domain analysis to extract modal parameters the other uses frequency domain analyses. Table 65.4 is the comparison of the two estimation algorithms (natural frequencies and damping ratios) for the medium noise case.





**Fig. 65.7** Frequency estimation with BS confidence interval for LSCE (a) and UMPA (b) for medium noise case

**Fig. 65.8** Damping estimation with BS confidence interval for UMPA (medium noise case)



As evident from the above Table 65.4 for a medium level of noise the values of frequency obtained are highly reliable for LSCE and UMPA. We can also note that UMPA results for damping values are often correct.

The Fig. 65.7 clearly shows that the standard deviation of the LSCE method is relatively less important as compared to the UMPA codes for frequency. At the same time both methods have higher values of standard deviation when taking into account the damping ratio.

For damping estimation, LSCE results are slightly better than UMPA. Fig. 65.8 shows typical results for damping estimation with confidence interval for the first four modes (UMPA). Speaking on noise dependency, the two algorithms have reliable mean values for damping ratios except for the lowest SNR, and globally the standard deviation is reducing when SNR is increasing.

## 65.4 Ongoing Works

This chapter will introduce the two main perspectives of our works. The first ongoing work is to improve artificially the data consistency of our set of FRFs for solving the inverse problem of modal parameter estimation. So far, we need to introduce virtual FRFs, which are the FRF from an unknown measurement point such as a point that does not belong to the



measurement grid points. Virtual FRFs will be built from the experimental FRFs set using surrogate modeling [9]. One way to do this is to link the residue of the transfer function (or imaginary part of the FRF) at resonance with a harmonic (Fourier) solution of the spatial mode shape (for each resonance). Thus by solving a classical inverse problem using least squares solution for example, we will be able to synthesize the missing data (virtual FRFs). This will lead to a larger data set for the modal parameter estimation and probably lead to more reliable results.

One of our previous works at IMAC will help us to deal with non-regular measurement grids [8, 10]. Mode shapes can be viewed as an  $n$ -dimensional vector ( $n = 2$ ). To acquire this signal, we consider a linear measurement model, in which we measure an  $m$ -dimensional vector  $b = Ax \in R^m$  for some  $m \times n$  measurement matrix  $A$  (thus we measure the inner products of  $x$  with the rows of  $A$ ). For instance, if we are measuring a time series in the frequency domain,  $A$  would be some sort of *Fourier* matrix.

$$x = \operatorname{argmin}_{x:Ax=b} \|x\|_{l_2} = A^*(AA^*)^{-1}b \quad (65.6)$$

For regular grid the least square solution is interesting. But let's take the example of non-regular grid for mode shape reconstruction. Then another approach based on sparsity must be used; it is called compressive sampling [11–13]. The sparse basis for 2D signal would be collections of mode shapes  $(\sin(\omega_j \frac{t_m}{a})) \cdot (\sin(\omega_j \frac{t_m}{b}))$  at the desired resolution ( $5 \times 5$  modes for example). A suitable incoherent measurement system for this basis is to select random samples (6 sensors) in the space domain, obtaining measurements  $y_k = f(t_k)$ , where the  $t_k, k = 1, 2 \dots K$ , are selected randomly.

An optimal sparse representation in a given basis is obtained by performing a constrained  $L_1$  optimization over the linear coefficients that appear in the representation of the signal. That is, given some signal  $f$  and basis elements  $f$ , a minimization is performed, as:

$$\min \sum_{j=1}^N |a_j| \text{ s.t. } y_m = \sum_{j=1}^N a_j \cos(\omega_j t_m) \quad \text{with } m = 1, 2, \dots, M \quad (65.7)$$

The  $L_1$  minimization tends to concentrate the energy of the signal on to a few non-zero coefficients  $a_j$ , unlike the least squares ( $L_2$  minimization), which tends to spread the energy around. By replacing the absolute value of the  $a_j$  with the difference of the positive and negative parts, the  $L_1$  function becomes a linear objective solved by linear programming method (simplex).

The second part will be the validation of our method using experimental data of the monitoring of composites beams subjected to different level of impact [14]. Using the confidence interval, we will be able to link the relationship between pole shifts and delamination zone with higher confidence especially when dealing with damping ratio changes estimation, which are often subjected to uncertainties.

## 65.5 Conclusions

Modal parameters are often the inputs of SHM algorithms. It is clear that uncertainties will propagate from the modal parameters to the damage identifications parameters. Starting from the numerical data extracted from Nastran, we have tested the behavior of the two classical identification methods (LSCE and UMPA) respect to the presence of noise on the data (FRFs). It is essential to consider which methods (time method LSCE or frequency method UMPA) will suppress the sources of variability. We have then presented a way to quantify the uncertainties on identified modal parameters. These uncertainties provide a measure of the efficiency and reliability of the extraction method. Finally we introduce virtual FRFs paradigm in order to artificially enlarge the set of FRFs in the inverse problem, and so finally should enhance the reliability of the modal parameters estimation.

## References

1. Farrar CR, Doebling SW, Cornwell PJ (1998) A comparison study of modal parameter confidence intervals computed using the Monte Carlo and Bootstrap techniques. In: Proceedings of the 16th international modal analysis conference, Santa Barbara, USA
2. Doebling SW, Farrar CR (2000) Estimation of statistical distributions for modal parameters identified from averaged frequency response function data. ASME J Vibr Contr 7:603–624
3. Moaveni B, Barbosa AR, Conte JP, Hemez FM (2007) Uncertainty analysis of modal parameters obtained from three system identification methods. In: Proceedings of the 25th international modal analysis conference, Orlando, FL, USA

4. Brown DL, Allemang RJ, Zimmerman R, Mergeay M (1979) Parameter estimation techniques for modal analysis. Society of Automotive Engineers, Paper No. 790221
5. Kouroussis G, Fekih LB, Conti C, Verlinden O (2012) EasyMod: a MatLab/SciLab toolbox for teaching modal analysis. In: Proceedings of the international congress on sound and vibration, Vilnius, 9–12 July 2012
6. Allemang RJ, Philips AW (2004) The unified matrix polynomial approach to understanding modal parameter estimation: an update. In: Proceedings of international conference on noise and vibration, Dearborn, MI, USA
7. Efron B, Gong G (1983) A leisurely look at the bootstrap the jackknife and cross-validation. *Am Stat* 37(1):36–48
8. Morlier J, Chermain B, Gourinat Y (2009) Original statistical approach for the reliability in modal parameters estimation. In: Proceedings of the 27th international modal analysis conference, Orlando, FL, USA
9. Forrester AII, Sobester A, Keane J (2008) *Engineering design via surrogate modelling: a practical guide*, John Wiley & Sons Ltd, Chichester, UK
10. Morlier J, Bettebghor D (2011) Compressed sensing applied to modeshapes reconstruction. In: Proceedings of the 29th international modal analysis conference, Jacksonville, FL, USA
11. Candès EJ, Romberg J, Tao T (2006) Stable signal recovery from incomplete and inaccurate measurements. *Comm Pure Appl Math* 59:1207–1223
12. Donoho DL (2006) Compressed sensing. *IEEE Trans Inform Theor* 52(4):1289–1306
13. Candès EJ, Wakin MB (2008) An introduction to compressive sampling. *IEEE Signal Process Mag* 25(2):21–30
14. Shahdin A, Morlier J, Gourinat Y (2009) Correlating low energy impact damage with changes in modal parameters: a preliminary study on composite beams. *Struct Health Mon* 8(6):523–536

# Chapter 66

## A Bayesian Framework of Transmissibility Model Selection and Updating

Zhu Mao and Michael Todd

**Abstract** For the purpose of system identification and structural health monitoring, transmissibility, as an output-output transfer function, plays a very important role because of its compatibility with input absent data and local parameter sensitivity. However, data-driven transmissibility estimations are always subject to uncertainties, and tremendously increasing the length of measurements and/or number of averages to suppress some types of uncertainty influence are often impractical. Based upon the likelihood function established in previous work, this paper adopts a Bayesian framework to probabilistically select the most plausible class of models and update parameters with a limited amount of test data. A structural computational model is considered as a test-bed on which the approximated transmissibility model is computed; consequently, under a quantified confidence, the quality of transmissibility estimations is enhanced via a lower order approximate model, with a much lower demand on data acquisition requirements.

**Keywords** Bayesian model selection • Likelihood function • System identification • Damage detection • Structural health monitoring

### 66.1 Introduction

In the past couple of decades, model selection and updating regarding various applications of system identification have attracted increasing attention, such as in finite element analysis, modal analysis, time series (e.g., auto-regressive) modeling, and other applications that require system identification, for example, structural health monitoring and damage detection. An accurate yet low-order (as “simple as possible”) model would be an ideal solution for all engineering problems. However, uncertainty degrades the modeling performance and affects to all the aforementioned implementations. Moreover, when the object being modeled is subject to any time-variant factors, the system identification outcomes must adjusted in a synchronized fashion [1, 2]. In other words, there are errors in the system identification models, not only from uncertainties and details that are difficult to model, but also from the change of system as time goes by. Therefore, the model selection and updating dealing with the model errors are essentially a statistical inference problem, in which the most plausible identification is investigated and kept updated via information from data observations (evidences) [2–4].

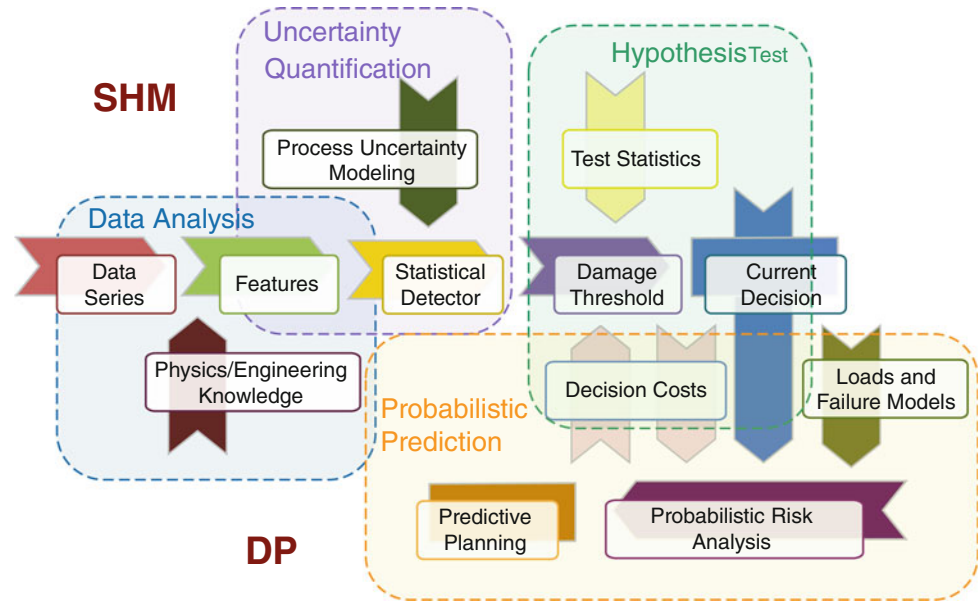
Specifically for structural health monitoring problems, model selection and updating play an important role in each step of the general structural health monitoring and damage prognosis (SHM/DP) flow, as shown in Fig. 66.1. The general flow includes four steps, namely, data analysis, uncertainty quantification, hypothesis testing, and probabilistic prediction parts. In the data analysis part, information from measurements is extracted to form a feature set, with a physics/engineering model of some kind selected. Uncertainty quantification part quantifies the variabilities or uncertainties appearing in the feature evaluations ending up with a statistical model. In the hypothesis test part, the uncertainty quantification model is utilized to make a decision between the baseline or damaged model in a statistical sense. The last step considers the decision cost and future information involving in the detection process, and predicts the future performance in terms of, for example, remaining service life, time to failure, or time to next maintenance action.

---

Z. Mao (✉) • M. Todd

Department of Structural Engineering, University of California San Diego, La Jolla, CA 92093-0085, USA  
e-mail: [zmao@ucsd.edu](mailto:zmao@ucsd.edu); [mdtodd@ucsd.edu](mailto:mdtodd@ucsd.edu)

**Fig. 66.1** General flow of SHM and DP



This paper focuses on the hypothesis testing part, by using the uncertainty quantification model established in previous work, and using a Bayesian inference framework to decide which model is more plausible to the system according to the data observation. In fact, this model selection approach can be directly related to damage detection problem, where the baseline and damaged model are the models to be selected from.

## 66.2 Model Selection Via Bayesian Inference

The motivation for this paper is to adopt Bayesian inference framework to select the correct, i.e. more plausible, system identification model given the observation of data measurements, so the first thrust is to recall Bayes theorem:

$$p(M|D) = \frac{p(D|M)p(M)}{p(D)}, \quad (66.1)$$

in which  $M$  denotes a single model in the entire possible class and  $D$  is the data observation, which usually is a vector. The terms  $p(M)$  and  $p(M|D)$  are prior and posterior probability respectively, indicating the plausibility of accepting model  $M$  and accepting model  $M$  given the observation of data  $D$ . Likelihood  $p(D|M)$  is interpreted as the probability of observing data  $D$  given the condition that model  $M$  is true, while the probability of occurrence of  $D$  is a constant and usually eliminated in Bayesian analysis.

A more practical form of the Bayes formula in (66.1) considers the ratio between the a posteriori probabilities of different models given the same set of data observation:

$$\frac{p(M_d|D)}{p(M_u|D)} = \left[ \frac{p(D|M_d)}{p(D|M_u)} \right] \cdot \left[ \frac{p(M_u)}{p(M_d)} \right], \quad (66.2)$$

where the subscript  $u$  and  $d$  denotes different model selections. This form represents quantitatively how the decision should be biased to the more possible model, considering any prior knowledge and the information from operating data. The likelihood ratio of the operational data under each model is also called Bayes factor  $\mathbf{B}$ , which reflects the influence of data observation in the  $M_u/M_d$  binary decision process.

In a practical implementation, “model” is often more similar to a “parameter”, and therefore the model selection and updating is indeed a parameter selection and updating process. Because Bayes factor links the information from data with

the actual model (parameter) state, a logarithm form of Bayes factor in terms of the likelihood of data given “parameters” is derived via series expansion and a Laplace approximation [1]:

$$\log(B) \approx \log \left( p \left( D | \hat{\theta}_d, M_d \right) \right) - \log \left( p \left( D | \hat{\theta}_u, M_u \right) \right) - \frac{\Delta k}{2} \log(N). \tag{66.3}$$

In (66.3),  $N$  is the total length of data vector and  $\Delta k$  is the difference between numbers of parameters in the two models. The third term on the right hand side is a penalty term for using more complex model structure causing the data over fitted. Based on this concept, Ref. [5] gives a scalar criterion for interpretation of Bayes factor. For small number of Bayes factors, around 1, the observe data does not obviously support any of the model more than the other. On the contrary, for very big Bayes factor, the  $M_d$  hypothesis is accepted while the  $M_u$  is denied with good confidence. If the logarithm is negative, that means the Bayes factor is less than 1, indicating support of model  $M_u$ .

### 66.3 Damage Detection Implementation

The Bayesian framework in last section will be implemented with transmissibility data from a simulation test structure shown in Fig. 66.2. A 3-DOF mass-spring-damper system is considered, on which the noise excitation is input at DOF#3, and acceleration responses are recorded at the rest two. Stiffness of spring#1 is tuned less than the original value to simulate change of the system, i.e.  $M_d$  in the context of model selection.

Transmissibility is picked as the feature of system status, which is defined as the ratio between two output spectra:

$$T_{ij}(\omega) \triangleq \frac{F[y_i(t)]}{F[y_j(t)]} = \frac{G_{xy_i}(\omega)}{G_{xy_j}(\omega)}. \tag{66.4}$$

In this part, the Bayes factor criterion will be used to deploy model selection among the original structure model  $M_u$  and the damaged (degraded) model  $M_d$ . FRF and transmissibility spectra are available analytically for this discrete system, as shown in Fig. 66.3. However, as stated in the beginning of this paper, the uncertainty and external measurement noise in the Gaussian system identification process will cause the change of structure not to be distinguished, and the actual transmissibility estimations will not be as smooth as Fig. 66.3 shows.

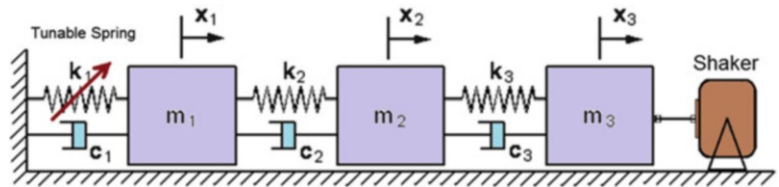


Fig. 66.2 Simulation test structure

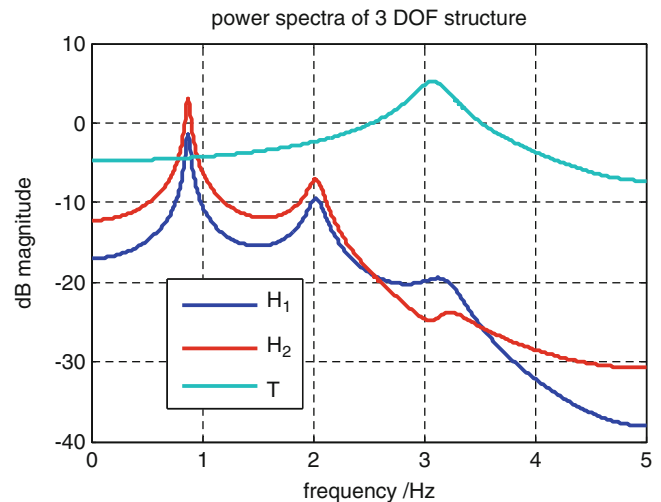
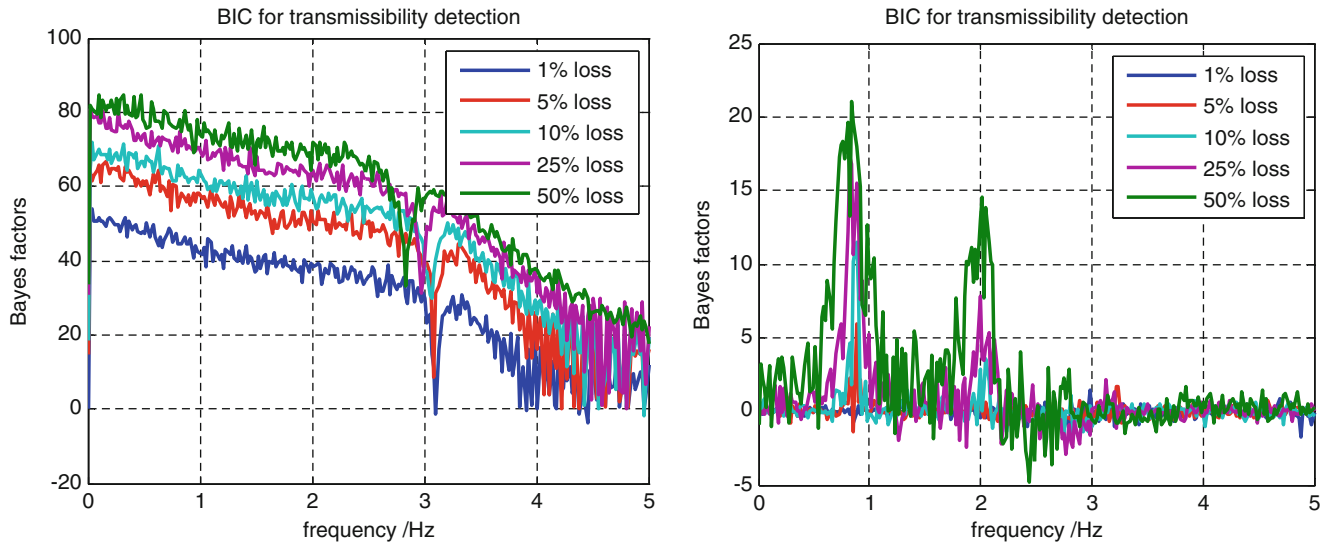


Fig. 66.3 Analytical spectra of 3-DOF system



**Fig. 66.4** Log of Bayes factor for  $N = 4$  realizations. *Left*: external noise free; *Right*: 10 dB external Gaussian white noise

### 66.3.1 Likelihood Function

Since the Bayes factor is only determined by the likelihood ratio,  $p(D|\hat{\theta}, M)$  in (66.3) is the key term in this entire Bayesian framework. In this specific model selection problem, as addressed above, the model class is the undamaged or damaged transmissibility evaluation, and data  $D$  is the transmissibility estimation from Gaussian random process simulation.

Probability density function of transmissibility estimation  $\hat{T}_{ij}$  is given by [6]:

$$pdf(t) = \frac{\gamma}{\pi\alpha} \cdot e^{-\frac{1}{2(1-\rho^2)}\left(\frac{\mu_{C_i}^2}{\sigma_{C_i}^2} - 2t\frac{\mu_{C_i}\mu_{C_j}}{\sigma_{C_i}\sigma_{C_j}} + \frac{\mu_{C_j}^2}{\sigma_{C_j}^2}\right)} + \frac{\beta}{\sqrt{2\pi}\alpha^{3/2}} \cdot e^{-\frac{(\mu_{C_i} - t\mu_{C_j})^2}{2\alpha}} \cdot \text{Erf}\left(\frac{\beta}{\sqrt{2\alpha}\gamma}\right) \quad (66.5)$$

in which  $\alpha = \sigma_{C_i}^2 - 2\rho t\sigma_{C_i}\sigma_{C_j} + t^2\sigma_{C_j}^2$ ,  $\beta = \sigma_{C_i}(\rho\mu_{C_i}\sigma_{C_j} - \mu_{C_j}\sigma_{C_i}) + t\sigma_{C_j}(\rho\mu_{C_j}\sigma_{C_i} - \mu_{C_i}\sigma_{C_j})$ ,  $\gamma = \sqrt{1-\rho^2}\sigma_{C_i}\sigma_{C_j}$  and  $\rho = \frac{\text{cov}(g_i, g_j)}{\sigma_{C_i}\sigma_{C_j}}$ , where it is assumed that the cross power density magnitude has a Gaussian bivariate distribution  $\hat{G} \sim N(\mu_C, \sigma_C^2)$ . By converting (66.5) into likelihood function in the Bayes factor, the model selection criterion will be formed in next section.

### 66.3.2 Model Selection

Recall the definition of Bayes factor in (66.3), the likelihood of data  $D$  is actually the product of all the probabilities of each single element  $t_i$  in  $D$ , assuming an independent sampling. Because the selection is implemented among two models with the same frame, thus same number of model parameters, the  $\Delta k$  term vanishes. The derived log Bayes factor is then expressed in (66.6):

$$\begin{aligned} \log(B) &\approx \log\left(\prod_{i=1}^N\right) - \log\left(\prod_{i=1}^N pdf\left(t_i|\hat{\theta}_u\right)\right) \\ &= \sum_{i=1}^N \log\left(pdf\left(t_i|\hat{\theta}_d\right)\right) - \sum_{i=1}^N \log\left(pdf\left(t_i|\hat{\theta}_u\right)\right). \end{aligned} \quad (66.6)$$

After running transmissibility identification for four times, i.e.  $N = 4$ , the Bayes factor of model selection among the original structure and structure with 1%, 5%, 10%, 25%, 50% of stiffness loss at spring #1 are calculated and plotted in Fig. 66.4. To be more realistic, extra artificial Gaussian white noise is added to the simulation data at a 10% level, making some extraneous uncertainty to the process. It is very clear to see that noise drops the Bayes factor dramatically and degrades



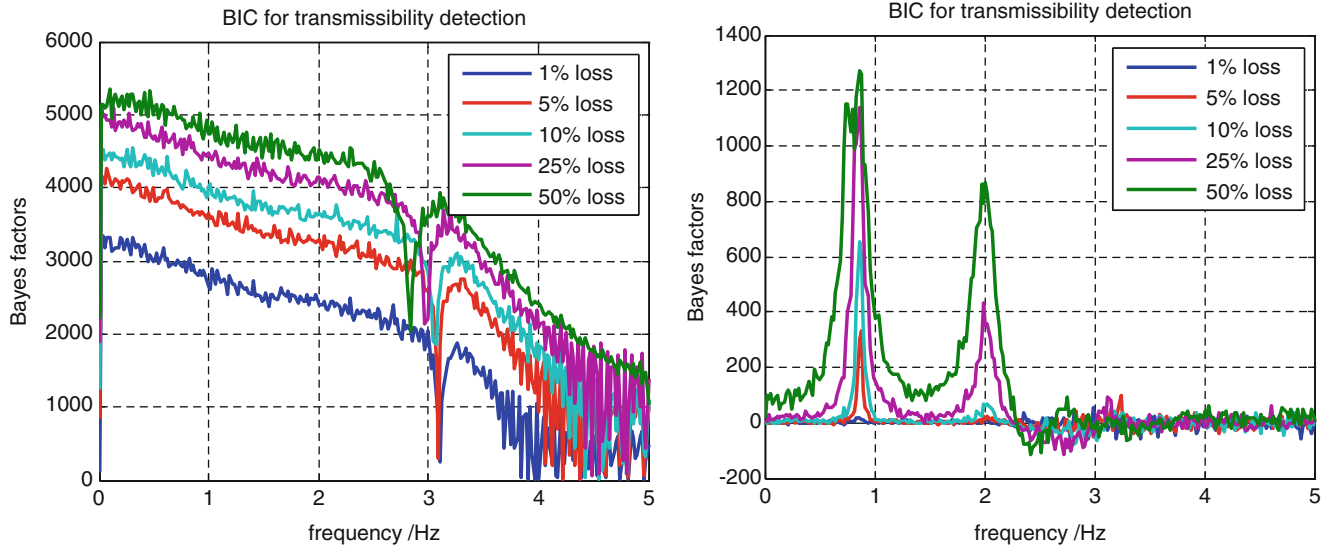


Fig. 66.5 Log of Bayes factor for  $N = 256$  realizations. *Left*: external noise free; *Right*: 10 dB external Gaussian white noise

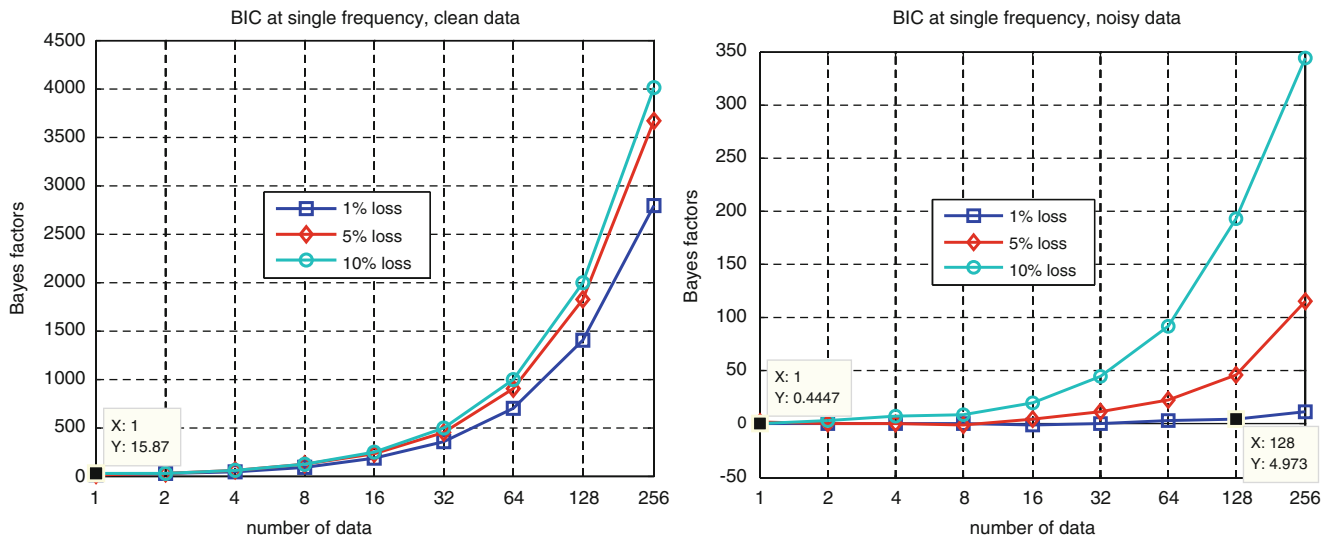


Fig. 66.6 Parametric study of log of Bayes factor for different amount evidences ( $N$ ). *Left*: external noise free; *Right*: 10 dB external Gaussian white noise

most of the frequencies near zero log value, ending up with good model selection capability only near resonances. On the other hand, for the external noise free case, almost all frequency lines have good Bayes factor evaluation, indicating strong support of  $M_d$  in stead of  $M_u$ .

In the context of damage identification, the Bayes factor shows a very good consistency with increasing of damage severity, as shown in Fig. 66.4. But where there is noise contamination, the detection of changes is not easy to be found, only except for the resonance where the local signal-to-noise level is sufficiently good. To enhance the capability of model selection and severity evaluation, more data (evidences) are necessary, considering the Bayesian essence. By adding more realizations of transmissibility features, there are increasing amount of evidences supporting the model selection, and mathematically a greater Bayes factor will be available.

Figure 66.5 plots the Bayes factor results after improving the amount of data and thus more evidence coming into the selection of plausible models. The Bayes factors are much higher than the factors in Fig. 66.4 indicating easier model selection. And moreover, the differentiability between those damaged cases is also enhanced given more data observations.

For a parametric study across the length  $N$  of data vector, Bayes factors calculated with different amount of evidences (in terms of  $N$ ) are plotted in Fig. 66.6. For external noise free condition, Bayes factor is good enough for an effectual model

selection, even with a couple of data points (realizations) observed, and even for only 1% of stiffness loss. Despite of the increase of Bayes factor as damage goes more severe, the result in contaminated condition is much smaller compare with the noise free condition, and for small  $N$  (small amount of evidence) and light damage (1% of stiffness loss), the Bayes factor is not sufficiently large for supporting the model selection, i.e., for performing any decision-making with high confidence.

## 66.4 Summary and Conclusion

This paper adopts Bayesian model selection frame and applied it onto damage detection applications. Results from a simulation test structure, with respect to Bayesian factor, show a clear insight of making decisions considering data measurements. Noise contamination will unsurprisingly degrade the model selection capability, with only the transmissibility evaluated near resonances still useful. However, with putting more data into the selection problem, there comes more evidences supporting the decision-making, and with sufficient data, the Bayes factor is capable at distinguishing structural changes as small as 1% of stiffness loss.

Future work is considered extending current Bayesian model selection framework to a more generalized scheme, and model updating regarding structural change will also be investigated.

**Acknowledgements** The authors acknowledge the Air Force Office of Scientific Research (AFOSR) Grant #FA9550-10-1-0455 (Dr. David Stargel, Program Manager) for support of this work.

## References

1. Burnham KP, Anderson DR (1998) Model selection and inference: a practical information-theoretic approach. Springer, New York
2. Vanik MW, Beck JL, Au SK (2000) Bayesian probabilistic approach to structural health monitoring. *J Eng Mech* 126:738–749
3. Sivia DS, David WIF, Knight KS (1993) An introduction to Bayesian model selection. *Physica D* 66:234–242
4. Saito T, Beck JL (2010) Bayesian model selection for ARX models and its application to structural health monitoring. *Earthquake Eng Struct Dynam* 39:1737–1759
5. Jeffreys H (1961) *The theory of probability*, 3rd edn. Clarendon, Oxford, p 432
6. Mao Z, Todd M (2012) Rapid structural condition assessment using transmissibility with quantified confidence for decision making. In: *Topics in model validation and uncertainty quantification*, vol 4. Conference proceedings of the society for experimental mechanics series, Jacksonville, FL USA, vol 29, pp 133–140

# Chapter 67

## Monitoring of Torsion of Guyed Mast Shafts

Shota Urushadze and Miroš Pirner

**Abstract** Systematic monitoring of torsion (swivelling) of guyed mast shafts has been performed in ITAM since 2005. The occurrence of this phenomenon is conditioned by the fact that the guy ropes are attached to the surface of the shaft, i.e. out of its axis.

The presented two examples of experimental verification describe the analysis of dynamic response of the shaft of real masts and on an aerodynamic model.

The simple calculation model serves for making the proof of the occurrence of the moment, affecting the shaft, which is guyed by three ropes. The exact theoretical solution of the real phenomenon assumes the introduction of dynamics of guy ropes, which vibrate in 3D shapes during the shaft's movement along the orbit and its torsion (swivelling).

**Keywords** Dynamics of guyed masts • Dynamic response • Swivelling of the shaft • Wind tunnel • Aerodynamic model

### 67.1 Introduction

The statics of guyed masts was sufficiently elaborated as early as the first half of the twentieth century, also with respect to the nonlinearity of the effect of ropes [1].

The basis for the dynamics of guyed masts was published by Koloušek [2], with the use of his deformation method. Since then the field of dynamics of guyed masts has extended by the knowledge of the effects of nonlinear phenomena, parametric resonance and self-excitation. Out of these, let us state at least [3, 4].

The theoretical analysis of the mast should always be corrected on the basis of monitoring of the real structure.

From the measuring of the dynamic response of masts or of their models it was known that the resulting movement of the shaft in ground plan appears as an ellipse,<sup>1</sup> whose major semi-axis forms an angle less than 90° with the direction of the wind. Usually low intensity of turbulence and smooth surface of the shaft are conditions for the regularity and intensity of the vortex shedding. High intensity of turbulence disturbs the regularity of the shedding and thus also the cross-wind direction excitation and then the ellipse becomes more a circle [5, 6, 10].

### 67.2 Torsion or Swivelling of the Mast Shaft

The shifting from zero position will result in changes of the forces in the ropes and moments in the points of connection to the shaft, which are out of the axis of the shaft. If the shaft is guyed by three ropes, there are six points on the elliptical track, in which the sum of the moments from the eccentric connection of the ropes is zero, and thus also the swivelling is zero (see

---

<sup>1</sup>The orbit may degenerate into a line, it may also be circular.

S. Urushadze (✉) • M. Pirner

Institute of Theoretical and Applied Mechanics of the Academy of Sciences of the Czech Republic v.v.i, Prosecká, 76, Prague, Czech Republic  
e-mail: [urushadze@itam.cas.cz](mailto:urushadze@itam.cas.cz); [pirner@itam.cas.cz](mailto:pirner@itam.cas.cz)

**Fig. 67.1** Rotation of the shaft owing to the eccentricity of the ropes

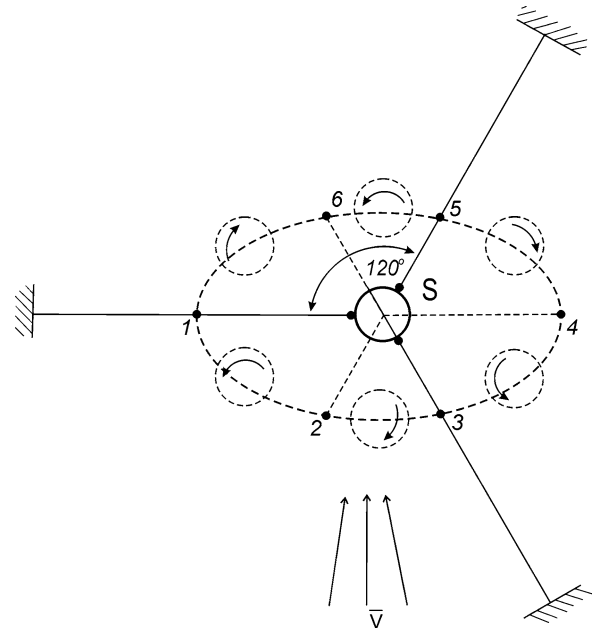


Fig. 67.1). These points delimit the domains with positive or negative rotation of the shaft. The zero points may lie close to each other; in such case the domains prevail with their size at the apexes of the ellipse. If the ellipse degenerates into a line, there are two domains of rotation which differ in the plus/minus sign.

The frequency of torsion or swivelling of the shaft depends on the position of the zero points on the ellipse (see Fig. 67.1): if the zero points are far enough from each other, the torsion of the shaft is governed by the six domains of moments and the frequency of swivelling  $f_{tor}$

$$f_{tor} = 3 f_b \tag{67.1}$$

If points (see Fig. 67.1) 2 and 3 merge into one, and so do points 5 and 6, then:

$$f_{tor} = f_b \tag{67.2}$$

Under certain conditions<sup>2</sup> there also appear other ratios of  $f_{tor}$  and  $f_b$ .

The proof of the occurrence of moments which swivel (torsion) the shaft will be made using a simple calculation model, in which we take into account only static effects. The ropes are in a horizontal plane, without sag. Figure 67.2 shows the ground plan of a shaft of triangular cross section, guyed in one level by three ropes (1., 2. and 3.).

When moving the shaft by  $\Delta r$  in the direction of X-axis, the ropes 1. and 2. of a length of  $l_1$  and  $l_2$  will lengthen by

$$\left. \begin{aligned} \Delta l_1 &= \sqrt{l_1^2 + \Delta r^2} - l_1 \\ \Delta l_2 &= l_2 (\cos \varphi_2 - 1) + \Delta r \cdot \cos(30^\circ - \varphi_2) \end{aligned} \right\} \tag{68.3}$$

and the 3rd rope will shorten by

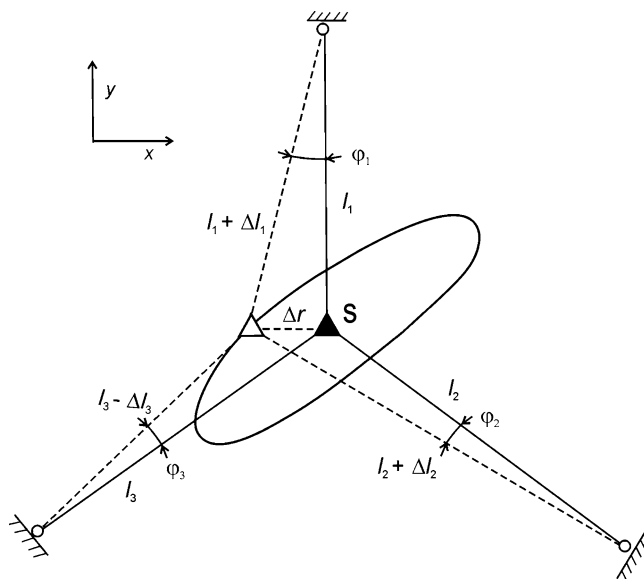
$$\Delta l_3 = \frac{l_3 - \Delta r \cdot \cos 30^\circ}{\cos \varphi_3} - l_3$$

where  $l_i$  are the lengths of rope

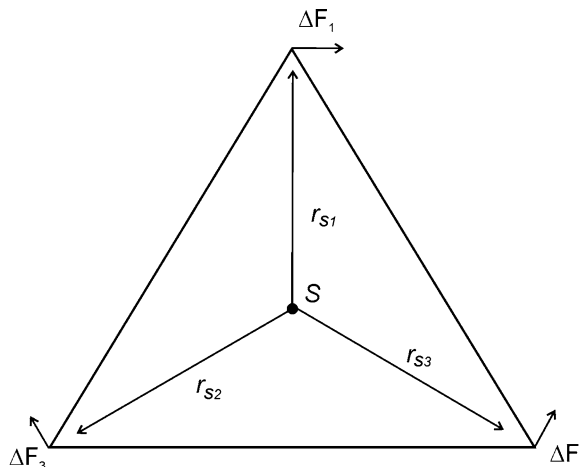
When  $\Delta r$  is || the axis X then  $\Delta y = 0$ ,  $\Delta x = \Delta r$ ,  $\cos \varphi_1 = \frac{l_1}{l_1 + \Delta l_1}$

<sup>2</sup>These conditions include the fact that the point of intersection of guy ropes; forces may lie “behind” the centre of gravity of the shaft cross section; “behind” means out of the orbit.

**Fig. 67.2** Deriving the length strain of the ropes



**Fig. 67.3** Components of forces and their moment arms to the rotation axis



$$k_i = \frac{A \cdot E}{l_i} \tag{67.4}$$

$$\Delta F_i = k_i \cdot \Delta l_i \tag{67.5}$$

Using the length transformations of the ropes  $\Delta l_i$  and the chosen spring constant  $k_i$  of the rope we will determine the increments of forces in the ropes  $\Delta F_i$ , whose components on the arms  $r_{si}$  create the resulting moment (see Fig. 67.3)

$$M = \sum_1^3 \Delta F_i \cdot r_{si} \tag{67.6}$$

### 67.3 Monitoring of Torsion (Swivelling) on Real Structures

The torsion of the mast shaft was monitored on three masts [5, 7]. In the year 2011 were monitored the other two guyed masts. Lets us see results. The first one is on the Fig. 67.4. The movements of the shaft were monitored at a height of 124.88 m by means of two accelerometers ENDEVCO, type 86, the signals of which could have been mutually added or subtracted.

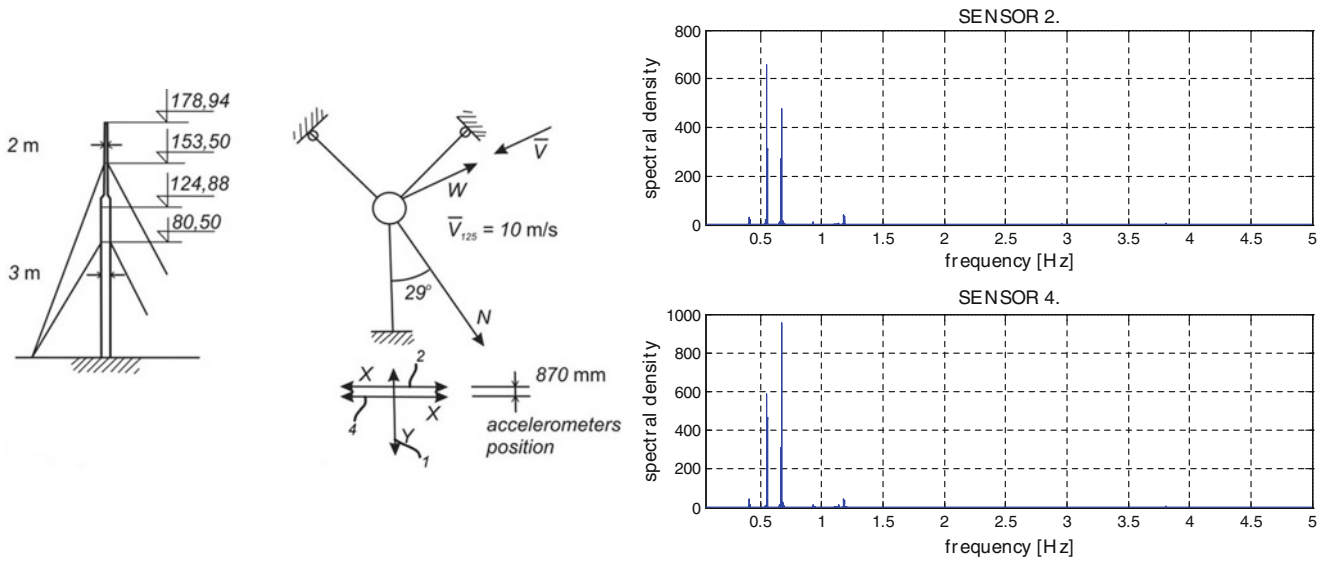
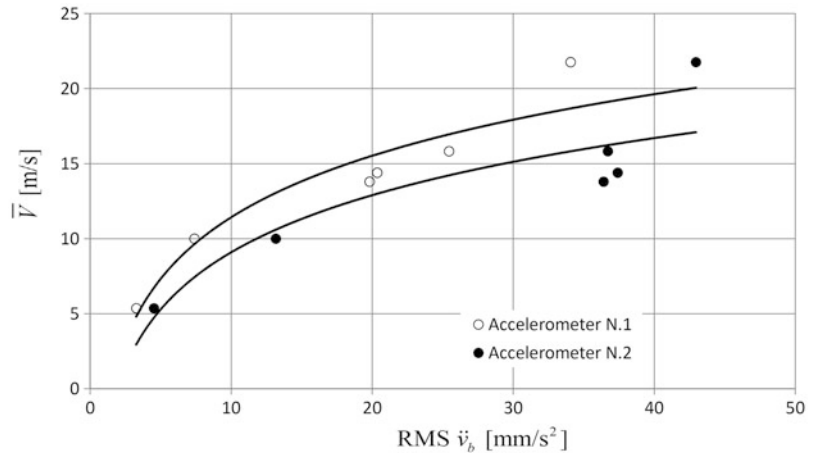


Fig. 67.4 The first guyed masts. The spectral density of response

Fig. 67.5 Relation between mean wind speed  $\bar{V}$  [m/s] and RMS acceleration of bending  $\text{RMS } \ddot{v}_b$  [mm/s<sup>2</sup>]



In Fig. 67.5 is the relation between mean wind speed  $\bar{V}$  in the height 125 m and the acceleration of bending  $\ddot{v}_b$ ; the frequency range from 0 up to 5 Hz. In Fig. 67.6 is the relation between mean speed  $\bar{V}$  in the height 125 m and RMS value of torsional acceleration<sup>3</sup>; the frequency range from 3.5 up to 4 Hz. In Fig. 67.7 is as an example the relation between max  $\ddot{v}_b$  from one our record. In all records the relation between bending and torsional frequencies is

$$\frac{f_t}{f_e} = \frac{3.794}{0.54} \doteq 7$$

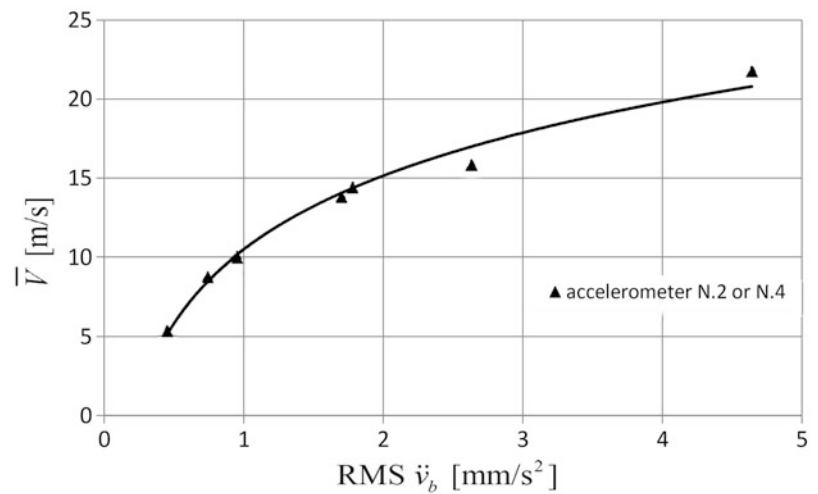
The sketch of the second mast is in Fig. 67.8; top left there is indicated the position of the sensors (4 and 6) at a height of 100 m, by means of which the spectral density (see Fig. 67.9) of swiveling and the spectral densities of acceleration were determined [8, 9].

On the bottom are spectral densities of bending acceleration and torsional acceleration, if we take for the ratio  $f_t/f_b$  the top peaks from spectral densities we received  $f_t/f_b = 4.2$ , which is near value 4

<sup>3</sup>Could be expressed in the angle.



**Fig. 67.6** Relation between mean wind speed  $\bar{V}$  [m/s] and RMS acceleration of bending  $\text{RMS } \ddot{v}_b$  [mm/s<sup>2</sup>]



**Fig. 67.7** Relation between mean wind speed  $\bar{V}$  [m/s] and max  $\ddot{v}_i$  [mm/s<sup>2</sup>]

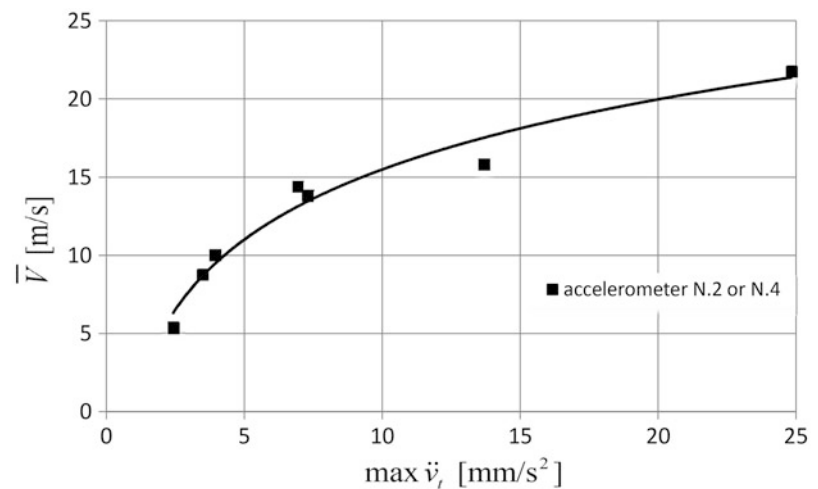


Figure 67.10, as an illustration, shows the superposition of two components of the shaft's motion: the blue line is the orbit from the signals of sensors No. 5 and 6 and the red line is the swivel according to the sensors No. 4 and 6.

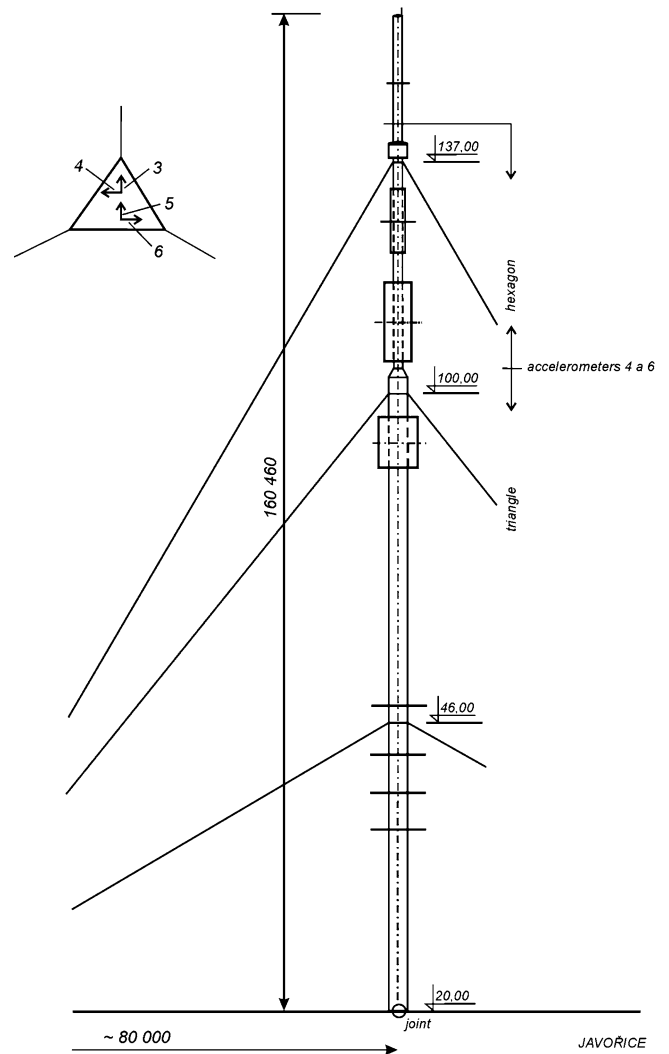
## 67.4 Monitoring of Swivelling on a Model

In more detail and more stable aerodynamic conditions was the phenomenon of swivelling of the mast shaft examined on a simple model [5]. The shaft is a tube of hardened PVC, of an outer diameter of 62 mm, supported by a point at the bottom. It is guyed by three wires.

The flexural rigidity of the shaft is not modelled; the bending is substituted by the tilting. That is why there are no higher shapes of tilting and the orbit is always close to ellipse.

The top end of the shaft is outside the tunnel, therefore it was equipped with a horizontal arm with two accelerometers Brüel-Kjaer, type 4370 attached on its ends; the distance between the accelerometers is 566 mm, alternatively 165 mm – see Fig. 67.11. Accelerometers 1 and 2 sense the motion in the direction perpendicular to the horizontal arm. Besides the two accelerometers on the horizontal arm there is also the third accelerometer at the upper end of the shaft, which senses the motions perpendicular to the direction of the above pair of accelerometers.

**Fig. 67.8** Sketch of the second mast



The mast model was adjusted within the admissible limits by means of stressing of the wires and increasing of the mass concentrated on the top of the shaft. The air flow velocity was  $\bar{V} = 15 \div 25 \text{ m/s}$ .

Figure 67.12 shows the records of the orbit and swivelling of the shaft relative to it.<sup>4</sup>

## 67.5 Conclusions

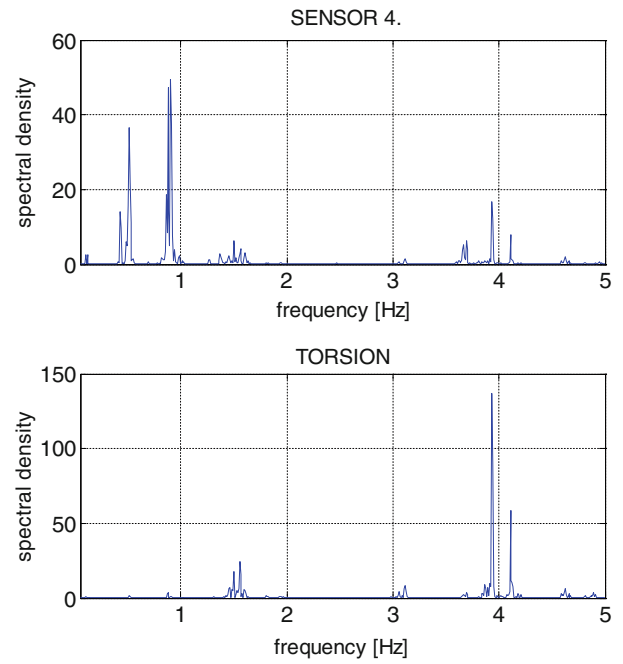
The existence of torsion (swivelling) takes short time in which orbit of the shafts the shape near the ellipse.

The curve which intersects the ellipse in several points (at first masts in 14 points, and second masts in 8 points) formulates shaft rotation in place of the sensors.

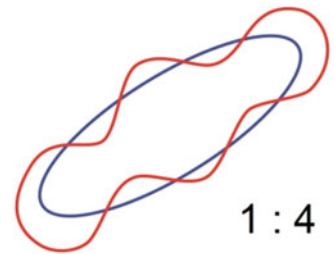
The torsion (swivelling) of the shaft as expressed for the 1st and 2nd masts is very little and insignificant for the stress of the shaft. But it is important for the quality of broadcasted (for example) telephone signal in case of longer transmission distance.

<sup>4</sup>The deviations from ideal elliptical orbits and the courses of swivelling are caused for example by imperfect smoothness of the air flow.

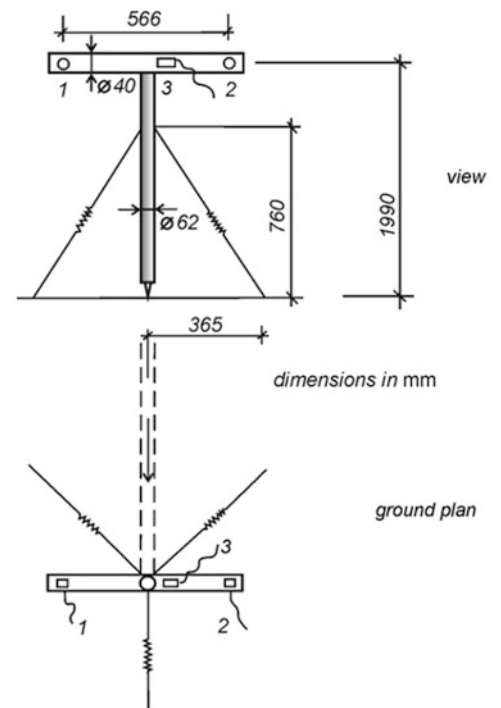
**Fig. 67.9** *Top*: spectral density of acceleration (sensor 4), *bottom*: spectral density of acceleration of the torsion motion (sensor 4 and 6)



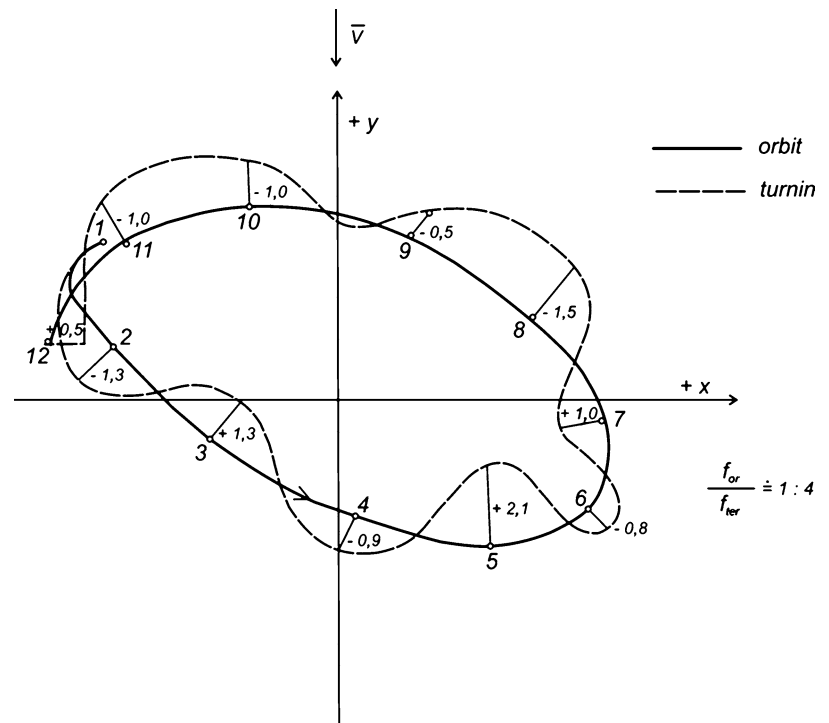
**Fig. 67.10** Superposition of the shaft motions at a level of 100 m above the ground



**Fig. 67.11** Sketch of the model of guyed mast



**Fig. 67.12** Examples of the masts swivelling and tilting



**Acknowledgements** The support of the grants GA CR 103/09/0094, MPO TIP FR-TI3/654 and GA CR P105/10/2159 are gratefully acknowledged. Identification code of research project of the ITAM AS CR v.v.i. RVO: 68378297.

## References

1. Bleich F (1933) *Stahlhochbauten*. Springer, Berlin
2. Koloušek V (1947) *Solution statique et dynamique de pylones d'antenne harbenes*, Mem. De IAIPCV, VII, Zürich
3. Peil U (1998) Collapse behaviour of guyed masts under gales and guy-rupture. In: *Proceedings of the 2nd EECWE*, Prague
4. Sparling BF (2001) Comparison of frequency and time domain analyses for guyed masts in turbulent winds, IASS, Group 4 on Masts and Towers, Oslo
5. Fischer O, Pirner M (1987) *Dynamics of guyed masts*, Study 2/87. Academia, Prague
6. Koloušek V et al (1983) *Wind effects on civil engineering structures*. Academia-Elsevier, Prague
7. Pirner M (1985) *The loading test of the guyed mast Kleř*, report TZUS, Prague
8. Pospíšil S, Janata V, Lahodný J, Urushadze Sh (2009) *Determination of dynamic characteristics TV tower Kleř*, report ÚTAM, AV ČR v.v.i., Prague
9. Pospíšil S, Janata V, Lahodný J, Urushadze Sh (2009) *Determination of dynamic characteristics TV tower Javořice*, report ÚTAM, AV ČR v.v.i., Prague
10. Fischer O, Náprstek J, Pirner M (1979) *Dynamic response of guyed masts to wind action*. In: *Proceedings congress IASS*, Madrid